Luca Saba · João Miguel Sanches
Luís Mendes Pedro · Jasjit S. Suri *Editors*

Multi-Modality Atherosclerosis Imaging and Diagnosis

Springer

Multi-Modality Atherosclerosis Imaging and Diagnosis

Luca Saba • João Miguel Sanches
Luís Mendes Pedro • Jasjit S. Suri
Editors

Multi-Modality Atherosclerosis Imaging and Diagnosis

Springer

Editors
Luca Saba
Department of Radiology
A.O.U Cagliari - Polo di Monserrato
Di Cagliari Polo Di Monserrato
Bivio per Sestu, Italy

Luís Mendes Pedro
Hospital de Santa Maria
Lisboa, Portugal

João Miguel Sanches
Institute for Systems and Robotics
Instituto Superior Técnico
Lisboa, Portugal

Jasjit S. Suri
Stroke Research and Monitoring Division
AtheroPoint(TM) LLC
Roseville, CA USA

ISBN 978-1-4614-7424-1 ISBN 978-1-4614-7425-8 (eBook)
DOI 10.1007/978-1-4614-7425-8
Springer New York Heidelberg Dordrecht London

Library of Congress Control Number: 2013942493

Printed on acid-free paper

Springer is part of Springer Science+Business Media (www.springer.com)

Luca Saba dedicates this book to his parents Giovanni and Raffaela Saba who first taught him to love science.
Jasjit S. Suri dedicates this book to his family and collaborators around the world.

Foreword

I gladly accept the invitation to write a few words of presentation to this book dedicated to the diagnosis and treatment of atherosclerosis with multimodality imaging procedures.

The development of atherosclerotic carotid plaque and the plaque's rupture as cause of stroke requires a multidisciplinary approach; the imaging procedures represent the most relevant practical methodology to study this important clinical problem.

Over the next year improvement in instrumentation and radiopharmaceuticals contributed to the important growth of this scientific field.

In this volume the authors, in a remarkable international representation, present an encyclopedic compilation of the more relevant methodological approaches in the study of atherosclerosis. Special thanks go to the editors: Dr. Saba, Dr. Sanches, Dr. Pedro, and Dr. Suri for the outstanding contributions and dedications.

The text comprises 29 chapters organized into five major sections dealing with atherosclerosis anatomy imaging, MR atherosclerosis imaging, CT atherosclerosis imaging, Ultrasound Atherosclerosis Imaging, and Molecular Imaging and Therapy.

The contributors, well-known authorities, and younger authors who have achieved particular renown in specialized aspects, are well matched to permit each topic to be considered in depth and with expertise. They have defined the technology and identified the methodology and areas for its effective application.

I feel confident that this volume will put a diagnostically significant specialty into perspective to all physicians who deal with atherosclerosis imaging diagnosis. I express my warmest congratulations to the authors for having taken that important scientific aim.

Cagliari, Italy — Mario Piga

Preface

Stroke is one of the leading causes of death in the world, resulting mostly from the sudden ruptures of atherosclerosis carotid plaques. However, until now, the exact plaque development/rupture mechanism has not been fully understood, and also the plaque rupture risk stratification. From biomechanical viewpoint, plaque initiation and development could be attributed to the disturbed flow in those arteries, and the sudden rupture of plaque can be resulted from plaque structure stability failure due to the mechanical stress in/outside plaque structure. Understanding this phenomenon why and how plaque develops and ruptures requires a multidisciplinary approach such as radiology, biomedical engineering, medical physics, software engineering, hardware engineering, and pathological and histological imaging.

This book presents a new dimension of understanding Atherosclerosis in 2D and 3D. For example, Finite element/Finite volume models have been developed from 2D to 3D, from idealized models to patient-specific plaques in terms of geometrical accuracy, from structure/blood flow analysis only to fluid structure interaction analysis in terms of physical phenomenon reality. Recent studies have demonstrated that the predicted stress combined with plaque morphological features can be used for plaque risk assessment, which will be helpful in clinic. The book presents work on plaque stress analysis in order to provide a general framework of computational modeling with atherosclerosis plaques.

Another field in predicting plaque development is in understanding the 3D fluid dynamics and distributed flow pattern analysis with plaque morphological features. The book also presents the atherosclerosis lesions with respect to the 3D geometry of the arteries due to the resulted complex blood flow patterns, such as the regions with high curvature, or near bifurcations. Computational fluid dynamic based on patient-specific 3D carotid geometries will be helpful in identifying the area in risk and might be used for predicting plaque development.

Limited research has been devoted to advancing plaque stress analysis into the field of patient-specific modeling; however, most existed studies on plaque stress analysis are not patient-specific modeling due to the lack of patient-specific boundary condition or material properties. Patient-specific modeling in plaque stress analysis still is a bit challenging in the field. Recent studies have demonstrated that it is possible to obtain patient-specific material model from in vivo human data, which enable plaque stress analysis to be much closer to the real situation rather than a general material model from existed literatures or obtained by ex vivo experiments. The book also presents the related difficulties in patient-specific modeling for plaque stress analysis, and focus on patient-specific material property characterization by using in vivo MRI data. It is believed that the procedure of using patient-specific material model will yield more realistic plaque stresses, which may play an important role in understanding plaque development and rupture.

Much research has been devoted to studying plaque risk stratification by using modern medical imaging technology for characterization of plaque burdens, including stenosis degree, arterial wall thickness, etc., and further studies on medical image-based plaque modeling, such as plaque stress analysis. The first step for those studies is to accurately segment diseased vascular structure manually or semiauto/automatic. Semiautomatic segmentation applications with the ability of manual adjustment and correction become particularly useful in the clinical application and research as rapidly advancing scanner technology capable of generating larger

sets of images for each patient. The book is also going to present and evaluate the performance of a semiautomatic computational algorithm for segmenting carotid arterial wall boundaries by using variational level set methods, and validate this method by comparing with manual segmentation.

Today, 2D Ultrasound is the preferred medical image modality to assess the atherosclerotic disease of the carotid. However, this technique highly depends on the subjective criteria of the clinician in the selection of the cross sections used for the analysis. Additionally, 2D ultrasound images only provide partial information of the anatomy and morphology of the organs, and the overall picture is composed by the medical doctor that subjectively integrates this partial information. The natural evolution is 3D Ultrasound where an accurate and objective representation of the region of interest is provided to the medical doctor. Recent advances on matrix-array ultrasound transducers and on spatial locators that can be coupled to the traditional linear transducers permitted the development of new reliable applications of 3D and 4D Ultrasound in several domains, namely, obstetrics.

In this book, new algorithms based on 3D and 4D Ultrasound are presented to assess the atherosclerotic disease. Indicators computed today from 2D Ultrasound images to characterize plaque by extrapolation can be accurately computed from the reconstructed 3D anatomy without the need of any subjective assumptions about the morphology and texture of the plaque. This 3D approach can be used to accurately estimate not only the degree of stenosis, the main indicator used today for plaque risk stratification, but most important the morphology of the plaque, which is crucial for plaque stress analysis, as referred before.

Very recent advances in plaque multimodality image fusion analysis are also described in this book. The goal is to fuse information obtained from different 3D medical image modalities, such as 3D US, CT, and MRI, providing the medical doctor with some sort of augmented reality information about the atherosclerotic plaque in order to improve the accuracy of the diagnosis.

Analysis of the plaque dynamics along the cardiac cycle is also a valuable indicator for plaque instability assessment and therefore for risk stratification. 4D Ultrasound, a sequence of 3D reconstructions of the region of interest along the time, can be used for this dynamic analysis. 4D US is particularly suitable for this type of analysis due to the high temporal resolution of ultrasound imaging in comparison with other modalities.

By this, Multimodality Image Fusion is a very appealing approach because it puts together the best characteristics of each modality, such as the high temporal resolution of US and the high spatial resolutions of MRI and CT.

Cagliari, Italy — Luca Saba
Lisbon, Portugal — João Miguel Sanches
Lisbon, Portugal — Luís Mendes Pedro
Roseville, CA, USA — Jasjit S. Suri

Contents

Contributors

U. Rajendra Acharya Department of Electronics and Computer Engineering, Ngee Ann Polytechnic, Clementi, Singapore

Takashi Akasaka Department of Cardiovascular Medicine, Wakayama Medical University, Wakayama, Japan

Michele Anzidei Department of Radiological Sciences of the Sapienza, University of Rome, Rome, Italy

Teresa Arcadi Department of Radiology, Giovanni XXIII Hospital, Monastier, Treviso, Italy

Sara Avansari Department of Computer Science, University of Tehran, Tehran, Iran

Efthimios Avgerinos Department of Vascular Surgery, Athens University Medical School, "Attikon" Hospital, Athens, Greece

Sebastián Baldi Department of Endovascular Therapy, Hospiten Rambla Hospital, Santa Cruz de Tenerife, Spain

Ali Bigdelou Informatic Department, Technical University of Munich, Munich, Germany

Fabrizio Boni Department of Radiological Sciences of the Sapienza, University of Rome, Rome, Italy

Gerd Brunner Division of Atherosclerosis and Vascular Medicine, Baylor College of Medicine, Houston, TX, USA

Filippo Cademartiri Department of Radiology, Giovanni XXIII Hospital, Monastier, Treviso, Italy

Department of Radiology, Erasmus Medical Center University, Rotterdam, The Netherlands

Aurélio Campilho INEB – Instituto de Engenharia Biomédica, Universidade do Porto, Porto, Portugal

Faculdade de Engenharia, Universidade do Porto, Porto, Portugal

Carlo Catalano Department of Radiological Sciences of the Sapienza, University of Rome, Rome, Italy

Nuno V. Dias Vascular Center, Skåne University Hospital, Malmö, Sweden

Luca Famiglietti Department of Radiology, Azienda Ospedaliero Universitaria di Cagliari, Cagliari, Italy

Oliver Faust Department of Electronics and Computer Engineering, Ngee Ann Polytechnic, Clementi, Singapore

Rafael Feldman Department of Interventional Cardiology and Cardiovascular Surgery, Clínica Sarmiento, San Miguel de Tucumán, Argentina

J. Fernandes e Fernandes Instituto Superior Técnico, Lisboa, Portugal

Ruy Fernandes e Fernandes Department of Vascular Surgery, Hospital Santa Maria-CHLN, Faculty of Medicine University of Lisbon, Lisbon Academic Medical Centre, Lisbon, Portugal

Lisbon Cardiovascular Institute, Lisbon, Portugal

M. Martín-Fernández Laboratoria de Procesado de Imagen (LPI), Universidad de Valladolid, Valladolid, Spain

Zsolt Garami Division of Atherosclerosis and Vascular Medicine, Baylor College of Medicine, Houston, TX, USA

Nick Georgiou Vascular Screening and Diagnostic Centre, London, UK

Department of Biological Sciences, University of Cyprus, Nicosia, Cyprus

K. Hameeteman Biomedical Imaging Group Rotterdam, Department of Radiology, Erasmus MC, University Medical Center Rotterdam, Rotterdam, The Netherlands

Biomedical Imaging Group Rotterdam, Department of Medical Informatics, Erasmus MC, University Medical Center Rotterdam, Rotterdam, The Netherlands

Hao Gao Centre for Excellence in Signal and Image Processing, Department of Electronic and Electrical, University of Strathclyde, Glasgow, UK

Massimo Imbriaco Department of Radiology, University Federico II, Naples, Italy

Department of Biomorphological and Functional Sciences, University Federico II, Naples, Italy

Nikolaos Kadoglou Department of Vascular Surgery, Athens University Medical School, "Attikon" Hospital, Athens, Greece

John D. Kakisis Department of Vascular Surgery, Athens University Medical School, "Attikon" Hospital, Athens, Greece

Amin Katouzian Informatic Department, Technical University of Munich, Munich, Germany

Takashi Kubo Department of Cardiovascular Medicine, Wakayama Medical University, Wakayama, Japan

Hannah Kuper Faculty of Infectious and Tropical Diseases, London School of Hygiene and Tropical Medicine, London, UK

Elena Ladich CVPath Institute, Inc., Gaithersburg, MD, USA

Christos D. Liapis Department of Vascular Surgery, Athens University Medical School, "Attikon" Hospital, Athens, Greece

William Liboni Neurology Division, Gradenigo Hospital, Torino, Italy

Christos P. Loizou Department of Computer Science, School of Sciences, Intercollege, Limassol, Cyprus

Quan Long Brunel Institute for Bioengineering, Brunel University, London, UK

Erica Maffei Department of Radiology, Giovanni XXIII Hospital, Monastier, Treviso, Italy

Raja Sriswan Mamidi National Institute of Nutrition, Hyderabad, Andhra Pradesh, India

Cesare Mantini Department of Radiology, "G. D'Annunzio" University, Chieti, Italy

Department of Neuroscience and Imaging, Section of Diagnostic Imaging and Therapy,"G. D'Annunzio" University, Chieti, Italy

Beatrice Cavallo Marincola Department of Radiological Sciences of the Sapienza, University of Rome, Rome, Italy

Chiara Martini Department of Radiology, Giovanni XXIII Hospital, Monastier, Treviso, Italy

Manuel Maynar Department of Endovascular Therapy, Hospiten Rambla Hospital, Santa Cruz de Tenerife, Spain

Kristen M. Meiburger Biolab, Department of Electronics, Politecnico di Torino, Torino, Italy

Giancarlo Messalli Department of Radiology, University Federico II, Naples, Italy

Department of Biomorphological and Functional Sciences, University Federico II, Naples, Italy

Filippo Molinari Biolab, Department of Electronics, Politecnico di Torino, Torino, Italy

Joel D. Morrisett Division of Atherosclerosis and Vascular Medicine, Baylor College of Medicine, Houston, TX, USA

Konstantinos Moulakakis Department of Vascular Surgery, Athens University Medical School, "Attikon" Hospital, Athens, Greece

Masataka Nakano CVPath Institute, Inc., Gaithersburg, MD, USA

Vijay Nambi Division of Atherosclerosis and Vascular Medicine, Baylor College of Medicine, Houston, TX, USA

Nassir Navab Informatic Department, Technical University of Munich, Munich, Germany

Andrew Nicolaides Vascular Screening and Diagnostic Centre, London, UK

Department of Biological Sciences, University of Cyprus, Nicosia, Cyprus

Luis García Nielsen Department of Interventional Cardiology and Cardiovascular Surgery, Clínica Sarmiento, San Miguel de Tucumán, Argentina

W.J. Niessen Biomedical Imaging Group Rotterdam, Department of Radiology, Erasmus MC, University Medical Center Rotterdam, Rotterdam, The Netherlands

Biomedical Imaging Group Rotterdam, Department of Medical Informatics, Erasmus MC, University Medical Center Rotterdam, Rotterdam, The Netherlands

Imaging Science and Technology, Delft University of Technology, Delft, The Netherlands

Vincenzo Noce Department of Radiological Sciences of the Sapienza, University of Rome, Rome, Italy

Marios Pantzaris The Cyprus Institute of Neurology and Genetics, Nicosia, Cyprus

Luís Mendes Pedro Instituto Cardiovascular de Lisboa, University of Lisbon, Lisbon, Portugal

Timothy Resch Vascular Center, Skåne University Hospital, Malmö, Sweden

Rui Rocha INEB – Instituto de Engenharia Biomédica, Universidade do Porto, Porto, Portugal

ISEP – Institute Superior de Engenhariado Porto, Porto, Portugal

Alireza Roodaki Department of SSE, SUPELEC, Gif-sur-Yvette, France

Luca Saba Department of Radiology, Azienda Ospedaliero Universitaria di Cagliari, Cagliari, Italy

Tobias Saam Institute of Radiology, University of Munich, Munich, Germany

Chandra dev Sahu Diagnostic and Interventional Neuroradiology Division, Department of Radiology and Medical Imaging, University of Virginia, Charlottesville, VA, USA

J. Miguel Sanches Department of Bioengineering, Institute for Systems and Robotics, Instituto Superior Técnico/Technical University of Lisbon, Lisbon,
Portugal

G. Vegas-Sánchez-Ferrero Laboratoria de Procesado de Imagen (LPI), Universidad de Valladolid, Valladolid, Spain

Andreas Schindler Department of Clinical Radiology, University of Munich, Munich, Germany

Arend F.L. Schinkel Division of Pharmacology, Vascular and Metabolic Diseases, Department of Internal Medicine, Erasmus University Medical Center, Rotterdam, The Netherlands

Department of Cardiology, Thoraxcenter, Erasmus Medical Center, Rotterdam, The Netherlands

José Seabra Institute for Systems and Robotics, Lisbon, Portugal

Department of Bioengineering (DBEng), Instituto Superior Técnico, Lisbon,
Portugal

George Sfyroeras Department of Vascular Surgery, Athens University Medical School, "Attikon" Hospital, Athens, Greece

Eric J. G. Sijbrands Division of Pharmacology, Vascular and Metabolic Diseases, Department of Internal Medicine, Erasmus University Medical Center, Rotterdam, The Netherlands

Department of Cardiology, Thoraxcenter, Erasmus Medical Center, Rotterdam, The Netherlands

Jorge Silva INEB – Instituto de Engenharia Biomédica, Universidade do Porto, Porto, Portugal

Faculdade de Engenharia, Universidade do Porto, Porto, Portugal

Luís L. Silvestre INEB – Instituto de Engenharia Biomédica, Universidade do Porto, Porto, Portugal

Faculdade de Engenharia, Universidade do Porto, Porto, Portugal

Jasjit S. Suri Stroke Research and Monitoring Division, AtheroPoint(TM) LLC, Roseville, CA, USA

Global Biomedical Technologies, Roseville, CA, USA

Arash Taki Informatic Department, Technical University of Munich, Munich, Germany

Gerrit L. ten Kate Division of Pharmacology, Vascular and Metabolic Diseases, Department of Internal Medicine, Erasmus University Medical Center, Rotterdam, The Netherlands

Department of Cardiology, Thoraxcenter, Erasmus Medical Center, Rotterdam, The Netherlands

Rikin A. Trivedi Department of Neurosurgery, Addenbrooke's Hospital, Cambridge, UK

Max van Gils Department of Radiology, Erasmus MC, University Medical Center Rotterdam, Rotterdam, The Netherlands

M. van Straten Department of Radiology, Erasmus MC, University Medical Center Rotterdam, Rotterdam, The Netherlands

Stijn C. H. van den Oord Department of Cardiology, Thoraxcenter, Erasmus Medical Center, Rotterdam, The Netherlands

Department of Biomedical Engineering, Thoraxcenter, Erasmus Medical Center, Rotterdam, The Netherlands

Aad van der Lugt Department of Radiology, Erasmus MC, University Medical Center Rotterdam, Rotterdam, The Netherlands

Antonius F. W. van der Steen Department of Biomedical Engineering, Thoraxcenter, Erasmus Medical Center, Rotterdam, The Netherlands

S. Vinitha Sree Global Biomedical Technologies Inc., Roseville, CA, USA

Renu Virmani CVPath Institute Inc., Gaithersburg, MD, USA

Max Wintermark Diagnostic and Interventional Neuroradiology Division, Department of Radiology and Medical Imaging, University of Virginia, Charlottesville, VA, USA

Eric Y. Yang Division of Atherosclerosis and Vascular Medicine, Baylor College of Medicine, Houston, TX, USA

Tobias Zander Department of Endovascular Therapy, Hospiten Rambla Hospital, Santa Cruz de Tenerife, Spain

Chiara Zini Department of Radiological Sciences of the Sapienza, University of Rome, Rome, Italy

Rohitashwa Sinha Department of Neurosurgery, Addenbrooke's Hospital, Hills Road, Box 166, CB2 0QQ Cambridge, UK

Karol P. Budohoski Department of Neurosurgery, Addenbrooke's Hospital, Hills Road, Box 166, CB2 0QQ Cambridge, UK

Victoria E. L. Young Department of Neurosurgery, Addenbrooke's Hospital, Hills Road, Box 166, CB2 0QQ Cambridge, UK

Isabel Gonçalves Department of Cardiology, Skåne University Hospital, Lund University, Malmö, Sweden

Part I

Introduction: Anatomy and Imaging

Imaging Occlusive Atherosclerosis

1

J. Fernandes e Fernandes, L. Mendes Pedro, R. Fernandes e Fernandes, and L. Silvestre

Atherosclerosis is a global disease affecting the entire arterial system and it is a major cause of morbidity and mortality in all continents. It is the commonest form of arteriosclerosis, a term used to indicate thickening of the arterial walls.

Atherosclerosis derives from the Greek language: *athere* meaning soft paste-like material and *sclero* for hard which results from the proliferation of fibrous tissue and the presence of calcification.

Its pathogenesis is complex and multifactorial and several epidemiological studies have identified risk factors, which are associated with its severity and widespread involvement of the arterial tree. Smoking, hypertension, dyslipidemia, and diabetes mellitus have all been associated with atherosclerosis and the mechanisms leading to arterial injury became clear in extensive research conducted in the last two decades.

Atherosclerosis is a common process associated with human development and aging. Usually starts at arterial bifurcations and *ostia*, where it appears as a localized thickening or elevation of the inner side of the artery—atheromatous plaque—which proliferates in the sub-endothelial layer and determines narrowing of the artery. This atheromatous plaque can act as a focus for localized thrombosis—atherothrombosis—or as a source of distal embolization—atheroembolism. Necropsy studies conducted in young children [1] have documented the presence of lipid deposition in coronary arteries and aortas, suggesting that atherosclerotic changes may occur silently even in infants.

To better understand the pathogenesis of atherosclerosis and what could be achieved with modern imaging methods available in today's clinical practice, from morphological to functional and molecular technologies, it is important to briefly review the basic structure and histology of the arterial system and the morphological changes produced by atherosclerosis.

J. Fernandes e Fernandes (✉) • L.M. Pedro • R. Fernandes e Fernandes • L. Silvestre
Faculty of Medicine, University of Lisbon, Lisbon, Portugal

Department of Vascular Surgery, Hospital Santa Maria, Lisbon, Portugal

Instituto Cardiovascular de Lisboa, Lisbon, Portugal
e-mail: jmfernandes@fm.ul.pt

1 Arterial Wall Structure and Function

Usually arteries are divided into larger or central arteries with predominant elastic component (like the aorta), medium size or muscular arteries, and small arteries and arterioles, distributing blood flow into the vast capillary network.

The wall of the arteries is composed of three layers separated by elastic laminas: intima, media, and adventitia. The inner layer—*intima*—is composed by a single layer of endothelial cells providing the interface with the circulating blood and an extracellular component with connective tissue, smooth muscle cells, and macrophages, within a biochemical complex matrix rich in proteoglycans occupying the sub-endothelial space from the endothelial cells to the internal *lamina elastica* which separates the intima from the *media* layer. Connective tissue, collagen fibrils, elastin, and smooth muscle cells essentially compose the media and its relative composition varies according to size a function of the arteries. Elastic fibers are dominant in large transport arteries like the aorta, and muscular fibers predominate in medium size arteries like the superficial femoral artery. The media is separated from the outer layer—*adventitia*—by the external *lamina elastica*. This external layer contains undifferentiated dendritic cells, collagen fibers, and smooth muscle cells through which penetrates a rich network of very small vessels—the *vasa vasorum*—responsible for cell nutrition in the arterial wall, plus multiple nerve fibers from the autonomic system which are essential to regulate vascular tone through muscle cell contraction. Thickness of these different layers varies according to the size and function of the arteries in the body and it is early affected by atherogenesis, a process that leads to a remarkable thickening of the arterial wall.

L. Saba et al. (eds.), *Multi-Modality Atherosclerosis Imaging and Diagnosis*,
DOI 10.1007/978-1-4614-7425-8_1,

Endothelial cells are connected through junctional complexes, forming tight and gap junctions and they have a wide range of membrane receptors for circulating blood cells and plasma components [2–4]. Its functions are diverse and very important: barrier to penetration of plasma proteins and lipids, non-thrombogenic interface with circulating blood through the production of prostacyclin (PGI2) and thrombomodulin–thrombin complex preventing adhesion and aggregation of circulating cells and plasma components to the arterial wall, regulator of vascular tone by the production of nitric oxide which has a dilating effect and endothelin 1, a potent constrictor, modulation for immune and inflammatory reactions mediated through cytokines and growth factors, and production of extracellular matrix proteins including a monocyte chemoattractant protein MCP-1.

Endothelial dysfunction seems to be the initial trigger of a very complex process called *atherogenesis* leading to established arterial lesions.

Increased permeability of the endothelial cells and deposition of lipids within the extracellular matrix in the sub-endothelial space induce an inflammatory reaction in the arterial wall mediated by circulating monocytes and T-lymphocytes and leading to migration and proliferation of smooth muscle cells (SMCs) through known biochemical mediators. Evidence has been recently published associating both systemic and intraplaque markers of inflammation with symptomatic stroke and plaque instability [5].

Several mechanisms have been considered responsible for endothelial injury leading to its dysfunction. Physical injury may be caused by hemodynamic flow disturbances resulting from turbulence, increased pulse pressure associated with arterial hypertension, low shear stress in arterial segments close to bifurcations and *ostia*, and low flow situations which increase contact between chemical agents affecting endothelial function [6, 7]. Chemical agents include lipids and oxidized lipid molecules, oxidative stress from exposure to oxygen-derived free radicals that inactivate nitric oxide and reduce its availability, and cytokines from damaged tissues or infection. These injuries promote coagulation changes leading to thrombosis and enhanced production of inflammatory mediators, which have been extensively studied and described [8–10]. Gene de-regulation has been implied in changes in nitric oxide synthesis, tissue-plasminogen activation, monocyte chemoattractant protein-1, and platelet-derived growth factor offering insight and possible explanation on the mechanisms of genetic susceptibility to atherosclerosis in some families and its increased incidence in younger age patients.

Endothelial dysfunction results in monocyte penetration and activation in the sub-endothelial space, thus initiating a complex inflammatory and proliferative reaction leading to thickening of the artery and narrowing of its lumen, reducing blood flow, and further enhancing hemodynamic changes that in turn aggravate cell damage within the arterial wall.

Smooth muscle cells (SMCs) have two different phenotypes: contractile and synthetic [11]. Contractile plays an essential role to maintain vascular tone regulation required for an effective blood flow distribution according to the needs of organs- and tissues: borrowing–lending effect. It is through the synthetic phenotype that SMCs are directly involved in atherogenesis, through migration from the media to the sub-endothelial matrix, proliferation in response to various mitogens, and synthesis of collagen, proteoglycans, and elastin.

Macrophages are closely associated with the changes in the arterial wall during atherogenesis and play a substantial role in the stability of established atheroma. These cells derive from circulating monocytes which following penetration of the endothelial layer differentiate into macrophages. They respond to several chemoattractants such as MCP-1, tumor necrosis factor (TNF) alpha, and interleukins. They are scavengers of lipids and cell debris resulting in the formation of the foam cell within the atherosclerotic plaque, but also secrete a large amount of enzymes such as proteases, hydrolases, elastase, and growth factors and act as modulators of immune responses [12, 13].

2 Atherogenesis and Evolution of Atheromatous Plaques

Atherosclerosis begins with deposition of cholesterol and lipoproteins and macrophages filled with lipid components—foam cells—in the sub-endothelial matrix without destruction of the endothelial layer and appearing in susceptible arterial segments. These changes are designated by fatty streak, produce a yellowish discoloration of the intima of the artery, and may remain quiescent or progress forming multiple cell layers in the intima, as described by Stary [14].

There is strong evidence that accumulation of plasma-derived lipoproteins initiates the formation of foam cells and this is the key element conducting the formation of the atherosclerotic lesion. The progression of the lesion is related to increased deposition and accumulation of extracellular lipids favored by local hemodynamic factors and endothelial injury as described previously. Cell necrosis in which debris tend to accumulate within the media layerand to form a core nucleus with deposits of lipids, cell degradation products, and calcium. The fibrous proliferation at the luminal surface constitutes a fibrous cap that protects the inner components of the lesion from the circulating blood and replaces the damaged endothelial layer.

This lesion is usually designated as fibrous plaque disrupting the normal architecture of the arterial wall with destruction of inner and outer elastic laminas.

On direct examination it protrudes in the arterial lumen causing localized narrowing stenosis. When it affects

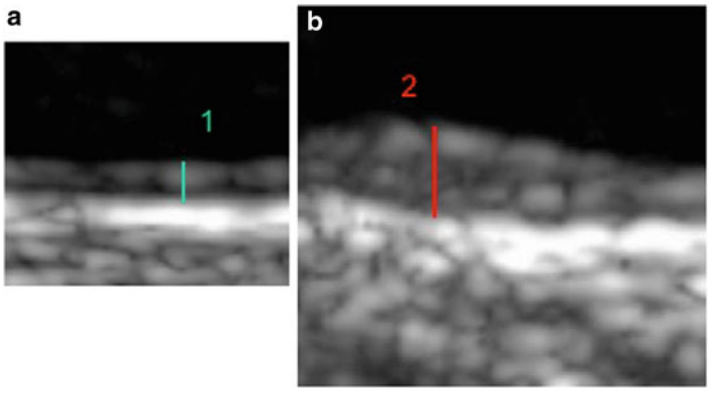

Fig. 1.1 (**a**) Ultrasonographic morphology of the normal arterial wall with quantification of the intima–media thickness (IMT). (**b**) Increased IMT with destruction of the normal artery morphology

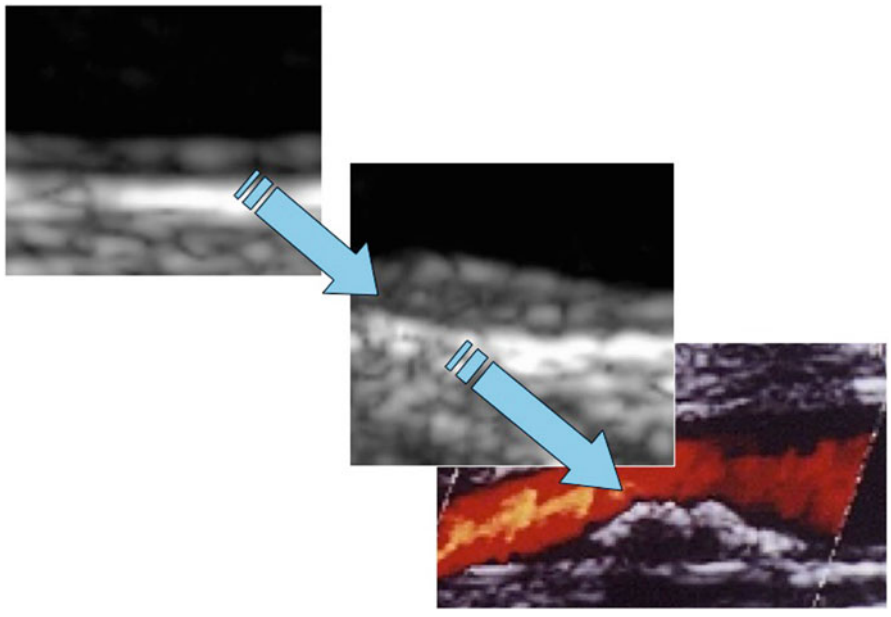

Fig. 1.2 Progression from the normal arterial wall morphology to atheromatous plaque

normal laminar flow and causes localized acceleration and turbulence it is considered to be hemodynamically significant. It determines high shear stress further increasing the endothelial injury. Areas of flow stagnation also coexist increasing endothelial exposure to chemical injuries from plasma components and promoting adhesion of blood cells and platelets to the arterial wall [15] a persistent mechanism that further damages the arterial wall.

These lesions can be visualized with high-definition B-mode echography (Figs. 1.1 and 1.2) and are markers of early atherosclerosis and increased risk of cardiovascular clinical events [16, 17]. Hemodynamic studies conducted in these group of patients with early atherosclerotic lesions suggest impairment of reactive hyperemia following induced ischemia, indicating associated endothelial dysfunction with reduced production of endothelial-derived relaxing factor [18].

More advanced (Figs. 1.2 and 1.3) or complicated lesions result from persistence of the injury mechanisms to the arterial wall, promoting an inflammatory reaction with development of neovascularization from the *vasa vasorum* which can also be detected in vivo by enhanced color-flow Doppler imaging technologies using microparticles [19] or by using micro-CT assessment of symptomatic coronary arteries [20]. Extensive plaque neovascularization in carotid endarterectomy specimens was predictor of late cardiovascular events [21]. This process is associated with higher production of several proteases and other enzymes inducing cell destruction and loss of tensile strength of the plaque by the hemodynamic stress resulting from flow disturbances which

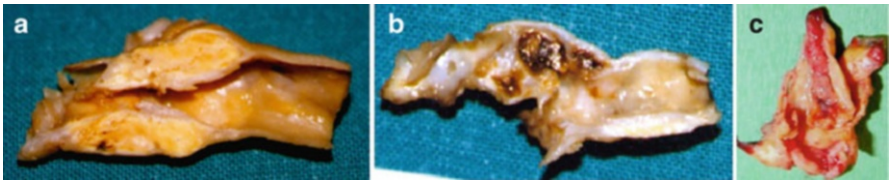

Fig. 1.3 (**a**) Stable carotid plaque. (**b**) Carotid lesion with intraplaque hemorrhage. (**c**) Carotid plaque showing extensive surface thrombosis (atherothrombosis)

lead to rupture of the fibrous cap, intraplaque hemorrhage, and thrombosis inside the lesion and at its surface [22–24] as shown in Fig. 1.3b, c.

These morphologic changes lead to an increase in the volume of the lesion, rupture of the plaque with extrusion of material from its core nucleus, associated thrombosis and increased severity of the stenosis, or complete arterial occlusion.

It is important to understand the underlying mechanisms that increase plaque progression and its biological markers in order to improve our capability for its recognition.

The concept of vulnerable plaque introduced by Fuster and others [25, 26] shifted the emphasis from degree of stenosis to plaque composition and structure, which increases the risk of rupture and associated clinical acute events.

The major determinants of plaque's vulnerability to rupture may be listed as follows [26]:

- Size and location of the core nucleus rich in lipids and cell debris.
- Thickness and collagen content of the fibrous cap overlying the core.
- Distance from the core to the lumen [27, 28].
- Exposure of plaque components to circulating blood, which have a potent thrombogenic effect.
- Active inflammatory and immunological processes resulting from increased deposition and activation of macrophages, T lymphocytes, and mast cells.
- Local flow disturbances usually associated with severity of stenosis [29, 30].
- Systemic thrombotic propensity from the individual patient.

In vivo detection of plaque morphology, recognition of individual inflammatory activity, and immunological status plus increased propensity to intravascular thrombosis completely changed the scope of diagnostic methods in atherosclerosis. The challenge is no longer the assessment of severity of stenosis and its hemodynamic effect but the identification of these potentially dangerous lesions, which are associated with increased risk of adverse clinical events.

The new developments on imaging technology, both morphological and functional, will be briefly dealt subsequently.

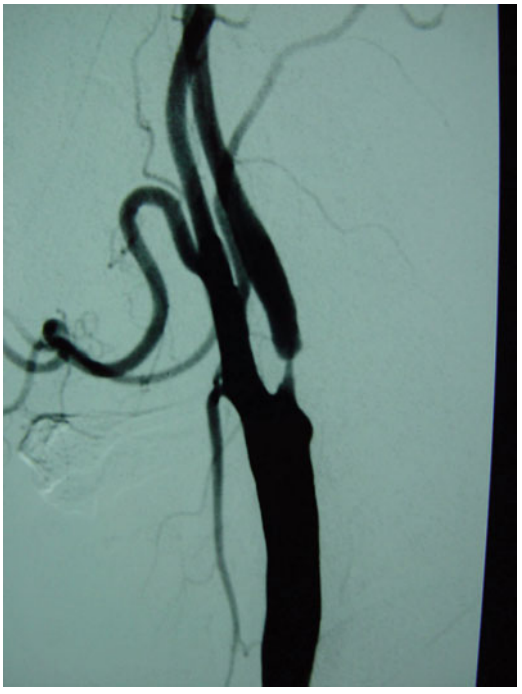

Fig. 1.4 Arteriography of the carotid bifurcation with tight stenosis in the origin of the internal carotid artery

3 Imaging Technologies

3.1 Arteriography

Introduced by Egas Moniz in 1926 [31] for the diagnosis of brain tumors it provided the first clinical correlations between ischemic stroke and occlusion of extracraneal internal carotid [32]. It was subsequently extended to visualize the abdominal aorta and peripheral arteries [33]. Selective intra-arterial catheterization by Seldinger [34] provided an extraordinary expansion of the arteriographic method, which for decades was only available method to study atherosclerosis in vivo (Fig. 1.4).

The development of arterial reconstructive surgery, from endarterectomy introduced by Cid dos Santos in 1946 [35] and bypass techniques popularized by M.E. DeBakey in the early 1950s, to present-day endovascular intervention rested upon arteriography.

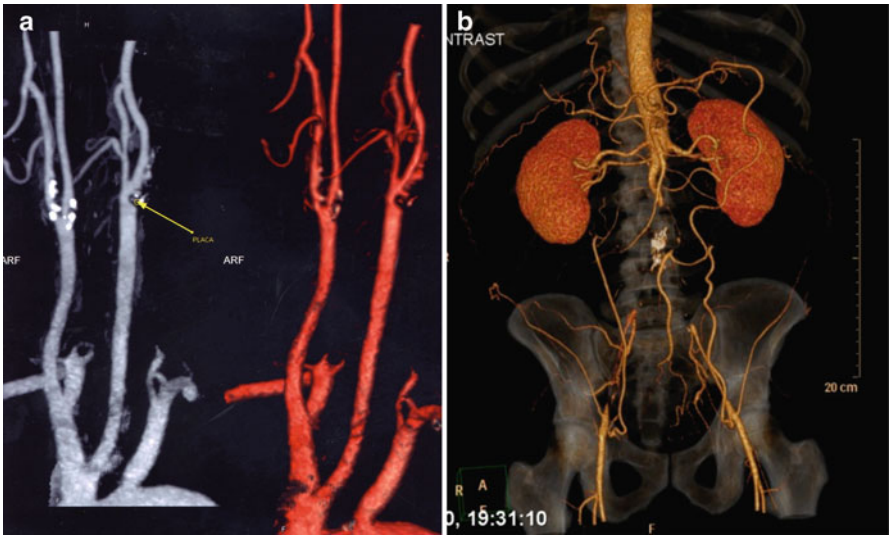

Fig. 1.5 (**a**) CT-angio of the supra-aortic trunks (calcified carotid plaques). (**b**) CT-angio of the abdominal vessels (aortic thrombosis)

Arteriography is a luminography: its images are of the contrasted blood flow and indentations upon the circulating flow produced by the diseased arterial wall. It does not provide any image of the vessel wall and nature of the disease, but only its effect upon blood flow.

It does not also provide accurate information on plaque morphology characteristics relevant to clinical management as previously described, although the presence of irregularities and/or ulceration in carotid arteriography performed within the scope of the ECST trial were markers of higher risk for stroke in the medical arm of the study [36].

Its invasiveness, toxicity associated with contrast injection, X-ray exposure, and high costs have reduced its scope for diagnostic purposes. In today's clinical practice conventional or digital arteriography for management of atherosclerotic patients is part of the interventional treatment procedure aimed to correct both occlusive and dilating disease.

3.2 CT Angiography and Magnetic Resonance Angiography

New developments in computed tomography technology including multi-detector CT and ECG-gated CT for accurate visualization of coronary circulation provided an useful tool to study atherosclerosis by combining flow assessment with arterial wall imaging (Fig. 1.5a, b).

Identification of plaque morphology in carotid bifurcation disease using CT angiography (CTA) provided identification of intraplaque hemorrhage and ulceration confirmed by histology [37].

For coronary circulation CTA has been correlated with conventional arteriography and used to quantify thecalcium content of the lesions (calcium score) and to correlate with symptoms.

A recent trial [38] using a 64 row multi-detector CTA confirmed its accuracy for identification of coronary stenosis and to assess disease severity in symptomatic patients with calcium score <600, but could not replace conventional coronary angiography because of negative predictive value of 83 % and positive predictive value of 91 %.

Failure to use this technology to identify vulnerable plaques and to discriminate between fibrous tissue and lipids was reported [39], although experimental evidence for the detection of macrophages in a rabbit model of atherosclerosis [40].

For peripheral lower limb arterial disease CTA provides acceptable visualization of the arteries useful for planning the treatment particularly in the absence of extensive calcification.

Although less invasive than conventional arteriography, CTA requires iodine contrast use and radiation exposure which limits its use.

Magnetic resonance imaging is safer, without conventional radiation and less toxic contrast agents. It provides flow images equivalent to conventional arteriography, with better visualization of low flow perfusion situations, like in critical lower limb ischemia, but it has limitations for the assessment of coronary circulation due to its low specificity [41]. Technical refinements provided suitable information to assess arterial remodeling in the presence of moderate stenosis [42] and to characterize unstable fibrous caps in advanced carotid atherosclerosis [43].

New molecular imaging tools and the use of nanotechnology are promising developments for MR imaging of atherosclerotic lesions and to provide more objective iden-

tification of markers of plaque vulnerability [44, 45] both in animal models and in humans.

However, this is an expensive technology and time-consuming, which reduces its applicability for routine clinical use.

3.3 B-Mode High-Definition Ultrasound and Color-Flow Duplex Scan

Color-flow duplex scan (CF DS) provides accurate visualization of the arterial system, from extracraneal to intracranial vessels from abdominal aorta and its major visceral branches to the arteries of both upper and lower limbs. It provides visualization of the arterial wall and its changes as well as the flow abnormalities directly induced by the lesions.

Extensive literature has been published to validate objective criteria from flow velocity changes to quantify the degree of stenosis [46–49] from carotids to renal and mesenteric circulation to peripheral limb occlusive disease.

Accurate quantification of stenosis severity is a key factor for clinical management in carotid bifurcation disease and it is extensively dealt in another chapter.

However high-definition B-mode echography offers an objective, noninvasive, reliable, and inexpensive tool to identify early atherosclerotic lesions (Fig. 1.1) and to measure intima–media thickness (IMT) a powerful marker of late occurrence of cardiovascular events. It also provides an objective quantification of the total atherosclerotic burden by using as windows to the arterial system, both the common carotid and femoral bifurcations [50, 51].

By using computerized technology and image standardization of carotid bifurcation plaques (Fig. 1.6a, b) it is possible to quantify the echogenicity of the plaque, to assess its homogenous or heterogeneous quality, and to identify markers of plaque vulnerability and obtain correlations with its biochemical composition and clinical outcomes [28, 30, 52–60].

In a previously published report using computer-assisted HD echography we described ultrasonographic equivalents to histological markers of lesion instability and showed a good separation between symptomatic and asymptomatic lesions and also a positive correlation with ipsilateral brain hemispheric infarcts [28, 61, 62].

Extending further the analysis an indicator of plaque activity was obtained [63]—Activity Index—which had an excellent correlation with appropriate neurological symptoms and was a predictor of late ipsilateral cerebrovascular events in asymptomatic patients followed for a period of 4 years (Fig. 1.6c).

Recently the ACSRS trial was published [64] providing evidence on the value of plaque morphology analysis to stratify clinical and neurological risk in asymptomatic patients with carotid bifurcation stenosis >50 %.

Also the efficacy of lipid-lowering agents like statins can be monitored by changes in echogenicity of the plaque and increased thickness of the fibrous cap [65].

There is now substantial evidence pointing to the possibility of this simple, noninvasive, and inexpensive technology to provide adequate imaging for atherosclerotic lesions in accessible sites, accurate measurements of lesion severity, and its direct hemodynamic repercussion and to obtain reliable information on plaque structure to identify vulnerable/unstable plaques.

Using a 2 MHz probe and injecting echogenic particles it has been possible to identify increased vascularization in segments of unstable carotid plaques, which could be a marker of active inflammation [66].

3.4 Intravascular Ultrasound

This is an invasive technology catheter-based providing two-dimensional and cross-section images of the arteries, thus providing accurate measurement of stenosis severity and plaque volume. It has been used associated with catheter-based techniques to improve selection of lesions for treatment and for completion assessment following interventional procedures [67].

Advances in intravascular ultrasound (IVUS) technology with spectral analysis of the signals provide plaque characterization and evaluation of its composition, which has been referred as Virtual Histology [68].

Several studies have provided validation of this technology. However it is invasive, expensive, and not suitable for routine clinical use and epidemiological studies.

3.5 Optical Coherence Tomography

It is an optical analogue of intravascular ultrasound with excellent spatial resolution and providing also a cross-sectional image of the artery [69].

Its clinical advantage seems to provide completion assessment following angioplasty and stent deployment in both coronary and carotid arteries and to identify intimal hyperplasia in early re-stenosis.

3.6 Fluorescence Imaging

This technology is available and provides the visualization of the inflammatory reaction within the plaque. [70] and visualize the inflammatory reaction within the plaque. It targets molecules and follows its incorporation and degradation in the structures. Its use has been experimental to test new imaging tools, but the recent developments with catheter

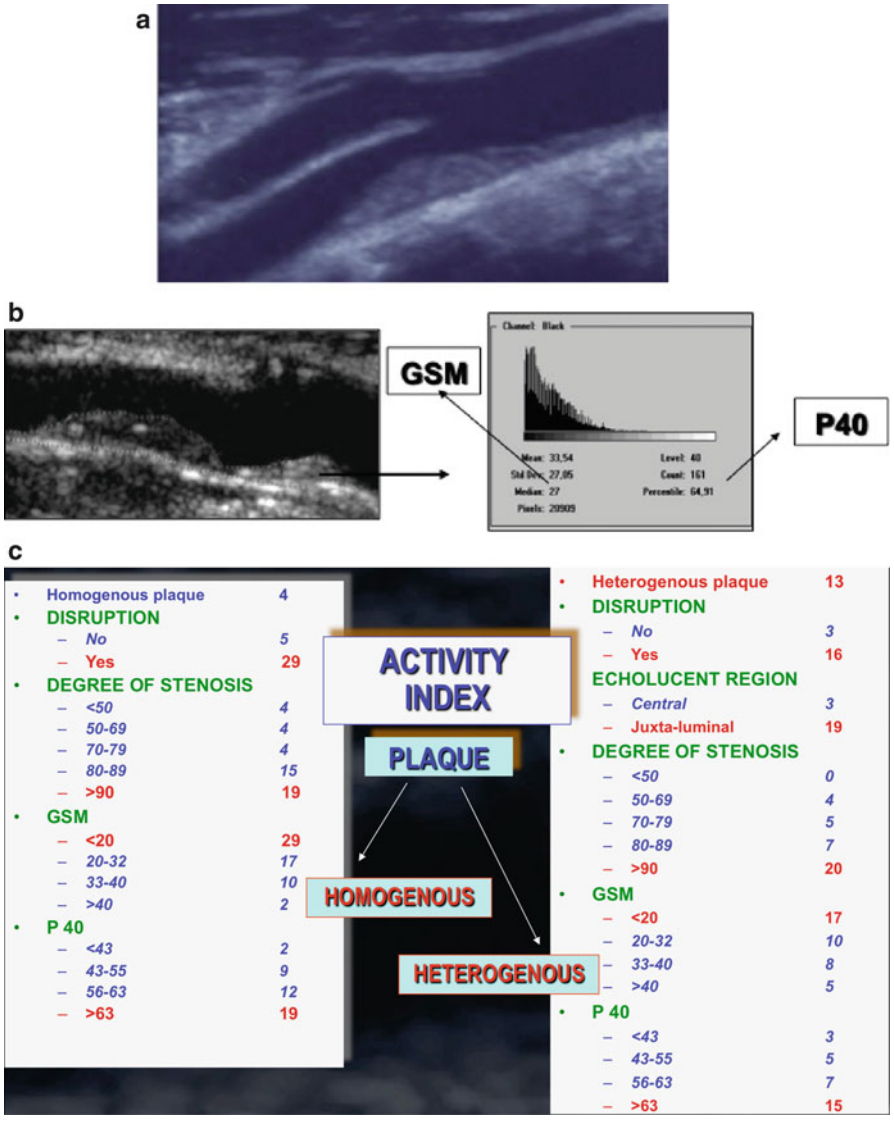

Fig. 1.6 (**a**) Homogenous carotid plaque visualized by high-definition ultrasonography. (**b**) Computer-assisted plaque analysis. (**c**) Activity index

technology allowed incorporation of a fluorescence probe which can be directed to coronary or other arterial bed. By injecting fluorochromes and activating them with the laser probe it is feasible to track down enzymes or other molecules involved in plaque instability [71].

3.7 Nuclear Imaging PET-SCAN

Single photon emission computed tomography (SPECT) and PET imaging of vascular structures have improved their sensitivity and accuracy by accurate anatomic location of the radiation source. Using 18 FDG (fluorodeoxyglucose), which is taken by active cells, has provided interesting images of carotid plaques correlating with neovascularization [72, 73]. It targets individual molecules involved in different metabolic pathways (VCAM-1), which adhere to endothelial cell in early atherosclerosis.

These technologies are promising tools for research, but its use in clinical practice requires further improvements on its sensitivity and specificity and also easier and less expensive instrumentation.

We have briefly described several technologies, some already tested in clinical studies and used in practice, and others still within the realm of experimentation and animal models.

There is a fundamental need to achieve better diagnosis of the unstable plaque, which often is not associated with severe stenosis and is a major cause of atherothrombosis and leads to acute cardiovascular events.

Some of the technologies provide only morphological imaging, but a new era of functional biological imaging

is beginning with new optical devices and nuclear-based technology often used with combined MR and CT Imaging to achieve better resolution and accuracy. They offer new ways to visualize the ongoing metabolic process that leads to the morphological changes that are markers of plaque instability.

Also a new area of clinical research will be the combined use of these technologies with biomarkers of inflammation like CPR or others, which may help to identify the vulnerable lesions and the patients at a higher risk of cardiovascular events.

The road from arteriography to molecular and biological imaging is fascinating and provides a good example of translational research from the bench and animal experiments to the bedside, by allowing a better selection of patients who really need of interventional treatment and thus saving a relevant number from unnecessary procedures.

References

1. Stary HC (1987) Macrophages, macrophage foam cells and eccentric intimal thickening in the coronary arteries of young children. Atherosclerosis 64:91–108
2. Napoli C, D'Armiento FP, Mancini F, Postiglione A, Witztum JL, Palumbo G, Palinski W (1997) Fatty streak formation occurs in human fetal aortas and is greatly enhanced by maternal hypercholesterolemia. Intimal accumulation of low density lipoprotein and its oxidation precede monocyte recruitment into early atherosclerotic lesions. J Clin Invest 100:2680
3. Yuan XM, Brunk UT, Hazel L (2000) The morphology and natural history of atherosclerosis. In: Dean RT, Klly DT (eds) Atherosclerosis: gene expression, cell interactions and oxidation. Oxford University Press, Oxford
4. Haudenschild CC (1994) Vascular wall physiology. In: White RA, Hollier LH (eds) Vascular surgery basic science and clinical correlations. JB Lippincott, Philadelphia, PA
5. Montecucco F, Lenglet S, Gayet-Ageron A et al (2010) Systemic and intraplaque mediators of inflammation are increased in patients symptomatic for ischemic stroke. Stroke 41:1394–1404
6. Koskinas KC, Feldman CL, Chatzizissis YS et al (2010) Natural history of experimental coronary atherosclerosis and vascular remodeling in relation to endothelial shear stress: a serial in vivo intravascular ultrasound study. Circulation 121:2092–2101
7. Markl M, Wegent F, Zech T et al (2010) In vivo wall shear stress distribution in the carotid artery: effect of bifurcation geometry, internal carotid artery stenosis and recanalization therapy. Circ Cardiovasc Imaging 3:647–655
8. Wolin MS (2000) Interactions of oxidants with vascular signaling systems. Arterioscler Thromb Vasc Biol 20:1430
9. Muhlestein JB (1998) Bacterial infections and atherosclerosis. J Investig Med 46:396
10. Ford PJ, Yamazaki K, Seymour GJ (2007) Cardiovascular and oral disease interactions: what is the evidence? Prim Dent Care 14:59
11. Ross R (1999) Atherosclerosis – an inflammatory disease. New Engl J Med 340:115
12. Kovanen PT (1996) Mast cells in human fatty streaks and atheromas: implications for intimal lipid accumulation. Curr Opin Lipidol 7:281
13. Raines EW, Rosenfeld ME, Ross R (1996) The role of macrophages. In: Fuster V, Topol EJ (eds) Atherosclerosis and coronary artery disease. Lippincott-Raven, Philadelphia, PA
14. Stary HC (1993) The evolution of human atherosclerotic lesions. Merck, West Point, PA
15. Glagov S, Zarins CK, Giddens DP, Ku DN (1988) Hemodynamics and atherosclerosis. Insights and perspectives gained from studies of human arteries. Arch Pathol Lab Med 112:1018–1031
16. O'Leary DH, Polak JF, Kronmal RA, Manolio TA, Burke GL, Wolfson SK Jr (1999) Carotid-artery intima and media thickness as a risk factor for myocardial infarction and stroke in older adults. Cardiovascular Health Study Collaborative Research Group. N Engl J Med 340:14–22
17. Salonen JT, Salonen R (1991) Ultrasonographically assessed carotid morphology and the risk of coronary heart disease. Arterioscler Thromb 11:1245–1249
18. Dickinson LE, Rand DR, Tsao J, Eberle W, Gerecht S (2012) Endothelial cell responses to micropillar substrates of varying dimensions and stiffness. J Biomed Mater Res A 100(6):1457–1466. doi:10.1002/jbm.a.34059
19. Vicenzini E, Giannoni MF, Benedetti-Valentini F, Lenzi GL (2009) Imaging of carotid plaque angiogenesis. Cerebrovasc Dis 27(Suppl 2):48–54
20. Gossl M, Versari D, Hildebrandt HA et al (2010) Segmental heterogeneity of vasa-vasorum neovascularization in human coronary atherosclerosis. J Am Coll Cardiol 3:32–40
21. Hellings WE, Peeters W, Moll F et al (2010) Composition of carotid atherosclerotic plaque is associated with cardiovascular outcome: a prognostic study. Circulation 121:1941–1950
22. Falk E, Shah PK, Fuster V (1995) Coronary plaque disruption. Circulation 92:657–671
23. Arroyo LH, Lee RT (1999) Mechanisms of plaque rupture: mechanical and biological interactions. Cardiovasc Res 41:369–375
24. Zhou J, Chew M, Ravn HB, Falk E (1999) Plaque pathology and coronary thrombosis in the pathogenesis of acute coronary syndromes. Scand J Clin Lab Invest Suppl 230:3–11
25. Falk E, Fuster V, Shah PK (1998) Interrelationship between atherosclerosis and thrombosis. In: Verstraete M, Fuster V, Topol EJ (eds) Cardiovascular thrombosis: thrombocardiology and thromboneurology. Lippincott-Raven, Philadelphia, PA, pp 45–58
26. Korsholm T-L, Lyngdorf LG, Falk E (2002) Atherosclerotic lesions: vulnerability. In: Lanzer P, Topol E (eds) Pan vascular medicine. Springer, Heidelberg
27. Bassiouny HS, Sakaguchi Y, Mikucki SA et al (1997) Juxtalumenal location of plaque necrosis and neoformation in symptomatic carotid stenosis. J Vasc Surg 26:585
28. Pedro LM, Pedro MM, Goncalves I, Carneiro TF, Balsinha C, Fernandes e Fernandes R, Fernandes e Fernandes J (2000) Computer-assisted carotid plaque analysis: characteristics of plaques associated with cerebrovascular symptoms and cerebral infarction. Eur J Vasc Endovasc Surg 19:118–123
29. Steffen CM, Gray-Weale AC, Byrne KE, Lusby RJ (1989) Carotid artery atheroma: ultrasound appearance in symptomatic and asymptomatic vessels. Aust N Z J Surg 59(7):529–534
30. Pedro LM (2003) A window to atherosclerosis: high definition ultrasonography in the study of the arterial wall. University of Lisbon, Lisbon
31. Moniz E (1927) L'éncephalographie artérielle: son importance dans la localization des tumeurs cérébrales. Rev Neurol 2:172
32. Moniz E, Lima A, Lacerda R (1937) Hemiplegies par thrombose de la carotide interne. Presse Med 45:977
33. Cid dos Santos J (1971) In memoriam Reynaldo dos Santos: profile of a scientist. J Cardiovasc Surg 12:78–81
34. Seldinger SI (1953) Catheter replacement of the needle in percutaneous arteriograhy. Acta Radiol 39:368–376
35. Cid dos Santos J (1947) Sur la desobliteration des thromboses arterièlles anciènnes. Mem Acad Chir (Paris) 73:409
36. Rothwell PM, Gibson R, Warlow CP (2000) Interrelation between plaque surface morphology and degree of stenosis on carotid

angiograms and the risk of ischemic stroke in patients with symptomatic carotid stenosis. On behalf of the European Carotid Surgery Trialists' Collaborative Group. Stroke 31:615–621
37. Heller RS, Malek AM (2012) Successful detection of embologenic ulceration in a symptomatic non-hemodynamic intracranial stenosis using C-arm cone beam CT. J Neurointerv Surg 5(2):e3
38. Miller JM, Rochitte CE, Dewey M et al (2008) Diagnostic performance of coronary angiography by 64-row CT. N Eng J Med 359:2324–2336
39. Hoffmann U, Moselewski F, Nieman K et al (2006) Non-invasive assessment of plaque morphology and composition in culprit and stable lesions in acute coronary syndrome and stable lesions in stable angina by multidetector computed tomography. J Am Coll Cardiol 47:1655–1662
40. Hyafil F, Cornily JC, Feig JE et al (2007) Noninvasive detection of macrophages using a nanoparticle contrast agent for computed tomography. Nat Med 13:636–641
41. Sakuma H, Ichikawa Y, Chino S et al (2006) Detection of coronary artery stenosis with whole-heart coronary magnetic resonance angiography. J Am Coll Cardiol 48:1946–1950
42. Kim WY, Stuber M, Bornert P et al (2002) Three-dimensional black-blood cardiac magnetic resonance coronary vessel wall imaging detects positive arterial remodeling in patients with nonsignificant coronary artery disease. Circulation 106:296–299
43. Mitsumori LM, Hatsukami TS, Ferguson MS et al (2003) In vivo accuracy of multisequence MR imaging for identifying unstable fibrous caps in advanced human carotid plaques. J Magn Resson Imaging 17:410–420
44. Ruehm SG, Corot C, Vogt P et al (2001) Magnetic resonance imaging of atherosclerotic plaque with ultra small superparamagnetic particles of iron oxide in hyperlipidemic rabbits. Circulation 103:415–422
45. Botnar RM, Perez AS, White S et al (2004) In vivo molecular imaging of acute and subacute thrombosis using a fibrin-binding magnetic resonance imaging contrast agent. Circulation 109:2023–2029
46. Alexandrov AV, Bladin CF, Maggisano R, Norris JW (1993) Measuring carotid stenosis. Time for a reappraisal. Stroke 24:1292–1296
47. Grant EG, Benson CB, Moneta GL et al (2003) Carotid artery stenosis: gray-scale and Doppler US diagnosis – Society of Radiologists in Ultrasound Consensus Conference. Radiology 229(2):340–346
48. Grant EG, Duerinckx AJ, El Saden S et al (1999) Doppler sonographic parameters for detection of carotid stenosis: is there an optimum method for their selection? AJR Am J Roentgenol 172:1123–1129
49. von Reutern GM, Goertler MW, Bornstein NM et al (2012) Grading carotid stenosis using ultrasonic methods. Stroke 43:916–921
50. Ebrahim S, Papacosta O, Whincup P, Wannamethee G, Walker M, Nicolaides AN, Dhanjil S, Griffin M, Belcaro G, Rumley A, Lowe GD (1999) Carotid plaque, intima media thickness, cardiovascular risk factors, and prevalent cardiovascular disease in men and women: the British Regional Heart Study. Stroke 30:841–850
51. Belcaro G, Laurora G, Cesarone MR, Barsotti A, Trevi GP, Renton S, Veller M, Fisher C, Gerulakos G, Nicolaides AN (1993) Noninvasive ultrasonic biopsy: evaluation of early arteriosclerotic lesions progression in normal asymptomatic, hyperlipidemic, and diabetic subjects. Angiology 44:93–99
52. Gronholdt ML, Nordestgaard BG, Wiebe BM (1998) Echolucency of computerized ultrasound images of carotid atherosclerotic plaques are associated with increased levels of triglyceride-rich lipoproteins as well as increased plaque lipid content. Circulation 97:34–40
53. Gonçalves I, Moses J, Dias N, Pedro LM, Fernandes e Fernandes J, Nilsson J, Ares MP (2003) Changes related to age and cerebrovascular symptoms in the extracellular matrix of human carotid plaques. Stroke 34:616–622
54. Gonçalves I, Moses J, Pedro LM, Dias N, Fernandes e Fernandes J, Nilsson J, Ares MP (2003) Echolucency of carotid plaques correlates with plaque cellularity. Eur J Vasc Endovasc Surg 26:32–38
55. Gonçalves I, Lindholm MW, Pedro LM, Dias N, Fernandes e Fernandes J, Fredrikson GN, Nilsson J, Moses J, Ares MP (2004) Elastin and calcium rather than collagen or lipid content determine the echogenicity of human carotid plaques. Stroke 35:2795–2800
56. Sabetai MM, Tegos TJ, Nicolaides AN, El Atrozy TS, Dhanjil S, Griffin M, Belcaro G, Geroulakos G (2000) Hemispheric symptoms and carotid plaque echomorphology. J Vasc Surg 31:39–49
57. Biasi GM, Froio A, Diethrich EB, Deleo G, Galimberti S, Mingazzini P, Nicolaides AN, Griffin M, Raithel D, Reid DB, Valsecchi MG (2004) Carotid plaque echolucency increases the risk of stroke in carotid stenting: the Imaging in Carotid Angioplasty and Risk of Stroke (ICAROS) study. Circulation 110:756–762
58. Tegos TJ, Sabetai MM, Nicolaides AN, Elatrozy TS, Dhanjil S, Stevens JM (2001) Patterns of brain computed tomography infarction and carotid plaque echogenicity. J Vasc Surg 33:334–339
59. Tegos TJ, Sabetai MM, Nicolaides AN, Robless P, Kalodiki E, Elatrozy TS, Ramaswami G, Dhanjil S (2001) Correlates of embolic events detected by means of transcranial Doppler in patients with carotid atheroma. J Vasc Surg 33:131–138
60. Tegos TJ, Sohail M, Sabetai MM, Robless P, Akbar N, Pare G, Stansby G, Nicolaides AN (2000) Echomorphologic and histopathologic characteristics of unstable carotid plaques. AJNR Am J Neuroradiol 21:1937–1944
61. Pedro LM, Pedro MM, Goncalves I, Carneiro TF, Balsinha C, Fernandes e Fernandes R, Fernandes e Fernandes J (1999) Placa de ateroma da bifurcação carotídea. Como identificar a lesão activa? Rev Port Cardiol 18:699–708
62. Tegos TJ, Kalodiki E, Nicolaides AN, Sabetai MM, Stevens JM, Thomas DJ (2001) Brain CT infarction in patients with carotid atheroma. Does it predict a future event? Int Angiol 20:110–117
63. Pedro LM, Fernandes e Fernandes J, Pedro MM, Gonçalves I, Dias NV, Fernandes e Fernandes R, Carneiro TF, Balsinha C (2002) Ultrasonographic risk score of carotid plaques. Eur J Vasc Endovasc Surg 24:492–498
64. Nicolaides AN, Kakkos SK, Kyriacou E, Griffin M, Sabetai M, Thomas DJ, Tegos T, Geroulakos G, Labropoulos N, Doré CJ, Morris TP, Naylor R, Abbott AL, Asymptomatic Carotid Stenosis and Risk of Stroke (ACSRS) Study Group (2010) Asymptomatic internal carotid artery stenosis and cerebrovascular risk stratification. J Vasc Surg 52(6):1486–1496
65. Kadoglou NP, Gerasimidis T, Moumtzouoglou A et al (2008) Intensive lipid-lowering therapy ameliorates novel calcification markers and GSM score in patients with carotid stenosis. Eur J Vasc Endovasc Surg 35(6):661–668
66. Moustafa RR, Izquierdo-Garcia D, Fryer TD et al (2010) Carotid plaque inflammation is associated with cerebral microembolism in patients with recent transient ischemic stroke or stroke: a pilot study. Circ Cardiovasc Imaging 3:536–541
67. Nair A, Kuban BD, Tuzcu EM et al (2002) Coronary plaque classification with intravascular ultrasound radiofrequency data analysis. Circulation 106:2200–2206
68. Hong MK, Mintz GS, Lee CW et al (2008) A three-vessel virtual histology intravascular ultrasound analysis of frequency and distribution of thin-cap fibroatheromas in patients with acute coronary syndrome or stable angina pectoris. Am J Cardiol 101:568–572
69. Tearney GJ, Waxman S, Shiskov M et al (2008) Three-dimensional coronary artery microscopy by intracoronary optical frequency domain imaging. JACC Cardiovasc Imaging 1:752–761
70. Matter CM, Stuber M, Nahrendorf M (2009) Imaging of the unstable plaque: how far have we got? Eur Heart J 30:2566–2574

71. Jaffer FA, Kim DE, Quinti L et al (2007) Optical visualization of cathepsin K activity in atherosclerosis with a novel protease-activatable fluorescence sensor. Circulation 115: 2292–2298
72. Aziz K, Berger K, Claycombe K et al (2008) Noninvasive detection and localization of vulnerable plaque and arterial thrombosiswith computed tomography angiography/positron emission tomography. Circulation 117:2061–2070
73. Calcagno C, Cornily JC, Hyafil F et al (2008) Detection of neovessels in atherosclerotic plaques of rabbits using dynamic contrast enhanced MRI and 18F-FDG PET. Arterioscler Thromb Vasc Biol 28:1311–1317

Part II

MR Atherosclerosis

Histopathology of Atherosclerosis Progression: What Imagers Need to Know

2

Masataka Nakano, Elena Ladich, and Renu Virmani

Abbreviations

ACS	Acute coronary syndrome
AHA	American Heart Association
AMI	Acute myocardial infarction
CTO	Chronic total occlusion
CVD	Cardiovascular disease
Hb	Hemoglobin
HO-1	Hemoxygenase-1
Hp	Haptoglobin
HPR	Healed plaque rupture
ICAM-1	Intercellular adhesion molecule 1
MMP	Matrix metalloprotease
MPO	Myeloperoxidase
NO	Nitric oxide
PCI	Percutaneous coronary intervention
PIT	Pathologic intimal thickening
SCD	Sudden coronary death
SEM	Scanning electron microscopy
SMC	Smooth muscle cell
TCFA	Thin-cap fibroatheroma
TF	Tissue factor
VCAM-1	Vascular cell adhesion molecule 1

1 Introduction

Atheromatous coronary artery disease is the leading causes of death worldwide, constituting approximately 7,000,000 cases each year. Atherosclerotic plaque rupture with thrombosis is the pathologic mechanism responsible for the majority of acute myocardial infarction (AMI) and sudden coronary death (SCD). Insights into the mechanism of luminal thrombosis have been elucidated from the study of the diseased arterial wall, largely through detailed analysis of the underlying plaque morphologies observed in pathologic studies of sudden death victims. While formerly the emphasis has been on luminal narrowing, the interventionalists today must have an understanding of specific plaque composition to potentially identify rupture-prone arterial plaques. This understanding is critical, especially as new imaging modalities emerge, which are targeted at identifying vulnerable plaques.

In the early 1990s, the American Heart Association (AHA) proposed a classification scheme for coronary atherosclerosis progression by which atherosclerotic lesions were classified into six numerical categories categorized in relation to plaque rupture. In this classification scheme, plaque rupture was identified as the sole etiology of coronary thrombosis [1, 2]. Sudden luminal thrombosis however may arise from three different plaque morphologies: plaque rupture, erosion, and calcified nodule. Moreover, the AHA nomenclature failed to describe healing mechanisms, which contribute to severe luminal narrowing with or without acute plaque rupture. These silent plaque ruptures may also lead to chronic total occlusion (CTO), which is reported to occur in approximately 30 % of SCDs. These limitations led us to modify the AHA classification, forgoing the more complicated numeric categories in favor of a simpler descriptive classification. This classification system can easily be translated and utilized by new invasive and noninvasive imaging modalities to improve our predictive ability in patients that are at high risk of developing acute coronary syndromes (ACSs) [3]. Moreover, to improve the outcome of patients with ACS, it is essential to have a comprehensive understanding of pathological processes involved in the progression of atherosclerosis as discussed below.

M. Nakano, MD • E. Ladich, MD • R. Virmani, MD (✉)
CVPath Institute, Inc., 19 Firstfield Rd., Gaithersburg, MD 20878, USA
e-mail: mnakano@tokai-u.jp; eladich@cvpath.org; rvirmani@cvpath.org

L. Saba et al. (eds.), *Multi-Modality Atherosclerosis Imaging and Diagnosis*,
DOI 10.1007/978-1-4614-7425-8_2,

Table 2.1 Modified AHA consensus classification based on morphologic description

	Description	Thrombosis
Non-atherosclerotic intimal lesions		
Intimal thickening	Normal accumulation of smooth muscle cells (SMCs) in the intima in the absence of lipid or macrophage foam cells	Absent
Intimal xanthoma	Superficial accumulation of foam cells without a necrotic core or fibrous cap. Based on animal and human data, such lesions usually regress	Absent
Progressive atherosclerotic lesions		
Pathologic intimal thickening	SMC-rich plaque with proteoglycan matrix and focal accumulation of extracellular lipid	Absent
Fibrous cap atheroma	Early necrosis: focal macrophage infiltration into areas of lipid pools with an overlying fibrous cap Late necrosis: loss of matrix and extensive cellular debris with an overlying fibrous cap	Absent
Thin-cap fibroatheroma	A thin fibrous cap (<65 μm) infiltrated by macrophages and lymphocytes with rare or absence of SMCs and relatively large underlying necrotic core. Intraplaque hemorrhage/fibrin may be present	Absent
Lesions with acute thrombi		
Plaque rupture	Fibroatheroma with cap disruption; the luminal thrombus communicates with the underlying necrotic core	Occlusive or non-occlusive
Plaque erosion	Plaque composition, as above; no communication of the thrombus with necrotic core. Can occur on a plaque substrate of pathologic intimal thickening or fibroatheroma	Usually non-occlusive
Calcified nodule	Eruptive (shedding) of calcified nodule with an underlying fibrocalcific plaque with minimal or absence of necrosis	Usually non-occlusive
Lesions with healed thrombi		
Fibrotic (without calcification) Fibrocalcific (±necrotic core)	Collagen-rich plaque with significant luminal stenosis. Lesions may contain large areas of calcification with few inflammatory cells and absence of necrosis. These lesions may represent healed erosions or ruptures	Absent

(Modified from Virmani R et al (2000) Lessons from sudden coronary death: a comprehensive morphological classification scheme for atherosclerotic lesions. Arterioscler Thromb Vasc Biol 20:1262–1275)

2 Progression of Atherosclerotic Plaque

In the modified classification (Table 2.1, Figs. 2.1 and 2.2), the numeric AHA types I to IV are replaced by descriptive terminology: adaptive intimal thickening, intimal xanthoma (fatty streak), pathologic intimal thickening (PIT), and fibroatheroma. AHA type V and type VI lesions were discarded since they failed to account for the three different causes of thrombotic morphologies (rupture, erosion, and calcified nodule) and their relationship to healed plaque rupture (HPR) that is representative of stable angina. Since atherosclerosis is a dynamic process with a complicated pathogenesis, it is useful to review the stages of development of atherosclerosis. As the mechanistic underpinnings of the disease are better understood, however, the classification should be revised periodically and improved as new knowledge is gained.

2.1 Adaptive Intimal Thickening and Intimal Xanthoma (Fatty Streaks)

The earliest manifestation of vascular change is "adaptive intimal thickening" (AHA Type I), which consists of several layers of smooth muscle cells (SMCs) in an extracellular matrix with no or little inflammatory cell infiltration. Intimal thickening is observed in 35 % of neonates, and the intima/media ratio at birth is 0.1 increasing progressively to reach 0.3 by 2 years of life [4]. This change is considered adaptive (non-atherosclerotic) since the SMCs exhibit a very low proliferative activity and exhibit an anti-apoptotic phenotype [5]. Although the adaptive intima increases in thickness with aging, very rarely does it grow into a disease compromising blood flow. The change of shear stress is a trigger for abnormal responses in the endothelial lining [6] as well as changes secondarily induced in SMC phenotype [7]; however, the detailed mechanism remain elusive.

"Fatty streak" or "Intimal xanthoma" (AHA Type II) is a lesion that is not raised and is primarily composed of abundant foamy macrophages interspersed between SMCs. Although the AHA classification alludes to this entity as the earliest lesion of atherosclerosis, from our experience and reports of human and animal studies, the lesion is reversible at least in some locations [8, 9]. Some reports suggest that the modification of extracellular matrix is responsible for the progression of macrophage infiltration implying a role for biglycan and decorin proteoglycans [10], but the mechanism remains largely uncertain.

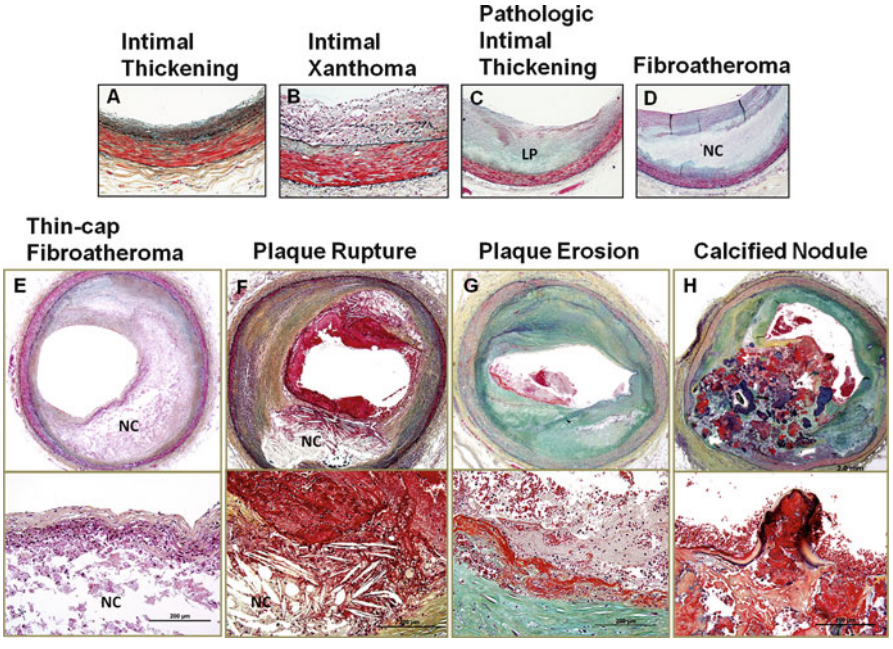

Fig. 2.1 Plaque atherosclerotic progression in human coronary arteries. These histologic images illustrate the various lesion morphologies of human coronary atherosclerosis. (**a**) Adaptive intimal thickening is present from birth and consists of a smooth muscle-rich intima. (**b**) Intimal xanthoma are predominantly foam cell-rich lesions that are found in the young, but known to regress in adults. (**c**) Pathologic intimal thickening (PIT) is the first of the progressive plaques marked by an acellular lipid pool rich in proteoglycan; inflammation in macrophages when present is typically confined to the most luminal aspect of this plaque. (**d**) Fibroatheroma (FA) are lesions with areas of necrosis characterized by cellular debris and cholesterol monohydrate with varying degrees of calcification or hemorrhage. (**e**) Thin-cap fibroatheroma (TCFA) or vulnerable plaques are recognized by their relatively large necrotic core and thin fibrous cap which is infiltrated by numerous macrophages. (**f**) Plaque rupture leads to exposure of necrotic contents to the blood flow, resulting in the triggering of the coagulation cascade. The luminal thrombus at the site of rupture is platelet rich (*white thrombus*). (**g**) Erosion is another entity that gives rise to coronary thrombosis. Erosions can occur on a substrate of PIT or FA. (**h**) Calcified nodules (a minor but viable mechanisms of thrombosis) depict eruptive fragments of calcium that protrude into the lumen causing a thrombotic event. *LP* lipid pool, *NC* necrotic core

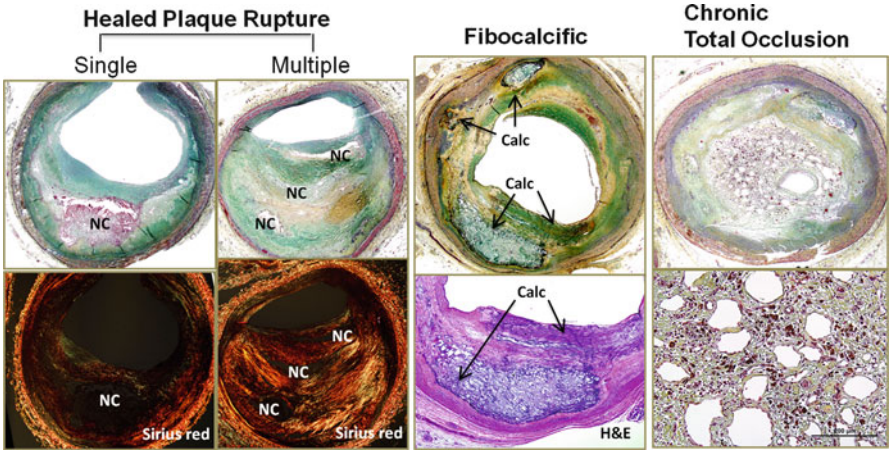

Fig. 2.2 Fate of atherosclerotic plaque. *Boxes* on the *left* show healed plaque ruptures where the newly formed fibrous cap is rich in proteoglycans and type III collagen (type III collagen appears *green* with Sirius red stain under polarized light) with interspersed smooth muscle cells. Repeated ruptures lead to a multilayered appearance with necrotic cores and overlying fibrous layers, resulting in severe luminal narrowing. Multiple healed plaque ruptures are thought responsible for progressive luminal narrowing. Fibrocalcific plaque (*middle column*) is thought to be a burnt-out lesion, which is associated with a calcified sheet of plaque matrix (*arrows*). *Boxes* on the *right* show histologic features of chronic total occlusion. The lumen is characterized by recanalized organized thrombus that is rich in proteoglycan matrix with presence of iron deposition and macrophages. *Calc* calcification, *NC* necrotic core

2.2 Pathologic Intimal Thickening

"Pathologic intimal thickening" (PIT, AHA Type III) is recognized as the earliest progressive (irreversible) lesion by most research groups. The lesion is characterized by layers of proliferating SMCs near the lumen and an underlying lipid pool present at the intimal medial border. The origin of lipid pool is not fully understood. The area of the lipid pool is rich in proteoglycan versican and hyaluronan as well as extracellular lipid deposits but is devoid of SMCs and macrophages. It has been demonstrated that there is an affinity of the lipid pool to retain plasma lipoprotein, which suggests that the accumulation of extracellular lipid is likely derived from the influx of plasma lipoproteins [11]. Williams et al. proposed a "response-to-retention" hypothesis: the retention of atherogenic lipoprotein associated with the extracellular matrix such as proteoglycan versican and hyaluronan is an initiating event in early atherogenesis [12]. Recent studies reinforce this hypothesis by demonstrating that structural changes in the glycosaminoglycan chain of proteoglycans are an initial proatherogenic step that promotes the binding and retention of lipoproteins [13]. An alternative hypothesis suggests that the membranes of apoptotic SMC may be an alternative source for lipid in PIT [14]. Apoptotic SMCs within lipid pools are recognized by membrane remnants (cages of basal lamina) and the presence of microcalcification representing calcified mitochondria [15]. However, the proof supporting this mechanism remains speculative.

Another important hallmark of PIT is the presence of varying degrees of foamy macrophage accumulation near the luminal aspect of the plaque (apart from the lipid pool) albeit this does not necessarily apply to all cases. Lesions demonstrating PIT with foamy macrophages are considered a more advanced stage of atherosclerosis as reported by Nakashima et al. in their systematic study of early coronary plaques [16]. We believe that macrophages invade the plaque from the luminal surface. Although the precise nature of focal macrophage accumulation in PIT is not fully elucidated, it is speculated that retention or modified lipoprotein along with activation of vascular adhesion molecules like VCAM-1 and ICAM-1 expressed by endothelial cells stimulates the recruitment of macrophages [17, 18]. In addition, lesions with PIT exhibit varying degrees of free cholesterol represented by empty fine crystalline structures in paraffin-embedded sections that accumulate within lipid pools. Although it is assumed that free cholesterol originates from dead foam cells, this is not a likely source in PIT as the majority of macrophages when present are confined to the more luminal aspect of the plaque.

2.3 Fibroatheroma

Fibroatheroma (AHA type IV) represents a further progressive stage of atherosclerotic disease and is histologically characterized by the presence of acellular necrotic cores, which are distinct from the lipid pools of PIT as they lack expression of hyaluronan and proteoglycan versican. Recognition of early macrophage infiltration into the lipid pools and cell death along with a substantial increase in free cholesterol and breakdown of extracellular matrix, which is presumably degraded by the matrix proteases released by macrophages, is classified as "early" necrotic cores. In the early phase of the necrotic core formation an efficient system of clearance of apoptotic bodies by macrophages is present, however, the system is soon overwhelmed and there is defective phagocytic clearance of apoptotic cells and this is thought to further contribute to the vicious circle of enlargement of necrotic core and plaque progression (Fig. 2.3) [19]. As total plaque burden increases, compensatory enlargement of the vessel, i.e., positive coronary arterial remodeling, occurs to preserve arterial lumen. According to Glagov, the lumen compromise only begins to occur when the luminal narrowing exceeds >40 % cross-sectional luminal narrowing [20]. We have further classified fibroatheromas into "early" and "late" based on the type of necrotic core observed. A necrotic core that is devoid of proteoglycan versican and hyaluronan or any collagen expression is termed "late" necrotic core but a thick fibrous cap fully contains the necrotic core. On the other hand "early" necrotic cores focally express the proteoglycan versican and hyaluronan, especially towards the media, but towards the lumen there is absence of matrix with macrophages infiltration.

2.4 Intraplaque Hemorrhage

It is not only apoptotic macrophages that contribute to the accumulation of free cholesterol but other source such as red blood cells may also contribute to the expansion of the necrotic core (Fig. 2.4). Studies from our SCD registry showed that hemorrhage into a necrotic core is commonly observed in cases of plaque rupture and late necrotic core. The membranes of red blood cells are enriched with lipid, which constitutes 40 % by weight, and are rich in free cholesterol content that exceeds that of all other cell membranes [21]. Excess membrane cholesterol of red blood cells can phase separate and form immiscible membrane domains consisting of pure cholesterol arranged in a tail-to-tail orientation favoring crystal formation [22]. The extent of accumulated erythrocytes incorporated into the plaque and abundant lipids, together with impaired phagocytic efficiency of macrophages to effectively clean up red blood cells and

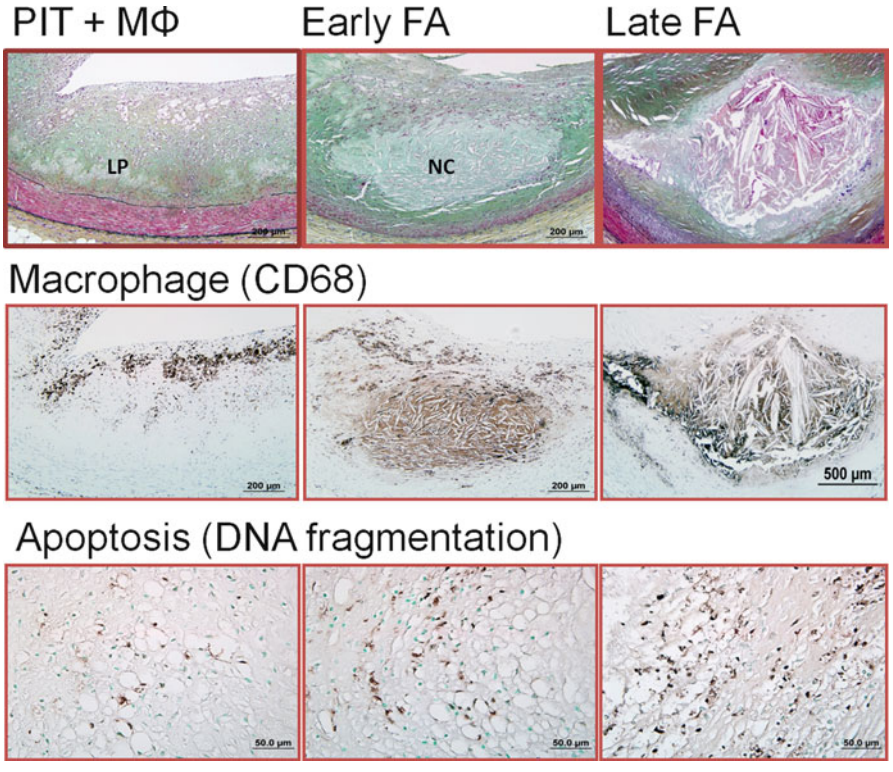

Fig. 2.3 Mechanism of necrotic core expansion in human coronary plaques. (*Left column*) Pathologic intimal thickening (PIT) is characterized by an underlying lipid pool (LP), which is devoid of macrophages (MΦ). The majority of macrophages when present are confined to the more luminal aspect of the plaque. Apoptotic cells are rarely seen in PIT. (*Middle column*) The presence of necrotic core (NC) infiltrated by CD68-positive macrophages characterizes the early stage of fibroatheroma (FA). Macrophages in early FA are capable of engulfing apoptotic bodies. (*Right column*) Late FA is represented by increased macrophage death and cell lysis. Free apoptotic bodies are commonly seen, possibly indicating defective clearance (efferocytosis) by resident macrophages

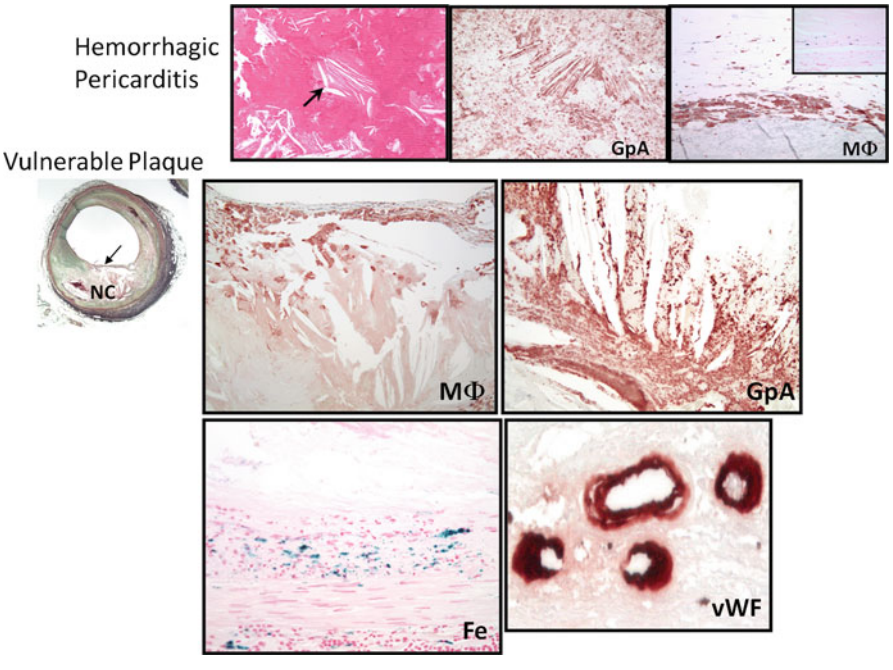

Fig. 2.4 Intraplaque hemorrhage in fibroatheroma with a late-stage necrotic core. Intraplaque hemorrhage leads to the accumulation of cholesterol monohydrate and increased lesion vulnerability. Illustrated in the *top panel* is the initial observation of hemorrhage in nonvascular sites showing accumulated free cholesterol. Note free cholesterol clefts in hemorrhagic pericarditis (*arrow*). Stained by Glycophorin A (GpA) which is specific for red blood cells, it is noted that positive staining surrounds the crystal structure of cholesterol. At the periphery of the hemorrhage, foamy macrophage (MΦ) were observed. The *bottom panel* shows a vulnerable plaque with macrophage positivity within the thin fibrous cap. GpA is strongly positive along with iron (Fe). Moreover, leaky microvessels within the plaque are detected as illustrated by the diffuse staining of von Willebrand factor (vWF) (reproduced with permission from Nakano et al. Vulnerable plaque. In: Zeev Vlodaver (ed) Coronary heart disease: clinical, pathological, imaging and molecular profiles. Springer)

other debris, influences both the biochemical composition and size of the necrotic core [23, 24].

The origin of intraplaque hemorrhage is also debatable between those claiming blood influx from luminal subsequent to plaque fissuring and proponents of leakage from intraplaque microcapillaries. However, we are in favor of the latter since often intraplaque erythrocyte extravasation is seen in the absence of plaque fissure and is associated with a high density of small vessels within the plaque. Further, some reports demonstrated the presence of incomplete mural cells coverage and dysfunctional endothelial cells of capillaries and arterioles with focal absence of basement membranes and poorly formed endothelial junctions [25]. It is possible that these immature or leaky vessels also allow diffusion of plasma proteins and diapedesis of leukocytes and erythrocytes spillage [26], which may serve as a driving force of further centripetal angiogenesis from the adventitia [27].

2.5 Hemoglobin Toxicity and Oxidative Stress

Intraplaque hemorrhage could potentially also recruit inflammatory cells [28]. The precise signaling pathways for the cellular response are not fully understood but it is postulated that hemoglobin–haptoglobin receptor CD163 on macrophages may be involved in the clearance of the complex with release of anti-inflammatory cytokines that may contribute to a decrease in inflammation [29]. However more importantly, our recent studies have elucidated the significance of oxidative stress associated with extravasated erythrocytes providing a rapid increase of hemoglobin (Hb) and continued inflammation in the intraplaque area [30]. Free Hb binds to and inactivates nitric oxide (NO), a potent molecule that plays a critical role in the regulation of smooth muscle vaso-reactivity and endothelial adhesion molecule expression, events that lead to inflammation within the vessel wall [31].

The function of haptoglobin (Hp) is primarily to handle hemoglobin released from red blood cells following intravascular or extravascular hemolysis. There are two common alleles at the Hp genetic locus denoted as 1 and 2, with two homozygous (1-1 and 2-2) and one heterozygous (2-1) genotype possible. There are functional differences between the Hp 1 and Hp 2 protein products in protecting against hemoglobin-driven oxidative stress with important functional and clinical significance. It is reported that there is a three- to fivefold increased risk of cardiovascular disease (CVD) in individuals with diabetes mellitus (DM) having the Hp 2-2 genotype as compared to DM individuals without the Hp 2-2 genotype. In particular, individuals with the Hp 2-2 genotype and diabetes mellitus appear to be at significantly higher risk of microvascular and macrovascular complications.

In atherosclerotic plaques, the primary route for clearance of the Hb–Hp complex involves the CD163 receptor expressed on immunosuppressive macrophages with M2 phenotype [32]. Physiologically low concentrations of hemoglobin (Heme) are cytoprotective as they induce the rapid upregulation of hemoxygenase-1 (HO-1). Excess pathological amounts of heme outstrip the ability of HO-1 to metabolize it so that residual heme (librating free iron) may act deleteriously on tissue by pro-oxidative and pro-inflammatory effects [33]. Also, when the capacity of protective hemoglobin-scavenging mechanisms has been saturated, levels of cell-free hemoglobin increase, resulting in the consumption of nitric oxide and resulting in clinical sequelae. NO plays a major role in vascular homeostasis and has been shown to be a critical regulator of basal and stress-mediated smooth muscle relaxation and vasomotor tone, endothelial adhesion molecule expression, and platelet activation and aggregation. Another product of excessive heme is bilirubin, which has potential antioxidant activity. Free ferrous iron has potential pro-oxidant activity, although this may be limited by its sequestration by ferritin.

2.6 Thin-Cap Fibroatheroma and Plaque Rupture

Thin-cap fibroatheroma (TCFA), traditionally designated as vulnerable plaque, is characterized by having a morphological appearance that resembles ruptured plaque [3]. TCFA generally contain a large necrotic core with overlying thin intact fibrous caps consisting mainly of type I collagen with varying degrees of macrophages and lymphocytes and very few, if any, α-actin-positive SMCs. The fibrous cap thickness is an indicator of plaque vulnerability and a TCFA is defined as having a cap thickness ≤ 65 μm since the thinnest portion of the remnant cap of a ruptured plaque was measured as 23 ± 19 μm, with 95 % of ruptured caps measuring ≤ 65μm [34]. As compared to ruptured plaque, TCFA tend to have smaller necrotic cores and less macrophage infiltration. Cross-sectional luminal narrowing is also typically less in TCFA compared to ruptures and occlusive thrombus generally shows greater underlying stenosis than lesions with non-occlusive thrombus [35].

It has been shown that the site of rupture usually occurs at its weakest point, often near shoulder regions. However, in our experience, this is not always the case as we have observed an equivalent number of ruptures at the mid portion of fibrous cap, especially in individuals who are dying during exertion [36]. Therefore, it is reasonable to speculate that several processes may be involved in the mechanisms of plaque rupture, e.g., fibrous cap degradation

by matrix metalloproteases (MMPs) [37], high shear stress [38], macrophage and smooth muscle cell death [39], and microcalcification and iron accumulation within the fibrous cap [40] all have been implicated.

Once plaque rupture occurs and necrotic contents are exposed to the flowing blood, this results in the triggering of the coagulation cascade in response to lipids, collagen, and tissue factors (TF). The luminal thrombus at the site of rupture is platelet rich (white thrombus) while proximal and distal to the rupture site, i.e., sites of propagation of the thrombus consist of a red thrombus composed of layers of fibrin and erythrocyte. A study of aspirated thrombi from patients presenting with AMI when examined by scanning electron microscopy (SEM) confirmed a decrease of platelet content and an increase of fibrin content as the duration of ischemia increased [41].

2.7 Plaque Erosion

Plaque rupture of an atherosclerotic plaque is the primary cause of AMI and SCD, occurring in 60–75 % of cases [42]. In the mid-1990s, our laboratory and that of van der Wal et al. reported an alternative mechanism of coronary thrombosis, referred to as "plaque erosion". In plaque erosion, the thrombus is confined to the luminal plaque surface with an absence of fissures or communication with the underlying necrotic core (when present), a finding validated by serial sectioning. In a study of 20 AMI patients, van der Wal et al. showed that the incidence of plaque ruptures (60 %) was more frequent than "superficial erosion" (40 %) [43]. In our series of 50 consecutive cases of sudden death due to coronary artery thrombosis plaque rupture was identified in 28 (56 %) cases, while superficial erosion was observed in 22 (44 %) cases, all of which had a smooth muscle cell and proteoglycan-rich underlying plaque [44]. In more recent studies, of AMI and SCD cases plaque erosion is identified as an important substrate of coronary thrombosis with its frequency being higher in women than men [45].

The term "erosion" was used since the luminal surface underneath the thrombus was devoid of endothelium. In addition, there were clear morphologic differences between rupture and erosion with plaque erosions having fewer macrophages and T-lymphocytes as compared to plaque rupture [44, 46]. In addition, eroded plaques tend to be more frequently eccentric with lesions rich in proteoglycan versican, hyaluronan, and type III collagen, unlike ruptured or stable plaques. Further, thrombi from erosion express a greater number of myeloperoxidase (MPO)-positive cells and have a higher incidence of distal micro-emboli than ruptures [47, 48]. Taken together, the above facts suggest a great necessity to better understand mechanistic differences between erosion and rupture, where different strategies may be required for the diagnosis and treatment of erosions.

2.8 Calcified Nodule

Calcified nodules is the least frequent cause of coronary thrombosis. It is characterized as a lesion with underlying calcification that is fragmented into small amorphous nodules on the luminal surface with surrounding fibrin, while the deeper portions more often show sheets of calcification. It morphologically resembles eruptive nodules (often multiple nodules with or without bone formation) protruding into the lumen, accompanied by a platelet-rich thrombus, which is usually non-occlusive. Little is known about the origin of nodular calcification. Histologically, fibrin is often present between the bony or calcified spicules, along with osteoblasts, osteoclasts, and inflammatory cells, indicating possible entrapment of circulating stem cells or cell transformation occurring from existing plaque cells [3]. Lesions with nodular calcification are more common in older individuals, more likely seen in males and chronic renal failure patients, and are preferentially found in tortuous middle right coronary or left anterior descending coronary arteries. They also appear to be more prevalent in the carotid arteries than coronary, which may be related to a greater frequency of calcification in carotid disease. The necrotic core is usually small, if present, in comparison to other atherothrombotic lesions.

2.9 Healed Plaque Rupture

The prevalence of silent plaque rupture or erosion in the clinical setting remains unknown as there are few studies that have demonstrated plaque progression following clinical events. Overall, it has been demonstrated in the NHLBI Dynamic Registry involving consecutive patients undergoing percutaneous coronary interventions (PCI) having a 6 % rate of nontarget lesion PCI by 1 year, and that the greater the coronary artery disease burden the higher the risk. Another recent study in patients who presented with an ACS and underwent PCI, major cardiovascular events in nontarget lesions were 11.6 % at 30 months. These lesions had angiographically mild disease, most often were TCFA, and were characterized by a large plaque burden and a small lumen area or some combination of these characteristics. Also, autopsy studies provide evidences that plaque progression defined as cross-sectional luminal narrowing occurs following repeated thrombotic events. Ruptured lesions with healed repair sites, referred to as the HPR, are discernible by breaks in the underlying old fibrous cap with a newly formed overlying tissue consisting of SMC surrounded by

proteoglycans and/or a collagen-rich matrix depending on the phase of healing [49]. It is likewise the case for healed erosion, i.e., similarly to that of rupture sites, erosion lesions heal and lead to luminal narrowing. Early stage of healing towards the lumen is characterized by lesions that are rich in proteoglycans and type III collagen, with an underlying necrotic core and ruptured fibrous cap rich in type I collagen.

Davies showed that the mechanism of plaque progression was through HPRs. The frequency of HPR correlates with the degree of luminal narrowing such that HPR was identified in 8 % of lesions with <20 % diameter stenosis, 19 % with 21–50 % diameter stenosis, and 73 % with >50 % stenosis [49]. We showed in patients with SCD that the incidence of HPR was 61 %; the percent luminal narrowing increased with increased number of healed rupture sites of previous ruptures. These data provided evidence that silent plaque ruptures is a form of wound healing that results in increased percent stenosis [50].

2.10 Calcified Stable Plaque (Fibrocalcific Plaque)

Although extent of calcification has been shown to be a predictor of diffuse coronary disease by CT, calcification of atherosclerotic plaque in SCD patients is observed in 80 % of patients, and the degree of calcification significantly varies from patient to patient and does not necessarily correlate with the disease severity or plaque vulnerability. Calcification is likely a consequence of multiple risk factors which include age/gender [51], renal function, diabetes [52], vitamin D levels and other aspects of bone metabolism [53], and genetic markers [54].

The initiation of calcification at least in man in atherosclerotic plaque is a marker of cell death, which is an essential component of all atherosclerotic plaques. The apoptotic smooth muscle cell is considered to be the earliest source of plaque calcification by an active or passive process involving calcification of the cell organelles referred to as matrix vesicles, which are observed as microcalcifications by histology, and only appreciated following utilization of special stains like von Kossa [55]. Macrophage cell death is thought to be another source of early calcium deposition. The calcified macrophages are present as small blocky calcifications and are morphologically distinct from those of SMCs. We have observed that the microcalcifications, derived from the apoptotic SMCs and macrophages, generally begin within the lipid pool and in "early" necrotic cores close to the luminal surface. It remains to be elucidated how the calcifications extend and lead to diffuse calcification involving other extracellular matrix proteins such as collagen and proteoglycans or through the expression of bone-forming proteins. The eventual transformation into plates of calcification that may appear as pipestem calcification, which involves necrotic core, collagen, and inflammatory cells, and in late stages even bone formation may be observed. Immunohistochemical studies and gene expression studies have demonstrated the presence of bone morphogenic protein, osteopontin, bone sialoprotein, and the osteoblast specific transcription factor for bone formation is highly expressed in the calcified arteries as compared to the control. In heavily calcified lesions which are regarded as burnt-out lesions, there is little if any macrophage infiltration and absence of other inflammatory cells. Nevertheless, a fair proportion of the calcification is passive, being purely degenerative without biological regulation and consists of calcium phosphate crystals [56].

3 Plaque Morphologies and Clinical Significance

In histological studies of patients dying of SCD, fresh thrombus has been reported in 50–75 % of cases while the remaining cases succumb to stable plaque with severe stenosis (>75 % cross-sectional luminal narrowing) of major coronary arteries. Of the various cases of fresh thrombus, the underlying pathologic lesions are mainly plaque rupture (60–75 %), followed by erosion (30–40 %), and calcified nodules (2–7 %) [3, 57–60]. In cases where death is attributed to plaque rupture, 70 % of cases show the presence of TCFAs at the site remote from the ruptured lesion. On the contrary, the incidence of TCFAs is markedly less (30 % of cases) where death is associated with stable plaques with severe stenosis. Also, the incidence of thin-cap fibroatheroma is highest in patient dying of plaque rupture, less in stable plaques, and least in patients dying with plaque erosion. The majority of TCFAs occur predominantly in the proximal portion of the three major coronary arteries; the proximal portion of the left anterior descending artery is the most frequent location (43 %) followed by the proximal right coronary artery (20 %) and the least frequent is the left circumflex artery (18 %) [35].

While plaque rupture may lead to unstable angina, myocardial infarction, or sudden death, however, rupture may also occur without causing symptoms. Silent ruptures heal and their repeated occurrence at the same location leads to greater luminal area stenosis with each new rupture. These lesions exhibit multiple necrotic cores separated by layers of collagen. These repeated thrombotic events contribute to gradual luminal narrowing and plaque progression. This significant increase in plaque burden and luminal narrowing due to previous repeated thrombosis often occurring silently in the absence of cardiac symptoms. The prevalence of silent episodes of rupture in living patients is unknown. In our experience, 61 % of SCD victims show at least one HRP lesion, where the incidence is greatest in the deaths from stable plaques with severe stenosis (80 %), followed by acute plaque rupture (75 %), and the least in plaque erosions (9 %) [50].

Although lipids along with other traditional risk factors play an essential role in the causation of coronary artery disease, the mechanistic link between lipid and disease remains unknown. Similarly, plaque progression studies in humans have been derived mostly from autopsy studies and for the most part clinical studies in the last century concentrated on study of luminograms and not the arterial wall where most of the disease of atherosclerosis is located. Our animal models have also failed to show events such as plaque rupture that occur commonly in man. There is no doubt we have learned many disease mechanisms from genetically altered mice but the atherosclerotic lesions in no way resemble those of man. Similarly, the animal models have not helped predict the responsiveness of newer treatments in humans. Therefore, identification of various plaque characteristics in man by invasive or noninvasive means may be the only way we are likely to enhance our knowledge of plaque types and plaque progression in man. We must continue to improve our imaging tools for the detection and characterization of coronary artery disease, targeting detailed plaque morphology or specific metabolic processes, e.g., local inflammation or biomarkers, which may permit strict monitoring of the activity of atherosclerotic disease. The development of noninvasive imaging device for screening purposes in asymptomatic individuals may prove an indispensable tool for the prediction and management of patients at high risk of clinical events.

References

1. Stary HC, Blankenhorn DH, Chandler AB et al (1992) A definition of the intima of human arteries and of its atherosclerosis-prone regions. A report from the Committee on Vascular Lesions of the Council on Arteriosclerosis, American Heart Association. Arterioscler Thromb 12:120–134
2. Stary HC, Chandler AB, Dinsmore RE et al (1995) A definition of advanced types of atherosclerotic lesions and a histological classification of atherosclerosis. A report from the committee on vascular lesions of the council on arteriosclerosis, american heart association. Arterioscler Thromb Vasc Biol 15:1512–1531
3. Virmani R, Kolodgie FD, Burke AP et al (2000) Lessons from sudden coronary death: a comprehensive morphological classification scheme for atherosclerotic lesions. Arterioscler Thromb Vasc Biol 20:1262–1275
4. Ikari Y, McManus BM, Kenyon J et al (1999) Neonatal intima formation in the human coronary artery. Arterioscler Thromb Vasc Biol 19:2036–2040
5. Orekhov AN, Andreeva ER, Mikhailova IA et al (1998) Cell proliferation in normal and atherosclerotic human aorta: proliferative splash in lipid-rich lesions. Atherosclerosis 139:41–48
6. Davies PF, Civelek M, Fang Y et al (2010) Endothelial heterogeneity associated with regional athero-susceptibility and adaptation to disturbed blood flow in vivo. Semin Thromb Hemost 36:265–275
7. Wang L, Karlsson L, Moses S et al (2002) P2 receptor expression profiles in human vascular smooth muscle and endothelial cells. J Cardiovasc Pharmacol 40:841–853
8. Aikawa M, Rabkin E, Okada Y et al (1998) Lipid lowering by diet reduces matrix metalloproteinase activity and increases collagen content of rabbit atheroma: a potential mechanism of lesion stabilization. Circulation 97:2433–2444
9. Velican C (1981) A dissecting view on the role of the fatty streak in the pathogenesis of human atherosclerosis: culprit or bystander? Med Interne 19:321–337
10. Nakashima Y, Wight TN, Sueishi K (2008) Early atherosclerosis in humans: role of diffuse intimal thickening and extracellular matrix proteoglycans. Cardiovasc Res 79:14–23
11. Hoff HF, Bradley WA, Heideman CL et al (1979) Characterization of low density lipoprotein-like particle in the human aorta from grossly normal and atherosclerotic regions. Biochim Biophys Acta 573:361–374
12. Williams KJ, Tabas I (1995) The response-to-retention hypothesis of early atherogenesis. Arterioscler Thromb Vasc Biol 15: 551–561
13. Merrilees MJ, Beaumont BW, Braun KR et al (2011) Neointima formed by arterial smooth muscle cells expressing versican variant v3 is resistant to lipid and macrophage accumulation. Arterioscler Thromb Vasc Biol 31:1309–1316
14. Preston Mason R, Tulenko TN, Jacob RF (2003) Direct evidence for cholesterol crystalline domains in biological membranes: role in human pathobiology. Biochim Biophys Acta 1610:198–207
15. Kockx MM, De Meyer GR, Muhring J et al (1998) Apoptosis and related proteins in different stages of human atherosclerotic plaques. Circulation 97:2307–2315
16. Nakashima Y, Fujii H, Sumiyoshi S et al (2007) Early human atherosclerosis: accumulation of lipid and proteoglycans in intimal thickenings followed by macrophage infiltration. Arterioscler Thromb Vasc Biol 27:1159–1165
17. Cushing SD, Berliner JA, Valente AJ et al (1990) Minimally modified low density lipoprotein induces monocyte chemotactic protein 1 in human endothelial cells and smooth muscle cells. Proc Natl Acad Sci USA 87:5134–5138
18. Klouche M, Gottschling S, Gerl V et al (1998) Atherogenic properties of enzymatically degraded LDL: selective induction of mcp-1 and cytotoxic effects on human macrophages. Arterioscler Thromb Vasc Biol 18:1376–1385
19. Tabas I (2000) Cholesterol and phospholipid metabolism in macrophages. Biochim Biophys Acta 1529:164–174
20. Glagov S, Weisenberg E, Zarins CK et al (1987) Compensatory enlargement of human atherosclerotic coronary arteries. N Engl J Med 316:1371–1375
21. Yeagle PL (1985) Cholesterol and the cell membrane. Biochim Biophys Acta 822:267–287
22. Tulenko TN, Chen M, Mason PE et al (1998) Physical effects of cholesterol on arterial smooth muscle membranes: evidence of immiscible cholesterol domains and alterations in bilayer width during atherogenesis. J Lipid Res 39:947–956
23. Kolodgie FD, Gold HK, Burke AP et al (2003) Intraplaque hemorrhage and progression of coronary atheroma. N Engl J Med 349:2316–2325
24. Tabas I (2005) Consequences and therapeutic implications of macrophage apoptosis in atherosclerosis: the importance of lesion stage and phagocytic efficiency. Arterioscler Thromb Vasc Biol 25:2255–2264
25. Sluimer JC, Kolodgie FD, Bijnens AP et al (2009) Thin-walled microvessels in human coronary atherosclerotic plaques show incomplete endothelial junctions relevance of compromised structural integrity for intraplaque microvascular leakage. J Am Coll Cardiol 53:1517–1527
26. Zhang Y, Cliff WJ, Schoefl GI et al (1993) Plasma protein insudation as an index of early coronary atherogenesis. Am J Pathol 143:496–506

27. Michel JB, Thaunat O, Houard X et al (2007) Topological determinants and consequences of adventitial responses to arterial wall injury. Arterioscler Thromb Vasc Biol 27:1259–1268
28. Tavora F, Kutys R, Li L et al (2010) Adventitial lymphocytic inflammation in human coronary arteries with intimal atherosclerosis. Cardiovasc Pathol 19:e61–e68
29. Davis GE (1992) The mac-1 and p150,95 beta 2 integrins bind denatured proteins to mediate leukocyte cell-substrate adhesion. Exp Cell Res 200:242–252
30. Finn AV, Nakano M, Polavarapu R et al (2012) Hemoglobin directs macrophage differentiation and prevents foam cell formation in human atherosclerotic plaques. J Am Coll Cardiol 59:166–177
31. Rother RP, Bell L, Hillmen P et al (2005) The clinical sequelae of intravascular hemolysis and extracellular plasma hemoglobin: a novel mechanism of human disease. JAMA 293:1653–1662
32. Boyle JJ, Harrington HA, Piper E et al (2009) Coronary intraplaque hemorrhage evokes a novel atheroprotective macrophage phenotype. Am J Pathol 174:1097–1108
33. Wagener FA, van Beurden HE, von den Hoff JW et al (2003) The heme-heme oxygenase system: a molecular switch in wound healing. Blood 102:521–528
34. Burke AP, Farb A, Malcom GT et al (1997) Coronary risk factors and plaque morphology in men with coronary disease who died suddenly. N Engl J Med 336:1276–1282
35. Kolodgie FD, Burke AP, Farb A et al (2001) The thin-cap fibroatheroma: a type of vulnerable plaque: the major precursor lesion to acute coronary syndromes. Curr Opin Cardiol 16:285–292
36. Burke AP, Farb A, Malcom GT et al (1999) Plaque rupture and sudden death related to exertion in men with coronary artery disease. JAMA 281:921–926
37. Sukhova GK, Schonbeck U, Rabkin E et al (1999) Evidence for increased collagenolysis by interstitial collagenases-1 and -3 in vulnerable human atheromatous plaques. Circulation 99:2503–2509
38. Gijsen FJ, Wentzel JJ, Thury A et al (2008) Strain distribution over plaques in human coronary arteries relates to shear stress. Am J Physiol Heart Circ Physiol 295:H1608–H1614
39. Kolodgie FD, Narula J, Burke AP et al (2000) Localization of apoptotic macrophages at the site of plaque rupture in sudden coronary death. Am J Pathol 157:1259–1268
40. Vengrenyuk Y, Carlier S, Xanthos S et al (2006) A hypothesis for vulnerable plaque rupture due to stress-induced debonding around cellular microcalcifications in thin fibrous caps. Proc Natl Acad Sci USA 103:14678–14683
41. Silvain J, Collet JP, Nagaswami C et al (2011) Composition of coronary thrombus in acute myocardial infarction. J Am Coll Cardiol 57:1359–1367
42. Falk E, Shah PK, Fuster V (1995) Coronary plaque disruption. Circulation 92:657–671
43. van der Wal AC, Becker AE, van der Loos CM et al (1994) Site of intimal rupture or erosion of thrombosed coronary atherosclerotic plaques is characterized by an inflammatory process irrespective of the dominant plaque morphology. Circulation 89:36–44
44. Farb A, Burke AP, Tang AL et al (1996) Coronary plaque erosion without rupture into a lipid core. A frequent cause of coronary thrombosis in sudden coronary death. Circulation 93:1354–1363
45. Kramer MC, van der Wal AC, Koch KT et al (2009) Histopathological features of aspirated thrombi after primary percutaneous coronary intervention in patients with ST-elevation myocardial infarction. PLoS One 4:e5817
46. Kolodgie FD, Burke AP, Farb A et al (2002) Differential accumulation of proteoglycans and hyaluronan in culprit lesions: insights into plaque erosion. Arterioscler Thromb Vasc Biol 22:1642–1648
47. Ferrante G, Nakano M, Prati F et al (2010) High levels of systemic myeloperoxidase are associated with coronary plaque erosion in patients with acute coronary syndromes: a clinicopathological study. Circulation 122:2505–2513
48. Schwartz RS, Burke A, Farb A et al (2009) Microemboli and microvascular obstruction in acute coronary thrombosis and sudden coronary death: relation to epicardial plaque histopathology. J Am Coll Cardiol 54:2167–2173
49. Mann J, Davies MJ (1999) Mechanisms of progression in native coronary artery disease: role of healed plaque disruption. Heart 82:265–268
50. Burke AP, Kolodgie FD, Farb A et al (2001) Healed plaque ruptures and sudden coronary death: evidence that subclinical rupture has a role in plaque progression. Circulation 103:934–940
51. Burke AP, Farb A, Malcom G et al (2001) Effect of menopause on plaque morphologic characteristics in coronary atherosclerosis. Am Heart J 141:S58–S62
52. Burke AP, Taylor A, Farb A et al (2000) Coronary calcification: insights from sudden coronary death victims. Z Kardiol 89(Suppl 2):49–53
53. Watson KE, Abrolat ML, Malone LL et al (1997) Active serum vitamin d levels are inversely correlated with coronary calcification. Circulation 96:1755–1760
54. Keso T, Perola M, Laippala P et al (2001) Polymorphisms within the tumor necrosis factor locus and prevalence of coronary artery disease in middle-aged men. Atherosclerosis 154:691–697
55. Proudfoot D, Shanahan CM (2001) Biology of calcification in vascular cells: intima versus media. Herz 26:245–251
56. Sage AP, Tintut Y, Demer LL (2010) Regulatory mechanisms in vascular calcification. Nat Rev Cardiol 7:528–536
57. Davies MJ, Thomas A (1984) Thrombosis and acute coronary-artery lesions in sudden cardiac ischemic death. N Engl J Med 310:1137–1140
58. El Fawal MA, Berg GA, Wheatley DJ et al (1987) Sudden coronary death in glasgow: nature and frequency of acute coronary lesions. Br Heart J 57:329–335
59. Davies MJ, Bland JM, Hangartner JR et al (1989) Factors influencing the presence or absence of acute coronary artery thrombi in sudden ischaemic death. Eur Heart J 10:203–208
60. Burke AP, Farb A, Malcom GT et al (1998) Effect of risk factors on the mechanism of acute thrombosis and sudden coronary death in women. Circulation 97:2110–2116

Clinical MRA of the Carotid Arteries

3

Michele Anzidei, Beatrice Cavallo Marincola, Fabrizio Boni, and Carlo Catalano

1 Introduction

Atherosclerosis disease, and in particular its coronary and carotid location, is nowadays the major cause of morbidity and mortality in western countries [1, 2]. The development of less invasive techniques such as computed tomography angiography (CTA) and magnetic resonance angiography (MRA) has led to an almost complete replacement of the conventional catheter angiography for imaging of cerebrovascular arteries preserving excellent diagnostic accuracy in the evaluation of grade of stenosis; anyway this technique still holds an important role in the treatment of this pathology (angioplasty and stenting).

Among the benefits of the MRA, the lack of ionizing radiation and the ability to perform angiographic sequences without using contrast medium represents two of many benefits of the MRA technique; anyway, the study performed with contrast medium (contrast-enhanced MR angiography, CE-MRA) reaches higher diagnostic accuracy.

2 Patient Preparation

After signing an informed consent to evaluate any condition that might contraindicate the study of MRA, the patient is asked to remove any metal objects on the body surface. Contraindications to MRA of carotid arteries are general contraindication to perform any MR study: presence of a pacemaker noncompatible with MR, presence of intracranial vascular clip or embolizing material, permanent acoustic or ocular prosthesis, cardiac valves prosthesis noncompatible with MR, or any other material that might be susceptible to electromagnetic field. Patient is positioned supine inside the magnetic field, with the surface bobine on head and neck. If the use of contrast medium is required, it is important to have a superficial venous access of about 20 G, possibly at the level of the right arm. Moreover, in these cases it is mandatory to know the patient's renal function levels (glomerular filtration rate, GFR) of the last 30 days. In fact, the recent discovery of nephrogenic systemic fibrosis (NSF) contraindicates the use of contrast medium in subjects with a GFR < 30 mL/min.

3 Technical Requirements

Technical execution of a MRA study can be potentially performed on any system (0.5–1 T magnet, gradients < 25 mT/m^2), although the actual availability of high field magnet (1.5–3 T; gradients > 30 mT/m^2) allows in the majority of cases to perform MRA studies at the state of the art. In addition, the recent introduction of radiofrequency coils integrated with multichannel technology and the development of parallel imaging acquisition techniques have resulted in a significant reduction in the acquisition time and in an increase of the spatial and contrast resolution: currently an ideal study of carotid MRA provides the use of high field gradient magnets, rapid and integrated coils, and parallel imaging techniques.

4 Examination Techniques

The widespread development of magnetic resonance imaging techniques currently provides a wide range of sequences, coils, and contrast agents for carotid arteries imaging. However, for the execution of this type of study in a clinical contest the techniques that have proven a real indication and demonstrated applicability are essentially two:

M. Anzidei (✉) • B. Cavallo Marincola • F. Boni • C. Catalano
Department of Radiological Sciences, University of Rome,
Viale Regina Elena 324, Rome 00161, Italy
e-mail: Michele.Anzidei@gmail.com;
beatrice.cavallomarincola@gmail.com; fabrizioboni00@libero.it;
carlo.catalano@uniroma1.it

L. Saba et al. (eds.), *Multi-Modality Atherosclerosis Imaging and Diagnosis*,
DOI 10.1007/978-1-4614-7425-8_3,

4.1 Imaging with Time of Flight Sequences

Time of flight (ToF) sequences have the classic structure of gradient-echo pulses and are generally acquired with very short TR (shorter than those of stationary tissues) on planes perpendicular to the direction of blood flow within the studied vessel. The difference in protons spin saturation between stationary tissues and flowing blood contributes to the creation of the difference in signal intensity at the base of the vascular studies using ToF sequences: for each new TR, blood flow carries within the scanning plane protons with desaturated spin; the contrast between the latter and the signal coming from the protons of stationary tissues (completely saturated) creates the angiographic effect also known as "in-flow enhancement". The TR of the sequence must be properly calibrated to achieve the maximum possible signal from the incoming blood flow in the scanning plane; as the TR calibration set on flow velocity, the signal intensity inside the vessels will be dependent on this last parameter. The use of previous additional selective saturation or excitation pulses in the layers adjacent to the vascular structures of interest allows suppression of signal coming from the arterial or venous structures depending on the type of required assessment (arterial or venous studies). ToF sequences can be performed with 2D or 3D acquisitions [3]; the use of 3D scans with thin slabs known as multiple overlapping thin slab acquisitions (MOTSA) produced a substantial increase in spatial resolution and diagnostic accuracy of this approach [4]. Currently the use of ToF sequences for carotid arteries MRA studies has been reduced in favor of the newest and most reliable approaches with the use of contrast medium, mainly due to some important technical limitations including artifacts caused by saturation of the flow in the presence of severe stenosis (evaluation of false vessel occlusions) or in vessels with very tortuous course (overestimation of the degree of stenosis) (Fig. 3.1), motion artifacts due to long acquisition times, and reduced fields of view [5]. ToF sequences are still indicated for the evaluation of the intracranial circulation and carotid imaging in patients with known intolerance or contraindication to paramagnetic contrast agent.

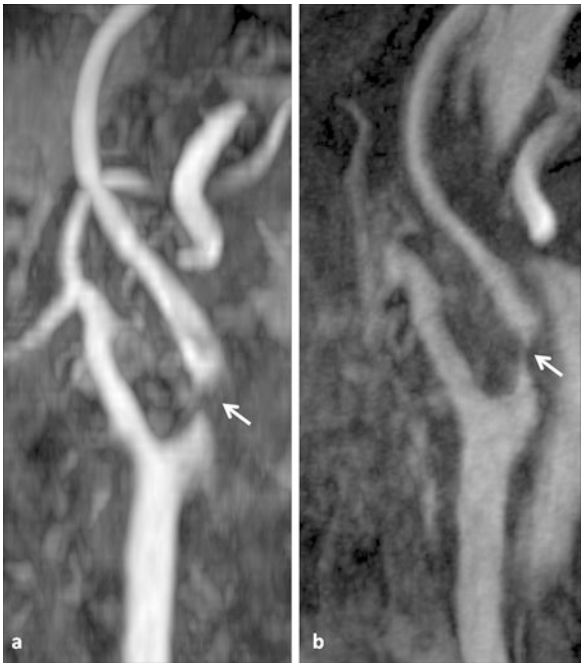

Fig. 3.1 Sixty-one-year-old female with carotid stenosis. In TOF images proton dephasation occurs at the site of stenosis causing intraluminal loss of signal simulating focal occlusion. Contrast-enhanced images demonstrate lumen patency at the site of stenosis, with severe reduction of lumen caliper

4.2 Imaging with 3D T1-Weighted Sequences After Injection of Contrast Medium

Contrast-enhanced MRA techniques are based on the capability of paramagnetic agents (Gd chelates) to reduce the T1 of flowing blood inside the vascular structures in comparison to that of stationary tissues; the main advantage of these techniques is to eliminate the dependence of signal intensity of blood from the blood flow velocity in the vessel (Fig. 3.2). The importance of this feature appears to be more important in small arteries such as carotids, which, if affected by stenosing lesions, may have significant reductions in the flow rate at the level of irregularity of the wall, simulating stenosis, or occlusion in the flow-dependent sequences. The technical and diagnostic success of these studies with contrast medium is based on the conjugation of three parameters: spatial resolution, temporal resolution, and synchronization between image acquisition and contrast agent administration [6]. The study is performed using 3D T1-weighted gradient-echo sequences with spoiler gradient, acquired with low values of TR and FA (in order to optimize the difference in signal intensity between blood and stationary tissue) and low values of TE to minimize T2* effects; the acquisition is performed before and after administration of contrast medium using subtraction techniques to remove the signal of the anatomical extravascular structures and increase image contrast. The setting of scanning parameters should be adjusted to the reduced size of the vascular segments in question, to the relatively large field of view (from aortic arch to the intracranial circulation), and especially to the rapid circulation time of the cervical vessels. Using state-of-the-art equipment, acquisition may be performed with semi-isotropic or isotropic voxel size (maximum 1 mm^3) and a minimum of 384×384 matrix; acquisition time must be optimized for a duration between 14 and 18 s depending

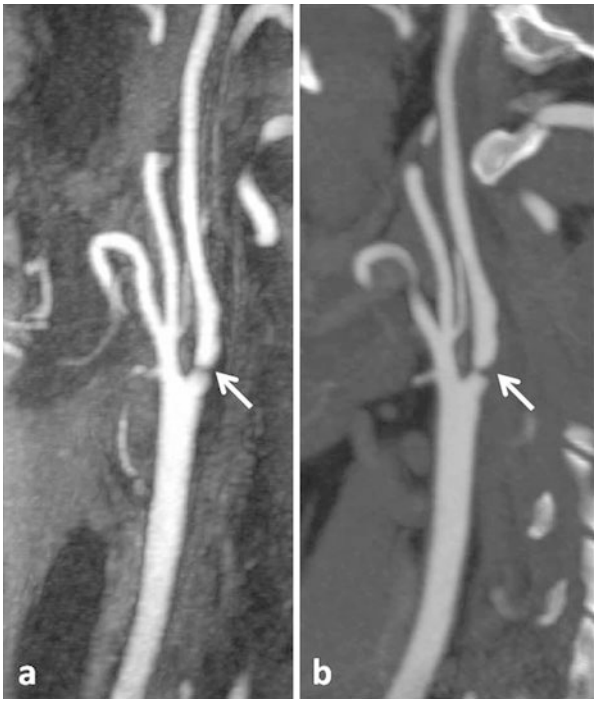

Fig. 3.2 (**a**) Contrast-enhanced MRA performed with 3D T1-weighted sequences after injection of contrast medium shows the presence of a tight stenosis at the base of the internal carotid artery (*arrow*). CTA findings (**b**) are superimposable to that of MRA (*arrow*)

also on the flow speed of contrast medium administration. Synchronization between contrast medium administration and acquisition start is generally set by fluoro-MR bolus-tracking techniques, with multiple low spatial resolution scans acquired at the aortic arch in order to display in real time the arrival of the contrast agent [7]. Contrast administration rate affects both the duration and intensity of peak enhancement: at low flows the rate corresponds to reduced but lasting enhancement, while at high flows it corresponds to greater but shorter enhancement. The use of high relaxivity contrast agent allows low flow administrations with high and prolonged enhancement.

It is very important to combine acquisition parameters and contrast injection protocols with adequate techniques of K-space sampling: the most effective approach is the elliptic-centric sampling [8], through which the central portion of the K-space (containing data on the image contrast resolution) is first sampled using the highest concentration of contrast medium into the vessel, while the peripheral portion (containing data on the spatial resolution) is sampled during more delayed acquisition, where the concentration of the contrast agent begins to decline leading to a progressive loss of signal and contrast resolution within the vascular structures. The integration of all these parameters has been simplified by the introduction of parallel imaging techniques and the use of integrated multichannel coils, whose combined use makes possible the acquisition of sequences with high spatial resolution in significantly reduced times. However, the technical progress in the field of MRA has not remained confined to the equipment and the development of new sequences: thanks to a wide experience in different experimental protocols developed during the past decade, the first contrast agent belonging to the family of compound blood pool has recently been approved and made available for trading. This innovative new class of contrast agents has been designed with the intent of combining profiles of R1 relaxivities higher than those of conventional compounds with specific binding properties to plasma proteins, making possible an extended stay within the vascular bed. These features allow to bring the adaptation of the acquisition protocols beyond the current limits imposed by first-pass imaging which is linked to the MRA (Fig. 3.3): taking advantage of the prolonged vascular enhancement reached during the equilibrium phase of contrast medium, 3D sequences with sub-millimeter voxel can be acquired virtually without time limits, obtaining a spatial resolution equal or even greater than the latest generation multislice CT [9]. Currently the spread of blood-pool compounds is limited and its clinical experience is reduced [10]; anyway, thanks to the potential increase in the quality and in diagnostic accuracy for vascular studies, it is desirable its wide diffusion. Recently, high-resolution sequences acquired during the equilibrium phase have been performed using an interstitial contrast agent (gadobenate dimeglumine) that differs from conventional gadolinium contrast agents because of its interaction with serum albumin. The consequent decreased T1 relaxation time and increased R1 relaxivity of gadobenate dimeglumine are sufficient to permit reliable acquisition of SS images of the carotid vasculature subsequent to routine FP image acquisition [11]. Finally, it cannot be neglected to mention the importance of 4D techniques, or time-resolved imaging, in MRA innovative applications and clinical indications: these techniques, known by commercial acronyms TRICKS (GE), TWIST (Siemens), 4D-TRACK (Philips), DRKS (Toshiba), combine the high spatial resolution of 3D datasets acquired with gradient-echo sequences and the ability to repeatedly examine the same vascular segment in very short time intervals, thus obtaining a dynamic view of contrast medium flowing within the vessels. In carotid MR imaging the application of 4D techniques is very useful in the evaluation of hemodynamic features in the vascular malformations, arteriovenous fistulas, and dissection imaging. Other interesting technical issues in MRA of the carotid arteries have been widely investigated, while remaining mostly confined to the clinical fields of research studies.

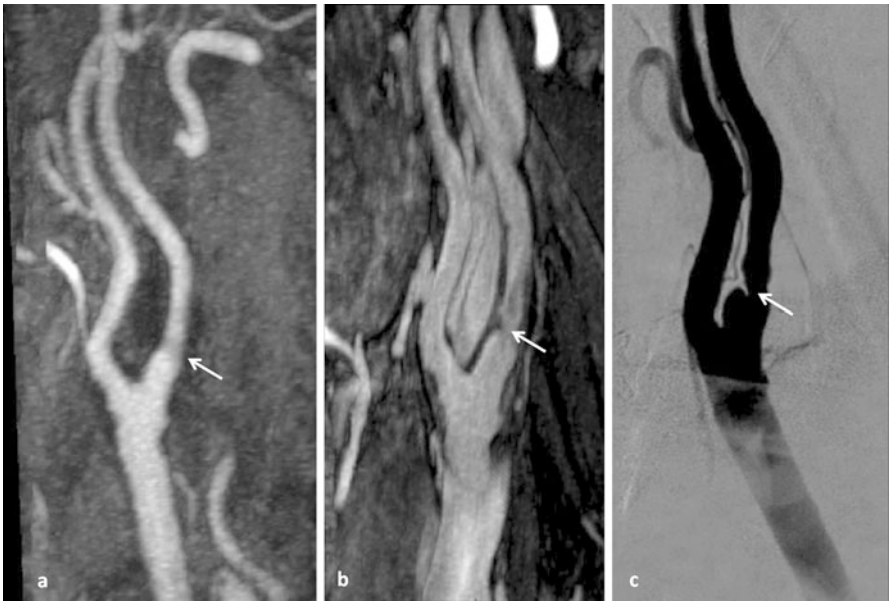

Fig. 3.3 (**a**) Contrast-enhanced MRA shows mild irregularity of the wall without significant stenosis (*arrow*); (**b**) high-resolution sequence acquired during the equilibrium phase shows ulceration of the wall with moderate stenosis (*arrow*); (**c**) DSA confirmed both ulceration of the wall and stenosis (*arrow*)

4.3 Imaging with Phase-Contrast Sequences

Phase-contrast sequences exploit blood protons speed of changing phase that move parallel to the static magnetic field. Through the activation of a pair of bipolar gradients that sequentially diphase and phase again the spins during the acquisition, it is possible to obtain images where pixels signal intensity directly corresponds to the moving speed values inside the anatomical segment in question: by changing the velocity encoding parameters (velocity encoding—VENC) it is possible to have a selective imaging of arterial (VENC factor > 40 cm/s) or venous (VENC factor <20 cm/s) vessels, without any signal derived from stationary tissues, whose protons remain static. In carotid imaging, the application of phase-contrast sequences has limited utility, mainly for long acquisition times and low immediacy in image interpretation in clinical and surgical fields; however, their application has been described in the evaluation of carotid artery stenosis [12] but also in the study of vascular malformations, aneurysms, and dissections, in which the morphological alteration of the vessel wall is frequently associated with changes of the blood flow velocity and flow direction.

4.4 Imaging of Atherosclerotic Plaque with High-Resolution Sequences

Some important histopathological studies have demonstrated a strong correlation between morphostructural changes in carotid atherosclerotic plaques and symptomatic cerebrovascular thromboembolic events [13]: the presence of irregularities of the plaque surface, ulcers, the prevalence of soft component instead of the calcified one, and hemorrhages inside the plaque were described as significant risk factors, independent from the degree of vascular stenosis in facilitating ischemic events (Fig. 3.4). The study of such alterations, also known as "vulnerable plaque", was proposed and realized with MR technology [14]. The dedicated plaque imaging is not an angiographic study, but rather a morphological evaluation (T1, T2 also with superparamagnetic contrast medium) using very high spatial resolution sequences that in the future could join the conventional MRA: currently the clinical use of this approach is limited because of the technical requirements that are not available on a large scale (high field magnets, dedicated surface coils, and endovascular micro-coils) and of the long acquisition times, often not easily tolerated by patients clinical conditions.

5 Post-processing

Digital imaging, 3D datasets, and post-processing techniques have become routinely using tools in diagnostic radiology: almost all the methods (most of all CT and MRI) use these techniques to speed up and simplify radiologist work. In MRI post-processing techniques are very useful in vascular imaging, even with the recent development of acquisition protocols that allow obtaining images with isotropic voxels.

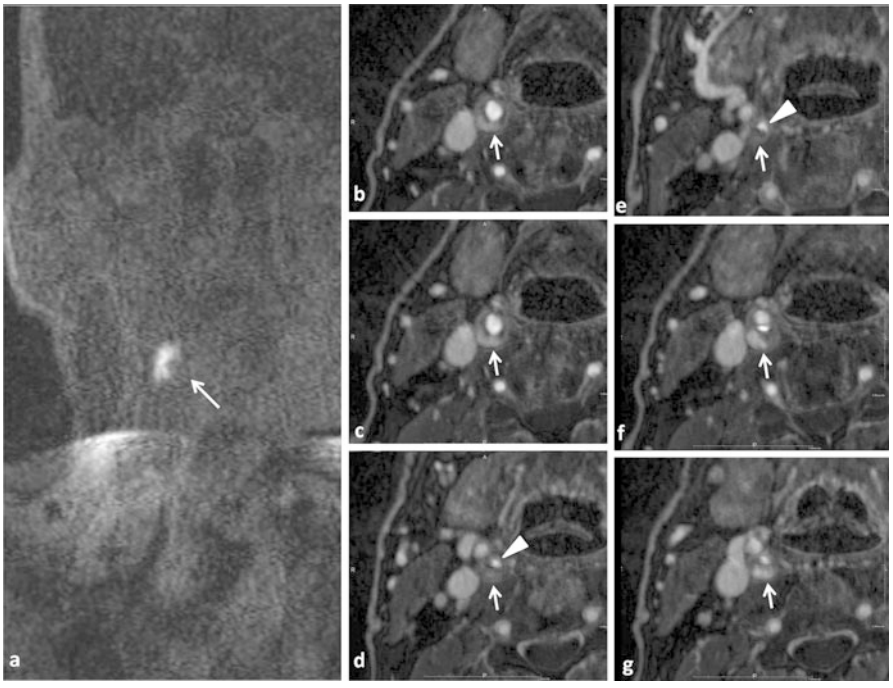

Fig. 3.4 (**a**) Pre-contrast T1-weighted images show the presence of a hyperintense area in the right cervical region (*arrow*); (**b**–**g**) high-resolution sequences acquired at the equilibrium phase demonstrate the presence of a severe stenosis of the right internal carotid artery (*arrowheads* in **d** and **e**); the enhancement of the soft component (*arrows*) demonstrates the presence of an hemorrhagic and inflammatory component (*arrows*)

Compared to CT, the possibilities and perspectives of application in MRI seem small, but their importance remains high to reduce reporting times and provide immediate and easily interpretable images to clinicians and surgeons. The available approaches are generally divided into:

– Section techniques (MPR, curved-MPR, thick-MPR, c-MPR): multiplanar reformatting techniques (MPR) use 3D datasets acquired on a single plane (i.e., coronal) to reproduce two-dimensional images on different orthogonal planes (i.e., axial or sagittal) or curved planes (curved-MPR, in which the entire vessel is "rolled out" on the longitudinal axis) (Fig. 3.5). Generally, the slice thickness obtained with this reconstruction technique does not exceed that of the native slices of the dataset; anyway it is possible to get thicker slices using a technique with partially projective characteristics (thick-MPR). In carotid imaging, section techniques are very important not much in atherosclerotic lesion identification or in panoramic assessment of vascular structures, but especially in small wall irregularities characterization and in the exact evaluation of stenosis degree, in order to have an accurate surgical planning [15].
– Projective techniques (MIP and thin-MIP): MIP images are obtained by projecting all the voxels contained within the dataset having the higher signal intensity on the same plan (approximately 10 % of the total information), excluding all others voxels. The optimal application of MIP images is obtained when the structure in question shows greater signal intensity compared to tissues in the background (MRA, MRCP). The main advantage of MIP techniques in carotid MRA is to provide panoramic views and rapid interpretation of the images (simultaneous display extending from aortic arch to the intracranial circulation), but losing fine details (i.e., small wall irregularities, small ulcers) that are masked by voxels with greater intensity.

  For this type of evaluations the use of thin-MIP is preferable; similar to the thick-MPR, this technique projected on the same plane data obtained from a limited number of voxels (i.e., those contained in 5, 10, or 15 mm slice thickness) without hide background structures and allowing the evaluation of small changes in the vessel wall. Before the widespread use of software, 3D reconstruction console, and the advent of high-resolution acquisitions with isotropic or semi-isotropic voxels, MIP images were used to measure the degree of stenosis; currently this approach has been replaced by the evaluation with MPR and its variants, for greater accuracy in measurements [16].
– Surface techniques and volume techniques (SSD and VR): these techniques use 3D data segmentation algorithms and artificial light and color sources (only in VR) based on signal intensity or attenuation values for each voxel. Compared with projective techniques, SSD and VR introduce significant innovation of the artificial light source: this factor creates in the observer the perception of the sense of depth and three dimensionality that is almost completely

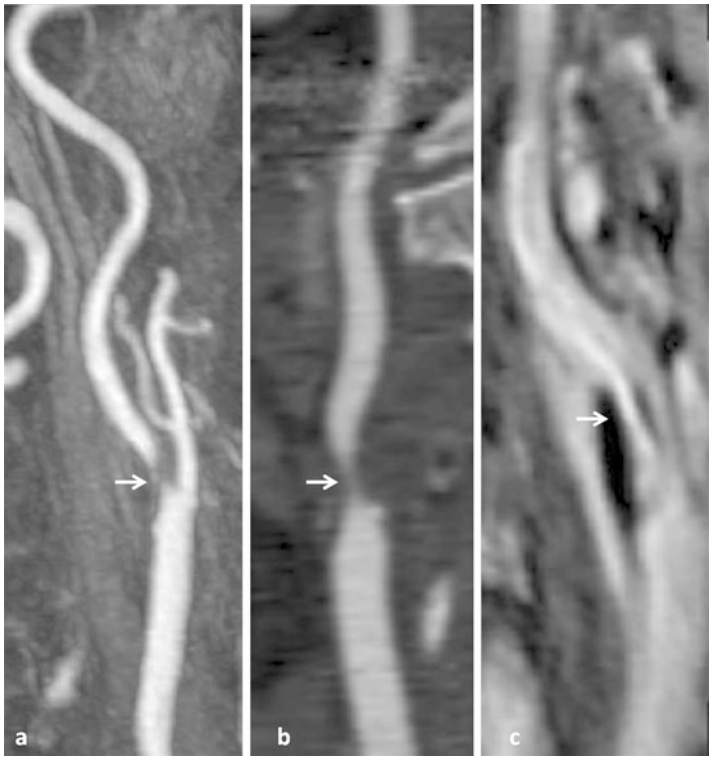

Fig. 3.5 (**a**) Contrast-enhanced MRA shows a long plaque localized at carotid bifurcation causing severe stenosis at the origin of the internal carotid artery; (**b**) curved-MPR allows to roll out the entire vessel on its longitudinal axis and visualize the stenosis from different angles (*arrow*); (**c**) high-resolution sequence acquired during the equilibrium phase better demonstrates plaque morphology and stenosis degree (*arrow*)

absent in MIP images. The applications of SSD and VR techniques in conventional MRI and in particular in MRA are usually reduced and almost completely replaced by MIP techniques: such restriction in the use is mainly dictated by the most difficult segmentation and color and brightness values assignment in MRI than CT.

6 Current Role of MRA in the Diagnosis of Carotid Artery Pathologies

Since the advent of multidetector technology, CT angiography has been a step forward in the study of vascular structures, especially in districts such as the carotid arteries, where the rapid circulation time and the small size of the vessels require a faster and accurate imaging in anatomical detail. Currently, progress obtained in the field of structural technologies (magnets, gradients), of the coils (multichannel technology, parallel imaging) and of the contrast media (compounds with high relaxivity, blood-pool agents) have made the MRA such a valid alternative in the study of carotid disease. Today the MRA of the carotid circulation has different indications, advantages and disadvantages in relation to different clinical conditions in analysis, beyond the steno-obstructive disease alone.

6.1 Steno-Obstructive Atherosclerotic Disease

Steno-obstructive atherosclerotic disease of carotid arteries is now one of the main causes of ischemic cerebrovascular events with adverse clinical outcome. According to the criteria of the North American Symptomatic Carotid Endoarterectomy Trial Collaborators (NASCET), the thromboendoarterectomy can provide a significant clinical benefit in patients with carotid stenosis > 70 % and in selected cases with stenosis grade between 50 and 69 % [17]. Therefore it's obvious that the adequate evaluation of stenosis degree and the identification of additional independent risk factors, such as irregularities or ulcerations on the plaque surface are essential for proper therapeutic planning. Conventional angiography or digital subtraction angiography technique (DSA) is the current gold standard for the evaluation of stenosis degree; however because of the costs and procedure risks, the diagnostic role of DSA has been largely reduced in favor of noninvasive techniques such as CTA and MRA. The rapid development of multislice CT technology has made possible a wider diffusion and clinical application of angiographic studies, which have been long predominant in applications for the evaluation of carotid stenosis. In recent years, the advances in MRI and in particular

the implementation of dedicated protocols for angiographic studies have made contrast-enhanced MRA nearly equivalent to CTA for diagnostic accuracy in the carotid vascular district [18]: technical limitations such as flow-related artifacts, conflict between spatial and temporal resolution, long-term examinations, and reduced fields of view have been substantially overcome by the spread and application of technologies at the state of the art. A wide panorama of recent comparative studies with DSA shows that the assessment of steno-obstructive carotid disease using contrast-enhanced MRA is superior to ToF-MR and can be considered a non-invasive diagnostic tool as reliable as CTA, with sensitivity and specificity values over 90 % for clinically significant stenosis (>70 %) and with a perfect correlation with DSA in differentiating obstruction from pseudo-obstruction [19–22]. A moderate propendency of contrast-enhanced MRA has been documented in overestimating the stenosis in comparison to DSA, initially related to acquisition technique characteristics (non-isotropic voxel, spin dephasing artifacts, magnetic susceptibility artifacts). The recent introduction of rotational angiography, a technique which can acquire three-dimensional images (in contrast to DSA), has shown that conventional angiographic studies may underestimate the degree of carotid stenosis [23]. From a clinical and surgical point of view, it is therefore demonstrated that the MRA shows in almost all cases vascular stenosis requiring surgical treatment, with a modest propendency to overtreatment of stenosis otherwise manageable: in patient management is then mandatory taking into account of potential risks due to unnecessary treatment (and therefore related to surgical or endovascular procedure), compared to a non-performed treatment (and then related to disease progression). The study of atherosclerotic plaque morphology and tandem lesions represents other parameters of preoperative assessment adequately quantified with MRA, allowing the prior exclusion from treatment protocols of patients with risk factors that are not compatible with the procedure. To date, therefore, MRA can be used in preoperative planning for stenosis measurement, differentiation between occlusion and pre-occlusion, identification of tandem lesions, and definition of plaque morphology; diagnostic questions to which it is not possible to provide answers are represented by the assessment of plaque composition (particularly with regard to the presence of calcification), hemodynamic effect of stenosis, and quantification of compensating cerebral circulation. The gradual spread of advanced MR techniques such as a dedicated plaque evaluation and 4D imaging will enable in the future to add additional diagnostic value to this technique, which currently has reached diagnostic accuracy levels equivalent to those of CT.

6.2 Steno-Obstructive Disease Caused by Non-atherosclerotic Systemic Pathologies

Carotid steno-obstructive disease due to non-atherosclerotic causes, although less frequent, represents an important application area of MRA techniques [24]. Among the most common causes of non-atherosclerotic steno-obstructive disorders, acute inflammatory systemic disease and post-actinic and dysplastic arteriopathies on a post-vasculitic base are included. Among the first, the most common form is represented by Takayasu arteritis, an autoimmune inflammatory disease involving the large arteries, particularly the ascending aorta and supra-aortic vessels. In these patients carotid involvement is common, with symptoms that can mimic the presence of steno-obstructive lesions without intimal alterations: the pathologic pattern is characterized by a prevalent granulomatous involvement of the outer layers of the wall with the development of an inflammatory tissue and a progressive reduction of the residual lumen. In this context MRA allows an optimal evaluation of arterial involvement and caliper reduction [25], allowing also the execution of dedicated sequences (inversion recovery, T2 weighted with fat saturation) in order to study the degree of wall inflammation; an additional data is also represented by the possibility of acquiring repeated sequences after contrast medium administration (preferably made with blood-pool agents) showing a potential enhancement of the wall related to the inflammatory status of the vasa vasorum (Fig. 3.6). Another common form of non-atherosclerotic arterial disease is represented by post-actinic changes, common after radiation therapy (greater incidence 10 years after treatment) in oropharynx and upper airway cancers, represented by long stenosis; even in these cases MRA represents an excellent choice for assessing the degree and extent of lumen reduction of the vessels. Fibromuscular dysplasia is another important cause of carotid wall alteration resulting from vasculitic disease; this disease involves medium caliper arteries and occurs in young women, mainly affecting renal arteries and secondly carotid vessels, which may facilitate the onset of aneurysms and dissections. Carotid involvement, more often bilateral, occurs predominantly in the middle part of the internal carotid artery, with alternate stenosis and small dilatations, giving the vessel a typical appearance.

6.3 Trauma, Dissections, Aneurysms

Cervico-facial injuries caused by deceleration and impact or penetrating injury are another common cause predisposing

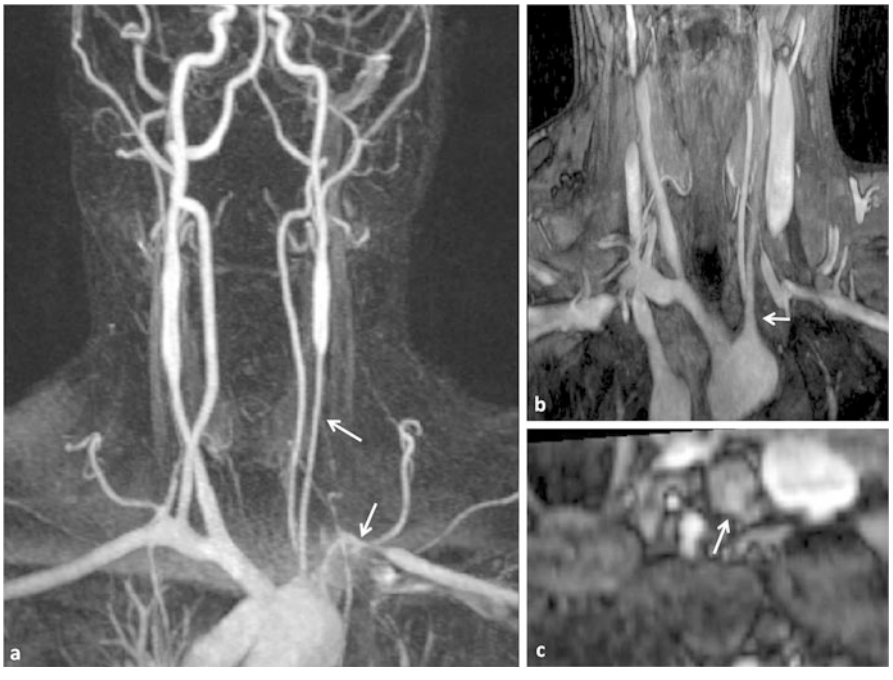

Fig. 3.6 Seventeen-year-old male with a barely palpable left radial pulse. (**a**) Contrast-enhanced MR angiography shows a severe caliper reduction of the proximal portion of left common carotid and subclavian artery (*arrows*). High-resolution sequences acquired during the equilibrium phase of contrast agent demonstrate the presence of an enhancing inflammatory tissue surrounding these vessels (*arrows*) and causing the stenosis. The final diagnosis was Takayasu arteritis

to the development of carotid disease. If in the presence of trauma from penetrating injury it is possible the onset of aberrant communications between arterial and venous vascular structures and the consequent development of fistulas, in the first two cases the intima involvement is more frequent, resulting in occurrence of intramural hematoma and aortic dissection, or structural failure of the wall with the development of pseudoaneurysm. In the evaluation of intramural hematoma, which represent an early and potentially evolutionary state of the dissection, MRA is able to highlight the location and extent of the reduction in size of the perfused vascular lumen determined from hematoma with the classical crescent image (the overall size of the vessel will be increased in comparison to the contralateral); however for a precise characterization is essential the integration with conventional MR sequences, able to highlight and differentiate intraparietal hemorrhagic extravasation (low signal in acute phase in both T1- and T2-weighted sequences, high signal with conversion of the content in methemoglobin). In real dissections a good assessment of blood flow and a differentiation between true and false lumen can be obtained with both conventional contrast-enhanced MRA and alternative techniques (flow-dependent imaging and phase-contrast) [26]; currently the availability of the acquisition with 4D approach allows real-time evaluation of the differences in speed and volume of blood flow along the vascular segment dissected (Fig. 3.7). The formation of aneurysms and pseudoaneurysms in the carotid district is another common consequence of traumatic events, with a small percentage of these changes that have post-fungal or vasculitis origin; in these pathologies, the study MRA is able to ensure an optimal assessment of the vascular segment involved, allowing accurate planning in view of therapy, whether surgical or endovascular. The ideal approach for the study of aneurysms, mainly because of intraluminal turbulent flow, is represented by imaging with contrast medium and evaluation on MPR reconstruction or axial scans acquired after the dynamic examination for optimal identification of possible wall thrombotic appositions.

6.4 Arteriovenous Fistula, Vascular Neoplasms, and Vascular Malformations

One area in which the role of MRA is still in transition and not yet fully defined is one that concerns the study of fistulas, vascular malformations, and tumors (Figs. 3.8 and 3.9) [27, 28]. In this clinical setting appears to be more easily found on the morphological data the possibility of dynamic imaging, capable to provide immediate information acquired in real time on the characteristics of blood flow and on vascular composition of lesions; in cases treated with endovascular approach it is of great importance the

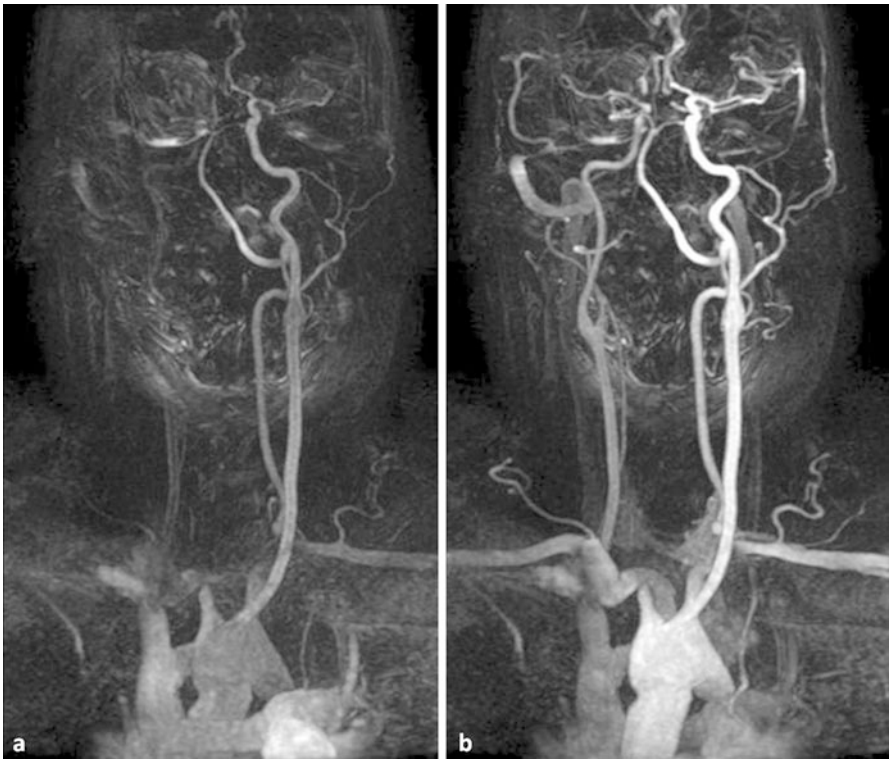

Fig. 3.7 Patient with brachiocephalic trunk dissection: (**a**, **b**) contrast-enhanced MRA performed with time-resolved sequences demonstrates the presence of asymmetric circulation between right and left carotid arteries, due to the origin of the right common carotid from the false lumen

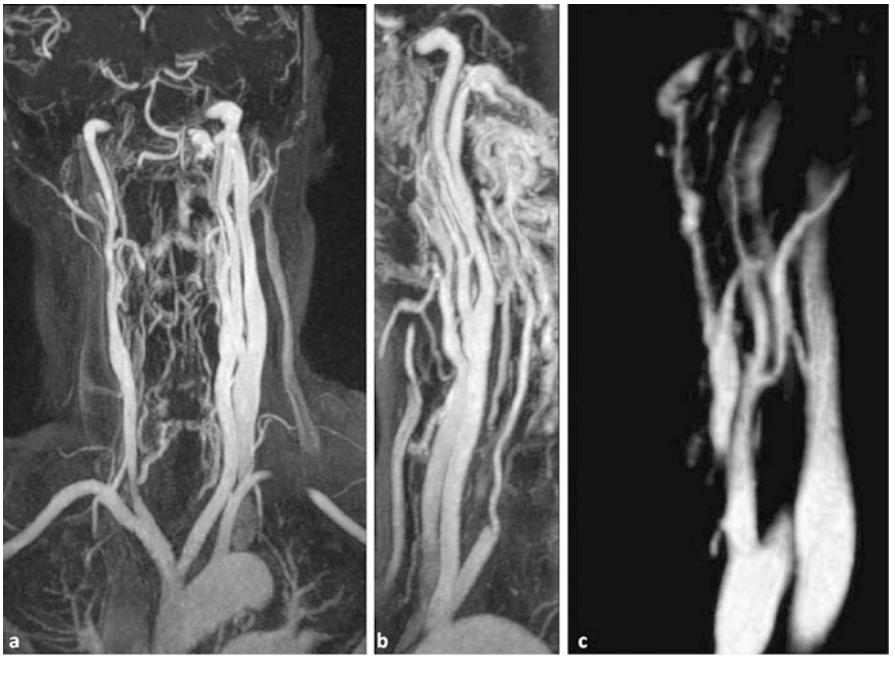

Fig. 3.8 Conventional flash 3D T1 sequences acquired during the arterial phase show an early enhancement of the left venous structures (**a**). Sagittal MIP reconstruction demonstrates the presence of an arteriovenous fistula between external carotid artery and internal jugular vein (**b**). (**c**) VR reconstruction

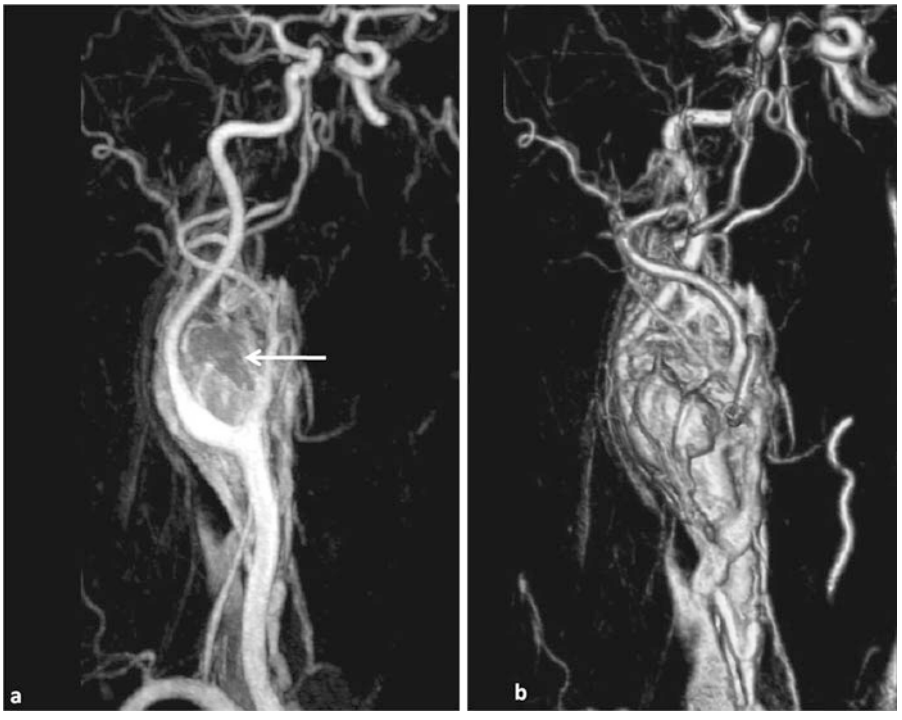

Fig. 3.9 Fifty-six-year-old male with right cervical palpable mass. (**a**) Contrast-enhanced MRA showed the presence of a vascular, well-defined mass, localized at the level of carotid bifurcation that separates internal from external carotid artery (*arrow*). (**b**) VR reconstruction of the same image. The final diagnosis was chemodectoma

possibility to differentiate arterial and venous structures of small size and to identify the so-called "arterial feeders," the arterial tributaries that support the flow in most of these pathologies. In this context, the prospects offered by the different 4D approaches appear as a promising alternative compared to conventional angiography and the use of the new blood-pool contrast agents would allow a diagnostic approach not only effective in terms of functional evaluation, but also extremely accurate in anatomical detail available in high-resolution sequences.

References

1. Reddy KS, Yusuf S (1998) Emerging epidemic of cardiovascular disease in developing countries. Circulation 97:597–601
2. McNeill AM, Rosamond WD, Girman CJ, Golden SH, Schmidt MI, East HE, Ballantyne CM, Heiss G (2005) The metabolic syndrome and 11-year risk of incident cardiovascular disease in the atherosclerosis risk in communities study. Diabetes Care 28(2):385–390
3. Willig DS, Turski PA, Frayne R, Graves VB, Korosec FR, Swan JS, Mistretta CA, Grist TM (1998) Contrast-enhanced 3D MR DSA of the carotid artery bifurcation: preliminary study of comparison with unenhanced 2D and 3D time-of-flight MR angiography. Radiology 208(2):447–451
4. De Marco JK, Nesbit GM, Wesbey GE, Richardson D (1994) Prospective evaluation of extracranial carotid stenosis: MR angiography with maximum-intensity projections and multiplanar reformation compared with conventional angiography. AJR Am J Roentgenol 163(5):1205–1212
5. Mitra D, Connolly D, Jenkins S, English P, Birchall D, Mandel C, Shrikanth K, Gregson B, Gholkar A (2006) Comparison of image quality, diagnostic confidence and interobserver variability in contrast enhanced MR angiography and 2D time of flight angiography in evaluation of carotid stenosis. Br J Radiol 79(939):201–207
6. Thurnher S (2005) MRA of the carotid arteries. Eur Radiol 15(Suppl 5):E11–E16
7. Huston J 3rd, Fain SB, Riederer SJ, Wilman AH, Bernstein MA, Busse RF (1999) Carotid arteries: maximizing arterial to venous contrast in fluoroscopically triggered contrast-enhanced MR angiography with elliptic centric view ordering. Radiology 211(1):265–273
8. Huston J 3rd, Fain SB, Wald JT, Luetmer PH, Rydberg CH, Covarrubias DJ, Riederer SJ, Bernstein MA, Brown RD, Meyer FB, Bower TC, Schleck CD (2001) Carotid artery: elliptic centric contrast-enhanced MR angiography compared with conventional angiography. Radiology 218(1):138–143
9. Essig M, Nikolaou K, Meaney JF (2007) Magnetic resonance angiography of the head and neck vessels. Eur Radiol 17(Suppl 2):B30–B37, Review
10. Nikolaou K, Kramer H, Grosse C, Clevert D, Dietrich O, Hartmann M, Chamberlin P, Assmann S, Reiser MF, Schoenberg SO (2006) High-spatial-resolution multistation MR angiography with parallel imaging and blood pool contrast agent: initial experience. Radiology 241(3):861–872, Epub 2006 Oct 10
11. Anzidei M, Napoli A, Marincola BC, Kirchin MA, Neira C, Geiger D, Zaccagna F, Catalano C, Passariello R (2009) High-resolution steady state magnetic resonance angiography of the carotid arteries: are intravascular agents necessary?: feasibility and preliminary experience with gadobenate dimeglumine. Invest Radiol 44(12):784–792

12. Vanninen RL, Manninen HI, Partanen PL, Vainio PA, Soimakallio S (1995) Carotid artery stenosis: clinical efficacy of MR phase-contrast flow quantification as an adjunct to MR angiography. Radiology 194(2):459–467
13. Mathiesen EB, Bonaa KH, Joakimsen O (2001) Echolucent plaques are associated with high risk of ischemic cerebrovascular events in carotid stenosis: the Tromso study. Circulation 103:2171–2175
14. Yuan C, Mitsumori LM, Beach KW, Maravilla KR (2001) Carotid atherosclerotic plaque: noninvasive MR characterization and identification of vulnerable lesions. Radiology 221(2):285–299, Review
15. Lell M, Fellner C, Baum U, Hothorn T, Steiner R, Lang W, Bautz W, Fellner FA (2007) Evaluation of carotid artery stenosis with multisection CT and MR imaging: influence of imaging modality and postprocessing. AJNR Am J Neuroradiol 28(1):104–110
16. Layton KF, Huston J 3rd, Cloft HJ, Kaufmann TJ, Krecke KN, Kallmes DF (2007) Specificity of MR angiography as a confirmatory test for carotid artery stenosis: is it valid? AJR Am J Roentgenol 188(4):1114–1116
17. North American Symptomatic Carotid Endarterectomy Trial (NASCET) Collaborators (1991) Beneficial effect of carotid endarterectomy in symptomatic patients with high-grade carotid stenosis. N Engl J Med 325(7):445–453
18. Alvarez-Linera J, Benito-León J, Escribano J, Campollo J, Gesto R (2003) Prospective evaluation of carotid artery stenosis: elliptic centric contrast-enhanced MR angiography and spiral CT angiography compared with digital subtraction angiography. AJNR Am J Neuroradiol 24(5):1012–1019
19. Borisch I, Horn M, Butz B et al (2003) Preoperative evaluation of carotid artery stenosis: comparison of contrast-enhanced MR angiography and duplex sonography with digital subtraction angiography. AJNR Am J Neuroradiol 24(6):1117–1122
20. Nederkoorn PJ, van der Graaf Y, Hunink MG (2003) Duplex ultrasound and magnetic resonance angiography comparedwith digital subtraction angiography in carotid artery stenosis: a systematic review. Stroke 34(5):1324–1332
21. Lenhart M, Framme N, Volk M et al (2002) Time-resolved contrast enhanced magnetic resonance angiography of the carotid arteries: diagnostic accuracy and inter-observer variability compared with selective catheter angiography. Invest Radiol 37(10): 535–541
22. U-King-Im JM, Trivedi RA, Graves MJ et al (2004) Contrast-enhanced MR angiography for carotid disease: diagnostic and potential clinical impact. Neurology 62(8):1282–1290
23. Anzalone N, Scomazzoni F, Castellano R, Strada L, Righi C, Politi LS, Kirchin MA, Chiesa R, Scotti G (2005) Carotid artery stenosis: intraindividual correlations of 3D time-of-flight MR angiography, contrast-enhanced MR angiography, conventional DSA, and rotational angiography for detection and grading. Radiology 236(1):204–213, Epub 2005 Jun 13
24. Lombardi M, Bartolozzi C (2005) Magnetic resonance imaging of the heart and vessels. Springer, Berlin, pp 136–141, cap. 6
25. Cantú C, Pineda C, Barinagarrementeria F, Salgado P, Gurza A, de Pablo P, Espinosa R, Martínez-Lavín M (2000) Noninvasive cerebrovascular assessment of Takayasu arteritis. Stroke 31(9):2197–2202
26. Yang CW, Carr JC, Futterer SF, Morasch MD, Yang BP, Shors SM, Finn JP (2005) Contrast-enhanced MR angiography of the carotid and vertebrobasilar circulations. AJNR Am J Neuroradiol 26(8):2095–2101
27. van den Berg R, Schepers A, de Bruïne FT, Liauw L, Mertens BJ, van der Mey AG, van Buchem MA (2004) The value of MR angiography techniques in the detection of head and neck paragangliomas. Eur J Radiol 52(3):240–245
28. Vattoth S, Cherian J, Pandey T (2007) Magnetic resonance angiographic demonstration of carotid-cavernous fistula using elliptical centric time resolved imaging of contrast kinetics (EC-TRICKS). Magn Reson Imaging 25(8):1227–1231, Epub 2007 Apr 18

Quantitative MR Analysis for the Assessment of Carotid Atherosclerosis

4

Andreas Schindler and Tobias Saam

Abbreviations

bb-MRI	Black-blood magnetic resonance imaging
CNR	Contrast-to-noise ratio
DCE	Dynamic contrast enhanced
DIR	Double inversion recovery
FC	Fibrous cap
ICC	Intraclass correlation coefficient
IOSB	Inflow/outflow saturation band
IPH	Intraplaque hemorrhage
IS	Inflow saturation
LR/NC	Lipid-rich/necrotic core
MACE	Major cardiovascular or cerebrovascular event
MP-RAGE	Magnetization-prepared rapid acquisition gradient echo
MSDE	Motion-sensitized driven equilibrium
NWI	Normalized wall index
PWS	Plaque wall stress
REX-DIR	Rapid extended coverage double inversion recovery
SNR	Signal-to-noise ratio
TI	Time of inversion
TOF	Time of flight
USPIO	Ultrasmall superparamagnetic iron oxide
WSS	Wall shear stress

1 Introduction

Atherosclerotic disease accounts for approximately 25 % of ischemic strokes and for the majority of myocardial infarctions and sudden cardiac deaths. Despite major advances in treatment ofatherosclerosis, a larger percentage of victims of the disease who are apparently healthy die without prior symptoms [1]. Since luminal obstruction is rather a feature of late-stage atherosclerosis than a basic requirement for ischemic symptoms, it is generally accepted that knowledge of the degree of luminal stenosis alone is insufficient to predict a plaque's vulnerability. Thus the concept of the "vulnerable plaque" has been introduced. "Vulnerable plaques" are atherosclerotic plaques which have a high likelihood to cause thrombotic complications, such as myocardial infarction or stroke. Plaques which tend to progress rapidly are also considered to be "vulnerable." A classification for clinical as well as pathological evaluation of vulnerable plaques was recently put forward, which proposed five major and five minor criteria to define vulnerable plaques [2, 3]. These plaque features were based on studies of coronary arteries and included thin fibrous caps (FC) with large lipid-rich/necrotic cores (LR/NC), active inflammation (including infiltration of inflammatory cells, and neovascularization), fissured plaque, stenosis >90 %, endothelial denudation with or without superficial platelet aggregation and fibrin deposition, endothelial dysfunction, calcified nodules, intraplaque hemorrhage (IPH), glistening yellow plaques (on angioscopy), and outward remodeling. Rupture of the thin fibrous cap results in exposure of the underlying thrombogenic LR/NC to the flowing blood and may cause thrombus and/or emboli formation with severe clinical consequences.

The challenge for screening modalities and diagnostic methods is to **identify** high-risk patients with vulnerable plaques, before the event occurs. In order to do so imaging methods should be able to identify and **quantify** the main components of atherosclerotic plaques. Noninvasive black-blood magnetic resonance imaging (bb-MRI) has unique potential to identify the key features of the vulnerable plaque [4]. BB-MRI is well suited for this role because it is non-invasive, does not involve ionizing radiation, enables the visualization of the vessel lumen and wall, and can be repeated serially. The ability to measure the plaque burden as well as the plaque components (e.g., LR/NC, IPH, FC) makes

A. Schindler • T. Saam (✉)
Department of Clinical Radiology, University of Munich,
Pettenkoferstr. 8a, 80336 München, Germany
e-mail: Tobias.Saam@med.lmu.de

L. Saba et al. (eds.), *Multi-Modality Atherosclerosis Imaging and Diagnosis*,
DOI 10.1007/978-1-4614-7425-8_4, © Springer Science+Business Media, LLC 2014

bb-MRI a suitable tool to **track progression or regression** of atherosclerosis. Atherosclerosis is a chronic systemic inflammatory disease of the arterial blood vessels. Thus, bb-MRI of the easily accessible carotid arteries can serve as a representative "window" allowing assessment of the systemic atherosclerotic load. This potential enables studies that are aimed at the **understanding of plaque development** and makes it a unique approach since histology, the gold standard, can only depict wall characteristics at one point in time. Furthermore, as surgery is only performed in stenotic symptomatic and highly stenotic asymptomatic vessels, histologic information about the early stages of atherosclerosis is difficult to obtain. Additionally bb-MR imaging of the carotids enables the identification of risk factors for plaque development, such as IPH. In a next step, this knowledge can be applied to **stratify** the risk of plaque-related events in asymptomatic patients. Based on these findings patients may be screened and assigned to the best suited individual therapy.

This book chapter will discuss the capabilities of bb-MRI for quantitative assessment of the composition and morphology of atherosclerotic lesions. Technical requirements, such as hardware, software, and sequence considerations, will be discussed. Studies, which evaluated the accuracy and reproducibility of carotid bb-MRI, will be shown. In addition, clinical studies will be shown which used bb-MRI to compare symptomatic and asymptomatic plaques, to study the natural history of atherosclerosis, and to evaluate the effect of anti-atherosclerotic drugs on the regression/progression of atherosclerosis.

2 Technical Considerations

2.1 Hardware

2.1.1 MRI Scanner

Most imaging of the vessel wall by MRI has been performed by 1.5 T scanners. Recently, 3.0 T scanners and their resulting high-resolution images have opened the field of vascular imaging to new potentials. These new scanners increase resolution and image quality. At the same time, the expected gain in image signal-to-noise ratio (SNR) at 3.0 T may be compromised due to increased T1 relaxation times. A recent study showed that wall SNR and lumen/wall contrast-to-noise ratio (CNR) significantly increased ($P < 0.001$) at 3.0 T with a 1.5-fold gain for T1-weighted images and a 1.7/1.8-fold gain for PD/T2-weighted images compared to 1.5 T. Quantitative plaque measurements of lumen and wall areas demonstrated good agreement between 1.5 and 3.0 T MRI with no significant bias ($P > 0.5$), a coefficient of variation of <10 %, and intraclass correlation coefficient (ICC) of >0.95 [5]. Another study [6] showed signal gains at 3.0 T relative to 1.5 T for carotid artery wall SNR of 223 % and wall lumen CNR of 255 % in all sequences ($P < 0.025$). T1-weighted (T1w) inflow/outflow saturation band (IOSB) and rapid extended coverage double inversion recovery (REX-DIR) were found to have different levels of SNR and CNR ($P < 0.05$) with IOSB values observed to be larger. While these variations can be resultant of different coil designs, pulse sequences, and contrast weightings, even the most conservative estimates (1.4–1.6 times) provide high potential for improved image resolution and/or shorter scan time.

A study by Underhill et al. [7] compared the interpretation and quantification of carotid vessel wall morphology and plaque composition at 1.5 T with those at 3.0 T MRI in 20 subjects with 16–79 % carotid stenosis at duplex ultrasonography. There was a strong level of agreement between field strengths for all morphologic variables, with intraclass correlation coefficients ranging from 0.88 to 0.96. Agreement in the identification of presence or absence of plaque components was very good for calcification ($\kappa = 0.72$), LR/NC ($\kappa = 0.73$), and hemorrhage ($\kappa = 0.66$). However, the visualization of hemorrhage was greater at 1.5 T than at 3.0 T (14.7 % vs. 7.8 %, $P < 0.001$) and calcifications measured significantly ($P = 0.03$) larger at 3.0 T. The authors concluded that at higher field strengths, the increased susceptibility of calcification and paramagnetic ferric iron in hemorrhage may alter quantification and/or detection. Nevertheless, imaging criteria at 1.5 T for carotid vessel wall interpretation are applicable at 3.0 T. Additionally Kerwin et al. investigated the impact of different field strengths on determining plaque composition with an automatic classifier and found the automated classification results of both 1.5 and 3.0 T to produce highly similar results, when using the identical algorithm [8].

2.1.2 Carotid Coils

MR phased-array (PA) surface coil techniques have been used in a variety of vascular beds and have been proven to be effective in improving the signal-to-noise ratio (SNR) in carotid arteries [9]. The carotid arteries are relatively large, superficial, and stationary vessels and therefore well suited for high-resolution MR imaging with a phased-array coil assembly consisting of several adjacent small surface coils that collect data simultaneously. Hayes et al. developed a 1.5 T MRI two-coil phased-array coil for carotid arteries with an effective longitudinal coverage of up to 5 cm [9]. Using this setup SNR could be improved by 37 % when compared to a commercially available single 3-in. surface coil. Various models of surface coils are available and some of them can be used in combination with head and body coils [10]. This allows combining the assessment of carotid plaque morphology and composition with an MR angiography of the supra-aortal vessels and/or with a brain MRI in one session.

2.2 Sequences

2.2.1 MR Protocol

MRI has emerged to be a one of the major noninvasive methods for the evaluation of the carotid arteries [4] and currently can be partitioned into three acquisition entities: luminography, vessel wall imaging, and tissue-specific imaging [11]. Consequently the application of MRI allows identification and quantification of plaques noninvasively and without radiation exposure of the patient. Up to date, however, there is not a single MR technique that allows to covering all the vulnerable plaque criteria (see Sect. 1) as proposed by the AHA. Various publications lead to a broad spectrum of proposed techniques, ranging from the acquisition of one [12] or two [13, 14] to multiple contrast-weighted MR sequences [15, 16]. Depending on the focus of the study, the number and type of sequences acquired may vary. For a sole evaluation of overall plaque burden, one sequence (T1w, PDw, or T2w) may be sufficient. In contrast the more complex evaluation of plaque composition and morphology in one imaging session requires the use of multiple MR sequences [4].

2.2.2 Bright-Blood Imaging

Multi-sequence protocols commonly used for atherosclerotic plaque imaging use two kinds of images: bright-blood and black-blood images. Bright-blood sequences, such as time-of-flight (TOF) sequences, facilitate the evaluation of the luminal signal by suppression of surrounding tissue and enhancing the luminal signal. These sequences are particularly useful for identifying calcified nodules—a feature of the vulnerable plaque—and large chunks of calcification adjacent to the lumen [17]. Furthermore, in combination with black-blood sequences TOF images can be helpful in the identification and characterization of IPH and thickness and integrity of the fibrous cap [18], which are important markers in the assessment of stroke risk. Depending on the desired information different techniques can be applied for luminography. Time-of-flight is a standard technique and basic component of most multi-sequence protocols. Alternative approaches for depiction and maximization of luminal signal-to-noise ratio are contrast-enhanced imaging [19] and phase-contrast imaging [20].

2.2.3 Black-Blood Imaging

The blood signal interferes with optimal evaluation of the vessel wall and its components. Consequently suppression of luminal signal is obligatory to evaluate the atherosclerotic wall, which has led to the introduction of the so-called black-blood sequences. Black-blood imaging is commonly performed using multiple spin-echo sequences [fast spin-echo (FSE) = turbo spin-echo (TSE)] in combination with a preceding module for blood flow suppression [21]. Black-blood images of the carotid arteries can be generated by generally three techniques such as inflow saturation (IS) [22], double inversion recovery (DIR) [23], and motion-sensitized driven equilibrium (MSDE) [24]. Inflow saturation is achieved by a selective RF pulse which saturates the blood within the vessel before it enters the imaging plane and replaces unsaturated blood [18]. Consequently problems, similar to those encountered in TOF imaging, may occur and limit the application of inflow saturation. Complicated flow patterns with slow flow, flow parallel to the imaging plane, and thick slab thickness may deteriorate quality of blood suppression, mimicking wall thickening and atherosclerotic plaque [25]. Despite these limitations, inflow saturation also has certain advantages. As blood pre-saturation can be achieved selectively by the placement of the saturation impulse, arterial and venous vessel separation is possible, making it suitable for MR angiograms [18]. This technique also allows fast and simple black-blood imaging which makes it suitable for screening on high signal intensities of IPH on T1-weighted images [26]. Furthermore inflow saturation may be combined with ECG-gated imaging. Coordination of imaging with the phase of the fastest blood flow shortly after peak systole can limit the appearance of flow artifacts [25].

The **DIR technique** is a commonly used method for blood suppression and, concerning the effectiveness, superior to inflow saturation. DIR modules consist of two 180° RF pulses. The first, nonselective pulse inverts the longitudinal magnetization of the whole body and is followed by a selective 180° pulse which reinverts the longitudinal magnetization of the slice of interest. After a precalculated inversion time (TI) during which the magnetization of the inflowing blood reaches the zero point due to its natural T1 relaxation an acquisition sequence records the signal [27]. Compared to inflow saturation, the DIR technique is less depending on the blood flow rate and is more effective in signal suppression in areas with complex flow patterns [28]. However, DIR is limited by the following: (1) like inflow saturation, DIR is dependent on outflow from the imaging slice; (2) due to the selective inversion pulse, DIR is basically a single-slice method—if more slices are to be acquired at the same pulse, this is only possible at suboptimal time points (i.e., loss of image quality) or in combination with longer imaging time [29]; and (3) a change of blood T1 (e.g., after administration of gadolinium contrast material) can hamper suppression of the luminal signal [30]. For multislice imaging, several other models based on the DIR technique have been proposed. These include the quadruple inversion recovery (QIR) technique, which basically consists of two consequent or simultaneous DIR modules. However, this technique also requires longer preparation time for the scan [31]. Developments in protocol structure, which are based on the above techniques, today allow simultaneous imaging of 8–16 slices [21].

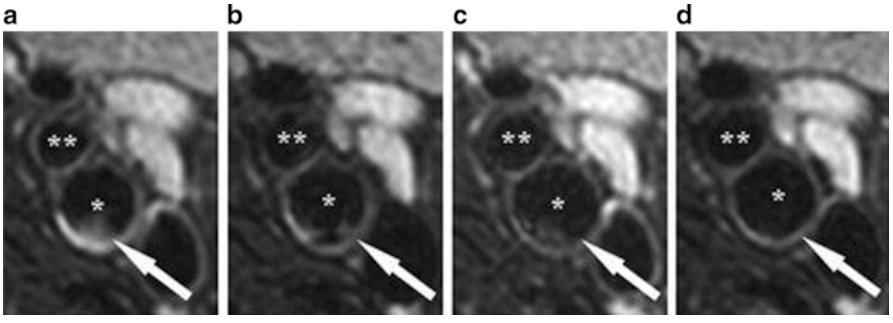

Fig. 4.1 Sample images illustrating the flow suppression capability of different BB-imaging techniques. (**a**) IS, (**b**) single-slice DIR, (**c**) multislice MDIR, and (**d**) MSDE. The residual flow signal is eliminated by the MSDE sequence but visible for other techniques (*arrows*). All images are presented using the identical window settings. *Single asterisk*, internal carotid lumen; *double asterisks*, external carotid lumen. Reprinted with permission from [24]

In contrast to inflow saturation and DIR, the recently developed **motion-sensitized driven equilibrium** (MSDE) technique can suppress blood signal without direct dependence on flow direction or velocity. Blood signal is suppressed by a preparative module via phase dispersion of spins of the flowing blood [24]. Independence of blood flow, relatively high vessel wall CNR, short scan times, and effective blood signal suppression even after contrast material application make MSDE a promising black-blood technique [24, 32]. Limitations of MSDE are the inherent T2 and diffusion weightings caused by the preparative sequence which lead to a reduction of SNR of approximately 12 % [24, 33] (see Fig. 4.1).

2.2.4 Fat Suppression

For accurate identification and characterization of plaque components, an effective suppression of subcutaneous fat is necessary [4]. Thus contrast of both intraplaque components and surrounding tissues can be increased in all commonly applied plaque imaging sequences, including T1-, T2-, and proton density-weighted sequences [26, 34]. Fat suppression is achieved by the application of a spectrally selective fat suppression technique, which suppresses signal and chemical shift artifacts of triglycerides by application of a fat-saturation pre-pulse. As triglycerides are mostly contained in subcutaneous fat, lipids within the necrotic core of plaques, consisting mainly of cholesterol and cholesteryl esters, are generally not affected by fat suppression [35].

2.2.5 Contrast Agents

In addition to the commonly used T1-, PD-, TOF-, and T2-weighted sequences, application of contrast material has been shown to improve the accuracy and reproducibility of quantitative plaque measurements [36]. Additionally plaque characteristics, which cannot be depicted by regular non-contrast-enhanced plaque MRI, such as inflammation and neovascularization may be detected and quantified.

The most widely used contrast agents in bb-MRI are nonselective gadolinium-based agents which reduce tissue T1 relaxation time and thereby significantly increase signal intensity on T1-weighted images [37]. This effect can be observed up to 30 min after injection, with a peak enhancement after 10 min [38]. Due to a higher blood supply, fibrous tissue and neovasculature have been reported to have higher signal enhancement compared to other plaque components, such as the poorly vascularized LR/NC, and thus help in the delineation of the fibrous cap and the LR/NC [37, 39]. Since regional plaque enhancement is also caused by increased permeability, a factor considered to be associated with plaque inflammation and rupture, gadolinium-based contrast agents can also be used to detect and quantify plaque inflammation using dynamic contrast-enhanced MRI (DCE), a technique which will be described in Sect. 5.3.

Intravenously administered ultrasmall superparamagnetic iron oxide (USPIO) particles are an example for a selective contrast agent in T2*-weighted imaging. USPIOs accumulate within macrophages, which are abundantly present in inflamed plaques, and thus cause a negative contrast by susceptibility effects. The application of USPIO and its possible role in characterization of the vulnerable plaque will be discussed in more detail in Sect. 5.4.

Recent research has focused on the development of gadolinium agents that bind to specific targets, by linking gadolinium chelates to polymers, polysaccharides [40], or nanoparticles. This approach has already allowed creation of specific agents that bind to thrombus [41] and factors which are correlated to angiogenesis (e.g., αvβ3-integrins) [42]. Recent animal studies have shown that Gadoflourine binds to lipid-rich plaque and thus can improve atherosclerotic plaque detection [43].

2.2.6 Image Processing/Processing Software

As information about plaque composition generally is derived by observations of images of various weightings, the complete review of the carotid vessels including evaluation

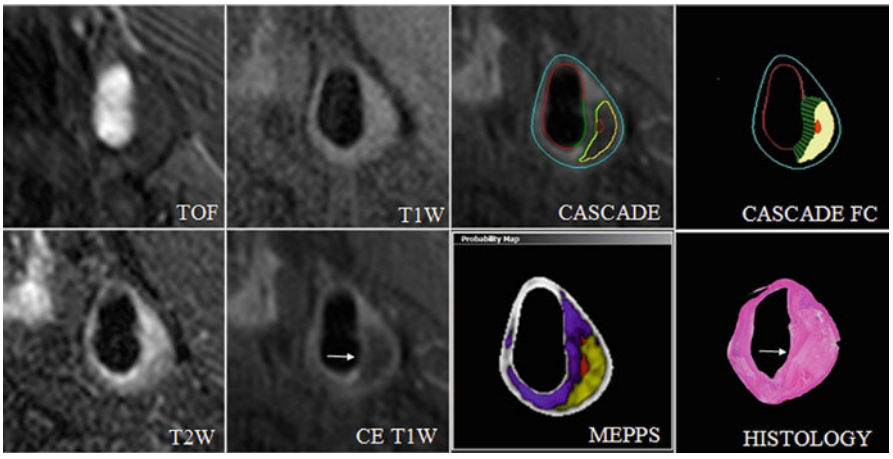

Fig. 4.2 Automated segmentation of bright- and black-blood, high-spatial-resolution, multicontrast in vivo CMR. Quantification of in vivo carotid magnetic resonance (CMR) (TOF, T1W, T2W, and CE T1W) using CASCADE to generate component outlines. The CASCADE fibrous cap (FC) is an additional algorithm that collects FC length, depth, and area. The automated map of the plaque is produced by the MEPPS algorithm. Loose matrix is shown in *purple*, lipid-rich necrotic core in *yellow*, and intraplaque hemorrhage in *red* on the MEPPS image. Histology from CEA confirms the components and the enhancing thick FC (*arrow*). In vivo CMR were acquired on a 3 T Philips Achieva scanner (Best, the Netherlands) along with the use of an 8-element phased-array carotid coil. *CASCADE* computer-aided system for cardiovascular disease evaluation, *CE* contrast enhanced, *CEA* carotid endarterectomy, *MEPPS* morphology-enhanced probabilistic plaque segmentation. Reprinted, with permission from [48]

of plaque characteristics and components may take a long time. Also certain conclusions such as volume measurements or wall thickness parameters can hardly be drawn by the naked eye. For quicker evaluation and quantification of morphology and plaque components several computer-aided tools, which are capable to implement this mass of information and present results in a simplified matter, have been proposed [21, 44]. These highly automated measurement techniques can reduce analysis time and reader-dependent bias and improve measurement reproducibility [45].

Essential steps in the evaluation process are image registration of multicontrast MRI images, segmentation of lumen and outer wall boundaries, and classification of tissue types based on their contrast properties [31]. Before the beginning of the reviewing process, images of all contrast weightings must be aligned. This step is necessary to account for patient movement during measurements and differences in coverage of the acquired image series. Furthermore the determination of certain landmarks, such as the carotid bifurcation and shape and size of the arterial lumen and the wall, allows matching of images acquired at various time points or with histology. For automated image registration several approaches, such as active edge maps [46] and voxel-based mutual information [47], have been proposed [31]. Automated or semiautomated image processing tools facilitate the assessment of three different basic types of plaque information: (1) plaque burden, (2) plaque composition, and (3) functional measurements that are determined by plaque composition. Figure 4.2 offers an insight into plaque information which has been generated by the use of the software tool CASCADE (University of Washington, Seattle, USA).

3 Plaque Burden

"Plaque burden" is the amount of atherosclerotic plaque within the vessel wall of a certain artery and it has been shown in coronary arteries [49] and in carotid arteries [50] that plaque burden is associated with cardio- and cerebrovascular events. Of note, diseased vessels can contain large amounts of atherosclerotic mass without significant luminal narrowing due to compensatory arterial outward remodeling [51]. Thus, imaging methods which can reliably depict the lumen and the wall are needed to quantify the atherosclerotic plaque burden.

Maximum and mean wall thickness are parameters of plaque burden that are relatively insensitive to artery size or coverage [44]. High wall thickness parameters correspond with increased lipid content within the intima of the vessel wall and are the first parameters that can be observed in early atherosclerosis. In a prospective study of 154 initially asymptomatic patients, Takaya et al. could show that an increase in maximum wall thickness is associated with the occurrence of subsequent cerebrovascular events (hazard ratio for a 1-mm increase, 1.6; $P = 0.008$) [52]. In a subsequent retrospective study, patients with prior major cardiovascular or cerebrovascular events (MACE) were reported to have a significantly higher plaque burden (wall thickness) and plaque eccentricity (standard deviation of wall thickness) than a matched patient group without MACE [53]. Also measurements of mean wall thickness by carotid MRI are highly associated with B-mode ultrasound measurements of

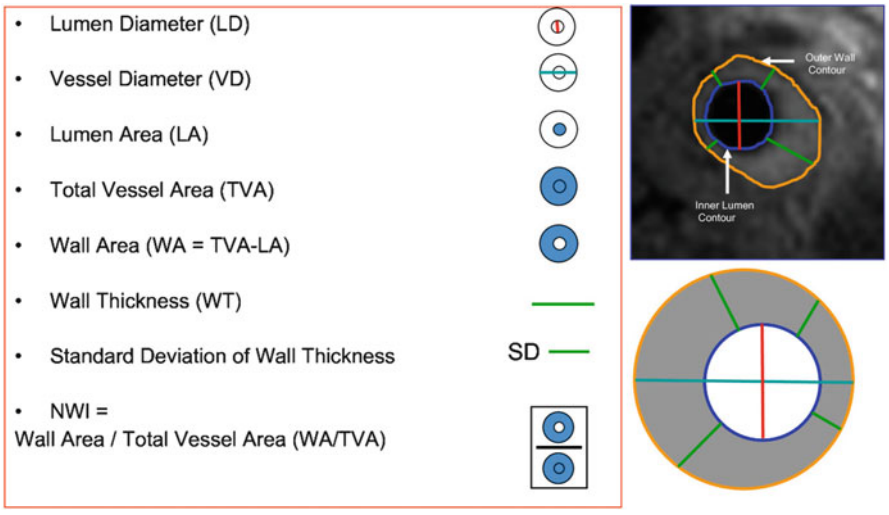

Fig. 4.3 MR imaging parameters measured for carotids and thoracic aorta. MR imaging parameters measured for carotids and thoracic aorta. The *red line* indicates the measure of the lumen diameter; the *teal line* represents the vessel diameter; the *green line* represents the wall thickness. The area enclosed by the *blue contour* represents the lumen area and the area enclosed by the *orange contour* represents the total vessel area. The difference between the total vessel area and the lumen area provides the wall area. The normalized wall index is determined by the ratio of the wall area to the total vessel area. The *top right panel* shows the contours on a sample carotid image. Reprinted with permission from [53] (Color figure online)

the carotid intima-media thickness [54], which has been associated with stroke in multiple long-term, prospective investigations [55].

The **total volume** of the wall or its components can be derived by addition of the total wall areas of the required section and multiplication with the slice thickness. However, care must be taken if volumes of various measurements are compared: Differences in body size and of the coverage of the artery may lead to false conclusions as both longer extent of coverage and larger vessel size may lead to high values, mimicking a larger disease burden [44].

The **normalized wall index (NWI)**, a promising marker in the assessment of atherosclerotic plaque burden, is calculated as wall area divided by the total vessel area and is a very accurate and reproducible measurement [44]. NWI values of a normal carotid artery scatter around 0.4 [44]. Higher mean arterial NWI values (>0.56) have been associated with FC rupture and IPH in the carotid artery. Figure 4.3 demonstrates a list of plaque burden parameters commonly used.

When aiming at comparisons with histology these measurements can be necessary for calculating the percentage content of wall components such as lipids, calcifications, and fibrous tissues, as in many cases specimen shrinkage won't allow comparison of absolute measurements.

A recent study sought to determine the strength of plaque burden and stenosis in classifying carotid high-risk features [56]. Analysis of 180 patients with either carotid stenosis >50 % by duplex ultrasound or suspected coronary artery disease by multicontrast carotid MRI revealed that measures of plaque burden do not substantially improve disease assessment compared to stenosis. This seems likely, since high-risk features such as IPH and surface disruption occur across wide range of both parameters. However, assessment and quantification of plaque burden are not useless: presence of atherosclerotic plaque in the carotid arteries is an indicator of systemic disease and thus may be useful as a surrogate marker in clinical trials with anti-atherosclerotic therapies.

Both accuracy and reproducibility are important characteristics of an approach which is aimed to clinically assess and observe progression/regression or therapeutic effects in atherosclerotic disease.

Various studies have been performed on the **accuracy** of morphological measurements in the carotid arteries using bb-MRI. Comparison of measurements derived from in vivo and ex vivo MRI images has shown excellent agreement for the plaque burden parameters maximum wall area and wall volume [57, 58]. Area measurements of the lumen and the vessel wall seem to be independent of the weighting of a multicontrast MRI protocol used and tend to provide similar results [59], provided they were acquired with the same bb-technique and sufficient image quality was achieved. Additionally, in comparison with corresponding and validated 2D images, accuracy of 3D imaging has been validated [60].

MRI imaging of the carotid arteries also is highly **reproducible** on multiple scanner platforms [61], between scans [62], and between readers [62, 63]. Variability of quantitative plaque burden measurements ranges from 1.5 to 4 % for lumen area, 4.5 to 5.8 % for wall area, and 1.9 to 3.3 % for outer wall area measurements. Variability of the NWI

Table 4.1 Modified MR criteria for identification of the main atherosclerotic plaque components [16, 39, 69]

	TOF	T1	PD	T2	CE-T1
Lipid-rich/necrotic core					
(A) Without hemorrhage	o/+	o/+	−	−	↓
(B) With type I hemorrhage	+	+	−/o	−/o	↓
(C) With type II hemorrhage	+	+	+	+	↓
Calcification	−	−	−	−	↓
Loose fibrous tissue	o	−/o	+	+	↔
Dense fibrous tissue	o	o	o	o	↑

TOF time-of-flight, *PD* proton density, *CE* contrast enhanced (↓, no contrast enhancement; ↔, contrast enhancement similar to the normal arterial wall; ↑, strong contrast enhancement; +, hyperintense; o, isointense; −, hypointense)
All signal intensities are relative to a reference segment of the normal arterial wall

is approximately 3.0 %. These measurements have excellent intraclass correlation coefficients, ranging from 0.90 to 0.98 [58, 64, 65].

4 Plaque Composition

MR plaque imaging techniques can not only be used for simple plaque burden measurements, but they are also well suited for the identification and quantification of plaque components. Focus in this field has been set on identification and quantification of components that characterize the previously mentioned "vulnerable plaque"—LR/NC, IPH, and fibrous cap. Multicontrast MRI plaque imaging has systemically been validated with histology to identify and quantify in vivo carotid plaque components, such as the LR/NC [17, 39, 66], calcification [16, 66], IPH [17, 66], surface disruption [67, 68], and markers of inflammation and neovasculature by the unique signal combination of different weightings [11].

These histology studies have shown that MR signal intensities of the main plaque components and the amount of contrast uptake are somewhat component specific (see Table 4.1); thus MRI is able to identify (and quantify) the main components of the atherosclerotic plaque with good correlation to histopathology [18, 26, 70] (see Fig. 4.4).

4.1 Intraplaque Hemorrhage

IPH occurs frequently during the development of atherosclerotic lesions and is a significant step in plaque development from stable to unstable plaque [71]. The fundamental mechanisms that result in IPH have not been completely understood, but may be caused by two different mechanisms: True plaque rupture with cracks or fissures that originate at the luminal surface connects the underlying vessel wall tissue to the lumen and causes deposition of blood cells within the vessel wall [72]. Alternatively, IPH may occur secondary to rupture of immature neovessels within the plaque. These vessels often lack support by smooth muscle cells within the arterial wall and focal discontinuity of the endothelial lining makes them prone to leakage [48].

Detection of IPH by carotid plaque imaging is based on the degradation of hemoglobin into methemoglobin, which takes place about 12 h after hemorrhage. Presence of methemoglobin shortens the longitudinal relaxation time of surrounding protons and thus appears hyperintense on T1w images [70], such as on black-blood T1w fast spin echocardiography, time-of-flight, and magnetization-prepared rapid acquisition gradient echo (MP-RAGE). Additionally to T1w images a T2w black blood sequence can be used to differentiate between early subacute or type I (hypointense signal on T2w images) and late subacute or type II hemorrhage (iso- or hyperintense signal on T2w images). IPH findings have been extensively validated by histology for both 1.5 and 3.0 T [70, 73]. However, due to inherently low contrast in IPH regions accurate outlining of the hemorrhage area remains difficult with Pearson's correlation coefficients for mean hemorrhage area between histology and MRI of $r = 0.66$ ($P < 0.001$) [16]. Application of tissue-specific imaging for IPH detection can improve performance, but has difficulties with the detection of small hemorrhages and the presence of heavy calcified plaques [73]. Recently, a new technique using a slab-selective phase-sensitive inversion recovery (SPI) sequence for assessment of IPH has been proposed and validated against histology specimens. In vivo and ex vivo measurements could show a significantly improved IPH wall contrast-to-noise ratio and blood suppression efficiency than the previously mentioned MP-RAGE and offer a better reproducibility of IPH measurements [74].

Since IPH has been shown to be one of the major driving forces in plaque development, assessment of presence of IPH in studies (work-up, risk assessment, therapeutically) is desirable. Instead of the general approach, which regards IPH as a dichotomous variable (present or absent), histology studies suggest that size [75] and age [76] of IPH might be important factors in disease severity. In the clinical setting, knowledge of the age of IPH can provide insight into the history and current condition of the biologically active plaque [21]. To date quantitative measurements of IPH area, sensitivity, specificity, and agreement with histology have remained problematic. For the combination of black-blood T1-weighted turbo spin echo and time-of-flight sequences in a multicontrast protocol, a good sensitivity of 90 % has been reported. However, specificity for the detection of IPH in this setting is moderate (74 %) and intra-reader agreement is limited [69]. When compared to matching histology, application of MP-RAGE for the in vivo detection of IPH provided the highest sensitivity and specificity with

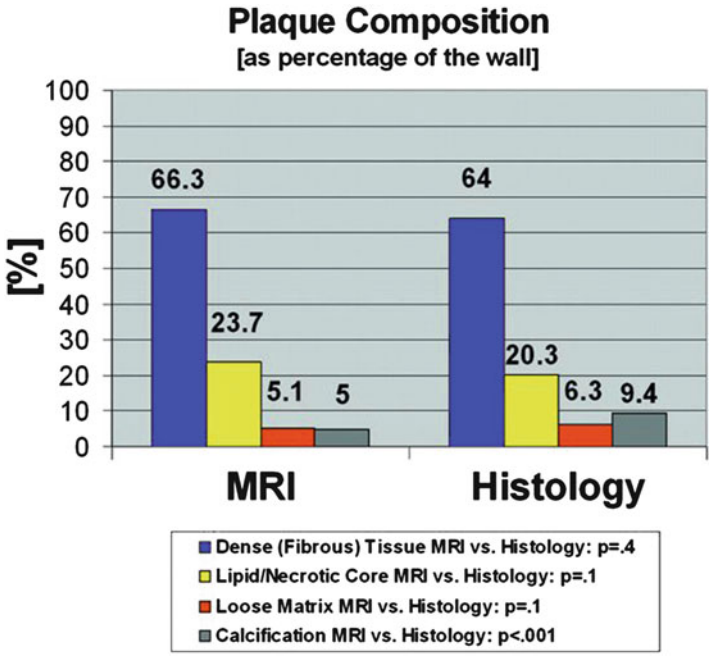

Fig. 4.4 Correlation of MRI and histology. Plaque composition calculated as the percentage of the vessel wall area for MRI and histology. Reprinted with permission from [16]

values of 84 % and 84 %, respectively. Application of the recently published SPI-Sequence showed a slightly higher accuracy than MP-RAGE and significantly higher IPH wall CNR [16].

MRI studies have shown that the presence of IPH may be a good indicator for unstable plaques. Together with fibrous cap status (thin or ruptured: hazard ratio, 17.0; $P \leq 0.001$), larger mean IPH area (hazard ratio for 10 mm^2 increase, 2.6; $P = 0.006$) and presence of IPH are the strongest predictors for the development of stroke in previously asymptomatic individuals (hazard ratio in patients with 50–79 % carotid stenosis, 5.2; 95 % confidence interval: 1.6–17.3; $P = 0.005$) [52]. Furthermore in symptomatic individuals with a stenosis degree between 30 and 69 %, IPH has been shown to be a good predictor of recurrent stroke [77]. In contrast patients with absence of IPH at MR plaque imaging are significantly less likely to suffer stroke due to a ruptured plaque. Thus the absence of IPH may be considered as a marker of plaque stability and a lower risk of thromboembolism [78].

In vivo plaque imaging of the carotids has revealed that occurrence of IPH is not limited to symptomatic patients or vessels with advanced stenosis [79]. A prevalence of IPH in up to 15 % of asymptomatic vessels with a stenosis <50 % has been reported [79]. To date the significance of these complicated atherosclerotic plaques is unclear. To comprehensively elucidate the significance of complicated plaques in stroke patients without significant stenosis, a systematic, prospective bicentric study (carotid plaque imaging in acute stroke, CAPIAS), which is registered on http://www.clinicaltrials.gov (NCT01284933), has recently been initiated.

To date the definite role of IPH in plaque development and rupture has not completely been understood, but is believed to be a factor promoting plaque progression and consequently plaque disruption. Repeated IPH leads to deposition of free cholesterol from erythrocyte membranes, macrophage infiltration, and enlargement of the necrotic core and thus represents a potent stimulus in the development from the subclinical to the complicated atherosclerotic plaque [80]. Furthermore, the destabilization process might be accelerated by inflammatory mediators which stimulate the expression of extracellular matrix metalloproteinase and consequently lead to degradation of extracellular matrix and plaque microvasculature. Repeated rupture events and micro hemorrhages into the LR/NC are the consequence [81]. Previous histology-based studies demonstrated that the prevalence of IPH increases with the severity of carotid stenosis [82]. Recent findings, however, suggest that IPH already occurs in low-grade stenosed vessels and that the presence of IPH is a driving force of luminal occlusion [83] raising the question of which factor appears first (see Fig. 4.5). Prospective studies of patients with and without IPH and stenosis degree between 16 and 79 % at baseline could show that after a period of 18 months percent change in wall volume and LR/NC was significantly higher in patients with IPH. Furthermore, patients with IPH at baseline showed an increased susceptibility to recurrent plaque hemorrhages [83, 85]. Additionally a significant impact of IPH on the vessel wall remodeling pattern was found: Lesions without IPH tend to expand outward and preserve the lumen (positive remodeling), while plaques containing IPH could be associated with inward (negative remodeling) remodeling and luminal narrowing [83].

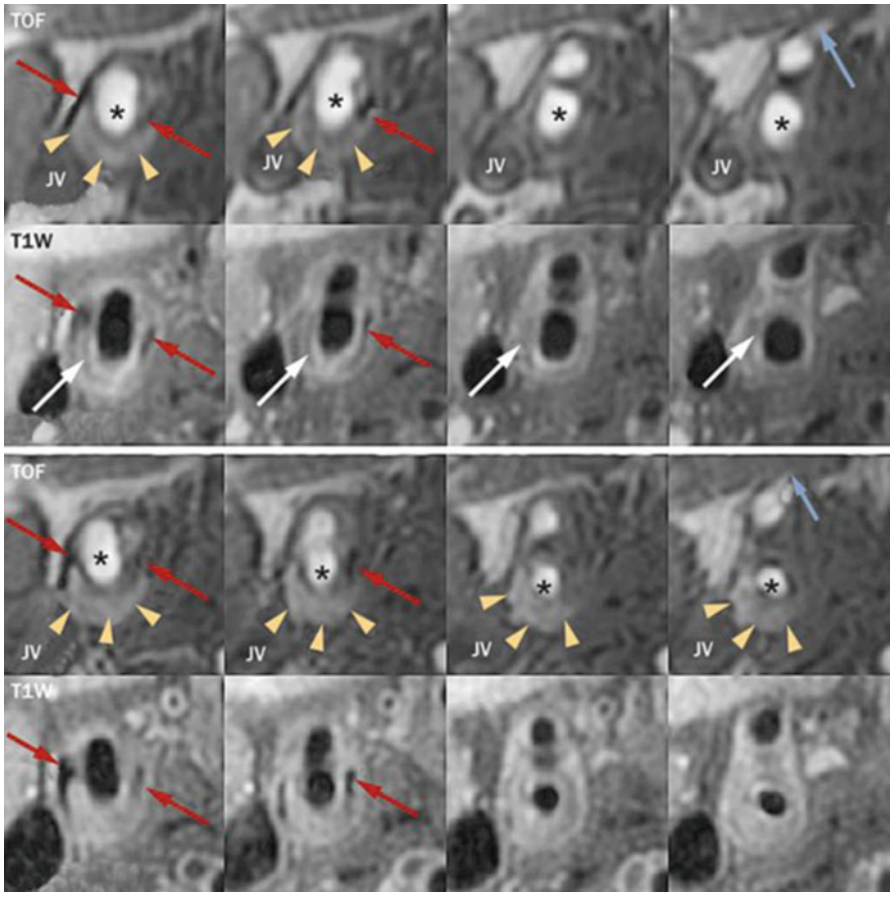

Fig. 4.5 In vivo evidence of the effects of IPH. Images are serial axial sections through a lesion of the carotid artery from TOF and contrast-enhanced T1W sequences. The *upper panel* is the baseline scan and the *lower panel* is the corresponding matched axial images at 36-month follow-up. Matching can be confirmed by calcification (*red arrows*), the flow divider (column 2), and the branching of the superior thyroidal artery off the external carotid (*blue arrow*, column 4). The *asterisk* indicates the lumen of the common and internal carotid arteries. The lesion contains a lipid-rich/necrotic core (*white arrows*, hypointense signal on CE-T1W) and IPH (*yellow arrowheads*, hyperintense signal on TOF). Notice the substantial increase in IPH at follow-up and corresponding reduction in lumen area most pronounced in columns 3 and 4. *IPH* intraplaque hemorrhage, *Jv* jugular vein, *T1W* T1 weighted, *TOF* time-of-flight. Reprinted, with permission from [84] (Color figure online)

4.2 Thrombus/Juxtaluminal Hemorrhage

In contrast to IPH, etiology of thrombus formation seems to be clear. Erosion, ulceration, or plaque rupture, each recognized markers of unstable plaque, leads to exposure of the thrombogenic LR/NC and subsequent platelet aggregation and fibrin deposition [1]. Formation of thrombus can lead to luminal occlusion of the affected vessel and acute cerebrovascular events, or promote plaque progression. Teng et al. examined the relation between juxtaluminal hemorrhage/thrombus (JLH/T) and subsequent events in 42 TIA patients with mild-to-moderate carotid stenosis by high-resolution multicontrast MRI. During a 2-year follow-up period 52.4 % of the patients with JLH/T at baseline experienced recurrent cerebrovascular events in the territory of the index carotid artery, while none of the patients without JLH/T had an ischemic event [86].

Various approaches have been suggested for the detection of thrombus, including diffusion-weighted MR [87] and combination of TOF-, intermediate-, T1-, and T2-weighted images [88]. Similar to imaging of IPH, thrombus imaging preferentially utilizes the T1-shortening effects of the degrading hemoglobin, which acts as an endogenous contrast agent. In a histology-validated study with 26 patients scheduled for carotid endarterectomy, Kampschulte et al. reported to not only correctly detect hemorrhage with a high sensitivity but also to distinguish juxtaluminal hemorrhage from intraplaque hemorrhage with an accuracy of 96 % by using an in vivo multicontrast-weighted MRI protocol at 1.5 T [88]. Thrombus was identified by a hyperintense signal on TOF- and T1-weighted images adjacent to the lumen and absent dark band in TOF images. This technique was also applied in a trial with 23 symptomatic patients with high-grade stenosis [89] in order to evaluate the potential of MR imaging to differentiate between symptomatic and asymptomatic plaques. Besides higher incidence of cap rupture, type I hemorrhage, and complicated AHA type VI lesions, symptomatic plaques were more likely to show juxtaluminal hemorrhage and thrombus, whereas IPH was common in both symptomatic and asymptomatic plaques. Although it has been shown that MRI is able to identify and detect juxtaluminal hemorrhage/thrombus, there is no data demonstrating that MRI is able to quantify these components.

4.3 Lipid-Rich/Necrotic Core

The LR/NC is a mixture of lipids, cellular debris, blood, and water in various concentrations and is separated from the carotid lumen by a smooth, cell-rich fibrous cap [33]. The main components of the LR/NC are cholesterol and cholesterol esters. Differences in the lipid mixture and presence/absence and type of hemorrhage within the LR/NC result in a wide spectrum of signal intensities in MRI images and represent different risks for plaque rupture (see also Sects. 4.1 and 4.2). Lesions with a thin fibrous cap and a relatively large necrotic core, so-called thin cap fibrous atheromas, are considered to be most prone to rupture and have been associated with symptoms [90, 91].

Cholesterol and cholesterol esters have a rapid transversal (T2) decay. Consequently, given the absence of IPH, the LR/NC has a characteristic hypointense signal on T2-weighted images and appears iso/hyperintense on T1w and TOF images [92]. However, IPH into the LR/NC can cause T1-shortening effects and increase the relative signal intensity within the LR/NC on T1w images [11] (see Table 4.1). In our experience the most reliable marker/indicator of LR/NC is the complete absence of contrast enhancement (see Fig. 4.6).

Initial experiments which were performed on ex vivo endarterectomy specimens by using T1-, T2-, and intermediate-weighted imaging demonstrated that the presence of the lipid-rich/necrotic core could be detected with sensitivities and specificities ranging from 92 to 100 % [93, 94]. Translation of this approach to in vivo imaging showed that the LR/NC and/or IPH could be identified with a sensitivity of 85 %, specificity of 92 %, and accuracy of 87 %. Additionally a good agreement between MRI and histological findings, with a value of $\kappa = 0.69$, was reported [17].

Recent reports have demonstrated that MR imaging is not only able to identify the LR/NC, but that it also offers information for quantification. The ability to quantitatively assess the LR/NC has two advantages: high-risk plaques with a large LR/NC, proximally located to the lumen, can be identified and the effect of lipid-lowering therapy on disease burden can be directly evaluated. In a first step ex vivo fat measurements, acquired with T1-, intermediate-, T2-weighted, and diffusion-weighted imaging, were compared with histological findings and showed a sensitivity and specificity for necrotic tissue of 83.9 % and 75 %, respectively [15]. Again, translation of these findings in vivo showed that by using TOF- and T1-, T2-, and intermediate-weighted sequences, measurements of the LR/NC did not differ significantly from findings on histologic specimens (23.7 % vs. 20.3 %; $P = 0.1$). Additionally a strong correlation between MR and histologic area measurements was found ($r = 0.75$; $P < 0.001$) [4, 16].

Comparison of T1-weighted pre- and post-contrast images yields a more accurate delineation of the LR/NC and thus improves reproducibility and quantification [39]. In contrast to the surrounding fibrous tissue, the necrotic core is poorly vascularized and therefore shows only little if any enhancement in images after administration of gadolinium-based contrast material [95]. Additionally, depiction of the fibrous cap, which is well vascularized and separates the LR/NC from the lumen, is improved after contrast administration, facilitating differentiation of the fibrous cap from the LR/NC [95]. Gadolinium-enhanced T1 images of the LR/NC have been shown to provide approximately twice the signal-to-noise ratio with a contrast-to-noise ratio similar or better than that of T2w images [37], resulting in an increased intraclass correlation coefficient from 0.94 to 0.99 and from 0.85 to 0.93 for the intra- and inter-reader measurements, respectively [36].

Qualitative and quantitative assessment of the LR/NC has been successfully applied in longitudinal studies, observing plaque development under anti-atherosclerotic therapy. Findings and results of these studies will be discussed in the Sect. 7.

4.4 Fibrous Tissue

The production of interstitial collagen is thought to be an attempt to repair damaged areas within the plaque following IPH or lipid accumulation [69]. It is generally believed that fibrous tissue is a marker of plaque stability. The MRI signal pattern of fibrous tissue has been reported to be similar to the signal of the LR/NC without IPH [16] and is almost isointense to the signal of the normal arterial wall. Differentiation of both tissue types can be achieved by contrast-enhanced T1w sequences; in contrast to the necrotic core, fibrous tissue usually does enhance [39]. A histology study which quantified the amount of dense fibrous tissue showed no significant differences between MRI and histology measurements (66.3 % vs. 64.0 %; $P = 0.4$) [16].

4.5 Fibrous Cap

Plaque rupture with subsequent thrombus formation is the most common cause for ischemic events [96]. Ulceration, discontinuity of the fibrous cap, and thrombus are markers of such an event (see Fig. 4.7a–c). Consequently the status of the fibrous cap, which has been defined as a distinct layer of connective tissue completely covering the lipid-necrotic core [1], is considered to be one of the key features of vulnerable plaques. Histopathology studies have shown that the prevalence of plaque rupture is significantly higher among patients with a past history of an ischemic neurological event

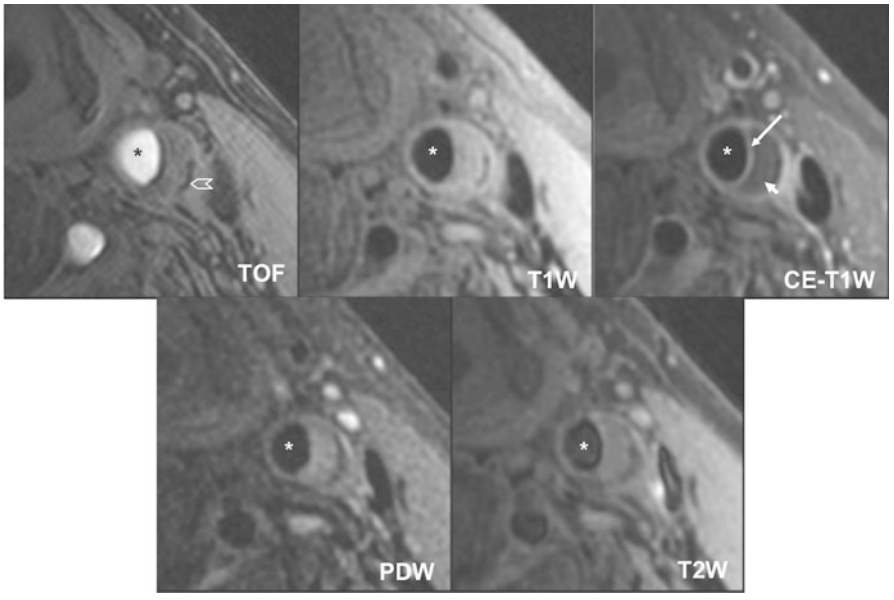

Fig. 4.6 Atherosclerotic carotid artery lipid-rich/necrotic core. Multicontrast *black*- and *bright*-blood sequences show a large lipid-rich/necrotic core (*small arrow*) with an intact thick fibrous cap best seen in the post-contrast T1-weighted (CE T1W) image (*long arrow*). Calcification is also visible at the base of the plaque (*chevron*). *Asterisks* are placed on the lumen. Reprinted with permission from [45]

[97]. Studies comparing histological carotid endarterectomy specimens with previously acquired MR images confirmed these findings. Patients with ruptured caps suffered significantly more often from ischemic symptoms (70 %) than those with thick fibrous caps (9 %). Compared with patients with thick fibrous caps, patients with ruptured caps were 23 times more likely to have had a recent TIA or stroke (95 % CI = 3, 210) [98]. For the carotids cutoff values for a high risk of plaque rupture have been reported to be a minimum cap thickness of <200 μm and a representative mean cap thickness of <500 μm [99]. Due to improvements in hardware and sequence setup, high-resolution MRI allows depiction of these small structures with diagnostic quality and thus not only allows detection of prior plaque rupture but also differentiation between stable lesions (thick cap) and high-risk disruption-prone (thin cap or ruptured cap) vulnerable plaques [16].

For optimal depiction of the lumen surface and the fibrous cap, a combination of black-blood and bright-blood imaging techniques is used. In 3D TOF MR angiography images the fibrous cap appears as hypointense band or rim surrounding the bright lumen [67]. This approach is already sufficient for discrimination of intact thick cap from intact thin and disrupted cap in vivo and has a high level of agreement with histology (with a Cohen's k (95 % CI) value of 0.83 (0.67–1.0) and a weighted k value of 0.87) [67]. Furthermore for this approach a high test sensitivity (0.81 %) and specificity (0.90 %) for identifying an unstable cap in vivo have been reported [100]. Additionally the fibrous cap shows hyperintense signal relatively to the underlying LR/NC on T2-weighted images [39] and is in strong agreement with histological findings [68]. Especially in cases in which IPH into the LR/NC increases signal intensity on T2-weighted images, gadolinium-based contrast imaging can help delineate the LR/NC and the fibrous cap by increasing the signal of the fibrous cap in T1-weighted post-contrast images and allows quantification of both components. In a MRI study this approach led to good intra- and inter-reader agreement ($k = 0.96$ for intra-reader; $k = 0.64$ for inter-reader) for the status of the fibrous cap [101]. Additionally measurements of the fibrous cap including fibrous cap length and area in contrast-enhanced T1w images showed a good correlation between MRI and histology measurements ($r = 0.73$–0.80, $P < 0.001$) [39].

4.6 Calcification

Calcification is commonly found in atherosclerotic vessels and may occur in both viable and necrotic parts of the plaque. The exact role of calcium deposition and its contribution to plaque stability have not completely been understood. While some studies report an association of presence and extent of calcium deposition with an increased risk of plaque rupture [102], others observed a stabilizing, protecting effect [103]. A systematic review reported that clinically symptomatic plaques tend to have a lower degree of calcification than asymptomatic plaques and that calcification percentage of the vessel wall may be a valuable parameter in the assessment of plaque stability [104]. Li et al. additionally conjectured that calcium within the LR/NC may even stabilize the plaque by adding bulk [105]. Plaques with a higher calcification percentage may have smaller LR/NC size, which could decrease plaque vulnerability [104].

Besides general calcium content within the plaque the location of the calcification might also be important.

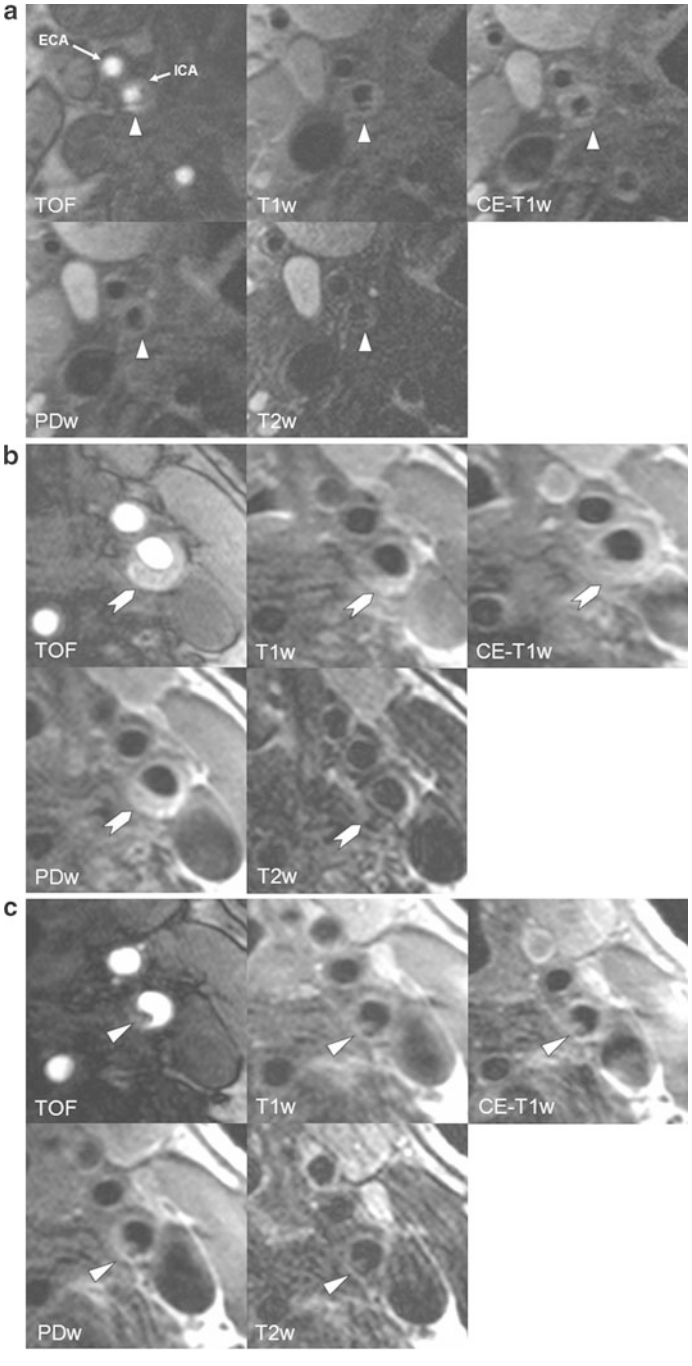

Fig. 4.7 In vivo identification of FCR, IPH, and thrombus. (**a**) MR images of the right internal carotid artery (ICA) of a 78-year-old patient with a right-hemispheric stroke ipsilateral to a 60 % carotid stenosis 4 days before the MRI scan. The surface of the plaque appears irregular and TOF images show a *very bright* area posterior to the lumen of the ICA, corresponding to a hypointense area in all other sequences, suggestive of a ruptured fibrous cap. It is tempting to assume that the rupture of the fibrous cap—which is known to cause thrombotic complications—is the reason for the ischemic stroke in this previously asymptomatic patient. (**b**) Complicated AHA type VI plaque of a 82-year-old symptomatic patient without cardiovascular risk factors. The patient suffered a stroke ipsilateral to the left carotid artery 5 days before the MRI scan. The *chevron* points to an eccentric plaque which is hyperintense on TOF and T1w images, indicative of intraplaque hemorrhage. (**c**) Images of the same patient (**b**) show a small mural thrombus 4 mm further distally (*arrow*)

Calcifications within or close to the fibrous cap, so-called superficial calcified nodules, may be encountered in plaques irrespective of the general calcification degree [1]. Those structures may protrude through the fibrous cap into the lumen or rupture the fibrous cap and may thus act directly or indirectly thrombogenic [3]. Model-based stress studies of carotid plaques could show that maximum wall stress increased by 47.5 %, when the calcification was located within the thin fibrous cap, indicating an increased risk of plaque rupture [105]. Calcium location within the FC further away from the lumen or within the LR/NC had no or little impact on plaque stress. Due to their pro-rupture characteristics, superficial calcified nodules are considered to be one of the minor criteria in the evaluation of the vulnerable plaque [3].

MRI has been successfully applied in carotid plaque imaging due to its high ability to distinguish soft tissue. However, for exact depiction and quantification of calcium other methods such as CT and ultrasonography are superior. Due to a low water (and thus proton) content, calcifications can be detected as areas of relative hypointensity on T1- and T2-weighted and proton density images and TOF MR

angiograms [16]. Measurements at 1.5 T demonstrated that multicontrast MR has a high sensitivity (98 %) and specificity (99 %) for detection of plaque calcification ex vivo and good in vivo sensitivity (84 %) and specificity (91 %). When measured as percentage of wall, a significant difference between calcium measurements in MRI and histology can be observed (9.4 % by histology vs. 5.0 % by MRI; $P < 0.001$). Absolute area measurements, however, have high correlation ($r = 0.74$; $P < 0.001$). This might be caused by signal averaging problems in hypointense areas within the plaque which make them appear smaller than they really are [16].

Since superficial small calcified nodules may present with the same hypointense signal as the background blood in black-blood sequences, identification can be more difficult than that of calcification deeper within the plaque. However, addition of a bright-blood sequence (e.g., TOF) facilitates delineation of juxtaluminal calcification from the bright lumen [4, 88].

At higher field strengths increased susceptibility may alter quantification and detection. Comparison of area measurements at 1.5 and 3.0 T found that calcification was significantly larger at 3.0 T ($P = 0.03$) with an intraclass correlation coefficient of 0.79 [7].

5 Functional Imaging

Multicontrast MRI enables to not only reliably assess plaque morphology but is increasingly used for functional and molecular measurements of the vessel wall. Even though these methods are not ready for everyday clinical use and remain for the time being experimental, studies have shown promising results. Current aims of research are imaging and quantification of macrophage content and neovasculature, both assumed to be related to plaque inflammation and subsequent plaque vulnerability. The currently applied techniques have the advantage that after application of contrast material, signal of those plaque characteristics can not only be localized but also quantified, enabling these techniques to deliver clinical markers for therapeutic studies and studies exploring factors of plaque progression.

5.1 Inflammation

Inflammation is considered to be an important factor in lesion progression and plaque destabilization and is a recognized risk factor for the vulnerable atherosclerotic plaque. Accumulation of lipids in the vessel wall leads to liberation of pro-inflammatory cytokines which is followed by tissue infiltration of inflammatory cells such as macrophages and lymphocytes [81]. During the process of plaque progression inflammation is characterized by increased endothelial permeability, macrophage infiltration, hypoxia within the vessel wall, and plaque angiogenesis [45]. The recruited macrophages absorb lipids, produce extracellular matrix degrading enzymes (e.g., MMP-1), undergo apoptosis, and contribute to the development and growth of the LR/NC and thus are considered to be one of the key cellular mediators in the inflammatory process [106]. Histological studies have shown that the extent and the distribution of inflammation, and consequently that of macrophages, are associated with plaque stability. Risk for rupture and subsequent thromboembolism has been reported to be especially elevated with inflammation and neovascularization in the shoulders of the fibrous cap or within the LR/NC [107, 108]. Thus, detection of macrophage activity and consequently inflammation within the atherosclerotic plaque could potentially help distinguish between vulnerable and more stable plaques and thus remains one of the key goals in atheroma imaging.

Image regions containing inflammation are associated with elevated tissue perfusion and increased permeability. Consistent with this notion, nonspecific contrast agents with relatively high molecular mass (e.g., Gadolinium) have been observed to accumulate in hyper-permeable plaque areas and can thus be used to identify plaque inflammation [48]. The advantage of this method is that assessment is not limited to the identification of inflammation, but also quantitative measurements of the enhancement pattern can be obtained [109]. This approach is also followed in dynamic contrast-enhanced (DCE) imaging which will be discussed below. Furthermore, specific ex vivo or in vivo labeling of cells which are involved in the inflammatory process allows observation of cell migration and accumulation into the high-risk plaque over time. Ultrasmall superparamagnetic iron oxide particles (USPIOs) accumulate especially in activated macrophages and generate a signal loss on T2*-weighted imaging. Like Gadolinium-enhanced imaging, USPIO uptake is considered to be a good marker for the extent of inflammation within the plaque [110].

5.2 Neovessels

Neoangiogenesis is generally associated with plaque inflammation, and has been explained as a response to the hypoxic conditions in the thickened tunica media of advanced plaques [111]. However, various recent observations suggest that the formation of new blood vessels may already begin in the early stages of plaque development and thus sustains inflammation by facilitated extravasation of recruited inflammatory cells [112]. In a previous study microvessel density was found to be not only correlated with the presence of inflammation within the plaque but also was increased in thin cap atheromas and ruptured plaques [113]. Since the newly formed blood vessels which originate from adventitial vasa vasorum often are immature and prone to leakage, they

also seem to play a major role in the etiology of IPH. High microvessel density thus is considered to be a driving force in plaque growth, destabilization, rupture, and symptoms [113, 114]. Techniques that allow specific in vivo identification of neoangiogenesis consequently may offer valuable information about the role of neoangiogenesis in the development of IPH, monitoring of agents that inhibit angiogenesis, and identification of high-risk plaques.

Angiogenic areas and vessels can be detected in MRI by contrast-enhanced imaging. Similar to imaging of inflammation this can be achieved by selective and nonselective agents. Nonselective dynamic contrast-enhanced (DCE) MRI using long circulating contrast agents (e.g., gadolinium) that accumulate in plaque over time detect vascular permeability which can be used to quantify vessel density [115]. Targeted contrast agents (e.g., αvβ3-integrin), however, may detect angiogenesis by specific binding to receptors which are overexpressed in angiogenically activated endothelial cells [116]. These selective mediators additionally have the advantage that besides combination with contrast agents also targeted therapies are possible [117].

5.3 Dynamic Contrast-Enhanced MRI

Due to the importance of plaque inflammation and neovascularization in plaque progression and development of vulnerable plaques, high effort is put into the detection of these factors. Since conventional carotid MR imaging is unsuited for quantification and assessment of functional parameters, contrast-enhanced MR techniques have been increasingly used for this purpose. Dynamic contrast-enhanced (DCE) MRI was primarily used to investigate vascular permeability in tumors but has also been considered to be useful in studies on atherosclerosis [118]. DCE-MRI permits assessment of parameters for neovascularization and permeability with kinetic analysis of contrast agent uptake from the bloodstream into the plaque. Strong enhancement after application of a contrast agent (preferably gadolinium-based agents) is considered to be an indicator for a vascular supply and increased permeability which facilitates contrast agent uptake into the plaque and is thus considered to be a sign of inflammation [115, 119].

For the acquisition of dynamic contrast-enhanced MR images, images are repetitively acquired at preselected locations before and after the administration of a gadolinium-based contrast agent [120]. Extravasation of the contrast agent alters the signal in the surrounding tissue proportional to its concentration [112]. In a next step the acquired signal intensities are converted into concentration curves, provided that a pre-contrast relaxation map has been obtained and the relationship between signal intensity and concentration is known for the specific MR sequence used. Alternatively a linear relationship between signal intensity and contrast agent concentration can be assumed. However, this linearity has been reported to be valid only for low contrast agent concentrations and may not be accurate in areas with high contrast agent uptake or in the blood plasma. The change of contrast agent concentration and consequently the signal intensity is followed over time during the dynamic scan and contains information on the amount of tissue vascularization and other tissue characteristics, such as surface area product, extraction fraction, and blood flow [112]. Images of a T1-weighted "localizer," which covers the area of the DCE sequence, can be acquired before or after the dynamic sequence and is useful for identification of the lumen and wall boundaries in the further evaluation process during which results of the T1-weighted sequence (anatomical) and the DCE sequence (functional) are merged. In a last step tissue parameters related to neovascularization and inflammation can be calculated by application of either model-based or model-free approaches [120]. Figure 4.8 offers an illustration of the necessary steps for obtaining quantitative data.

Based on the two compartment model, initially proposed by Tofts and Kermode for the study of multiple sclerosis, two valuable parameters $\boldsymbol{K^{trans}}$ and **vp** can be obtained. K^{trans} has been defined as the transfer constant from the plasma to the tissue compartment and is related to blood flow, capillary surface area, and permeability making it a good marker for inflammation. Studies comparing MR images with corresponding histology specimens found K^{trans} to correlate with macrophage ($r = 0.75$, $P < 0.001$), microvessel ($r = 0.71$, $P < 0.001$), and loose matrix ($r = 0.42$, $P = 0.03$) content [115]. Additionally measurements of K^{trans} in the carotid arteries were found to significantly correlate with serum markers of inflammation and pro-inflammatory risk factors, such as high C-reactive protein levels, low high-density lipoprotein (HDL), and smoking [119].

The partial volume of blood (**vp**) is a parameter which reflects the microvessel area within the plaque, which with increasing area may facilitate cell extravasation. In a comparison of DCE with histological measurements an overestimation of the neovessel amount was found. However, in the same study a correlation of 0.80 between vp and the fractional area of microvessels was reported, making vp an effective marker of plaque microvasculature [121].

Alternatives to kinetic modeling include model-free approaches including calculation of the area under the curve (AUC) of the contrast agent uptake, time to peak (TP), and wash-in or wash-out slopes [112]. Although these parameters are easy to acquire and calculate, their relationship with true physical quantities is not obvious and therefore can't be used for definite assumptions about capillary permeability or blood volume [122].

DCE-MRI is an experimental method which is easily integrated into preexisting MRI protocols for vessel wall

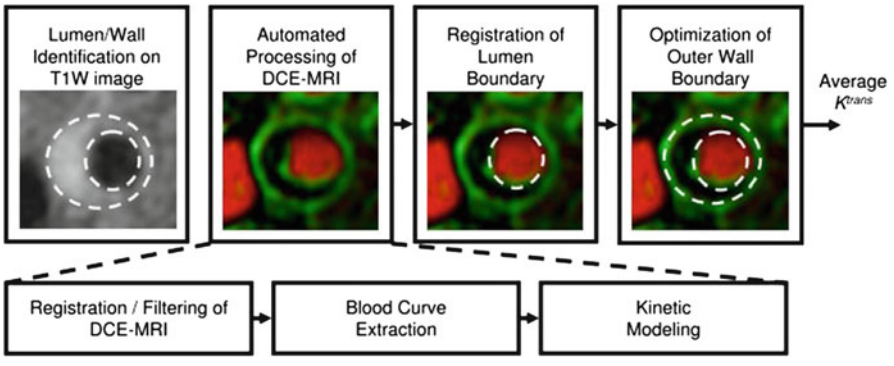

Fig. 4.8 Illustration of the processing steps in measuring adventitial K^{trans}. Reprinted with permission from [119]

characterization; image acquisition time is short (minutes) and clinically available and safe contrast agents are utilized [45]. Future developments in DCE-MRI of atherosclerosis may benefit from improvements in kinetic modeling algorithms and image quality. Current algorithms, such as the one used by Dong et al. [123], require a minimum of 2-mm carotid arterial wall thickness and thus preclude the evaluation of vessels with thinner walls. Imaging of those early lesions however could provide valuable information on plaque initiation and facilitate initiation of prospective studies. The major difficulty encountered in the use of bright-blood DCE-MRI is the influence of the hyperintense lumen signal, which impedes adequate evaluation of small structures adjacent to the lumen [123]. Thus development of black-blood DCE imaging sequences may lead to a clearer depiction of the vessel boundaries and enable imaging of thinner walls. Another limitation of the current technique is the relatively low SNR. Thus intraindividual measurements suffer from significant variations and by this still prevent a reliable assessment in individuals.

5.4 USPIO

Ultrasmall Superparamagnetic Iron Oxide (USPIO) particles can directly detect and quantify macrophage content within the plaque in vivo and thus provide information on the extent of plaque inflammation from a different approach than the previously described DCE-MRI [124]. USPIOs, such as Ferumoxtran (commercially known as Sinerem), are small iron particles which are administered intravenously after solution in suspension. A thick and complete cover of dextran promotes a long blood circulating time of more than 24 h in humans, before elimination by the reticulo-endothelial system in the liver [125]. The optimum time for imaging USPIO uptake has been found to be between 24 and 48 h with a peak at 36 h [126]. Forty-eight hours after contrast agent administration the signal-altering effect decreases but can be observed up to 96 h. Iron oxide particles create a large dipolar magnetic field gradient (magnetic field inhomogeneities) that acts on the water molecules surrounding the particles and reduce detectable magnetization [127]. This effect has its biggest influence on the transverse (T2) relaxivity of tissue and can be observed as T2 or T*2 shortening effects. Consequently USPIOs which have accumulated within activated macrophages can be recognized in T2*-weighted imaging as areas with focal signal loss. While the selective accumulation of USPIO in macrophages is well established, their uptake into the cell has not yet been completely understood. Several pathways including pinocytosis, phagocytosis, and cell surface receptor-bound uptake have been suggested for USPIO uptake, which seems to take place in an unsaturable manner [125]. Also the time point of USPIO uptake into the macrophage remains unclear. Possible mechanisms include (a) uptake into activated blood monocytes before extravasation into the plaque, (b) transcytosis of USPIOs from the blood into particularly inflamed tissue due to increased permeability, followed by uptake into in situ macrophages, and (c) transport of USPIOs into the pathological tissue [128].

Imaging of carotid plaque inflammation with USPIO has been performed in both animal [129] and in human studies [126, 130]. Application of USPIO-containing contrast agents allowed direct depiction of macrophages within atherosclerotic plaques. This assumption was validated by imaging the carotid arteries before and after application of USPIO in patients scheduled for carotid endarterectomy [124]. MRI images were correlated with the histological findings in the surgery specimens. Macrophages detected positive for iron in histology were visualized in 24 of 27 patients with an average reduction in signal intensity induced by the USPIO of 24 %. These findings and observations from animal studies suggest that USPIO accumulation and the resulting signal alternation can be used as biomarkers for inflammation in atherosclerotic plaques. This assumption has been strengthened by the finding that USPIO is detected preferentially more in ruptured and rupture-prone lesions than in stable lesions (75 % vs. 7 %) [130]. Interestingly USPIO enhancement cannot only be encountered in symptomatic plaques: A study by Tang et al. [131] compared truly asymptomatic plaques

of asymptomatic patients with contralateral asymptomatic vessels to the symptomatic side and found that inflammation could be detected by USPIO in both subject groups, suggesting subclinical inflammation to be a significant risk factor in asymptomatic disease.

Although USPIO imaging has proven to be a feasible method and has been applied in a variety of studies, larger scale studies are necessary to prove the diagnostic accuracy and potential effects on clinical management. Furthermore the analysis of serial MR measurements to quantify USPIO uptake still presents a number of challenges. The most important limitation of USPIO is that sometimes it creates only relatively modest negative contrast which can only be quantified by the use of dedicative quantitative algorithms [125]. This is especially a problem in images with a limited SNR, heavy calcified plaques, and blood degrading products, which can have strong susceptibility effects on gradient echo sequences. To date, the general approach in USPIO imaging relies on measurements performed at least at two time points (before and after administration of contrast medium) about 24 h apart. This not only poses a logistic challenge for patients but also might lead to signal alternation due to patient positioning, coil inhomogeneities, and noise between visits.

Additionally at the moment there is no consensus on the use of the methodology used on quantification of signal reduction. Some of the proposed approaches rely on normalization of the signal intensity to the adjacent sternocleidomastoid muscle. However, this suggests that the adjacent muscle does not enhance even though it is perfused by blood containing USPIOs. This might lead to a systemic bias of the measured USPIO uptake and hence the "true USPIO effect" [125].

6 Biomechanical Stress

The previous sections of this chapter have discussed the impact of morphological and compositional features of the vessel wall on the development of atherosclerotic lesions. However, atherosclerotic disease does depend not only on the influence from extraluminal plaque features that destabilize the plaque, but also on effects from the blood on the vessel wall. Comparison of postmortem plaque distribution to in vitro fluid dynamic models has provided a relatively direct insight into the association between wall shear stress (WSS) and the focal development of atherosclerotic lesions [132]. Both ultrasound and MR imaging are generally suited for direct assessment of wall thickness and blood velocities (from which WSSs are derived) in straight vessel sections. However, quantification of blood velocities remains difficult in areas with non-laminar flow, such as the carotid bifurcation, which is the preferred location for initiation of atherosclerotic disease [133].

When looking at the luminal site and blood flow, two primary mechanical forces of hemodynamic origin with impact on vessel structure and remodeling can be observed: fluid wall shear stress and tensile stress. Shear stress is the frictional force per unit area, exerted on the luminal vessel wall and endothelial surface by and in the direction of the blood flow [134]. Blood vessel segments with slow, turbulent flow and temporal fluctuations of flow direction, such as in the carotid bifurcation, experience only weak net hemodynamic shear stress and seem to be most vulnerable to atherosclerotic remodeling [132, 135, 136]. Fast and laminar flow, resulting in higher levels of shear stress, in contrast seems to have a protective effect [137]. Alternation in the gene expression of endothelial cells towards pro-atherogenic effects due to a low magnitude of shear stress might be one of the factors that induce lipid accumulation, thinning of vascular smooth muscle cells, outward remodeling, decrease of collagen content, and thinning of the fibrous cap [134, 138].

Tensile (or circumferential) stress is the normal mechanical transmural force along the arterial wall which originates from the internal pressure, created by mechanical loading with blood [134]. Studies reported that tensile stress is the highest in the shoulder areas of the plaque, which in consequence are the most typical areas of plaque rupture [139]. Plaque rupture, however, does not always have to take place in areas of the highest tensile stress, since also local variations in non-high stress regions (e.g., calcified nodules) may weaken the plaque surface [140].

Due to the lack of an in vivo "gold standard" for measurements of mechanical indicators that can be utilized to assess plaque vulnerability and rupture risk, models for depiction of stress exerted on the vessel wall have received increasing interest. Over the last decade advancement has been made from hardware models of the carotid bifurcation to image-based computational models that combine mechanical factors and morphological information from actual patient data. Recent studies increasingly additionally consider the effect of single plaque components on the general vascular stress profile. Description of the various applied techniques is beyond the scope of this chapter, but can be found in the following review: [141]. Although the mechanical approach remains extensively experimental, valuable data and a number of parameters can be received.

In a structural analysis based on in vivo MRI of five patients with vulnerable carotid arteries, Li et al. [142] found higher stress values in previously ruptured plaques than in unruptured plaques. Furthermore stress concentrations were high in the thinnest fibrous cap regions and the shoulder regions of the plaque, which is in accordance with previous findings [143]. However, as previously mentioned not only

thinning of the FC seems to increase plaque wall stress (PWS), but also microcalcification inclusions in the FC have been associated with elevated stress levels and may thus be related to plaque rupture [144]. Even though WSS seems to have a major role in plaque initiation and early lesions, mechanisms in plaque progression and rupture remain not well understood. In a recent serial study Yang et al. could show a positive correlation between WSS and wall thickness increase, while PWS was negatively correlated [145]. PWS, however, seems to be an important factor in plaque rupture. Teng et al. compared histological endarterectomy specimens to stress values derived by 3D fluid–structure interaction (FSI) models and found PWS values in previously ruptured plaques to be 100 % higher compared to plaques without rupture ($P < 0.05$), while the same trend in flow shear stress remained insignificant [146]. Significantly higher local stress concentrations in rupture sites and generally higher PWS levels in ruptured plaques were also reported by Gao et al.[147], supporting the stress-induced plaque rupture hypothesis. Various studies also report influences of the NWI [148] and other plaque structures such as IPH [149] and juxtaluminal hemorrhage/thrombus [86] on PWS and WSS and recurrent ischemic events.

Future advancements in resolution and implementation of component characteristics (e.g., LR/NC vs. calcification; soft LR/NC vs. solid LR/NC) into the computational model may give an even more exact insight into mechanical forces acting on the vessel wall and improve risk stratification. Furthermore new markers for vulnerability may be derived: A recent study by Teng et al. examined the relationship between the area of maximum principal stress along the lumen (stress-P), lumen irregularity (L-deltair), local FC thickness, and lumen curvature. If irregular luminal surface was present, a high correlation of stress-P with lumen curvature could be detected, while only a weak or no correlation with local FC thickness was found. For a relatively round lumen, exactly the opposite applied to stress-P. Consequently lumen shape was suggested as a method of identifying vulnerable plaque sites in mechanics-based plaque vulnerability assessment [150].

7 Plaque Imaging Biomarkers and Their Role in Studies

As demonstrated in the previous sections, MRI provides quantitative information on plaque burden and plaque composition and thus can be used for monitoring plaque progression or regression in serial studies. Besides angiography, B-mode ultrasound, and IVUS, MRI has emerged to be a promising tool for monitoring the efficacy in therapeutic studies and for studying the influence of plaque characteristics on plaque development.

7.1 Sample Size Calculation

In order to establish carotid MR imaging as a reliable tool for use in clinical trials, low variability due to measurement error must be ensured. In a recent multicenter trial, which acquired MR images of 20 asymptomatic placebo-controlled subjects in five clinical sites over 13 weeks, the intra- and inter-reader reproducibility of quantitative plaque measurements was evaluated [64]. Scans were performed on 1.5 T scanners using TOF, T1/PD/T2- and contrast-enhanced T1-weighted images. Analysis of the derived data showed a low inter-scan variability with measurement errors for wall volume, wall/outer wall ratio, %LR/NC volume, and %Ca volume of 5.8 %, 3.2 %, 11.1 %, and 18.6 %, respectively. Subsequent power analysis, based on these values, showed that a study with 14 participants in each group could detect a 5 % change in wall/outer wall ratio, 10 % change in wall volume, and 20 % change in %LR/NC volume (power = 80 %, $P < 0.05$). Recent studies at 3.0 T using parallel imaging techniques have shown even lower measurement errors [151], suggesting that the number of patients needed to show an anti-atherosclerotic effect might be even lower at 3.0 T. These results show that carotid MRI provides highly reproducible carotid wall measurements and that bb-MRI of the carotids can be a valuable maker in experimental, clinical, and/or therapeutical studies.

7.2 Therapeutical Studies

Over the last decades, anti-atherosclerotic therapy, aimed at various systemic risk factors, has been shown to be a valuable approach for the reduction of clinical events (e.g., myocardial infarct, ischemic stroke) in multiple, long-term, and randomized trials [152]. Especially statins have shown to reduce the overall rate of heart attacks and stroke significantly [153]. However, effect evaluation of newly introduced therapeutical approaches, which target inflammation and enzymatic targets, is difficult. Since changes of the cardiovascular risk due to the application of a new drug cannot always be observed directly, large and long-term morbidity and mortality studies are necessary to prove its superiority to previous drugs. Surrogate endpoint studies, in contrast, can evaluate dose-dependent changes and causality of drug effect and disease response in a shorter amount of time and thus may save organizational and financial resources. Thus, besides clinical surrogate markers such as LDL-c, HDL-c, or HbA1c, imaging of atherosclerosis is increasingly accepted as a valuable surrogate endpoint that enables depiction of the atherosclerotic process itself [154].

In one of the first therapeutic case–control studies involving bb-MRI, Zhao et al. demonstrated in eight patients with coronary artery disease that prolonged intensive

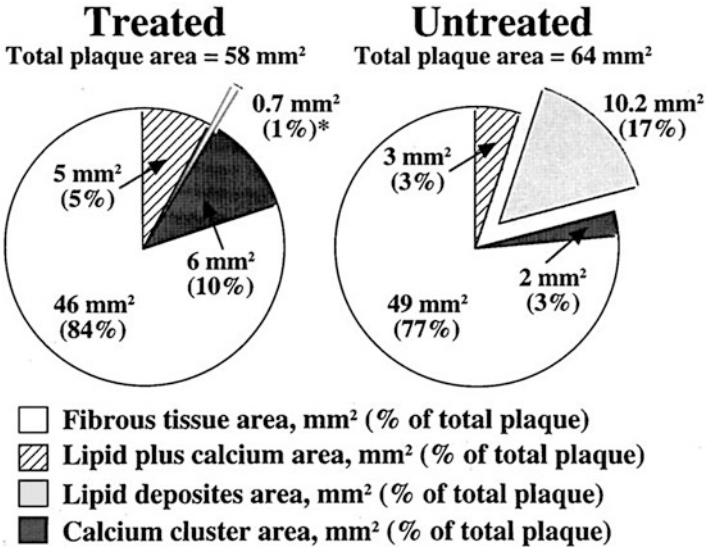

Fig. 4.9 Comparisons of carotid plaque tissue components and composition. The treated plaques contained significantly less lipid than did the untreated plaques ($P = 0.01$). Fibrous tissue, calcium, and calcium plus lipid were not statistically different between the two groups. Reprinted with permission from [155]

lipid-lowering therapy for 10 years is associated with a markedly decreased lipid content in carotid plaques (see Fig. 4.9) [155]. Patients treated with niacin, novastatin, and colestipol had a smaller lipid core area and a lower lipid content in the carotid artery compared to untreated control subjects.

Atherosclerosis is a chronic disease which starts early in life and develops over decades. In a natural history study with 68 asymptomatic subjects with ≥50 % stenosis [156], the wall area increased by 2.2 %/year ($P = 0.001$) and the mean NWI by 1.7 % per year ($P < 0.001$) and mean lumen area decreased by 1.9 % per year ($P = 0.02$). The mean total vessel area did not change significantly (0.5 % per year; $P = 0.3$).

This progression rate seems to be substantially higher in TIA/stroke patients. In a study by Kwee et al. 40 symptomatic patients with ipsilateral <70 % carotid stenosis underwent MRI of the plaque ipsilateral to the symptomatic side at baseline and after 1 year. Over a 1-year period, mean carotid lumen volume decreased by 4.8 % ($P = 0.013$) and mean wall volume increased by 11.2 % ($P < 0.001$). Total vessel volume did not significantly change ($P = 0.147$) [157].

Corti et al. reported that maintained lipid-lowering therapy with simvastatin can induce significant regression of atherosclerotic plaques in humans [158]. Subjects with atherosclerotic plaque in the carotid arteries or the aorta were followed by serial MRI studies in 6 month intervals over a period of 24 months. First significant reductions in vessel wall thickness and vessel wall area compared to baseline were observed after 12 months, and continued during the further observation process. A small but significant increase in lumen area (4–6 %) could be observed after 24 months only, implying a remodeling process of the arteries [159] (see Fig. 4.10).

In a recent study Underhill et al. [160] strengthened the assumption that plaque composition may be more sensitive to therapy than overall plaque burden. Change of wall *volume* (WV), *wall thickness* (WT), *normalized wall index* (NWI), *%LR/NC*, and *%fibrous tissue* was assessed by bb-MRI in patients before and after 24 months of rosuvastatin therapy. Statin treatment showed a significant reduction of the LR/NC content within the vessel wall (-41.4 ± 8.1 %; $P = 0.005$), an increase in percentage of fibrous tissue (1.8 ± 0.7 %; $P = 0.02$) and no significant change in plaque burden measurements (see Fig. 4.11).

Preliminary results from another clinical trial by Zhao et al., testing the lipid depletion therapy, have suggested similar results [161]. After 3 years of lipid therapy, the 33 subjects with measurable LR/NC at baseline had a significant reduction in plaque lipid content: LR/NC volume decreased from 60.4 ± 59.5 mm^3 to 37.4 ± 69.5 mm^3 ($P < 0.001$) and %LR/NC (LR/NC area/wall area in the lipid-rich regions) from 14.2 ± 7.0 % to 7.4 ± 8.2 % ($P < 0.001$). The time course showed that %LR/NC decreased by 3.2 ($P < 0.001$) in the first year, by 3.0 ($P = 0.005$) in the second year, and by 0.91 ($P = 0.2$) in the third year [162].

Since changes in plaque burden (assessed with 1.5 T) seem to be hardly noticed prior to 2 years of therapy, detection of changes in plaque composition may enable earlier evaluation of therapeutic effects already after 1 year of treatment [161]. According to a recent study by Migrino et al. [163] MR imaging at 3 T may shorten the period to detect changes in plaque volume to 6 months.

Besides metric measurements for therapeutic evaluation of plaque burden and composition, MRI affords depiction and quantification of "newer" parameters, such as inflammation and neovascularization. The ATHEROMA study evaluated the effects of low-dose and high-dose statins based on imaging via serial USPIO-enhanced MRI [164]. First treatment effects in the high-dose group could be visualized as significant signal reduction in comparison to baseline

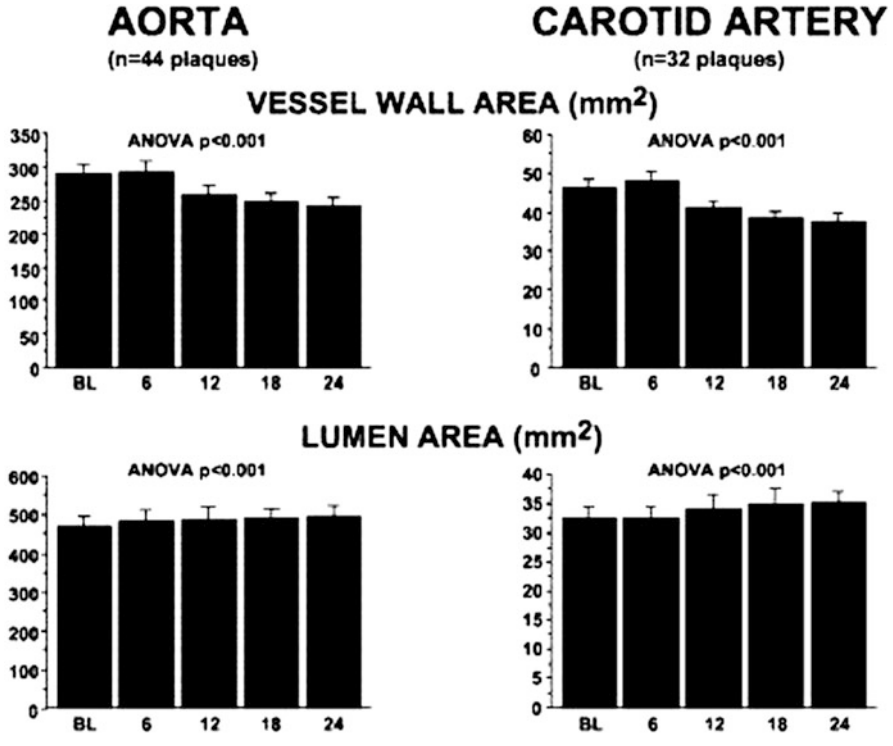

Fig. 4.10 Changes in atherosclerotic vessel wall dimensions after statin treatment. Data on vessel wall area (*top*) and lumen area (*bottom*) at baseline, 6, 12, 18, and 24 months on simvastatin for aorta (*left*) and the carotid arteries (*right*). Data are given as mean + SEM. Reprinted with permission from [159]

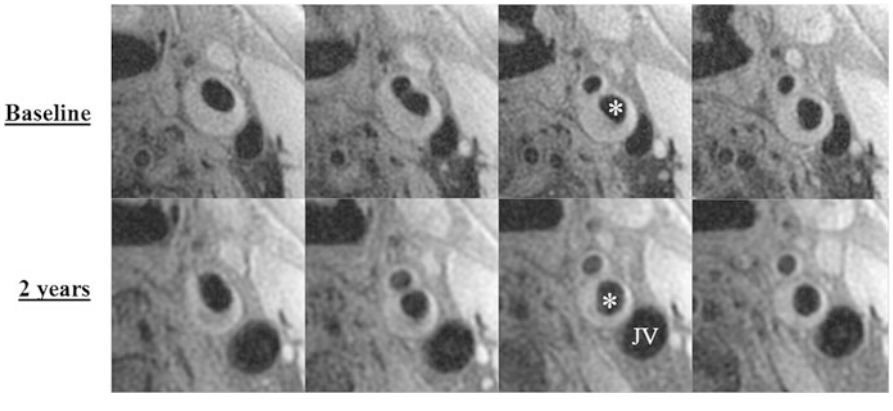

Fig. 4.11 Comparison of a baseline T1W carotid plaque (*top row*) with the same imaging locations 2 years after treatment (*bottom row*). Notice the decrease in wall area and subsequent increase in lumen area, particularly in the internal carotid artery. *Single asterisk*, lumen of the internal carotid artery. Reprinted with permission from [160]

USPIO-defined inflammation after 6 weeks (signal intensity change [ΔSI] 0.13, $P = 0.0003$) (see Fig. 4.12). Signal difference was even higher after high-dose treatment for duration of 12 weeks (ΔSI 0.20, $P < 0.0001$). However, the authors noted that measurements may have been compromised by the aforementioned drawbacks of USPIO imaging (i.e., due to the necessity of two imaging sessions, such as variations in coil positioning and image co-registration). Quantitative post-USPIO measurements in qT2* only, as described by Patterson et al. [165], however, might facilitate the use of USPIO imaging and pave the way for a wider use in therapeutic studies (see Fig. 4.13).

Alternatively inflammation can be indirectly monitored by DCE-MRI. In a study of 28 subjects receiving intensive lipid therapy, microvascular changes in the plaque were observed by DCE-MRI at baseline and after 1 year [123]. Results stated that intensive lipid therapy is associated with a significant reduction in the transfer constant (K^{trans}) (0.085 min $(-1) \pm 0.037$ [standard deviation] to 0.067 min $(-1) \pm 0.028$, $P = 0.02$) within 12 months after onset of treatment. Interestingly changes of K^{trans} were not significantly correlated with observed reductions in lipid-rich necrotic core area or reductions in HsCRP level, suggesting that DCE-MRI may be an alternative and independent method for assessing therapeutic effects on carotid artery atherosclerosis.

7.3 Multicenter Studies

Although the majority of therapeutic studies with application of bb-MRI were performed as single-center trials, the feasibility of using MRI techniques to evaluate carotid atherosclerosis in multicenter trials has been studied. In a

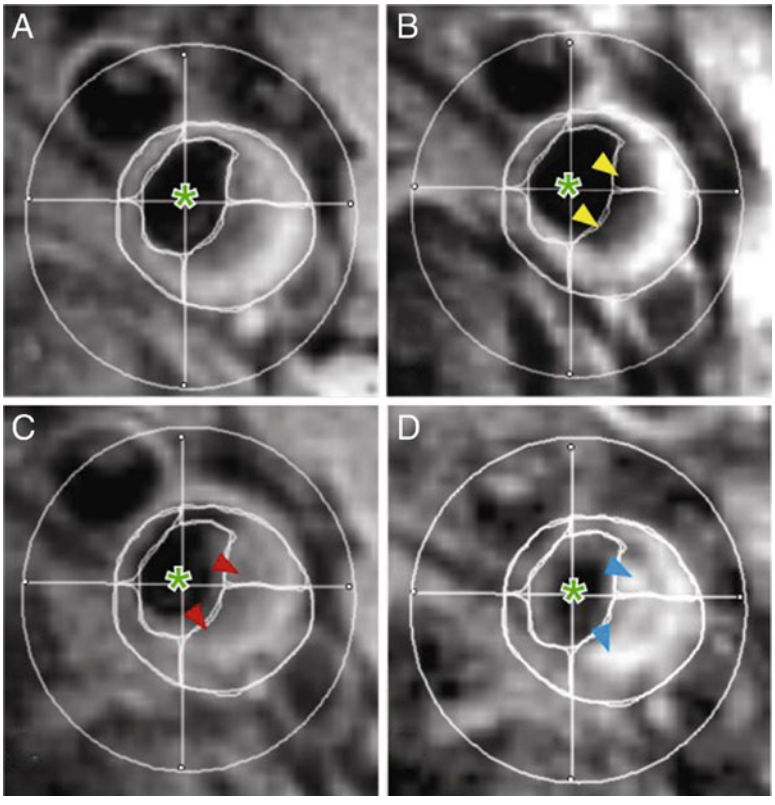

Fig. 4.12 Atorvastatin therapy: evaluation of macrophage activity using ultrasmall superparamagnetic iron oxide-enhanced carotid MRI. T2*-weighted imaging of a right common carotid artery before and after ultrasmall superparamagnetic iron oxide (USPIO) infusion at the 2 time points of 0 (**a** and **b**) and 12 (**c** and **d**) weeks. (**b**) USPIO uptake can clearly be seen in the plaque at baseline (*yellow arrowheads*). (**c**) Sinerem has been cycled out of the plaque before reinfusion at 12 weeks (*red arrowheads*). (**d**) The plaque enhances at 12 weeks (*blue arrowheads*), indicating that high-dose statin treatment has damped the USPIO-defined inflammation. Plaque segmentation was performed using a combination of multicontrast sequences. Signals from artifact, extravascular structures, and the luminal blood pool (*green asterisks*) are excluded from the analysis. Reprinted with permission from [164] (Color figure online)

study reported by Chu et al. [166] 39 asymptomatic subjects with atherosclerotic disease and >15 % stenosis as determined by ultrasound were recruited from five clinical sites and received four scans in 13 weeks on GE 1.5 T scanners with a standardized carotid imaging protocol (TOF, T1/T2 weighted, T1-contrast enhanced (CE), and proton density (PD)). The mean image quality per site was 3.5–4.2 (5-point scale, with image quality ≥3 acceptable for analysis) and across all four time points a matched coverage of at least six MRI-locations (which is considered to be necessary for reliable evaluation) was achieved by all participating centers.

Another study, which aimed at the creation of a carotid atherosclerosis score (CAS), was performed with 344 subjects from 4 imaging centers [167]. Using 60 % of the included patients as a training group, factors associated with IPH and fibrous cap rupture were evaluated by multivariate analysis. Maximum LR/NC-proportion of the arterial wall was found to be the strongest predictor of IPH ($P < 0.001$) and FCR ($P < 0.001$). Application of the subsequently derived CAS on the test group showed good identification of IPH (AUC = 0.91) and FCR (AUC = 0.93). Thus the authors concluded that quantification of the LR/NC may be an effective complementary strategy to stenosis for classifying carotid atherosclerotic disease severity [167]. Various other multicenter clinical studies on the imaging of atherosclerosis are currently ongoing [168, 169].

8 Future Developments

8.1 Hardware

MRI at 7 T is of significant interest because it provides an opportunity for increases in spatial resolution or acquisition speed while revealing novel imaging contrasts. At 7 T, fast gradient echo sequences show hyperintense vascular signal even without administration of contrast agents [170]. However, imaging of the carotid artery bifurcation at 7 T has been limited so far mainly by the lack of suitable coils.

Recent studies have suggested a potential using ^{18}FDG-Positron emission tomography (PET) to image atherosclerotic plaque inflammation [171, 172]. With the

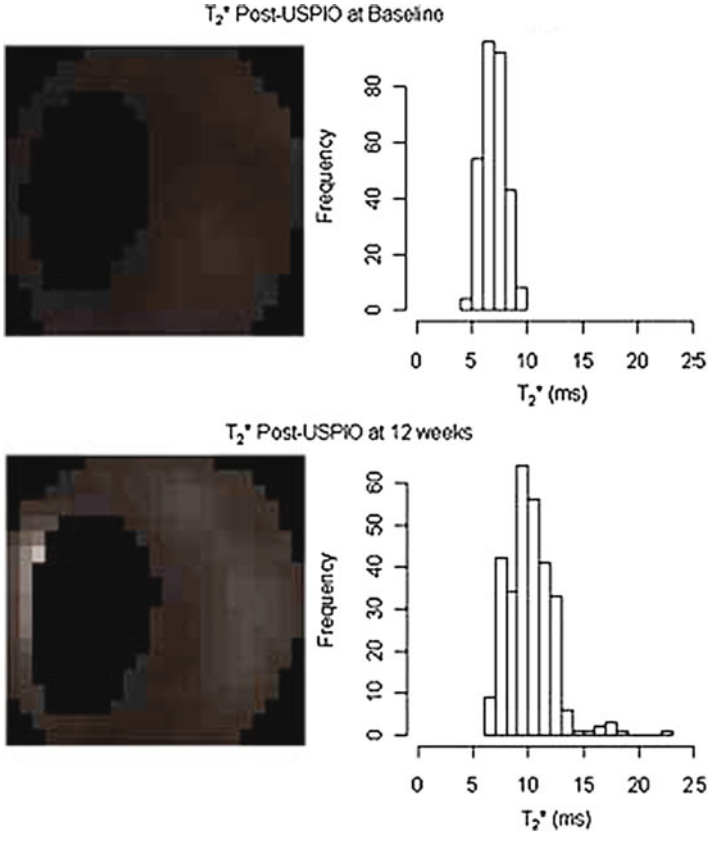

Fig. 4.13 Quantitative T2* (qT2*) maps illustrating the treatment response for a patient on high-dose statin therapy (80 mg of atorvastatin). The map was derived from multi-echo, quadruple inversion recovery-prepared, two-dimensional, ECG-gated images. The post-USPIO infusion scans at baseline and after 12 weeks, and the corresponding histograms from each pixel intensity within the plaque, are shown. The qT2* values were calculated at each pixel after performing spatial smoothing using a Gaussian kernel (matrix size, 33; full-width at half-maximum, 1), followed by the application of Miller's power correction and fitting to the linearization of Sc $(TE)^2 = S^20$ exp(−2TE/T2*) using standard linear interpolation. Reprinted with permission from [165]

recent introduction of clinical MRI/PET systems, the morphological information of MRI can be combined with the functional information of the PET component, and future studies will have to examine the potential of MRI/PET to image atherosclerosis.

With advances in sequence design and the use of higher field strengths for imaging the carotid arteries, the development of new coil designs has gained a new momentum. MR scanners are continuously equipped with an increasing number of receivers and make imaging with coils, consisting of larger amounts of elements, possible [173]. For example by the use of an eight-channel phased-array coil, SNR, CNR, and consequently vessel coverage can be improved significantly [174].

8.2 Minimizing Motion Artifacts

Motion has been the challenge of every imaging modality. Consequently image quality in carotid artery MR imaging can be compromised by motion artifacts, limiting the accuracy of plaque assessment. In particular artifacts due to swallowing or patient movement can be hard to overcome and can cause temporary changes of carotid location of up to almost 1 cm [175]. Comfortable patient bedding, short imaging sequences, and special neck holders can limit head motion and improve image quality. Additionally several hardware-based attempts for the detection of movements have been made. Motion-detection navigators, which are placed on the tongue, can detect motion and limit image acquisition to motion-less phases [176] only. Neck coils capable of motion detection have also been reported to improve image quality and minimize swallowing artifacts [177].

8.3 Parallel Imaging

Parallel imaging has been one of the biggest innovations in magnetic resonance imaging in the last decade. The use of multiple receiver coils to augment the time consuming Fourier encoding has reduced acquisition times significantly. A 3.0 T BB-MRI study using Parallel Imaging with an acceleration factor of 2 [65] demonstrated that the number of excluded scans due to insufficient image quality can be reduced substantially by using this technique. In this study the percentage of non-diagnostic scans was approximately 2 %, which is substantially smaller than the number of excluded scans in previous 1.5 T MRI studies [64, 178–180], where the number of excluded exams ranged from 5 to 33 %. The authors concluded that one of the reasons of the lower number of excluded exams compared to previous 1.5 T MR studies might be the signal gains associated with the higher

field strength in combination with the shorter scan time due to the Parallel Imaging technique, which is easier to tolerate for the patients and might therefore result in less motion artifacts and artifacts due to patient swallowing.

9 Conclusion

Noninvasive bb-MRI of the carotid arteries has unique potential to identify and quantify the key features of the vulnerable plaque. BB-MRI is well suited for this role because it has an excellent soft tissue contrast, is noninvasive, does not involve ionizing radiation, enables the visualization of the vessel lumen and wall, and can be repeated serially. The ability to measure the plaque burden as well as the plaque components (e.g., LR/NC, IPH, FC) makes bb-MRI a suitable tool to track progression or regression of atherosclerosis. This potential enables studies that are aimed at the understanding of plaque development and to test new anti-atherosclerotic therapies and makes it a unique approach since histology, the gold standard, can only depict wall characteristics at one point in time. Additionally bb-MR imaging of the carotid arteries enables the identification of risk factors for plaque development, such as IPH. In the future, a personalized medical approach could use bb-MRI to stratify the risk of plaque-related events in asymptomatic patients. Based on these findings patients may be screened and assigned to the best suited individual therapy.

References

1. Virmani R, Kolodgie FD, Burke AP, Farb A, Schwartz SM (2000) Lessons from sudden coronary death: a comprehensive morphological classification scheme for atherosclerotic lesions. Arterioscler Thromb Vasc Biol 20(5):1262–1275
2. Naghavi M, Libby P, Falk E, Casscells SW, Litovsky S, Rumberger J, Badimon JJ et al (2003) From vulnerable plaque to vulnerable patient: a call for new definitions and risk assessment strategies: part II. Circulation 108(15):1772–1778. doi:10.1161/01.CIR.0000087481.55887.C9
3. Naghavi M, Libby P, Falk E, Casscells SW, Litovsky S, Rumberger J, Badimon JJ et al (2003) From vulnerable plaque to vulnerable patient: a call for new definitions and risk assessment strategies: part I. Circulation 108(14):1664–1672. doi:10.1161/01.CIR.0000087480.94275.97
4. Saam T, Hatsukami TS, Takaya N, Chu B, Underhill H, Kerwin WS, Cai J, Ferguson MS, Yuan C (2007) The vulnerable, or high-risk, atherosclerotic plaque: noninvasive MR imaging for characterization and assessment. Radiology 244(1):64–77. doi:10.1148/radiol.2441051769, 244/1/64 [pii]
5. Yarnykh VL, Terashima M, Hayes CE, Shimakawa A, Takaya N, Nguyen PK, Brittain JH, McConnell MV, Yuan C (2006) Multicontrast black-blood MRI of carotid arteries: comparison between 1.5 and 3 tesla magnetic field strengths. J Magn Reson Imaging 23(5):691–698. doi:10.1002/jmri.20562
6. Koktzoglou I, Chung YC, Mani V, Carroll TJ, Morasch MD, Mizsei G, Simonetti OP, Fayad ZA, Li D (2006)Multislice dark-blood carotid artery wall imaging: a 1.5T and 3.0T comparison. J Magn Reson Imaging 23(5):699–705. doi:10.1002/jmri.20563
7. Underhill HR, Yarnykh VL, Hatsukami TS, Wang J, Balu N, Hayes CE, Oikawa M et al (2008) Carotid plaque morphology and composition: initial comparison between 1.5- and 3.0-T magnetic field strengths. Radiology 248(2):550–560. doi:10.1148/radiol.2482071114, 2482071114 [pii]
8. Kerwin WS, Liu F, Yarnykh V, Underhill H, Oikawa M, Yu W, Hatsukami TS, Yuan C (2008) Signal features of the atherosclerotic plaque at 3.0 Tesla versus 1.5 Tesla: impact on automatic classification. J Magn Reson Imaging 28(4):987–995. doi:10.1002/jmri.21529
9. Hayes CE, Mathis CM, Yuan C (1996) Surface coil phased arrays for high-resolution imaging of the carotid arteries. J Magn Reson Imaging 6(1):109–112
10. Saam T, Raya JG, Cyran CC, Bochmann K, Meimarakis G, Dietrich O, Clevert DA et al (2009) High resolution carotid black-blood 3T MR with parallel imaging and dedicated 4-channel surface coils. J Cardiovasc Magn Reson 11:41. doi:10.1186/1532-429X-11-41
11. Underhill HR, Yuan C (2011) Carotid MRI: a tool for monitoring individual response to cardiovascular therapy? Expert Rev Cardiovasc Ther 9(1):63–80. doi:10.1586/erc.10.172
12. Serfaty JM, Chaabane L, Tabib A, Chevallier JM, Briguet A, Douek PC (2001) Atherosclerotic plaques: classification and characterization with T2-weighted high-spatial-resolution MR imaging – an in vitro study. Radiology 219(2):403–410
13. Cappendijk VC, Cleutjens KB, Heeneman S, Schurink GW, Welten RJ, Kessels AG, van Suylen RJ, Daemen MJ, van Engelshoven JM, Kooi ME (2004) In vivo detection of hemorrhage in human atherosclerotic plaques with magnetic resonance imaging. J Magn Reson Imaging 20(1):105–110. doi:10.1002/jmri.20060
14. Corti R, Osende JI, Fayad ZA, Fallon JT, Fuster V, Mizsei G, Dickstein E, Drayer B, Badimon JJ (2002) In vivo noninvasive detection and age definition of arterial thrombus by MRI. J Am Coll Cardiol 39(8):1366–1373
15. Clarke SE, Hammond RR, Mitchell JR, Rutt BK (2003) Quantitative assessment of carotid plaque composition using multicontrast MRI and registered histology. Magn Reson Med 50(6):1199–1208. doi:10.1002/mrm.10618
16. Wang J, MS Ferguson, N Balu, C Yuan, TS Hatsukami, P Bornert. 2010b. Improved carotid intraplaque hemorrhage imaging using a slab-selective phase-sensitive inversion-recovery (SPI) sequence. Magn Reson Med 64(5): 1332–1340.doi:10.1002/mrm.22539
17. Yuan C, Mitsumori LM, Ferguson MS, Polissar NL, Echelard D, Ortiz G, Small R, Davies JW, Kerwin WS, Hatsukami TS (2001) In vivo accuracy of multispectral magnetic resonance imaging for identifying lipid-rich necrotic cores and intraplaque hemorrhage in advanced human carotid plaques. Circulation 104(17):2051–2056
18. Yuan C, Mitsumori LM, Beach KW, Maravilla KR (2001) Carotid atherosclerotic plaque: noninvasive MR characterization and identification of vulnerable lesions. Radiology 221(2): 285–299
19. Lin W, Abendschein DR, Haacke EM (1997) Contrast-enhanced magnetic resonance angiography of carotid arterial wall in pigs. J Magn Reson Imaging 7(1):183–190
20. Dumoulin CL, Hart HR Jr (1986) Magnetic resonance angiography. Radiology 161(3):717–720
21. Yuan C, Kerwin WS, Yarnykh VL, Cai J, Saam T, Chu B, Takaya N et al (2006) MRI of atherosclerosis in clinical trials. NMR Biomed 19(6):636–654. doi:10.1002/nbm.1065
22. Edelman RR, Mattle HP, Wallner B, Bajakian R, Kleefield J, Kent C, Skillman JJ, Mendel JB, Atkinson DJ (1990) Extracranial carotid arteries: evaluation with "black blood" MR angiography. Radiology 177(1):45–50

23. Edelman RR, Chien D, Kim D (1991) Fast selective black blood MR imaging. Radiology 181(3):655–660
24. Wang J, Yarnykh VL, Hatsukami T, Chu B, Balu N, Yuan C (2007) Improved suppression of plaque-mimicking artifacts in black-blood carotid atherosclerosis imaging using a multislice motion-sensitized driven-equilibrium (MSDE) turbo spin-echo (TSE) sequence. Magn Reson Med 58(5):973–981. doi:10.1002/mrm.21385
25. Steinman DA, Rutt BK (1998) On the nature and reduction of plaque-mimicking flow artifacts in black blood MRI of the carotid bifurcation. Magn Reson Med 39(4):635–641
26. Watanabe Y, Nagayama M (2010) MR plaque imaging of the carotid artery. Neuroradiology 52(4):253–274. doi:10.1007/s00234-010-0663-z
27. Simonetti OP, Finn JP, White RD, Laub G, Henry DA (1996) "Black blood" T2-weighted inversion-recovery MR imaging of the heart. Radiology 199(1):49–57
28. Fayad ZA, Fuster V (2002) Atherothrombotic plaques and the need for imaging. Neuroimaging Clin N Am 12(3):351–364
29. Yarnykh VL, Yuan C (2003) Multislice double inversion-recovery black-blood imaging with simultaneous slice reinversion. J Magn Reson Imaging 17(4):478–483. doi:10.1002/jmri.10278
30. Yarnykh VL, Yuan C (2002) T1-insensitive flow suppression using quadruple inversion-recovery. Magn Reson Med 48(5):899–905. doi:10.1002/mrm.10292
31. Balu N, Wang J, Dong L, Baluyot F, Chen H, Yuan C (2009) Current techniques for MR imaging of atherosclerosis. Top Magn Reson Imaging 20(4):203–215. doi:10.1097 / RMR.0b013e3181ea287d00002142-200908000-00001 [pii]
32. Koktzoglou I, Li D (2007) Diffusion-prepared segmented steady-state free precession: application to 3D black-blood cardiovascular magnetic resonance of the thoracic aorta and carotid artery walls. J Cardiovasc Magn Reson 9(1):33–42. doi:10.1080/10976640600843413
33. Wang J, Balu N, Canton G, Yuan C (2010) Imaging biomarkers of cardiovascular disease. J Magn Reson Imaging 32(3):502–515. doi:10.1002/jmri.22266
34. Yim YJ, Choe YH, Ko Y, Kim ST, Kim KH, Jeon P, Byun HS, Kim DI (2008) High signal intensity halo around the carotid artery on maximum intensity projection images of time-of-flight MR angiography: a new sign for intraplaque hemorrhage. J Magn Reson Imaging 27(6):1341–1346. doi:10.1002/jmri.21284
35. Yuan C, Petty C, O'Brien KD, Hatsukami TS, Eary JF, Brown BG (1997) In vitro and in situ magnetic resonance imaging signal features of atherosclerotic plaque-associated lipids. Arterioscler Thromb Vasc Biol 17(8):1496–1503
36. Takaya N, Cai J, Ferguson MS, Yarnykh VL, Chu B, Saam T, Polissar NL et al (2006) Intra- and interreader reproducibility of magnetic resonance imaging for quantifying the lipid-rich necrotic core is improved with gadolinium contrast enhancement. J Magn Reson Imaging 24(1):203–210. doi:10.1002/jmri.20599
37. Wasserman BA, Smith WI, Trout HH 3rd, Cannon RO 3rd, Balaban RS, Arai AE (2002) Carotid artery atherosclerosis: in vivo morphologic characterization with gadolinium-enhanced double-oblique MR imaging initial results. Radiology 223(2):566–573
38. Balu N, Wang J, Dong L, Baluyot F, Chen H, Yuan C (2009) Current techniques for MR imaging of atherosclerosis. Top Magn Reson Imaging 20(4):203–215. doi:10.1097/RMR.0b013e3181ea287d
39. Cai J, Hatsukami TS, Ferguson MS, Kerwin WS, Saam T, Chu B, Takaya N, Polissar NL, Yuan C (2005) In vivo quantitative measurement of intact fibrous cap and lipid-rich necrotic core size in atherosclerotic carotid plaque: comparison of high-resolution, contrast-enhanced magnetic resonance imaging and histology. Circulation 112(22):3437–3444. doi:10.1161/CIRCULATIONAHA.104.528174, CIRCULATIONAHA.104.528174 [pii]
40. Armitage FE, Richardson DE, Li KC (1990) Polymeric contrast agents for magnetic resonance imaging: synthesis and characterization of gadolinium diethylenetriaminepentaacetic acid conjugated to polysaccharides. Bioconjug Chem 1(6):365–374
41. Flacke S, Fischer S, Scott MJ, Fuhrhop RJ, Allen JS, McLean M, Winter P et al (2001) Novel MRI contrast agent for molecular imaging of fibrin: implications for detecting vulnerable plaques. Circulation 104(11):1280–1285
42. Winter PM, Morawski AM, Caruthers SD, Fuhrhop RW, Zhang H, Williams TA, Allen JS et al (2003) Molecular imaging of angiogenesis in early-stage atherosclerosis with alpha(v)beta3-integrin-targeted nanoparticles. Circulation 108(18):2270–2274. doi:10.1161/01.CIR.0000093185.16083.95
43. Barkhausen J, Ebert W, Heyer C, Debatin JF, Weinmann HJ (2003) Detection of atherosclerotic plaque with Gadofluorine-enhanced magnetic resonance imaging. Circulation 108(5):605–609. doi:10.1161/01.CIR.0000079099.36306.10
44. Kerwin W, Xu D, Liu F, Saam T, Underhill H, Takaya N, Chu B, Hatsukami T, Yuan C (2007) Magnetic resonance imaging of carotid atherosclerosis: plaque analysis. Top Magn Reson Imaging 18(5):371–378. doi:10.1097/rmr.0b013e3181598d9d
45. Dong L, Kerwin WS, Ferguson MS, Li R, Wang J, Chen H, Canton G, Hatsukami TS, Yuan C (2009) Cardiovascular magnetic resonance in carotid atherosclerotic disease. J Cardiovasc Magn Reson 11:53. doi:10.1186/1532-429X-11-53, 1532-429X-11-53 [pii]
46. Kerwin WS, Yuan C (2001) Active edge maps for medical image registration. Proc SPIE 4322:4516–4526
47. Fei B, Suri JS, Wilson DL (2005) Three-dimensional volume registration of carotid MR images. Stud Health Technol Inform 113:394–411
48. Chu B, Ferguson MS, Chen H, Hippe DS, Kerwin WS, Canton G, Yuan C, Hatsukami TS (2009) Magnetic [corrected] resonance imaging [corrected] features of the disruption-prone and the disrupted carotid plaque. JACC Cardiovasc Imaging 2(7):883–896. doi:10.1016/j.jcmg.2009.03.013, S1936-878X(09)00343-X [pii]
49. Greenland P, LaBree L, Azen SP, Doherty TM, Detrano RC (2004) Coronary artery calcium score combined with Framingham score for risk prediction in asymptomatic individuals. JAMA 291(2):210–215. doi:10.1001/jama.291.2.210
50. Ebrahim S, Papacosta O, Whincup P, Wannamethee G, Walker M, Nicolaides AN, Dhanjil S et al (1999) Carotid plaque, intima media thickness, cardiovascular risk factors, and prevalent cardiovascular disease in men and women: the British Regional Heart Study. Stroke 30(4):841–850
51. Glagov S, Weisenberg E, Zarins CK, Stankunavicius R, Kolettis GJ (1987) Compensatory enlargement of human atherosclerotic coronary arteries. N Engl J Med 316(22):1371–1375. doi:10.1056/NEJM198705283162204
52. Takaya N, Yuan C, Chu B, Saam T, Underhill H, Cai J, Tran N et al (2006) Association between carotid plaque characteristics and subsequent ischemic cerebrovascular events: a prospective assessment with MRI – initial results. Stroke 37(3):818–823. doi:10.1161/01.STR.0000204638.91099.91, 01.STR.0000204638.91099.91 [pii]
53. Mani V, Muntner P, Gidding SS, Aguiar SH, El Aidi H, Weinshelbaum KB, Taniguchi H et al (2009) Cardiovascular magnetic resonance parameters of atherosclerotic plaque burden improve discrimination of prior major adverse cardiovascular events. J Cardiovasc Magn Reson 11:10. doi:10.1186/1532-429X-11-10
54. Underhill HR, Kerwin WS, Hatsukami TS, Yuan C (2006) Automated measurement of mean wall thickness in the common carotid artery by MRI: a comparison to intima-media thickness by B-mode ultrasound. J Magn Reson Imaging 24(2):379–387. doi:10.1002/jmri.20636

55. Cao JJ, Thach C, Manolio TA, Psaty BM, Kuller LH, Chaves PH, Polak JF et al (2003) C-reactive protein, carotid intima-media thickness, and incidence of ischemic stroke in the elderly: the Cardiovascular Health Study. Circulation 108(2):166–170. doi:10.1161/01.CIR.0000079160.07364.6A
56. Zhao X, Underhill HR, Zhao Q, Cai J, Li F, Oikawa M, Dong L et al (2011) Discriminating carotid atherosclerotic lesion severity by luminal stenosis and plaque burden: a comparison utilizing high-resolution magnetic resonance imaging at 3.0 Tesla. Stroke 42(2):347–353. doi:10.1161/STROKEAHA.110.597328
57. Luo Y, Polissar N, Han C, Yarnykh V, Kerwin WS, Hatsukami TS, Yuan C (2003) Accuracy and uniqueness of three in vivo measurements of atherosclerotic carotid plaque morphology with black blood MRI. Magn Reson Med 50(1):75–82. doi:10.1002/mrm.10503
58. Yuan C, Beach KW, Smith LH Jr, Hatsukami TS (1998) Measurement of atherosclerotic carotid plaque size in vivo using high resolution magnetic resonance imaging. Circulation 98(24):2666–2671
59. Zhang S, Hatsukami TS, Polissar NL, Han C, Yuan C (2001) Comparison of carotid vessel wall area measurements using three different contrast-weighted black blood MR imaging techniques. Magn Reson Imaging 19(6):795–802, doi:S0730725X01004088 [pii]
60. Balu N, Chu B, Hatsukami TS, Yuan C, Yarnykh VL (2008) Comparison between 2D and 3D high-resolution black-blood techniques for carotid artery wall imaging in clinically significant atherosclerosis. J Magn Reson Imaging 27(4):918–924. doi:10.1002/jmri.21282
61. Saam T, Hatsukami TS, Yarnykh VL, Hayes CE, Underhill H, Chu B, Takaya N et al (2007) Reader and platform reproducibility for quantitative assessment of carotid atherosclerotic plaque using 1.5T Siemens, Philips, and General Electric scanners. J Magn Reson Imaging 26(2):344–352. doi:10.1002/jmri.21004
62. Duivenvoorden R, de Groot E, Elsen BM, Lameris JS, van der Geest RJ, Stroes ES, Kastelein JJ, Nederveen AJ (2009) In vivo quantification of carotid artery wall dimensions: 3.0-Tesla MRI versus B-mode ultrasound imaging. Circ Cardiovasc Imaging 2(3):235–242. doi:10.1161/CIRCIMAGING.108.788059
63. Alizadeh Dehnavi R, Doornbos J, Tamsma JT, Stuber M, Putter H, van der Geest RJ, Lamb HJ, de Roos A (2007) Assessment of the carotid artery by MRI at 3T: a study on reproducibility. J Magn Reson Imaging 25(5):1035–1043. doi:10.1002/jmri.20904
64. Saam T, Kerwin WS, Chu B, Cai J, Kampschulte A, Hatsukami TS, Zhao XQ et al (2005) Sample size calculation for clinical trials using magnetic resonance imaging for the quantitative assessment of carotid atherosclerosis. J Cardiovasc Magn Reson 7(5):799–808
65. Saam T, Raya JG, Cyran CC, Bochmann K, Meimarakis G, Dietrich O, Clevert DA et al (2009) High resolution carotid black-blood 3T MR with parallel imaging and dedicated 4-channel surface coils. J Cardiovasc Magn Reson 11:41. doi:10.1186/1532-429X-11-41, 1532-429X-11-41 [pii]
66. Toussaint JF, LaMuraglia GM, Southern JF, Fuster V, Kantor HL (1996) Magnetic resonance images lipid, fibrous, calcified, hemorrhagic, and thrombotic components of human atherosclerosis in vivo. Circulation 94(5):932–938
67. Hatsukami TS, Ross R, Polissar NL, Yuan C (2000) Visualization of fibrous cap thickness and rupture in human atherosclerotic carotid plaque in vivo with high-resolution magnetic resonance imaging. Circulation 102(9):959–964
68. Trivedi RA, U-King-Im J, Graves MJ, Horsley J, Goddard M, Kirkpatrick PJ, Gillard JH (2004) Multi-sequence in vivo MRI can quantify fibrous cap and lipid core components in human carotid atherosclerotic plaques. Eur J Vasc Endovasc Surg 28(2):207–213. doi:10.1016/j.ejvs.2004.05.001 S1078588404002199 [pii]
69. Chu B, Kampschulte A, Ferguson MS, Kerwin WS, Yarnykh VL, O'Brien KD, Polissar NL, Hatsukami TS, Yuan C (2004) Hemorrhage in the atherosclerotic carotid plaque: a high-resolution MRI study. Stroke 35(5):1079–1084. doi:10.1161/01.STR.0000125856.25309.86 01.STR.0000125856.25309.86 [pii]
70. Moody AR, Murphy RE, Morgan PS, Martel AL, Delay GS, Allder S, MacSweeney ST et al (2003) Characterization of complicated carotid plaque with magnetic resonance direct thrombus imaging in patients with cerebral ischemia. Circulation 107(24):3047–3052. doi:10.1161/01.CIR.0000074222.61572.44, 01.CIR.0000074222.61572.44 [pii]
71. Virmani R, Kolodgie FD, Burke AP, Finn AV, Gold HK, Tulenko TN, Wrenn SP, Narula J (2005) Atherosclerotic plaque progression and vulnerability to rupture: angiogenesis as a source of intraplaque hemorrhage. Arterioscler Thromb Vasc Biol 25(10):2054–2061. doi:10.1161/01.ATV.0000178991.71605.18
72. Davies MJ, Thomas AC (1985) Plaque fissuring – the cause of acute myocardial infarction, sudden ischaemic death, and crescendo angina. Br Heart J 53(4):363–373
73. Ota H, Yarnykh VL, Ferguson MS, Underhill HR, Demarco JK, Zhu DC, Oikawa M et al (2010) Carotid intraplaque hemorrhage imaging at 3.0-T MR imaging: comparison of the diagnostic performance of three T1-weighted sequences. Radiology 254(2):551–563. doi:10.1148/radiol.09090535, 254/2/551 [pii]
74. Wang J, Ferguson MS, Balu N, Yuan C, Hatsukami TS, Bornert P (2010) Improved carotid intraplaque hemorrhage imaging using a slab-selective phase-sensitive inversion-recovery (SPI) sequence. Magn Reson Med 64(5):1332–1340. doi:10.1002/mrm.22539
75. Arapoglou B, Kondi-Pafiti A, Katsenis K, Dimakakos P (1994) The clinical significance of carotid plaque haemorrhage. Int Angiol 13(4):323–326
76. Ammar AD, Wilson RL, Travers H, Lin JJ, Farha SJ, Chang FC (1984) Intraplaque hemorrhage: its significance in cerebrovascular disease. Am J Surg 148(6):840–843
77. Altaf N, Daniels L, Morgan PS, Auer D, MacSweeney ST, Moody AR, Gladman JR (2008) Detection of intraplaque hemorrhage by magnetic resonance imaging in symptomatic patients with mild to moderate carotid stenosis predicts recurrent neurological events. J Vasc Surg 47(2):337–342. doi:10.1016/j.jvs.2007.09.064
78. Singh N, Moody AR, Gladstone DJ, Leung G, Ravikumar R, Zhan J, Maggisano R (2009) Moderate carotid artery stenosis: MR imaging-depicted intraplaque hemorrhage predicts risk of cerebrovascular ischemic events in asymptomatic men. Radiology 252(2):502–508. doi:10.1148/radiol.2522080792, 2522080792 [pii]
79. Saam T, Underhill HR, Chu B, Takaya N, Cai J, Polissar NL, Yuan C, Hatsukami TS (2008) Prevalence of American Heart Association type VI carotid atherosclerotic lesions identified by magnetic resonance imaging for different levels of stenosis as measured by duplex ultrasound. J Am Coll Cardiol 51(10):1014–1021. doi:10.1016/j.jacc.2007.10.054, S0735-1097(07)03882-X [pii]
80. Kolodgie FD, Gold HK, Burke AP, Fowler DR, Kruth HS, Weber DK, Farb A et al (2003) Intraplaque hemorrhage and progression of coronary atheroma. N Engl J Med 349(24):2316–2325. doi:10.1056/NEJMoa035655
81. Libby P (2002) Inflammation in atherosclerosis. Nature 420(6917):868–874. doi:10.1038/nature01323
82. Bornstein NM, Krajewski A, Lewis AJ, Norris JW (1990) Clinical significance of carotid plaque hemorrhage. Arch Neurol 47(9):958–959
83. Underhill HR, Yuan C, Yarnykh VL, Chu B, Oikawa M, Polissar NL, Schwartz SM, Jarvik GP, Hatsukami TS (2009) Arterial remodeling in [corrected] subclinical carotid artery disease. JACC Cardiovasc Imaging 2(12):1381–1389. doi:10.1016/j.jcmg.2009.08.007

84. Underhill HR, Hatsukami TS, Fayad ZA, Fuster V, Yuan C (2010) MRI of carotid atherosclerosis: clinical implications and future directions. Nat Rev Cardiol 7(3):165–173. doi:10.1038/nrcardio.2009.246, nrcardio.2009.246 [pii]
85. Takaya N, Yuan C, Chu B, Saam T, Polissar NL, Jarvik GP, Isaac C et al (2005) Presence of intraplaque hemorrhage stimulates progression of carotid atherosclerotic plaques: a high-resolution magnetic resonance imaging study. Circulation 111(21):2768–2775. doi:10.1161/CIRCULATIONAHA.104.504167, CIRCULATIONAHA.104.504167 [pii]
86. Teng Z, Sadat U, Huang Y, Young VE, Graves MJ, Lu J, Gillard JH (2011) In vivo MRI-based 3D mechanical stress–strain profiles of carotid plaques with juxtaluminal plaque haemorrhage: an exploratory study for the mechanism of subsequent cerebrovascular events. Eur J Vasc Endovasc Surg 42(4):427–433. doi:10.1016/j.ejvs.2011.05.009
87. Toussaint JF, Southern JF, Fuster V, Kantor HL (1997) Water diffusion properties of human atherosclerosis and thrombosis measured by pulse field gradient nuclear magnetic resonance. Arterioscler Thromb Vasc Biol 17(3):542–546
88. Kampschulte A, Ferguson MS, Kerwin WS, Polissar NL, Chu B, Saam T, Hatsukami TS, Yuan C (2004) Differentiation of intraplaque versus juxtaluminal hemorrhage/thrombus in advanced human carotid atherosclerotic lesions by in vivo magnetic resonance imaging. Circulation 110(20):3239–3244. doi:10.1161/01.CIR.0000147287.23741.9A, 01.CIR.0000147287.23741.9A [pii]
89. Saam T, Cai J, Ma L, Cai YQ, Ferguson MS, Polissar NL, Hatsukami TS, Yuan C (2006) Comparison of symptomatic and asymptomatic atherosclerotic carotid plaque features with in vivo MR imaging. Radiology 240(2):464–472. doi:10.1148/radiol.2402050390, 240/2/464 [pii]
90. Stary HC, Chandler AB, Dinsmore RE, Fuster V, Glagov S, Insull W Jr, Rosenfeld ME, Schwartz CJ, Wagner WD, Wissler RW (1995) A definition of advanced types of atherosclerotic lesions and a histological classification of atherosclerosis. A report from the Committee on Vascular Lesions of the Council on Arteriosclerosis, American Heart Association. Arterioscler Thromb Vasc Biol 15(9):1512–1531
91. Underhill HR, Yuan C, Yarnykh VL, Chu B, Oikawa M, Dong L, Polissar NL, Garden GA, Cramer SC, Hatsukami TS (2010) Predictors of surface disruption with MR imaging in asymptomatic carotid artery stenosis. AJNR Am J Neuroradiol 31(3):487–493. doi:10.3174/ajnr.A1842, ajnr.A1842 [pii]
92. Toussaint JF, Southern JF, Fuster V, Kantor HL (1995) T2-weighted contrast for NMR characterization of human atherosclerosis. Arterioscler Thromb Vasc Biol 15(10):1533–1542
93. Fabiano S, Mancino S, Stefanini M, Chiocchi M, Mauriello A, Spagnoli LG, Simonetti G (2008) High-resolution multicontrast-weighted MR imaging from human carotid endarterectomy specimens to assess carotid plaque components. Eur Radiol 18(12):2912–2921. doi:10.1007/s00330-008-1091-x
94. Shinnar M, Fallon JT, Wehrli S, Levin M, Dalmacy D, Fayad ZA, Badimon JJ, Harrington M, Harrington E, Fuster V (1999) The diagnostic accuracy of ex vivo MRI for human atherosclerotic plaque characterization. Arterioscler Thromb Vasc Biol 19(11):2756–2761
95. Yuan C, Kerwin WS, Ferguson MS, Polissar N, Zhang S, Cai J, Hatsukami TS (2002) Contrast-enhanced high resolution MRI for atherosclerotic carotid artery tissue characterization. J Magn Reson Imaging 15(1):62–67. doi:10.1002/jmri.10030 [pii]
96. Berliner JA, Navab M, Fogelman AM, Frank JS, Demer LL, Edwards PA, Watson AD, Lusis AJ (1995) Atherosclerosis: basic mechanisms. Oxidation, inflammation, and genetics. Circulation 91(9):2488–2496
97. Mauriello A, Servadei F, Sangiorgi G, Anemona L, Giacobbi E, Liotti D, Spagnoli LG (2011) Asymptomatic carotid plaque rupture with unexpected thrombosis over a non-canonical vulnerable lesion. Atherosclerosis 218(2):356–362. doi:10.1016/j.atherosclerosis.2011.06.056
98. Yuan C, Zhang SX, Polissar NL, Echelard D, Ortiz G, Davis JW, Ellington E, Ferguson MS, Hatsukami TS (2002) Identification of fibrous cap rupture with magnetic resonance imaging is highly associated with recent transient ischemic attack or stroke. Circulation 105(2):181–185
99. Redgrave JN, Gallagher P, Lovett JK, Rothwell PM (2008) Critical cap thickness and rupture in symptomatic carotid plaques: the oxford plaque study. Stroke 39(6):1722–1729. doi:10.1161/STROKEAHA.107.507988, STROKEAHA.107.507988 [pii]
100. Mitsumori LM, Hatsukami TS, Ferguson MS, Kerwin WS, Cai J, Yuan C (2003) In vivo accuracy of multisequence MR imaging for identifying unstable fibrous caps in advanced human carotid plaques. J Magn Reson Imaging 17(4):410–420. doi:10.1002/jmri.10264
101. Kwee RM, van Engelshoven JM, Mess WH, ter Berg JW, Schreuder FH, Franke CL, Korten AG et al (2009) Reproducibility of fibrous cap status assessment of carotid artery plaques by contrast-enhanced MRI. Stroke 40(9):3017–3021. doi:10.1161/STROKEAHA.109.555052, STROKEAHA.109.555052 [pii]
102. Schmermund A, Erbel R (2001) Unstable coronary plaque and its relation to coronary calcium. Circulation 104(14):1682–1687
103. Huang H, Virmani R, Younis H, Burke AP, Kamm RD, Lee RT (2001) The impact of calcification on the biomechanical stability of atherosclerotic plaques. Circulation 103(8):1051–1056
104. Kwee RM (2010) Systematic review on the association between calcification in carotid plaques and clinical ischemic symptoms. J Vasc Surg 51(4):1015–1025. doi:10.1016/j.jvs.2009.08.072, S0741-5214(09)01788-1 [pii]
105. Li ZY, Howarth S, Tang T, Graves M, U-King-Im J, Gillard JH (2007) Does calcium deposition play a role in the stability of atheroma? Location may be the key. Cerebrovasc Dis 24(5):452–459. doi:10.1159/000108436
106. Deguchi JO, Aikawa M, Tung CH, Aikawa E, Kim DE, Ntziachristos V, Weissleder R, Libby P (2006) Inflammation in atherosclerosis: visualizing matrix metalloproteinase action in macrophages in vivo. Circulation 114(1):55–62. doi:10.1161/CIRCULATIONAHA.106.619056
107. Jeziorska M, Woolley DE (1999) Local neovascularization and cellular composition within vulnerable regions of atherosclerotic plaques of human carotid arteries. J Pathol 188(2):189–196. doi:10.1002/(SICI)1096-9896(199906)188:2<189::AID-PATH336>3.0.CO;2-N
108. Milei J, Parodi JC, Alonso GF, Barone A, Grana D, Matturri L (1998) Carotid rupture and intraplaque hemorrhage: immunophenotype and role of cells involved. Am Heart J 136(6):1096–1105
109. Papini GD, Di Leo G, Tritella S, Nano G, Cotticelli B, Clemente C, Tealdi DG, Sardanelli F (2011) Evaluation of inflammatory status of atherosclerotic carotid plaque before thromboendarterectomy using delayed contrast-enhanced subtracted images after magnetic resonance angiography. Eur J Radiol 80(3):e373–e380. doi:10.1016/j.ejrad.2011.01.029
110. Tang TY, Howarth SP, Miller SR, Graves MJ, U-King-Im JM, Li ZY, Walsh SR, Hayes PD, Varty K, Gillard JH (2008) Comparison of the inflammatory burden of truly asymptomatic carotid atheroma with atherosclerotic plaques in patients with asymptomatic carotid stenosis undergoing coronary artery bypass grafting: an ultrasmall superparamagnetic iron oxide enhanced magnetic resonance study. Eur J Vasc Endovasc Surg 35(4):392–398. doi:10.1016/j.ejvs.2007.10.019, S1078-5884(07)00683-1 [pii]

111. Moreno PR, Purushothaman KR, Sirol M, Levy AP, Fuster V (2006) Neovascularization in human atherosclerosis. Circulation 113(18):2245–2252. doi:10.1161/CIRCULATIONAHA.105.578955
112. Calcagno C, Mani V, Ramachandran S, Fayad ZA (2010) Dynamic contrast enhanced (DCE) magnetic resonance imaging (MRI) of atherosclerotic plaque angiogenesis. Angiogenesis 13(2):87–99. doi:10.1007/s10456-010-9172-2
113. Moreno PR, Purushothaman KR, Fuster V, Echeverri D, Truszczynska H, Sharma SK, Badimon JJ, O'Connor WN (2004) Plaque neovascularization is increased in ruptured atherosclerotic lesions of human aorta: implications for plaque vulnerability. Circulation 110(14):2032–2038. doi:10.1161/01.CIR.0000143233.87854.23
114. Mofidi R, Crotty TB, McCarthy P, Sheehan SJ, Mehigan D, Keaveny TV (2001) Association between plaque instability, angiogenesis and symptomatic carotid occlusive disease. Br J Surg 88(7):945–950. doi:10.1046/j.0007-1323.2001.01823.x
115. Kerwin WS, O'Brien KD, Ferguson MS, Polissar N, Hatsukami TS, Yuan C (2006) Inflammation in carotid atherosclerotic plaque: a dynamic contrast-enhanced MR imaging study. Radiology 241(2):459–468. doi:10.1148/radiol.2412051336
116. Choudhury RP, Fuster V, Fayad ZA (2004) Molecular, cellular and functional imaging of atherothrombosis. Nat Rev Drug Discov 3(11):913–925. doi:10.1038/nrd1548
117. Griffioen AW, Molema G (2000) Angiogenesis: potentials for pharmacologic intervention in the treatment of cancer, cardiovascular diseases, and chronic inflammation. Pharmacol Rev 52(2):237–268
118. Choyke PL, Dwyer AJ, Knopp MV (2003) Functional tumor imaging with dynamic contrast-enhanced magnetic resonance imaging. J Magn Reson Imaging 17(5):509–520. doi:10.1002/jmri.10304
119. Kerwin WS, Oikawa M, Yuan C, Jarvik GP, Hatsukami TS (2008) MR imaging of adventitial vasa vasorum in carotid atherosclerosis. Magn Reson Med 59(3):507–514. doi:10.1002/mrm.21532
120. Yankeelov TE, Gore JC (2009) Dynamic contrast enhanced magnetic resonance imaging in oncology: theory, data acquisition, analysis, and examples. Curr Med Imaging Rev 3(2):91–107. doi:10.2174/157340507780619179
121. Kerwin W, Hooker A, Spilker M, Vicini P, Ferguson M, Hatsukami T, Yuan C (2003) Quantitative magnetic resonance imaging analysis of neovasculature volume in carotid atherosclerotic plaque. Circulation 107(6):851–856
122. Walker-Samuel S, Leach MO, Collins DJ (2006) Evaluation of response to treatment using DCE-MRI: the relationship between initial area under the gadolinium curve (IAUGC) and quantitative pharmacokinetic analysis. Phys Med Biol 51(14):3593–3602. doi:10.1088/0031-9155/51/14/021
123. Dong L, Kerwin WS, Chen H, Chu B, Underhill HR, Neradilek MB, Hatsukami TS, Yuan C, Zhao XQ (2011) Carotid artery atherosclerosis: effect of intensive lipid therapy on the vasa vasorum – evaluation by using dynamic contrast-enhanced MR imaging. Radiology 260(1):224–231. doi:10.1148/radiol.11101264, radiol.11101264 [pii]
124. Trivedi RA, Mallawarachi C, U-King-Im JM, Graves MJ, Horsley J, Goddard MJ, Brown A et al (2006) Identifying inflamed carotid plaques using in vivo USPIO-enhanced MR imaging to label plaque macrophages. Arterioscler Thromb Vasc Biol 26(7):1601–1606. doi:10.1161/01.ATV.0000222920.59760.df, 01.ATV.0000222920.59760.df [pii]
125. Tang TY, Muller KH, Graves MJ, Li ZY, Walsh SR, Young V, Sadat U, Howarth SP, Gillard JH (2009) Iron oxide particles for atheroma imaging. Arterioscler Thromb Vasc Biol 29(7):1001–1008. doi:10.1161/ATVBAHA.108.165514, ATVBAHA.108.165514 [pii]
126. Trivedi RA, U-King-Im JM, Graves MJ, Cross JJ, Horsley J, Goddard MJ, Skepper JN et al (2004) In vivo detection of macrophages in human carotid atheroma: temporal dependence of ultrasmall superparamagnetic particles of iron oxide-enhanced MRI. Stroke 35(7):1631–1635. doi:10.1161/01.STR.0000131268.50418.b7
127. Winter PM, Caruthers SD, Yu X, Song SK, Chen J, Miller B, Bulte JW et al (2003) Improved molecular imaging contrast agent for detection of human thrombus. Magn Reson Med 50(2):411–416. doi:10.1002/mrm.10532
128. Rausch M, Hiestand P, Baumann D, Cannet C, Rudin M (2003) MRI-based monitoring of inflammation and tissue damage in acute and chronic relapsing EAE. Magn Reson Med 50(2):309–314. doi:10.1002/mrm.10541
129. Ruehm SG, Corot C, Vogt P, Kolb S, Debatin JF (2001) Magnetic resonance imaging of atherosclerotic plaque with ultrasmall superparamagnetic particles of iron oxide in hyperlipidemic rabbits. Circulation 103(3):415–422
130. Kooi ME, Cappendijk VC, Cleutjens KB, Kessels AG, Kitslaar PJ, Borgers M, Frederik PM, Daemen MJ, van Engelshoven JM (2003) Accumulation of ultrasmall superparamagnetic particles of iron oxide in human atherosclerotic plaques can be detected by in vivo magnetic resonance imaging. Circulation 107(19):2453–2458. doi:10.1161/01.CIR.0000068315.98705.CC
131. Tang TY, Howarth SP, Miller SR, Graves MJ, U-King-Im JM, Trivedi RA, Li ZY et al (2007) Comparison of the inflammatory burden of truly asymptomatic carotid atheroma with atherosclerotic plaques contralateral to symptomatic carotid stenosis: an ultra small superparamagnetic iron oxide enhanced magnetic resonance study. J Neurol Neurosurg Psychiatry 78(12):1337–1343. doi:10.1136/jnnp.2007.118901
132. Ku DN, Giddens DP, Zarins CK, Glagov S (1985) Pulsatile flow and atherosclerosis in the human carotid bifurcation. Positive correlation between plaque location and low oscillating shear stress. Arteriosclerosis 5(3):293–302
133. Steinman DA, Thomas JB, Ladak HM, Milner JS, Rutt BK, Spence JD (2002) Reconstruction of carotid bifurcation hemodynamics and wall thickness using computational fluid dynamics and MRI. Magn Reson Med 47(1):149–159
134. Kerwin WS, Canton G (2009) Advanced techniques for MRI of atherosclerotic plaque. Top Magn Reson Imaging 20(4):217–225. doi:10.1097/RMR.0b013e3181ea285300002142-200908000-00002 [pii]
135. Gnasso A, Irace C, Carallo C, De Franceschi MS, Motti C, Mattioli PL, Pujia A (1997) In vivo association between low wall shear stress and plaque in subjects with asymmetrical carotid atherosclerosis. Stroke 28(5):993–998
136. Lovett JK, Rothwell PM (2003) Site of carotid plaque ulceration in relation to direction of blood flow: an angiographic and pathological study. Cerebrovasc Dis 16(4):369–375. doi:10.1159/000072559
137. Malek AM, Alper SL, Izumo S (1999) Hemodynamic shear stress and its role in atherosclerosis. JAMA 282(21):2035–2042
138. Cheng C, Tempel D, van Haperen R, van der Baan A, Grosveld F, Daemen MJ, Krams R, de Crom R (2006) Atherosclerotic lesion size and vulnerability are determined by patterns of fluid shear stress. Circulation 113(23):2744–2753. doi:10.1161/CIRCULATIONAHA.105.590018
139. Richardson PD, Davies MJ, Born GV (1989) Influence of plaque configuration and stress distribution on fissuring of coronary atherosclerotic plaques. Lancet 2(8669):941–944
140. Cheng GC, Loree HM, Kamm RD, Fishbein MC, Lee RT (1993) Distribution of circumferential stress in ruptured and stable atherosclerotic lesions. A structural analysis with histopathological correlation. Circulation 87(4):1179–1187

141. Tang D, Yang C, Kobayashi S, Zheng J, Woodard PK, Teng Z, Billiar K, Bach R, Ku DN (2009) 3D MRI-based anisotropic FSI models with cyclic bending for human coronary atherosclerotic plaque mechanical analysis. J Biomech Eng 131(6):061010. doi:10.1115/1.3127253
142. Li ZY, Howarth S, Trivedi RA, U-King-Im JM, Graves MJ, Brown A, Wang L, Gillard JH (2006) Stress analysis of carotid plaque rupture based on in vivo high resolution MRI. J Biomech 39(14):2611–2622. doi:10.1016/j.jbiomech.2005.08.022
143. Loree HM, Kamm RD, Stringfellow RG, Lee RT (1992) Effects of fibrous cap thickness on peak circumferential stress in model atherosclerotic vessels. Circ Res 71(4):850–858
144. Vengrenyuk Y, Carlier S, Xanthos S, Cardoso L, Ganatos P, Virmani R, Einav S, Gilchrist L, Weinbaum S (2006) A hypothesis for vulnerable plaque rupture due to stress-induced debonding around cellular microcalcifications in thin fibrous caps. Proc Natl Acad Sci USA 103(40):14678–14683. doi:10.1073/pnas.0606310103
145. Yang C, Canton G, Yuan C, Ferguson M, Hatsukami TS, Tang D (2011) Impact of flow rates in a cardiac cycle on correlations between advanced human carotid plaque progression and mechanical flow shear stress and plaque wall stress. Biomed Eng Online 10(1):61. doi:10.1186/1475-925X-10-61
146. Teng Z, Canton G, Yuan C, Ferguson M, Yang C, Huang X, Zheng J, Woodard PK, Tang D (2010) 3D Critical plaque wall stress is a better predictor of carotid plaque rupture sites than flow shear stress: an in vivo MRI-based 3D FSI study. J Biomech Eng 132(3):031007. doi:10.1115/1.4001028
147. Gao H, Long Q, Das SK, Sadat U, Graves M, Gillard JH, Li ZY (2011) Stress analysis of carotid atheroma in transient ischemic attack patients: evidence for extreme stress-induced plaque rupture. Ann Biomed Eng 39(8):2203–2212. doi:10.1007/s10439-011-0314-5
148. Zhu C, Teng Z, Sadat U, Young VE, Graves MJ, Li ZY, Gillard JH (2010) Normalized wall index specific and MRI-based stress analysis of atherosclerotic carotid plaques: a study comparing acutely symptomatic and asymptomatic patients. Circ J 74(11):2360–2364
149. Sadat U, Teng Z, Young VE, Zhu C, Tang TY, Graves MJ, Gillard JH (2011) Impact of plaque haemorrhage and its age on structural stresses in atherosclerotic plaques of patients with carotid artery disease: an MR imaging-based finite element simulation study. Int J Cardiovasc Imaging 27(3):397–402. doi:10.1007/s10554-010-9679-z
150. Teng Z, Sadat U, Ji G, Zhu C, Young VE, Graves MJ, Gillard JH (2011) Lumen irregularity dominates the relationship between mechanical stress condition, fibrous-cap thickness, and lumen curvature in carotid atherosclerotic plaque. J Biomech Eng 133(3):034501. doi:10.1115/1.4003439
151. Syed MA, Oshinski JN, Kitchen C, Ali A, Charnigo RJ, Quyyumi AA (2009) Variability of carotid artery measurements on 3-Tesla MRI and its impact on sample size calculation for clinical research. Int J Cardiovasc Imaging 25(6):581–589. doi:10.1007/s10554-009-9468-8
152. (1998) Prevention of cardiovascular events and death with pravastatin in patients with coronary heart disease and a broad range of initial cholesterol levels. The Long-Term Intervention with Pravastatin in Ischaemic Disease (LIPID) Study Group. N Engl J Med 339(19):1349–1357. doi:10.1056/NEJM199811053391902
153. Libby P, Aikawa M (2003) Mechanisms of plaque stabilization with statins. Am J Cardiol 91(4A):4B–8B
154. Duivenvoorden R, de Groot E, Stroes ES, Kastelein JJ (2009) Surrogate markers in clinical trials – challenges and opportunities. Atherosclerosis 206(1):8–16. doi:10.1016/j.atherosclerosis.2008.12.009, S0021-9150(08)00899-X [pii]
155. Zhao XQ, Yuan C, Hatsukami TS, Frechette EH, Kang XJ, Maravilla KR, Brown BG (2001) Effects of prolonged intensive lipid-lowering therapy on the characteristics of carotid atherosclerotic plaques in vivo by MRI: a case–control study. Arterioscler Thromb Vasc Biol 21(10):1623–1629
156. Saam T, Yuan C, Chu B, Takaya N, Underhill H, Cai J, Tran N et al (2007) Predictors of carotid atherosclerotic plaque progression as measured by noninvasive magnetic resonance imaging. Atherosclerosis 194(2):e34–e42. doi:10.1016/j.atherosclerosis.2006.08.016
157. Kwee RM, van Oostenbrugge RJ, Mess WH, Prins MH, van der Geest RJ, ter Berg JW, Franke CL et al (2010) Carotid plaques in transient ischemic attack and stroke patients: one-year follow-up study by magnetic resonance imaging. Invest Radiol 45(12):803–809. doi:10.1097/RLI.0b013e3181ed15ff
158. Corti R, Fayad ZA, Fuster V, Worthley SG, Helft G, Chesebro J, Mercuri M, Badimon JJ (2001) Effects of lipid-lowering by simvastatin on human atherosclerotic lesions: a longitudinal study by high-resolution, noninvasive magnetic resonance imaging. Circulation 104(3):249–252
159. Corti R, Fuster V, Fayad ZA, Worthley SG, Helft G, Smith D, Weinberger J et al (2002) Lipid lowering by simvastatin induces regression of human atherosclerotic lesions: two years' follow-up by high-resolution noninvasive magnetic resonance imaging. Circulation 106(23):2884–2887
160. Underhill HR, Yuan C, Zhao XQ, Kraiss LW, Parker DL, Saam T, Chu B et al (2008) Effect of rosuvastatin therapy on carotid plaque morphology and composition in moderately hypercholesterolemic patients: a high-resolution magnetic resonance imaging trial. Am Heart J 155(3):584.e581–584.e588. doi:10.1016/j.ahj.2007.11.018
161. Zhao XQ, Phan BA, Chu B, Bray F, Moore AB, Polissar NL, Dodge JT Jr, Lee CD, Hatsukami TS, Yuan C (2007) Testing the hypothesis of atherosclerotic plaque lipid depletion during lipid therapy by magnetic resonance imaging: study design of carotid plaque composition study. Am Heart J 154(2):239–246. doi:10.1016/j.ahj.2007.04.035
162. Zhao XQ, Dong L, Hatsukami T, Phan BA, Chu B, Moore A, Lane T et al (2011) MR imaging of carotid plaque composition during lipid-lowering therapy a prospective assessment of effect and time course. JACC Cardiovasc Imaging 4(9):977–986. doi:10.1016/j.jcmg.2011.06.013
163. Migrino RQ, Bowers M, Harmann L, Prost R, Ladisa JF (2011) Carotid plaque regression following 6-month statin therapy assessed by 3T cardiovascular magnetic resonance: comparison with ultrasound intima media thickness. J Cardiovasc Magn Reson 13(1):37. doi:10.1186/1532-429X-13-37
164. Tang TY, Howarth SP, Miller SR, Graves MJ, Patterson AJ, U-King-Im JM, Li ZY et al (2009) The ATHEROMA (Atorvastatin therapy: effects on reduction of macrophage activity) study. Evaluation using ultrasmall superparamagnetic iron oxide-enhanced magnetic resonance imaging in carotid disease. J Am Coll Cardiol 53(22):2039–2050. doi:10.1016/j.jacc.2009.03.018
165. Patterson AJ, Tang TY, Graves MJ, Muller KH, Gillard JH (2011) In vivo carotid plaque MRI using quantitative T2* measurements with ultrasmall superparamagnetic iron oxide particles: a dose–response study to statin therapy. NMR Biomed 24(1):89–95. doi:10.1002/nbm.1560
166. Chu B, Zhao XQ, Saam T, Yarnykh VL, Kerwin WS, Flemming KD, Huston J 3rd et al (2005) Feasibility of in vivo, multicontrast-weighted MR imaging of carotid atherosclerosis for multicenter studies. J Magn Reson Imaging 21(6):809–817. doi:10.1002/jmri.20308
167. Underhill HR, Hatsukami TS, Cai J, Yu W, DeMarco JK, Polissar NL, Ota H et al (2010) A noninvasive imaging approach to assess plaque severity: the carotid atherosclerosis score. AJNR

Am J Neuroradiol 31(6):1068–1075. doi:10.3174/ajnr.A2007, ajnr.A2007 [pii]
168. Macedo R, Chen S, Lai S, Shea S, Malayeri AA, Szklo M, Lima JA, Bluemke DA (2008) MRI detects increased coronary wall thickness in asymptomatic individuals: the multi-ethnic study of atherosclerosis (MESA). J Magn Reson Imaging 28(5):1108–1115. doi:10.1002/jmri.21511
169. Wasserman BA, Sharrett AR, Lai S, Gomes AS, Cushman M, Folsom AR, Bild DE, Kronmal RA, Sinha S, Bluemke DA (2008) Risk factor associations with the presence of a lipid core in carotid plaque of asymptomatic individuals using high-resolution MRI: the multi-ethnic study of atherosclerosis (MESA). Stroke 39(2):329–335. doi:10.1161/STROKEAHA.107.498634, STROKEAHA.107.498634 [pii]
170. Maderwald S, Ladd SC, Gizewski ER, Kraff O, Theysohn JM, Wicklow K, Moenninghoff C, Wanke I, Ladd ME, Quick HH (2008) To TOF or not to TOF: strategies for non-contrast-enhanced intracranial MRA at 7T. MAGMA 21(1–2):159–167. doi:10.1007/s10334-007-0096-9
171. Rominger A, Saam T, Wolpers S, Cyran CC, Schmidt M, Foerster S, Nikolaou K, Reiser MF, Bartenstein P, Hacker M (2009) 18F-FDG PET/CT identifies patients at risk for future vascular events in an otherwise asymptomatic cohort with neoplastic disease. J Nucl Med 50(10):1611–1620. doi:10.2967/jnumed.109.065151
172. Rudd JH, Warburton EA, Fryer TD, Jones HA, Clark JC, Antoun N, Johnstrom P et al (2002) Imaging atherosclerotic plaque inflammation with [18F]-fluorodeoxyglucose positron emission tomography. Circulation 105(23):2708–2711
173. Hadley JR, Roberts JA, Goodrich KC, Buswell HR, Parker DL (2005) Relative RF coil performance in carotid imaging. Magn Reson Imaging 23(5):629–639. doi:10.1016/j.mri.2005.04.009
174. Balu N, Yarnykh VL, Scholnick J, Chu B, Yuan C, Hayes C (2009) Improvements in carotid plaque imaging using anew eight-element phased array coil at 3T. J Magn Reson Imaging 30(5):1209–1214. doi:10.1002/jmri.21890
175. Boussel L, Herigault G, de la Vega A, Nonent M, Douek PC, Serfaty JM (2006) Swallowing, arterial pulsation, and breathing induce motion artifacts in carotid artery MRI. J Magn Reson Imaging 23(3):413–415. doi:10.1002/jmri.20525
176. Crowe LA, Keegan J, Gatehouse PD, Mohiaddin RH, Varghese A, Symmonds K, Cannell TM, Yang GZ, Firmin DN (2005) 3D volume-selective turbo spin echo for carotid artery wall imaging with navigator detection of swallowing. J Magn Reson Imaging 22(4):583–588. doi:10.1002/jmri.20424
177. Chan CF, Gatehouse PD, Hughes R, Roughton M, Pennell DJ, Firmin DN (2009) Novel technique used to detect swallowing in volume-selective turbo spin-echo (TSE) for carotid artery wall imaging. J Magn Reson Imaging 29(1):211–216. doi:10.1002/jmri.21607
178. Boussel L, Arora S, Rapp J, Rutt B, Huston J, Parker D, Yuan C, Bassiouny H, Saloner D (2009) Atherosclerotic plaque progression in carotid arteries: monitoring with high-spatial-resolution MR imaging – multicenter trial. Radiology 252(3):789–796. doi:10.1148/radiol.2523081798
179. Parmar JP, Rogers WJ, Mugler JP 3rd, Baskurt E, Altes TA, Nandalur KR, Stukenborg GJ et al (2010) Magnetic resonance imaging of carotid atherosclerotic plaque in clinically suspected acute transient ischemic attack and acute ischemic stroke. Circulation 122(20):2031–2038. doi:10.1161/CIRCULATIONAHA.109.866053
180. Saam T, Underhill HR, Chu B, Takaya N, Cai J, Polissar NL, Yuan C, Hatsukami TS (2008) Prevalence of American Heart Association type VI carotid atherosclerotic lesions identified by magnetic resonance imaging for different levels of stenosis as measured by duplex ultrasound. J Am Coll Cardiol 51(10):1014–1021. doi:10.1016/j.jacc.2007.10.054

Contrast Agents in Carotid Angiography with Magnetic Resonance

5

Michele Anzidei, Chiara Zini, Vincenzo Noce, and Carlo Catalano

1 Introduction

Carotid MRA does not necessarily require contrast material, but contrast-enhanced MRA (CE-MRA) has become the standard of practice because it is faster and flow independent. CE-MRA era begun in 1988 with the approval of first MR contrast agent for clinical use by Food and Drugs Administration (FDA) [1]; the first contrast-enhanced MR angiograms (CE-MRA) required 5-min-and-10-s acquisition time [2] and its quality was not so high, but it led to an interesting scenario. In fact, the diagnostic accuracy of CE-MRA has been positively evaluated in a number of studies [3–5]: a recent meta-analysis of the noninvasive tests, available for imaging the carotid arteries, has determined that CE-MRA is the most accurate for detection of significant (70–99 %) symptomatic stenosis [6].

2 Principles of CE-MRA

CE-MRA is based on the principle of shortening the T1 relaxation of blood by intravenously injecting Gd-chelate-based contrast media (GBCM). This results in a significant difference in signal intensity between flowing blood and stationary tissue at heavily T1-weighted arterial phase imaging, leading to the high signal intensity of blood on contrast enhanced T1-weighted sequences.

When a GBCM is administered it decreases the observed tissue T1 and T2 relaxation times, changing the tissue signal intensity. In other words the same phenomenon can be expressed as increasing the tissue relaxivities R1 and R2 (i.e., observed 1/T1 and 1/T2); the effect is termed relaxation enhancement. Because the concentration of protons (water) is much greater (55,000 M) than the concentration of GBCM (0.1–5.0 mM), individual contrast complexes must exert relaxation effects on extremely large numbers of water molecules. The efficiency of this process can be expressed as the relaxivity of the contrast molecule (Rcontrast), which is linearly related to the concentration of the contrast agent and can be written [7]:

$$\text{R1 (observed)} = \text{R1 (intrinsic)} + c\text{R1 (contrast)}$$

$$\text{R2 (observed)} = \text{R2 (intrinsic)} + c\text{R2 (contrast)}$$

where c is the concentration of GBCM. The observed relaxivities R1,2 can be thought of as the sum of an intrinsic relaxivity (i.e., the true tissue T1 and T2) and a contrast-specific relaxivity proportional to the concentration of contrast present.

Based on their predominant relaxivity effects, GBCM can be classified as paramagnetic or superparamagnetic.

- *Paramagnetic or relaxation agents* (also called positive contrast agents) have relatively large numbers of unpaired electrons. These unpaired electrons generate a locally fluctuating magnetic field, which cause a shortening in relaxation time T1 and induce a positive enhancement of the signal in T1-weighted images. The effect on T2-weighted images is present but less evident than in T1-weighted images. The magnetic momentum is nulled when the paramagnetic substance is removed from the magnetic field. The most utilized paramagnetic substances are the lanthanides, among which the most used is gadolinium. Gadolinium chelates are the most CA used for MR angiography because of their shortening of the T1 relaxation of blood (bright blood sequence).
- *Superparamagnetic or susceptibility agents* (also called negative contrast agents) develop large magnetic moments when placed into a magnetic field much greater than those seen with paramagnetic agents such as gadolinium [8] and

M. Anzidei (✉) • C. Zini • V. Noce • C. Catalano
Department of Radiological Sciences of the Sapienza,
Univerity of Rome,Viale Regina Elena 324, Rome 00161, Italy
e-mail: Michele.Anzidei@gmail.com; zini.chiara@gmail.com;
vinc.noce@hotmail.it; carlo.catalano@uniroma.it

L. Saba et al. (eds.), *Multi-Modality Atherosclerosis Imaging and Diagnosis*,
DOI 10.1007/978-1-4614-7425-8_5,

Table 5.1 Physiochemical properties of interstitial GBCM

Genetic name	Product name	Manufacturer	Chemical abbreviation	R_1a	R_2a	Molarity	Osmolality	Viscosity
Gadopentetate	Magnevist	Berlex	Gd-DTPA	3.8		0.500	1.96	2.90
Gadoversetamide	MultiHance	Bracco	Gd-BOPTA	4.4	5.6	0.500	1.97	5.30
				9.7				
Gadodutrol	Gadovist	Bayer	Gd-DO3A-butrol	3.6		1.000	1.39	3.70
Gadoterate	Dotarem	Guerbet	Gd-DOTA	3.6	4.8	0.500	1.35	2.00
Gadoteridol	ProHance	Bracco	Gd-HPDO3A	3.7		0.500	0.63	1.30
Gadodiamide	Omniscan	Nycomed, Amersham	Gd-DTPA-BMA	3.9		0.500	0.79	1.40

Table 5.2 Physiochemical properties of blood pool GBCM

Genetic name	Product name	Manufacturer	Chemical abbreviation	R_1a	R_2a	Molarity	Osmolality	Viscosity
Gadofosveset	Vasovist	Shering	MS-325	6.6	53.0	0.250		
				44.0				
B22956		Bracco	B22956	6.5		0.250		
				27.0				
SHL 643	Gadomer-17	Bayer	Gadomer-17	18.7		0.500		
P792	P792	Guerbet	P792	39.0		0.035		
				44.5				

determine a local lack of homogeneity in the magnetic field at a macroscopic level which induces a marked fluctuation of the magnetic momentum between the blood and intracellular compartments, causing a shortening of T2* of the neighboring 1H nuclei, thus determining a decrease in signal. Two types of compounds are discriminated based on their aggregate size: large (>50 nm) particles, referred to as a SPIO (superparamagnetic iron oxide) and small (<50 nm) particles, referred to as a USPIO (ultrasmall superparamagnetic iron oxide). Examples of SPIOs include AMI-25 and SHU-555A; USPIOs include AMI-227 and NC100150. Superparamagnetic contrast agents have been proposed for studies on the cardiovascular system with satisfying results both in animal and human studies [9, 10].

3 Pharmacokinetic

Contrast agent's pharmacokinetic knowledge is necessary before approaching a carotid MRA. The principal characteristics are resumed in Table 5.1.

- *Molarity* is defined as the amount of a constituent divided by the volume of solvent. MR contrast agents must be formulated at adequate concentration to effectively alter relaxation at achievable blood concentrations and must be either soluble or homogeneously dispersible in blood. The molarity of CA employed are 0.1–1.0 M depending on agent relaxivity (Tables 5.1 and 5.2).
- *Viscosity* measures the fluid resistance and must be low enough that bolus injection can be performed through intravenous (IV) catheters. Warming the contrast agent to body temperature reduces viscosity, and it is useful when injecting high-viscosity agents such as gadopentetate dimeglumine through smaller IVs [24, 25]. Recently, some authors report viscosity as a risk factor for contrast-induced nephropathy (CIN) [11].
- *Osmolality* is the measure of solute concentration. Acceptable contrast agent osmolalities range from 0.3 to 2.0 Osm/kg [7].

The biodistribution of GBCMs is governed by the kinetics of distribution, clearance, and excretion. Simplifying kinetics is possible to identify two compartments with an intravascular space (arteries and veins) and extracellular extravascular space (EES). After injection, contrast media pass from the intravascular space into the EES due to the high intravascular concentration; this phenomenon takes variable time: extracellular fluid agents (ECF) agents diffuse rapidly; blood pool agents and SPIOs diffuse slowly. This process is measured by distribution half-life T1/2 that represents the time required for half of contrast to redistribute from the intravascular space to the EES. Elimination pathways vary according to the type of contrast agent. The gadolinium ECF agents, small and extremely hydrophilic, are predominately eliminated unmetabolized via a renal pathway (glomerular filtration, active secretion, or a combination of the two). The elimination half-life T1/2 represents the time required for elimination of one-half the total contrast from the body, and it is on the order of 90 min for conventional contrast media. The only exception to pure renal elimination is gadobenate dimeglumine (Gd-BOPTA), which is partially taken up by the hepatocytes and excreted in bile [12].

Based on GBCM biodistribution, it is possible to identify two class of molecules:

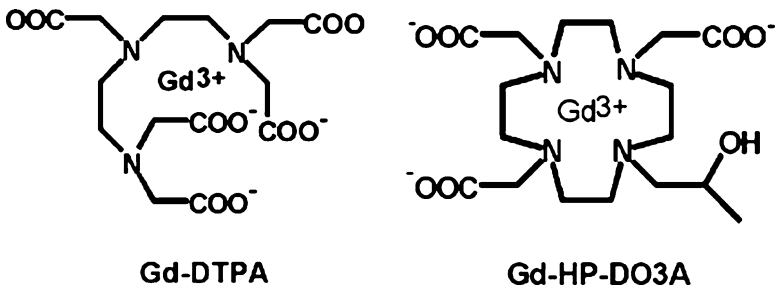

Fig. 5.1 Molecular structure of two GBCMs that differ for how Gd is chelated inside the molecule; the shell-like structure of the molecule avoids any contact between the Gd ion and the tissue components

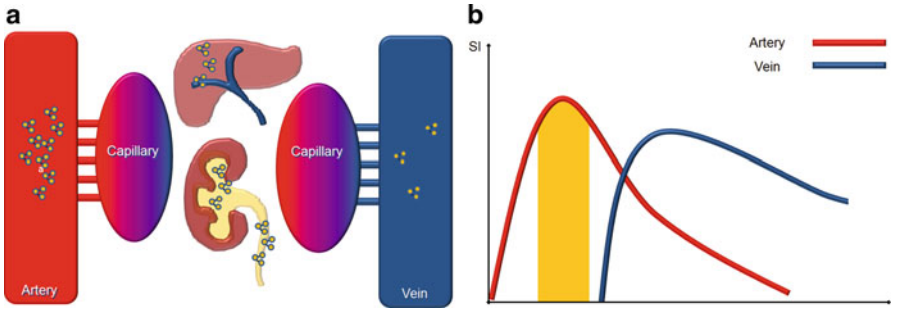

Fig. 5.2 Biodistribution (**a**) and effects on blood signal intensity (**b**) of interstitial GBMC. The initial arterial concentration of interstitial GBCM rapidly decreases owing to renal and, later on, hepatic excretion (in smaller percentage). This allows to acquire images only during a short time window (*yellow area* under the *curve*) corresponding to the peak of arterial enhancement (Color figure online)

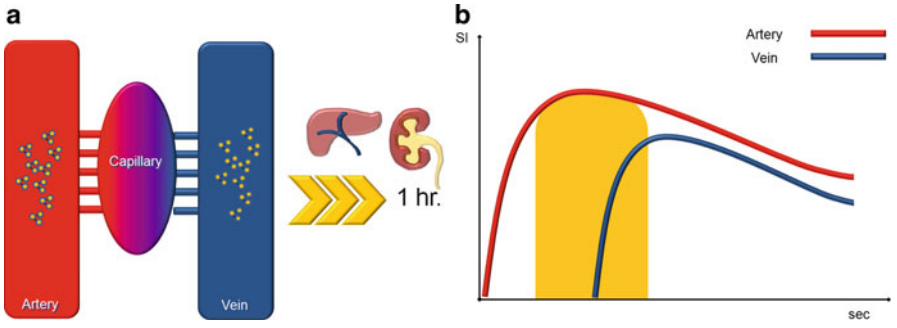

Fig. 5.3 Biodistribution (**a**) and effects on blood signal intensity (**b**) of blood pool GBMC. The arterial concentration of interstitial GBCM remains constant in time, since its interstitial filtration is minimal and the renal and hepatic excretion occur later (vascular half life of 1 h) as compared to conventional molecules. This allows to acquire images during a longer time window (*yellow area* under the *curve*), even if veins are enhanced, since the increased spatial resolution allowed by longer angiographic sequences reduces artery/veins superimposition issues, allowing at the same time the evaluation of smaller anatomic details that cannot be appreciated with conventional sequences used for arterial images with interstitial GBCM (Color figure online)

- *Extracellular fluid agents (ECF) or parenchymal agent (PA)* contain one gadolinium ion (see Fig. 5.1) and are quite small (<1,000 Da) so their distribution half-life T1/2 is low. Characteristics of PA are resumed in Table 5.1 and PA biodistribution is described in Fig. 5.2.
- *Intravascular contrast agent (ICA) or blood pool agents (BP)* remain intravascular for a much longer time and are eliminated from the body much more slowly (longer T1/2) as you can see in Fig. 5.3. These agents remain largely intravascular due to one of two mechanisms: (a) a substantial fraction (>80 % at any one time) reversibly binds to serum albumin or (b) the large inherent size (>20,000 Da) of the blood pool agent prevents it from diffusing through the endothelium. This particular property led to steady state sequence acquisition; these are particularly high definition sequence, acquired after traditional first pass sequence, in order to characterize plaque morphology. Intravascular CA are out of commerce or not yet approved by FDA or UE, so some authors [5] tried to acquire steady state sequence also with interstitial GBCM with good to excellent results. See Table 5.2 for BP agents' properties.

4 Safety

Historically, GBCMs are considered to have less adverse reactions than the other contrast media and no nephrotoxicity (at approved dosages for MR imaging). For several years MR with gadolinium has been used to replace contrast-enhanced CT in patients at risk for developing renal failure if exposed to iodinated contrast media. However, in the nephrogenic systemic fibrosis (NSF) era, this practice should only be considered after reviewing the recommendations for use of gadolinium-based contrast in this group of patients. Gadolinium chelates have been approved for parenteral use since the late 1980s, and they are extremely well tolerated by the vast majority of patients in whom they are injected. Acute adverse reactions are encountered with a lower frequency than is observed after administration of iodinated contrast media; the frequency of all acute adverse events after an injection of 0.1 or 0.2 mmol/kg of gadolinium chelate ranges from 0.07 to 2.4 % [13]. The majority of these reactions are mild, including coldness at the injection site, nausea with or without vomiting, headache, warmth or pain at the injection site, paresthesias, dizziness, and itching. Reactions resembling an "allergic" response (rash, hives, urticaria, and bronchospasm) are very unusual (0.004–0.7 %), and severe reactions (life-threatening anaphylactoid or nonallergic anaphylactic reactions) are exceedingly rare (0.001–0.01 %). Fatal reactions to gadolinium chelate agents occur but are extremely rare. Symptoms and treatments are resumed in Table 5.3. Literature [14, 15] reports some risk factors for adverse reaction as:

- *Previous adverse reaction to GBCM*: The frequency of acute adverse reactions to gadolinium contrast media is about eight times higher in patients with a previous reaction to gadolinium-based contrast media. Recurrent reactions to GBCM can be more severe than the first.
- *Atopic subjects*: Persons with asthma and various allergies (including to other medications or foods) are also at greater risk, with reports of adverse reaction rates as high as 3.7 %. Although there is no cross-reactivity, patients who have had previous allergic-like reactions to iodinated contrast media are also in this category.

Table 5.3 Classification of severity and manifestations of adverse reactions to contrast media

Mild	Signs and symptoms **self-limited** without evidence of progression *Treatment*: observation to confirm resolution and/or lack of progression, usually no treatment is require
Moderate	Signs and symptoms are **more pronounced** with evidence of focal or systemic signs or symptoms *Treatment*: prompt treatment with close, careful observation for possible progression to a life-threatening event
Severe	Signs and symptoms are often **life-threatening** *Treatment*: aggressive treatment, frequently hospitalization is necessary

Table 5.4 Administered doses of GBCM and associated NSF cases, according to data provided by the Food and Drug Administration (FDA) in December 2009

Agent	Approximate number of doses (in millions)	Number of reported NSF cases
Gadodiamide	13	382
Gadopentetate dimeglumine	23	195
Gadoversetamide	4.7	35

In the absence of any widely accepted policy for dealing with patients with prior contrast reactions in the need for subsequent exposure to GBCM, it does seem prudent to take pharmacologic precautions. It should be determined if gadolinium-based contrast medium is necessary, if a different molecule can be used, and if 12–24 h of premedication with corticosteroids and antihistamines could be initiated.

Recently, NSF has been described as a late complication of GDBC. NSF is a fibrosing disease, primarily identified in the skin and subcutaneous tissues but also known to involve other organs such as the lungs, esophagus, heart, and skeletal muscles. Initial symptoms typically include skin thickening and/or pruritus. Symptoms and signs may develop and progress rapidly, with some affected patients developing contractures and joint immobility. Death may result in some patients, presumably as a result of visceral organ involvement. NSF was first described in 2000 [16], but only in 2006 [17, 18] was related to patients with end stage chronic kidney disease (CKD), particularly in patients on dialysis, who underwent contrast enhanced MRI. Much data about NSF are still controversial and/or unknown but it is important to point on:

- *Precise quantification of the relative risk of NSF* development following administration of the various GBCMs: empirical data and theoretical lines of reasoning suggest that not all GBCMs are associated with an identical risk of NSF in at-risk patients. The majority of studies have reported on the incidence of NSF after gadodiamide exposure (Table 5.4). European Medicines Agency (EMEA) classified GBCM into different groups (when considering administration to at-risk patients) [19], resumed in Table 5.5.
- *Chronic renal failure* has been recognized as the principal risk factor for developing NFS; in particular, patients with severe CKD in stages 4 and 5 (corresponds to eGFR values of 15–29 and <15 ml/min/1.73 m^2, respectively) have a 1–7 % chance of developing NSF after exposure to GBCM [1, 2, 5, 8–11]; however, isolated

Table 5.5 EMEA recommendations re-elaborated by American College of Radiology (ACR) Committee on Drugs and Contrast Media and the ACR Subcommittee on MR Safety

Group I: Agents associated with the greatest number of NSF cases
Gadodiamide (Omniscan®—GE Healthcare)
Gadopentetate dimeglumine (Magnevist®—Bayer HealthCare Pharmaceuticals)
Gadoversetamide (OptiMARK®—Covidien)
Group II: Agents associated with few, if any, unconfounded cases of NSF
Gadobenate dimeglumine (MultiHance®—Bracco Diagnostics)
Gadoteridol (ProHance®—Bracco Diagnostics)
Gadoteric acid (Dotarem®—Guerbet)
Gadobutrol (Gadovist®—Bayer HealthCare Pharmaceuticals)
Group III: Agents that have only recently appeared on the market in the US
Gadofosveset (Ablavar®—Lantheus Medical Imaging)
Gadoxetic acid (Eovist®—Bayer HealthCare Pharmaceuticals)

reports of biopsy-proven NSF developing in patients with stage 3 CKD (which corresponds to an estimated glomerular filtration rate (eGFR) value between 30 and 59 ml/min/1.73 m^2). Moreover, NSF has also developed in patients with acute kidney injury [20]: in one series, up to 20 % of NSF cases were diagnosed in patients who had been in some element of transient acute renal failure at the time of GBCM administration [21].

- *Roles of the free gadolinium ion and/or the ligand component of GBCM*: in patients with significantly degraded renal function, gadolinium ion dissociates from its chelate due to the prolonged clearance times (transmetallation). The free gadolinium then binds with other anions (such as phosphate or bicarbonate), and the resulting insoluble precipitate is deposited in the skin and subcutaneous tissues (as well as at other locations) via a process that is still poorly understood [22].
- *Risk factors*: A number of factors have been postulated to explain why some patients with severe CKD who are exposed to GBCMdevelop NSF and some do not. These include: metabolic acidosis or medications that predispose patients to acidosis [17, 23], increased iron, calcium, and/or phosphate levels [23], high-dose erythropoietin therapy, immunosuppression [24], vasculopathy [25], an acute pro-inflammatory event [26], and infection [27], all at the time of GBCM exposure. None of these potential risk factors has been demonstrated consistently to be present in all affected patients in all studies . Therefore, at present, none of these risk factors can be considered to have been established as a true cofactor with a high degree of confidence.
- *Dose of GBCM*: Many authors suggested that renal failure patients are at highest risk when they are exposed to high doses or multiple doses of GBCM. Nonetheless, there are clearly reported instances of NSF occurring in patients who have been exposed to standard (0.1 mmol/kg) single dose of GBCM [28] or exceptionally rarely in those who have no known GBCM exposure [29]. Conversely, there are also patients with severe CKD, who have received high doses and/or many doses of GBCM, but who have not developed NSF [28]. In one study [30], of 30 patients who had an eGFR of under 30 ml/min/1.73 m^2 and who were exposed to high doses of gadodiamide (median dose of 90 ml and range of 40–200 ml), only one patient subsequently developed NSF, which calculates to an incidence of only about 3 %

Based on the recommendations for GBCM administration, it is mostly important to identify patients who are at increased risk of developing NSF prior to any GBCM injection. Patients at highest risk are those who have severe CKD (defined as eGFRs of <30 ml/min/1.73 m^2) or acute kidney injury. Patients can be screened verbally to identify the presence of a history of renal disease, but it is important to obtain the eGFR (within 6 weeks of anticipated GBCM injection) in patients who might have reduced renal function as the American College of Radiology Subcommittee on MR Safety recommended. The calculation of eGFR for adults should be performed using the modification of diet in renal disease (MDRD) equation:

$$\mathrm{eGFR(ml/\,min\,/1.73\ m^2)} = 175 \times (\text{serum creatinine in mg/dl}) - 1.154 \times (\text{age in years}) - 0.203 \times (0.742 \text{ if female}) \times (1.212 \text{ if African American})$$

The Schwartz equation should be used for children:

$$\mathrm{eGFR(ml/\,min\,/1.73\,m^2)} = \frac{0.413 \times \text{height in cm}}{\text{serum creatinine in mg/dl}}$$

Decisions concerning the appropriate time interval between the last eGFR determination and GBCM injection will be tempered by any interval change in the patient's clinical condition (which might increase the need for a more recent eGFR).

5 Technical Parameters You Need to Know to Perform a Successful Carotid CE-MRA Examination

The imaging success depends on:

- *Contrast resolution*: related to signal intensity difference between background and vascular enhancement; the intravascular signal depends on the amount of contrast agent concentrated within the vascular bed during acquisition.
- *Temporal resolution*: the arterial phase acquisition must be limited in duration to avoid venous overlap, with relevant constrains to spatial resolution [31–33]. This drawback is going to progressively overcome by the wider availability of advanced parallel imaging, dedicated multichannel coils, performing gradients, and high-field scanners.
- *Imaging acquisition*: should be ideally performed at the peak of vascular enhancement, when a maximum difference exists between signal intensity of the target vessel and the surrounding overlapping structures.

Acquisition parameters change between vendors widely; however, some concepts must be kept in mind when setting up protocols for carotid CE-MRA:

- TE, TR, and flip-angle values should be kept at minimum in order to maximize the differences in signal intensity between contrast agent and stationary tissues and T2* effects.
- Pre-contrast mask acquisition is mandatory for image subtraction in order to increase intrinsic contrast.
- Matrix values should not be lower than 384 × 384, with an effective slice thickness not wider than 1.5 mm.
- Acquisition time should not exceed 14–18 s (depending on individual changes in circulation physiology) to avoid jugular enhancement.
- Optimal delay between contrast agent administration and acquisition start should be evaluated with real-time monitoring techniques based on *k*-space filling evaluation or MR fluoroscopy; test bolus is also acceptable but is more prone to technical errors and longer to perform. It should strictly avoid the use of prefixed delay, and individual changes in circulation physiology may completely hamper arterial-only acquisitions [34].
- The modality of *k*-space sampling must be adapted for CE-MRA, with centric or elliptic-centric techniques being more convenient to achieve a compromise between the needs for spatial and temporal resolution [35].

References

1. Weinman H, Brasch R, Press W et al (1984) Characteristics of gadolinium-DTAP complex: a potential NMR contrast agent. Am J Roentgenol 142:619–624
2. Prince M, Yucel E, Kaufman J et al (1993) Dynamic gadolinium-enhanced three-dimensional abdominal MR arterography. J Magn Reson Imaging 3:877–881
3. Ismaeel MM, Abdel-Hamid A (2011) Role of high resolution contrast-enhanced magnetic resonance angiography (HR CeMRA) in management of arterial complications of the renal transplant. Eur J Radiol 79(2):e122–e127
4. Gutzeit A, Sutter R, Froehlich JM, Roos JE, Sautter T, Schoch E, Giger B, Wyss M, Graf N, von Weymarn C, Jenelten R, Binkert CA, Hergan K (2011) ECG-triggered non-contrast-enhanced MR angiography (TRANCE) versus digital subtraction angiography (DSA) in patients with peripheral arterial occlusive disease of the lower extremities. Eur Radiol 21(9):1979–1987
5. Anzidei M, Napoli A, Zaccagna F, Cavallo Marincola B, Zini C, Kirchin MA, Catalano C, Passariello R (2011) First-pass and high-resolution steady-state magnetic resonance angiography of the peripheral arteries with gadobenate dimeglumine: an assessment of feasibility and diagnostic performance. Invest Radiol 46(5):307–316
6. Chappell FM, Wardlaw JM, Young GR et al (2009) Carotid artery stenosis: accuracy of noninvasive tests – individual patient data meta-analysis. Radiology 251:493–502
7. Hohenschuh E, Watson A (1997) Theory and mechanisms of contrast-enhancing agents. In: Higgins C, Hricak H, Helms C (eds) Magnetic resonance imaging of the body. Lippencott-Raven, Philadelphia, PA, pp 1439–1464
8. Petersein J, Saini S, Weissleder R (1996) Liver. II: iron oxide-based reticuloendothelial contrast agents for MR imaging. Magn Reson Imaging Clin N Am 4:53–60
9. Stillman AE (2001) New contrast agents for cardiovascular MRI and MRA. Int J Cardiovasc Imaging 17:471–472
10. Priest AN, Ittrich H, Jahntz CL, Kooijman H, Weber C, Adam G (2006) Investigation of atherosclerotic plaques with MRI at 3 T using ultrasmall superparamagnetic particles of iron oxide. Magn Reson Imaging 24(10):1287–1293
11. Solomon R (2005) The role of osmolality in the incidence of contrast-induced nephropathy: a systematic review of angiographic contrast media in high risk patients. Kidney Int 68(5):2256–2263
12. Runge V, Nelson K (1999) Contrast agents. In: Stark D, Bradley W (eds) Magnetic resonance imaging. Mosby, St. Louis, MO, pp 257–275
13. ACR Manual on Contrast Media (2010) ACR Committee on Drugs and Contrast Media. Version 7, pp 45–47
14. Kanal E, Shellock FG, Talagala L (1990) Safety considerations in MR imaging. Radiology 176:593–606
15. Cochran ST, Bomyea K, Sayre JW (2001) Trends in adverse events after IV administration of contrast media. AJR Am J Roentgenol 176:1385–1388
16. (2000) NSF boost sends the right message to Congress. Nature 403(6770):579
17. Grobner T (2006) Gadolinium – a specific trigger for the development of nephrogenic fibrosing dermopathy and nephrogenic systemic fibrosis? Nephrol Dial Transplant 21:1104–1108
18. Marckmann P, Skov L, Rossen K et al (2006) Nephrogenic systemic fibrosis: suspected causative role of gadodiamide used for contrast-enhanced magnetic resonance imaging. J Am Soc Nephrol 17:2359–2362
19. European Medicines Agency (2009) Questions and answers on the review of gadolinium-containing contrast agents. Doc. Ref. EMEA/727399/2009, EMEA/H/A-31/1097. London, UK
20. Perez-Rodriguez J, Lai S, Ehst BD, Fine DM, Bluemke DA (2009) Nephrogenic systemic fibrosis: incidence, associations, and effect of risk factor assessment – report of 33 cases. Radiology 250:371–377
21. Prince MR, Zhang H, Morris M et al (2008) Incidence of nephrogenic systemic fibrosis at two large medical centers. Radiology 248:807–816

22. Abraham JL, Thakral C, Skov L, Rossen K, Marckmann P (2008) Dermal inorganic gadolinium concentrations: evidence for in vivo transmetallation and long-term persistence in nephrogenic systemic fibrosis. Br J Dermatol 158:273–280
23. Peak AS, Sheller A (2007) Risk factors for developing gadolinium-induced nephrogenic systemic fibrosis. Ann Pharmacother 41:1481–1485
24. Wertman R, Altun E, Martin DR et al (2008) Risk of nephrogenic systemic fibrosis: evaluation of gadolinium chelate contrast agents at four American universities. Radiology 248:799–806
25. Swartz RD, Crofford LJ, Phan SH, Ike RW, Su LD (2003) Nephrogenic fibrosing dermopathy: a novel cutaneous fibrosing disorder in patients with renal failure. Am J Med 114:563–572
26. Sadowski EA, Bennett LK, Chan MR et al (2007) Nephrogenic systemic fibrosis: risk factors and incidence estimation. Radiology 243:148–157
27. Golding LP, Provenzale JM (2008) Nephrogenic systemic fibrosis: possible association with a predisposing infection. AJR Am J Roentgenol 190:1069–1075
28. Shabana WM, Cohan RH, Ellis JH et al (2008) Nephrogenic systemic fibrosis: a report of 29 cases. AJR Am J Roentgenol 190:736–741
29. Wahba IM, Simpson EL, White K (2007) Gadolinium is not the only trigger for nephrogenic systemic fibrosis: insights from two cases and review of the recent literature. Am J Transplant 7:2425–2432
30. Bridges MD, St Amant BS, McNeil RB, Cernigliaro JG, Dwyer JP, Fitzpatrick PM (2009) High-dose gadodiamide forcatheter angiography and CT in patients with varying degrees of renal insufficiency: prevalence of subsequent nephrogenic systemic fibrosis and decline in renal function. AJR Am J Roentgenol 192:1538–1543
31. Borisch I, Horn M, Butz B, Zorger N, Draganski B, Hoelscher T, Bogdahn U, Link J (2003) Preoperative evaluation of carotid artery stenosis: comparison of contrast-enhanced MR angiography and duplex sonography with digital subtraction angiography. AJNR Am J Neuroradiol 24(6):1117–1122
32. Nederkoorn PJ, van der Graaf Y, Hunink MG (2003) Duplex ultrasound and magnetic resonance angiography compared with digital subtraction angiography in carotid artery stenosis: a systematic review. Stroke 34(5):1324–1332
33. Lenhart M, Framme N, Völk M, Strotzer M, Manke C, Nitz WR, Finkenzeller T, Feuerbach S, Link J (2002) Time-resolved contrast enhanced magnetic resonance angiography of the carotid arteries: diagnostic accuracy and inter-observer variability compared with selective catheter angiography. Invest Radiol 37(10): 535–541
34. Huston J 3rd, Fain SB, Riederer SJ, Wilman AH, Bernstein MA, Busse RF (1999) Carotid arteries: maximizing arterial to venous contrast in fluoroscopically triggered contrast-enhanced MR angiography with elliptic centric view ordering. Radiology 211(1):265–273
35. Madhuranthakam AJ, Hu HH, Barger AV, Haider CR, Kruger DG, Glockner JF, Huston J 3rd, Riederer SJ (2006) Undersampled elliptical centric view-order for improved spatial resolution in contrast-enhanced MR angiography. Magn Reson Med 55(1): 50–58

Quantitative Magnetic Resonance Analysis in the Assessment of Cardiac Diseases

6

Erica Maffei, Giancarlo Messalli, Cesare Mantini, Teresa Arcadi, Chiara Martini, Massimo Imbriaco, and Filippo Cademartiri

1 Introduction

The diagnosis of cardiovascular disease requires the precise assessment of both morphology and function. Cardiac magnetic resonance (CMR) offers several acquisition techniques for accurate and highly reproducible quantitative assessment of global and regional ventricular function, blood flow, myocardial perfusion at rest and stress, necrotic and scarred myocardium and heart iron load.

The ongoing clinical need for objective and accurate assessment of myocardial function and recent advances in CMR hardware and automated and semi-automated image analysis software resulted in significant improvements in image quality and a reduction in imaging time.

E. Maffei • T. Arcadi • C. Martini
Department of Radiology, Giovanni XXIII Hospital, Monastier, Treviso, Italy
e-mail: ericamaffei@gmail.com; teresaarcadi@yahoo.it; cesare.mantini@gmail.com

G. Messalli
Department of Radiology, SDN IRCCS – Institute of Diagnostic and Nuclear Research, Naples, Italy

Department of Biomorphological and Functional Sciences, University Federico II, Naples, Italy
e-mail: giancarlomessalli@hotmail.it

C. Mantini
Department of Neuroscience and Imaging, Section of Diagnostic Imaging and Therapy, "G. D'Annunzio" University, Chieti, Italy
e-mail: Chiaramartini10@gmail.com

M. Imbriaco
Department of Radiology, University Federico II, Naples, Italy

Department of Biomorphological and Functional Sciences, University Federico II, Naples, Italy
e-mail: mimbriaco@hotmail.com

F. Cademartiri (✉)
Department of Radiology, Erasmus Medical Center University, Rotterdam, The Netherlands

Cardio-Vascular Imaging Unit, Giovanni XXIII Hospital, Via Giovanni XXIII 7, 31050 Monastier di Treviso, Treviso, Italy
e-mail: filippocademartiri@gmail.com

2 Assessment of Global Ventricular Function

The accurate and reproducible quantification of left and right ventricular volumes, ejection fraction, and myocardial muscle mass is fundamental for evaluation of disease severity/progression, appropriate therapeutic procedures, timing of surgery, and prognostic stratification in patients with cardiac disease.

CMR is recognized as the reference standard for the assessment of left and right ventricular volume and mass; it has been shown to be accurate, highly reproducible, and independent from geometric models [1, 2].

Measurements of global ventricular function are typically derived from multislice cine 2D balanced steady-state free-precession (b-SSFP) images with 30 phases per cardiac cycle encompassing the entire left and right ventricle short axes in 8–12 consecutive parallel slices (usually 8 mm slice thickness and 2 mm slice gap) (Fig. 6.1). Tissue signal in the b-SSFP sequences is based on T2/T1 relaxation behavior and is largely inflow independent. As a result, a high contrast in blood-filled ventricular cavities (high signal) and myocardium (low signal), allowing an excellent detection of the endocardial border [3, 4].

During the post-processing, the precise delineation of the endocardial ventricular border in the end-diastolic and end-systolic phases is crucial for accurate quantification of ventricular volumes (Fig. 6.1). Ventricular volume and global function parameters can be derived using Simpson's rule including end-diastolic (EDV) and end-systolic volumes (ESV), ejection fraction (EF), stroke volume (SV), and left ventricular mass.

The difference between EDV and ESV is the SV (mL).

$$SV = EDV - ESV$$

L. Saba et al. (eds.), *Multi-Modality Atherosclerosis Imaging and Diagnosis*,
DOI 10.1007/978-1-4614-7425-8_6, © Springer Science+Business Media, LLC 2014

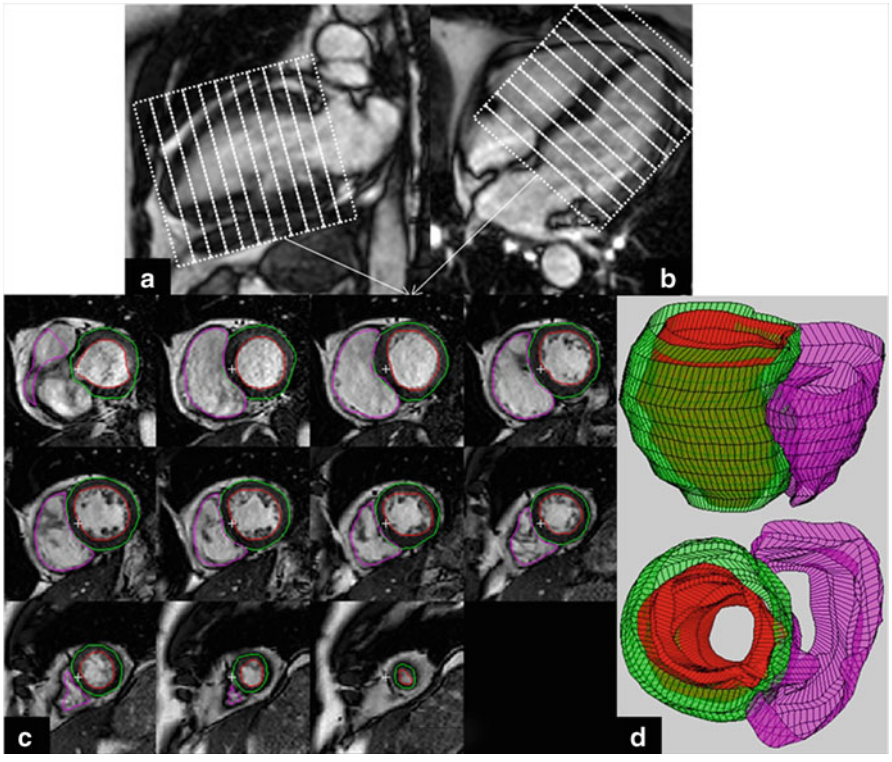

Fig. 6.1 Slice positioning on the vertical long-axis (VLA) (**a**) and 4-chamber (4CH) (**b**) planes to obtain multislice short axis (SAX) images (**c**) from base to apex of the ventricles. Note that all slices are parallel to the atrioventricular (AV) valves and perpendicular to the interventricular septum. Functional analysis of both ventricles using the Simpson's method is obtained by drawing endocardial borders in each plane (respectively *red* in the LV and *purple* in the RV). The delineation of the epicardial ventricular border (*green*) is important to quantify LV mass. (**d**) Surface-rendered 3D images of the left and right ventricle obtained from the automatic propagation of endocardial and epicardial contours to the all subsequent phases of the cardiac cycle

The SV divided by the EDV gives the EF (%).

$$\mathrm{EF} = \frac{\mathrm{SV\ [mL]}}{\mathrm{EDV\ [mL]}} \times 100$$

The SV multiplied by the heart rate (HR) gives the cardiac output (L/min).

$$\mathrm{CO} = \mathrm{SV} \times \mathrm{HR}$$

The trabeculations and the papillary muscles should be included in ventricular cavity, except in patient with hypertrofic cardiomyopathy. The delineation of the epicardial ventricular border is important for quantification of the overall volume of the ventricular wall and to obtain the ventricular mass multiplying the myocardial volume by the heart muscle-specific density (1.05 g/cm^3). All determinations are usually indexed for the body surface area to according parameters for individual body conformation.

Phase contrast (PC) images also play an important role in the evaluation of global ventricular function, in particular, the application of this technique to the proximal portion of the ascending aorta and pulmonary artery allows a precise quantification of anterograde flow over a complete cardiac cycle; left and right ventricular stroke volume can be measured by integrating the area under flow curve [5].

Literature data agree in considering CMR the reference standard for the assessment of right and left ventricular volumes, EF and myocardial mass, and functional parameters have always to be reported.

3 Assessment of Regional Ventricular Function

Evaluating the contribution of the different ventricular portions to the global ventricular performance is important in many cardiac diseases. The parameters used to study regional ventricular function are myocardial wall thickness, systolic wall thickening, and circumferential and longitudinal wall motion or shortening.

Preserved wall thickness is a good indicator of the presence of viable myocardium in the setting of a chronic infarction and wall thickening analysis is more sensitive in the detection of dysfunctional myocardium than wall motion analysis [6]. Some studies have shown that measuring regional contractility is a better prognostic indicator than left ventricular EF and that quantitative measurement of wall thickening provides a more precise indication of regional function than does visual estimation of wall motion [7, 8].

CMR short-axis acquisitions have proved their usefulness for the determination of left ventricular regional wall parameters [6]. In contrast to echocardiography, which only provide good visualization of the endocardial borders of the myocardium, CMR also provides excellent depiction of the epicardial borders of the myocardium. This allows

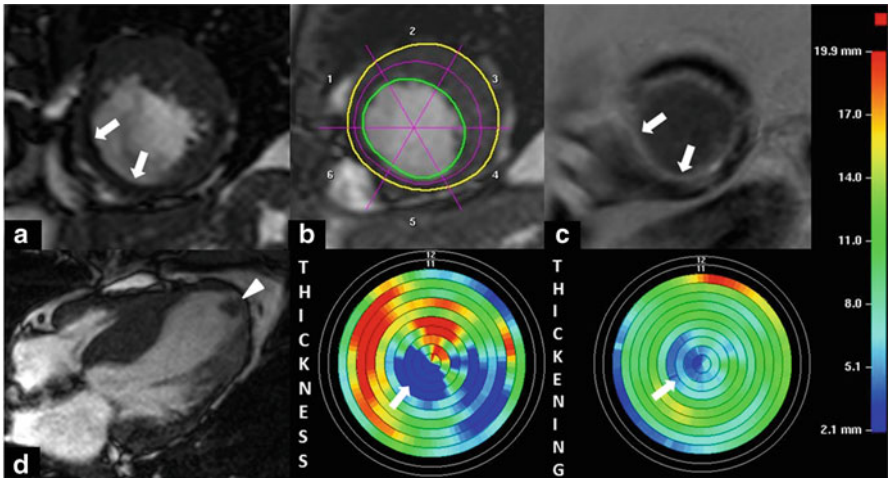

Fig. 6.2 (**b**) Application of the centerline method for wall thickness and wall thickening analysis of short-axis cine MR images obtained in a 68-year-old man with chronic myocardial infarction in the region of the left anterior descending artery (**a**). (**c**) Delayed-enhancement short-axis image shows transmural hyperenhancement (*arrows*) in the thinned myocardial wall of the septum and the infero-apical segment corresponding to scar tissue. Bull's-eye plots show a reduced wall thickness and wall thickening in the scarred tissue (*arrows*). (**d**) b-SSFP image depicts a dyskinetic aneurysm of the LV apex with the presence of an apical thrombus (*arrowhead*)

assessment of not only wall motion but also wall thickening and thinning. Local wall thickness and thickening can be derived from manually or automatically defined endocardial and epicardial profile in end diastole and end systole of left and right ventricle.

The commonest way to assess wall thickness and thickening is based on the centerline method (Fig. 6.2). In short-axis images, myocardial thickness is divided by a line into two equal parts, equidistant to the endocardium and epicardium; multiple lines are drawn perpendicular to this line, covering the entire myocardium at defined intervals. The length of each line indicates parietal thickness, while the relationship between the length of each line at the end of systole and diastole defines systolic thickening [9].

Normal values for end-systolic wall thickening can be used for comparison to determine which myocardial regions are impaired. The most important clinical application of regional functional analysis is the assessment of reversibly injured yet viable myocardium in ischemic heart disease [10, 11].

Although, for daily clinical use, wall motion is often visually assessed, contouring of endo- and epicardial borders may be helpful to quantify motion (e.g., amount of centripetal motion of endocardial border during systole).

Accurate regional function analysis has become feasible with the introduction of CMR myocardial tagging (Fig. 6.3) allowing an highly reproducible quantitative assessment of mechanical properties such as myocardial strain deformation. It consists in applying, on a standard SSPF sequence, a radiofrequency prepulse perpendicular to the plane of the image, immediately following the ECG R-wave, appearing in the image as a grid of dark saturated lines. Dedicated computer algorithms have been developed to track the intersection points of the tagging lines over the cardiac cycle, to analyze the deformation of the saturation grid and sequent quantification of regional myocardial deformations. By applying this technique in multiple slices in both short-axis and long-axis directions, 3D-myocardial strain measurements can be performed, allowing an accurate quantification of circumferential and longitudinal shortening [12].

4 Assessment of Blood Flow in the Heart and Great Vessels

Cardiac-gated phase-contrast (PC) sequences with flow-encoding gradients are used to quantify velocity and blood flow in the heart and great vessels. 2D PC CMR sequences are the most commonly used in clinical practice and the flow quantification is based on the phase shift measurement induced in the protons in motion by the application of pulsed gradients.

PC can accurately quantify the regurgitant volume, either as an absolute value or as the regurgitant fraction. Each PC acquisition produced two sets of cine-images: a magnitude image, used for anatomic orientation, and a phase image in which the gray value of each pixel represents the velocity information in that voxel. For flow quantification, phase information acquired on a perpendicular plane through the jet of regurgitation, just near the valve, are required (Fig. 6.4). Stationary spins are represented as mid-gray, while increasing velocities in either direction are shown in increasing grades of black or white. Black values show flow toward the viewer, whereas white values show flow away from

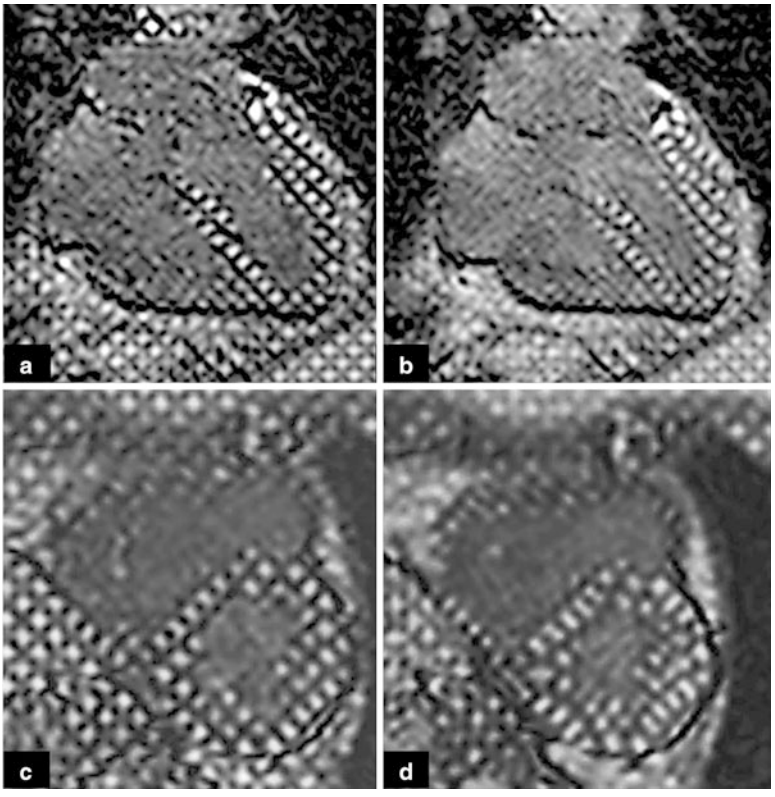

Fig. 6.3 End-diastolic (**a**, **c**) and end-systolic (**b**, **d**) 4-chamber and short-axis-tagged MR images

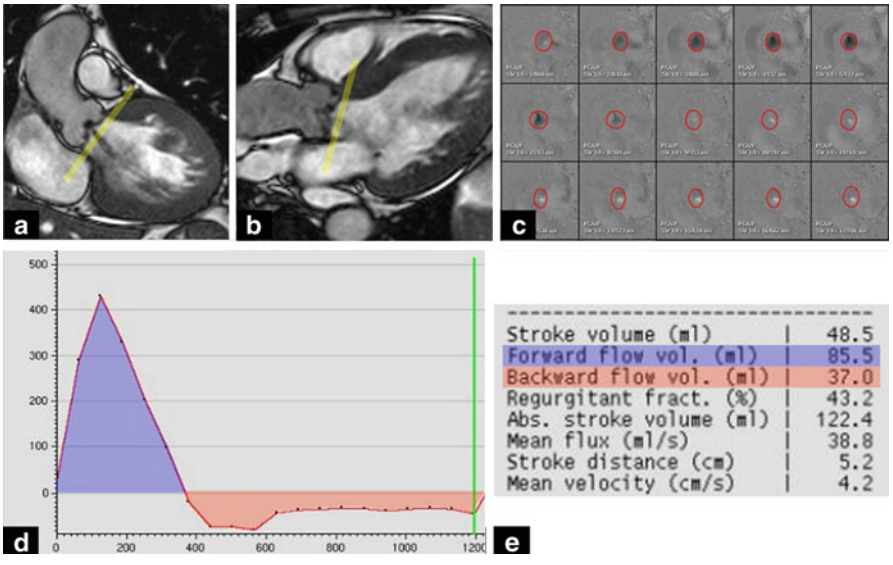

Fig. 6.4 Oblique coronal view (**a**) and oblique transverse long axis view (**b**) of the left ventricle outflow tract with slice positioned (*yellow lines*) for PC sequence (**c**) acquired in a through-aortic plane, just below the aortic valve annulus. (**c**) Phase image produced by PC sequence: *black values* show forward flow toward the viewer, whereas white values show backward flow away from the viewer. (**d**) Corresponding flow map obtained drawing the regions of interest (ROIs) on each phase. The regurgitant volume is obtained as the area under the curve of the negative portion (*red*) of the flow-time plot. The regurgitant fraction is obtained as the ratio of the regurgitant volume and the forward flow volume (**e**)

the viewer. It is important to define the size of velocity encode window as close to the peak velocity as possible, to reduce aliasing of peak velocities and maintaining sensitivity for flow measurements. Measurement of the spatial mean velocity for all pixels in a region of interest of known area enables the calculation of the instantaneous flow volume at any point in the cardiac cycle. Calculation of the flow volume per heart beat can be made by integrating the instantaneous

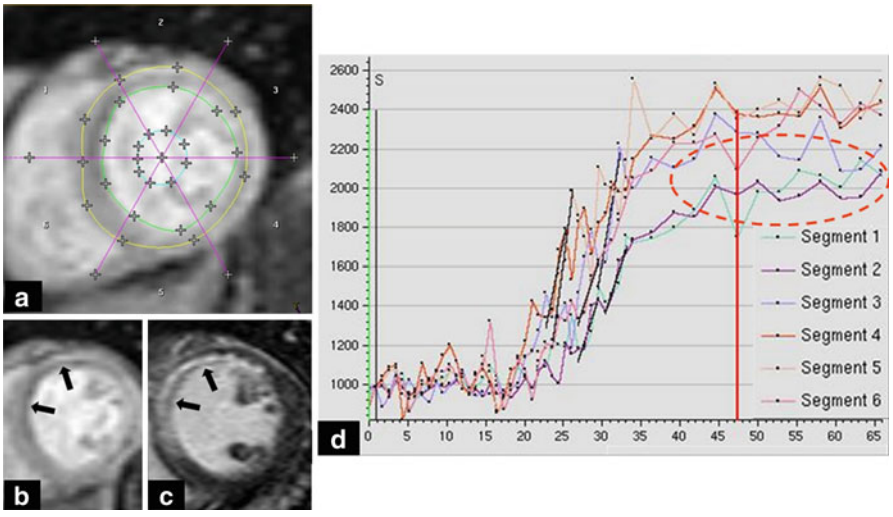

Fig. 6.5 Short-axis first-pass myocardial perfusion at a mid-ventricular slice level with endo- and epi-cardial contours defined and the myocardium divided into 6 segments (**a**). Signal-intensity versus time curve is derived for each of the myocardial segments (**d**). Short-axis resting first-pass myocardial perfusion (**b**) and delayed-enhancement (**c**) images show an area of microvascular obstruction localized in the anterior (segment 2) and antero-septal wall (segment 1) (*arrows* in **b** and **c**), characterized by a reduced myocardial signal intensity (SI) during the first pass (*red dotted circle* in **d**)

flow volumes for all frames throughout the cardiac cycle [13]. This technique has been validated in vitro and in vivo and is extremely accurate and reproducible [14]. The severity of regurgitation can be defined as mild (regurgitant fraction 15–20 %), moderate (regurgitant fraction 20–40 %), and severe (regurgitant fraction >40 %) [15].

Application of PC to the proximal portion of the ascending aorta allows the assessment of left ventricular systolic function by evaluating the flow over a complete cardiac cycle. Such a study requires a PC acquisition in the oblique axial plane crossing the ascending aorta and the left ventricular stroke volume can be obtained tracing the lumen of the vessels in every phase of the cardiac cycle [16].

Quantification of the right ventricular and left ventricular outputs can be compared using through-plane flow measurements from the proximal ascending aorta and pulmonary trunk (Qp/Qs ratio = 1 in normal individuals), thus allowing quantification of shunts in patients with congenital heart disease [17].

5 Assessment of Rest and Stress Myocardial Perfusion

In patients with known or suspected ischemic heart disease, diagnosis of an hemodynamically significant stenosis, and assessment of functional significance of an anatomical lesion, is of crucial importance in the evaluation and therapeutic decision-making.

The intrinsic mechanisms of coronary microvascular adaptation (coronary reserve) do not allow to appreciate myocardial perfusion defects at rest. To detect significant stenoses of the epicardial coronary arteries, it is helpful to stress the patient so that a measure of the coronary flow reserve, or similar measures such as the myocardial perfusion reserve index, can be obtained [18]. Stress conditions are induced by physical exercise or pharmacological agents such as dipyridamole, adenosine, or dobutamine.

Compared with the radionuclide techniques, myocardial MR perfusion imaging has several advantages, including its lack of ionizing radiation, higher spatial resolution to allow analysis of transmural differences in myocardial blood flow (MBF), no attenuation problem related to overlying breast shadow or obesity [19].

Myocardial CMR perfusion imaging is based on the changes in myocardial signal intensity (SI) during the first pass of an intravenously injected contrast agent (Gadolinium) acquired during stress and at rest. The simplest and most frequently used approach for interpreting CMR perfusion studies is the visual assessment of first-pass myocardial perfusion cineloop looking for regions of relative hypoperfusion visible as a nonenhancing part of the myocardium.

The time intensity curve, obtained contouring the endo- and epicardial borders, describes the changes in SI over time in the myocardium during the first pass of contrast through the heart (Fig. 6.5). A number of semiquantitative parameters can be obtained from this curve: maximum myocardial enhancement, transit time, time to maximal SI, area under the SI curve, and the upslope of myocardial enhancement (i.e.,

slope of the initial portion of the signal intensity versus time curve after gadolinium administration).

Of these parameters, the upslope of the SI curve has been most widely adopted for semiquantitative analysis and has been shown to improve diagnostic accuracy over visual analysis alone [20]. A recent meta-analysis showed an overall sensitivity of 91 % and specificity of 81 % for CMR perfusion imaging using qualitative and semiquantitative analysis for the diagnosis of CAD, compared to quantitative coronary angiography [21].

In addition to the semiquantitative methods, CMR perfusion imaging can also quantify the absolute MBF in mL/min/g evaluating time intensity curves for regions within the myocardium. The quantification of tissue perfusion is mathematically complex and involves a number of assumptions, including parameters such as water exchange rates, contrast agent distribution, and the relationship between signal intensity and the concentration of contrast agent [19, 22].

In healthy volunteers, MBF measurements by CMR have been found to be in agreement with published values based on invasive and noninvasive methods, and the magnitude of flow heterogeneity is similar to that seen in PET [23]. Quantitative perfusion CMR is thus a safe noninvasive test that represents a stenosis-specific alternative for determining the hemodynamic significance of CAD.

6 Assessment of the Necrotic and Scarred Myocardium

In patients with myocardial infarction (MI), delayed enhancement cardiac magnetic resonance (DE-CMR) is a well-validated technique for the detection, characterization, and accurate quantification of the necrotic (acute phase) and scarred (chronic phase) myocardium [24].

Viability imaging is based on contrast medium local concentration caused by an increase in the myocyte membrane permeability in acute MI and by enlargement of the extravascular space, and hence, an increased distribution volume for the extracellular contrast agent in chronic phase. Moreover, gadolinium chelates wash out of infarcted tissue more slowly than out of healthy myocardium resulting bright on delayed contrast-enhanced inversion recovery T1-weighted images. The size and location of the infarcted region, as demonstrated histochemically in animal models, correlate with the size and location of myocardial DE.

Findings of several studies have shown that the amount of delayed transmural enhancement predicts the degree of functional recovery after acute MI and relates to left ventricle remodeling.

The transmural extent of the infarction as seen on DE-CMR in chronic MI is inversely related to the likelihood of recovery following revascularization; conversely, absence of myocardial DE correlates with a likelihood of functional recovery [25]. Infarct size on DE-CMR has been shown to be superior to left ventricular EF and volume for predicting long-term mortality in patients with healed MI [26]. Myocardial scar forms a substrate for ventricular tachyarrhythmia and scar quantification by DE-CMR has the potential for allowing better identification of high risk patients.

The CMR high spatial resolution allows an accurately and reproducibly planimetric quantification of DE area by manual or automatic drawing of the contrast-enhanced region (Fig. 6.6).

The most important information used in daily clinical practice is the transmural extent of the infarction (Infarct size). Infarct size was computed by dividing the DE area by the total area of the corresponding myocardial wall and expressed as left ventricle percentage. The amount of DE areas assessed section by section gives the total volume of infarction expressed in grams by multiplying the volume of infarction for the myocardium-specific weight (equal to 1.05 g/cm^3). This value can also be expressed in percentage respect to left ventricular mass.

Considerable additional information is available through the use of supplementary techniques in acute infarction.

The DE short-axis images also allow an accurately planimetric quantification of the potential presence of microvascular obstruction (MO) by manually drawing the hypoenhanced region within infarcted myocardium. Infarcts with microvascular obstruction have a poorer prognosis, which is a predictor that is independent of EF [27].

In T2-weighted short-axis images, myocardial area at risk (AAR) can be obtained by manually tracing the hyperintense region and expressed as left ventricular percentage (Fig. 6.6). When present, an hypointense area within the hyperintense myocardium is considered an hemorrhagic component of infarcted myocardium and included in the AAR computation.

Myocardial salvage is defined as the amount of myocardium that is jeopardized by a coronary occlusion but spared from infarction. The myocardial salvage index (MSI) is calculated by correcting the amount of necrotic myocardium for the AAR extent.

$$\mathrm{MSI} = \frac{\text{AAR extent} - \text{Infarct size}}{\text{AAR extent}}$$

In reperfused ST-segment elevation MI patients, CMR-derived MSI is the strongest predictor of adverse left ventricle remodeling independent from the presence of microvascular obstruction, infarct transmurality, and baseline

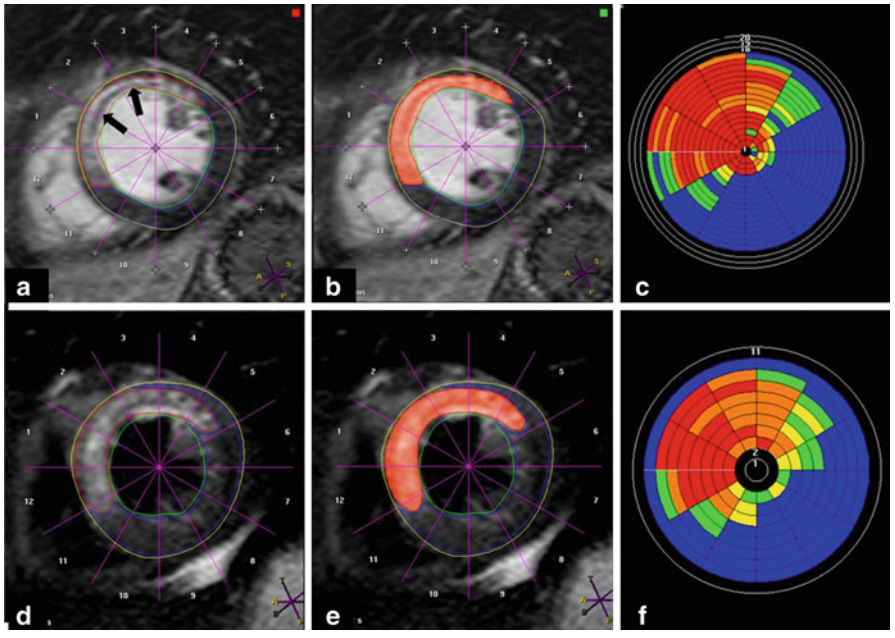

Fig. 6.6 Planimetric quantification of transmural extent of the infarction (infarct size) on DE-CMR short axis image (**a**–**c**) showing example of transmural subendocardial myocardial infarction within an area of microvascular obstruction depicted as a persisting area of hypoenhancement (*black arrows* in **a**) surrounded by hyperenhanced myocardial tissue. Planimetric quantification of area at risk (AAR) on short TI inversion recovery (STIR) short-axis image (**d**–**f**) of the same patient

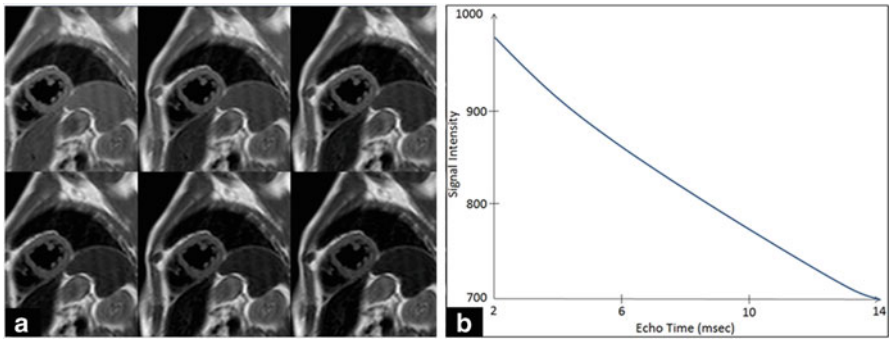

Fig. 6.7 Myocardial quantification of iron load in a patient with hemochromatosis on single breath-hold multi-echo T2* sequence acquired in mid-ventricular short axis (**a**). The images do not show a decrease of heart signal intensity while depicts a marked decrease of liver signal intensity. Myocardial signal intensities are measured in the ventricular septum for each image and then plotted against the echo time (**b**). The T2 decay is 36 ms (>20 ms), then the patient has not a myocardial iron overload

EF. These findings may open new perspectives on the use of this index as a surrogate end point in studies testing novel reperfusion strategies [28].

7 Assessment of Tissue Iron Overload

Iron overload cardiomyopathy (IOC) is a restrictive cardiomyopathy defined as the presence of diastolic and then systolic cardiac dysfunction secondary to increased deposition of iron in the heart [29]. It results from the accumulation of iron in the myocardium related to primary or secondary hemochromatosis. Initially, diastolic dysfunction whit restrictive filling pattern usually precede systolic function and regional abnormalities.

CMR is the only available noninvasive technique which can quantify myocardial iron load.

In iron-overloaded hearts, the iron paramagnetic effect disturbs the magnetic field homogeneity, produces changes in MR signal intensity and susceptibility, and shortens the T2 relaxation time causing a marked decrease in signal intensity on T2-weighted images [30]. The noninvasive quantification of myocardial iron overload is possible using a single breath-hold multi-echo T2* sequence acquired in mid-ventricular short axis. Myocardial signal intensities are measured in the ventricular septum for each image and then plotted against the echo time (Fig. 6.7). Patients with myocardial iron overload have a T2 decay <20 ms.

References

1. Pennell DJ, Sechtem UP, Higgins CB et al (2004) Clinical indications for cardiovascular magnetic resonance (CMR): Consensus Panel report. Eur Heart J 25:1940–1965

2. Shapiro EP, Rogers WJ, Beyar R et al (1989) Determination of left ventricular mass by magnetic resonance imaging in hearts deformed by acute infarction. Circulation 79:706–711
3. Barkhausen J, Ruehm SG, Goyen M et al (2001) MR evaluation of ventricular function: true fast imaging with steady-state precession versus fast low angle shot cine MR imaging-feasibility study. Radiology 219:264–269
4. Plein S, Bloomer TN, Ridgway JP et al (2001) Steady state free precession magnetic resonance imaging of the heart: comparison with segmented k-space gradient-echo imaging. J Magn Reson Imaging 14:230–236
5. Kondo C, Caputo GR, Semelka R et al (1991) Right and left ventricular stroke volume measurements with velocity-encoded cine MR imaging: *in vitro* and *in vivo* validation. AJR Am J Roentgenol 157:9–16
6. Azhari H, Sideman S, Weiss JL et al (1990) Three-dimensional mapping of acute ischemic regions using MRI: wall thickening versus motion analysis. Am J Physiol 259:H1492–H1503
7. Weintraub WS, Agarwal JB, Seeclaus PA et al (1983) Segmental wall motion score as a predictor of survival in coronary artery disease. Circulation 68:111–114
8. Lieberman AN, Weiss JL, Jugdutt BI et al (1981) Two dimensional echocardiography and infarct size: relationship of regional wall motion and thickening to the extent of myocardial infarction in the dog. Circulation 63:739–746
9. San Román JA, Candell-Riera J, Arnold R et al (2009) Quantitative analysis of left ventricular function as a tool in clinical research. Theoretical basis and methodology. Rev Esp Cardiol 62(5):535–551
10. Picano E, Lattanzi F, Orlandini A et al (1991) Stress echocardiography and the human factor: the importance of being expert. J Am Coll Cardiol 17:666–669
11. Nagel E, Lehmkuhl HB, Bocksch W et al (1999) Noninvasive diagnosis of ischemia-induced wall motion abnormalities with the use of high-dose dobutamine stress MRI: comparison with dobutamine stress echocardiography. Circulation 99:763–770
12. McVeigh ER, Zerhouni EA (1991) Noninvasive measurement of transmural gradients in myocardial strain with MR imaging. Radiology 180:677–683
13. Bogaert J, Dymarkowski S, Taylor AM (2005) Clinical cardiac MRI. 1. Springer, Berlin
14. Meier D, Maier S, Boesiger P (1988) Quantitative flow measurements on phantoms and on blood vessels with MR. Magn Reson Med 8:25–34
15. Sechtem U, Pflugfelder PW, Cassidy MM et al (1988) Mitral and aortic regurgitation: quantification of regurgitant volumes with cine MR imaging. Radiology 167:425–430
16. Longmore DB, Klipstein RH, Underwood SR (1985) Dimensional accuracy of magnetic resonance studies of the heart. Lancet 1:1360–1362
17. Kondo C, Caputo GR, Semelka R et al (1991) Right and left ventricular stroke volume measurements with velocity encoded cine NMR imaging: in vivo and in vitro evaluation. AJR Am J Roentgenol 157:9–16
18. Gallagher KP, Osakada G, Matsuzaki M et al (1982) Myocardial blood flow and function with critical coronary stenosis in exercising dogs. Am J Physiol 243(5):698–707
19. Schwitter J, Nanz D, Kneifel S et al (2001) Assessment of myocardial perfusion in coronary artery disease by magnetic resonance. A comparison with positron emission tomography and coronary angiography. Circulation 103:2230–2235
20. Nagel E, Klein C, Paetsch I et al (2003) Magnetic resonance perfusion measurements for the noninvasive detection of coronary artery disease. Circulation 108:432–437
21. Nandalur KR, Dwamena BA, Choudhri AF et al (2007) Diagnostic performance of stress cardiac magnetic resonance imaging in the detection of coronary artery disease: a meta-analysis. J Am Coll Cardiol 50:1343–1353
22. Milles J, Van der Geest RJ, Jerosch-Herold M et al (2008) Fully automated motion correction in first-pass myocardial perfusion MR image sequences. IEEE Trans Med Imaging 27:1611–1621
23. Lee DC, Johnson NP (2009) Quantification of absolute myocardial blood flow by magnetic resonance perfusion imaging. JACC Cardiovasc Imaging 2:761–770
24. Kim RJ, Fieno DS, Parrish TB et al (1999) Relationship of MRI delayed contrast enhancement to irreversible injury, infarct age, and contractile function. Circulation 100:1992–2002
25. Kim RJ, Wu E, Rafael A et al (2000) The use of contrast-enhanced magnetic resonance imaging to identify reversible myocardial dysfunction. N Engl J Med 343:1445–1453
26. Wu E, Ortiz JT, Tejedor P et al (2008) Infarct size by contrast enhanced cardiac magnetic resonance is a stronger predictor of outcomes than left ventricular ejection fraction or end-systolic volume index: prospective cohort study. Heart 94:730–736
27. Thomson LEJ, Kim RJ, Judd RM (2004) Magnetic resonance imaging for the assessment of myocardial viability. J Magn Reson Imaging 19:771–788
28. Masci PG, Ganame J, Strata E et al (2010) Myocardial salvage by CMR correlates with LV remodeling and early ST-segment resolution in acute myocardial infarction. JACC Cardiovasc Imaging 3(1):45–51
29. Liu P, Olivieri N (1994) Iron overload cardiomyopathies: new insights into an old disease. Cardiovasc Drugs Ther 8:101–110
30. Wood JC (2007) Magnetic resonance imaging measurement of iron overload. Curr Opin Hematol 14:183–190

Atherosclerosis Plaque Stress Analysis: A Review

7

Hao Gao and Quan Long

1 Introduction

Stroke is one of the leading causes of death in the world [58], mainly caused by atherosclerotic plaque rupture with subsequent thrombus formation [12]. In carotid arteries or coronary arteries, atherosclerotic plaques may develop into a high degree of stenosis, which could restrict blood supply to the downstream arteries, and cause reshaping of arterial wall. More often, the rupture of plaques with low-grade stenosis degree and subsequent thrombus formation, rather than stenosis, which can block blood flow in the arterial system, causes stroke or myocardial infarction.

However the exact mechanisms of plaque rupture still remain unclear. Plaques that are prone to rupture may often be clinically silent until the time of rupture. Research has been devoted to finding features for predicting plaque vulnerability. At present, some plaque features, such as large lipid pool, thin fibrous cap, and high content of inflammatory cells, have been believed to contribute to plaque instability [51]. Figure 7.1 shows a typical histological section of a vulnerable carotid plaque, where a thin fibrous cap can be found, covering the lipid region. The rupture of thin fibrous cap will let the lipid into blood flow, which will cause blockage at downstream arteries.

It has been accepted that both plaque morphology and biomechanical environment of the plaques influence their vulnerability [57]. The biomechanical factors such as plaque wall tensile stress and wall shear stress are considered to be important factors in plaque rupture process and should be taken into account for plaque vulnerability assessment. In this chapter, plaque wall stress analysis will be reviewed from 2D to 3D, from idealized models to patient-specific plaques in terms of geometrical accuracy, and from structure analysis only to fluid–structure interaction (FSI) analysis, with computational examples from our group, while hemodynamic studies of atherosclerotic plaques will not be reviewed in the chapter.

H. Gao (✉)
School of Mathematics and Statistics, University of Glasgow, Glasgow, UK
e-mail: hao.gao@glasgow.ac.uk

Q. Long
Brunel Institute for Bioengineering, Brunel University, London, UK
e-mail: quan.long@brunel.ac.uk

2 Biomechanical Study of Plaque Vulnerability

The hypothesis behind this group of studies is that plaque rupture is a mechanical failure of thin fibrous cap. The tendency of a plaque to rupture is due in part to increases in mechanical stress in fibrous cap [7, 16, 27, 56]. Various studies [53] have revealed that plaque rupture often occurs in the shoulder regions of plaques, the high stress concentration region due to the significant difference in stiffness between fibrous cap and underlying lipid pool [7, 27]. The main hypotheses for plaque rupture suggested by biomechanical community are as follows:

1. *Local maximum stress*: The local maximum stress in fibrous cap region, which is higher than the critical stress value which fibrous cap tissue can sustain, usually is considered to be the main reason of rupture in terms of biomechanics factors [7, 13, 15, 65, 66]. A critical value of 300 kPa has been proposed by Cheng et al. [7] for coronary arterial plaque, based on their 2D stress analysis with ruptured and stable atherosclerotic lesions.
2. *Fatigue failure*: Bank [1] hypothesized that mechanical fatigue on fibrous cap caused by pulsatile blood flow may be an important factor causing plaque rupture. The growth of plaque fatigue crack based on this hypothesis has been simulated by evolving stress distribution in plaques [76].
3. *Extremely high wall shear stress*: Recently extremely high wall shear stress has been linked to plaque rupture [20, 21] based on the findings that plaque ulceration occurs at the high wall shear stress location.

L. Saba et al. (eds.), *Multi-Modality Atherosclerosis Imaging and Diagnosis*,
DOI 10.1007/978-1-4614-7425-8_7, © Springer Science+Business Media, LLC 2014

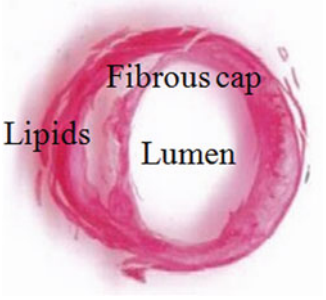

Fig. 7.1 A typical histological section of a vulnerable carotid plaque

4. *De-bonding effect by microcalcification*: The hypothesis for vulnerable plaque rupture due to stress-induced de-bonding around cellular microcalcification in thin fibrous caps was proposed [74] based on the fact that cellular-level microcalcifications in a thin cap can cause local stress concentrations that lead to interfacial de-bonding. It should be mentioned that the "de-bonding effect" also can be categorized into the hypothesis of "local maximum stress" because of extremely high stress caused by micro-calcifications.
5. *Other hypotheses*: Include injury due to turbulent flow in the stenosis [43], rupture of vasa vasorum [2], etc.

Comparing with the others, the local maximum stress hypothesis is the most wildly accepted one. However the biomechanical factors related to rupture hypothesis have not been fully verified in vivo, due to the difficulties such as (1) there is no technique that can directly measure wall stress in the plaque in vivo, and (2) the geometry of a specific plaque at pre- and post-rupture status is practically unachievable. Nonetheless, to work on any stress-related hypothesis, obtaining accurate stress distribution on the specific plaque is essential. While there is no better way to accurately measure the stress in the plaque, numerical methods have been extensively applied to obtain the stress in the plaque region, especially finite element method (FEM). The realistic plaque geometry with multicomponents including lipid region, fibrous cap, etc., is generally used to construct a FEM model together with physiological mechanical loading to predict the mechanical stress distribution in a plaque.

Finite element models have been developed from 2D to 3D, from idealized models to patient-specific plaques in terms of geometrical accuracy, and from structure analysis only to FSI analysis in terms of physical phenomenon reality. There are normally five main tasks involved in building a plaque mechanical stress analysis model which include (a) to acquire plaque components; (b) to reconstruct plaque geometry; (c) to apply mechanical load and dynamic boundary conditions; (d) to define suitable material constitutive models; and (f) to perform FEM simulation and post-processing. Table 7.1 lists breakdowns of each task for different levels of complexity of simulations. The following sections provide a brief review of the simulation technique developments, in the order of 2D structure-only stress analysis, 3D structure-only stress analysis, 3D fluid-only models and results, and 2D/3D FSI results.

2.1 Two-Dimensional Structure-Only Stress Analysis

Since 1990s, 2D structure stress analysis has been extensively applied to plaque models for predicting stress distributions from idealized models to patient-specific models. The advantage of using idealized models is that they allow easy changing of geometrical parameters to investigate effects of individual plaque features. Loree et al. [44] studied the effects of plaque structure features including stenosis severity and fibrous cap thickness on stress distributions based on idealized plaque models. They found that decreasing the fibrous cap thickness considerably increased the peak circumferential stress, while increasing the stenosis severity decreased peak stress, suggesting that ruptured plaques may not associate with high stenosis degree. Cheng et al. [7] studied the relation between the locations of peak stress in ruptured plaques and rupture sites for the same plaque. The results showed that most plaque rupture sites occurred very close to regions of high stress; however, the peak stress did not always coincide with the rupture site. They also found that the maximum circumferential stress in plaques that ruptured was significantly higher than maximum stress in stable specimens; a critical stress value of 300 kPa has been proposed for predicting plaque rupture. Finet et al. [11] studied the effect of fibrous cap thickness to plaque stress with 2D idealized models. They found that irrespective of plaque geometry and composition, a fibrous cap thickness of less than 60 μm results stresses greater than 300 kPa.

By using heterogeneous material model for stress analysis in human atherosclerotic aortas, Beattie et al. [4] found that the distribution of stress and strain energy was strongly influenced by plaque structure and compositions, indicating that a proper material model with multicomponents in plaque stress analysis is of very importance. Williamson et al. [79] studied the sensitivity of wall stresses in diseased human coronary arteries to varied material properties. They showed that stresses in the artery have low sensitivities to variations in elastic modulus and comparable among isotropic nonlinear, isotropic nonlinear with residual strains, and transversely isotropic linear models. However, the stress in the stress concentration regions can vary up to 30 % with different material models from the same work. Huang et al. [27] investigated the effect of calcification towards plaque stability in human atherosclerotic coronary arteries, suggesting that calcification does not decrease the stability of the plaque. However, Veress et al. [75] believed that the locationof calcification

Table 7.1 Summary of research on biomechanical study of plaques

Papers	Models source	Results
2D structure stress analysis		
[44]	Idealized models	Fibrous cap thickness is an critical factor affecting plaque stress
[7]	Histology	Plaque ruptures at high stress location
[11]	IVUS + Idealized model	The fibrous cap thickness can greatly affect the peak stress
[4]	Histology	Proper material models with multicomponents in plaque stress analysis are of very importance
[79]	Histology	Stress prediction showed low sensitivity to the chosen material models
[36]	Histology	Significant correlation between MMP-1 and circumferential stress
[26]	MRI + Histology	Macrophage locations correlated with peak plaque stress
[22]	Histology	A limited relation found between inflammation and extreme stress
[27]	Histology	Calcification may stabilize plaques
[6]	OCT	Realistic plaque geometry and components are important
[38–41]	MRI	Peak stress in symptomatic patients is much higher
[73]	MRI	Plaque stress related to plaque stability
[84]	MRI + Histology	Vulnerability index was proposed based on stress analysis
[68]	MRI	Local critical stress was suggested for plaque vulnerability assessment
[54]	Histology	Residual stress/strain may greatly affect plaque stability
[55]	Histology + US	Residual stress/strain may just have limited effects on the plaque stress
[70]	MRI	Luminal curvature can affect plaque stress condition
3D structure stress analysis		
[25]	Idealized 3D model	Calcification locations matter in plaque stability
[30]	Idealized 3D model	Plaque shape, size, remodeling, etc., affect longitudinal plaque stress
[23]	MRI	A nonlinear anisotropic multilayer material model was developed
[17]	Image-based 3D model	Plaque fissuring/dissection could cause localized mechanical trauma
[10]	MRI	Plaque rupture was simulated
[53]	IVUS	Plaque ruptures at locations of high stress
[80]	Cine angiographic images	Plaque structure/components are key issues in stress prediction
Fluid structure interaction analysis		
[83]	MRI	Certain locations with high wall stress and low wall shear stress were identified in healthy carotid artery
[82]	MRI	Biomechanical factors effects on atherogenesis
[31, 32]	MRI + Histology	Biomechanical factors were correlated with histological analysis
[40]	2D idealized model	Low stenosis plaque with thin fibrous cap may have high rupture risk
[41]	3D idealized model	The effects of wall motion in plaque development and rupture
[5]	3D idealized model	Microcalcification in fibrous cap could increase plaque vulnerability
[34]	MRI-based 2D model	Plaque stress can help in vulnerability assessment
[62–69]	MRI	3D FSI plaque stress with MRI has been developed and discussed
[81]	MRI	Comparison between structure-only and FSI model was conducted
[28, 29]	MRI	The determination of plaque shrinkage and stress-free state in plaque; intraplaque hemorrhage is associated with higher plaque stress
[8]	CT	Curvature difference in plaque region could be an important factor

could play an important role in plaque stability. Calcification deep in plaques could have little effect on stability, and may even stabilize the plaque from rupture, while calcification in the fibrous cap could contribute to the plaque rupture due to the great difference in stiffness, and increasing the stress in the fibrous cap, especially the interface between calcification and fibrous cap. Figure 7.2 presents a 2D plaque stress analysis from histology analysis of the carotid plaque corresponding to Fig. 7.1 from our group. The discretized carotid geometry is shown in Fig. 7.2a. Arterial wall was assumed to be linear in material properties with 1 MPa Young's modulus, and 0.45 for Poisson ratio. A luminal pressure of 110 mmHg was applied. Figure 7.2b shows the corresponding Von-Mises stress distribution. The fibrous cap experiences much higher stress than other regions and the maximum stress region can be found in the shoulder of the plaque with maximum value of 253 kPa. Figure 7.2c shows the detailed stress distribution in a local stress concentration adjacent to lipid core, which experiences very low stress. This high plaque wall stress level inside fibrous cap has been believed to be related to plaque rupture.

Stress analysis also has been combined with the findings from histological analysis to study the possible interaction between inflammatory activities and extreme stress

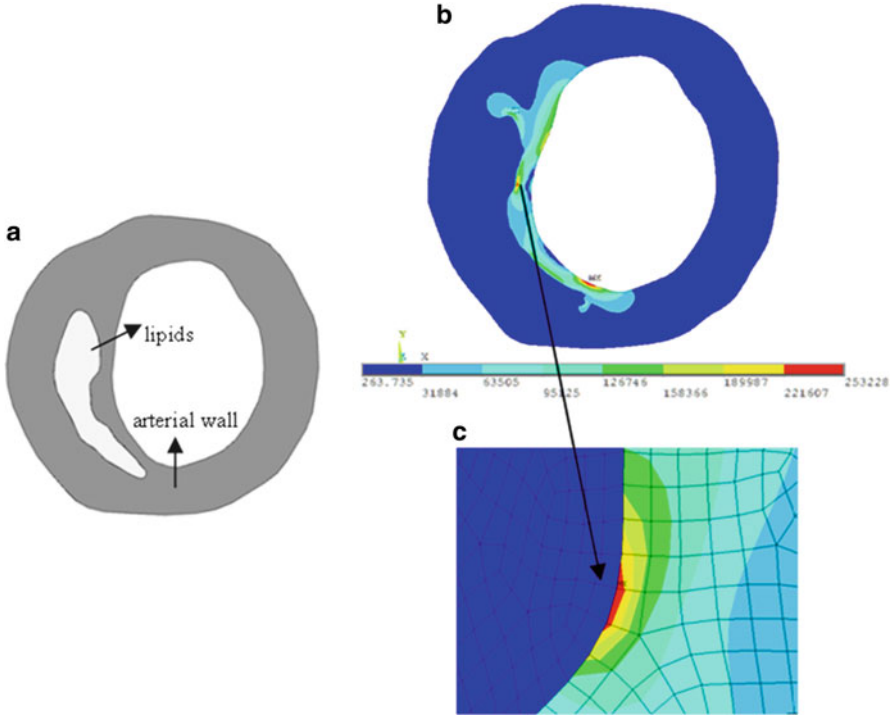

Fig. 7.2 (**a**) Discretized plaque geometry from histology section; (**b**) stress distribution; (**c**) detailed stress distribution in fibrous cap

environments in fibrous cap. Lee et al. [36] demonstrated that there are some correlations between high circumferential stress regions and MMP expression in human atherosclerotic coronary arteries, by considering that the degradation of the collagenous extracellular matrix at high stress regions will further weaken fibrous cap and promote plaque rupture. Howarth et al. [26] correlated the macrophage locations and plaque stress distributions by using ultrasmall superparamagnetic iron oxide contrast agent (USPIO)-enhanced MRI in a patient with symptomatic severe carotid stenosis. Their findings supported that macrophage locations correlated well with maximal predicted stresses in the plaque. Studies from Hallow et al. [22] by using a 2D heterogeneous finite element model and the corresponding distributions of selected inflammatory markers have identified the progression-dependent relationships between stress and both macrophage presence and MMP-1 expression, suggesting the role of mechanical stress in stimulating the inflammatory response, which will help explain how mechanical factors may regulate plaque remodeling.

However, many of those studies [4, 7, 27, 36] are based on the geometry from histology analysis of plaques for predicting stress distribution or on idealized plaque models. The distortion caused in the histological tissue processing procedure has not been considered in the models. Plaque geometry based on histological analysis may be totally different from in vivo state [47]. Figure 7.3a shows an ultrasound scanning slice of an ex vivo carotid plaque sample from our lab, and Fig. 7.3b shows the corresponding histological section; the great distortion in histological process can be found by comparing Figs. 7.3a and 7.3b. As the consequence, the predicted stress distribution based on the distorted/idealized geometry may not actually reflect the real stress distributions in plaques. Efforts have been made to use modern in/ex vivo medical imaging techniques for more realistic stress predictions. Ohayon et al. [52] used pre-angioplasty IVUS images of human atherosclerotic coronary arteries to predict plaque rupture locations. Chau et al. [6] performed stress and strain study by using optical coherence tomography images and compared those results with models from histological images. Though the stress distributions were comparable between those two models, the maximum stress was higher in the histological models. Tang et al. [62] used ex vivo MRI images for stress analysis and compared the results with histological models of human carotid plaques. The maximum and minimum stress values from histological models were 28 and 69 % higher than those from MRI-based models. From high resolution of in vivo multi-spectral magnetic resonance imaging of five human carotid atherosclerotic plaques, Li et al. [39] built up multicomponents of 2D plaque models. Incompressible hyper-elastic material prosperities were used for the stress analysis. Results showed that the mean maximum stresses in ruptured plaques were much higher than those in unruptured plaques. In their following study [38], they compared the stress concentrations between symptomatic and asymptomatic patients by 2D structure analysis based on in vivo magnetic resonance imaging and found that maximal predicted plaque stresses in symptomatic patients were significantly higher, indicating the possibility that plaques with higher stresses may be more prone to be symptomatic and rupture in the near future. Similar results can be found in the study by Trivedi et al. [73]. A recent study

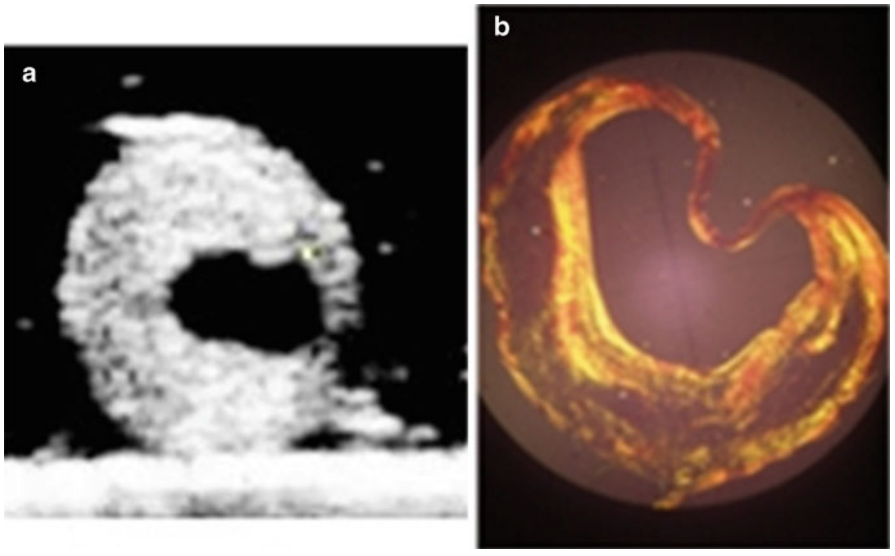

Fig. 7.3 (**a**) Ultrasound imaging of an ex vivo carotid plaque sample; (**b**) corresponding histological section of the ex vivo carotid plaque

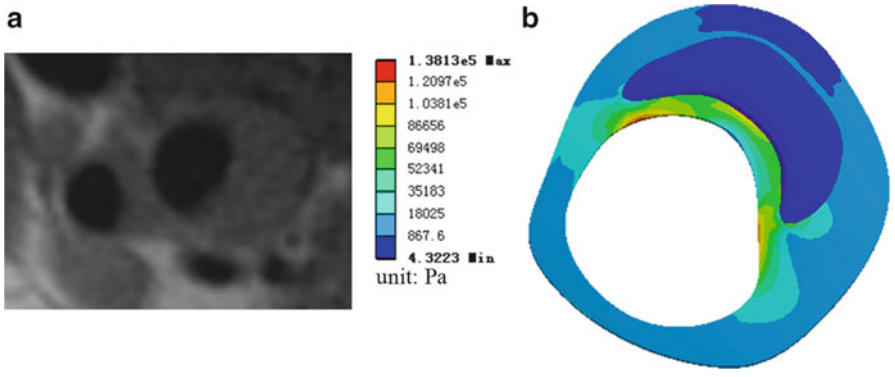

Fig. 7.4 (**a**) One carotid plaque MRI slice; (**b**) the corresponding plaque stress analysis

from Teng et al. [70] showed that arterial luminal curvature and fibrous cap thickness should be considered together for better mechanical risk assessment of atherosclerotic plaques by using 2D FEM models with in vivo MRI images.

Figure 7.4a presents one MRI slice from a carotid plaque, and by manual segmentation, the boundary points of the plaque geometry were inputted into ANSYS 11.0 to reconstruct plaque components. By applying the similar boundary condition and material properties as in Fig. 7.2, the static stress analysis was performed, shown in Fig. 7.4b. Still high stress region can be found in the fibrous cap and much lower stress level in lipid region as previous examples. Although MRI imaging can provide in vivo geometry, the classification of plaque components from MRI images still is a challenge, especially for a very thin fibrous cap.

Two-dimensional mechanical models of atherosclerotic plaques are abundant in the literature, and even though the results may be unrealistic, the findings could still shed some lights on the plaque rupture mechanics. The disadvantages of 2D models lie in (1) the assumptions of plane strain/stress; (2) simplified material model; and (3) distorted geometry compared to the in vivo state, which will lead to a possible overestimated plaque stress level. Therefore realistic 3D models are needed for accurate stress analysis in plaque region.

2.2 3D Structure-Only Stress Analysis

3D structure-only stress analysis has been carried out based on idealized plaque models and patient-specific geometries.

Idealized 3D Plaque Models By constructing an idealized 3D plaque model, Hoshino et al. [25] studied stress distributions around atherosclerotic calcifications and their effects on plaque vulnerability. Their findings suggested that the presence of a calcium deposit creates local increases in wall tensile stress, and it depends on the relative position of the deposit in the plaque region. Imoto et al. [30] studied the structure stress distributions in an idealized 3D plaque model in a cylindrical vessel model, and mapping the stress results with longitudinal IVUS plaque images, the effects of plaque size, shape, expansive remolding, calcification, and lipid core on the stress distributions were examined. Results showed that plaque shape, size and remodeling, as well as spatial configurations of plaque components have different effects on plaque stress.

Ex Vivo 3D Plaque Models Holzapfel et al. [23] have performed a series of stress studies in diseased vessels by introducing a multilayer anisotropic 3D model incorporating the histological structure of arterial wall. In their studies, MR images were used to develop 3D finite element models to simulate balloon angioplasty in atherosclerotic iliac arteries. Mechanical test was performed to provide the required raw data for the formulation of nonlinear material models. They compared their 3D models with existing biomechanical models, characterized by isotropic material response, assumption of plain strain, etc. The results showed those assumptions may give a wide range of stress levels, indicating those simplifications need to be well justified when interpreting stress results with plaque rupture. By using similar nonlinear material model, Gasser and Holzapfel [17] modeled plaque fissuring and dissection during balloon angioplasty intervention in a human external iliac artery with type V lesion. Ferrara and Pandolfi [10] presented three-dimensional finite element simulations of damaged arteries to investigate the influence of the geometry and tissue properties on plaque rupture. The cohesive elements were used to model the fracture surface induced by the mechanical action when the tensile strength of the material is reached.

In Vivo 3D Plaque Models Ohayon et al. [53] calculated the stress in a single diseased human coronary artery from IVUS images to decide the possible relation between high stress concentrations and plaque rupture sites. The diseased arterial wall was modeled by components of adventitia, media, dense fibrosis, and cellular fibrosis with isotropic materials. A physiological mean blood pressure of 13.33 kPa was applied for the luminal loading. They found the peak stress locations from 3D model well coincided with plaque rupture location, but not in the corresponding 2D FE models, which may overestimate the stress levels. The stress and strain distributions using FEM and in vivo patient-specific dynamic 3D coronary arterial tree reconstruction from cine angiographic images have been done by Wu et al. [80], the local stresses were calculated in the diseased wall, and results showed that a smaller vessel diameter, greater percentage narrowing, and large lesion size may result in higher stress in the fibrous cap.

Compared to 2D stress analysis, 3D structure analysis could incorporate more information in FE models, such as the multilayers of arterial wall, anisotropic material model considering fiber directions, and no plain stress or strain assumptions as in 2D FE models, while there are still places left for improving in order to achieve a realistic plaque stress prediction. In a physiological situation, plaque is under pulsating blood pressure loading, with reduced pressure value in the stenosis throat due to the narrowing effect in the stenosis part. Therefore a uniform pressure loading applied on the luminal surface which is generally adopted in 3D FE structure-only models cannot simulate the realistic stress distributions. In real situation, the mechanical environment of plaques includes the blood flow dynamics and wall structure dynamics. In order to accurately predict the biomechanical environment, one must consider the hemodynamics surrounding the plaque region, and the corresponding wall dynamics under pulsating loading caused by blood flow. Therefore 3D blood flow simulation in the plaque region is required as part of plaque stress analysis.

2.3 2D/3D FSI Results

In nature, blood flow in the arteries and arterial wall structure dynamics are interacted with each other. Blood flow provides the loading for arterial structure dynamics, such as pressure and the drag force in the wall. Arterial wall will deform under those loadings, and correspondingly change arterial geometry which will affect the blood flow. Therefore the FSI method simulates more accurate mechanical interaction phenomenon of artery and needs to be adopted for stress analysis in atherosclerotic plaques under physiological environment [13].

Zhao et al. [83] firstly introduced MRI-based FSI models to predict wall shear stress and wall stress patterns in healthy subjects, and tried to define regions of low wall shear stress and high wall stress. Their results demonstrated that there are certain regions with low wall shear stress and high mechanical stress, corresponding to the areas where atherosclerotic plaque develops. Younis et al. [82] used finite element simulations of fluid–solid interactions to investigate interindividual variations in flow dynamics and wall mechanics at carotid artery bifurcations from three healthy subjects. Subject-specific calculations were based on MR images of carotid artery geometries and ultrasound measured flow boundaries. Various biomechanics parameters such as wall shear stress, oscillatory shear index, and cyclic strain have been compared among subjects. Kaazempur-Morfrad et al. [31] proposed cyclic strain in describing the arterial wall dynamics under pulsatile blood pressure loading. They found that the regions of highest variations in cyclic strain are identified at frequent sites of atherosclerosis. In the study carried out by Kaazempur-Morfrad et al. [32], stress analysis was performed for four patients. In addition to the numerical study on the plaque models, the excised plaques were sectioned and stained for smooth muscle cells, macrophages, lipid, and collagen. Efforts have been given to correlate fluid dynamic parameters with histological markers of atherosclerosis.

Li et al. [40] used a 2D flow–plaque interaction model and tried to answer how critical is fibrous cap thickness to carotid plaque stability. They suggested that the presence of a moderate carotid stenosis (30–70 %) but with a thin

fibrous cap can also present a high risk for plaque rupture. Li et al. [41] constructed an idealized 3D plaque model with varying stenosis degrees of 30, 50, and 70 %, to study the wall motion in plaque throat. The results suggested that severe stenosis may inhibit wall motion. The numerical study on the role of microcalcifications in plaque vulnerability in an eccentric stenosis model [5] showed that the vulnerable plaque with embedded calcification spots presented higher wall stress concentration region in the fibrous cap, providing the evidence for the hypothesis that microcalcifications could increase the plaque vulnerability. Kock et al. [34] developed a 2D FSI model based on in vivo MR images of two symptomatic atherosclerosis patients, and the longitudinal stress levels for each patient were calculated. They concluded that the longitudinal fibrous cap stresses may be useful in assessing plaque vulnerability.

Tang et al. [62] have developed a 3D fluid–structure interaction model from 3D ex vivo MR images of a human atherosclerotic carotid artery to identify critical flow and stress/strain conditions, which may be related to plaque rupture. In the following years, Tang and colleagues did a series of studies on the stress analysis with atherosclerotic plaques from ex vivo to in vivo states [63]. Their results showed that large lipid pool and thin fibrous caps are associated with both extreme stress and strain levels. Large cyclic stress and strain resulted from pulsating pressure were identified, which may lead to plaque rupture by a fatigue procedure. Similarly as the results from 2D stress analysis, the plaque stress, and strain conditions are affected considerably by lipid pool size, shape and position, plaque cap thickness, and axial stretch, and so on, from their 3D FSI models [64, 65]. The study [81] on the comparison between fluid–wall (FSI) and wall-only (or structure-only) models with in vivo/ex vivo MRI-based 3D non-Newtonian FSI showed that there could be a great difference in wall shear stress and maximum principal stress between the two models. Huang [28] has proposed a method to determine 3D zero stress state of carotid atherosclerotic plaques from in vivo MRI data by a patient-specific artery shrinkage procedure in axial and inner circumferential directions. They suggested that accurate knowledge of artery shrinkage and the shrinkage process will considerably improve the accuracy of stress prediction from in vivo plaque models. Huang et al. [29] found that intraplaque hemorrhage is associated with higher structural stresses in human atherosclerotic plaques by using in vivo MRI-based 3D FSI models with ten plaque models. Creane et al. [8] suggested that the curvature difference in the inner and outer plaque surfaces could also be an important factor in the development of a symptomatic plaque.

Moreover, efforts have been made to use plaque stress for assessing and predicting plaque vulnerability [68]. The local maximal stress hypothesis and a stress-based computational plaque vulnerability index were proposed to assess plaque vulnerability by Tang et al. [66]. A critical stress form in the fibrous cap was chosen to determine the vulnerability index. Their results showed that the vulnerability index based on stress information was 85 % agreement with the assessment given by histopathological analysis. Similarly a pilot study was also performed on assessment of plaque vulnerability by MRI and computational biomechanics by Zheng et al. [84]. The stress/strain was calculated in plaque sections, and an index including entire plaque area, lipid-cap-thickness, and stress components was suggested for vulnerability assessment. A negative correlation between human carotid atherosclerotic plaque progression and plaque wall stress has been demonstrated by Tang et al. [67] with in vivo MRI-based 2D/3D FSI models. They also suggested that both lower wall stress and lower wall shear stress may contribute to continued plaque progression. Gao et al. [15] studied the plaque wall stress with four patients with carotid plaques by using FSI combining with morphological analysis, and a risk assessment based on plaque wall stress has been tried. Based on 12 carotid plaques, Tang et al. [69] compared plaque stress between a group of five ruptured plaques (confirmed by histology) and seven unruptured plaques by using 3D FSI methods. They found that the stress in the rupture sites was significantly higher than in the surrounding region.

The studies linking plaque stress to plaque progression/rupture would advance the understanding of biomechanical role in atherosclerosis plaque initiation, development, and rupture, providing insights into therapy options. Figure 7.5 shows an example of plaque stress analysis by using FSI with patient-specific carotid plaque geometry. Figure 7.5a is the pressure distribution at the end of systole phase on the luminal surface, and due to moderate stenosis, the pressure drop is not significant in plaque region; Fig. 7.5b is the wall shear stress distribution, and slightly higher wall shear stress could be found in the plaque region; Fig. 7.5c is the corresponding plaque wall tensile stress distribution, represented by the first principle stress. The local high stress concentration at downstream of the plaque can be identified, which has been believed to be related to plaque rupture. From Fig 7.5, the stress factors from hemodynamics and plaque structure dynamics are available for analysis, providing a more complete framework for analyzing stress-related plaque rupture.

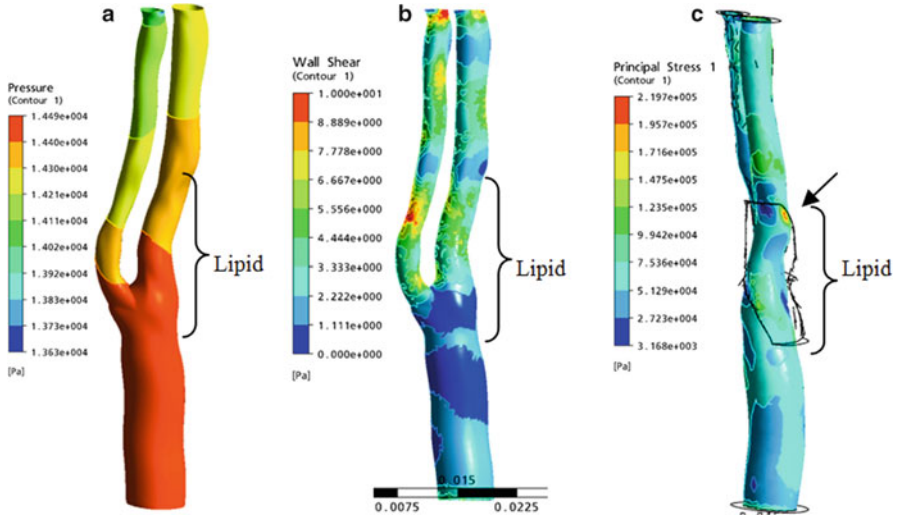

Fig. 7.5 Stress analysis with fluid–structure interaction. (**a**) Pressure distribution on luminal surface at the end of systole phase; (**b**) wall shear stress distribution; (**c**) plaque wall stress distribution, represented by first principal stress

3 Factors Influencing the Simulation Accuracy of FEM Models on Plaque Stress Analysis

3.1 Model Reconstruction

The computational biomechanics simulation with two/three-dimensional medical imaging provides a new approach for advancing our understanding between biomechanics factors and arterial disease. In order to perform biomechanical study on plaques, the first step after the image acquisition is to reconstruct the plaque model either 2D or 3D. However, the reconstruction procedure is subject to several potential uncertainties, especially for 3D models. From previous studies, it has been demonstrated that the accurate reconstruction of plaque geometry will greatly affect the biomechanics results, and more effort should be given to a more accurate and detailed geometry reconstructions, the primary influence on physiologically significant indicators [37, 61].

With the development of modern medical imaging technique, increasing number of different kinds of in vivo images can be used for geometry reconstruction. The reconstructions of patient-specific diseased artery model from medical images have been studied for a long time, and the procedure has been well established, either using third-party software [59] for image analysis and geometry extraction or in-house software based on established image processing techniques [60]. Most of the methods in existed literatures are based on the extraction of arterial cross-sectional boundaries, alignment of those boundaries in 3D context, and construction of 3D surfaces and bodies from the stack of 2D boundary profiles. Figure 7.6 shows the general plaque geometry reconstruction from in vivo MRI carotid plaque geometries from our group.

The overall accuracy of 3D luminal wall geometry reconstruction has been investigated by Moore et al. [50] by using a carotid bifurcation phantom and a human carotid bifurcation. Five different reconstruction procedures were applied to the reconstructions with or without smoothing. Results showed that for phantom model, all reconstructions gave acceptable results, while in vivo models need to be properly smoothed for use in computational studies of in vivo hemodynamics. Long et al. [42] studied the reproducibility of 3D geometrical reconstructions of eight human carotid bifurcations from in vivo MRI. Smoothed lumen contours were aligned in the longitudinal direction, B-spline interpolation was applied to reconstruct the 3D surface of carotid bifurcation, and two steps of smoothing were employed to improve the quality of the 3D reconstruction, including centerline smoothing and surface smoothing. They concluded that the geometry of common carotid artery was well reproduced by the reconstruction procedure in most of the cases, while the external carotid artery showed the worst reproducibility. 3D ultrasound also has been used for carotid geometry reconstruction for image-based CFD modeling [19].

However most of studies have been focused on the arterial luminal reconstruction and the effects on the hemodynamic factors. The stress analysis in the plaque region requires the accurate reconstructions of plaque components, which could be much harder than the reconstruction of arterial lumen. Compared to the lumen geometry reconstruction, the structures involved in the plaque structure analysis are different in size, shape, etc. especially when coming to thin fibrous cap reconstruction. A vulnerable plaque could have a thin fibrous cap less than 65 μm, which may be represented by one or two pixels in medical images. Therefore the relative uncertainties in fibrous cap reconstruction will be higher than other plaque components.

Although structure stress analysis has been applied in plaques with modern medical imaging to assess plaque vulnerability for many years, there are few studies on assessing the plaque geometry reconstruction uncertainties and their

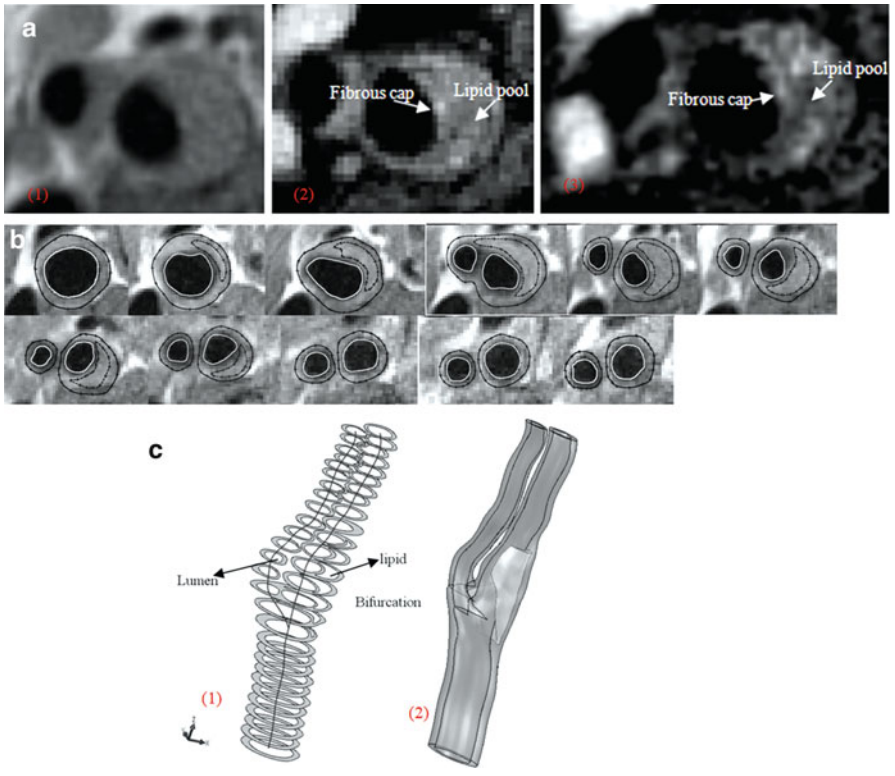

Fig. 7.6 The general procedure of patient-specific plaque geometry reconstruction from in vivo MRI. (**a**) Carotid plaque MRI imaging with difference sequences [(*1*) T_2 weighted; (*2*) T_2 weighted with fat saturation; (*3*) short T_1 inversion recovery]; (**b**) segmentation of plaque component from multi-sequence MRI images; (**c**) 3D reconstruction of plaque geometry

effects on stress distributions in plaque region. In order to provide the uncertainty analysis in plaque stress analysis from MRI image processing to 3D reconstruction, and to final plaque stress analysis, Gao et al. [14] studied three carotid plaques to estimate the possible uncertainties. They found that inter-operator reproducibility for the arterial wall reconstruction based on T2W images was high, with the disagreement among the operators being at one pixel level. The reproducibility was lower for the segmentation of lipid core and fibrous cap. The uncertainties caused during 3D surface interpolation and smoothing and bifurcation 3D reconstruction were minor and negligible. The stress analysis showed that the overestimation of the lipid region would induce a higher stress concentration and general higher stress level in the plaque region. The impacts on the stress distribution in the plaque region caused by over/underestimation of arterial wall are much less and insignificant comparing with the variations caused by the over/underestimation of the lipid region. The improved resolution/quality in plaque imaging with newly developed MRI protocols would generate more realistic stress predictions, while the uncertainties involved in MRI image acquisition have not been assessed in that study, which is equally important.

3.2 Material Properties

Quantifying the mechanical properties of healthy and diseased arterial tissue is essential for realistic stress prediction. Histological studies in the arterial wall have shown that arterial wall is heterogeneous, nonlinear, anisotropic, and viscous-elastic. Richardson [57] has pointed out that the lack of accurate plaque material properties data is possibly the most uncertain aspect in the existing literature on plaque rupture study. The main components of the plaque are lipid core, calcification, and fibrous cap tissue. While there has been much research on the healthy arterial tissue [18, 77], studies on the mechanical properties of plaque components are much less. A review of published data showed a wide range of material properties for plaque components [79]. In general, lipid is much softer compared to other plaque components, while calcification is much stiffer. The stiffness of fibrous cap is essential to the plaque stability. Because of the complex fiber organization and content variation, the stiffness of fibrous cap shows a great range of variation. Therefore, to obtain a proper material data for structure stress analysis is a key step towards on developing biomechanical plaque models, especially for fibrous cap tissue.

Lee et al. [35] determined the mechanical properties of plaque fibrous cap from human abdominal aortas by static

and dynamic loading tests. The stiffness of the fibrous cap was depended on its microstructure, including calcification, collagen content, and organization. They also found that fibrous cap stiffness increased with the increased frequency of loadings, indicating fibrous cap stiffness is nonlinear in nature. Loree et al. [45] investigated the static circumferential modulus of human atherosclerotic tissue. They found that the static circumferential tangential modulus was not significantly affected by the degree of cellularity and calcification, compared to the compressive modulus. Later, Loree et al. [46] did the mechanical test on lipid pools with different lipid compositions by using a torsion rheometer. Results showed that the stiffness of lipid pools depended on the concentration of cholesterol monohydrate crystals.

Topoleski et al. [71] used a custom-built experimental system to test segments of a whole human atherosclerotic plaque by uniaxial radial cyclic compressive testing, and plaques showed nonlinear characteristic under finite deformation, related to the plaque composition and load history. Topoleski and Salunke [72] studied the mechanical behavior of calcified plaques with compression and stress-relaxation experiments, and the calcified plaques are significantly different from other plaques. Holzapfel et al. [24] measured anisotropic mechanical properties of tissue components in human atherosclerotic plaque tissue, including ultimate tensile stresses/stretches. Results showed that plaque components are highly nonlinear and different in the different layers, and the lowest fracture stress occurred in the circumferential direction of the fibrous cap. Ebenstein et al. [9] used nano-indentation to measure the mechanical properties of blood clots, fibrous tissue, and calcified fibrous tissue from human atherosclerotic plaque tissue and demonstrated that the stiffness of plaque tissue increases with increasing mineral content. Recently Barrett et al. [3] measured the indentation response of eight human carotid atherothrombotic plaque samples by fitting the experimental results to finite element simulations. Maher et al. [48] measured the tensile and compressive properties of fresh human carotid atherosclerotic plaques and found that calcified plaques had the stiffest response.

Modern medical imaging has been employed to quantify the material properties in diseased vessels recently, which provides a possibility to characterize material properties under in vivo situation for realistic patient-specific stress simulation. Based on 3D IVUS model, Vonesh et al. [78] developed a method to estimate the regional material properties in diseased iliac and femoral arteries by using FEM, and results showed that the elastic modulus for non-diseased tissue was significantly different from plaque tissue. Karimi et al. [33] proposed a new method for estimation of nonlinear elastic properties of soft tissue by combining the nonlinear FEMs for estimating tissue stiffness profile. The proposed method has been applied to realistic 2D and idealized 3D arterial plaque models and proved the possibility for the estimation of intraplaque distribution of nonlinear material properties. Masson et al. [49] developed an approach to identify material properties and wall stress prediction for human common carotid arteries based on noninvasive in vivo clinical data by measuring the dynamical intra-luminal pressure, medial diameter, and intimal–medial thickness. The method provided a way to characterize patient-specific material parameters directly from noninvasive in vivo human data.

3.3 Residual Stress/Strain

It is accepted that biological tissue does not become free of stress when all external loads are removed. Previous studies have shown that such residual stress/strain tends to maintain the integrity of vessel structure, and make the stress distribution more uniform throughout the arterial wall. However the effects of residual stress on plaque stability have not been well studied. Ohayon's study [54] showed the residual stress/strain in plaques is not negligible, and may dramatically affect the physiological peak stress in thin fibrous cap, and suggested that plaque rupture should be treated as a combination of external loading and intraplaque residual stress/strain. The study from our group showed that the circumferential residual stress has limited effects on the actual stress distribution under normal physiological loadings [55]. Those controversial results indicated that more efforts need to be made to understand the residual stress/strain to plaque stability.

4 Discussion and Conclusion

Atherosclerotic plaque has been considered to be one of the leading causes of death all over the world, caused by the plaque rupture and subsequent thrombus formation. Until now the exact mechanism of plaque rupture is not clear, from biomechanical aspect, the rupture can be considered to be a mechanical event. Therefore it is essential to predict plaque stress with high accuracy. Results from those models will help understand how plaque ruptures. Plaque stress has been studied for several decades from 2D structure-only to fully coupled 3D plaque stress in both structure dynamics and hemodynamics. The extremely high stress locations in plaque region also have been considered to be a main factor responsible for plaque rupture. The biggest challenge lies in how to predict plaque stress with patient-specific simulations, for example, realistic geometry reconstruction, boundary conditions, and material models. Studies have demonstrated that 2D plaque models are prone to overestimate the stress levels because of assumptions;

3D plaque stress analysis with coupled FSI emerges to advance the accuracy of analysis, not just the stress in the plaque structure, but also the flow pattern around the plaque.

The development of medical imaging provides the possibility of realistic 3D plaque geometry with a high resolution, and the plaque components (fibrous cap, lipid region) could be obtained from multi-spectral MR images, for example. However the resolution of MR images is not high enough for very thin fibrous cap reconstruction, and also the contrast is not high, which impose certain uncertainties on plaque stress analysis based on in vivo MRI. The study on plaque components' effects to plaque stress distribution showed that plaque stress level is significantly affected by the thickness of fibrous cap compared to lipid size; therefore efforts to increase the accuracy of plaque reconstruction from in vivo MRI need to be made in the near future. The accuracy of stress analysis based on plaque geometry is subject to MR image quality. The improved resolution/quality in plaque imaging with newly developed MRI protocols would generate more realistic stress predictions. Although FSI simulation can provide a more realistic stress prediction than 2D/3D structure stress analysis, some major limitations existing in the current modeling techniques are (1) realistic material property modeling; (2) the choice of blood flow model, such as laminar flow assumption; (3) patient-specific boundary conditions, especially the real pressure inside plaque lumen; and (4) residual stress/strain incorporation, etc. Therefore attention needs to be paid when interpreting plaque stress results with patient situation, the uncertainties should be acknowledged.

Rupture of the fibrous cap is a very complex process. It is not only the mechanical factors that matter, but other abnormalities in tissue and cells, such as elevated inflammatory activity and degraded collagen structures, may also influence the rupture process [57]. Comprehensive plaque vulnerability assessment should involve a combination of systemic markers, morphological features, and biomechanical factors. Considering only a few factors may not give a complete picture of plaque rupture risk.

In conclusion, the summary of main plaque stress analysis research in recent years, but not limited, is presented in the following Table 7.1. The progress in numerical modeling in stress analysis has made fluid–structure interaction analysis with patient-specific plaque models possible. Extreme stress distributions in the plaque region could be predicted, and may be used for plaque rupture risk assessment, and these assessments could be helpful in clinical practice. The combination of plaque MR imaging analysis, computational modeling, and clinical study/validation would advance our understandings of plaque rupture, and establish new procedures for patient diagnose, management, and treatment.

Acknowledgements This project is supported by the British Heart Foundation (FS/06/048). The authors like to thank Dr ZY Li, Dr M Graves, MD, and JH Gillard from Department of Radiology, Cambridge University, for their contributions to all MR images, and collaborations in the project.

References

1. Bank AJ, Versluis A, Dodge SM, Douglas WH (2000) Atherosclerotic plaque rupture: a fatigue process? Med Hypotheses 55(6):480–484
2. Barger AC, Beeuwkee R, Lainey LL, Silverman KJ (1984) Hypothesis: vasa vasorum and neovascularization of coronary arteries. A possible role in the pathophysiology of atherosclerosis. N Engl J Med 310:175–177
3. Barrett SRH, Sutcliffe MPF, Howarth S, Li ZY, Gillard JH (2009) Experimental measurement of the mechanical properties of carotid atherothrombotic plaque fibrous cap. J Biomech 42(11):1650–1655
4. Beattie D, Xu C, Vito R, Glagov S, Whang MC (1998) Mechanical analysis of heterogeneous, atherosclerotic human aorta. J Biomech Eng 120(5):602–607
5. Bluestein D, Alemu Y, Avrahami I et al (2008) Influence of microcalcifications on vulnerable plaque mechanics using FSI modeling. J Biomech 41(5):1111–1118
6. Chau AH, Chan RC, Shishkov M, MacNeill B, Iftimia N, Teraney GJ et al (2004) Mechanical analysis of atherosclerotic plaques based on optical coherence tomography. Ann Biomed Eng 32(11):1494–1503
7. Cheng GC, Loree HM, Kamm RD, Fishbein MC, Lee RT (1993) Distribution of circumferential stress in ruptured and stable atherosclerotic lesions. A structure analysis with histopathological correlation. Circulation 87(4):1179–1187
8. Creane A, Maher E, Sultan S, Hynes N, Kelly D, Lally C (2010) Finite element modeling of diseased carotid bifurcations generated from in-vivo computerized tomographic angiography. Comput Biol Med 40(4):419–429
9. Ebenstein DM, Coughlin D, Chapman J, Li C, Pruitt LA (2008) Nanomechanical properties of calcification, fibrous tissue, and hematoma from atherosclerotic plaques. J Biomed Mater Res A 295(2):H717–H727. doi:10.1002/jbm.a.32321
10. Ferrara A, Pandolfi A (2008) Numerical simulation of arterial plaque ruptures. Int J Mater Form 1(Suppl 1):1095–1098
11. Finet G, Ohayon J, Rioufol G (2004) Biomechanical interaction between cap thickness, lipid core composition and blood pressure in vulnerable coronary plaque: impact on stability or instability. Coron Artery Dis 15(1):13–20
12. Fuster V (1994) Mechanisms leading to myocardial infarction: insights from studies of vascular biology. Circulation 90(4):2126–2146
13. Gao H, Long Q (2008) Effects of varied lipid core volume and fibrous cap thickness on stress distribution in carotid arterial plaques. J Biomech 41(14):3053–3059
14. Gao H, Long Q, Howarth SPS, Tang TY, Li ZY, Graves MJ, Gillard JH (2009) The reproducibility study of 3D arterial plaque reconstruction and its effects to the stress analysis based on multiple sequence MRI images. J Magn Reson Imaging 30(1):85–93
15. Gao H, Long Q, Graves M, Gillard JH, Li ZY (2009) Carotid arterial plaque stress analysis using fluid–structure interactive simulation based on in vivo magnetic resonance images of four patients. J Biomech 42(10):1416–1423
16. Gao H, Long Q, Sadat U, Graves M, Gillard JH, Li ZY (2009) Stress analysis of carotid atheroma in a TIA patient using MRI-based fluid–structure interaction method. Br J Radiol 82(s46-s54):46–54. doi:10.1259/bjr/20307071

17. Gasser TC, Holzapfel GA (2007) Modeling plaque fissuring and dissection during balloon angioplasty intervention. Ann Biomed Eng 35(5):711–723
18. Gerhard AH (2006) Determination of material models for arterial walls from uniaxial extension tests and histological structure. J Theor Biol 238(2):290–302
19. Glor FP, Ariff B, Crowe LA, Hughes AD, Cheong PL, Thom SA et al (2003) Carotid geometry reconstruction: a comparison between MRI and ultrasound. Med Phys 30(12):3251–3261
20. Groen HC, Gijsen FJH, van der Lugt A, Ferguson MS, Hatsukami TS, van der Steen AFW, Yuan C, Wentzel JJ (2007) Plaque rupture in the carotid artery is localized at the high shear stress region: a case report. Stroke 38(8):2379–2381
21. Groen HC, Gijsen FJH, van der Lugt A, Ferguson MS, Hatsukami TS, van der Steen AFW, Yuan C, Wentzel JJ (2008) High shear stress influences plaque vulnerability. Neth Heart J 16(7–8):280–283
22. Hallow KM, Taylor WR, Rachev A, Vito RP (2009) Markers of inflammation collocate with increased wall stress in human coronary arterial plaque. Biomech Model Mechanobiol 8(6):473–486
23. Holzapfel GA, Stadler M, Schulze-Bauer CA (2002) A layer-specific three dimensional model for the simulation of balloon angioplasty using magnetic resonance imaging and mechanical testing. Ann Biomed Eng 30(6):753–767
24. Holzapfel GA, Sommer G, Regitnig P (2004) Anisotropic mechanical properties of tissue components in human atherosclerotic plaques. J Biomech Eng 126(5):657–665
25. Hoshino T, Chow LA, Hsu JJ, Perlowski AA et al (2009) Mechanical stress analysis of a rigid inclusion in distensible material: a model of atherosclerotic calcification and plaque vulnerability. Am J Physiol Heart Circ Physiol 297:H802–H810
26. Howarth S, Li ZY, Trivedi RA, U-King-Im JM, Graves MJ, Kirkpatrick PJ, Gillard JH (2007) Correlation of macrophage location and plaque stress distribution using USPIO-enhanced MRI in a patient with symptomatic severe carotid stenosis: a new insight into risk stratification. Br J Neurosurg 21(4):396–398
27. Huang H, Virmani R, Younis H, Burke AP, Kamm RD, Lee RT (2001) The impact of calcification on the biomechanical stability of atherosclerotic plaques. Circulation 103(8):1051–1056
28. Huang X, Yang C, Yuan C, Liu F, Canton G, Zheng J, Woodard PK, Sicard GA, Tang D (2009) Patient specific artery shrinkage and 3D zero-stress state in multi-component 3D FSI models for carotid atherosclerotic plaques based on in vivo MRI data. Mol Cell Biomech 6(2):121–134
29. Huang X, Teng Z, Canton G, Ferguson M, Yuan C, Tang D (2010) Intraplaque hemorrhage is associated with higher structural stresses in human atherosclerotic plaques: an in vivo MRI-based 3d fluid–structure interaction study. Biomed Eng Online 9(1):86
30. Imoto K, Hiro T, Fujii T, Murashige A et al (2005) Longitudinal structural determinants of atherosclerotic plaque vulnerability: a computational analysis of stress distribution using vessels models and three dimensional intravascular ultrasound imaging. J Am Coll Cardiol 46(8):1507–1515
31. Kaazempur-Morfrad MR, Younis HF, Patel S, Isasi S, Chung C et al (2003) Cyclic strain in human carotid bifurcation and its potential correlation to atherogenesis: idealized and anatomically-realistic models. J Eng Math 47:299–314
32. Kaazempur-Mofrad MR, Isasi AG, Younis HF, Chan RC, Hinton DP, Sukhova G, Lamuraglia GM, Lee RT, Kamm RD (2004) Characterization of the atherosclerotic carotid bifurcation using MRI, Finite element modeling, and histology. Ann Biomed Eng 32(7):932–946
33. Karimi R, Zhu T, Bouma BE, Kaazempur Mofrad Mohammad R (2008) Estimation of nonlinear mechanical properties of vascular tissues via elastography. Cardiovasc Eng 8(4):191–202
34. Kock SA, Nygaard JV, Eldrup N, Frund E-T, Klarke A, Paaske WP, Falk E, Kimi WY (2008) Mechanical stresses in carotid plaques using MRI-based fluid–structure interaction models. J Biomech 41(8):1651–1658
35. Lee RT, Grodzinsky AJ, Frank EH, Kamm RD, Schoen FJ (1991) Structure-dependent dynamic mechanical behavior of fibrous caps from human atherosclerotic plaques. Circulation 83(5):1764–1770
36. Lee RT, Schoen FJ, Loree HM, Lark MW, Libby P (1996) Circumferential stress and matrix metalloproteinase 1 in human coronary atherosclerosis. Implications for plaque rupture. Arterioscler Thromb Vasc Biol 16(8):1070–1073
37. Lee S-W, Steinman DA (2007) On the relative importance of Rheology for image-based CFD models of the carotid bifurcation. J Biomed Eng 129(2):273–278
38. Li MX, Beech-Brandt JJ, John LR, Hoskins PR, Easson WJ (2007) Numerical analysis of pulsatile blood flow and vessel wall mechanics in different degrees of stenosis. J Biomech 40(16):3715–3724
39. Li ZY, Howarth S, Trivedi RA, U-King-Im JM, Graves MJ, Brown A, Wang L, Gillard JH (2006) Stress analysis of carotid plaque rupture based on in vivo high resolution MRI. J Biomech 39(14):2611–2622
40. Li ZY, Howarth Simon PS, Tang TJ, Gillard JH (2006) How critical is fibrous cap thickness to carotid plaque stability? A flow-plaque interaction model. Stroke 37:1195–1199
41. Li ZY, Howarth SPS, Tang T, Graves MJ, U-King-Im J, Trivedi RA, Kirkpatrick PJ, Gillard JH (2007) Structure analysis and magnetic resonance imaging predict plaque vulnerability: a study comparing symptomatic and asymptomatic individuals. J Vasc Surg 45(4):768–775
42. Long Q, Ariff B, Zhao SZ, Thom SA, Hughes AD, Xu XY (2003) Reproducibility study of 3D geometrical reconstruction of the human carotid bifurcation from magnetic resonance images. Magn Reson Med 49(4):665–674
43. Loree HM, Kamm RD, Atkinson CM, Lee RT (1991) Turbulent pressure fluctuations on surface of model vascular stenosis. Am J Physiol Heart Circ Physiol 261:H644–H650
44. Loree HM, Kamm RD, Stringfellow RG, Lee RT (1992) Effects of fibrous cap thickness on peak circumferential stress in model atherosclerotic vessels. Circ Res 71(4):850–858
45. Loree HM, Grodzinsky AJ, Park SY, Gibson LJ, Lee RT (1994) Static circumferential tangential modulus of human atherosclerotic tissue. J Biomech 27(2):195–204
46. Loree HM, Tobias BJ, Gibson LJ, Kamm RD, Small DM, Lee RT (1994) Mechanical properties of model atherosclerotic lesion lipid pools. Arterioscler Thromb 14(2):230–234
47. Lowder ML, Li S, Carnell PH, Vito RP (2007) Correction of distortion of histologic sections of arteries. J Biomech 40(2):445–450
48. Maher E, Creane A, Sultan S, Hynes N, Lally C, Kelly D (2009) Tensile and compressive properties of fresh human carotid atherosclerotic plaques. J Biomech 42:2760–2767
49. Masson I, Boutouyrie P, Laurent S, Humphrey JD, Zidi M (2008) Characterization of arterial wall mechanical behavior and stresses from human clinical data. J Biomech 41(12):2618–2627
50. Moore JA, Steinman DA, Holdworth DW, Ethier CR (1999) Accuracy of computational hemodynamics in complex arterial geometries reconstructed from magnetic resonance imaging. J Biomed Eng 27(1):32–41
51. Naghavi M, Libby P et al (2003) From vulnerable plaque to vulnerable patient: a call for new definition and risk assessment strategies: Part I. Circulation 108:1664–1672
52. Ohayon J, Teppaz P, Finet G, Rioufol G (2001) In-vivo prediction of human coronary plaque rupture locations using intravascular ultrasound and the finite element method. Coron Artery Dis 12(8):655–663

53. Ohayon J, Finet G, Treyve F, Rioufol G, Dubreuil O (2005) A three dimensional finite element analysis of stress distribution in a coronary atherosclerotic plaque: in vivo prediction of plaque rupture location. Biomech Appl Comput Assist Surg 37:225–241
54. Ohayon J, Dubreuil O, Tracqui P, Le Floch S, Rioufol G, Chalabreysse L, Thivolet F, Pettiqrew RI, Finet G (2007) Influence of residual stress/strain on the biomechanical stability of vulnerable coronary plaques: potential impact for evaluating the risk of plaque rupture. Am J Physiol Heart Circ Physiol 293(3):H1987–H1996
55. Pocaterra M, Gao H, Das S, Pinelli M, Long Q (2009) Circumferential residual stress distribution and its influence in a diseased carotid artery. In: Proceedings of 2009 ASME summer bioengineering conference, Lake Tahoe, CA, 17–21 June 2009
56. Richardson PD, Davies MJ, Born GV (1989) Influence of plaque configuration and stress distribution on fissuring of coronary atherosclerotic plaques. Lancet 2(8669):941–944
57. Richardson PD (2002) Biomechanics of plaque rupture: progress, problems, and new frontiers. Ann Biomed Eng 30(4):524–536
58. Rosamond W, Flegal K, Friday G, Furie K, Go A, Greenlund K (2007) Heart disease and stroke statistics—2007 update: a report from the American Heart Association Statistics Committee and Stroke Statistics Subcommittee. Circulation 115(5):e69–e171
59. Shojima M, Oshima M, Takagi K et al (2004) Magnitude and role of wall shear stress on cerebral aneurysms: computational fluid dynamic study of 20 middle cerebral aneurysms. Stroke 35:2500–2505
60. Steinman DA, Milner JS, Norley CJ, Stephen PL, Holdsworth DW (2003) Image based computational simulation of flow dynamics in a giant intracranial aneurysm. AJNR Am J Neuroradiol 24:559–566
61. Steinman DA (2004) Image-based computational fluid dynamics: a new paradigm for monitoring hemodynamics and atherosclerosis. Curr Drug Targets Cardiovasc Haematol Disord 4(2):183–197
62. Tang D, Yang C, Zheng J, Woodard PK, Sicard GA, Saffitz JE, Yuan C (2004) 3D MRI-based multicomponent FSI models for atherosclerotic plaques. Ann Biomed Eng 32(7):947–960
63. Tang D, Yang C, Zheng J, Woodard PK, Sicard GA, Saffitz JE et al (2004) 3D computational mechanical analysis for human atherosclerotic plaques using MRI-based models with fluid–structure interactions. Lect Notes Comput Sci 3217(1):328–336
64. Tang D, Yang C, Kobayashi S, Ku DN (2004) Effect of a lipid pool on stress/strain distributions in stenotic arteries: 3-D fluid structure interactions(FSI) models. J Biomech Eng 126(3):363–370
65. Tang D, Yang C, Zheng J, Woodard PK, Saffitz JE, Sicard GA, Pilgram TK, Yuan C (2005) Quantifying effects of plaque structure and material properties on stress distributions in human atherosclerotic plaques using 3D FSI models. J Biomed Eng 127(7):1185–1194
66. Tang D, Yang C, Zheng J, Woodard PK, Saffitz JE, Peteruccelli JD, Sicard GA, Yuan C (2005) Local maximal stress hypothesis and computational plaque vulnerability index for atherosclerotic plaque assessment. Ann Biomed Eng 33(12 special issue):1789–1801
67. Tang D, Yang C, Mondal S, Liu F, Canton G, Hatsukami TS, Yuan C (2008) A negative correlation between human carotid atherosclerotic plaque progression and plaque wall stress: in vivo MRI-based 2D/3D FSI models. J Biomech 41(4):727–736
68. Tang D, Teng Z, Canton G, Hatsukami TS, Dong L, Huang X, Yuan C (2009) Local critical stress correlates better than global maximum stress with plaque morphological features linked to atherosclerotic plaque vulnerability: an in vivo multi-patient study. Biomed Eng Online 8:15
69. Tang D, Teng Z, Canton G, Yang C et al (2009) Sites of rupture in human atherosclerotic carotid plaques are associated with high structure stresses: an in-vivo MRI-based 3D fluid structure interaction study. Stroke 40:3258–3263
70. Teng Z, Sadat U, Li Z, Huang X, Zhu C, Young V, Graves MJ, Gillard JH (2010) Arterial luminal curvature and fibrous-cap thickness affect critical stress conditions within atherosclerotic plaque: an in-vivo MRI-based 2D finite element study. Ann Biomed Eng 38(10):3096–3101
71. Topoleski LD, Salunke NV, Humphrey JD, Mergner WJ (1997) Composition and history dependent radial compressive behavior of human atherosclerotic plaque. J Biomed Mater Res 35(1):117–127
72. Topoleski LD, Salunke NV (2000) Mechanical behavior of calcified plaques: a summary of compression ad stress relaxation experiments. Z Kardiol 89(Suppl 2):85–91
73. Trivedi RA, Li ZY, U-King-Im J, Graves MJ, Kirkpatrick PJ, Gillard JH (2007) Identifying vulnerable carotid plaques in vivo using high resolution magnetic resonance imaging-based finite element analysis. J Neurosurg 107(3):536–542
74. Vengrenyuk Y, Carlier S, Xanthos S, Cardoso L, Ganatos P, Virmnani R, Einav S, Gilchrist L, Weinbaum S (2006) A hypothesis for vulnerable plaque rupture due to stress-induced debonding around cellular microcalcifications in thin fibrous cap. Proc Natl Acad Sci USA 103(40):14678–14683
75. Veress AI, Vince DG, Anderson PM, Cornhill JF et al (2000) Vascular mechanics of the coronary artery. Z Kardiol 89(Suppl 2):92–100
76. Versluis A, Bank AJ, Douglas WH (2006) Fatigue and plaque rupture in myocardial infarction. J Biomech 39(2):339–347
77. Vito RP, Dixon SA (2003) Blood vessel constitutive models-1995-2002. Annu Rev Biomed Eng 5:413–439
78. Vonesh MJ, Cho CH, Pinto JV Jr, Kane BJ, Lee DS et al (1997) Regional vascular mechanical properties by 3D intravascular ultrasound with finite element analysis. Am J Physiol 272(1):H425–H437
79. Williamson SD, Lam Y, Younis HF, Huang H, Patel S, Kaazempur-Mofrad MR, Kamm RD (2003) On the sensitivity of wall stresses in diseased arteries to variable material properties. J Biomech Eng 125(1):147–155
80. Wu H-C, Chen SY, James S, Sanjeev G, Carroll JD (2003) Stress analysis using anatomically realistic coronary tree. Med Phys 30(11):2927–2936
81. Yang C, Tang D, Yuan C, Hatsukami TS, Zheng J, Woodard PK (2007) In vivo/ex vivo MRI-based 3D non-Newtonian FSI models for human atherosclerotic plaques compared with fluid/wall-only models. Comput Model Eng Sci 19(3):233–245
82. Younis HF, Kaazempur-Mofrad MR, Chan RC, Isasi AG, Hinton DP, Hinton DP et al (2004) Hemodynamics and wall mechanics in human carotid bifurcation and its consequences for atherogenesis: investigation of inter-individual variation. Biomech Model Mechanobiol 3(1):17–32
83. Zhao SZ, Ariff B, Long Q, Thom SA, Hughes AD, Xu XY (2002) Inter-individual variations in wall shear stress and mechanical stress distribution at the carotid artery bifurcation of healthy humans. J Biomech 35:1367–1377
84. Zheng J, EI Naga I, Rowold FE, Pilgram TK, Woodard PK, Saffitz JE, Tang D (2005) Quantitative assessment of coronary artery plaque vulnerability by high-resolution magnetic resonance imaging and computational biomechanics: a pilot study ex vivo. Magn Reson Med 54(6):1360–1368

Carotid Plaque Stress Analysis: Issues on Patient-Specific Modeling

8

Hao Gao and Quan Long

1 Introduction

From the previous chapter, it is demonstrated that stress analysis in plaques can provide critical information on plaque vulnerability assessment, which will be helpful in clinic. Currently, to obtain the accurate stress field inside carotid plaques is still a great challenge in the biomechanics community, especially for the patient-specific modeling, including patient-specific geometry, patient-specific boundary conditions, patient-specific material models, and so on [12]. To our best knowledge, there is no kind of study to incorporate all those above issues together for the plaque stress analysis.

Plaque stress analysis by finite element models have been developed from 2D to 3D, from idealized models to patient-specific plaques in terms of geometrical accuracy, from structure analysis only to fluid structure interaction (FSI) analysis in terms of physical phenomenon reality [8, 13, 16, 19, 20, 31]. There are normally five main tasks involved in building a plaque mechanical stress analysis model which include the following: (a) to acquire plaque components, (b) to reconstruct plaque geometry, (c) to apply mechanical load and dynamic boundary conditions, (d) to define suitable material constitutive models, and (e) to perform FEM simulation and post-processing. In order to carry out the numerical simulation, certain assumptions are applied during the above five main tasks, such as idealized plaque geometry [8] or general material properties [5, 29–31] and so on.

In this chapter, we will focus on the issues related to patient-specific modeling, including (1) stress analysis based on patient-specific geometry and (2) stress analysis by using patient-specific material model. The chapter is divided into two parts as; (1) the first part is plaque stress analysis on one symptomatic patient and one asymptomatic patient based on high resolution in vivo carotid MRI; (2) the second part is plaque stress by using anisotropic material constitutive model, which is derived from in vivo high resolution carotid MRI.

H. Gao (✉)
School of Mathematics and Statistics, University of Glasgow, Glasgow, UK
e-mail: hao.gao@glasgow.ac.uk

Q. Long
Brunel Institute for Bioengineering, Brunel University, London, UK
e-mail: quan.long@brunel.ac.uk

2 Plaque Stress Analysis: Patient-Specific Plaque Geometry

Recent developments in high-resolution multispectral MRI have allowed plaque components to be visualized in vivo [2, 15, 35, 36], providing more realistic plaque geometries for stress analysis [9, 27]. In this part, two plaque geometries were reconstructed from high-resolution in vivo MR images with detailed plaque stress analysis.

2.1 MRI Image Acquisition

Patient selection and image acquisition were performed by investigators who were not involved in the stress analysis. The protocol was approved by the local ethics committee, and written informed consent was obtained from each patient before the study. In vivo multispectral MRI scanning was performed on one symptomatic patient and one asymptomatic patient recruited from a specialist neurovascular clinic. The symptomatic patient had recently experienced either a retinal or cortical transient ischemic attack and was scanned less than 6 months of the event. The asymptomatic patient had not experienced any symptom before imaging.

Multicontrast imaging was carried out using a 1.5 T MRI system (GE Diagnostic Imaging, WI) and a four-channel phased-array neck coil (PACC, Machnet BV, Elde, The Netherlands). Axial images were acquired through the common carotid artery 12 mm below the carotid bifurcation to a point 12 mm distal to the extent of the stenosis identified on the TOF sequence to cover a large

L. Saba et al. (eds.), *Multi-Modality Atherosclerosis Imaging and Diagnosis*,
DOI 10.1007/978-1-4614-7425-8_8, © Springer Science+Business Media, LLC 2014

range of carotid bifurcation. The following 2D, ECG-gated, blood-suppressed, fast spin echo pulse sequences were used in the plaque region: intermediate T_2 Weighted (ImT2W_FatSat: TR/TE: $2 \times$ RR/46) with fat saturation; T_2 Weighted (T2W: TR/TE: $2 \times$ RR/100); short T_1 inversion-recovery (STIR: TR/TE/TI: $2 \times$ RR/46/150). The field of view was 10×10 cm^2, matrix size 256×256, slice thickness was 3 mm. It made the pixel size of $0.39 \times 0.39 \times 3$ mm in all cases except the TOF images. These images were used to delineate the various plaque components such as fibrous cap, lipid core. More details can be found in refs. [32, 33].

2.2 General Plaque Geometry Reconstruction Procedure

The artery and plaque geometries were obtained from the multispectral MR scans. An in-house program developed in Matlab was used to facilitate the segmentation of lipid core, arterial wall, and lumen, which have different signal characteristics when imaged using multispectral protocol. The plaque region was identified and reconstructed based on T2W, ImT2W_FatSat, STIR images (if existed), and the healthy arterial part was reconstructed based on TOF images. Figure 8.1 shows a general procedure for patient-specific geometry reconstruction based on multispectral MRI images. Details regarding plaque geometry reconstruction can be found in ref. [10]. Figure 8.2 shows the segmentation results for the symptomatic patient and the reconstructed 3D plaque geometry.

2.3 Plaque Stress Analysis by FSI Simulation

The carotid arterial wall was assumed to be nonlinear, isotropic, and incompressible. The 3D nonlinear Mooney–Rivlin model in ANSYS11.0 was used to describe the material property, the strain energy density function W was

$$W = C_{10}(I_1 - 3) + C_{01}(I_2 - 3) + C_{20}(I_1 - 3)^2 + C_{11}(I_1 - 3)(I_2 - 3) + C_{02}(I_2 - 3)^2 + \frac{1}{d}(J - 1)^2 \tag{8.1}$$

where I_1 and I_2 are the first and second strain invariants, d is the material incompressible parameter, J stands for the ratio of the deformed volume over the un-deformed volume of materials, C_{10}, C_{01}, C_{20}, C_{11}, and C_{02} are material constants. In the study, $C_{10} = 50.445$ kPa, $C_{01} = 30.491$ kPa, $C_{20} = 40$ kPa, $C_{11} = 120$ kPa, $C_{02} = 10$ kPa, and $d = 1.44\text{e}{-7}$, derived from existed literatures [29]. Lipid core was much softer with 2 kPa for the Young's modulus and 0.49 for Poisson ratio. The structure model was meshed with an unstructured mesh consisting of nearly 90,000 10-node 3D tetra elements. The computational nodes at the efferent planes of ICA and ECA were fixed in all directions and an axial pre-stretch of 11 % (based on the shunk procedure in plaque geometry reconstruction).

The fluid domain was meshed in ICEM CFD11.0 with a much finer grid of around 1,000,000 3D tetra cells. Blood was treated as an incompressible, Newtonian fluid with a viscosity of 4×10^{-3} Pa s and a density of 1,067 kg m^{-3}. The flow was assumed to be laminar. Transient simulations were carried out with time-dependent pressure at the inlet of the CCA and mass flow rates at the ICA and ECA. In this study, the boundary conditions for the two subjects were assumed to be the same as in Fig. 8.3. The fully coupled FSI simulation details also can be found in ref. [10].

2.4 Stress Analysis Results

The first principle stress (FPS) was used to represent the plaque wall tensile stress, the strongest stretching stress. Figure 8.4 shows the stress distributions between the symptomatic (column 1) and asymptomatic (column 2) patients. Figure 8.4a1, b1 shows the FPS distribution in the whole plaque with longitudinal cutting view. Generally FPS is higher at the luminal wall, lower at the outer arterial wall, and lowest in the lipid region. The local high stress concentrations could be identified in the plaque region at both patients, indicated by arrows in Fig. 8.4a1, b1. The maximum FPS value is much higher in the symptomatic patient (227.7 kPa) than the asymptomatic patient (134.9 kPa). Figure 8.4a2, b2 presents FPS distributions in the transversal planes covering the whole plaque region. For the sections with a thin fibrous cap, the stress concentration regions appear at one or both edges of the lipid core (or plaque shoulders).

Stress distribution in the fibrous cap has been considered to be closely related to plaque rupture. The fibrous cap surface in the lumen side was extracted, covering the lipid core, to clearly show the stress distribution in the plaque region. The fibrous cap thickness (FCT), defined as the shortest distance between the fibrous cap surface (lumen side) and lipid region, is shown in Fig. 8.5a1, b1. Although MR image spatial resolution is 0.39 mm, the 3D surface interpolation during model reconstruction can still produce fibrous cap regions with a thickness less than 0.39 mm. The minimum FCT in the symptomatic subject is much smaller than the asymptomatic subjects (0.087 mm vs. 0.177 mm). Figure 8.5a2, b2 shows corresponding FPS distributions in fibrous cap surfaces. Generally, the high stress regions are well correlated with the thin fibrous cap regions; especially

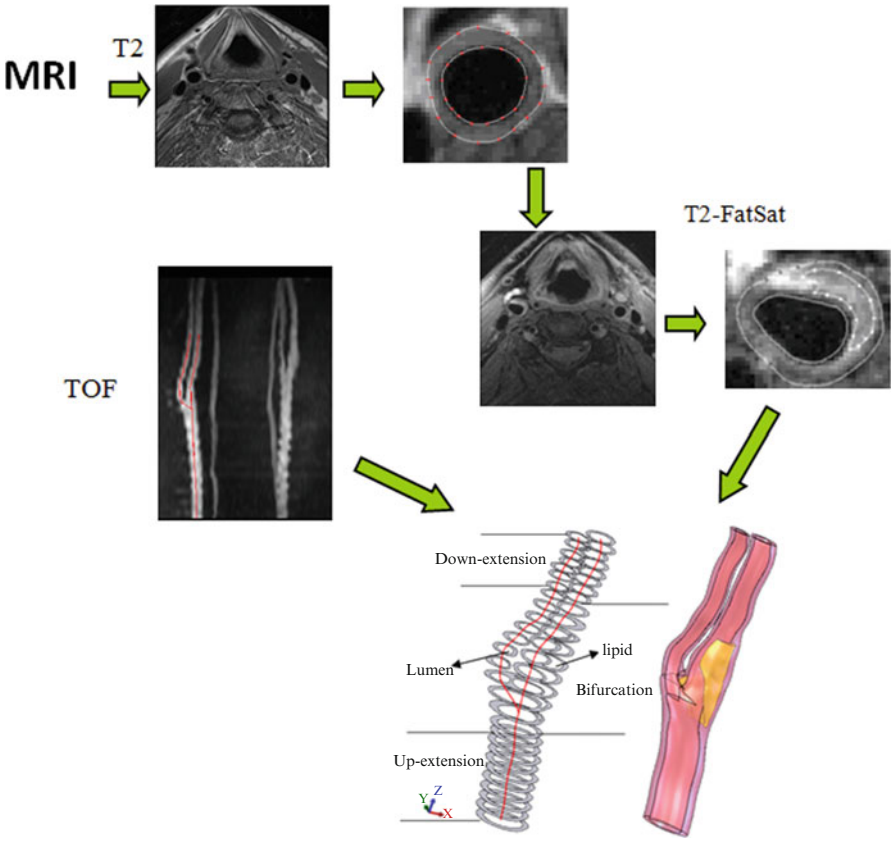

Fig. 8.1 General procedure of 3D plaque geometry reconstruction

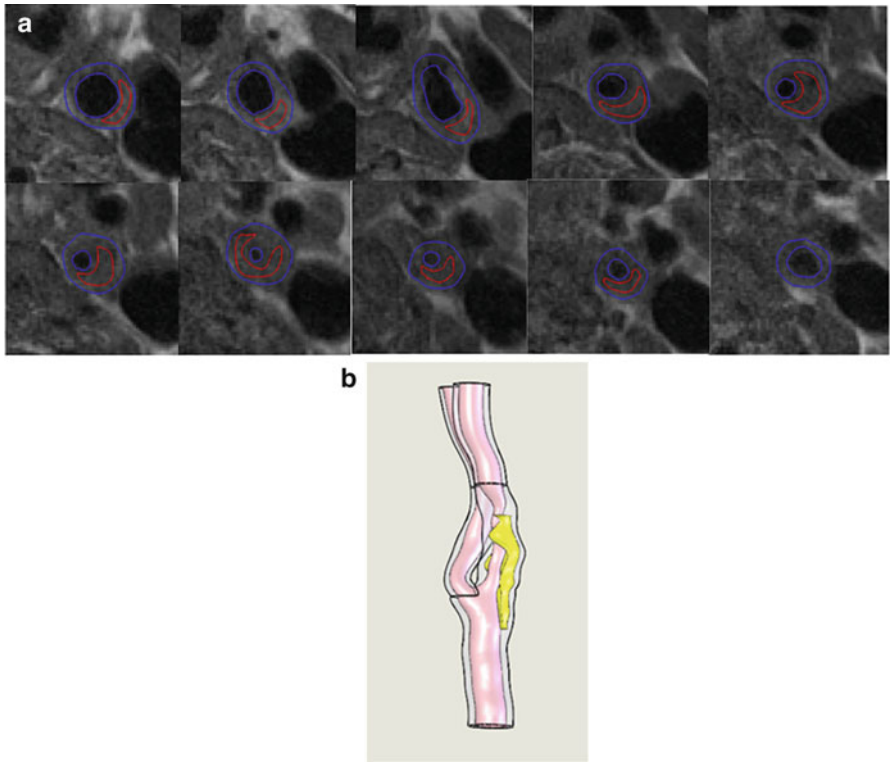

Fig. 8.2 Segmentation results for the symptomatic patients superimposed on T2-weighted MRI images (**a**) and reconstructed 3D plaque geometry (**b**)

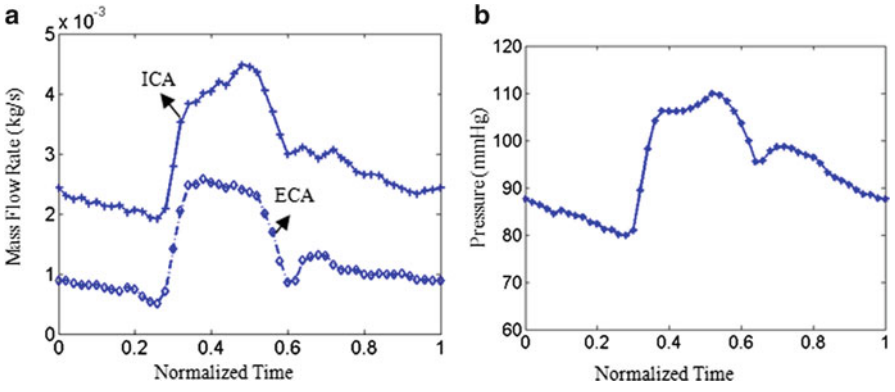

Fig. 8.3 Mass flow rates for ICA and ECA (**a**) and pressure profile at CCA (**b**)

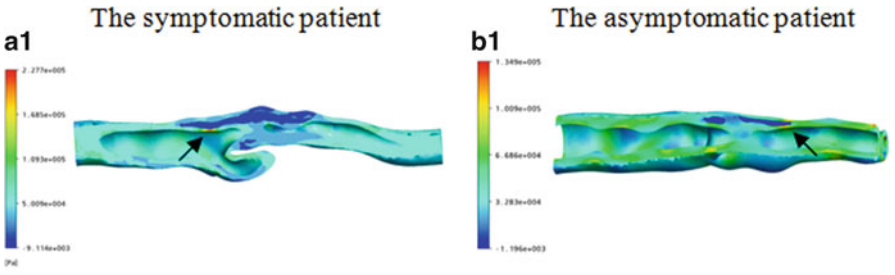

Fig. 8.4 FPS distributions for one symptomatic patient (**a**) and one asymptomatic patient (**b**)

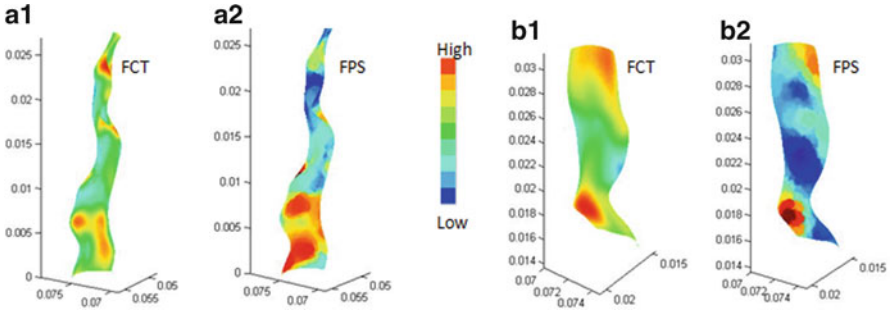

Fig. 8.5 FCT and FPS distributions for symptomatic (**a**) and asymptomatic (**b**) patients

for the asymptomatic patient, the high stress region upstream is corresponding to a very thin fibrous cap location. While in symptomatic patient, the highest stress region does not locate in the thinnest fibrous cap region (downstream plaque); this may be resulted in part from the blood pressure drop at downstream plaque. Linear correlation analysis of the FPS and FCT was performed for the two plaques by comparing the FPS and FCT value at every computational node on the fibrous cap surface in the lumen side. Figure 8.6a, b presents the scatter plot between FCT and FPS. The correlation results were $r = -0.434$ with $p < 0.05$ for the symptomatic patient and $r = -0.692$ with $p < 0.05$ for the asymptomatic patient.

3 Patient-Specific Material Model Based on In Vivo MRI

Recent studies have demonstrated that it is possible to obtain patient-specific material model from in vivo human data [22], which enable plaque stress analysis to be much closer to the real situation rather than a general material model from existed literatures or obtained by ex vivo experiments. Therefore in this part, the method proposed by Masson [22] was used to determine arterial properties from in vivo data and applied the material properties to plaque stress analysis for

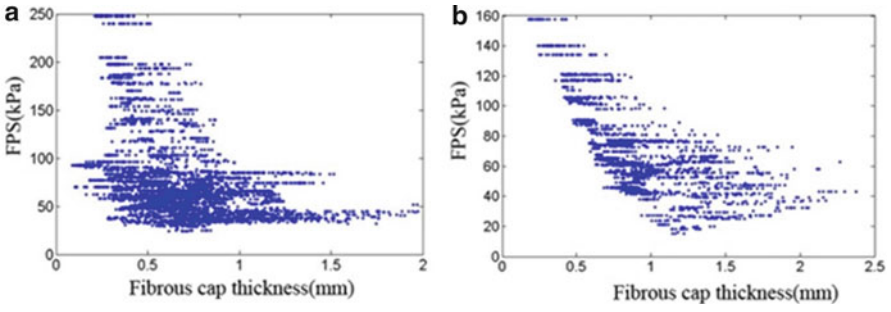

Fig. 8.6 Scatter plots of fibrous cap thickness and plaque wall stress for the symptomatic (**a**) and asymptomatic patients (**b**)

one subject. An idealized 3D arterial wall section representing CCA was constructed based on in vivo MR images. Phase contrast MR images, residual stress, perivascular stress, and fiber-reinforced, hyperelastic effect of arterial tissue were included in the mechanical model. The fitted material parameters were applied to a real plaque stress analysis. It is believed that the procedure of using patient-specific material model will yield more realistic plaque stresses.

3.1 MRI Data Acquisitions

The MRI acquisition protocol was the same as in Sect. 2. Phase contrast MR images at common carotid artery were obtained to provide the luminal area change over one cardiac cycle as in Fig. 8.7a; the bright region, indicated by the arrow, is the lumen region; however there is little information regarding arterial wall. Figure 8.7b shows the luminal radius change of the CCA section over one cardiac cycle. Due of lack of pressure information, a pressure profile (denoted as measured pressure) was chosen as in Fig 8.3b by rescaling the pressure range of 80–110 mmHg according to luminal area change over time at CCA.

3.2 Kinematics of Idealized Arterial Wall

CCA section in Fig. 8.7a was considered to be a thick-walled circular cylinder in order to theoretically calculate stretch ratio in radial and circumferential directions by using a cylindrical coordinate system, that is, (e_r, e_θ, e_z). Therefore the deformation field of the CCA section over one cardiac cycle could be calculated from two successive motions [17]. Three configurations were considered as Ω_0: stress free and excised configuration (R, Θ, Z); Ω_1: intact and unloaded configuration (ρ, ϕ, ξ); Ω_2: in vivo loaded configuration (r, θ, z). The three configurations can be found in Fig. 8.8.

If a material particle is considered in the arterial wall, such as the particle indicated by '✦' in Fig. 8.8, then $X(R, \Theta, Z)$, $\tilde{x}(\rho, \phi, \xi)$, $x(r, \theta, z)$ are the configurations of Ω_0, Ω_1, and Ω_2, respectively. By employing the relations from Humphrey [17],

$$\rho = \rho(R), \quad \phi = \left(\frac{\pi}{\Theta_0}\right)\Theta, \quad \xi = \Lambda Z \tag{8.2}$$

$$r = r(\rho, t), \quad \theta = \phi, \quad z = \lambda\xi \tag{8.3}$$

where t is the time, Θ_0 is the open angle when arterial wall is excised. Λ is the axial stretch accounting for axial residual stress from Ω_0 to Ω_1. λ is the in vivo load-induced axial stretch, which is assumed to be constant over cardiac cycles. R_i and r_i are the inner radiuses in Ω_0 and Ω_2; R_m and r_m are the radiuses at the medial–adventitial interface.

The deformation gradient tensor from Ω_0 to Ω_2 can be defined as $F = \partial x(X)/\partial X$, that is

$$F = \begin{bmatrix} \frac{\partial r}{\partial R} & & \\ & \frac{\pi r}{\Theta_0 R} & \\ & & \lambda\Lambda \end{bmatrix} = \begin{bmatrix} \lambda_r & & \\ & \lambda_\theta & \\ & & \lambda_z \end{bmatrix} \tag{8.4}$$

where λ_r, λ_θ, and λ_z are principle stretch ratios in radial, circumferential, and axial directions. The left and right Cauchy–Green tensors are

$$B = FF^\mathrm{T}, \quad C = F^\mathrm{T}F \tag{8.5}$$

The local volume ratio is

$$J = \det(F) = \lambda_r\lambda_\theta\lambda_z \tag{8.6}$$

Generally arterial wall is considered to be impressible, therefore $J = 1$. Then by applying (8.2)–(8.6) with $J = 1$,

$$R\partial R = \frac{\pi\lambda\Lambda}{\Theta_0} r\partial r \tag{8.7}$$

Integrating from r_i and R_i to r and R respectively,

$$R = \sqrt{\left(R_\mathrm{m}^2 - \frac{\pi\lambda\Lambda}{\Theta_0}\left(r_\mathrm{m}^2 - r^2\right)\right)} \tag{8.8}$$

Therefore the stretch ratio in radial direction is

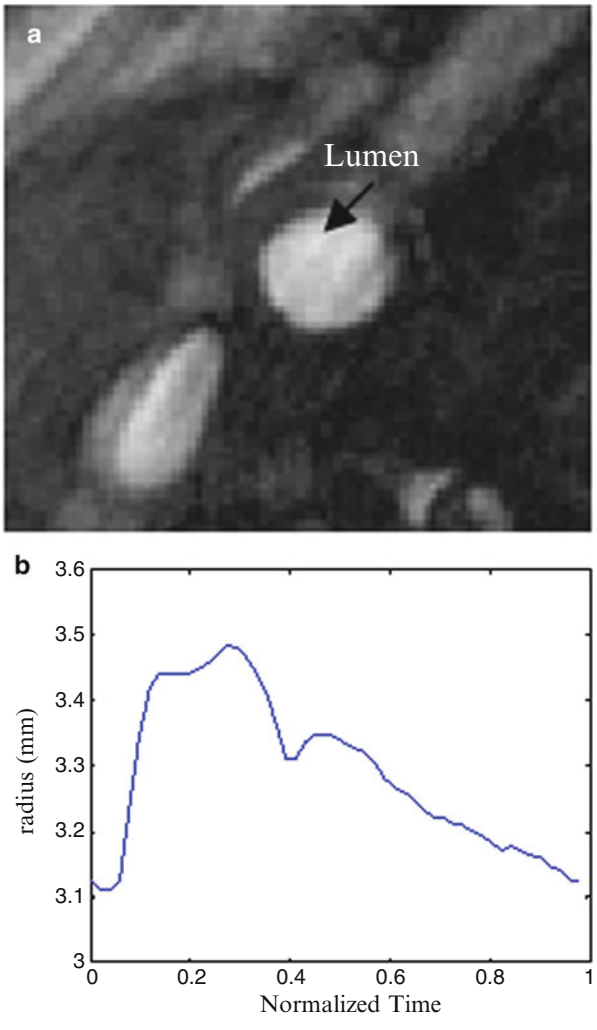

Fig. 8.7 In vivo data in CCA. (**a**) Phase contrast MRI of a CCA section; (**b**) luminal radius change

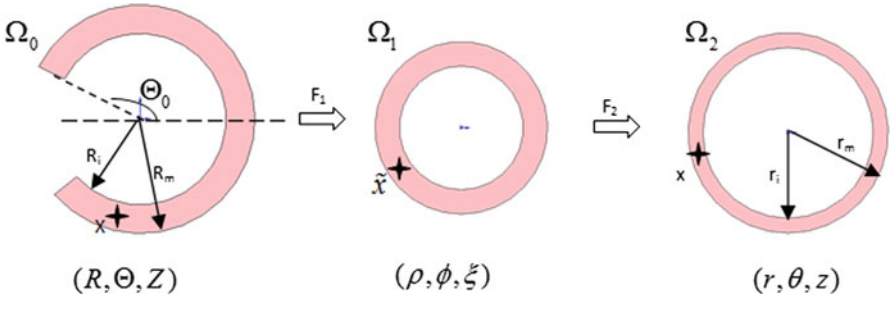

Fig. 8.8 Three different configurations of the intact CCA from stress free to load free and loaded state

$$\lambda_r = \frac{\Theta_0}{\pi\lambda\Lambda}\cdot\frac{R}{r} = \frac{\Theta_0}{\pi\lambda\Lambda}\cdot\frac{\sqrt{\left(R_{\mathrm{m}}^2 - \frac{\pi\lambda\Lambda}{\Theta_0}\left(r_{\mathrm{m}}^2 - r^2\right)\right)}}{r} \tag{8.9}$$

3.3 Constitutive Modeling of Arterial Wall

The mechanical response of the CCA section is considered to be anisotropic hyperelastic. Because the material properties in adventitial layer is different from medial layer, and different collagen fiber configurations compared to medial layer, in order to simplify the solution procedure, as in Masson's study [22], only medial and intimal layers were studied in this study. The strain energy function proposed by Gasser [14] was used to model the CCA section with two families of collagen fibers embedded in a soft incompressible ground matrix, which is also available in Abaqus 6.8. The associated strain energy function W is

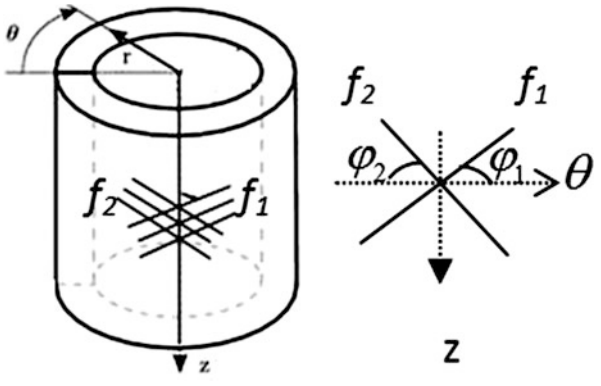

Fig. 8.9 Two families of collagen fibers in medial layer of artery

$$W = a(I_1 - 3) + \frac{k_1}{2k_2}\sum_{f=1}^{N}\left(e^{k_2\langle E_f\rangle^2} - 1\right) + \frac{1}{D}\left(\frac{(J)^2 - 1}{2} - \ln J\right) \tag{8.10}$$

$$E_f = \kappa(I_1 - 3) + (1 - 3\kappa)(I_{4(ff)} - 1) \tag{8.11}$$

a, D, k_1, and k_2 are material parameters. κ denotes the level of dispersion in the fiber directions, in this study $\kappa = 0$, which means fibers from one family are perfectly aligned along one direction. f represents one fiber family, N is the total number of fiber families. Two families of fibers (f_1, f_2) are considered in this study ($N = 2$), and the fibers only distribute in circumferential and axial directions, no fiber in radial direction, as shown in Fig. 8.9. The angles of f_1 and f_2 with circumferential direction are φ_1 and φ_2. In this study, φ_1 is equal to φ_2.

The fiber orientations can be defined in the reference configuration by unit factor $A_{f_1}(0, \cos(\varphi_1), \sin(\varphi_1))$ and $A_{f_2}(0, \cos(\varphi_2), \sin(\varphi_2))$, which depend on the angle of φ_1 and φ_2. I_1 is the first strain invariants, defined as $I_1 = \text{trace}(C)$. $I_{4(ff)}$ is the pseudo-invariants of C combined with A_{f_1} and A_{f_2}

$$I_{4(f_1 f_1)} = A_{f_1} C {A_{f_1}}^{\mathrm{T}} \tag{8.12}$$

$$I_{4(f_2 f_2)} = A_{f_2} C {A_{f_2}}^{\mathrm{T}} \tag{8.13}$$

The first term in the strain energy function W represents the contributions of the noncollagenous isotropic ground material; the second term represents the contributions from the different families of collagen fibers; and the third term is the contributions from volumetric change. A basic assumption of the model is that the fibers can only support tension, therefore, the anisotropic contribution in the second term appears only when the strain of the fibers is positive, that is $E_f > 0$, enforced by the term $\langle E_f \rangle$, where the operator $\langle * \rangle$ stands for the Macauley bracket and is defined as $\langle E \rangle = 1/2(|E| + E)$. The second Piola–Kirchhoff stress S for nonlinear elastic incompressible material from strain energy equation is

$$S = -pC^{-1} + 2\frac{\partial W}{\partial C} \tag{8.14}$$

where p is the hydrostatic-like pressure, then the Cauchy stress tensor σ can be computed from S as

$$\sigma = FSF^{\mathrm{T}}J^{-1} \tag{8.15}$$

From above equations, and $\varphi_1 = \varphi_2 = \varphi$, the components of Cauchy stress tensor σ are

$$\sigma_{rr} = -p + 2a{\lambda_r}^2 \tag{8.16}$$

$$\sigma_{\theta\theta} = -p + 2a{\lambda_\theta}^2 + 4k_1 e^{k_2 {E_4}^2} E_4 \cos(\varphi)^2 \tag{8.17}$$

$$\sigma_{zz} = -p + 2a{\lambda_z}^2 + 4k_1 e^{k_2 {E_4}^2} E_4 \sin(\varphi)^2 \tag{8.18}$$

$$E_4 = A_{f_1} C {A_{f_1}}^{\mathrm{T}} = A_{f_2} C {A_{f_2}}^{\mathrm{T}} = \lambda_\theta^2 \cos(\varphi)^2 + \lambda_z^2 \sin(\varphi)^2 - 1 \tag{8.19}$$

3.4 Equilibrium of Arterial Dynamics

From Humphrey's [18] study, if no body force is included, the motion equation of the idealized CCA section as shown in Fig. 8.8 at Ω_2 configuration can be expressed as

$$\frac{\partial \sigma_{rr}}{\partial r} + \frac{\sigma_{rr} - \sigma_{\theta\theta}}{r} = \rho a_{\mathrm{r}} \tag{8.20}$$

ρ is the density of the CCA section. a_{r} is the radial acceleration, due to the insignificant contribution of inertial term, the quasi-statically assumption is applied [18]. Equation (8.20) can be solved by numerical integration over r from the inner wall r_{i} to the interface between media and adventitial layers r_{m}.

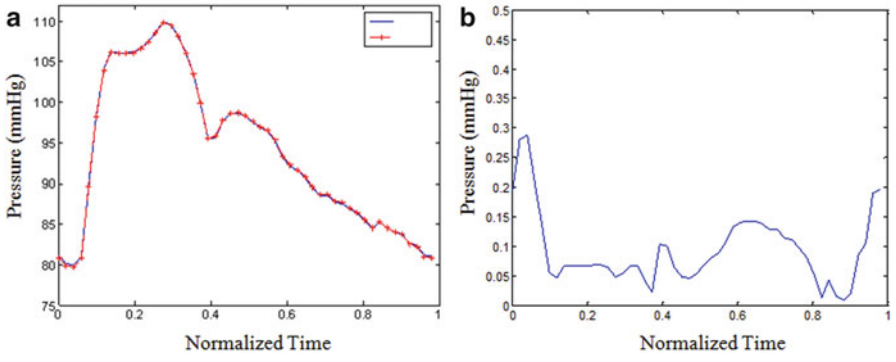

Fig. 8.10 (**a**) Predicted pressure compared to the real pressure profiles; (**b**) residual between predicted and real pressure profiles

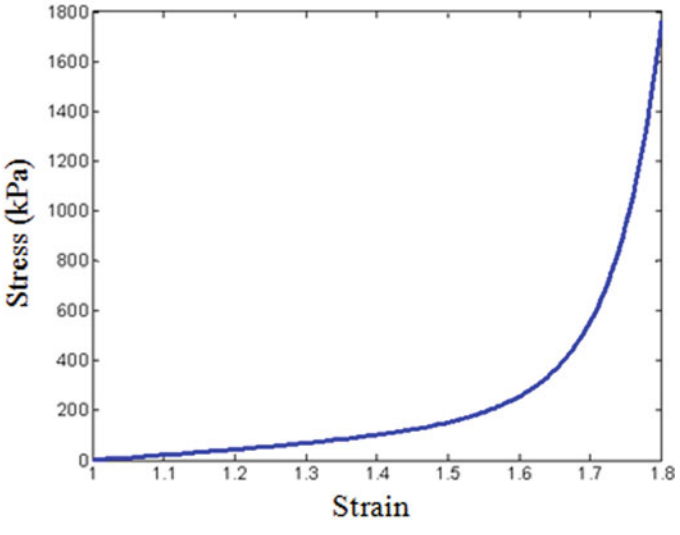

Fig. 8.11 $\sigma_{\theta\theta}$ response under uni-axial stretch

$$P_{\mathrm{i}}(t) = P_{\mathrm{a}}(t) + \int_{r_{\mathrm{i}}(t)}^{r_{\mathrm{m}}(t)} \frac{\sigma_{\theta\theta}(r,t) - \sigma_{rr}(r,t)}{r} \qquad (8.21)$$

where $P_{\mathrm{i}}(t)$ is the computed luminal pressure and $P_{\mathrm{a}}(t)$ is the pressure-like contribution from the adventitial layer on the medial layer (perivascular stress). Equation (8.21) can allow the computation of luminal pressure by given information of arterial wall motion, residual stress effects, and pressure contribution from adventitial layer. The exact form of (8.21) can be obtained from Matlab by Symbolic Math Toolbox.

3.5 Material Parameters Fitting

The material parameters are estimated based on noninvasive in vivo data. The residual stress-related axial stretch Λ is chosen to be 1 from existed literatures [6]. The in vivo loading induced axial stretch ratio λ is assumed to be 1.1. Θ_0 is assigned to be 130°, a static pressure of 2 kPa is assigned to $P_{\mathrm{a}}(t)$ [22]. In order to define r_{m}, which is not available in phase contrast MR images, an assumed thickness (0.6 mm) of medial and intima was assigned in the beginning of the cardiac cycle, then the change of r_{m} over one cardiac cycle can be calculated by applying the constraint of constant area of arterial wall because of incompressibility. Therefore the undetermined parameters are a, k_1, k_2, φ, and R_{m}. Best-fit values for those parameters can be obtained using a nonlinear least-square minimization of the difference between predicted and measured luminal pressures over one cardiac cycle. The function *lsqnonlin* in Matlab was used for the fitting procedure. The best fitted parameter from *lsqnonlin* is $[a, k_1, k_2, \varphi, R_{\mathrm{m}}] = [32.1\ \mathrm{kPa}, 9.6\ \mathrm{kPa}, 3.8, 45.7, 4.8\ \mathrm{mm}]$.

Figure 8.10a shows the predicted pressured compared to the assumed measured pressure, the predicted pressure agrees well with measured pressure, no noticeable difference can be identified. The residual of the fitted procedure is in Fig. 8.10b, the maximum difference between predicted and measured pressure is about 0.288 mmHg. Figure 8.11 shows $\sigma_{\theta\theta}$ under uniaxial stretch in circumferential direction. $\sigma_{\theta\theta}$ increases dramatically when stretch ratio increases because of the engagement of fibers in circumferential direction.

A cross section of plaque sample with lipid from the same subject was chosen for stress analysis with the fitted material parameters for arterial wall material model. Static stress analysis was performed in Abaqus 6.8, which has implemented the strain energy function (8.10). The geometry is shown in Fig. 8.12, the cross section was extruded to

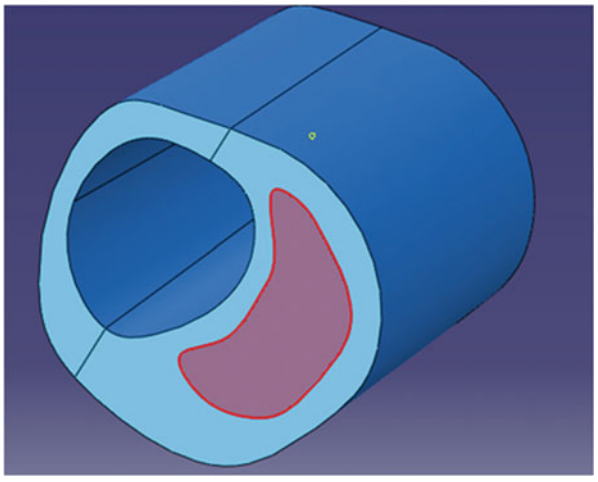

Fig. 8.12 3D plaque geometry

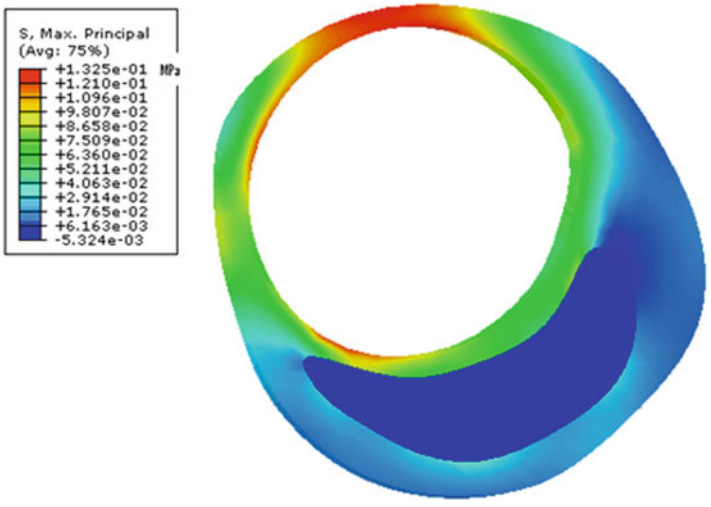

Fig. 8.13 Maximum principle stress distribution

construct the 3D plaque geometry, a cylindrical coordinate system was created in the luminal center. A pressure load of 110 mmHg was applied in the luminal surface. Lipid was considered to be very soft with 2 kPa for Young's modulus and 0.49 for Poisson ratio.

Figure 8.13 shows the FPS distribution. The stress distribution pattern from the patient-specific material model is similar as existed literatures on plaque stress analysis. However the stress levels and detailed distribution pattern would be much closer to the real situation. In Fig. 8.13, a local high stress concentration can be found in the thin fibrous cap region. Due to the thin wall region in the opposite side of lipid core, a high region of stress appears.

4 Discussion

Atherosclerotic plaque has been considered to be one of the leading causes of death all over the world, caused by the plaque rupture and subsequent thrombus formation. Until now the exact mechanism of plaque rupture is not clear. From biomechanical aspect, the rupture can be considered to be a mechanical failure event. Therefore it is essential to numerically predict plaque stress with high accuracy. Results from those models will be helpful in understanding how and why plaque ruptures.

Plaque stress has been studied for several decades from 2D structure only to fully coupled 3D plaque stress in both structure dynamics and hemodynamics. The extremely high stress locations in plaque region have been considered to be main factors responsible for plaque rupture [11]. The biggest challenge lies in how to predict plaque stress with patient-specific simulations and high accuracy, such as realistic geometry reconstruction, patient-specific boundary conditions, and material models. Studies have demonstrated that 2D plaque models are prone to overestimate the stress levels because of simplifications. 3D plaque stress analysis with coupled FSI emerges to advance the accuracy of analysis, not just the stress in the plaque structure but also the flow pattern around the plaque. In this chapter, two issues regarding 3D patient-specific plaque stress analysis were studied.

The development of medical imaging provides the possibility of realistic 3D plaque geometry reconstruction with a high resolution [27, 34]. However the resolution of MR images is not high enough for tiny plaque component reconstruction at present, the thin fibrous cap may go beyond the highest resolution of in vivo MRI (in this study, the MRI resolution was 0.39 mm, which was impossible to image a fibrous cap with less than 0.39 mm thickness). Furthermore the contrast between fibrous tissue and lipid region is poor in general, which impose uncertainties on plaque stress analysis based on in vivo MRI. Our previous study [9] on plaque components' effects to plaque stress distribution showed that plaque stress level is significantly affected by the thickness of fibrous cap compared to lipid size, therefore efforts in increasing the accuracy of fibrous cap reconstruction from in vivo MRI need to be paid in the near future. The improved resolution/quality in plaque imaging with newly developed MRI protocols would generate more realistic stress predictions.

Plaque stress analysis on a symptomatic and asymptomatic patients showed that the wall stress in the symptomatic patient is much higher than the value in asymptomatic patient (227.7 kPa vs. 134.9 kPa). According to Li's 2D stress analysis study [21], which was based on 2D in vivo MRI images of 30 patients (15 symptomatic compared to 15 asymptomatic), the stress in asymptomatic patients was lower than that in symptomatic patients (269.6 ± 107.9 vs. 508.2 ± 193.1 kPa, $p = 0.004$). Our 3D stress analysis confirmed the conclusion that the maximum stress in the symptomatic patient was much higher than that in the asymptomatic patient. However in Li's study, the 2D stress model may not identify the maximum stress location in a plaque with highly irregular 3D geometry; also the pressure loading was not realistic since it did not consider the pressure drop in the plaque region. From Tang's study [31] based on 12 patient data, it was demonstrated that ruptured plaques experienced much higher wall stress value than non-ruptured plaques (247.3 ± 121.4 vs. 109.1 ± 21.0 kPa), which are similar to the stress values in our study for the symptomatic and asymptomatic patients. The great difference in plaque wall stress between symptomatic and asymptomatic patient may be used in the future for predicting plaque vulnerability, while a large sample of different plaque prototypes is needed in order to validate the procedure.

A vulnerable plaque usually is associated with a thinner fibrous cap and a large lipid region [7, 25]. The comparison between the two patients in minimum FCT and actual lipid core size shows that the symptomatic patient had a thinner FCT and larger lipid core size than the asymptomatic patient (the symptomatic patients: 0.087 mm for minimum FCT, 247 mm^3 for lipid core size; the asymptomatic patients: 0.177 mm for minimum FCT, 70 mm^3 for lipid core size). FCT is an important morphological feature associated with plaque rupture. A very thin fibrous cap usually indicates a more vulnerable plaque. According to Burke's [1] study on 133 coronary plaques from male patients, a cap thickness of 65 μm was defined as a critical value of instability. While the critical cap thickness of coronary plaque may not directly be applied to carotid plaques. Redgrave et al. [24] studied the critical cap thickness and rupture in symptomatic carotid plaques, suggested that the optimum cut-off FCT value for discriminating between ruptured and non-ruptured plaques was a minimum FCT <200 μm. In the present study, the minimum cap thickness for the symptomatic patient is much less than 200 μm, while the asymptomatic patient had a thin FCT close to 200 μm, which could serve for an indirect evidence that a carotid plaque with a thin fibrous cap less than 200 μm is more prone to rupture from biomechanical aspect. However, until now, there is no clear indication of the threshold value for lipid core size above which the plaque will become unstable, as for the cases of FCT, 200 μm is the critical value for carotid plaques. From a 2D study, Ohayon [23] suggested that plaque instability is to be viewed as a consequence of the combination of FCT, lipid core thickness, and remodeling index, and the lipid core thickness is more important than its area in determining plaque stability. When we consider the lipid core in 3D context, it is expected that the morphological feature is much harder to be represented. It includes the volume, the shape occupied by lipids, interface smoothness between fibrous tissue and lipids, lipid core depths, and so on. The soft characteristic of lipid will cause extreme stress concentrations in plaque shoulder region, a frequent location of plaque rupture. Our study on the two plaque samples showed that the symptomatic patient had much larger lipid region than the asymptomatic patient.

Quantifying the mechanical properties of healthy and diseased arterial tissue is essential for realistic stress prediction. Histological studies in the arterial wall have shown that arterial wall is heterogeneous, nonlinear, anisotropic, and viscous-elastic. Richardson [26] has pointed out that the lack of accurate plaque material properties data is possibly the most uncertain aspect in the existing literature on plaque rupture study. Based on the in vivo MR images of carotid plaques, it is possible to characterize material properties of arterial wall, which has been studied in the research as in the second part. Based on phase contrast MRI, the time evolution of arterial wall motion is available, and then the material parameters for a specific material model could be obtained by minimizing the difference between predicted arterial wall dynamic and MRI-measured arterial wall dynamics. The patient-specific material model will greatly advance plaque stress analysis in terms of patient-specific model. However there is still a long way to go for robust and reliable material model characterization and application to real 3D patient-specific plaque models for the fact that material properties vary at different locations even for the same subject.

Extracranial internal carotid artery stenosis accounts for 15–20 % of ischemic strokes, depending on the population studied. Carotid endarterectomy is the most frequently performed operation to prevent stroke. A recent study showed that Carotid endarterectomy reduces the stroke risk compared to medical therapy alone for patients with 70–99 % symptomatic stenosis (16 % absolute risk reduction at 5 years) and number needed to treatment (NNT) on preventing a stroke is 6.3. There is a smaller benefit for patients with 50–69 % symptomatic stenosis (absolute risk reduction 4.6 % at 5 years), NNT = 22. The benefit/risk ratio is smaller for asymptomatic patients with 60–99 % stenosis compared to symptomatic patients and individual decisions must be made [4]. Patient plaque rupture risk assessment could be potentially a key factor on providing the best result on preventing stroke and enhancing the ratio of benefit/risk. The current patient-selecting criteria used in clinical practice are based on whether the plaque is symptomatic or asymptomatic and the degree of stenosis. Current studies have clearly demonstrated that degree of stenosis is not a good criterion on assessing plaque rupture risk [3, 28]. The significant differences in plaque stress levels and difference in minimum FCT and lipid core size between symptomatic and asymptomatic patients indicate that those parameters can be used for plaque vulnerability assessment. A validated plaque rupture risk assessment will enhance the CEA efficiency on preventing rupture and reduce unnecessary procedure for low risk patients, which will save money and unnecessary operation risk. With the accumulated data of this kind of study will eventually provide a useful risk predicting index for individual plaque.

5 Conclusion

Two issues regarding patient-specific plaque stress analysis are studied in this chapter: (1) patient-specific geometry; (2) patient-specific material model. Based on high-resolution in vivo MRI, patient-specific plaque geometry is available for the followed plaque stress analysis. The comparison between a symptomatic and asymptomatic patient showed that plaque stress level in the symptomatic patient is much higher than the asymptomatic patient. Furthermore, from the patient-specific geometries for the two patients, the minimum FCT is much thinner and the lipid core size is much larger in the symptomatic patient than that in the asymptomatic patient. Based on phase-contrast MRI sequence, a procedure for obtaining patient-specific material model has been successfully carried out, and the predicted plaque stress pattern is consistent with existed results. Plaque stress analysis with patient-specific modeling will be helpful in the identification of high-rupture risk patients.

Acknowledgements This project is supported by the British Heart Foundation (FS/06/048). The authors like to thank Dr ZY Li, Dr M Graves, M.D. JH Gillard from Department of Radiology, Cambridge University, for their contributions to all MR images, and collaborations in the project.

References

1. Burke AP, Farb A, Malcom GT, Liang YH, Smialek J, Virmani R (1997) Coronary risk factors and plaque morphology in men with coronary disease who died suddenly. N Engl J Med 336(18):1276–1282
2. Cai J, Hatsukami TS, Ferguson MS, Kerwin WS, Saam T, Chu B, Takaya N, Polissar NL, Yuan C (2005) In vivo quantitative measurement of intact fibrous cap and lipid-rich necrotic core size in atherosclerotic carotid plaque. Circulation 29:3437–3444
3. Casscells W, Naghavi M, Eillerson JT (2003) Vulnerable atherosclerotic plaque: a multifocal disease. Circulation 107(16):2072–2075
4. Chaturvedi S et al (2005) Carotid endarterectomy – an evidence-based review. Neurology 65:794–801
5. Cheng GC, Loree HM, Kamm RD, Fishbein MC, Lee RT (1993) Distribution of circumferential stress in ruptured and stable atherosclerotic lesions. A structure analysis with histopathologicla correlation. Circulation 87(4):1179–1187
6. Chuong CJ, Fung YC (1983) Three-dimensional stress distribution in arteries. J Biomed Eng 105(3):268–274
7. Davies MJ (1990) A macro and micro view of coronary vascular insult in ischemic heart disease. Circulation 82(3 suppl):II38–II46
8. Finet G, Ohayon J, Rioufol G (2004) Biomechanical interaction between cap thickness, lipid core composition and blood pressure in vulnerable coronary plaque: impact on stability or instability. Coron Artery Dis 15(1):13–20
9. Gao H, Long Q, Howarth SPS, Tang TY, Li ZY, Graves MJ, Gillard JH (2009) The reproducibility study of 3D arterial plaque reconstruction and its effects to the stress analysis based on multiple sequence MRI images. J Magn Reson Imaging 30(1):85–93
10. Gao H, Long Q, Graves M, Gillard JH, Li ZY (2009) Carotid arterial plaque stress analysis using fluid–structure interactive simulation based on in vivo magnetic resonance images of four patients. J Biomech 42(10):1416–1423
11. Gao H, Long Q et al (2009) Stress analysis of carotid atheroma in a transient ischaemic attack patient using the MRI-based fluid–structure interaction method. Br J Radiol 82(Spec No 1):S46–S54
12. Gao H, Long Q (2011) Stress analysis on carotid atherosclerotic plaques by fluid structure interaction. In: Jasjit SS, Chirinjeev K, Filippo M (eds) Atherosclerosis disease management. Springer, Berlin, pp 87–118
13. Gao H et al (2011) Stress analysis of carotid atheroma in transient ischemic attack patients: evidence for extreme stress-induced plaque rupture. Ann Biomed Eng. doi:10.1007/s10439-011-0314-5
14. Gasser TC, Holzapfel GA (2007) Modeling plaque fissuring and dissection during balloon angioplasty intervention. Ann Biomed Eng 35(5):711–723
15. Hatsukami TS, Ross R, Polissar NL et al (2000) Visualization of fibrous cap thickness and rupture in human atherosclerotic carotid plaque in vivo with high-resolution magnetic resonance imaging. Circulation 102:959–964
16. Huang X, Teng Z, Canton G, Ferguson M, Yuan C, Tang D (2010) Intraplaque hemorrhage is associated with higher structural stresses in human atherosclerotic plaques: an in vivo MRI-based 3D fluid–structure interaction study. Biomed Eng Online 9:86
17. Humphrey JD (2002) Cardiovascular solid mechanics: cells, tissues, and organs. Springer, New York

18. Humphrey JD, Na S (2002) Elastodynamics and arterial wall stress. Ann Biomed Eng 30(4):509–523
19. Kock SA, Nygaard JV, Eldrup N, Frund ET, Klarke A, Paaske WP, Falk E, Kimi WY (2008) Mechanical stresses in carotid plaques using MRI-based fluid–structure interaction models. J Biomech 41(8):1651–1658
20. Leach JR, Rayz VL, Soares B, Wintermark M, Mofrad MR, Saloner D (2010) Carotid atheroma rupture observed in vivo and FSI-predicted stress distribution based on pre-rupture imaging. Ann Biomed Eng 38(8):2748–2765
21. Li ZY, Howarth SPS, Tang T, Graves MJ, U-King-Im J, Trivedi RA, Kirkpatrick PJ, Gillard JH (2007) Structure analysis and magnetic resonance imaging predict plaque vulnerability: a study comparing symptomatic and asymptomatic individuals. J Vasc Surg 45(4):768–775
22. Masson I, Boutouyrie P, Laurent S, Humphrey JD, Zidi M (2008) Characterization of arterial wall mechanical behavior and stresses from human clinical data. J Biomech 41(12):2618–2627
23. Ohayon J, Finet G, Gharib AM, Heerzka DA et al (2008) Necrotic core thickness and positive arterial remodeling index: emergent biomechanical factors for evaluating the risk of plaque rupture. Am J Physiol Heart Circ Physiol 295(2):H717–H727
24. Redgrave JN, Gallaqher P, Lovett JK, Rothwell PM (2008) Critical cap thickness and rupture in symptomatic carotid plaques: the oxford plaque study. Stroke 39(6):1722–1729
25. Richardson PD, Davies MJ, Born GV (1989) Influence of plaque configuration and stress distribution on fissuring of coronary atherosclerotic plaques. Lancet 2(8669):941–944
26. Richardson PD (2002) Biomechanics of plaque rupture: progress, problems, and new frontiers. Ann Biomed Eng 30(4):524–536
27. Saam T, Ferguson M, Yarnykh VL, Takaya N, Xu D, Polissar NL, Hatsilao TS, Yuan C (2005) Quantitative evaluation of carotid plaque composition by in vivo MRI. Arterioscler Thromb Vasc Biol 25:234–239
28. Shah PK (2003) Mechanisms of plaque vulnerability and rupture. J Am Coll Cardiol 41(4 suppl S):15S–22S
29. Tang D, Yang C, Zheng J, Woodard PK, Sicard GA, Saffitz JE, Yuan C (2004) 3D MRI-based multicomponent FSI models for atherosclerotic plaques. Ann Biomed Eng 32(7):947–960
30. Tang D, Yang C, Zheng J, Woodard PK, Sicard GA, Saffitz JE et al (2004) 3D computational mechanical analysis for human atherosclerotic plaques using MRI-based models with fluid–structure interactions. Lect Notes Comput Sci 3217(1):328–336
31. Tang D, Teng Z, Canton G, Hatsukami TS, Dong L, Huang X, Yuan C (2009) Local critical stress correlates better than global maximum stress with plaque morphological features linked to atherosclerotic plaque vulnerability: an in vivo multi-patient study. Biomed Eng Online 8:15
32. Trivedi RA, U-king-Im JM, Graves MJ, Horsley J, Goddard M, Kirkpatrick PJ, Gillard JH (2004) MRI-derived measurements of fibrous-cap and lipid-core thickness: the potential for identifying vulnerable carotid plaques in vivo. Neuroradiology 46:738–743
33. Trivedi RA, Mallawarachi C, U-king-Im JM et al (2006) Identifying Inflamed carotid plaques using in vivo USPIO-enhanced MR imaging to label plaque macrophages. Arterioscler Thromb Vasc Biol 26:1601–1606
34. Underhill HR, Hatsukami TS, Fayad ZA, Fuster V, Yuan C (2010) MRI of carotid atherosclerosis: clinical implications and future directions. Nat Rev Cardiol 7(3):165–173
35. Yuan C, Kerwin WS, Ferguson MS, Polissar N, Zhang S, Cai J et al (2002) Contrast-enhanced high resolution MRI for atherosclerotic carotid artery tissue characterization. J Magn Reson Imaging 15:62–67
36. Yuan C, Zhang S, Polissar NL, Echelard D et al (2002) Identification of fibrous cap rupture with magnetic resonance imaging is highly associated with recent transient ischemic attack or stroke. Circulation 105:181–185

Magnetic Resonance Imaging of Vulnerable Carotid Plaques

9

Rohitashwa Sinha, Karol P. Budohoski, Victoria E.L. Young, and Rikin A. Trivedi

1 Introduction

In 1951, C. Miller Fisher first recognized the connection between an occluded carotid artery and cerebral infarction [1]. Since this seminal finding, carotid atherosclerotic disease has been recognized as a thromboembolic source, which may precipitate cerebral ischemic episodes. The present management of carotid atherosclerotic disease is directed at reducing the risk of stroke. This can be achieved surgically, by means of carotid endarterectomy (CEA), however, not without significant perioperative risks involved. Indications for surgical treatment are largely based on investigations that assess the degree of luminal narrowing. The reason behind this is a series of multicentre, randomized controlled trials (RCTs), which have stratified the risk of stroke for symptomatic and asymptomatic patients with various degrees of luminal stenosis undergoing CEA [2–5].

An analysis of the pooled results from the major RCTs: European Carotid Surgery Trial (ECST), North American Symptomatic Carotid Endarterectomy Trial (NASCET), and Veterans' Affairs Trial, demonstrated that a significant benefit can only be achieved in patients with severe stenosis (70–99 %) [6]. The absolute risk reduction (ARR) of ipsilateral stroke within the next 5 years was found to be 16 % [6]. Only a marginal benefit was observed for patients with moderate stenosis (50–69 %) with an ARR of 4.6 % [6]. Furthermore, combined data from the Asymptomatic Carotid Atherosclerosis Study (ACAS) and the Asymptomatic Carotid Surgery Trial (ACST) showed a 5-year stroke risk reduction from 11.5 to 6 %, but only in patients with a significantnarrowing $\geq$70 % [7, 8] It is also worth noting that the benefit was significant only for males aged >75 years [8].

Digital subtraction angiography (DSA) was used to assess the extent of luminal narrowing in the major RCTs for CEA in symptomatic patients [2–5]. However, as an investigation, DSA has low availability, suffers inherent measurement errors with a reported inter-observer variability approaching 10 % [9]. The costs associated with DSA are greater than modern noninvasive vascular imaging such as ultrasonography (US), computed tomography angiography (CTA), or even magnetic resonance angiography (MRA). Furthermore, DSA is time consuming, requires highly skilled interventional radiologists, and has a significant risk burden (0.5–1.3 % permanent neurological complications and 0.4–1.3 % of transient neurological complications) [10–12]. Hence, in asymptomatic patients, ultrasound has been the gold standard first-line investigation in assessing luminal stenosis, despite being undermined by considerable variability in intraobserver measurement readings as well as between interobserver readers [8, 9].

Recently, as the understanding of carotid atherosclerosis pathophysiology has developed, the emphasis on luminal stenosis has diminished, further demonstrating the limitations of DSA and ultrasonography as the first-line investigation modalities. For example, adaptive arterial remodeling mechanisms described first by Glagov et al. [13] in diseased carotid arteries, which allow for large plaques to dilate the outer wall circumference without reducing the lumen may not be detected using DSA alone.

Histological analysis of plaques which were known to have caused cerebrovascular events such as stroke or transient ischemic attack (TIA) have helped to elicit features of the diseased arterial walls which may prove to be more sensitive and accurate markers of disease progression [14, 15]. Recent research using Magnetic Resonance Imaging(MRI) have shown it to be sensitive in identifying features of carotid arterial walls which have been implicated in a significant risk of disease progression [16–18].

R. Sinha (✉) • K.P. Budohoski • V.E.L. Young • R.A. Trivedi
Department of Neurosurgery, Addenbrooke's Hospital, Hills Road, Box 166, CB2 0QQ Cambridge, UK
e-mail: rohitashwa.sinha@addenbrookes.nhs.uk; karol.budohoski@gmail.com; victoria.young@addenbrookes.nhs.uk; rikitrivedi@hotmail.com; rt256@cam.ac.uk; rikin.trivedi@addenbrookes.nhs.uk

L. Saba et al. (eds.), *Multi-Modality Atherosclerosis Imaging and Diagnosis*,
DOI 10.1007/978-1-4614-7425-8_9,

This chapter aims to describe the recent developments in MRI, which make it a promising tool in the evaluation of carotid atherosclerotic disease. The markers of high-risk atherosclerotic plaques visible on MRI and evidence obtained from long-term observational studies will be described.

2 From Luminal Stenosis to Wall Characteristics

Histological characteristics studied in excised carotid specimens from stroke or TIA patients have been fundamental to understanding disease progression in atherosclerosis [19, 20]. Subsequently, the term "vulnerable plaque" was coined, referring to carotid plaques, which exhibit the characteristics that have been commonly found in plaques that were found to have caused cerebrovascular events. Nagahavi et al. proposed the systematic classification of plaques at high risk for thrombosis, rupture, and embolization. Major and minor criteria were proposed. Major criteria include active inflammation within the plaque, a thin fibrous cap (FC) with a large lipid rich necrotic core (LRNC), fibrous cap disruption, as well as severe stenosis. Minor criteria include intraplaque hemorrhage (IPH), expansive remodeling, superficial calcified nodules, yellow coloring on angioscopy, and endothelial dysfunction [21, 22].

Various MRI sequences have been used successfully to depict all of the aforementioned major and minor characteristics within carotid plaques (with the exception of endothelial dysfunction and yellow coloring on angioscopy). Furthermore, studies have ascertained a relationship between MRI signs of "vulnerability" and subsequent risk of stroke and/or TIA. For example, Takaya et al. found a significant correlation between the presence of a thin or ruptured fibrous cap on carotid MRI and ipsilateral ischemic stroke [23]. These characteristics infer a significant risk of future ischemic events for the affected patients irrespective of the extent luminal stenosis. Indeed, several reports indicate that the majority of people with neurological symptoms attributable to ipsilateral internal carotid artery (ICA) atherosclerosis have only moderate ICA stenosis [24].

This shift in emphasis, described above, from hemodynamic compromise caused by luminal stenosis to thromboembolism arising from "vulnerable" atherosclerotic plaques is based on an evolving understanding of the pathophysiology of atherosclerosis. As the disease progresses, an ongoing inflammatory process occurs whereby cholesterol carried by low density lipoproteins (LDL) in the blood is deposited and oxidized in the subendothelial layer of medium and large arteries such as the carotid arteries [25]. Subsequently the LDL become oxidized, attract macrophages, and later also smooth muscle cells. Both these cell types phagocytose the oxidized LDL. The internalized lipids within smooth muscle cells and macrophages interspersed by discrete foci of extruded lipid are histological and, on imaging, seen as the characteristic lipid-rich necrotic core (LRNC). Furthermore, the amount of activated macrophages can be quantitatively assessed and is one of the markers used for imaging the inflammatory process. Both the LRNC and activated macrophages, i.e., inflammation have been classified by Naghavi et al. as major criteria characteristic of vulnerable plaques [21, 22].

The fibrous cap (FC), on the other hand, is formed by the vascular endothelial layer along collagen fibers and matrix glycoproteins which overlie the lipid core [25]. As the intimal lipid core progresses, it incurs local hypoxia leading to necrosis. Hypoxia and necrosis render the delicate neovascular bed of the atherosclerotic plaque prone to the development of intraplaque hemorrhage (IPH) [26–28]. All the above-described processes alongside the increasing biomechanical stress due to deformation of vessel wall and the action of inflammation-induced proteolytic enzymes such as matrix metalloproteinases (MMPs) may lead to the rupture of the fibrous cap and thromboembolism [26, 29–31].

In summary the characteristic stages of the pathophysiology of atherosclerotic plaque formation have been identified and described as the major and minor criteria of plaque vulnerability. The presence of these characteristics increases the risk of subsequent TIA and/or stroke. It has been postulated that the described characteristics may be more sensitive in predicting the risk of TIA and/or stroke than the extent of luminal stenosis. Therefore, the ability to image and monitor their progression is of great clinical importance (Fig. 9.1). Table 9.1 shows the different criteria outlined by Naghavi et al. and the investigative modalities that can be used to assess them [21, 22]. As can be seen at present MRI has the broadest application [32].

3 Magnetic Resonance Imaging

MRI has many advantages, which make it likely to become the investigative modality of choice for imaging carotid disease. It yields images of high spatial resolution, even of soft tissue. Additionally, MRI-derived measurements have been shown to be reproducible and can be used in classifying plaques according to the American Heart Association criteria [33]. It has been shown that imaging plaques in vivo using MRI corresponds well to postoperative histological examination of the excised plaques. It is noninvasive and does not entail patient exposure to ionizing radiation. These particular benefits mean that MRI can safely be used sequentially on the same patient to assess disease progression or response to treatment.

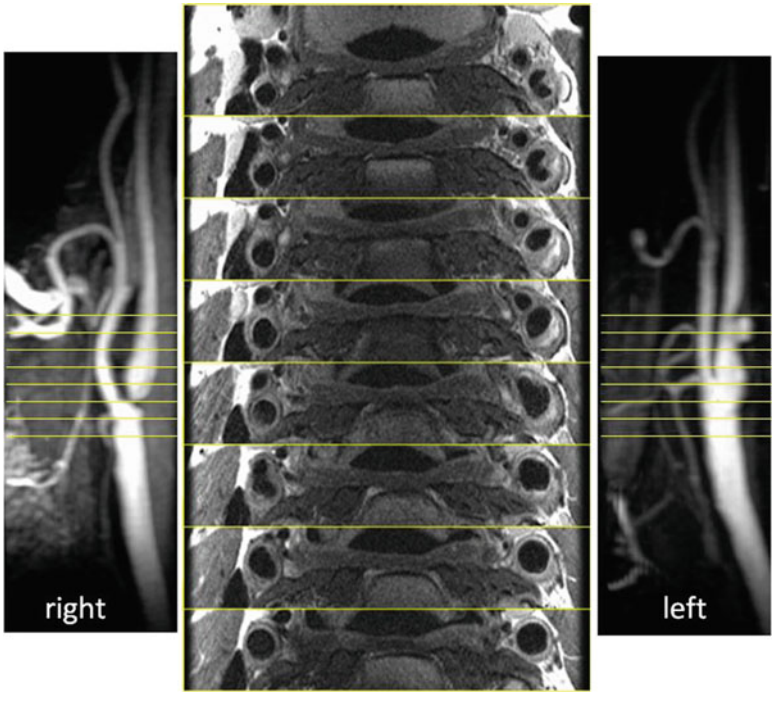

Fig. 9.1 Sequential imaging of bilateral carotid artery stenosis. TOF depicts the area of luminal narrowing. Axial slices depict the full extent of the atherosclerotic process, including expansive remodeling. The atherosclerotic process includes a larger area than seen only by looking at the extent of luminal narrowing. *TOF* time of flight

Table 9.1 Imaging modalities available to assess atherosclerotic carotid plaque characteristics

Plaque characteristic	MRI	CT	US	PET	SPECT	DSA
Active inflammation	✓	X	X	✓	X	X
Thin FC with large LRNC	✓	✓	X	X	X	X
FC disruption	✓	X	X	X	✓	X
Severe stenosis	✓	✓	✓	X	X	✓
Intraplaque hemorrhage	✓	X	X	X	X	X
Expansive remodeling	✓	X	✓	X	X	X
Superficial calcified nodules	✓	✓	X	X	X	X
Yellow coloring on angioscopy	X	X	X	X	X	X
Endothelial dysfunction	✓	X	X	✓	X	X

MRI magnetic resonance imaging, *CT* computed tomography, *US* ultrasonography, *PET positron emission tomography*, *SPECT* single photon, emission computed tomography, *DSA* digital subtraction angiography

The disadvantages of MRI include its costs; it is an expensive technology requiring skilled staff, trained in imaging carotid vessels and using specialist equipment. Furthermore, MRI involves long-image acquisition times and this can pose problems for patients suffering with impaired neurological status, which is often encountered in patients following stroke. MRI is absolutely contraindicated in an important subsection of the patient population with metallic implants, especially those with concomitant coronary atherosclerotic disease who might have implanted cardiac devices. Different techniques using MRI have been used to investigate the key characteristics of "vulnerable" plaques. In the subsequent sections we will outline recent research studies that demonstrate how MRI is being used to investigate each of those characteristics.

4 Fibrous Cap

As discussed earlier, the fibrous cap overlying the lipid core of an atherosclerotic plaque is implicated as the thromboembolic component which, when ruptured, leads to TIA or stroke. Indeed, a number of histological studies have shown that a thin fibrous cap overlying a large lipid-rich necrotic core is a common feature of plaques prone to rupture [15, 21, 34, 35].

High resolution MRI using a 3D "multiple overlapping thin slab angiography" sequence was employed in a study by Hatsukami et al. to assess the feasibility of differentiation types of FC depending on thickness into thin FC, thick FC, and ruptured FC [36]. Their results had an 89 % agreement

with ex vivo histological assessment of the imaged plaques. In a study by Trivedi et al., the authors were able to quantify both fibrous cap and the lipid-rich necrotic core using 2D, blood-suppressed, fast spin echo, T2W MRI sequences with high interobserver agreement [37]. The fibrous cap/lipid-rich necrotic core ratio was introduced. Similar results were later confirmed by other authors, who also found good agreement of the MRI measurements with histological specimens [38]. The specific sequence employed included double inversion recovery, T1W, time of flight, and proton density weighted, which were statistically more accurate than T2-weighted MRI.

These studies demonstrate that fibrous cap identification and measurement can reliably be achieved using specialized high-resolution MRI sequences with reliable comparison to the histological measurements from the same plaques postoperatively. These results suggest that the imaging techniques could be used sequentially to assess disease progression. Additionally, there is wide scope for the morphological parameters visualized with MR to be used for the assessment of therapeutic interventions aimed at stabilizing the plaques and their fibrous caps.

5 Lipid-Rich Necrotic Core

Larger sized LRNC in atherosclerotic plaques have been postulated as inferring greater risk of plaque vulnerability owing to the increased likelihood of hypoxia and necrosis in the LRNC and the increased fragility of neovascularization leading to intraplaque hemorrhage; all of which perpetuate atherosclerotic disease progression. Recent studies have used various different MRI techniques to reliably image and measure the LRNC in vivo.

Echo-planar diffusion-weighted imaging (DWI) was used alongside high resolution MRI to generate apparent diffusion coefficient (ADC) maps in 26 patients with moderate to severe carotid stenosis to distinguish between LRNC and FC. They report a significant difference between the ADC values for the FC and LRNC ($p < 0.0001$) as well as a significant correlation ($p = 0.005$) between ADC values and histology post CEA; lower ADC values matched with heavier lipid staining in the excised specimens.

Underhill et al. [39] used multicontrast MRI in a prospective observational study in 108 asymptomatic individuals with carotid stenosis, imaging at baseline and at 3 years to assess for new ulceration or plaque disruption. Regression analysis revealed that the proportion of wall volume occupied by the LRNC was the strongest predictor of subsequent "surface disruption" and that a new surface disruption was associated with a significant increase in percentage LRNC volume. This particular target step in the pathophysiology may be of special relevance as the point where a stable plaque becomes unstable. The use of high resolution MRI to assess therapy effects on LRNC at this stage is likely to be of great clinical importance.

In a randomized, double-blind, placebo-controlled prospective study over 3 years, [40] used high resolution, multicontrast bilateral carotid MRI scans at baseline and annually in 33 patients to assess the effect of lipid lowering therapy on LRNC volume and as percentage of the diseased wall. They report significant LRNC volume reduction ($p < 0.001$) and significant reduction in LRNC percentage of arterial wall ($p < 0.001$) over 3 years with intensive lipid lowering therapy. The statistically significant reduction in LRNC percentage of the arterial reduction over the first 2 years precedes "plaque regression"; although longer term follow-up would be required to verify whether this change in imaged LRNC will translate into a lower incidence of stroke or TIA in the future.

6 Fibrous Cap Disruption

Histopathological studies have shown that fibrous cap disruption is more frequently found in patients who have suffered from a transient ischemic attack or stroke in the past [26, 41]. Specific assessment of the FC has been shown to be able to detect with good accuracy situations of disrupted fibrous caps, suggestive of plaque rupture (Figs. 9.2 and 9.3). This has been obtained using high resolution MRI with multicontrast protocols [38]. A case series study has demonstrated it possible to use multisequence, cross-sectional MRI with black and bright blood sequences to identify carotid plaques with disrupted fibrous caps [42]. However, the spatial resolution of conventional scanners is approximately 250 μm, which is the dimension of a thin fibrous cap. This demonstrates the existing pitfalls of imaging of carotid atherosclerosis with conventional MRI scanners.

7 Intraplaque Hemorrhage

Fragile neovascularization in the inflammation-ridden atherosclerotic plaque is prone to hemorrhage. Current thinking suggests that hemorrhage within the atherosclerotic plaque perpetuates the inflammatory processes and induces further necrosis. All these increase the risk of ipsilateral stroke.

As with imaging of the lipid-rich necrotic core, a variety of recent studies have used different MRI techniques to successfully investigate intraplaque hemorrhage in carotid atherosclerotic lesions (Fig. 9.4).

One study compared contrast-enhanced MR angiography (CE-MRA) with time-of-flight (TOF) MRA sequences in 15 patients and validated their accuracy with histological

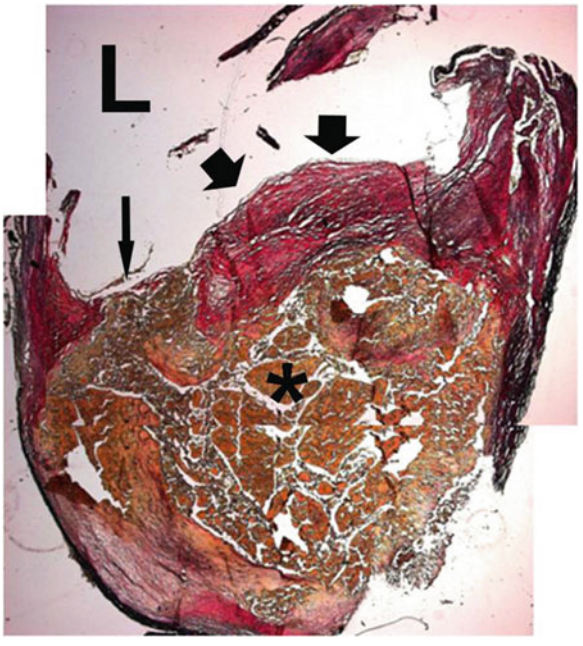

Fig. 9.2 Histological specimen of a atherosclerotic carotid artery. A thin fibrous cap is seen (*short arrow*), with a rupture at one of the edges (*long arrow*). Below the fibrous cap the lipid-rich necrotic core can be seen (*asterisk*). L signifies arterial lumen

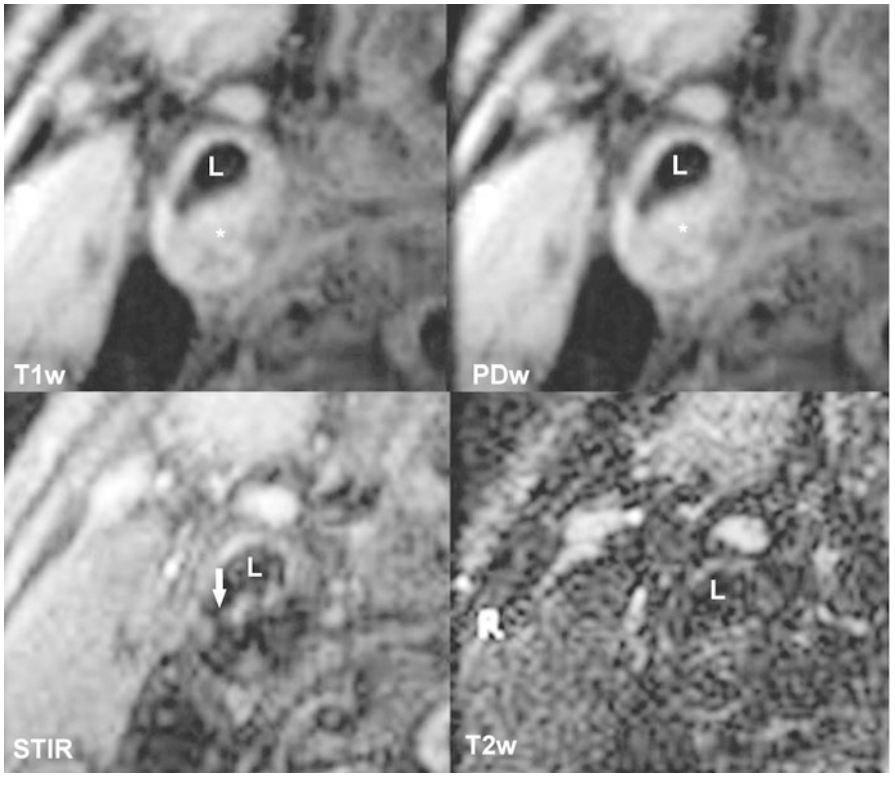

Fig. 9.3 T1w, PDw, STIR, T2w images of the same plaque as in Fig. 9.2. Ruptured fibrous cap is visible in the STIR sequence (*long arrow*). L signifies arterial lumen, *asterisk* signifies the lipid-rich necrotic core. *T1w* T1-weighted sequence, *PDw* proton density-weighted sequence, *STIR* short T1 inversion recover sequence, *T2w* T2-weighted sequence

findings from the ex vivo post-CEA plaque specimens. They report a 94 % accuracy with CE-MRA over 84 % using TOF sequences, with excellent intra and interobserver agreement [43].

Improvements in the technique for imaging intraplaque hemorrhage have been made. One study reported the use of a novel technique to improve on IPH identification, which has previously relied on methemoglobin detection with T1-weighted sequences and blood suppression [44]. They report their novel technique "slab-selective phase-sensitive inversion-recovery" (SPI) optimizes IPH detection and is validated against histology, with significantly

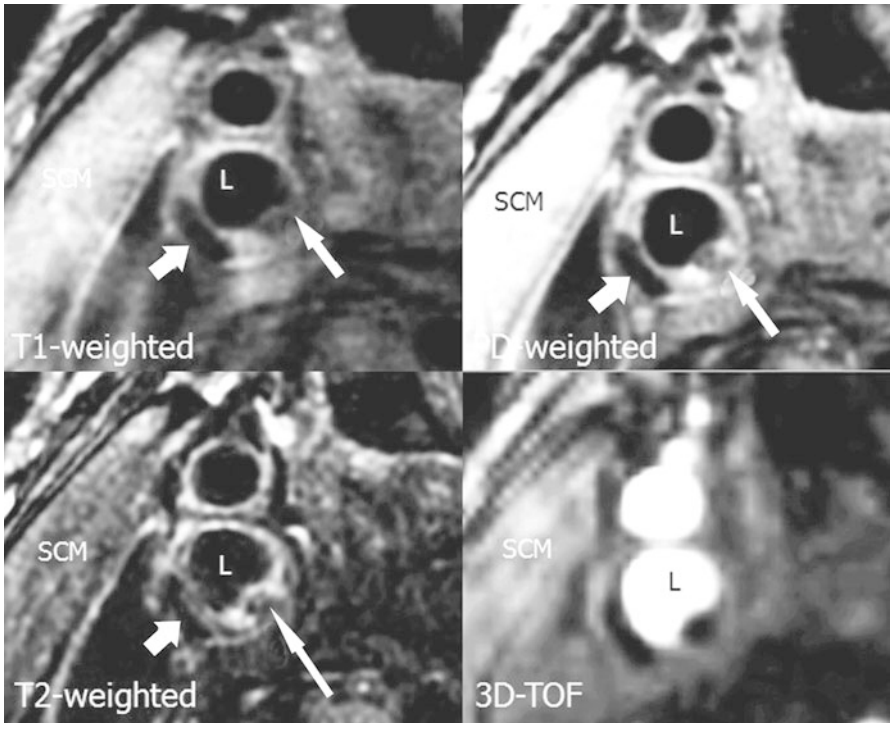

Fig. 9.4 MRI image with T1w, PDw, T2w, and 3D-TOF demonstrating thrombus within a carotid artery plaque (*short arrow*). Additionally thrombus with partial calcifications is seen in adjacent area (*long arrow*). L indicates arterial lumen. *T1w* T1-weighted sequence, *PDw* proton density-weighted sequence, *T2w* T2-weighted sequence, *3D-TOF* 3-dimensional time of flight

improved intraplaque hemorrhage-wall contrast-to-noise ratio ($p < 0.01$) and blood suppression efficiency ($p < 0.01$) when compared with recently used 3D rapid acquisition gradient echo sequences.

8 Wall Thickness

As the focus has shifted from vessel lumen stenosis to the arterial vessel wall, the relationship between the overall wall thickness and the percentage of the wall occupied by the LNRC has also been emphasized as a risk-stratifying characteristic. In the Carotid Atherosclerosis Score (CAS) [39], maximal vessel wall thickness (VWT) and the percentage of the wall occupied by the LRNC were the strongest predictors of FC disruption and IPH.

VWT and vessel wall area (VWA) have been used as surrogate markers of expansive remodeling, whereby the plaque progression occurs by enlarging the vessel wall outwards rather than encroaching on the lumen size. Black-blood fast spin-echo sequences were used in a prospective clinical trial of the effects of 12, 18, and 24 months of simvastatin lipid lowering therapy on VWT and VWA [45, 46]. Changes in both VWT and VWA at all the predefined times were statistically significant; the reduction in VWA size at 24 months compared to baseline ($p < 0.0001$) and VWT ($p < 0.001$). This feasibility study showed that MRI can be used in clinical trials to evaluate treatment efficacy, by means of assessing the change in wall characteristics rather than the degree of lumen stenosis in a longitudinal manner.

9 Inflammation

The inflammatory process within the plaque itself plays a major role in all aspects of atherosclerosis, i.e., plaque initiation, plaque progression, and plaque rupture. Systemic markers of inflammation, such as C-reactive protein (CRP) have been correlated with the cardiovascular events due to atherosclerotic disease [47]. Furthermore, inflammation has become a target of new therapies for atherosclerosis. While the exact mechanisms of inflammation related to atherosclerosis are beyond the scope of this chapter, macrophage infiltration of the plaque and neovascularization are of the plaque are two aspects, which have been recognized as potential markers of plaque vulnerability. MRI using a specific, macrophage-directed contrast agent, such as ultrasmall superparamagnetic iron oxide (USPIO) and dynamic contrast-enhanced MRI (DCE-MRI) using traditional gadolinium-based contrast agents have been used [48–51].

10 USPIO-Enhanced MRI and Macrophage Content

Ultrasmall superparamagnetic iron oxide (USPIO) is a non-gadolinium-based contrast agent that has been shown to be useful in MRI. The USPIO particle consists of a microcrystalline magnetite core, within dextran coating. Typically the diameter of USPIO is around 30 nm [52]. The particles are

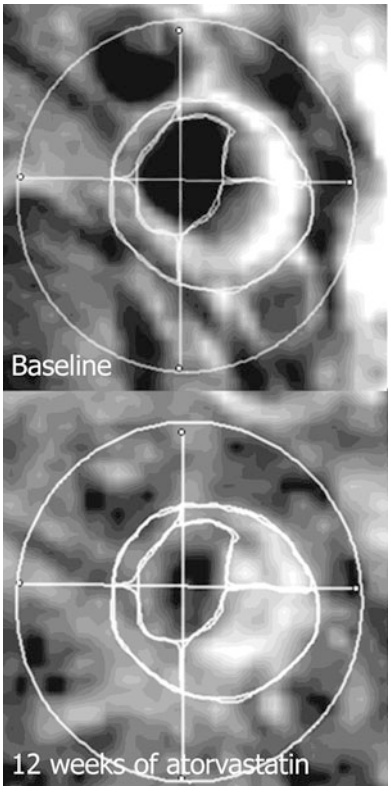

Fig. 9.5 USPIO-enhanced MRI at baseline and after 12 weeks of atorvastatin therapy. Note the increased enhancement in the *right upper* and *lower quadrant* signifies a lower USPIO accumulation, thus, reduced inflammatory process

absorbed by the reticuloendothelial system (RES) of the liver and spleen and are subsequently nonselectively absorbed by activated macrophages. Activated macrophages accumulate in areas of active inflammation, such as atherosclerotic plaques, but not only, and thus can be visualized using MRI [53, 54].

The effect of USPIO on MRI imaging has been described by Bulte et al. [55]. Briefly, USPIO particles create a large dipolar magnetic field, which acts on water molecules thus reducing the T2 relaxation times. USPIO acts as a negative contrast is on T2-weighted (T2W) sequences [55] (Fig. 9.5).

The uptake of USPIO particles by macrophages has been demonstrated in experimental studies [53] and later confirmed in plaques from carotid arteries of humans [49, 54, 56, 57]. Later, Trivedi et al. described the temporal relationship of the magnitude of signal loss following USPIO administration, establishing an optimal window for imaging between 24 and 36 h following administration of contrasting medium [57].

Interestingly no relationship between USPIO uptake of carotid plaques and luminal narrowing was demonstrated [58]. On the other hand, a relationship between inflammation as seen using USPIO-enhanced MRI and biomechanical stress has been demonstrated [59]. These results suggest the degree of inflammation may be an independent factor in determining the risk of plaque progression and subsequent risk of cerebrovascular events. Such findings prompted the question whether inflammation can be used as a surrogate end-point in clinical trials aimed at medical reduction of plaque burden.

The first use of USPIO-enhanced MRI for this purpose was published by Tang et al. in the ATHEROMA trial [60]. Forty-seven patients with asymptomatic carotid atherosclerosis (≥40 % stenosis) were randomized into two groups of high-dose (80 mg/day) and low-dose (10 mg/day) atorvastatin. While a significant reduction in USPIO uptake was demonstrated in the high-dose atorvastatin group as early as 6 weeks after initiation of treatment, no such effect was noted in the low-dose group. Previously interventional studies aimed at reducing plaque burden have focused on morphological characteristics [15, 45, 46, 61, 62]. Similarly, these studies showed that improvements in gross morphological parameters such as vessel wall thickens and vessel wall area, precede changes in luminal stenosis. However, the earliest changes were visible after 12 months of treatment. In contrast using USPIO-enhanced MRI quantifiable changes were demonstrated as early as 6 weeks following start of therapy. These results demonstrate the potential of novel imaging techniques in the rapid assessment of plaque vulnerability and therefore patient risk stratification. It needs to be noted that only patients with baseline uptake of USPIO particles were included in the ATHEROMA study, potentially limiting the generalization of the results to a wider population [60]. However, the potential of imaging inflammation has been demonstrated giving incentive for further development in this area.

11 Dynamic Contrast-Enhanced MRI

Gadolinium-based contrast media are used for their T1-shortening ability. The accumulation of the contrast causes T1 hyperintensity. With the implementation of gadolinium chelates, investigation of the late-phase enhancement is possible. Late enhancement is used as a surrogate marker of contrast diffusion into the extracellular compartment. In order to visualize the vessel wall, sufficient suppression of the blood signal is essential, hence the choice of image acquisition is essential when DCE-MRI is used. Commonly black blood T1W sequences with either double inversion-recovery (DIR) [63] or even, quadruple inversion-recovery (QIR) are used [64].

Studies have shown that the extent of microvasculature within a plaque corresponds to the risk of intraplaque hemorrhage and subsequent rupture [30, 65]. Neovascularization

is induced by the chronic inflammatory process occurring in the plaque. Dynamic contrast-enhanced MRI (DCE-MRI), a method, which was originally developed for in neuro-oncology to determine the extent of tumor neovascularization, has been recently implemented in the study of carotid atherosclerosis. The main advantage of this method is that it can utilize routinely available contrasting media [66]. The first human observation of enhancement of atherosclerotic plaques was observed by Aoki et al. [67]. However, two separate aspects of plaque enhancement have been noted. In the first reports a hyperintense rim surrounding the diseased vessel was reported [67]. This was thought to represent vasa vasorum in the adventitia of the artery. However, direct enhancement within the plaque, in particular the FC was also noted [51, 68].

Kinetic modeling plays the role in the image analysis today [48, 69, 70]. Two parameters which are considered for analysis are fractional plasma volume (V_p) and transfer constant of the contrast agent (K^{trans}) and represent the two compartments: intravascular space and extravascular, extracellular space. V_p is thought to represent the actual microvascular volume [48]. It was found to be a good marker of plaque neovasculature when compared with histology ($r = 0.68$, $p < 0.001$) [48, 70]. K^{trans}, on the other hand, is used to estimate the permeability of the microvasculature. Interestingly, it was K^{trans} which was found to correlate with macrophage content within the plaque suggesting that there may be distinct features of the neovascular bed which are associated with inflammation [48].

One major pitfall of MRI-contrasting agents is the non-specific enhancement, which may unfavorably alter results. MRI contrasting media development is currently concentrating on designing new markers, which would bind to specific targets in the atherogenic process. This progress is being done on the molecular and cellular level. Contrast media that bind to lipid [71, 72], thrombus [73], specific inflammatory mediators [74–76], apoptotic cells [77], and proteolytic enzymes, which could contribute to plaque destabilization [77], are currently under investigation and have the potential to obtain similar binding specificity as the one found in nuclear medicine.

12 Biomechanical Stress Modeling

The biomechanical forces acting on diseased arterial walls with atherosclerotic plaques prone to rupture have also been successfully modeled using MRI techniques [78]. As the inflamed endothelial layers are subject to biomechanical stress from hyperkinetic and turbulent blood flow, the structural integrity becomes progressively compromised which may lead to plaque rupture [78]. Such stresses can be measured using finite elements analysis (FEA) [79].

Trivedi et al. have used MRI-derived 2D geometrical arterial models to perform FEA to predict the differences in plaque tensile stress between symptomatic and asymptomatic patients with carotid atherosclerosis [80]. They reported a substantial difference in principal tensile stress calculated between the two groups.

A recent study used MRI-derived FEA, in a series of 45 patients with carotid atherosclerosis, to demonstrate that plaques with IPH had significantly higher stress than non-hemorrhagic plaques ($p = 0.003$) [81]. Furthermore, biomechanical stress has been used to determine the effect of lipid lowering therapies on carotid atherosclerotic plaques [82]. A reduction in arterial wall strain following aggressive lipid lowering therapy was determined using MR-based modeling. Maximum arterial wall strain at 12 weeks of treatment was significantly lower in the high dose Atorvastatin (80 mg) patient group versus the low dose (10 mg) group [82].

13 Recent Trends and Future Directions

The described studies illustrating how different MR techniques have been used to evaluate the individual "high risk" components of atherosclerotic carotid plaques are by no means the only research employing MR for this purpose. MRI-derived measurements have been shown to be reproducible and that they can be used in classifying plaques according to the American Heart Association criteria [33]. Furthermore, it has been shown that imaging plaques in vivo using MRI corresponds well to postoperative histological examination of the excised plaques [34, 51]. The efficacy and feasibility of MRI in imaging vulnerable carotid plaques has been repeatedly demonstrated [32, 33, 37, 39, 42, 48, 83]. MRI is increasingly being adopted as the imaging tool in prospective studies. It has been successfully used in longitudinal studies [46, 61, 84], as well as clinical intervention trials [60, 85, 86] (Table 9.2).

A recent study by Bianda et al. [84] used high spatial resolution MRI to quantify the progression of atherosclerotic disease in 30 patients over 2 years, looking at both their carotid and femoral arteries. Crucially, patients' medication regimens remained stable throughout the whole study period. The authors were able to quantitatively measure the changes in lumen area, total vessel area, and vessel wall area at baseline and at 1 and 2-year follow-up. Interestingly, differences in plaque progression were found between femoral artery plaques and carotid artery plaques. During the 2 years observation period, the authors demonstrated disease progression (as demonstrated by an increase in vessel wall area), despite standard medical therapy with good compliance. However, only in carotid arteries the increase in plaque size was accompanied by a significant decrease in lumen area. Despite methodological limitations, (inclusion criteria required

Table 9.2 Summary of recent longitudinal studies and clinical trials using MRI measures as primary or secondary end points

Author	Design	*n*	Intervention	Time	Imaging	Results
Corti et al. [45, 46]	Long.	18	Simvastatin	24 months	DIR, FSE PDw, T2w	VWA: decrease of 15 % and 18 % at 12 and 24 months; VWT: decrease of 11 % and 19 % at 12 and 24 months; LA: increase of 5 % at 24 months
Lima (2004) [87]	RCT	27	20 vs. 80 mg/day simvastatin	6 months	DIR, FSE PDw, T2w	PV: decrease of 12 % from baseline; PA: decrease of 12 % from baseline; no difference between groups
Corti et al. [61]	RCT	51	20 vs. 80 mg/day simvastatin	24 months	DIR, FSE PDw, T2w	VWA: decrease of 14 % and 18 % at 12 and 24 months, respectively; VWT: decrease of 10 % and 17 % at 12 and 24 months, respectively; LA: increase of 4 % and 5 % at 12 and 24 months, respectively; no differences between groups
Underhil et al. [62]	RCT	43	5 vs. 40/80 mg/day rosuvastatin	24 months	DIR, FSE T1w, PDw, T2w, 3D TOF	LV, WV, NWI: no changes neither between groups nor between baseline and 24 months; %LRNC: decrease of 37.0 % in high-dose group, no change in low-dose group
Tang et al. [60]	RCT	47	10 vs. 80 mg/day atorvastatin	12 weeks	USPIO-enhanced	ΔSI: 0.203 (95 % CI: 0.065, 0.198) reduction from baseline at 6 weeks (high-dose); difference of 0.240 (95 % CI: 0.134, 0.347) between groups at 12 weeks
Fayad et al. [85]	RCT	130	Dalcetrapib vs. placebo	48 months	TOF, DCE	Reduction in VA in dalcetrapib vs. placebo after 24 months; absolute change from baseline relative to placebo: -4.01 mm^2 (90 % CI: -7.23 to -0.80; nominal $p = 0.04$)
Bianda et al. [84]	Long.	30	Standard medical management	48 months	DIR, FSE T1w, PDw, T2w, 3D TOF	LA decreased (-3.19 %/year, $p = 0.018$); VWA increased ($+3.83$ %/year, $p = 0.019$)

DIR double inversion recovery, *FSE* fast spin echo, *T1w* T1 weighted, *T2w* T2 weighted, *PDw* proton density weighted, *TOF* time of flight, *DCE* dynamic contrast enhanced, *Long* longitudinal, *USPIO* ultrasmall superparamagnetic iron oxide, *VWT* vessels wall thickness, *VWA* vessel wall area, *LA* lumen area, *PA* plaque area, *PV* plaque volume, *ΔSI* signal intensity change, *SUV* standardized uptake value

<70 % stenosis in the carotid arteries while all grades of stenosis in the femoral arteries were permitted) the study successfully demonstrated the sensitivity and usefulness of MRI in monitoring atherosclerosis disease progression.

The recently published dal-PLAQUE (Safety and efficacy of dalcetrapib on atherosclerotic disease using novel noninvasive multimodality imaging) study [85], was designed to assess the efficacy of Dalcetrapib (a cholesterol ester transfer protein inhibitor) on atherosclerotic disease. Simultaneous MR and PET imaging was undertaken to assess the primary endpoints at 2 years from baseline. MRI was used to assess structural changes in carotid arterial walls (total vessel area, wall area, wall thickness, and normalized wall index). Patients treated with Dalcetrapib not only did not demonstrate progression of carotid plaques but were also found to have significant reductions in plaque burden as compared with placebo. Together with the atorvastatin therapy: effects on reduction of macrophage activity (ATHEROMA) study [60], dal-PLAQUE have been the first interventional clinical trials in the field of carotid atherosclerosis to use noninvasive imaging as primary endpoints. The authors of dal-PLAQUE conclude by stating that the imaged vascular endpoints will need even further and longer term clinical validation of the safety of Dalcetrapib on cardiovascular morbidity and mortality. These results are to be published in the "dal-OUTCOMES" trial.

Another study used MR to quantitatively detect changes in the size and composition of carotid plaques following cilostazol therapy; an antiplatelet agent [88]. They prospectively imaged 16 patients at baseline and at 6 months, using methodology where analysis of atherosclerotic plaques is performed calculating a contrast ratio between the imaged plaque and the sternocleidomastoid muscle. They also analyzed the intraplaque components and their relative size in percentage of total area (i.e., fibrous tissue, lipid/necrosis, and hemorrhage components). It was shown that the fibrous component increased significantly, while the lipid and hemorrhagic components decreased. Unfortunately, due to factors such as the small sample size and the lack of a control group, these findings cannot reliably be attributed to the therapeutic effects of Cilostazol.

Aside from MR evaluation of plaque morphology in vivo clinical studies, a recent longitudinal study simultaneously assessed the relationship of biomechanical structural stresses on the atherosclerotic plaques of previously symptomatic patients with a past history of a recent (<1 month) transient ischemic attack or a minor, nondisabling stroke in the last month [89]. They followed up patients clinically from a baseline MR assessment for up to 2 years or until they suffered a cerebrovascular event in the territory of the previously imaged carotid artery. The baseline MR imaging underwent "finite elements analysis" to integrate information regarding plaque morphology, material properties of the plaque constituents, and patient-specific blood pressure during the computational simulations. The additional information provided by the stress factors, the authors' state, give a much more comprehensive assessment of plaque vulnerability compared with plaque morphology alone. This is especially useful in the subset of patients in whom there may be a history of neurological symptoms but who have a moderate degree of luminal stenosis. They report that plaques with hemorrhage or fibrous cap rupture had six to seven times greater likelihood of being associated with subsequent ischemic events, high structural stresses were seen to increase the chance of subsequent events by 13 times.

Further adaptation of currently used MR protocols in clinical studies look likely to refine the use of MR to evaluate prognostic risk, therapeutic effects, and the natural pathophysiology of carotid atherosclerosis with even greater reliability than currently seen. Future work incorporating stress analysis and plaque morphology with bigger patient sample sizes may well prove to be of vital importance in stratifying risk more accurately than the cumbersome luminal stenosis assessment by ultrasound. Such dynamic evaluation of vulnerable plaques could indicate another group of patients who may benefit from CEA, such as those who currently have mild to moderate degrees of luminal stenosis but have "high risk" plaque morphological characteristics and high stresses exerted on the plaques. Alternatively, using 3D volumetric MR measurements of vulnerable plaques, as suggested by [88] and Bianda et al. [84], may be another route for development of MR in imaging carotid atherosclerosis.

14 Conclusions

Current research is unanimous in its shift of focus from the stenosed lumens of atherosclerotic carotid arteries to the arterial wall characteristics that signify earlier phases in the pathophysiology of atherosclerotic plaque progression than the relatively late feature of luminal stenosis. Morphological features such as the vessel wall thickness, lipid-rich necrotic core, intraplaque hemorrhage, fibrous cap size, and disruption as well as biomechanical stress can all be reliably assessed with a variety of high-resolution MRI techniques which are well validated against histological measurements from the same plaques ex vivo. Even inflammatory characteristics of the wall, such as neovascularization and macrophage infiltration in the plaque can be visualized with the use of gadolinium contrast and ultrasmall superparamagnetic iron oxide-enhanced MRI.

As a result, the crude and outdated assessments of degree of lumen stenosis by modalities such as digital subtraction angiography and ultrasound have largely been replaced with MRI as the modality of choice to investigate further details in the pathophysiology of carotid atherosclerosis, to establish patient risk stratification on more sensitive characteristics, and to assess the efficacy of therapeutic interventions at a much earlier stage than previously possible. With newer molecular contrast media being developed to depict in even more detail the full functional history of carotid atherosclerotic plaques, MRI as a modality seems to be indispensable in the future management of this disease.

References

1. Fisher M (1951) Occlusion of the internal carotid artery. AMA Arch Neurol Psychiatry 65:346–377
2. Barnett HJ, Taylor DW, Eliasziw M, Fox AJ, Ferguson GG, Haynes RB, Rankin RN, Clagett GP, Hachinski VC, Sackett DL, Thorpe KE, Meldrum HE, Spence JD (1998) Benefit of carotid endarterectomy in patients with symptomatic moderate or severe stenosis. North American Symptomatic Carotid Endarterectomy Trial Collaborators. N Engl J Med 339:1415–1425
3. Hobson RW 2nd, Weiss DG, Fields WS, Goldstone J, Moore WS, Towne JB, Wright CB (1993) Efficacy of carotid endarterectomy for asymptomatic carotid stenosis. The Veterans Affairs Cooperative Study Group. N Engl J Med 328:221–227
4. Mayberg MR, Wilson SE, Yatsu F, Weiss DG, Messina L, Hershey LA, Colling C, Eskridge J, Deykin D, Winn HR (1991) Carotid endarterectomy and prevention of cerebral ischemia in symptomatic carotid stenosis. Veterans Affairs Cooperative Studies Program 309 Trialist Group. JAMA 266:3289–3294
5. (1998) Randomised trial of endarterectomy for recently symptomatic carotid stenosis: final results of the MRC European Carotid Surgery Trial (ECST). Lancet 351:1379–1387
6. Rothwell PM, Eliasziw M, Gutnikov SA, Fox AJ, Taylor DW, Mayberg MR, Warlow CP, Barnett HJ (2003) Analysis of pooled data from the randomised controlled trials of endarterectomy for symptomatic carotid stenosis. Lancet 361:107–116
7. (1995) Endarterectomy for asymptomatic carotid artery stenosis. Executive Committee for the Asymptomatic Carotid Atherosclerosis Study. JAMA 273:1421–1428
8. Halliday A, Mansfield A, Marro J, Peto C, Peto R, Potter J, Thomas D (2004) Prevention of disabling and fatal strokes by successful carotid endarterectomy in patients without recent neurological symptoms: randomised controlled trial. Lancet 363:1491–1502
9. Young GR, Humphrey PR, Shaw MD, Nixon TE, Smith ET (1994) Comparison of magnetic resonance angiography, duplex ultrasound, and digital subtraction angiography in assessment of extracranial internal carotid artery stenosis. J Neurol Neurosurg Psychiatry 57:1466–1478

10. Hankey GJ, Warlow CP, Molyneux AJ (1990) Complications of cerebral angiography for patients with mild carotid territory ischaemia being considered for carotid endarterectomy. J Neurol Neurosurg Psychiatry 53:542–548
11. Johnston DC, Chapman KM, Goldstein LB (2001) Low rate of complications of cerebral angiography in routine clinical practice. Neurology 57:2012–2014
12. Willinsky RA, Taylor SM, TerBrugge K, Farb RI, Tomlinson G, Montanera W (2003) Neurologic complications of cerebral angiography: prospective analysis of 2,899 procedures and review of the literature. Radiology 227:522–528
13. Glagov S, Weisenberg E, Zarins CK, Stankunavicius R, Kolettis GJ (1987) Compensatory enlargement of human atherosclerotic coronary arteries. N Engl J Med 316:1371–1375
14. Stary HC, Chandler AB, Glagov S, Guyton JR, Insull W Jr, Rosenfeld ME, Schaffer SA, Schwartz CJ, Wagner WD, Wissler RW (1994) A definition of initial, fatty streak, and intermediate lesions of atherosclerosis. A report from the Committee on Vascular Lesions of the Council on Arteriosclerosis, American Heart Association. Circulation 89:2462–2478
15. Stary HC, Chandler AB, Dinsmore RE, Fuster V, Glagov S, Insull W Jr, Rosenfeld ME, Schwartz CJ, Wagner WD, Wissler RW (1995) A definition of advanced types of atherosclerotic lesions and a histological classification of atherosclerosis. A report from the Committee on Vascular Lesions of the Council on Arteriosclerosis, American Heart Association. Circulation 92:1355–1374
16. Saam T, Hatsukami TS, Takaya N, Chu B, Underhill H, Kerwin WS, Cai J, Ferguson MS, Yuan C (2007) The vulnerable, or high-risk, atherosclerotic plaque: noninvasive MR imaging for characterization and assessment. Radiology 244:64–77
17. Stemme S, Faber B, Holm J, Wiklund O, Witztum JL, Hansson GK (1995) T lymphocytes from human atherosclerotic plaques recognize oxidized low density lipoprotein. Proc Natl Acad Sci USA 92:3893–3897
18. Yuan C, Zhang SX, Polissar NL, Echelard D, Ortiz G, Davis JW, Ellington E, Ferguson MS, Hatsukami TS (2002) Identification of fibrous cap rupture with magnetic resonance imaging is highly associated with recent transient ischemic attack or stroke. Circulation 105:181–185
19. Imparato AM, Riles TS, Gorstein F (1979) The carotid bifurcation plaque: pathologic findings associated with cerebral ischemia. Stroke 10:238–245
20. Moore WS, Hall AD (1968) Ulcerated atheroma of the carotid artery. A cause of transient cerebral ischemia. Am J Surg 116:237–242
21. Naghavi M, Libby P, Falk E, Casscells SW, Litovsky S, Rumberger J, Badimon JJ, Stefanadis C, Moreno P, Pasterkamp G, Fayad Z, Stone PH, Waxman S, Raggi P, Madjid M, Zarrabi A, Burke A, Yuan C, Fitzgerald PJ, Siscovick DS, de Korte CL, Aikawa M, Airaksinen KE, Assmann G, Becker CR, Chesebro JH, Farb A, Galis ZS, Jackson C, Jang IK, Koenig W, Lodder RA, March K, Demirovic J, Navab M, Priori SG, Rekhter MD, Bahr R, Grundy SM, Mehran R, Colombo A, Boerwinkle E, Ballantyne C, Insull W Jr, Schwartz RS, Vogel R, Serruys PW, Hansson GK, Faxon DP, Kaul S, Drexler H, Greenland P, Muller JE, Virmani R, Ridker PM, Zipes DP, Shah PK, Willerson JT (2003) From vulnerable plaque to vulnerable patient: a call for new definitions and risk assessment strategies: Part II. Circulation 108:1772–1778
22. Naghavi M, Libby P, Falk E, Casscells SW, Litovsky S, Rumberger J, Badimon JJ, Stefanadis C, Moreno P, Pasterkamp G, Fayad Z, Stone PH, Waxman S, Raggi P, Madjid M, Zarrabi A, Burke A, Yuan C, Fitzgerald PJ, Siscovick DS, de Korte CL, Aikawa M, Juhani Airaksinen KE, Assmann G, Becker CR, Chesebro JH, Farb A, Galis ZS, Jackson C, Jang IK, Koenig W, Lodder RA, March K, Demirovic J, Navab M, Priori SG, Rekhter MD, Bahr R, Grundy SM, Mehran R, Colombo A, Boerwinkle E, Ballantyne C, Insull W Jr, Schwartz RS, Vogel R, Serruys PW, Hansson GK, Faxon DP, Kaul S, Drexler H, Greenland P, Muller JE, Virmani R, Ridker PM, Zipes DP, Shah PK, Willerson JT (2003) From vulnerable plaque to vulnerable patient: a call for new definitions and risk assessment strategies: Part I. Circulation 108:1664–1672
23. Takaya N, Yuan C, Chu B, Saam T, Underhill H, Cai J, Tran N, Polissar NL, Isaac C, Ferguson MS, Garden GA, Cramer SC, Maravilla KR, Hashimoto B, Hatsukami TS (2006) Association between carotid plaque characteristics and subsequent ischemic cerebrovascular events: a prospective assessment with MRI – initial results. Stroke 37:818–823
24. Brown PB, Zwiebel WJ, Call GK (1989) Degree of cervical carotid artery stenosis and hemispheric stroke: duplex US findings. Radiology 170:541–543
25. Berliner JA, Navab M, Fogelman AM, Frank JS, Demer LL, Edwards PA, Watson AD, Lusis AJ (1995) Atherosclerosis: basic mechanisms. Oxidation, inflammation, and genetics. Circulation 91:2488–2496
26. Fisher M, Paganini-Hill A, Martin A, Cosgrove M, Toole JF, Barnett HJ, Norris J (2005) Carotid plaque pathology: thrombosis, ulceration, and stroke pathogenesis. Stroke 36:253–257
27. Garcia de Tena J (2005) Inflammation, atherosclerosis, and coronary artery disease. N Engl J Med 353:429–430, author reply 429–430
28. Hansson GK (2005) Inflammation, atherosclerosis, and coronary artery disease. N Engl J Med 352:1685–1695
29. Galis ZS, Khatri JJ (2002) Matrix metalloproteinases in vascular remodeling and atherogenesis: the good, the bad, and the ugly. Circ Res 90:251–262
30. Mofidi R, Crotty TB, McCarthy P, Sheehan SJ, Mehigan D, Keaveny TV (2001) Association between plaque instability, angiogenesis and symptomatic carotid occlusive disease. Br J Surg 88:945–950
31. Newby AC (2005) Dual role of matrix metalloproteinases (matrixins) in intimal thickening and atherosclerotic plaque rupture. Physiol Rev 85:1–31
32. Nighoghossian N, Derex L, Douek P (2005) The vulnerable carotid artery plaque: current imaging methods and new perspectives. Stroke 36:2764–2772
33. Cai JM, Hatsukami TS, Ferguson MS, Small R, Polissar NL, Yuan C (2002) Classification of human carotid atherosclerotic lesions with in vivo multicontrast magnetic resonance imaging. Circulation 106:1368–1373
34. Saam T, Ferguson MS, Yarnykh VL, Takaya N, Xu D, Polissar NL, Hatsukami TS, Yuan C (2005) Quantitative evaluation of carotid plaque composition by in vivo MRI. Arterioscler Thromb Vasc Biol 25:234–239
35. Virmani R, Kolodgie FD, Burke AP, Farb A, Schwartz SM (2000) Lessons from sudden coronary death: a comprehensive morphological classification scheme for atherosclerotic lesions. Arterioscler Thromb Vasc Biol 20:1262–1275
36. Hatsukami TS, Ross R, Polissar NL, Yuan C (2000) Visualization of fibrous cap thickness and rupture in human atherosclerotic carotid plaque in vivo with high-resolution magnetic resonance imaging. Circulation 102:959–964
37. Trivedi RA, U-King-Im JM, Graves MJ, Horsley J, Goddard M, Kirkpatrick PJ, Gillard JH (2004) MRI-derived measurements of fibrous-cap and lipid-core thickness: the potential for identifying vulnerable carotid plaques in vivo. Neuroradiology 46: 738–743
38. Cai J, Hatsukami TS, Ferguson MS, Kerwin WS, Saam T, Chu B, Takaya N, Polissar NL, Yuan C (2005) In vivo quantitative measurement of intact fibrous cap and lipid-rich necrotic core size in atherosclerotic carotid plaque: comparison of high-resolution, contrast-enhanced magnetic resonance imaging and histology. Circulation 112:3437–3444

39. Underhill HR, Hatsukami TS, Cai J, Yu W, Demarco JK, Polissar NL, Ota H, Zhao X, Dong L, Oikawa M, Yuan C (2010) A noninvasive imaging approach to assess plaque severity: the carotid atherosclerosis score. AJNR Am J Neuroradiol 31(6):1068–1075
40. Zhao XQ, Dong L, Hatsukami T, Phan BA, Chu B, Moore A, Lane T, Neradilek MB, Polissar N, Monick D, Lee C, Underhill H, Yuan C (2011) MR imaging of carotid plaque composition during lipid-lowering therapy a prospective assessment of effect and time course. JACC Cardiovasc Imaging 4:977–986
41. Spagnoli LG, Mauriello A, Sangiorgi G, Fratoni S, Bonanno E, Schwartz RS, Piepgras DG, Pistolese R, Ippoliti A, Holmes DR Jr (2004) Extracranial thrombotically active carotid plaque as a risk factor for ischemic stroke. JAMA 292:1845–1852
42. Chu B, Ferguson MS, Chen H, Hippe DS, Kerwin WS, Canton G, Yuan C, Hatsukami TS (2009) Magnetic [corrected] resonance imaging [corrected] features of the disruption-prone and the disrupted carotid plaque. JACC Cardiovasc Imaging 2:883–896
43. Qiao Y, Hallock KJ, Hamilton JA (2011) Magnetization transfer magnetic resonance of human atherosclerotic plaques ex vivo detects areas of high protein density. J Cardiovasc Magn Reson 13:73
44. Wang J, Ferguson MS, Balu N, Yuan C, Hatsukami TS, Bornert P (2010) Improved carotid intraplaque hemorrhage imaging using a slab-selective phase-sensitive inversion-recovery (SPI) sequence. Magn Reson Med 64:1332–1340
45. Corti R, Fayad ZA, Fuster V, Worthley SG, Helft G, Chesebro J, Mercuri M, Badimon JJ (2001) Effects of lipid-lowering by simvastatin on human atherosclerotic lesions: a longitudinal study by high-resolution, noninvasive magnetic resonance imaging. Circulation 104:249–252
46. Corti R, Fuster V, Fayad ZA, Worthley SG, Helft G, Smith D, Weinberger J, Wentzel J, Mizsei G, Mercuri M, Badimon JJ (2002) Lipid lowering by simvastatin induces regression of human atherosclerotic lesions: two years' follow-up by high-resolution noninvasive magnetic resonance imaging. Circulation 106:2884–2887
47. Kriszbacher I, Koppan M, Bodis J (2005) Inflammation, atherosclerosis, and coronary artery disease. N Engl J Med 353:429–430, author reply 429–430
48. Kerwin WS, O'Brien KD, Ferguson MS, Polissar N, Hatsukami TS, Yuan C (2006) Inflammation in carotid atherosclerotic plaque: a dynamic contrast-enhanced MR imaging study. Radiology 241:459–468
49. Kooi ME, Cappendijk VC, Cleutjens KB, Kessels AG, Kitslaar PJ, Borgers M, Frederik PM, Daemen MJ, van Engelshoven JM (2003) Accumulation of ultrasmall superparamagnetic particles of iron oxide in human atherosclerotic plaques can be detected by in vivo magnetic resonance imaging. Circulation 107:2453–2458
50. Trivedi RA, U-King-Im JM, Graves MJ, Kirkpatrick PJ, Gillard JH (2004) Noninvasive imaging of carotid plaque inflammation. Neurology 63:187–188
51. Yuan C, Kerwin WS, Ferguson MS, Polissar N, Zhang S, Cai J, Hatsukami TS (2002) Contrast-enhanced high resolution MRI for atherosclerotic carotid artery tissue characterization. J Magn Reson Imaging 15:62–67
52. EMA (2008) International Nonproprietary Name (INN): superparamagnetic iron oxide nanoparticles stabilised with dextran and sodium citrate
53. Schmitz SA, Coupland SE, Gust R, Winterhalter S, Wagner S, Kresse M, Semmler W, Wolf KJ (2000) Superparamagnetic iron oxide-enhanced MRI of atherosclerotic plaques in Watanabe hereditable hyperlipidemic rabbits. Invest Radiol 35:460–471
54. Schmitz SA, Taupitz M, Wagner S, Wolf KJ, Beyersdorff D, Hamm B (2001) Magnetic resonance imaging of atherosclerotic plaques using superparamagnetic iron oxide particles. J Magn Reson Imaging 14:355–361
55. Bulte JW, Brooks RA, Moskowitz BM, Bryant LH Jr, Frank JA (1999) Relaxometry and magnetometry of the MR contrast agent MION-46L. Magn Reson Med 42:379–384
56. Trivedi R, U-King-Im JM, Gillard J (2003) Accumulation of ultrasmall superparamagnetic particles of iron oxide in human atherosclerotic plaque. Circulation 108:e140, author reply e140
57. Trivedi RA, U-King-Im JM, Graves MJ, Cross JJ, Horsley J, Goddard MJ, Skepper JN, Quartey G, Warburton E, Joubert I, Wang L, Kirkpatrick PJ, Brown J, Gillard JH (2004) In vivo detection of macrophages in human carotid atheroma: temporal dependence of ultrasmall superparamagnetic particles of iron oxide-enhanced MRI. Stroke 35:1631–1635
58. Tang TY, Howarth SP, Miller SR, Graves MJ, U-King-Im JM, Li ZY, Walsh SR, Patterson AJ, Kirkpatrick PJ, Warburton EA, Varty K, Gaunt ME, Gillard JH (2008) Correlation of carotid atheromatous plaque inflammation using USPIO-enhanced MR imaging with degree of luminal stenosis. Stroke 39:2144–2147
59. Tang TY, Howarth SP, Li ZY, Miller SR, Graves MJ, U-king-Im JM, Trivedi RA, Walsh SR, Brown AP, Kirkpatrick PJ, Gaunt ME, Gillard JH (2008) Correlation of carotid atheromatous plaque inflammation with biomechanical stress: utility of USPIO enhanced MR imaging and finite element analysis. Atherosclerosis 196:879–887
60. Tang TY, Howarth SP, Miller SR, Graves MJ, Patterson AJ, U-King-Im JM, Li ZY, Walsh SR, Brown AP, Kirkpatrick PJ, Warburton EA, Hayes PD, Varty K, Boyle JR, Gaunt ME, Zalewski A, Gillard JH (2009) The ATHEROMA (atorvastatin therapy: effects on reduction of macrophage activity) study. Evaluation using ultrasmall superparamagnetic iron oxide-enhanced magnetic resonance imaging in carotid disease. J Am Coll Cardiol 53:2039–2050
61. Corti R, Fuster V, Fayad ZA, Worthley SG, Helft G, Chaplin WF, Muntwyler J, Viles-Gonzalez JF, Weinberger J, Smith DA, Mizsei G, Badimon JJ (2005) Effects of aggressive versus conventional lipid-lowering therapy by simvastatin on human atherosclerotic lesions: a prospective, randomized, double-blind trial with high-resolution magnetic resonance imaging. J Am Coll Cardiol 46:106–112
62. Underhill HR, Yuan C, Zhao XQ, Kraiss LW, Parker DL, Saam T, Chu B, Takaya N, Liu F, Polissar NL, Neradilek B, Raichlen JS, Cain VA, Waterton JC, Hamar W, Hatsukami TS (2008) Effect of rosuvastatin therapy on carotid plaque morphology and composition in moderately hypercholesterolemic patients: a high-resolution magnetic resonance imaging trial. Am Heart J 155(584):e1–e8
63. Simonetti OP, Finn JP, White RD, Laub G, Henry DA (1996) "Black blood" T2-weighted inversion-recovery MR imaging of the heart. Radiology 199:49–57
64. Yarnykh VL, Yuan C (2002) T1-insensitive flow suppression using quadruple inversion-recovery. Magn Reson Med 48:899–905
65. Moreno PR, Purushothaman KR, Fuster V, Echeverri D, Truszczynska H, Sharma SK, Badimon JJ, O'Connor WN (2004) Plaque neovascularization is increased in ruptured atherosclerotic lesions of human aorta: implications for plaque vulnerability. Circulation 110:2032–2038
66. Jackson A, O'Connor JP, Parker GJ, Jayson GC (2007) Imaging tumor vascular heterogeneity and angiogenesis using dynamic contrast-enhanced magnetic resonance imaging. Clin Cancer Res 13:3449–3459
67. Aoki S, Aoki K, Ohsawa S, Nakajima H, Kumagai H, Araki T (1999) Dynamic MR imaging of the carotid wall. J Magn Reson Imaging 9:420–427
68. Wasserman BA, Smith WI, Trout HH 3rd, Cannon RO 3rd, Balaban RS, Arai AE (2002) Carotid artery atherosclerosis: in vivo morphologic characterization with gadolinium-enhanced double-oblique MR imaging initial results. Radiology 223:566–573
69. Akella NS, Twieg DB, Mikkelsen T, Hochberg FH, Grossman S, Cloud GA, Nabors LB (2004) Assessment of brain

tumorangiogenesis inhibitors using perfusion magnetic resonance imaging: quality and analysis results of a phase I trial. J Magn Reson Imaging 20:913–922
70. Kerwin W, Hooker A, Spilker M, Vicini P, Ferguson M, Hatsukami T, Yuan C (2003) Quantitative magnetic resonance imaging analysis of neovasculature volume in carotid atherosclerotic plaque. Circulation 107:851–856
71. Briley-Saebo KC, Shaw PX, Mulder WJ, Choi SH, Vucic E, Aguinaldo JG, Witztum JL, Fuster V, Tsimikas S, Fayad ZA (2008) Targeted molecular probes for imaging atherosclerotic lesions with magnetic resonance using antibodies that recognize oxidation-specific epitopes. Circulation 117:3206–3215
72. Chen W, Vucic E, Leupold E, Mulder WJ, Cormode DP, Briley-Saebo KC, Barazza A, Fisher EA, Dathe M, Fayad ZA (2008) Incorporation of an apoE-derived lipopeptide in high-density lipoprotein MRI contrast agents for enhanced imaging of macrophages in atherosclerosis. Contrast Media Mol Imaging 3:233–242
73. Spuentrup E, Botnar RM, Wiethoff AJ, Ibrahim T, Kelle S, Katoh M, Ozgun M, Nagel E, Vymazal J, Graham PB, Gunther RW, Maintz D (2008) MR imaging of thrombi using EP-2104R, a fibrin-specific contrast agent: initial results in patients. Eur Radiol 18:1995–2005
74. Laitinen I, Saraste A, Weidl E, Poethko T, Weber AW, Nekolla SG, Leppanen P, Yla-Herttuala S, Holzlwimmer G, Walch A, Esposito I, Wester HJ, Knuuti J, Schwaiger M (2009) Evaluation of alphavbeta3 integrin-targeted positron emission tomography tracer 18F-galacto-RGD for imaging of vascular inflammation in atherosclerotic mice. Circ Cardiovasc Imaging 2:331–338
75. Mulder WJ, Strijkers GJ, Briley-Saboe KC, Frias JC, Aguinaldo JG, Vucic E, Amirbekian V, Tang C, Chin PT, Nicolay K, Fayad ZA (2007) Molecular imaging of macrophages in atherosclerotic plaques using bimodal PEG-micelles. Magn Reson Med 58:1164–1170
76. Nahrendorf M, Jaffer FA, Kelly KA, Sosnovik DE, Aikawa E, Libby P, Weissleder R (2006) Noninvasive vascular cell adhesion molecule-1 imaging identifies inflammatory activation of cells in atherosclerosis. Circulation 114:1504–1511
77. Lancelot E, Amirbekian V, Brigger I, Raynaud JS, Ballet S, David C, Rousseaux O, Le Greneur S, Port M, Lijnen HR, Bruneval P, Michel JB, Ouimet T, Roques B, Amirbekian S, Hyafil F, Vucic E, Aguinaldo JG, Corot C, Fayad ZA (2008) Evaluation of matrix metalloproteinases in atherosclerosis using a novel noninvasive imaging approach. Arterioscler Thromb Vasc Biol 28:425–432
78. Kaazempur-Mofrad MR, Isasi AG, Younis HF, Chan RC, Hinton DP, Sukhova G, LaMuraglia GM, Lee RT, Kamm RD (2004) Characterization of the atherosclerotic carotid bifurcation using MRI, finite element modeling, and histology. Ann Biomed Eng 32:932–946
79. Baldewsing RA, de Korte CL, Schaar JA, Mastik F, van der Steen AF (2004) Finite element modeling and intravascularultrasound elastography of vulnerable plaques: parameter variation. Ultrasonics 42:723–729
80. Trivedi RA, Li ZY, U-King-Im JM, Graves MJ, Kirkpatrick PJ, Gillard JH (2007) Identifying vulnerable carotid plaques in vivo using high resolution magnetic resonance imaging-based finite element analysis. J Neurosurg 107:536–542
81. Sadat U, Teng Z, Young VE, Li ZY, Gillard JH (2011) Utility of magnetic resonance imaging-based finite element analysis for the biomechanical stress analysis of hemorrhagic and non-hemorrhagic carotid plaques. Circ J 75:884–889
82. Li ZY, Tang TY, Jiang F, Zhang Y, Gillard JH (2011) Reduction in arterial wall strain with aggressive lipid-lowering therapy in patients with carotid artery disease. Circ J 75:1486–1492
83. Moody AR, Murphy RE, Morgan PS, Martel AL, Delay GS, Allder S, MacSweeney ST, Tennant WG, Gladman J, Lowe J, Hunt BJ (2003) Characterization of complicated carotid plaque with magnetic resonance direct thrombus imaging in patients with cerebral ischemia. Circulation 107:3047–3052
84. Bianda N, Di Valentino M, Periat D, Segatto JM, Oberson M, Moccetti M, Sudano I, Santini P, Limoni C, Froio A, Stuber M, Corti R, Gallino A, Wyttenbach R (2012) Progression of human carotid and femoral atherosclerosis: a prospective follow-up study by magnetic resonance vessel wall imaging. Eur Heart J 33:230–237
85. Fayad ZA, Mani V, Woodward M, Kallend D, Abt M, Burgess T, Fuster V, Ballantyne CM, Stein EA, Tardif JC, Rudd JH, Farkouh ME, Tawakol A (2011) Safety and efficacy of dalcetrapib on atherosclerotic disease using novel non-invasive multimodality imaging (dal-PLAQUE): a randomised clinical trial. Lancet 378:1547–1559
86. Yonemura A, Momiyama Y, Fayad ZA, Ayaori M, Ohmori R, Higashi K, Kihara T, Sawada S, Iwamoto N, Ogura M, Taniguchi H, Kusuhara M, Nagata M, Nakamura H, Tamai S, Ohsuzu F (2005) Effect of lipid-lowering therapy with atorvastatin on atherosclerotic aortic plaques detected by noninvasive magnetic resonance imaging. J Am Coll Cardiol 45:733–742
87. Lima JA, Desai MY, Steen H, Warren WP, Gautam S, Lai S (2004) Statin-induced cholesterol lowering and plaque regression after 6 months of magnetic resonance imaging-monitored therapy. Circulation 110:2336–2341
88. Yamaguchi M, Sasaki M, Ohba H, Mori K, Narumi S, Katsura N, Ohura K, Kudo K, Terayama Y (2012) Quantitative assessment of changes in carotid plaques during cilostazol administration using three-dimensional ultrasonography and non-gated magnetic resonance plaque imaging. Neuroradiology 54:939–945
89. Sadat U, Li ZY, Young VE, Graves MJ, Boyle JR, Warburton EA, Varty K, O'Brien E, Gillard JH (2010) Finite element analysis of vulnerable atherosclerotic plaques: a comparison of mechanical stresses within carotid plaques of acute and recently symptomatic patients with carotid artery disease. J Neurol Neurosurg Psychiatry 81:286–289

Part III

CT Atherosclerosis Imaging

Clinical CT Imaging of Carotid Arteries

10

Chandra dev Sahu and Max Wintermark

1 Introduction

Carotid artery atherosclerotic disease occurs frequently in the general population, with a prevalence of 75 % in men and 62 % in women over 64 years of age [1, 2]. It is the reported cause for 30 % of all ischemic strokes. As such, imaging assessment of the carotid arteries is an important component of the prevention and management of acute stroke [3, 4].

Computed tomography (CT), and CT-angiography in particular, have grown to occupy a preponderant role in the evaluation of carotid arteries, almost completely replacing diagnostic carotid angiograms. CT is widely available in the emergent setting because of its speed and relative safety and as such as become the imaging modality of choice in patients with acute cerebral ischemic symptoms. New generations of CT scanners can image the neck arteries from the aortic arch to the vertex in less than 15 s. This short acquisition times translates into few artifacts from patient motion and reduced contrast requirement with accurate timing of contrast [5]. CTA is non flow-dependent technique, and has high spatial resolution, which results into high accuracy for stenosis measurements and carotid plaque characterization. CTA can assess carotid arteries for near occlusion, tandem lesions, collateral flow, and concomitant intracranial atherosclerotic disease [5].

2 CTA Imaging Protocol

The CTA imaging protocol we are using at our institution for the cervical carotid arteries on our 64-slice scanner is as follows: number of activated detectors, 64; gantry rotation time, 0.5 s; caudocranial acquisition; collimation, 0.625 mm; pitch, 1.375:1; 120 kV; 200–350 mA; dose modulation with noise index of 4. Slices are reconstructed at 1.25-mm thickness with a 1-mm reconstruction interval for evaluation of the vasculature, while the 0.625-mm raw data images are used to create maximum-intensity-projection (MIP) images. Sections are also reconstructed at 2.5-mm thickness with a 2-mm reconstruction interval for evaluation of soft tissues.

For the above-described CTA acquisition, a bolus of 50 mL of iodinated contrast material is injected at a 5-mL/s injection rate followed by a 25-mL saline bolus chaser. For contrast material infusion, an 18-gauge intravenous catheter is typically used. We generally attempt to administer intravenous contrast material from a right-sided injection for two reasons. First, the left brachiocephalic vein takes a more transverse course into the superior vena cava, which produces a higher likelihood of undiluted contrast material obscuring the origins of the great vessels. Second, compression of the brachiocephalic vein by an ectatic aorta, which is especially common in elderly patients, can lead to contrast material pooling and subsequent reflux into neck veins [5].

Proper timing of contrast material administration is a key determinant of optimal arterial opacification and CTA image quality. With multidetector scanners of up to 16 sections, a fixed delay (e.g., 25 s) between contrast material injection and the start of scanning has been successfully used by some authors [6]. However, given the physiologic variability of blood flow among patients (especially those with cardiac dysfunction or vascular stenoses) and the very fast imaging times of 64-section CT, accurately timing the delay between contrast material administration and scanning initiation with either a bolus-tracking technique or a preprocedure timing bolus becomes important [7–9]. In bolus tracking, the main contrast material bolus is injected and then a designated vessel of interest is monitored in real-time with low-dose dynamic scanning. When a certain enhancement threshold is reached in the monitored vessel, the table moves to the start position and scanning begins. The main drawback of this technique is the inherent delay between when the threshold

C. dev Sahu, M.D • M. Wintermark, M.D (✉)
Diagnostic and Interventional Neuroradiology Division, Department of Radiology and Medical Imaging, University of Virginia, PO Box 800170, 1215 Lee Street, Charlottesville, VA 22903, USA
e-mail: cds9m@virginia.edu; mw4vh@virginia.edu

L. Saba et al. (eds.), *Multi-Modality Atherosclerosis Imaging and Diagnosis*,
DOI 10.1007/978-1-4614-7425-8_10,

value is reached and when scanning begins (approximately 4 s), as well as the delay in computer reconstruction of bolus-tracking images (2 s). The combined 6-s lag often requires that an increased amount of contrast material be injected.

In our opinion, the timing bolus approach is superior because CTA can be performed in pure arterial phase with optimal enhancement of the carotid and vertebral arteries and minimal enhancement in cervical veins. Also, there is no intrinsic delay with the timing-bolus approach; the volume of contrast material given for the CTA can be kept as low as possible (60 ml for CTA). Finally, the perfusion-CT series obtained prior to CTA can be used as a timing bolus, so no additional amount of contrast needs to be injected [5].

In a study that used a phantom model of carotid stenosis and nonionic contrast material, other authors have shown that contrast densities between 150 and 200 HU yield the most accurate assessments of stenoses on CTA [10]. With our carotid CTA protocol, high arterial opacification is achieved, with a mean arterial attenuation of approximately 310 HU [5].

Post-processing is performed by the technologist at the scanner or in the 3D laboratory. MIP images of the carotid bifurcations are obtained bilaterally in sagittal oblique planes, and MIP images of the origins of the great vessels and extracranial carotid arteries are obtained in the coronal plane. Additional computer-aided analysis of the degree of carotid artery stenosis is undertaken by using the North American Symptomatic Carotid Endarterectomy Trial (NASCET) criteria (described below).

The rapid acquisition of CTA images with modern CT scanners can generate a variety of flow artifacts, which are very important for radiologist to recognize in order not to be mislead by pseudodissection, pseudoocclusion, and pseudo venous thrombosis appearances [5].

The typical radiation dose with CTA is in the range of 5–7 milli-Sievert (mSv) [6]. Various methods can be used to reduce the radiation dose such as manipulation of acquisition parameters (KVp, pitch, gantry rotation time, and milliampere) and use of *x*–*y*–*z* axis modulation, in which the tube current applied within each section varies depending on the patient girth and attenuation at each level [11, 12].

3 Carotid Luminal Measurements Using CT

Luminal narrowing is the standard parameter to report on the extent and severity of carotid artery stenosis. The widespread use of this measure is based primarily on the results of several randomized clinical trials, including the NASCET [13], the European Carotid Surgery Trial (ECST) [14], and the Veterans Affairs Cooperative Studies Program trial [15]. These trials demonstrated a significant reduction in the risk of ischemic stroke in patients with luminal stenosis of ≥70 %, as assessed on conventional angiograms, after carotid endarterectomy compared with medical treatment alone. The degree of luminal narrowing has been traditionally measured on catheter angiography [16, 17]; however it is increasingly being measured using CTA and other noninvasive techniques [18, 19]. These have been shown to be equivalent to conventional angiograms in characterizing the degree of luminal narrowing [18, 20, 21].

Measuring the degree of luminal narrowing using CTA or MRA raises some issues in the clinical setting. First, several methods have been reported to characterize the degree of carotid stenosis, including the NACSET method (Fig. 10.1) [13, 22], the ECST method [14, 22], and the common carotid method [23], which differ as to the reference arterial segment used resulting in different percent measurements for the same absolute residual lumen [23–26]. Also, different visualization methods (MIP, volume rendering, surface-shaded display (SSD)) are available for the display of the same dataset [21, 27–31], adding to the variability of the luminal narrowing measurements. Furthermore, interobserver variability results since, in typical clinical practice, neuroradiologists simply "eyeball" the carotid artery lumen and only obtain quantitative measurements in a limited number of cases. The highest precision in measuring carotid stenosis is known to be attained by using magnified axial images and by getting measurements exactly perpendicular to the longitudinal axis of the vessel [19, 31]. Finally, the measurement of the luminal narrowing is influenced by the image quality and particularly by the quality of the contrast injection [32]. The proper window width and level must be used to avoid variability in quantifying carotid stenosis. Too narrow window may lead to overestimation of the degree of stenosis; a wide window is desirable for carotid artery stenosis evaluation.

An alternative method to calculating directly percent of stenosis has been proposed by Fox et al. [33] (Table 10.1). It consists of measuring the minimal luminal diameter in millimeters and infer the corresponding degree of stenosis. A minimal lumen of 1.3 mm corresponds with 70 % stenosis and a minimal lumen of 2.2 mm with 50 % stenosis [34].

Recently, software has become available on post-processing workstations that performs semiautomatic segmentation of the carotid artery lumen on CTA studies and automatic quantitative measurements of diameter and area. This approach could potentially alleviate some of the limitations listed above, and the use of such software has recently been validated [35].

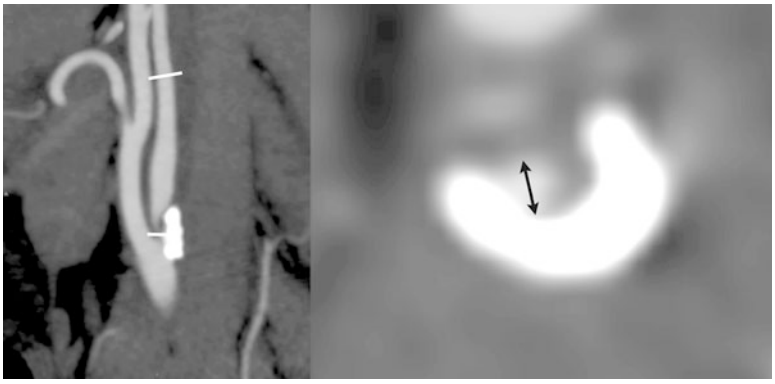

Fig. 10.1 Measuring the degree of luminal narrowing using the NASCET method involves measuring the minimal residual lumen diameter at the level of maximal stenosis (*double arrow*), measuring the lumen diameter at the level of the distal cervical internal carotid artery, and reporting the difference of the two as a percentage of the later

Table 10.1 Correspondence between minimal luminal diameter in millimeters and degree of stenosis in %, as proposed by Fox et al. [33]

Stenosis (mm)	Stenosis (%)
2.2	**50–55**
2.0	54–59
1.7	61–66
1.5	66–70
1.3	**70–74**
1.0	77–80
0.9	80–82
0.6	86–88
0.4	91–92
0.2	95–96

4 Carotid Wall Characterization Using CT

The widespread use of the luminal narrowing to assess the severity of carotid artery stenosis is based primarily on the results of several randomized clinical trials that demonstrated a reduction in the risk of ischemic stroke in patients with luminal stenosis of ≥70 % (assessed on conventional angiograms), after carotid endarterectomy compared with medical treatment alone [13, 15, 22]. However, ≥70 %-carotid stenosis occurs in fewer than 10 % of patients, whereas <70 %-carotid stenosis is extremely frequent in the general population (70 % in men and 60 % in women over 64 years of age) [1, 2]. In patients with <70 % carotid stenosis, high-resolution lumenography fails to provide any insight into the associated risk of stroke, because angiography is able to detect atherosclerosis only when >40 % of the area of the vessel wall is occupied by the plaque [36].

Luminal narrowing on conventional angiogram is only an indirect measure of the carotid atherosclerosis process as it occurs in the vessel wall, not the lumen. Angiography is not able to detect atherosclerosis at early stages because luminal narrowing begins only when >40 % of the vessel wall is occupied by plaque [36, 37]. However, plaque complications that result in strokes can occur in these early stages of atherosclerosis, a phenomenon that has also been described for coronary arteries (where a significant proportion of acute myocardial infarcts occur as a result of plaque rupture in coronary arteries with normal or subcritical narrowing) [38, 39]. For this reason, parameters other than luminal narrowing are needed to predict the risk of stroke more reliably, particularly in patients with <70 % stenosis. Plaque morphology and composition have been suggested as a complement to luminal narrowing measurements for assessing carotid atherosclerotic disease, giving rise to the concept of "vulnerable plaque" [40–44]. A number of carotid plaque morphological features have been suggested as potential markers of the "vulnerable plaque" and are possibly associated with an increased risk of stroke, the most studied of which being the common carotid artery (CCA) intima–media thickness [1, 2, 45–49]. Also, embolic phenomena have been reported as being associated with thinning and subsequent ulceration of the fibrous cap on the surface of the atherosclerotic plaque [40, 44, 50–52] resulting in release into the parent vessel of necrotic lipoid debris from the plaque substance, especially in the case of a high plaque lipid content [53, 54]. On the contrary, carotid plaque calcifications appear to be protective [55, 56].

Noninvasive in vivo imaging of carotid atherosclerotic plaques holds considerable promise for clinical decision-making and treatment [53, 57, 58]. Such imaging has classically been achieved using ultrasound [1, 2, 45–49] and also magnetic resonance imaging (MRI) [13, 59–64].

More recently, the ability of modern, multidetector-row, isotropic resolution CTA (Fig. 10.2) studies to assess the histological composition (including non-calcified components) and characteristics of carotid artery atherosclerotic plaques were demonstrated, using histology as the gold standard. In this study, there was 72.6 % agreement between

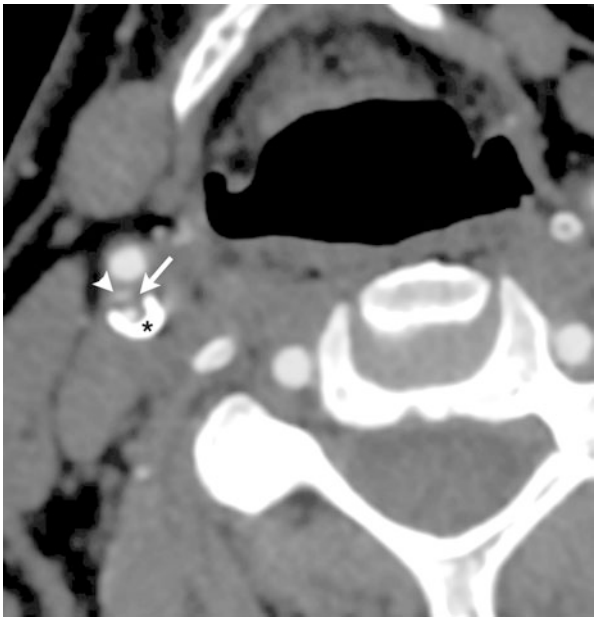

Fig. 10.2 CTA image showing a complex plaque at the right internal carotid artery bulb, with an ulceration (*arrowhead*), lipid-rich necrotic plaque (*arrow*), and calcified plaque (*star*)

CTA and histology for carotid plaque classification, perfect concordance for calcifications, and good correlation with histology for large lipid cores. CTA was also accurate in the detection of ulcerations and in the measurement of fibrous cap thickness [51]. Utilizing the standardized, computerized assessment of CTA studies described above, Wintermark et al. performed a retrospective, cross-sectional study to identify the CT features of carotid atherosclerotic plaques that were significantly associated with the occurrence of ischemic stroke [65]. This study revealed that a small number of carotid wall CT features were significantly associated with acute carotid stroke. Specifically, increased risk of acute carotid stroke was associated with an increased wall volume, a thinner fibrous cap, a higher number of lipid clusters, and lipid clusters closer to the lumen [65]. The number of calcium clusters was a protective factor [65]. Unfortunately, there were several limitations to the pilot study. The design of the study was cross-sectional, and it involved only a small number of patients. The authors concluded that their results needed to be confirmed in a large cohort study.

In a subsequent study, involving a retrospective cohort of a large sample of patients, 14 patients who developed a new, carotid ischemic stroke between the time when they underwent their baseline CTA of the neck and a follow-up imaging study of the brain were identified. Three risk factors that would predict 10 of the 14 carotid ischemic strokes were identified, including two clinical risk factors (age ≥ 75 and antihypertensive treatment) and one CT feature of carotid atherosclerotic disease—the maximal carotid wall thickness > 4 mm. This new rule appears straightforward to remember and apply clinically.

5 Conclusion

A better understanding of the role of carotid plaque components in predicting ischemic stroke will be important in designing future treatment trials for carotid artery stenosis. A decade ago, studies demonstrated a clear advantage in certain populations of endarterectomy compared with medical therapy. However, these studies were conducted before the widespread use of medical treatments that have been demonstrated to reduce stroke risk in patients with vascular disease, such as clopidogrel; extended-release dipyridamole; and aspirin, statins, and more aggressive blood pressure control [66].

With the development of both improved medical therapy and less invasive percutaneous stenting approaches over the last few years, some of the same questions must be addressed again [1]. Should our hypotheses prove correct, these results will provide a relevant, standardized, and validated method of interpreting the carotid artery wall findings using a routine imaging technique that could be used in future trials to monitor the carotid wall composition, both to select patients for treatment and to determine whether drug treatments are effective in altering the size and composition of the atheroma.

References

1. O'Leary DH, Polak JF, Kronmal RA et al (1992) Distribution and correlates of sonographically detected carotid artery disease in the Cardiovascular Health Study. The CHS Collaborative Research Group. Stroke 23(12):1752–1760
2. Ebrahim S, Papacosta O, Whincup P et al (1999) Carotid plaque, intima media thickness, cardiovascular risk factors, and prevalent cardiovascular disease in men and women: the British Regional Heart Study. Stroke 30(4):841–850
3. Pasternak RC, Criqui MH, Benjamin EJ et al (2004) Atherosclerotic vascular disease conference: Writing Group I: epidemiology. Circulation 109(21):2605–2612
4. Faxon DP, Fuster V, Libby P et al (2004) Atherosclerotic vascular disease conference: Writing Group III: pathophysiology. Circulation 109(21):2617–2625
5. Kim JJ, Dillon WP, Glastonbury CM, Provenzale JM, Wintermark M (2010) Sixty-four-section multidetector CT angiography of carotid arteries: a systematic analysis of image quality and artifacts. AJNR Am J Neuroradiol 31(1):91–99
6. González RG, Hirsch JA, Koroshetz WJ, Lev M, Schaefer PW, SpringerLink (Online service) (2006) Acute ischemic stroke imaging and intervention. Springer, Berlin
7. Bae KT (2005) Test-bolus versus bolus-tracking techniques for CT angiographic timing. Radiology 236(1):369–370, author reply 370
8. Cademartiri F, Nieman K, van der Lugt A et al (2004) Intravenous contrast material administration at 16-detector row helical CT coronary angiography: test bolus versus bolus-tracking technique. Radiology 233(3):817–823

9. Hallett RL, Fleischmann D (2006) Tools of the trade for CTA: MDCT scanners and contrast medium injection protocols. Tech Vasc Interv Radiol 9(4):134–142
10. Claves JL, Wise SW, Hopper KD, Tully D, Ten Have TR, Weaver J (1997) Evaluation of contrast densities in the diagnosis of carotid stenosis by CT angiography. AJR Am J Roentgenol 169(2):569–573
11. Smith AB, Dillon WP, Gould R, Wintermark M (2007) Radiation dose-reduction strategies for neuroradiology CT protocols. AJNR Am J Neuroradiol 28(9):1628–1632
12. Smith AB, Dillon WP, Lau BC et al (2008) Radiation dose reduction strategy for CT protocols: successful implementation in neuroradiology section. Radiology 247(2):499–506
13. Barnett HJ, Taylor DW, Eliasziw M et al (1998) Benefit of carotid endarterectomy in patients with symptomatic moderate or severe stenosis. North American Symptomatic Carotid Endarterectomy Trial Collaborators. N Engl J Med 339(20):1415–1425
14. (1998) Randomised trial of endarterectomy for recently symptomatic carotid stenosis: final results of the MRC European Carotid Surgery Trial (ECST). Lancet 351(9113):1379–1387
15. Mayberg MR, Wilson SE, Yatsu F et al (1991) Carotid endarterectomy and prevention of cerebral ischemia in symptomatic carotid stenosis. Veterans Affairs Cooperative Studies Program 309 Trialist Group. JAMA 266(23):3289–3294
16. Eliasziw M, Fox AJ, Sharpe BL, Barnett HJ (1997) Carotid artery stenosis: external validity of the North American Symptomatic Carotid Endarterectomy Trial measurement method. Radiology 204(1):229–233
17. Gagne PJ, Matchett J, MacFarland D et al (1996) Can the NASCET technique for measuring carotid stenosis be reliably applied outside the trial? J Vasc Surg 24(3):449–455, discussion 455–446
18. Young GR, Humphrey PR, Shaw MD, Nixon TE, Smith ET (1994) Comparison of magnetic resonance angiography, duplex ultrasound, and digital subtraction angiography in assessment of extracranial internal carotid artery stenosis. J Neurol Neurosurg Psychiatry 57(12):1466–1478
19. Anderson GB, Ashforth R, Steinke DE, Ferdinandy R, Findlay JM (2000) CT angiography for the detection and characterization of carotid artery bifurcation disease. Stroke 31(9):2168–2174
20. Berg M, Zhang Z, Ikonen A et al (2005) Multi-detector row CT angiography in the assessment of carotid artery disease in symptomatic patients: comparison with rotational angiography and digital subtraction angiography. AJNR Am J Neuroradiol 26(5):1022–1034
21. Marks MP, Napel S, Jordan JE, Enzmann DR (1993) Diagnosis of carotid artery disease: preliminary experience with maximum-intensity-projection spiral CT angiography. AJR Am J Roentgenol 160(6):1267–1271
22. (1991) Beneficial effect of carotid endarterectomy in symptomatic patients with high-grade carotid stenosis. North American Symptomatic Carotid Endarterectomy Trial Collaborators. N Engl J Med 325(7):445–453
23. Bladin CF, Alexandrova NA, Murphy J, Alexandrov AV, Maggisano R, Norris JW (1996) The clinical value of methods to measure carotid stenosis. Int Angiol 15(4):295–299
24. Rothwell PM, Gibson RJ, Slattery J, Sellar RJ, Warlow CP (1994) Equivalence of measurements of carotid stenosis. A comparison of three methods on 1001 angiograms. European Carotid Surgery Trialists' Collaborative Group. Stroke 25(12):2435–2439
25. Rothwell PM, Gibson RJ, Slattery J, Warlow CP (1994) Prognostic value and reproducibility of measurements of carotid stenosis. A comparison of three methods on 1001 angiograms. European Carotid Surgery Trialists' Collaborative Group. Stroke 25(12):2440–2444
26. Eliasziw M, Smith RF, Singh N, Holdsworth DW, Fox AJ, Barnett HJ (1994) Further comments on the measurement of carotid stenosis from angiograms. North American Symptomatic Carotid Endarterectomy Trial (NASCET) Group. Stroke 25(12):2445–2449
27. Marcus CD, Ladam-Marcus VJ, Bigot JL, Clement C, Baehrel B, Menanteau BP (1999) Carotid arterial stenosis: evaluation at CT angiography with the volume-rendering technique. Radiology 211(3):775–780
28. Leclerc X, Godefroy O, Pruvo JP, Leys D (1995) Computed tomographic angiography for the evaluation of carotid artery stenosis. Stroke 26(9):1577–1581
29. Leclerc X, Godefroy O, Lucas C et al (1999) Internal carotid arterial stenosis: CT angiography with volume rendering. Radiology 210(3):673–682
30. De Marco JK, Nesbit GM, Wesbey GE, Richardson D (1994) Prospective evaluation of extracranial carotid stenosis: MR angiography with maximum-intensity projections and multiplanar reformation compared with conventional angiography. AJR Am J Roentgenol 163(5):1205–1212
31. Dix JE, Evans AJ, Kallmes DF, Sobel AH, Phillips CD (1997) Accuracy and precision of CT angiography in a model of carotid artery bifurcation stenosis. AJNR Am J Neuroradiol 18(3):409–415
32. Rothwell PM, Gibson RJ, Villagra R, Sellar R, Warlow CP (1998) The effect of angiographic technique and image quality on the reproducibility of measurement of carotid stenosis and assessment of plaque surface morphology. Clin Radiol 53(6):439–443
33. Bartlett ES, Walters TD, Symons SP, Aviv RI, Fox AJ (2008) Classification of carotid stenosis by millimeter CT angiography measures: effects of prevalence and gender. AJNR Am J Neuroradiol 29(9):1677–1683
34. Bartlett ES, Walters TD, Symons SP, Fox AJ (2006) Quantification of carotid stenosis on CT angiography. AJNR Am J Neuroradiol 27(1):13–19
35. Wintermark M, Glastonbury C, Tong E et al (2008) Semi-automated computer assessment of the degree of carotid artery stenosis compares favorably to visual evaluation. J Neurol Sci 269(1–2):74–79
36. Glagov S, Weisenberg E, Zarins CK, Stankunavicius R, Kolettis GJ (1987) Compensatory enlargement of human atherosclerotic coronary arteries. N Engl J Med 316(22):1371–1375
37. Corti R, Fayad ZA, Fuster V et al (2001) Effects of lipid-lowering by simvastatin on human atherosclerotic lesions: a longitudinal study by high-resolution, noninvasive magnetic resonance imaging. Circulation 104(3):249–252
38. Falk E (1991) Coronary thrombosis: pathogenesis and clinical manifestations. Am J Cardiol 68(7):28B–35B
39. Fuster V, Stein B, Ambrose JA, Badimon L, Badimon JJ, Chesebro JH (1990) Atherosclerotic plaque rupture and thrombosis. Evolving concepts. Circulation 82(3 Suppl):II47–59
40. Ballotta E, Da Giau G, Renon L (2000) Carotid plaque gross morphology and clinical presentation: a prospective study of 457 carotid artery specimens. J Surg Res 89(1):78–84
41. Lovett JK, Gallagher PJ, Hands LJ, Walton J, Rothwell PM (2004) Histological correlates of carotid plaque surface morphology on lumen contrast imaging. Circulation 110(15):2190–2197
42. McCarthy MJ, Loftus IM, Thompson MM et al (1999) Angiogenesis and the atherosclerotic carotid plaque: an association between symptomatology and plaque morphology. J Vasc Surg 30(2):261–268
43. Naghavi M, Libby P, Falk E et al (2003) From vulnerable plaque to vulnerable patient: a call for new definitions and risk assessment strategies: Part I. Circulation 108(14):1664–1672
44. Rothwell PM, Gibson R, Warlow CP (2000) Interrelation between plaque surface morphology and degree of stenosis on carotid angiograms and the risk of ischemic stroke in patients with symptomatic carotid stenosis. On behalf of the European Carotid Surgery Trialists' Collaborative Group. Stroke 31(3):615–621

45. Bonithon-Kopp C, Scarabin PY, Taquet A, Touboul PJ, Malmejac A, Guize L (1991) Risk factors for early carotid atherosclerosis in middle-aged French women. Arterioscler Thromb 11(4):966–972
46. Bonithon-Kopp C, Touboul PJ, Berr C et al (1996) Relation of intima-media thickness to atherosclerotic plaques in carotid arteries. The Vascular Aging (EVA) Study. Arterioscler Thromb Vasc Biol 16(2):310–316
47. Lorenz MW, von Kegler S, Steinmetz H, Markus HS, Sitzer M (2006) Carotid intima-media thickening indicates a higher vascular risk across a wide age range: prospective data from the Carotid Atherosclerosis Progression Study (CAPS). Stroke 37(1):87–92
48. O'Leary DH, Polak JF, Kronmal RA, Manolio TA, Burke GL, Wolfson SK Jr (1999) Carotid-artery intima and media thickness as a risk factor for myocardial infarction and stroke in older adults. Cardiovascular Health Study Collaborative Research Group. N Engl J Med 340(1):14–22
49. Zureik M, Touboul PJ, Bonithon-Kopp C et al (1999) Cross-sectional and 4-year longitudinal associations between brachial pulse pressure and common carotid intima-media thickness in a general population. The EVA study. Stroke 30(3):550–555
50. Prabhakaran S, Rundek T, Ramas R et al (2006) Carotid plaque surface irregularity predicts ischemic stroke: the northern Manhattan study. Stroke 37(11):2696–2701
51. Wintermark M, Jawadi SS, Rapp JH et al (2008) High-resolution CT imaging of carotid artery atherosclerotic plaques. AJNR Am J Neuroradiol 29(5):875–882
52. Troyer A, Saloner D, Pan XM, Velez P, Rapp JH (2002) Major carotid plaque surface irregularities correlate with neurologic symptoms. J Vasc Surg 35(4):741–747
53. Bassiouny HS, Sakaguchi Y, Mikucki SA et al (1997) Juxtalumenal location of plaque necrosis and neoformation in symptomatic carotid stenosis. J Vasc Surg 26(4):585–594
54. Biasi GM, Froio A, Diethrich EB et al (2004) Carotid plaque echolucency increases the risk of stroke in carotid stenting: the Imaging in Carotid Angioplasty and Risk of Stroke (ICAROS) Study. Circulation 110(6):756–762
55. McKinney AM, Casey SO, Teksam M et al (2005) Carotid bifurcation calcium and correlation with percent stenosis of the internal carotid artery on CT angiography. Neuroradiology 47(1):1–9
56. Nandalur KR, Hardie AD, Raghavan P, Schipper MJ, Baskurt E, Kramer CM (2007) Composition of the stable carotid plaque: insights from a multidetector computed tomography study of plaque volume. Stroke 38(3):935–940
57. Carr S, Farb A, Pearce WH, Virmani R, Yao JS (1996) Atherosclerotic plaque rupture in symptomatic carotid artery stenosis. J Vasc Surg 23(5):755–765, discussion 765–756
58. Glagov S, Bassiouny HS, Giddens DP, Zarins CK (1995) Pathobiology of plaque modeling and complication. Surg Clin North Am 75(4):545–556
59. Adame IM, van der Geest RJ, Wasserman BA, Mohamed MA, Reiber JH, Lelieveldt BP (2004) Automatic segmentation and plaque characterization in atherosclerotic carotid artery MR images. MAGMA 16(5):227–234
60. Clarke SE, Hammond RR, Mitchell JR, Rutt BK (2003) Quantitative assessment of carotid plaque composition using multicontrast MRI and registered histology. Magn Reson Med 50(6):1199–1208
61. Coombs BD, Rapp JH, Ursell PC, Reilly LM, Saloner D (2001) Structure of plaque at carotid bifurcation: high-resolution MRI with histological correlation. Stroke 32(11):2516–2521
62. Shinnar M, Fallon JT, Wehrli S et al (1999) The diagnostic accuracy of ex vivo MRI for human atherosclerotic plaque characterization. Arterioscler Thromb Vasc Biol 19(11):2756–2761
63. Worthley SG, Helft G, Fuster V et al (2000) Serial in vivo MRI documents arterial remodeling in experimental atherosclerosis. Circulation 101(6):586–589
64. Yuan C, Mitsumori LM, Ferguson MS et al (2001) In vivo accuracy of multispectral magnetic resonance imaging for identifying lipid-rich necrotic cores and intraplaque hemorrhage in advanced human carotid plaques. Circulation 104(17):2051–2056
65. Wintermark M, Arora S, Tong E et al (2008) Carotid plaque computed tomography imaging in stroke and nonstroke patients. Ann Neurol 64(2):149–157
66. Cunningham EJ, Bond R, Mehta Z, Mayberg MR, Warlow CP, Rothwell PM (2002) Long-term durability of carotid endarterectomy for symptomatic stenosis and risk factors for late postoperative stroke. Stroke 33(11):2658–2663

Quantitative CT Imaging of Carotid Arteries

11

Max J. van Gils, K. Hameeteman, M. van Straten, W.J. Niessen, and Aad van der Lugt

1 Background

Stroke is the second leading cause of mortality in the Western world after coronary heart disease. Although stroke death rate declined to 44 % in the last decade, the burden of disease remains high [1]. Of all strokes, 87 % are ischemic, 10 % are intracerebral hemorrhage and 3 % are subarachnoid hemorrhage strokes [1]. About 50 % of the ischemic strokes are due to atherosclerotic disease, which is preferentially located in the carotid artery [2].

Till now, the degree of luminal narrowing of the carotid arteries, caused by atherosclerosis, has been the only image-based risk factor for (recurrent) stroke that is used in therapeutic decision making. Large, randomized clinical trials (the North American Symptomatic Carotid Endarterectomy Trial (NASCET) and the European Carotid Surgery Trial (ECST)) have established the imaging criteria for surgical treatment in symptomatic patients. Carotid endarterectomy (CEA) is indicated for symptomatic patients with high-grade stenosis (>70 %) and in selected patients with recent symptoms and moderate stenosis (50–69 %) [3–5]. In asymptomatic carotid artery stenosis, a modest benefit of CEA is described in selected patient groups (relatively young male patients) who had a severe stenosis [6–8]. However, most patients with a stenosis >70 % are asymptomatic and most symptomatic patients have a carotid stenosis <70 %, which suggest that other factors play an important role in the pathophysiological cascade of ischemic stroke. Especially in the group of patients with moderate carotid stenosis, it is of clinical importance to improve risk prediction.

The last decades, extensive research has been performed to increase our knowledge of the pathophysiology of atherosclerosis. Apart from luminal narrowing of the carotid artery resulting in blood flow compromise, rupture of the atherosclerotic plaque and subsequent thromboembolism is thought to result in ischemic events. Histological studies of coronary arteries and carotid arteries have found that certain atherosclerotic plaque characteristics increase the vulnerability of the plaque to rupture. Inflammation is the hallmark of vulnerability and plaques with active inflammation may be identified by extensive macrophage infiltration. Plaques with a thin cap of <100 μm and a lipid core accounting for >40 % of total plaque volume are also considered highly vulnerable. Plaques with a fissured or ruptured cap are prone to thrombosis and thromboembolization [9]. Carotid plaque ulcerations on digital subtraction angiography (DSA) have been associated with plaque rupture [10] and with an increased risk of acute recurrent ischemic events [11, 12]. Advanced invasive and noninvasive imaging technologies enable the visualization of these atherosclerotic plaque characteristics in vivo.

DSA has long been the modality of choice for imaging carotid arteries, since it accurately visualizes the vascular lumen and its contours. However, DSA has several

Max J. van Gils (✉) • M. van Straten • Aad van der Lugt
Department of Radiology, Erasmus MC, University Medical Center Rotterdam, 'sGravendijkwal 230, 3015 CE Rotterdam, The Netherlands
e-mail: m.j.vangils@erasmusmc.nl; a.vanderlugt@erasmusmc.nl; marcel.vanstraten@erasmusmc.nl

K. Hameeteman
Biomedical Imaging Group Rotterdam, Department of Radiology, Erasmus MC, University Medical Center Rotterdam, Rotterdam, The Netherlands

Biomedical Imaging Group Rotterdam, Department of Medical Informatics, Erasmus MC, University Medical Center Rotterdam, Rotterdam, The Netherlands
e-mail: k.hameeteman@erasmusmc.nl

W.J. Niessen
Biomedical Imaging Group Rotterdam, Department of Radiology, Erasmus MC, University Medical Center Rotterdam, Rotterdam, The Netherlands

Biomedical Imaging Group Rotterdam, Department of Medical Informatics, Erasmus MC, University Medical Center Rotterdam, Rotterdam, The Netherlands

Imaging Science and Technology, Delft University of Technology, Delft, The Netherlands
e-mail: w.niessen@erasmusmc.nl

L. Saba et al. (eds.), *Multi-Modality Atherosclerosis Imaging and Diagnosis*,
DOI 10.1007/978-1-4614-7425-8_11,

disadvantages: it is invasive, laborious, time intensive, and expensive. Moreover, DSA requires skilled operators and is therefore less readily available. More importantly, cerebrovascular DSA has a non-negligible morbidity and mortality, with a complication rate of 0.4–12.2 % for neurological deficits [13, 14]. These drawbacks and the increasing interest in the arterial vessel wall have driven the use of other, less invasive modalities for imaging the carotid arteries.

Nowadays, noninvasive imaging techniques like duplex ultrasound (DUS), magnetic resonance imaging (MRI), and computed tomography (CT) not only enable grading of carotid stenosis but also provide a window to the atherosclerotic process in vivo [15]. They also allow for the quantification of plaque measures like plaque burden and plaque composition.

Using serial imaging, the early natural development of the atherosclerotic plaque can now be studied in vivo. Furthermore, it provides a tool to monitor changes in atherosclerotic plaque in response to secondary preventive therapies. The development of new pharmaceutical therapies is a slow and costly process, since the most reliable way to measure their clinical impact is to study its effect on clinical endpoints. The use of imaging biomarkers of atherosclerotic disease could speed up this process and reduce the number of subjects studied. For an effective use, imaging biomarkers should be derived in a robust, noninvasive way and the imaging modality should be broadly available [16]. Further, standardized image acquisition parameters and post-processing methods are required and the imaging biomarkers should be carefully validated and highly reproducible. The changes in an imaging biomarker should be correlated to the biological effect and the clinical endpoints [16]. Quantification, and especially automated quantification, of the degree of stenosis and atherosclerotic plaque measures is therefore important in the development of reliable surrogate endpoints for atherosclerosis.

Computed tomography angiography (CTA) is a potential imaging modality for monitoring atherosclerosis in vivo. It is a readily available and fast imaging technique causing minimal inconvenience for the patient. Although CTA involves potentially harmful ionizing radiation, the effective dose during a diagnostic CTA is relatively low (1–5 mSv) [17]. The increased acquisition speed of multidetector CT angiography (MDCTA) reduces motion artifacts. Current multidetector row CTA enables fast vascular imaging from the aortic arch to the intracranial vessels. This enables simultaneous investigation of other vascular territories, which makes that MDCTA can compete with other noninvasive imaging techniques and is increasingly used in the clinical evaluation of stroke patients. In this chapter, the state-of-the-art CTA technique used to evaluate carotid artery stenosis and atherosclerotic plaque is described.

2 Luminal Imaging Using CTA

2.1 Technical Aspects

In the early 1990s spiral CT was introduced, which enabled a volumetric data acquisition through continuous X-ray source rotation and simultaneous continuous table movement. Using this technique noninvasive imaging of blood vessels became widely available. The steady increase of the longitudinal coverage of the X-ray detectors, i.e., the number of slices, even further improved the feasibility of luminography.

Contrast material is necessary for the visualization of the lumen. Stenosis measurement relies upon the contrast difference between the lumen and its environment. Several technical factors should be taken into account when imaging vessel lumen using MDCTA.

The contrast difference between lumen and surrounding tissue is varying and depends mainly on the amount of lumen attenuation which is artificially increased by contrast material. The attenuation caused by contrast material can vary depending on patient-related factors like cardiac output and weight and on scan parameters and contrast protocol-specific factors. Peak tube voltage (kVp) influences the difference in HU values between different tissues. The lumen contrast density increases as tube voltage decreases. The lumen enhancement pattern is determined by the injection volume, the injection rate, and the iodine concentration in the contrast material [18]. Timing of contrast bolus arrival should be such that a maximum contrast density is achieved in the carotid artery with a concomitant low contrast density in the neighboring jugular vein. Use of a saline bolus chaser reduces the amount of contrast material needed by 20–40 % and reduces the extent of perivenous artifacts caused by a high contrast density in the jugular vein [18]. Synchronization between passage of the contrast bolus and data acquisition can be achieved by real-time bolus tracking at the level of the ascending aorta. Moreover, a craniocaudal scan direction also reduces contrast material-related perivenous artifacts [19]. The contrast injection protocol for carotid artery imaging is generally standardized with a fixed contrast volume of 80–125 mL (iodine concentration of >300 mg/mL) and a saline bolus chaser of 40 mL, both at an injection rate of 2–4 mL/s. The disadvantage of intravenous contrast in CT angiography remains its limited application in patients with renal insufficiency and hyperthyroidism.

Because of the limited spatial resolution of the CT scanner partial volume averaging occurs, leading to the so-called blooming artifact. This is easily appreciated at the boundary of the enhanced lumen and the vessel wall where differences in density are large. In subtle cases this is reflected in a blurred interface between structures as well. Partial volume averaging may influence the appreciation of the real lumi-

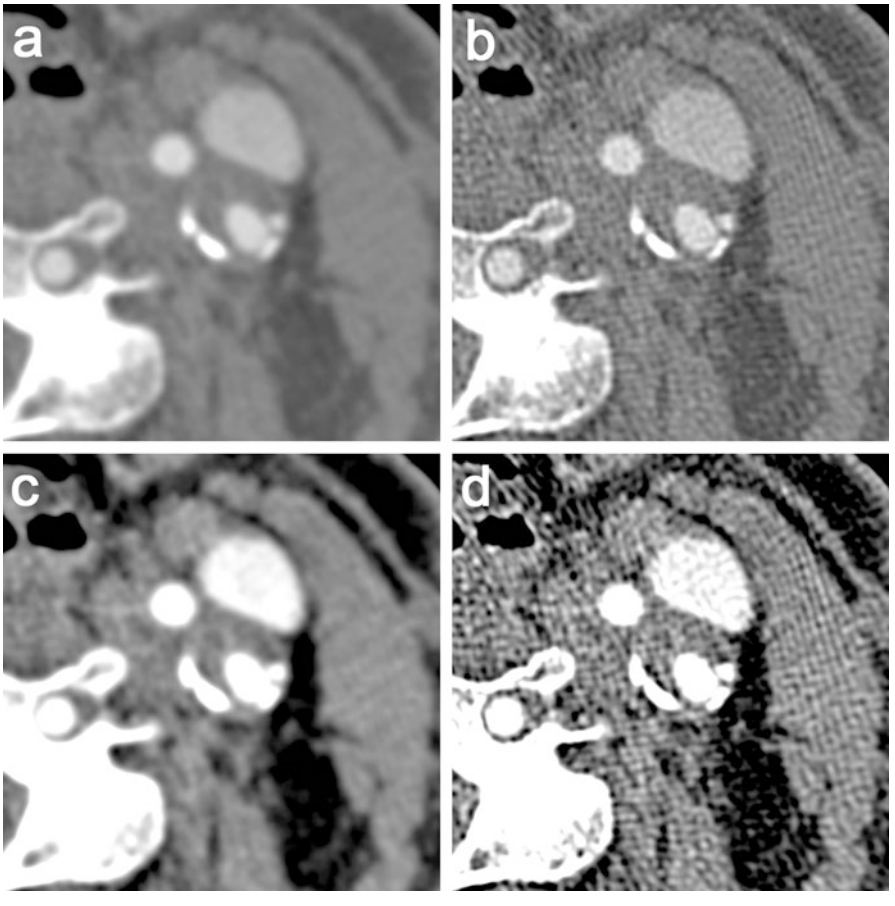

Fig. 11.1 Influence of window-level setting and convolution kernels on the evaluation of lumen and plaque. Four axial MDCT images through the carotid bifurcation obtained with a smooth (**a**, **c**) or a sharp (**b**, **d**) kernel and with a larger (W1000 L200; **a**, **b**) or smaller (W400 L100; **c**, **d**) window width setting. A large window width (**a**, **b**) gives a better differentiation between lumen and neighboring calcifications, which mostly appear brighter. A smaller window width (**c**, **d**) enables visualization of the small density differences inside the non-calcified part of the plaque. A sharper reconstruction kernel (**b**, **d**) increases the contrast between the small dense calcifications and the surrounding structures, whereas a smoother kernel (**a**, **c**) leads to averaging of contrast differences, which gives a smoother appearance to the structures

nal dimensions and therefore the accuracy of the stenosis measurements. The extent of blooming also depends on the convolution kernel chosen in the filtered-back projection algorithm. Sharp convolution kernels increase the contrast of small dense structures as the blurring is reduced, whereas smooth kernels lead to averaging of contrast differences. The signal-to-noise-ratio on the other hand improves when applying a smooth kernel because the image noise is reduced.

The appearance of the lumen–wall interface is influenced by adjustment of the window-level setting. Each lumen contrast opacification has been shown to theoretically have its own optimal window-level setting for which lumen measurements are most accurate [20]. When calcifications border the lumen, the two hyperdense structures may be difficult to differentiate from each other, impeding accurate lumen measurement. Normally, in CTA a large window width (500–1,000 HU) is used, which can be adjusted by the reader dependent on the lumen attenuation and the presence of calcifications near the lumen in order to improve the visual differentiation between dense structures. Figure 11.1 illustrates the influence of window-level setting and convolution kernels on the evaluation of the lumen.

In MDCTA images a challenge is formed by the artifacts from extra luminal dense structures like dental material, bone, and atherosclerotic calcifications which might obscure a clear visualization of the lumen. Correct head positioning with a slight tilt of the head and an upright position of the chin reduces the effect of beam hardening artifacts from dental material at the level of the carotid bifurcation, the predilection place for atherosclerotic disease in the carotid artery (Fig. 11.2). As described, convolution kernels and window-level settings highly influence the appearance of high density structures like calcifications. In addition, with a fixed window-level setting, calcification volumes appear smaller in higher kVp-settings [21].

From the cross-sectional source images, 2D or 3D image reconstructions can be created which aid in the identification and measurement of the maximal stenosis. Multiplanar

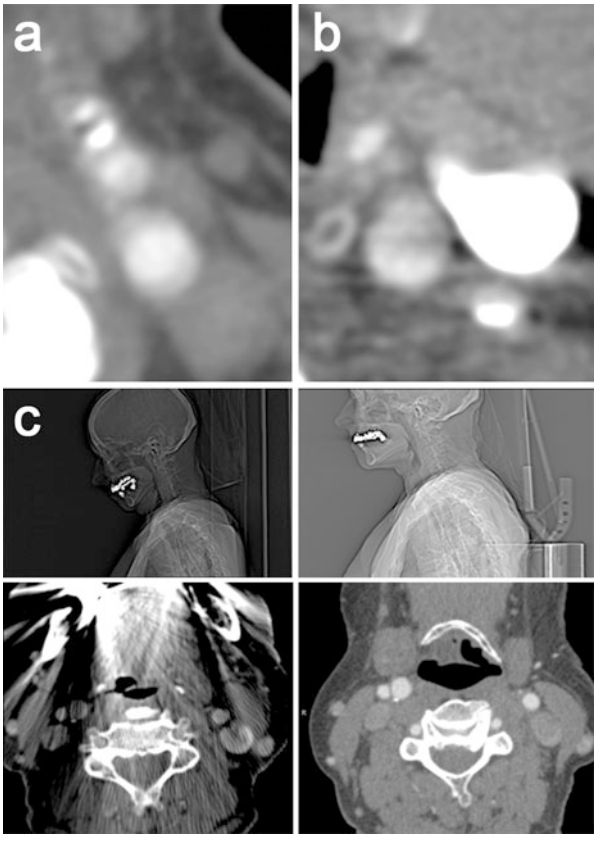

Fig. 11.2 Influence of artifacts on MDCTA imaging. (**a**) Axial image at a level above the carotid bifurcation showing motion artifacts due to swallowing. The tissue boundaries are heavily blurred. (**b**) The dependent part of the jugular vein is filled with high density contrast material, which causes streaks of low attenuation, artificially introducing a low contrast area in the neighboring carotid artery and hampering visualization of its wall. (**c**) Dental material can cause enormous streak artifacts (images on the *left*), impeding correct judgment of surrounding structures. A slight upward tilt of the chin moves these artifacts away from the region of interest and allows a normal visualization of the larger part of the carotid bifurcation (as shown on the *right*)

reconstructions (MPR) and curved planar reconstructions (CPR) provide 2D images of any predefined plane and enable accurate stenosis measurement. For creating a longitudinal view of the artery, CPR has the advantage over MPR that it corrects for vessel curvature outside of the plane. Shaded surface display (SSD), volume rendering (VR), and maximum intensity projection (MIP) are all 3D techniques with their own strengths and weaknesses. In SSD all pixels with densities below a certain threshold are excluded and the remaining data are viewed as if their surfaces are illuminated by a point source. VR utilizes the image intensities directly, by assigning opacity and color coding, to create 3D reconstructions. Both techniques are less useful for carotid artery stenosis measurements. MIPs are created by projection of the maximum intensity pixels from a 3D data set on a predefined 2D plane and give a simple overview of the vessel and its stenosis. However, this technique is limited in arteries with atherosclerotic calcifications, since calcifications in the vessel wall can easily cover the contrasted lumen causing overestimation of the degree of luminal stenosis. In addition, bony structure like the spine, thyroid cartilage, cricoid, and hyoid might interfere with a clear overview of the artery in 3D post-processing techniques (Fig. 11.3).

New techniques have been investigated that might solve the problem of artifacts from bone and calcifications on images. Matched mask bone elimination (MMBE) is a technique for the automated removal of bone pixels from CTA data sets. Preceding to the CT angiography a nonenhanced data set is acquired on which the bone pixels are identified. The corresponding pixels on the registered CT angiography are assigned an arbitrarily low value and MIP images free from overprojecting bone can then be obtained [22, 23]. Whereas for MMBE, acquisition and registration of two separate datasets is necessary, in dual-energy CT (DECT) two image data sets can be simultaneously acquired with different tube voltages (for example 80 and 140 kVp). Tissues can be differentiated by analysis of their attenuation differences depending on the tube voltage. The attenuation difference is especially large in materials with a high atomic number, such as iodine. Bone and calcifications, which show a smaller attenuation difference, can therefore be differentiated from iodine in the carotid lumen. As a result, calcifications can be removed from the contrast-filled lumen, enabling quantification of carotid stenosis in heavily calcified arteries [24]. However, because in both techniques an additional rim around the calcified pixels is removed due to blooming artifacts, overestimation of the grade of stenosis can still be introduced.

2.2 Stenosis Measurement

The accuracy of the stenosis measurement is important, seen its role in clinical decision making about carotid endarterectomy. Traditionally, the stenosis in the carotid artery was assessed using intra-arterial digital subtraction angiography (DSA), which is still considered the gold standard. The degree of stenosis was defined as the residual lumen at the stenosis as a percentage of the normal lumen in the distal internal carotid artery (according to the NASCET criteria) or as the residual lumen as a percentage of the estimated original diameter of the artery at the level of the stenosis (according to the ECST criteria). In the large symptomatic carotid surgery trials, conventional DSA was performed in two or three projections (lateral, posterio-anterior, and/or oblique) which were investigated for the most severe stenosis. Whereas rotational DSA, using multiple planes, showed to provide a benefit in detecting the smallest diameter in a stenosed artery compared to conventional DSA [25], the association

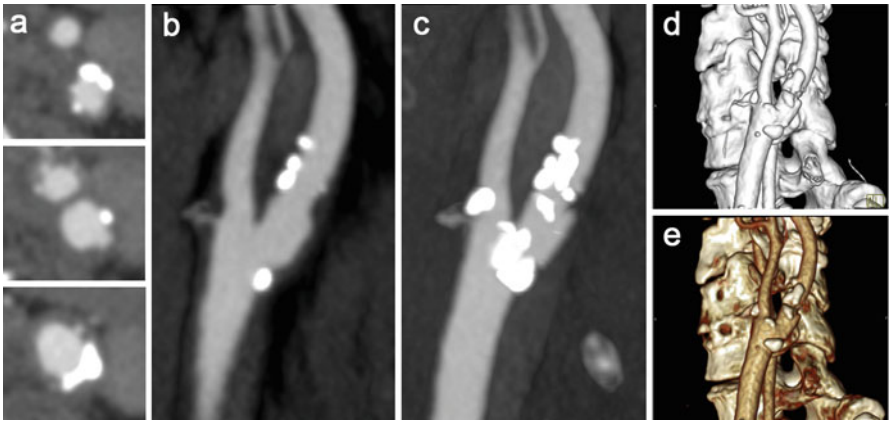

Fig. 11.3 [!t]Different post-processing techniques in MDCTA images of a moderately stenosed carotid artery. (**a**) Axial slices through the common carotid artery (*lower image*), the level of the carotid bifurcation (*middle*), and a level above the bifurcation (*upper image*). (**b**) Multiplanar reformat (MPR) in the sagittal plane visualizing the atherosclerotic plaque around the bifurcation. (**c**) Maximum intensity projection (MIP, 8.8 mm) in the same plane. Over projection of calcifications hampers a clear visualization of the lumen. (**d**) Volume rendering (VR) shows a 3D reconstruction of the carotid artery. (**e**) Shaded surface display (SSD) of the same carotid bifurcation. Both last techniques suffer from over projection of calcifications

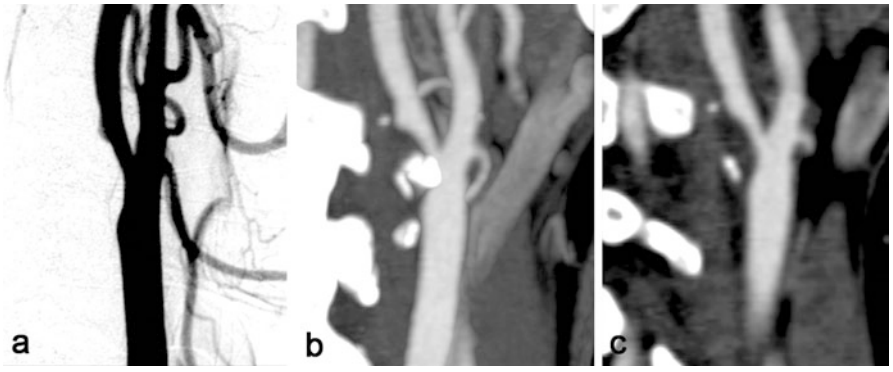

Fig. 11.4 Assessment of carotid stenosis with DSA and MDCT angiography. (**a**) Digital subtraction angiography (DSA) of a right carotid artery shows a 50 % stenosis at the level of the bifurcation. (**b**) A maximum intensity projection (MIP, 6 mm) of MDCTA images of the same artery. MIP has the disadvantage of overprojection of calcifications over the lumen, causing overestimation of stenosis measurement. (**c**) A multiplanar reformatted image (MPR, 1 mm) in the same plane as the MIP in (**b**); the problem of overprojection does not occur here. Using MPR reconstruction of 3D data the point of maximum stenosis can be found easier compared to using DSA

between the severity of stenosis and stroke risk and therefore the indication for surgical intervention remained based on conventional DSA.

The volumetric CTA datasets allow for MPRs and MIPs in any plane and therewith provide much more information on the lumen and its morphology than conventional DSA. The residual lumen is almost never circular and DSA performed in a limited number of projections does not always reveal the narrowest lumen. Analysis of 3D information therefore may provide a more realistic way to assess the true maximum stenosis.

In case CTA replaces DSA in clinical decision making, stenosis measurements on CTA should be performed in a comparable way, i.e., measuring the diameter of the remaining lumen at the level of the maximal stenosis and of the normal lumen distal to the stenosis. This can be done in several ways using different post-processing techniques. Although with MIP reconstructions images comparable to those in DSA can be obtained, this technique is limited in calcified plaques and it is recommended not to use MIP images for stenosis measurements in arteries with calcifications (Fig. 11.4). Generally, one uses 3D software to create MPRs and/or CPRs in oblique planes parallel to the carotid lumen to seek the point of maximum stenosis and measures the smallest diameter in the cross-sectional plane perpendicular to the central lumen line at that level. Figure 11.5 shows this method of stenosis measurement using 3D software. The reference diameter is measured in the same way at a level above the carotid bulb where the lumen walls run parallel to each other (i.e., the healthy distal carotid artery).

When using the ECST criteria to assess the degree of stenosis, CTA directly enables visualization of the outer

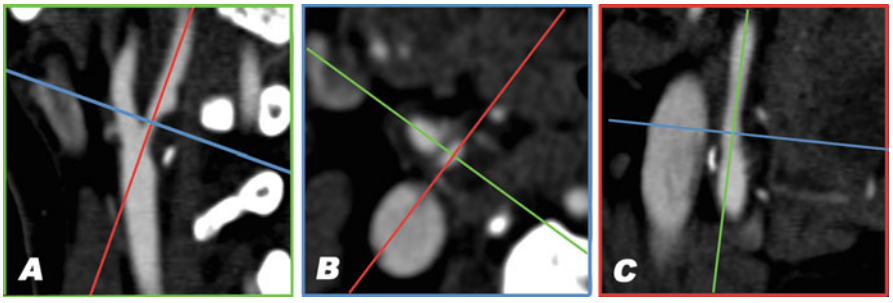

Fig. 11.5 Stenosis measurement in MDCT angiography using 3D software. Multiplanar reformatted images are created in planes parallel and perpendicular to the lumen axis; the smallest lumen diameter in the cross-sectional plane can then be measured using calipers. (**a**) A sagittal view of the carotid bifurcation. The *blue* and *red lines* correspond to the planes that are depicted in **b** and **c**, respectively. A large atherosclerotic plaque is visible at the origin of the internal carotid artery, causing a high-grade stenosis. (**b**) The cross-sectional image perpendicular to the central lumen line at the level of the smallest vessel diameter. The residual lumen has an *oval shape*. (**c**) The view perpendicular to those in **a** and **b**. In this plane the stenosis is not very prominent (Color figure online)

vessel wall, whereas on DSA the vessel diameter has to be estimated by delineating the projected lumen contour. Therewith, CTA takes into account the changes in vessel diameter caused by vascular remodeling, whereas this phenomenon is ignored when measured on DSA. This might cause differences in ECST stenosis measurements between CTA and DSA.

2.3 Diagnostic Accuracy

Several diagnostic studies have been performed which compared single slice CTA with DSA in the assessment of carotid stenosis. From a meta-analysis of studies published between 1990 and 2003, single slice CTA has been shown to have a pooled sensitivity of 85 % and a pooled specificity of 93 % for detection of a 70–99 % stenosis. Sensitivity and specificity for detection of an occlusion were 97 % and 99 %, respectively [26]. Another systemic review reported a pooled sensitivity of 95 % and a specificity of 98 % for the detection of a 70–99 % stenosis [27]. The latter study also found that CTA was sensitive (95 %), but slightly less specific (92 %) in depicting stenosis >30 %. In 2006, Wardlaw and colleagues performed a meta-analysis comparing noninvasive imaging techniques with intra-arterial angiography. They found only 11 studies on CTA, published between 1980 and 2004, that explicitly met the Standards for Reporting of Diagnostic Accuracy (STARD) criteria [28] and they reported a sensitivity of 77 % and a specificity of 95 % for diagnosing 70–99 % stenosis using CTA [29]. The authors warned for the methodological shortcomings of many studies evaluating diagnostic imaging. They concluded that the existing data might support the cautious use of noninvasive imaging to diagnose 70–99 % stenosis, but that more data are needed from carefully designed trials to determine true sensitivity and specificity of noninvasive imaging techniques in routine clinical practice, especially for 50–69 % stenosis, or when used in combination [29]. In 2009, Chappell and colleagues performed an individual patient data meta-analysis to find clinically significant estimates of the accuracy of non-invasive imaging in diagnosing severe and moderate symptomatic artery stenosis [30]. They also concluded that existing primary studies provide limited data and that the literature overestimates the accuracy of noninvasive imaging techniques. The small CTA dataset included in this analysis revealed a sensitivity and specificity of 65 % and 56 % for detection of 70–99 % stenosis, respectively [30].

A difficulty in the evaluation of the accuracy of stenosis measurement using noninvasive imaging techniques is that both acquisition and post-processing procedures evolve rapidly. Although multidetector CTA is now widespread and is expected to improve diagnostic accuracy, this has barely been tested. Only one study compared MDCTA with DSA and found MDCTA to have a high specificity and a high negative predictive value for significant carotid disease [31]. Since DSA is not routinely used anymore in clinical practice, the assessment of new noninvasive imaging techniques against DSA can not be justified ethically anymore. Therefore there is an increasing need for practical, reliable methods for evaluating new technologies, for example, by standardized comparison with other non-invasive tests or test phantoms.

Both aforementioned systemic reviews [26, 27] did not provide enough evidence to draw robust conclusions about the diagnostic accuracy of the different post-processing techniques, although stenosis assessment using axial slices and MIPs seemed to be better than when using VR and SSD [27]. Most studies did not report on the exact—combinations of—reformatting techniques used, which hampers a solid meta-analysis. More recent studies comparing the post-processing techniques in MDCTA revealed that stenosis measurements on axial source images are highly reproducible and accurate and that the additional use of MPRs or other reconstructions

is not necessary, but might aid in finding the location of the maximum stenosis [32–34].

2.4 (Semi)automated Quantification of Luminal Measures

Manual lumen segmentation and stenosis quantification are laborious and suffer from interobserver and intraobserver variability. Consequently much work has been performed on the development of (semi)automated lumen quantification. The majority of publications with respect to lumen quantification focus on the segmentation of the lumen while the assessment of the severity of luminal stenosis is addressed by few.

Lumen segmentation methods have been reviewed and grouped according to the mathematical framework used [35] or categorized with respect to (1) the way vessel geometry and appearance are modeled, (2) the image features which are used for vessel extraction, and (3) the methodology used in vessel extraction [36].

Some of the published methods have been tailored to or evaluated on carotid CTA images [37–40]. Reported values vary highly. However the comparison of these methods is hampered by the fact that they all use different imaging data and evaluation measures, like Dice similarity coefficient, mean surface distances, or visual inspection. In addition, most studies were performed on small and selected data sets. Figure 11.6 illustrates a 3D lumen segmentation of a carotid bifurcation.

To facilitate an objective comparison of carotid artery segmentation and stenosis quantification algorithms, the Carotid Bifurcation Algorithm Evaluation Framework was set up in 2009 (http://cls2009.bigr.nl/) [41]. This framework consists of a publically available image database, annotated data for training and evaluation, and standardized evaluation measures. Till date nine algorithms have been evaluated by the framework, of which only one is fully automatic, whereas the others require three initialization points. The three best performing methods evaluated by the framework have dice similarity coefficients of 0.92, 0.88, and 0.90, mean surface distances of 0.18, 0.54, and 0.17 mm and Hausdorff distances of 1.5, 4.4, and 1.7 mm, respectively [41]. Figure 11.7 shows three examples of lumen segmentations with three different dice values.

These three best performing methods are based on three different approaches, i.e., graph cut, level set, and active surface algorithms [41].

In the graph cut framework voxels are assigned to vessel lumen or background by considering all image voxels as nodes in a three-dimensional graph and creating an optimal surface which separates (cuts) the foreground (lumen) from the background. To compute this optimal cut the image gradient can be used.

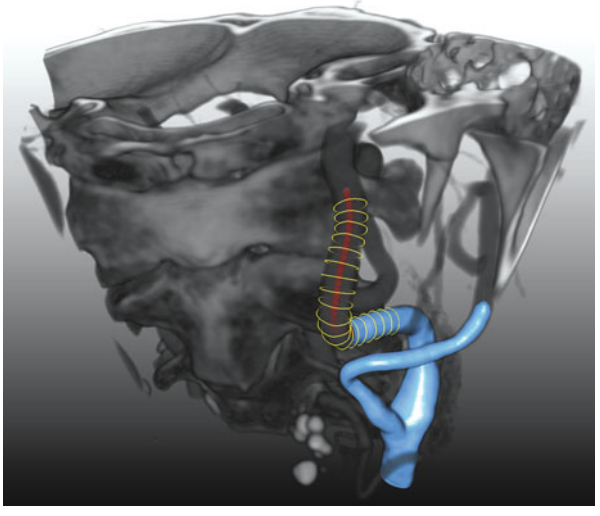

Fig. 11.6 3D-segmentation of the lumen of a carotid artery. An example is shown of a carotid artery lumen segmentation using three different segmentation representations. The *red dots* indicate a centerline through the centroids of the vessel cross sections. The *yellow* "*circles*" show the lumen contours perpendicular to the centerline. The *blue* surface shows an interpolated surface through the *yellow* contours (Color figure online)

In the level set framework, the vessel surface is represented implicitly by the zero level lines (zero level set) of an embedding function (similar as, e.g., sea level in a height map). This embedding function is then changed (evolved), implicitly resulting in deformation of the zero level set. This representation has the advantage that the zero level set can change topology (Fig. 11.8). The evolution of the embedding function should ensure that the zero level set halts at the vessel lumen boundary. This is achieved by defining a speed function derived from the image data. Both the initial segmentation and the design of the speed image are the key ingredients in the design of a level set-based segmentation method.

Active surfaces are a generalization of active contours (also called snakes). Using active surfaces the segmentation is also the result of the evolution of an initially segmented surface. However changing topology is much harder to model in this framework. The segmentation is modeled as a surface on which forces are acting which causes the evolution of the segmentation. This evolution can be constrained by properties of the used surface representation.

Although considerable research has been performed on vessel lumen segmentation, only few researchers have published on automatic vessel stenosis grading [42–44]. Also, approaches differ widely in the evaluation that has been performed, both with respect to evaluation measures and number of data sets used.

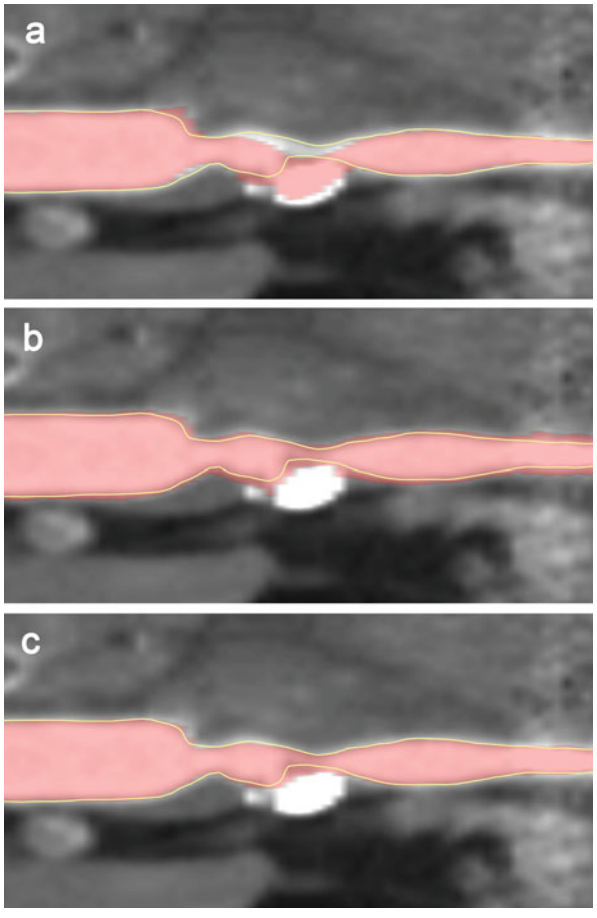

Fig. 11.7 (Semi)automated lumen segmentations of a carotid artery of different qualities. Shown are curved multiplanar reformats (CMPR) of a carotid artery with a calcified atherosclerotic plaque that causes a high-grade stenosis. A visual impression is shown of the reference standard (*yellow line*) based on manual annotations by three observers and automated lumen segmentations (in *red*) that have different qualities: (**a**) with a bad Dice similarity index (SI) of 0.881, (**b**) a moderate Dice SI of 0.884 and (**c**) a good Dice SI of 0.945. The Dice similarity indices are calculated on the whole volume of which the shown CMPR is just a single plane (Color figure online)

The evaluation framework discussed previously also allows objective comparison of performance in stenosis quantification. To date only three stenosis grading methods have been evaluated using this framework, also indicating that this field has received less attention [41]. Clinically, the minimal diameter is often used to calculate the stenosis degree. However, the minimal diameter of a non-elliptical shape is not uniquely defined and is therefore prone to measurement errors and is hard to measure automatically. The evaluation framework evaluates two stenosis measures: an area-based measure which compares the area of the lumen at the stenosis to the area of a distal vessel part and a measure that compares the minimal diameter at the two positions. In the framework, the diameter-based stenosis degree is defined by the smallest line that divides the cross-sectional area in two equal parts. Using automated lumen segmentation, the minimal diameter can easily be replaced by the lumen cross-sectional area. This is a much more accurate measure for the obstruction of the blood flow as carotid arteries, especially at the site of atherosclerotic plaque, generally do not have circular luminal cross sections and also do not run exactly perpendicular to the axial plane of the CT scan. Zhang et al. investigated the use of area measurements and found that assessment of area stenosis on CTA was highly reproducible and showed a satisfactory agreement with diameter stenosis on DSA, although it provides a less-severe estimate of the degree of carotid stenosis, especially in noncircular lumens [45]. The average error in assessing carotid artery stenosis of the best stenosis grading method according to the evaluation framework was 16.9 % for area-based and 17.0 % for diameter-based measurements [41].

Besides stenosis grading, lumen segmentation also enables the extraction of other quantitative measures. The extracted lumen model can, e.g., be used for Computation Fluid Dynamic calculations to assess the shear stress in the atherosclerotic carotid bifurcation [46] and the quantification of geometric parameters such as vessel tortuosity and bifurcation angles [47].

3 Plaque Imaging Using CTA

3.1 Technical Aspects

Assessment of different atherosclerotic plaque components in CTA relies on the differences in linear attenuation coefficient expressed in Hounsfield Units (HU) of the plaque components. Plaque component differentiation is highly dependent on scan parameters.

Reconstruction of thin slices is very important for plaque evaluation. Thin slices allow for datasets with isotropic and higher resolution and therefore enhance the differentiation of plaque components. Especially for plaque components of which HU values are close, like lipid and fibrous tissue, thin slices are crucial.

Where blooming artifacts from vessel wall calcifications can hamper correct stenosis measurements, it also causes a problem in the evaluation of plaque, since it interferes with optimal plaque characterization of the non-calcified part of the plaque. The finite spatial resolution of CT causes partial volume averaging and therefore blooming artifacts. Blooming of calcifications leads to overestimation of calcification size and inability to evaluate the atherosclerotic regions that border the calcifications. Moreover, the calcification volume appears larger when using lower kVp settings [21].

For accurate differentiation of plaque components a high signal-to-noise ratio (SNR) is necessary. Image noise depends mainly on the product of the tube current and rotation

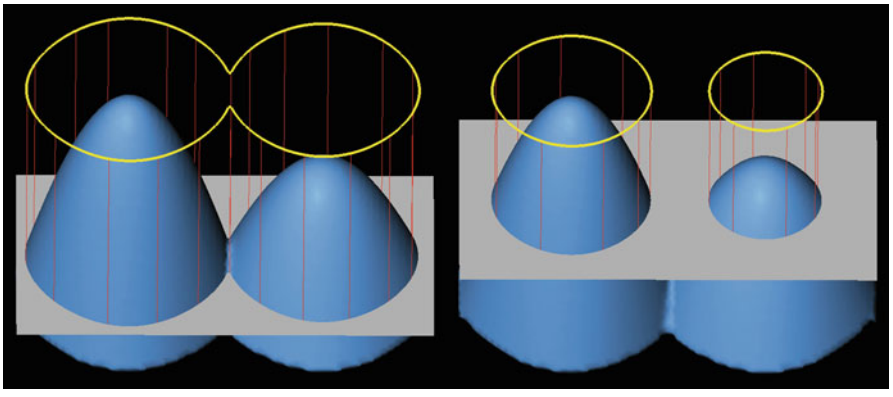

Fig. 11.8 Level set method for lumen segmentation. Using the level set framework a segmentation (indicated by the *yellow contours*) is seen as the zero level (*gray plane*) of an embedding function in a higher dimension (*blue surface*). If the embedding function changes as is indicated by the two *blue* surfaces which are slightly different, the zero level (segmentation) changes. Using this framework a segmentation can easily change topology. The segmentation on the *left* has one object (*contour*) while the segmentation on the *right* consists of two distinct objects (Color figure online)

time (mAs), the tube voltage, and reconstruction kernel. Because the atherosclerotic plaque is a relative small structure, a thin slice thickness and a small field-of-view are required. These result in a decrease of SNR, which should be compensated by a higher radiation exposure.

High intraluminal contrast material density may influence the density measurements in the plaque. Ex vivo studies in coronary arteries revealed that intraluminal attenuation strongly affects the measured attenuation of the plaque [48]. This can be explained not only by partial volume effects but also by the entrance of contrast material in the plaque via the vaso vasorum. It is unknown yet if this effect is also seen in the larger carotid artery, but it underlines the necessity of standardized scan protocols, especially since carotid plaque enhancement in CTA is thought to be associated with increased risk for neurological events [49, 50].

Another technical aspect influencing accurate differentiation of plaque components in CTA is the convolution kernel used for reconstruction of the image dataset. The convolution kernels allow for influencing the image characteristics; a smooth algorithm will reduce spatial resolution, image noise, and image contrast for tiny structures, whereas a sharp algorithm has the opposite effect. Plaque characterization and quantification of the different plaque components based on measurement of HU densities is thus highly influenced by the convolution kernel used. Smooth kernels hamper the correct differentiation between tissues with small differences in density, as is the case for lipid and fibrous tissue. In contrast, sharp kernels not only increase contrast differentiation but also lead to an increase in calcium size and low-intensity rings around calcifications (edge-enhancement artifacts), which hamper further plaque interpretation. Intermediate reconstruction kernels turned out to allow optimal plaque interpretation [21].

The window-level setting also influences the visualization of the different plaque components. Whereas a large window-width is used in luminography to differentiate lumen from calcifications that border the lumen, a small window-width is necessary to enhance the small differences in HU density inside the non-calcified plaque (Fig. 11.1).

3.2 Diagnostic Accuracy

3.2.1 Plaque Surface Morphology

The accuracy of DSA in the detection of plaque ulceration, as compared to macroscopic surgical observations, has been found to be low (sensitivity 46 % and sensitivity 74 %) [51]. CTA allows for analysis of the plaque surface (Fig. 11.9) and the differentiation between ulcerations and irregularities and has been demonstrated to perform better than DSA [52]. A validation study, comparing single slice CTA with histological specimens reported a sensitivity and specificity of 60 % and 74 %, respectively [53]. However, MDCTA has been found to have a high sensitivity and specificity (94 % and 99 %, respectively) in detecting plaque ulcerations compared to surgical observation [54]. Assessment of plaque ulceration on MDCTA is highly reproducible ($\kappa > 0.86$) [55, 56].

3.2.2 Plaque Composition

The first validation studies compared 3 mm single slice CT images with histological sections from carotid endarterectomy specimens and did not show clear-cut results. Whereas two studies reported that calcifications, lipid, and fibrous tissue could be differentiated based on density measurements [57, 58], another study concluded that single slice CT was not sufficiently robust to reliably characterize plaque composition and plaque morphology [53]. The introduction of multidetector CT enabled a more detailed analysis of the

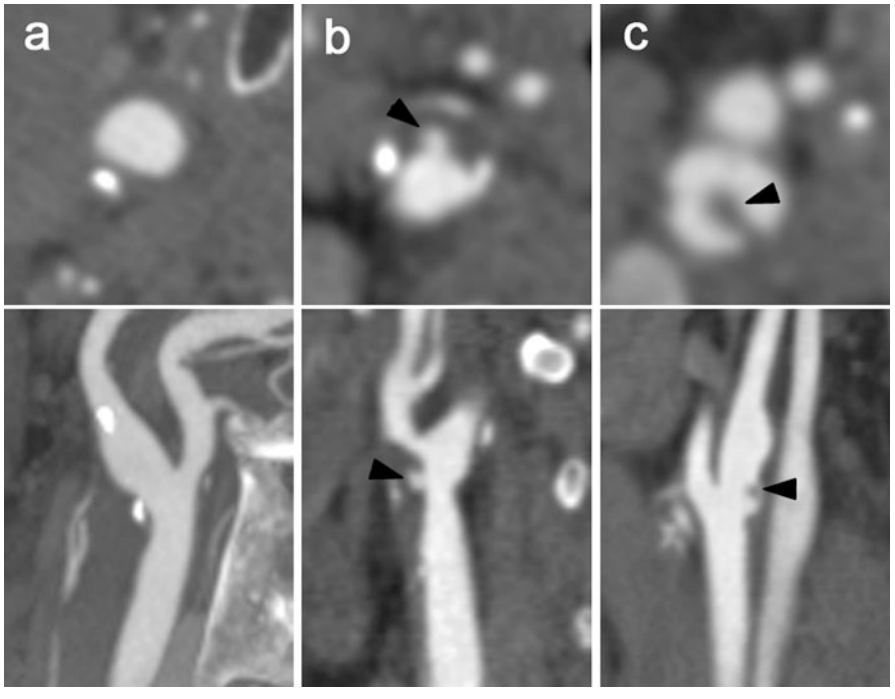

Fig. 11.9 Assessment of plaque surface morphology using MDCT angiography. Cross-sectional images (*upper panels*) perpendicular to the central lumen line and multiplanar reformats (*lower panels*) of carotid bifurcations. (**a**) An atherosclerotic carotid plaque with a smooth surface. (**b**) A plaque at the level of the carotid bifurcation with an ulceration (*arrowhead*). (**c**) An ulcerated plaque with thrombus material (*arrow head*) that protrudes into the lumen

atherosclerotic carotid plaque composition and the differentiation of plaque components.

Several validation studies have been performed, in carotid arteries as well as in coronary arteries. In coronary artery studies, intravascular ultrasound (IVUS) is used as a gold standard. In carotid artery studies, the availability of histological carotid plaque specimens from carotid endarterectomy enables reliable validation against histology. An additional advantage is that the characterization of the separate plaque components can be performed easier and in more detail in the larger carotid arteries. In 2005, we performed an ex vivo validation study, in which CEA specimens were scanned and the images were compared with the histological slices (Fig. 11.10). The CT value of lipid-rich regions differed significantly from that of fibrous-rich regions (45 ± 21 HU versus 79 ± 20 HU, $p < 0.001$). An ROC analysis revealed 60 HU as the optimal cut-off point for differentiation between lipid and fibrous tissue, with a sensitivity of 89 % and a specificity of 93 % [21]. The study was repeated in vivo, in which the CT values for lipid- and fibrous-rich tissue were 25 ± 19 HU and 88 ± 18 HU, respectively. Again an optimal threshold value of 60 HU was found, with a sensitivity and specificity of both 100 % [59]. Calcifications are easily detected on CT images as high density structures and equivalent to coronary calcium scoring in electron beam CT, 130 HU is generally taken as a threshold for differentiating calcifications.

Wintermark and colleagues performed a validation study in which they compared in vivo MDCTA images with histological sections for the non-calcified plaque components and with ex vivo MDCTA images for the calcifications [56]. They found the following scan-parameter dependent cut-off values, determined as the half way HU attenuation value between the average HU values of each plaque component: 39.5 HU between lipid-rich necrotic core and connective tissue, 72.0 HU between connective tissue and hemorrhage, and 177.1 HU between hemorrhage and calcifications. They further compared the CT classification with the histological classification of type of atherosclerotic plaque and stage of lesion development according to the system derived from the AHA classification and found an overall agreement of 72.6 % (unweighted κ of 67.6 %) [56]. The concordance for calcifications was perfect, whereas the reliability of the identification of the non-calcified plaque components was limited due to overlap of the values between the soft components. However, CTA showed good correlation with histology for larger lipid cores and larger hemorrhages. Further they demonstrated that CTA performed well in measuring fibrous cap thickness ($R^2 = 0.77$, $p < 0.001$) [56].

3.3 Quantification of Plaque Components

Calcifications in the vessel wall can easily be measured in a quantitative way. Agatston and colleagues were the first to quantify coronary calcifications with electron beam CT [60]. As a default, the threshold to differentiate calcification is $\geq$130 HU in non-contrast CT scans. Although the Agatston score as a quantification tool can be used in carotid arteries, other scoring methods like a volume score are more frequently used [61]. However, when CTA images are used, the threshold has to be higher in order to automatically

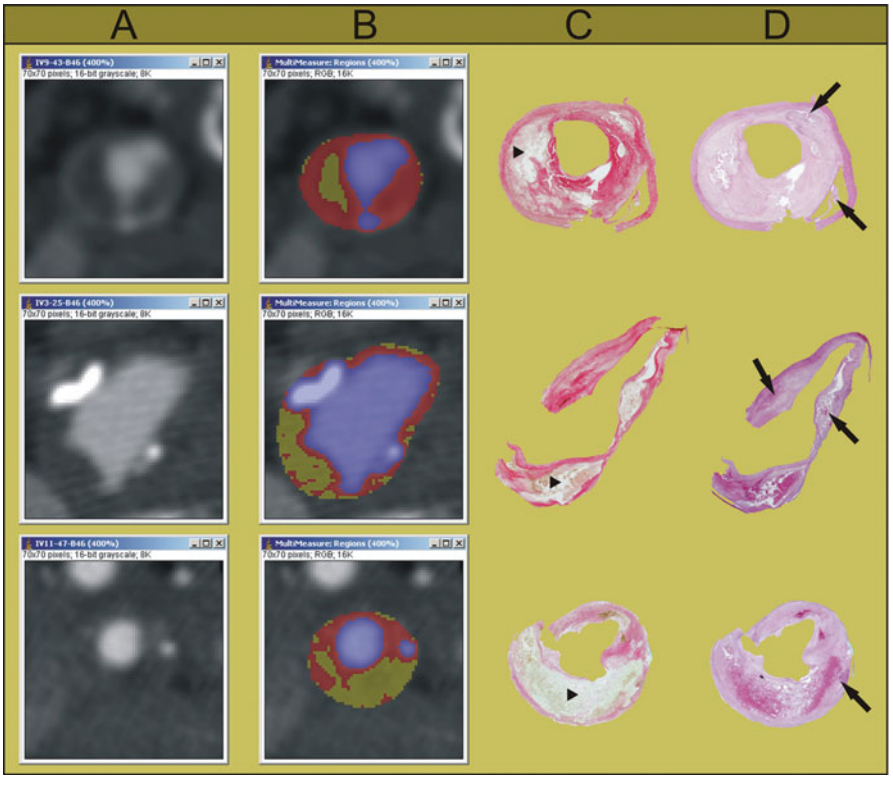

Fig. 11.10 Hounsfield attenuation-based differentiation of plaque components—validation against histological sections. Column **a**: axial MDCT images of a carotid artery with atherosclerotic plaque. Column **b**: MDCT plaque composition based on HU differences. Column **c**, **d**: Corresponding histological sections with Sirius Red (SR) and hematoxylin eosin (HE) staining, respectively. *Blue* regions in the MDCT plaque composition images correspond well with lumen and calcifications on HE stained histological sections (*arrows*). The *red* regions correspond well with the *red* collagen-rich regions in the SR stained sections. *Yellow* regions correspond with the lipid core (i.e., lipid, hemorrhage, and necrotic debris) (*arrowhead*) regions on histology (the *non-red* regions on the SR stained sections that are not calcified areas on the HE stained sections). (Reprinted with permission from de Weert TT, Ouhlous M, Meijering E, et al (2006) In vivo characterization and quantification of atherosclerotic carotid plaque components with multidetector computed tomography and histopathological correlation. Arterioscler Thromb Vasc Biol 26(10):2366–2372) (Color figure online)

differentiate calcifications from the bordering luminal contrast. Another possibility is to first delineate the inner and outer borders of the carotid plaque and subsequently discriminate calcifications using a threshold of 130 HU within the plaque. In this way, 3D volumetric MDCTA datasets also allow for quantification of the soft plaque components.

Annotation of the luminal area can be done (semi)automatically based on thresholds that separate the bright, contrast-filled lumen from the lower density plaque. However, calcifications bordering the lumen might be included in the lumen segmentation and therefore manual correction is necessary. Using lumen and outer vessel wall contours, the plaque area can be calculated by subtracting lumen area from total vessel area.

Validation studies of plaque area measurements with histology as gold standard are hampered by the fact that histological preparation leads to shrinkage of the specimens. Nevertheless, strong correlations have been found between ex vivo and in vivo MDCTA and histology for the assessment of plaque area ($R^2 = 0.81$ and 0.73, respectively) [21, 59]. Intraobserver reproducibility of plaque area measurements with MDCTA was good (coefficient of variation of 8 %) [59].

The CT value thresholds in HU that differentiate between plaque components create the opportunity to quantify plaque composition. The aforementioned in vivo validation study, comparing MDCTA images with histological specimens, showed that area measurements of calcifications were overestimated by MDCTA; however the correlation with histology was good ($R^2 = 0.74$). The correlation between MDCTA and histology for fibrous area measurements was also good ($R^2 = 0.76$) but was poor for lipid ($R^2 = 0.24$). Further investigation, however, showed that this correlation improved in mildly calcified plaques and non-calcified plaques ($R^2 = 0.77$ and 0.81, respectively). The intraobserver variability of area measurements of the different plaque components was low, with a coefficient of variation of 8 %, 11 %, and 15 % for calcifications, fibrous tissue, and lipid, respectively [59].

Plaque volume and plaque component volumes can be calculated by multiplying area measurements with slice increment and the number of slices in the range of interest.

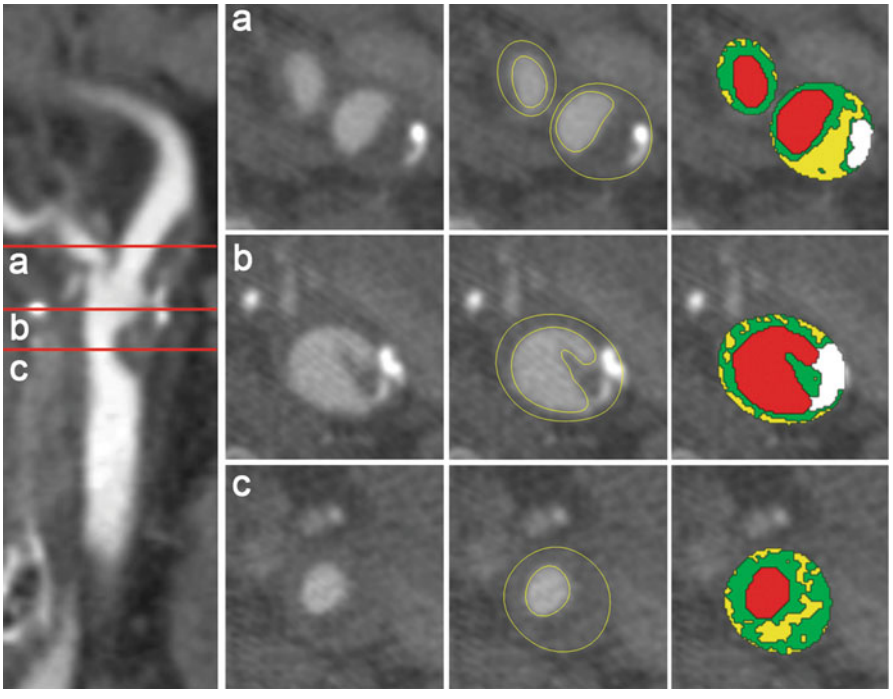

Fig. 11.11 (Semi)automated segmentation of lumen and plaque components. (Semi)automated segmentation of lumen and plaque is performed on axial images within a predefined range. Contours of lumen and plaque are generated and can be manually adjusted if necessary. Within the plaque area (outer vessel wall contour minus lumen contour) the plaque components are differentiated based on Hounsfield Unit thresholds (lipids: <60 HU, fibrous 60–130 HU, calcification >130 HU). The *color overlay* shows the different structures; lumen = *red*, lipid = *yellow*, fibrous = *green*, calcification = *white*. This figure shows a CPR image of a carotid bifurcation on the *left* and plaque segmentation on axial slices at three levels: (**a**) through the internal and external carotid artery, showing a large, mainly non-calcified atherosclerotic plaque in the internal carotid artery; (**b**) through the distal common carotid artery just below the bifurcation on which an ulcerated surface is visible; and (**c**) through the common carotid artery at the level of the smallest vessel diameter (Color figure online)

In an in vivo study in 56 patients, plaque volume and plaque component volumes could be assessed in a reproducible way. The difficulty of defining the transition of normal wall into atherosclerotic plaque contributes highly to the interobserver variability. Consensus about the longitudinal dimensions of the plaque improved the reproducibility of plaque volumes strongly [62].

3.4 (Semi)automated Plaque Measurements

Manually assessing lumen and vessel contours is a time-consuming task and is highly influenced by the window-level setting. Segmentation of the outer vessel wall and subsequent automated plaque characterization has received considerably less attention than luminal analysis.

The challenge of automated analysis of carotid atherosclerotic plaque lies in the difficulty of defining the outer vessel wall. This is a challenging task due to the low and varying contrast between the plaque and its surrounding soft tissue. Vukadinovic et al. developed a semiautomated method to segment the outer vessel wall [63], which only required clicking initialization points for lumen segmentation and clicking seed points for defining the range of interest for plaque segmentation. The method uses a level-set framework for vessel lumen segmentation [37], followed by classification of calcium objects using a set of image features related to the appearance, shape, and size of bright objects in the CTA data set. Subsequently, image voxels are identified as lying inside or outside the vessel wall, using a same set of image features. Finally, the outer vessel wall is determined by fitting an ellipsoid that utilizes the information from the calcium and inner/outer vessel classification step. After generation of the inner and outer vessel wall contours, the plaque components (lipid, fibrous tissues, and calcifications) are automatically differentiated based on the aforementioned HU-thresholds. Figure 11.11 shows the results of (semi)automatically generated plaque segmentations.

The method has been trained and tested on manually annotated MDCTA datasets of the carotid arteries and validated against manually segmented carotid arteries. The average Dice similarity index was 91 %, which was comparable to the similarity index between two observers [63]. Subsequently, the performance of this plaque segmentation method in quantifying plaque volume and plaque component

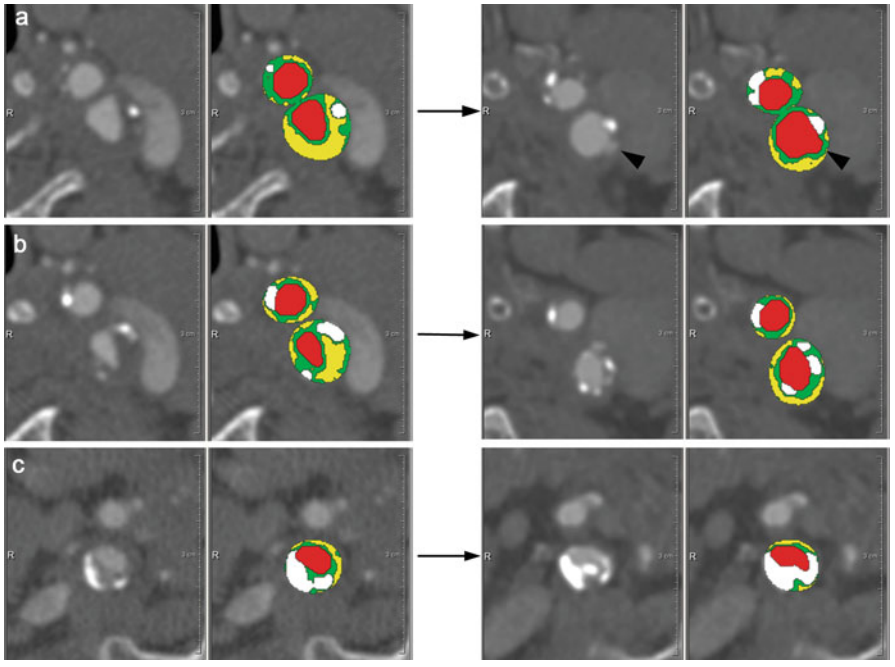

Fig. 11.12 Serial quantitative plaque imaging. Serial plaque imaging in a 67-year-old male patient (**a**, **b**) and a 62-year-old male patient (**c**). On the *left*, axial MDCTA images and the *plaque color overlays* of the baseline scan and on the *right* the corresponding images of the follow-up scan. (**a**) Predominantly non-calcified plaque at a level just above the bifurcation. At follow-up imaging after 6 years an ulceration is visible (*arrow head*). (**b**) Images from the same artery at a more distal site. (**a**, **b**) At follow-up a decrease in plaque volume and a change in plaque composition is demonstrated. (**c**) Internal carotid artery demonstrating an increase in calcification of the vessel wall at follow-up (after 6 years) (Color figure online)

volumes was studied by comparing measurement error of the automated method using manual contours as a reference standard with the interobserver variability in manual annotations. The differences between the automated method and the manual observers were comparable to the interobserver differences [64].

Although the method is highly automated some observer interventions are still needed and the outer vessel wall segmentations should still be checked manually for erroneous in or exclusion of calcifications, and therewith over-segmentation or under-segmentation of the plaque. Taken these manual interventions into account, the intraobserver and interobserver reproducibility of the semiautomated method is better as compared to the reproducibility of manual annotating, with intraclass correlation coefficients of 0.93/0.84 for plaque volume and 0.86–1.00/0.76–0.99 for plaque component volumes (unpublished data).

4 Applications of Quantitative Atherosclerotic Measures

MDCTA-based quantitative plaque measures have been used in several studies to investigate atherosclerotic development. Rozie et al. investigated in a cross-sectional study the correlation between cardiovascular risk factors and plaque volume and plaque composition. They found that plaque volume and severity of stenosis were just moderately correlated, which means that plaque volume could be an additional predictor for ischemic stroke. An increasing plaque volume was associated with increased lipid and calcium proportion and a decreased fibrous proportion. Age and smoking were independently related to plaque volume. Patients with hypercholesterolemia had a significantly higher contribution of calcifications and a significantly lower contribution of lipid in the atherosclerotic plaque [65]. Another study investigated whether plaque features could be correlated with the presence of ulcerations, which is thought to be a marker of plaque rupture [10]. It was demonstrated that degree of stenosis, plaque volume, and the proportion of lipid-rich necrotic-core were associated with the presence of carotid plaque ulcerations [66]. In another cross-sectional study, carotid atherosclerotic plaque features were identified that were significantly different in acute carotid stroke patients compared to non-stroke patients and on the infarct side compared to the contralateral side in stroke patients. These features included increased vessel wall, thinner fibrous caps, greater number of lipid cores, and their location closer to the lumen. The number of calcium clusters was a protective factor [67].

Numerous studies report on the role of plaque calcifications in plaque stability. The findings are not conclusive. A recent systemic review suggests that clinically symptomatic plaques have a lower degree of calcifications than asymptomatic plaques [61]. The percentage calcification within a plaque of a stenosed artery, rather than the absolute volume seems to be associated with plaque stability [68]. This underscores why the (automated) quantification of the relative contribution of the plaque components might add to the improvement of stroke risk prediction.

The MDCTA plaque imaging studies performed so far had a cross-sectional study design. The ability to quantify atherosclerotic features in vivo creates the potential to further explore atherosclerotic plaque development by prospective, serial in vivo imaging of the carotid plaque (Fig. 11.12). Currently, a prospective serial MDCTA plaque imaging study is being performed, which investigates the temporal changes in plaque burden and plaque composition and its determinants in TIA and stroke patients.

5 Summary and Future Directions

Currently, MDCTA is a noninvasive imaging technique frequently used in clinical practice for the assessment of carotid stenosis grading and is replacing the more invasive technique of DSA. MDCTA can perfectly be combined with a native CT scan and a perfusion CT scan of the brain in the evaluation of stroke patients.

Although plaque imaging is currently only used in research settings, the same MDCTA data set might provide further clinically important information on the atherosclerotic plaque burden, plaque surface morphology, and plaque composition for a more individualized risk prediction. Large, prospective studies demonstrating significant associations between CTA-based risk factors and (recurrent) events are yet lacking. Future research should focus on the role of plaque measures in stroke risk prediction and on the use of MDCTA-based quantified plaque measurements in monitoring efficacy of medical therapy. Large—preferably multicenter—studies should pay attention to the standardization of data acquisition and postprocessing across centers and imaging time points, since several technical parameters highly influence quantification of plaque features as is broadly depicted in this chapter. More effort should further be put in the development of robust, accurate, automated quantification of plaque measures in order to minimize measurement variability.

References

1. Roger VL, Go AS, Lloyd-Jones DM, Adams RJ, Berry JD, Brown TM, Carnethon MR, Dai S, de Simone G, Ford ES, Fox CS, Fullerton HJ, Gillespie C, Greenlund KJ, Hailpern SM, Heit JA, Ho PM, Howard VJ, Kissela BM, Kittner SJ, Lackland DT, Lichtman JH, Lisabeth LD, Makuc DM, Marcus GM, Marelli A, Matchar DB, McDermott MM, Meigs JB, Moy CS, Mozaffarian D, Mussolino ME, Nichol G, Paynter NP, Rosamond WD, Sorlie PD, Stafford RS, Turan TN, Turner MB, Wong ND, Wylie-Rosett J, American Heart Association Statistics Committee and Stroke Statistics Subcommittee (2011) Heart disease and stroke statistics – 2011 update: a report from the American Heart Association. Circulation 123(4):e18–e209. doi:10.1161/CIR.0b013e3182009701, CIR.0b013e3182009701 [pii]
2. Warlow C, Sudlow C, Dennis M, Wardlaw J, Sandercock P (2003) Stroke. Lancet 362(9391):1211–1224. doi:10.1016/S0140-6736(03)14544-8, S0140-6736(03)14544-8 [pii]
3. (1991) Beneficial effect of carotid endarterectomy in symptomatic patients with high-grade carotid stenosis. North American Symptomatic Carotid Endarterectomy Trial Collaborators. N Engl J Med 325(7):445–453. doi:10.1056/NEJM199108153250701
4. (1998) Randomised trial of endarterectomy for recently symptomatic carotid stenosis: final results of the MRC European Carotid Surgery Trial (ECST). Lancet 351(9113):1379–1387. doi:S0140673697092921 [pii]
5. Rothwell PM, Eliasziw M, Gutnikov SA, Fox AJ, Taylor DW, Mayberg MR, Warlow CP, Barnett HJ, Carotid Endarterectomy Trialists C (2003) Analysis of pooled data from the randomised controlled trials of endarterectomy for symptomatic carotid stenosis. Lancet 361(9352):107–116, doi:S0140673603122283 [pii]
6. (1995) Endarterectomy for asymptomatic carotid artery stenosis. Executive Committee for the Asymptomatic Carotid Atherosclerosis Study. JAMA 273(18):1421–1428
7. Halliday A, Mansfield A, Marro J, Peto C, Peto R, Potter J, Thomas D, Group MRCACSTC (2004) Prevention of disabling and fatal strokes by successful carotid endarterectomy in patients without recent neurological symptoms: randomised controlled trial. Lancet 363(9420):1491–1502. doi:10.1016/S0140-6736(04)16146-1, S0140673604161461 [pii]
8. Hobson RW 2nd, Weiss DG, Fields WS, Goldstone J, Moore WS, Towne JB, Wright CB (1993) Efficacy of carotid endarterectomy for asymptomatic carotid stenosis. The Veterans Affairs Cooperative Study Group. N Engl J Med 328(4):221–227. doi:10.1056/NEJM199301283280401
9. Naghavi M, Libby P, Falk E, Casscells SW, Litovsky S, Rumberger J, Badimon JJ, Stefanadis C, Moreno P, Pasterkamp G, Fayad Z, Stone PH, Waxman S, Raggi P, Madjid M, Zarrabi A, Burke A, Yuan C, Fitzgerald PJ, Siscovick DS, de Korte CL, Aikawa M, Juhani Airaksinen KE, Assmann G, Becker CR, Chesebro JH, Farb A, Galis ZS, Jackson C, Jang IK, Koenig W, Lodder RA, March K, Demirovic J, Navab M, Priori SG, Rekhter MD, Bahr R, Grundy SM, Mehran R, Colombo A, Boerwinkle E, Ballantyne C, Insull W Jr, Schwartz RS, Vogel R, Serruys PW, Hansson GK, Faxon DP, Kaul S, Drexler H, Greenland P, Muller JE, Virmani R, Ridker PM, Zipes DP, Shah PK, Willerson JT (2003) From vulnerable plaque to vulnerable patient: a call for new definitions and risk assessment strategies: part I. Circulation 108(14):1664–1672. doi:10.1161/01.CIR.0000087480.94275.97 , 108/14/1664 [pii]
10. Lovett JK, Gallagher PJ, Hands LJ, Walton J, Rothwell PM (2004) Histological correlates of carotid plaque surface morphology on lumen contrast imaging. Circulation 110(15):2190–2197. doi:10.1161/01.CIR.0000144307.82502.32, 01.CIR.0000144307.82502.32 [pii]
11. Eliasziw M, Streifler JY, Fox AJ, Hachinski VC, Ferguson GG, Barnett HJ (1994) Significance of plaque ulceration in symptomatic patients with high-grade carotid stenosis. North American Symptomatic Carotid Endarterectomy Trial. Stroke 25(2):304–308
12. Rothwell PM, Gibson R, Warlow CP (2000) Interrelation between plaque surface morphology and degree of stenosis on carotid angiograms and the risk of ischemic stroke in patients with symptomatic carotid stenosis. On behalf of the European Carotid Surgery Trialists' Collaborative Group. Stroke 31(3):615–621
13. Hankey GJ, Warlow CP, Molyneux AJ (1990) Complications of cerebral angiography for patients with mild carotid territory ischaemia being considered for carotid endarterectomy. J Neurol Neurosurg Psychiatry 53(7):542–548
14. Willinsky RA, Taylor SM, TerBrugge K, Farb RI, Tomlinson G, Montanera W (2003) Neurologic complications of cerebral angiography: prospective analysis of 2,899 procedures and re-

view of the literature. Radiology 227(2):522–528. doi:10.1148/radiol.2272012071, 2272012071 [pii]
15. Saba L, Anzidei M, Sanfilippo R, Montisci R, Lucatelli P, Catalano C, Passariello R, Mallarini G (2011) Imaging of the carotid artery. Atherosclerosis 220(2):294–309. doi:10.1016/j.atherosclerosis.2011.08.048, S0021-9150(11)00852-5 [pii]
16. European Society of Radiology (2010) White paper on imaging biomarkers. Insights Imaging 1:42–45. doi:10.1007/s13244-010-0025-8
17. Beitzke D, Wolf F, Edelhauser G, Plank C, Schernthaner R, Weber M, Nolz R, Lammer J, Loewe C (2011) Computed tomography angiography of the carotid arteries at low kV settings: a prospective randomised trial assessing radiation dose and diagnostic confidence. Eur Radiol 21(11):2434–2444. doi:10.1007/s00330-011-2188-1
18. Cademartiri F, van der Lugt A, Luccichenti G, Pavone P, Krestin GP (2002) Parameters affecting bolus geometry in CTA: a review. J Comput Assist Tomogr 26(4):598–607, doi:00004728-200207000-00022 [pii]
19. de Monye C, de Weert TT, Zaalberg W, Cademartiri F, Siepman DA, Dippel DW, van der Lugt A (2006) Optimization of CT angiography of the carotid artery with a 16-MDCT scanner: craniocaudal scan direction reduces contrast material-related perivenous artifacts. AJR Am J Roentgenol 186(6):1737–1745. doi:10.2214/AJR.05.0143, 186/6/1737 [pii]
20. Liu Y, Hopper KD, Mauger DT, Addis KA (2000) CT angiographic measurement of the carotid artery: optimizing visualization by manipulating window and level settings and contrast material attenuation. Radiology 217(2):494–500
21. de Weert TT, Ouhlous M, Zondervan PE, Hendriks JM, Dippel DW, van Sambeek MR, van der Lugt A (2005) In vitro characterization of atherosclerotic carotid plaque with multidetector computed tomography and histopathological correlation. Eur Radiol 15(9):1906–1914. doi:10.1007/s00330-005-2712-2
22. van Straten M, Venema HW, Streekstra GJ, Majoie CB, den Heeten GJ, Grimbergen CA (2004) Removal of bone in CT angiography of the cervical arteries by piecewise matched mask bone elimination. Med Phys 31(10):2924–2933
23. Venema HW, Hulsmans FJ, den Heeten GJ (2001) CT angiography of the circle of Willis and intracranial internal carotid arteries: maximum intensity projection with matched mask bone elimination-feasibility study. Radiology 218(3):893–898
24. Uotani K, Watanabe Y, Higashi M, Nakazawa T, Kono AK, Hori Y, Fukuda T, Kanzaki S, Yamada N, Itoh T, Sugimura K, Naito H (2009) Dual-energy CT head bone and hard plaque removal for quantification of calcified carotid stenosis: utility and comparison with digital subtraction angiography. Eur Radiol 19(8):2060–2065. doi:10.1007/s00330-009-1358-x
25. Elgersma OE, Buijs PC, Wust AF, van der Graaf Y, Eikelboom BC, Mali WP (1999) Maximum internal carotid arterial stenosis: assessment with rotational angiography versus conventional intraarterial digital subtraction angiography. Radiology 213(3):777–783
26. Koelemay MJ, Nederkoorn PJ, Reitsma JB, Majoie CB (2004) Systematic review of computed tomographic angiography for assessment of carotid artery disease. Stroke 35(10):2306–2312. doi:10.1161/01.STR.0000141426.63959.cc, 01.STR.0000141426.63959.cc [pii]
27. Hollingworth W, Nathens AB, Kanne JP, Crandall ML, Crummy TA, Hallam DK, Wang MC, Jarvik JG (2003) The diagnostic accuracy of computed tomography angiography for traumatic or atherosclerotic lesions of the carotid and vertebral arteries: a systematic review. Eur J Radiol 48(1):88–102, doi:S0720048X03002006 [pii]
28. Bossuyt PM, Reitsma JB, Bruns DE, Gatsonis CA, Glasziou PP, Irwig LM, Lijmer JG, Moher D, Rennie D, de Vet HC, Standards for Reporting of Diagnostic Accuracy (2003) Towards complete and accurate reporting of studies of diagnostic accuracy: the STARD initiative. Clin Radiol 58(8):575–580, doi:S0009926003002587 [pii]
29. Wardlaw JM, Chappell FM, Best JJ, Wartolowska K, Berry E, NHS Research and Development Health Technology Assessment Carotid Stenosis Imaging Group (2006) Non-invasive imaging compared with intra-arterial angiography in the diagnosis of symptomatic carotid stenosis: a meta-analysis. Lancet 367(9521):1503–1512. doi:10.1016/S0140-6736(06)68650-9, S0140-6736(06)68650-9 [pii]
30. Chappell FM, Wardlaw JM, Young GR, Gillard JH, Roditi GH, Yip B, Pell JP, Rothwell PM, Brown MM, Gough MJ, Randall MS (2009) Carotid artery stenosis: accuracy of noninvasive tests – individual patient data meta-analysis. Radiology 251(2):493–502. doi:10.1148/radiol.2512080284, 2512080284 [pii]
31. Josephson SA, Bryant SO, Mak HK, Johnston SC, Dillon WP, Smith WS (2004) Evaluation of carotid stenosis using CT angiography in the initial evaluation of stroke and TIA. Neurology 63(3):457–460, doi:63/3/457 [pii]
32. Hacklander T, Wegner H, Hoppe S, Danckworth A, Kempkes U, Fischer M, Mertens H, Caldwell JH (2006) Agreement of multislice CT angiography and MR angiography in assessing the degree of carotid artery stenosis in consideration of different methods of postprocessing. J Comput Assist Tomogr 30(3):433–442, doi:00004728-200605000-00014 [pii]
33. Howard P, Bartlett ES, Symons SP, Fox AJ, Aviv RI (2010) Measurement of carotid stenosis on computed tomographic angiography: reliability depends on postprocessing technique. Can Assoc Radiol J 61(3):127–132. doi:10.1016/j.carj.2009.10.013, S0846-5371(09)00220-4 [pii]
34. Puchner S, Popovic M, Wolf F, Reiter M, Lammer J, Bucek RA (2009) Multidetector CTA in the quantification of internal carotid artery stenosis: value of different reformation techniques and axial source images compared with selective carotid arteriography. J Endovasc Ther 16(3):336–342. doi:10.1583/08-2636.1, 08-2636 [pii]
35. Kirbas C, Quek F (2004) A review of vessel extraction techniques and algorithms. ACM Comput Surv 36(2):81–121. doi:10.1145/1031120.1031121
36. Lesage D, Angelini ED, Bloch I, Funka-Lea G (2009) A review of 3D vessel lumen segmentation techniques: models, features and extraction schemes. Med Image Anal 13(6):819–845. doi:10.1016/j.media.2009.07.011, S1361-8415(09)00067-X [pii]
37. Manniesing R, Schaap M, Rozie S, Hameeteman R, Vukadinovic D, van der Lugt A, Niessen W (2010) Robust CTA lumen segmentation of the atherosclerotic carotid artery bifurcation in a large patient population. Med Image Anal 14(6):759–769. doi:10.1016/j.media.2010.05.001, S1361-8415(10)00046-0 [pii]
38. Manniesing R, Viergever MA, Niessen WJ (2007) Vessel axis tracking using topology constrained surface evolution. IEEE Trans Med Imaging 26(3):309–316. doi:10.1109/TMI.2006.891503
39. Milwer MB, Valencia LF, Hoyos MH, Magnin IE, Orkisz M (2007) Fast-marching contours for the segmentation of vessel lumen in CTA cross-sections. Conf Proc IEEE Eng Med Biol Soc 2007:791–794. doi:10.1109/IEMBS.2007.4352409
40. Cuisenaire O, Virmani S, Olszewski M, Ardon R (2008) Fully automated segmentation of carotid and vertebral arteries from contrast enhanced CTA. In: Reinhardt (ed) Med imaging 2008: image processing, SPIE. pp R–R-8. doi:10.1117/12.770481
41. Hameeteman K, Zuluaga MA, Freiman M, Joskowicz L, Cuisenaire O, Valencia LF, Gulsun MA, Krissian K, Mille J, Wong WC, Orkisz M, Tek H, Hoyos MH, Benmansour F, Chung AC, Rozie S, van Gils M, van den Borne L, Sosna J, Berman P, Cohen N, Douek PC, Sanchez I, Aissat M, Schaap M, Metz CT, Krestin GP, van der Lugt A, Niessen WJ, van Walsum T (2011) Evaluation framework for carotid bifurcation lumen segmentation and stenosis grading. Med Image Anal 15(4):477–488. doi:10.1016/j.media.2011.02.004, S1361-8415(11)00026-0 [pii]
42. Scherl H, Hornegger J, Prummer M, Lell M (2007) Semi-automatic level-set based segmentation and stenosis quantification

of the internal carotid artery in 3D CTA data sets. Med Image Anal 11(1):21–34. doi:10.1016/j.media.2006.09.004, S1361-8415(06)00076-4 [pii]
43. Wintermark M, Glastonbury C, Tong E, Lau BC, Schaeffer S, Chien JD, Haar PJ, Saloner D (2008) Semi-automated computer assessment of the degree of carotid artery stenosis compares favorably to visual evaluation. J Neurol Sci 269(1–2):74–79. doi:10.1016/j.jns.2007.12.023, S0022-510X(07)00816-7 [pii]
44. Berg M, Zhang Z, Ikonen A, Manninen H, Vanninen R (2005) Carotid stenosis assessment with CT angiography using advanced vessel analysis software. Int Congr Ser 1281:322–327
45. Zhang Z, Berg M, Ikonen A, Kononen M, Kalviainen R, Manninen H, Vanninen R (2005) Carotid stenosis degree in CT angiography: assessment based on luminal area versus luminal diameter measurements. Eur Radiol 15(11):2359–2365. doi:10.1007/s00330-005-2801-2
46. Groen HC, Gijsen FJ, van der Lugt A, Ferguson MS, Hatsukami TS, van der Steen AF, Yuan C, Wentzel JJ (2007) Plaque rupture in the carotid artery is localized at the high shear stress region: a case report. Stroke 38(8):2379–2381. doi:10.1161/STROKEAHA.107.484766, STROKEAHA.107.484766 [pii]
47. Lee SW, Antiga L, Spence JD, Steinman DA (2008) Geometry of the carotid bifurcation predicts its exposure to disturbed flow. Stroke 39(8):2341–2347. doi:10.1161/STROKEAHA.107.510644, STROKEAHA.107.510644 [pii]
48. Cademartiri F, Mollet NR, Runza G, Bruining N, Hamers R, Somers P, Knaapen M, Verheye S, Midiri M, Krestin GP, de Feyter PJ (2005) Influence of intracoronary attenuation on coronary plaque measurements using multislice computed tomography: observations in an ex vivo model of coronary computed tomography angiography. Eur Radiol 15(7):1426–1431. doi:10.1007/s00330-005-2697-x
49. Romero JM, Babiarz LS, Forero NP, Murphy EK, Schaefer PW, Gonzalez RG, Lev MH (2009) Arterial wall enhancement overlying carotid plaque on CT angiography correlates with symptoms in patients with high grade stenosis. Stroke 40(5):1894–1896. doi:10.1161/STROKEAHA.108.529008, STROKEAHA.108.529008 [pii]
50. Saba L, Mallarini G (2011) Carotid plaque enhancement and symptom correlations: an evaluation by using multidetector row CT angiography. AJNR Am J Neuroradiol 32(10):1919–1925. doi:10.3174/ajnr.A2605, ajnr.A2605 [pii]
51. Streifler JY, Eliasziw M, Fox AJ, Benavente OR, Hachinski VC, Ferguson GG, Barnett HJ (1994) Angiographic detection of carotid plaque ulceration. Comparison with surgical observations in a multicenter study. North American Symptomatic Carotid Endarterectomy Trial. Stroke 25(6):1130–1132
52. Randoux B, Marro B, Koskas F, Duyme M, Sahel M, Zouaoui A, Marsault C (2001) Carotid artery stenosis: prospective comparison of CT, three-dimensional gadolinium-enhanced MR, and conventional angiography. Radiology 220(1):179–185
53. Walker LJ, Ismail A, McMeekin W, Lambert D, Mendelow AD, Birchall D (2002) Computed tomography angiography for the evaluation of carotid atherosclerotic plaque: correlation with histopathology of endarterectomy specimens. Stroke 33(4):977–981
54. Saba L, Caddeo G, Sanfilippo R, Montisci R, Mallarini G (2007) Efficacy and sensitivity of axial scans and different reconstruction methods in the study of the ulcerated carotid plaque using multidetector-row CT angiography: comparison with surgical results. AJNR Am J Neuroradiol 28(4):716–723, doi:28/4/716 [pii]
55. de Weert TT, Cretier S, Groen HC, Homburg P, Cakir H, Wentzel JJ, Dippel DW, van der Lugt A (2009) Atherosclerotic plaque surface morphology in the carotid bifurcation assessed with multidetector computed tomography angiography. Stroke 40(4):1334–1340. doi:10.1161/STROKEAHA.108.538439, STROKEAHA.108.538439 [pii]
56. Wintermark M, Jawadi SS, Rapp JH, Tihan T, Tong E, Glidden DV, Abedin S, Schaeffer S, Acevedo-Bolton G, Boudignon B, Orwoll B, Pan X, Saloner D (2008) High-resolution CT imaging of carotid artery atherosclerotic plaques. AJNR Am J Neuroradiol 29(5):875–882. doi:10.3174/ajnr.A0950, ajnr.A0950 [pii]
57. Estes JM, Quist WC, Lo Gerfo FW, Costello P (1998) Noninvasive characterization of plaque morphology using helical computed tomography. J Cardiovasc Surg (Torino) 39(5):527–534
58. Oliver TB, Lammie GA, Wright AR, Wardlaw J, Patel SG, Peek R, Ruckley CV, Collie DA (1999) Atherosclerotic plaque at the carotid bifurcation: CT angiographic appearance with histopathologic correlation. AJNR Am J Neuroradiol 20(5):897–901
59. de Weert TT, Ouhlous M, Meijering E, Zondervan PE, Hendriks JM, van Sambeek MR, Dippel DW, van der Lugt A (2006) In vivo characterization and quantification of atherosclerotic carotid plaque components with multidetector computed tomography and histopathological correlation. Arterioscler Thromb Vasc Biol 26(10):2366–2372. doi:10.1161/01.ATV.0000240518.90124.57, 01.ATV.0000240518.90124.57 [pii]
60. Agatston AS, Janowitz WR, Hildner FJ, Zusmer NR, Viamonte M Jr, Detrano R (1990) Quantification of coronary artery calcium using ultrafast computed tomography. J Am Coll Cardiol 15(4):827–832, doi:0735-1097(90)90282-T [pii]
61. Kwee RM (2010) Systematic review on the association between calcification in carotid plaques and clinical ischemic symptoms. J Vasc Surg 51(4):1015–1025. doi:10.1016/j.jvs.2009.08.072, S0741-5214(09)01788-1 [pii]
62. de Weert TT, de Monye C, Meijering E, Booij R, Niessen WJ, Dippel DW, van der Lugt A (2008) Assessment of atherosclerotic carotid plaque volume with multidetector computed tomography angiography. Int J Cardiovasc Imaging 24(7):751–759. doi:10.1007/s10554-008-9309-1
63. Vukadinovic D, van Walsum T, Manniesing R, Rozie S, Hameeteman R, de Weert TT, van der Lugt A, Niessen WJ (2010) Segmentation of the outer vessel wall of the common carotid artery in CTA. IEEE Trans Med Imaging 29(1):65–76. doi:10.1109/TMI.2009.2025702
64. Vukadinovic D, Rozie S, van Gils M, van Walsum T, Manniesing R, van der Lugt A, Niessen WJ (2011) Automated versus manual segmentation of atherosclerotic carotid plaque volume and components in CTA: associations with cardiovascular risk factors. Int J Cardiovasc Imaging 28(4):877–887. doi:10.1007/s10554-011-9890-6
65. Rozie S, de Weert TT, de Monye C, Homburg PJ, Tanghe HL, Dippel DW, van der Lugt A (2009) Atherosclerotic plaque volume and composition in symptomatic carotid arteries assessed with multidetector CT angiography; relationship with severity of stenosis and cardiovascular risk factors. Eur Radiol 19(9):2294–2301. doi:10.1007/s00330-009-1394-6
66. Homburg PJ, Rozie S, van Gils MJ, van den Bouwhuijsen QJ, Niessen WJ, Dippel DW, van der Lugt A (2011) Association between carotid artery plaque ulceration and plaque composition evaluated with multidetector CT angiography. Stroke 42(2):367–372. doi:10.1161/STROKEAHA.110.597369, STROKEAHA.110.597369 [pii]
67. Wintermark M, Arora S, Tong E, Vittinghoff E, Lau BC, Chien JD, Dillon WP, Saloner D (2008) Carotid plaque computed tomography imaging in stroke and nonstroke patients. Ann Neurol 64(2):149–157. doi:10.1002/ana.21424
68. Nandalur KR, Hardie AD, Raghavan P, Schipper MJ, Baskurt E, Kramer CM (2007) Composition of the stable carotid plaque: insights from a multidetector computed tomography study of plaque volume. Stroke 38(3):935–940. doi:10.1161/01.STR.0000257995.74834.92, 01.STR.0000257995.74834.92 [pii]

Quantitative Computed Tomography Analysis in the Assessment of Coronary Artery Disease

12

Erica Maffei, Giancarlo Messalli, Cesare Mantini, Teresa Arcadi, Chiara Martini, Massimo Imbriaco, and Filippo Cademartiri

1 Introduction

Coronary artery disease (CAD) is one of the leading causes of death in developed countries. The correct evaluation of CAD presence and severity is fundamental for establish an appropriate clinical management. Recent literature confirmed multi detector computed tomography (MDCT) as a noninvasive imaging technique able to rule out and rule in CAD with a very high accuracy compared with conventional coronary angiography (CCA) [1–3].

Numerous studies successfully investigated the incremental prognostic value of MDCT over other noninvasivetests and, as a result, this tool is increasingly being used in CAD evaluation [4–9].

However the plaque burden and stenosis severity on MDCT is usually visually assessed with sequent inherent limitations. Recent technologies have permitted a real quantitative assessment of CAD.

2 Calcium Score

Coronary calcium (CA) is widely recognized as a remnant of passed atherosclerosis and it reflects the epicardial coronary artery total plaque burden [10–12]. Numerous studies report CA as a predictor of cardiac events in patients, providing independent and incremental prognostic information over factor-based risk calculators, such as Framingham and Procam [13].

Electron beam computed tomography was the first tool able to identify and quantify CA and extensive database have been drawn up to correlate the extent of CA to cardiac events, according to ethnicity [14–18]. Relative recent studies demonstrated MDCT is comparable to electron-beam CT for coronary calcification screening and nowadays MDCT is routinely used for this issue [19].

According to the method described by Agatston, a calcified lesion (CL) is defined as an area ≥ 1 mm^2 lying on coronary arteries and having a density ≥ 130 HU; these cut-off values permit to eliminate single pixels with a computed tomographic density ≥ 130 HU due to noise or non CL. Today most of post-processing workstations allow a colored display of CL simplifying the operator job who has just to trace a "region of interest" (ROI) around colored plaque (Fig. 12.1). Automated measurements of the lesion area in square millimeters and the maximal computed tomographic number of each ROI are recorded by the workstation [14]; for each lesion, a score is determined based on the CL area and maximal computed tomographic number; in particular, the area is multiplied for the density score which is:

E. Maffei • T. Arcadi • C. Martini
Department of Radiology, Giovanni XXIII Hospital, Monastier, Treviso, Italy
e-mail: ericamaffei@gmail.com; teresaarcadi@yahoo.it; Chiaramartini10@gmail.com

G. Messalli
Department of Radiology, SDN IRCCS – Institute of Diagnostic and Nuclear Research, Naples, Italy

Department of Biomorphological and Functional Sciences, University Federico II, Naples, Italy
e-mail: giancarlomessalli@hotmail.it

C. Mantini
Department of Neuroscience and Imaging, Section of Diagnostic Imaging and Therapy, "G. D'Annunzio" University, Chieti, Italy
e-mail: cesare.mantini@gmail.com

M. Imbriaco
Department of Radiology, University Federico II, Naples, Italy

Department of Biomorphological and Functional Sciences, University Federico II, Naples, Italy
e-mail: mimbriaco@hotmail.com

F. Cademartiri (✉)
Department of Radiology, Erasmus Medical Center University, Rotterdam, The Netherlands

Cardio-Vascular Imaging Unit, Giovanni XXIII Hospital, Via Giovanni XXIII 7, 31050 Monastier di Treviso, Treviso, Italy
e-mail: filippocademartiri@gmail.com

L. Saba et al. (eds.), *Multi-Modality Atherosclerosis Imaging and Diagnosis*,
DOI 10.1007/978-1-4614-7425-8_12,

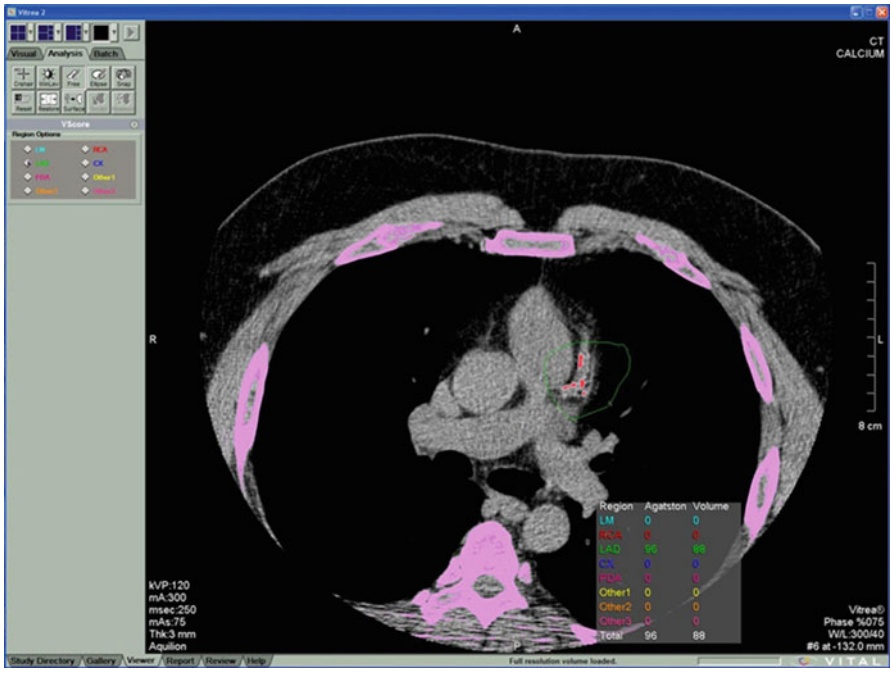

Fig. 12.1 Calcified plaques on left anterior descending quantified with Agatston score and volume evaluation

(a) One, if the density plaque (DP) is $130 < DP < 199$
(b) Two, if $200 < DP < 299$
(c) Three, if $300 < DP < 399$
(d) Four, if $DP \geq 400$

The total calcium score (CaS) according to Agatston is calculated summing all the scores of all CLs present in epicardial coronary arteries (Fig. 12.1) [14].

Recent guidelines for interpretation of MDCT state that when reporting, the calcium score for each vessel and a total calcium score should be written [20].

Different papers showed an interscan variability too large to make monitoring annual change meaningful on an individual basis, so on other techniques of calcium quantification have been proposed, such as calcium volume (CV) and calcium mass (CM) [21]. CV is calculated tracing a ROI around each CL, then the software multiplies each area with slice thickness. The total sum is the CV in mm^3 (Fig.12.1). CM is calculated tracing a ROI around each CL, then the software multiplies every plaque area with its density in HU; finally, the sum of all measurements is multiplied by a scanner and scan protocol-specific calibration factor allowing for calculating the absolute mass of coronary calcium in mg calcium hydroxyapatite (CaHA) [22–24]. Of worth, the volume and mass score are less commonly used in clinical practice, since there is no current validation data for this measures (no normograms and outcome studies) and the Society of Cardiovascular Computed Tomography suggests these scores should be accompanied by reporting of the more traditional Agatston score [20]; furthermore non-contrast

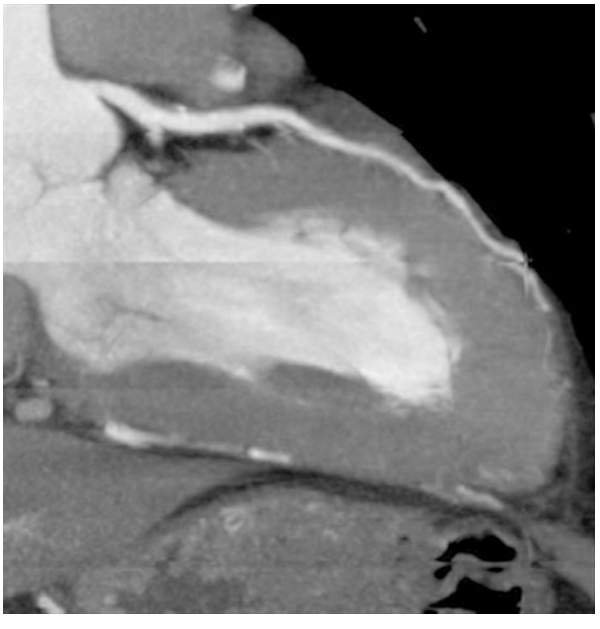

Fig. 12.2 MPR thick of non-calcified eccentric plaque positively remodeled lying on distal left main and proximal LAD, without significant stenosis; visual assessment = caliper reduction <50 %

CT is nowadays considered as appropriate for intermediate coronary heart disease (CHD) risk patients and for a specific subgroup of low-risk patients in whom a family history of CHD was present in relatives at a young age [20].

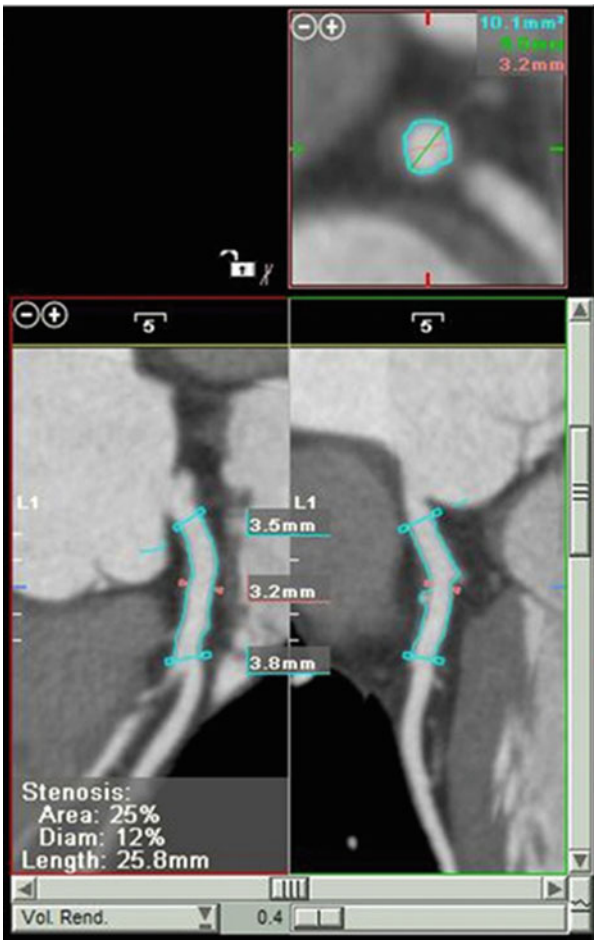

Fig. 12.3 MPR thick of non-calcified eccentric plaque positively remodeled lying on distal left main and proximal LAD, without significant stenosis; quantitative assessment of %AS = 25 %

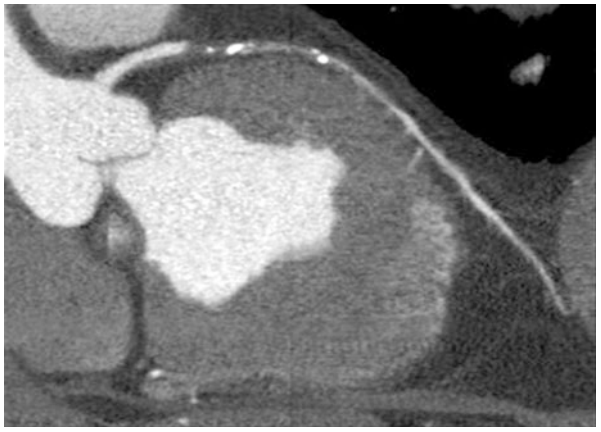

Fig. 12.4 MPR reconstruction of a totaled occluded mid-portion left anterior descending reperfused in distal tract

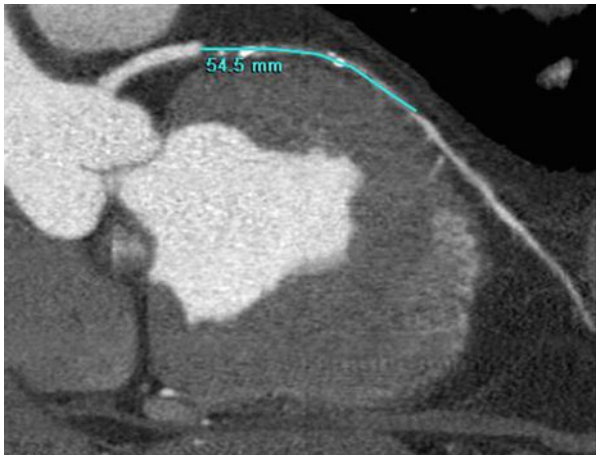

Fig. 12.5 MPR reconstruction of a totaled occluded mid-portion left anterior descending reperfused in distal tract. The image shows the length stenosis quantification

3 Quantification of Coronary Artery Stenosis

Molecular and cellular events leading to atherosclerosis, such as lipoprotein deposition, inflammation, smooth muscle cell proliferation, apoptosis, necrosis, calcification, and fibrosis, cause specific geometric and compositional changes in coronary vessels [25, 26]. Some of these changes, such as increased plaque volume, positive remodeling, lipoprotein deposition in the form of non-calcified plaques, and calcification, can be detected by contrast-enhanced MDCT [26].

MDCT has gained acceptance as an accurate, noninvasive tool to evaluate coronary artery disease, in most of the cases with a dichotomous score assessment (cutoff value 50 %) for significant stenosis [1–3, 27] (Fig. 12.2); however, the visual score assessment represents a major limitation of this technique and quantitative analysis of coronary stenosis is aimed to overcoming this drawback. With recent imaging technology and user-friendly post-processing tools, a quantitative evaluation of stenosis, which may be preferred in terms of diagnostic accuracy and reproducibility, has become feasible. Recent papers explored the role of MDCT in quantify coronary artery stenosis; in most of the cases CCA was considered the reference standard but last literature confirmed the limitation of CCA in the assessment of complex vasculature anatomy [28]. Because of its tomographic nature, MDCT allows the display of coronary vessels in unlimited projections, including cross-sectional views and three-dimensional vessel reconstructions and studies using intravascular ultrasound (IVUS) as the gold standard found superior accuracy for MDCT stenosis quantification compared to CCA [28–30].

Different geometrical parameters are nowadays used to quantify CAD with MDCT. They include plaque length (PL), minimal lumen diameter (MLD), percentage of diameter stenosis (%DS), minimal lumen area (MLA), percentage of

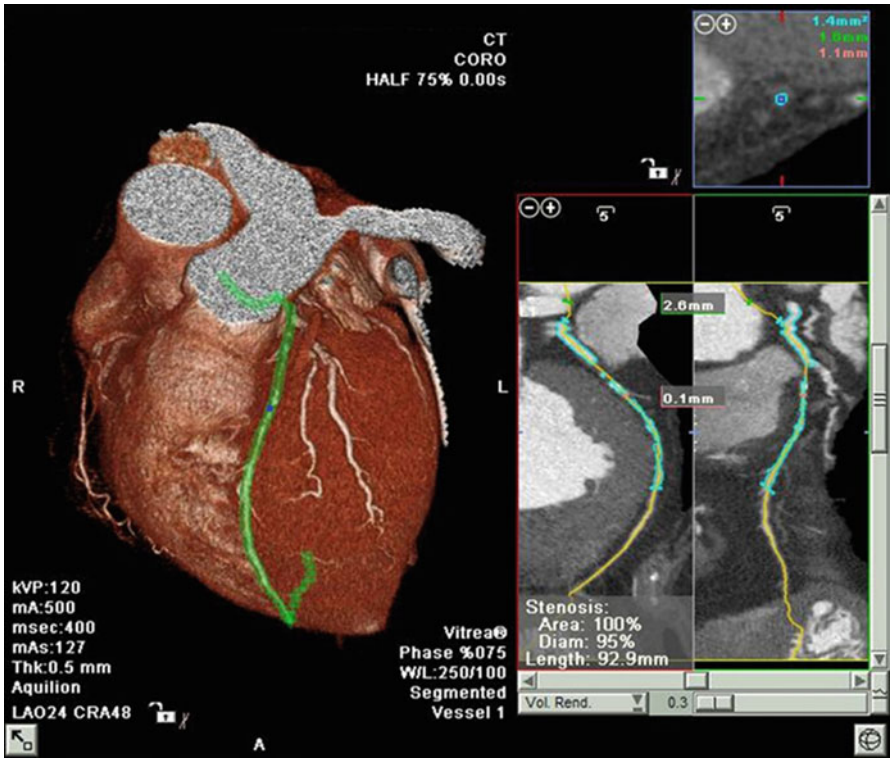

Fig. 12.6 Volume rendering and MPR reconstructions of a totaled occluded mid-portion left anterior descending with %AS quantification

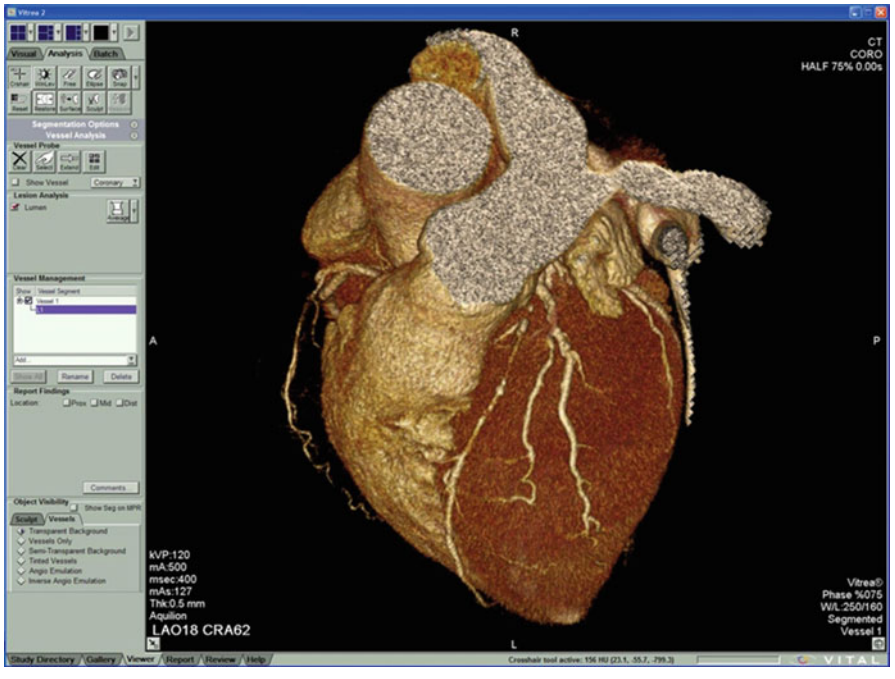

Fig. 12.7 Volume rendering reconstruction of a totaled occluded mid-portion left anterior descending

area stenosis (%AS), percentage of atheroma volume (%AV), and remodeling index (RI) [29, 30]. The %DS is calculated as (diameter lesion/diameter mean reference diameter) × 100, where the mean reference diameter is calculated by averaging the diameter of the proximal and distal reference slices to correct for vessel tapering; similarly, %AS is calculated as (area lesion/area mean reference area) × 100, where the mean reference area is calculated by averaging the area of

the proximal and distal reference slices to correct for vessel tapering. %AV is calculated with the following equation: (total vessel volume − total lumen volume)/total vessel volume × 100. RI is calculated as (total vessel area)/(mean of proximal and distal reference areas) [31].

Geometrical parameters are usually accompanied by compositional parameters in particular dividing plaques in three calcified, non-calcified, and mixed with some authors distinguishing between Calcified Plaque (CP) (attenuation values 150 HU or greater), High Density Non-calcified Plaques (HD-NCP) (30–149 HU), and Low Density Non-calcified Plaques (LD-NCP) (−100 to +30 HU) [31].

Literature data confirmed the feasibility of quantitative coronary MDCT stenosis and plaque measurements with heterogeneous sensitivity ($I^2 = 82\,\%$) reported by a recent meta-analysis, in part explained by scanner type (16-slice MDCT 0.84; 95 % CI: 0.80–0.88 and 64-slice MDCT 0.94; 95 % CI: 0.83–0.98) [26]. For quantitative stenosis assessment, MDCT slightly overestimated lumen area by 0.46 mm^2 (95 % CI: 0.14–0.79), or by 6.7 % ($p = 0.005$), with plaque area and volume being similar between CT and IVUS (plaque area mean difference 0.09 mm^2, 95 % CI: −1.00 to 1.18 mm^2, $p = 0.88$; plaque volume mean difference 5.30 mm^3, 95 % CI: −3.01 to 13.60 mm^3, $p = 0.21$); %AS is very similar between CT and IVUS (weighted mean difference −1.81 %, 95 % CI: −4.10 to 0.49, $p = 0.12$) and represent the most concordant parameter (Fig. 12.3).

Different papers showed a slight overestimation of calcified plaque stenosis due to blooming effect with sequent poor correlation and a larger limit of agreement in the lesions with calcified plaque compared with non-calcified plaques [32]; anyway the quantitative approach is found to be reproducible and may be used for the assessment of plaque progression [26, 30, 33, 34].

The powerful of tomographic nature of MDCT may be useful also to quantify lesion length and density in totaled occluded coronary artery, furnishing an added value over CCA for stent planning in chronic occlusion [35] (Figs. 12.4, 12.5, 12.6, and 12.7).

The characterization of plaque components is one of the biggest challenges of MDCT with different papers dealing with this issue; a significant overlap exists between lipid and fibrous material, making interpretation of plaque HU problematic [20, 30, 34, 36]; anyway all studies agree on the fact that a correlation is found for all plaque components but with large limits of agreement.

In summary, although future technical developments may improve the accuracy, at the state, the relatively wide limits of agreement for geometrical and compositional parameters with MDCT suggest that quantification should only supplement and not replace the more descriptive report in the clinical practice [20, 30]. Of worth, they can be used in well-selected clinical trials.

4 Future Directions

Even if MDCT has been one of the greatest advances in the noninvasive diagnosis of CAD in the past decade, it is a poor discriminator of the functional impact of identified plaques [2, 3, 37]. The mismatch between anatomic and functional evaluation of CAD can be due to microvascular dysfunction independent of epicardial coronary arteries, multiple non-significant stenoses in series, difficult assessment of stenoses grading in calcified plaques, and to collateral blood flow [37].

Nowadays, recent technologies allowed a rest and stress myocardial perfusion with MDCT and preliminary and satisfying results are available in animals and humans showing MDCT is able to furnish qualitative and quantitative measurements of myocardial perfusion [38–40]. The confirm of these results in the next future will give to this tool the unique capability of providing anatomic as well as coronary stenosis-related functional data increasing the potential of MDCT to revolutionize the way we diagnose and treat ischemic heart disease [37].

References

1. Miller JM, Rochitte CE, Dewey M et al (2008) Diagnostic performance of coronary angiography by 64-row CT. N Engl J Med 359:2324–2336
2. Meijboom WB, Meijs MF, Schuijf JD et al (2008) Diagnostic accuracy of 64-slice computed tomography coronary angiography: a prospective, multicenter, multivendor study. J Am Coll Cardiol 52:2135–2144
3. Schuijf JD, Pundziute G, Jukema JW et al (2006) Diagnostic accuracy of 64-slice multislice computed tomography in the noninvasive evaluation of significant coronary artery disease. Am J Cardiol 98:145–148
4. de Azevedo CF, Hadlich MS, Bezerra SG, Petriz JL, Alves RR, de Souza O, Rati M, Albuquerque DC, Moll J (2011) Prognostic value of CT angiography in patients with inconclusive functional stress tests. JACC Cardiovasc Imaging 4(7):740–751
5. Buechel RR, Pazhenkottil AP, Herzog BA, Brueckner M, Nkoulou R, Ghadri JR, Küest SM, Wyss CA, Husmann L, Kaufmann PA (2011) Prognostic performance of low-dose coronary CT angiography with prospective ECG triggering. Heart 97(17):1385–1390
6. Yiu KH, de Graaf FR, Schuijf JD, van Werkhoven JM, Marsan NA, Veltman CE, de Roos A, Pazhenkottil A, Kroft LJ, Boersma E, Herzog B, Leung M, Maffei E, Leung DY, Kaufmann PA, Cademartiri F, Bax JJ, Jukema JW (2012) Age- and gender-specific differences in the prognostic value of CT coronary angiography. Heart 98(3):232–237, Epub 2011 Sep 13
7. La Grutta L, Runza G, Gentile G, Russo E, Lo Re G, Galia M, Bartolotta TV, Alaimo V, Malagò R, Cademartiri F, Cardinale AE, Midiri M (2011) Prognostic outcome of routine clinical noninvasive multidetector-row computed tomography coronary angiography in patients with suspected coronary artery disease: a 2-year follow-up study. Radiol Med 116(4):521–531
8. Maffei E, Seitun S, Martini C, Aldrovandi A, Arcadi T, Clemente A, Messalli G, Malagò R, Weustink A, Mollet N, Nieman K, Ardissino D, de Feyter P, Krestin G, Cademartiri F (2011) Prog-

nostic value of CT coronary angiography: focus on obstructive vs. nonobstructive disease and on the presence of left main disease. Radiol Med 116(1):15–31
9. Van Werkhoven JM, Cademartiri F, Seitun S, Maffei E, Palumbo A, Martini C, Tarantini G, Kroft LJ, de Roos A, Weustink AC, Jukema JW, Ardissino D, Mollet NR, Schuijf JD, Bax JJ (2010) Diabetes: prognostic value of CT coronary angiography – comparison with a nondiabetic population. Radiology 256(1):83–92
10. Rumberger JA, Simons DB, Fitzpatrick LA et al (1995) Coronary artery calcium areas by electron beam computed tomography and coronary atherosclerotic plaque area: a histopathologic correlative study. Circulation 92:2157–2162
11. Baumgart D, Schmermund A, Goerge G et al (1997) Comparison of electron beam computed tomography with intracoronary ultrasound and coronary angiography for detection of coronary atherosclerosis. J Am Coll Cardiol 30:57–64
12. Schmermund A, Baumgart D, Gorge G et al (1997) Coronary artery calcium in acute coronary syndromes: a comparative study of electron beam CT, coronary angiography, and intracoronary ultrasound in survivors of acute myocardial infarction and unstable angina. Circulation 96:1461–1469
13. Hecht HS, Budoff MJ, Berman DS, Ehrlich J, Rumberger JA (2006) Coronary artery calcium scanning: clinical paradigms for cardiac risk assessment and treatment. Am Heart J 151(6):1139–1146
14. Agatston AS, Janowitz WR, Hildner FJ, Zusmer NR, Viamonte M Jr, Detrano R (1990) Quantification of coronary artery calcium using ultrafast computed tomography. J Am Coll Cardiol 15(4):827–832
15. Budoff MJ, Yang TP, Shavelle RM (2002) Ethnic differences in coronary atherosclerosis. J Am Coll Cardiol 39:408–412
16. Newman AB, Naydeck BL, Whittle J et al (2002) Racial differences in coronary artery calcification in adults. Arterioscler Thromb Vasc Biol 22:424–430
17. Khuran C, Rosenbaum CG, Howard BV et al (2003) Coronary artery calcification in black women and white women. Am Heart J 145:724–729
18. Jain T, Peshock R, Darren K et al (2004) African Americans and Caucasians have a similar prevalence of coronary calcium in the Dallas Heart Study. J Am Coll Cardiol 44:1011–1017
19. Stanford W, Thompson BH, Burns TL, Heery SD, Burr MC (2004) Coronary artery calcium quantification at multi-detector row helical CT versus electron-beam CT. Radiology 230(2):397–402
20. Raff GL, Abidov A, Achenbach S, Berman DS, Boxt LM, Budoff MJ, Cheng V, DeFrance T, Hellinger JC, Karlsberg RP, Society of Cardiovascular Computed Tomography (2009) SCCT guidelines for the interpretation and reporting of coronary computed tomographic angiography. J Cardiovasc Comput Tomogr 3(2):122–136
21. Takahashi N, Bae KT (2003) Quantification of coronary artery calcium with multi-detector row CT: assessing interscan variability with different tube currents pilot study. Radiology 228(1):101–106
22. Becker CR, Majeed A, Crispin A, Knez A, Schoepf UJ, Boekstegers P, Steinbeck G, Reiser MF (2005) CT measurement of coronary calcium mass: impact on global cardiac risk assessment. Eur Radiol 15(1):96–101
23. Ohnesorge B, Flohr T, Fischbach R et al (2002) Reproducibility of coronary calcium quantification in repeat examinations with retrospectively ECG-gated multisection spiral CT. Eur Radiol 12(6):1532–1540
24. Ulzheimer S, Kalender WA (2003) Assessment of calcium scoring performance in cardiac computed tomography. Eur Radiol 13(3):484–497
25. Voros S (2009) Does imaging paint a sugarcoated picture of diabetic vessels? Plaque composition in diabetics by IVUS and CT angiography. J Nucl Cardiol 16:339–344
26. Voros S, Rinehart S, Qian Z, Joshi P, Vazquez G, Fischer C, Belur P, Hulten E, Villines TC (2011) Coronary atherosclerosis imaging by coronary CT angiography: current status, correlation with intravascular interrogation and meta-analysis. JACC Cardiovasc Imaging 4(5):537–548
27. Ropers D, Rixe J, Anders K, Küttner A, Baum U, Bautz W, Daniel WG, Achenbach S (2006) Usefulness of multidetector row spiral computed tomography with 64- × 0.6-mm collimation and 330-ms rotation for the noninvasive detection of significant coronary artery stenoses. Am J Cardiol 97:343–348
28. Arbab-Zadeh A, Texter J, Ostbye KM, Kitagawa K, Brinker J, George RT, Miller JM, Trost JC, Lange RA, Lima JA, Lardo AC (2010) Quantification of lumen stenoses with known dimensions by conventional angiography and computed tomography: implications of using conventional angiography as gold standard. Heart 96(17):1358–1363
29. Caussin C, Larchez C, Ghostine S et al (2006) Comparison of coronary minimal lumen area quantification by sixty-four-slice computed tomography versus intravascular ultrasound for intermediate stenosis. Am J Cardiol 98:871e6
30. Rinehart S, Vazquez G, Qian Z, Murrieta L, Christian K, Voros S (2011) Quantitative measurements of coronary arterial stenosis, plaque geometry, and composition are highly reproducible with a standardized coronary arterial computed tomographic approach in high-quality CT datasets. J Cardiovasc Comput Tomogr 5(1): 35–43
31. Voros S, Rinehart S, Qian Z, Vazquez G, Anderson H, Murrieta L, Wilmer C, Carlson H, Taylor K, Ballard W, Karmpaliotis D, Kalynych A, Brown C III (2011) Prospective validation of standardized, 3-dimensional, quantitative coronary computed tomographic plaque measurements using radiofrequency backscatter intravascular ultrasound as reference standard in intermediate coronary arterial lesions: results from the ATLANTA (assessment of tissue characteristics, lesion morphology, and hemodynamics by angiography with fractional flow reserve, intravascular ultrasound and virtual histology, and noninvasive computed tomography in atherosclerotic plaques) I study. JACC Cardiovasc Interv 4(2):198–208
32. Kang DK, Im NJ, Park SM, Lim HS (2011) CT comparison of visual and computerized quantification of coronary stenosis according to plaque composition. Eur Radiol 21(4):712–721
33. Otsuka M, Bruining N, Van Pelt NC, Mollet NR, Ligthart JM, Vourvouri E, Hamers R, De Jaegere P, Wijns W, Van Domburg RT, Stone GW, Veldhof S, Verheye S, Dudek D, Serruys PW, Krestin GP, De Feyter PJ (2008) Quantification of coronary plaque by 64-slice computed tomography: a comparison with quantitative intracoronary ultrasound. Invest Radiol 43(5):314–321
34. Brodoefel H, Reimann A, Heuschmid M et al (2008) Characterization of coronary atherosclerosis by dual-source computed tomography and HU-based color mapping: a pilot study. Eur Radiol 18:2466–2474
35. Choi JH, Song YB, Hahn JY, Choi SH, Gwon HC, Cho JR, Jang Y, Choe Y (2011) Three-dimensional quantitative volumetry of chronic total occlusion plaque using coronary multidetector computed tomography. Circ J 75(2):366–375
36. Leber AW, Becker A, Knez A et al (2006) Accuracy of 64-slice computed tomography to classify and quantify plaque volumes in the proximal coronary system: a comparative study using intravascular ultrasound. J Am Coll Cardiol 47:672–677
37. Sato A, Hiroe M, Tamura M, Ohigashi H, Nozato T, Hikita H, Takahashi A, Aonuma K, Isobe M (2008) Quantitative measures of coronary stenosis severity by 64-Slice CT angiography and relation to physiologic significance of perfusion in nonobese patients: comparison with stress myocardial perfusion imaging. J Nucl Med 49(4):564–572

38. San Roman JA, Vilacosta I, Castillo JA, Rollan MJ, Hernandez M, Peral V et al (1998) Selection of the optimal stress test for the diagnosis of coronary artery disease. Heart 80:370–376
39. Valdiviezo C, Ambrose M, Mehra V, Lardo AC, Lima JA, George RT (2010) Quantitative and qualitative analysis and interpretation of CT perfusion imaging. J Nucl Cardiol 17(6):1091–1100
40. Christian TF, Frankish ML, Sisemoore JH, Christian MR, Gentchos G, Bell SP, Jerosch-Herold M (2010) Myocardial perfusion imaging with first-pass computed tomographic imaging: measurement of coronary flow reserve in an animal model of regional hyperemia. J Nucl Cardiol 17(4):625–630

Part IV

Ultrasound Atherosclerosis Imaging

A Gamma Mixture Model for IVUS Imaging

13

G. Vegas-Sánchez-Ferrero, M. Martín-Fernández, and J. Miguel Sanches

1 Introduction

Cholesterol and collections of blood cells in the wall artery conforms what is commonly called vulnerable plaque, which is prone to cause cardiovascular problems like heart attack and brain stroke [1,2]. The presence of these structures in the arterial wall causes mechanical stress, which leads to rupture of the vulnerable plaque and clots. Stenosis is also one of the problems derived from the presence of plaques.

The coronary angiography has been considered the standard imaging modality among all the imaging techniques commonly used for detecting atherosclerotic plaques in the coronary arteries. However, this modality has shown a limited ability to accurately measure the degree of stenosis and to characterize the plaque. Concretely, most patients with acute coronary syndromes have minimal or mild coronary lumen obstruction detected by angiography [2]. Given these limitations, the importance of detecting stenosis areas and the presence of different kinds of plaque becomes evident. Instead of angiography, intravascular ultrasonography (IVUS) has demonstrated to provide clear visualization of arterial wall inner morphology and turns out to be a convenient alternative method for assessing the severity of morphology lesions [2]. The IVUS data acquisition procedure consists of introducing a catheter similar to the standard catheters employed in coronary angioplasty. The catheter is inserted inside the artery and moved until it reaches the artery segment to be studied. A piezoelectric transducer transmits acoustic pulses in a rotating fashion and collects the A-lines that correspond to the reflected echoes along the depth, ρ, for each direction θ. This results in a polar representation of a 360° cross-sectional view. Then, the image is interpolated and geometrically arranged to build the Cartesian image. In Fig. 13.1 an example of an IVUS image in polar and Cartesian coordinates is depicted.

The acoustic response of different kinds of plaque is qualitative known: lipidic plaque presents low echolucent response; fibrous plaque presents intermediate level echogenicity; calcified plaque is hyperechogenic and usually presents an acoustic shadow due to the series of echoes created by multiple reflections within a small but highly reflective tissue [2–5].

However, although this qualitative characterization of the plaques offers an intuitive interpretation of IVUS images, an important effort has been done to understand the echomorphology and pathological evolution [6]. A quantitative characterization of plaques allows developing or refining methods for plaque detection, risk predictions, and potentially suggesting different therapies.

Obtaining a quantitative characterization of the ultrasonic responses of plaques involve the analysis of the physics of ultrasound imaging throughout the acquisition process.

Basically, the process of image formation in medical ultrasound begins with the propagation of a pulse packet emission along the beam vector axis. This pulse changes its shape according to media properties The traveling pulse is scattered by objects placed at different scattering depths and cause delays in the pulse.

As a result, the backscattered (received) signal is corrupted by a characteristic granular pattern noise called *speckle* which depends on the number of scatterers per resolution cell as well as their size [7, 8]. This type of multiplicative noise, in the sense its variance depends on the underlying signal, is observed in other modalities using coherent radiation such as LASER [9] and Synthetic-Aperture Radar (SAR) [10].

Speckle mainly depends on the microstructure of the tissues and thus its statistics can be used as tissue histological

G. Vegas-Sánchez-Ferrero (✉) • M. Martín-Fernández
Laboratorio de Procesado de Imagen (LPI), Universidad de Valladolid, Valladolid, Spain
e-mail: gvegsan@lpi.tel.uva.es; marcma@tel.uva.es

J.M. Sanches
Department of Bioengineering, Institute for Systems and Robotics, Instituto Superior Técnico/Technical University of Lisbon, Lisbon, Portugal
e-mail: jmrs@ist.utl.pt

L. Saba et al. (eds.), *Multi-Modality Atherosclerosis Imaging and Diagnosis*,
DOI 10.1007/978-1-4614-7425-8_13,

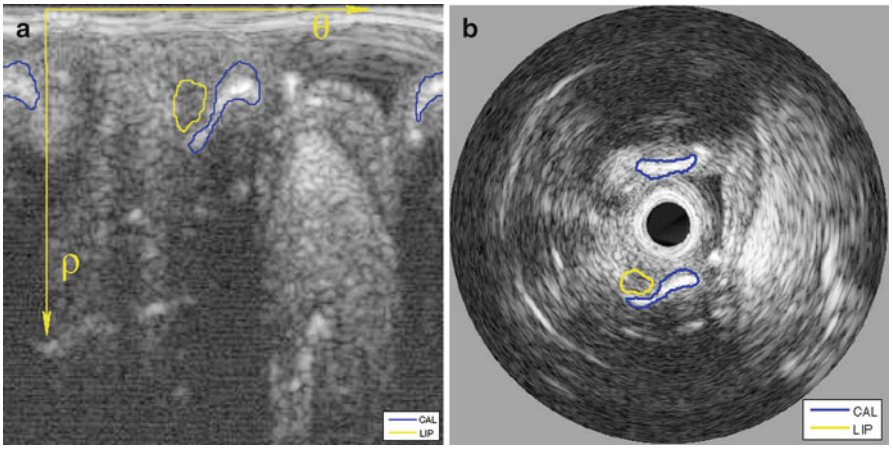

Fig. 13.1 IVUS image in polar coordinates (**a**) and Cartesian coordinates (**b**) with the presence of lipidic (LIP) and calcified (CAL) plaques that were histologically identified

descriptors [11]. These statistics strongly depend on the scatter density, that is, on the number and intensity distribution of the scatters in each resolution cell and the resulting *speckle* noise can be grouped in the following main classes:

- Fully developed: large number of scatters (central limit theorem can be applied) per resolution cell and nonexistence of deterministic component, modeled by Rayleigh distribution [12, 13].
- Fully resolved: large number of scatters per resolution cell and existence of deterministic component, modeled by Rice distribution [14].
- Partially developed: small number of scatters per resolution cell and nonexistence of deterministic component, modeled by K distribution [15, 16].
- Partially resolved: small number of scatters per resolution cell and existence of deterministic component, modeled by K-Homodyne distribution [17].

Fully developed speckle is the most common model for speckle formation. It considers a tissue or region composed of a large number of scatterers, acting as echo diffusers. These scatterers arise from inhomogeneity and structures approximately equal to or smaller in size than the wavelength of the ultrasound, such as tissue parenchyma, where there are changes in acoustic impedance on a microscopic level within the tissue.

There are different approximations for this model, the one-parameter probabilistic model that describe the pixel intensities in envelope data is by Rayleigh probability density function (PDF) [7, 13, 18].

Other distributions have been proposed for the characterization of speckle. Probably, the most noticeable distribution is the Nakagami proposed in [19]. This distribution has two parameters and can be considered as a generalization of the Rayleigh distribution. In [20], a model based on Nakagami distributions is proposed for the characterization of backscattered echo. This model is motivated from the fact that the Nakagami distribution generalizes the Rayleigh distribution and also appears to be similar to Rician distribution, which is also a generalization of the Rayleigh (see [20]).

Plaque echo-morphology is the contribution result of different tissue types (components). The lipidic plaque usually presents a fibrotic cap which has different acoustic response and thus different distributions [2]. Additionally, accumulation of blood cells (macrophages) within plaques may change their probabilistic models. Hence, a mixture model becomes an opportune strategy for statistically describing the echo-morphology of the plaque.

The Rayleigh mixture model (RMM) was first proposed in [8, 21] for plaque characterization and classification. In that work, a RMM was obtained by Expectation–Maximization method [22, 23]. Three kinds of plaque were considered in that study: fibrotic, lipidic, and calcified. The RMM parameters were estimated for each kind of plaque and were used, in combination to other textural features, to provide a descriptor of plaque composition. On the other hand, a Nakagami mixture model (NMM) was proposed in [24] for segmentation of arteries. This approach uses the Nakagami as a generalization of Rayleigh distribution as a good candidate to characterize the speckle.

Although the characterization of speckle can be modeled by different PDFs, the echo-morphology of plaque presents a more complicated nature than an isolated kind of speckle. It is the contribution result of different tissue types (components): the lipidic plaque usually presents a fibrotic cap which has different acoustic response and thus different distribution [2]. Additionally, the presence of macrophages within plaques change their probabilistic models.

The complexity of the composition of the plaque introduce difficulties when the echolucent response is modeled by a simple model such as a unimodal PDF (Rayleigh,

Rice, K or K-Homodyne). Instead of that, a mixture model offers a good strategy for statistically describing the echomorphology of the plaque. Among mixture models proposed in the literature for describing plaque characterization, two are of capital importance. On the one hand, a RMM which was first proposed in [8, 21] for plaque characterization and classification. In that work, a RMM was obtained by Expectation–Maximization method [22, 23]. Three kinds of plaque were considered in that study: fibrotic, lipidic, and calcified. The RMM parameters were estimated for each kind of plaque and were used, in combination to other textural features, to provide a descriptor of plaque composition.

On the other hand, a NMM was proposed in [24] for segmentation of arteries. This approach uses the Nakagami as a generalization of Rayleigh distribution as a good candidate to characterize the speckle. Note that both mixture models describe the behavior of speckle in the case of fully formed speckle. And the NMM could be considered as a generalization of the RMM.

Both the Rayleigh and the Nakagami have been commonly accepted assumptions for fully developed speckle. The former is justified because it is based on the physics of the data generation process, the later has proven to provide a better description since it is a two-parameter generalization of the Rayleigh. However, real-life cases of ultrasound images have shown that Rayleigh or Nakagami models do not describe it as good as expected. In [18, 25], many distributions were empirically fitted to real data and showed that fully developed speckle is better described by the Gamma distribution. Those distributions were tested in the resulting image after the reconstruction process, so it is clear that the different reconstruction stages modify dramatically the statistical behavior. This result was also confirmed in [7] where the PDFs were tested after the interpolation stage when no logarithmic compression is performed. In that work, experimental tests showed the superiority of the Gamma distribution over the Rayleigh and Nakagami for describing US data—85 % of the fully developed speckle areas passed the χ^2 test when a Gamma distribution was fitted, whereas 70 % and less than 10 % passed in the Nakagami and Rayleigh cases respectively.

The interpolation operation performed in the A-lines of the raw RF signal to resample the data and equalize the resolution in both dimensions, angle and depth seems to be the key element to explain why Gamma describes better the data than the Rayleigh or Nakagami distributions. The interpolation process can be formulated as linear filter that linearly combines different pixels that are Rayleigh distributed. As shown in [7], a linear combination of Rayleigh random variables can be accurately fitted by Gamma distributions even when the central limit theorem can be applied (when the number of combinations of Rayleigh distributions is high enough to apply the central limit theorem). Note that the interpolation process consists of a weighted sum of values that, in the case of Rayleigh distributed data, results in a different random variable. Hence, not only interpolation processes but every linear filter applied to a Rayleigh distributed data is a weighted sum of Rayleigh random variables, which is better described by a Gamma random variable than a Rayleigh.

A common stage of the acquisition process of US images is to downsample the acquisition in order to provide an isotropic resolution of the image. This resampling stage usually involves an interpolation stage where linear filtering is applied. This interpolation is performed when the final resolution is not a multiple of the initial resolution. In these conditions, the results obtained in [7, 18, 25] still hold and the Gamma distribution better describe US RF envelope downsampled data than the Rayleigh or Nakagami distributions.

In this chapter we propose a *Gamma mixture model* (GMM) to describe the interpolated/resampled RF envelope US data. This model is compared with the other mixture models (Rayleigh and Nakagami) for different sort of plaques.

The characterization method provides probability maps which can be of help for physicians or for automatic postprocessing techniques such as filtering or segmenting methods. Concretely, a filtering method based on the estimation of the underlying parameters of the speckle is presented.

The rest of the chapter is structured as follows: in Sect. 2 we justify the better behavior of the Gamma PDF when linear filters and/or interpolation are applied. This justification follows that one presented in [7]. In Sect. 3 we describe the dataset, the acquisition protocols, and histological validation for plaques for which the comparison between methods is performed. Section 5 is devoted to the GMM, where the GMM is derived. The comparison between mixture models and experiments are presented in Sect. 6. As an application of the characterization of the GMM probability maps, a filter is proposed in Sect. 7. Finally, we conclude in Sect. 8.

2 Interpolation on Probabilistic Models for Ultrasonic Images

2.1 Overview

Some image filtering and segmentation techniques for ultrasound imaging, as those approaches based on maximum likelihood and maximum a posteriori [25], rely on an accurate statistical model for the different regions in the image. This model is usually derived from the analysis of the acoustic physics and the information available of the ultrasound probe [7, 26]. However, the whole information during the acquisition process is not usually available, and therefore some suppositions must be considered. For example, images provided by practitioners usually do not include the

acquisition parameters as gain and/or contrast adjustment. Additionally, some of the steps of the acquisition process may be unknown, depending on the commercial firm of the ultrasound equipment.

In this section we focus on fully formed speckle. In fully formed speckle regions, acquired signal can be modeled following a Rayleigh distribution [13]. However, to form the final Cartesian image, these Rayleigh distributed data have to be interpolated. Thus, the resulting image will no longer follow a Rayleigh distribution. This section is devoted to model this final distribution taking into account the interpolation process [7, 26].

If no compression of the data is done (which will be an assumption throughout the section), we show that the results provided in literature [18, 25] hold with the interpolation probabilistic model here presented and that this approach can be extended easily to other distributions.

2.2 Interpolation Model

Ultrasonic images are constructed from a number of acoustic "lines" or vectors usually organized in a sequential pattern [26]. These vectors form lines in the image after conversion by envelope detection. Each line represents a time record of the scattered waves from different depths. The process of image formation begins with a pulse packet emission which travels along the beam vector axis and changes shape according to characteristics of the media. The traveling pulse is scattered by objects placed at different scattering depths and cause delays in the pulse. Reflections are received by the transducer and, considering a constant sound speed, the depths of the scattering objects can be estimated. These intercepted waves are integrated over the surface of the transducer with a suitable weighting and time delays are added for focusing and beamforming. The amplitude of the envelope record is usually logarithmically compressed but this is optional depending on the ultrasonic machine. At this point, when fully formed speckle regions are observed, a Rayleigh probabilistic distribution is often considered [9]. After this step all the lines are interpolated to form a complete Cartesian image from a number of image lines arranged in their geometrical attitude [7, 26].

Let $\{X_i\}$ be independent and identically distributed (IID) random variables (RVs) which follow a Rayleigh distribution $f_X(x)$:

$$f(x) = \frac{x}{\sigma^2} \exp \frac{-x^2}{2\sigma^2}, \quad x \geq 0. \tag{13.1}$$

When a simple scheme of interpolation is considered such the bilinear one in the 2D-case or trilinear in the 3D-case (which is likely to be the one used by the ultrasound machine because of its computational efficiency), the resultant interpolated value of the pixel can be calculated as

$$Y = \sum_{i=1}^{n} w_i X_i, \quad \text{where} \quad \sum_{i=1}^{n} w_i = 1. \tag{13.2}$$

The resultant PDF of the interpolated RV has no closed expression and several ways for calculating it has been presented in the last years [27]. In this work, we will consider a numerical approach based on quadrature methods due to its simple implementation, since we want to study the behavior of this PDF in order to validate the empirical approaches of the literature.

One simple way to calculate $f_Y(y)$ is to see it as the convolution of the weighted PDFs of independent RV. This way, a closed expression can be obtained when characteristic functions are used since a Rayleigh distribution admits a characteristic function which is known, though not simple [27]:

$$\begin{aligned} \phi_X(t) &= E\{e^{tX}\} = 1 + i\sigma t e^{-\sigma^2 t^2/2} \sqrt{\pi} 2 \left(\operatorname{erf}\left(i \frac{\sigma t}{\sqrt{2}} \right) + 1 \right) \\ &= {}_1F_1\left(1, \frac{1}{2}, \frac{-t^2\sigma^2}{2}\right) + i\sqrt{\frac{\pi}{2}} t\sigma e^{-t^2\sigma^2/2}, \end{aligned} \tag{13.3}$$

where $\operatorname{erf}(\cdot)$ is the error function defined as

$$\operatorname{erf}(x) = \frac{2}{\sqrt{\pi}} \int_0^x e^{-t^2} dt \tag{13.4}$$

and ${}_1F_1(a, b, x)$ is the confluent hypergeometric function of the first kind defined as

$${}_1F_1(a, b, x) = 1 + \frac{a}{b}x + \frac{a(a+1)}{b(b+1)} \frac{x^2}{2!} + \cdots. \tag{13.5}$$

So, the characteristic function of Y is

$$\phi_Y(t) = \prod_{i=1}^{n} \phi_i(t), \tag{13.6}$$

where $\phi_i(t)$ is the characteristic function of each $w_i X_i$. Note that w_i affects X_i in such a way that Y can be considered as the sum of Rayleigh RVs with different σ. The PDF is obtained from (13.6) by numerical quadrature.

This distribution is not practical in statistical estimation of real data, due to the large number of parameters to estimate. A simplified model is more suitable. Concretely, the sum of Rayleighs is approximated by a Gamma distribution. Note that a Gamma PDF has only two free parameters and the behavior of the tails is *similar* to the PDF of Y. In addition, in literature Gamma PDFs has also been used to model this kind of speckle [25], but no justification has been given.

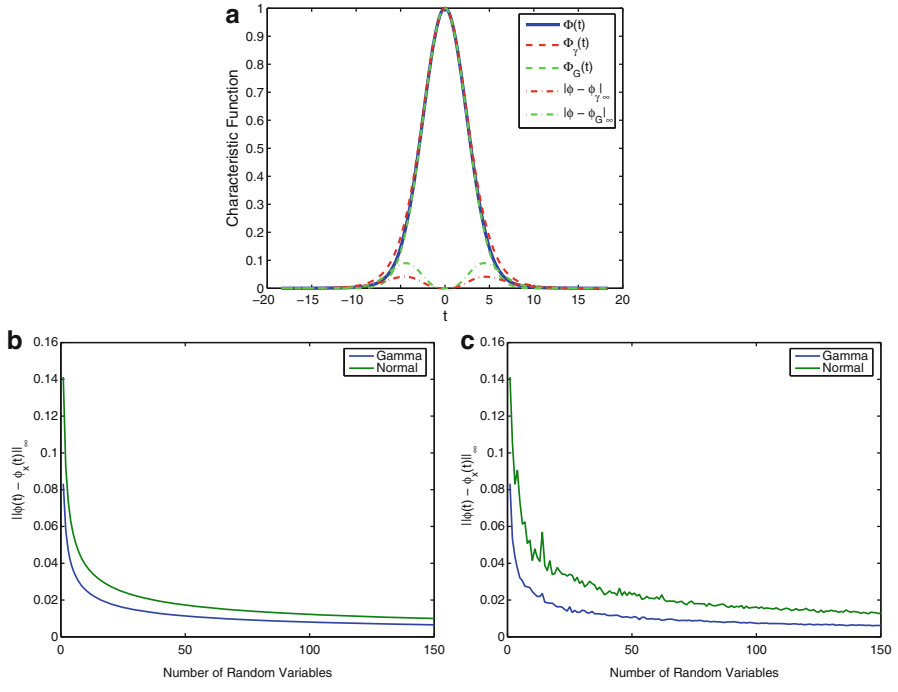

Fig. 13.2 Characteristic functions for Gamma, Normal, and interpolated Rayleighs RVs. (**a**) Four terms characteristic functions and the error committed (*dash–dotted lines*). (**b**) Error of the approach of Gamma and Normal when number of terms increases. (**c**) Error of the approach of Gamma and Normal when number of terms increases for random weights for each case. The errors were calculated by using the uniform norm of the difference between both functions

In Fig. 13.2 we show the characteristic function of a Gamma ϕ_γ, Gaussian ϕ_G, and theoretical sum of Rayleigh ϕ for four terms and the error committed in the approximation for an increasing number of terms by using the uniform norm of the difference.

In that figure we can see that the characteristic function of a Gamma distribution offers a better behavior than the Normal distribution even when the central limit theorem can be applied. Experiments were made considering the same weights of the RVs, however this approach can be done for arbitrary weights and the result still holds (see Fig. 13.2c).

In order to test this assumption we simulate speckle based in the acquisition model in the same fashion as it is done in [28]. This method scans an image and records the data in a matrix which is corrupted by means of the speckle formation model of [13] where the tissue is modeled as a collection of scatters that are so numerous and of size comparable to the wavelength. The speckle pattern is obtained by means of random walk which does not assume any statistical distribution in order to avoid any bias of the results.

In Fig. 13.3 we show the reconstructed image when no coherent echoes exist and the number of scatters is high enough to consider the speckle as a fully formed speckle pattern. As it is shown, the histogram of the image before interpolation follows a Rayleigh distribution whereas, in the case of the interpolated image, the result shows clearly that a Gamma distribution accurately fits to the data histogram.

3 Materials

In this work, the characterization is tested with the golden standard recently presented in [29]. This IVUS dataset consists of nine postmortem coronary arteries. From these arteries, 50 different images with the presence of plaques of different nature were selected. Then the arteries are sliced in order to characterize plaques by histological analysis.

The acquisition of the images was performed in the following way: the artery is separated from the heart fixed in a mid-soft plane and filled (using a catheter) with physiological saline solution at constant pressure (around 120 mmHg), simulating blood pressure. References of distal, proximal, left, and right positions are marked. The probe is introduced through the catheter and RF data are acquired in correspondence of plaques.

Real-time radio-frequency (RF) data acquisition was performed with the Galaxy II IVUS Imaging System (Boston Scientific) using a catheter Atlantis SR Pro 40 MHz (Boston Scientific). To collect and store the RF data, the imaging system has been connected to a workstation equipped with a 12-bit Acquiris acquisition card with a sampling rate of 200 MHz.

The RF data for each frame is arranged in a data matrix of $N \times M$ samples, where $M = 1{,}024$ isthe number of samples

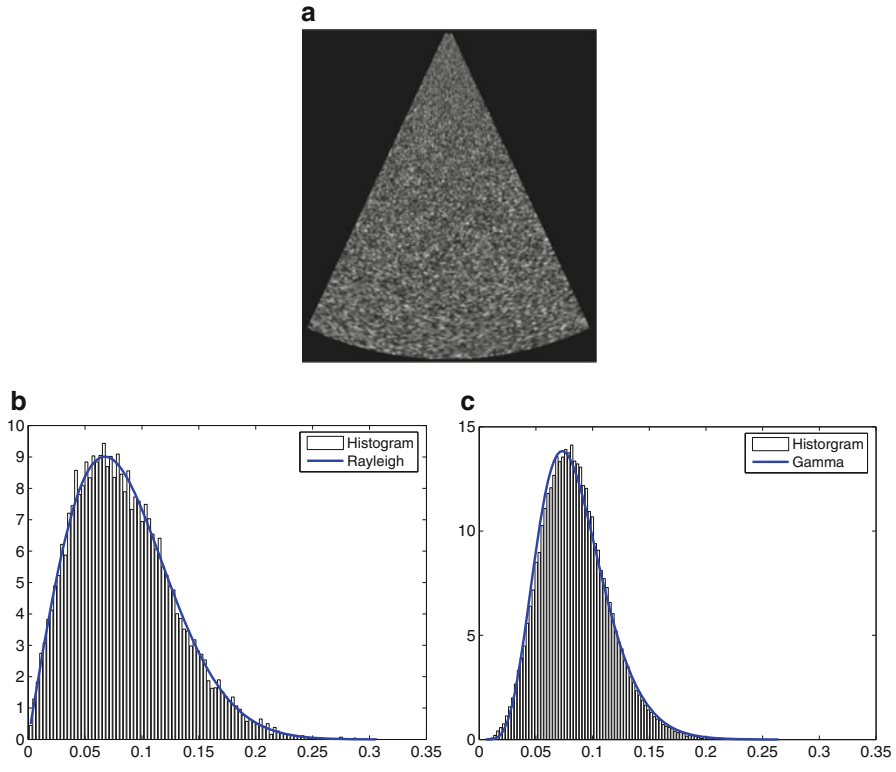

Fig. 13.3 (**a**) Fully formed speckle pattern. (**b**) Histogram of the received signal and Rayleigh distribution estimate. (**c**) Histogram of the reconstructed image and Gamma distribution estimate

per A-line, and $N = 256$ is the number of positions assumed by the rotational ultrasound probe.

The histological validation of plaques comprises the following steps: vessels are cut in correspondence with previously marked positions and plaque composition is determined by histological analysis. A correspondence between detected plaques by histology and respective IVUS image is established by means of the reference positions by expert interventionists in cooperation with pathologists. With the purpose of preserving a reliable correspondence between histological tissue and regions of the IVUS image, the medical team manually performs the plaque labeling task discarding pairs of images in which a correspondence cannot be obtained.

Finally, the dataset comprises 50 different images (with the presence of one or more plaques), all of them present segmentations of the lumen, a set of 69 plaques was identified in the images and histologically characterized in the following types: 30 calcified, 14 lipidic, 25 fibrotic.

The IVUS images were directly reconstructed from the raw RF signals rather than using the ones produced by the IVUS equipment. The image reconstruction algorithm used is the one described in [29], which is shown in Fig. 13.4. The process comprises the following stages:

1. Time Gain Compensation, with $\mathrm{TGC}(r) = 1 - e^{-\beta r}$ where $\beta = \log 10^{\alpha f/20}$, α is the attenuation coefficient for biological soft tissues ($\alpha \approx 0.8$ dB/MHz cm for $f = 40$ MHz [29]), f is the central frequency of the transducer in MHz, and r is the radial distance from the catheter in cm.
2. Butterworth Band pass filter with cut frequencies $f_L = 20$ MHz and $f_u = 60$ MHz.
3. Envelope recovering with Hilbert Transform.
4. Downsampling of the image in order to obtain isotropic resolution with linear interpolation.
5. Log-compression.
6. Digital Development Process (DDP). A nonlinear adjustment of the gain and edge-emphasis process to enhance the tissue visualization.

After this reconstruction process, the IVUS displayed image can be easily obtained by interpolating polar coordinates into Cartesian coordinates, resulting in a noncompressed, 256×256 pixels image (cf. Fig. 13.1a where the polar coordinate image is shown and Fig. 13.1b where the interpolation into Cartesian coordinates is depicted).

The traditional displayed IVUS image is obtained from the polar representation (ρ, θ) by interpolating in a rectangular (Cartesian) grid, (i, j). However, in this work, the image used for the analysis is the noncompressed polar one obtained after the Downsampling step (cf. Fig. 13.4). This stage of the reconstruction process involves linear filtering and, thus, Rayleigh or Nakagami models do not

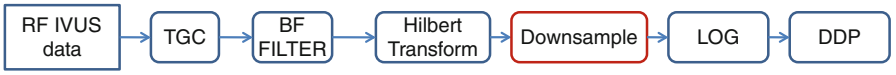

Fig. 13.4 Image reconstruction process. A Time Gain Compensation (TGC) operation is applied to the RF IVUS data acquired. The envelope is recovered by a Hilbert Transform. A downsample stage is applied to obtain isotropic resolution, all the analysis of this work is applied after this stage where the Gamma assumption is applied. Log-compression and Digital Development Process (DDP) stages are usually applied for visualization

hold. This linear filtering is performed by default in order to obtain an isotropic resolution even if the final resolution is a multiple of the initial one.

4 Statistical Analysis of Envelope Data

In this section we test the performance of the Gamma distribution for describing the speckle when internal preprocessing such as linear filtering and interpolation (due to the downsampling stage, see Fig. 13.4). We perform a comparison with the Rayleigh distribution and its generalization, the Nakagami distribution, since they are considered as good candidates for describing the statistics of speckle.

Two measures were used for testing the performance: Kullback–Leibler divergence and uniform norm of the cumulative distribution function (CDF). The former is a non-symmetric measure of the difference between two probability distributions defined as

$$D_{\mathrm{KL}}(p_n, f_X) = \sum_{i=1}^{N} p_n(i) \log \frac{p_n(i)}{f_X(i)}, \tag{13.7}$$

where p_n is the empirical PDF estimate and f_X is the theoretical distribution: Rayleigh, Gamma, or Nakagami.

The approximation of the PDF was estimated by means of the histogram of the neighborhood of the pixel under study. The size of the neighborhood used was 11×11, which is a reasonable number of samples to provide an estimate of the PDF of homogeneous regions. The number of bins used of the histogram is $n = 30$. Parameters of Rayleigh and Gamma distributions were calculated by maximum likelihood estimates of the data in the defined neighborhood. Parameters of the Nakagami distribution were calculated as in [24].

The uniform norm of the CDF, also called Kolmogorov–Smirnov (KS) statistic, is defined as

$$D_{\mathrm{KS}} = \sup |\hat{F}_n(i) - F_X(i)|, \tag{13.8}$$

where $\hat{F}_n$ is the empirical CDF of data and F_X is the CDF of either Gamma or Rayleigh distributions.

This last metric was chosen since it does not depend on the PDF estimate and can be calculated with a few number of samples. Additionally, the Glivenko–Cantelli theorem states that, if the samples are drawn from distribution F_X, then D_{KS} converges to 0 almost surely [30].

The comparison between Gamma, Nakagami, and Rayleigh distributions was done by applying a Welch t-test for both measures, D_{KL} and D_{KS}. To that end, both measures were calculated in each neighborhood (with size 11×11). The average value was calculated for each image (50 images of the dataset) and the Welch t-test is performed with 50 samples. This test was chosen since no equal variance should be assumed. The test was performed by considering pairs of distributions (Gamma vs. Rayleigh, Gamma vs. Nakagami, and Rayleigh vs. Nakagami). The null hypothesis considers that both population means are the same. The boxplot of both measures obtained for the 50 samples (images) is depicted in Fig. 13.5.

Note that boxplots reveals the better performance of the Nakagami when compared to the Rayleigh distribution. This result was expected since the Nakagami distribution is a generalization of the Rayleigh one. However, for the Gamma distribution case, the mean values of both measures is below the Rayleigh and the Nakagami. This result evidences the better performance of the Gamma distribution for describing the probabilistic behavior of speckle. In order to confirm this result, the p-values of the Welch t-test for the case of KL divergence and uniform norm of the CDF are shown in Table 13.1. Note that all values are negligible and the null hypothesis has to be rejected in all cases. Consequently, these three distributions fit in a different way, and the Gamma is the one with best fitting for both measures.

This result confirms that Gamma distribution better describes the probabilistic nature of speckle when internal preprocessing such as linear filtering and interpolation (due to the downsampling stage) are taking place and confirms the result obtained in [7, 18, 25].

5 Gamma Mixture Model

In this section the GMM is proposed and the method for the computation of its parameters and coefficients is described. The aim of using GMMs is that the echo-morphology may result from the contribution of different echogenic components of the plaque that follow different distributions. Under the assumption of Gamma distributed speckle, the GMM arises in a natural way.

Let $\mathbf{X} = \{x_i\}$, $1 \leq i \leq N$ be a set of samples (pixel intensities) of a given region of the ultrasound image.

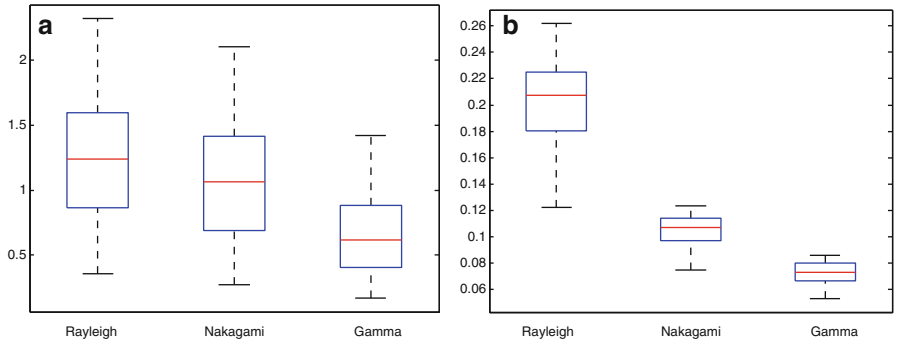

Fig. 13.5 Boxplots for both measures D_{KL} and D_{KS} are represented in (**a**) and (**b**) respectively. Welch t-test results show that populations are statistically different and thus the Gamma distributions fits better than Rayleigh or Nakagami distributions

Table 13.1 p-Values the Welch t-test for the case of D_{KL} and D_{KL}

	Rayleigh	Nakagami	Gamma
Rayleigh		$7.54{\cdot}10^{-35}$	$7.9{\cdot}10^{-38}$
Nakagami	$1.83{\cdot}10^{-30}$		$3.67{\cdot}10^{-46}$
Gamma	$1.92{\cdot}10^{-22}$	$1.05{\cdot}10^{-18}$	

Kullback-Leibler Divergence **Kolmogorov-Smirnov Statistic**

These samples can be considered as IID random variables (RVs). This assumption is taken since the downsampling stage reduces the possible correlation between neighboring pixels. The GMM considers that these variables result from the contributions of J distributions[1]:

$$p(x_i|\Theta) = \sum_{j=1}^{J} \pi_j f_X(x_i|\Theta_j), \tag{13.9}$$

where Θ is a vector of the parameters of the GMM $(\pi_1, \ldots, \pi_J, \Theta_1, \ldots, \Theta_J)$ and Θ_j are the parameters of the PDF (in our case the parameters of a Gamma distribution are represented as α_j and β_j). The Gamma PDF is defined as

$$f_X(x|\alpha,\beta) = \frac{x^{\alpha-1}}{\beta^{\alpha}\Gamma(\alpha)} e^{-(x/\beta)}, \quad x \geq 0 \text{ and } \alpha, \beta > 0, \tag{13.10}$$

where $\Gamma(x)$ is the Euler Gamma function defined as $\Gamma(x) = \int_0^{\infty} t^{x-1} e^{-t}\, dt$, for $x > 0$. Thecondition $\sum_{j=1}^{J} \pi_j = 1$ must hold to guarantee that $p(x_i|\Theta)$ is a well-defined probability distribution.

The joint distribution of IID samples is given by

$$p(\mathbf{X}|\Theta) = \prod_{i=1}^{N} p(x_i|\Theta). \tag{13.11}$$

The Expectation–Maximization method is applied here to maximize the log-likelihood function when some hidden discrete random variables, $\mathbf{Z} = \{Z_i\}$, are introduced to the model. These RVs take values in $\{1, \ldots, J\}$, their meaning is that the sample x_i belongs to the distributions class j when $Z_i = j$.

Now, let $\Theta^{(n)}$ be an estimate of the parameters of the mixture in the nth iteration, the expectation step is performed by calculating the expected value of the log-likelihood $\mathcal{L}(\Theta|\mathbf{X}, \mathbf{Z})$:

$$\mathcal{Q}(\Theta|\Theta^{(n)}, \mathbf{X}) = E_{\mathbf{Z}|\Theta^{(n)},\mathbf{X}}\{\mathcal{L}(\Theta|\mathbf{X}, \mathbf{Z})\}. \tag{13.12}$$

In the maximization step the new estimate $\Theta^{(n)}$ is obtained by maximizing the expectation of the likelihood function $\mathcal{Q}(\Theta|\Theta^{(n)}, \mathbf{X})$. These steps are iterated until a stop criterion such as $||\Theta^{(n+1)} - \Theta^{(n)}|| < \mathrm{TOL}$ for some pre-established threshold (TOL) is reached.

The application of the EM algorithm for general distributions is not new, see for example [23, 31]. In the case of a GMM, it was firstly derived by Webb in [32]; another similar derivation was obtained in [24]. For the sake of completeness we give in this chapter our own derivation.

[1]The notation used, from here forth, refers to random variables in capital letters and samples of random variables in lower case letters. The expectation operator is denoted as $E\{\cdot\}$.

The expectation of the likelihood function with respect to the hidden RVs when data $\mathbf{x}$ and the previous estimate $\Theta^{(n)}$ are known is

$$\begin{aligned}\mathcal{Q}(\Theta|\Theta^{(n)},\mathbf{x}) &= E_{Z|\Theta^{(n)},\mathbf{x}}\{\mathcal{L}(\Theta|\mathbf{X},\mathbf{Z})\}\\ &= \sum_{i=1}^{N} E_{Z_i|\Theta^{(n)},x_i}\{\log p(x_i|\Theta_{z_i}, Z_i = z_i) + \log p(Z_i = z_i|\Theta)\}\\ &= \sum_{i=1}^{N}\sum_{j=1}^{J} p(Z_i = j|x_i,\Theta^{(n)})\left(\log p(x_i|\Theta_j) + \log \pi_j\right), \end{aligned} \tag{13.13}$$

where $p(Z_i = j|\Theta)$ is the probability of x_i to belong to the class j, denoted as π_j. On the other hand, $p(Z_i = j|x_i,\Theta^{(n)})$ can be derived by the Bayes theorem as

$$p(Z_i = j|x_i,\Theta^{(n)}) = \frac{p(x_i|\Theta_j^{(n)})p(Z_i = j|\Theta^{(n)})}{f_X(x_i|\Theta^{(n)})}, \tag{13.14}$$

where, as in (13.9),

$$\sum_{j=1}^{J} p(x_i|\Theta_j^{(n)})p(Z_i = j|\Theta^{(n)}) = \sum_{j=1}^{J}\pi_j f_X(x_i|\Theta_j^{(n)}). \tag{13.15}$$

Since (13.13) is composed of two terms, the maximization step can be done to each term independently. For the term depending on π_j an optimization via *Langrange Multipliers* can be done in a straightforward way, where the constraint is the well-defined probability condition $\sum_{j=1}^{J}\pi_j = 1$. The Lagrange method of multipliers guarantees a necessary condition for optimality in this problem. The new *Lagrange function* with the Lagrange multiplier, λ, is the following:

$$\Lambda(\boldsymbol{\pi},\lambda) = \sum_{i=1}^{N}\sum_{j=1}^{J}\gamma_{i,j}\log\pi_j + \lambda\left(\sum_{j=1}^{J}\pi_j - 1\right), \tag{13.16}$$

where $\gamma_{i,j} = p(Z_i = j|x_i,\Theta^{(n)})$ to make notation simpler.

Now, one can calculate the derivative with respect to each π_j and equaling to 0, the following expression is derived:

$$\sum_{i=1}^{N}\gamma_{i,j} = -\lambda\pi_j. \tag{13.17}$$

By summing both terms of the equation over j, we obtain $\lambda = -N$. Finally, the values of $\hat{\pi}_j$ that maximize the Lagrange function (and the likelihood term) are

$$\hat{\pi}_j = \frac{1}{N}\sum_{i=1}^{N}\gamma_{i,j} = \frac{1}{N}\sum_{i=1}^{N}p(Z_i = j|\Theta). \tag{13.18}$$

Now, we can maximize the term of (13.13) which depends on $\Theta_j = (\alpha_j,\beta_j)$. First with respect to β_j

$$\frac{\partial}{\partial\beta_j}\left\{\sum_{i=1}^{N}\sum_{j=1}^{J}\gamma_{i,j}\log p(x_i|\Theta_j)\right\} = 0, \tag{13.19}$$

where the loglikelihood of $p(x_i|\Theta_j)$ is

$$\log p(x_i|\Theta_j) = (\alpha_j - 1)\log x_i - \frac{x_i}{\beta_j} - \alpha_j\log(\beta_j) - \log(\Gamma(\alpha_j)) \tag{13.20}$$

it results in the following expressions:

$$\sum_{i=1}^{N}\gamma_{i,j}\left(\frac{x_i}{\beta_j^2} + \frac{\gamma_{i,j}}{\alpha_j}\right) = 0 \tag{13.21}$$

which gives the following result:

$$\beta_j = \frac{1}{\alpha_j}\frac{\sum_{i=1}^{N}\gamma_{i,j}x_i}{\sum_{i=1}^{N}\gamma_{i,j}}. \tag{13.22}$$

Now, plugging (13.22) into (13.13) and deriving with respect to α_j

$$\frac{\partial}{\partial\alpha_j}\left\{\sum_{i=1}^{N}\sum_{j=1}^{J}\gamma_{i,j}\log p\left(x_i|\alpha_j,\frac{1}{\alpha_j}\frac{\sum_{i=1}^{N}\gamma_{i,j}x_i}{\sum_{i=1}^{N}\gamma_{i,j}}\right)\right\} = 0. \tag{13.23}$$

The result is

$$\begin{aligned}&\sum_{i=1}^{N}\gamma_{i,j}\log(x_i) - \sum_{i=1}^{N}\gamma_{i,j}\log\left(\frac{\sum_{k=1}^{N}\gamma_{k,j}x_k}{\sum_{k=1}^{N}\gamma_{k,j}}\right)\\ &\quad + \sum_{i=1}^{N}\gamma_{i,j}\log(\alpha_j) - \sum_{i=1}^{N}\gamma_{i,j}\psi(\alpha_j) = 0, \end{aligned} \tag{13.24}$$

where $\psi(x)$ is the *Digamma* function defined as $\psi(x) = \Gamma'(x)/\Gamma(x)$.

Finally, reordering terms, the following equality is derived:

$$\log(\alpha_j) - \psi(\alpha_j) = \log\left(\frac{\sum_i^N \gamma_{i,j} x_i}{\sum_i^N \gamma_{i,j}}\right) - \frac{\sum_i^N \gamma_{i,j} \log x_i}{\sum_i^N \gamma_{i,j}}. \tag{13.25}$$

This expression has no closed solution; however it can be obtained by numerical methods since the function $f(x) = \log(x) - \psi(x)$ is well behaved.

From the estimated value $\hat{\alpha}_j$ that maximizes the log-likelihood, the estimate of $\hat{\beta}$ is directly obtained from (13.22).

6 Results

In this section we test the GMM, RMM, and NMM are tested for fitting different tissue classes for an increasing number of components. Both measures, D_{KL} and D_{KS} were used for this purpose. The measure Kullback–Leibler divergence, D_{KL}, was calculated by estimating the empirical PDF with 300 bins. Note that this measure strongly depends not only on the number of samples but also on the selections of bins and, thus, some discrepancies can be obtained depending on these selections. The Kolmogorov–Smirnov statistic is more robust in the sense that only depends on the samples. For this reason, this measure can be considered as a better descriptor of the fitting performance. An example of the performance of the all the mixture models is depicted in Fig. 13.6 where three components are used for each tissue model. Results are shown in Table 13.2.

Note that these results evidence the better fit for the GMM in almost every case for both measures (D_{KS} and D_{KL}). There are some exceptions that are worth to comment, concretely the case of Lumen for four to seven components. In those cases the D_{KL} measure of the RMM shows a better result, while the D_{KS} measure shows a better performance for the GMM. This effect is due to the problems of estimating the PDF from the samples since the dynamic range of the values for Lumen is too big and the concentration of the PDF is closer to lower values. This provokes a narrow peak that is difficult to describe by approximating the PDF by bins. The variations of the values of the PDF estimate in this peak decrease the precision of D_{KS}. On the other hand, the D_{KL} measure just takes into account the samples of the Lumen and gives a better error measure.

In some other cases, the NMM and RMM show a lower D_{KS} measure compared to the GMM. However, note that the differences of the D_{KS} measures of RMM and NMM with respect the GMM are almost negligible (these differences are about 0.0005 in the worst case) and one can conclude that, in those cases, the GMM fits as good as the others.

These results can be used in order to select the number of components of the GMM model. Note that, as the number of components increases, the measure decreases with slower rate. In Fig. 13.7 the rate of decreasing of both measures for GMM and RMM are depicted for each tissue class. This rate is calculated as $f_{\mathrm{rate}}(n) = D(n-1) - D(n)$, where $D(n)$ is D_{KL} or D_{KS} measures and n is the number of components of the mixture model. The global maximum is obtained for $n = 3$ so this can be considered the optimal number of components for describing every plaque and lumen.

7 Application: A Probabilistic Filter with Detail Preservation

In this section we show the potential of the GMM probability maps provided by the Bayes theorem, that we describe again by convenience:

$$p(Z_i = j|x_i, \Theta^{(n)}) = \frac{p(x_i|\Theta_j^{(n)})p(Z_i = j|\Theta^{(n)})}{f_X(x_i|\Theta^{(n)})}. \tag{13.26}$$

These probability maps can be used for determining the most probable contours between tissue classes, which is a valuable information for developing segmenting of filtering algorithms.

As an example of the potential of this probability maps, we present a novel and fast method for filtering ultrasonic images which takes into account any linear filtering or interpolation of the original image.

Let X_i be a set of IID RVs which follow a Rayleigh distribution with parameter σ. After the interpolation/filtering stage,[2] this RV is transformed in the following way:

$$Y = \sum_{i=1}^{4} w_i X_i = \sigma \sum_{i=1}^{4} w_i R_i, \quad \text{where } \sum_{i=1}^{4} w_i = 1, \tag{13.27}$$

where R_i are IID normalized Rayleigh random variables ($\sigma_R = 1$) and w_i are weights which, in the case of the 2D interpolation, come from two IID uniform random U_1, U_2variables in $[0, 1]$ which conform the coefficients as

$$w_1 = U_1U_2,\ w_2 = U_1(1-U_2),\ w_3 = (1-U_1)U_2,$$
$$w_4 = (1-U_1)(1-U_2).$$

Note that this new RV, Y does not follow a Rayleigh distribution but a Gamma-like distribution as was shown in Sect. 2. By means of GMMs, the distributions that describe the probabilistic behavior of the RVs can be obtained easily. This offers an effective way to calculate local conditioned moments of the random variables that correspond to each

[2]Throughout the derivation of the equations, the linear filter will be considered as an interpolation filter for 2D images. The derivation can be easily extended for other linear filters for 2D or 3D.

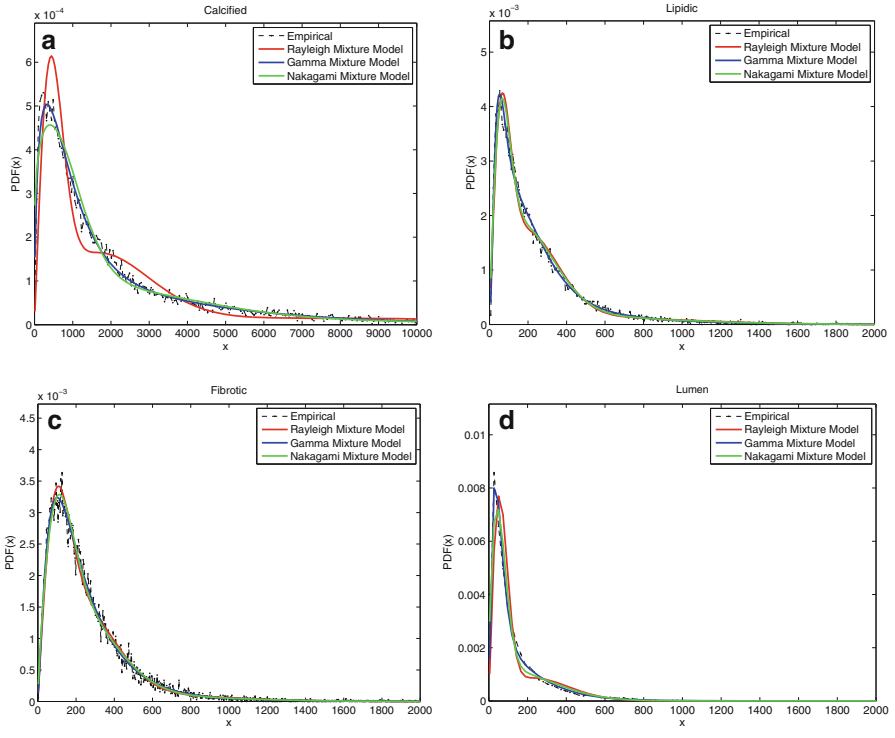

Fig. 13.6 Gamma mixture model and Rayleigh mixture model and Nakagami mixture model fitting for different kinds of tissue. In all the methods the tolerance was fixed to $||\Theta^{(n+1)} - \Theta^{(n)}|| < 10^{-4}$ with a maximum number of iterations of 1,000 and three components in each mixture. (**a**) Calcified. (**b**) Lipidic. (**c**) Fibrotic. (**d**) Lumen

tissue class. The use of local conditional moments offer a powerful information to develop a Linear Minimum Mean Square Error Estimation (LMMSE) of the underlying parameter σ.

7.1 Formulation

The LMMSE filter can be defined in the following way [33]:

$$\hat{\sigma} = E\{\sigma\} + C_{\sigma Y} C_{YY}^{-1}(Y - E\{Y\}), \tag{13.28}$$

where C_{YY}^{-1} is the covariance of Y and $C_{\sigma Y}$ is the cross-covariance. Both covariance terms and $E\{\sigma\}$ can be calculated by directly applying (13.27):

$$E\{\sigma\} = \sqrt{\frac{2}{\pi}} E\{Y\}, \tag{13.29}$$

$$C_{YY} = E\{Y^2\} - E\{Y\}^2, \tag{13.30}$$

$$C_{\sigma Y} = E\{(Y - E\{Y\})(\sigma - E\{\sigma\})\} = (E\{\sigma^2\} - E\{\sigma\}^2)\sqrt{\frac{\pi}{2}}. \tag{13.31}$$

Note that $C_{\sigma Y}$ depends on the calculation of the variance of σ, $\text{var}\{\sigma\} = E\{\sigma^2\} - E\{\sigma\}^2$. This parameter could de obtained by the estimation of local moments of Y in the following way:

$$\begin{aligned} E\{Y^2\} &= E\left\{\sigma^2 \left(\sum_{i=1}^{4} w_i R_i\right)^2\right\} \\ &= E\{\sigma^2\}\left(\frac{4}{9}E\{R_i^2\} + \frac{5}{9}E\{R_i\}^2\right) \\ &= E\{\sigma^2\}\left(\frac{8}{9} + \frac{5}{9}\frac{\pi}{2}\right) \end{aligned} \tag{13.32}$$

so, the variance of σ is

$$\text{var}\{\sigma\} = E\{Y^2\}\frac{9}{8 + 5\frac{\pi}{2}} - E\{Y\}^2\frac{2}{\pi}. \tag{13.33}$$

This value could be calculated by means of the local moments calculated over Y in a similar way as was done in [34,35]. However, since equation does not depend directly on the value of $\text{var}\{Y\}$, the estimate of $\text{var}\{\sigma\}$ by means of local moments could result in negative values. This is a nondesired property which strongly depends on the image (the values of Y).

As a solution to this problem we can make use of the probability maps in order to obtain a suitable C in the modified LMMSE equation:

Table 13.2 Gamma mixture model, Rayleigh mixture model, and Nakagami mixture model fitting for different kinds of tissue and number of components. Bold values are the best results for each tissue and metric

♯ components = 2	D_{KL}			D_{KS}		
Tissue	GMM	NMM	RMM	GMM	NMM	RMM
Calcified	**0.0269**	0.0521	0.1974	**0.0126**	0.0331	0.1087
Lipidic	**0.0211**	0.0403	0.1037	**0.0198**	0.0410	0.1059
Fibrotic	**0.0156**	0.0272	0.0449	**0.0085**	0.0257	0.0445
Lumen	**0.0444**	0.1378	0.6712	**0.0277**	0.0768	0.4110
♯ components = 3	D_{KL}			D_{KS}		
Tissue	GMM	NMM	RMM	GMM	NMM	RMM
Calcified	**0.0197**	0.0279	0.0607	**0.0080**	0.0180	0.0359
Lipidic	**0.0119**	0.0192	0.0222	**0.0054**	0.0114	0.0161
Fibrotic	**0.0145**	0.0166	0.0178	**0.0038**	0.0078	0.0117
Lumen	**0.0128**	0.0322	0.0697	**0.0167**	0.0341	0.0894
♯ components = 4	D_{KL}			D_{KS}		
Tissue	GMM	NMM	RMM	GMM	NMM	RMM
Calcified	**0.0189**	0.0197	0.0253	0.0079	**0.0072**	0.0141
Lipidic	**0.0117**	0.0152	0.0159	**0.0055**	0.0076	0.0083
Fibrotic	**0.0144**	0.0152	0.0148	**0.0032**	0.0062	0.0036
Lumen	0.0261	0.0315	**0.0153**	**0.0043**	0.0339	0.0126
♯ components = 5	D_{KL}			D_{KS}		
Tissue	GMM	NMM	RMM	GMM	NMM	RMM
Calcified	**0.0170**	0.0188	0.0253	**0.0042**	0.0071	0.0141
Lipidic	**0.0110**	0.0134	0.0140	**0.0044**	0.0070	0.0060
Fibrotic	**0.0144**	0.0151	0.0147	**0.0029**	0.0062	0.0033
Lumen	0.0258	0.0153	**0.0119**	**0.0044**	0.0117	0.0110
♯ components = 6	D_{KL}			D_{KS}		
Tissue	GMM	NMM	RMM	GMM	NMM	RMM
Calcified	**0.0170**	0.0184	0.0178	0.0041	0.0068	**0.0036**
Lipidic	**0.0104**	0.0119	0.0133	**0.0029**	0.0057	0.0065
Fibrotic	**0.0143**	0.0148	0.0146	**0.0031**	0.0054	**0.0031**
Lumen	0.0295	0.0151	**0.0073**	**0.0031**	0.0110	0.0118
♯ components = 7	D_{KL}			D_{KS}		
Tissue	GMM	NMM	RMM	GMM	NMM	RMM
Calcified	**0.0170**	0.0186	0.0178	0.0041	0.0069	**0.0036**
Lipidic	**0.0103**	0.0118	0.0133	**0.0026**	0.0059	0.0066
Fibrotic	**0.0142**	0.0146	0.0146	**0.0024**	0.0047	0.0029
Lumen	0.0293	0.0197	**0.0072**	**0.0031**	0.0052	0.0118

$$\hat{\sigma} = E\{\sigma\} + C(Y - E\{Y\}). \tag{13.34}$$

This equation is a linear estimate. Now, we define a new constant C with some desired properties similar to that one of the LMMSE $C_{\sigma Y} C_{YY}^{-1}$. This coefficient should describe the statistical discrepancies of the covariance and the cross-covariance. When the coefficient is close to zero, the statistical behavior of the Normalized RV Y is closed to σ. Conversely, when the coefficient is close $\sqrt{2/\pi}$, the estimate leads to $\hat{\sigma} = \sqrt{(2/\pi)}Y$, which is the unbiased estimate of σ (since $E\{\hat{\sigma}\} = E\{\sqrt{(2/\pi)}Y\} = \sigma$).

For the definition of C, we propose to obtain the gradient of the probability maps for each tissue class. This way, the coefficient will be closer to zero in areas with the same statistical behavior; conversely, it will be closer to one in heterogeneous areas, where the estimate should maintain the details of the image. Formally, the proposed coefficient is defined as

$$C_i = \frac{\sum_j^J ||\nabla_\varepsilon p(Z_i = j\,|y_i, \Theta)||}{\max \sum_j^J ||\nabla_\varepsilon p(Z_i = j\,|y_i, \Theta)||} \sqrt{\frac{2}{\pi}}, \tag{13.35}$$

where Z_i are the hidden RVs that express that variable Y_i belongs to the jth class. The operator ∇_ε means the gradient operator calculated over the image convolved with a Gaussian kernel with ε as the standard deviation. The index i refers to each pixel; hence, the definition of the coefficient is for each pixel of the image.

The definition in (13.35) ranges in $[0, \sqrt{2/\pi}]$ since the discrete implementation of the gradient by finite differences over the probability maps with unitary step is always bounded in $[0, 1]$.

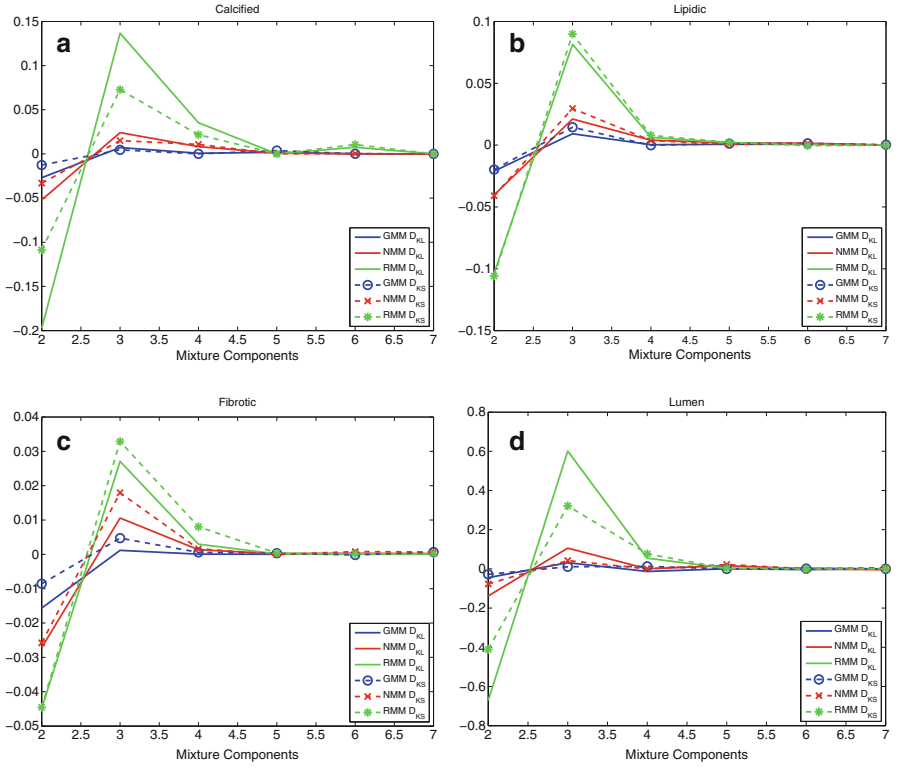

Fig. 13.7 Difference rate ($f_{\text{rate}}(n)$) of D_{KL} and D_{KS} for GMM, RMM, and NMM models. (**a**) Calcified. (**b**) Lipidic. (**c**) Fibrotic. (**d**) Lumen

In order to obtain a better estimate of σ, the probability maps can be used as well to calculate it as the contribution of each local mean in the local neighborhood, $\eta(m,n)$ conditioned to each tissue class. When the moments are calculated in this way, only those pixels belonging to each tissue class contribute to the estimate of each local moment, resulting in a more accurate estimate of local moments. This result can be considered as a non-isotropic way to calculate the local moments since each pixel is not equally treated when the local moments are calculated. The main advantage of local conditional moments is that it provides robustness to the method. In other words, bigger windows for the calculation of local moments may include different tissues (different statistics) which introduce deviations in the calculation of the moments. The inclusion of conditional probabilities allows to discard or attenuate the effect of the presence of pixels belonging to other tissues.

By introducing the probability of belonging to each tissue class in the calculation of the local moments, they are calculated as

$$\langle Y(m,n)\rangle = \sum_{j=1}^{J} P(Z=j)\langle Y(m,n)|Z=j\rangle, \quad (13.36)$$

where the local mean for each tissue class, j is

$$\langle Y(m,n)|Z=j\rangle = \frac{\sum_{(m',n')\in\eta(m,n)} Y(m',n')\,p(Z(m',n')=j|Y,\Theta)}{\sum_{(m',n')\in\eta(m,n)} p(Z(m',n')=j|Y,\Theta)} \quad (13.37)$$

with

$$p(Z(m',n')=j|Y,\Theta) = \frac{\pi_j\, p(Y(m',n')|\Theta_j)}{p(Y(m',n')|\Theta)}. \quad (13.38)$$

The weight $P(Z=j)$, is the probability of belonging to the jth tissue class for the neighborhood of (m,n) and is calculated as

$$P(Z(m,n)=j) = \frac{\prod_{(m',n')\in\eta(m,n)} p(Z(m',n')=j|Y,\theta)}{\sum_{j=1}^{J}\prod_{(m',n')\in\eta(m,n)} p(Z(m',n')=j|Y,\theta)}. \quad (13.39)$$

As an example, a real IVUS in the downsample stage is filtered with the proposed method. The image is depicted in Fig. 13.8a and the filtered image is represented in Fig. 13.8b. The parameters of the filter for this image are neighborhood radius 7, $\varepsilon = 1$, and 12 components for the GMM. Note that these 12 components were selected in order to describe the presence of all possible plaques (three for each plaque and three more for the lumen).

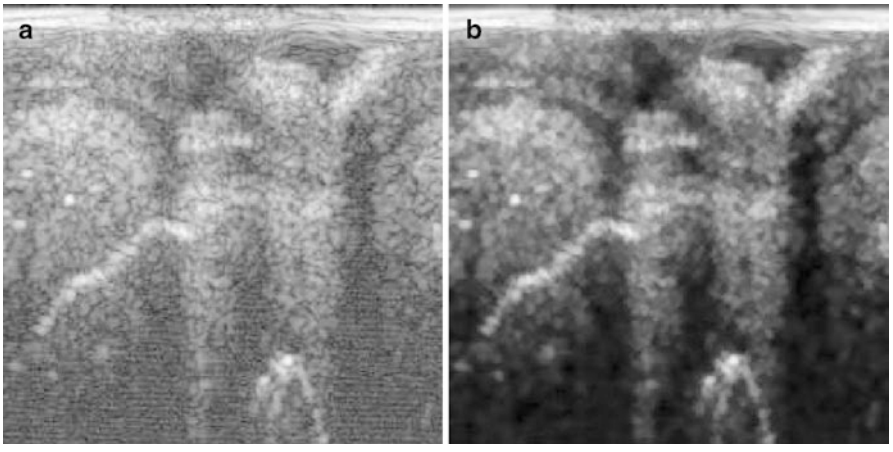

Fig. 13.8 (**a**) IVUS image in polar coordinates in the downsampling stage of the acquisition protocol. (**b**) Filtered image with the proposed method. Both images are log compressed only for representation purposes

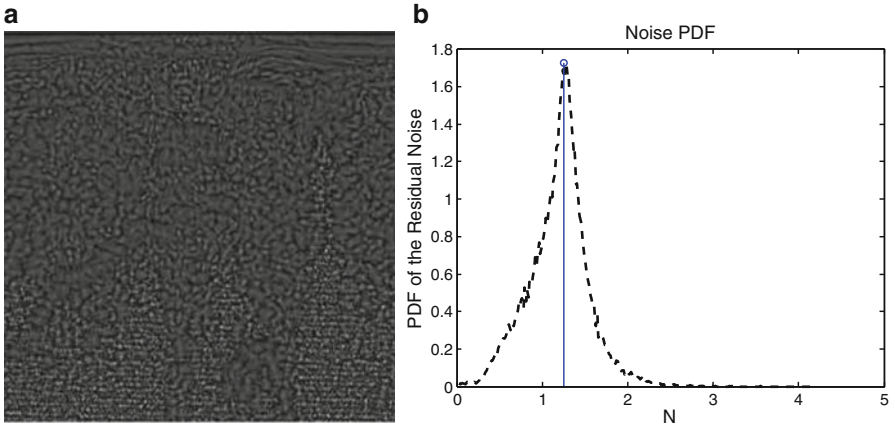

Fig. 13.9 (**a**) Residual noise of Fig. 13.8a. (**b**) Probability density function of the residual noise. Note that the mode of the residual noise PDF is clearly placed in $\sqrt{\pi/2}$

In order to see whether this estimate of σ is properly calculated, an analysis of the residual noise after the filter can be performed. Note that the residual noise, N, of the image can be calculated by simply dividing the original image by the estimate of σ:

$$N = \frac{1}{\hat{\sigma}} \sum_{i=1}^{4} w_i X_i = \frac{\sigma}{\hat{\sigma}} \sum_{i=1}^{4} w_i R_i . \tag{13.40}$$

If a perfect estimate was obtained, N would behave as the probability distribution of $\sum_{i=1}^{4} w_i R_i$. This distribution would have a mean value of $\sqrt{\pi/2}$. Since $\hat{\sigma}$ is estimated by conditioned local means in homogeneous areas, the PDF of the residual noise should have its mode at the mean value of $\sum_{i=1}^{4} w_i R_i$, which is $\sqrt{\pi/2}$.

In Fig. 13.9a the residual noise is represented as well as its PDF, Fig. 13.9b. Note that the noise presents its mode close to the ideal value. Concretely, the relative error of the mode is 2.23 %. This result shows that the proposed method provides a good estimate of the underling σ.

7.2 Robustness of the Method

The advantages of introducing conditional moments in the calculation of local moments lie in the robustness of the estimation of the moments. This allows to consider neighborhoods of any sizes without the typical blurring effect of isotropic local means (which actually is a convolution with a constant value that acts like a low pass filter).

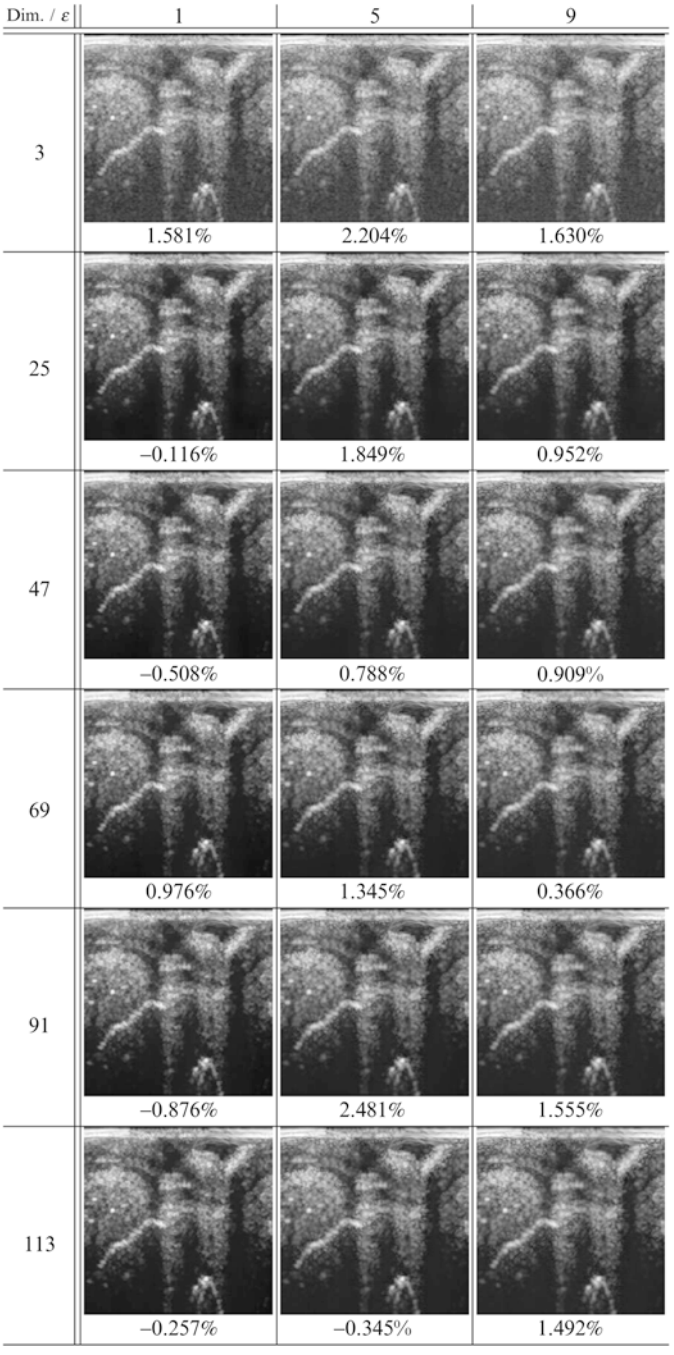

Fig. 13.10 Filtered images for different parameters. The size of the neighborhood (Dim.) windows ranges in [3, 113], while the ε ranges in [1, 9]. Note that the performance of the filter si stable for all the ranges of the parameters. This is due to the robustness introduced by the calculation of the conditioned moments to each tissue class

The effect of increasing the neighborhood size in the proposed method is that local variations are discarded while the moments estimates are calculated with more samples from the same nature (same tissue class and, thus, same probability distribution), resulting in a more accurate estimate.

The parameter ε is a detail preservation. Note that this parameter extends the effect of the edges of its boundaries; so, when the ε parameter takes a higher value, the filtered image preserves the details of the most probable edges between tissues.

To see the effect of the variation of both parameters, in Fig. 13.10, some of the filtered image obtained from that one of Fig. 13.8a are depicted. Additionally, we include the relative error of the residual error mode.

The size of the neighborhood windows ranges in $\{3, 113\}$ and the detail parameter, ε, ranges in $\{1, 9\}$. Note that resultant filtered provide an enhanced image for all the cases in which the blurring effect due to bigger neighborhoods is avoided. Note that, in the case of a small neighborhood, the local varying intensities are maintained, this is the most

restrictive case of the filter which can be used in situations where physicists want a good enhancement of the image but preserving the speckle texture.

As the dimension of the neighborhood (Dim.) increases, the estimate of local moments is calculated with more samples and, thus, the resulting moments vary in a smooth way but always preserving edges between tissues. Note that even for a huge dimension such as 113 (the size of the image is 256×256), the filtered image does not present any evidence of blurring effect due to inaccurate calculation of moments.

8 Conclusions

In this chapter we have analyzed the acquisition process of IVUS images and the probabilistic distributions that better fit the statistical properties of speckle.

We put emphasis on the effect that linear filters or interpolation processes have in the probabilistic models, which are commonly applied during the acquisition stage. As it was shown, the fully formed speckle distribution is transformed in a Gamma-like distribution. This distribution was tested against the Nakagami and the Rayleigh which are the most widespread models used in the case of fully formed speckle. Results evidence the better fitting of the Gamma distribution in the case of IVUS images.

A GMM was proposed as a model for fitting the echomorphology which results from the contribution of different echogenic components of the plaque. This GMM was tested against the NMM and the RMM. Results have proved that the GMM provides a better fitting than NMM or RMM.

As an application to the GMM for IVUS images, a detail preserving filter is proposed. This filter takes advantage of the probabilistic information that provides the GMM. Concretely, the GMM provides the probability of belonging to each tissue class for each pixel. This information procure a useful and robust way to calculate local moments, even for huge neighborhoods. Additionally, probability maps can be used for detecting the most probable edges between tissue classes.

The combination of a robust way for calculating local moments and the probability of edges can be used for defining an estimation of the underling parameters of the fully formed speckle filtering which preserves details while estimates. This filter was tested with real IVUS images without log-compression transformation. The residual noise obtained by directly dividing the σ estimate from the original image presents its mode about the ideal value $\sqrt{\pi/2}$ (the mean of a Rayleigh distribution with parameter 1); this result evidences the consistence of the proposed filter.

References

1. Spagnoli LG, Mauriello A, Sangiorgi G, Fratoni S, Bonanno E, Schwartz RS, Piepgras DG, Pistolese R, Ippoliti A, Holmes DR (2004) Extracranial thrombotically active carotid plaque as a risk factor for ischemic stroke. J Am Med Assoc 292(15):1845–1852
2. Escolar E, Weigold G, Fuisz A, Weissman NJ (2006) New imaging techniques for diagnosing coronary artery disease. Can Med Assoc J 174(4):487–495
3. Wilhjelm JE, Gronholdt M-LM, Wiebe B, Jespersen SK, Hansen LK, Sillesen H (1998) Quantitative analysis of ultrasound B-mode images of carotid atherosclerotic plaque: correlation with visual classification and histological examination. IEEE Trans Med Imaging 17(6):910–922
4. El-Barghouty N, Geroulakos G, Nicolaides A, Androulakis A, Bahal V (1995) Computer-assisted carotid plaque characterisation. Eur J Vasc Endovasc Surg 9(4):389–393
5. El-Barghouty NM, Levine T, Ladva S, Flanagan A, Nicolaides A (1996) Histological verification of computerised carotid plaque characterisation. Eur J Vasc Endovasc Surg 11(4):414–416
6. Matsagas MI, Vasdekis SN, Gugulakis AG, Lazaris A, Foteinou M, Sechas MN (2000) Computer-assisted ultrasonographic analysis of carotid plaques in relation to cerebrovascular symptoms, cerebral infarction, and histology. Ann Vasc Surg 14(2):130–137
7. Vegas-Sánchez-Ferrero G, Martín-Martínez D, Aja-Fernández S, Palencia C (2010) On the influence of interpolation on probabilistic models for ultrasonic images. In: IEEE international symposium on biomedical imaging, pp 292–295
8. Seabra J, Sanches J, Ciompi F, Radeva P (2010) Ultrasonographic plaque characterization using a Rayleigh mixture model. In: IEEE international symposium on biomedical imaging, pp 1–4
9. Goodman JW (1975) Some fundamental properties of laser speckle. In: Laser speckle and related phenomena. Topics in applied physics, vols 9–75. Springer, Berlin, pp 1145–1150
10. Copsey K, Webb A (2003) Bayesian gamma mixture model approach to radar target recognition. IEEE Trans Aero Electron Syst 39(4):1201–1217
11. Thijssen JM (2003) Ultrasonic speckle formation, analysis and processing applied to tissue characterization. Pattern Recognit Lett 24(4–5):659–675
12. Wagner RF, Smith SW, Sandrik JM, Lopez H (1983) Statistics of speckle in ultrasound B-scans. IEEE Trans Son Ultrason 30(3):156–163
13. Burckhardt CB (1978) Speckle in ultrasound b-mode scans. IEEE Trans Son Ultrason 25(1):1–6
14. Tuthill TA, Sperry RH, Parker KJ (1988) Deviations from rayleigh statistics in ultrasonic speckle. Ultrason Imaging 10(2):81–89
15. Jakeman E (1984) Speckle statistics with a small number of scatterers. Opt Eng 23(4):453–461
16. Jakeman E (1980) On the statistics of K-distributed noise. J Phys A Math Gen 13(1):31–48
17. Jakeman E, Tough RJA (1987) Generalized K distribution: a statistical model for weak scattering. J Opt Soc Am A 4(9):1764–1772
18. Eltoft T (2006) Modeling the amplitude statistics of ultrasonic images. IEEE Trans Med Imaging 25(2):229–240
19. Nakagami M (1960) The m-distribution, a general formula of intensity of rapid fading. In: Proceedings of statistical methods in radio wave propagation. Permagon, Oxford, pp 3–36
20. Shankar PM (2000) A general statistical model for ultrasonic backscattering from tissues. IEEE Trans Ultrason Ferroelectr Freq Control 47(3):727–736
21. Seabra JC, Ciompi F, Pujol O, Mauri J, Radeva P, Sanches J (2011) Rayleigh mixture model for plaque characterization in intravascular ultrasound. IEEE Trans Biomed Eng 58(5):1314–1324

22. Dempster AP, Laird NM, Rubin DB (1977). Maximum likelihood from incomplete data via the EM algorithm. J R Stat Soc Ser B 39(1):1–38
23. Moon TK (1996) The expectation-maximization algorithm. IEEE Signal Process Mag 13(6):47–60
24. Destrempes F, Meunier J, Giroux MF, Soulez G, Cloutier G (2011) Segmentation of plaques in sequences of ultrasonic B-mode images of carotid arteries based on motion estimation and a bayesian model. IEEE Trans Biomed Eng 58(8):2202–2211
25. Tao Z, Tagare HD, Beaty JD (2006) Evaluation of four probability distribution models for speckle in clinical cardiac ultrasound images. IEEE Trans Med Imaging 25(11):1483–1491
26. Szabo T (2004) Diagnostic ultrasound imaging: inside out. Elsevier, Burlington
27. Beaulieu NC (1990) An infinite series for the computation of the complementary probability distribution function of a sum of independent random variables and its application to the sum of rayleigh random variables. IEEE Trans Commun 38(9):1463–1474
28. Perreault C, Auclair-Fortier M-F (2007) Speckle simulation based on B-mode echographic image acquisition model.In: Fourth Canadian conference on computer and robot vision, 2007 (CRV '07), pp 379–386
29. Ciompi F, Pujol O, Gatta C, Rodriguez-leor O, Mauri-ferre J, Radeva P (2010) Fusing in-vitro and in-vivo intravascular ultrasound data for plaque characterization. Int J Cardiovasc Imaging 26(7):763–779
30. Dudley RM (1999) Uniform central limit theorems, 1st edn. Cambridge University Press, Cambridge
31. Figueiredo MAT, Jain AK (2000) Unsupervised learning of finite mixture models. IEEE Trans Pattern Anal Mach Intell 24:381–396
32. Webb AR (2000) Gamma mixture models for target recognition. Pattern Recognit 33(12):2045–2054
33. Kay SM (1993) Fundamentals of statistical signal processing: estimation theory. Prentice Hall, Upper Saddle River
34. Aja-Fernández S, Niethammer M, Kubicki M, Elizabeth Shenton M, Westin C-F (2008) Restoration of dwi data using a rician lmmse estimator. IEEE Trans Med Imaging 27(10): 1389–1403
35. Aja-Fernández S, Alberola-López C, Westin C-F (2008) Noise and signal estimation in magnitude MRI and Rician distributed images: a LMMSE approach. IEEE Trans Image Process 17(8):1383–1398

Ultrasound Profile of Carotid Plaque: A New Approach Towards Stroke Prediction

14

José Seabra, L.M. Pedro, J. Fernandes e Fernandes, and J. Miguel Sanches

1 Introduction

Carotid artery atherosclerosis is an important cause of death and disability due to stroke. Among patients with carotid plaques, only a few show warning events, whereas the majority present cerebral events associated with previous asymptomatic plaques.

Numerous studies reported the importance of the degree of stenosis as an indicator of stroke in both symptomatic and asymptomatic groups [1, 2]. Indeed, disease severity and selection of patients for surgery is based on previous occurrence of clinical symptoms, such as stroke, transient ischemic attack (TIA), amaurosis fugax (AF), and the degree of stenosis presented by the plaque.

Moreover, it has been shown [1,2] that surgery associated with a degree of stenosis of more than 70 % resulted in an absolute reduction of 17 % in the risk of ipsilateral stroke after 2 years and 11.6 % at 3 years. These observations suggest that not all severe stenotic plaques are harmful; in fact, as reported by Inzitari et al. [3], the majority of asymptomatic high-grade stenotic plaques remain asymptomatic. Moreover, a study performed by Polak et al. [4] reported evidence that atheromatous plaques with relatively low degree of stenosis may produce symptoms as well. In addition, endarterectomy carries a non-negligible risk for the patient as well as significant financial costs for the patient, hospital, and health system in general. Consequently, an optimized characterization and identification of symptomatic lesions must be carried out to objectively select patients which should be treated with surgery among those to whom a correct medication represent a better solution.

While preliminary studies [5, 6] were based on a subjective evaluation of the plaque appearance to interpret the lesion severity, nowadays advanced methods of image processing allow the extraction of a large number of features from B-mode ultrasound (BUS) images of the carotid plaque. Furthermore, specialized techniques can be employed to identify a subset of salient features, which may be used as input to a classification system. The use of feature selection methods significantly simplifies the classification task, which will be faster and use less memory, while usually achieving a high classification performance. The evolution of artificial intelligence methods in conjunction with optimized computer performance has allowed the development of computer-aided diagnosis (CAD) systems [7]. Such systems are expected to help physicians on supporting the evaluation of pathologic findings during the diagnostic procedure.

1.1 Background

Different techniques relying on both qualitative and quantitative assessment of carotid plaque echo-morphology can be found in the literature, although no single technique has emerged as the method of choice.

As suggested by histopathological studies, other factors besides stenosis, including plaque structure and echomorphology (information on plaque gray-scale intensities) have shown to be associated with neurological symptoms [8–10]. Echogenic material reflects strongly the ultrasound signal and comprises fibrous tissue and calcium deposits, whereas echolucent material has less reflecting ability and includes blood and lipids. As previously referred, echolucent plaques are more likely to lead to development of neurologic events than echogenic ones.

El-Barghouty et al. [8] in a study with 94 plaques has provided a characterization of plaques based on the

J. Seabra • J.M. Sanches (✉)
Instituto de Sistemas e Robótica, Instituto Superior Técnico, Torre Norte, 6° Piso, Av. Rovisco Pais, 1049-001 Lisboa, Portugal
e-mail: jseabra@ist.ist.utl.pt; jmrs@ist.utl.pt

L.M. Pedro • J. Fernandes e Fernandes
Cardiovascular Institute and the Lisbon University Medical School, Hospital de Santa Maria, 1649-035 Lisbon, Portugal
e-mail: lmendespedro@clix.pt; fernandes456@hotmail.it

L. Saba et al. (eds.), *Multi-Modality Atherosclerosis Imaging and Diagnosis*,
DOI 10.1007/978-1-4614-7425-8_14, © Springer Science+Business Media, LLC 2014

gray-scale median (GSM), reporting an association between echolucency (GSM ≤ 32) and the incidence of cerebral computed tomography brain infractions. Subsequently, the study conducted by Iannuzzi et al. [11] in 242 stroke and 336 transient ischemic attack patients showed that the features more consistently associated with cerebrovascular events were low echogenicity, thicker plaques, and presence of longitudinal motion.

Then, Wilhjelm et al. [12] in a study with 52 patients scheduled for surgery, presented a comparison between subjective visual classification of the plaque appearance, first and second-order statistical features, and histological analysis of the excised plaques. Some correlation was found between the three types of information, where the best performing feature was found to be the histogram contrast.

From thereon, various studies have emerged, either using exclusively or combining texture information, based on first and second order statistics [13], Fourier power spectrum [13], fractal properties [14], and Law's texture energy [7]. Particularly, Christodoulou et al. used statistical, model-based, and Fourier-based methods as well as a combination of classifiers and found an average diagnostic performance (accuracy) of 73.1 % in identifying symptomatic lesions, using a dataset composed of 230 plaque images.

The comprehensive study conducted by Pedro et al. [15] in 215 carotid plaques, combined quantitative (e.g., the degree of stenosis and histogram features) and qualitative information resulting from visual inspecting the plaques on BUS images for developing an ultrasound score. This score, designated as Activity Index (AI) provides promising results in identifying plaques with a high likelihood of developing symptoms despite the significant number of false positive samples.

Moreover, the work developed by Mougiakakou et al. [7] extended previous studies on the characterization of carotid plaques from BUS images, by systematically studying all available first-order statistics, as well as Law's texture energy features. In that study, a CAD system is used to support diagnosis based on a neural network trained via a combination of back propagation with a genetic algorithm. This study produced promising results in identifying atheromatous lesions at high risk of stroke in a population of 108 plaques, thus suggesting the use of CAD systems as valuable tools in modern clinical practice. A rather interesting study performed by Kyriacou et al. [16] in a population of 137 asymptomatic and 137 symptomatic plaques proposed a multilevel binary and gray-scale morphological analysis method that have strong connections to prior clinical studies on what constitutes an unstable, symptomatic plaque. The multilevel approach is used to decompose the BUS image in its low-image, middle-image, and hi-image parts corresponding to hypoechoic, isoechoic, and hyperechoic image components, as originally proposed by AbuRahma [17]. The power spectra was computed from such images, showing significant differences between the symptomatic and asymptomatic spectra. Moreover, the derived pattern spectra were used as classification features with two different classifiers, the Probabilistic Neural Network (PNN) and the Support Vector Machine (SVM) and, as noted by the authors, the low-images alone provide better results than complicated multifeature classifier systems ($\approx$74 % versus 73 % [13]). An elegant explanation of why the pattern spectra for low-images performed better is that such images capture the (more echolucent) lipid components and there is clinical evidence that unstable plaques have large lipid components.

Furthermore, the importance of speckle in BUS images as well as its statistical modeling for tissue characterization has been previously documented [18]. In this chapter, we investigate the usefulness of a recently proposed de-speckling algorithm [19] which is able to decompose an ultrasound image into its noiseless and speckle components for feature extraction and, consequently, for tissue characterization. It is expected that such echo-morphology and texture parameters obtained from these image sources could contribute to a better analysis of the symptomatic plaque and differentiation from the asymptomatic lesion.

Here, it is argued that an optimal method for identifying vulnerable lesions should attempt to include not only morphological and textural features extracted from pixel intensity information within the plaque but also diagnostic information regarding plaque structure and appearance (e.g., stenosis, evidence of surface disruption, and presence of echogenic cap), interpreted and given by experienced physicians. The combination of this information is expected to produce a more comprehensive description of the profile of an active plaque, potentially providing the identification of lesions that would developed symptoms in the future.

1.2 Chapter Organization

This chapter is composed of two main parts, reflecting two different studies that were performed. The workflow of the current chapter is presented in Fig. 14.1.

Section 2 describes a cross-sectional study for characterizing the symptomatic plaque including a detailed descrip-

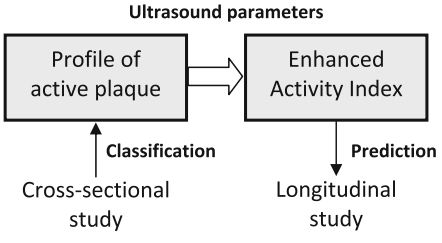

Fig. 14.1 Framework presented in the current chapter

tion of the data (Sect. 2.1) and methods (Sect. 2.2) used. Then, the results and main observations about the first study are drawn in Sect. 2.3.

The second study, presented in Sect. 3, involves the development and testing of a diagnostic measure to quantify plaque activity in a group of asymptomatic subjects. The data used in the longitudinal study is described in Sect. 3.1. The design of the plaque activity measure is described in Sect. 3.2 and experimental results are given in Sect. 3.3. Finally, Sect. 4 concludes the chapter.

2 Cross-Sectional Study

This study introduces a classification framework which enables to distinguish between symptomatic and asymptomatic lesions (Fig. 14.1). This method uses a collection of ultrasound image processing methods for feature extraction and tissue classification. In addition, it provides the identification of the most relevant parameters for plaque classification, consequently yielding an ultrasound profile of the "active," symptomatic plaque.

2.1 Data Management

This study included 221 carotid bifurcation plaques acquired from 99 patients, 75 males and 24 females. Mean age in this group of subjects was 68 years old (41–88). This data set was specifically assigned for training and testing the performance of a classification framework in separating symptomatic from asymptomatic lesions.

Patients were observed through neurological consultation at Instituto Cardiovascular and Hospital de Santa Maria, Lisbon, Portugal. A typical exam included a noninvasive examination with color-flow duplex scan of one or both carotids, performed with ATL-HDI 3000 equipment (Philips Medical Systems, Bothell, WA, USA) using a L12-5 scan probe (5–12 MHz broadband linear-array transducer). A plaque was considered symptomatic when AF or focal transitory, reversible or established neurological symptoms in the ipsilateral carotid territory, was observed in the previous 6 months. From this data set, 70 plaques were symptomatic while the remaining 151 did not reveal symptoms. This study was based on ultrasound images of plaques acquired at a fixed time frame (cross-sectional study).

2.2 Methods: CAD System

The conceptual idea of the cross-sectional study relies on a computer-assisted diagnostic framework (Fig. 14.2) designed with the purpose of distinguishing between symptomatic and asymptomatic lesions and, consequently, providing an accurate description of the vulnerable plaque.

The CAD system is supported by an user-friendly graphical interface, developed in MATLAB (Version R2007b, The Mathworks, Natick, MA, USA). This program provides the physician with several functionalities, including image normalization, definition of plaque(s) contour(s), adding relevant patient information (e.g., age, clinical history, medication, risk factors) and about subjective plaque structural characteristics (e.g., degree of stenosis, evidence of surface disruption, presence of fibrous cap and echolucent areas). Physicians can easily give their clinical input through an application designed for this purpose. In addition, the CAD system incorporates a chain of image processing tasks, such as image normalization as well as estimation of the envelope image and de-speckling. Operations involving envelope RF (ERF) image retrieval and de-speckling are employed to create new sources of information used for plaque characterization. Finally, the designed CAD system supplies the calculation of a measure which indicates the risk of the plaque to developing symptoms formulated in two

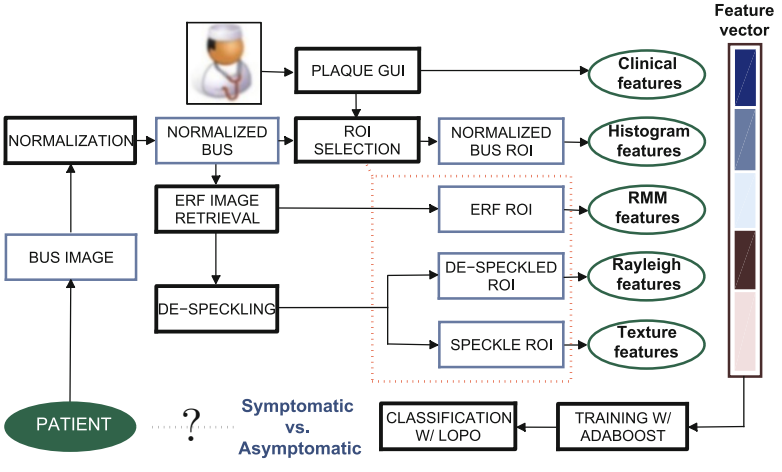

Fig. 14.2 Plaque classification framework

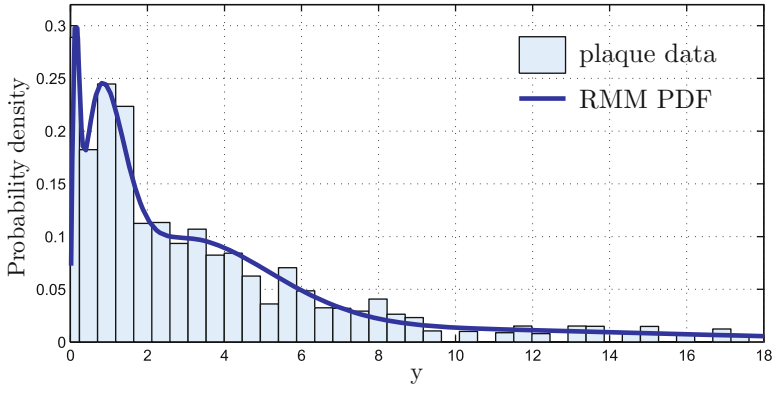

Fig. 14.3 RMM applied to plaque intensities in the ERF image: the RMM PDF is obtained as in (14.1) using the estimated *weights* and *Rayleigh* parameters

different ways: the *Activity Index*, early proposed by Pedro et al. [15] and the *Enhanced Activity Index* (EAI), which is detailed ahead in this chapter.

The main steps of the CAD system, supported by the described application, are explained next.

2.2.1 Image Processing

Image normalization is an important step to guarantee that images acquired under different conditions yield comparable and reproducible features and classification results. Image normalization was achieved as previously reported [9]; in particular, pixel intensities across the image were linearly scaled so that the adventitia and blood intensities would be in the range of 185–195 and 0–5, respectively (Fig. 14.3, top-left). This is an interactive procedure since the user must select two regions in the image, one corresponding to the adventitia (accounting for the most echogenic part) and the other to the blood (corresponding to the less echogenic component).

The normalized image is used to segment existing plaque(s) in the image. Each plaque is delineated by drawing around its structure and the obtained contour is a result of a two-step procedure: (a) contour interpolation according to a maximum distance (10 pixels) allowed between two consecutive points defined manually and (b) contour smoothing using basis functions (sinc functions).

De-speckled and speckle components of the image are required to compute echo-morphological and textural features. It is argued that the speckle-free (noiseless) component of the ultrasound image contains echogenic contents providing important insight on plaque morphology (and surrounding tissues). On the other hand, the speckle component, due to its multiplicative nature which makes it possible to dissociate it from the underlying anatomy, enables to better investigate the spatial relationship among pixels (texture) in the image. In a first step, an estimate of the envelope image (Fig. 14.3, top-right) is obtained from the normalized BUS image through the proposed decompression method. Subsequently, the ERF image is used to compute speckle-free and speckle components, displayed in Fig. 14.3, bottom-left and Fig. 14.3, bottom-right.

2.2.2 Feature Extraction

Features used for training the plaque classifier comprise subjective input given by the physician together with information automatically extracted from the normalized BUS, ERF, de-speckled and speckle images. As a consequence, features used for the purpose of plaque characterization include:

- *BUS morphological features* given by a physician during BUS examination. The 4-element vector of morphological parameters include (a) *evidence of plaque disruption*, defined by an interruption in the echogenic surface of the plaque; (b) *presence of echogenic cap*, identified as an equivalent of a thick fibrous cap and characterized by an echogenic line over the visible structure of the plaque; (c) *the degree of stenosis*, quantified using cross-section area measurement combined with hemodynamic assessment; and (d) *plaque echo-structure appearance*, where uniform plaques are defined as homogeneous while plaques presenting significant areas of echolucency are defined as heterogeneous.
- *Histogram features* extracted from the histogram of normalized pixel intensities inside the plaque. A total of 13 histogram features is estimated, including the *mean gray value*, *median gray value*, *percentage of pixels with grey value lower than 40*, *standard deviation of gray values*, *kurtosis*, *skewness*, *energy*, *entropy*, *10-, 25-, 50-, 75-, and 90-percentiles*.
- *RMM features* consist of the parameters of a mixture of Rayleigh distribution (RMM), early proposed in [20], used to model plaque echo-morphology contents. The RMM method is applied on envelope data, whose pixel intensities approximately follow Rayleigh statistics. Given this, gray-scale intensities within the plaque are considered random variables described by the following mixture of K distributions:

$$p(y_i|\Psi) = \sum_{k=1}^{K} \theta_k \, p(y_i|\sigma_k), \tag{14.1}$$

where $p(y_i|\sigma_k)$ is the Rayleigh PDF. θ_k and σ_k are the weights and Rayleigh parameters of the mixture, respectively, which are estimated using the *Expectation–Maximization* method, $K = 6$ (see Fig. 14.3) and $\Psi = \{\theta_1, \ldots, \theta_k, \ \sigma_1, \ldots, \sigma_k\}$. Hence, a 13-element feature vector is obtained, consisting of 6 *mixture weights*, 6 *Rayleigh parameters*, and the *effective number of RMM components*, determined by the number of mixture components with nonzero weight.

- *Rayleigh features* consist of average theoretical estimators of the Rayleigh distribution, whose parameters are given by the pixels on the de-speckled which contains the plaque. The Rayleigh features include the *mean*, $\mu_\sigma = \overline{\sigma_{i,j}}\sqrt{\pi/2}$, *median*, $\upsilon_\sigma = \overline{\sigma_{i,j}}\sqrt{2\log(2)}$, *variance*, $\sigma_\sigma = \overline{\sigma_{i,j}}\sqrt{(4-\pi)/2}$ of *Rayleigh values* and *percentage of pixels with Rayleigh value lower than 40*, $\sigma_{PP40} = 100 - \exp(-(40^2/2\overline{\sigma_{i,j}{}^2}))$.
- *Texture features* involve the study of the spatial distribution of gray levels inside the plaque region extracted from the speckle image. These features are estimated from gray level cooccurrence matrices (GLCMs), autoregressive (AR) models, and wavelet models. GLCMs are constructed using the relative frequencies $P(i, j, d, \theta)$ with which two neighboring pixels with gray levels i and j at a given distance d and orientation θ occur on the image. The distances used are $d = \{1, 2, 3, 4\}$ pixels and the angles $\theta = \{0, 45, 90, 135\}°$, thus creating 16 different GLCMs. From each computed GLCM different statistics can be derived, namely the *Contrast*, *Correlation*, *Energy*, and *Homogeneity* thus producing a 64-element feature vector. *Contrast* measures the local variations in the GLCM, while *Correlation* gives the joint probability occurrence of the specified pixel pairs. The *Energy* provides the sum of squared elements in the GLCM and, finally, *Homogeneity* measures the closeness of the distribution of elements in the GLCM to the GLCM diagonal. Furthermore, to investigate a possible relation between each pixel and its neighborhood, the AR model is used on the speckle image, $\mathbf{N} = \{\eta_{i,j}\}$. This model assumes $\eta_{i,j}$ to be a 2D random variable where each pixel depends on its causal neighbors according to [21]:

$$\eta_{i,j} = \sum_{n,m}^{p,q} a_{n,m}\eta_{i-m,j-n} + u_{i,j}, \tag{14.2}$$

where $a_{n,m}$ are the AR coefficients to be estimated and $u_{i,j}$ are the residues. Considering a 1st order model such that $(p, q) = (1, 1)$, we estimate 3 *AR coefficients*. Alternatively, plaque texture can be studied using multi-level 2D wavelet decomposition. This technique consists of using low and high pass filters onto the approximation coefficients at level l in order to obtain the approximation at level $l + 1$ and the details in three orientations (horizontal, vertical, and diagonal). Here, decomposition is made along $l = 4$ levels. For each level, the *percentage of energy* for the approximation E_A as well as horizontal E_H, vertical E_V, and diagonal E_D details is computed. Hence, a 13-element wavelet-based feature vector is obtained composed of 4 (E_H) + 4 (E_V) + 4 (E_D) + E_A.

Therefore, each plaque is described by a feature vector $\mathbf{x}$ of 4 (Clinical) + 13 (Histogram) + 13 (RMM) + 4 (Rayleigh) + 80 (Texture) = 114 features.

2.2.3 Classification

The aforementioned features which describe each plaque are used to train the AdaBoost (Adaptive Boosting) classifier [22]. The use of such classifier is motivated by the promising results achieved when classifying plaque components on IVUS images [23]. AdaBoost is a binary classifier which consists in designing a *strong* classifier by linearly combining a set of *weak* classifiers. At each round of the boosting algorithm, the classification error in classifying the training data set is minimized by selecting the best discriminative value of one feature in the vector $\mathbf{x}$. The classifier performance is assessed by means of the LOPO cross-validation technique, where the training set is built taking at each time all patients' data, except one, used for testing. Performance results are given in terms of Sensitivity: Sens = TP/(TP + FN), Specificity: Spec = TN/(TN + FP), Precision or PPV (*Positive Predictive Value*): Prec = TP/(TP + FP) and Accuracy: Acc = (TP + TN)/(TP + TN + FP + FN), where TP = True Positive, TN = True Negative, FP = False Positive and FN = False Negative. Hence, a good classifier for diagnostic purposes would present a high sensitivity, meaning that it would be able to detect most of the symptomatic lesions, and a high PPV, which indicates that few asymptomatic lesions were identified as symptomatic.

2.2.4 Feature Analysis

A considerable amount of features was collected after ultrasound image processing. Naturally, not all the features are important to accurately characterize the plaque status, whether it is symptomatic or not. Hence, at this point an attempt is made to identify the most relevant ultrasound parameters for this particular problem. Hypothesis testing is a common method of drawing inferences about one or more populations based on statistical evidences from population samples (features). Here, we want to investigate if the statistical properties of a given feature significantly differ from the symptomatic to the asymptomatic group. Different hypothesis tests, including the z-, t-, Kolmogorov–Smirnov, and Mann–Whitney U-tests, make different assumptions

about the distribution of the random variable (feature value) being sampled in the data. For example, the z-test and the t-test both assume that the data are independently sampled from a normal distribution. In this work, the Mann–Whitney U-test [24] was chosen because it was the one providing the most promising results. This method performs a two-sided rank sum test of the null hypothesis that feature values in symptomatic and asymptomatic populations are independent samples from identical continuous distributions with equal medians, against the alternative that they do not have equal medians. Moreover, the *p-value* is the probability of rejecting the null hypothesis assuming that the null hypothesis is true. Clinically significant features will have a *p-value* which is typically lower than 0.05 or 0.01. In this work, features were considered to be relevant for differentiating between symptomatic and asymptomatic groups when the $p\text{-}value < 0.05$.

2.3 Experimental Results

This section presents three types of results. First, a suitable feature set, which is statistically relevant for the plaque classification problem is investigated and identified. Secondly, AdaBoost is trained with different ultrasound feature sets in order to evaluate which feature source is more effective to distinguish between plaques with and without symptoms. Then, an overall comparison study between state-of-the-art classifiers (degree of stenosis and AI) and the proposed method is provided.

Before implementing AdaBoost, it is of crucial importance to investigate the best feature set to describe and identify symptomatology in carotid plaques. This will allow to draw some conclusions about the different sources of information employed for plaque classification.

The use of a Mann–Whitney (M–W) U hypothesis test, described in Sect. 2.2.4, enables to identify ultrasound parameters with statistical significance. Table 14.1 presents the parameters and corresponding sources and *p-values* of the so-called *best feature set*.

Table 14.1 Optimal ultrasound parameter set

Ultrasound parameter	Type
Degree of stenosis	Clinical
Plaque echo-structure appearance	Clinical
Evidence of plaque disruption	Clinical
Presence of echogenic cap	Clinical
Mean	Histogram
Skewness	Histogram
Percentile 10, 50	Histogram
4th; 5th; 6th Rayleigh parameters	Rayleigh mixture models
5th; 6th mixture components	Rayleigh mixture models
# mixture components	Rayleigh mixture models
Wavelet decomposition energy	Speckle
GLCM homogeneity	Speckle

A closer look at the 16-element feature set allows to verify that both subjective and image-based parameters are useful for plaque classification. In particular, features from different image sources, namely the normalized image, the envelope RF image, and speckle field are considered statistically relevant. This preliminary observation justifies the use of an ultrasound preprocessing set of operations since it enables to estimate useful parameters for plaque classification.

Furthermore it is interesting to study the classifier performance under different conditions. Hence, AdaBoost is trained with five different parameter sets, considering only morphological information ($F.1$), parameters used to estimate the AI ($F.2$), the total feature set ($F.3$), and a feature set composed of the most relevant features ($F.4$), summarized in Table 14.1. Moreover, a last feature set ($F.5$) is also considered, including again the best feature set except that now all parameters were computed from just one image source—the normalized image, thus discarding information contained on de-speckled and speckle images. After training, the diagnostic value of each classifier is tested on the validated database, according to the LOPO technique. Classification performance is shown in Fig. 14.4, while a detailed description is given in Table 14.2.

Several observations can be made: first, morphological features are important markers of symptomatology as justified by the significant accuracy and specificity values

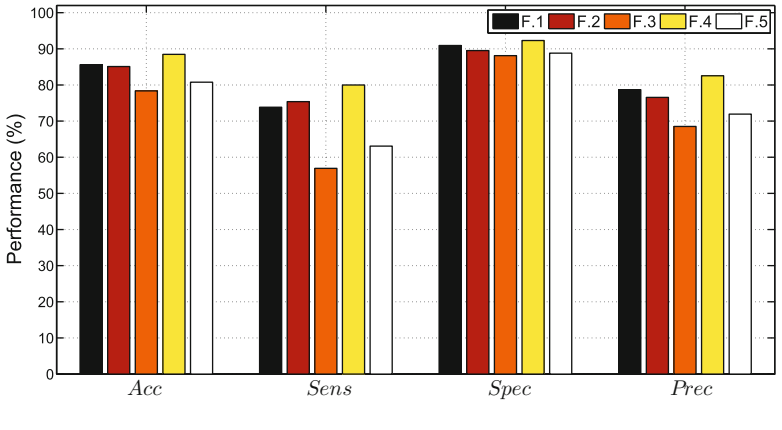

Fig. 14.4 Plaque classification with AdaBoost trained with different feature sets

Table 14.2 Detailed classification of results obtained with AdaBoost (results obtained with best feature set are highlighted)

LOPO (%)	$F.1$	$F.2$	$F.3$	$F.4$	$F.5$
Acc	85.57	85.10	78.37	**88.46**	80.77
Sens	73.85	75.38	56.92	**80.00**	63.08
Spec	90.91	89.51	88.11	**92.31**	88.81
Prec	78.69	76.56	68.52	**82.54**	71.93

obtained with $F.1$. However, it is important to bear in mind that this result is attained exclusively with subjective parameters, quantified and interpreted by physicians, which naturally know the patient clinical status. It is not quantifiable to what extent this a priori knowledge influences the estimation of morphological parameters. Secondly, morphological parameters are combined with histogram parameters, namely the GSM and P40, thus determining the feature set used in the AI method. Results obtained with $F.2$ are similar to $F.1$, except for sensitivity which is higher in $F.1$ meaning that it is able to detect more TP at the expense of getting more FP (lower precision).

Moreover, in order to investigate the usefulness of the proposed feature set we have trained AdaBoost with all the ultrasound parameters proposed in this work. Naturally, $F.3$ results in lower classifier performance and this can be mostly explained by the fact that some undesirable features are cluttering the classifier, which tweaks in favor of those features thus leading to poor classification performance. Finally, the collection of features which were found to be statistically relevant for this particular problem were used to train the studied classifier. Using $F.4$, all the performance criteria are significantly better than the reference classifier ($F.2$) up to 80 % sensitivity (improvement of 5 %) and 88.5 % accuracy (improvement of 3 %).

Hence, it was clearly identified a set of features, including morphology, echogenicity, and texture, which proved to be suitable for identifying symptomatic plaques among plaques presenting no symptoms. As it was previously detailed, such features were extracted after applying a set of processing operations, including envelope RF estimation and de-speckling.

In order to assess the usefulness of the aforementioned sources of information, a comparison is made between classification results when features are computed from different image sources ($F.4$), as proposed along this chapter, and when such features are exclusively obtained from normalized images ($F.5$). Results clearly show that the classification performance is substantially improved from $F.5$ to $F.4$ showing that it is preferable to use the mentioned RMM and textural features when these are extracted from their sources, envelope RF image, and speckle, respectively, rather than computing such features on the normalized image.

A third result, presented in Fig. 14.5 and Table 14.3, is designed to show a general perspective of the classification performances obtained with different approaches. Hence, in this study we have included the gold-standard method, based on the degree of stenosis with a clinical meaningful cut-off of 80 %, together with a recent approach based on the AI score and, finally, the best classifier investigated so far throughout this chapter, that is, the AdaBoost method trained with the so-called *best feature set*.

By comparing the outcomes of each classifier, it is observed that AdaBoost trained with the estimated *best feature set* outperforms the other two approaches which are often referred in literature. In particular, specificity and precision values are significantly higher for AdaBoost with respect to the other classifiers which suggests that the number of detected FP is relatively small. As a consequence, the accuracy obtained in correct plaque classification is also high.

Furthermore, it should be interesting to perform a direct comparison between the effectiveness of the proposed classification method and other related work [13, 16]. Even if this is not possible because the ultrasound data used is not the same, the margin between the accuracy obtained with the AdaBoost method (≈88 %) and these studies (≈74 %) is large enough to argue that the proposed method indeed outperforms other related plaque classification approaches.

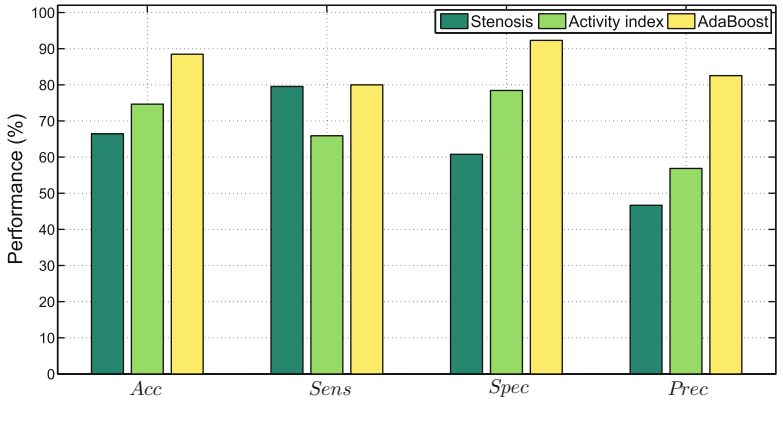

Fig. 14.5 Plaque classification using two state-of-the-art approaches together with proposed method

Table 14.3 Detailed classification results according to different feature sets and performance criteria

LOPO (%)	Degree of stenosis	AI	AdaBoost w/*best feature set*
Acc	66.44	74.66	**88.46**
Sens	79.55	65.91	**80.00**
Spec	60.78	78.43	**92.31**
Prec	46.67	56.86	**82.54**

3 Longitudinal/Natural History Study

A study which aims at classifying plaques with and without symptoms using both morphological- and image-based features has just been presented. However, despite its clinical significance, the CAD system as it has been described so far is not capable of identifying those asymptomatic lesions at high risk of becoming symptomatic. In fact, this kind of information would be more useful for physicians because they would be able to observe an asymptomatic lesion and quantitatively evaluate if such lesion is prone to develop symptoms.

As a consequence, the identification of a subset of "dangerous" or "active" plaques, featuring high neurological risk would help in the indication of treatment. Needless to say, this decision has important clinical and economical consequences for all the parts involved in this process.

As mentioned before, the absolute benefit of surgical intervention based on the degree of stenosis alone as a decision-making criterion is low in the asymptomatic disease and in symptomatic disease with moderate obstruction [1,2]. This clearly motivates the need for developing new strategies for plaque risk prediction.

In this study, a quantitative tool to evaluate plaque activity is proposed, designated by EAI. This method makes use of information gained during the cross-sectional study, particularly the estimated feature set which provides the best discrimination of symptomatic lesions among those that are harmless. Hence, the so-called *best feature set* represents an ultrasound *input* for an algorithm which aims at predicting the occurrence of symptoms in a longitudinal study conducted in a group of asymptomatic subjects (Fig. 14.1).

Again, the diagnostic power of the proposed EAI is compared to other strategies for identifying plaques at high risk, namely the one based on the degree of stenosis and the AI [15].

3.1 Data Management

This study presents a score that correlates with plaque activity and tests its diagnostic power on a group of 112 asymptomatic plaques, acquired from 112 patients. BUS images were collected from the ACSRS (*Asymptomatic Carotid Stenosis and Risk Study*) [25], consisting in a multicentre natural history study of patients with asymptomatic internal carotid diameter stenosis greater than 50 % in relation to the bulb. The degree of stenosis was graded using multiple established ultrasonic duplex criteria. The distribution of plaques according to the degree of stenosis was an average value of ≈75 % (50–99) and no. of plaques with degree of stenosis > 70 % = 80. Patients were followed for possible occurrence of symptoms for a mean time interval of 37.1 weeks. At the end of the study, 13 out of 112 patients (11.6 %) had developed symptoms (3 AF, 6 TIA, 4 stroke).

3.2 Methods: Enhanced Activity Index

A quantitative diagnostic measure—EAI—is developed considering the knowledge gathered in the cross-sectional study. Recall that the first study enabled to identify the "profile" of the "active" plaque by taking into account a set of parameters that are statistically relevant for separating symptomatic and asymptomatic lesions. Hence, the implementation of EAI is performed as follows:

1. The ultrasound "profile" of the "active" plaque is considered, by taking the features which are relevant for plaque classification, using the M–W U statistical test.
2. Reference values are taken for each ultrasound feature, f_i, and group, symptomatic (S), and asymptomatic (A), considering the mean $(\mu_i(S), \mu_i(A))$ and variance $(\sigma_i^2(S), \sigma_i^2(A))$.
3. The EAI*, renamed for convenience, is computed as the Bayes factor given by

$$\mathrm{EAI}^* = \frac{R_S}{R_A}, \tag{14.3}$$

where

$$R_k = \sum_i p(f_i|\omega_k) \approx \mathcal{N}(\mu_i(k), \sigma_i^2(k)), \quad k = \{S, A\} \tag{14.4}$$

are the marginal likelihoods of each group (S or A) and correspond to the sum of the conditional probabilities of each feature belonging to each group, respectively. Such conditional probabilities in (14.4) are computed assuming a normal distribution (Fig. 14.6). In (14.3), R_S and R_A represent the likelihoods of each plaque producing symptoms or stabilize, respectively. Hence, when $\mathrm{EAI} = 1$, the result is inconclusive, while for $\mathrm{EAI} < 1$ the plaque will stay harmless with a significant probability which is higher as EAI decreases. Contrarily, plaques showing an $\mathrm{EAI} > 1$ are prone to produce symptoms, being more "dangerous" when EAI increases.

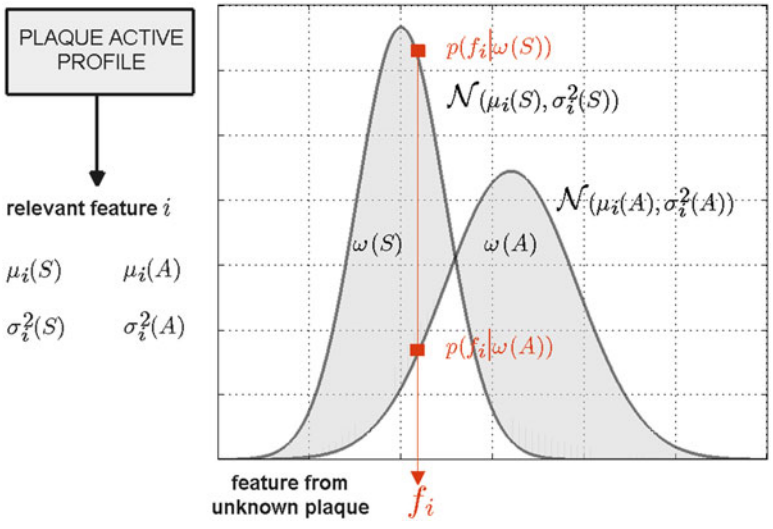

Fig. 14.6 Illustrative concept of conditional probabilities for a particular plaque feature f_i used to compute the EAI

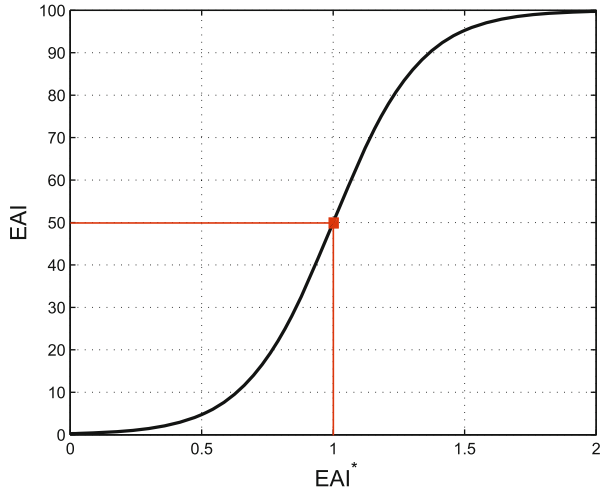

Fig. 14.7 Mapping function for re-scaling the EAI onto a 0–100 scale, where 100 represents maximum risk and 0 accounts for stability

4. The EAI is rescaled using a sigmoid mapping function which places the EAI onto a 0 100 scale. This function, sketched in Fig. 14.7 is defined as

$$\mathrm{EAI} = \frac{100}{1 + \exp -(\mathrm{EAI}^* - 1)}. \qquad (14.5)$$

This mapping technique is useful to make the predictive power of the proposed EAI method comparable to AI [15] and degree of stenosis [2].

3.3 Experimental Results

The longitudinal study (Fig. 14.1) investigates the diagnostic power of EAI for identifying plaques at high risk of originating cerebrovascular events. To make this study feasible, the proposed method should be compared with other strategies of plaque risk prediction (e.g. degree of stenosis and AI).

Such comparison is here performed using ROC (*Receiver Operating Characteristic*) curve analysis [26]. In general, when considering the results of a particular test in two populations, one population with a disease, the other population without the disease, one rarely observes a perfect separation between the two groups. For every possible cut-off point or criterion value which one selects to discriminate between the two populations, there will be some cases with the disease correctly classified as positive (TPF = True Positive fraction) but some samples with the disease classified as negative (FNF = False Negative fraction). On the other hand, some cases without the disease will be correctly classified as negative (TNF = True Negative fraction) but some samples without the disease will be classified as positive (FPF = False Positive fraction). In a ROC curve the TPF (Sensitivity) is plotted as function of the FPF (100-Specificity) for different cut-off points, therefore each point on the ROC plot represents a sensitivity/specificity pair corresponding to a particular decision threshold. A test with perfect discrimination (no overlap in the two distributions) has a ROC plot that passes through the upper left corner (100 % TPF and 0 % FPF). Sometimes, the ROC is used to generate a summary statistic.

Moreover, the area under the ROC curve (ROC AUC) statistic is often used in machine learning for model comparison. This measure indicates that a predictive method is more accurate as higher is the ROC AUC. Similarly, it can be interpreted as the probability that when one randomly picks one positive and one negative example, the classifier will assign a higher score to the positive example than to the negative. In engineering, the area between the ROC curve and the no-discrimination line is also used. This area is often simply known as the discrimination. Moreover, the intersection of the ROC curve with the line at 90° to the no-

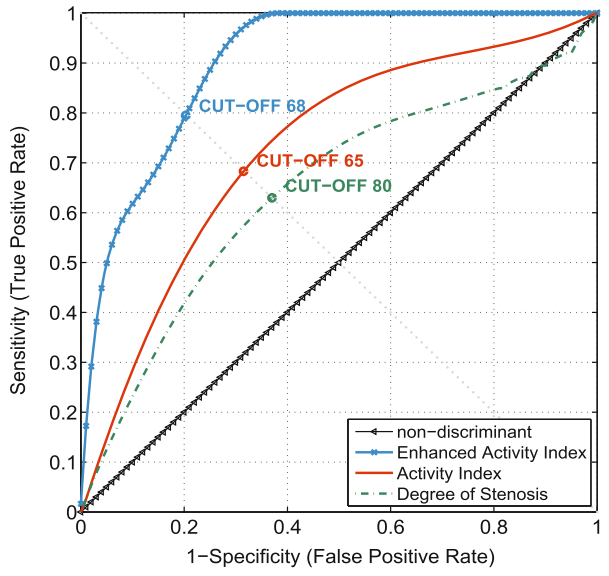

Fig. 14.8 ROC curves for different prediction methods

discrimination line is also considered as an heuristic method to investigate the cut-off providing the best discriminative power of the test (or predictive method).

Figure 14.8 presents the ROC curves obtained with the three studied predictive methods. The ROC AUCs are 0.6496 (64.96 %), 0.7329 (73.29 %), and 0.9057 (90.57 %) for degree of stenosis, AI and EAI, respectively. Naturally, the ROC AUC of the no-discrimination line is 0.5000 (50.00 %). These results markedly show that the EAI method is the most accurate method among the ones tested. Additionally, the AI method is also better than the degree of stenosis, as expected, because the former includes other parameters besides the stenosis degree. When computing the differences between the ROC AUCs and the no-discrimination line, one obtains 14.96 %, 23.29 %, and 40.57 % of discrimination for degree of stenosis, AI and EAI, respectively. This observation gives a clue about the amount of effective diagnostic information that is gained since the no-discrimination line corresponds to random guessing. The results reinforce the idea that the EAI method is the most discriminant among the investigated approaches.

According to the aforementioned heuristic method, the cut-off values providing the best trade-off between TP and FP rates for each predictive method are respectively 80, 65, and 68 for degree of stenosis, AI, and EAI (Fig. 14.8).

Note that the choice of a method to identify the best cut-off value is critical for the performance of the predictive method. The heuristic method that was presented (a diagonal line perpendicular to the nondiscriminant line, intersecting it at 0.5 FPR and 0.5 TPR) assigns equal importance to the detection of TP (TPR) and TN (1-FPR). In practice, we can argue that the relative importance of TPR and TNR should change according to each scenario. Hence, when the decision-making strategy intends to assign more relevance to the TPR, the cut-off line (or curve) should be shifted upper right while the opposite should happen when an increase importance is to be given to the TNR.

Figure 14.9 provides a different viewpoint about the diagnostic power of the proposed EAI prediction method when compared to the other methods. Particularly, this result allows the comparison of FP and FN samples according to different cut-offs applied for each studied method. Hence, the shorter the bars corresponding to the FP and FN are, the better is the cut-off or the predictive method, depending on if one is studying a particular method or comparing the three methods at the same time. To make an equivalence between the results shown in Fig. 14.9 and the ROC curves, it can be said that as the bars of FN and FP get smaller (hence, the TPR increases and the FPR decreases), the predictive method moves up and left, respectively.

It can be clearly observed that the application of the EAI method provides lower FP values when compared to the other methods regardless the cut-off chosen. Also evident is the fact that the prediction method based on stenosis is the one resulting in the highest number of FP, which is a natural observation because it is by far the simplest discriminative test used. Other observation that can be made from comparing Fig. 14.9b, c is that, generally, the number of FP is significantly lower for EAI when compared to AI.

In fact, Fig. 14.9 provides an objective interpretation of the trade-off between FP and FN. However, choosing an optimal cut-off is highly subjective. The reader should bear in mind that a method with a good diagnostic power should be naturally able to identify as much TP samples as possible, while providing a small number of FN and FP. In fact, the cut-off should be chosen according to a justifiable criterion: (a) is it more important to identify and treat all subjects that will develop a neurological complication even though a large number of patients must be operated? (b) should one be worried about sparing as many patients as we can from surgery?, or (c) should one decide on combining low FP and FN rates? If we pick the latter, the most suitable cut-off for degree of stenosis is 70 % while the best cut-offs for AI are 56 and 50, respectively. Additionally, it is worth to note that the application of EAI with the mentioned cut-off is able to identify all TP, in other words, is capable of predicting all plaques that developed symptoms.

Results presented in Fig. 14.9 are detailed in Table 14.4, providing different performance criteria for each method and cut-offs. For instance, note that the EAI method with cut-off 52 shows 100 % sensitivity and 30.95 % positive predictive value. This is, indeed, the most important result to outline since the EAI, with this particular cut-off, is able to identify all the plaques which will develop symptoms while detecting the smallest number of false positives.

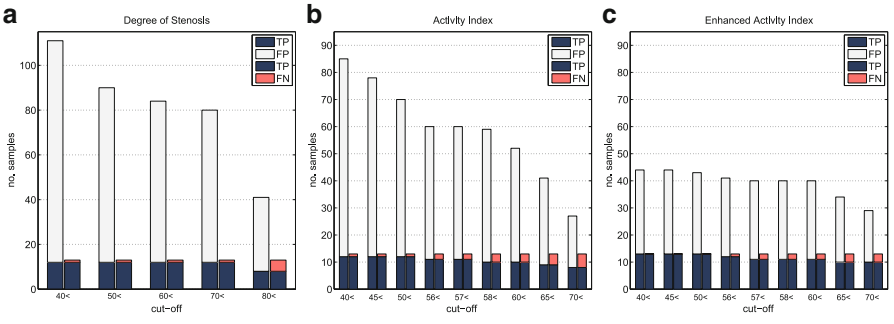

Fig. 14.9 Bar plot with TP, FP and FN values for different cut-offs, according to the stenosis predictor (**a**), AI (**b**) and EAI (**c**)

Table 14.4 Diagnostic (discriminative) power of the investigated methods for different cut-offs, according to performance criteria including sensitivity, specificity, accuracy, PPV and NPV

	Cut-off	Sens (%)	Spec (%)	Acc (%)	PPV (%)	NPV (%)
Stenosis	**>40**	92.31	0	10.71	10.81	0
	>50	92.31	21.21	29.46	13.33	95.46
	>60	92.31	27.27	34.82	14.29	96.43
	>70	***92.31***	***31.31***	***38.39***	***15.00***	***96.87***
	>80	61.54	66.67	66.07	19.51	92.96
AI	**>40**	92.31	26.26	33.93	14.12	96.30
	>45	92.31	33.33	40.18	15.36	97.06
	>50	***92.31***	***41.41***	***47.32***	***17.14***	***97.62***
	>56	84.62	50.50	54.46	18.33	96.15
	>60	76.92	57.58	59.82	19.23	95.00
	>65	69.23	67.68	67.86	21.95	94.37
	>70	61.54	80.81	78.57	29.63	94.12
EAI	**>40**	100	68.69	72.32	29.55	100
	>50	100	69.70	73.21	30.23	100
	>52	***100***	***70.71***	***74.10***	***30.95***	***100***
	>56	92.31	70.71	73.21	29.27	98.59
	>60	84.61	70.71	72.32	27.50	97.22
	>65	76.92	75.76	75.89	29.41	96.15
	>70	76.92	80.81	80.36	34.48	96.39

Results obtained for the best cut-off for each method (combination of best Sens and PPV) are highlighted

In predictive analysis, a table of confusion, also known as a confusion matrix, is a table with two rows and two columns that reports the number of TN, FP, FN, and TP. Table 14.5 summarizes the true predictive value of each method according to the aforementioned cut-offs, selected after comprehensive appreciation of Table 14.4.

As it is observed in Table 14.5 the EAI method was able to identify the 13 patients who had developed symptoms by the end of the follow-up (longitudinal) study, whereas the degree of stenosis and the AI methods were unable to identify, respectively, 1 and 2 patients who developed neurological complications later. Moreover, as far as the false positive number is concerned, the EAI method yields 29 FP against 49 and 68, respectively, for the AI and degree of stenosis. This means that if the decision of surgery for plaque removal was based in the former method, only 29 patients were unnecessarily operated. This number is significantly smaller than the one observed for the other methods, suggesting that the EAI is the most cost-effective method. Thus, the EAI method demonstrates to have the best diagnostic power among the methods investigated because it provides the most accurate selection of a subset of patients potentially at high risk within a population of asymptomatic patients.

Table 14.5 Confusion matrix with prediction outcome of the investigated methods: stenosis (underlined), AI (italics), and EAI (bold)

		Actual value					
		P			N		
Prediction	P′	12	*11*	**13**	68	*49*	**29**
	N′	1	*2*	**0**	31	*50*	**70**

4 Conclusions

Carotid plaques are the commonest source of neurological symptoms due to embolization or flow reduction.

Throughout this chapter it has been motivated the need for defining accurately the ultrasound "profile" of the "active" plaque, that is, the asymptomatic lesion with an increased likelihood of becoming symptomatic. This is of considerable importance because currently the treatment planning, based only on the patient's clinical history and degree of stenosis, is not optimal and cost-effective.

First, a cross-sectional study was performed for training and testing the Adaptive Boosting classifier using the LOPO cross-validation technique. This classifier consists of ultrasound parameters, accounting for morphology, echogenicity, and texture, extracted from different image sources, after application of a set of processing operations, described in previous chapters. A suitable statistical hypothesis test is applied in order to identify a subset of features which are statistically meaningful to discriminate between plaques with and without symptoms. An AdaBoost classifier based on the so-called *best feature set* outperforms other state-of-the-art methods, yielding an accuracy of 88 % and sensitivity of 80 % in identifying symptomatic plaques. Moreover, a comparative study of classifiers performance clearly suggests the usefulness of the preprocessing ultrasound methods, proposed throughout this thesis, as well as the value of mixture model and textural features for plaque classification.

Once a suitable ultrasound profile of the symptomatic or active plaque was established, an EAI that quantifies the degree of plaque activity or likelihood to rupture was proposed. This measure was evaluated on a longitudinal study of asymptomatic plaques and compared to other approaches (degree of stenosis and AI), demonstrating the best diagnostic power. In particular, EAI provides correct identification of all plaques that developed symptoms while giving the smallest number of false positives. This result suggests that the EAI could have a significant impact on stroke prediction and treatment planning.

References

1. North American Symptomatic Carotid Endarterectomy Trial Collaborators (1998) Benefit of carotid endarterectomy in patients with symptomatic moderate or severe stenosis. N Engl J Med 339(20):1445–1453
2. European Carotid Surgery Trialists Collaborative Group (1998) Randomised trial of endarterectomy for recently symptomatic carotid stenosis: final results of the MRC European Carotid Surgery Trial (ECST). Lancet 351:1379–1387
3. Inzitari D et al (2000) The causes and risk of stroke in patients with asymptomatic internal carotid artery stenosis. N Engl J Med 342(23):1693–1700
4. Polak JF et al (1998) Hypoechoic plaque at US of the carotid artery: an independent risk factor for incident stroke in adults aged 65 years or older. Cardiovascular Health Study. Radiology 208(3):649–654
5. Widder B, Paulat K, Hackspacher J, Hamann H, Hutschenreiter S, Kreutzer C, Ott F, Vollmar J (1990) Morphological characterization of carotid artery stenoses by ultrasound duplex scanning. Ultrasound Med Biol 16(4):349–354
6. Belcaro G, Nicolaides AN, Laurora G, Cesarone MR, Sanctis M, Incandela L, Barsotti A (1996) Ultrasound morphology classification of the arterial wall and cardiovascular events in a 6-year follow-up study. Arterioscler Thromb Vasc Biol 16:851–856
7. Mougiakakou S, Golemati S, Gousias I, Nicolaides AN, Nikita KS (2007) Computer-aided diagnosis of carotid atherosclerosis based on ultrasound image statistics, laws' texture and neural networks. Ultrasound Med Biol 33(1):26–36 .
8. El-Barghouty NM, Levine T, Ladva S, Flanagan A, Nicolaides A (1996) Histological verification of computerised carotid plaque characterisation. Eur J Vasc Endovasc Surg 11(4): 414–416
9. Elatrozy T, Nicolaides A, Tegos T, Griffin M (1998) The objective characterization of ultrasonic carotid plaque features. Eur J Vasc Endovasc Surg 16:223–230
10. Tegos TJ, Kalodiki E, Daskalopoulou SS, Nicolaides AN (2000) Stroke: epidemiology, clinical picture, and risk factors—part i of iii. Angiology 51(10):793–808
11. Iannuzzi A, Wilcosky T, Mercuri M, Rubba P, Bryan AF, Bond MG (1995) Ultrasonographic correlates of carotid atherosclerosis in transient ischemic attack and stroke. Stroke 26(4):614–619
12. Wilhjelm JE, Grnholdt ML, Wiebe B, Jespersen SK, Hansen LK, Sillesen H (1998) Quantitative analysis of ultrasound b-mode images of carotid atherosclerotic plaque: correlation with visual classification and histological examination. IEEE Trans Med Imaging 17(6):910–922
13. Christodoulou CI, Pattichis CS, Pantziaris M, Nicolaides A (2003) Texture-based classification of atherosclerotic carotid plaques. IEEE Trans Med Imaging 22(7):902–912
14. Asvestas P, Golemati S, Matsopoulos GK, Nikita KS, Nicolaides AN (2002) Fractal dimension estimation of carotid atherosclerotic plaques from b-mode ultrasound: a pilot study. Ultrasound Med Biol 28(9):1129–1136
15. Pedro LM, Fernandes JF, Pedro MM, Gonalves I, Dias NV (2002) Ultrasonographic risk score of carotid plaques. Eur J Vasc Endovasc Surg 24:492–498
16. Kyriacou E et al (2009) Classification of atherosclerotic carotid plaques using morphological analysis on ultrasound images. Appl Intell 30(1):3–23
17. AbuRahma AF, Thiele SP, Wulu JT Jr (2002) Prospective controlled study of the natural history of asymptomatic 60 % to 69 % carotid stenosis according to ultrasonic plaque morphology. J Vasc Surg 36(3):437–443
18. Thijssen J (2003) Ultrasonic speckle formation, analysis and processing applied to tissue characterization. Pattern Recognit Lett 24(4–5):659–675
19. Seabra J, Sanches J (2010) On estimating de-speckled and speckle components from B-mode ultrasound images. In: Proceedings of IEEE international symposium on biomedical imaging, Rotterdam, April 2010. IEEE Engineering in Medicine and Biology Society, pp 284–287
20. Seabra J, Sanches J, Ciompi F, Radeva P (2010) Ultrasonographic plaque characterization using a rayleigh mixture model. In: Proceedings of IEEE international symposium on biomedical imaging, Rotterdam, The Netherlands, April 2010. IEEE Engineering in Medicine and Biology Society, pp 1–4
21. Wear K, Wagner R, Garra B (1995) A comparison of autoregressive spectral estimation algorithms and order determination methods in ultrasonic tissue characterization. IEEE Trans Ultrason Ferroelectr Freq Control 42(4):709–716

22. Schapire RE (2002) The Boosting Approach to Machine Learning An Overview In MSRI Workshop on Nonlinear Estimation and Classification
23. Ciompi F, Pujol O, Gatta C, Rodriguez O, Mauri F, Radeva P (2009) Fusing in-vitro and in-vivo intravascular ultrasound data for plaque characterization. Int J Cardiovasc Imaging 26:763–779
24. Gibbons J, Chakraborti S (1992) Nonparametric statistical inference. CRC Press, Boca Raton
25. Nicolaides AN, Kakkos SK, Griffin M, Sabetai M, Dhanjil S et al (2005) Severity of asymptomatic carotid stenosis and risk of ipsilateral hemispheric ischaemic events: results from the ACSRS study. Eur J Vasc Endovasc Surg 30(3):275–284
26. Zweig MH, Campbell G (1993) Receiver-operating characteristic (ROC) plots: a fundamental evaluation tool in clinical medicine. Clin Chem 39(4):561–577

Ultrasonographic Quantification of Carotid Stenosis: A Reappraisal Using a New Gold Standard

15

Luís Mendes Pedro, Ruy Fernandes e Fernandes, Luís M. Silvestre, and J. Fernandes e Fernandes

1 Introduction

Atherosclerotic disease involving the carotid bifurcation is a major cause of cerebrovascular events and its treatment, by endarterectomy or stenting, aims to prevent stroke and disability.

The choice for medical treatment or intervention (surgical or endovascular) is largely dependent on the degree of stenosis as defined in major level 1 trials for the management of symptomatic (NASCET [1], ECST [2]) and asymptomatic disease (ACAS [3], ACST [4]). The NASCET and ECST concluded that a clear benefit was obtained when symptomatic patients with >70 % stenosis were submitted to carotid endarterectomy (CEA). In patients with <50 % stenosis, CEA did not provide any benefit, and in the 50–70 % group only in the NASCET study (and not the ECST) the CEA was associated with some reduction in the risk of stroke (absolute risk reduction of 6.5 % and relative risk reduction of 29 %) [5].

In asymptomatic patients, the ACAS trial published in 1995 demonstrated a 55 % reduction of the relative risk of stroke in the group submitted to CEA over best medical treatment alone, but only for lesions associated with >60 % stenosis. The Asymptomatic Carotid Stenosis Trial (ACST) [4] published in 2004 also confirmed a benefit of CEA in asymptomatic patients for stenosis higher than 80 %.

Adequate quantification of the degree of stenosis is therefore mandatory, particularly concerning 50 %, 60 %, and 70 % cutoffs. Also, in most of these studies the calculation of the severity of obstruction was determined in bi-planar angiography, which is not widely used anymore.

Despite an overall similarity between the results of NASCET and ECST for the threshold of 70 %, major methodological differences were present in both trials as the stenosis quantification method in angiographies was substantially different (Fig. 15.1a). In NASCET the minimal luminal diameter at the level of stenosis was compared with the diameter of the distal internal carotid artery according to the formula:

$$\%\,\text{Stenosis} = 1 - \left(\frac{\text{ICA minimal luminal diameter at maximal stenosis level}}{\text{distal ICA luminal diameter}}\right) \times 100$$

In ECST the minimal luminal diameter at the level of stenosis was compared with the diameter of the carotid bulb at the level of stenosis according to the formula:

$$\%\,\text{Stenosis} = 1 - \left(\frac{\text{ICA minimal luminal diameter at maximal stenosis level}}{\text{diameter of the carotid bulb}}\right) \times 100$$

This methodological difference led to an underestimation of stenosis in the NASCET study when compared to the ECST. For example, a 70 % NASCET[1] stenosis corresponds

L.M. Pedro (✉) • R. Fernandes e Fernandes • L.M. Silvestre • J. Fernandes e Fernandes
Faculty of Medicine, University of Lisbon, Lisbon, Portugal

Department of Vascular Surgery, Hospital Santa Maria, Lisbon, Portugal

Instituto Cardiovascular de Lisboa, Lisbon, Portugal
e-mail: jmrs@ist.utl.pt; jsuri@comcast.net; jmfernandes@fm.ul.pt

[1] In the following text, the method for stenosis American quantification (used in NASCET and ACAS) will be designated as N (e.g., 70 %N) and the European method (used in ECST) will be designated as E (e.g., 70 %E).

L. Saba et al. (eds.), *Multi-Modality Atherosclerosis Imaging and Diagnosis*,
DOI 10.1007/978-1-4614-7425-8_15, © Springer Science+Business Media, LLC 2014

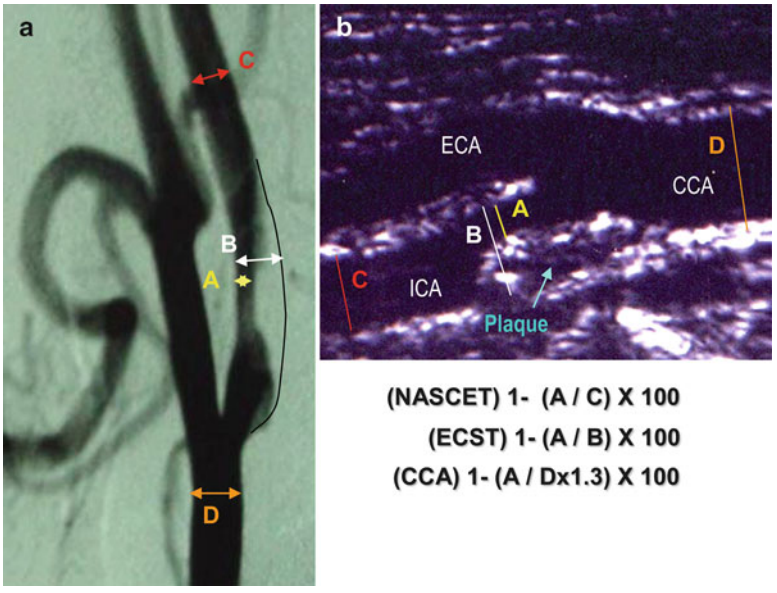

Fig. 15.1 Methods for stenosis quantification in angiography (**a**) and their equivalents in ultrasonography (**b**). NASCET, method used in the American studies NASCET and ACAS; ECST, method used in the European study ECST; (CCA), method that uses the distal CCA diameter as the reference; CCA, common carotid artery; CE, external carotid artery; CI, internal carotid artery

Table 15.1 Theoretical correspondence of the percentage of stenosis calculated according to the American (NASCET) and European (ECST) methods

Study	Percentage of stenosis							
NASCET	11	30	40	50	60	70	80	90
ECST	50	65	70	75	80	85	91	97

to 85 % ECST (see footnote 1) and a 70 %E corresponds to 40 %N stenosis (Table 15.1). For more severe lesions this difference tends to be less relevant and above 70 %N all the lesions are also >70 %E.

However, only stenoses >85 %E are also >70 %N, suggesting that the population of both trials was not exactly comparable. Lesions 70–85 %E correspond to 50–70 %N, and in fact a later analysis of the NASCET trial showed a significant benefit of CEA in this group of patients.

The understanding of all these discrepancies is very important, as the correct quantification of the degree of stenosis remains the key parameter used for therapeutical decision [6–9]. On the other hand, angiography is not used anymore in general clinical practice for the purpose of stenosis quantification, being replaced by other methods like color-flow duplex scan (CFDS), angio-magnetic resonance (Angio-MR), or angio-computerized tomography (Angio-CT) [10, 11].

2 Quantification of Carotid Stenosis Using Color-Flow Duplex Scan

The use of CFDS as a screening and also as a treatment decision method prompted the introduction of quantification criteria, which were considered accurate when compared with angiography, and associated with high sensitivity, with low rate of false positives. Also, the therapeutical decision-making strategy based on CFDS requires the need of diagnostic criteria with high specificity and negligible number of false negatives.

In view of the generalized use of CFDS examination, a reappraisal of the diagnostic parameters for stenosis measurement is pertinent.

CFDS is a unique method to study arterial stenosis as it permits the assessment of a number of morphologic and hemodynamic aspects related to the lesion.

It may visualize the plaque longitudinally, allowing the quantification of stenosis according to the angiographic criteria used in NASCET and ECST. In fact, the minimal luminal diameter can be compared to the clearly visualized bulb diameter (European criteria), to the distal common carotid artery (CCA), and also to the distal ICA diameter (American criteria) (Fig. 15.1b).

Beyond this, the carotid axis can also be evaluated in transversal views, providing cross-sectional assessments of the stenosis (Fig. 15.2). After identifying the point of tighter stenosis, one can measure the obstruction comparing the minimal luminal area with the outer arterial area (cross-sectional area measurement).

Finally, the CFDS is also able to evaluate the flow repercussion caused by the obstruction by quantification of flow velocities, thus providing hemodynamic objective parameters, which correlated well with the degree of stenosis, allowing its classification in different subgroups of severity [12].

The quantification of carotid stenosis by CFDS should include and combine the information emerging from morphologic and hemodynamic assessments, thus incorporating the unique capabilities of the method on the decision process [13].

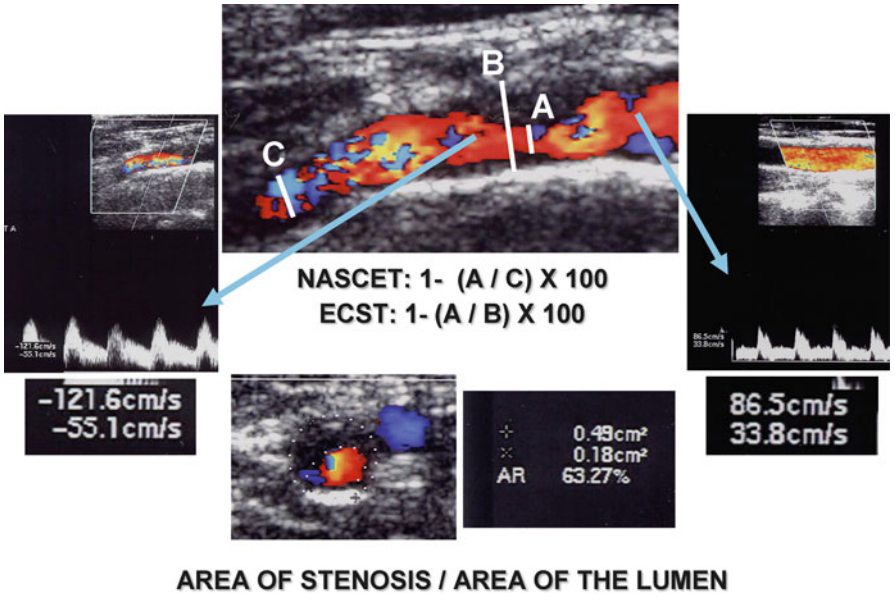

Fig. 15.2 Quantification of carotid stenosis by CFDS, according to the linear longitudinal methods (NASCET and ECST), according to the cross-sectional area measurement, and according to the hemodynamic assessment

3 Hemodynamic Assessment

Several hemodynamic criteria were introduced to quantify carotid stenosis. They include the systolic and/or diastolic velocities as well as relations between velocities obtained at different levels (Fig. 15.2).

The more useful parameters were shown to be the peak systolic velocity (PSV) and the end-diastolic velocity (EDV) measured immediately after the more stenotic part of the lesion.

In the 1980s, D. E. Strandness introduced the first original criteria based on flow velocity to classify carotid stenosis according to the cutoffs: A: Normal; B: 1–15 %; C: 15–50 %; D: 50–80 %; D+: 80–99 % [14].

Other authors, aiming to differentiate the levels of stenosis that were found to be clinically relevant after the multicenter trials, proposed other criteria based on PSV, EDV, or combinations of these values [15].

Flow acceleration with increase of PSV appears with diameter reduction of >50 % (>75 % area reduction) and it seems to be one of the earliest hemodynamic manifestations of a significant lesion. EDV increase is a later feature as only severe stenosis (>70 % diameter reduction) is related to the persistence of gradient during diastole, meaning a lower distal peripheral resistance.

The measurement of proximal velocities is usually performed at the CCA and is used to compare with velocities obtained at the level of the stenosis or 1 cm beyond. This is the location where higher velocities can be found.

Fujitani [16] called the attention to the normal increase of ipsilateral carotid velocities when the contralateral carotid artery is occluded. This fact requires reappraisal of the criteria for stenosis quantification in the presence of severe contralateral disease. Others [17, 18] suggested the importance of using indexes comparing velocities at the stenosis with the ones obtained in the CCA. Examples of these ratios are the Systolic Index (PSV_{ica}/PSV_{cca}), the Diastolic Index (EDV_{ica}/EDV_{cca}), and the PSV_{ica}/EDV_{cca} Index.

Refinement of these criteria aimed to improve the diagnostic accuracy of the relevant cutoffs for symptomatic and asymptomatic carotid stenosis (50 % [4], 60 % [3], and 70 % [1, 2]), which could have impact on clinical decision.

The pitfalls [9, 10, 19] of these investigations are related to the multiplicity of criteria and protocols suggested for the CFDS examination, and also by the lack of uniformity in the validation process against angiography, which depends largely on the quantification technique and criteria used (NASCET, ECST, or CCA criteria?). This controversy is very relevant, as in later years CFDS was established as the major technique used in clinical practice for the management of patients with carotid stenosis and correlation of flow velocities with diameter reduction according to ECST or NASCET criteria and area reduction—the four more significant parameters—became imperative.

4 Morphologic Assessment: The Advantages of Cross-sectional Area Measurement

The measurement of stenosis by bidimensional (2D) ultrasonography may include longitudinal and transversal evaluations.

The assessment of the carotid axis in longitudinal plane allows the definition and quantification of the minimal luminal

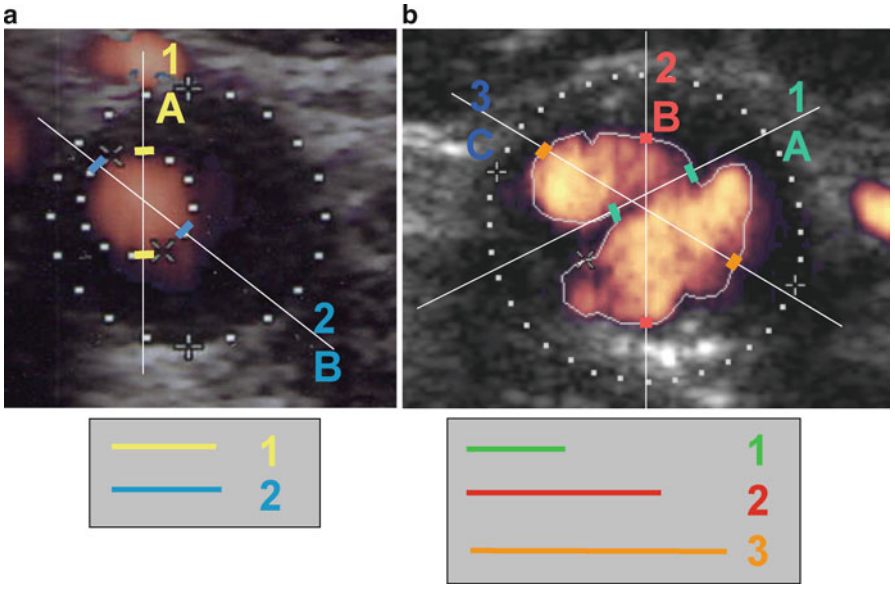

Fig. 15.3 (**a**) Cross-sectional image of a stenosis with regular and circular lumen: both linear diameters (1, 2) are identical. (**b**) Cross-sectional image of a stenosis with irregular lumen: the three diameters (1, 2, 3) are significantly different

diameter, which is then compared with the diameter of the bulb, the ICA, or the CCA. This evaluation is always dependent on a subjective choice of the operator according to his perception of the higher stenosis point. When the lumen is regular and circular the determination of the minimal luminal diameter is predictable and independent on the chosen plane of assessment. However, very often, lesions are complex and eccentric and the geometry of the lumen in the region of the plaque is elliptical or irregular, rendering the calculation of the minimal luminal diameter highly dependent on the plane chosen and subject to remarkable variations (Fig. 15.3). Porsche et al. [20] found that the lumen was not circular in 18 % and the ACSEPT study [21] characterized the carotid lumen at the level of the stenosis and demonstrated that it was circular in 28 %, eliptical in 50 %, and irregular in 22 %. This is in consonance with the need to evaluate the luminal shape and to assess its repercussion on the longitudinal plane used for diameter quantification.

Therefore, characterization of the lumen geometry is imperative and is better accomplished using a cross-sectional approach that permits the choice of the point where the stenosis is tighter. Severity of stenosis should then be assessed by the ratio of the area at the minimal lumen and the area obtained from the peripheral contour of the artery. In the future, a tridimensional (3D) assessment of plaque structure and lumen may provide more realistic estimation of the degree of stenosis as well as the total volume of the lesion [22].

Physiologically, the cross-sectional area reduction is the most relevant parameter to induce hemodynamic effect, and, therefore, area measurement appears to be more adequate to quantify carotid stenosis, because it is independent on the longitudinal plane used for the evaluation.

This method of quantification of stenosis using area measurements was recognized as being superior to the linear measurement, in studies based on the reconstruction of the plaques removed by CEA [13, 23, 24].

Another approach to challenge the longitudinal diameter method was made by Alexandrov et al. [13] who compared several parameters: angiographic longitudinal measurements by the NASCET and ECST methods, area quantification extrapolated by the formula πr^2, ultrasonographic velocity assessment, determination of stenosis by conversion to area using diameter–area conversion tables, area quantification after assembling and measuring removed surgical specimens, and finally the subjective ("eye-driven") method for calculation on angiography.

The authors concluded that both NASCET and ECST methods underevaluate the lesions, when comparisons were made with CEA specimens. Area of stenosis as extrapolated from the angiography-driven NASCET and ECST diameters as well as from CFDS diameters was not significantly different from area measurements in CEA specimens. Using velocity parameters, the linear NASCET measurement had a correlation of 0.75, higher than the one obtained from linear ECST method ($r = 0.57$). Area extrapolation (πr^2) method correlated well with the NASCET ($r = 0.92$) and ECST ($r = 0.63$) methods.

The limitation of this study derives from the inaccuracy of the extrapolation of diameter measurements to area in irregular lesions [20, 21], but points out that assessments based on area reduction calculations are closer to the reality from endarterectomy specimens [23]. However, the obvious drawbacks result from the difficulty to perfectly assemble surgical specimens, with inevitable modifications and distortions in the size and shape of the structure of the lesion.

These studies suggest the need to define new gold standards to compare and validate the different methods for carotid stenosis quantification.

The aim of our research was to compare the different measurement methods of carotid stenosis with area ratios at the point of highest velocity acceleration obtained intra-operatively with the probe applied directly over the artery, which gives a real image of the lesion area (and "volume") [25] in physiological conditions.

5 A New Gold Standard: Intra-operative Cross-sectional Area Measurement [25]

The intra-operative CFDS (IO CFDS) was performed during the procedure of CEA, after the dissection of the carotid bifurcation but before arteriotomy, thus obtaining in vivo high-definition images of the plaque and stenosis, as the sterile probe is directly applied over the artery (Fig. 15.4).

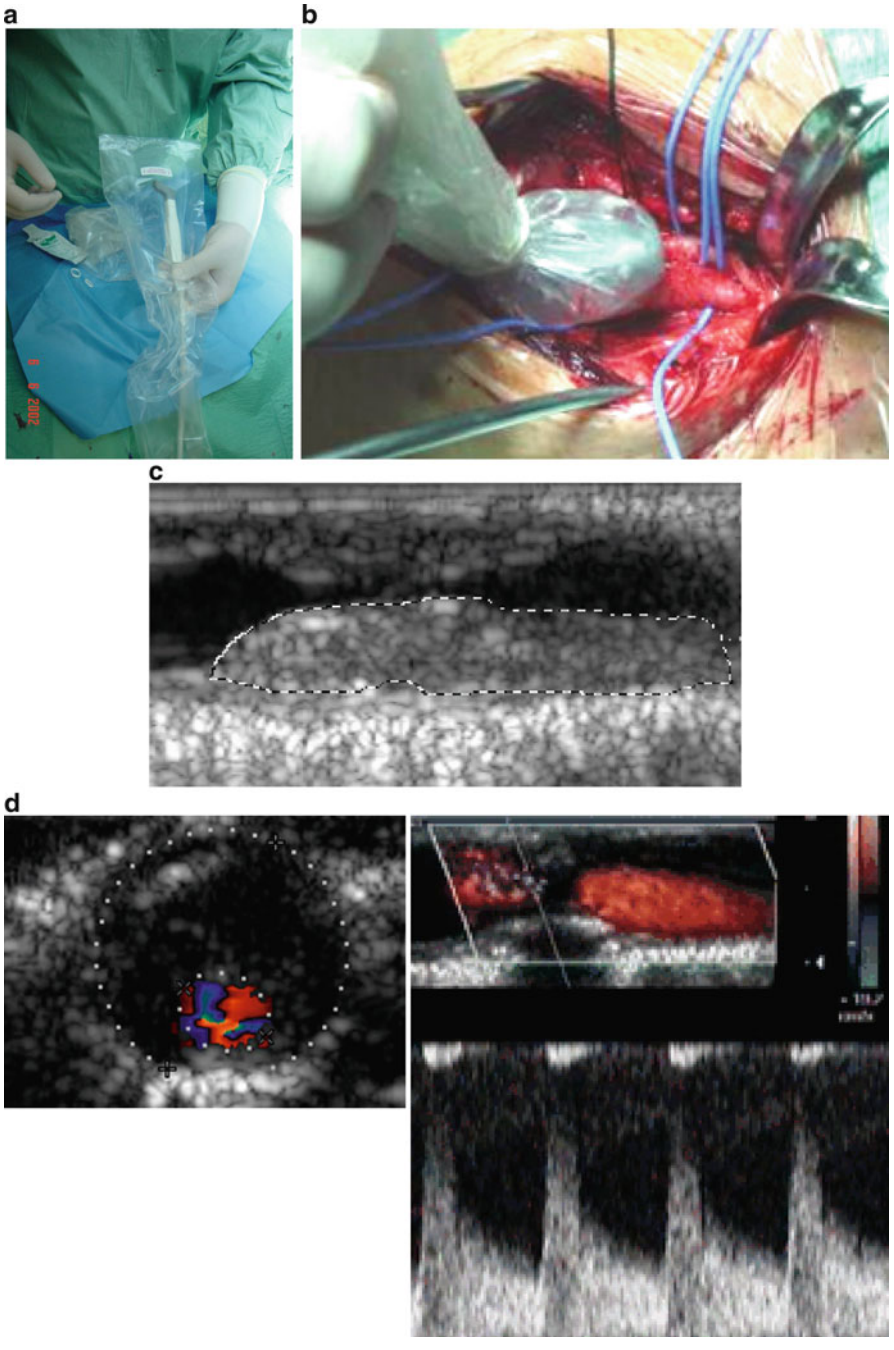

Fig. 15.4 Intra-operative CFDS. (**a**) Specially designed "hockey-stick" probe and the plastic kit for surgical use; (**b**) detail of the examination; (**c**) plaque structure characterisation; (**d**) quantification of stenosis morphologically (área) and hemodynamically

This approach eliminates the distortion associated with the models using the in vitro reconstruction of the removed plaque by endarterectomy. On the other hand, the IO CFDS permits the easy identification of the higher stenotic point and the direct quantification of the luminal and arterial area and thus the determination of the percentage of obstruction. This IO CFDS evaluation can afterwards be compared with the transcervical area measurement and we assumed that it represents the most reliable method to determine the degree of carotid stenosis.

The technique used for IO CFDS included an equipment ATL-Philips® HDI 3000, a 5–10 MHz multifrequency probe specially designed for intra-operative studies, and a kit for sterile surgical protection of the probe and cable (Fig. 15.4a, b).

After arterial exposure the probe is located directly over the carotid axis and high-quality images of the lesion are obtained (Fig. 15.4c). Then, the point of higher stenosis is located in cross-sectional views and another image is taken after ensuring that the probe is located perpendicularly to the artery. The quantification of the percentage of stenosis was determined in this image using the area measurement technique (Fig. 15.4d).

Table 15.2 Hemodynamic criteria A[14] (University of Washington)

Degree of stenosis (%)			
NASCET	ECST	PSV (cm/s)	EDV (cm/s)
• <11	• <50	<125	<140
• 11–60	• 50–80	>125	<140
• >60	• >80	>125	>140

Table 15.3 Hemodynamic criteria B[17,19]

Degree of stenosis (%)			
NASCET	ECST	PSV (cm/s)	EDV (cm/s)
• <11	• <50	<120	<40
• 11–40	• 50–70	121–150	40–80
• 41–70	• 71–85	151–250	<140
• >70	• >85	>250	>141

Table 15.4 Hemodynamic criteria C[19]—Quotient VSM ci/VSM cp

Degree of stenosis (%)		
NASCET	ECST	PSV_{ica}/PSV_{cca}
• <11	• <50	<1.5
• 11–40	• 50–70	1.5–2
• 41–50	• 71–75	2–3.2
• 51–70	• 76–85	3.2–4
• >70	• >85	>4

6 Comparison of Conventional Methods for Stenosis Quantification with IO CFDS Cross-sectional Area Measurement [25]

A study was conducted to validate conventional morphologic and hemodynamic criteria for stenosis quantification against the new gold standard (cross-sectional area measurement in IO CFDS evaluation).

The study included the comparison of IO CFDS with three parameters: (1) transcervical cross-sectional area measurement; (2) transcervical longitudinal diameter measurement according to the NASCET and ECST methods; and (3) commonly used hemodynamic criteria (Tables 15.2, 15.3, and 15.4).

Tests of accuracy were determined whenever indicated, and in general, the correspondence between the NASCET (American) and ECST (European) levels of stenosis was adapted from Nicolaides et al. [19].

Statistical analysis was based in Stata software. The Pearson's Correlation Coefficient was used to compare cross-sectional areas with longitudinal measurements. The statistical significance was determined with Qui-Square and Student's test and a p value <0.05 was considered significant. Transcervical area measurement was compared with hemodynamic criteria using the Qui-Square test.

The study included 214 carotid bifurcation plaques prospectively analyzed in 139 patients (105 male and 34 female) with a mean age of 68 (41–87) years. All these patients underwent a careful transcervical CFDS with quantification of stenosis according to morphologic (longitudinal diameter NASCET, longitudinal diameter ECST, and cross-sectional area) and hemodynamic criteria.

From the global population of the study, a group of 48 lesions obtained in 44 patients (mean age 68, 23 male) that were submitted to CEA was selected for IO CFDS quantification of stenosis in order to validate the transcervical area reduction (by comparison with the gold standard IO CFDS).

The results of the study were as follows:

(a) *Comparison of IO CFDS cross-sectional area measurement with other parameters for stenosis quantification in 48 carotid lesions.*

– *Comparison of IO CFDS cross-sectional area measurement with transcervical cross-sectional area measurement.*

The comparison between both methods was carried out on those 48 lesions from patients submitted to surgery. In this group the mean degree of stenosis was 82 % (60–95 %) in the transcervical evaluation and 84 % (63–95 %) in the intra-operative assessment (Table 15.2).

The correlation coefficient was 0.86 ($r = 0.86$) and the overall concordance was highly significant ($p < 0.01$) (Fig. 15.5).

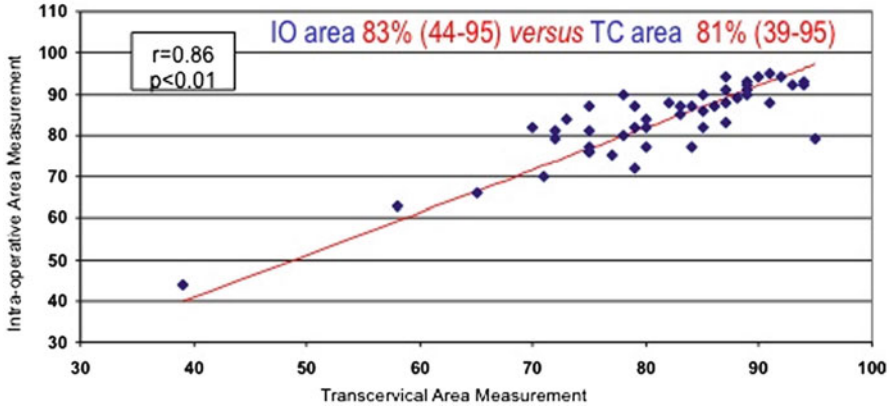

Fig. 15.5 Agreement between the quantification by IO CFDS area measurement and transcervical area measurement in the same lesions

This suggests that transcervical cross-sectional area measurement is comparable to intra-operative measurements and it was subsequently used to compare the other established methods for carotid stenosis quantification.

– *Comparison of IO CFDS cross-sectional area measurement with transcervical longitudinal diameter measurement (ECST and NASCET).*

According to the longitudinal linear quantification by the ECST method, the mean degree of stenosis was 78 % (50–95 %) and a correlation coefficient of 0.70 ($p = 0.004$) was observed in the comparison of IO area measurement.

According to the longitudinal linear quantification by the NASCET method, the mean degree of stenosis in was 55 % (−16 to 81 %) and there was no correlation ($r = 0.45$, $p =$ NS) with IO area measurement.

– *Comparison of IO CFDS cross-sectional area measurement with hemodyna- mic criteria.*

We tested three commonly used hemodynamic criteria:

Criteria A: Introduced by Strandness [14] permits the definition of the cutoffs 50 % and 80 % and were validated against angiography using the European method (Table 15.2).
Criteria B: Validated against the European method to measure stenosis on angiography and aims to identify the cutoffs 50 %, 70 %, and 85 % (Table 15.3).
Criteria C: Based on a quotient between end-diastolic velocities in ICA and CCA and was validated in angiographies measured by the American (NASCET) method allowing the identification of the cutoffs 50 %N (75 %E) and 80 %N (Table 15.4).

The comparison between IO area measurement with the hemodynamic criteria A revealed an overall correlation of 0.63 ($p = 0.013$) with sensitivity of 93.8 %, specificity of 40.6 % and accuracy of 58.3 % in the identification of >70 % obstruction.

The testing of criteria B was associated with an overall correlation of 0.62 ($p = 0.004$) with sensitivity of 93 %, specificity of 20 %, and accuracy of 85.4 % for the identification of the 70 % threshold of stenosis.

Finally, the criteria C had an overall correlation of 0.64 ($p = 0.0002$) with sensitivity of 69 %, specificity of 33.3 %, and accuracy of 64.6 % in the discrimination of the 80 % stenosis cutoff.

The results showed a good correlation between intra-operative area measurements and transcervical cross-sectional area quantification. In the further analysis this later criteria was used as the gold standard and was compared with the other established methods for carotid stenosis quantification.

(b) *Comparison of transcervical cross-sectional area measurement with transcervical longitudinal diameter measurement (NASCET and ECST).*

These comparisons were made in the overall population of the study ($n = 214$ plaques).

The mean degree of stenosis by transcervical cross-sectional area measurement was 70 % (20–99 %).

The mean degree of stenosis by transcervical longitudinal diameter measurement according to the NASCET method was 45 % (−45 to 90 %) (Table 15.5). This means that the correlations between both methods are weak with a correlation index of 0.09 ($r = 0.09$, $p = 0.99$) (Fig. 15.6).

These results confirm an underestimation of the degree of stenosis by the NASCET method when compared to the area measurement.

The mean degree of stenosis by transcervical longitudinal diameter measurement according to the ECST method was 68 % (20–93 %) (Table 15.5). The correlation between this method and area assessment was strong ($r = 0.75$, $p < 0.01$) (Fig. 15.7).

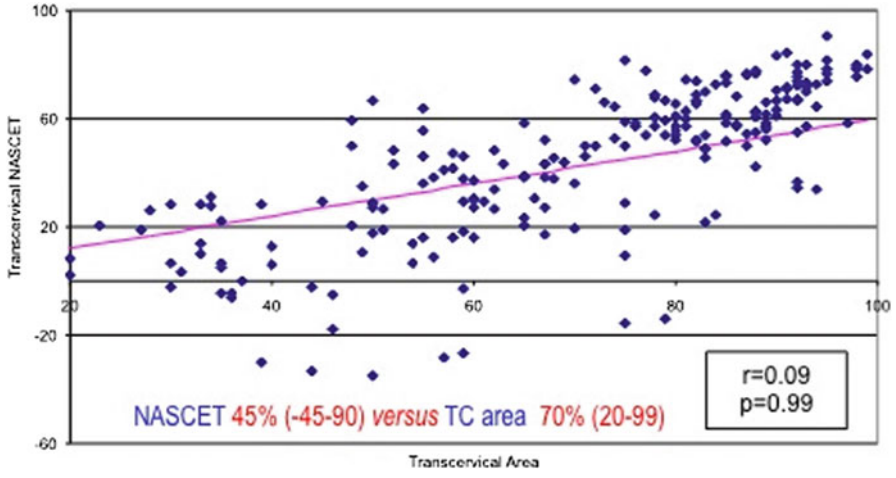

Fig. 15.6 Agreement between transcervical area measurement and transcervical linear diameter measurement according to the NASCET method

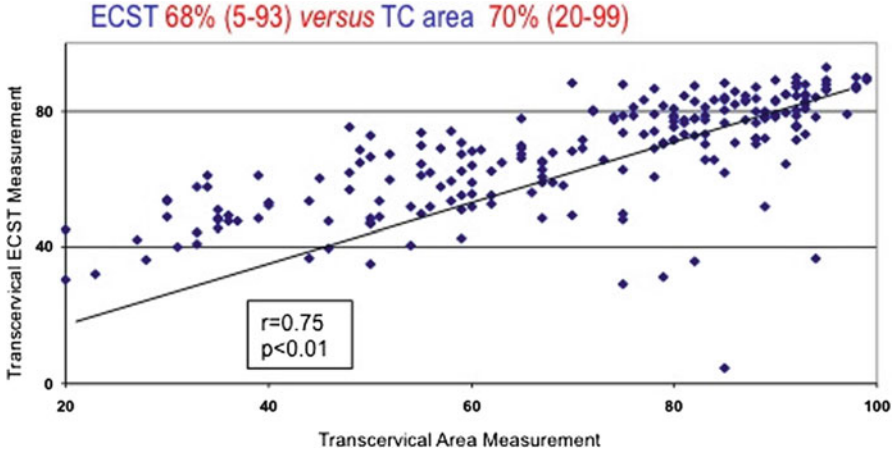

Fig. 15.7 Agreement between transcervical area measurement and transcervical linear diameter measurement according to the ECST method

Table 15.5 Comparison of the CFDS morphologic criteria for quantification of carotid stenosis

	Mean stenosis (min–max) (SD)	Correlation
• Area IO versus Area TC	84 % (63–95) (9.78) versus 82 % (60–95) (10–16)	$r = 0.86$, $p < 0.01$
• Area TC versus NASCET	70 % (20–99) (19.99) versus 45 % (−45 to 90) (31.98)	$r = 0.09$, $p = 0.99$
• Area TC versus ECST	70 % (20–99) (19.99) versus 68 % (20–93) (18.65)	$r = 0.75$, $p < 0.01$

Area IO, intra-operative area measurement; Area TC, transcervical area measurement; NASCET, linear measurement according to the NASCET method; ECST, linear measurement according to the ECST method

The results showed a good correlation between area measurement and the longitudinal method used in the European trial and an extrapolation of the cutoffs in clinical decisions is acceptable. However, no correlation was found with the longitudinal NASCET method, confirming that area quantification is not adequate to manage patients according to the American thresholds of stenosis.

(c) *Comparison between transcervical cross-sectional area measurement and hemodynamic criteria*.

We tested three hemodynamic criteria, commonly used in clinical practice, which were compared with the cross-sectional area measurement.

– *Hemodynamic criteria A (University of Washington)*.

The comparison of the criteria A with CFDS area measurement did not show overall concordance for all the intervals of stenosis ($p < 0.01$). However, for the identification of >50 %E stenosis the diagnostic parameters were as follows: sensitivity—80.3 %, specificity—97.1 %, PPV—99.3 %, NPV—49.3 %, and overall accuracy—83.1 % (Table 15.6).

Considering the cutoff of stenosis >80 %E (or >60 %N) the sensitivity was 65.6 %, the specificity

Table 15.6 Diagnostic accuracy of hemodynamic criteria

			Area measurement				
	ECST (%)	NASCET (%)	SENS	SPEC	PPV	NPV	ACC
• Criteria A	>50	–	80.3	97.1	99.3	49.3	83.1
	>80	>60	65.6	97.5	95.3	78.5	83.6
• Criteria B	>50	–	82.6	94.3	98.7	51.6	84.5
	>70	–	95	88.2	91.2	93.2	92.0
	>85	>70	85.3	92.1	81.3	94	90.1
• Criteria C	>50	–	83.6	85.7	96.7	50.9	84.0
	>75	>50	67	92.5	89.9	73.9	81.0

was 97.5 %, the PPV was 95.3 %, the NPV was 78.5 %, and the accuracy was 83.6 % (Table 15.6).

– *Hemodynamic criteria B* [17, 26].

The results showed that there was any overall agreement between the hemodynamic criteria B and the area measurement ($p < 0.01$).

The diagnostic parameters to identify stenosis >50 %E were sensitivity—82.6 %, specificity—94.3 %, PPV—98.7 %, NPV—51.6 %, and overall accuracy—84.5 %; for stenosis >70 %E were sensitivity—95 %, specificity—88.2 %, PPV—91.2 %, NPV—93.2 %, and overall accuracy—92 %; and for stenosis >85 %E were sensitivity—85.3 %, specificity—92.1 %, PPV—81.3 %, NPV—94 %, and overall accuracy—90.1 % (Table 15.6).

– *Hemodynamic criteria C* [27]

There was general concordance between criteria C and transcervical area measurement to discriminate the cutoff 75 %E (p = NS).

The results were as follows: the diagnostic parameters to identify stenosis >75 %E (>50 %N) were (Table 15.6): sensitivity—87.6 %, specificity—86 %, PPV—87.6 %, NPV—86 %, and overall accuracy—86.9 %; for stenosis >90 %E (or >80 %N) the sensitivity was 75 %, the specificity was 84.2 %, the PPV was 48.2.6 %, the NPV was 94.3 %, and the overall accuracy was 82.2 %.

In *conclusion*, for the identification of the cutoff 70 %E and 75 %E to 50 %N the criteria B was associated with high sensitivity (95 %) but less specificity (88.2 %). This criteria presented also high global accuracy (90.1 %) to identify stenosis >85 %E (>70 %N) with sensitivity of 85.3 % and specificity of 92.1 %.

The discrimination of stenosis >80 %E (60 %N) was better accomplished by the criteria A, with high specificity (97.5 %) but less sensitivity (65.6 %).

7 Conclusion

The present study aimed to define a new approach to the quantification of carotid stenosis with CFDS. Advantages of area measurements obtained by transcervical cross-sectional area method were validated against the direct ultrasonographic evaluation of the carotid arteries during operations and before endarterectomy, which we considered closer to the physiologic reality. This method allows a direct view and high image quality (high definition) of the lesion, in vivo and in physiological conditions, with the possibility of assessing the morphology of the lumen.

This technique then was used to compare and validate the transcervical measurement in area that is adequate for systematic application. Between these two methods we observed a good correlation ($r = 0.86$, $p < 0.01$), which suggests that the transcervical area measurement reflects a reliable assessment of the two-dimensional morphological reality of the plaque and stenosis.

Subsequently, the study compared the transcervical area quantification with linear longitudinal measurements by the NASCET and ECST methods and also with hemodynamic parameters frequently used in practice.

This analysis is important in order to understand how appropriate is the extrapolation of the methodology used in multicenter trials (European and American methods) for measurements in area.

In fact, area measurements showed a discrepancy with the NASCET method ($r = 0.09$), which undergrads the stenosis in relation to area (average 45 % versus 70 %). It also confirms the well-known paradox that makes possible "negative" stenosis (luminal diameter of stenosis greater than the minimum diameter of the distal internal carotid) when obstructions are moderate.

The ECST method of measuring stenosis presents a good correlation with the quantification in area ($r = 0.75$, $p < 0.01$) and we can conclude that area quantification can "match", in general, the concept of diameter quantification used in ECST. However, it should be noted that this global "equivalence" only makes sense when the lumen is fairly regular and uniform; when it is irregular and asymmetrical the measurement in diameter can be inaccurate.

Nevertheless, the results of the study show some discrepancy with the theoretical tables of conversion what can be explained by the construction of those ratios in in vitro circular tubular models, away from the biological reality, where only rarely the carotid bifurcation stenosis is regular and produces uniform reduction of arterial lumen.

The next stage of the study consisted in assessing various hemodynamic parameters in its relationship with the area measurement. Indeed, these were reexamined in multiple studies to provide a higher diagnostic accuracy in the identification of thresholds of stenosis resulting from multicentre trials, although, as stated above, there has not been consensus on appropriate criteria.

The study compared the diagnostic accuracy of some of those criteria with area measurement looking for its performance in the identification of clinically relevant thresholds which are, for symptomatic disease, 50 %N (75 %E), 70 %N (85 %E), and 70 %E and for asymptomatic disease 60 %N (80 %E). As we observed an overall agreement between area and diameter by the European method, the most relevant cutoffs are 70–75 %E in symptomatic patients and 80 %E in asymptomatic disease.

As regards the threshold 70–75 %E, criteria B and C have the best overall accuracy and criteria B showed greater sensitivity, suggesting that it will be adequate for screening. However, their use in therapeutic selection implies greater specificity than the one that was observed meaning that the hemodynamic evaluation should always be combined with other hemodynamic or morphological parameters.

Concerning the threshold 80–85 %E the criterion A was the more specific while the criterion B was more sensitive.

Thus, the quantification of carotid artery stenosis by CFDS should include a careful combination of measurement in cross-sectional area and at least one of the hemodynamic methods mentioned above, which should be chosen according to the purpose of the examination (screening or therapeutical decision).

References

1. North American Symptomatic Carotid Endarterectomy Trial Collaborators (1991) Beneficial effect of carotid endarterectomy in symptomatic patients with high grade carotid stenosis. N Engl J Med 325:445–463
2. European Carotid Surgery Trialists' Collaborative Group (1991) MRC European Carotid Surgery Trial: interim results for symptomatic patients with severe (70-99 %) and with mild (0-29 %) stenosis. Lancet 337:1235–1243
3. Executive Committee for the Asymptomatic Carotid Atherosclerosis Study (1995) Endarterectomy for asymptomatic carotid artery stenosis. JAMA 273:1421–1428
4. Halliday A, Mansfield A, Marro J, Peto C, Peto R, Potter J, Thomas D, MRC Asymptomatic Carotid Surgery Trial (ACST) Collaborative Group (2004) Prevention of disabling and fatal strokes by successful carotid endarterectomy in patients without recent neurological symptoms: randomised controlled trial. Lancet 363:1491–1502
5. Barnett HJ, Taylor DW, Eliasziw M, Fox AJ, Ferguson GG, Haynes RB, Rankin RN, Clagett GP, Hachinski VC, Sackett DL, Thorpe KE, Meldrum HE (1998) Benefit of carotid endarterectomy in patients with symptomatic moderate or severe stenosis. North American Symptomatic Carotid Endarterectomy Trial Collaborators. N Engl J Med 339:1415–1425
6. Rothwell PM, Gibson R, Warlow CP (2000) Interrelation between plaque surface morphology and degree of stenosis on carotid angiograms and the risk of ischemic stroke in patients with symptomatic carotid stenosis. On behalf of the European Carotid Surgery Trialists' Collaborative Group. Stroke 31:615–621
7. Walker J, Naylor AR (2006) Ultrasound based measurement of 'carotid stenosis >70 %': an audit of UK practice. Eur J Vasc Endovasc Surg 31:487–490
8. Cuffe RL, Rothwell PM (2006) Effect of nonoptimal imaging on the relationship between the measured degree of symptomatic carotid stenosis and risk of ischemic stroke. Stroke 37: 1785–1791
9. Bucek RA, Puchner S, Haumer M et al (2006) Grading of internal carotid artery stenosis: comparative analysis of different flow velocity criteria and multidetector computed tomographic angiography. J Endovasc Ther 13:182–189
10. Bucek RA, Puchner S, Haumer M et al (2006) Grading of internal carotid artery stenosis: can CTA overcome the confusion? J Endovasc Ther 13:443–450
11. Puchner S, Popovic M, Wolf F et al (2009) Multidetector CTA in the quantification of internal carotid artery stenosis: value of different reformation techniques and axial source images compared with selective carotid arteriography. J Endovasc Ther 16:336–342
12. Grant EG, Benson CB, Moneta GL et al (2003) Carotid artery stenosis: gray-scale and Doppler US diagnosis – Society of Radiologists in Ultrasound Consensus Conference. Radiology 229(2):340–346
13. Alexandrov AV, Bladin CF, Maggisano R, Norris JW (1993) Measuring carotid stenosis. Time for a reappraisal. Stroke 24:1292–1296
14. Strandness JD (1993) Chapter 6: Extracranial arterial disease. In: Duplex scan in vascular disorders, 2nd edn. Raven, New York, pp 113–157
15. Grant EG, Duerinckx AJ, El Saden S et al (1999) Doppler sonographic parameters for detection of carotid stenosis: is there an optimum method for their selection? AJR Am J Roentgenol 172:1123–1129
16. Fujitani RM, Mills JL, Wang LM, Taylor SM (1992) The effect of unilateral internal carotid arterial occlusion upon contralateral duplex study: criteria for accurate interpretation. J Vasc Surg 16:459–467
17. Zweibel WJ (1987) Spectrum analysis in carotid sonography. Ultrasound Med Biol 13:625–636
18. AbuRahma AF, Richmond BK, Robinson PA, Khan S, Pollack JA, Alberts S (1995) Effect of contralateral severe stenosis or carotid occlusion on duplex criteria of ipsilateral stenoses: comparative study of various duplex parameters. J Vasc Surg 22:751–761
19. Nicolaides AN, Shifrin EG, Bradbury A, Dhanjil S, Griffin M, Belcaro G, Williams M (1996) Angiographic and duplex grading of internal carotid stenosis: can we overcome the confusion? J Endovasc Surg 3:158–165
20. Porsche C, Walker L, Mendelow D, Birchall D (2001) Evaluation of cross-sectional luminal morphology in carotid atherosclerotic disease by use of spiral CT angiography. Stroke 32:2511–2515
21. Troyer A, Saloner D, Pan XM, Velez P, Rapp JH (2002) Major carotid plaque surface irregularities correlate with neurologic symptoms. J Vasc Surg 35:741–747
22. Seabra JC, Pedro LM, Fernandes e Fernandes J, Sanches JM (2009) A 3-D ultrasound-based framework to characterize the echo morphology of carotid plaques. IEEE Trans Biomed Eng 56:1442–1453
23. Jmor S, El Atrozy T, Griffin M, Tegos T, Dhanjil S, Nicolaides A (1999) Grading internal carotid artery stenosis using B-mode ultrasound (in vivo study). Eur J Vasc Endovasc Surg 18:315–322
24. Pan XM, Saloner D, Reilly LM, Bowersox JC, Murray SP, Anderson CM, Gooding GA, Rapp JH (1995) Assessment of carotid artery stenosis by ultrasonography, conventional angiography, and magnetic resonance angiography: correlation with ex vivo measurement of plaque stenosis. J Vasc Surg 21:82–88

25. Pedro LM (2003) A window to atherosclerosis: high definition ultrasonography in the study of the arterial wall. University of Lisbon, Portugal
26. Mittl RL Jr, Broderick M, Carpenter JP, Goldberg HI, Listerud J, Mishkin MM, Berkowitz HD, Atlas SW (1994) Blinded-reader comparison of magnetic resonance angiography and duplex ultrasonography for carotid artery bifurcation stenosis. Stroke 25:4–10
27. Knox RA, Greene FM, Beach K, Phillips DJ, Chikos PM, Strandness DE Jr (1982) Computer based classification of carotid arterial disease: a prospective assessment. Stroke 13:589–594

Histologic and Biochemical Composition of Carotid Plaque and Its Impact on Ultrasonographic Appearance

16

Isabel Gonçalves

1 Pathophysiology of Atherosclerosis

The pathophysiology of atherosclerosis has been described long time ago in a brief manner. Aschoff [1] recognized two components of the disease: lipid deposition, called *atherosis* or *atheromatosis*, and fibrosis or *sclerosis*. The fibrolipid state was then designated *atherosclerosis*. Nowadays atherosclerosis depicts a whole pathology and not only one single stage of the disease. Some authors still use three simple concepts: fatty streak, fibrous plaques, and complicated plaques. Fatty streaks are accumulations of foam cells, some T cells, and extracellular cholesterol, in the intima, covered by an intact endothelium. Fibrous plaques are those with an enlarged intima, where smooth muscle cells (SMCs) have accumulated surrounded by extracellular matrix proteins, constituting a fibrous cap that covers a core region. The core is composed mostly of lipids, cell debris, extracellular matrix proteins, and macrophages. Some T, very few B cells, and masts cells can also be found in the plaques. These plaques are often eccentric. In an attempt to preserve the dimensions of the lumen, remodeling of the media occurs with an enlargement of the vessel outwards. As a result the artery may look normal when assessed by angiography. The concept of complicated lesion refers to those plaques that, in addition to the previously named components, contain signs of hemorrhage or thrombus. Complicated lesions usually develop after rupture of a fibrous plaque. Plaques can also present surface erosions, fissures, or ulcerations. Lesions can also be calcified, probably in advanced stages mostly.

I. Gonçalves, M.D (✉)
Department of Cardiology, Skåne University Hospital, Lund University, Malmö, Sweden
e-mail: Isabel.Goncalves@med.lu.se

2 Formation of the Atherosclerotic Plaque

LDL can enter the arterial intima through an intact endothelium, particularly at sites of increased permeability, which exist at branches of the arterial tree. As the media can be seen as a permeability barrier, LDL stays relatively stagnant in the intima. Additionally, it is trapped in the extracellular matrix [2]. LDL is modified in the intima, by aggregation, oxidation, and degradation of its components. Oxidatively modified peptide sequences can function as haptens and become targets for the immune system [3, 4]. Aggregates of oxidized LDL (ox-LDL) can activate complement, which generates chemotactic signals [5]. At the same time, modified lipids activate endothelial and smooth muscle cells. Circulating cells, such as the monocytes, adhere to the vessel wall and migrate from the endothelial surface through intercellular clefts into the subendothelial space. These activated cells produce a cascade of cytokines that attract even more circulating leukocytes to the inflammatory site in the vessel wall. Hemodynamic stress can also induce expression of intercellular adhesion molecule (ICAM)-1 [6].

Monocytes differentiate into macrophages in the vessel wall, which upregulate scavenger receptors and internalize ox-LDL, in the intima [7]. The cholesteryl esters present in ox-LDL are hydrolyzed and later free cholesterol can be re-esterified, forming a pool of intracellular droplets of cholesteryl esters. ox-LDL contains platelet-activating factor (PAF)-like lipids that are highly inflammatory and activate not only macrophages, but also endothelial cells [8, 9].

When the macrophages become lipid laden, they are called foam cells. Macrophages act as antigen-presenting cells, by processing the apolipoproteins into peptides, and present them bound to major histocompatibility complex (MHC) class II for T cells. The antigen–MHC complexes are recognized by CD4+ T cells, which are the T cell subtype that predominates in plaques [10]. T cells can be activated or reactivated if they had been primed by that

L. Saba et al. (eds.), *Multi-Modality Atherosclerosis Imaging and Diagnosis*,
DOI 10.1007/978-1-4614-7425-8_16,

antigen before. A significant proportion of T cells from human plaques recognize ox-LDL [11]. This activation leads to a chain reaction of intracellular signaling, which leads to DNA synthesis, cytokine secretion, and cytotoxicity.

CD8+ T cells are present in plaques in varying proportions. They have cytotoxic activity and are activated by cells that express peptide fragments in the context of MHC I. They can cause apoptosis in lesions and they secrete cytokines. B and NK (natural killer) cells are found in advanced lesions. B cell infiltrates can be prominent in the adventitia or periadventitial connective tissue [12]. In hypercholesterolemic animals, they become quite abundant and clones of immunoglobulin (Ig)-producing cells can be found [13]. Plasma cells can also be present in lesions and are likely to locally produce IgG. IgG might additionally enter the lesions by filtration [13]. Mast cells are less frequent, but produce proteases and accumulate at rupture sites [14]. The dendritic cells, the only ones to activate naïve T cells, have high migratory capacity and "patrol" the arterial wall. Only a few are present in plaques. They engulf antigens by endocytosis and take them to lymph nodes, to present them to T cells, inducing adaptive immunity. In the plaques they can also present lipid antigens on CD1 receptors to the few CD3+4–8- or γδ T cell subtypes, for instance [15, 16].

Complex cascades of signals are involved in plaque formation. Cytokines stimulate further cytokine production. In endothelial cells, they promote further expression of adhesion molecules and procoagulant activity. In macrophages, they activate proteases, endocytosis, and nitric oxide (NO), and in SMC they induce NO production and inhibition of collagen expression.

3 Plaque Destabilization

The progressive reduction of the lumen can lead to hypoperfusion symptoms, but the majority of ischemic symptoms arise due to thrombus formation or embolization. In 30 % of the cases, surface damage is simply endothelial erosion, while in the 70 % small fissures occur of variable depth in the plaque, leading to thrombus formation.

Another mechanism that has been considered as associated with plaque destabilization is intraplaque hemorrhage [17, 18]. Initially when finding hemorrhage in plaques, it was considered that the blood came in after plaque rupture. However, there is also the possibility that the plaques become more and more vascularized by vasa vasorum and other friable neovessels [19]. These vessels may leak or rupture and cause intraplaque hemorrhage, which can function further as an inflammatory stimulus [20–22]. This sudden increase of volume in the plaque may contribute to its disruption. However, it can be difficult to imagine such a rupture against the much higher pulse pressure [23].

Macrophages progressively infiltrate the plaque, accumulating in the shoulder regions and invading the fibrous cap. They produce matrix metalloproteinases (MMPs), which degrade matrix molecules, like collagen, elastin, and proteoglycans. The expression of collagen synthesis can be inhibited by cytokines, as IFN-γ and TNF-α, which may inhibit SMC proliferation and induce apoptosis. Taken together, these mechanisms decrease the tensile strength of the fibrous cap.

Extrinsic factors that might "trigger" rupture have been described [23]. High blood velocity, possibly shearing the endothelium away, [24] cyclic plaque deformations both longitudinally [25] and circumferentially, [26, 27] as well as changes in vascular tone [28] can precipitate disruption in vulnerable plaques.

When the plaque ruptures, blood elements reach the subendothelial components. Vasospasm occurs frequently. The platelets are immediately activated, adhere, and aggregate, due to the binding of glycoproteins IIb/IIIa to fibrinogen and glycoprotein Ib to von Willebrand factor. The coagulation cascade is initiated after tissue factor is exposed. Tissue factor is expressed in the normal vessel wall and even more abundantly in the atherosclerotic vessel, particularly in plaques associated with symptoms [29, 30]. Finally the fibrin clot is formed, stabilizing the platelet thrombus. In parallel the fibrinolytic system is activated, to prevent complete obstruction. Tissue-type and urokinase plasminogen activators depend on the milieu of mediators of inflammation and innate immunity, such as IL-1 and TNF-α [31]. They are produced by endothelial cells and lead to the formation of plasmin, a serine protease that can degrade cross-linked fibrin, fibrinogen, and factors V and VIII. Plasmin levels are tightly regulated by plasminogen activator inhibitor-1, also expressed by endothelial cells, and α2-plasmin inhibitor. Therefore, in conclusion, one should keep in mind that plaque rupture and thrombus formation may be associated both with characteristic of the plaque and with thrombogenicity of the blood elements.

4 Plaque Types

In the 1990s, a detailed classification in eight types of plaques [32, 33] was proposed, mostly based on coronary autopsies. It indicates in part the sequence of the lesion progression. Type I lesion is characterized by small lipids depositions and some scattered foam cells. Type II lesions are accumulations of more foam cells and correspond to the previously mentioned fatty streaks. In type III lesions, the extracellular lipid droplets become larger. In type IV lesions, a visible, confluent core has developed. In addition, capillaries can be present in these lesions. This type of lesion has also been called as atheroma. Type V lesions are defined as those in which prominent new fibrous tissue has formed.

If the new tissue is part of a lesion with an exuberant lipid core, it can be referred as Va, whereas if the lipid in general is minimal and the fibrosis predominates as Vc or VIII. If parts of the lesion are calcified, it can be referred as Vb or sometimes as VII. Type V lesions are usually too large to compensate by outwards remodeling, resulting in various degrees of narrowing of the lumen. In this classification the complicated lesion are designated as type VI, meaning type IV or V lesions with disruption of the surface (VIa), hematoma or hemorrhage (VIb), or thrombosis (VIc). Morbidity and mortality from atherosclerosis are largely due to type VI lesions. Often lesions type I and II occur in infants and children, type III around puberty, and after the third decade of life, lesions type V and VI begin to appear.

The previous classification created by pathologists based on histological aspects of the plaques was attractive by its simplicity, but has raised some discussion. According to this classification thrombosed lesions would be included in type VI, but it has been noted that thrombi can be formed at any stage of the disease, as it can result from endothelial dysfunction even in less complex lesions.

In the 1980s, Falk [34] and Davies and Thomas [35] described plaque disruption related to acute coronary syndromes. Since then it has become clear that culprit coronary lesions correspond to ruptured plaques in approximately 70 % of the cases and to non-ruptured plaques in 30 %. These non-ruptured plaques may present, e.g., erosions or calcified nodules. From the 70 % of plaques that are ruptured, 50 % are nonstenotic. In the coronaries, myocardial infarction evolves most frequently from plaques that are only mildly to moderately obstructive before infarction [23]. This means that angiography only detects around 20 % of all culprit lesions. The risk of plaque rupture correlates only weakly with the degree of stenosis. So, other factors than simply the degree of stenosis are relevant for vulnerability.

In 2003, in a review series in Circulation, some of the leading scientists on atherosclerotic plaques [36, 37] collected the most important aspects associated with the "vulnerable" patients and plaques. They suggested major and minor criteria for defining the vulnerable plaque, mostly based on histology, as summarized in Table 16.1. Some of these features suspected to be present in vulnerable plaques still require validation in longitudinal, prospective studies, but they raise interesting perspectives.

Nomenclature has motivated many discussions and meetings. The use of terms like the unstable, high-risk, thrombosis-prone, symptomatic, disrupted, or vulnerable plaque has been somewhat confusing. The language can be misleading as plaques are not symptomatic as the patients are the ones who may have symptoms, but that term is supposed to be a simplification of "plaque associated with symptoms". Unstable is not a very specific term, while the prospective definitions, such as vulnerable/high-risk/thrombosis-prone, seem more adequate. Independently of the nomenclature, one should aim at the identification of the plaques that have a high likelihood of causing clinical events. To this end, many different methods have been used and are still being developed and improved, from histological and biochemical methods to ultrasonographic and magnetic resonance imaging and others, such as elastography and thermography [50].

Table 16.1 Summary of possible plaque structure characteristics conditioning vulnerability, assessed by histology and ultrasound [38–49]

Histology	Carotid ultrasound
Major	Echolucency (low gray-scale median)
Thickness of the fibrous cap	Thickness of the echogenic cap
Large inflammatory cells infiltrate	Surface irregularity/ulceration
Superficial erosion or fissure	Proximity of the echolucent region to the lumen
Presence of thrombus	Severe stenosis
Size of the lipid core	Lesion motion
Severe stenosis	Others?
Minor	
Superficial calcified nodule	
Intraplaque hemorrhage	
Endothelial dysfunction	
Outward remodeling	
Others	
Rich in proteoglycans	
Others?	

5 Ultrasound

Nowadays, the indications for carotid endarterectomy are based on the presence of symptoms and on the degree of stenosis. However, atherosclerotic plaques causing low grades of stenosis have been associated with clinical events, while others causing high degrees of stenosis may remain asymptomatic [51, 52]. Because of this, the degree of luminal narrowing may not be the optimal criterion for defining clinical risk and indications for treatment. As a result, some patients may undergo unnecessary surgery. Improved techniques are, therefore, needed to enable reliable identification of high-risk plaques that lead to cerebrovascular events. In the last decade, ultrasound has been further developed using compound imaging, [53, 54] and 3D reconstructions [55, 56].

Carotid ultrasonography has known limitations in discriminating subtotal from total occlusion, in assessing plaques that have an acoustic shadow, and in patients with short neck, high carotid bifurcation, or severe arterial kinking. Operator dependency has also been a limitation that has been discussed widely, but is beyond the scope of this chapter.

Newer generations of ultrasound equipment have appeared, as attempts to overcome some of the limitations. An example is the high-definition ultrasonography. It has higher spatial, contrast, and temporal resolution, allowing also direct digital image recording. The latest strategy in our group is to use open platform equipments and design homemade algorithms to characterize plaque morphology.

Several subjective classifications for the ultrasonographic aspect of plaques have been proposed: Reilly et al. [57] divided plaques into homogeneous and heterogeneous; Johnson et al. [58] into calcified, dense, or soft; Gray-Weale et al. [59] into echolucent, predominantly echolucent, and predominantly echogenic and echogenic ones; Langsfeld et al. [60] also graded as to the ratio of echolucency to echogenicity, with type 1 being most echolucent and type 4 being most echogenic, and the normal-appearing artery was classified as type 5; for Geroulakos et al. [61] the type 5 consisted of plaques that could not be classified owing to acoustic shadows; the European Carotid Plaque Study Group [62] divided plaques into echolucent, intermediate, and echorich. In summary these studies suggested that the soft, echolucent, and heterogeneous plaques were those associated with symptoms. In Geroulakos' study the association of symptoms and echolucency was only true for stenosis >70 %. Others could not find associations between the ultrasonographic aspect and neurologic events [63, 64]. Many of these studies were based on small cohorts of patients and the ultrasonographic evaluation was done subjectively.

Actually, the most important limitation of ultrasonography is the intra- and inter-observer variability. Standardization methods to process plaque images have been found to overcome differences in the evaluation of plaque echogenicity between the different equipments and observers. This way, the group from the Irvine Laboratory at the St. Mary's Hospital, London [65, 66], created a method, based on the gray-scale values of pixels in a scale of gray intensities (0 darkest and 255 brightest). They used the gray-scale median (GSM), as a score of global echogenicity. The reference values were the blood as 0 (the darkest structure in the image) and the adventitia as 190 (the brightest structure in the image). The whole plaque image outlined would be processed by linear scaling, compressing the scale. Making the blood and adventitia of all the plaques have the same values allowed the comparison of different plaques, assessed with different equipments and setups and by different observers. Intra- and inter-observer variabilities improved considerably [65].

Plaques with low GSM have been associated with higher incidence of cerebral infarction [67, 68]. These authors found a cutoff value of 32 for GSM that could discriminate best between the plaques associated with symptoms or not. The same cutoff was identified by our group [69]. Other studies have found other cutsoff values of GSM,namely 40, using the same method [66], or 50, without using the linear scaling [70].

Gronholdt et al. [38] showed that echolucent plaques causing stenosis >50 % are associated with increased risk of stroke in symptomatic but not asymptomatic individuals. Using GSM = 74 as a cutoff point, echolucency was an age-independent predictor of ischemic stroke in symptomatic patients. In symptomatic patients, relative risk of ipsilateral ischemic stroke for echolucent versus echorich plaques was 3.1. Based on the degree of stenosis, when comparing 80–99 % versus 50–79 % stenosis, the relative risk was 1.4. This association between echolucency and high risk for ipsilateral symptoms has also been verified on other studies, though the influence of the degree of stenosis is not widely accepted [71, 72]. Whereas some suggested hypertension and progressive lesions to be important additional determinants of risk [73], others proposed that echolucent plaques were associated with increased risk of neurological events, even independently of degree of stenosis and cardiovascular risk factors [74].

Some other studies evaluated heterogeneity of the plaque image and found that heterogeneous and/or echolucent plaques are associated with higher risk of stroke [60, 75–79]. The ability of ultrasonography to study other characteristics that could be associated with the presence of symptoms has been intensively studied. The identification of ulceration by ultrasonography in different studies showed large variation. Rubin et al. [39] using ultrasonography detected 93 % of the ulcerated lesion, whereas Comerota et al. [80] argued that the possibility of detecting ulceration varied with different degrees of stenosis, being particularly difficult in high-grade stenoses. Bluth et al. [81] reported that merely sonography for evaluating the surface of the plaque to determine if it was smooth or irregular could not be used as a successful means to identify which patients were at risk for ulceration. O'Leary et al. [82] came to a similar conclusion. Bassiouny et al. [83] found that the proximity of plaque necrotic core to the lumen is associated with clinical ischemic events. Our group [40] showed that in heterogeneous plaques, juxtaluminal location of the echolucent region was associated with increased risk. On the contrary, in homogenous plaques the absence of an echogenic cap and disruption of the plaque surface correlated with symptoms. In an attempt to determine the relative importance of the ultrasonographic structural characteristic of the plaques, besides GSM, an activity index was calculated. This activity index was associated with symptoms [84]. The parameters associated with the presence of ipsilateral symptoms were surface disruption, severe stenosis, and low GSM and, in heterogeneous plaques, the presence of a juxtaluminal echolucent area. Though all these results are interesting, large-scale studies on different ultrasonographic aspects that can reflect risk and on the natural history of the plaques are needed.

Although the association of echolucent plaques with higher neurological risk has become accepted, no ultrasonographic characteristics have been associated with a single type of symptom. The majority of the studies did not separate those end-points. One study, by Sabetai et al. [85], reported that plaques associated with amaurosis fugax are more hypoechoic and more stenotic than those associated with TIA or stroke or those without symptoms. In another study by Iannuzi et al. [86] TIA patients showed more hypoechoic carotid plaques with longitudinal motion. The association between plaque radial and longitudinal motion and neurological events was demonstrated by four-dimensional ultrasound examinations in another study [41].

In order to better understand the ultrasonographic appearance of plaques, histological analyses have been used in several studies. Wolverson et al. [87] compared echolucent and echogenic plaques in vitro, relatively to their composition. Aggregates of amorphous lipid residue appeared less echogenic than adjacent tissues and regions of dense fibrosis more echogenic. Densely calcified foci in plaques were highly echogenic and associated with acoustic shadowing. Gray Weale et al. [59] when creating the classification of ultrasound appearance in 1988 observed the plaques macroscopically and histologically. There was a significant relationship between plaques type 1 and 2 (the echolucent and predominantly echolucent) and the presence of either intraplaque hemorrhage or ulceration. Montauban van Swijndregt et al. [88] concluded in a first study that B-mode ultrasound and subsequent subjective categorization of atherosclerotic plaques cannot adequately determine the volume of fibrosis or lipids within the plaque. Later [89] they found that plaques associated with symptoms contained more fibrosis than lipids. Apart from agreeing that echolucent plaques were most common in symptomatic patients Kardoulas et al. [90] reported that the fibrous tissue was significantly greater in echogenic plaques. According to Lammie et al. [91] echolucent areas in the plaque corresponded histologically to necrosis or hemorrhage, and the thickness of the fibrous cap could be determined reliably with ultrasound. On the other hand a possible association between clinical events and the presence of hemorrhage in the plaques has not been consensual. Some supported that association [17, 18], while others did not [92, 93]. Similarly, the ability of ultrasound to detect plaques with hemorrhage is also not consensual. Actually in most ultrasound studies comparing with histology, the criteria to define plaque hemorrhage varied or no distinction was made between lipid and hemorrhage. They have often been called "soft tissue" [62]. Nevertheless, plaques with a high lipid and hemorrhage content as established histologically had low GSM, whereas those with a high fibrous content had a high GSM [94]. According to Gronholdt et al. echolucent carotid artery plaques were associated with elevated levels of acute phase reactants, [95] and circulating triglyceride-rich lipoproteins in the fasting or postprandial state [96]. Some years later, they reported that echolucency was associated with increased macrophage density and lipid content in the plaques [97]. Histologically, echogenic plaques contained more calcification and fibrous tissue than echolucent plaques. Intraplaque hemorrhage was directly related to lipid content and inversely related to amount of fibrous tissue in the plaque [98].

In many of the previous studies, the histological analysis was done only by semiquantitative or not quantitative techniques, using unspecific stainings and analyzing only parts of the plaques. Moreover, many of them only used the subjective classifications for the ultrasound images. Analyzing plaque components by other methods, such as biochemical methods in relation to echogenicity, has been done by our group, allowing the measurement of components in the whole plaque and not only on some sections. We used fast-performance liquid chromatography and high-performance thin-layer chromatography to measure matrix and lipid components in plaque homogenates [99]. Echolucent plaques contained less hydroxyapatite (the most prevalent calcium salt in plaques), more total elastin, and more intermediate-size elastin forms. There was no difference in collagen amount between echogenic and echolucent plaques, neither biochemically nor histologically. Cholesterol esters, unesterified cholesterol, and triglycerides were increased in plaques associated with symptoms, but no differences were detected between echolucent and echogenic plaques. Similar results were obtained by Oil Red O staining (for lipids) in symptomatic versus asymptomatic and in echolucent versus echogenic plaques. Our study was the first to study elastin and its fragments (known to be chemoattractant) in relation to echogenicity. Echogenicity seemed to be mainly determined by their elastin and calcium but not collagen or lipid content.

As inflammatory cells are so relevant in the atherosclerotic process, we also studied the cellularity in relation to echogenicity. Echolucency of carotid plaques correlates with plaque cellularity [100]. More recently it was found that annexin A1, a calcium and phospholipid-binding protein, known as endogenous modulator of inflammation, correlates with GSM in high-grade carotid stenosis [101]. This reinforces the idea of complex regulatory mechanisms of inflammation, which might be reflected in the ultrasound aspects of the plaques. Inflammatory cells secrete proteinases such as the metalloproteinases (MMP). Turu et al. [102] showed that hypoechogenic plaques had increased MMP activity and asymptomatic patients with plaque progression showed increase intraplaque MMP-8 levels.

Vascular calcification is a frequent process in the advanced lesions. Osteoprotegerin is one of the proteins involved in the regulation of bone metabolism and vascular calcification and high serum values of osteoprotegerin are

associated with cardiovascular disease in humans. Vik et al. [103] showed that patients with echogenic carotid plaques had lower levels of serum osteoprotegerin, supporting its role in arterial calcification.

Intraplaque neovascularization is a common characteristic of advanced lesions. Feinstein's group used contrast-enhanced ultrasound to visualize neovessels in the plaque and correlated that to the lesion severity and morphologic features of plaque instability [104]. An additional concept attempted by Owen et al. has been to measure the retention of nontargeted microbubbles using contrast-enhanced ultrasound to depict difference in plaques from asymptomatics or symptomatics [105].

The rate of remodeling of human plaque tissue has not been studied. We were the pioneers in measuring for the first time in humans the biological age of different components of advanced atherosclerotic plaques by analyzing tissue levels of ^{14}C. The turnover time of human plaque tissue is very long (20 years or more) [106]. This may explain why regression of atherosclerotic plaque size rarely is observed in cardiovascular intervention trials. Simultaneously it recalls the interest of early lesion monitoring for instance on the fatty streak level. At that early biological phase, a possible intima–media thickening will be seen that would correspond to small accumulation of lipids and inflammatory cells in the intima. Recently, inspired by the measurements of GSM performed in advanced lesions, Lind et al. started to measure the GSM on the intima–media complex. Considering the fact that echolucency may correspond to lipid accumulation it was easy to understand their results showing that low shear stress in the common carotid is associated with a thick intima–media and with an echolucent intima–media complex. Furthermore, they found that echolucent carotid intima–media complex was a predictor of all-cause mortality after age 75 years [107]. In another large study, they found that the GSM of the intima–media of the common carotid artery is closely related to the echogenicity in over carotid plaques [108].

6 Possible Future Trends

In the future one would like to overcome some of the current limitations of ultrasound, such as resolution, different tissue characterization, three-dimensional reconstruction, or maybe combining algorithms of different characteristics to be able to detect the plaques that are associated with higher risk for rupture and consequent symptoms. Targeted imaging could also be an approach, although there is no consensus on what is/are the best target/s yet. Some techniques like optical imaging have started to implement this targeting to image proteases [109]. There have been attempts on direct tissue characterization based on the integrated backscatter showing that the index in fatty/necrotic atheromatous sites was lower than that in fibrous or calcified sites and the same as that in intraplaque hemorrhagic sites [110].

Plaque morphology assessed by ultrasound will potentially give insights into the disease and why some patients have higher risk than others. One example of this type of study was published by Östling et al.,[111] showing that type 2 diabetics have more echolucent moderate plaques than nondiabetics. Plaque size and echogenicity are related to different cardiovascular risk factors in the elderly [112]. Further developments in ultrasound will definitely improve risk stratification.

A final important use of carotid plaque ultrasound is to monitor the effect of interventions, considering the possible effects on plaque composition that lay behind those interventions. Several studies have shown the favorable effect of statins on echogenicity [113]. More recently even other interventions have been studied such as the illustrative study showing the association of low-dose metoprolol CR/XL with increased plaque echogenicity [114].

References

1. Aschoff L (1930) Die arteriosklerose. Mediz Klinik (suppl 1):1–20
2. Nordestgaard BG (1996) The vascular endothelial barrier – selective retention of lipoproteins. Curr Opin Lipidol 7(5):269–273
3. Palinski W, Hörkkö S, Miller E, Steinbrecher UP, Powell HC, Curtiss LK et al (1996) Cloning of monoclonal autoantibodies to epitopes of oxidized lipoproteins from apolipoprotein E-deficient mice. demonstration of epitopes of oxidized low density lipoprotein in human plasma. J Clin Invest 98(3):800–814
4. Palinski W, Rosenfeld ME, Ylä-Herttuala S, Gurtner GC, Socher SS, Butler SW et al (1989) Low density lipoprotein undergoes modification in vivo. Proc Natl Acad Sci USA 86:1372–1376
5. Seifert PS, Hugo F, Hansson GK, Bhakdi S (1989) Prelesional complement activation in experimental atherosclerosis. Terminal C5b-9 complement deposition coincides with cholesterol accumulation in the aortic intima of hypercholesterolemic rabbits. Lab Invest 60(6):747–754
6. Walpola PL, Gotlieb AI, Cybulsky MI, Langille BL (1995) Expression of ICAM-1 and VCAM-1 and monocyte adherence in arteries exposed to altered shear stress. Arterioscler Thromb Vasc Biol 15(1):2–10
7. Brown MS, Goldstein JL (1983) Lipoprotein metabolism in the macrophage: implications for cholesterol deposition in atherosclerosis. Annu Rev Biochem 52:223–261 [Review]
8. Lehr HA, Seemuller J, Hubner C, Menger MD, Messmer K (1993) Oxidized LDL-induced leukocyte/endothelium interaction in vivo involves the receptor for platelet-activating factor. Arterioscler Thromb 13(7):1013–1018
9. Watson AD, Navab M, Hama SY, Sevanian A, Prescott SM, Stafforini DM et al (1995) Effect of platelet activating factor-acetylhydrolase on the formation and action of minimally oxidized low density lipoprotein. J Clin Invest 95:774–782
10. Hansson GK (1997) Cell-mediated immunity in atherosclerosis. Curr Opin Lipidol 8(5):301–311
11. Stemme S, Faber B, Holm J, Wiklund O, Witztum JL, Hansson GK (1995) T lymphocytes from human atherosclerotic plaques

recognize oxidized low density lipoprotein. Proc Natl Acad Sci USA 92:3893–3897
12. Parums DV, Chadwick DR, Mitchinson MJ (1986) The localisation of immunoglobulin in chronic periaortitis. Atherosclerosis 61(2):117–123
13. Sohma Y, Sasano H, Shiga R, Saeki S, Suzuki T, Nagura H et al (1995) Accumulation of plasma cells in atherosclerotic lesions of Watanabe heritable hyperlipidemic rabbits. Proc Natl Acad Sci USA 92(11):4937–4941
14. Kovanen PT, Kaartinen M, Paavonen T (1995) Infiltrates of activated mast cells at the site of coronary atheromatous erosion or rupture in myocardial infarction. Circulation 92(5):1084–1088
15. Kleindienst R, Xu Q, Willeit J, Waldenberger FR, Weimann S, Wick G (1993) Immunology of atherosclerosis. Demonstration of heat shock protein 60 expression and T lymphocytes bearing alpha/beta or gamma/delta receptor in human atherosclerotic lesions. Am J Pathol 142(6):1927–1937
16. Melian A, Geng YJ, Sukhova GK, Libby P, Porcelli SA (1999) CD1 expression in human atherosclerosis. A potential mechanism for T cell activation by foam cells. Am J Pathol 155(3):775–786
17. Imparato AM, Riles TS, Mintzer R, Baumann FG (1983) The importance of hemorrhage in the relationship between gross morphologic characteristics and cerebral symptoms in 376 carotid artery plaques. Ann Surg 197(2):195–203
18. Aburahma AF, Robinson P, Decanio R (1989) Prospective clinicopathologic study of carotid intraplague hemorrhage. Am Surg 55(3):169–173
19. McCarthy MJ, Loftus IM, Thompson MM, Jones L, London NJ, Bell PR et al (1999) Angiogenesis and the atherosclerotic carotid plaque: an association between symptomatology and plaque morphology. J Vasc Surg 30(2):261–268
20. Neote K, Darbonne W, Ogez J, Horuk R, Schall TJ (1993) Identification of a promiscuous inflammatory peptide receptor on the surface of red blood cells. J Biol Chem 268(17):12247–12249
21. Yuan XM, Brunk UT, Olsson AG (1995) Effects of iron- and hemoglobin-loaded human monocyte-derived macrophages on oxidation and uptake of LDL. Arterioscler Thromb Vasc Biol 15(9):1345–1351
22. Kolodgie FD, Gold HK, Burke AP, Fowler DR, Kruth HS, Weber DK et al (2003) Intraplaque hemorrhage and progression of coronary atheroma. N Engl J Med 349(24):2316–2325
23. Falk E, Shah PK, Fuster V (1995) Coronary plaque disruption. Circulation 92(3):657–671
24. Gertz SD, Roberts WC (1990) Hemodynamic shear force in rupture of coronary arterial atherosclerotic plaques. Am J Cardiol 66(19):1368–1372
25. Stein PD, Hamid MS, Shivkumar K, Davis TP, Khaja F, Henry JW (1994) Effects of cyclic flexion of coronary arteries on progression of atherosclerosis. Am J Cardiol 73(7):431–437
26. Cheng GC, Loree HM, Kamm RD, Fishbein MC, Lee RT (1993) Distribution of circumferential stress in ruptured and stable atherosclerotic lesions. A structural analysis with histopathological correlation. Circulation 87(4):1179–1187
27. Richardson PD, Davies MJ, Born GV (1989) Influence of plaque configuration and stress distribution on fissuring of coronary atherosclerotic plaques. Lancet 2(8669):941–944
28. Bogaty P, Hackett D, Davies G, Maseri A (1994) Vasoreactivity of the culprit lesion in unstable angina. Circulation 90(1):5–11
29. Crawford ES, Crawford JL (1984) Aortitis. In: Tracy TT (ed) Disease of the aorta Including an atlas of angiographic pathology and surgical technique. Williams & Wilkins, Baltimore/London, pp 272–86
30. Jander S, Sitzer M, Wendt A, Schroeter M, Buchkremer M, Siebler M et al (2001) Expression of tissue factor in high-grade carotid artery stenosis: association with plaque destabilization. Stroke 32(4):850–854
31. Bevilacqua MP, Schleef RR, Gimbrone MA Jr, Loskutoff DJ (1986) Regulation of the fibrinolytic system of cultured human vascular endothelium by interleukin 1. J Clin Invest 78(2):587–591
32. Fuster V, Lewis A (1994) Conner Memorial Lecture. Mechanisms leading to myocardial infarction: insights from studies of vascular biology. Circulation 90(4):2126–2146
33. Stary HC, Chandler AB, Dinsmore RE, Fuster V, Glagov S, Insull W Jr et al (1995) A definition of advanced types of atherosclerotic lesions and a histological classification of atherosclerosis : a report from the Committee on Vascular Lesions of the Council on Arteriosclerosis, American Heart Association. Circulation 92(5):1355–1374
34. Falk E (1983) Plaque rupture with severe pre-existing stenosis precipitating coronary thrombosis. Characteristics of coronary atherosclerotic plaques underlying fatal occlusive thrombi. Br Heart J 50(2):127–134
35. Davies MJ, Thomas AC (1985) Plaque fissuring – the cause of acute myocardial infarction, sudden ischaemic death, and crescendo angina. Br Heart J 53(4):363–373
36. Naghavi M, Libby P, Falk E, Casscells SW, Litovsky S, Rumberger J et al (2003) From vulnerable plaque to vulnerable patient: a call for new definitions and risk assessment strategies: part I. Circulation 108(14):1664–1672
37. Naghavi M, Libby P, Falk E, Casscells SW, Litovsky S, Rumberger J et al (2003) From vulnerable plaque to vulnerable patient: a call for new definitions and risk assessment strategies: part II. Circulation 108(15):1772–1778
38. Gronholdt ML, Nordestgaard BG, Schroeder TV, Vorstrup S, Sillesen H (2001) Ultrasonic echolucent carotid plaques predict future strokes. Circulation 104(1):68–73
39. Rubin JR, Bondi JA, Rhodes RS (1987) Duplex scanning versus conventional arteriography for the evaluation of carotid artery plaque morphology. Surgery 102(4):749–755
40. Pedro LM, Pedro MM, Goncalves I, Carneiro TF, Balsinha C, Fernandes e Fernandes R et al (2000) Computer-assisted carotid plaque analysis: characteristics of plaques associated with cerebrovascular symptoms and cerebral infarction. Eur J Vasc Endovasc Surg 19(2):118–123
41. Meairs S, Hennerici M (1999) Four-dimensional ultrasonographic characterization of plaque surface motion in patients with symptomatic and asymptomatic carotid artery stenosis. Stroke 30(9):1807–1813
42. Kolodgie FD, Burke AP, Farb A, Gold HK, Yuan J, Narula J et al (2001) The thin-cap fibroatheroma: a type of vulnerable plaque: the major precursor lesion to acute coronary syndromes. Curr Opin Cardiol 16(5):285–292
43. Virmani R, Kolodgie FD, Burke AP, Farb A, Schwartz SM (2000) Lessons from sudden coronary death. A comprehensive morphological classification scheme for atherosclerotic lesions. Arterioscler Thromb Vasc Biol 20:1262–1275
44. Goldstein JA, Demetriou D, Grines CL, Pica M, Shoukfeh M, O'Neill WW (2000) Multiple complex coronary plaques in patients with acute myocardial infarction. N Engl J Med 343(13):915–922
45. Moulton KS (2001) Plaque angiogenesis and atherosclerosis. Curr Atheroscler Rep 3(3):225–233
46. Targonski PV, Bonetti PO, Pumper GM, Higano ST, Holmes DR Jr, Lerman A (2003) Coronary endothelial dysfunction is associated with an increased risk of cerebrovascular events. Circulation 107(22):2805–2809
47. Varnava AM, Mills PG, Davies MJ (2002) Relationship between coronary artery remodeling and plaque vulnerability. Circulation 105(8):939–943
48. Farb A, Burke AP, Tang AL, Liang TY, Mannan P, Smialek J et al (1996) Coronary plaque erosion without rupture into a lipid

core. A frequent cause of coronary thrombosis in sudden coronary death. Circulation 93(7):1354–1363
49. Kolodgie FD, Burke AP, Wight TN, Virmani R (2004) The accumulation of specific types of proteoglycans in eroded plaques: a role in coronary thrombosis in the absence of rupture. Curr Opin Lipidol 15(5):575–582
50. Waksman R, Serruys PW (2004) Handbook of the vulnerable plaque. Taylor & Francis Group, London
51. Falk E (1992) Why do plaques rupture? Circulation 86(6 Suppl):III30–III42
52. Falk E, Fuster V (1995) Angina pectoris and disease progression. Circulation 92(8):2033–2035
53. Jespersen SK, Wilhjelm JE, Sillesen H (1998) Multi-angle compound imaging. Ultrason Imaging 20(2):81–102
54. Kern R, Szabo K, Hennerici M, Meairs S (2004) Characterization of carotid artery plaques using real-time compound B-mode ultrasound. Stroke 35(4):870–875
55. Delcker A, Schurks M, Polz H (1999) Development and applications of 4-D ultrasound (dynamic 3-D) in neurosonology. J Neuroimaging 9(4):229–234
56. Fenster A, Landry A, Downey DB, Hegele RA, Spence JD (2004) 3D ultrasound imaging of the carotid arteries. Curr Drug Targets Cardiovasc Haematol Disord 4(2):161–175
57. Reilly LM, Lusby RJ, Hughes L, Ferrell LD, Stoney RJ, Ehrenfeld WK (1983) Carotid plaque histology using real-time ultrasonography. Clinical and therapeutic implications. Am J Surg 146(2):188–193
58. Johnson JM, Kennelly MM, Decesare D, Morgan S, Sparrow A (1985) Natural history of asymptomatic carotid plaque. Arch Surg 120(9):1010–1012
59. Gray-Weale AC, Graham JC, Burnett JR, Byrne K, Lusby RJ (1988) Carotid artery atheroma: comparison of preoperative B-mode ultrasound appearance with carotid endarterectomy specimen pathology. J Cardiovasc Surg (Torino) 29(6):676–681
60. Langsfeld M, Gray-Weale AC, Lusby RJ (1989) The role of plaque morphology and diameter reduction in the development of new symptoms in asymptomatic carotid arteries. J Vasc Surg 9(4):548–557
61. Geroulakos G, Ramaswami G, Nicalaides A, James K, Labropoulos N, Belcaro G et al (1993) Characterization of symptomatic and asymptomatic carotid plaques using high-resolution real-time ultrasonography. Br J Surg 80:1274–1277
62. Group ECPS (1995) Carotid artery plaque composition: relationship to clinical presentation and ultrasound B-mode imaging. Eur J Vasc Endovasc Surg 10:23–30
63. Hallerstam S, Carlstrom C, Zetterling M, Konrad P, Rosfors S (2000) Carotid atherosclerosis in relation to symptoms from the territory supplied by the carotid artery. Eur J Vasc Endovasc Surg 19(4):356–361
64. Holdsworth RJ, McCollum PT, Bryce JS, Harrison DK (1995) Symptoms, stenosis and carotid plaque morphology. Is plaque morphology relevant? Eur J Vasc Endovasc Surg 9(1):80–85
65. Elatrozy T, Nicolaides A, Tegos T, Zarka AZ, Griffin M, Sabetai M (1998) The effect of B-mode ultrasonic image standardisation on the echodensity of symptomatic and asymptomatic carotid bifurcation plaques. Int Angiol 17(3):179–186
66. Elatrozy T, Nicolaides A, Tegos T, Griffin M (1998) The objective characterisation of ultrasonic carotid plaque features. Eur J Vasc Endovasc Surg 16(3):223–230
67. el-Barghouty N, Geroulakos G, Nicolaides A, Androulakis A, Bahal V (1995) Computer-assisted carotid plaque characterisation. Eur J Vasc Endovasc Surg 9(4):389–393
68. El-Barghouty N, Nicoalides A, Bahal V, Geroulakos G, Androulakis A (1996) The identification of the high risk carotid plaque. Eur J Vasc Endovasc Surg 11:470–478
69. Pedro LM, Pedro MM, Goncalves I, Carneiro TF, Balsinha C, Fernandes e Fernandes R et al (1999) [Atheroma plaque of the carotid bifurcation: how to identify an "active" lesion?]. Rev Port Cardiol 18(7–8):699–708
70. Biasi GM, Mingazzini PM, Baronio L, Piglionica MR, Ferrari SA, Elatrozy TS et al (1998) Carotid plaque characterization using digital image processing and its potential in future studies of carotid endarterectomy and angioplasty. J Endovasc Surg 5(3):240–246
71. O'Holleran LW, Kennelly MM, McClurken M, Johnson JM (1987) Natural history of asymptomatic carotid plaque. Five year follow-up study. Am J Surg 154(6):659–662
72. Polak JF, Shemanski L, O'Leary DH, Lefkowitz D, Price TR, Savage PJ et al (1998) Hypoechoic plaque at US of the carotid artery: an independent risk factor for incident stroke in adults aged 65 years or older. Cardiovascular Health Study. Radiology 208(3):649–654
73. Liapis CD, Kakisis JD, Kostakis AG (2001) Carotid stenosis. Factors affecting symptomatology. Stroke 32:2782–2786
74. Mathiesen EB, Bonaa KH, Joakimsen O (2001) Echolucent plaques are associated with high risk of ischemic cerebrovascular events in carotid stenosis: the tromso study. Circulation 103(17):2171–2175
75. Sterpetti AV, Schultz RD, Feldhaus RJ, Davenport KL, Richardson M, Farina C et al (1988) Ultrasonographic features of carotid plaque and the risk of subsequent neurologic deficits. Surgery 104(4):652–660
76. Leahy AL, McCollum PT, Feeley TM, Sugrue M, Grouden MC, O'Connell DJ et al (1988) Duplex ultrasonography and selection of patients for carotid endarterectomy: plaque morphology or luminal narrowing? J Vasc Surg 8(5):558–562
77. Matalanis G, Lusby RJ (1988) Is there still a place for carotid endarterectomy? Clin Exp Neurol 25:17–26
78. Giannoni MF, Speziale F, Faraglia V, Sbarigia E, Zaccaria A, Lauri D et al (1991) Minor asymptomatic carotid stenosis contralateral to carotid endarterectomy (CEA): our experience. Eur J Vasc Surg 5(3):237–245
79. Belcaro G, Laurora G, Cesarone MR, De Sanctis MT, Incandela L, Fascetti E et al (1993) Ultrasonic classification of carotid plaques causing less than 60 % stenosis according to ultrasound morphology and events. J Cardiovasc Surg (Torino) 34(4):287–294
80. Comerota AJ, Katz ML, White JV, Grosh JD (1990) The preoperative diagnosis of the ulcerated carotid atheroma. J Vasc Surg 11(4):505–510
81. Bluth EI, McVay LV 3rd, Merritt CR, Sullivan MA (1988) The identification of ulcerative plaque with high resolution duplex carotid scanning. J Ultrasound Med 7(2):73–76
82. O'Leary DH, Holen J, Ricotta JJ, Roe S, Schenk EA (1987) Carotid bifurcation disease: prediction of ulceration with B-mode US. Radiology 162(2):523–525
83. Bassiouny HS, Sakaguchi Y, Mikucki SA, McKinsey JF, Piano G, Gewertz BL et al (1997) Juxtalumenal location of plaque necrosis and neoformation in symptomatic carotid stenosis. J Vasc Surg 26:589–594
84. Pedro LM, Fernandes e Fernandes J, Pedro MM, Goncalves I, Dias NV, Fernandes e Fernandes R et al (2002) Ultrasonographic risk score of carotid plaques. Eur J Vasc Endovasc Surg 24(6):492–498
85. Sabetai MM, Tegos TJ, Nicolaides AN, El-Atrozy TS, Dhanjil S, Griffin M et al (2000) Hemispheric symptoms and carotid plaque echomorphology. J Vasc Surg 31(1 Pt 1):39–49
86. Iannuzzi A, Wilcosky T, Mercuri M, Rubba P, Bryan FA, Bond MG (1995) Ultrasonographic correlates of carotid atherosclerosis in transient ischemic attack and stroke. Stroke 26(4):614–619

87. Wolverson MK, Bashiti HM, Peterson GJ (1983) Ultrasonic tissue characterisation of atheromatous plaques using a high resolution real time scanner. Ultrasound Med Biol 9:599–609
88. Montauban van Swijndregt AD, Elbers HR, Moll FL, de Letter J, Ackerstaff RG (1998) Ultrasonographic characterization of carotid plaques. Ultrasound Med Biol 24(4):489–493
89. Montauban van Swijndregt AD, Elbers HR, Moll FL, de Letter J, Ackerstaff RG (1999) Cerebral ischemic disease and morphometric analyses of carotid plaques. Ann Vasc Surg 13(5):468–474
90. Kardoulas DG, Katsamouris AN, Gallis PT, Philippides TP, Anagnostakos NK, Gorgoyannis DS et al (1996) Ultrasonographic and histologic characteristics of symptom-free and symptomatic carotid plaque. Cardiovasc Surg 4(5):580–590
91. Lammie GA, Wardlaw J, Allan P, Ruckley CV, Peek R, Signorini DF (2000) What pathological components indicate carotid atheroma activity and can these be identified reliably using ultrasound? Eur J Ultrasound 11(2):77–86
92. Leen EJ, Feeley TM, Colgan MP, O'Malley MK, Moore DJ, Hourihane DO et al (1990) "Haemorrhagic" carotid plaque does not contain haemorrhage. Eur J Vasc Surg 4(2):123–128
93. Milei J, Parodi JC, Ferreira M, Barrone A, Grana DR, Matturri L (2003) Atherosclerotic plaque rupture and intraplaque hemorrhage do not correlate with symptoms in carotid artery stenosis. J Vasc Surg 38(6):1241–1247
94. El-Barghouty NM, Levine T, Ladva S, Flanagan A, Nicolaides A (1996) Histological verification of computerised carotid plaque characterisation. Eur J Vasc Endovasc Surg 11(4):414–416
95. Gronholdt ML, Sillesen H, Wiebe BM, Laursen H, Nordestgaard BG (2001) Increased acute phase reactants are associated with levels of lipoproteins and increased carotid plaque volume. Eur J Vasc Endovasc Surg 21(3):227–234
96. Gronholdt ML, Nordestgaard BG, Nielsen TG, Sillesen H (1996) Echolucent carotid artery plaques are associated with elevated levels of fasting and postprandial triglyceride-rich lipoproteins. Stroke 27(12):2166–2172
97. Gronholdt ML, Nordestgaard BG, Bentzon J, Wiebe BM, Zhou J, Falk E et al (2002) Macrophages are associated with lipid-rich carotid artery plaques, echolucency on B-mode imaging, and elevated plasma lipid levels. J Vasc Surg 35(1):137–145
98. Gronholdt ML, Wiebe BM, Laursen H, Nielsen TG, Schroeder TV, Sillesen H (1997) Lipid-rich carotid artery plaques appear echolucent on ultrasound B-mode images and may be associated with intraplaque haemorrhage. Eur J Vasc Endovasc Surg 14(6):439–445
99. Goncalves I, Lindholm MW, Pedro LM, Dias N, Fernandes e Fernandes J, Fredrikson GN et al (2004) Elastin and calcium rather than collagen or lipid content are associated with echogenicity of human carotid plaques. Stroke 35(12):2795–2800
100. Goncalves I, Moses J, Pedro LM, Dias N, Fernandes e Fernandes J, Nilsson J et al (2003) Echolucency of carotid plaques correlates with plaque cellularity. Eur J Vasc Endovasc Surg 26(1):32–38
101. Cheuk BL, Cheng SW (2011) Annexin A1 expression in atherosclerotic carotid plaques and its relationship with plaque characteristics. Eur J Vasc Endovasc Surg 41(3):364–371
102. Turu MM, Krupinski J, Catena E, Rosell A, Montaner J, Rubio F et al (2006) Intraplaque MMP-8 levels are increased in asymptomatic patients with carotid plaque progression on ultrasound. Atherosclerosis 187(1):161–169
103. Vik A, Mathiesen EB, Noto AT, Sveinbjornsson B, Brox J, Hansen JB (2007) Serum osteoprotegerin is inversely associated with carotid plaque echogenicity in humans. Atherosclerosis 191(1):128–134
104. Staub D, Partovi S, Schinkel AF, Coll B, Uthoff H, Aschwanden M et al (2011) Correlation of carotid artery atherosclerotic lesion echogenicity and severity at standard US with intraplaque neovascularization detected at contrast-enhanced US. Radiology 258(2):618–626
105. Owen DR, Shalhoub J, Miller S, Gauthier T, Doryforou O, Davies AH et al (2010) Inflammation within carotid atherosclerotic plaque: assessment with late-phase contrast-enhanced US. Radiology 255(2):638–644
106. Goncalves I, Stenström K, Skog G, Mattsson S, Nitulescu M, Nilsson J (2010) Dating components of human atherosclerotic plaques. Circ Res 106:1174–1177
107. Wohlin M, Sundstrom J, Andren B, Larsson A, Lind L (2009) An echolucent carotid artery intima-media complex is a new and independent predictor of mortality in an elderly male cohort. Atherosclerosis 205(2):486–491
108. Lind L, Andersson J, Ronn M, Gustavsson T (2007) The echogenecity of the intima-media complex in the common carotid artery is closely related to the echogenecity in plaques. Atherosclerosis 195(2):411–414
109. Kim DE, Kim JY, Schellingerhout D, Kim EJ, Kim HK, Lee S et al (2010) Protease imaging of human atheromata captures molecular information of atherosclerosis, complementing anatomic imaging. Arterioscler Thromb Vasc Biol 30(3):449–456
110. Nagano K, Yamagami H, Tsukamoto Y, Nagatsuka K, Yasaka M, Nagata I et al (2008) Quantitative evaluation of carotid plaque echogenicity by integrated backscatter analysis: correlation with symptomatic history and histologic findings. Cerebrovasc Dis 26(6):578–583
111. Ostling G, Hedblad B, Berglund G, Goncalves I (2007) Increased echolucency of carotid plaques in patients with type 2 diabetes. Stroke 38(7):2074–2078
112. Andersson J, Sundstrom J, Gustavsson T, Hulthe J, Elmgren A, Zilmer K et al (2009) Echogenecity of the carotid intima-media complex is related to cardiovascular risk factors, dyslipidemia, oxidative stress and inflammation: the Prospective Investigation of the Vasculature in Uppsala Seniors (PIVUS) study. Atherosclerosis 204(2):612–618
113. Kadoglou NP, Gerasimidis T, Moumtzouoglou A, Kapelouzou A, Sailer N, Fotiadis G et al (2008) Intensive lipid-lowering therapy ameliorates novel calcification markers and GSM score in patients with carotid stenosis. Eur J Vasc Endovasc Surg 35(6):661–668
114. Ostling G, Goncalves I, Wikstrand J, Berglund G, Nilsson J, Hedblad B (2011) Long-term treatment with low-dose metoprolol CR/XL is associated with increased plaque echogenicity: the Beta-blocker Cholesterol-lowering Asymptomatic Plaque Study (BCAPS). Atherosclerosis 215(2):440–445

17 Automated Carotid IMT Measurement and Its Validation in Low Contrast Ultrasound Database of 885 Patient Indian Population Epidemiological Study: Results of AtheroEdge® Software

Filippo Molinari, Kristen M. Meiburger, Luca Saba, U. Rajendra Acharya, Luca Famiglietti, Niki Georgiou, Andrew Nicolaides, Raja Sriswan Mamidi, Hannah Kuper, and Jasjit S. Suri

1 Introduction

The World Health Organization (WHO) [1] estimated cardiovascular disease (CVD) to be responsible for one-third of all global deaths. Although, nowadays, CVD is a major problem for high-income countries, WHO forecasts that CVD will also become common in low- and middle-income countries (LMIC) where it is predicted to be responsible for one-third of deaths by 2040. Multicenter assessment protocols and epidemiological studies are the basis for understanding the risk factors and for developing public health messages, including in LMIC.

The earliest manifestation of the possible onset of a CVD is atherosclerosis, which refers to the degeneration of the arterial wall and the deposition of lipids within the latter [2–4]. Atherosclerosis causes increase of the arterial intima–media thickness (IMT). Carotid IMT is the most widely adopted and validated ultrasonic marker for the assessment of atherosclerosis and cardiovascular risk [5–9] and has been used as the principal marker of CVD in studies ranging across Japan [10], Europe [8, 9, 11], China [12], North America [13–17], and Latin America [18]. There are several advantages to the use of carotid IMT as a marker for CVD in epidemiological studies. The ultrasound-based carotid IMT measurement is accurate and reproducible [19, 20]. Also, ultrasound is an imaging modality with low associated costs, minimal invasiveness, and cheap and portable scanners. The IMT is measured by an expert operator. The operator places a marker in correspondence of the intima and media boundary (LI) and another in correspondence of the media and adventitia boundary (MA). The distance between LI and MA corresponds to the IMT. However, manual measurements are discouraged in multicenter and epidemiological studies because they are user-dependent, not fully standardized, subjective, time-consuming, and prone to errors [21]. Therefore, the availability of a computer-based IMT measurement algorithm is fundamental.

The quality of the image is compromised unless a high-level scanner is used. Figure 17.1 show four sample images acquired by a high-level scanner (Fig. 17.1a), a medium-level scanner (Fig. 17.1b), and two low-end equipments (Fig. 17.1c, d). In Fig. 17.1a the LI and MA interfaces are clearly represented, the line corresponding to the distal LI

F. Molinari, Ph.D. (✉) • K.M. Meiburger, M.S.
Biolab, Department of Electronics, Politecnico di Torino, Corso Duca degli Abruzzi 24, 10129 Torino, Italy
e-mail: filippo.molinari@polito.it; kristen.meiburger@polito.it

L. Saba, M.D. • L. Famiglietti, M.D.
Department of Radiology, Azienda Ospedaliero Universitaria di Cagliari, Cagliari, Italy
e-mail: lsaba@tiscali.it

U.R. Acharya, Ph.D.
Department of Electronics and Computer Engineering, Ngee Ann Polytechnic, Clementi Road, Singapore

Department of Biomedical Engineering, University of Malaya, Malaysia
e-mail: aru@np.edu.sg

N. Georgiou • A. Nicolaides, Ph.D.
Vascular Screening and Diagnostic Centre, London, UK

Department of Biological Sciences, University of Cyprus, Nicosia, Cyprus
e-mail: georgnik@cytanet.com.cy; anicolaides1@gmail.com

R.S. Mamidi, M.D.
National Institute of Nutrition, Hyderabad, Andhra Pradesh, India
e-mail: srishwan@gmail.com

H. Kuper, Sc.D.,M.D.
Faculty of Infectious and Tropical Diseases, London School of Hygiene and Tropical Medicine, London, UK
e-mail: hannah.kuper@lshtm.ac.uk

J.S. Suri, M.S., Ph.D., M.B.A., Fellow AIMBE
Department of Biomedical Engineering (Aff.), Idaho State University, Pocatello, ID, USA

Fellow AIMBE, CTO, Diagnostic and Monitoring Division, AtheroPoint LLC, Roseville, CA, USA
e-mail: jsuri@comcast.net

L. Saba et al. (eds.), *Multi-Modality Atherosclerosis Imaging and Diagnosis*,
DOI 10.1007/978-1-4614-7425-8_17,

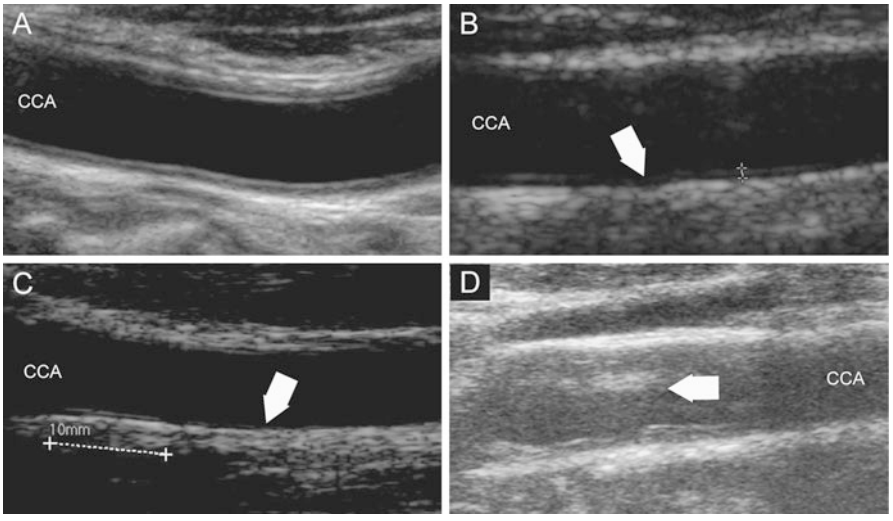

Fig. 17.1 Samples of high-resolution and low-resolution images. (**a**) High-resolution image where the intima and adventitia layers are neatly defined, noise is low, and pixel density is high (about 20 pixels/mm). (**b**) Image acquired by a medium-end scanner without compound imaging, where LI is hypoechoic. (**c**) Images acquired by a low-end equipment without harmonic imaging and compound, where LI is almost invisible and pixel resolution is very low (about 12 pixels/mm). (**d**) Example of low-resolution image with high level of image noise

is echoic and not interrupted, and the noise level is very low (i.e., the lumen is dark and homogeneous). This is an example of what we consider a high-resolution image. Figure 17.1b shows an image where the LI is hypoechoic due to lack of compound imaging. The LI is not focused and it is not well represented. However, the noise level is low and the image has a pixel density comparable to Fig. 17.1a. This is an example of a medium-resolution image. In Fig. 17.1c the LI is almost anechoic and the pixel density is very low. This results in a low-resolution image. Figure 17.1d shows an image where noise is very high due to the lack of despeckling filters embedded in the system and the lack of compound and harmonic imaging. This is another example of a low-resolution image.

The characteristics that make an image suitable for automated delineation are (see Fig. 17.1) (1) high spatial resolution, (2) high dynamic range, (3) low noise level, (4) compound imaging, and (5) harmonic imaging. When an image has the above-mentioned five characteristics, we can say that it is a high-resolution image and automated IMT measurement algorithms can process it [22, 23]. If the image does not possess one or more of the above-mentioned characteristics, specific image enhancement and delineation or segmentation strategies must be adopted [24]. Compound and harmonic imaging are available on most of the medium-level and high-level ultrasound OEM scanners. However, they are not present in the majority of the entry-level and cheaper equipment so that compound imaging and harmonic imaging are not supported. As a consequence, the image quality becomes low with poor contrast and automated segmentation is difficult and sometimes nearly impossible. As an example, Fig. 17.2 shows three samples of low-resolution images. The left column (Fig. 17.2a, c, e) shows B-Mode longitudinal projections of the images of our low-resolution database. The dashed line represents a region of interest, which is zoomed on the right (Fig. 17.2b, d, f). The white arrows indicate where the lack of contrast is more evident. It can be seen that in Fig. 17.2b, the adventitia layer (MA) is bright, but the intima is sometimes broken and not represented (white arrow). In Fig. 17.2d, the intima layer cannot be clearly distinguished from the media and adventitia, because all three layers have almost the same gray color. In Fig. 17.2f, the adventitia is bright, but the intima is almost invisible. These three conditions can represent a very difficult challenge to automated segmentation techniques.

In this chapter we will present the results of a completely automated epidemiological study devoted to the IMT measurement of healthy subjects from around Hyderabad in India. We used CALEX in its last empowered version 3.0. CALEX3 is a novel and improved technique, which incorporates the rejection of the jugular vein, hard constraints of the seed points, and an optimized fuzzy *K-means* classifier [25, 26].

2 Image Dataset and Image Characteristics

The database consisted of 885 ultrasound carotid images in longitudinal projection. The subjects for the images were identified through the Hyderabad DXA Study, which included participants drawn from two groups. The first was the participants of the Hyderabad arm of the Indian Migrant Study that included migrants of rural origin, their rural dwelling sibs, and those of urban origin together with their urban dwelling sibs. The second was the participants

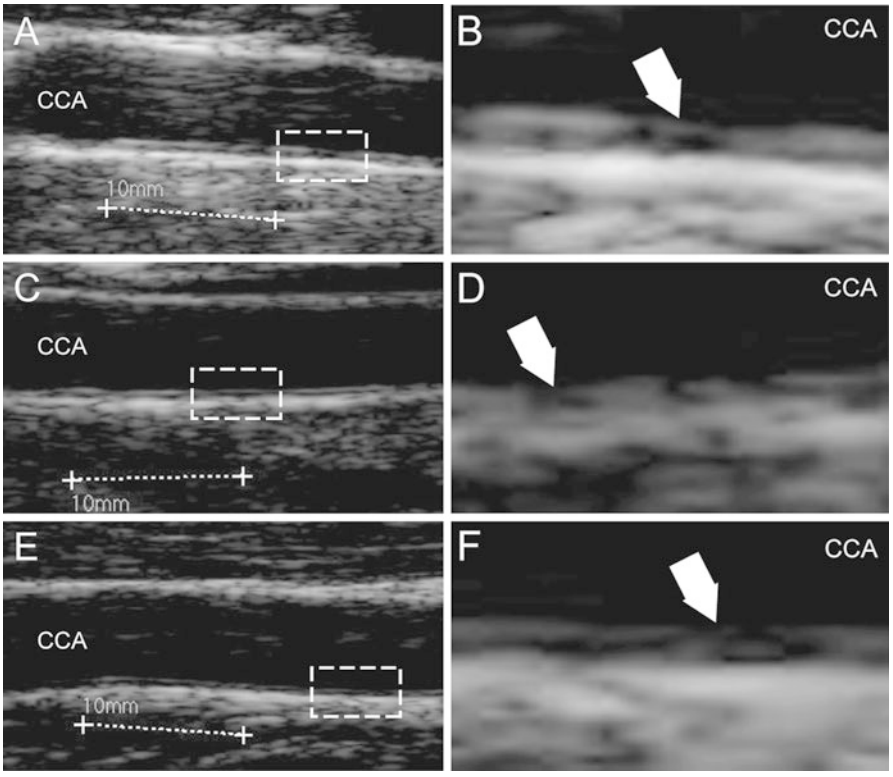

Fig. 17.2 Samples of low-resolution images extracted from the dataset. Panels (**a**, **c**), and (**e**) show the carotid. Panels (**b**, **d**), and **f** show the zoomed portion of the corresponding *dashed rectangle* on the *left*. The *white arrows* indicate the challenges of these images: interrupted intima representation (panel **b**), low contrast between intima, media, and adventitia (panel **d**), and well represented adventitia, but hypoechoic intima (panel **f**)

of the Hyderabad Nutrition Trial which was made up of people born within an earlier controlled, community trial of nutritional supplementation integrated with other public health programs, now aged 18–21. Participants attended screening examination between January 2009 and December 2010, which included assessment of carotid IMT. The study received Ethical Approval by the local Committee of the National Institute of Nutrition and the London School of Hygiene & Tropical Medicine.

The challenging aspect of these images is that they were acquired with low-end ultrasound equipment. Figure 17.3a shows an example of ultrasound B-Mode image. As can be seen, the operator traced calibration lines during the image acquisition. Such lines are 10 mm long. However, such lines are often not horizontally placed, and, therefore, they cannot be used for computing the vertical and horizontal conversion factor independently. The white arrows in Fig. 17.3a indicate the vertical calibration scale. The distance between the white lines indicated by the arrows is 10 mm. We computed the number of pixels between the two white lines and used them to derive the vertical conversion factor. All the images had a vertical pixel density equal to 127 pixels/cm, or 12.7 pixels/mm, which is a very low pixel density that is typical of low-end OEM ultrasound scanners. Therefore, the conversion factor for the images was 0.0787 mm/pixel.

All the images were JPEG formatted. In several previous studies, we showed that the black frame surrounding the ultrasound image is detrimental to the automated processing algorithm and must be removed [25–29]. We adopted an automated autocropping strategy we previously published [27]. By computing the horizontal Sobel gradient of the image, we marked the first and last nonzero column, which marked the horizontal extension of the ultrasound data area. By computing the vertical Sobel gradient, we marked the vertical extension of the image area. The result of the automated cropping is shown in Fig. 17.3b.

An expert operator (L.S.) manually traced the far wall LI and MA boundaries by using an ad hoc developed graphical user interface (called ImgTracer™ [30, 31]). As the images were in low contrast and low resolution, the use of ImgTracer™ was justified by zooming the image before tracing. The final LI/MA profiles were saved in numerical form on text file and made available for IMT computation. The manual tracings were considered as ground truth (GT).

3 Brief Architecture of CALEX 3.0

The completely automated technique we used to perform automated IMT measurement was called CALEX (Com-

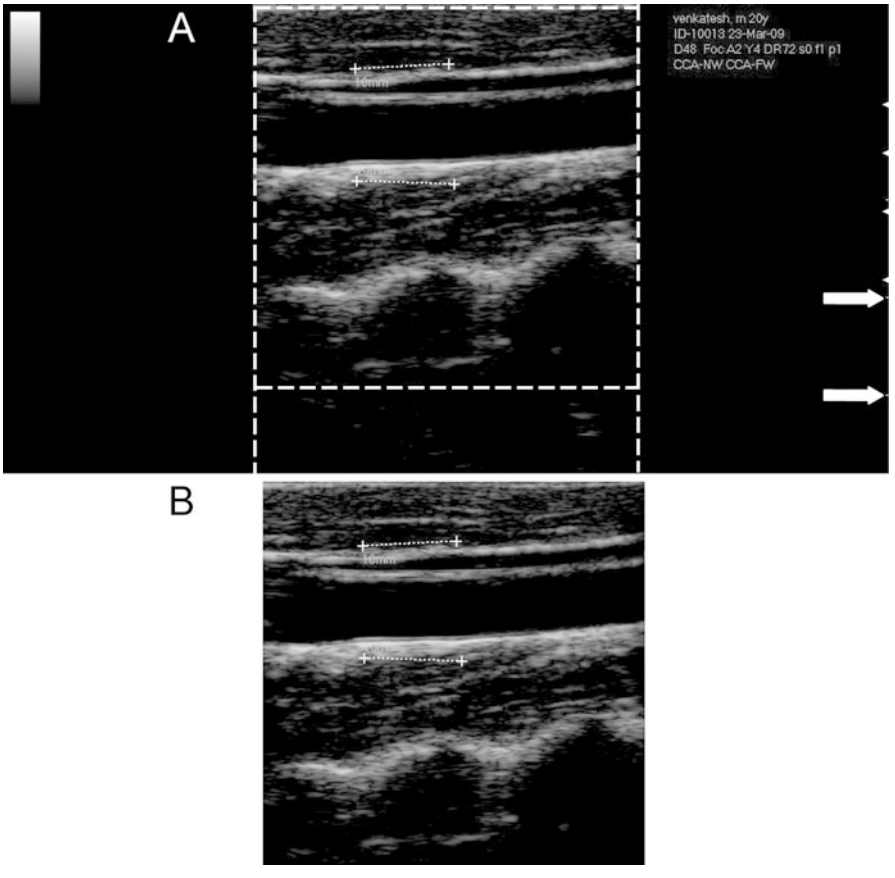

Fig. 17.3 CALEX 3.0 automated cropping. (**a**) Original image. The *dashed lines* delimit the region containing the ultrasound data. Outside the *dashed lines*, the vertical and horizontal gradients are null. The *white arrows* on the *right* indicate the vertical scale for the measurement of the conversion factor. (**b**) Cropped image

pletely Automated Layers EXtraction). We had previously developed this technique in 2010 [25, 26], but we modified it in order to improve the performance for low contrast and low-resolution carotid ultrasound images. For the purposes of this study, we used the CALEX 3.0 version, which is the latest improvement of our CALEX system architecture. CALEX 3.0 consists of three cascaded stages. Stage-I is the artery recognition phase based on feature extraction, line fitting, and classification [22]. This system was further improved by differentiating the CCA and JV. This was called intelligent carotid artery recognition processor—CALEX 3.0. The output of this stage is the adventitia borders (ADF). Stage-II consists of delineation or segmentation of walls or LI/MA segmentation based on fuzzy *K-means* classifier for the delineation of the automated LI and MA boundaries. Stage-III consists of LI/MA refinement.

3.1 Stage-I: Automatic Recognition of the CA

Stage-I is based on the pixel analysis through local statistics. The fundamental hypothesis of this recognition stage is that carotid appearance in B-Mode longitudinal images can be modeled in a relatively simple way as a black region (the artery lumen) in between two bright lines, which are the near and far adventitia layers. Therefore, Stage-I of CALEX 3.0 essentially searches for the carotid adventitia layers [25].

First of all, all the local intensity maxima of the images are automatically found and marked. Such maxima are called "seed points." Seed points are linked to form lines. Figure 17.4a shows the original cropped image and Fig. 17.4b the automatically detected line segments. In all our images, the carotid artery was represented as horizontally placed. Therefore, we kept all the horizontal lines in the image and discarded inclined lines. By using linear discriminators and a very solid classification procedure [32], we detected, among all the line segments, the two that comprised the artery lumen (Fig. 17.4c). The final output of Stage-I is the profiles of the far adventitia layer (AD_F), depicted by Fig. 17.4d.

The AD_F profile was used to derive a Guidance Zone (GZ) used by the subsequent Stage-II. This GZ must comprise the entire far wall along the carotid artery. Since the nominal IMT value is lower than 1 mm, it means that the distance between intima and media is about 13 pixels (since the pixel density of these images is 12.7 pixel/mm). Therefore, our GZ had the same horizontal width of the AD_F profile, and

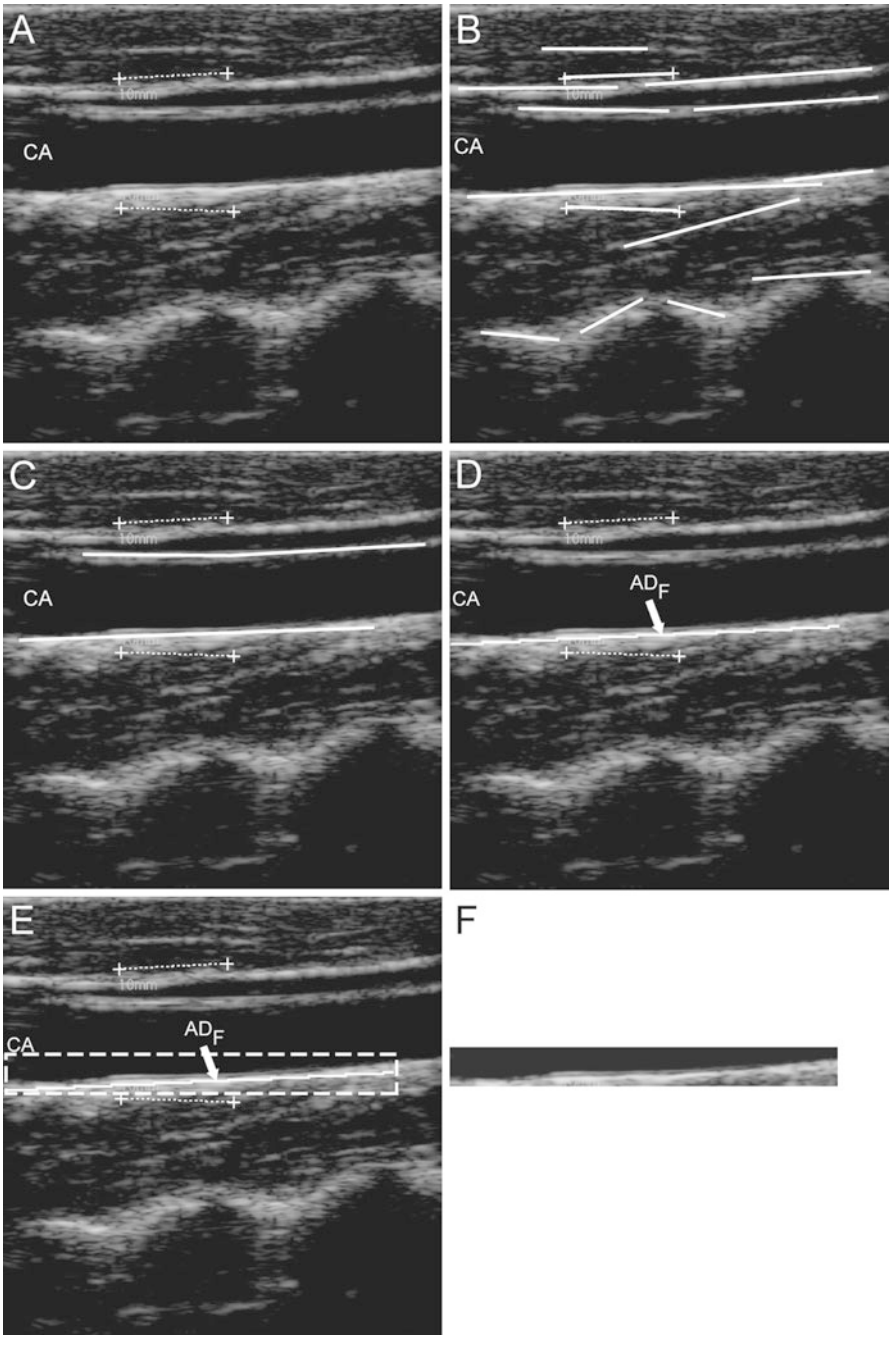

Fig. 17.4 Automated carotid identification (Stage-I) by CALEX 3.0. (**a**) Original cropped image. (**b**) Line segments. (**c**) Line segments corresponding to the near and far adventitia layers obtained through validation and classification [25]. (**d**) Final profile of the far adventitia (AD_F). (**e**) Determination of a Guidance Zone in which segmentation is performed (*white dashed line*). (**f**) Extracted Guidance Zone of the distal wall

height equal to 30 pixels, which means about twice the size of the IMT. With this value, our GZ always comprised the distal (far) wall and a portion of the carotid lumen. The pixels in the GZ were then processed by Stage-II. Figure 17.4e shows the Guidance Zone automatically detected (white dashed rectangle), and Fig. 17.4f the cropped Guidance Zone containing the distal carotid wall.

3.2 Stage-II: Fuzzy-Based LI-MA Segmentation Strategy

The automated delineation or segmentation of the far wall is performed by relying on a fuzzy *K-means* classifier. The GZ was processed column-wise. The intensity profile of each column was fed as input to the fuzzy *K-means* classifier.

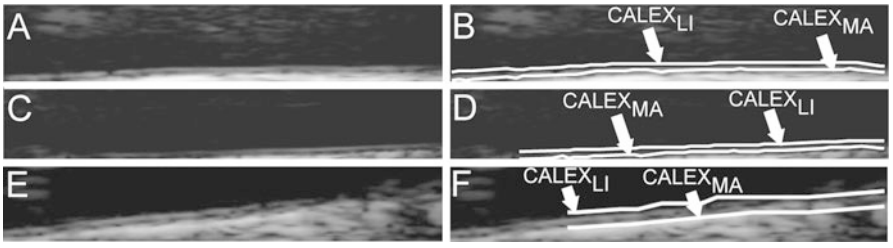

Fig. 17.5 Samples of CALEX 3.0 automated segmentation. The image is zoomed in the Guidance Zone

Basically, we modeled the intensity profile as a mixture of three clusters of pixels: (1) the pixels belonging to the lumen, which have a low intensity; (2) the pixels belonging to the intima and media layers, which are characterized by an intermediate gray intensity; and (3) the pixels belonging to the far adventitia, which are bright and with high associated values. Therefore, we forced the number of clusters of our *K-means* classifier equal to three. The pixel at the boundary between the first and the second class was then taken as marker of the LI interface; the pixels at the boundary between the second and the third class were taken as the marker of the MA interface. The final LI and MA boundaries were obtained by the sequence of the LI and MA marker points of every column of the GZ. Figure 17.5 shows three samples of CALEX 3.0 LI/MA profiles.

3.3 Stage-III: LI/MA Boundaries Refinement

Computer-generated boundaries might present local inaccuracies, caused by noise and image artifacts. Such inaccuracies are problematic in the framework of automated IMT measurement, because they can introduce a substantial error in the computer measurement of the IMT. Our CALEX 3.0 system is equipped with a third stage of post-processing that regularizes the LI/MA profiles and avoids inaccuracies. The two refinement strategies we introduced in CALEX 3.0 are lumen region detection and spike removal.

Lumen Region Detection via Pixels Classification We introduced a lumen detection step to prevent the computer-generated profiles crossing or penetrating into the lumen region. Particularly, we observed that when the carotid lumen was characterized by a high degree of blood backscattering, the LI profile could become inaccurate and protrude or bleed into the carotid lumen. This error condition is caused by the incorrect pixel classification by Stage-II. The pixels belonging to the lumen can be easily detected by relying on the bidimensional distribution of the intensities and standard deviations. Specifically, we computed the average intensity and the standard deviation of the intensity values of the 10×10 square neighborhood of each pixel. We found that lumen points have a very low average intensity and a very low standard deviation, since they are almost black and surrounded by homogeneous dark pixels. Hence, by plotting a bidimensional histogram, we could mark all the pixels possibly belonging to the artery lumen. Figure 17.6 shows an example of lumen region detection on an image from our dataset.

All the pixels possibly belonging to the artery lumen were marked according to the described procedure. Then, we forced the fuzzy *K-means* classifier of Stage-II to classify such lumen pixels into the first cluster. This avoided the LI profile bleeding into the artery lumen in 100 % of the images.

Spike Detection and Removal Small spikes can be present in the final LI/MA profiles. Again, such spikes can be generated by noise. Since the conversion factor of our database was 0.0787 mm/pixel, an IMT of 1 mm was be equivalent to 12.7 pixels. Therefore, we defined spike as a jump higher than six pixels in the LI/MA profiles, which means about half the nominal IMT value. All the spikes were detected and substituted by the average value of the 10 points neighboring the spiky point (5 points to the left and 5 to the right).

4 IMT Measurement and Performance Metric

The segmentation errors were computed by comparing automated tracings by CALEX 3.0 with manual segmentations, which were traced by expert sonographers by using a custom-made research prototype available system (IMgTracer™, Global Biomedical Technologies, Inc., California, USA). We used the Polyline Distance measure (PDM) as performance metric. A detailed description of the PDM can be found in previous works [33]. The fundamental equations of the PDM metric are reported in Appendices 1–3. Consider that the output of the CALEX 3.0 system consists of two profiles: LI and MA. Both the profiles consist of a certain number of vertices or points on the LI/MA borders. First, we compute the average distance of the vertices of LI with respect to the segments of MA and we call this value as $D_{\text{LI-MA}}$. Then, we compute the average distance between the

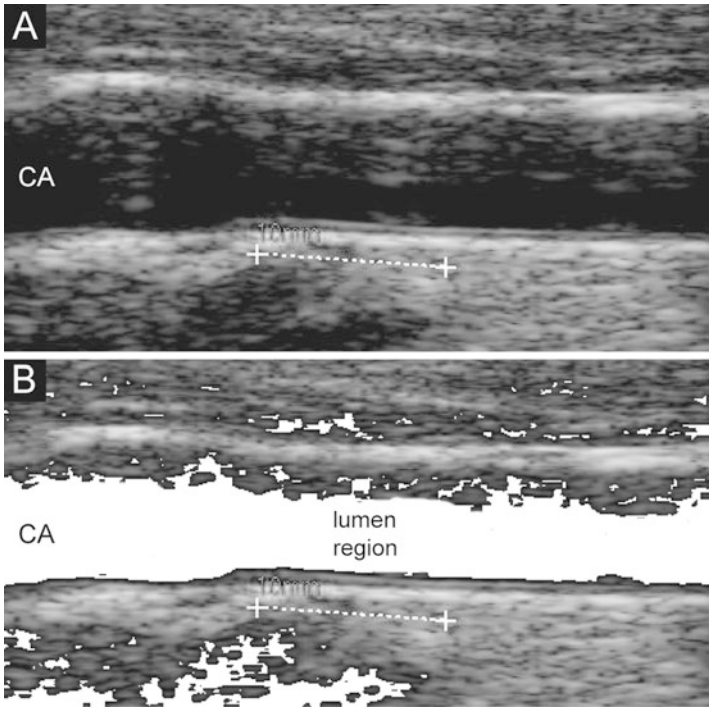

Fig. 17.6 Lumen region detection. (**a**) Original cropped image. (**b**) Lumen region detection. The pixels possibly belonging to the lumen are mapped to *white*

vertices of MA with respect to the segments of LI and call such distance as $D_{\text{MA-LI}}$. The PDM is defined as the sum of $D_{\text{LI-MA}}$ with $D_{\text{MA-LI}}$ divided by the total number of vertices of the two profiles. The main advantage of using the PDM as performance metric is that it is almost insensible to the number of points constituting a profile.

For each image, we compared the IMT measured by CALEX 3.0 with the IMT value calculated from manual delineations (GT). We then computed the IMT bias (i.e., the difference between CALEX 3.0 measurement and GT IMT), the IMT absolute value (i.e., the absolute difference between CALEX 3.0 measurement and GT IMT), and the IMT squared error (i.e., the squared absolute difference between CALEX 3.0 measurement and GT IMT). A detailed description of the error metrics is reported by Appendix 1. We also computed the Figure-of-Merit (FoM) for CALEX 3.0, which corresponds to the percent agreement between the computer-estimated IMT, and manually measured IMT values (mathematical details are reported in Appendix 3).

The performance evaluation analysis was completed by Bland–Altmann plots, correlation plots, and distribution histogram of the IMT measurement errors.

5 IMT Measurement Results in Low Contrast Images

CALEX 3.0 successfully segmented all the 885 images of the database. Table 17.1 reports the IMT measurement performance for CALEX 3.0 in comparison to Ground Truth. CALEX 3.0 measured an average IMT of 0.407 ± 0.083 mm, whereas the GT IMT value was 0.429 ± 0.052 mm. The IMT bias was as low as 0.022 ± 0.081 mm, the absolute error was 0.061 ± 0.058 mm, and the squared error was 0.007 ± 0.015 mm^2. The FoM was equal to 94.7 %.

Table 17.1 clearly shows the reliability and reproducibility of the technique.

Table 17.1 Overall system performance for CALEX 3.0

	CALEX 3.0	Ground truth
IMT mean	0.407 ± 0.083 mm	0.429 ± 0.052 mm
IMT bias	0.022 ± 0.081 mm	–
IMT absolute error	0.061 ± 0.058 mm	–
IMT squared error	0.007 ± 0.015 mm^2	–
FoM	94.7 %	–

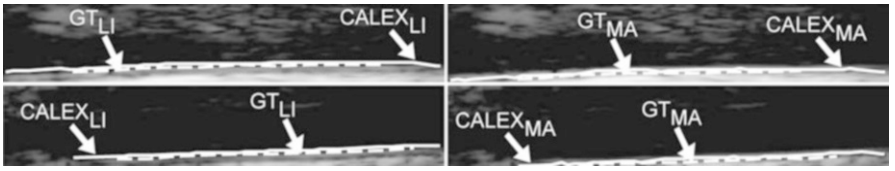

Fig. 17.7 Samples of CALEX 3.0 automated segmentation (*white lines*) compared to manual segmentations (*white dashed lines*). The *left column* reports the lumen–intima profiles, the *right* the media–adventitia

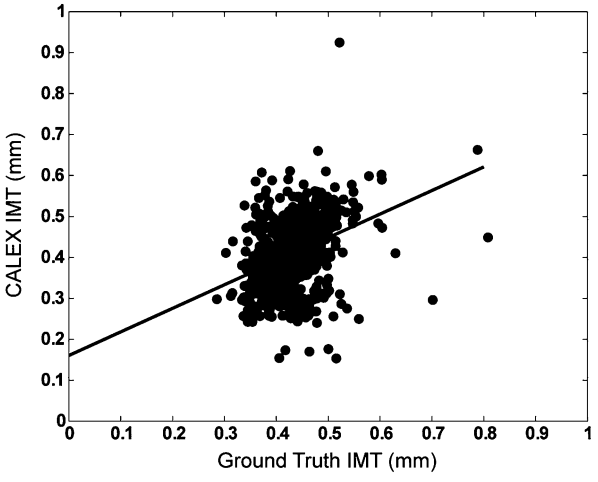

Fig. 17.8 Correlation plot between CALEX 3.0 IMT values (*vertical axis*) and GT IMT values (*horizontal axis*)

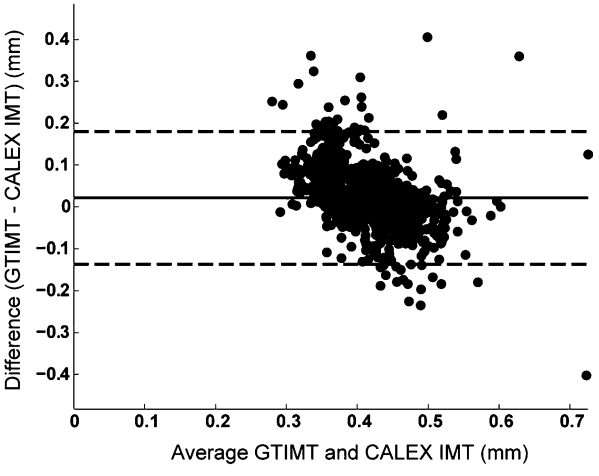

Fig. 17.9 Bland–Altmann plot of the CALEX 3.0 IMT measurements compared to ground truth

Figure 17.6 reports samples of CARES 3.0 automated segmentation. Figure 17.7 reports samples of CALEX 3.0 automated segmentation compared to ground truth (GT). The left column of Fig. 17.7 shows the comparison of the LI profiles w.r.t. GT, while the right column of Fig. 17.7 shows for the MA profiles. The CALEX 3.0 profiles are depicted by continuous white lines, whereas the GT profiles by dashed lines. Figure 17.7 clearly demonstrates that the overall agreement between automated and manual profiles.

Figures 17.8, 17.9, and 17.10 depict the overall CALEX 3.0 performance. Specifically, Fig. 17.8 reports the correlation plot between the CALEX 3.0 IMT measurements and the corresponding GT IMT values.

Figure 17.9 reports the Bland–Altmann plot for CALEX 3.0 compared to GT. Finally, Fig. 17.10 reports the histogram distribution of the IMT measurement bias (as defined in Appendix 1). The black line on the histogram is the cumulative function. From Fig. 17.9 it is possible to observe that CALEX 3.0 IMT error is as low as 0.022 mm (black line) with reproducibility lower than 1 mm (equal to 0.081 mm—dashed lines). This IMT measurement error was about 5 % of the average IMT value on the population (manually measured as 0.429 mm—Table 17.1). The Bland–Altmann plot (Fig. 17.9) did not evidence any clear trend in the IMT measurement error. The distribution of the IMT error was in

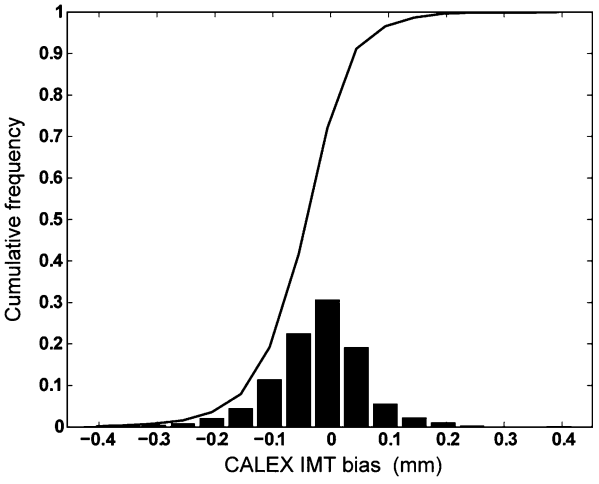

Fig. 17.10 Histogram distribution of the IMT measurement bias. It can be noticed that the average IMT bias is very low and the standard deviation of the histogram is lower than 0.1 mm

the range [−0.2, 0.2] mm (Fig. 17.10), which was an index of high system reproducibility. The cumulative function of the histogram revealed that less than 7 % of the images had an IMT error higher than 0.1 mm. Also, the average IMT error is centered on zero and the error distribution is symmetrical, thus evidencing that there is not a clear tendency towards

under- or overestimation of the IMT value. This was an indication of high system accuracy.

The optimization of the system and the integrated architecture lowered the computational time to be about 1 s for each image. With this automated tool, therefore, we could process the 885 images of our database in less than 15 min.

6 Are Fully Automated Systems Ready for Epidemiological Studies?

In this chapter we showed the potential of CALEX 3.0—an automated IMT measurement applied to an epidemiological study. This study is novel for many reasons:

1. It is the first time a fully automated method for carotid IMT measurement (a class of patented AtheroEdge® systems) has been applied to an epidemiological study
2. The dataset was relatively large (about 885 images) with low contract and low resolution
3. The CALEX 3.0 is accurate and provides reproducible results
4. The system takes 2 s per image and is near real time
5. There is no user interaction involved and is thus fully automated
6. The system parameters are automatically and dynamically adjusted

Our technique showed very good performance when applied to this database. The major challenge we had to face was the low pixel density of the B-Mode ultrasound images. We measured a pixel density of 12.7 pixels/mm, which led to a pixel physical dimension of 0.0787 mm/pixel (conversion factor). Since the average IMT value manually measured by an expert sonographer came out to be about 0.42 mm, it means that the IMT was represented on about 5.7 pixels in thickness. Thus it is very challenging for an automated system to find the LI/MA borders which are just 5–6 pixels apart. For example, if the IMT measurement error was of 0.5 pixels (that is a sub-pixel error), the measurement error would be of about 0.04 mm; this accounts to 10 % of the average IMT value on the sample population. Our IMT measurement bias and reproducibility was 0.022 ± 0.081 mm, nearly less than a quarter of a pixel—hence highly accurate.

From a technical point of view, CALEX 3.0 performance was satisfactory both in terms of measurement accuracy and of reproducibility. The accuracy of about 0.02 mm is in line with that of semiautomated techniques. For example, Stein et al. [34] tested their semiautomated edge-based system for IMT measurement on 300 images, acquired on 25 consecutive controls and 25 consecutive patients referred to the IMT measurement by their physician. They got an error of 0.012 ± 0.006 mm. Faita et al. [35] obtained an IMT measurement bias equal to 0.01 ± 0.038 mm and tested their semiautomated algorithm based on an edge snapper on 150 images taken from 80 healthy subjects and 70 patients with increased cardiovascular risk. Though there the difference between our method and Faita et al. and Stein's is in the range of 0.012 mm, we have to keep in mind that a great amount of user interaction was done in these methods. Further, their techniques were fine-tuned for a specific ultrasound scanner, while CALEX 3.0 was not specifically modified in order to work with the images of this Asian Indian database.

We believe that the most important results of CALEX 3.0 were the high reproducibility of the IMT measurement. The standard deviation of the IMT bias (i.e., what is called reproducibility) was as low as 0.081 mm. Compared to Stein's technique, which is the most reproducible method we found in the literature, CALEX 3.0 could still have scope of improvement. Nevertheless, the value of 1 mm for reproducibility can be nowadays considered as the threshold limit for automated techniques [36]. In fact, fully automated techniques need superior architecture and quality controls in order to optimize the IMT computation with respect to the semiautomated and user-driven techniques, and the lack of such controls increases the IMT bias standard deviation (thus lowering reproducibility).

Finally, CALEX 3.0 is an IMT automated measurement paradigm that has been integrated into a versatile and commercial platform called AtheroEdge® (Global Biomedical Technologies, Inc., CA, USA).

7 Conclusion

We demonstrated the usage of AtheroEdge® class of system on a low contrast and low-resolution (pixel density was 12.7 pixels/mm) epidemiological study consisting of a database of 885 carotid ultrasound images. The CALEX 3.0 fully automated system processed 100 % of the images in the dataset and shows an IMT measurement bias (compared to human tracings) of 0.022 ± 0.081 mm, comparable to previous semiautomated methods on accuracy and reproducibility. This CALEX 3.0 can therefore be used in large multicentric and epidemiological studies involving low-resolution imaging acquired by low-end ultrasound equipments.

Acknowledgements The Hyderabad DXA Study was funded by the Wellcome Trust (WT083707MA).

Appendix 1. Polyline Distance

The polyline distance metric (PDM) is a robust metric to define the distance between two boundaries. The basic idea is to measure the distance of each vertex of a boundary to the segments of the other boundary. The polyline distance from vertex v to the boundary B_2 can be defined as the minimum

distance between v and the segments of B_2. The distance between the vertexes of B_1 and the segments of B_2 is then defined as the sum of the distances from the vertexes of B_1 to the closest segment of B_2. Let's call this distance as $d(B_1,B_2)$. Similarly, it is possible to calculate the distance between the vertices of B_2 and the closest segment of B_1 (let's call this distance as $d(B_2,B_1)$). The polyline distance between boundaries is the defined as

$$D\left(B_1, B_2\right) = \frac{d\left(B_1, B_2\right) + d\left(B_2, B_1\right)}{(\#\text{ of vertices of } B_1 + \#\text{ of vertices of } B_2)} \tag{17.1}$$

Appendix 2. Definition of the IMT Bias, Absolute Error, and Squared Errors

Let IMT_i be the intima–media thickness value automatically computed by CALEX 3.0 on the ith image of the database. Let GTIMT_i be the IMT value computed by manual measurements.

The IMT measurement bias ε_i is defined as

$$\varepsilon_i = \mathrm{GTIMT}_i - \mathrm{IMT}_i \tag{17.2}$$

The absolute value μ_i of the IMT bias is defined as

$$\mu_i = |\mathrm{IMT}_i - \mathrm{GTIMT}_i| \tag{17.3}$$

The squared error η_i is, finally, defined as

$$\eta_i = |\mathrm{IMT}_i - \mathrm{GTIMT}_i|^2 \tag{17.4}$$

By averaging all these error metrics on the N images of the database, we computed the overall system errors as:

$$\overline{\varepsilon} = \frac{1}{N}\sum_{i=1}^{N}\varepsilon_i \tag{17.5}$$

$$\overline{\mu} = \frac{1}{N}\sum_{i=1}^{N}\mu_i \tag{17.6}$$

$$\overline{\eta} = \frac{1}{N}\sum_{i=1}^{N}\eta_i \tag{17.7}$$

Appendix 3. Figure-of-Merit

Let IMT_i be the intima–media thickness value automatically computed by CALEX 3.0 on the ith image ofthe database. Let GTIMT_i be the IMT value computed by manual measurements. If we consider a database of N images, then the overall system IMT estimate can be defined as

$$\overline{\mathrm{IMT}} = \frac{1}{N}\sum_{i=1}^{N}\mathrm{IMT}_i \tag{17.8}$$

$$\overline{\mathrm{GTIMT}} = \frac{1}{N}\sum_{i=1}^{N}\mathrm{GTIMT}_i \tag{17.9}$$

The Figure-of-Merit (FoM) is mathematically represented as

$$\mathrm{FoM} = 100 - \left|\frac{\overline{\mathrm{IMT}} - \overline{\mathrm{GTIMT}}}{\overline{\mathrm{GTIMT}}}\right| \times 100 \tag{17.10}$$

References

1. WHO. Cardiovascular disease [WWW document]. http://www.who.int/cardiovascular_diseases/en/
2. Badimon JJ, Ibanez B, Cimmino G (2009) Genesis and dynamics of atherosclerotic lesions: implications for early detection. Cerebrovasc Dis 27(Suppl 1):38–47
3. Walter M (2009) Interrelationships among HDL metabolism, aging, and atherosclerosis. Arterioscler Thromb Vasc Biol 29:1244–1250
4. Kampoli AM, Tousoulis D, Antoniades C, Siasos G, Stefanadis C (2009) Biomarkers of premature atherosclerosis. Trends Mol Med 15:323–332
5. U-King-Im JM, Young V, Gillard JH (2009) Carotid-artery imaging in the diagnosis and management of patients at risk of stroke. Lancet Neurol 8:569–580
6. Kastelein JJ, Wiegman A, de Groot E (2003) Surrogate markers of atherosclerosis: impact of statins. Atheroscler Suppl 4:31–36
7. Polak JF, Pencina MJ, Meisner A, Pencina KM, Brown LS, Wolf PA, D'Agostino RB Sr (2010) Associations of carotid artery intima-media thickness (IMT) with risk factors and prevalent cardiovascular disease: comparison of mean common carotid artery IMT with maximum internal carotid artery IMT. J Ultrasound Med 29:1759–1768
8. Touboul PJ, Hennerici MG, Meairs S, Adams H, Amarenco P, Bornstein N et al (2007) Mannheim carotid intima-media thickness consensus (2004–2006). An update on behalf of the Advisory Board of the 3rd and 4th Watching the Risk Symposium, 13th and 15th European Stroke Conferences, Mannheim, Germany, 2004, and Brussels, Belgium, 2006. Cerebrovasc Dis 23:75–80
9. Touboul PJ, Hennerici MG, Meairs S, Adams H, Amarenco P, Desvarieux M et al (2004) Mannheim intima-media thickness consensus. Cerebrovasc Dis 18:346–349
10. Watanabe H, Yamane K, Egusa G, Kohno N (2004) Influence of westernization of lifestyle on the progression of IMT in Japanese. J Atheroscler Thromb 11:330–334
11. van der Meer IM, Bots ML, Hofman A, del Sol AI, van der Kuip DA, Witteman JC (2004) Predictive value of noninvasive measures of atherosclerosis for incident myocardial infarction: the Rotterdam Study. Circulation 109:1089–1094
12. Liu L, Zhao F, Yang Y, Qi LT, Zhang BW, Chen F et al (2008) The clinical significance of carotid intima-mediathickness in cardiovas-

cular diseases: a survey in Beijing. J Hum Hypertens 22:259–265
13. (1991) Beneficial effect of carotid endarterectomy in symptomatic patients with high-grade carotid stenosis. North American Symptomatic Carotid Endarterectomy Trial Collaborators. N Engl J Med 325:445–453
14. Fisher M, Martin A, Cosgrove M, Norris JW (1993) The NASCET-ACAS plaque project. North American Symptomatic Carotid Endarterectomy Trial. Asymptomatic Carotid Atherosclerosis Study. Stroke 24:I24–I25, discussion I31–I32
15. Grogan JK, Shaalan WE, Cheng H, Gewertz B, Desai T, Schwarze G et al (2005) B-mode ultrasonographic characterization of carotid atherosclerotic plaques in symptomatic and asymptomatic patients. J Vasc Surg 42:435–441
16. Johnsen SH, Mathiesen EB (2009) Carotid plaque compared with intima-media thickness as a predictor of coronary and cerebrovascular disease. Curr Cardiol Rep 11:21–27
17. Bhuiyan AR, Srinivasan SR, Chen W, Paul TK, Berenson GS (2006) Correlates of vascular structure and function measures in asymptomatic young adults: the Bogalusa Heart Study. Atherosclerosis 189:1–7
18. Schargrodsky H, Hernandez-Hernandez R, Champagne BM, Silva H, Vinueza R, Silva Aycaguer LC et al (2008) CARMELA: assessment of cardiovascular risk in seven Latin American cities. Am J Med 121:58–65
19. de Groot E, van Leuven SI, Duivenvoorden R, Meuwese MC, Akdim F, Bots ML, Kastelein JJ (2008) Measurement of carotid intima-media thickness to assess progression and regression of atherosclerosis. Nat Clin Pract Cardiovasc Med 5:280–288
20. Rothwell PM, Gibson RJ, Slattery J, Warlow CP (1994) Prognostic value and reproducibility of measurements of carotid stenosis. A comparison of three methods on 1001 angiograms. European Carotid Surgery Trialists' Collaborative Group. Stroke 25:2440–2444
21. Naqvi TZ (2006) Ultrasound vascular screening for cardiovascular risk assessment. Why, when and how? Minerva Cardioangiol 54:53–67
22. Sipila O, Blomqvist P, Jauhiainen M, Kilpelainen T, Malaska P, Mannila V et al (2011) Reproducibility of phantom-based quality assurance parameters in real-time ultrasound imaging. Acta Radiol 52(6):665–669
23. Lieu D (2010) Ultrasound physics and instrumentation for pathologists. Arch Pathol Lab Med 134:1541–1556
24. Loizou CP, Pattichis CS, Pantziaris M, Tyllis T, Nicolaides A (2006) Quality evaluation of ultrasound imaging in the carotid artery based on normalization and speckle reduction filtering. Med Biol Eng Comput 44:414–426
25. Molinari F, Zeng G, Suri JS (2010) An integrated approach to computer-based automated tracing and its validation for 200 common carotid arterial wall ultrasound images: a new technique. J Ultrasound Med 29:399–418
26. Molinari F, Zeng G, Suri JS (2010) Intima-media thickness: setting a standard for completely automated method for ultrasound. IEEE Trans Ultrason Ferroelectr Freq Control 57:1112–1124
27. Molinari F, Liboni W, Giustetto P, Badalamenti S, Suri JS (2009) Automatic computer-based tracings (ACT) in longitudinal 2-D ultrasound images using different scanners. J Mech Med Biol 9:481–505
28. Molinari F, Zeng G, Suri J (2010) Greedy technique and its validation for fusion of two segmentation paradigms leads to an accurate intima-media thickness measure in plaque carotid arterial ultrasound. J Vasc Ultrasound 34:63–73
29. Molinari F, Zeng G, Suri J (2011) Inter-greedy technique for fusion of different segmentation strategies leading to high-performance carotid IMT measurement in ultrasound images. J Med Syst 35(5):905–919
30. Saba L, Montisci R, Molinari F, Tallapally N, Zeng G, Mallarini G, Suri JS (2012) Comparison between manual and automated analysis for the quantification of carotid wall by using sonography. A validation study with CT. Eur J Radiol 81(5):911–918
31. Saba L, Sanfilippo R, Tallapally N, Molinari F, Montisci R, Mallarini G, Suri JS (2011) Evaluation of carotid wall thickness by using computed tomography (CT) and semi-automated ultrasonographic software. J Vasc Ultrasound 35(3):136–142
32. Molinari F, Zeng G, Suri JS (2010) Effect of learning algorithm on automated tracings of adventitia borders in atherosclerotic common carotid artery (CCA) ultrasound. In: 2010 AIUM annual convention, San Diego, CA
33. Suri JS, Haralick RM, Sheehan FH (2000) Greedy algorithm for error correction in automatically produced boundaries from low contrast ventriculograms. Pattern Anal Appl 3:39–60
34. Stein JH, Korcarz CE, Mays ME, Douglas PS, Palta M, Zhang H et al (2005) A semiautomated ultrasound border detection program that facilitates clinical measurement of ultrasound carotid intima-media thickness. J Am Soc Echocardiogr 18:244–251
35. Faita F, Gemignani V, Bianchini E, Giannarelli C, Ghiadoni L, Demi M (2008) Real-time measurement system for evaluation of the carotid intima-media thickness with a robust edge operator. J Ultrasound Med 27:1353–1361
36. Molinari F, Zeng G, Suri JS (2010) A state of the art review on intima-media thickness (IMT) measurement and wall segmentation techniques for carotid ultrasound. Comput Methods Programs Biomed 100:201–221

Carotid Artery Recognition System (CARS): A Comparison of Three Automated Paradigms for Ultrasound Images

18

Filippo Molinari, Kristen Mariko Meiburger, U. Rajendra Acharya, William Liboni, Andrew Nicolaides, and Jasjit S. Suri

1 Introduction

Ultrasound imaging showed a rapid rise in last 5 years in several diagnostic fields. The cutting edge of ultrasound diagnostics is represented by cardiovascular and cerebrovascular applications. There are an increasing number of computer-aided techniques dedicated to the assessment of the artery wall status. This chapter illustrates a unique and innovative framework for the automated localization of the arterial morphology in the ultrasound image frame.

Several studies from around the world have demonstrated the correlation between the characteristics of the carotid artery wall and the risk of cerebrovascular diseases (CVDs) [1–3]. The most used and validated marker of progression of atherosclerosis and CVDs is the intima–media thickness (IMT) [4–6]. It has been shown that the carotid IMT is a valuable risk marker for CVDs [4, 5] with specific predictive value for incident myocardial infarction [7]. Ultrasound is commonly used to assess the carotid status and for monitoring. The most used and validated marker of progression of carotid artery diseases is the intima–media thickness (IMT) [4, 5]. The IMT value can be measured by using ad hoc computer techniques and image processing strategies. The goal is to segment the carotid artery distal wall, in order to find the lumen–intima (LI) and media–adventitia (MA) interfaces. The distance between such interfaces is taken as estimate of IMT.

Conceptually, the segmentation process can be thought as sequence of two steps [8, 9]:

- Stage-I: recognition of carotid artery (CA) in an ultrasound image
- Stage-II: delineation of the wall boundaries in the ROI of the recognized CA

In Stage-I, the carotid artery must be located or recognized in the image frame. This step is usually better performed by human experts, who mark the position of the carotid artery by placing markers or by tracing rectangular region of interests (ROIs). In Stage-II, segmentation of the walls is performed in the region of interest where the carotid distal wall portion has been recognized. Once the LI and MA borders are determined during the segmentation process, IMT can be measured. These two steps may not be independent. In fact, an incorrect ROI of the region containing the carotid walls may preclude the optimal performance of the wall segmentation algorithm and IMT measurement. Therefore, complete automation can be achieved only by designing both Stage-I and Stage-II independent of the user. This means that appropriate detection strategies are required in order to automatically localize the carotid artery in the image during the Stage-I process. Such strategies must be robust with respect to noise. Also, they must be able to process carotids with different geometrical appearance (i.e., horizontal, inclined, curved, kinked, or walls with intermittent gaps).

F. Molinari (✉) • K.M. Meiburger
Biolab, Department of Electronics, Politecnico di Torino, Corso Duca degli Abruzzi 24, 10129 Torino, Italy
e-mail: filippo.molinari@polito.it; kristen.meiburger@polito.it

U.R. Acharya
Department of Electronics and Computer Engineering, Ngee Ann Polytechnic, Clementi Road, Singapore

Department of Biomedical Engineering, Faculty of Engineering, University of Malaya, Malaysia
e-mail: aru@np.edu.sg

W. Liboni
"Un Passo Insieme" ONLUS Fundation, Valdellatorre, Torino, Italy
e-mail: wil.liboni@alice.it

A. Nicolaides
Vascular Screening and Diagnostic Centre, London, UK

Department of Biological Sciences, University of Cyprus, Nicosia, Cyprus
e-mail: anicolaides1@gmail.com

J.S. Suri
Diagnostic and Monitoring Division, AtheroPoint LLC, Roseville, CA, USA

Department of Biomedical Engineering (Aff.), Idaho State University, Pocatello, ID, USA
e-mail: jsuri@comcast.net

L. Saba et al. (eds.), *Multi-Modality Atherosclerosis Imaging and Diagnosis*,
DOI 10.1007/978-1-4614-7425-8_18, © Springer Science+Business Media, LLC 2014

The majority of the IMT measurement and segmentation techniques that can be found in the literature are user driven [10]. This means that Stage-I (i.e., carotid localization or recognition) usually requires human operator or a trained sonographer. In a recent review by Molinari and Suri, we analyzed the most recent and adopted techniques for carotid wall segmentation and IMT measurement [10]. Any user interaction precludes real automation of the technique, slows the analysis process, as it can be iterative, and introduces a dependence on the operator if the gain settings are not optimal. This brings subjectivity in the process. Different studies reported inter-subject variability associated with the IMT measurement that could be as high as 0.05 mm [11–13]. Complete automation, conversely, enables the processing of large image volumes and can be an asset for multicenter large studies. Further, correct intelligent automation of CA recognition aids in Stage-II, i.e., accurate wall segmentation. Thus, the goal of this chapter is to automatically estimate the far adventitia border (AD_F) automatically.

Since 2005, our team developed completely automated methods for ultrasound vascular wall image segmentation and IMT measurement [14–17]. Our first method was based on local statistics [14]. We observed that speckle and noise sources like blood backscattering and image artifacts could alter the carotid lumen, thus weakening the local statistic approach. We then proposed a feature-based technique [16], which exploited the image brightness features, but had the drawback of requiring a strong fitting and classification scheme. In 2011, we proposed a versatile and multiresolution approach [18] that is very robust to noise. Hence, continuous research in improving performance was carried out by our team in last 5 years. We demonstrated that in spite of the presence of the noise, automated techniques could reach performance similar to those of semiautomated ones only by adopting intelligent and integrated approaches [19]. Therefore, we always paid particular attention to Stage-I. In fact, we showed that the inaccuracies in this Stage-I could easily propagate to Stage II and can affect the overall performance of the algorithm [9, 16]. In this chapter, therefore, we will provide an extended overview of our recognition architectures along with their experimental characterization.

There are no studies available in the literature that compare the performance of different techniques for Stage-I, i.e., the automated recognition of CA. Recently, two groups (Rossi et al. [20] and Golemati et al. [21]) published fully automated techniques for carotid images processing. However, in these studies, the performance relative to Stage-I was missing. Specifically, Rossi et al. [20] measured the distance between the computer-based carotid lumen centerline and the centerline traced by a semiautomated method. If the distance was lower than 2 mm, they considered the carotid as correctly recognized. However, they did not state which distance metric they had used to measure the distance between the two centerline profiles. Golemati et al. [21] focused their paper on carotid segmentation and IMT measurement; thus they did not provide performance evaluation on carotid recognition.

We show the comparative characterization of Stage-I of three completely automated paradigms we developed. The techniques are named as CARSgd, CARSsa, and CARSia, off shoots of some of our previous work [15–17]. CARSgd (carotid artery recognition system using first-order derivative Gaussian edge approach) is the most recent and innovative approach and is based on first-order derivative Gaussian edge analysis. CARSia (carotid artery recognition system using integrated approach) detects the carotid artery by relying on a combined approach of feature extraction, fitting, and classification [16]. CARSsa (carotid artery recognition system using signal processing approach) is based on local statistics and distribution of the pixels and its features [9, 15].

We benchmarked the three techniques on a database consisting of 365 images consisting of normal and pathological arteries. We used the Hausdorff Distance as performance metric and we measured the distance between the far adventitial border traced by the three automated CA recognition techniques and the corresponding adventitia and LI/MA profiles that were manually drawn by experts, so-called ground truth. Also, the three expert sonographers visually inspected results and determined the pass or fail for each image.

The chapter is organized as follows. We will start with describing each technique in detail, and then we will present our image testing set and our validation and benchmarking methods. We will then discuss the results and show how this automated carotid artery recognition system (CARS) could be used in large epidemiological and multi-centric studies about atherosclerosis.

2 CARS System Overview: Three Different and Complementary Paradigms

In this section, we will describe the CARS system in detail. We will mathematically define the architecture of the three automated subsystems and their behavior. We will show the fundamental ideas, which are the basis of each component.

Usually, B-Mode ultrasound images cannot be directly processed as they come from the ultrasound scanner. This because ultrasound data (i.e., the region of interest for processing) are confined in a limited and defined region of the image, which must be individuated prior to any further processing. Hence, preliminarily, the ultrasound image was automatically cropped in order to discard the surrounding black frame containing device headers and image/patient text data [9]. For a DICOM formatted image,

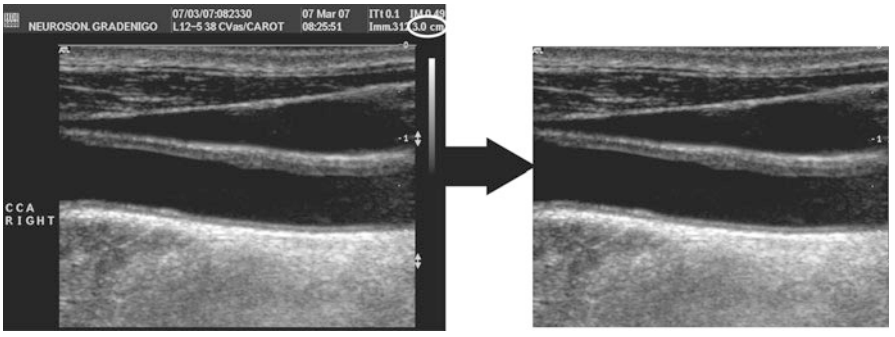

Fig. 18.1 Automated cropping of the ultrasound DICOM image. The original image frame (*left*) is cropped (*right*). The *white circle* indicates the scanning depth, which could be used for manual computation of the calibration factor

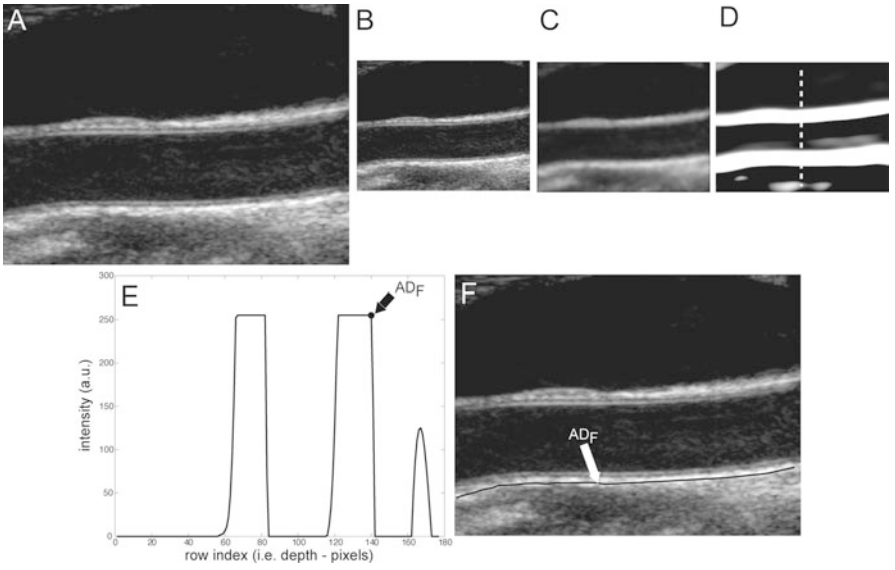

Fig. 18.2 CARSgd procedure for AD_F tracing. (**a**) Original cropped image. (**b**) Downsampled image. (**c**) Despeckled image. (**d**) Image after convolution with first-order Gaussian derivative ($\sigma = 8$). (**e**) Intensity profile of the column indicated by the *vertical dashed line* in panel **d** (AD_F indicates the position of the far adventitia wall). (**f**) Cropped image with far adventitia profile overlaid

we relied on the data contained in the specific field named "`SequenceOfUltrasoundRegions`," which contains four subfields that mark the location of the image containing the ultrasound representation. The raw B-Mode DICOM image was then cropped in order to extract only the portion that contains the carotid morphology. Alternatively, if the image was in a non-DICOM format, or if the DICOM tags were not fully formatted, we adopted a gradient-based procedure. We computed the horizontal and vertical Sobel gradients of the image. The beginning of the image region containing the ultrasound data can be calculated as the first row/column with gradient different from zero. Similarly, the end of the ultrasound region was computed as the last nonzero row/column of the gradient. Figure 18.1 depicts a sample of automated cropping: the original DICOM raw image (left) is cropped (right). The cropped image was then fed as input to the CARSgd, CARSia, or CARSsa algorithm, respectively.

2.1 CARSgd: Far Adventitia Border Detection Based on First-Order Derivative Gaussian Edge Analysis

The completely automated technique we developed and named CARSdg consists of a novel and low-complexity procedure. Figure 18.2 shows the steps of the automatic CA recognition, starting with the automatically cropped image (Fig. 18.2a), which constitutes the input to the recognition procedure. This is discussed in more detail here:

- *Step 1*: Fine to coarse downsampling. The image was first downsampled by a factor of two (i.e., the number of rows and columns of the image was halved) (Fig. 18.2b). We implemented the downsampling method discussed by Zhen et al. [22], adopting a bi-cubic interpolation. This method was tested on ultrasound images and showed a good accuracy and a low computational cost [22]. Downsampling prepares the vessel wall's edge boundary

such that the vessel wall thickness tends to be equivalent to the scale of the Gaussian kernels (used in Step 3 for wall recognition). This paradigm will yield an automated recognition of the distal (far) adventitia layer. Thus a guidance zone can be built around this far adventitia border for wall segmentation. Fan et al. [23] adopted a similar approach to measure the diameter of the brachial artery. They used a Gaussian higher order filtering to create a guidance zone. Segmentation was then performed by relying on a template matching strategy.

- *Step 2*: Speckle reduction. Speckle was attenuated by using a first-order local statistics filter (named as *lsmv* by the authors [24, 25]), which gave the best performance in the specific case of carotid imaging. This filter is defined by the following equation:

$$J_{x,y} = \bar{I} + k_{x,y}(I_{x,y} - \bar{I}) \tag{18.1}$$

where $I_{x,y}$ is the intensity of the noisy pixel, $\bar{I}$ is the mean intensity of a $N \times M$ pixel neighborhood, and $k_{x,y}$ is a local statistic measure. The speckle-free central pixel in the moving window is indicated by $J_{x,y}$. Loizou et al. [24] mathematically defined $k_{x,y} = \frac{\sigma_I^2}{\bar{I}^2\sigma_I^2+\sigma_n^2}$, where σ_I^2 represents the variance of the pixels in the neighborhood, and σ_n^2 is the variance of the noise in the cropped image. An optimal neighborhood size was shown to be 7×7. Figure 18.2c shows the despeckled image. Note that the despeckle filter is useful in removing the spurious peaks if any during the distal (far) adventitia identification in subsequent steps.

- *Step 3*: First-order derivative Gaussian edge (FODGE) operator. The despeckled image was filtered by using a 35×35 pixels first-order derivative of a Gaussian kernel. Figure 18.2d shows the results of the filtering by the Gaussian derivative. The scale parameter of the Gaussian derivative kernel was taken equal to 8 pixels, i.e., half the expected dimension of the IMT value in an original fine resolution image. In fact, an average IMT value of say 1 mm corresponds to about 16 pixels in the original image scale and, consequently, to 8 pixels in the coarse or downsampled image. The white horizontal stripes of Fig. 18.2d are relative to the proximal (near) and distal (far) adventitia layers.
- *Step 4*: Automated far adventitia (AD_F) tracing. Figure 18.2e shows the intensity profile of one column of the filtered image of Fig. 18.2d. The proximal and distal walls are visible as intensity maxima saturated to the value of 255. To automatically trace the profile of the distal wall, we used a heuristic search applied to the intensity profile of each column. Starting from the bottom of the image, we search for the first white region consisting of width of at least 6 pixels (computed empirically). The deepest point of this region (i.e., the pixel with the higher row index) marked the position of the far adventitia (AD_F) layer on that column. The sequence of the points resulting from the heuristic search for all the image columns constituted the overall automated AD_F tracing.
- *Step 5*: Upsampling of far adventitia (AD_F) boundary locator. The AD_F profile was then upsampled to the original fine scale and superimposed over the original cropped image (Fig. 18.2f) for both visualization and performance evaluation.

This Stage-I essentially consists of an architecture combining fine-to-coarse downsampling for wall scale reduction, despeckle filtering, first-order derivative Gaussian Kernel edge (FODGE) filtering for wall extraction, and Heuristic-based peak detection for final segmentation of the far adventitia borders. The matching between the downsampled wall thickness and the Gaussian Kernel size (scale) ensured optimal representation of the artery. If the FODGE kernel size did not match the theoretical IMT of 8 pixels, the overall CARSgd performance decreased from 100 % ($\sigma = 8$) to 94 % for $\sigma = 6$ and 97 % for $\sigma = 10$. We chose to downsample the image and match the wall size to the FODGE kernel and not vice versa to avoid higher error propagation and to reduce the computational burden.

2.2 CARSia: Far Adventitia Border Detection Using Feature Extraction and Fitting

CARSia exploits the image information in order to automatically detect far adventitia [16]. This is based on the assumption that there exists a dark, low-intensity region (the lumen region) between the two bright, higher intensity regions (the near and far wall adventitia layers). Thus, the basic idea of CARSia is to exploit the geometrical and intensity features of the carotid artery representation to recognize the artery walls. The first step is the definition of "seed points." A seed point is a local intensity maxima located on the CA wall. Seed points are clustered from the other intensity maxima by a linear discriminator (which we preliminary trained on a subset of 15 images [16]). Once detected, seed points are then linked to form line segments. An intelligent procedure is applied to remove short or false line segments by computing the *validation* probability $P(D_{\text{valid}}|s_i)$ [see (18.2) and (18.3)] and join close and aligned segments by computing the *connectability* probability $P(D_{\text{conn}}|s_i)$ [see (18.4) and (18.5)]. This procedure avoids over-segmentation of the artery wall. Therefore, line segments classification extracts the line pair that contains the artery lumen in between.

$$P(D_{\text{valid}}|s_i) = \exp\{-\psi(D_{\text{valid}}|s_i)\} \tag{18.2}$$

where the energy function $\psi(\cdot)$ is based on the support $g_1(s_i)$ and the width stability $g_4(s_i)$ and is defined according to the following formula:

$$\psi(D_{\text{valid}}|s_i) = \omega_1 g_1(s_i) + \omega_4 g_4(s_i) \tag{18.3}$$

$$P(D_{\text{conn}}|s_i, s_j) = \exp\{-\psi(D_{\text{conn}}|s_i, s_j)\} \tag{18.4}$$

where the energy function $\psi(\cdot)$ is based on proximity $h_1(s_i, s_j)$ and alignment $h_2(s_i, s_j)$:

$$\psi(D_{\text{conn}}|s_i, s_j) = \omega'_1 h_1(s_i, s_j) + \omega'_2 h_2(s_i, s_j) \tag{18.5}$$

Here, ω_1, ω_4, ω'_1, and ω'_2 are weights determined by the training data. For each line segment s_i we defined four features:

(a) *Support*, defined as the number of seed points contained by the segment s_i (indicated by $g_1(s_i)$)
(b) *Residue*, defined as the mean squared error of the seed points with respect to their perpendicular distance from s_i (indicated by $g_2(s_i)$)
(c) *Spread*, defined as the shortest path length connecting the seed points divided by the number of seed points s_i contains (indicated by $g_3(s_i)$)
(d) *Width stability*, defined as the percentage of points along the fitted line segments s_i whose width (perpendicular distance to the nearest intensity edge) is within some tolerance of the estimated width of the adventitial layers (indicated by $g_4(s_i)$)

These are computed as follows: $g_1(s_i)$ is mathematically defined and computed as the number of seed points present on the line segment s_i.

$g_2(s_i)$ is the residue and is computed as the average Euclidean distance from the seed points to the line segment s_i. Thus it is the perpendicular distance from the seed point to the line segment s_i.

$g_3(s_i)$ is the spread function defined as the shortest path length connecting the seed points divided by the number of seed points s_i contains.

We compute the length of s_i as follows: (a) selection of any two seed points that s_i contains, and then, calculate the Euclidean distance; (b) the maximum Euclidean distance is the length of s_i.

$g_4(s_i)$ is mathematically defined as the percentage of points along the fitted line segments s_i whose width (perpendicular distance to the nearest intensity edge) is within some tolerance of the estimated width of the adventitial layers. The algorithmic steps for computation of $g_4(s_i)$ are as follows:

1. Application of the Canny edge detector on the original image. Canny edge detector uses a multistage algorithm to detect a wide range of edges in images. Because it is susceptible to noise present on rawunprocessed image data, we thus convolve the raw image with an optimal Gaussian filter.
2. For each line segment, find its closest edge. This can be done by applying connected component analysis to the binary Canny edges. Then calculate the distance from a line segment to an edge and then sort the distance values.
3. For each seed point on a line segment, we calculate the distance $\mathbf{d}_i$ to the closest edge.
4. We then compute the average distance R as the average radius of this line segment s. To remove the outliers caused by the background noise we calculate the threshold, which is the ratio $r_i = \mathbf{d}_i/R$. Our lower threshold bound is 0.8 and upper threshold bound is 1.25. Setting these threshold values can effectively remove most of outliers.
5. Finally, calculate the percentage of seed points that meet the criteria above which is called the width stability [16, 17].

Details about the definition of the above parameters are described in our previous paper [16]. Figure 18.3 summarizes CARSia functioning.

2.3 CARSsa: Local Statistics Approach

The automated approach based on local statistics was one of the first we developed and was the basis of many studies we conducted [14, 15, 17, 26–32].

This approach is based on the assumption that carotid representation can be thought of as a mixture model with varying intensity distributions. This is because the (a) pixels belonging to the vessel lumen are characterized by low mean intensity and low standard deviation; (b) pixels belonging to the adventitia layer of the carotid wall are characterized by high mean intensity and low standard deviation; and (c) all remaining pixels should have high mean intensity and high standard deviation. As a result, we derived a bi-dimensional histogram (2DH) of the carotid image. For each pixel, we considered a 10×10 neighborhood of which we calculated the mean value and the standard deviation. The mean values and the standard deviations were normalized to 0 and 1 and were grouped into 50 classes each having an interval of 0.02. The 2DH was then a joint representation of the mean value and standard deviation of each pixel neighborhood. In previous studies, we showed that pixels belonging to the lumen of the artery are usually classified into the first classes of this 2DH [9]: expert sonographer manually traced the boundaries of the CA lumen and observed the distribution of the lumen pixels on the 2DH. Overall results revealed that pixels of the lumen have a mean values classified in the first four classes and a standard deviation in the first seven classes. We therefore consider a pixel as possibly belonging to the carotid lumen if its neighborhood intensity is lower than

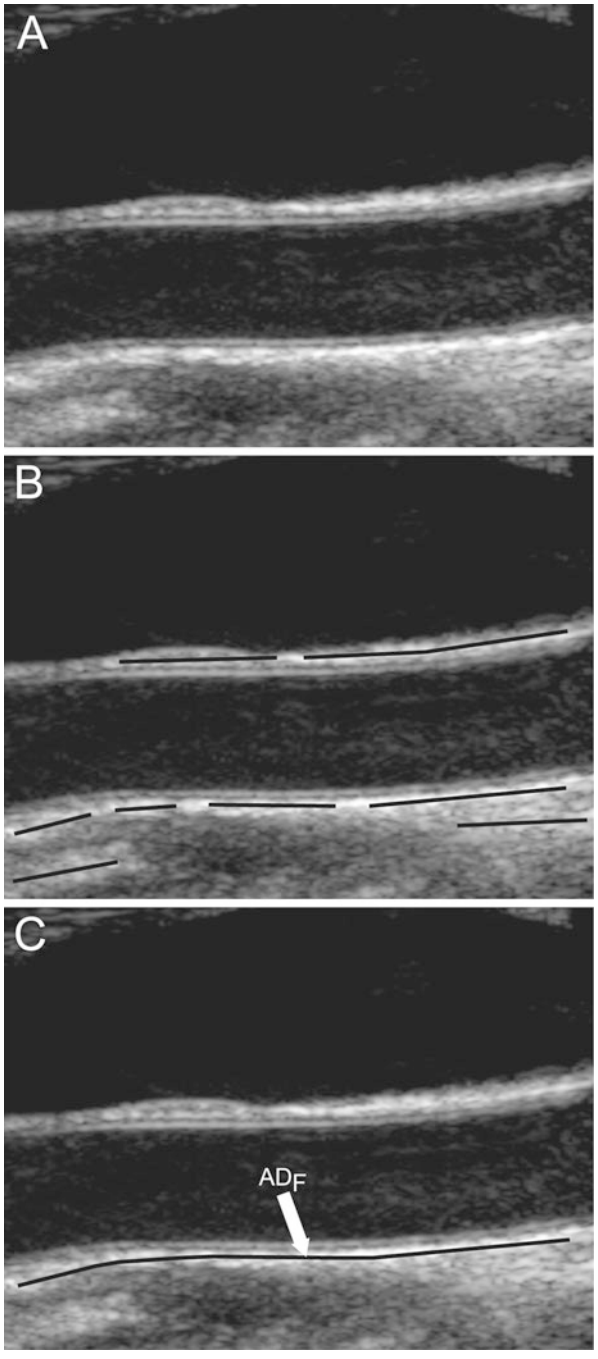

Fig. 18.3 CARSia (integrated approach) recognition strategy. (**a**) Original image. (**b**) Automatically identified line segments (*black lines*). (**c**) Final AD_F tracing after line segments validation and combination

0.08 and if its neighborhood standard deviation is lower than 0.14. Figure 18.4 shows the lumen region selection process in four images: Fig. 18.4a depicts the original image after automatic cropping; Fig. 18.4b depicts the 2D histogram (2DH) showing the relationship between the normalized mean and normalized standard deviation. The gray region in the 2DH represents what we consider the lumen region of the carotid artery. All the image pixels falling into this region have been depicted in gray in Fig. 18.4c. This example shows how the local statistic is effective in detecting image pixels that can be considered as belonging to the CA lumen.

To avoid incorrect detection of our ADF, we had to attenuate the superimposed noise and random intensity peaks. We therefore used the low-pass filter (Gaussian Kernel Size 29×29, with $\sigma = 1$) and convolved it with the image to lessen the noise and speckle effect. Schematically, the following are the steps for processing the intensity profile:

(i) *AD_F tracing*: the procedure started from the bottom most point and searched for the first maxima with an intensity value above the 90th percentile of the intensity distribution along that profile. This point was marked as possible far adventitia (AD_F) candidate. Starting from the bottom most point and searching for a local intensity maximum yielded the AD_F candidate selection quite robust, due to the hyperechoic appearance of the adventitia layer. The strong low-pass filtering preliminary to this choice attenuated possible high-intensity noisy points located above the adventitia layer.

(ii) *Lumen tracing*: For lumen estimation point, the algorithm moved upwards along the row (decreasing row value) and searched for a pixel (point) possibly belonging to the lumen. The lumen candidate was the first minima point whose neighborhood mean intensity and standard deviation values matched the criteria of the 2DH (i.e., normalized mean value lower than 0.08 and normalized standard deviation lower than 0.14, respectively).

When the two candidate points along the column were found, they were plotted on the original image in correspondence of their row index (and of the column index under analysis). If the row index reached 1 (or the last row) before the two points were found, the column was discarded and marked as unsuitable to segmentation. Figure 18.4d shows the marked points on a sample image column.

3 Image Database and Preprocessing Steps

We describe here the image dataset we used for performance analysis and validation of CARS.

Our database consisted of 365 B-model images collected from four different institutions/hospitals around the world. They are as follows:

- The Neurology Division of the Gradenigo Hospital of Torino (Italy), which provided 200 images.

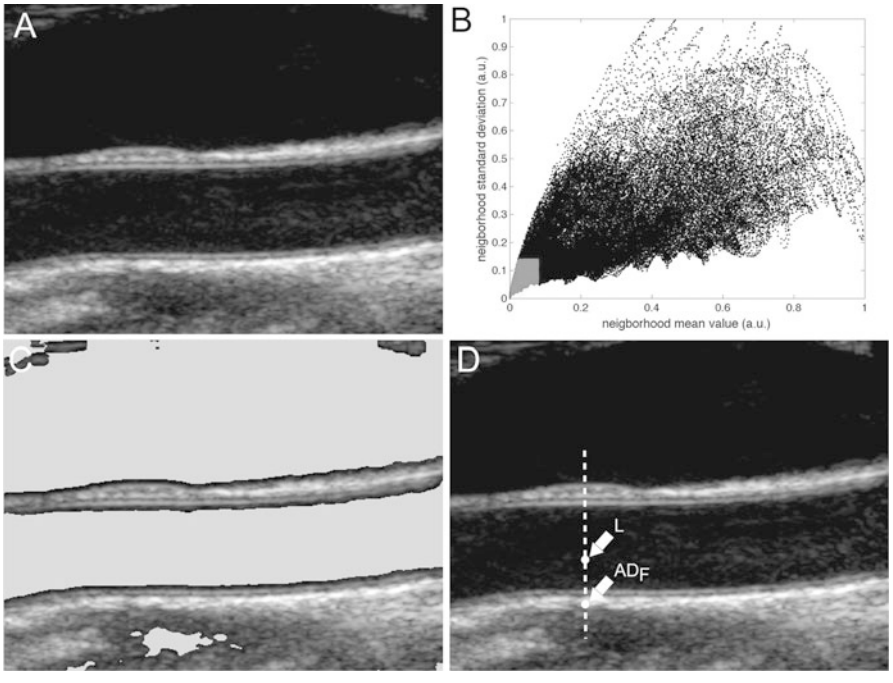

Fig. 18.4 CARSsa (signal processing) strategy for far wall adventitial tracing. (**a**) Original image. (**b**) Bidimensional histogram (2DH). The *gray portion* of the 2DH denotes the region in which we suppose to find only lumen pixels. (**c**) Original image with lumen pixels overlaid in *gray*. (**d**) Sample processing of one column, with the marker points of the far (AD_F) adventitia layer and of the lumen (L)

Table 18.1 Image database and patient demographics

Institution	Total images (N)	Conversion factor (τ) (mm/pixel)	Ultrasound scanner	Patients	Age
Torino (Italy)	200	$\tau_{\text{Torino}} = 0.0625$	ATL HDI5000	150	69 ± 16 years (50–83 years)
Nicosia (Cyprus)	100	$\tau_{\text{Nicosia}} = 0.0600$	ATL HDI3000	100	54 ± 24 years (25–95 years)
Porto (Portugal)	23	$\tau_{\text{Porto}} = 0.0900$	ATL HDI5000	23	(Not published—see refs. [15] and [16])
Cagliari (Italy)	42	$\tau_{\text{Cagliari}} = 0.0789$	Esaote MyLab 70	21	68 ± 8 years (59–81 years)

Characteristics of the image dataset coming for four different institutions and relative patient demographics. The first column reports the institution, the second the number of image, the third the conversion factor, and the fourth the scanner used. Finally, the last two columns report the number of patients and their demographics

- The Cyprus Institute of Neurology of Nicosia (Cyprus), which provided 100 images.
- The Hospital de S. João do Porto (Portugal), which provided 23 images [33, 34].
- The Department of Radiology of the University Hospital of Cagliari (Italy), which provided 42 images.

The complete description of the image database and of the patient's demographics is reported by Table 18.1. All the Institutions took care of obtaining written informed consent from the patients prior to enrolling them in the study. The experimental protocol and data acquisition procedure were approved by the respective local Ethical Committees.

Considering 342 patients (excluding the 23 from Porto), 236 subjects were male. One-hundred and twenty subjects had hypertension history, 75 had hypercholesterolemia, and 30 had both. Ten patients were diabetic. Sixty-seven patients had carotid plaque onset and 40 showed neurological signs (minor stroke, transient ischemic attack, or amaurosis fugax). The demographics for the patients from Porto were not published. Three expert sonographers (a neurologist, a vascular surgeon, and a cardiologist—all with at least 30 years of experience in their field) independently manually segmented the images by tracing the boundaries of the lumen–intima (LI) and media–adventitia (MA) interfaces. The average tracings were considered as ground truth (GT). One of the experts also manually traced the 365 adventitia profiles.

4 Hausdorff Distance Metric: How Good Is the Carotid Artery Recognition?

The Hausdorff distance (HD) between two boundaries is a measure of the longest distance that one has to travel if moving from a given point on a boundary and going to the other boundary. In other words, given the boundaries B_1 and B_2, one has to calculate the Euclidean distances of each

vertex of B_1 from the vertices of B_2. Let's indicate with d_{12} the minimum distance of the most distant vertex of B_1 from the vertices of B_2. Similarly, let's define d_{21} the minimum distance of the most distant vertex of B_2 from the vertices of B_1. The HD can be mathematically defined as

$$\mathrm{HD} = \max\{d_{12}, d_{21}\} \tag{18.6}$$

The performance of the far adventitial border automated tracing was assessed in two ways: (a) by computing the distance between AD_F and the ground-truth average LI profile and (b) by computing the distance between AD_F and the ground-truth average MA profile. Since the HD is sensible to the longest distance from the points of one boundary to the points of the other, we reduced the computer profiles to the same support of GT. This means shrinking the AD_F border, which spans the GT LI/MA profiles (or borders). In such conditions, the HD is unbiased by points that could be located out of the GT support. To make this clear and simple and easy to use ahead, we symbolize the HD between AD_F and the GT AD_F profiles as $H^{AD_F}_{GT-AD_F}$, that between AD_F and GT LI as $H^{AD_F}_{GT-LI}$, and that between AD_F and GT MA $H^{AD_F}_{GT-MA}$.

The accuracy of carotid recognition was validated using three methods: (1) comparing the AD_F tracings to the gold standard LI/MA profiles, (2) visual inspection by expert sonographers, and (3) comparison of computer traced AD_F to the gold standard AD_F.

5 Is the Hausdorff Distance a Suitable Distance Metric for Evaluating the Artery Recognition?

The Hausdorff distance, or Hausdorff metric, measures how far two subsets of a metric space are from each other. Informally, two sets are close in the HD if every point of either set is close to some point of the other set. The HD is the longest distance you can be forced to travel by an adversary who chooses a point in one of the two sets, from where you then must travel to the other set. Here the GT_{LI} boundary is a smooth lumen interface boundary actually drawn by the vascular sonographer or vascular surgeon. This boundary has no bumps as it is drawn using the knowledge of gradient information. This boundary represents the true lumen interface boundary drawn by the sonographer or physician. On the contrary, the far adventitia boundary is the boundary, which is automatically detected representing the adventitia border. Note that this is not a MA boundary, but a boundary approximately computed representing the adventitia border as a by-product of CA recognition process. This is a guiding boundary, which is actually representing the region of coarse identification of the common or internal carotid artery, corresponding to the distal wall or far fall. Because this boundary is a coarser boundary, it is very likely to be a boundary with less smoothness or more or less like a spiky nature of the boundary. Since this is an observed boundary, this spiky nature of the boundary may have sharp curvature changes. As a result, we are interested in finding the farthest distance between the AD_F and the GT_{LI} and/or between AD_F and GT_{MA}. Note that the farthest distance computation can be done using HD since it tells about the worst limit of the AD_F boundary. This helps in appreciating how worst the AD_F boundary is with respect to ground-truth LI/MA profiles. This HD will tell how good the AD_F is, given the distance limits of the AD_F with respect to LI/MA GT borders. If AD_F's limiting distance is Δ_{limit}, then AD_F should be less than the Δ_{limit}. The Δ_{limit} is computed as the maximum ROI one can support to efficiently compute accurate LI/MA borders. For our techniques we took Δ_{limit} to be about 50 pixels. This means if HD must be less than Δ_{limit} for a technique to perform better. Thus, HD is an ideal choice for evaluating the performance of the AD_F boundary, keeping the Δ_{limit} in mind.

6 IMT Measurement by First-Order Absolute Moment Operator

The final goal of automated AD_F tracing is the development of accurate IMT measurement techniques. To test the effect of AD_F accuracy and, thus, of $H^{AD_F}_{GT-LI}$ and $H^{AD_F}_{GT-MA}$ on the IMT estimation, we implemented a first-order absolute moment (FOAM) based technique. FOAM operator is a regularized edge-based operator, was first introduced by Demi et al. [35], and was then extended by Faita et al. [36] for an accurate semiautomated IMT measurement in ultrasound images. Preliminary, we built a guidance zone (GZ) around the automatically traced *far adventitia* AD_F profile. The GZ had the same width of the AD_F and height of 50 pixels (which roughly corresponds to 1/2 of the artery diameter). The GZ was then processed by FOAM, which was defined according to Faita et al. [36] as

$$e(x,y) = \iint_{\theta_2} |\, I_1(x,y) - I_2(x-k, y-l)\,| \cdot G(k,l,\sigma_3)\, \mathrm{d}k\, \mathrm{d}l \tag{18.7}$$

where $I_1(x,y) = \iint_{\theta_1} I(x-k, y-l) \cdot G(x,y,\sigma_1)\, \mathrm{d}k\, \mathrm{d}l$ and $I_2(x,y) = \iint_{\theta_2} I(x-k, y-l) \cdot G(x,y,\sigma_2)\, \mathrm{d}k\, \mathrm{d}l$ are computed by low-pass filtering the input image by a Gaussian kernel with standard deviations equal to σ_1 and σ_2, on circular domains θ_1 and θ_2, respectively. When computed in homogeneous regions (i.e., in regions without intensity changes and that are of the same gray level), the FOAM edge value is close to zero. When computed in proximity

of an intensity gradient, the FOAM edge value rises to a maximum. We linked the Gaussian Kernel sizes and σ values to the image conversion factor (the best conversion factor was $\tau_{\text{Nicosia}} = 0.06\,\text{mm/pixel}$, as reported by Table 18.1), and chose the value of $\eta_{\text{MRAFOAM}} = 0.3\,\text{mm}$ as pixel conversion factor for the FOAM operator. Hence, we used the kernel size $\theta_1 = \theta_3 = \eta_{\text{MRAFOAM}}/\tau_{\text{Nicosia}}$. This yields $\theta_1 = \theta_3 = 0.3/0.06 = 5\,\text{pixels}$. As suggested by Faita et al. [36], we took $\theta_2 = 2\theta_1 = 10\,\text{pixels}$. The Gaussian Kernel parameters were then taken equal to:

$$\begin{aligned} \sigma_1 = \sigma_3 &= \lceil \theta_1/3 \rceil = 2\ \text{pixels} \\ \sigma_2 &= \lceil \theta_2/3 \rceil = 3\ \text{pixels} \end{aligned} \tag{18.8}$$

The LI and MA edge interfaces in the GZ were then searched by relying on heuristic search, which basically searched for the two most echogenic peaks in the GZ, starting from the bottom of the GZ (and marking the MA peak) and then moving towards lumen (and marking the LI peak).

If $H^{\text{AD}_\text{F}}_{\text{GT}-\text{LI}}$ was higher than 50 pixels (3 mm; the vertical size of the Guidance Zone), the image could not be correctly processed, whereas if it was in the range, the LI/MA segmentation was possible. Hence, we considered the value Δ_{limit} of 50 pixels (3 mm) as threshold criteria for evaluating the AD_F segmentation as pass or fail for CCA carotid recognition. We however kept this threshold distance criterion in pixels as units because we had images with different pixel density (see Table 18.1).

7 CARS Performance and Challenges

In this last section of the chapter, we will show the overall CARS system performance and we will describe and discuss the challenges, the innovative solutions, the unique CARS features, the system robustness, and its weaknesses.

7.1 CARS Recognition Performance

Figure 18.5 shows the comparison of the AD_F traced by CARSgd, CARSia, and CARSsa, compared to the human traced AD_F (left column). The right column of Fig. 18.5 shows the computer traced AD_F profiles compared to human LI/MA tracings.

Table 18.2 reports the average HD results (in pixels and mm) between the three computer-based AD_F tracings and the manual AD_F and LI/MA profiles. CARSgd (first-order derivative Gaussian edge) showed AD_F tracings that were closer to the manually traced LI/MA profiles compared to CARSia (integrated approach) and CARSsa (signal processing approach). The average HD between the computer traced AD_F and the actual AD_F position was 24.93 ± 24.47 pixels (corresponding to 1.53 ± 1.51 mm) for CARSgd, 29.51 ± 50.03 pixels (1.82 ± 3.08 mm) for CARSia, and 41.60 ± 46.95 pixels (2.56 ± 2.89 mm) for CARSsa. The average HD between GT_LI and AD_F for CARSgd was equal to 35.11 ± 18.82 pixels (2.16 ± 1.16 mm), whereas that of CARSia was 43.78 ± 46.43 pixels (2.71 ± 2.89 mm) and that of CARSsa was 43.09 ± 25.33 pixels (2.66 ± 1.52 mm). The average HD between GT_MA and AD_F for CARSgd was 25.03 ± 19.47 pixels (1.54 ± 1.19 mm), which was lower than both CARSia (30.07 ± 42.88 pixels, which was 1.86 ± 2.66 mm) and CARSsa (31.67 ± 27.42 pixels, equal to 1.95 ± 1.64 mm). An F-Test performed on the HD distances from LI profiles revealed that the variance of CARSgd was statistically lower than that of CARSia (two-sided F-Test, $\alpha = 0.05$; $p < 10^{-33}$) and CARSsa (two-sided F-Test, $\alpha = 0.05$; $p < 5 \times 10^{-3}$). When testing the distances from MA profiles, only the difference between CARSgd and CARSia was significant ($p < 10^{-18}$), because CARSia showed a very variable distance between the AD_F generated boundary and the GT LI/MA profiles.

Due to this variability in CARSia tracings, the average HD between CARSgd and CARSia profiles did not prove statistically significant (Student's t-test; $p > 0.05$ for LI and MA). Also, since CARSgd variability was lower than CARSsa, the average HD values of the two techniques did not prove different ($p > 0.05$).

Figure 18.6 reports a 3×3 panel showing a possible explanation of such variability source. Our dataset incorporated normal and pathological carotids. Also, it contained arteries with different morphology: the first row of Fig. 18.6 is relative to a straight and horizontal artery, the second row to a curved artery, and the third row to a straight and inclined artery in the image frame. The white dashed lines correspond to the ground-truth LI while black corresponds to the ground-truth MA. The first column (panels a, d, and g) reports CARSgd tracings, the second column (panels b, e, and h) reports CARSia, and the third column (panels c, f, and i) CARSsa. It is possible to observe how, despite the different carotid morphology, the three techniques show correct results and identify the far adventitial border. However, the variability in the carotid appearance increased the standard deviations of the HD values. This is because AD_F tracings of straight arteries were closer to the LI/MA profiles than those of curved arteries (see Fig. 18.6a compared to Fig. 18.6d).

We used the AD_F tracings by CARSgd, CARSia, and CARSsa to assess the effect of the AD_F accuracy on the IMT measurement error by using FOAM. The original AD_F profile was progressively shifted towards the bottom of the image of 1 pixel, for a total of 16 iterations (i.e., a total shift of 16 pixels). The HD between AD_F and the MA, therefore, progressively increased. Figure 18.7 reports the average IMT measurement error (Fig. 18.7a) and its standard

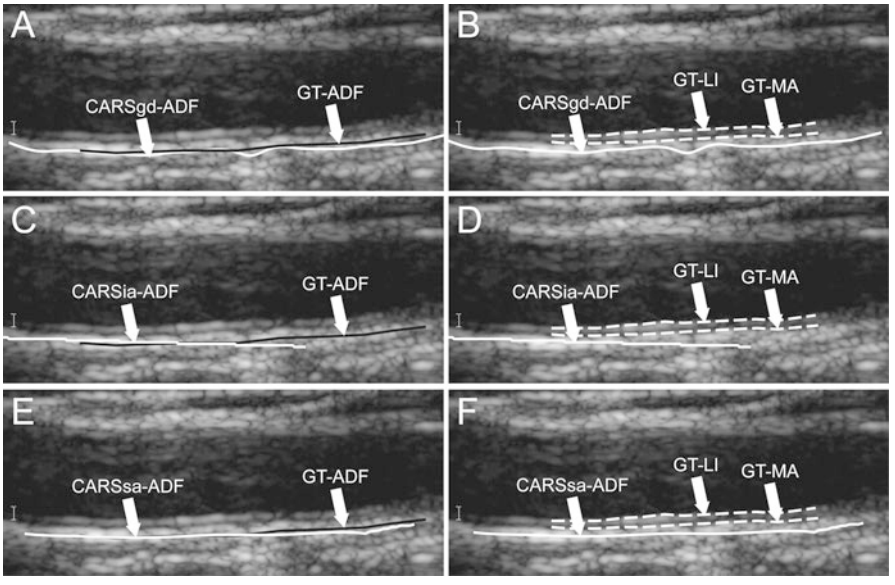

Fig. 18.5 The *left column* reports a sample of automated carotid recognition by CARSgd (**a**), CARSia (**c**), and CARSsa (**e**) compared to the human traced AD_F profile. In the *right column*, the CARSgd (**b**), CARSia (**d**), and CARSsa (**f**) AD_F profile is compared to the ground-truth LI/MA boundaries

Table 18.2 Hausdorff distance between the average ground-truth (GT) ADF (first row), LI (second row), and MA (third row) boundaries and the AD_F automated tracings by the three considered techniques

	CARSgd	CARSia	CARSsa
$H_{GT-ADF}^{AD_F}$	24.93 ± 24.47 pixels	29.51 ± 50.03 pixels	41.60 ± 46.95 pixels
	1.53 ± 1.51 mm	1.82 ± 3.08 mm	2.56 ± 2.89 mm
$H_{GT-LI}^{AD_F}$	35.11 ± 18.82 pixels	43.78 ± 46.43 pixels	43.09 ± 25.33 pixels
	2.16 ± 1.16 mm	2.71 ± 2.89 mm	2.66 ± 1.52 mm
$H_{GT-MA}^{AD_F}$	12.30 ± 11.87 pixels	16.61 ± 33.10 pixels	35.43 ± 50.49 pixels
	0.76 ± 0.73 mm	1.02 ± 2.03 mm	2.18 ± 3.10 mm

deviation (Fig. 18.7b) for the three techniques. It is possible to notice that when the shift of the AD_F reached about 6–8 pixels (half a mm), the average system error jumped rapidly. Thus, the stable value of AD_F zone was within the tolerance of 6–8 pixels (half a mm). The end of the tolerance zone can be the shoulder when the error shoots more rapidly and the effect of the AD_F on Stage-II is more profound. It is this tolerance zone where AD_F can be thought to give stable IMT measurement. Beyond the tolerance zone, the IMT measurement can be unstable. The IMT change was from 72 to 84 μm 12 μm. Thus, the error change was as low as 0.12 % when compared to the wall thickness of 1 mm. This clearly showed the robustness of the CARS systems.

We considered a Δ_{limit} value of 50 pixels (3 mm) to discriminate between correctly and incorrectly recognized carotids. CARSgd showed an identification accuracy of 100 % and correctly recognized the CA in all 365 images. With the same Δ_{limit} value, CARSia did not recognize 27 arteries out of 365 (identification accuracy of 93 %), whereas CARSsa did not recognize 15 images out of 365 (identification accuracy of 96 %). Table 18.3 reports the visual validation made by the experts who assessed the pass/fail for each image and for each technique. The visual inspection by experts gave substantially the same results we reported in the paper: CARSgd showed 100 % accuracy, CARSsa 96 %, and CARSia 93 %.

Figure 18.8 reports the distribution of the HD between ADF and LI (left column) and ADF and MA (right column) for the three techniques. Each of the three rows represents the corresponding computer-based methods. CARSia technique is reported in the first row, CARSsa technique in the second, and the CARSgd technique in the last row. The horizontal axis is the distance in mm, while the *y*-axis is the cumulative frequency normalized between 0 and 1. The cumulative frequency is also drawn as black line on the histogram. CARSgd showed 100 % reliability and correctly identified the carotid artery in all 365 images, as can be noticed by the cumulative frequency line.

The original implementation of these three techniques was done in MATLAB environment. The average computation

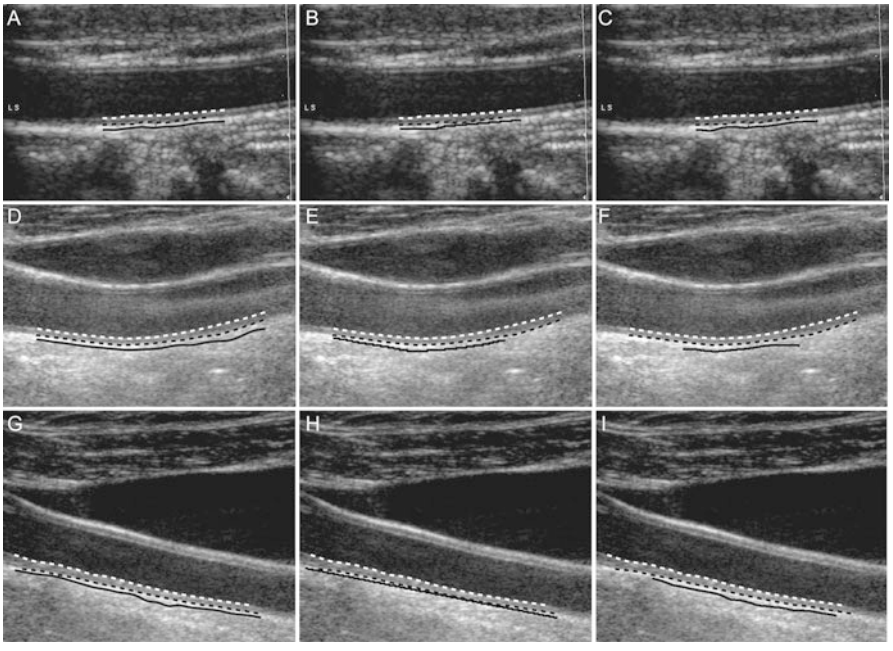

Fig. 18.6 Samples of automated far adventitia tracing by the three techniques. CARSgd is represented by panels (**a**, **d**), and (**g**). CARSia is shown in panels (**b**, **e**), and (**h**). CARSsa is represented in panels (**c**, **f**), and (**i**). The *white dashed line* represents the GT_{LI} profile, and the *black dashed line* the GT_{MA}. The *continuous black line* represents the AD_F. The first row is relative to a straight and horizontal artery; the second row to a curved artery; and the third row to a straight but inclined artery

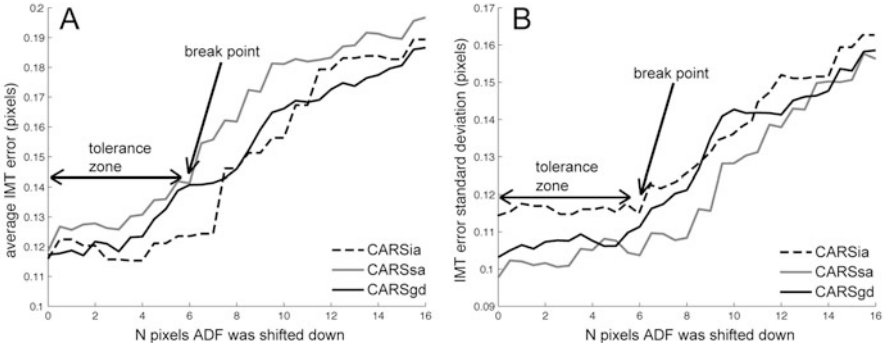

Fig. 18.7 Effect of AD_F distance from MA on the IMT measurement error. The AD_F profile was progressively shifted towards the bottom of the image (i.e., the HD from MA increased). (**a**) Average IMT measurement error for the three techniques. (**b**) Standard deviation of the IMT measurement error for the three techniques. The tolerance zone, where the error remains stable, is between 0 and 6 pixels of shift. Around 6–8 pixels there is a break point and the error increases (CARSia—*black dashed line*; CARSsa—*gray line*; CARSgd—*black line*)

Table 18.3 Performance of three techniques using visual inspection of CCA recognition

Technique types	Observer 1	Observer 2	Observer 3
CARSgd	365/365 ∼ 100 %	365/365 ∼ 100 %	365/365 ∼ 100 %
CARSia	340/365 ∼ 93.1 %	338/365 ∼ 92.6 %	341/365 ∼ 93.4 %
CARSsa	355/365 ∼ 97.2 %	352/365 ∼ 96.4 %	349/365 ∼ 95.6 %

time was 1.1 ± 0.3 s for CARSgd, 2.0 ± 1.1 for CARSia, and 20.4 ± 1.8 for CARSsa. CARSgd was the technique with lower computational burden, whereas CARSsa required a substantial amount of time to perform carotid location. From a practical point of view, CARSgd and CARSia can be considered real-time techniques, since their average processing time is of 2 s in the worst case, whereas CARSsa is not suited for real-time implementation.

We have now developed a research tool called "AtheroEdge," which runs all the three systems in 1 s per image. AtheroEdge is a cross-platform medical application written in Java and has a component framework.

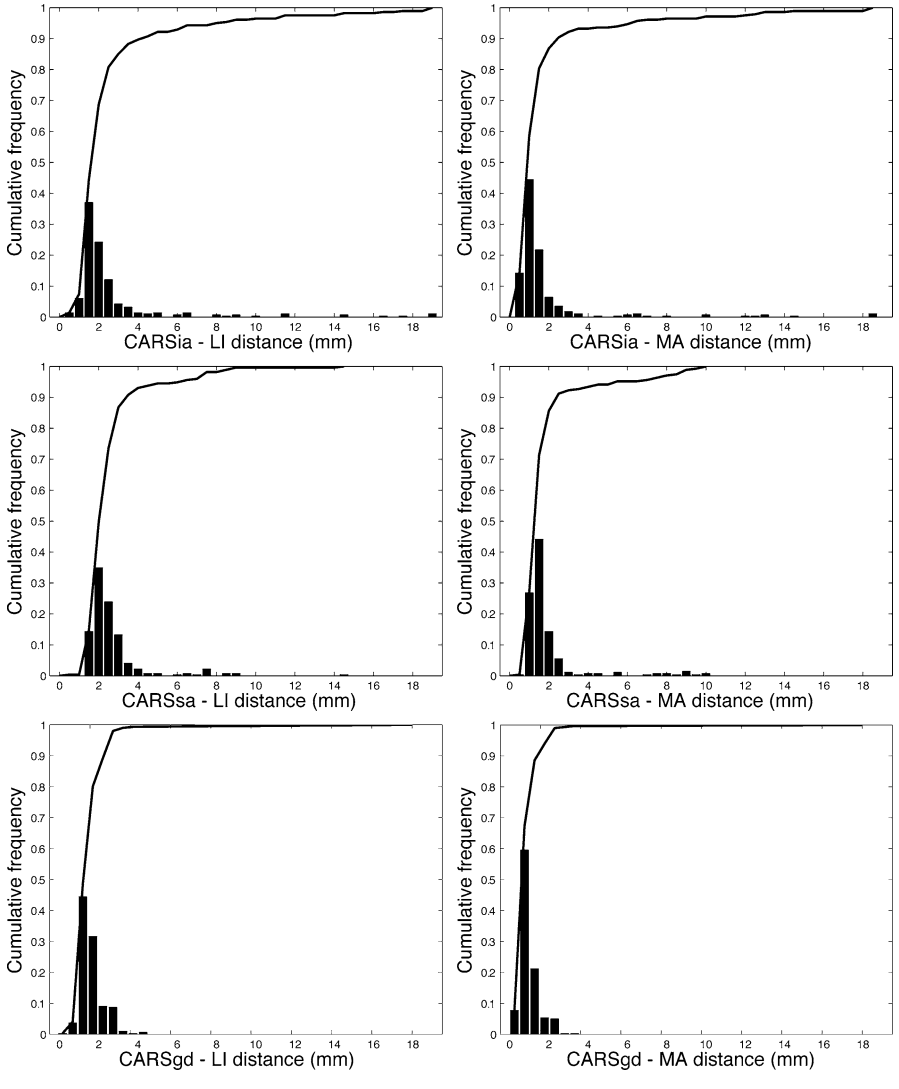

Fig. 18.8 Distribution of the HD between AD_F profiles and the LI (*left panels*) and MA (*right panels*) interfaces. The *top row* is relative to CARSia, the *middle* to CARSsa, and the *bottom* to CARSgd

Functionality can be enhanced through the use of pluggable modules. These modules may be written in pure Java or C/C++. It interfaces with C/C++ modules through the use of the Java Native Interface. C/C++ modules can be used when interfacing with hardware is necessary or extreme performance is demanded from the system (for e.g., the use of a GPU through CUDA).

7.2 Effect of the Pixel Size and of the Calibration Factor

To convert the HD into millimeters, a calibration factor was required. When the image is DICOM formatted, an automated conversion was possible. The DICOM header was automatically scanned. The field named `SequenceOfUltrasound Regions`, coded by the field (0018,6011) as per the NEMA specifications (http://medical.nema.org/), contained two subfields providing the calibration factors, called `PhysicalDeltaX` (for the horizontal *x*-axis) and `PhysicalDeltaY` (for the vertical *y*-axis). These two numbers specify the physical dimension of a pixel (which is squared) in millimeters. The inverse of the calibration factor is the image pixel density (expressed in pixels/mm).

If the image was not provided in DICOM format, a manual calibration was performed. The ultrasound image frame surrounding the region containing the ultrasound data usually reports the scanning depth in a corner, as shown by the white circle in Fig. 18.1. The scanning depth, expressed in centimeters, is relative to the last row of the image (i.e., it is relative to the physical depth of the last image row). Therefore, we measured the number of rows of the image after automatic cropping and divided the scanning depth by

the number of rows, obtaining the calibration factor. In the example of Fig. 18.1, the scanning depth was equal to 3.0 cm and the number of rows was 480. Therefore, the calibration factor was 0.0625 mm.

The calibration factors of the images we used in this study are reported by Table 18.1.

7.3 Possible Inaccuracy Sources and Developed Strategic Solutions

Jugular Vein Issue: One of the major challenges in automatic carotid recognition is avoiding the jugular vein (JV). The appearance of the jugular vein is similar to that of the carotid artery (CA); thus, an automated technique could incorrectly recognize the JV instead of the CA. Our automated techniques are equipped by many checks in order to minimize the probability of having detected the JV. CARSsa is intrinsically very robust, since it searches for the far adventitia and lumen starting from the bottom of the image. Therefore, we did not found incorrect behavior of CARSsa. CARSgd and CARSsa are more affected by the presence of the JV. We observed that CARSgd recognized the JV instead of CA in 29 images out of 365; CARSia in 33 out of 365. To correct this possible error condition, we inserted a final check: if the row index of the traced AD_F profile was too low (i.e., if the AD_F profile was not located towards the bottom of the image), we assumed that the algorithm had identified the JV and not the CA. Hence, we checked for the presence of a hyperechoic structure located below: if it was present, then we considered that this structure was the actual AD_F. If it was not present, we kept the first AD_F tracing. This check solved the error condition in all the images for CARSgd, and in 27 out of 33 for CARSia. This check was totally automated.

Spike Detection and Smoothing: The AD_F tracing might also be inaccurate due to the presence of excessive spikes. We developed an intelligent spike-removal algorithm that checks for the presence of spikes and counts them. We find zero-crossing points on the LI/MA border using a simple difference operator. We reapply the difference operator on these zero-crossing points and compute the absolute difference. The point whose absolute difference is above a predetermined threshold determines spikes location. Detected spikes are removed using the linear interpolation method by utilizing the neighborhood non-spike border points. Finally, the ADF tracings were regularized by a cubic spline interpolation.

Presence of Hyperechoic Structures: Inaccurate AD_F tracings were observed in four images for CARSgd, five for CARSia, and two for CARSsa. Some possible but sporadic challenges might be present. Figure 18.9 reports samples of inaccurate AD_F tracings by the three techniques. Figure 18.9a is relative to CARSgd. The white arrow indicates a portion of the AD_F profile that overlaps to GT_{MA}. This problem is given by the presence of image markers that attract the AD_F profile. However, this local inaccuracy in the AD_F tracing did not preclude the correct definition of the guidance zone for the IMT measurement. Figure 18.9b is relative to CARSia and shows the AD_F that overlaps to the GT_{MA} boundary. This error condition is caused by incorrect tracings of the line segments by CARSia. Finally, Fig. 18.9c is relative to CARSsa and shows an incorrect AD_F boundary that is located neatly below the actual adventitial layer. This error condition is determined by a hypoechoic adventitia layer and by the presence of a hyperechoic deep structure (located below the artery and indicated by the white arrow). In such condition, the intensity-based strategy for AD_F detection fails and recognizes the hyperechoic deep structure instead of the adventitia layer.

7.4 Robustness to Noise

To assess the robustness to noise of the CARS techniques, we performed a systematic characterization of the three CARS techniques with respect to noise. We corrupted the images with random additive noise, with Gaussian distribution, and with variance equal to 0.03 and 0.06. We ran the CARS systems computations on the noisy images and we computed the HDs from LI/MA boundaries. We found that despite the increased noise level, the automatically traced AD_F profiles did not change significantly. When we corrupted the images with variance equal to 0.06, we did not experiment changes in the CARS technique performances: CARSgd showed an accuracy of 100 % (365 images out of 365 correctly processed); CARSia showed an accuracy of 92 % (337 images out of 365 correctly processed); CARSsa showed an accuracy of 95 % (349 images out of 365 correctly processed). Therefore, the performance of CARS was as expected and be categorized as robust with respect to noise.

7.5 Comparison with Other Methods

The direct comparison of the herein presented results to other published studies is not straightforward. In 2008, Rossi et al. presented an efficient technique for the automatic recognition of the carotid artery in the longitudinal images [20]. In their approach, the longitudinal image is considered column-wise and decimated, so that a finite and small number of spatial envelopes are processed. Each spatial envelope is equivalent to the intensity profile of one column of the image, where two intensity peaks indicate the position of the adventitia layers. A template-matching algorithm processes each envelope in

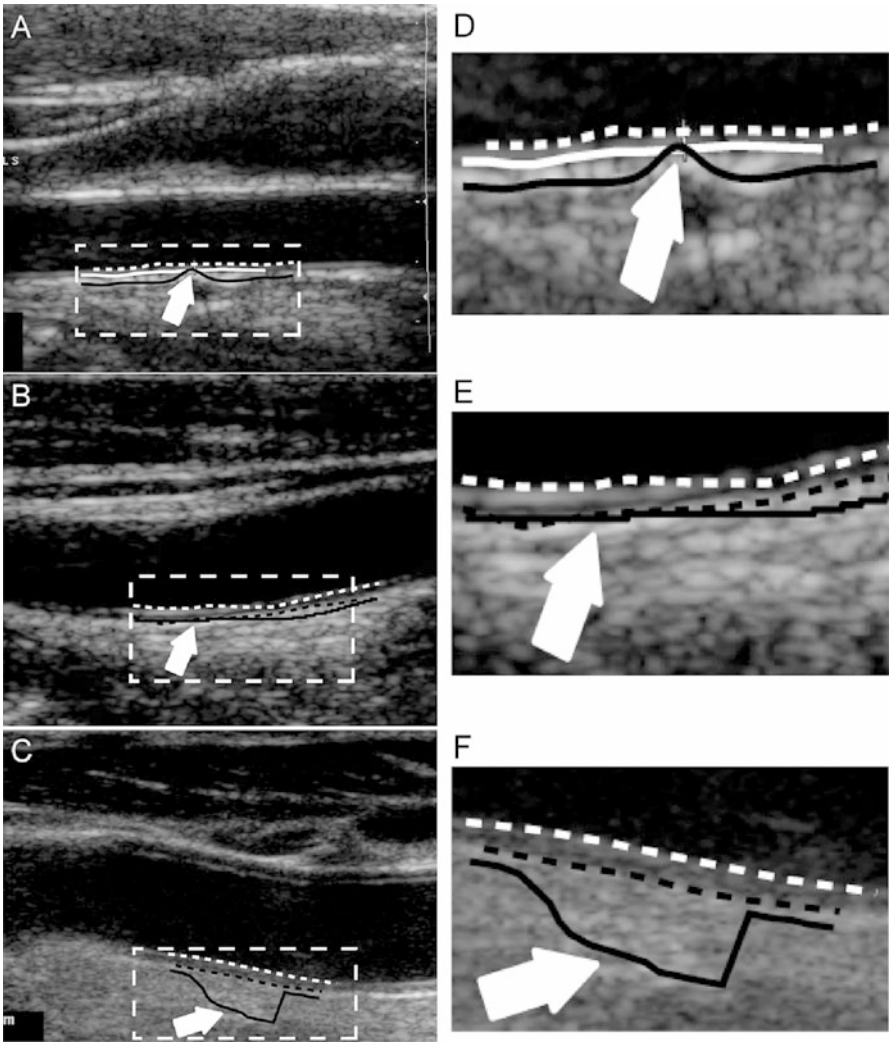

Fig. 18.9 Samples of inaccurate AD_F tracings by CARSgd (**a**); CARSia (**b**); and CARSsa (**c**). *Dashed lines* are the average GT_{LI} (*white*) and GT_{MA} (*black*). The *continuous black line* represents the AD_F. The *white arrows* indicate the inaccurate adventitia tracing. Panels (**d**), (**e**), and (**f**) depict the zoomed region of the white dashed box of panels (**a**), (**b**), and ©, respectively

order to find the center of the carotid lumen, which is the midpoint of the intensity peaks given representing the artery walls. This approach, once tuned for the specific image scanner and completed by a clustering post-processing, presented very accurate results (about 99 % of the carotid artery is correctly identified in each frame). This technique proved effective in the presence of fibrous plaques and noise. The computational burden was low enough for a real-time intermittent implementation (about 0.2 s on average). This method required the tuning of some parameters and, in the paper, it was optimized for a specific scanner. Therefore, it would be difficult to use it on a dataset. Moreover, this method localized the artery lumen by identifying its lumen, but no information was provided about the detection of the near and far adventitia layers. This method did not trace the AD_F profile and the authors did not assess performance by using a robust distance metric. Therefore, numerical comparison of the results is impossible.

Similar considerations can be done for the approach proposed by Golemati et al. in 2007 [21]. They developed a Hough transform based algorithm that first detected the carotid artery in the image frame, followed by wall segmentation and IMT measurement. The major advantage of this technique was the possibility of processing longitudinal and transverse images. The drawback, in longitudinal images, was the need for a straight and horizontally placed carotid in the image frame. Performance was assessed by measuring segmentation accuracy (in terms of sensitivity and specificity) with respect to manual tracings. However, no data were provided about the quality of carotid localization in the image.

The closer the AD_F tracing is to the actual distal wall LI/MA borders, the easier is the definition of a guidance zone for IMT computation. With this hypothesis in mind, CARSgd was the preferable technique. CARSgd showed very accurate

AD_F profiles coupled with a low computational burden. Therefore it can be thought of as a reference technique for carotid localization. CARSgd did not require specific tuning and worked with images acquired from different scanners. We believe that these results are very encouraging and even acceptable for real clinical settings.

8 Concluding Remarks

Ultrasound imaging is rapidly evolving methodology. Technical advances coupled to new possibilities (provided by improvement in the contrast agents and in complementary scanning modalities such as elastography, strain imaging, 3D volumetric reconstruction, 4D imaging, perfusion) force the development of performing and robust techniques to aid the sonographer. The CARS system we developed aims at providing a general solution in the field of vascular ultrasound. Robustness, versatility, and recognition accuracy are the key features of this system.

References

1. Amato M, Montorsi P, Ravani A, Oldani E, Galli S, Ravagnani PM, Tremoli E, Baldassarre D (2007) Carotid intima-media thickness by B-mode ultrasound as surrogate of coronary atherosclerosis: correlation with quantitative coronary angiography and coronary intravascular ultrasound findings. Eur Heart J 28(17):2094–2101
2. Rosvall M, Janzon L, Berglund G, Engstrom G, Hedblad B (2005) Incidence of stroke is related to carotid IMT even in the absence of plaque. Atherosclerosis 179(2):325–331
3. Saba L, Mallarini G (2009) A comparison between NASCET and ECST methods in the study of carotids evaluation using multidetector-row CT angiography. Eur J Radiol 76(1):42–47
4. Touboul PJ, Hennerici MG, Meairs S, Adams H, Amarenco P, Bornstein N, Csiba L, Desvarieux M, Ebrahim S, Fatar M, Hernandez Hernandez R, Jaff M, Kownator S, Prati P, Rundek T, Sitzer M, Schminke U, Tardif JC, Taylor A, Vicaut E, Woo KS, Zannad F, Zureik M (2007) Mannheim carotid intima-media thickness consensus (2004-2006). An update on behalf of the Advisory Board of the 3rd and 4th Watching the Risk Symposium, 13th and 15th European Stroke Conferences, Mannheim, Germany, 2004, and Brussels, Belgium, 2006. Cerebrovasc Dis 23(1):75–80
5. Touboul PJ, Hennerici MG, Meairs S, Adams H, Amarenco P, Desvarieux M, Ebrahim S, Fatar M, Hernandez Hernandez R, Kownator S, Prati P, Rundek T, Taylor A, Bornstein N, Csiba L, Vicaut E, Woo KS, Zannad F (2004) Mannheim intima-media thickness consensus. Cerebrovasc Dis 18(4):346–349
6. Saba L, Montisci R, Molinari F, Tallapally N, Zeng G, Mallarini G, Suri JS (2012) Comparison between manual and automated analysis for the quantification of carotid wall by using sonography. A validation study with CT. Eur J Radiol 81(5):911–918
7. van der Meer IM, Bots ML, Hofman A, del Sol AI, van der Kuip DA, Witteman JC (2004) Predictive value of noninvasive measures of atherosclerosis for incident myocardial infarction: the Rotterdam Study. Circulation 109(9):1089–1094
8. Molinari F, Meiburger KM, Zeng G, Acharya RU, Liboni W, Nicolaides A, Suri JS (2012) Carotid artery recognition system: a comparison of three automated paradigms for ultrasound images. Med Phys 39(1):378–391
9. Molinari F, Liboni W, Giustetto P, Badalamenti S, Suri JS (2009) Automatic computer-based tracings (ACT) in longitudinal 2-D ultrasound images using different scanners. J Mech Med Biol 9(4):481–505
10. Molinari F, Zeng G, Suri JS (2010) A state of the art review on intima-media thickness (IMT) measurement and wall segmentation techniques for carotid ultrasound. Comput Methods Programs Biomed 100:201–221
11. Polak JF, Funk LC, O'Leary DH (2011) Inter-reader differences in common carotid artery intima-media thickness: implications for cardiovascular risk assessment and vascular age determination. J Ultrasound Med 30(7):915–920
12. Touboul PJ, Vicaut E, Labreuche J, Belliard JP, Cohen S, Kownator S, Pithois-Merli I (2005) Design, baseline characteristics and carotid intima-media thickness reproducibility in the PARC study. Cerebrovasc Dis 19(1):57–63
13. de Groot E, van Leuven SI, Duivenvoorden R, Meuwese MC, Akdim F, Bots ML, Kastelein JJ (2008) Measurement of carotid intima-media thickness to assess progression and regression of atherosclerosis. Nat Clin Pract Cardiovasc Med 5(5):280–288
14. Delsanto S, Molinari F, Giustetto P, Liboni W, Badalamenti S (2005) CULEX-completely user-independent layers extraction: ultrasonic carotid artery images segmentation. Conf Proc IEEE Eng Med Biol Soc 6:6468–6471
15. Delsanto S, Molinari F, Giustetto P, Liboni W, Badalamenti S, Suri JS (2007) Characterization of a completely user-independent algorithm for carotid artery segmentation in 2-D ultrasound images. IEEE Trans Instrum Meas 56(4):1265–1274
16. Molinari F, Zeng G, Suri JS (2010) An integrated approach to computer-based automated tracing and its validation for 200 common carotid arterial wall ultrasound images: a new technique. J Ultrasound Med 29:399–418
17. Molinari F, Zeng G, Suri JS (2010) Intima-media thickness: setting a standard for completely automated method for ultrasound. IEEE Trans Ultrason Ferroelectr Freq Control 57(5):1112–1124
18. Molinari F, Pattichis C, Zeng G, Saba L, Acharya U, Sanfilippo R, Nicolaides A, Suri J (2012) Completely automated multi-resolution edge snapper (CAMES) inverted question mark a new technique for an accurate carotid ultrasound IMT measurement: clinical validation and benchmarking on a multi-institutional database. IEEE Trans Image Process 21(3):1211–1222
19. Molinari F, Zeng G, Suri JS (2010) Greedy technique and its validation for fusion of two segmentation paradigms leads to an accurate intima-media thickness measure in plaque carotid arterial ultrasound. J Vasc Ultrasound 34(2):63–73
20. Rossi AC, Brands PJ, Hoeks AP (2008) Automatic recognition of the common carotid artery in longitudinal ultrasound B-mode scans. Med Image Anal 12(6):653–665
21. Golemati S, Stoitsis J, Sifakis EG, Balkizas T, Nikita KS (2007) Using the Hough transform to segment ultrasound images of longitudinal and transverse sections of the carotid artery. Ultrasound Med Biol 33(12):1918–1932
22. Zhen Y, Jasjit S, Yajie S, Janer R (2005) Four image interpolation techniques for ultrasound breast phantom data acquired using Fischer's full field digital mammography and ultrasound system (FFDMUS): a comparative approach. In: IEEE international conference on image processing, 2005. ICIP 2005
23. Fan L, Santago P, Riley W, Herrington DM (2001) An adaptive template-matching method and its application to the boundary detection of brachial artery ultrasound scans. Ultrasound Med Biol 27(3):399–408
24. Loizou CP, Pattichis CS, Christodoulou CI, Istepanian RSH, Pantziaris M, Nicolaides A (2005) Comparative evaluation of despeckle filtering in ultrasound imaging of the carotid artery. IEEE Trans Ultrason Ferroelectr Freq Control 52(10):1653–1669

25. Loizou CP, Pattichis CS, Pantziaris M, Tyllis T, Nicolaides A (2006) Quality evaluation of ultrasound imaging in the carotid artery based on normalization and speckle reduction filtering. Med Biol Eng Comput 44(5):414–426
26. Delsanto S, Molinari F, Liboni W, Giustetto P, Badalamenti S, Suri JS (2006) User-independent plaque characterization and accurate IMT measurement of carotid artery wall using ultrasound. Conf Proc IEEE Eng Med Biol Soc 1:2404–2407
27. Molinari F, Delsanto S, Giustetto P, Liboni W, Badalamenti S, Suri JS (2008) User-independent plaque segmentation and accurate intima-media thickness measurement of carotid artery wall using ultrasound. In: Suri JS, Chang RF, Kathuria C, Molinari F, Fenster A (eds) Advances in diagnostic and therapeutic ultrasound imaging. Artech House, Norwood, MA, pp 111–140
28. Molinari F, Liboni W, Giustetto P, Pavanelli E, Marsico A, Suri J (2010) Carotid plaque characterization with contrast-enhanced ultrasound imaging and its histological validation. J Vasc Ultrasound 34(4):1–10
29. Molinari F, Liboni W, Pantziaris M, Suri JS (2011) CALSFOAM—completed automated local statistics based first order absolute moment" for carotid wall recognition, segmentation and IMT measurement: validation and bench-marking on a 300 patient database. Int Angiol 30(3):227–241
30. Molinari F, Liboni W, Pavanelli E, Giustetto P, Badalamenti S, Suri JS (2007) Accurate and automatic carotid plaque characterization in contrast enhanced 2-D ultrasound images. Conf Proc IEEE Eng Med Biol Soc 2007:335–338
31. Molinari F, Zeng G, Suri J (2010) Inter-greedy technique for fusion of different segmentation strategies leading to high-performance carotid IMT measurement in ultrasound images. J Med Syst 35(5):905–919
32. Suri JS, Kathuria C, Molinari F (Eds.) (2011) Atherosclerosis disease management. Springer, New York
33. Rocha R, Campilho A, Silva J, Azevedo E, Santos R (2011) Segmentation of ultrasound images of the carotid using RANSAC and cubic splines. Comput Methods Programs Biomed 101(1):94–106
34. Rocha R, Campilho A, Silva J, Azevedo E, Santos R (2010) Segmentation of the carotid intima-media region in B-Mode ultrasound images. Image Vis Comput 28(4):614–625
35. Demi M, Paterni M, Benassi A (2000) The first absolute central moment in low-level image processing. Comput Vis Image Underst 80(1):57–87
36. Faita F, Gemignani V, Bianchini E, Giannarelli C, Ghiadoni L, Demi M (2008) Real-time measurement system for evaluation of the carotid intima-media thickness with a robust edge operator. J Ultrasound Med 27(9):1353–1361

Atherosclerotic Carotid Plaque Segmentation in Ultrasound Imaging of the Carotid Artery

19

Christos P. Loizou and Marios Pantzaris

Abbreviations

2D	Two-dimensional
3D	Three-dimensional
4D	Four-dimensional
ACSRS	Asymptomatic carotid stenosis and risk of stroke
AS	Automated segmentation
ATL	Advanced Technology Laboratories
CCA	Common carotid artery
DsFlsmv	Despeckle filter linear scaling mean variance
F	Effectiveness
FNF	False-negative fraction
FPF	False-positive fraction
GT	Ground truth
GVF	Gradient vector flow
IMT	Intima–media thickness
IVUS	Intravascular ultrasound
KI	Kappa index
MR	Magnetic resonance
MRI	Magnetic resonance image
P	Precision
ROC	Receiver operating characteristics
Sp	Specificity
TIA	Transient ischemic attack
TNF	True-negative fraction
TPF	True-positive fraction

C.P. Loizou (✉)
Department of Computer Science, School of Sciences and Engineering, Intercollege, 92 Ayias Phylaxeos Street, P.O. Box 51604, 3507 Limassol, Cyprus
e-mail: loizou.c@lim.intercollege.ac.cy; loizou.christos@ucy.ac.cy

M. Pantzaris
The Cyprus Institute of Neurology and Genetics, P.O. Box 23462, 1683 Nicosia, Cyprus
e-mail: pantzari@cing.ac.cy

1 Introduction

Carotid artery atherosclerosis is the primary cause of stroke and the third leading cause of death in the USA Almost twice as many people die from cardiovascular disease than from all forms of cancer combined. Atherosclerosis is a disease of the large and medium size arteries, and it is characterized by plaque formation due to progressive intimal accumulation of lipid, protein, and cholesterol esters in the blood vessel wall [1], which reduces blood flow significantly. The risk of stroke increases with the severity of carotid stenosis and is reduced after carotid endarterectomy [2]. The degree of internal carotid stenosis is the only well-established measurement that is used to assess the risk of stroke [3]. Indeed, it is the only criterion at present used to decide whether carotid endarterectomy is indicated or not [4]. The objective of this study was to propose an integrated system for the segmentation of the atherosclerotic carotid plague in ultrasound imaging.

Several studies investigated the segmentation of atherosclerotic carotid plaque in ultrasound imaging, intravascular ultrasound (IVUS) imaging, and magnetic resonance (MR) imaging. An overview of these techniques is given in Table 19.1. Zahalka et al. [5] applied a geometrically deformable model on two 3D ultrasound images of the carotid artery to detect the blood borders in the carotid artery. Hamou et al. [6] proposed a method, which was based on the Canny edge detector to detect the plaque regions in longitudinal carotid artery ultrasound images. A morphological-based approach for the carotid contour extraction was proposed in [7] for longitudinal ultrasound images of carotid artery, incorporating speckle reduction filtering, contour quantization, morphological contour detection, and a contour enhancement stage. Mao et al. [8]

L. Saba et al. (eds.), *Multi-Modality Atherosclerosis Imaging and Diagnosis*,
DOI 10.1007/978-1-4614-7425-8_19, © Springer Science+Business Media, LLC 2014

Table 19.1 An overview of atherosclerotic carotid plaque segmentation techniques

Study	Segmentation method	2D/3D	AIC	*N*
Ultrasound imaging				
Zahalka et al. [5]	Deformable models	3D	No	69
Hamou et al. [6]	Canny edge detection	2D	No	–
Abdel-Dayen et al. [7]	Morphological based	2D	No	–
Mao et al. [8]	Discrete dynamic contour	2D	No	7
Abolmaesumi et al. [9]	Kalman filtering	2D	No	1
Gill et al. [10]	Balloon	3D	No	2
Delsanto et al. [11]	Deformable parametric model	2D	No	45
Loizou et al. [12]	Snakes	2D	Yes	80
Guerrero et al. [13]	Star–Kalman algorithm	2D	No	–
Golemati et al. [14]	Hough transforms	2D	No	56
Slabaugh et al. [15]	Region-based active contour	2D	No	–
IVUS imaging				
Zhang [16]	Optimal graph searching	2D	No	20
Cardinal [17]	Fast-marching method	2D	No	200
Brusseau [18]	Statistical approach	2D	Yes	15
Olszewski [19]	Knowledge based	3D	No	21
Magnetic resonance imaging (MRI)				
Xu [20]	Mean shift	2D	Yes	22
Adams [21]	Snakes, GVF	2D	No	20
Yang [22]	Dynamic programming	2D	Yes	62

AIC automatic initial contour, *N* number of cases investigated

proposed a discrete dynamic contour model for extracting the carotid artery lumen in 2D transversal ultrasound images, whereas Abolmaesumi et al. [9] introduced an algorithm based on the star algorithm improved by Kalman filtering, for extracting the carotid artery boundaries from transversal carotid ultrasound images. A semiautomatic method for tracking the progression of atherosclerotic plaque in 3D images of the carotid artery using the Balloon model introduced in [23] was proposed by Gill et al. [10]. In [11], Delsanto et al. proposed a user-independent plaque characterization and intima–media thickness (IMT) segmentation method, based on area of interest identification stage, gradient segmentation stage, and a contour refinement stage, using deformable parametric model. The overall accuracy of the system determined as normalized error was overall to 8 %. Loizou et al. [12] proposed an integrated system for the segmentation of the atherosclerotic carotid plaque on ultrasound images based on initial contour estimation and speckle reduction filtering. It was also shown that normalization and speckle reduction filtering improve the outcome of the plaque segmentation. The user was able to interact and correct the segmentation results manually. A limitation of the proposed method includes the presence of acoustic shadowing together with strong speckle noise, which hinders the visual and automatic analysis in ultrasound images. Furthermore, only vessels without atherosclerotic plaques were segmented in this study. In [13], a method based on a Star–Kalman algorithm was used to determine vessel contours and ellipse parameters using an extended Kalman filter with an elliptical model. The segmentation and tracking were implemented in real time and validated using simulated ultrasound data with known features and real data, for which expert segmentation was performed. Results indicate that mean errors between segmented contours and expert tracings are on the order of 1–2 % of the maximum feature dimension, and that the transverse cross-sectional vessel area as computed from estimated ellipse parameters as determined by the algorithm is within 10 % of that determined by experts. Hough transforms were used in [14] to perform the segmentation of 2D longitudinal and cross-sectional ultrasound images of plaques. Slabaugh et al. [15] presented an ultrasound-specific segmentation approach that addressed both the spatial correlation of the data as well as its intensity distribution. The image is first decorrelated and then a region-based active contour whose motion is derived from an appropriate parametric distribution for maximum likelihood image segmentation was applied. A zero-mean complex Gaussian, Rayleigh, and Fisher–Tippett flows were considered, which were designed to model fully formed speckle in the in-phase/quadrature, envelope detected, and display (log compressed) images, respectively. The effectiveness of the method was compared with other parametric and nonparametric active contours.

Furthermore, a number of studies investigated the use of IVUS imaging of the carotid artery. Although, IVUS provides better quality images when compared with ultrasound images, it poses a certain risk to the patients due to the insertion of a catheter in the patient's artery. A graph-searching

approach to detect the wall and plaque borders from IVUS images of the carotid artery was documented in [16]. A semi-automatic segmentation method for IVUS images based on gray-scale statistics of the image was proposed in [17], where the lumen, IMT, and the plaque were segmented in parallel by utilizing a fast marching method. In [18], an automated luminal contour segmentation method based on a statistical approach was introduced, whereas in [19] IVUS images were segmented using knowledge-based methods.

Several studies also investigated the automated segmentation in MRI of the carotid artery. Xu et al. [20] applied a mean shift density estimation algorithm to segment 22 multiple transversal MRI's of the carotid artery. Adams et al. [21] attempted to segment the carotid plaque by using snakes based on the GVF method, in order to detect the artery, lumen, and plaque borders, where the initial contour was placed manually by the expert. The results showed a good accuracy of the segmentation algorithm. Yang et al. [22] proposed a dynamic programming approach to detect the plaque borders in each MRI frame where seed points were placed by the expert for estimating the initial plaque contour.

As shown in Table 19.1, different methods were investigated for the segmentation of the atherosclerotic carotid plaque, however, these studies were evaluated on a limited number of subjects for ultrasound imaging (although this is not the case for IVUS, see study [17]). Therefore, the need still exists for the development, implementation, and evaluation of an integrated system enabling the automated segmentation of ultrasound imaging carotid plaque. In this chapter, we propose and evaluate such a system based on normalization, speckle reduction filtering, and snakes segmentation. Four different snake methods were investigated, namely (1) the Williams and Shah [12, 24], (2) the Balloon [23], (3) the Lai and Chin [25], and (4) the GVF [26]. Preliminary results of this study were also published in [27].

2 Materials and Methods

2.1 Recording of Ultrasound Images

A total of 80 B-mode and blood flow longitudinal ultrasound images of the common carotid artery (CCA) bifurcation were selected at random representing different types of atherosclerotic plaque formation with irregular geometry typically found in this blood vessel. The images were acquired by the ATL HDI-3000 ultrasound scanner (Advanced Technology Laboratories, Seattle, USA) [28] and were recorded digitally on a magneto optical drive, with a resolution of 768×576 pixels with 256 gray levels. Digital images were resolution normalized at 16.66 pixels/mm (see Sect. 2.3). This was carried out due to the small variations in the number of pixels per mm of image depth (i.e., for deeply situated carotid arteries, image depth was increased and therefore digital image spatial resolution would have decreased) and in order to maintain uniformity in the digital image spatial resolution [28, 29]. The images were recorded at the Saint Mary's Hospital, Imperial College of Medicine, Science and Technology, UK, from 32 female and 48 male symptomatic patients aged between 26 and 95 years old, with a mean age of 54 years. These subjects were at risk of atherosclerosis and have already developed clinical symptoms, such as a stroke or a transient ischemic attack (TIA).

2.2 Manual Plaque Segmentation and Classification

An expert manually delineated the plaque borders, between plaque and artery wall, and those borders between plaque and blood, on 80 longitudinal B-mode ultrasound images of the carotid artery, after image normalization and speckle reduction filtering (see Sects. 2.3 and 2.4), using MATLAB software developed by other researchers from our group. The procedure for carrying out the manual delineation process was established by a team of experts and was documented in the asymptomatic carotid stenosis and risk of stroke (ACSRS) project protocol [4]. The correctness of the work carried out by a single expert was monitored and verified by at least another expert. Usually the plaques are classified into type I–type V as documented in [4, 12]. In this study the plaques delineated were of type II, III, and IV because it is easier to make a manual delineation since the fibrous cap, which is the border between blood and plaque, is more easily identified. If the plaque is of type I, borders are not visible well. Plaques of type V produce acoustic shadowing and the plaque is also not visible well.

2.3 Image Normalization

Brightness adjustments of ultrasound images were carried out in this study based on the method introduced in [30]. It was shown that this method improves image compatibility by reducing the variability introduced by different gain settings, different operators, different equipment and facilitates ultrasound tissue comparability [30]. Algebraic (linear) scaling of the image was manually performed by linearly adjusting the image so that the median gray level value of the blood was 0–5, and the median gray level of the adventitia (artery wall) was 180–190 [30, 31]. The scale of the gray level of the images ranged from 0 to 255. Thus the brightness of all pixels in the image was readjusted according to the linear scale defined by selecting the two reference regions. It is noted that a key point to maintaining a high reproducibility was to ensure that the ultrasound beam was at right angles to the adventitia, adventitia was visible adjacent to the plaque and that for image normalization a standard sample consisting of the half of the width of the brightest area of adventitia was obtained.

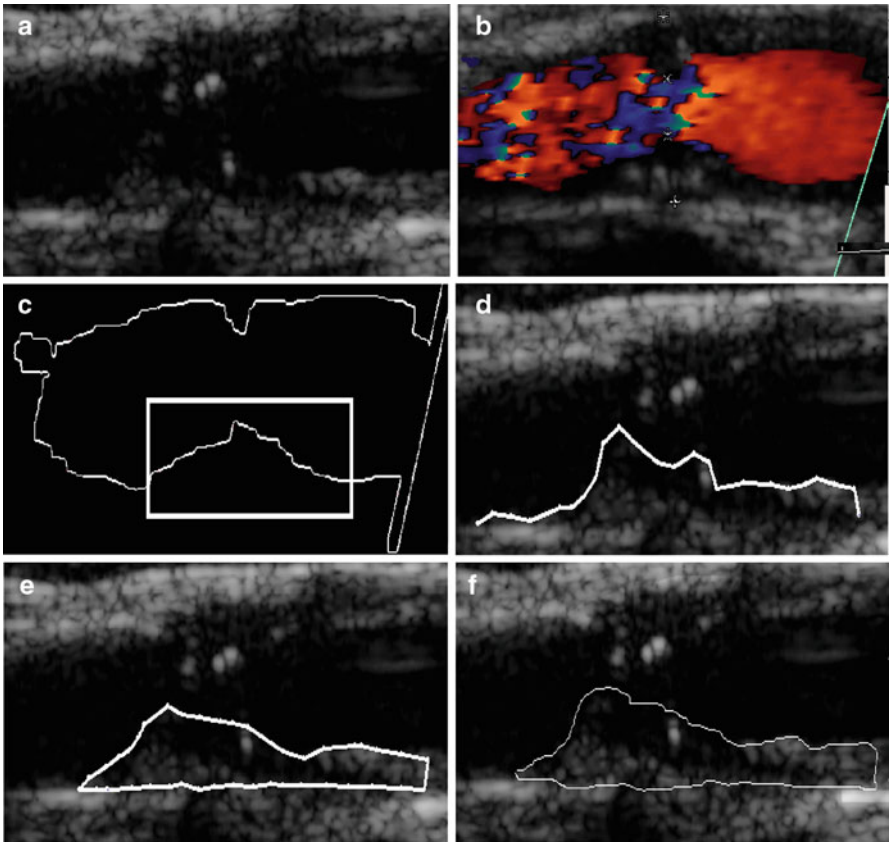

Fig. 19.1 Plaque initialization using the blood flow image: (**a**) original ultrasound B-mode image of a carotid artery with plaque at the far wall, (**b**) blood flow of the image in (**a**), (**c**) initial blood flow edge contour with the area for the initial contour selected by the user, (**d**) sampled initial snake contour, (**e**) Williams and Shah snakes segmentation of plaque, and (**f**) manual segmentation of plaque. Source [12], © IEEE, 2007

2.4 Speckle Reduction Filtering

In this study, a linear scaling filter (DsFlsmv—*Despeckle filter linear scaling mean variance*) utilizing the mean and the variance of a pixel neighburhood was used. This filter was introduced in [32] and evaluated on ultrasound imaging of the carotid giving best results in [33]. The DsFlsmv filter may be described by a weighted average calculation using subregion statistics to estimate statistical measurements over 7×7 pixel windows applied for five iterations [31–33].

2.5 Plaque Contour Initialization

In most of the cases a plaque is visualized in a B-mode longitudinal ultrasound image and its size confirmed in transverse section using color blood flow imaging. However, uniformly echolucent plaques are not obvious on B-mode, and color flow imaging is needed. These echolucent plaques are seen as black filling defects. PW Doppler is used to measure velocity in order to grade the degree of stenosis and blood flow can be detected at a specific depth by selecting the time interval between the transmitted and received pulses.

In this work the blood flow image was used, in order to extract the initial snake contour for the plaque borders in the carotid artery. The plaque snakes contour initialization procedure, carried out using both the blood flow and the B-mode images, may be described as follows (see also Fig. 19.1):

1. The blood flow area is extracted from the blood flow image (Fig. 19.1b) by searching to find all color pixels (i.e., if the red, green, and blue pixel values are different). Otherwise, pixels belong to a grayscale area. All color pixels are (set to zero) in the blood flow image. The resulting image is then cross-correlated with the B-mode image (Fig. 19.1a) so that the blood flow edge is mapped on the B-mode image.
2. Dilate the extracted blood flow edge image to eliminate small gaps and remove small-undesired regions.
3. From the dilated edge blood flow image, detect the blood flow edge contour (see Fig. 19.1c). Mark a region of

interest on the edge contour (a task carried out by the user of the proposed system, illustrated by a rectangle in Fig. 19.1c) where the lower or the upper boundary of plaque is covered. This is used as an initial snake contour.
4. Sample the initial snake contour at 20–40 consecutive points to construct an interpolating B-spline.
5. Connect the first and the last snake points on the initial contour to form a closed contour.
6. Perform image normalization (see Sect. 2.3) and speckle reduction on the B-mode image by the DsFlsmv filter described in Sect. 2.4.
7. Map the initial plaque contour on the B-mode image (see Fig. 19.1d).
8. Deform the initial contour by the snake to accurately locate the plaque–blood borders (see Sect. 2.6).
9. Save the final plaque contour and display it on the B-mode image (see Fig. 19.1e).

2.6 Snake Segmentation

Four different snake segmentation methods were investigated in this study, namely (1) the Williams and Shah [12, 24], (2) the Balloon [23], (3) the Lai and Chin [25], and (4) the GVF [26]. Preliminary results of this study were also published in [27]. The parameter values for the four different snakes segmentation methods were the same in all experiments. For the Williams and Shah snake, the strength, tension, and stiffness parameters were equal to $\alpha_s = 0.6$, $\beta_s = 0.4$, and $\gamma_s = 2$, respectively. For the Lai and Chin, the regularization parameter, λ_π, was varied as documented in [25]. For the GVF snake, the elasticity, rigidity, and the regularization parameters were, $\alpha_{GVF} = 0.05$, $\beta_{GVF} = 0$, and $\mu_{GVF} = 0.2$, respectively [26].

2.7 Evaluation of the Segmentation Methods

ROC analysis [34] was used to assess the specificity and sensitivity of the four segmentation methods by the true-positive fraction, TPF and false-positive fraction, FPF [34]. The TPF is calculated when the expert detects a plaque (when a plaque is present) and the computerized method identifies it as so, whereas the FPF is calculated when the expert detects no plaque and the computerized method incorrectly detects that there is a plaque present. The TNF fraction is calculated when the expert identifies no plaque and the computerized method identifies it as so (absent), whereas the FNF is calculated when the expert identifies plaque presence and the computerized method incorrectly identifies plaque absence. Ratios of overlapping areas can also be assessed by applying the similarity kappa index, KI, [35] and the overlap index [36]. These indices were computed as follows:

$$\begin{aligned} TPF &= \frac{|AS \cap GT|}{|GT|},\ FPF = \frac{|AS| - |GT|}{|\overline{GT}|}, \\ TNF &= \frac{|AS \cap GT|}{|AS|}, \\ FNF &= \frac{|AS| - |GT|}{|AS|},\ KI = 2\frac{|GT \cap AS|}{|GT| + |AS|}, \\ \text{and } overlap &= \frac{|GT \cap AS|}{|GT \cup AS|} \end{aligned} \tag{19.1}$$

where $||$ denotes the magnitude, $\cap$ denotes the intersection (the number of common pixels in the manual and the snakes-segmented areas), and $\cup$ the union (the number of all pixels defined by the manual and the snakes-segmented areas where the common pixels are considered only once). GT, denotes the number of pixels defined by the segmented area, representing ground truth delineated by the expert, $\overline{\text{GT}}$, its complement, and AS the number of pixels belonging in the area, obtained by the snakes segmentation method. The intersection gives the probability that both AS and GT occur and the union is the probability that either AS or GT occur. The specificity, Sp $= 1 -$ FPF, the precision, P, and the effectiveness measure, $F = 1 - E$, [34] were also calculated to describe the ROC characteristics of the segmentation methods.

2.8 Univariate Statistical Analysis

The Wilcoxon matched-pairs signed rank sum test was used in order to detect if for each metric, TPF, TNF, FPF, FNF, KI, overlap index, Sp, P, and F, a significant difference or not exists between all the segmentation methods at $p < 0.05$. The test was applied on all 80 segmented plaques for all different segmentation methods.

3 Results

3.1 Examples of Plaque Segmentation

Figure 19.2 illustrates the original longitudinal ultrasound B-mode image of a carotid plaque with a manual delineation made by the expert in (a), and the results of the William and Shah segmentation in (b), the Balloon segmentation in (c), the Lai and Chin segmentation in (d), and the GVF segmentation in (e). Figure 19.2f shows the superimposition of the segmentation contours computed in Fig. 19.2b, e. As illustrated in Fig. 19.2f, both the manual and the snakes segmentation contours are visually very similar. It sould be noted that the despeckle filter DsFlsmv [31, 33] with a moving sliding window of $[5 \times 5]$, was iteratively four times applied on all images before segmentation.

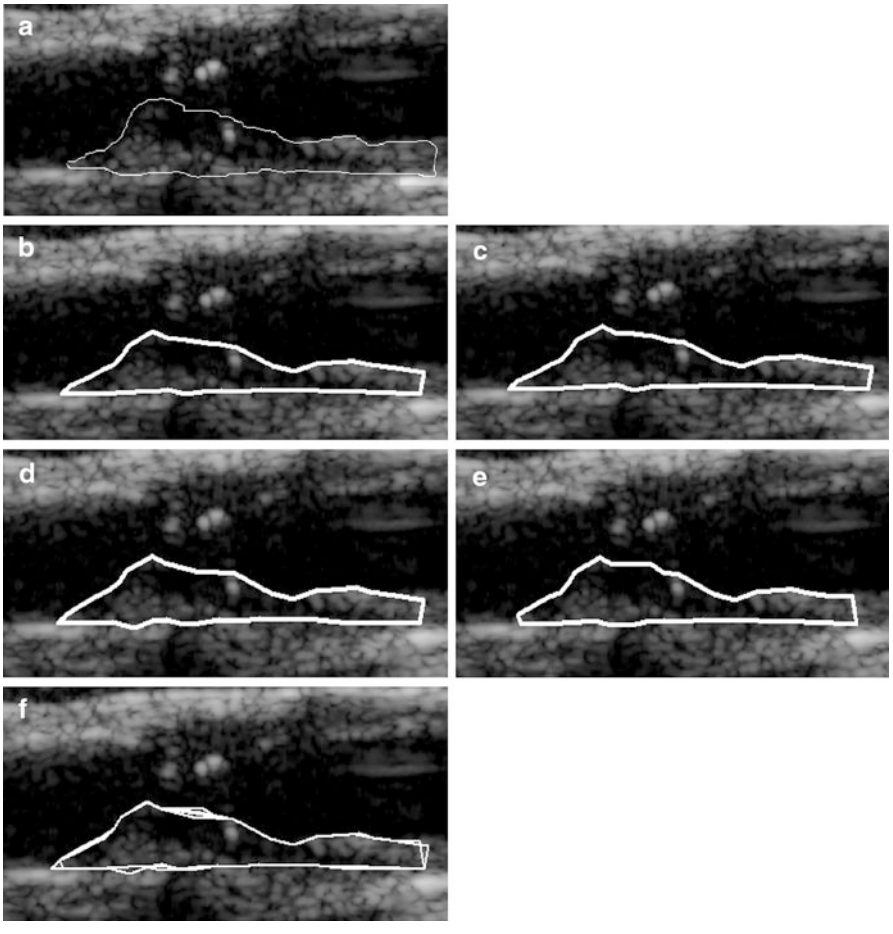

Fig. 19.2 Plaque segmentation results on a longitudinal ultrasound B-mode image of the carotid artery: (**a**) manual, (**b**) Williams and Shah, (**c**) Balloon, (**d**), Lai and Chin, (**e**) GVF snake, and (**f**) superimposition of segmentation contours computed in (**b**)–(**e**). Source [12], © IEEE, 2007

Table 19.2 ROC analysis based on TNF, TPF, FNF, FPF, KI, overlap index, Sp, P, and $F = 1 - E$, for the four different plaque snakes segmentation methods on 80 ultrasound images of the carotid artery

Segmentation method	System detects	Expert detects no plaque	Expert detects plaque	KI (%)	Overlap index (%)	Sp	P	$F=1-E$
Williams and Shah	No plaque	TNF = 77.59 %	FNF = 19.64 %	78.86	67.60	0.935	0.926	0.862
	Plaque	FPF = 6.50 %	TPF = 81.76 %					
Balloon	No plaque	TNF = 77.12 %	**FNF = 13.90 %**	77.87	67.79	**0.946**	0.927	**0.888**
	Plaque	**FPF = 5.40 %**	TPF = 80.35 %					
Lai and Chin	No plaque	**TNF = 80.89 %**	FNF = 15.59 %	**80.66**	**69.30**	0.942	**0.934**	0.885
	Plaque	FPF = 5.86 %	**TPF = 82.70 %**					
GVF	No plaque	TNF = 79.44 %	FNF = 14.90 %	77.25	66.60	0.937	0.926	0.883
	Plaque	FPF = 6.30 %	TPF = 79.57 %					

Bolded values show best performance
Source [12], © IEEE, 2007

3.2 Evaluation of Plaque Segmentation Methods

Table 19.2 tabulates the results of the ROC analysis based on TNF, TPF, FNF, FPF, KI, overlap index, Sp, P, and F, for the four different plaque snakes segmentation methods on 80 longitudinal ultrasound images. Although all methods demonstrated similar performance with nonsignificant differences (see Sect. 3.3), the best overall performance was demonstrated by the Lai and Chin segmentation method. Bolded values in Table 19.2 show best performance. The results showed that the Lai and Chin method agrees with the expert by correctly detecting no plaque (TNF) in 80.89 % of the cases, by correctly detecting a plaque (TPF) in 82.70 % of the cases, disagrees with the expert by detecting no plaque

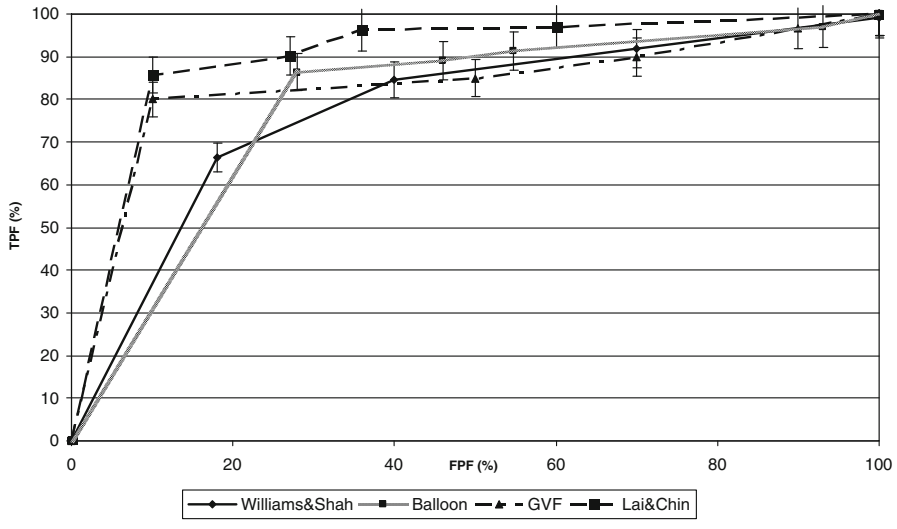

Fig. 19.3 ROC curve analysis based on the TPF and FPF fractions for the four snakes segmentation methods. Source [12], © IEEE, 2007

(FNF) in 15.59 % of the cases, and by detecting a plaque (FPF) in 5.86 % of the cases. The similarity kappa index KI, and the overlap index, for the Lai and Chin snakes segmentation method were the highest, equal to 80.66 % and 69.3 %, respectively. The best FPF and FNF fractions were given by the Balloon, with 5.4 % and 13.90 %, respectively. The GVF gave the worst results with the lowest similarity kappa index, KI, (77.25 %), and the lowest overlap index (66.6 %). The best specificity, Sp, was given by the Balloon (0.946), followed by the Lai and Chin (0.942) snakes segmentation method. The Lai and Chin gave the best precision, P, (0.934), whereas the best F, was given by the Balloon (0.888), followed by the Lai and Chin (0.885) snakes segmentation method.

Figure 19.3 shows the ROC curves for the four snakes segmentation methods, based on the TPF and FPF fractions with 95 % confidence margins. The area below the ROC curve was 0.90, 0.83, 0.79, and 0.67 for the Lai and Chin, GVF, Balloon, and Williams and Shah snakes segmentation method, respectively. It is clear that the largest area under the ROC curve was obtained by the Lai and Chin snakes segmentation method.

3.3 Univariate Statistical Analysis

The Wilcoxon matched-pairs signed rank sum test was performed to check if significant differences exist between the different segmentation methods at $p < 0.05$ for the measures TPF, TNF, FPF, FNF, KI, the overlap index, Sp, P, and F. There were no significant differences between the four segmentation methods for all measures, except for the case of the FNF between the Balloon and the Lai and Chin snake segmentation methods.

4 Discussion

The comparison of the four different snakes segmentation methods proposed in this chapter showed that the Lai and Chin gave slightly better results, although these results were not statistically significant when compared with the other three snakes segmentation methods.

4.1 Normalization and Speckle Reduction Filtering

To the best of our knowledge no other study carried out ultrasound image normalization as described in this study, prior to segmentation of the atherosclerotic carotid plaque. However, in [6], histogram equalization was performed on carotid artery ultrasound images for increasing the image contrast. The normalization method used in this study was documented to be helpful in the manual contour extraction as well as in the snake's segmentation of the IMT [37, 38]. Moreover, this method increased the classification accuracy of different plaque types as assessed by the experts [38].

In this chapter, speckle reduction filtering was used as a preprocessing step based on our previous work [33, 38]. More, specifically, in [38], it was shown that image normalization followed by speckle reduction produces better quality images, whereas the reverse (speckle reduction followed by normalization) might produce distorted edges. Speckle reduction filtering of the carotid was also proposed by [12, 37, 39], where it was shown that this improves the image quality and the visual evaluation of the image. However in

other segmentation studies for extracting the carotid artery plaque borders in IVUS imaging, speckle was used as useful information [16–19].

4.2 Plaque Contour Initialization

Initial contour estimation using the blood flow image was proposed in this work where the limitations of this method based on the color imaging were outlined in Sect. 2.5. Initial contour estimation was also proposed in [18], which was derived from the polar image by combining information extracted from the probability function of the contour position, and more specifically from the function maximum location and the first zero crossing of its derivative. Then, starting from the initial contour, a region of interest was automatically selected and the process iterated until the snake contour evolution could be ignored. In [19], a cost function was calculated and used as an input to the segmentation algorithm. In [10], a dynamic balloon model [23] represented by a triangular mesh was applied for detecting the plaque borders on two 3D ultrasound carotid images where the initial contour was placed manually. In all of these studies as well as in the present study, the significance of the initial contour placement was not investigated in order to estimate how this influences the final segmentation result.

4.3 Plaque Segmentation

The four different snakes segmentation methods presented in this study gave very satisfactory results, with the best performance obtained by the Lai and Chin. Snakes were only investigated by other researchers, for segmenting 3D ultrasound images of the carotid artery in a small number of cases with very promising results [10, 19]. Additional effort, for segmenting the atherosclerotic carotid plaque, was made on IVUS images [16], where the insertion of a catheter in the patients artery for acquiring the IVUS images posed a certain risk to the patient. This method was based on graph searching, which required that the expert must provide the initial plaque border contour. Furthermore, a time consuming methodology based on the Balloon snake [23] was proposed in [10] for 3D ultrasound carotid artery images, by triangulating the image in a finite element mesh. The method proposed in [9], for longitudinal images of the carotid artery, was time consuming and results were not that satisfactory as the lumen borders of the carotid artery were not that accurately found. Furthermore, in a recent study [6], where morphological processing was applied, the results were not in agreement with the manual delineations of an expert, and the expert had no interaction with the system. In [17] a semiautomatic segmentation method for IVUS images, based on gray-scale statistics of the image was proposed, where the lumen, IMT and the plaque were successfully segmented in parallel by utilizing a fast-marching model. The performance of the segmentation methods proposed above was not compared with other different segmentation methods, nor was investigated under different preprocessing conditions, such as normalization and speckle reduction filtering, as in this study.

The evaluation of the four plaque snakes segmentation methods based on ROC curves (see Fig. 19.3) showed that the best ROC curve was obtained for the Lai and Chin snakes segmentation method. The area under this curve was larger than the others.

Some attempts were made from other researchers to segment the carotid plaque in MRI by using the GVF field [21], snakes [21], and dynamic programming [22]. In all of the above studies, the initial snake contour was placed manually, and a smaller number of images compared with this study were tested. More specifically, a segmentation method for the arterial walls and plaque in transversal MRI images based on dynamic programming was proposed in [22]. In [20], the plaque borders in transversal MRI carotid images were segmented based on the mean shift density estimation algorithm. In [21], a snakes segmentation method was applied on MRI transversal carotid images to detect the lumen and the outer wall boundaries of the artery by using the GVF force field [26].

There are some limitations in the proposed methodology which are summarized as follows: (a) The color flow sometimes overlaps with areas of the tissue wall or the plaque. (b) The color does not always fill up places where the blood flow velocity is very low. Therefore the contour initialization estimation may not be that accurate. The contour initialization can be improved by using a statistical approach to initialize and train the snake about blood flow [40]. (c) The snake contour may be some times attracted by local minima and converge to a wrong location. (d) Cases of plaque type I and type V (see Sect. 2.2) were not considered for segmentation.

5 Concluding Remarks and Future Directions

The method presented in this study proposes an integrated system for plaque segmentation in longitudinal ultrasound images of the carotid artery. Such a system cannot only reduce significantly the time required for the image analysis but also it can reduce the subjectivity that accompanies manual delineations and measurements. The method will be further evaluated on a larger number of ultrasound images and using multiple experts. In this chapter, the cases of totally occlusive dissections and side-branches, as well as cases of plaque type I and type V (see Sect. 2.2) were not considered for segmentation. Future work will focus on

improving the segmentation procedure, such that it can process satisfactorily these special cases and difficult to segment images, taking for example into consideration a statistical approach to initialize and teach the snake about the blood flow and plaque area [40]. Furthermore, the segmentation system proposed in this study will be incorporated into a computer-aided diagnostic system that supports the texture analysis of the segmented plaque, as documented in [41], providing an automated system for the early diagnosis and the assessment of the risk of stroke.

The majority of plaque image analysis studies are focused on the development of 2D ultrasound systems. In general these studies present effective methods for image segmentation, image de-speckling, and texture feature extraction. Due to the large number of parameters involved, we can see many variations in the results. Thus, even for 2D systems, there will always be an interest in developing more robust segmentation methods, new multiscale texture features, and the application of innovative classification techniques. Some of the most interesting challenges are associated with emerging studies [42]. These methods can be used in order to focus on new 2D problems associated with early plaque formation.

The extraction of 3D shape and structure information can be used to further our understanding of carotid plaque morphology. We believe that research will continue in establishing 3D volumetric changes and their associations with atherosclerosis.

Plaque motion analysis holds significant promise as well. The relative motion among different plaque components should be investigated [43]. The future development of very accurate 3D/4D systems will also help with the development of accurate motion analysis systems. Finally, in [44] a method for the segmentation of plaques in video sequences of ultrasound images of the internal carotid artery was presented. The method was formulated in a Bayesian framework.

It would be interesting to develop noninvasive, multimodality plaque image analysis systems. The advancement of 3D ultrasound will help these efforts. Basically, high-resolution 3D ultrasound reconstructions will be much easier to fuse with 2D slices from other modalities. To do this, we would need to register the geometric features of the 2D slice to the 3D volume or to use a mutual information registration method. It would also be interesting to examine how 2D histological studies match 3D ultrasound reconstructions.

References

1. Zarins CK, Xu C, Glagov S (2001) Atherosclerotic enlargement of the human abdominal aorta. Atherosclerosis 155(1):157–164
2. ACAS Clinical Advisory (1994) Carotid endarterectomy for patients with asymptomatic internal carotid artery stenosis. Stroke 25(12):2523–2524
3. Executive Committee for the Asymptomatic Carotid Atherosclerosis study (2002) Endarterectomy for asymptomatic carotid stenosis. J Am Med Assoc 273:1421–1428
4. Nicolaides A, Sabetai M, Kakkos SK, Dhanjil S, Tegos T, Stevens JM (2003) The asymptomatic carotid stenosis and risk of stroke study. Int Angiol 22(3):263–272
5. Zahalka A, Fenster A (2001) An automated segmentation method for three-dimensional carotid ultrasound images. Phys Med Biol 46:1321–1342
6. Hamou A, El-Sakka M (2004) A novel segmentation technique for carotid ultrasound images. In: International conference on acoustic speech and signal processing ICASSP, vol 521, p 524
7. Abdel-Dayen AR, El.-Sakka MR (2004) A novel morphological-based carotid artery contour extraction. Can Conf Electr Comput Eng 4:1873–1876
8. Mao F, Gill J, Downey D, Fenster A (2000) Segmentation of carotid artery in ultrasound images: method development and evaluation technique. Med Phys 27(8):1–10
9. Abolmaesumi P, Sirouspour MR, Salcudean SE (2000) Real-time extraction of carotid artery contours from ultrasound images. In: Proceedings of IEEE international conference on computer based medical systems, pp 181–186
10. Gill JD, Ladak HM, Steinman DA, Fenster A (2000) Segmentation of ulcerated plaque: a semi-automatic method for tracking the progression of carotid atherosclerosis. In: World congress on medical physics and biomedical engineering, pp 1–4
11. Delsanto S, Molinari F, Liboni W, Giustetto P, Patalamenti S, Suri JS (2006) User-independent plaque characterization and accurate IMT measurement of carotid artery wall using ultrasound. In: Proceedings of 28th annual international conference IEEE EMBS, pp 2404–2407
12. Loizou CP, Pattichis CS, Pantziaris M, Nicolaides AN (2007) An integrated system for the segmentation of atherosclerotic carotid plaque. IEEE Trans Inf Technol Biomed 11(6):661–667
13. Guerrero J, Salcudean SE, McEwen SE, Masri JA (2007) Real-time vessel segmentation and tracking for ultrasound imaging applications. IEEE Trans Med Imaging 26(8):1079–1090
14. Golemati S, Stoitsis E, Sifakis G, Balkisas T, Nikita KS (2007) Using the Hough transform to segment ultrasound images of longitudinal and transverse sections of the carotid artery. Ultrasound Med Biol 33(12):1918–1932
15. Slabaugh G, Unal G, Wels M, Fang T, Rao B (2009) Statistical region-based segmentation of ultrasound images. Ultrasound Med Biol 35(5):781–795
16. Zhang X, McKay CR, Sonka M (1998) Tissue characterization in intravascular ultrasound images. IEEE Trans Med Imaging 17(6):889–899
17. Cardinal MR, Meunier J, Soulez G, Thérasse E, Cloutier G (2003) Intravascular ultrasound image segmentation: a fast-marching method. In: Proceedings of MICCAI LNCS 2879, pp 432–439
18. Brusseau E, De Korte CL, Mastick F, Schaar J, Van der Steen AFW (2004) Fully automatic luminal contour segmentation in intracoronary ultrasound imaging – a statistical approach. IEEE Trans Med Imaging 23(5):554–566
19. Olszewski ME, Wahle A, Vigmostad SC, Sonka M (2005) Multidimensional segmentation of coronary intravascular ultrasound images using knowledge-based methods. In: Proceedings of SPIE medical imaging: image processing, vol 5747, pp 496–504
20. Xu D, Hwang J-N, Yuan C (2001) Atherosclerotic plaque segmentation at human carotid artery based on multiple contrast weighting MR images. In: IEEE ICIP, pp 849–852
21. Adams GJ, Vick GW, Ballantyne CM, Insull W, Morrisett JD (2002) Estimation of carotid atherosclerotic plaque volume in vivo magnetic resonance images. In: Proceedings of EMBS/BMES conference, pp 1072–1073

22. Yang F, Holzapfel GA, Schulze-Bauer CAJ, Stollberger R, Thedens D, Bolinger L, Stolpen A, Sonka M (2003) Segmentation of wall and plaque in in-vitro vascular MR images. Int J Cardiovasc Imaging 19:419–428
23. Cohen LD (1991) On active contour models and balloons. Comput Vis Graph Image Process Image Underst 53(2):211–218
24. Williams D, Shah M (1992) A fast algorithm for active contour and curvature estimation. CVGIP Image Underst 55(1):14–26
25. Lai KF, Chin RT (1995) Deformable contours-modeling and extraction. IEEE Trans PAMI 17(11):1084–1090
26. Xu C, Prince J (1998) Generalized gradient vector flow external forces for active contours. Signal Process 71:131–139
27. Loizou CP, Pattichis CS, Pantziaris M, Nicolaides AN (2005) Performance evaluation of active contour models for carotid plaque segmentation. In: EMBEC European medical and biological engineering conference IFMBE on biomedical engineering, Prague, Czech Republic, vol 11, issue 1, pp 1–6
28. A Philips Medical System Company (2001) Comparison of image clarity, SonoCT real-time compound imaging versus conventional 2D ultrasound imaging. ATL Ultrasound Report
29. Kyriakou E, Pattichis MS, Christodoulou C, Pattichis CS, Kakkos S, Griffin M, Nicolaides A (2005) Ultrasound imaging in the analysis of carotid plaque morphology for the assessment of stroke. In: Suri JS, Yuan C, Wilson DL, Laxminarayan S (eds) Plaque imaging: pixel to molecular level. IOS Press, Washington, DC, pp 241–275
30. Elatrozy T, Nicolaides A, Tegos T, Zarka A, Griffin M, Sabetai M (1998) The effect of B-mode ultrasonic image standardization of the echodensity of symptomatic and asymptomatic carotid bifurcation plaque. Int Angiol 17(3):179–186
31. Loizou CP, Pattichis CS (2008) Despeckle filtering algorithms and software for ultrasound imaging. Synthesis lectures on algorithms and software for engineering. Morgan & Claypool, San Rafael, CA
32. Lee JS (1980) Digital image enhancement and noise filtering by use of local statistics. IEEE Trans Pattern Anal Mach Intell PAMI-2(2):165–168
33. Loizou CP, Pattichis CS, Christodoulou CI, Istepanian RSH, Pantziaris M, Nicoliades A (2005) Despeckle filtering inultrasound imaging of the carotid artery. IEEE Trans Ultrason Feroelectr Freq Control 52(2):1653–1669
34. Metz C (1978) Basic principles of ROC analysis. Semin Nucl Med 8:283–298
35. Fleiss JL, Cohen J, Everitt BS (1969) Large sample standard errors of kappa and weighted kappa. Psychol Bull 72(5):323–327
36. Rosenfield GH, Fitzpatrick-Lins K (1986) A coefficient of agreement as a measure of thematic classification accuracy. Photogramm Eng Remote Sensing 52(2):223–227
37. Loizou CP, Pattichis CS, Pantziaris M, Tyllis T, Nicolaides A (2007) Snakes based segmentation of the common carotid artery intima media. Med Biol Eng Comput 45(1):35–49
38. Loizou CP, Pattichis CS, Pantziaris M, Tyllis T, Nicolaides A (2006) Quantitative quality evaluation of ultrasound imaging in the carotid artery. Med Biol Eng Comput 44(5):414–426
39. Abd-Elmonien K, Youssef A-B, Kadah Y (2002) Real-time speckle reduction and coherence enhancement in ultrasound imaging via nonlinear anisotropic diffusion. IEEE Trans Biomed Eng 49(9):997–1014
40. Gil D, Hernandez A, Mauri J, Radeva P (2006) Statistical strategy for anisotropic adventitia modeling in IVUS. IEEE Trans Med Imaging 25(6):768–778
41. Christodoulou CI, Pattichis CS, Pantziaris M, Nicolaides A (2003) Texture based classification of atherosclerotic carotid plaques. IEEE Trans Med Imaging 22(7):902–912
42. Kyriacou E, Pattichis CS, Pattichis MS, Loizou CP, Christodoulou C, Kakos S, Nicolaides A (2010) A review of non-invasive ultrasound imaging processing methods in the analysis of carotid plaque morphology for the assessment of stroke. IEEE Trans Inf Technol Biomed 14(4):1027–1038
43. Loizou CP, Pantziaris M, Pattichis CS, Kyriakou E (2010) M-mode state-based identification in ultrasound videos of the common carotid artery. In: Proceedings of 4th international symposium on communications, control and signal processing ISCCSP, pp 1–6
44. Destrempes F, Meunier J, Giroux M-F, Soulez G, Cloutier G (2011) Segmentation of plaques in sequences of ultrasonic B-mode images of carotid arteries based on motion estimation and a Bayesian model. IEEE Trans Biomed Eng 58(8):2202–2210

Relationship Between Plaque Echogenicity and Atherosclerosis Biomarkers

20

John D. Kakisis, Efthimios Avgerinos, Nikolaos Kadoglou, George Sfyroeras, Konstantinos Moulakakis, and Christos D. Liapis

1 Introduction

Prediction of the outcome of carotid stenosis is currently based on two main factors: the history of neurologic events and the degree of stenosis. However, even for the highest risk group of recently symptomatic patients with severe carotid stenosis, the majority of the patients will remain asymptomatic, indicating that our ability to predict future strokes needs further improvement. Several imaging modalities have been used for the identification of the vulnerable carotid plaque, including duplex ultrasound, computed tomography, magnetic resonance imaging, fluorine-18-labeled fluorodeoxyglucose positron emission tomography, optical coherence tomography and laser-induced fluorescence spectroscopy [1]. The most widely used of all these techniques is duplex ultrasound, with the prognostic significance of plaque echolucency having been demonstrated in more than 8,000 patients [2–6]. The underlying mechanism is plaque rupture, with subsequent embolization to the brain, which is more likely in a lipid-rich, fragile, echolucent plaque.

Advances in cellular and molecular pathophysiology and the demand to accurately predict stroke risk and choose the optimal prevention strategy (carotid endarterectomy, carotid stenting, or medical treatment) have stimulated great interest in the development of novel diagnostic markers [7]. Serum biomarkers have emerged as potential predictors of carotid artery disease natural history and perioperative risk, while recent data suggest that they may guide carotid intervention and bio-oriented therapies [8].

Serum biomarkers are molecules produced and secreted by several cells that are present in the atherosclerotic plaque such as monocyte-derived macrophages, T-lymphocytes, activated endothelial cells, and proliferating smooth muscle cells. Such molecules include C-reactive protein (CRP), matrix metalloproteinases and their inhibitors, soluble CD40 ligand, cytokines, oxidized LDL, lipoprotein-associated phospholipase A2, type II secretory phospholipase A2, myeloperoxidase, monocyte chemoattractant protein-1, etc. [1, 9, 10]. These molecules induce a local inflammatory response, activation and proliferation of smooth muscle cells, lesion progression, and matrix degradation of the fibrous cap [9]. In this context, there is an interesting link between biomarkers and carotid plaque echogenicity, with biomarkers representing a part of the pathophysiologic process that leads to the development of a plaque with the respective morphological characteristics.

2 Cytokines

Serum IL-6 levels have been found to be significantly higher in patients with symptomatic compared with those with asymptomatic carotid disease. Symptomatic patients have also more intense macrophage infiltration of the atherosclerotic plaque suggesting that inflammatory process may contribute to the destabilization of the carotid plaque [11]. Intracellular cytokine expression in peripheral blood has also been found to be significantly higher in patients undergoing carotid endarterectomy who had previous stroke (IFN-g, IL-1b, IL-6, IL-8, IL-4, and IL-10) or amaurosis fugax (IFN-g, IL-6, IL-4, and IL-10) than in patients not undergoing endarterectomy [12].

The theory of the link between cytokine expression and plaque vulnerability has been verified by an ultrasonographic study demonstrating that elevated serum IL-6 levels are associated with lower echogenicity of carotid plaques as quantified by integrated backscatter analysis [13]. The association remained significant when traditional atherosclerotic risk factors, plaque thickness, and medication use were controlled for.

IL-6 is also released from carotid stenotic lesions after stenting, with the level of local IL-6 release being higher in

J.D. Kakisis (✉) • E. Avgerinos • N. Kadoglou • G. Sfyroeras • K. Moulakakis • C.D. Liapis
Department of Vascular Surgery, Athens University Medical School, "Attikon" Hospital, Rimini 1, 12462 Athens, Haidari, Greece
e-mail: kakisis@med.uoa.gr

L. Saba et al. (eds.), *Multi-Modality Atherosclerosis Imaging and Diagnosis*,
DOI 10.1007/978-1-4614-7425-8_20,

plaques with lower echogenicity and less plaque calcification [14]. Prominent secretion of IL-6 from symptomatic lesions and lower echogenic lesions support the close association of plaque instability and IL-6 production in vulnerable plaques. IL-6 release after carotid stenting has also been found to be associated with periprocedural new ischemic lesions [15]. On the other hand, carotid plaques retrieved at endarterectomy from patients taking statins showed significantly reduced concentrations of IL-6, suggesting a lesser degree of localized inflammation within the plaques of patients on statin therapy [16].

Although the association between IL-6 and plaque vulnerability has been proven, it is not clear whether IL-6 is the cause or the effect of this vulnerability. High levels of IL-6 in peripheral blood may reflect the increased production of IL-6 by inflammatory cells in unstable plaques and, thus, be a simple marker of increased inflammatory activity within the plaque [17]. On the other hand, IL-6 may itself facilitate the formation of unstable plaques through:

- Activation of mononuclear cells to secrete monocyte chemotactic protein 1 (MCP-1), a chemokine pivotal for monocyte recruitment [18]
- Stimulation of the synthesis of all the acute phase proteins involved in the inflammatory response (CRP, serum amyloid A, fibrinogen, α_1-chymotrypsin, and haptoglobin) [19, 20]
- Stimulation of the production of MMP-9, MMP-2, and MMP-1 [21, 22]

3 Vascular Calcification Markers

Atherosclerotic plaque calcification enhances plaque stability and decreases the likelihood of clinical events. A growing number of stimulatory and inhibitory molecules suggest that vascular calcification is an actively regulated process. Among these molecules, osteopontin (OPN), an acidic phosphoprotein, and osteoprotegerin (OPG), a member of the TNF-a receptor superfamily, have recently been demonstrated to inhibit mineral deposition as well as osteoclastogenesis, and they are constitutively expressed by a wide range of cell types in vasculature [23]. Although the large prospective study by Nybo et al. found no association of baseline OPG with ischemic stroke [24], a recent comparative study (symptomatic vs. asymptomatic patients with carotid stenosis) showed a strong relationship of serum OPN and OPG levels with low carotid plaque echogenicity and symptomatology [25].

These findings support the notion that OPN downregulates plaque calcification and may promote plaque instability [25]. Aside from direct effects, OPN may facilitate plaque destabilization indirectly. Available data suggest that OPN may induce matrix metalloproteinases release and angiogenesis within the atherosclerotic plaque leading to fibrous cap degradation and hemorrhage, respectively [26–28]. Taken all together, OPN seems to assume a key role in atherogenesis and cerebral ischemic events occurrence, but the underlying mechanisms require further research.

OPG comprises a crucial inhibitor of vascular calcification. OPG-deficient mice exhibit severe osteoporosis and vascular calcification of the aorta and renal arteries [29]. This phenotype can be prevented by delivery of the recombinant OPG and transgenic overexpression of OPG [30]. Consequently, the elevated OPG levels in symptomatic patients and their independent relationship with GSM suggest less calcification and a contributory role of OPG to plaque vulnerability [25]. Probably targeting OPG may provide a novel therapeutic strategy against carotid plaque rupture.

4 Glycated Hemoglobin

HbA1c is an indicator of average glucose levels over the previous 6–8 weeks. Apart from its common use as an indicator of intermediate-term glycemic control, HbA1c can also be used as a marker of increased mortality and cardiovascular disease in both diabetic and nondiabetic persons [31–36].

With regard to carotid disease, increasing levels of HbA1c are associated with both IMT [37–39] and carotid plaque prevalence [40]. In the Tromsø study, HbA1c level was found to be strongly related to the prevalence of echogenic and predominantly echogenic plaques but not, or if anything negatively, associated with the risk of echolucent plaques in nondiabetic individuals [41]. The authors postulate that the high prevalence of echogenic plaques may reflect the fact that subjects with high HbA1c levels have had plaques for a longer period than euglycemic persons at the same age, or that the progression from soft to hard plaque is accelerated in hyperglycemic subjects [41]. Another possible mechanism is that activation of transforming growth factor-β occurs at an early stage of diabetes mellitus triggering fibrotic changes in the tissue and, thus, leading to a high content of fibrous tissue within the developing plaque [41, 42].

5 Matrix Metalloproteinases

Matrix metalloproteinases are an ever-expanding family of zinc-dependent endopeptidases with proteolytic activity toward one or more components of the extracellular matrix [43]. Growing evidence supports the strong relationship of MMPs with plaque instability and consequent cardiovascular events. Insights from human pathological studies and experimental models of atherosclerosis have revealed the overproduction of MMPs by inflammatory cells in the rupture-prone regions of atherosclerotic plaques [44, 45].

In a follow-up study, the MMP-9 plasma concentrations predicted stroke and cardiovascular death in patients with ≥50 % carotid stenosis, although not independently [45]. These findings were further confirmed by two nonprospective studies comparing symptomatic and asymptomatic patients [46, 47]. The positive predictive value of MMP-9 was significantly enhanced when combined with other members of the MMP family (MMP-7 and MMP-8 and their tissue inhibitor of metalloproteinases-1) [47] or with plaque echolucency [27].

Pregnancy-associated plasma protein A (PAPP-A) is a high-molecular-weight metalloproteinase that is typically measured during pregnancy in maternal blood for the fetal diagnosis of Down syndrome [48]. However, circulating PAPP-A is physiologically present in both men and women; moreover, it is abundantly expressed in plaque cells and extracellular matrix of ruptured and eroded unstable coronary plaques, but not in stable plaques [49]. In patients with carotid artery disease, circulating levels of the metalloproteinase PAPP-A were found to be significantly higher in those who exhibited hyperechoic or isoechoic, echogenic plaques compared with patients with hypoechoic plaques [48]. The significant positive correlation observed between CRP and PAPP-A levels supports the notion that PAPP-A is produced by activated cells and released into the extracellular matrix during the local inflammatory process occurring within the arterial wall [48].

6 Soluble CD36

CD34 is a surface glycophosphoprotein expressed on lymphohematopoietic stem and progenitor cells, small-vessel endothelial and embryonic fibroblasts [50]. It has been shown to be involved in angiogenesis, inflammation, lipid metabolism, platelet activation, and atherosclerosis. CD36 is present in lipid-laden macrophages in atherosclerotic lesions [51–53], whereas CD36-apo E double-null animals have been found to be markedly resistant to lesion formation even in areas of enhanced predisposition [54]. These findings underscore the essential role of CD34 in the atherogenic process.

The association between CD36 and advanced atherosclerosis is also supported by the finding of strong immunostaining of CD36 in symptomatic as compared with asymptomatic carotid plaques, primarily located to lipid-loaded macrophages in the fatty core of the atherosclerotic plaque [55]. Plasma levels of soluble CD36 were markedly elevated in those with recently symptomatic carotid plaques, within the last 2 months, as compared with other patients. Furthermore, patients with echolucent carotid plaques tended to have higher soluble CD36 levels in plasma compared with those with echogenic/heterogenic plaque [55]. It is speculated that apoptosis of lipid-loaded macrophages may lead to enhanced release of CD36. In this context, soluble CD36 can be used as a marker of plaque echolucency and destabilization.

7 Soluble CD40 Ligand

CD40 ligand (CD40L) is a transmembrane protein and a member of the TNF superfamily. It is expressed by all major cells implicated in inflammation and atherosclerosis, including activated T-lymphocytes, vascular endothelial cells, smooth muscle cells, monocytes/macrophages, and platelets [56, 57]. Ligation of CD40 enhances the expression of proinflammatory and atherogenic molecules such as cytokines, chemokines, matrix metalloproteinases, growth factors, and adhesion molecules, as well as prothrombotic mediators such as tissue factor [10].

In a prospective, nested case–control evaluation of healthy middle-aged women, mean concentrations of soluble CD40L at baseline were significantly higher among the participants who subsequently developed myocardial infarction, stroke, or cardiovascular death, compared with the age- and smoking-matched women who remained free of cardiovascular disease during a 4-year follow-up [58]. These findings, however, were not verified by a recent study, in an older (aged 60–69 years) general population cohort [59].

In an MRI study of carotid plaques in patients with carotid atherosclerosis on ultrasonography, baseline levels of soluble CD40L were higher among patients with evidence of intraplaque lipid than among those without it [60]. In contrast, soluble CD40L levels were not correlated with percent diameter stenosis. The relative risk for intraplaque lipid associated with soluble CD40L levels above the median was 6.0, with the magnitude of this predictive effect remaining practically the same after adjustment for traditional cardiovascular risk factors.

There are several ways by which soluble CD40L may participate in the destabilization of atheromatous plaques. CD40L induces apoptosis and the formation of necrotic core in atheromatous plaques [61]. In addition, CD40L stimulates endothelial cell proliferation and promotes in vivo angiogenesis, thus representing a major determinant of intraplaque neovascularization and plaque vulnerability [62].

In mice, inhibition of CD40 signaling reduced the size of aortic atherosclerotic lesions by 59 % and their lipid content by 79 % [63]. Furthermore, atheroma of mice treated with anti-CD40L antibody contained significantly fewer macrophages and T lymphocytes, more smooth muscle cells and collagen and exhibited decreased expression of vascular cell adhesion molecule-1 [63, 64]. Similarly, in an

animal model of progressive atherosclerosis, a pronounced increase in collagen content, vascular smooth muscle cell/myofibroblast content, and fibrous cap thickness was observed, while the lipid core and macrophage content decreased [65].

8 Retinol-Binding Protein 4

Retinol-binding protein 4 (RBP4) is a recently identified adipokine suggested to link obesity with its comorbidities, especially insulin resistance, type 2 diabetes, and certain components of the metabolic syndrome [66]. RBP4 may also elicit subclinical inflammation leading to cardiovascular disease [67]. A strong correlation between RBP4 and inflammation markers, such as CRP, monocyte chemoattractant protein-1, and CD68, has been found [67, 68]. Studies in patients with type 2 diabetes or coronary artery disease have also revealed an association between RBP4 levels and markers of lipid metabolism, such as total cholesterol, LDL-cholesterol, VLDL cholesterol, triacylglycerol levels, and hepatic lipase activity [69].

The lipid-modulating activities of RBP4 may explain the finding that circulating RBP4 concentrations are inversely associated with intima media and plaque echogenicity in carotid arteries [70]. The higher fat content in the vessel wall and in atherosclerotic plaques of subjects with higher RBP4 levels implies that RBP4 could be involved not only in the development of atherosclerosis but also in the development of vulnerable atherosclerotic plaques as well. Interestingly, in the Uppsala Longitudinal Study of Adult Men, which recruited among all 50-year-old men living in Uppsala in 1970–1974, RBP4 concentrations were significantly associated with prior cerebrovascular disease and any prior hospitalization for cardiovascular disease in age-adjusted analyses, whereas no significant associations were found between RBP4 concentrations and prior myocardial infarction [71].

9 Oxidized LDL

LDL cholesterol is one of the major risk factors for atherosclerosis, since it is causally associated with the development of atherosclerosis, whereas a reduction in LDL levels leads to a reduction of atherosclerosis progression or even regression of atherosclerosis, lower incidence of cardiovascular events (myocardial infarction and stroke), and even reduced total mortality [72–74]. Plasma LDL is transported across the endothelium to the subendothelial space where it is subjected to oxidative modifications to produce highlyoxidized LDL (OxLDL). OxLDL is a potent inducer of inflammatory molecules and is believed to be the most atherogenic form of LDL.

In accordance with this notion, the plasma OxLDL level has been found to be significantly higher in patients with carotid stenosis than in controls, suggesting that OxLDL is involved in carotid artery disease, as is the case in coronary artery disease [75]. The plaque OxLDL level was nearly 70 times higher than plasma OxLDL. There was also a strong correlation between the plaque OxLDL level and the extent of macrophage infiltration. The macrophage-rich plaques were associated with plaque rupture, fibrous cap thinning, and a large-sized lipid core and correlated with ultrasonographic echolucency but not with angiographical carotid stenosis [75].

Similarly, in a cross-sectional population-based study of 61-year-old men, plasma OxLDL turned out to be independently associated with the occurrence of echolucent plaques both in the femoral and the carotid artery [76, 77]. The source of OxLDL in plasma could be the direct release of OxLDL from ruptured or permeable plaques, ischemic injury to damaged cell membranes, or a turnover of OxLDL in newly formed or progressing lesions in the arterial tree [76].

10 C-Reactive Protein

CRP is currently the most studied biomarker used in clinical practice. In several prospective studies, baseline CRP has been related to the risk of cerebrovascular events among healthy adults, patients with asymptomatic carotid lesions, and other patient cohorts [78–85]. A meta-analysis of studies with a long-term follow-up showed that the risk of stroke in healthy individuals with the highest quartile of CRP concentrations increased by 70 % compared with those in the lowest quartile [86]. Nonprospective studies comparing symptomatic vs. asymptomatic patients with carotid stenosis advocate that CRP may identify carotid plaque at risk of symptomatic conversion [87, 88].

Despite these findings that support an association between CRP levels and plaque instability, there have not been any data, so far, correlating CRP with plaque echogenicity. CRP has been found to be associated with total carotid plaque area among men in models controlling for traditional atherosclerotic risk factors, but did not discriminate echolucent from echogenic carotid plaques in neither women nor men [89]. In another study, high-sensitivity CRP concentrations were negatively correlated with carotid plaque echogenicity in univariate analysis, but when traditional atherosclerotic risk factors, plaque thickness, and medication use were controlled for, the association was of borderline significance [13]. Other reports have further supported the notion that carotid plaque echolucency is not related to systemic levels of CRP [90, 91].

References

1. Liapis CD, Bell PR, Mikhailidis D, Sivenius J, Nicolaides A, Fernandes e Fernandes J, Biasi G, Norgren L, ESVS Guidelines Collaborators (2009) ESVS guidelines. Invasive treatment for carotid stenosis: indications, techniques. Eur J Vasc Endovasc Surg 37(4 Suppl):1–19
2. Nicolaides AN, Kakkos SK, Griffin M, Sabetai M, Dhanjil S, Thomas DJ et al (2005) Asymptomatic Carotid Stenosis and Risk of Stroke (ACSRS) Study Group. Effect of image normalization on carotid plaque classification and the risk of ipsilateral hemispheric ischemic events: results from the asymptomatic carotid stenosis and risk of stroke study. Vascular 13:211–221
3. Liapis CD, Kakisis JD, Kostakis AG (2001) Carotid stenosis: factors affecting symptomatology. Stroke 32:2782–2786
4. Mathiesen EB, Bonaa KH, Joakimsen O (2001) Echolucent plaques are associated with high risk of ischemic cerebrovascular events in carotid stenosis: the tromso study. Circulation 103:2171–2175
5. Gronholdt ML, Nordestgaard BG, Schroeder TV, Vorstrup S, Sillesen H (2001) Ultrasonic echolucent carotid plaques predict future strokes. Circulation 104:68–73
6. Pedro LM, Pedro MM, Goncalves I, Carneiro TF, Balsinha C, Fernandes e Fernandes R et al (2000) Computer-assisted carotid plaque analysis: characteristics of plaques associated with cerebrovascular symptoms and cerebral infarction. Eur J Vasc Endovasc Surg 19:118–123
7. Loftus I, Thompson M (2008) Plaque biology: interesting science or pharmacological treasure trove? Eur J Vasc Endovasc Surg 36:507–516
8. Avgerinos ED, Kadoglou NP, Moulakakis KG, Giannakopoulos TG, Liapis CD (2011) Current role of biomarkers in carotid disease: a systematic review. Int J Stroke 6:337–345
9. Ding S, Zhang M, Zhao Y, Chen W, Yao G, Zhang C et al (2008) The role of carotid plaque vulnerability and inflammation in the pathogenesis of acute ischemic stroke. Am J Med Sci 336:27–31
10. Koenig W, Khuseyinova N (2007) Biomarkers of atherosclerotic plaque instability and rupture. Arterioscler Thromb Vasc Biol 27:15–26
11. Koutouzis M, Rallidis LS, Peros G, Nomikos A, Tzavara V, Barbatis C, Andrikopoulos V, Vassiliou J, Kyriakides ZS (2009) Serum interleukin-6 is elevated in symptomatic carotid bifurcation disease. Acta Neurol Scand 119:119–125
12. Profumo E, Buttari B, Tosti ME, Siracusano A, Ortona E, Margutti P, Capoano R, Salvati B, Riganò R (2008) Association of intracellular pro- and anti-inflammatory cytokines in peripheral blood with the clinical or ultrasound indications for carotid endarterectomy in patients with carotid atherosclerosis. Clin Exp Immunol 152:120–126
13. Yamagami H, Kitagawa K, Nagai Y, Hougaku H, Sakaguchi M, Kuwabara K, Kondo K, Masuyama T, Matsumoto M, Hori M (2004) Higher levels of interleukin-6 are associated with lower echogenicity of carotid artery plaques. Stroke 35:677–681
14. Abe Y, Sakaguchi M, Furukado S, Okazaki S, Fujinaka T, Sakoda S, Yoshimine T, Kitagawa K (2010) Associations of local release of inflammatory biomarkers during carotid artery stenting with plaque echogenicity and calcification. Cerebrovasc Dis 30:402–409
15. Abe Y, Sakaguchi M, Furukado S, Fujinaka T, Sakoda S, Yoshimine T, Kitagawa K (2010) Interleukin-6 release after carotid artery stenting and periprocedural new ischemic lesions. J Cereb Blood Flow Metab 30:857–863
16. Molloy KJ, Thompson MM, Schwalbe EC, Bell PR, Naylor AR, Loftus IM (2004) Comparison of levels of matrix metalloproteinases, tissue inhibitor of metalloproteinases, interleukins, and tissue necrosis factor in carotid endarterectomy specimens from patients on versus not on statins preoperatively. Am J Cardiol 94:144–146
17. Schieffer B, Schieffer E, Hilfiker-Kleiner D, Hilfiker A, Kovanen PT, Kaartinen M, Nussberger J, Harringer W, Drexler H (2000) Expression of angiotensin II and interleukin 6 in human coronary atherosclerotic plaques: potential implications for inflammation and plaque instability. Circulation 101:1372–1378
18. Biswas P, Delfanti F, Bernasconi S, Mengozzi M, Cota M, Polentarutti N, Mantovani A, Lazzarin A, Sozzani S, Poli G (1998) Interleukin-6 induces monocyte chemotactic protein-1 in peripheral blood mononuclear cells and in the U937 cell line. Blood 91:258–265
19. Woods A, Brull DJ, Humphries SE, Montgomery HE (2000) Genetics of inflammation and risk of coronary artery disease: the central role of interleukin-6. Eur Heart J 21:1574–1583
20. Castell JV, Gomez-Lechon MJ, David M et al (1989) Interleukin- is the major regulator of acute phase protein synthesis in adult human hepatocytes. FEBS Lett 24:237–239
21. Kossakowska AE, Edwards DR, Prusinkiewicz C, Zhang MC, Guo D, Urbanski SJ, Grogan T, Marquez LA, Janowska-Wieczorek A (1999) Interleukin-6 regulation of matrix metalloproteinase (MMP-2 and MMP-9) and tissue inhibitor of metalloproteinase (TIMP-1) expression in malignant non-Hodgkin's lymphomas. Blood 94:2080–2089
22. Zhu Y, Hojo Y, Ikeda U, Takahashi M, Shimada K (2000) Interaction between monocytes and vascular smooth muscle cells enhances matrix metalloproteinase-1 production. J Cardiovasc Pharmacol 36:152–161
23. Johnson RC, Leopold JA, Loscalzo J (2006) Vascular calcification: pathobiological mechanisms and clinical implications. Circ Res 99:1044
24. Nybo M, Johnsen SP, Dethlefsen C et al (2008) Lack of observed association between high plasma osteoprotegerin concentrations and ischemic stroke risk in a healthy population. Clin Chem 54:1969–1974
25. Kadoglou NP, Gerasimidis T, Golemati S et al (2008) The relationship between serum levels of vascular calcification inhibitors and carotid plaque vulnerability. J Vasc Surg 47:55–62
26. Isoda K, Nishikawa K, Kamezawa Y, Yoshida M, Kusuhara M, Moroi M et al (2002) Osteopontin plays an important role in the development of medial thickening and neointimal formation. Circ Res 91:77–82
27. Kadoglou NP, Daskalopoulou SS, Perrea D, Liapis CD (2005) Matrix metalloproteinases and diabetic vascular complications. Angiology 56:173–189
28. Tureyen K, Vemuganti R, Salamat MS, Dempsey RJ (2006) Increased angiogenesis and angiogenic gene expression in carotid artery plaques from symptomatic stroke patients. Neurosurgery 58:971–977
29. Bucay N, Sarosi I, Dunstan CR, Morony S, Tarpley J, Capparelli C et al (1998) Osteoprotegerin deficient mice develop early onset osteoporosis and arterial calcification. Genes Dev 12: 1260–1268
30. Min H, Morony S, Sarosi I, Dunstan CR, Capparelli C, Scully S et al (2000) Osteoprotegerin reverses osteoporosis by inhibiting endosteal osteoclasts and prevents vascular calcification by blocking a process resembling osteoclastogenesis. J Exp Med 192:463–474
31. Liu Y, Yang YM, Zhu J, Tan HQ, Liang Y, Li JD (2011) Prognostic significance of hemoglobin A1c level in patients hospitalized with coronary artery disease. A systematic review and meta-analysis. Cardiovasc Diabetol 10:98
32. Khaw KT, Wareham N, Luben R et al (2001) Glycated haemoglobin, diabetes, and mortality in men in Norfolk cohort of European Prospective Investigation of Cancer and Nutrition (EPIC-Norfolk). BMJ 322:15–18

33. Park S, Barrett-Connor E, Wingard DL et al (1996) GHb is a better predictor of cardiovascular disease than fasting or postchallenge plasma glucose in women without diabetes: the Rancho Bernardo Study. Diabetes Care 19:450–456
34. Singer DE, Nathan DM, Anderson KM et al (1992) Association of HbA1c with prevalent cardiovascular disease in the original cohort of the Framingham Heart Study. Diabetes 41:202–208
35. Stratton IM, Adler AI, Neil HA, Matthews DR, Manley SE, Cull CA, Hadden D, Turner RC, Holman RR (2000) Association of glycaemia with macrovascular and microvascular complications of type 2 diabetes (UKPDS 35): prospective observational study. BMJ 321:405–412
36. Selvin E, Coresh J, Golden SH, Brancati FL, Folsom AR, Steffes MW (2005) Glycemic control and coronary heart disease risk in persons with and without diabetes: the Atherosclerosis Risk in Communities study. Arch Intern Med 165:1910–1916
37. Gerstein HC, Anand S, Yi QL et al (2003) The relationship between dysglycemia and atherosclerosis in South Asian, Chinese, and European individuals in Canada: a randomly sampled cross-sectional study. Diabetes Care 26:144–149
38. Okada M, Miida T, Hama H et al (2000) Possible risk factors of carotid artery atherosclerosis in the Japanese population: a primary prevention study in non-diabetic subjects. Intern Med 39:362–368
39. Vitelli LL, Shahar E, Heiss G et al (1997) Glycosylated hemoglobin level and carotid intimal-medial thickening in nondiabetic individuals: the Atherosclerosis Risk in Communities Study. Diabetes Care 20:1454–1458
40. Ishizaka N, Ishizaka Y, Takahashi E et al (2003) Association between insulin resistance and carotid arteriosclerosis in subjects with normal fasting glucose and normal glucose tolerance. Arterioscler Thromb Vasc Biol 23:295–301
41. Jørgensen L, Jenssen T, Joakimsen O, Heuch I, Ingebretsen OC, Jacobsen BK (2004) Glycated hemoglobin level is strongly related to the prevalence of carotid artery plaques with high echogenicity in nondiabetic individuals: the Tromsø study. Circulation 110:466–470
42. Hosomi N, Noma T, Ohyama H et al (2002) Vascular proliferation and transforming growth factor-beta expression in pre- and early stage of diabetes mellitus in Otsuka Long-Evans Tokushima fatty rats. Atherosclerosis 162:69–76
43. Kadoglou NP, Liapis CD (2004) Matrix metalloproteinases: contribution to pathogenesis, diagnosis, surveillance and treatment of abdominal aortic aneurysms. Curr Med Res Opin 20:419–432
44. Alvarez B, Ruiz C, Chacon P, Alvarez-Sabin J, Matas M (2004) Serum values of metalloproteinase-2 and metalloproteinase-9 as related to unstable plaque and inflammatory cells in patients with greater than 70 % carotid artery stenosis. J Vasc Surg 40:469–475
45. Eldrup N, Gronholdt ML, Sillesen H, Nordestgaard BG (2006) Elevated matrix metalloproteinase-9 associated with stroke or cardiovascular death in patients with carotid stenosis. Circulation 114:1847–1854
46. Jefferis BJ, Whincup P, Welsh P et al (2010) Prospective study of matrix metalloproteinase-9 and risk of myocardial infarction and stroke in older men and women. Atherosclerosis 208:557–563
47. Heider P, Pelisek J, Poppert H, Eckstein HH (2009) Evaluation of serum matrix metalloproteinases as biomarkers for detection of neurological symptoms in carotid artery disease. Vasc Endovascular Surg 43:551–560
48. Beaudeux JL, Burc L, Imbert-Bismut F, Giral P, Bernard M, Bruckert E, Chapman MJ (2003) Serum plasma pregnancy-associated protein A: a potential marker of echogenic carotid atherosclerotic plaques in asymptomatic hyperlipidemic subjects at high cardiovascular risk. Arterioscler Thromb Vasc Biol 23:e7–e10
49. Bayes-Genis A, Conover CA, Overgaard MT, Bailey KR, Christiansen M, Holmes DR Jr, Virmani R, Oxvig C, Schwartz RS (2001) Pregnancy-associated plasma protein A as a marker of acute coronary syndromes. N Engl J Med 345:1022–1029
50. Krause DS, Fackler MJ, Civin CI, May WS (1996) CD34: structure, biology, and clinical utility. Blood 87:1–13
51. Nakagawa-Toyama Y, Yamashita S, Miyagawa J, Nishida M, Nozaki S, Nagaretani H, Sakai N, Hiraoka H, Yamamori K, Yamane T, Hirano K, Matsuzawa Y (2001) Localization of CD36 and scavenger receptor class A in human coronary arteries–a possible difference in the contribution of both receptors to plaque formation. Atherosclerosis 156:297–305
52. Suzuki H, Kurihara Y, Takeya M et al (1997) A role for macrophage scavenger receptors in atherosclerosis and susceptibility to infection. Nature 386:292–296
53. Ren Y, Silverstein RL, Allen J, Savill J (1995) CD36 gene transfer confers capacity for phagocytosis of cells undergoing apoptosis. J Exp Med 181:1857–1862
54. Febbraio M, Podrez EA, Smith JD, Hajjar DP, Hazen SL, Hoff HF, Sharma K, Silverstein RL (2000) Targeted disruption of the class B scavenger receptor CD36 protects against atherosclerotic lesion development in mice. J Clin Invest 105:1049–1056
55. Handberg A, Skjelland M, Michelsen AE, Sagen EL, Krohg-Sørensen K, Russell D, Dahl A, Ueland T, Oie E, Aukrust P, Halvorsen B (2008) Soluble CD36 in plasma is increased in patients with symptomatic atherosclerotic carotid plaques and is related to plaque instability. Stroke 39:3092–3095
56. Tousoulis D, Androulakis E, Papageorgiou N, Briasoulis A, Siasos G, Antoniades C, Stefanadis C (2010) From atherosclerosis to acute coronary syndromes: the role of soluble CD40 ligand. Trends Cardiovasc Med 20:153–164
57. Chatzigeorgiou A, Lyberi M, Chatzilymperis G, Nezos A, Kamper E (2009) CD40/CD40L signaling and its implication in health and disease. Biofactors 35:474–483
58. Schönbeck U, Varo N, Libby P, Buring J, Ridker PM (2001) Soluble CD40L and cardiovascular risk in women. Circulation 104:2266–2268
59. Jefferis BJ, Whincup PH, Welsh P, Wannamethee SG, Rumley A, Lawlor DA, Ebrahim S, Lowe GD (2011) Prospective study of circulating soluble CD40 ligand concentrations and the incidence of cardiovascular disease in a nested prospective case-control study of older men and women. J Thromb Haemost 9:1452–1459
60. Blake GJ, Ostfeld RJ, Yucel EK, Varo N, Schonbeck U, Blake MA, Gerhard M, Ridker PM, Libby P, Lee RT (2003) Soluble CD40 ligand levels indicate lipid accumulation in carotid atheroma: an in vivo study with high resolution MRI. Arterioscler Thromb Vasc Biol 23:e11–e14
61. Schönbeck U, Libby P (2001) CD40 signaling and plaque instability. Circ Res 89:1092–1103
62. Leroyer AS, Rautou PE, Silvestre JS, Castier Y, Lesèche G, Devue C, Duriez M, Brandes RP, Lutgens E, Tedgui A, Boulanger CM (2008) CD40 ligand+ microparticles from human atherosclerotic plaques stimulate endothelial proliferation and angiogenesis a potential mechanism for intraplaque neovascularization. J Am Coll Cardiol 52:1302–1311
63. Mach F, Schonbeck U, Sukhova GK, Atkinson E, Libby P (1998) Reduction of atherosclerosis in mice by inhibition of CD40 signalling. Nature 394:200–203
64. Schonbeck U, Sukhova GK, Shimizu K, Mach F, Libby P (2000) Inhibition of CD40 signaling limits evolution of established atherosclerosis in mice. Proc Natl Acad Sci USA 97:7458–7463
65. Lutgens E, Cleutjens KB, Heeneman S, Koteliansky VE, Burkly LC, Daemen MJ (2000) Both early and delayed anti-CD40L antibody treatment induces a stable plaque phenotype. Proc Natl Acad Sci USA 97:7464–7469
66. Kotnik P, Fischer-Posovszky P, Wabitsch M (2011) RBP4: a controversial adipokine. Eur J Endocrinol 165:703–711
67. Balagopal P, Graham TE, Kahn BB, Altomare A, Funanage V, George D (2007) Reduction of elevated serum retinol binding protein in obese children by lifestyle intervention: association with subclinical inflammation. J Clin Endocrinol Metab 92:1971–1974

68. Yao-Borengasser A, Varma V, Bodles AM, Rasouli N, Phanavanh B, Lee MJ, Starks T, Kern LM, Spencer HJ 3rd, Rashidi AA, McGehee RE Jr, Fried SK, Kern PA (2007) Retinol binding protein 4 expression in humans: relationship to insulin resistance, inflammation, and response to pioglitazone. J Clin Endocrinol Metab 92:2590–2597
69. von Eynatten M, Lepper PM, Liu D, Lang K, Baumann M, Nawroth PP, Bierhaus A, Dugi KA, Heemann U, Allolio B, Humpert PM (2007) Retinol-binding protein 4 is associated with components of the metabolic syndrome, but not with insulin resistance, in men with type 2 diabetes or coronary artery disease. Diabetologia 50:1930–1937
70. Ingelsson E, Lind L (2009) Circulating retinol-binding protein 4 and subclinical cardiovascular disease in the elderly. Diabetes Care 32:733–735
71. Ingelsson E, Sundström J, Melhus H, Michaëlsson K, Berne C, Vasan RS, Risérus U, Blomhoff R, Lind L, Arnlöv J (2009) Circulating retinol-binding protein 4, cardiovascular risk factors and prevalent cardiovascular disease in elderly. Atherosclerosis 206:239–244
72. Heart Protection Study Collaborative Group, Bulbulia R, Bowman L, Wallendszus K, Parish S, Armitage J, Peto R, Collins R (2011) Effects on 11-year mortality and morbidity of lowering LDL cholesterol with simvastatin for about 5 years in 20,536 high-risk individuals: a randomised controlled trial. Lancet 378:2013–2020
73. Cholesterol Treatment Trialists' (CTT) Collaboration, Baigent C, Blackwell L, Emberson J, Holland LE, Reith C, Bhala N, Peto R, Barnes EH, Keech A, Simes J, Collins R (2010) Efficacy and safety of more intensive lowering of LDL cholesterol: a meta-analysis of data from 170,000 participants in 26 randomised trials. Lancet 376:1670–1681
74. Ridker PM, Danielson E, Fonseca FA, Genest J, Gotto AM Jr, Kastelein JJ, Koenig W, Libby P, Lorenzatti AJ, Macfadyen JG, Nordestgaard BG, Shepherd J, Willerson JT, Glynn RJ, JUPITER Trial Study Group (2009) Reduction in C-reactive protein and LDL cholesterol and cardiovascular event rates after initiation of rosuvastatin: a prospective study of the JUPITER trial. Lancet 373:1175–1182
75. Nishi K, Itabe H, Uno M, Kitazato KT, Horiguchi H, Shinno K, Nagahiro S (2002) Oxidized LDL in carotid plaques and plasma associates with plaque instability. Arterioscler Thromb Vasc Biol 22:1649–1654
76. Sigurdardottir V, Fagerberg B, Wikstrand J, Schmidt C, Hulthe J (2008) Circulating oxidized LDL is associated with the occurrence of echolucent plaques in the carotid artery in 61-year-old men. Scand J Clin Lab Invest 68:292–297
77. Sigurdardottir V, Fagerberg B, Wikstrand J, Schmidt C, Hulthe J (2007) Circulating oxidized low-density lipoprotein is associated with echolucent plaques in the femoral artery independently of hsCRP in 61-year-old men. Atherosclerosis 190:187–193
78. Everett BM, Kurth T, Buring JE, Ridker PM (2006) The relative strength of C reactive protein and lipid levels asdeterminants of ischemic stroke compared with coronary heart disease in women. J Am Coll Cardiol 48:2235–2242
79. Makita S, Nakamura M, Satoh K et al (2009) Serum C-reactive protein levels can be used to predict future ischemic stroke and mortality in Japanese men from the general population. Atherosclerosis 204:234–238
80. Bos MJ, Schipper CM, Koudstaal PJ, Witteman JC, Hofman A, Breteler MM (2006) High serum C-reactive protein level is not an independent predictor for stroke: the Rotterdam Study. Circulation 114:1591–1598
81. Tanne D, Benderly M, Goldbourt U et al (2006) C-reactive protein as a predictor of incident ischemic stroke among patients with preexisting cardiovascular disease. Stroke 37:1720–1724
82. Tzoulaki I, Murray GD, Lee AJ, Rumley A, Lowe GD, Fowkes FG (2007) Relative value of inflammatory, hemostatic, and rheological factors for incident myocardial infarction and stroke: the Edinburgh Artery Study. Circulation 115:2119–2127
83. Corrado E, Rizzo M, Tantillo R et al (2006) Markers of inflammation and infection influence the outcome of patients with baseline asymptomatic carotid lesions: a 5-year follow-up study. Stroke 37:482–486
84. Chou CY, Kuo HL, Lin HH, Liu JS, Liu YL, Huang CC (2009) C-reactive protein predicts ischaemic stroke in haemodialysis patients. Int J Clin Pract 63:243–248
85. Rizzo M, Corrado E, Coppola G, Muratori I, Carella M, Novo S (2008) Prediction of cerebrovascular and cardiovascular events in patients with subclinical carotid atherosclerosis: the role of C-reactive protein. J Investig Med 56:32–40
86. Kuo HK, Yen CJ, Chang CH, Kuo CK, Chen JH, Sorond F (2005) Relation of C-reactive protein to stroke, cognitive disorders, and depression in the general population: systematic review and meta-analysis. Lancet Neurol 4:371–380
87. Papas TT, Maltezos CK, Papanas N et al (2008) High-sensitivity CRP is correlated with neurologic symptoms and plaque instability in patients with severe stenosis of the carotid bifurcation. Vasc Endovascular Surg 42:249–255
88. Anan F, Shimomura T, Kaku T et al (2008) High-sensitivity C-reactive protein level is a significant risk factor for silent cerebral infarction in patients on hemodialysis. Metabolism 57: 66–70
89. Halvorsen DS, Johnsen SH, Mathiesen EB, Njølstad I (2009) The association between inflammatory markers and carotid atherosclerosis is sex dependent: the Tromsø Study. Cerebrovasc Dis 27:392–397
90. Sirico G, Brevetti G, Lanero S, Laurenzano E, Luciano R, Chiariello M (2009) Echolucent femoral plaques entail higher risk of echolucent carotid plaques and a more severe inflammatory profile in peripheral arterial disease. J Vasc Surg 49:346–351
91. Grønholdt ML, Sillesen H, Wiebe BM, Laursen H, Nordestgaard BG (2001) Increased acute phase reactants are associated with levels of lipoproteins and increased carotid plaque volume. Eur J Vasc Endovasc Surg 21:227–234

Hypothesis Validation of Far Wall Brightness in Carotid Artery Ultrasound for Feature-Based IMT Measurement Using a Combination of Level Set Segmentation and Registration

21

Filippo Molinari, U. Rajendra Acharya, Luca Saba, Andrew Nicolaides, and Jasjit S. Suri

1 Introduction

Atherosclerosis is the thickening and narrowing of the arteries due to formation of plaque on the walls of the artery. It is one of the leading causes of stroke and is the first clinical manifestation of cardiovascular disease. Recent research has been focused on determining early indicators of atherosclerosis. IMT is an early indicator of atherosclerosis [1] and precedes luminal narrowing due to plaque formation. Since plaque formation starts in the walls of the artery, IMT could be a better indicator than lumen area or blood velocity. Population studies have shown a strong correlation between carotid IMT and several cardiovascular risk factors [2], and IMT has also been found to be associated with the extent of atherosclerosis and end organ damage of high-risk patients [3]. B-mode ultrasound (US) is a noninvasive method to measure IMT especially in easily accessible arteries like the carotid. IMT measurements using ultrasonography correlate well with histopathology and are reproducible [4].

Automated segmentation facilitates real-time IMT measurements and is very helpful in the clinical evaluation of large databases which can be done either semiautomatically or by running automated methods (so-called batch mode processing). These methods can be applied to several blood vessels. However, several groups such as Liguori et al. [5], Cheng et al. [6], and Gutierrez et al. [7] have proposed methods that require the user to interactively place markers or draw regions of interest to initiate the segmentation. None of these methods are fully automated, and therefore, we seek to define an approach that would require no user interaction. Our patented system Completely Automated Layers EXtraction (CALEX) (a Class of AtheroEdge™ systems) [8] quantifies IMT using a feature-based approach and is fully automated with minimal user intervention. This system extracts features from the far wall based on the hypothesis that the far wall is brighter [8] compared to the near wall in the US image. Delsanto et al. [9] characterized the performance of an automated carotid wall segmentation algorithm based on the same hypothesis by validating against expert segmentation. The algorithm localized the adventitial wall based on the intensity local maxima of every column in the image, i.e., the far wall brightness compared to the near wall. Several systems developed by our group that were based on this hypothesis for IMT measurements produced results that were in good agreement with expert segmentation [8–10]. However, the validation was based on manual intensity measurements on several representative US images.

In this chapter, we validate the hypothesis of far wall maximum brightness by registering our entire database of 200 US images of the carotid artery and showing that the far wall has higher intensity. In addition, we also look at the

F. Molinari (✉)
Biolab, Department of Electronics, Politecnico di Torino, Torino, Italy
e-mail: filippo.molinari@polito.it

U.R. Acharya
Department of Electronics and Computer Engineering, Ngee Ann Polytechnic, Clementi Road, Singapore

Department of Biomedical Engineering, Faculty of Engineering, University of Malaya, Malaysia
e-mail: aru@np.edu.sg

L. Saba
Department of Science of the Images, Policlinico Universitario, Cagliari, Italy

Department of Radiology, Azienda Ospedaliero Universitaria di Cagliari, Cagliari, Italy
e-mail: lsaba@tiscali.it

A. Nicolaides
Vascular Screening and Diagnostic Centre, London, UK

Department of Biological Sciences, University of Cyprus, Nicosia, Cyprus
e-mail: anicolaides1@gmail.com

J.S. Suri
Fellow AIMBE, CTO, Diagnostic and Monitoring Division, AtheroPoint LLC,
Roseville, CA, USA

Department of Biomedical Engineering (Aff.), Idaho State University, Pocatello, ID, USA
e-mail: jsuri@comcast.net

L. Saba et al. (eds.), *Multi-Modality Atherosclerosis Imaging and Diagnosis*,
DOI 10.1007/978-1-4614-7425-8_21,

feasibility of automatic lumen segmentation and registration of B-mode US carotid artery images for clinical studies. Here, we are registering images to a "standard carotid artery" but we can adapt the same method for images obtained during follow-up studies involving the same patient. After registration, we segment the images using an automated technique, in order to show the performance and exploit the potentialities of the registered images. The concept of joint registration and segmentation in one system is not new and it has been adapted before to mammographic images by Suri et al. [11]. In fact, it has been shown that registration can improve segmentation performance and vice versa, thereby improving the overall quality of the examination [11].

This chapter is organized as follows. We will first describe the image dataset, the acquisition protocol, and the patients' characteristics. Then, we will describe the segmentation and registration methods. A detailed presentation of the results along with a discussion of the new insights of this method constitutes the core of this chapter. Finally, in the last section, we look at how we can exploit the higher intensity of the far wall for automatic carotid artery segmentation and we conclude the chapter.

2 Image Dataset and Patients Demographics

The image database consists of 200 B-mode 2D US longitudinal images of the common tract of the carotid artery. All the images were transferred to a computer via a DICOM communication port in log-compressed 8-bit grayscale. The pixel density of all the images was equal to 16 pixels/mm in the axial direction, thus leading to a conversion factor of 0.0625 mm/pixel. The images were taken from 130 subjects: 50 normal subjects and 80 patients suffering from atherosclerosis who were recruited by the Neurology division of the Gradenigo Hospital (Torino, Italy) where all the US examinations were conducted. One hundred images were relative to the left and right carotid artery of the 50 healthy subjects. One hundred and sixty images were acquired from the 80 patients, one each from the left and right carotid arteries. However, among these 160 images, we had to discard 60 images: 35 carotids had a plaque protruding in the artery lumen, whereas 25 images were relative to pretreated carotids (i.e., the carotid was either closed or with an implanted stent). These 60 images were unsuitable to test our hypothesis, because our methodology has not been developed for vessels with plaque. Such images were removed from the database, thus leading to a total of 200 images. The subjects' age ranged from 25 to 83 years (mean: 48.3 years; standard deviation: 9.9 years). Seventy subjects were male. All the patients were clinically evaluated before being included in the study and all the subjects signed an informed consent before the US examination. The study received the approval by the Institutional Committee of the Gradenigo Hospital

3 Segmentation and Registration Techniques

In this section, we will describe the segmentation and registration technique we used. Such techniques constitute the mathematical basis we exploited for testing and validating our hypothesis relative to the brightness of the carotid far wall adventitia layer.

3.1 Automated Lumen Segmentation

The objective of this segmentation is to automatically segment the lumen in the carotid artery frame. The concept of automated lumen segmentation is based on finding the far adventitia (AD_F) border and reconstructing the Region of Interest (ROI) in which lumen lies. The ROI is then utilized to capture the lumen region. For automated AD_F computation, we first remove the black frame surrounding the image [12]. This frame, which is a standard in all B-mode US images, interferes with the automated lumen segmentation system. We, therefore, cropped the images to maintain only the region containing the US data. This procedure was completely automated and relied on the data contained in the DICOM header of the images [12].

Subsequently, our procedure automatically recognizes the carotid artery in the image. We adopted a patented multi-resolution approach (CAMES [13]—a class of AtheroEdge™ systems from Global Biomedical Technologies, Inc., CA, USA), consisting of the following steps:

1. Downsampling: We downsampled the image (Fig. 21.1a) by a factor of 2 and attenuated the speckle noise (Fig. 21.1b). This process scaled the size of the carotid wall (nominally about 1 mm = about 16 pixels) to the optimal size of 8 pixels for the automated recognition.
2. Convolution with higher order derivative: We filtered the image (Fig. 21.1b) by using a first-order derivative Gaussian filter (Fig. 21.1c). This filter is the equivalent of a high-pass filter, which enhances the representation of the objects having the same size of the kernel. Since we aimed at enhancing the representation of the carotid walls, we chose a kernel size of 8 pixels.
3. Heuristic search for AD_F: Starting from the bottom of the image, the far carotid wall was recognized as it was a bright stripe of about 8 pixels size (Fig. 21.1d). As mentioned in step 1, the nominal value of the IMT is about 1 mm which is equivalent to 8 pixels in the downsampled domain. Thus, the first-order Gaussian derivative kernel is size matched to the IMT and it outputs a white stripe of the

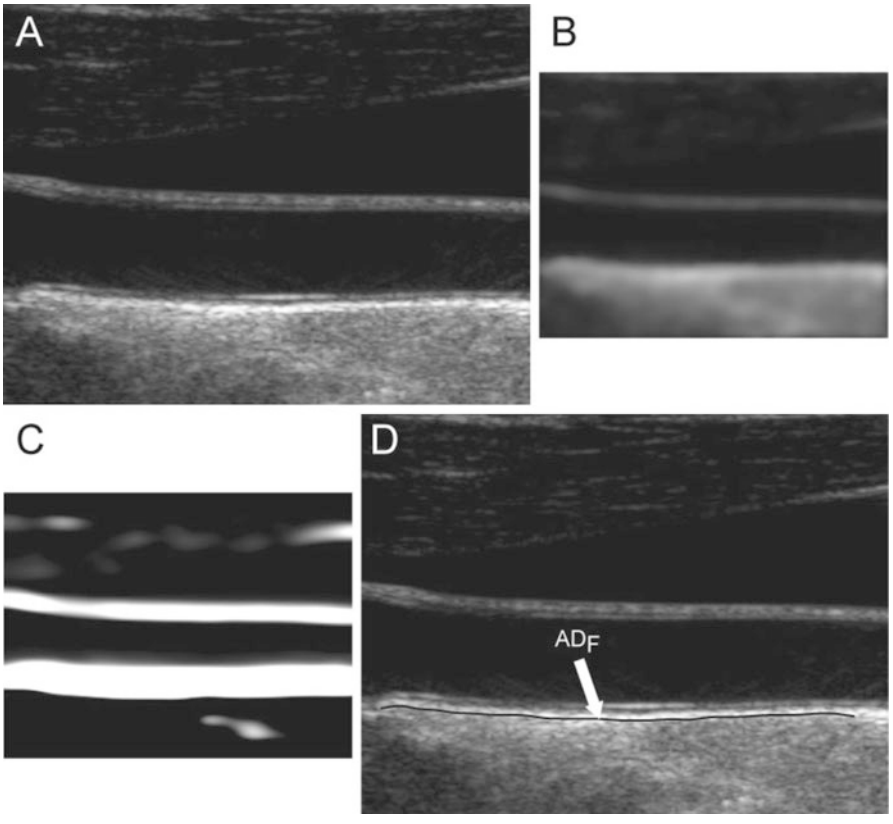

Fig. 21.1 (**a**) Original B-mode image. (**b**) Downsampled and despeckled image. (**c**) Convolution of image (**b**) with a first-order Gaussian kernel. (**d**) Automated tracing of the far adventitia layer (AD_F) in image (**a**)

same size as the far wall thickness. Our heuristic search considered the image column-wise. The intensity profile of each column was scanned from bottom to top (i.e., from the deepest pixel moving upwards). The deepest region which had a width of at least 8 pixels was considered as the far wall.

4. Guidance zone creation: The output of this carotid recognition stage was the tracing of the far adventitia layer (AD_F) (a complete description of this procedure is given in [13]). We selected a Guidance Zone (GZ) in which we performed segmentation. The basic idea was to draw a GZ that comprised the far wall (i.e., the intima, media, and adventitia layers) and the near wall. The average diameter of the carotid lumen is 6 mm, which roughly corresponded to 96 pixels at a pixel density of 16 pixels/mm. Therefore, we traced a GZ that had the same horizontal support of the AD_F profile, and a vertical height of about 200 pixels. With this vertical size, which is double the normal size of the carotid, we ensured the presence of both artery walls in the GZ.
5. Lumen segmentation: The lumen segmentation consists of a preprocessing step followed by a level set based segmentation method. The first preprocessing step is the inversion of the image, i.e., we subtract every pixel in the image from the maximum value of the image. We then multiply the image by a function of the gradient of the original image given by (21.1) below.

$$f(\nabla u) = \frac{1}{1 + |\nabla u|} \tag{21.1}$$

Here u indicates the image. The function is such that it takes low values ($\ll 1$) at the edges in the image and takes a maximum value of 1 in regions that are "flat." The lumen is then segmented using the active contour without edges algorithm or the Chan–Vese algorithm as described in [14] (Appendix). The algorithm was chosen because of the piecewise constant nature of the cropped carotid artery images obtained from the previous step. The lumen, after preprocessing, is white and its grayscale intensity is high (>100) with noise. The walls of the artery that initially appear bright become dark (i.e., <50 grayscale intensity) after preprocessing. The Chan–Vese method is very effective for segmenting images made up of two piecewise constant regions which in our case correspond to the lumen and the carotid wall. The segmentation produces

a binary image where the lumen is white (intensity of 1) and the wall intensity is 0. We would also like to point out that the algorithm is not influenced by the actual gray scale values in the carotid images giving us the flexibility to analyze images acquired with different settings. The algorithm is also robust to noise as it does not directly depend on the edges in the images. The pseudo-code for the entire automated segmentation algorithm is as follows:

(A) Invert image, i.e., subtract image from maximum value in the image.
(B) Multiply with function given in (21.1).
(C) Downsample image by a factor of 4. Since numerical Partial Differential Equations require long computing times, we downsampled the image to achieve convergence in a reasonable amount of time.
(D) Initialize level set contour as a rectangle. The initial contour placement is automated. We computed a rectangular contour centered on the image.
(E) Run the Chan–Vese algorithm for 1,000 iterations. The number of iterations was arrived at by trial and error and it was sufficient for all test images across different databases.
(F) Upsample the segmentation result, which is a binary image where the lumen is 1, to the original size of the image.
(G) The presence of the jugular vein in some images causes the algorithm to segment both the carotid and the vein. In this case, employ a connected component analysis to determine which connected group is closer to the AD_F. The connected group closest to the AD_F is taken as the carotid artery.
(H) Apply morphological hole filling to remove holes in the binary segmentation result caused by the backscatter noise in the lumen.

3.2 Image Alignment for Composite Image Generation

The first step in the automated IMT measurement algorithms like CALEX is the recognition of the Common Carotid Artery (CCA). For this purpose, the assumption by most of these feature-based algorithms is that the far wall of the CCA has the highest intensity in the image. To validate this assumption, it is necessary to locate the far wall and determine its intensity. If the ultrasound probe is exactly along the longitudinal axis of the CCA, the resulting image will show a nearly horizontal straight CCA with respect to the base edge of the image. However, not all CCA images are acquired parallel to the longitudinal axis. Sometimes, the probe can make a slight angle with the longitudinal axis of the CCA, and therefore, the resultant image will not have the CCA absolutely horizontal with respect to the base of the image. Such images will show a slightly tilted CCA. In order to superimpose all these images to show that the cumulative far wall intensity is the highest, we register all CCA images with respect to an ideal image in which the CCA is parallel to the base edge. This is the main motivation for registering the images in our work.

A near straight artery image is used as a target image for all other images in the database. Lumen segmentations of binary images are affine transformed to estimate the rotation and translation of the floating image into the same orientation and position as target image. The free form deformation registration method using B-spline described in [15] was used for nonrigid registration. The method is a hierarchical transformation model where the local deformations are described by free form deformations modeled using B-splines. Registration is performed by minimizing a cost function that is a combination of sum of squared differences and a cost function associated with the smoothness of the transformation. The free form deformation based on B-splines deforms the object by altering an underlying mesh of spline control points. The alteration produces smooth and continuous transformations. In two dimensions, we denote x and y as the coordinates of the image volume. Let φ_{ij} denote the mesh of control points ($n_1 \times n_2$). The deformations produced by the B-splines can be written as

$$d(x,y,z) = \sum_{l=0}^{3}\sum_{m=0}^{3} B_i(u)B_j(v)\varphi_{i+l,j+m}$$
$$i = \left\lfloor \frac{x}{n_1} \right\rfloor - 1, \quad j = \left\lfloor \frac{y}{n_2} \right\rfloor - 1 \tag{21.2}$$

In (21.2), B_l represents the basis functions of the B-splines, given by (21.3):

$$\begin{aligned} B_0(u) &= \frac{(1-u)^3}{6} \\ B_1(u) &= \frac{(3u^3 - 6u^2 + 4)}{6} \\ B_2(u) &= \frac{(-3u^3 + 3u^2 + 3u + 1)}{6} \\ B_3(u) &= \frac{u^3}{6} \end{aligned} \tag{21.3}$$

The cost function for the registration is mathematically given as

$$C = \sum (I - T(F))^2 + \sum_x \sum_y \left[\left(\frac{\partial^2 d}{\partial x^2}\right)^2 + \left(\frac{\partial^2 d}{\partial y^2}\right)^2 + 2\left(\frac{\partial^2 d}{\partial x \partial y}\right) \right] \tag{21.4}$$

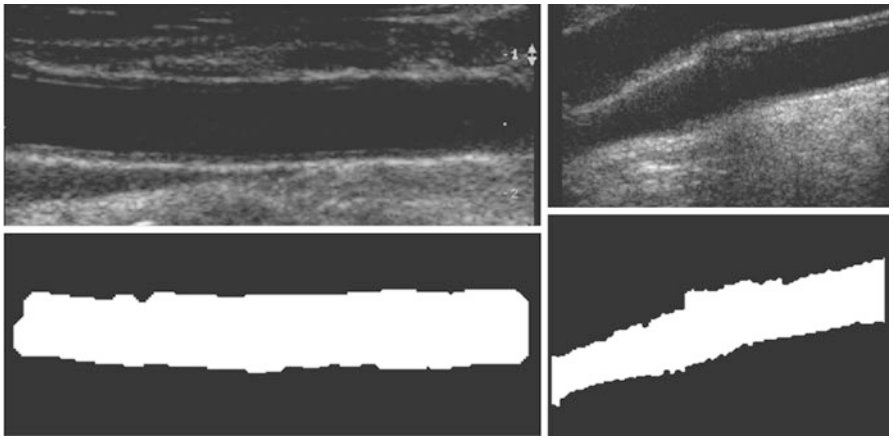

Fig. 21.2 Segmentation results. Fixed reference image of carotid artery (*top left*) and one of the 200 floating carotid artery images (*top right*). Binary image of segmented fixed reference image lumen (*bottom left*) and binary image of segmented floating image lumen (*bottom right*)

where I is the fixed target reference image, and F is the floating image transformed by T (combined rigid and nonrigid transformation). The deformation d is defined in (21.2) and the derivatives are with respect to spatial coordinates. In (21.4), the second term is the penalty term for smooth deformations and is the bending energy of a thin plate of metal. The optimization solves for the control point grid from which the deformations are calculated.

Nonrigid registration using B-splines based free form deformations is one of the popular methods for nonrigid registration of multi-modality images. The algorithm's main advantage compared to other methods is that it produces very smooth deformations due to B-splines and the transformed images are not overly distorted. Because of its use in multi-modality registration, information theoretic metrics are used as the cost function. For our application, we used the least squares criterion as we were registering 2D binary images oriented differently. It proved to be more effective than directly registering the grayscale carotid artery images. Several implementations of this algorithm are readily available in various languages. We used the Matlab implementation by Dr. Dirk-Jan Kroon available from Mathworks file exchange. The algorithm is generally slow (5 min per image pair). But in our case we are using it only for validation purposes and will not be a part of any commercial implementation. We also perform an initial affine registration that scales and aligns the floating image. The nonrigid registration is the final step to obtain a more accurate transformation field.

4 Segmentation and Registration Performance

4.1 Segmentation and Registration Results

The average distance between the manually traced Media–Adventitia (MA) boundary and the automatically traced AD_F was 25.03 ± 19.47 pixels (1.54 ± 1.19 mm). This small distance indicates that the automatically traced AD_F profile and the manually traced MA profile match, and therefore, the recognition of the carotid artery was successful. The segmented lumen of the fixed base carotid artery and a floating carotid artery image belonging to different patients are shown Fig. 21.2. The images are chosen to highlight the requirement for an affine transformation prior to a nonrigid registration.

In Fig. 21.3, a typical registration result is shown. We have chosen two carotid artery images that were at an angle with respect to the horizontal. The transformation is the result of an affine transformation followed by the free form deformation. We chose a weighting factor of 0.01 for the smoothing term in the cost function. Typically, it took about 35 iterations for the affine registration to converge. Following affine, the nonrigid registration took 60 iterations to converge.

In Fig. 21.4, a surface plot of the sum of all registered images is shown. The grayscale sum image is also displayed. The window and level of the grayscale image are set to its minimum and maximum values. The results in Fig. 21.4 confirm our hypothesis qualitatively. To obtain quantitative evidence, we calculated the maximum value along every column in the sum image and confirmed that the maximum value along each column was from the far wall. In Fig. 21.5, the mean intensity and standard deviation from a 5×5 window centered on the same column along the near and far wall are shown. The far wall intensity is clearly higher and well separated from the average values along the near wall. A z-score was calculated by dividing the difference between the mean values of the corresponding 11×11 window along the far and near walls and sum of their standard deviations. For all windows considered, the z-score was greater than 2.

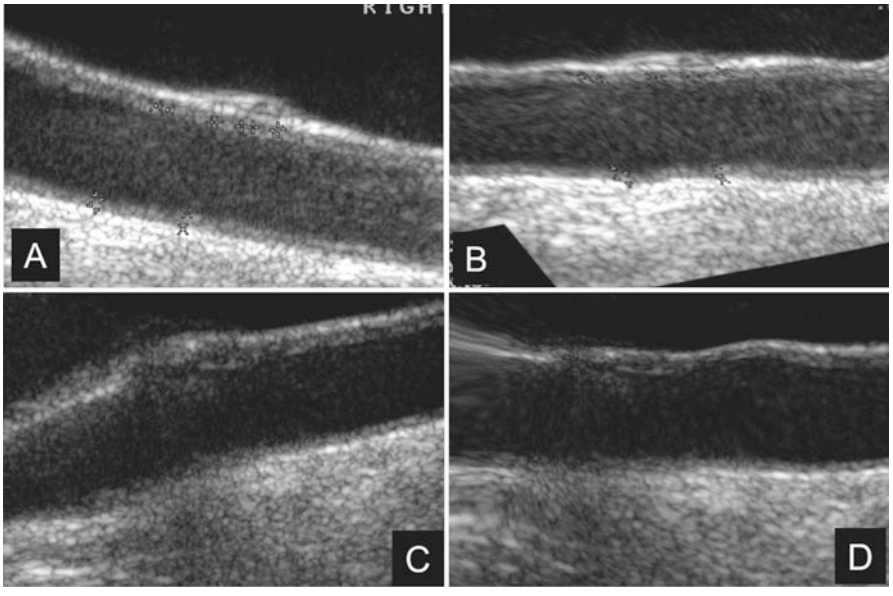

Fig. 21.3 Result of nonrigid free form deformation of two carotid artery images with the carotid artery at an angle with respect to the horizontal. (**a**) and (**b**) are the acquired and transformed image pairs of one carotid artery. Similarly (**c**) and (**d**) are acquired and transformed image pairs of the second carotid artery

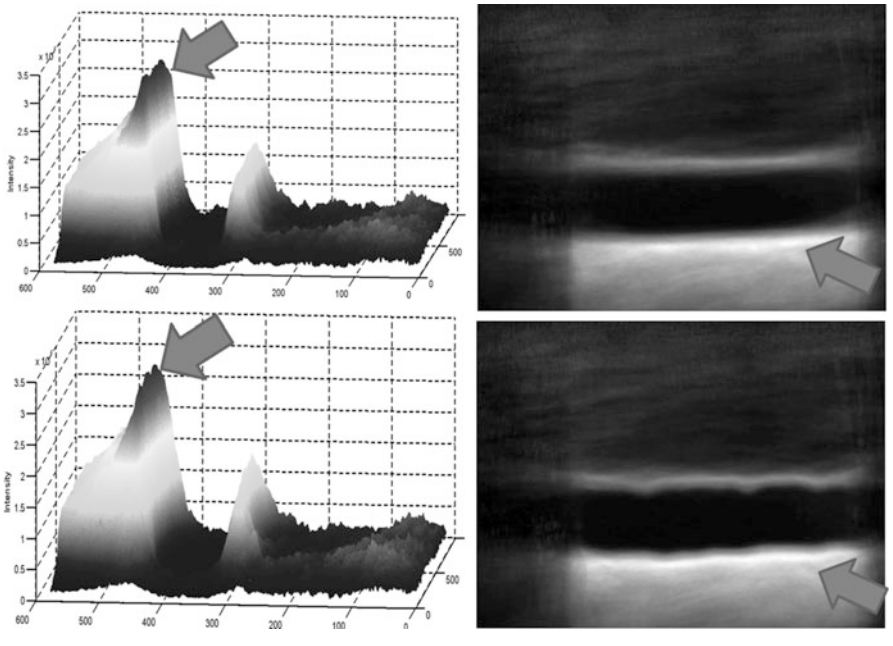

Fig. 21.4 Surface plot of the registered sum of 200 images showing intense far wall (*left*). The same displayed as a 2D image (*right*). The *top row image* is the result of nonrigid registration while the *bottom row image* is the results using affine registration. The *arrows point* to the far wall

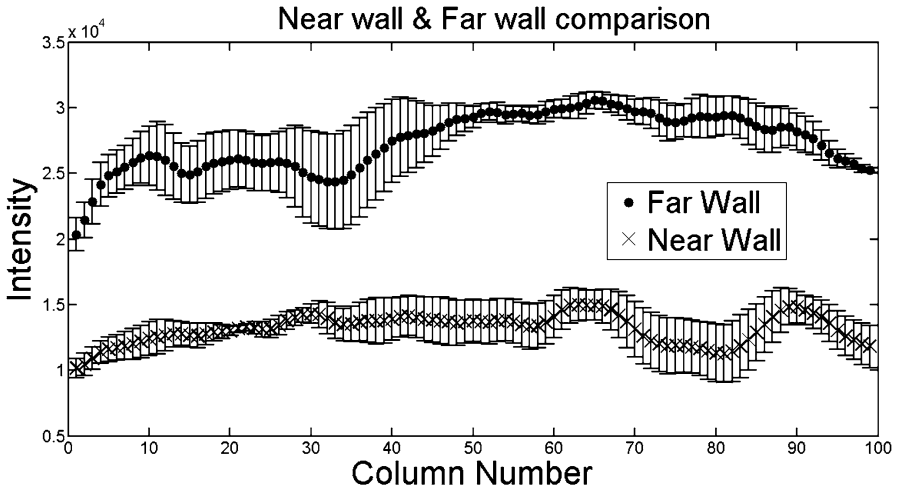

Fig. 21.5 Mean intensity and standard deviation along the far wall and near wall

4.2 Far Wall Brightness Hypothesis Validation and Discussion

In this work, we validated the hypothesis of far wall maximum brightness using a much larger dataset comprising of 200 images. Our approach was to register all the B-mode US images to a base fixed image which is considered carotid "straight." The US images of the carotid artery do not have many structures and there are no landmarks that can be used to assess the quality of registration. We used the intensity sum image to verify that the lumen volumes coincided. Since we used a nonrigid registration algorithm, we manually verified that the deformations are smooth and do not overly distort the carotid artery. Since the artery in different patients can be oriented at different angles and consequently be of different lengths in the image, we require an affine transformation to orient and scale the arteries appropriately. The nonrigid transformation aligns the edges of the segmented lumen. In many cases, nonrigid registration might not be required as the artery images are straight and do not have any distortions.

The registration accuracy in terms of sub-pixel metrics is not a hard requirement for this work. We wanted to verify that the far wall has higher intensity than the near wall in all images and for that purpose it is sufficient that the images be registered within the thickness of the far wall. Our hypothesis can be easily verified by visual inspection of Figs. 21.3 and 21.4 (3D plots). In Fig. 21.4, it can be seen that the far wall has a relatively higher intensity compared to that of the near wall. Quantitative results are depicted in Fig. 21.5, and the z-score of >2 also verifies our hypothesis.

The automated AD_F detection method proved very robust and had a 100% success rate. This ensured the possibility of an accurate segmentation, which is based on AD_F tracing. The major merits of this automated adventitia recognition is that the multiresolution stage is strictly linked to the pixel density of the image. This gave robustness to the method, as in the multiresolution framework, we always worked with a Gaussian kernel size equal to the expected IMT value.

The binary lumen image has a jagged appearance. The binary image edges can be smoothed to obtain a continuous line edge, but the impact on the registration is not significant. We are using the lumen binary images to estimate affine transforms and correct for orientation and scaling. The final nonrigid transformation makes small changes to arteries that are bent or slightly curved and aligns them with the straight fixed image. Small errors in segmentation do not impact the affine transformation in terms of orientation angle and scaling. Also, any significant curve in the arteries would be adjusted by the nonrigid transform despite the presence of these jagged edges.

The segmentation and subsequent registration of the binary image of the lumen can be further improved by increasing the dynamic range (DR) of the acquisition [16]. Increasing DR improves the contrast and reduces the variance of the image producing sharply peaked histograms of carotid US images. Increased contrast and variance improve the segmentation as it is based on the assumption that the image is made up of regions of constant intensity.

We also evaluated affine registration on our datasets. Although the nonrigid registration provides a more accurate registration, an affine registration scheme is sufficient for alignment of the lumen. The lumen edges can be smoothed to remove the kinks or jaggedness prior to registration. For the purposes of this chapter, we conclude that affine registration would be sufficient.

5 CCA Recognition and IMT Measurement

The brightness of the far wall is exploited by the CALEX 3.0 system to measure IMT. CALEX 3.0 is the latest release of an integrated approach combining feature extraction, fitting, and fuzzy classification we developed in 2010 [9, 17]. In Fig. 21.6, we show a typical carotid artery and the result of the adventitia localization by our system, CALEX 3.0. In this work, we acquired longitudinal images wherein the ultrasound probe head is held along the axis of the CCA. Therefore, even if the probe head is slightly tilted away from the longitudinal axis of the CCA, the angle of acquisition has a very subtle change and the resulting tilt in the carotid artery will only be minor. This subtle change/tilt is compensated by the registration algorithm described earlier, and therefore, the carotid shape does not influence the algorithm. Measuring IMT involves automatic identification and segmentation of the carotid artery lumen and localizing the MA boundary and the lumen–intima (LI) boundary. In this section, we present the steps involved in these processes, and the resultant IMT values.

5.1 Automated Carotid Localization/Recognition

Despite the use of a validation procedure, previous version of CALEX 1.0 could still inaccurately trace the far adventitia. In Fig. 21.6, we show how the far wall adventitia is localized. Initial seed points are chosen based on local maxima, which are assumed to be in the far wall. We have validated this assumption by registering an entire database of images. For selecting the true seed points, we used a linear discriminator that bins the true seed points and false-negative seed points separately. The objective is to find the possible seed points that are above a certain threshold u_T and are likely to be the edges of the lumen but not inside the lumen. To distinguish true seed points from local maxima due to background noise, we used a linear discriminator $\mathbf{v}$ applied to the vector of seed candidates with the property vector $\mathbf{p}$ made up of *Intensity*, e (which corresponds to the height of the seed candidate on the vertical intensity profile), and *Breadth*, b (which corresponds to the distance between the two neighbouring local minima that are on the opposite sides of the seed candidate). Now, the criteria for seed point selection were based on the threshold u_T, mathematically laid out to follow the equality: $\mathbf{p} \cdot \mathbf{v} > u_T$

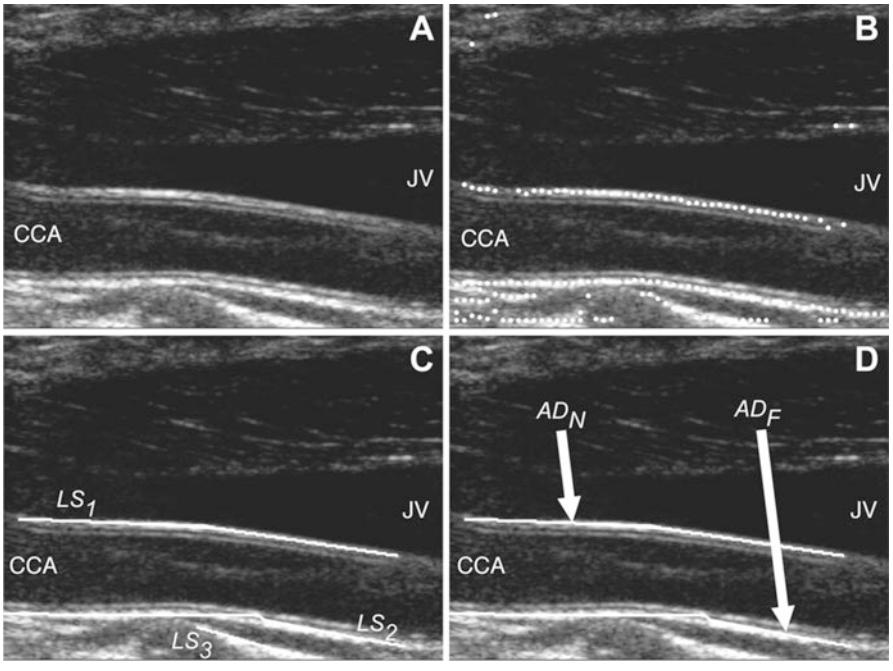

Fig. 21.6 CALEX process for adventitia localization. US image of carotid artery (**a**). Automatic selection of seed points based on higher intensity of far wall (**b**). Rejection of seed points not belonging to adventitia and connecting seed points to obtain line segments (**c**). Identification of far and near adventitia (**d**)

(here, denotes the dot product between two vectors). Here, u_T is equal to 0 [8]. The existing points were then connected according to their proximity and orientation and classified as near and far wall of the adventitia [8].

CALEX 3.0 incorporates a robust algorithm to avoid the Jugular Vein (JV) and to avoid incorrect tracings of the AD_F. As depicted in Fig. 21.7, the typical far wall identification errors of CALEX 1.0 are as follows:

1. Selected line segments are along the JV above common carotid artery.
2. The whole (or part) of selected line segments deviates from the adventitia layer of the far wall of CCA.

The first error can be fixed by observing that when the line segment is traced on the JV instead of the AD_F, its upper side is brighter than its lower side, while it should be the opposite. Based on this observation, we introduce a new feature, called *isadf*, for each valid line segment. Conceptually, the higher the value of the *isadf* of a line segment, the higher the probability that line segment corresponds to the far adventitia. For each valid line segment, the *isadf* feature is calculated as follows:

$$isadf = \frac{\sum_{i=0}^{N}\sum_{j=0}^{M} I(x_i, y_i + j)}{\sum_{i=0}^{N}\sum_{j=0}^{M} I(x_i, y_i - j)} \tag{21.5}$$

In (21.5), N is the number of points on the line segment, M (=30 pixels) is the sample distance, and I is the input image. When the *isadf* value of a given line segment is lower than 1, it means that the upper side of that segment is brighter than the lower side. Therefore, it cannot be the adventitia layer (which we proved to be the brightest image feature) and should be discarded.

The second error is fixed by a refinement procedure. For each point p on the detected far wall adventitia, we extract the column-wise signal as given by (21.6):

$$s = f(I(x, y + i)), D_{\text{lower}} < i < D_{\text{upper}} \tag{21.6}$$

where D_{upper} (=50) is upper sample limit, and D_{lower} (= −5) is lower sample limit. Then, we find the nearest local maxima (or minimum) point q such that the absolute intensity difference between point p and q is larger than a predefined threshold I_T; otherwise point p is discarded.

Figure 21.8 shows the original and initial CALEX 1.0 AD_F profile (*left panel*) and the refinement made by CALEX 3.0 (*right panel*).

5.2 Far Wall Segmentation

Once the near and far adventitia layers are automatically traced, a guidance zone (GZ) is delineated based on the far adventitia profile (AD_F). The GZ has same horizontal length of the AD_F profile and a height equal to 30 pixels. We determined this specific value of 30 pixels after an extensive benchmark on our image dataset. Since the pixel dimension was 0.0625 mm in both the vertical and horizontal directions, and since the average IMT is about 1 mm (i.e., 16 pixels), we took a GZ vertical size that was double the average IMT. Therefore, we made sure that we included the entire distal wall and a portion of the carotid lumen.

CALEX 3.0 was then used to classify the pixels into the GZ. We input the intensity profile of each column of the image into a fuzzy *K-means* classifier. We fixed the number of classes equal to three: (i) the carotid wall (made of dark pixels); (ii) the intima and media layers (made of pixels with an average gray level), and (iii) the adventitia layer (made of bright pixels). The transition point between class (i) and class (ii) was the LI interface, whereas the transition between classes (ii) and (iii) was the MA interface. The IMT value was computed as distance between the LI and MA profiles for each image.

Figure 21.9 shows samples of automated CALEX 3.0 segmentation of the far carotid wall and LI/MA tracings. To show the robustness of the method and the validity of our registration hypothesis in all the possible conditions, we have reported in Fig. 21.9 the CALEX 3.0 segmentations for different carotid morphologies.

5.3 Distance and Performance Metric

We adopted the Polyline Distance Metric (PDM) to compute the IMT value from the LI/MA profiles. This metric was proposed by Suri et al. [18] and used in cardiological studies. The PDM is an optimal distance metric to compute the distance between boundaries given by vertices, because it is almost insensitive to the number of points constituting the boundaries. For each vertex i belonging to LI, the minimum distance from the line segments of MA is computed. Let this distance be $d_{i\text{–MA}}$. Then, the overall distance between vertices of LI and the segments of MA is computed as in (21.7):

$$d_{\text{LI–MA}} = \sum_{i=1}^{N_{\text{LI}}} d_{i-\text{MA}} \tag{21.7}$$

where N_{LI} is the number of vertices of the LI boundary. Similarly, the distance $d_{\text{MA–LI}}$ is computed, which is the overall distance of the vertices of MA from the segments of

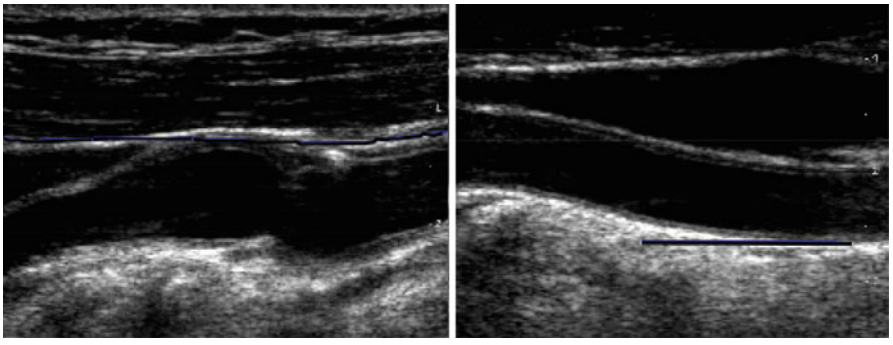

Fig. 21.7 Typical far wall identification errors of the former version CALEX

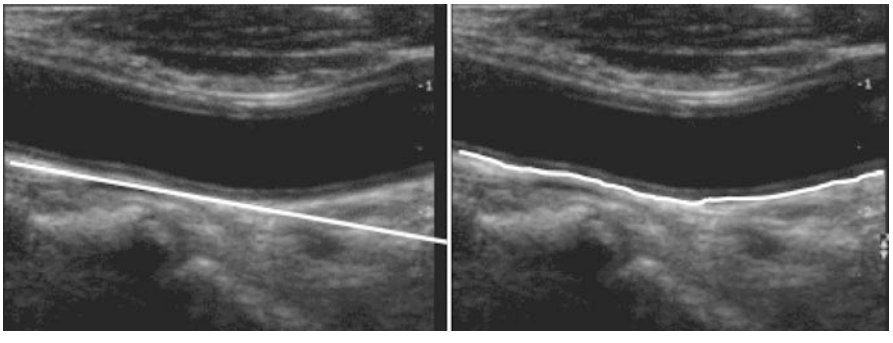

Fig. 21.8 *Left panel*: detection of the AD_F by CALEX 1.0. *Right panel*: refined and optimized AD_F profile detected by CALEX 3.0

LI. The PDM is defined as:

$$\mathrm{PDM}_{\mathrm{LI,MA}} = \frac{d_{\mathrm{LI-MA}} + d_{\mathrm{MA-LI}}}{N_{\mathrm{LI}} + N_{\mathrm{MA}}} \tag{21.8}$$

In (21.8), N_{MA} is the number of vertices of the MA profile. The IMT by CALEX 3.0 and the reference IMT ($\mathrm{IMT}_{\mathrm{GT}}$) were computed as:

$$\begin{aligned} \mathrm{IMT}_{\mathrm{CALEX}} &= \mathrm{PDM}_{\mathrm{CALEX_{LI}},\mathrm{CALEX_{MA}}} \\ \mathrm{IMT}_{\mathrm{GT}} &= \mathrm{PDM}_{\mathrm{GT_{LI}},\mathrm{GT_{MA}}} \end{aligned} \tag{21.9}$$

In (21.9), GT is relative to manually traced profiles, which we considered as Ground Truth. The IMT value was measured for each image and the overall system performance was computed in terms of IMT measurement bias, absolute error, and squared error compared to $\mathrm{IMT}_{\mathrm{GT}}$.

5.4 IMT Measurement Performance

Table 21.1 reports the overall system performance of CALEX 3.0 compared to GT. To completely characterize the system performance, we compared the IMT measurements by CALEX 3.0 to the manual measurements (GT). The results are given as mean value ± standard deviation on the 200 images database. We computed the IMT measurement bias ε, the absolute error δ, and the squared error ε^2 defined as follows:

Table 21.1 Overall system performance of CALEX 3.0 compared to ground truth

	CALEX 3.0	Ground truth
IMT value (mm)	0.836 ± 0.206	0.864 ± 0.221
IMT bias (mm)	-0.029 ± 0.228	
IMT absolute error (mm)	0.144 ± 0.179	
IMT squared error (mm^2)	0.052 ± 0.151	

$$\begin{aligned} \varepsilon &= \frac{1}{N}\sum_{i=1}^{N}\left(\mathrm{IMT}^i_{\mathrm{CALEX}} - \mathrm{IMT}^i_{\mathrm{GT}}\right) \\ \delta &= \frac{1}{N}\sum_{i=1}^{N}\left|\mathrm{IMT}^i_{\mathrm{CALEX}} - \mathrm{IMT}^i_{\mathrm{GT}}\right| \\ \varepsilon^2 &= \frac{1}{N}\sum_{i=1}^{N}\left(\mathrm{IMT}^i_{\mathrm{CALEX}} - \mathrm{IMT}^i_{\mathrm{GT}}\right)^2 \end{aligned} \tag{21.10}$$

where N is the number of the images in the testing database, $\mathrm{IMT}^i_{\mathrm{CALEX}}$ is the IMT measurement by CALEX 3.0 relative to the ith image, and $\mathrm{IMT}^i_{\mathrm{GT}}$ is the ground-truth IMT measurement of the ith image. The IMT bias was equal to -0.029 ± 0.228 mm, the IMT absolute

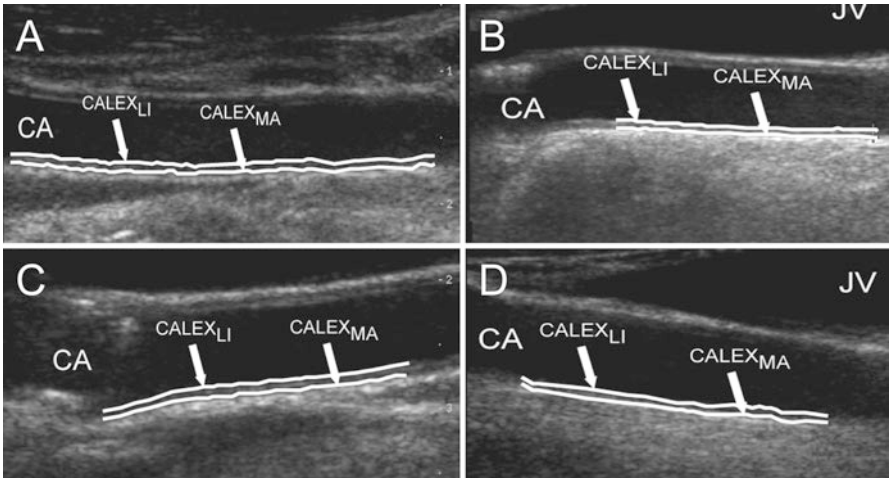

Fig. 21.9 Samples of CALEX 3.0 automated segmentation for different carotid morphologies, showing the robustness of the technique. (**a**) Straight and horizontally placed carotid. (**b**) Curved carotid with jugular vein overlapped (JV). (**c**) Inclined carotid with positive slope. (**d**) Inclined carotid with negative slope ($CALEX_{LI}$ CALEX lumen–intima boundary, $CALEX_{MA}$ CALEX media–adventitia boundary)

error to 0.144 ± 0.179 mm, and the IMT squared error to 0.052 ± 0.151 mm^2. The IMT estimated by CALEX 3.0 on the dataset was 0.836 ± 0.206 mm, which is very close to the ground truth of 0.864 ± 0.221 mm.

We also defined the Figure-of-Merit (FoM) for CALEX 3.0, which was defined as

$$\text{FoM} = 100 - \left| \frac{\overline{\text{IMT}}_{\text{CALEX}} - \overline{\text{IMT}}_{\text{GT}}}{\overline{\text{IMT}}_{\text{GT}}} \right| \times 100 \qquad (21.11)$$

where $\overline{\text{IMT}}_{\text{GT}}$ was the average IMT value by GT, and $\overline{\text{IMT}}_{\text{CALEX}}$ the average IMT value by CALEX 3.0 (i.e., these two values are those reported in the first row of Table 21.1). The FoM was equal to 96.7%. Figure 21.10a reports the Bland–Altmann plot for the CALEX 3.0 and GT estimates of the IMT. It can be shown that CALEX 3.0 has a much reduced bias (equal to 0.029 mm, which means about 3% of bias with respect to a nominal IMT value of 1 mm). Moreover, the reproducibility of CALEX 3.0 is good, because the standard deviation of the IMT error is 0.206 mm. Previous studies documented that the reproducibility of the IMT measurements made by expert sonographers can as low as 0.15 mm [1]. Figure 21.10b shows the distribution of the IMT bias. The black line represents the cumulative function.

From a clinical point of view, the Bland–Altmann is the most important representation of the performance of a technique. The accuracy of the technique (i.e., the IMT bias) was <3% of the nominal IMT value. In this regard, a bias of 30 μm is clinically acceptable. The reproducibility of the IMT measurement (i.e., the standard deviation of the IMT bias, which determines the width of the dashed lines in the Bland–Altmann plot) is a scope of improvement. Currently, the most accurate IMT measurement techniques are user driven. When an expert operator drives and corrects the segmentation, the IMT bias can be reduced to 0.01 ± 0.02 mm [19]. Automated techniques usually have a reproducibility that is between five and ten times worse [8, 10, 17]. Our team is now working specifically to increase the reproducibility of automated IMT measurement strategies.

6 Final Remarks

The far wall appears bright in a typical US carotid artery image. We have exploited this feature for automatic IMT measurement in our CAD software (a class of AtheroEdge® system from Global Biomedical Technologies, Inc., CA, USA). In this work, we validated the hypothesis that the far wall is bright compared to the near wall by taking into consideration a US database of 200 images. In the process, we have also put together a scheme for carotid artery segmentation and registration in follow-up US studies. Since we were able to register our database of images successfully we believe that this system can be used for registering multiple studies corresponding to the same patient. We have used a novel and completely automated segmentation algorithm based on level sets. We also applied our IMT measurement system (CALEX) and showed its error of about 30 μm. This system will be useful not only as a stand-alone technique but also as part of more complex systems as described in [20] that can improve image data retrieval, storage, and diagnosis.

A.1 Appendix

Following the description in [14], we formulate the segmentation problem as an energy minimization problem to find the

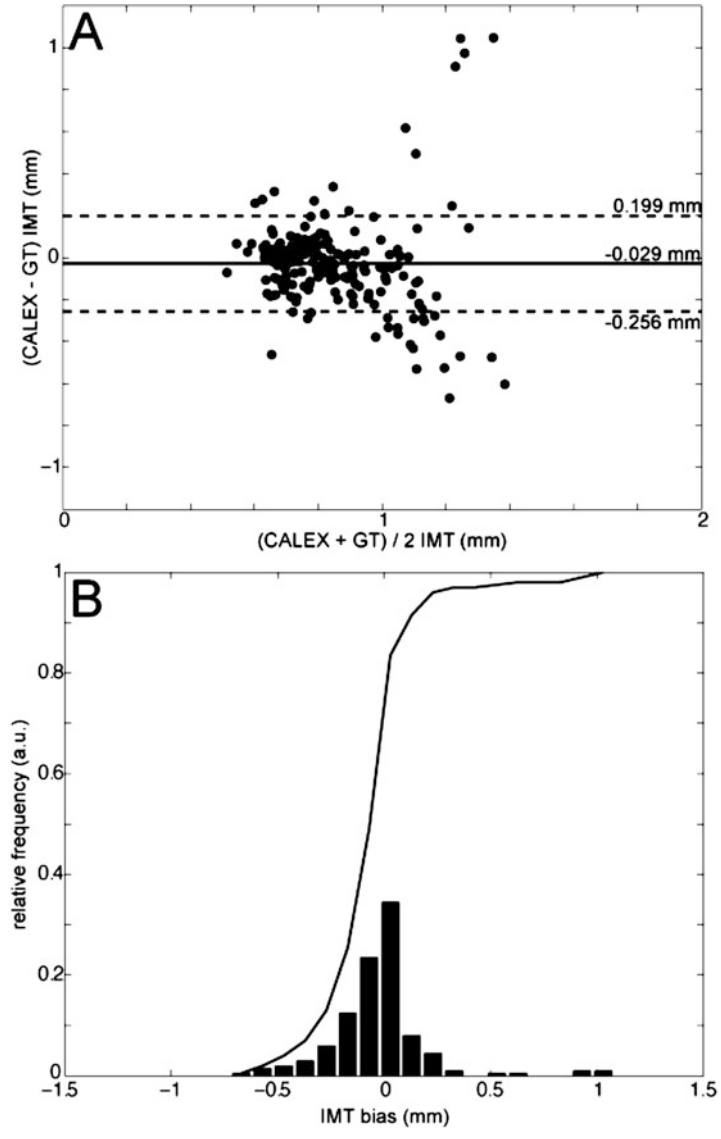

Fig. 21.10 Characterization of the CALEX 3.0 IMT performance. (**a**) Bland–Altmann plot of the CALEX 3.0 and GT IMT values. (**b**) Histogram distribution of the IMT measurement bias. The *black line* represents the cumulative function

optimum curve segmenting the regions. The energy term to be minimized can be written as

$$E = \int_{c_{\text{in}}} |u_0 - c_1|^2 \mathrm{d}x\mathrm{d}y + \int_{c_{\text{out}}} |u_0 - c_2|^2 \mathrm{d}x\mathrm{d}y \quad (21.12)$$

where c_{in} and c_{out} refer to the regions enclosed by the optimum curve C that separates the two regions in the image u_0. The terms c_1 and c_2 are the average values of the two regions. We can also add regularization terms that are proportional to the length of the curve (L_{c}) and the area of the curve (A_{c}).

$$\lambda_1 \int_{c_{\text{in}}} |u_0 - c_1|^2 \mathrm{d}x\mathrm{d}y + \lambda_2 \int_{c_{\text{out}}} |u_0 - c_2|^2 \mathrm{d}x\mathrm{d}y + \nu A_{\text{c}} + \mu \cdot L_{\text{c}} \quad (21.13)$$

Here, μ, ν, λ_1, and λ_2 are fixed parameters. The level set formulation is obtained by replacing the curve C with a level set function ϕ such that C is the level set with value 0. The function ϕ takes values less than zero inside the contour and positive values outside the contour. The energy is rewritten as

$$\begin{aligned} &\lambda_1 \int_{\Omega} |u_0 - c_1|^2 H_\varepsilon(\phi(x,y))\mathrm{d}x\mathrm{d}y \\ &+ \lambda_2 \int_{\Omega} |u_0 - c_2|^2 (1 - H_\varepsilon(\phi(x,y))\mathrm{d}x\mathrm{d}y \\ &+ \mu \int_{\Omega} \delta_\varepsilon |\nabla\phi(x,y)|\mathrm{d}x\mathrm{d}y \end{aligned} \quad (21.14)$$

where H_ε is the regularized version of the Heaviside function given by (21.15):

$$H_\varepsilon(z) = 1, \quad z > \varepsilon$$
$$H_\varepsilon(z) = 0, \quad z < -\varepsilon \tag{21.15}$$
$$H_\varepsilon(z) = \frac{1}{2}\left[1 + \frac{z}{\varepsilon} + \frac{1}{\pi}\sin\left(\frac{\pi z}{\varepsilon}\right)\right], \quad |z| \le \varepsilon$$

We used a value of 10e−5 for ε. The Heaviside function is defined as 1 if its argument is nonnegative and 0 otherwise. The derivative of the Heaviside function is the delta function (δ_ε). Ω is the domain of the level set function. The associated Euler–Lagrange equation for ϕ is given by (21.16) below:

$$\frac{\partial \phi}{\partial t} = \delta_\varepsilon(\phi)\left[\mu \cdot \mathrm{div}\left(\frac{\nabla \phi}{|\nabla \phi|}\right) - \lambda_1 \cdot (u_0 - c_1)^2 + \lambda_2 \cdot (u_0 - c_2)^2\right] \tag{21.16}$$

The boundary conditions are

$$\frac{\delta_\varepsilon(\phi)}{|\Delta \phi|}\frac{\partial \phi}{\partial \vec{n}} = 0, \partial\Omega$$
$$\phi(0, x, y) = \phi_0(x, y) \tag{21.17}$$

The equation is discretized and solved numerically.

References

1. Touboul PJ, Hennerici MG, Meairs S et al (2007) Mannheim carotid intima-media thickness consensus (2004–2006). An update on behalf of the Advisory Board of the 3rd and 4th Watching the Risk Symposium, 13th and 15th European Stroke Conferences, Mannheim, Germany, 2004, and Brussels, Belgium, 2006. Cerebrovasc Dis 23(1):75–80
2. van der Meer IM, Bots ML, Hofman A, del Sol AI, van der Kuip DA, Witteman JC (2004) Predictive value of noninvasive measures of atherosclerosis for incident myocardial infarction: the Rotterdam Study. Circulation 109(9):1089–1094
3. Poredos P (2004) Intima-media thickness: indicator of cardiovascular risk and measure of the extent of atherosclerosis. Vasc Med 9(1):46–54
4. Nasu K, Tsuchikane E, Katoh O, Tanaka N, Kimura M, Ehara M, Kinoshita Y, Matsubara T, Matsuo H, Asakura K, Asakura Y, Terashima M, Takayama T, Honye J, Hirayama A, Saito S, Suzuki T (2009) Effect of fluvastatin on progression of coronary atherosclerotic plaque evaluated by virtual histology intravascular ultrasound. JACC Cardiovasc Interv 2(7):689–696
5. Liguori C, Paolillo A, Pietrosanto A (2001) An automatic measurement system for the evaluation of carotid intima–media thickness. IEEE Trans Instrum Meas 50(6):1684–1691
6. Cheng D, Schmidt-Trucksass A, Cheng K, Burkhardt H (2002) Using snakes to detect the intimal and adventitial layers of the common carotid artery wall in sonographic images. Comput Methods Programs Biomed 67(1):27–37
7. Gutierrez MA, Pilon PE, Lage SG, Kopel L, Carvalho RT, Furuie SS (2002) Automatic measurement of carotid diameter and wall thickness in ultrasound images. Comput Cardiol 29:359–362
8. Molinari F, Zeng G, Suri JS (2010) An integrated approach to computer-based automated tracing and its validation for 200 common carotid arterial wall images. J Ultrasound Med 29(3):399–418
9. Delsanto S, Molinari F, Giustetto P, Liboni W, Badalamenti S, Suri JS (2007) Characterization of a completely user-independent algorithm for carotid artery segmentation in 2-D ultrasound images. IEEE Trans Instrum Meas 56(4):1265–1274
10. Molinari F, Rajendra Acharya U, Zeng G, Meiburger KM, Suri JS (2011) Completely automated robust edge snapper for carotid ultrasound IMT measurement on a multi-institutional database of 300 images. Med Biol Eng Comput 49(8):935–945
11. Suri JS, Guo Y, Janer R (2005) Entropy-based vs. spline-based registration techniques for X-ray phantom mammograms produced by Fischer's full field digital mammography and ultrasound system (FFDMUS): combined segmentation and registration framework. In: IASTED, BioMed
12. Molinari F, Liboni W, Giustetto P, Badalamenti S, Suri JS (2009) Automatic computer-based tracings (ACT) in longitudinal 2-D ultrasound images using different scanners. J Mech Med Biol 9(4):481–505
13. Molinari F, Pattichis C, Zeng G, Saba L, Rajendra AU, Sanfilippo R, Nicolaides A, Suri JS (2012) Completely automated multiresolution edge snapper (CAMES) – a new technique for an accurate carotid ultrasound IMT measurement: clinical validation and benchmarking on a multi-institutional database. IEEE Trans Image Process 21(3):1211–1222
14. Chan TF, Vese LA (2001) Active contours without edges. IEEE Trans Image Process 10(2):266–277
15. Rueckert D, Sonoda LI, Hayes C, Hill DLG, Leach MO, Hawkes DJ (1999) Nonrigid registration using free-form deformations: application to breast MR images. IEEE Trans Med Imaging 18(8):712–721
16. Golemati S, Stoitsis JS, Perakis DA, Varela E, Alexandridi A, Davos CH, Nikita KS (2009) Carotid artery motion estimation from sequences of B-mode ultrasound images: effect of scanner settings and image normalization. IEEE Trans Instrum Meas 58(7):2102–2112
17. Molinari F, Zeng G, Suri JS (2010) Intima-media thickness: setting a standard for completely automated method for ultrasound. IEEE Trans Ultrason Ferroelectr Freq Control 57(5):1112–1124
18. Suri JS, Haralick RM, Sheehan FH (2000) Greedy algorithm for error correction in automatically produced boundaries from low contrast ventriculograms. Pattern Anal Appl 3(1):39–60
19. Faita F, Gemignani V, Bianchini E, Giannarelli C, Ghiadoni L, Demi M (2008) Real-time measurement system for evaluation of the carotid intima-media thickness with a robust edge operator. J Ultrasound Med 27(9):1353–1361
20. Mougiakakou SG, Valavanis IK, Mouravliansky NA, Nikita KS, Nikita A (2009) Diagnosis: a telematics-enabled system for medical image archiving, management, and diagnosis assistance. IEEE Trans Instrum Meas 58(7):2113–2120

Segmentation of Carotid Ultrasound Images

22

Rui Rocha, Jorge Silva, and Aurélio Campilho

1 Introduction

According to the World Health Organization, cerebrovascular diseases are leading causes of death in the middle- and high-income countries [1]. Prevention is the key to reduce the impact of these diseases on the number of global deaths, and here imaging techniques play a crucial role. Despite the burden of disease, progress in stroke medicine has not been successful when compared with related cardiovascular conditions. In contrast to myocardial infarction, which is usually caused by rupture of the thrombosed plaque, in the coronary arteries stroke can have many causes: embolic or thrombotic large vessel occlusion (ischemic stroke), vessel rupture (primary intracerebral hemorrhage), or small vessel disease (ischemic stroke of the lacunar type or also primary intracerebral hemorrhage). The possibility to accurately differentiate the multiple processes leading to stroke in presymptomatic individuals can provide not only new insights into its pathophysiology but also opens a window of opportunity to achieve preventive treatment. Large vessel disease is related to the atherosclerotic process causing degeneration of the arterial wall and the deposition of lipids and other blood-borne material within the arterial wall of almost all vascular territories [2–4].

The diagnosis of atherosclerosis is one of the most important medical examinations for the prevention of cardiovascular events, like myocardial infarction and stroke [5, 6]. The carotid intima–media thickness (IMT) is a measure of the lesion of the macrovasculature and it is related with the cerebral cognitive functions [7]. IMT provides an index of atherosclerosis and is used for cardiovascular risk assessment [8]. The IMT can be measured using ultrasound (US) imaging, which uses safe nonionizing radiations. Ultrasound images are characterized by having low signal-to-noise ratio and several imaging artifacts that make their interpretation and segmentation very difficult [9]. They are affected by (1) speckle, a multiplicative noise that gives a granular texture to the images; (2) echo reverberations, which introduce false boundaries; (3) acoustic shadowing or echo attenuations, which can hinder boundaries or boundary segments. On the other hand, ultrasound IMT measures are highly repeatable, are noninvasive, and can be used to monitor pathologies and drug therapy efficacy. As shown in Fig. 22.1, B-mode US displays the vascular wall as a regular pattern that correlates with anatomical layers. The wall layers appear as two almost parallel echogenic lines (intima and adventitia layers) separated by the hypoechogenic media layer, forming an intensity valley known as the "double line" pattern [10]. The intima–media (IM) portion of this pattern is represented by the area of tissue starting at the lumen–intima (LI) edge of the artery and ending at the boundary between the media and the adventitia (MA) [11]. IMT measurements are usually made at the far wall (FW) of the common carotid artery (CCA), where the "double line" pattern is easier to visualize [10]. However, the segmentation of the near wall (NW) may also be required for some applications like the reconstruction of the 3D artery surface [12].

2 Segmentation of Carotid Ultrasound Images. Brief Survey

In carotid images the challenge is to obtain accurate IMT measures. This requires the detection of both the MA and the LI boundaries. Several approaches for the segmentation of the carotid wall and IMT measurement have been published

R. Rocha (✉)
INEB – Instituto de Engenharia Biomédica, Universidade do Porto, Rua Dr. Roberto Frias, s/n, 4200-465 Porto, Portugal

ISEP – Instituto Superior de Engenharia do Porto, Porto, Portugal
e-mail: rhr@isep.ipp.pt

J. Silva • A. Campilho
INEB – Instituto de Engenharia Biomédica, Universidade do Porto, Rua Dr. Roberto Frias, s/n, 4200-465 Porto, Portugal

Faculdade de Engenharia, Universidade do Porto, Porto, Portugal

L. Saba et al. (eds.), *Multi-Modality Atherosclerosis Imaging and Diagnosis*,
DOI 10.1007/978-1-4614-7425-8_22,

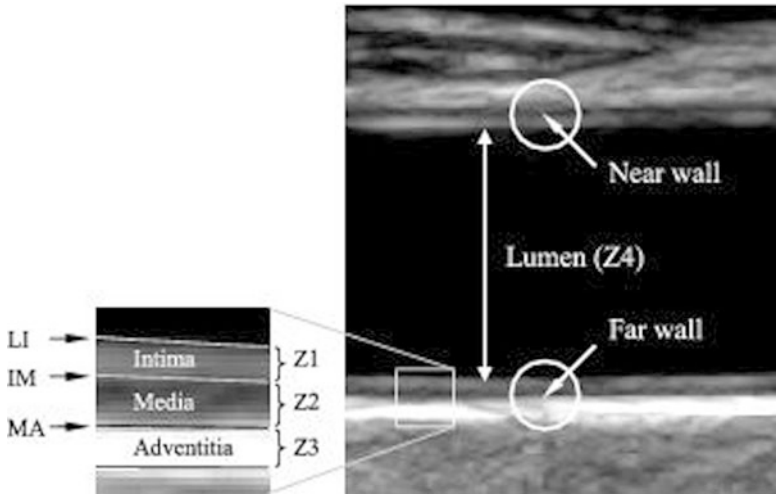

Fig. 22.1 Intima–media complex in a B-mode image of the common carotid artery (CCA). The lumen (zone Z4) is the region where the blood flows. The CCA wall is formed by the intima (zone Z1), the media (zone Z2), and the adventitia (zone Z3) regions. The interfaces between these four regions are represented by the *lines* LI (lumen–intima), IM (intima–media), and MA (media–adventitia)

in the last two decades. A wide range of methodologies have been tested, namely, edge detection [13–19]; gray level density analysis [20]; dynamic programming [21–24]; snakes [25–36]; discrete dynamic contour and multi-scale analysis [37]; Hough transform [36, 38, 39]; template matching [40, 41]; Nakagami modeling [42]; feature extraction, fitting, and classification [43–45]; feature extraction, cubic splines, geometric contours, and dynamic programming [46, 47]; and watershed transform [48]. A fusion of different segmentation methods using an inter-greedy technique was also introduced in [49–51], but a ground truth (manual tracings) is required to estimate the errors in each iteration. A description of most of these methods can also be found in [52].

2.1 Edge Detection

In 1998, Pignoli and Longo published the first computer-assisted method for the segmentation of 2D B-mode images of the carotid [13]. This method detects the edges of the vessel structure when moving from the lumen to the far wall. The edges corresponding to the LI and MA interfaces were used to measure the IMT. In [14], Touboul et al. used a similar approach and proved that semiautomatic computer-aided segmentation reduces the intra and inter-observer variability.

An edge detection based method was used by Selzer et al. [15, 16] to make IMT measurements and to evaluate their variability over time. The operator uses the mouse to identify a few points along the LI and the MA interfaces, over the first frame of a set of successive image frames. The artery interfaces in the first frame are then detected by searching for the edges in the vicinity of the smooth curves that pass through the identified points. The same procedure is repeated for the subsequent frames, using as guides the LI and MA interfaces detected on the preceding frame. The process may require manual correction of detection errors.

Another approach based on edge detection was proposed by Liguori et al. [18], where a statistical thresholding was used to reduce the noise before computing the intensity gradient. A manual selection of the region of interest (ROI) is required.

In [17], Stein et al. used an edge detection method to prove that computer-aided IMT measurements are faster, more reproducible, and more accurate when compared to manual measurements. The ROI must contain a portion of the lumen and the corresponding intimal, medial, and adventitial layers. The operator defines the length of the ROI and manually identifies a point in the lumen region at the left limit of this ROI. The LI and MA interfaces are then detected automatically. Manual corrections are performed by editing the boundaries incorrectly detected.

One of the most accurate edge detection approaches was introduced by Faita et al. [19]. This method improves the edge detection in the presence of noise by using a first-order absolute moment edge operator (FOAM) and a pattern recognition approach. This approach also has the advantage of being real time. However, it has two important limitations. First, the difficulty in processing vessels that are curved or non-horizontal in the image axis. Second, it needs a manual selection of the ROI.

2.2 Gray Level Density Analysis

In [20], Gariepy et al. used a computerized method, based on gray level intensity and tissue recognition, to demonstrate a strong correlation between ultrasonic and histological IMT measurements and to prove that hypertension is associated with an abnormal increase of the IMT in large arteries. Patients with plaque were excluded from the study to avoid disruptions of the double line arterial pattern. The ROI was selected manually and consisted of a rectangle containing

the far wall segment to analyze. The method detects the LI interface of both walls and the MA interface of the far wall. These interfaces were used to compute the average lumen diameter and the average IMT at the far wall. The computerized method was not evaluated against any manual tracings. It was used mainly to reduce the intra-observer variability.

2.3 Dynamic Programming

Gustavsson et al. [21] and Wendelhag et al. [22] proposed related dynamic programming procedures for the automatic detection of the carotid boundaries in B-mode images. Their approach linearly combines measurements of local intensity, intensity gradient, and boundary continuity into a cost function. Low values of the cost function are associated with pixels of the desired boundaries and high values are associated with other pixels. The weights of the three terms of the cost function (intensity, gradient, and continuity) were estimated in a training phase, using manual tracings as the ground truth. The procedure is completely automatic but allows the interaction of the operator in order to correct erroneous detections. To reduce the computational burden, Liang et al. [23] introduced a multi-scale version of the dynamic programming scheme proposed in [22]. The global position of the artery is computed for the coarser scale and iteratively refined down to the finer scale. The main disadvantages of these methods are the need for a training phase and the fact that the systems may need to be retrained when the scanner or its settings are changed.

More recently, a different approach based on dynamic programming was introduced in [24]. The instantaneous coefficient of variation (ICOV) was used to improve the edge detection in ultrasound images, where the noise has a multiplicative nature. The ICOV-based edge detection, the intensity gradient, robust statistics, and the a priori knowledge about the spatial distribution of the artery boundaries are used to compute fuzzy score maps for the LI and MA interfaces. These score maps are then passed to a dynamic programming procedure that computes the contour with the largest accumulated score, for each interface. The method is able to detect the LI and the MA interfaces at near and far walls, for both healthy and atherosclerotic arteries, with a wide range of plaque types and sizes. But results are significantly better for the far wall, where the automatic detection shows an accuracy similar to manual detections. The main disadvantages are the need for a manual selection of the ROI and for a training phase.

2.4 Snakes

Traditional snakes are often attracted by the wrong boundaries due to the influence of noise. In order to overcome this limitation and prevent the trapping of the snake in between the LI and the MA interfaces, Cheng et al. [25, 27] used a more robust formulation of the snake's external energy. A manual initialization of the snake is required. In another study [26], the same authors showed that using the contours estimated by their snake-based method, instead of manual tracings, significantly reduces the intra-observer and inter-observer variability.

Loizou et al. [28–30] showed that results obtained with snake-based methods can be improved if the snake is preceded by intensity normalization and despeckling of the image. The intensity normalization consists in setting the intensity median of the lumen region to a value between 0 and 5 and the intensity median of the adventitia layer to a value between 180 and 190. The best despeckling method found consisted in iterating five times a linear scaling filter, based on statistics taken from 7×7 pixel windows. Both the intensity normalization and the snake initialization require user interaction. The authors presented a large statistical validation of their results against manual tracings.

Delsanto et al. [32, 34] proposed a completely user-independent scheme that combines local statistics and a snake. Local statistics were used, first, to locate the carotid artery lumen, followed by a snake-based detection of the LI and MA interfaces. It was assumed that pixels associated with neighborhoods with low intensity mean and standard deviation usually belong to the lumen. So, the lumen was located by clustering the image into two classes, by separating the pixels with those two properties from all the remaining pixels. The threshold for the mean and the one for the standard deviation were both determined empirically, using a bidimensional histogram representing the intensity standard deviation as a function of the intensity mean, computed over 10×10 pixel windows. Once the lumen region is located, the adventitia layers are estimated by searching below the lumen, along each image column, for the intensity peak above a given threshold. The contour that links these intensity maxima in the longitudinal direction is used to initialize the snake that refines the estimate of the MA interface. A similar procedure is followed in the detection of the LI interface, but using the largest intensity peaks between the lumen and the MA interface to initialize the snake. The method was validated against manual tracings, showing good results. However, there are several parameters that were chosen empirically, the computational burden is too high for real-time applications and the noise caused wrong detections in 10% of the cases. An improvement of this method was proposed by the same authors in [31, 33], where the near wall and diseased vessel were also processed. Three clusters were considered: (i) lumen; (ii) intima and media layers; (iii) adventitia layer. The clustering was implemented using a fuzzy K-means classifier. The boundary between class (i) and class (ii) was taken as the initial guess for the LI interface while the boundary between class (ii) and

class (iii) was the initial guess for the MA interface. These boundaries were used to initialize snakes that refined the estimates of the LI and MA interfaces. The chapter reports an improvement of the IMT measurement error, as well as robustness in segmenting plaques, although with worse results for echolucent ones. The method failed in 8% of the images due to low signal-to-noise ratio or to failure of the ROI selection. A more recent version of the same approach [35] was tested on a set of 200 images acquired with three different ultrasound scanners. It was demonstrated that the segmentation performance did not depend on the scanner used. An improvement of the IMT measurement error was reported, when compared to the initial version of the method.

2.5 Discrete Dynamic Contour and Multi-scale

In [37], Gutierrez et al. used a discrete dynamic contour in a multi-scale scheme to automatically detect the carotid boundaries in B-mode images. The contour evolution was implemented as a function of a linear combination of three weighted forces: (1) an internal force, proportional to the curvature of the contour; (2) an external force, equal to the local magnitude of the intensity gradient; (3) and a damping force, proportional to the velocity of each vertex of the contour. The results showed a low accuracy in the IMT measurements.

2.6 Hough Transform

Golemati et al. [38, 39] proposed a scheme based on the Hough transform. The LI and MA boundaries are assumed to be straight horizontal lines in longitudinal sections and circular lines in transversal sections. The method is completely automatic, it is real time and both longitudinal and transversal sections of the carotid artery can be segmented. However, the need for straight horizontal or circular LI and MA interfaces is a serious limitation, since the appearance of these boundaries is often irregular. Another disadvantage is the large number of parameters that are set empirically. A normalization of the ultrasound images is required in order to minimize the variability introduced by different operators, scanners, and gain settings. More recently, the same authors [36] introduced a snake-based refinement of the carotid boundaries in transversal sections, where the snakes are initialized by the circles computed by the Hough transform approach. The results were validated using receiver operating characteristics (ROC) analysis measures between automatic contours and manual tracings.

2.7 Template Matching

Rossi et al. [40, 41] introduced an interesting parametric template matching approach for the automatic lumen detection in longitudinal sections of the CCA. The LI and MA interfaces are not computed because the method was conceived to estimate only the location of the lumen. But this technique may be useful as a first step for complete automation of the LI and MA detection, since it avoids the need for a manual location of the lumen. To decrease the computational load, the image columns are decimated. The proposed template matching scheme is based on a priori knowledge of the expected diameter range and of the typical intensity pattern of the arterial wall–lumen complex. Spatial and temporal clustering is performed over a sequence of frames in order to reject incorrect estimates. The method is real time but a training phase is required. The performance of the method is generally high but it may fall significantly when the jugular vein is present or when the signal-to-noise ratio in the lumen region is low. The algorithm was validated by comparing the lumen center positions estimated automatically with the ones traced by an operator, taken as the reference positions. The automatic recognition was considered correct if it did not deviate more than 2 mm from the reference position.

2.8 Nakagami Modeling

Destrempes et al. [42] used a segmentation scheme based on stochastic optimization that assumes the Nakagami model for the intensity distributions in a small ROI containing the CCA wall. The lumen and the adventitia were associated with the distributions with the lower and the higher means, respectively. The intima–media complex was considered the mixture. Although a good performance was reported, this approach may be of little use for images containing pathological structures, like plaque, where the assumptions about the statistical distributions of the wall layers may not be valid. For example, in the presence of a calcified plaque, the adventitia layer may not be the one with the highest mean. Another disadvantage is the need for manual initialization.

2.9 Feature Extraction, Fitting, and Classification

An integrated approach, consisting of feature extraction, fitting, and classification, was proposed by Molinari et al. [43, 44]. The authors divided the technique into two main steps: (1) the automatic location of the CCA; (2) the detection of the LI and MA interfaces of the far wall. The first step begins with the location of the seed points, defined as the local intensity maxima above a given threshold, in

each image column. Line segments are fitted to these seed points. Close and aligned segments are fused while the other segments are eliminated, producing an estimate of the location of the adventitia layer. In the second step, a fuzzy K-means classifier is applied to the intensity profile of each image column, in order to assign the pixels to the lumen, to the intima–media structure, or to the adventitia layer. The boundaries that separate these three clusters were taken as the estimates of the LI and the MA interfaces. There is also a preprocessing block that uses a low pass filter to reduce speckle. A large validation against manual tracings showed a very accurate detection of the MA interface but a poor detection of the LI interface. Another disadvantage is the need for a training phase in the first step.

More recently, the same authors [45] introduced an improved version of this approach, where the detection of the LI and MA interfaces, in the second step of the method, is based on the FOAM edge operator previously used by Faita et al. [19]. This approach was validated against manual tracings on a database of 300 carotid images from two different institutions, producing very accurate detections for both LI and MA interfaces of the far wall. The authors reported an average computation time of 2.3 s per image and a failure rate of 4%.

2.10 Watershed Transform

In [48], Molinari et al. adopted an approach similar to the one used in [43, 44], but using an algorithm based on watershed transform in the CCA location step. After erosion with a 12 pixel disk-shaped structuring element, the image was reconstructed against the original one. A black and white image was computed through thresholding and the white areas were used to perform marker-based watershed segmentation. The CCA location was then selected as the segmented image region with the greater value of an ad hoc score function. The CCA region includes the lumen and the walls of the artery, but the lumen is much darker and larger than the walls. When present, the jugular vein has similar properties, but appears above the CCA. Therefore, the score function was made proportional to the percentage of dark pixels in the region and inversely proportional to the average region intensity and the average region height. The method was tested against manual tracings. The failure rate reported for this method (9.5%) was only slightly lower than the one reported for the approach presented in [43, 44]. The evaluation in a database of 165 images showed some improvement of the accuracy when compared to the one reported in [43, 44], but a lower accuracy compared to the one found in [45]. The average segmentation time per image was equal to 18 s.

2.11 Limitations of the Current Solutions

The methods described above present several important limitations. Semiautomatic approaches [13–22, 24–30, 37, 42] are not suited for the treatment of large databases and the results are affected by the user interaction. Several automatic methods are computationally heavy [31–35, 43, 44, 48], making them unattractive for clinical practice. Some studies [13–16, 20, 21, 25, 27, 37] do not consider the segmentation of plaques. Few studies [18, 24, 31, 33, 46, 47] measure the IMT at the near wall.

There are already a few commercial systems available for the IMT measurement, namely, Vivid 7, created by General Electrics (http://www.vivid7ultrasound.com); SonoCalc IMT, commercialized by SonoSite (http://www.sonosite.com); and M'Ath from Intelligence in Medical Technologies (http://www.iimt.fr). These systems compute a set of IMT measurements, like the mean and maximum, over the specified section. But they also have some limitations. For instance, they all require user interaction. Vivid 7 and Sono-Calc require the manual selection of a rectangular ROI containing the section of the artery wall where the IMT is to be measured. M'Ath requires the user to draw a longitudinal line inside the lumen in order to locate the lumen and to define the section of the wall to be segmented. They only work properly if the boundaries to detect are well visible in the specified section of the wall. Also, at least in the case of M'Ath, this section cannot include plaque.

3 Cubic Splines and Dynamic Programming for Carotid Image Segmentation

The proposed method for the segmentation of the NW and FW intima–media regions of the CCA in B-mode ultrasound images begins with an edge detection step. The final edge map is made by the edges that are compatible with the carotid wall boundaries to be detected. The MA interface is detected by a RANSAC search for the best fit of a cubic spline to edges having features compatible with the MA boundary. Several discriminating features of the MA interface are used to reduce the attraction of the automatic contour by other edges. A smooth estimate of the LI interface is obtained using dynamic programming, smooth intensity thresholding surfaces, and geometric snakes.

3.1 Edge Estimation

The edge estimation consists in the determination of an edge map representing the set of the pixels whose properties (e.g., the gradient orientation) are compatible with the carotid wall

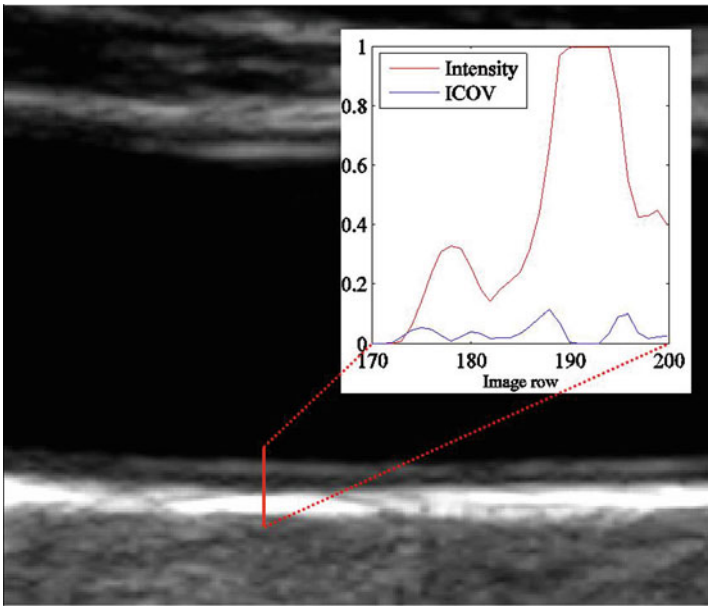

Fig. 22.2 Intensity and corresponding ICOV profiles along the line segment represented as a *red line* over a B-mode image

boundaries to be detected. These edges are estimated in four steps: edge detection (Sect. 3.1.1); estimation of the dominant gradient direction at edges (Sect. 3.1.2); determination of the final edge map (Sect. 3.1.3); and determination of the valley edge map (Sect. 3.1.4).

3.1.1 Edge Detection

In [46, 47], a new smoothing filter was proposed for the edge detection in B-mode images. This filter smoothes out the noise while producing well-localized edges and preserving important weak boundaries. It takes advantage of the instantaneous coefficient of variation (ICOV) edge detector [53, 54], which is well adapted to US images. The ICOV value at pixel (*x*,*y*) is computed by (22.1), using the intensities of the pixels in its 8-neighborhood.

$$\mathrm{ICOV}(x,y) = \sqrt{\frac{\left|\frac{1}{2}\|\nabla I(x,y)\|^2 - \frac{1}{16}(\nabla^2 I(x,y))^2\right|}{\left(I(x,y) + \frac{1}{4}\nabla^2 I(x,y)\right)^2}} \tag{22.1}$$

In (22.1), $I(x,y)$ represents the image intensity at (x,y), $\nabla I(x,y)$ is the intensity gradient at (x,y), and $\|(u,v)\| = \sqrt{(u^2+v^2)}$ is the norm of a vector (u,v). As explained in [53], the ICOV is an edge detector for speckled images that combines a normalized gradient magnitude operator and a normalized Laplacian. At edge pixels, the Laplacian term becomes zero, the gradient term becomes dominant, and $\mathrm{ICOV}(x,y) \rightarrow |\nabla I(x,y)|/I(x,y)$. This normalization of the gradient magnitude allows the ICOV to detect edges both in bright regions and in dark regions, in images with multiplicative noise. As shown in Fig. 22.2, the ICOV produces local maxima at the points associated with edge pixels, where the intensity changes more rapidly.

As in [55], robust statistics is used to decide where diffusion should take place and where it should be inhibited. The diffusion coefficient at pixel (x,y) and time t is a Tukey's function [56], given by

$$c(x,y;t) = \begin{cases} \frac{1}{2}\left[1 - \left(\frac{\mathrm{ICOV}(x,y;t)}{\sigma_s(t)}\right)^2\right]^2, & \mathrm{ICOV} < \sigma_s \\ 0, & \mathrm{ICOV} \geq \sigma_s \end{cases} \tag{22.2}$$

where $\sigma_s = \sqrt{5}\sigma_e$ and σ_e is the image edge scale [55], computed as

$$\begin{aligned} \sigma_e &= C\,\underset{\Omega}{\mathrm{MAD}}(\mathrm{ICOV}) + \underset{\Omega}{\mathrm{med}}(\mathrm{ICOV}) \\ &= C\,\underset{\Omega}{\mathrm{med}}\left|\mathrm{ICOV} - \underset{\Omega}{\mathrm{med}}(\mathrm{ICOV})\right| + \underset{\Omega}{\mathrm{med}}(\mathrm{ICOV}) \end{aligned} \tag{22.3}$$

where MAD represents the median absolute deviation, $\underset{\Omega}{\mathrm{med}}(r)$ is the median of r over the image domain, Ω, and $C = 1.4826$ is a constant.

The proposed filter has the advantage of preserving some important anatomical boundaries even when they have a low ICOV. It is based on concepts from the total variation theory [57, 58] and embeds the curvature information, as described by

$$\begin{cases} \frac{\partial I(x,y;t)}{\partial t} = c(x,y;t)\kappa(x,y;t)\,\|\nabla I(x,y;t)\| \\ I(x,y;t) = I_0(x,y) \\ \frac{\partial I(x,y;t)}{\partial \vec{n}} = 0 \quad \forall (x,y) \in \partial\Omega \end{cases} \tag{22.4}$$

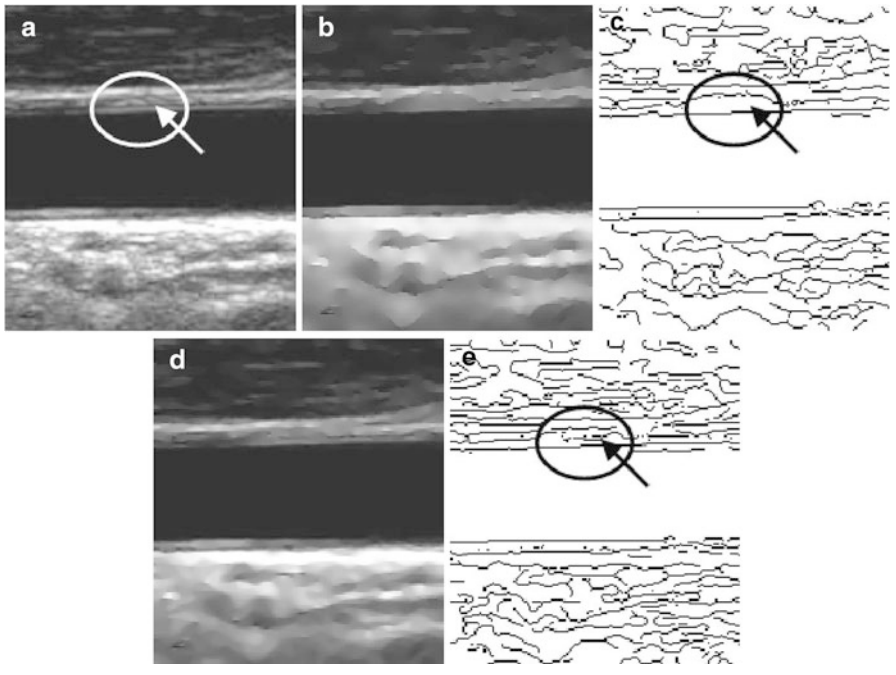

Fig. 22.3 Edge maps produced by nonlinear filtering: (**a**) a longitudinal section of a CCA and weak valley edges pointed out by an *arrow*; (**b**) smoothed image obtained with the filter proposed in [55]; (**c**) edge map of image (**b**) showing erosion of weak valley edges; (**d**) smoothed image obtained with the filter proposed in [46, 47]; (**e**) edge map of image (**d**) showing a better preservation of weak valley edges

where $c(x,y;t)$ is the Tukey's function given by (22.2), ∇I is the intensity gradient, I_0 is the initial image, at time $t=0$, $\partial\Omega$ is the image boundary, and $\vec{n}$ is the outward normal at the image boundary. $\kappa(x,y)$ is the mean curvature, updated at each time step, given by

$$\kappa(x,y) = \text{div}\left(\frac{\nabla I(x,y)}{\|\nabla I(x,y)\|}\right) \tag{22.5}$$

With this filter, the diffusion is inhibited both where the ICOV is high and where the curvature is small. This way, since the LI and MA boundaries usually have low curvature, they can be preserved even when they have a low ICOV. The noise is strongly smoothed out because it usually has high curvature and low ICOV. Figure 22.3 shows the improvement introduced by this new filter when compared with a related filter previously proposed in [55]. Figure 22.3c shows the erosion of weak edges produced by the filter proposed in [55]. Figure 22.3e shows that the new filter is better at preserving the carotid wall boundaries.

The edge map is computed from the smoothed version of the image produced by the new filter, using the ICOV as a measure of the edge strength, non-maxima suppression, and hysteresis [59]. The lower threshold for the hysteresis was set to $T_1 = \sigma_e$ and the higher threshold was set to $T_2 = 0.4T_1$. Morphological thinning [60] is applied to the edge map to make sure the edges are one pixel thick.

3.1.2 Dominant Gradient Direction

In [46, 47], the gradient orientation errors were reduced by using the local dominant gradient direction, computed as follows. Let $\nabla I^n(x,y)$ be the intensity gradient at pixel (x,y), in iteration n, and ∇I_k^n the gradient at the kth pixel in the 8-neighborhood of (x,y), in iteration $n-1$. Then $\nabla I^n(x,y)$ is computed as the average of ∇I_k^{n-1}, for $k=1,2,\ldots,9$, considering only the neighbors whose gradient makes an angle less than 45° with the gradient at the central pixel, to avoid the interference of close contours with very different orientations.

The stopping criterion of this iterative procedure was based on the stability of the gradient orientation. Let α be the angle change in the gradient orientation between consecutive iterations, at each edge pixel. Outliers can be defined as the edge pixels whose value of α does not stabilize. The threshold, σ_α^*, above which no inliers of α are expected can be estimated as $\sigma_\alpha^* = \sqrt{5}\sigma_\alpha$ [56], where $\sigma_\alpha = C\text{MAD}(\alpha) + \text{med}(\alpha)$ is a statistically robust estimate of the threshold at which the outliers start to appear [55]. Therefore, iterations stop when $\sigma_\alpha^* < \epsilon$, setting $\varepsilon = 0.1°$ in order to insure a good stability to all inliers.

3.1.3 Final Edge Map

The final edge map is determined by selecting only the edges that are compatible with the carotid wall boundaries to be detected, using criteria based on their gradient orientation, their distance to the lumen axis, and their signed distance to the lumen boundary (SDL) value. The elimination of incompatible edges reduces the computational cost and the chances of the automatic contour being attracted to other edges.

Since the gradient is expected to point outward at the carotid wall boundaries, edges with gradients pointing to the

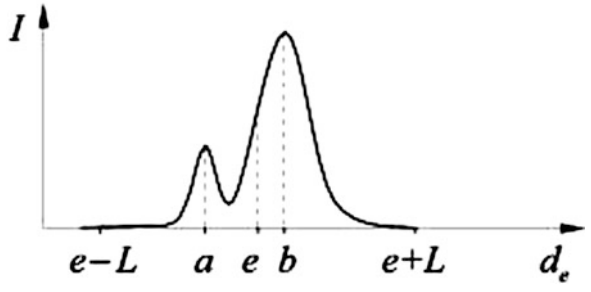

Fig. 22.4 Typical intensity profile of a valley edge, where I is the intensity, e is the location of the edge, d_e is the distance from the edge in the direction of its intensity gradient, $\nabla I(e)$, a is the location of the lower peak, b is the location of the higher peak, and L is the maximum distance of search

interior of the artery should be removed. If $\gamma(x,y)$ is the angle, at (x,y), between the intensity gradient and the gradient of the distance map to the estimated medial axis, all edge pixels for which $\gamma(x,y) < \gamma_{\max}$ are removed from the edge map, where $\gamma_{\max}$ is the threshold above which the probability of finding an edge of the carotid MA interface is virtually zero.

All edges in the ROI whose distance to the lumen axis is larger than a certain threshold, $d_{\max}$, or such that $\mathrm{SDL}_{\min} < \mathrm{SDL} < \mathrm{SDL}_{\max}$ are also removed from the edge map.

3.1.4 Valley Edge Map

The MA interface is often associated with a valley-shaped intensity profile (Fig. 22.4), called "double line" pattern [10].

As explained in [46, 47], the valley edge map is a subset of the final edge map described in Sect. 3.1.3. The determination of the valley edge map begins with a search, up to a certain distance, L, for the first local intensity maximum (Fig. 22.4) in both directions along the line defined by each edge point, e, and the corresponding intensity gradient, $\nabla I(e)$. The intensity profile of a valley edge has two intensity peaks, at locations a and b, one of these being usually lower. Only profiles with a strong lower peak should be classified as valley edges. Using hysteresis, as in Sect. 3.1.1, and representing the amplitude of the lower peak by A, the high threshold can be set to $T_A = C\mathrm{MAD}(A) + \mathrm{med}(A)$ and the low threshold to $0.4T_A$. However, experimentation showed that valley edge detection is better if an edge pixel is classified as a valley edge when $A > 0.4T_A$.

3.2 Estimation of the Media–Adventitia Interface Using RANSAC

The method proposed in [46, 47] for the segmentation of the MA boundary is based on a RANSAC search for the best fit of a cubic spline [61] model according to a specified cost function. The RANSAC algorithm allows for the estimation of the model parameters from a dataset containing a large number of outliers. It works by repeatedly extracting a random sample, with the minimum number of data points required to determine the model parameters. The consensus of the model is then evaluated for the rest of the population and the model with the best consensus is selected. The process is terminated when there is a high confidence in having drawn at least one good sample.

The cubic spline [61] model was chosen for the MA boundary because it gives smooth curves, it is relatively easy to implement, it offers a stable behavior, and the results showed that it is able to adequately follow the MA interface in longitudinal sections. A dedicated gain function was conceived to evaluate the spline consensus.

3.2.1 Sample Generation and the Adventitia Model

In longitudinal sections of the CCA, samples of the MA edges must have different abscissas. Therefore, a set of n different abscissas is randomly drawn and used to determine n vertical lines above and below the lumen axis, separately. Good abscissas are those for which the corresponding vertical line contains a good point, that is, an edge point of the MA boundary.

To detect the NW MA, a cubic spline is built from each sample of n edge points with different abscissas, above the lumen axis. Since there are usually several edge points for each abscissa, the algorithm evaluates all the splines fitted to the samples of n edge points for each sample of n abscissas. The best spline, according to a predefined criterion, is then selected. A similar procedure is used for the detection of the FW MA interface. Setting $n = 5$ gives some flexibility to the spline without compromising its robustness to noise.

3.2.2 Model Consensus

The consensus of the fitted spline is measured by a gain function integrating the response to several discriminating features of the carotid boundaries.

One feature is related to the type of edges. Since valley edges are not always present, step edges are also considered, giving more emphasis to valley edges and edges closer to the detected lumen boundary. Another feature is the SDL. A stronger penalty is given to larger absolute value of the SDL, in order to reduce the influence of other anatomical boundaries. However, the possible presence of plaque requires this penalty to have a slower growth for positive values of SDL (those outside the lumen). A third feature is the gradient orientation. It must be consistent with the normal to the carotid MA interface model. In summary, the gain function must integrate the following features:

1. Distance of the fitted spline to any edge points, *de*
2. Distance of the fitted spline to valley edge points, *dve*

3. Angle, θ, between the orientation of the normal to the fitted spline and the intensity gradient
4. Signed distance of the fitted spline to the lumen boundary, SDL

These features are integrated into the gain function presented in (22.6) in a way that reflects the probability of each spline point belonging to the carotid boundary. A spline point, P_k, has a high probability of belonging to the carotid boundary if it is close to a valley edge or a step edge, and it has an intensity gradient orientation similar to the orientation of the normal to the spline and it falls inside the expected distance limits to the lumen axis. The chance of each spline point being a good candidate should increase as each feature becomes stronger. Therefore, best spline fit is chosen as the one with the highest score for the following gain function

$$G = \frac{1}{2m}\sum_{k=1}^{m}[g_1(P_k) + g_2(P_k)]g_3(P_k)g_4(P_k) \quad (22.6)$$

where m is the number of P_k points of the digital spline and $g_j(P_k)$, $1 \le j \le 4$, are fuzzy functions representing the contribution of feature j at P_k.

In (22.6), $g_1(P_k) = f(de(P_k))$, $g_2(P_k) = f(dve(P_k))$, and $g_3(P_k) = f(\theta(P_k))$, where $f(z)$ is the Tukey's function, given in (22.7), with scale $\sigma = \sigma_d$ for features *de* and *dve* and scale $\sigma = \sigma_\theta$ for θ.

$$f(z) = \begin{cases} \left[1 - \left(\frac{z}{\sigma}\right)^2\right]^2, & z < \sigma \\ 0, & z \ge \sigma \end{cases} \quad (22.7)$$

The scale, σ, of each fuzzy function represents the threshold of the corresponding feature above which MA boundary pixels are no longer expected to be found. Function g_4 gives preference to curves that are closer to the lumen boundary and a larger tolerance to those outside the lumen. This is expressed as

$$g_4(P_k) = \begin{cases} f^-(-\mathrm{SDL}(P_k)), & \mathrm{SDL}(P_k) < 0 \\ f^+(\mathrm{SDL}(P_k)), & \mathrm{SDL}(P_k) \ge 0 \end{cases} \quad (22.8)$$

where $f^-(z)$ and $f^+(z)$ are given by (22.7), with scales $\sigma = \sigma^-$ and $\sigma = \sigma^+$, respectively.

The gain function produces values in the range [0, 1], where unity means a perfect fit. Its score reflects the percentage of good points along the path of the spline and can be viewed as an estimate of the probability of drawing a good abscissa.

To reduce the computational cost, two bailout tests and a digital spline are used. The digital spline avoids interpolations. The first bailout test rejects any sample of n abscissas not well spread along the columns of the image, in order to guarantee a good support for the spline model. A good spreading of the abscissas in each sample was obtained by selecting only samples where the distance between consecutive abscissas is not smaller than a specified distance, $\Delta = (m-1)/(2(n+1))$, where n is the size of the sample and m is the number of columns in the image. For $n = 5$ (4 polynomials), $\Delta = (m-1)/12$. The second bailout test rejects any sample of n points if the angle, θ, between the gradient intensity and the spline normal is larger than a threshold σ_θ at any point of the sample.

3.2.3 Stopping Criterion

The minimum number of samples, k, that should be inspected can be determined by adding a few standard deviations, σ, to the expected number of samples, μ, necessary to get a good sample [62], that is:

$$k > \mu + N\sigma = \omega^{-n} + N\frac{\sqrt{1-\omega^n}}{\omega^n} \quad (22.9)$$

where N is the number of standard deviations added to the mean, n is the size of the sample, and ω is the proportion of inliers in the dataset.

After the processing of each sample of n abscissas, ω is updated as the highest value found for the gain function, up to that moment. The procedure is terminated when the number, k, of drawn samples of abscissas exceeds the number given by the second member of (22.9).

Two examples of detections of the MA interfaces are presented in Fig. 22.5.

3.3 Estimation of the Lumen–Intima Interface Using DP

The method proposed for the detection of the LI boundary uses DP and assumes the carotid MA interface was previously detected (using the approach described in Sect. 3.2). It is summarized in the following steps:

1. Set $E_{\mathrm{all}}(x,y) = 1$ if (x,y) is a local maximum of the ICOV in the direction of $\nabla I(x,y)$. Otherwise, $E_{\mathrm{all}}(x,y) = 0$. E_{all} is the edge map with all edges (Fig. 22.6b), obtained as described in Sect. 3.1 but without any constraint on the edge strength, measured by the ICOV. This edge map is important because some edges of the lumen boundary may be quite weak.
2. Set $E_{\mathrm{strong}}(x,y) = E_{\mathrm{all}}(x,y)$ if $\mathrm{ICOV}(x,y) > T$, where T is a threshold automatically estimated with robust statistics [12]. Otherwise, set $E_{\mathrm{strong}}(x,y) = 0$. E_{strong} is the edge map with the strong edges (Fig. 22.6c).
3. Set $E(x,y) = E_{\mathrm{all}}(x,y)$ if $(x,y) \in \Omega$, where Ω is the inner region delimited by the detected MA contours. Otherwise, $E(x,y) = 0$.

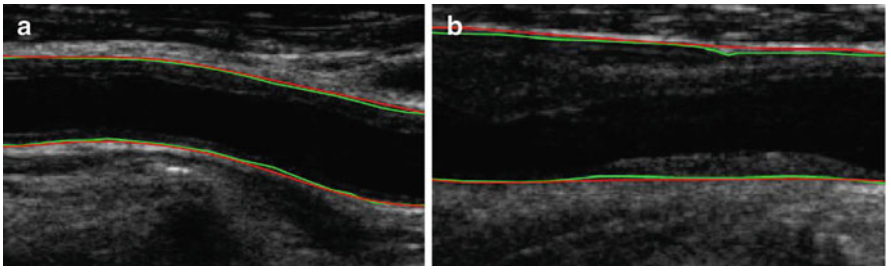

Fig. 22.5 Ground truth (*green*) and the MA interfaces estimated by the spline fitting model (*red*)

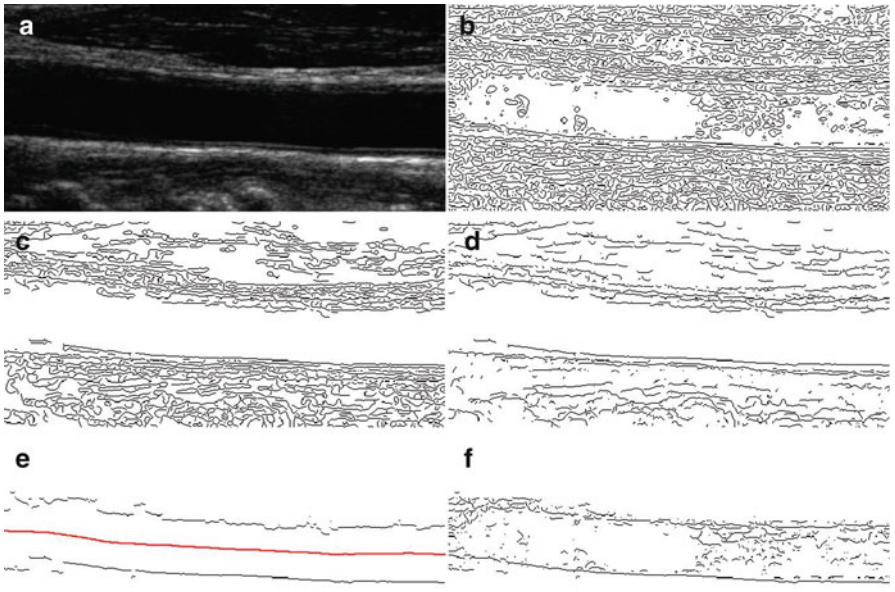

Fig. 22.6 (**a**) ROI from a B-mode image of a longitudinal section; (**b**) edge map E_{all}, with all edges (strong and weak); (**c**) edge map E_{strong}, containing only strong edges; (**d**) E_{strong} after removing all edges with a gradient direction incompatible with the LI interface; (**e**) edges of E_{strong} that are "visible" from the interpolated lumen axis (*red curve*); (**f**) final version of edge map E

4. Set $E(x, y) = 0$ and $E_{\text{strong}}(x, y) = 0$ if $\gamma(x, y) \geq 90^0$, where γ is the angle between $\nabla I(x,y)$ and $\nabla D(x,y)$, and D is the distance map to the lumen medial axis. This step removes the edges of E and E_{strong} that have a gradient pointing inwards the artery, which means they are incompatible with the LI interface. Fig. 22.6d illustrates the result of this step for E_{strong}.
5. If $E(x,y) = 1$, compute $\text{ICOV}^*(x, y) = \text{ICOV}(x, y) / \max_y (\text{ICOV}(x, y))$, the normalized ICOV at (x,y) in the vertical direction. ICOV* is computed separately for edges above and below the lumen axis, for each abscissa. This procedure gives a chance to the usually weaker lumen boundary edges to compete with the MA interface edges. Otherwise, the DP contour tends to be attracted toward the MA interface, where the ICOV is much stronger.
6. Set $E(x, y) = 1$ if $E_{\text{strong}}(x, y) = 1$ and there are no other edges in E_{strong} between (x,y) and the lumen axis, in the vertical direction (Fig. 22.6e, f). This is required because the carotid MA interface is the best estimate of the lumen boundary when the intima–media region is not visible. Set $\text{ICOV}^*(x,y) = 1$ for these edges.
7. Using DP, look for the path in E, between the first and the last columns of the ROI, that minimizes the cost function

$$C_t = \sum_{j=1}^{N} \psi(x_j, y_j) \tag{22.10}$$

where $\psi(x_j, y_j) = 1 - \text{ICOV}^*(x_j, y_j)$ if $E(x_j, y_j) = 1$ and $\psi(x_j, y_j) = 1$; otherwise, N is the number of columns of the ROI. The DP algorithm is applied directly to E, with independent searches made above and below the lumen axis, to detect the NW and the FW LI interfaces.

3.4 Smoothing and Improving the Detected Lumen Boundaries

The output of the DP algorithm needs to be smoothed because it is often irregular due to noise. This smoothing was not implemented by adding a geometric term in (22.10) because a strong geometric term would often be necessary, leading to bypasses of the contour through tissue regions

at sections of the LI boundary with high curvature. The smoothing was introduced by a geometric snake, which can also improve detections in the presence of deep concavities or sharp saliences, as the one in the left part of the upper lumen boundary in Fig. 22.6b. For this purpose, a hybrid version of the Chan–Vese piecewise constant segmentation model [63, 64] was introduced in [46, 47].

The Chan–Vese geometric snake is a successful region-based active contour embedded in a level set framework [65, 66] that does not depend on gradients, making it robust to the initial position of the active contour and to small gaps in the boundaries. It also has the ability to automatically detect inner contours, its topological changes are treated in a natural way, and the direction of its evolution in space is automatically determined from the image data.

The Chan–Vese active contour assumes a two-phase piecewise constant image and is described by the functional

$$\begin{aligned} F(c_1, c_2, C) &= \mu \text{Length}(C) \\ &+ \lambda_1 \int_{\text{inside}(C)} [u_0(x,y) - c_1]^2 \text{d}x\text{d}y \\ &+ \lambda_2 \int_{\text{outside}(C)} [u_0(x,y) - c_2]^2 \text{d}x\text{d}y \end{aligned} \tag{22.11}$$

where μ, λ_1, and λ_2 are positive parameters, u_0: $\Omega \rightarrow \Re$ represents the input image, c_1 and c_2 are, respectively, the averages of u_0 inside and outside the region boundaries represented by C. In [63] a level set formulation was introduced for (22.11), where the active contour, C, is represented as the zero level set of an implicit function. Constants c_1 and c_2 can be viewed as functions of an intensity threshold that is updated as the active contour evolves in space.

The major difficulty in the application of this active contour to B-mode images of the carotid is their non-piecewise constant nature. This problem was addressed in [46, 47] by introducing some modifications to the Chan–Vese model, making it also faster than the original model. The intensity threshold estimate of the Chan–Vese model was replaced by a thresholding surface, keeping the other attractive properties. The implementation of the hybrid model can be divided into two steps:

1. Before the initialization of the active contour, an optimal smooth thresholding surface, $T_{\text{opt}}(x,y)$, is interpolated from the intensities at the edges along the contours produced by the DP algorithm.
2. The image is then processed by the modified version of the Chan–Vese two-phase piecewise constant active contour, where c_1 and c_2 are determined as functions of $T_{\text{opt}}(x,y)$, such that the intensity threshold at each pixel is given by the thresholding surface.

In the hybrid model, $c_1(x,y) = 2\,T_{\text{opt}}\,(x,y)$ and $c_2(x,y) = 0$, to keep the intensity threshold as the mean of c_1 and c_2. The values of c_1 and c_2 are not updated during the evolution of the contour. The active contour is used only to smooth and to improve the position accuracy of the estimated boundaries.

A new method was introduced in [46, 47] to estimate the thresholding surface, $T_{\text{opt}}\,(x,y)$, by interpolating the image intensities at edge pixels, where good local thresholds are expected to be found. As in [67], the interpolation surface is obtained by solving the Laplace's equation

$$\frac{\partial^2 u}{\partial x^2} + \frac{\partial^2 u}{\partial y^2} = 0 \tag{22.12}$$

for the thresholding surface, u.

Equation (22.12) is computed in two steps. First, an approximate solution is obtained with a fast algorithm that propagates the intensity values at the interpolating pixels to the rest of the image. Second, the Laplace's equation is solved with the following numerical scheme:

$$\begin{aligned} u^{n+1}(x,y) &= 0.25[u^n(x+1,y) + u^n(x-1,y) \\ &\quad + u^n(x,y+1) + u^n(x,y-1)] \\ u^{n+1}(x,y) &= \beta u^{n+1}(x,y) + (1-\beta)u^n(x,y), \\ n &= 0, 1, 2, \ldots \end{aligned} \tag{22.13}$$

where $u^n(x,y)$ is the value of the thresholding surface at pixel (x,y) and at iteration n, $\beta = 1.5$, and the initial solution, u^0, is the surface in the first step.

The second equality in (22.13) introduces over-relaxation [61] to speed up the convergence. The iterations are stopped when the relative intensity difference for every pixel is $<1\%$ between two consecutive iterations.

Two examples of the final smoothed contour are presented in Fig. 22.7.

3.5 Parameter Settings

Parameters were estimated either automatically (σ_e, T_A, etc.) or through experimental tests. For instance, the ROI size was chosen as small as possible but large enough to contain the carotid region.

The nonlinear smoothing filter (22.4) was discretized with the numerical scheme proposed in [68]. Two parameters of this scheme are the image grid size, h, which was normalized to one, and the time step, Δt, that was set to 0.25 in order to obtain a good convergence speed without losing numerical stability. The value of the edge scale, σ_e (22.3), as well as the slope of the corresponding curve, decreases as the number of iterations increase. Iterations are stopped when the rate of change of σ_e falls below 5×10^{-4}, after which the smoothing increases very slowly.

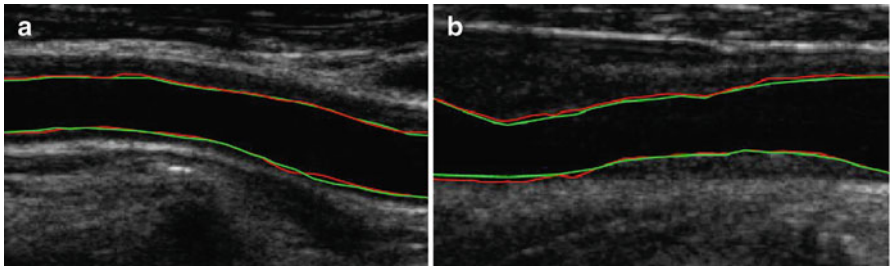

Fig. 22.7 Ground truth (*green*) and the LI interfaces estimated by the hybrid Chan–Vese model (*red*) applied to the output of the DP algorithm

In literature related to RANSAC (e.g., [62, 69]) it is common to select parameter N (22.9) such that $1/N^2 \approx 0.05$, which gives $N \approx 4.5$. Therefore, $N = 5$ was chosen.

In the used dataset, the distance from a carotid MA interface pixel to the lumen medial axis is less than 70 pixels. So, $d_{\max} = 90$ pixels was used in order to keep some of the image data outside the carotid boundaries.

The value of γ was computed in the neighborhood of the manually traced carotid boundaries, along each image column, for the edge pixel closest to these boundaries. It was observed that $\gamma < 30°$ in at least 99% of the cases, which means that $\gamma_{\max} = 30°$ is an adequate value.

The parameter $\mathrm{SDL}_{\min}$ represents the threshold of SDL below which no edge pixel of the carotid MA interface is expected to be found. It was observed that $\mathrm{SDL} > -6.4$ in every image of the dataset, leading to the choice of $\mathrm{SDL}_{\min} = -7$ and $\sigma^- = -\mathrm{SDL}_{\min} = 7$. Parameters $\mathrm{SDL}_{\max}$ and σ^+ represent the threshold of SDL above which no edge pixel of the MA interface is expect to be found. A natural value for this threshold is $d_{\max}$, leading to $\mathrm{SDL}_{\max} = \sigma^+ = d_{\max}$.

The width measurement of the valley edges in the dataset showed that $L = 10$ is enough for valley edges belonging to the MA interface.

To estimate the values of σ_d and σ_θ, the values of de and θ were computed for each point of the MA interfaces manually traced by one of the experts (MA1). Parameter θ was computed from the image gradient map, obtained with the local dominant gradient direction filter. Parameter de was computed from the edge map, described in Sect. 3.1. Parameters σ_d and σ_θ are scales of Tukey's functions. Therefore, they can be computed as $\sigma_d = \sqrt{5}[C\,\mathrm{MAD}(de) + \mathrm{med}(de)]$ and $\sigma_\theta = \sqrt{5}[C\,\mathrm{MAD}(\theta) + \mathrm{med}(\theta)]$, respectively, which gives $\sigma_\theta \approx 11°$ and $\sigma_d \approx 4$.

The threshold σ_θ was also used in one of the bailout tests, as the limit for the angle, θ, between the intensity gradient and the normal to the fitted spline.

There are several parameters in the hybrid Chan–Vese model. With the exception of parameter μ, which determines the elastic strength of the contour, all the others were set as suggested in [63, 64]. Equal importance is given to both phases in the image by choosing $\lambda_1 = \lambda_2 = 1$. Equation (22.11) was solved with the semi-implicit numerical scheme proposed in [63, 64], using a time step $\Delta t = 0.1\Delta x$ and setting $\Delta x = \Delta y = 1$, where $(\Delta x, \Delta y)$ represents the image grid size. This numerical scheme was iterated until the maximum distance covered by the active contour became less than $0.01\Delta x$, between two consecutive iterations.

Since parameter μ can be seen as a scale parameter, it was defined as a function of the scale of the segmented lumen, measured by the length, L, of the LI interface produced by the DP algorithm. In longitudinal sections, L is the perimeter of the region delimited by the two estimated contours (one above and the other below the medial axis). The scale parameter was set as $\mu = \rho L \times 255^2$, where $\rho = 10^{-4}$ was empirically determined as a compromise between a satisfactory level of smoothing and the fidelity to the data. The factor 255^2, also used in [63, 64], is necessary to keep unity consistence in the level set equation, since the image intensities are represented in the range $\{0, \ldots, 255\}$.

4 Image Database

The image database consists of a set of 47 longitudinal B-mode images of the CCA, acquired with a Philips HDI 5000 ultrasound system and recorded with 256 gray levels. The image set was taken from 24 different symptomatic patients, with several classes (class II to class IV), sizes, and shapes of plaque. The pixel size was normalized to 0.09 mm, a common value used in clinical practice.

All images were manually segmented by two medical experts, A and B, and twice by one of the experts (A), at two moments separated by a period of 1 year. These segmentations consisted of a manual delineation of the LI and MA interfaces of the CCA and are considered the ground truth. Hereafter, the manual segmentations of expert A and expert B and the automatic segmentation will be referred to as MA1, MA2, MB1, and A, respectively.

5 Evaluation Methodology

In [46, 47], several statistics and statistical analysis were used in the evaluation. They were based on the vertical distance between contours at every abscissa that is common to manual and automatic contours.

One statistic is D_{max}, the maximum vertical distance between corresponding contours obtained from two different detections. Another statistic is D_{mean}, the mean vertical distance between homologous contours obtained from two different detections. Other used statistics are IMT_{min}, IMT_{mean}, and IMT_{max}, the minimum, mean, and maximum IMT of each segmented intima–media region, respectively.

The inter-method (manual versus automatic), the intra-observer, and the inter-observer errors, defined as $se = sd/\sqrt{2}$ [21], were computed from the pooled mean, $\bar{x}$, and the standard deviation, sd, of the differences in IMT_{min}, IMT_{mean}, and IMT_{max} measures between two different detections. The coefficient of variation, CV, for IMT_{min}, IMT_{mean} and IMT_{max} was also estimated using the following equation:

$$CV = 100\frac{se}{\bar{x}}\% \tag{22.14}$$

The agreement between methods and between observers was assessed using box plots and Bland–Altman plots [70].

6 Results

Examples of good segmentations of the intima–media region are presented in Fig. 22.8 while Fig. 22.9 shows examples of defective segmentations. The corresponding MA1 segmentations are also shown, for comparison.

In the tested set of 47 B-mode images of the CCA, 86.2% of the MA boundaries (81 out of the 94) presented $D_{max} < 1$ mm between the automatic contour and any of the corresponding manual versions. Figure 22.10 shows the distribution of D_{max} for the subset of MA contours with $D_{max} < 1$ mm.

The statistical analysis for the LI interface was computed only for the subset of 81 intima–media complexes where the MA interface has $D_{max} < 1$ mm. For this subset of LI boundaries, 81.5% (66 out of the referred 81) presented $D_{max} < 1$ mm. The distribution of D_{max} and D_{mean} for the subset of LI interfaces with $D_{max} < 1$ mm can be found in Figs. 22.11 and 22.12.

The following statistical analysis, which evaluates the intra-observer, inter-observer, and inter-method errors and the degree of agreement between the methods, is computed only for the 66 LI boundaries with $D_{max} < 1$ mm.

Table 22.1 shows the inter-method (manual versus automatic), the intra-observer, and the inter-observer errors, as well as the coefficient of variation, CV, for IMT_{min}, IMT_{mean}, and IMT_{max}.

Figure 22.13 shows the Bland–Altman plots of the differences between the mean IMT of two given segmentations against their average. The standard deviation is represented by SD and the limits of agreement, in the form mean $\pm$ 2SD mm, are 0.03 ± 0.22 between MB1 and A, -0.07 ± 0.24 between MA2 and A, -0.10 ± 0.20 between MA2 and MB1, 0.11 ± 0.24 between MA1 and A, 0.08 ± 0.24 between MA1 and MB1, and 0.18 ± 0.24 between MA1 and MA2.

Using Matlab, on a computer equipped with an Intel Core 2 Duo processor at 2.13 GHz, the estimated median computing time is 0.0470 s for the DP algorithm, 18.5 s for the Chan–Vese algorithm, and 18.9 s for the whole LI interface segmentation procedure. The median computing time required to segment the MA interface is 28.5 s.

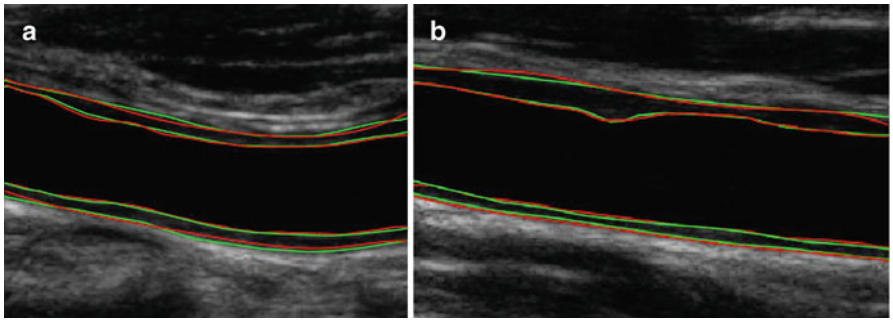

Fig. 22.8 Examples of good automatic segmentations of the intima–media region (*red curves*) along with the corresponding MA1 segmentations (*green curves*)

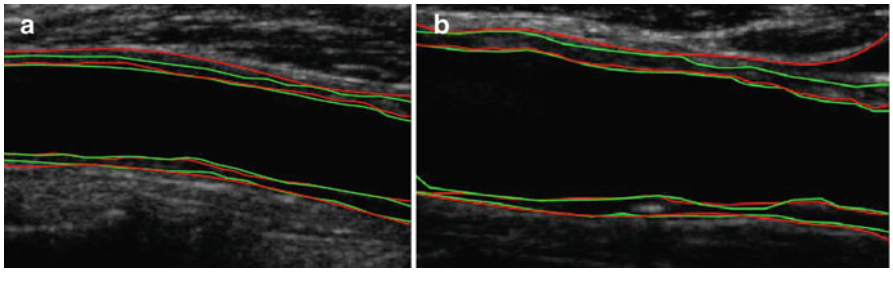

Fig. 22.9 Examples of defective automatic detections of the intima–media region (*red curves*) along with the corresponding MA1 segmentations (*green curves*)

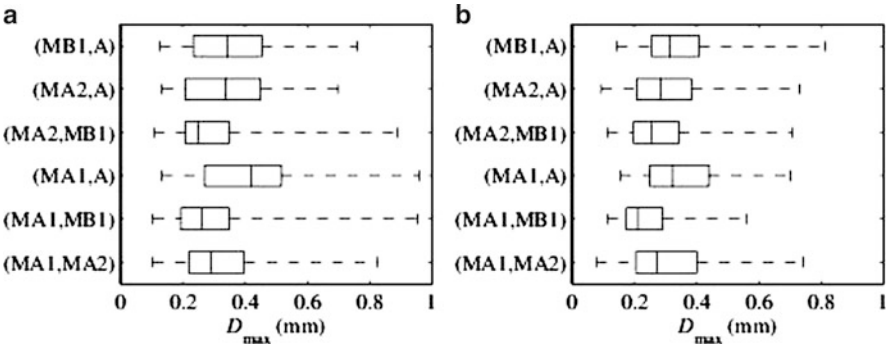

Fig. 22.10 D_{max} statistics for the MA interface detections with $D_{max} < 1$ mm: (**a**) NW boundary and (**b**) FW boundary

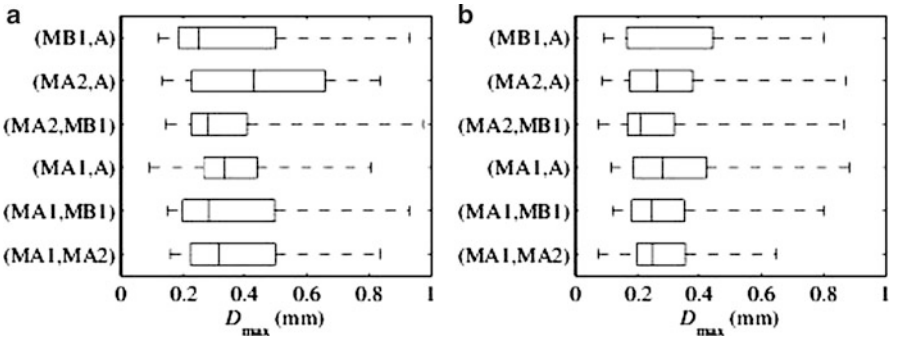

Fig. 22.11 D_{max} statistics for the LI interface detections with $D_{max} < 1$ mm: (**a**) NW boundary and (**b**) FW boundary

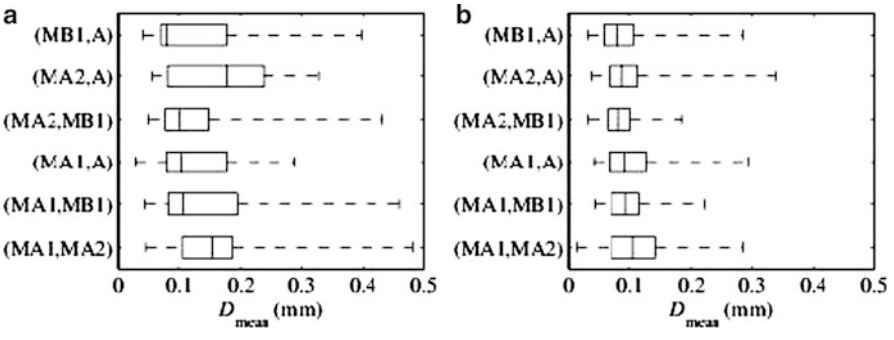

Fig. 22.12 D_{mean} statistics for the LI interface detections with $D_{max} < 1$ mm: (**a**) NW boundary and (**b**) FW boundary

Table 22.1 Comparison between manual and automatic measures of the IMT at NW and FW boundaries

		IMT_{min}		IMT_{mean}		IMT_{max}	
		se	*CV*	*se*	*CV*	*se*	*CV*
(MB1,A)	NE	0.15	21.3	0.09	8.7	0.13	9.0
	FE	0.13	25.0	0.08	7.7	0.16	10.3
(MA2,A)	NE	0.12	16.9	0.09	8.6	0.13	9.1
	FE	0.12	21.9	0.09	8.4	0.15	9.3
(MA2,MB1)	NE	0.08	10.2	0.08	7.4	0.14	9.7
	FE	0.09	15.4	0.07	6.9	0.11	6.9
(MA1,A)	NE	0.11	18.0	0.09	9.1	0.12	8.7
	FE	0.13	26.7	0.08	8.3	0.15	9.9
(MA1,MB1)	NE	0.10	15.5	0.10	10.9	0.13	10.0
	FE	0.10	18.4	0.06	6.5	0.09	6.2
(MA1,MA2)	NE	0.09	12.2	0.09	8.7	0.12	9.0
	FE	0.11	18.7	0.07	7.2	0.11	7.0

se: inter-observer, intra-observer, and inter-method error in mm; *CV*: coefficient of variation in percentage

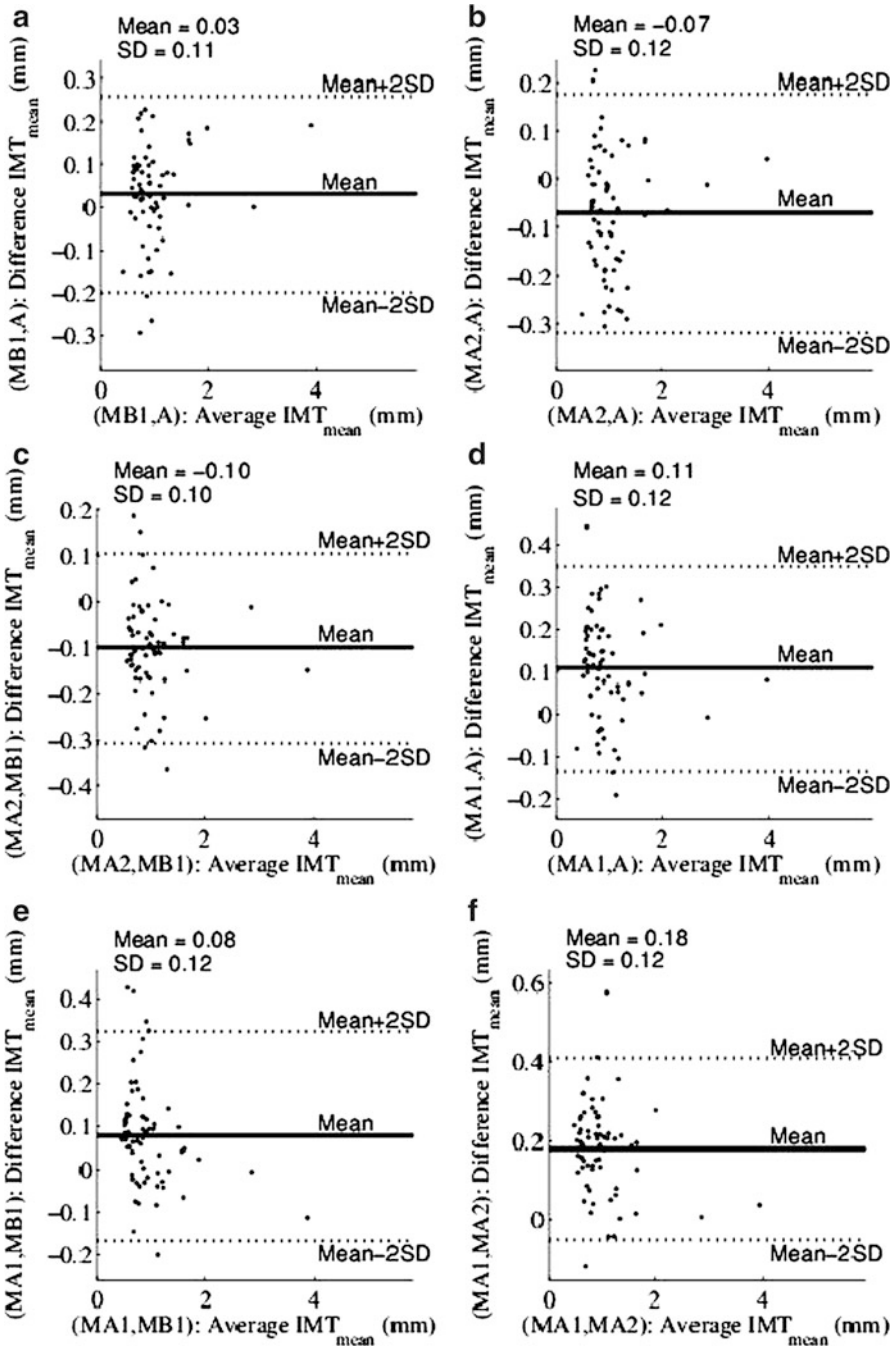

Fig. 22.13 Bland–Altman plots of the mean IMT for the automatic and the manual segmentations, where SD represents the standard deviation

7 Discussion

As shown in the previous section, the method proposed in [46, 47] is able to segment the carotid walls in B-mode images of the CCA, even in the presence of plaques of different sizes, shapes, and classes. It can segment both the far and the near walls. It requires a minimal user interaction. The automatically detected interfaces were not subjected to any manual corrections. The error dispersion observed for the automatic measures was slightly larger than for manual ones, especially for images of poor quality and for near walls. However, the statistical analysis showed promising results.

For the MA interface, the distribution of $D_{\max}$ (Fig. 22.10) leads to three main observations. First, the values of $D_{\max}$ and their variability are larger for near wall boundaries, which is in agreement with the lower visibility of these boundaries and the greater difficulty of their detection by both the medical experts and the computer. Second, $D_{\max}$ tends to be higher when one of the compared contours is automatic,

although the difference is small in general and very small for far wall boundaries. In at least 75% of the near wall cases, $D_{max} < 0.40$ mm when comparing two manual MA contours while $D_{max} < 0.51$ mm when one of the compared contours is automatic. Considering the same percentile for the far wall MA boundaries, $D_{max} < 0.40$ mm for pairs of manual contours and $D_{max} < 0.43$ mm for the other pairs. Third, some automatic detections are too far away from the manual versions. In some of these cases, the distances between different manual contours are also high, probably due to a poor quality of the images. However, $D_{max} > 1$ mm for 13.8% of the automatic detections of the MA boundaries.

For the LI interface, the detection results (Figs. 22.11 and 22.12) are also worse at the near wall than at the far wall. The larger values of D_{max} for the LI interface, when compared to the MA interface, are a consequence of the poorer visibility of the LI boundaries. This also explains why the percentage of automatic detections with $D_{max} > 1$ mm is higher for the LI interface (18.5%) than for the MA1.

The larger variability for IMT_{min} (values of *se* and *CV* in Table 22.1) than for IMT_{mean} and IMT_{max} can be explained by the poor definition of the LI boundaries at some very thin intima–media regions. The corresponding inter-method variability is higher because, when there are gaps in LI boundaries close to the MA interface, the expert can infer the correct location of the LI interface while the automatic procedure just looks for the closest compatible edges. Compared to IMT_{min}, the inter-method variability for IMT_{mean} and IMT_{max} is more important to the diagnosis of atherosclerosis and it is only slightly larger than the homologous variability of manual segmentations.

The Bland–Altman plots of the mean IMT (Fig. 22.13) for manual segmentations show a high intra-observer and inter-observer agreement, with mean differences close to zero (-0.10 mm $\leq$ mean ≤ 0.18 mm), small values of the standard deviation (0.10 mm $\leq$ SD ≤ 0.12 mm), and almost all differences within the limits of agreement ([mean $-$ 2SD; mean $+$ 2SD]). The plots indicate a good agreement between the automatic and the manual segmentations, with similar values of the mean differences (-0.07 mm $\leq$ mean ≤ 0.11 mm) and of the standard deviation (0.11 mm $\leq$ SD ≤ 0.12 mm).

8 Summary

A survey of methodologies for the segmentation of carotid ultrasound images has been presented in this chapter. A method for the segmentation of the NW and FW intima–media regions of the CCA in B-mode ultrasound images was also described. The MA interface is detected by searching for the best fit of a cubic spline to edges having features compatible with the MA boundary. Several discriminating features of the MA interface are used to reduce the attraction of the automatic contour by other edges. A smooth estimate of the LI interface is obtained using dynamic programming, smooth intensity thresholding surfaces, and geometric snakes.

The method was subjected to statistical evaluation, using a set of 47 images from 24 different symptomatic patients, including several classes (II–IV), sizes, and shapes of plaques. The results showed that the proposed approach is able to produce segmentations with accuracy comparable to the manual tracings of medical experts.

Despite the promising results, the detection of the LI interface can fail in images with very poor quality. In many cases, the plaque can only be detected with complementary information, like power-Doppler imaging or other B-scans taken from different angles. Therefore, the integration of this type of complementary data may be required to reduce the automatic detection error to levels comparable to the ones found for expert manual tracings.

Acknowledgements The authors would like to acknowledge the support of Dr. Elsa Azevedo and Dr. Rosa Santos, from Hospital de S. João, Porto, Portugal, for providing the image database and the ground truth reference contours.

References

1. World Health Organization. http://www.who.int/mediacentre/factsheets
2. Badimon JJ, Ibanez B, Cimmino G (2009) Genesis and dynamics of atherosclerotic lesions: implications for early detection. Cerebrovasc Dis 27(suppl 1):38–47
3. Walter M (2009) Interrelationships among HDL metabolism, aging, and atherosclerosis. Arterioscler Thromb Vasc Biol 29(9):1244–1250
4. Kampoli AM, Tousoulis D, Antoniades C, Siasos G, Stefanadis C (2009) Biomarkers of premature atherosclerosis. Trends Mol Med 15(7):323–332
5. O'Leary D, Polak J, Kronmal R, Manolio T, Burke G, Wolfson S Jr (1999) Carotid-artery intima and media thickness as a risk factor for myocardial infarction and stroke in older adults. N Engl J Med 340:14–22
6. Hodis H, Mack W, LaBree L, Selzer R, Liu CR, Liu CH, Azen S (1998) The role of carotid arterial intima-media thickness in predicting clinical coronary events. Ann Intern Med 128(4):262–269
7. Wendell C, Zonderman A, Metter E, Najjar S, Waldstein S (2009) Carotid intimal medial thickness predicts cognitive decline among adults without clinical vascular disease. Stroke 40:3180–3185
8. Baldassarre D, Amato M, Bondioli A, Sirtori CR, Tremoli E (2000) Carotid artery intima-media thickness measured by ultrasonography in normal clinical practice correlates well with atherosclerosis risk factors. Stroke 31:2426–2430
9. Noble JA (2010) Ultrasound image segmentation and tissue characterization. Proc Inst Mech Eng H 224(2):307–316
10. Halenka M (1999) Noninvasive measurement of early atherosclerosis by high-resolution B-mode ultrasonography. Acta Univ Palacki Olomuc Fac Med 142:7–12

11. Pignoli P, Tremoli E, Poli A, Oreste P, Paoletti R (1986) Intimal plus medial thickness of the arterial wall: a direct measurement with ultrasound imaging. Circulation 74:1399–1406
12. Rocha R (2007) Image segmentation and reconstruction of 3D surfaces from carotid ultrasound images. Ph.D. dissertation, Faculdade de Engenharia da Universidade do Porto, Porto
13. Pignoli P, Longo T (1988) Evaluation of atherosclerosis with B-mode ultrasound imaging. J Nucl Med Allied Sci 32(3):166–173
14. Touboul PJ, Prati P, Scarabin P, Adrai V, Thibout E, Ducimetiere P (1992) Use of monitoring software to improve the measurement of carotid wall thickness by B-mode imaging. J Hypertens 10(5):37–41
15. Selzer RH, Hodis HN, Kwong-Fu H, Mack WJ, Lee PL, Liu CR, Liu CH (1994) Evaluation of computerized edge tracking for quantifying intima-media thickness of the common carotid artery from B-mode ultrasound images. Atherosclerosis 111:1–11
16. Selzer RH, Mack WJ, Lee PL, Kwong-Fu H, Hodis HN (2001) Improved common carotid elasticity and intima-media thickness measurements from computer analysis of sequential ultrasound frames. Atherosclerosis 154(1):185–193
17. Stein JH, Korcarz CE, Mays ME, Douglas PS, Palta M, Zhang H, LeCaire T, Paine D, Gustafson D, Fan L (2005) A semiautomated ultrasound border detection program that facilitates clinical measurement of ultrasound carotid intima-media thickness. J Am Soc Echocardiogr 18(3):244–251
18. Liguori C, Paolillo A, Pietrosanto A (2001) An automatic measurement system for the evaluation of carotid intima-media thickness. IEEE Trans Instrum Meas 50(6):1684–1691
19. Faita F, Gemignani V, Bianchini E, Giannarelli C, Ghiadoni L, Demi M (2008) Real-time measurement system for evaluation of the carotid intima-media thickness with a robust edge operator. J Ultrasound Med 27(9):1353–1361
20. Gariepy J, Massonneau M, Levenson J, Heudes D, Simon A, Groupe de Prevention Cardio-vasculaire en Medecine du Travail (1993) Evidence for in vivo carotid and femoral wall thickness in human hypertension. J Hypertens 22(1):111–118
21. Gustavsson T, Liang Q, Wendelhag I, Wikstrand J (1994) A dynamic programming procedure for automated ultrasonic measurement of the carotid artery. In: Computers in cardiology conference, Bethesda, MD, USA, 25-28 Sept., pp 297–300
22. Wendelhag I, Liang Q, Gustavsson T, Wikstrand J (1997) A new automated computerized analyzing system simplifies readings and reduces the variability in ultrasound measurement of intima-media thickness. Stroke 28(11):2195–2200
23. Liang Q, Wendelhag I, Wikstrand J, Gustavsson T (2000) A multiscale dynamic programming procedure for boundary detection in ultrasound artery images. IEEE Trans Med Imaging 19(2):127–142
24. Rocha R, Silva J, Campilho A (2011) Dynamic programming and fuzzy classification for the automatic segmentation of the carotid in ultrasound images. In: 12th IAPR conference on machine vision and applications, pp 552–556
25. Cheng D, Schmidt-Trucksass A, Cheng K, Sandrock M, Pu Q, Burkhardt H (1999) Automatic detection of the intimal and the adventitial layers of the common carotid artery wall in ultrasound B-mode images using snakes. In: Werner B (ed) International conference on image analysis and processing, pp 452–457
26. Schmidt-Trucksass A, Cheng D, Sandrock M, Schulte-Monting J, Rauramaa R, Huonker M, Burkhardt H (2001) Computerized analysing system using the active contour in ultrasound measurement of carotid artery intima-media thickness. Clin Physiol 5:561–569
27. Cheng D, Schmidt-Trucksass A, Cheng K, Burkhardt H (2002) Using snakes to detect the intimal and adventitial layers of the common carotid artery wall in sonographic images. Comput Methods Programs Biomed 67(1):27–37
28. Loizou CP, Pattichis CS, Pantziaris M, Tyllis T, Nicolaides A (2007) Snakes based segmentation of the common carotid artery intima media. Med Biol Eng Comput 45(1):35–49
29. Loizou CP, Pattichis CS, Nicolaides A, Pantziaris M (2009) Manual and automated media and intima thickness measurements of the common carotid artery. IEEE Trans Ultrason Ferroelectr Freq Control 56(5):983–994
30. Loizou CP, Pattichis CS, Pantziaris M, Nicolaides A (2007) An integrated system for the segmentation of atherosclerotic carotid plaque. IEEE Trans Inf Technol Biomed 11(6):661–667
31. Molinari F, Delsanto S, Giustetto P, Liboni W, Badalamenti S, Suri J (2008) User-independent plaque segmentation and accurate intima-media thickness measurement of carotid artery wall using ultrasound. Artech House, Norwood, MA, pp 111–140
32. Delsanto S, Molinari F, Giustetto P, Liboni W, Badalamenti S (2005) CULEX-completely user-independent layers extraction: ultrasonic carotid artery images segmentation. Conf Proc IEEE Eng Med Biol Soc 6:6468–6471
33. Delsanto S, Molinari F, Liboni W, Giustetto P, Badalamenti S, Suri J (2006) User-independent plaque characterization and accurate IMT measurement of carotid artery wall using ultrasound. Conf Proc IEEE Eng Med Biol Soc 1:2404–2407
34. Delsanto S, Molinari F, Giustetto P, Liboni W, Badalamenti S, Suri J (2007) Characterization of a completely user-independent algorithm for carotid artery segmentation in 2D ultrasound images. IEEE Trans Instrum Meas 56(4):1265–1274
35. Molinari F, Liboni W, Giustetto P, Badalamenti S, Suri J (2009) Automatic computer-based tracings (ACT) in longitudinal 2D ultrasound images using different scanners. J Mech Med Biol 9:481–505
36. Stoitsis J, Golemati S, Kendros S, Nikita K (2008) Automated detection of the carotid artery wall in B-mode ultrasound images using active contours initialized by the Hough transform. In: Proceedings of IEEE Engineering in Medicine Biology Society, pp 3146–3149
37. Gutierrez M, Pilon P, Lage S, Kopel L, Carvalho R, Furuie S (2002) Automatic measurement of carotid diameter and wall thickness in ultrasound images. Comput Cardiol 29:359–362
38. Golemati S, Stoitsis J, Balkizas T, Nikita K (2005) Comparison of B-mode, M-mode and Hough transform methods for measurement of arterial diastolic and systolic diameters. Proc IEEE Eng Med Biol Soc 2(1):1758–1761
39. Golemati S, Stoitsis J, Sifakis E, Balkizas T, Nikita K (2007) Using the Hough transform to segment ultrasound images of longitudinal and transverse sections of the carotid artery. Ultrasound Med Biol 33(12):1918–1932
40. Rossi AC, Brands PJ, Hoeks AP (2008) Automatic recognition of the common carotid artery in longitudinal ultrasound B-mode scans. Med Image Anal 12(6):653–665
41. Rossi AC, Brands PJ, Hoeks AP (2009) Nonlinear processing in B-mode ultrasound affects carotid diameter assessment. Ultrasound Med Biol 35(5):736–747
42. Destrempes F, Meunier J, Giroux M, Soulez G, Cloutier G (2009) Segmentation in ultrasonic B-mode images of healthy carotid arteries using mixtures of Nakagami distributions and stochastic optimization. IEEE Trans Med Imaging 28(2):215–229
43. Molinari F, Zeng G, Suri J (2010) An integrated approach to computer-based automated tracing and its validation for 200 common carotid arterial wall ultrasound images: a new technique. J Ultrasound Med 29:399–418
44. Molinari F, Zeng G, Suri J (2010) Intima-media thickness: setting a standard for completely automated method of ultrasound measurement. IEEE Trans Ultrason Ferroelectr Freq Control 57(5):1112–1124

45. Molinari F, Acharya UR, Zeng G, Meiburger KM, Suri J (2011) Completely automated robust edge snapper for carotid ultrasound IMT measurement on a multi-institutional database of 300 images. Med Biol Eng Comput 49(8):935–945
46. Rocha R, Campilho A, Silva J, Azevedo E, Santos R (2010) Segmentation of the carotid intima media region in B-mode images. Image Vis Comput 28:614–625
47. Rocha R, Campilho A, Silva J, Azevedo E, Santos R (2011) Segmentation of ultrasound images of the carotid using RANSAC and cubic splines. Comput Methods Programs Biomed ?>101: 94–106
48. Molinari F, Zeng G, Suri JS (2010) Carotid wall segmentation and IMT measurement in longitudinal ultrasound images using morphological approach. In: International symposium on biomedical imaging, Rotterdam
49. Molinari F, Zeng G, Suri J (2010) Greedy technique and its validation for fusion of two segmentation paradigms leads to an accurate intima-media thickness measure in plaque carotid arterial ultrasound. J Vasc Ultrasound 34(2):63–73
50. Molinari F, Zeng G, Suri J (2011) Inter-Greedy technique for fusion of different segmentation strategies leading to high-performance carotid IMT measurement in ultrasound images. J Med Syst 35(5):905–919
51. Molinari F, Zeng G, Suri JS (2010) Inter-Greedy technique for fusion of different carotid segmentation boundaries leading to high performance IMT measurement. In: Conference of the IEEE EMBS, Buenos Aires, Argentina
52. Molinari F, Zeng G, Suri J (2010) A state of the art review on intima-media thickness (IMT) measurement and wall segmentation techniques for carotid ultrasound. Comput Methods Programs Biomed 100:201–221
53. Yu Y, Acton S (2002) Speckle reducing anisotropic diffusion. IEEE Trans Image Process 11(11):1260–1270
54. Yu Y, Acton S (2004) Edge detection in ultrasound imagery using the instantaneous coefficient of variation. IEEE Trans Image Process 13(12):1640–1655
55. Tauber C (2005) Filtrage anisotrope robuste et segmentation par b-spline snake: application aux images échographiques, Ph.D. thesis, Institut National Polytechnique de Toulouse, Toulouse
56. Black MJ, Sapiro G, Marimont DH, Heeger D (1998) Robust anisotropic diffusion. IEEE Trans Image Process 7(3):421–432
57. Rudin L, Osher S, Fatemi E (1992) Nonlinear total variation based noise removal algorithms. In: Proceedings of the 11th annual international conference of the Center for Nonlinear Studies on Experimental Mathematics: Computational Issues in Nonlinear Science, Elsevier North-Holland, Inc., pp 259–268
58. Rudin L, Osher S (1994) Total variation based image restoration with free local constraints. Proc IEEE Int Conf Image Proc 1: 31–35
59. Canny J (1986) A computational approach to edge detection. IEEE Trans Pattern Anal Mach Intell 8(6):679–698
60. Guo Z, Hall RW (1989) Parallel thinning with two-subiteration algorithms. Commun ACM 32(3):359–373
61. Burden R, Faires JD (2000) Numerical analysis. Brooks Cole, Belmont, CA
62. Forsyth DA, Ponce J (2003) Computer vision: a modern approach. Prentice Hall, Upper Saddle River, NJ
63. Chan T, Vese L (2001) Active contours without edges. IEEE Trans Image Process 10(2):266–277
64. Vese LA, Chan TF (2002) A multiphase level set framework for image segmentation using the Mumford and Shah model. Int J Comput Vis 50(3):271–293
65. Sethian JA (1999) Level set methods and fast marching methods. Cambridge University Press, Cambridge, MA
66. Osher S, Fedkiw R (2003) Level set methods and dynamic implicit surfaces. Springer, New York
67. Yanowitz SD, Bruckstein AM (1989) A new method for image segmentation. Comput Graph Image Process 46:82–95
68. Marquina A, Osher S (2000) Explicit algorithms for a new time dependent model based on level set motion for nonlinear deblurring and noise removal. SIAM J Sci Comput 22(2):387–405
69. Chum O, Matas J, Kittler J (2003) Locally optimized RANSAC. In: Lecture notes in computer science. Pattern recognition, vol 2781. Springer, Berlin, pp 236–243
70. Bland JM, Altman DG (1986) Statistical methods for assessing agreement between two methods of clinical measurement. Lancet 1(8476):307–310

Part V

Nuclear Medicine, Molecular Imaging and Therapy

Imaging of Aortic Aneurysms: What Do We Need to Know and Which Techniques Should Be Chosen?

23

Nuno V. Dias and Timothy Resch

This chapter will review the different modalities available for aortic aneurysm imaging, their background, current applications, areas of development, and the advantages and drawbacks of the different techniques in specific areas such as preoperative planning and follow-up after EVAR.

Aneurysms are localized dilatations of the arteries. They have been recognized as a medical condition requiring treatment since the old Egypt (Ebers Papyrus, 2000 BC). However, it was not until the sixteenth century that abdominal aortic aneurysms (AAA) were described by Vesalius. There are several AAA definitions. Some authors consider as an aneurysm a 50% focal increase in diameter compared to the expected normal diameter of the artery according to the imaging method used [1]. Others use the ratio between the infra- and suprarenal aorta $\geq$1.5 [2] or an absolute diameter >3 cm [3]. The comparison to the expected diameter tries to take into account the fact that, even after complete growth, the aorta of the adult continues to enlarge throughout life (about 25%) [4–7]. Besides, after the age of 25 the aorta is usually larger in men than in women, most likely due to the differences in body surface area.

Given an infinite life span, all aneurysms are destined to rupture. The natural history of aortic aneurysms is not completely known but there is a tendency for progressive expansion, with an increased risk for rupture. However, there are sporadic ruptures of small aneurysms, while other patients have large aneurysms that do not rupture [8–10]. The vast majority of aortic aneurysms are usually asymptomatic until the rupture occurs. Non-ruptured aortic aneurysms are, therefore, usually diagnosed sporadically while investigating other conditions or findings [11]. Clinical suspicion and physical examination should not be ignored [12], but have been considered to have low sensitivity and predictive values, especially in obese patients [13–16]. Imaging methods are, therefore, required to establish the diagnosis and the indication for treatment that has been essentially based on the aneurysm size [17].

The introduction of endovascular aneurysm repair (EVAR) in the late 1980s—early 1990s [18–20] and its subsequent popularization has further increased the demands on preoperative imaging. EVAR relies on the choice of a graft suitable for the patient anatomy since the possibilities of intra-operative adjustments are much more limited compared to open surgery. Good imaging of the aorta is therefore essential for the preoperative EVAR planning. The extent of the disease needs to be clearly defined, and the quality of the access arteries and the relation between the different aortic branches need also to be assessed. Moreover postoperative follow-up after EVAR relies also on imaging techniques.

This chapter will review the different imaging modalities available for imaging of aortic aneurysms in the arch, descending, thoracoabdominal, and abdominal aorta.

1 Plain X-Ray

Initially, when no other methods were available, plain X-ray was used for the diagnosis of aneurysms. However, they rely on indirect signs and identify only aneurysms with calcified walls or that produce changes in the mediastinal contour. This modality is, therefore, rarely diagnostic, and when suggestive findings appear while performing the exam for other reasons, confirmation is required by the use of other methods.

Plain X-ray does, nevertheless, have a role in the follow-up after EVAR. They provide good definition images defining the integrity of the stent-graft skeleton and development of kinks (Fig. 23.1). Component migration can also be easily identified taking advantage of the multiple markers the grafts have. Migration of the graft in relation to the aorta can indirectly be suspected by using the bony landmarks. This requires the X-ray to be obtained with a standardized protocol in order to avoid parallax [21, 22] and can also

N.V. Dias (✉) • T. Resch
Vascular Center, Skåne University Hospital, Malmö, Ruth Lundskogsgatan 10, 20502 Malmö, Sweden
e-mail: nuno.dias@med.lu.se; Timothyresch@gmail.com

L. Saba et al. (eds.), *Multi-Modality Atherosclerosis Imaging and Diagnosis*,
DOI 10.1007/978-1-4614-7425-8_23,

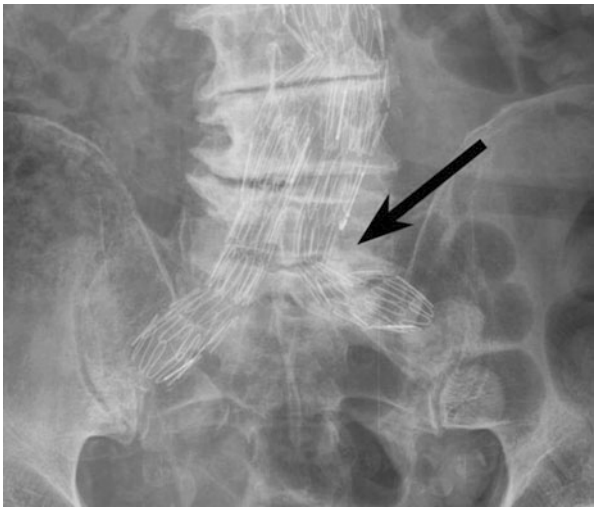

Fig. 23.1 Plain abdominal film showing kink of the left iliac limb of an aorto-biiliac EVAR

be done in a simple fashion on computer tomography (CT) whenever this is available.

2 Ultrasound

Ultrasound is a noninvasive method that does not use ionizing radiation. It is inexpensive and can be rapidly performed bedside, thus being the method usually chosen for screening programs [23]. Ultrasound can be performed transthoracically for imaging of the ascending aorta or transabdominally for imaging of AAA. Trans-esophagic ultrasound (TEE) allows the imaging of the ascending, parts of the arch, and descending aorta. Due to its higher invasiveness, TEE has been mostly applied intra-operatively during endovascular repair of type B dissections to identify the position of the guidewire in the true lumen and the flow in the true and false lumen.

The use of ultrasound in an emergency situation when suspecting a ruptured AAA, though feasible [24], provides limited information on detailed anatomy. Moreover, it has been reported to slightly underestimate aneurysm diameter when compared to computed tomography [25–27].

The diagnostic sensitivity and specificity of ultrasound to diagnose and follow aneurysms larger than 3 cm exceed 90% [28, 29]. Ultrasound is nevertheless observer dependent and there is a need for standardized protocols and education [30, 31]. These should include a clear definition of the measurement method since this seems to slightly influence the reproducibility of the method [32]. The reproducibility of the method is very high and ultrasound is therefore also useful for control after finding a dilated aorta. The frequency of the exams should increase with increasing aortic diameters [17].

Ultrasound has also been widely used for the follow-up after EVAR of AAA. This may be based on diameter measurement with CT whenever expansion is suspected [33], but some authors also suggest the combined use with duplex to identify endoleaks, which may be further potentiated by the use of contrast enhancement [34]. Ultrasound has a high temporal resolution which has been utilized in analyzing aneurysm pulsatility, especially in the follow-up after EVAR. The clinical value of the pulsatile wall motion is nevertheless limited [35, 36].

The latest developments in ultrasound that may have the potential of giving some advantages in aneurysm imaging include the use of targeted contrast agents against important pathogenic elements such as P-selection. Moreover, 3D ultrasound imaging seems to be possible with rapid acquisition and may allow follow-up of the AAA after treatment. This has the potential of increasing the anatomic detail obtained in terms of special resolution in the preoperative assessment of AAA. The value of the application of this technology remains to be demonstrated.

3 Intravascular Ultrasound

Intravascular ultrasound (IVUS) is an invasive application of ultrasound where a high-frequency probe is mounted on a catheter introduced into the vasculature. It has been widely used for occlusive disease especially in the coronaries where different modalities such has virtual histology possibilities are being developed [37, 38].

Automated vessel analysis has been developed to study the sealing zones in preoperative aortic aneurysm imaging [39]. IVUS has not gained the same popularity for aneurysm imaging mostly due to its invasiveness and the uncertainty in length measurements in patients with tortuous anatomy since the IVUS probe may follow a different path compared to grafts which may condition the length measures. IVUS has been used with some success during EVAR procedures [40], but the advantages seem modest when modern angiographic equipments are used. Some authors have found IVUS to be a good complement during endovascular repair of type B dissections that extend into the abdominal aorta, since it may assist in the assessment of the guidewire position in the true or false lumen [41].

4 Computer Tomography

CT is based on the use of a series of 2D X-ray data obtained around a single axis of rotation that are computed into 3D imaging through digital geometrical processing. The first CT scans provided single axial reconstructions with relatively poor definition. The development of the technique

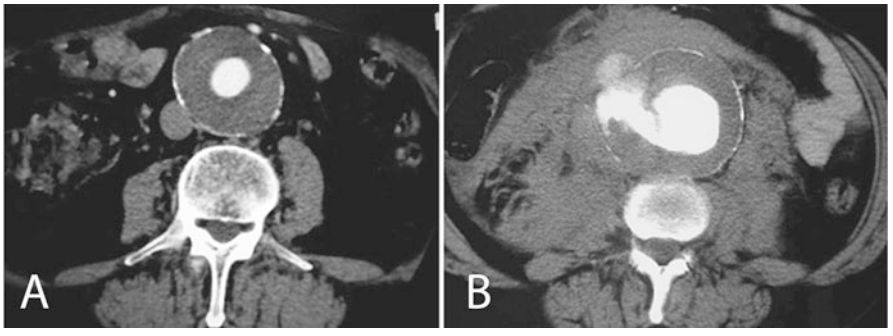

Fig. 23.2 Axial contrast-enhanced CT-scans showing non-ruptured (**a**) and ruptured (**b**) abdominal aortic aneurysms

was fast and multidetector-row CT has not only increased the resolution of the technique but also made the exam faster [42]. This allows the performance of rapid CT scans even in the acute setting for the diagnosis of aneurysm rupture while the patients are still hemodynamically stable, which usually is the case when they are admitted to the hospital (Fig. 23.2) [43].

CT of the aorta includes a scan performed with intravenous iodine contrast enhancement. This is obtained by the peripheral venous injection followed by a saline bolus injection. The contrast dose is adjusted according to patient weight. The timing of the scan adjusted by the placement of a region of interest (ROI) in the ascending or aortic arch when the entire aorta is being studied and at the level of the diaphragm if only the abdominal aorta is of interest. Consecutive single scans at the level of the ROI are done and as soon as the Hounsfield unit (HU) threshold is surpassed the scan is started. Patients with renal insufficiency are difficult to exam with intravenous contrast due to the risk of contrast induced nephropathy. This can be dealt with using intra-arterial injection through a transfemoral catheter. thus reducing the contrast dose. Low-dose CT protocols with reduced contrast dose have been used in other areas with good diagnostic result [44], but the applicability in aortic aneurysm imaging is still unclear.

4.1 Preoperative Imaging

Preoperative CT is useful for the assessment of the aneurysm size even in patients where ultrasound imaging is impossible. Diameter measurements can be done without contrast. However, a complete preoperative assessment of the aortic anatomy by the CT should include scans with and without contrast and have thin axial reconstruction ($\leq$1 mm). The scan should be in the arterial phase and extend from the skull base to the lesser femoral trochanter. This will allow mapping of the supraaortic circulation in cases of thoracic aneurysms as well as the access vessels. The assessment of the supraaortic circulation is of importance since it allows evaluation of anatomic variations such as separate origin of the left vertebral artery or aberrant right subclavian artery. Moreover it depicts the completeness of the circle of Willis and thereby assists in the decision on the need for revascularization of the left subclavian artery. CTs done for dissections or aneurysms involving the arch and the ascending aorta are preferably done with EKG-gated technique in order to avoid movement artifacts. Furthermore the EKG-gated CT offers the possibility of triple rule-out diagnostic [45]. Retrospective EKG-gated CT scanning allows for dynamic imaging of the aorta, while maintaining the radiation dose comparable to conventional CT. Dynamic CT can also identify pulsatile changes in the thoracic and abdominal aorta during the heart cycle [46]. The significance of these findings and their implications for stentgraft oversizing during planning as well any consequences for the long-term durability are still uncertain. Other applications of CT imaging are computational post-processing for the refinement of the rupture risk using finite element analysis [47].

4.2 Postoperative Imaging

EVAR relies on the remote insertion of the stent-graft without disrupting the physical integrity of the aneurysm wall. Aneurysm size can, therefore, be used as an indicator of the effectiveness of EVAR in a similar way as it was for the preoperative evaluation of the rupture risk. Aneurysms that become well excluded after EVAR are expected to decrease in size (Fig. 23.3). Consequently, imaging methods have been used for the periodical follow-up after EVAR, evaluating aneurysm size, stent-graft integrity, and/or migration and endoleak status. The use of spiral CT scans for the postoperative follow-up after aortic aneurysm repair was very frequent during the first 15 years after the introduction of EVAR. Currently there has been a trend for changing follow-up after standard EVAR of AAA replacing CTA with ultrasound. However, CT is still the cornerstone for thoracic and more complex EVAR.

Follow-up CTA scans are performed with nonionic contrast medium enhancement as described above for the preoperative work-up. In addition, the scan is repeated 60 s later

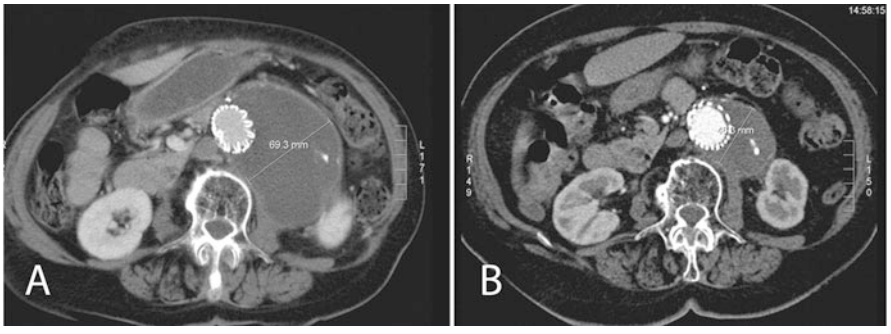

Fig. 23.3 Axial contrast-enhanced CT scans showing aneurysm shrinkage between the 1-year postoperative scan (**a**) and the 2 year's one (**b**)

to obtain a delayed scan. The inclusion of a delayed scan to obtain a late arterial phase has the potential of identifying type II endoleaks that could otherwise remain unnoticed [48]. Even during follow-up, low-dose CT protocols can be used to reduce radiation in the repeated exams, without affecting the diagnostic outcome [49].

The increase of the number of detectors up to 320 rows has increased the amount of information and the time required to obtain it. The other significant development in CT scanners in recent years has been the introduction of dual energy CT also called dual source. This consists of two X-ray tubes that simultaneously transmit at different energy levels (usually 80 and 140 kV). This will give different attenuations at the same time and has the potential to reduce the radiation of the exams during EVAR follow-up since it permits the production of virtual non-enhanced images by subtraction of the contrast medium which will allow the identification of endoleaks without the need of a non-enhanced scan [50–54].

4.3 Data Post-processing

As mentioned above, the introduction of multidetector CT scanning increased the definition of the imaging and allowed for 3D imaging which increased the post-processing possibilities. Axial, coronal, and sagittal reconstructions are currently a standard of CT imaging. The transfer of the DICOM raw images to workstations specifically dedicated to vascular imaging post-processing increases the possibilities of the imaging analysis vastly. This is important when planning for EVAR, especially when more advanced prostheses such as fenestrated and branched endografts are needed. It is important to emphasize the need for good quality raw imaging to be able to perform good post-processing. This means high-resolution imaging with thin axial reconstruction of less than 1 mm with good arterial phase enhancement.

Data post-processing allows the reconstruction of multiple multiplanar reconstructions (MPRs) as well as maximum intensity projections (MIPs) with free rotational ability at different angles allowing detailed assessment of different parts of the anatomy such as aortic branch takeoff. These may be useful to plan for the EVAR procedure including the best projections to visualize the different vessels [55]. Another tool of particular importance for EVAR planning is the center line of flow analysis (CLF, Fig. 23.4). This involves the manual or semiautomatic creation of a CLF and thereafter length measurements along that line with evaluation of orthogonal reconstructions along the CLF. Length measurements along CLF are helpful in determining the length of standard grafts since the aorto-iliac segment tends to elongate and become more tortuous upon aneurysm development which makes it difficult to measure lengths in the traditional axial, coronal, or sagittal reconstructions [56]. Moreover, when planning more complex endografts CLF lengths are also helpful in assessing the distance between the different aortic branches that are included in endovascular repair (Fig. 23.4c). The position of the target vessel fenestrations on the endograft also needs to be planned according to their position on the circumference (clock position) and the orthogonal reconstructions can be very useful in very tortuous cases (Fig. 23.4d, e). All CLF measurements are dependent on the accuracy of the graft following the CLF and this is not always the case, especially in cases of high tortuosity. For this reason, one needs to check the CLF path and manually adjust it whenever needed before performing the measurements.

Post-processing is also very useful in the follow-up after EVAR. Applications such as the creation of multiple MIPs with different window settings and projections will allow assessment of stent-graft integrity and possible dislocation. Fly-through applications that allow virtual angioscopy assist in the assessment of the different branches and possible compression or kinking of stents or stent-grafts [57] CLF is useful even in the assessment of stent-graft migration especially when the endograft is located in a tortuous region such as the distal aortic arch [58]. The use of workstations with the possibility of simultaneous visualization of different exams is very useful during the follow-up after EVAR since it allows the synchronization of images at the same level and in that way evaluation of any changes during follow-up including the evolution of the aneurysm size. This synchronization is also very useful using scans with and without contrast to

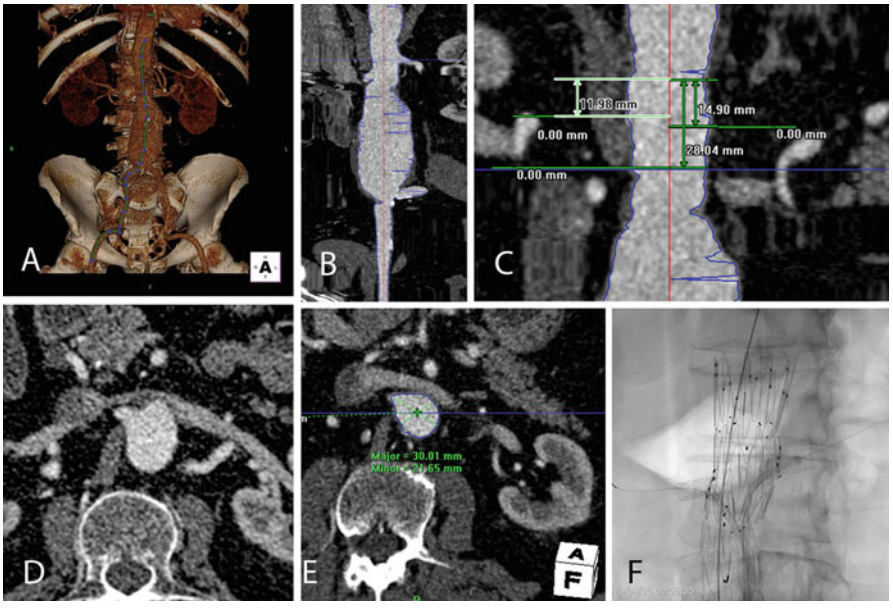

Fig. 23.4 (**a**) Semiautomated creation of a central line of flow (CLF). (**b**) Stretch vessel view allowing for length measurements along the CLF. (**c**) Measurement of the distances along the CLF between the different visceral vessels for the planning of fenestrated stent-graft. (**d**) Axial slice showing the origin of the right renal artery. The aortic lumen is oval in its appearance due to the postero-anterior angulation of the segment making it difficult to decide the clock position of the vessel origin. (**e**) Correspondent right renal artery origin in orthogonal reconstruction. (**f**) Intra-operative image with balloon-expandable stent-grafts deployed in the renal arteries through the respective fenestrations

distinguish between calcifications and endoleaks. Moreover, workstations also provide different methods of measuring the aneurysm size, such as axial diameter, orthogonal diameter, and volume of the aneurysm size. These methods seem to have increasing reliability in the assessment of the evolution of the aneurysm size during follow-up [27, 59, 60], but also require increasing amount of post-processing. A good strategy is therefore to successively take advantage of these different methods in doubtful cases, but using axial diameter measurements in the vast majority. These should be done perpendicular to the longest diameter at the chosen level in order to avoid overestimation caused by tortuosity.

5 Magnetic Resonance Imaging

Magnetic resonance imaging (MRI) is another advanced imaging technique. It is possible to use it in a similar way as CT scanning in order to obtain complete imaging of the aorta. It has, nevertheless, not gained the same popularity as CT due to its cost, lower availability, and longer time required for scanning.

MRI is based on the use of magnetic fields created by the imaging equipment that thereafter uses the different relaxation times of the different tissues finally converting them to images. Gadolinium contrast agents can be used to shorten the T1 (longitudinal) relaxation time of and thereby enhance the contrast and shorten the examination time [61]. This is nowadays applied for dynamic MR angiography which is the most common method for the evaluation of the aortic anatomy [62, 63].

The most common presentation of MR angiography images is subtracted MIP. These images are similar to the ones obtained during conventional angiography depicting only the lumen. The raw images should therefore be available and analyzed in order to be able to measure the aneurysm diameter, identify possible dissection, and assess any other changes surrounding the aneurysm such as inflammatory reactions. MR angiography imaging can be post-processed in a way similar to CT in order to obtain an identical morphological evaluation of the aorta and thereby perform EVAR planning [64]. MRI has also been shown to have high diagnostic accuracy in the follow-up after EVER, especially for the identification of type II endoleaks [65–67]. Moreover, the value of the method seems to be further increased by the use of blood-pool contrast agents [68, 69].

MRI used to be the method of choice for patients with reduced renal function. However, reports on the development of nephrogenic systemic fibrosis (NSF) in patients with renal insufficiency who have received Gadolinium-based contrast medium has made the use more restrictive in this category of patients [70]. The risks seem nevertheless to be small and should be weighed against the need for the examination [71]. The preliminary results of unenhanced MRI in EVAR planning seem promising [72] and future technical refinements may make this a valid alternative for patients with renal

insufficiency. One final remark should be done on the signal void caused by stainless steel endografts or ferromagnetic markers that make MRI inappropriate or difficult for EVAR follow-up on these cases [73].

Another interesting area of MRI is the use of ultrasmall superparamagnetic iron oxide contrast agents (USPIOs). After injection, these particles are slowly taken up by macrophages, which may reflect the biological activity in the aneurysm wall [74–77]. Dynamic and cine MRI have shown promising results similar to the ones obtained with CT imaging [46, 78–81]. These applications together with the possibility of performing EVAR with MRI may be the upcoming areas of development of the technique [82, 83].

6 Digital Subtraction Angiography

Angiography depicts an outline of the arterial lumen only and has, therefore, low capacity in determining the aneurysm diameter, especially when the aneurysm is partially thrombosed or when the wall is not calcified. For the same reasons, digital subtraction angiography (DSA) is inappropriate for evaluating sealing zones. In the past, angiography was used to complete the diagnosis of concomitant occlusive disease in the access vessels and aortic branches, to define anatomic variations or anomalies before open surgical repair, or to assist in length measurement before EVAR. However, this has been replaced by the use of volume rendering software for CT and MR [84, 85] which are noninvasive alternatives and can provide accurate measurements. Angiography is therefore currently used primarily to guide interventions. Hybrid rooms are the ideal environment for the performance of EVAR since it provides an operating room associated with high-quality angiographic imaging. However, current C-arms are feasible alternatives [86].

DSA is usually performed with iodine intra-arterial contrast agents that provide high-quality images but have the drawback of nephrotoxicity. Current angiographic equipments allow adjustments to retain the imaging quality while decreasing the amount and concentration of contrast used [87]. Moreover, carbon dioxide is a good alternative for abdominal EVAR [88, 89], but may be difficult to use for the imaging of dorsally oriented arterial takeoff due to the tendency of the gas to float in the blood. On the contrary it is excellent for arteries with ventral origins, but may should not be used above the diaphragm (Fig. 23.5).

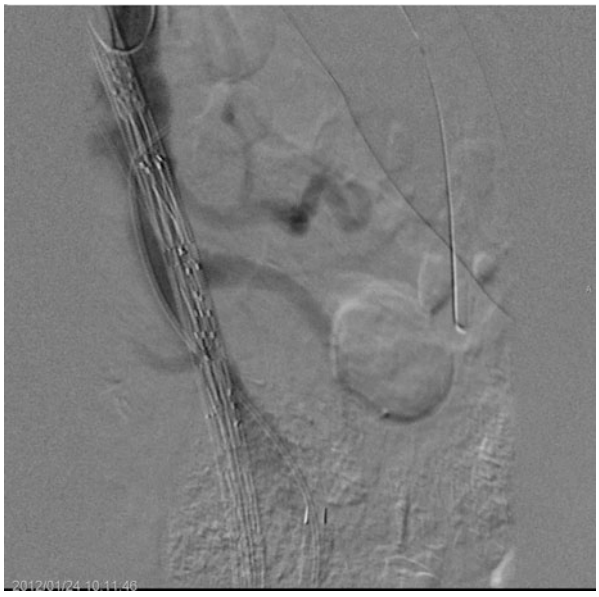

Fig. 23.5 Digital subtraction angiography during the placement of a triple fenestrated stent-graft. Carbon dioxide is used as contrast agent showing the superior mesenteric artery origin

7 Rotation Angiography, Cone Beam CT, and Fusion

Modern angiographic suits with flat digital panels have given the possibility of doing runs to obtain high-definition volume-rendering data. One of the possibilities is to obtain digitally subtracted rotational angiographies that may even be used as overlay reference into the fluoroscopy. This has limited application in aneurysm imaging since it conveys only an outline of the contrast-filled. However, it can be useful for intra-procedural orientation and characterization as well as during reinterventions for intraluminal endoleak embolization.

The other alternative is to use the flat panel as a CT detector to perform a cone beam CT (CB-CT). This has a high spatial resolution but the volume is limited to the length of the detector and centered in the iso-center. Good quality imaging can be obtained with low dose of iodine contrast. Preliminary results from the application of this technique seem promising compared to the preoperative anatomic evaluation [90–92] and in the assessment of the intra-operative final result (Fig. 23.6) [93]. CB-CT has limited use in the routine follow-up due to its invasive nature with an intra-arterial injection. However there is high potential in the assessment of the reintervention result especially when the location of the failure is difficult to visualize on standard DSA. In the current setup, CB-CT will not be able to totally replace the standard preoperative CTA or MRA since these are able to depict the entire aorta and access vessels while CB-CT is limited to the cone area as mentioned above.

Another technical advancement that seems to have great potential is the ability to obtain fusion of the preoperative CTA data with the fluoroscopy. This is achieved by matching the bony references of the preoperative CTA with a non-contrast-enhanced CB-CT. In this way the software will

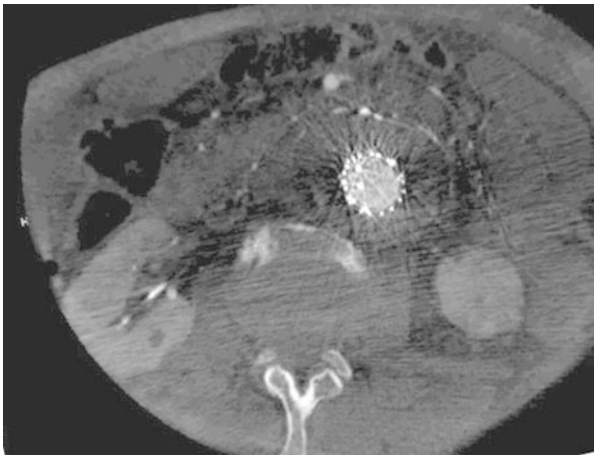

Fig. 23.6 Axial reconstruction of contrast-enhanced cone beam CT as intra-operative control after EVAR deployment

be able to use the preoperative CTA as an overlay reference in the fluoroscopy screen. There were some theoretical concerns on the potential deviation of the anatomy by the insertion of stiff large bore introducer in the aorta which could be misleading. The first results of the application of this technique in branched and fenestrated EVAR are nevertheless very promising [94]. Other applications are being developed with similar results [95].

8 Integrated Positron Emission Tomography and Computed Tomography

Aortic imaging with positron emission tomography (PET) uses fluorine 18-fluorodesoxyglucose (FDG) that is taken up by metabolically active cells such as activated leukocytes in the arterial wall [96, 97]. FDG disintegrates resulting in positron and gamma ray emission which are then detected by the cameras. Multidetector CT scanners can currently be used in integrated equipments with PET. This provides high-quality fusion imaging with the detailed morphological imaging of the CT and the functional information of the PET. The results of positron emission tomography and computed tomography (PET-CT) in pre- and postoperative imaging of aortic aneurysms have been contradictory and further studies are needed to establish the value of the technique [98–105].

9 Conclusion

Current imaging of aortic aneurysm requires multiple modalities. Ultrasound has an established role when diameter measurements of AAA are the objective. Contrast-enhanced CT scanning with post-processing on dedicated vascular workstations is essential in the planning and follow-up of EVAR, especially for more complex aneurysms. Refinement of intraoperative imaging, alongside with preoperative functional imaging focusing on prediction of rupture risk, are the areas where the greatest developments are expected in the future.

References

1. Johnston KW, Rutherford RB, Tilson MD, Shah DM, Hollier L, Stanley JC (1991) Suggested standards for reporting on arterial aneurysms. Subcommittee on Reporting Standards for Arterial Aneurysms, Ad Hoc Committee on Reporting Standards, Society for Vascular Surgery and North American Chapter, International Society for Cardiovascular Surgery. J Vasc Surg 13(3):452–458
2. Sterpetti AV, Schultz RD, Feldhaus RJ, Cheng SE, Peetz DJ Jr (1987) Factors influencing enlargement rate of small abdominal aortic aneurysms. J Surg Res 43(3):211–219
3. McGregor JC, Pollock JG, Anton HC (1975) The value of ultrasonography in the diagnosis of abdominal aortic aneurysm. Scott Med J 20(3):133–137
4. Sonesson B, Hansen F, Stale H, Lanne T (1993) Compliance and diameter in the human abdominal aorta – the influence of age and sex. Eur J Vasc Surg 7(6):690–697
5. Sonesson B, Lanne T, Hansen F, Sandgren T (1994) Infrarenal aortic diameter in the healthy person. Eur J Vasc Surg 8(1):89–95
6. Lederle FA, Johnson GR, Wilson SE, Gordon IL, Chute EP, Littooy FN et al (1997) Relationship of age, gender, race, and body size to infrarenal aortic diameter. The Aneurysm Detection and Management (ADAM) Veterans Affairs Cooperative Study Investigators. J Vasc Surg 26(4):595–601
7. Pearce WH, Slaughter MS, LeMaire S, Salyapongse AN, Feinglass J, McCarthy WJ et al (1993) Aortic diameter as a function of age, gender, and body surface area. Surgery 114(4):691–697
8. Bergqvist D, Bengtsson H (1990) Risk factors for rupture of abdominal aortic aneurysm. Clinical review. Acta Chir Scand 156(1):63–68
9. Bickerstaff LK, Hollier LH, Van Peenen HJ, Melton LJ 3rd, Pairolero PC, Cherry KJ (1984) Abdominal aortic aneurysms: the changing natural history. J Vasc Surg 1(1):6–12
10. Nicholls SC, Gardner JB, Meissner MH, Johansen HK (1998) Rupture in small abdominal aortic aneurysms. J Vasc Surg 28(5):884–888
11. Karkos CD, Mukhopadhyay U, Papakostas I, Ghosh J, Thomson GJ, Hughes R (2000) Abdominal aortic aneurysm: the role of clinical examination and opportunistic detection. Eur J Vasc Endovasc Surg 19(3):299–303
12. Venkatasubramaniam AK, Mehta T, Chetter IC, Bryce J, Renwick P, Johnson B et al (2004) The value of abdominal examination in the diagnosis of abdominal aortic aneurysm. Eur J Vasc Endovasc Surg 27(1):56–60
13. Fink HA, Lederle FA, Roth CS, Bowles CA, Nelson DB, Haas MA (2000) The accuracy of physical examination to detect abdominal aortic aneurysm. Arch Intern Med 160(6):833–836
14. Lederle FA, Simel DL (1999) The rational clinical examination. Does this patient have abdominal aortic aneurysm? JAMA 281(1):77–82
15. Beede SD, Ballard DJ, James EM, Ilstrup DM, Hallet JW Jr (1990) Positive predictive value of clinical suspicion of abdominal aortic aneurysm. Implications for efficient use of abdominal ultrasonography. Arch Intern Med 150(3):549–551
16. Chervu A, Clagett GP, Valentine RJ, Myers SI, Rossi PJ (1995) Role of physical examination in detection of abdominal aortic aneurysms. Surgery 117(4):454–457

17. Moll FL, Powell JT, Fraedrich G, Verzini F, Haulon S, Waltham M et al (2011) Management of abdominal aortic aneurysms clinical practice guidelines of the European Society for Vascular Surgery. Eur J Vasc Endovasc Surg 41(Suppl 1):S1–S58
18. Volodos NL, Karpovich IP, Shekhanin VE, Troian VI, Iakovenko LF (1988) A case of distant transfemoral endoprosthesis of the thoracic artery using a self-fixing synthetic prosthesis in traumatic aneurysm. Grudn Khir Nov-Dec(6):84–86
19. Volodos NL, Karpovich IP, Troyan VI, Kalashnikova Yu V, Shekhanin VE, Ternyuk NE et al (1991) Clinical experience of the use of self-fixing synthetic prostheses for remote endoprosthetics of the thoracic and the abdominal aorta and iliac arteries through the femoral artery and as intraoperative endoprosthesis for aorta reconstruction. Vasa Suppl 33:93–95
20. Parodi JC, Palmaz JC, Barone HD (1991) Transfemoral intraluminal graft implantation for abdominal aortic aneurysms. Ann Vasc Surg 5(6):491–499
21. Hodgson R, McWilliams RG, Simpson A, Gould DA, Brennan JA, Gilling-Smith GL et al (2003) Migration versus apparent migration: importance of errors due to positioning variation in plain radiographic follow-up of aortic stent-grafts. J Endovasc Ther 10(5):902–910
22. Murphy M, Hodgson R, Harris PL, McWilliams RG, Hartley DE, Lawrence-Brown MM (2003) Plain radiographic surveillance of abdominal aortic stent-grafts: the Liverpool/Perth protocol. J Endovasc Ther 10(5):911–912
23. Wilmink AB, Forshaw M, Quick CR, Hubbard CS, Day NE (2002) Accuracy of serial screening for abdominal aortic aneurysms by ultrasound. J Med Screen 9(3):125–127
24. Tayal VS, Graf CD, Gibbs MA (2003) Prospective study of accuracy and outcome of emergency ultrasound for abdominal aortic aneurysm over two years. Acad Emerg Med 10(8):867–871
25. Sprouse I, Richard L, Meier I, George H, LeSar CJ, DeMasi RJ, Sood J, Parent FN et al (2003) Comparison of abdominal aortic aneurysm diameter measurements obtained with ultrasound and computed tomography: is there a difference? J Vasc Surg 38(3):466–471
26. Lederle FA, Wilson SE, Johnson GR, Reinke DB, Littooy FN, Acher CW et al (1995) Variability in measurement of abdominal aortic aneurysms. Abdominal Aortic Aneurysm Detection and Management Veterans Administration Cooperative Study Group. J Vasc Surg 21(6):945–952
27. Manning BJ, Kristmundsson T, Sonesson B, Resch T (2009) Abdominal aortic aneurysm diameter: a comparison of ultrasound measurements with those from standard and three-dimensional computed tomography reconstruction. J Vasc Surg 50(2):263–268
28. Lindholt JS, Vammen S, Juul S, Henneberg EW, Fasting H (1999) The validity of ultrasonographic scanning as screening method for abdominal aortic aneurysm. Eur J Vasc Endovasc Surg 17(6):472–475
29. Wilmink AB, Hubbard CS, Quick CR (1997) Quality of the measurement of the infrarenal aortic diameter by ultrasound. J Med Screen 4(1):49–53
30. Beales L, Wolstenhulme S, Evans JA, West R, Scott DJ (2011) Reproducibility of ultrasound measurement of the abdominal aorta. Br J Surg 98(11):1517–1525
31. Grondal N, Bramsen MB, Thomsen MD, Rasmussen CB, Lindholt JS (2012) The cardiac cycle is a major contributor to variability in size measurements of abdominal aortic aneurysms by ultrasound. Eur J Vasc Endovasc Surg 43(1):30–33
32. Hartshorne TC, McCollum CN, Earnshaw JJ, Morris J, Nasim A (2011) Ultrasound measurement of aortic diameter in a national screening programme. Eur J Vasc Endovasc Surg 42(2):195–199
33. Dias NV, Riva L, Ivancev K, Resch T, Sonesson B, Malina M (2009) Is there a benefit of frequent CT follow-up after EVAR? Eur J Vasc Endovasc Surg 37(4):425–430
34. Mirza TA, Karthikesalingam A, Jackson D, Walsh SR, Holt PJ, Hayes PD et al (2010) Duplex ultrasound and contrast-enhanced ultrasound versus computed tomography for the detection of endoleak after EVAR: systematic review and bivariate meta-analysis. Eur J Vasc Endovasc Surg 39(4):418–428
35. Lindblad B, Dias N, Malina M, Ivancev K, Resch T, Hansen F et al (2004) Pulsatile wall motion (PWM) measurements after endovascular abdominal aortic aneurysm exclusion are not useful in the classification of endoleak. Eur J Vasc Endovasc Surg 28(6):623–628
36. Malina M, Länne T, Ivancev K, Lindblad B, Brunkwall J (1998) Reduced pulsatile wall motion of abdominal aortic aneurysms after endovascular repair. J Vasc Surg 27(4):624–631
37. Kaneda H, Ako J, Terashima M (2010) Intravascular ultrasound imaging for assessing regression and progression in coronary artery disease. Am J Cardiol 106(12):1735–1746
38. Garcia-Garcia HM, Gogas BD, Serruys PW, Bruining N (2011) IVUS-based imaging modalities for tissue characterization: similarities and differences. Int J Cardiovasc Imaging 27(2): 215–224
39. van Essen JA, Gussenhoven EJ, Blankensteijn JD, Honkoop J, van Dijk LC, van Sambeek MR et al (2000) Three-dimensional intravascular ultrasound assessment of abdominal aortic aneurysm necks. J Endovasc Ther 7(5):380–388
40. Pearce BJ, Jordan WD Jr (2009) Using IVUS during EVAR and TEVAR: improving patient outcomes. Semin Vasc Surg 22(3):172–180
41. Koschyk DH, Nienaber CA, Knap M, Hofmann T, Kodolitsch YV, Skriabina V et al (2005) How to guide stent-graft implantation in type B aortic dissection? Comparison of angiography, transesophageal echocardiography, and intravascular ultrasound. Circulation 112(9 Suppl):I260–I264
42. Rubin GD (2003) MDCT imaging of the aorta and peripheral vessels. Eur J Radiol 45(Suppl 1):S42–S49
43. Lloyd GM, Bown MJ, Norwood MG, Deb R, Fishwick G, Bell PR et al (2004) Feasibility of preoperative computer tomography in patients with ruptured abdominal aortic aneurysm: a time-to-death study in patients without operation. J Vasc Surg 39(4):788–791
44. Kristiansson M, Holmquist F, Nyman U (2010) Ultralow contrast medium doses at CT to diagnose pulmonary embolism in patients with moderate to severe renal impairment: a feasibility study. Eur Radiol 20(6):1321–1330
45. Shapiro MD (2009) Is the “triple rule-out” study an appropriate indication for cardiovascular CT? J Cardiovasc Comput Tomogr 3(2):100–103
46. van Keulen JW, van Prehn J, Prokop M, Moll FL, van Herwaarden JA (2009) Dynamics of the aorta before and after endovascular aneurysm repair: a systematic review. Eur J Vasc Endovasc Surg 38(5):586–596
47. Georgakarakos E, Ioannou CV, Papaharilaou Y, Kostas T, Katsamouris AN (2011) Computational evaluation of aortic aneurysm rupture risk: what have we learned so far? J Endovasc Ther 18(2):214–225
48. Rozenblit AM, Patlas M, Rosenbaum AT, Okhi T, Veith FJ, Laks MP et al (2003) Detection of endoleaks after endovascular repair of abdominal aortic aneurysm: value of unenhanced and delayed helical CT acquisitions. Radiology 227(2):426–433
49. Iezzi R, Cotroneo AR, Giammarino A, Spigonardo F, Storto ML (2011) Low-dose multidetector-row CT-angiography of abdominal aortic aneurysm after endovascular repair. Eur J Radiol 79(1):21–28
50. Ascenti G, Mazziotti S, Lamberto S, Bottari A, Caloggero S, Racchiusa S et al (2011) Dual-energy CT for detection of endoleaks after endovascular abdominal aneurysm repair: usefulness of colored iodine overlay. AJR Am J Roentgenol 196(6):1408–1414

51. Chandarana H, Godoy MC, Vlahos I, Graser A, Babb J, Leidecker C et al (2008) Abdominal aorta: evaluation with dual-source dual-energy multidetector CT after endovascular repair of aneurysms – initial observations. Radiology 249(2):692–700
52. Numburi UD, Schoenhagen P, Flamm SD, Greenberg RK, Primak AN, Saba OI et al (2010) Feasibility of dual-energy CT in the arterial phase: imaging after endovascular aortic repair. AJR Am J Roentgenol 195(2):486–493
53. Sommer WH, Graser A, Becker CR, Clevert DA, Reiser MF, Nikolaou K et al (2010) Image quality of virtual noncontrast images derived from dual-energy CT angiography after endovascular aneurysm repair. J Vasc Interv Radiol 21(3):315–321
54. Stolzmann P, Frauenfelder T, Pfammatter T, Peter N, Scheffel H, Lachat M et al (2008) Endoleaks after endovascular abdominal aortic aneurysm repair: detection with dual-energy dual-source CT. Radiology 249(2):682–691
55. van Keulen JW, Moll FL, van Herwaarden JA (2010) Tips and techniques for optimal stent graft placement in angulated aneurysm necks. J Vasc Surg 52(4):1081–1086
56. Higashiura W, Kichikawa K, Sakaguchi S, Tabayashi N, Taniguchi S, Uchida H (2009) Accuracy of centerline of flow measurement for sizing of the Zenith AAA endovascular graft and predictive factor for risk of inadequate sizing. Cardiovasc Intervent Radiol 32(3):441–448
57. Louis N, Bruguiere E, Kobeiter H, Desgranges P, Allaire E, Kirsch M et al (2010) Virtual angioscopy and 3D navigation: a new technique for analysis of the aortic arch after vascular surgery. Eur J Vasc Endovasc Surg 40(3):340–347
58. O'Neill S, Greenberg RK, Resch T, Bathurst S, Fleming D, Kashyap V et al (2006) An evaluation of centerline of flow measurement techniques to assess migration after thoracic endovascular aneurysm repair. J Vasc Surg 43(6):1103–1110
59. Lee JT, Aziz IN, Haukoos JS, Donayre CE, Walot I, Kopchok GE et al (2003) Volume regression of abdominal aortic aneurysms and its relation to successful endoluminal exclusion. J Vasc Surg 38(6):1254–1263
60. Wever JJ, Blankensteijn JD, Th M Mali WP, Eikelboom BC (2000) Maximal aneurysm diameter follow-up is inadequate after endovascular abdominal aortic aneurysm repair. Eur J Vasc Endovasc Surg 20(2):177–182
61. Zhang Z, Nair SA, McMurry TJ (2005) Gadolinium meets medicinal chemistry: MRI contrast agent development. Curr Med Chem 12(7):751–778
62. Leung DA, Debatin JF (1997) Three-dimensional contrast-enhanced magnetic resonance angiography of the thoracic vasculature. Eur Radiol 7(7):981–989
63. Leung DA, Hany TF, Debatin JF (1998) Three-dimensional contrast-enhanced magnetic resonance angiography of the abdominal arterial system. Cardiovasc Intervent Radiol 21(1):1–10
64. Ludman CN, Yusuf SW, Whitaker SC, Gregson RH, Walker S, Hopkinson BR (2000) Feasibility of using dynamic contrast-enhanced magnetic resonance angiography as the sole imaging modality prior to endovascular repair of abdominal aortic aneurysms. Eur J Vasc Endovasc Surg 19(5):524–530
65. Haulon S, Lions C, McFadden EP, Koussa M, Gaxotte V, Halna P et al (2001) Prospective evaluation of magnetic resonance imaging after endovascular treatment of infrarenal aortic aneurysms. Eur J Vasc Endovasc Surg 22(1):62–69
66. Alerci M, Oberson M, Fogliata A, Gallino A, Vock P, Wyttenbach R (2009) Prospective, intraindividual comparison of MRI versus MDCT for endoleak detection after endovascular repair of abdominal aortic aneurysms. Eur Radiol 19(5):1223–1231
67. van der Laan MJ, Bartels LW, Viergever MA, Blankensteijn JD (2006) Computed tomography versus magnetic resonance imaging of endoleaks after EVAR. Eur J Vasc Endovasc Surg 32(4):361–365
68. Cornelissen SA, Prokop M, Verhagen HJ, Adriaensen ME, Moll FL, Bartels LW (2010) Detection of occult endoleaks after endovascular treatment of abdominal aortic aneurysm using magnetic resonance imaging with a blood pool contrast agent: preliminary observations. Invest Radiol 45(9):548–553
69. Ersoy H, Jacobs P, Kent CK, Prince MR (2004) Blood pool MR angiography of aortic stent-graft endoleak. AJR Am J Roentgenol 182(5):1181–1186
70. Sadowski EA, Bennett LK, Chan MR, Wentland AL, Garrett AL, Garrett RW et al (2007) Nephrogenic systemic fibrosis: risk factors and incidence estimation. Radiology 243(1):148–157
71. Abu-Alfa AK (2011) Nephrogenic systemic fibrosis and gadolinium-based contrast agents. Adv Chronic Kidney Dis 18(3):188–198
72. Saida T, Mori K, Sato F, Shindo M, Takahashi H, Takahashi N et al (2012) Prospective intraindividual comparison of unenhanced magnetic resonance imaging vs contrast-enhanced computed tomography for the planning of endovascular abdominal aortic aneurysm repair. J Vasc Surg 55(3):679–687
73. van der Laan MJ, Bartels LW, Bakker CJ, Viergever MA, Blankensteijn JD (2004) Suitability of 7 aortic stent-graft models for MRI-based surveillance. J Endovasc Ther 11(4):366–371
74. Howarth SP, Tang TY, Graves MJ, U-King-Im JM, Li ZY, Walsh SR et al (2007) Non-invasive MR imaging of inflammation in a patient with both asymptomatic carotid atheroma and an abdominal aortic aneurysm: a case report. Ann Surg Innov Res 1:4
75. Richards JM, Semple SI, MacGillivray TJ, Gray C, Langrish JP, Williams M et al (2011) Abdominal aortic aneurysm growth predicted by uptake of ultrasmall superparamagnetic particles of iron oxide: a pilot study. Circ Cardiovasc Imaging 4(3):274–281
76. Sadat U, Taviani V, Patterson AJ, Young VE, Graves MJ, Teng Z et al (2011) Ultrasmall superparamagnetic iron oxide-enhanced magnetic resonance imaging of abdominal aortic aneurysms – a feasibility study. Eur J Vasc Endovasc Surg 41(2):167–174
77. Truijers M, Futterer JJ, Takahashi S, Heesakkers RA, Blankensteijn JD, Barentsz JO (2009) In vivo imaging of the aneurysm wall with MRI and a macrophage-specific contrast agent. AJR Am J Roentgenol 193(5):W437–W441
78. Merkx MA, van't Veer M, Speelman L, Breeuwer M, Buth J, van de Vosse FN (2009) Importance of initial stress for abdominal aortic aneurysm wall motion: dynamic MRI validated finite element analysis. J Biomech 42(14):2369–2373
79. van der Laan MJ, Bakker CJ, Blankensteijn JD, Bartels LW (2006) Dynamic CE-MRA for endoleak classification after endovascular aneurysm repair. Eur J Vasc Endovasc Surg 31(2):130–135
80. van Herwaarden JA, Bartels LW, Muhs BE, Vincken KL, Lindeboom MY, Teutelink A et al (2006) Dynamic magnetic resonance angiography of the aneurysm neck: conformational changes during the cardiac cycle with possible consequences for endograft sizing and future design. J Vasc Surg 44(1):22–28
81. van Prehn J, Vincken KL, Sprinkhuizen SM, Viergever MA, van Keulen JW, van Herwaarden JA et al (2009) Aortic pulsatile distention in young healthy volunteers is asymmetric: analysis with ECG-gated MRI. Eur J Vasc Endovasc Surg 37(2):168–174
82. Eggebrecht H, Kuhl H, Kaiser GM, Aker S, Zenge MO, Stock F et al (2006) Feasibility of real-time magnetic resonance-guided stent-graft placement in a swine model of descending aortic dissection. Eur Heart J 27(5):613–620
83. Raman VK, Karmarkar PV, Guttman MA, Dick AJ, Peters DC, Ozturk C et al (2005) Real-time magnetic resonance-guided endovascular repair of experimental abdominal aortic aneurysm in swine. J Am Coll Cardiol 45(12):2069–2077
84. Wyers MC, Fillinger MF, Schermerhorn ML, Powell RJ, Rzucidlo EM, Walsh DB et al (2003) Endovascular repair of abdominal

aortic aneurysm without preoperative arteriography. J Vasc Surg 38(4):730–738
85. Beebe HG, Kritpracha B, Serres S, Pigott JP, Price CI, Williams DM (2000) Endograft planning without preoperative arteriography: a clinical feasibility study. J Endovasc Ther 7(1):8–15
86. Maurel B, Sobocinski J, Perini P, Guillou M, Midulla M, Azzaoui R et al (2012) Evaluation of radiation during EVAR performed on a mobile C-arm. Eur J Vasc Endovasc Surg 43(1):16–21
87. Walker TG, Kalva SP, Ganguli S, Oklu R, Salazar GM, Waltman AC et al (2012) Image optimization during endovascular aneurysm repair. AJR Am J Roentgenol 198(1):200–206
88. Criado E, Upchurch GR Jr, Young K, Rectenwald JE, Coleman DM, Eliason JL et al (2012) Endovascular aortic aneurysm repair with carbon dioxide-guided angiography in patients with renal insufficiency. J Vasc Surg 55(6):1570–1575
89. Lee AD, Hall RG (2010) An evaluation of the use of carbon dioxide angiography in endovascular aortic aneurysm repair. Vasc Endovascular Surg 44(5):341–344
90. Eide KR, Odegard A, Myhre HO, Hatlinghus S, Haraldseth O (2011) DynaCT in pre-treatment evaluation of aortic aneurysm before EVAR. Eur J Vasc Endovasc Surg 42(3):332–339
91. Eide KR, Odegard A, Myhre HO, Lydersen S, Hatlinghus S, Haraldseth O (2009) DynaCT during EVAR – a comparison with multidetector CT. Eur J Vasc Endovasc Surg 37(1):23–30
92. Nordon IM, Hinchliffe RJ, Malkawi AH, Taylor J, Holt PJ, Morgan R et al (2010) Validation of DynaCT in the morphological assessment of abdominal aortic aneurysm for endovascular repair. J Endovasc Ther 17(2):183–189
93. Biasi L, Ali T, Hinchliffe R, Morgan R, Loftus I, Thompson M (2009) Intraoperative DynaCT detection and immediate correction of a type Ia endoleak following endovascular repair of abdominal aortic aneurysm. Cardiovasc Intervent Radiol 32(3):535–538
94. Dijkstra ML, Eagleton MJ, Greenberg RK, Mastracci T, Hernandez A (2011) Intraoperative C-arm cone-beam computed tomography in fenestrated/branched aortic endografting. J Vasc Surg 53(3):583–590
95. Carrell TWG, Modarai B, Brown JRI, Penney GP (2010) Feasibility and limitations of an automated 2D-3D rigid image registration system for complex endovascular aortic procedures. J Endovasc Ther 17(4):527–533
96. Joshi F, Rosenbaum D, Bordes S, Rudd JH (2011) Vascular imaging with positron emission tomography. J Intern Med 270(2):99–109
97. Rudd JH, Warburton EA, Fryer TD, Jones HA, Clark JC, Antoun N et al (2002) Imaging atherosclerotic plaque inflammation with [18F]-fluorodeoxyglucose positron emission tomography. Circulation 105(23):2708–2711
98. Kotze CW, Groves AM, Menezes LJ, Harvey R, Endozo R, Kayani IA et al (2011) What is the relationship between (1)F-FDG aortic aneurysm uptake on PET/CT and future growth rate? Eur J Nucl Med Mol Imaging 38(8):1493–1499
99. Kotze CW, Menezes LJ, Endozo R, Groves AM, Ell PJ, Yusuf SW (2009) Increased metabolic activity in abdominal aortic aneurysm detected by 18F-fluorodeoxyglucose (18F-FDG) positron emission tomography/computed tomography (PET/CT). Eur J Vasc Endovasc Surg 38(1):93–99
100. Palombo D, Morbelli S, Spinella G, Pane B, Marini C, Rousas N et al (2011) A positron emission tomography/computed tomography (PET/CT) evaluation of asymptomatic abdominal aortic aneurysms: another point of view. Ann Vasc Surg 26(4):491–499
101. Reeps C, Essler M, Pelisek J, Seidl S, Eckstein HH, Krause BJ (2008) Increased 18F-fluorodeoxyglucose uptake in abdominal aortic aneurysms in positron emission/computed tomography is associated with inflammation, aortic wall instability, and acute symptoms. J Vasc Surg 48(2):417–423, discussion 24
102. Truijers M, Kurvers HA, Bredie SJ, Oyen WJ, Blankensteijn JD (2008) In vivo imaging of abdominal aortic aneurysms: increased FDG uptake suggests inflammation in the aneurysm wall. J Endovasc Ther 15(4):462–467
103. Wasselius J, Malmstedt J, Kalin B, Larsson S, Sundin A, Hedin U et al (2008) High 18F-FDG uptake in synthetic aortic vascular grafts on PET/CT in symptomatic and asymptomatic patients. J Nucl Med 49(10):1601–1605
104. Xu XY, Borghi A, Nchimi A, Leung J, Gomez P, Cheng Z et al (2010) High levels of 18F-FDG uptake in aortic aneurysm wall are associated with high wall stress. Eur J Vasc Endovasc Surg 39(3):295–301
105. Cavalcanti Filho JL, de Souza Leao Lima R, de Souza Machado Neto L, Kayat Bittencourt L, Domingues RC, da Fonseca LM (2011) PET/CT and vascular disease: current concepts. Eur J Radiol 80(1):60–67

Molecular Imaging of Inflammation and Intraplaque Vasa Vasorum

24

Gerrit L. ten Kate, Stijn C.H. van den Oord, Eric J.G. Sijbrands, Antonius F.W. van der Steen, and Arend F.L. Schinkel

Abbreviations

CT	Computed tomography
ED-B	Fibronectin extra-domain B
FDG	^{18}F-Fluorodeoxyglucose
HIF-1α	Hypoxia-inducible factor-1α
ICAM-1	Intercellular adhesion molecule-1
MMP	Matrix metalloproteinase
MRI	Magnetic resonance imaging
PET	Positron emission tomography
SPECT	Single photon emission tomography
SPIO	Super paramagnetic iron oxide
VCAM-1	Vascular cell adhesion molecule-1
VEGF	Vascular endothelial growth factor

G.L. ten Kate (✉) • A.F.L. Schinkel
Division of Pharmacology, Vascular and Metabolic Diseases, Department of Internal Medicine,
Erasmus University Medical Center, Office Ba-304, 's Gravendijkwal 230, 3015 CE, Rotterdam, The Netherlands

Department of Cardiology, Thoraxcenter, Erasmus University Medical Center, Rotterdam, The Netherlands
e-mail: gltenkate@gmail.com; a.schinkel@erasmusmc.nl

S.C.H. van den Oord
Department of Cardiology, Thoraxcenter, Erasmus University Medical Center, Office Ba-304, 's Gravendijkwal 230, 3015 CE, Rotterdam, The Netherlands

Department of Biomedical Engineering, Thoraxcenter, Erasmus University Medical Center, Rotterdam, The Netherlands
e-mail: s.vandenoord@erasmusmc.nl

E.J.G. Sijbrands
Division of Pharmacology, Vascular and Metabolic Diseases, Department of Internal Medicine,
Erasmus University Medical Center, Office D-434, 's Gravendijkwal 230, 3015 CE, Rotterdam, The Netherlands
e-mail: e.sijbrands@erasmusmc.nl

A.F.W. van der Steen
Department of Biomedical Engineering, Thoraxcenter, Erasmus University Medical Center, Office Ee-2302, Gravendijkwal 230, 3015 CE, Rotterdam, The Netherlands
e-mail: a.vandersteen@erasmusmc.nl

1 Introduction

For about half a century invasive angiography has been considered the gold standard in cardiovascular imaging. Angiography provides a high-resolution image of the lumen diameter which makes it able to accurately identify the presence of a lumen narrowing atherosclerotic plaque. In clinical practice the degree of lumen stenosis determined by angiography is frequently the main determinant for the initiation of invasive therapy.

In recent decades it has become apparent that the majority of acute cardiovascular events result from plaques that do not cause a significant stenosis on angiography. A plaque's composition, morphology, and biological processes influence its risk on rupture and thrombosis, which consequently may cause acute cardiovascular events [1–4]. Plaques with properties that make it at risk for rupture and thrombosis have been defined as vulnerable plaques [5]. Two major types of vulnerable plaques have been identified, the rupture prone plaques and the eroded plaques. The rupture prone plaques are thin-cap fibroatheromas, which are characterized by a thin fibrous cap overlying a large necrotic core, containing little smooth muscle cells but numerous macrophages. Eroded plaques have a loss or dysfunction of the luminal endothelium leading to thrombosis, without structural defect to the plaque beyond the endothelium. Eroded plaques are often rich in smooth muscle cells and proteoglycans (Fig. 24.1) [6, 7].

The identification of these vulnerable plaques is expected to improve the prediction of future cardiovascular events. The noninvasive imaging techniques currently available in clinical practice are, besides identifying the degree of lumen stenosis, capable of evaluating plaque size, plaque morphology, and a number of plaque components. However,

L. Saba et al. (eds.), *Multi-Modality Atherosclerosis Imaging and Diagnosis*,
DOI 10.1007/978-1-4614-7425-8_24, © Springer Science+Business Media, LLC 2014

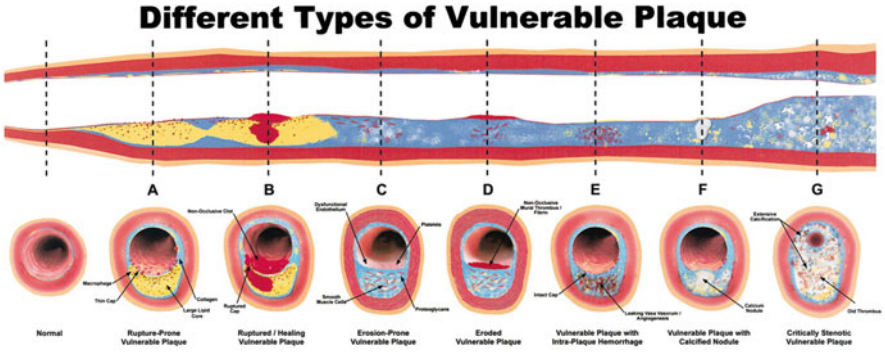

Fig. 24.1 Different types of vulnerable plaque as underlying cause of acute coronary events and sudden cardiac death. (**a**) Rupture-prone plaque with large lipid core and thin fibrous cap infiltrated by macrophages. (**b**) Ruptured plaque with subocclusive thrombus and early organization. (**c**) Erosion-prone plaque with proteoglycan matrix in a smooth muscle cell-rich plaque. (**d**) Eroded plaque with subocclusive thrombus. (**e**) Intraplaque hemorrhage secondary to leaking vasa vasorum. (**f**) Calcific nodule protruding into the vessel lumen. (**g**) Chronically stenotic plaque with severe calcification, old thrombus, and eccentric lumen. Reproduced with permission from Naghavi et al. [5]

especially in the early stages of development the size of most plaque components is too small to accurately image with the current spatial resolution [8, 9]. To date the identification of individual plaque components has not yet resulted in a clinically relevant improvement in prediction [10].

The use of molecular imaging to identify biological processes associated with plaque development and vulnerability could further improve prediction of cardiovascular events. Additionally molecular imaging could detect plaque in an earlier phase of development and provide new insights into the natural history of atherosclerotic disease, and aid the development of new therapies by target selection and validation in vivo, and monitoring of treatment effects [11–13].

The members of the Molecular Imaging Center of Excellence Standard Definitions Task Force have defined molecular imaging as the visualization, characterization, and measurement of biological processes at the molecular and cellular levels in humans or other living systems [14]. Jaffer and Weisleder have formulated four key questions that need to be addressed before molecular imaging can be applied [15].

1. Is there a molecular target relevant to the disease of interest?
2. Once the target is selected, is there a high-affinity ligand that will bind to the target?
3. What is the appropriate molecular imaging modality to provide the required spatial resolution, sensitivity, and depth penetration for the disease?
4. For a given imaging modality, can a molecular imaging agent be synthesized to detect the desired molecular target?

This chapter will review the use of noninvasive molecular imaging for the detection of inflammation and intraplaque neovascularization, two closely related and essential factors in plaque vulnerability. We will focus on the challenges in molecular imaging using nuclear imaging, magnetic resonance imaging (MRI), ultrasound, computed tomography (CT), and multimodality imaging for the evaluation of vulnerable plaques. Implementation of these modalities, for both molecular imaging and molecular guided therapy, will be addressed.

2 Inflammation and Intraplaque Neovascularization

Several molecular targets involved in atherosclerosis have been identified in basic research [16]. Inflammation and neovascularization are of special interest for molecular imaging due to their expression of endothelial markers in the lumen. Many of the molecular contrast agents are relatively large and are therefore restricted to intraluminal targets. The intraluminal expression of molecules associated with neovascularization and inflammation allows for easy targeting. Furthermore, their involvement in the earliest stages of plaque development makes them interesting targets for early detection of plaque development, even before intimal thickening occurs.

The development of an atherosclerotic plaque has long been thought of as a disease originating from the lumen–intima border, initiated by the diffusion of lipids and transportation of monocytes over the luminal endothelium. However, in recent years evidence has been gathered to support the role of the adventitial side of the vessel wall, especially the vasa vasorum, in plaque development [17]. The vasa vasorum form a microvascular network in the vessel wall of large arteries that provides the vessel wall with oxygen and nutrients. The vasa vasorum have been reported to provide an additional endothelial surface area of 17% of the main lumen endothelial surface in normal coronary arteries [18]. This number can rise to about almost 70% in regions with non-calcified plaques [18, 19].

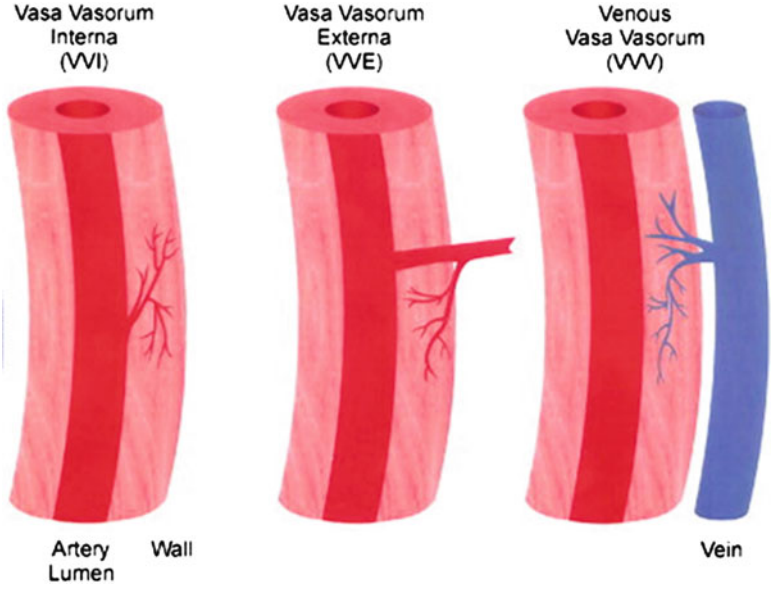

Fig. 24.2 Sketches of the three types of vasa vasorum found in the wall of cow aortae [inspired by Schoenenberger and Mueller 157]. In the Schoenenberger and Mueller study, vasa vasorum interna (*left panel*) originated directly from the aorta's main lumen, and vasa vasorum externa (*mid panel*) originated from intercostal branches deriving from the main lumen and dived back into the aortic wall. Venous vasa vasorum (*right panel*) developed in the aortic wall and finally drained into branches of concomitant veins. Reproduced with permission from Gössl et al. [25]

All cells in the human body are dependent on the vascular system for delivery of oxygen and nutrients. The majority of cells of the arterial vessel wall obtain their oxygen and nutrients by diffusion from the main lumen. However, in vessel walls more than 29 lamellar units thick, diffusion from the lumen is no longer sufficient. In these arteries the delivery to the adventitia and outer media is supplemented by vasa vasorum [20–24].

In humans vasa vasorum are present in all arteries with a vessel wall thickness >0.5 mm [24]. The majority of vasa vasorum originate from side branches of the main artery and enter the arterial wall from the abluminal side (vasa vasorum externa; Fig. 24.2), though vasa vasorum originating directly from the main lumen (vasa vasorum interna) are present as well. Additionally a network of venous vasa vasorum has been identified that drains to veins in proximity to the artery [25]. In a normal vessel the vasa vasorum are restricted to the adventitia and outer parts of the media. However, in atherosclerotic vessels neovascularization sprouting from the vasa vasorum into the intimal parts of the plaque has been found [26, 27]

Intraplaque neovascularization has gained interest as a factor in the development, progression, and vulnerability of atherosclerotic plaques. Pathologic studies have shown that the presence of intraplaque neovascularization, especially in the plaque shoulder where the plaque is most vulnerable to rupture, is associated with vulnerable and symptomatic plaques [18, 26–28]. Additionally, the presence of intraplaque neovascularization has been found to be an independent predictor of intraplaque hemorrhage and plaque rupture [27, 29]. Hellings et al. [30] investigated whether plaque composition is associated with the occurrence of future cardiovascular events. Endarterectomy specimens were collected for histology and patients were followed for 3 years after endarterectomy. Patients with intraplaque neovascularization or intraplaque hemorrhage were found to be at increased risk for a combined endpoint of cardiovascular events (fatal or nonfatal stroke, fatal or nonfatal myocardial infarction, sudden death or other vascular death) and any arterial vascular intervention not planned at time of inclusion (Fig. 24.3). The presence of macrophages, a large lipid core, calcifications, collagen, or smooth muscle cells was not associated with clinical outcome [30].

The association between intraplaque neovascularization, intraplaque hemorrhage, and cardiovascular events is thought to be due to the poor structural integrity of the newly formed vasa vasorum [31]. The majority of neovessels in symptomatic plaques are highly irregular in shape, while very few of these irregular vessels are present in asymptomatic plaques [32]. The newly formed microvessels are thin-walled, with incomplete or absent endothelial gap junctions. This may result in the extravasation of lipids, inflammatory cells, and red blood cells, and risks the collapse of microvessels, causing intraplaque hemorrhage (Fig. 24.4). This will contribute to lipid core growth and sustained plaque inflammation, thus the progression into more advanced plaques [33, 34]. Consequently plaques with a high density of neovascularization are at an increased risk of plaque rupture [35, 36].

Angiogenesis, the sprouting of new microvessels from an existing microvascular network, is the main process resulting in neovascularization of atherosclerotic plaques [35, 37]. Key factors initiating angiogenesis in atherosclerosis are still largely unknown. Developments in tumor research have greatly increased our knowledge about the processes that take place during neovascularization and identified several factors that can initiate neovascularization such as metabolic stress (hypoxia, acidosis, or hypoglycaemia),

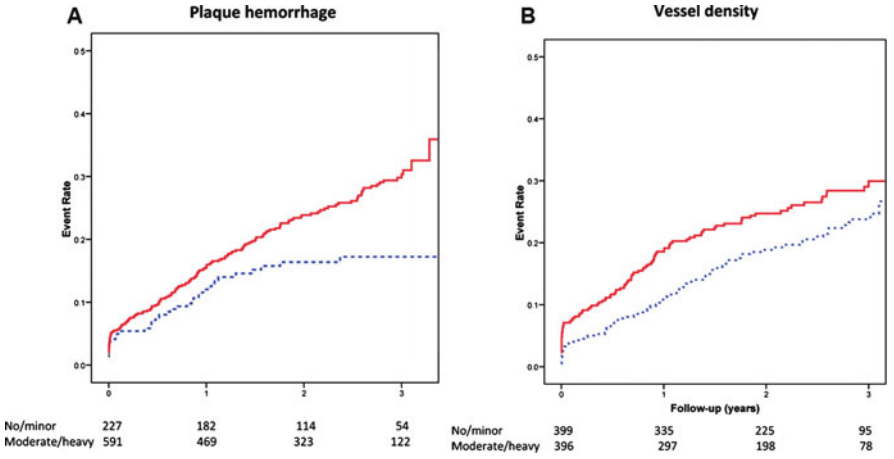

Fig. 24.3 Kaplan–Meier survival curves of plaque histology vs. primary outcome (vascular event and vascular intervention) for plaque hemorrhage (**a**): absent (*dashed line*) vs. present (*continuous line*) and intraplaque vessel density (**b**): <8 (average number of vessels per hot spot, dashed line) vs. ≥8 vessels (*continuous line*). The number of patients at risk for systemic cardiovascular events at 0, 1, 2, and 3 years is provided. Reproduced with permission from Hellings et al. [30]

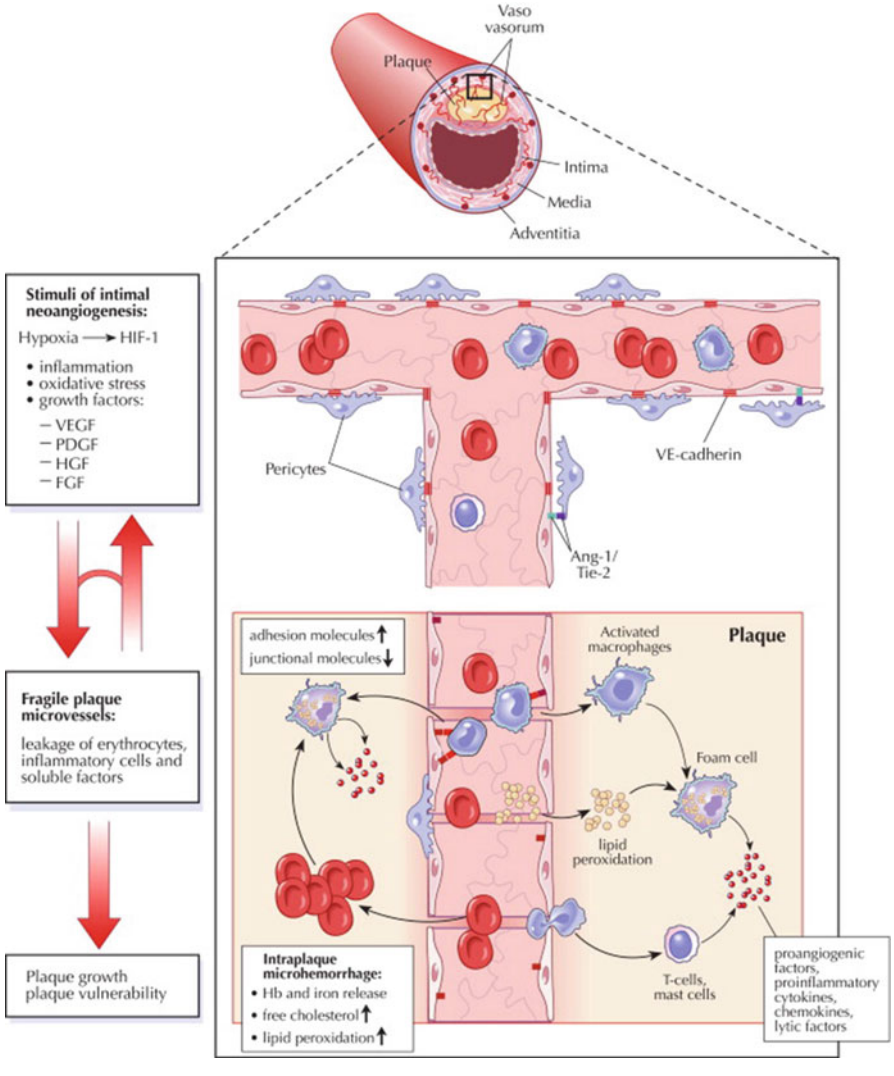

Fig. 24.4 Plaque microvessels show a compromised structural integrity and a modified expression profile of adhesion and junctional molecules, thus permitting extravasation of inflammatory cells and soluble factors as well as the occurrence of microhemorrhages. The resulting reactive microenvironment may support further plaque growth and plaque vulnerability. *Ang* angiopoietin, *FGF* fibroblast growth factor, *Hb* hemoglobin, *HGF* hepatocyte growth factor, *HIF* hypoxia-inducible factor, *PDGF* platelet-derived growth factor, *VE* vascular endothelial, *VEGF* vascular endothelial growth factor. Figure illustration by Rob Flewell. Reproduced with permission from Mause and Weber [31]

mechanical stress (pressure generated by proliferating cells), immune/inflammatory response (immune/inflammatory cells that have infiltrated the tissue), and genetic mutations [38].

Hypoxia has been found to be one of the most important stimuli for angiogenesis in several diseases [39, 40]. Upregulation of hypoxia-inducible factors has been found in

Table 24.1 Brief comparison of technological features of noninvasive imaging modalities used in clinical practice

Imaging modality	Spatial resolution (mm)	Acquisition time/frame (s)	Sensitivity of detection (g/ml)	Anatomical detail	Plaque composition	Advantages	Disadvantages
PET	3–8	1–300	$<10^{-12}$	−	−	Quantitative measurements	Ionizing radiation
							Short half-life tracers
							Expensive equipment
							Requires on-site cyclotron
SPECT	5–12	60–2,000	$>10^{-9}$	−	−	Multiple isotope imaging	Ionizing radiation
MRI	0.1–0.2	50–3,000	$>10^{-6}$	++	+++	No ionizing radiation	Contrast-induced systemic fibrosis
						Widely available	
Ultrasound	0.1–1.0	0.05–1	NA	+	+	No ionizing radiation	Limited penetration depth
						Widely available	Obligatory intravascular contrast agent
						Inexpensive	
						Real-time imaging	
CT	0.5–1	1–300	$>10^{-3}$	+++	+	Coronary imaging	Ionizing radiation
						Widely available	Contrast nephrotoxicity

CT computed tomography, *MRI* magnetic resonance imaging, *NA* not available, *PET* positron emission tomography, *SPECT* single photon emission computed tomography. Table based on ten Kate et al. [154]

atherosclerotic plaques [41, 42]. Though hypoxia may arise due to the increasing distance between the vessel lumen and plaque core, this is unlikely to be the main culprit, since angiogenesis is already present in early stages of plaque development when intimal thickening is negligible [43–46]. Hypoxia is thought to be primarily determined by the increased oxygen demand caused by plaque inflammation [35].

Inflammation is one of the hallmarks of plaque development and vulnerability and inflammatory cells have generally been accepted to play a key role in the early stages of plaque formation. In the early stages the vessel wall is infiltrated by lipoproteins and as a response the endothelium expresses leukocyte adhesion molecules. Monocytes in the lumen adhere to the adhesion molecules and extravasate into the subintimal space [47]. The influx of monocytes and their subsequent differentiation into mature and activated inflammatory cells increases the metabolic demand in the vessel wall. If the supporting vasculature is insufficient this will result in a hypoxic state and increased oxidative stress. This hypothesis has been supported by the presence of both hypoxic and inflammatory factors, such as hypoxia-inducible factor-1α (HIF-1α), nuclear transcription factor-kappa B, tumor necrosis factor-α, and interleukin-6 and an increased number of superoxide anions in atherosclerotic plaques. Furthermore, these factors have been found to be co-localized with intraplaque neovascularization [41, 48, 49].

3 Imaging Modalities

The noninvasive imaging modalities currently utilized in clinical practice are after the administration of a specialized contrast agent (e.g., iron oxide, gadolinium, microbubbles, radionuclides, iodine, gold, bismuth) capable of molecular imaging (Table 24.1).

Nuclear Imaging Nuclear imaging includes a number of techniques that are all dependent on a physical signal emitted by a radionuclide tracer. The two predominant techniques currently in use are positron emission tomography (PET) and single photon emission computed tomography (SPECT). Both techniques have a high penetration depth and are capable of 3D whole body scanning.

Inherent to the dependency on a physical signal is the very high sensitivity with which nuclear imaging can detect the molecular tracer [50]. The main drawbacks of nuclear imaging are the limited spatial resolution, and the lack of anatomical information. This is partially overcome by co-registration with either CT or MRI to provide high-resolution anatomical information. The use of radionuclide tracers has the inherent problem of radiation exposure of both personnel and patient. Though the radiation doses currently used in clinical practice are safe, the effect of cumulative radiation

exposure should be taken into account when performing repeated measurements.

Magnetic Resonance Imaging MRI molecular imaging is performed using either gadolinium or superparamagnetic iron oxide compounds (SPIOs) that influence the magnetic resonance signal. MRI provides a sub-millimeter spatial resolution and good soft tissue contrast, thus providing an excellent evaluation of anatomical structures. In recent years increasing field strengths and improved coil designs have resulted in higher signal-to-noise ratios, contrast-to-noise ratios, and resolutions, while reducing scanning times. Additionally MRI can obtain anatomic, physiologic, and metabolic information in one session.

The primary disadvantage is the low sensitivity for the detection of the contrast agent compared to nuclear techniques [51]. Additionally the use of gadolinium has been associated with nephrogenic systemic fibrosis, especially in patients with reduced renal function [52].

Ultrasound B-mode and Doppler ultrasound are the most frequently utilized imaging modalities in clinical practice. Ultrasound has a high spatial resolution, which provided excellent anatomical information. Ultrasound contrast agents consist of gas-filled microbubbles stabilized by a lipid or protein shell. For molecular imaging ligands can be bound to these microbubbles. When using specific pulse sequences ultrasound is capable of specific contrast imaging, which eliminates the signal of the surrounding tissue. This makes ultrasound very sensitive for the detection of contrast agent [53]. Untargeted ultrasound contrast agents have been used in echocardiography for decades and have been proven safe in large multicenter studies [54, 55].

Ultrasound has a superior temporal resolution, which makes it the only technique currently available for real-time imaging. However, the penetration depth and 3D scanning capabilities are limited. Another important limitation is the relatively large size (1–5 μm) of the microbubbles, making them obligatory intravascular tracers. However, this makes them well suited for identifying the presence of vasculature, since the presence of contrast agent indicates the presence of a vessel.

Computed Tomography CT (especially the latest generations of multislice and dual source CT) provides a high-resolution image with very short acquisition times, good penetration depth, and full body scanning capabilities. CT is currently the only noninvasive technique in clinical practice with sufficient resolution, penetration, and speed to accurately image the coronary arteries in a beating heart. CT provides good anatomical information; however, it is poor in soft tissue contrast. However, the use of CT for molecular imaging of the coronary arteries has not yet been investigated.

Molecular CT contrast agents are in early stage of development. Molecular contrast agents based on iodine, gold, and bismuth have been developed; however, they have not yet been investigated in humans [56–59]. The use of ionizing radiation potentially limits the use of CT, though the radiation dose in cardiovascular imaging has substantially been reduced in recent years [60]. From clinical practice it is known that iodine contrast agents can induce a contrast nephropathy, limiting its use in patients with decreased renal function [61].

Multimodality Imaging is being explored to improve the accuracy of examinations. The currently available modalities each have their limitations as previously described. When using multiple imaging modalities the advantages of each individual modality can be used to the other modalities' limitations, in order to improve the overall accuracy. In clinical practice multimodality imaging is already used by combining nuclear imaging with co-registration of either CT or MRI. This allows for the combination of the highly accurate and quantifiable assessment of biological activity by nuclear imaging with the high-resolution anatomical information provided by CT or MRI (Fig. 24.5) [62, 63].

The use of multimodal contrast agents is currently limited to preclinical research. A number of probes have been developed that enable both in vivo and ex vivo molecular imaging (e.g., MRI and fluorescence [64]). However, probes that are detectable with multiple in vivo imaging modalities (e.g., MRI and PET [65]) are sparse. The development of multimodal probes could help achieve high sensitivity and high spatial resolution.

4 Molecular Targets

Leukocyte Adhesion Molecules The expression of leukocyte adhesion molecules is a marker of endothelial dysfunction and is pivotal in the initiation of vessel wall inflammation [47]. Since adhesion molecules are expressed in the vascular lumen they are easily accessible to molecular contrast agents. Frequently investigated adhesion molecules include vascular cell adhesion molecule-1 (VCAM-1), intercellular adhesion molecule-1 (ICAM-1), and selectins. VCAM-1 and ICAM-1 and selectins are expressed by the luminal endothelium overlying the atherosclerotic plaque. However, the most dominant expression has been found at the adventitial site of the plaque and correlated with sites of vasa vasorum neovascularization, vascular permeability, and a high number of inflammatory cells [66, 67].

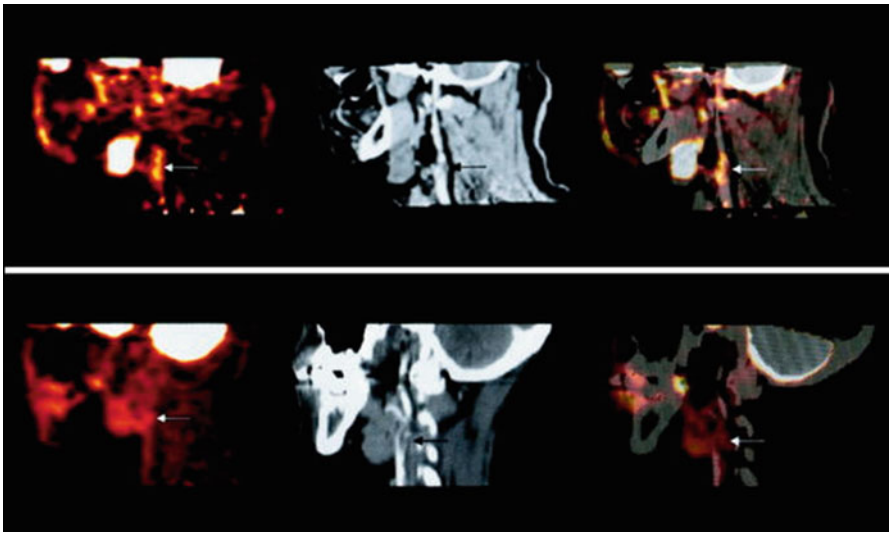

Fig. 24.5 The *upper row* (from *left* to *right*) shows PET, contrast CT, and co-registered PET/CT images in the sagittal plane, from a 63-year-old man who had experienced two episodes of left-sided hemiparesis. Angiography demonstrated stenosis of the proximal right internal carotid artery; this was confirmed on the CT image (*black arrow*). The *white arrows* show FDG uptake at the level of the plaque in the carotid artery. As expected, there was high FDG uptake in the brain, jaw muscles, and facial soft tissues. The *lower row* (from *left* to *right*) demonstrates a low level of FDG uptake in an asymptomatic carotid stenosis. The *black arrow* highlights the stenosis on the CT angiogram, and the *white arrows* demonstrate minimal FDG accumulation at this site on the FDG-PET and co-registered PET/CT images. Reproduced with permission from Ross et al. [93]

VCAM-1-targeted MRI contrast agents have utilized VCAM-1's ability to internalize ligands, resulting in accumulation of the contrast agent. In vivo VCAM-1-targeted magnetofluorescent nanoparticles were shown to be able to identify VCAM-1 expression in atherosclerotic lesions by MRI, which was confirmed by fluorescence imaging and histology [68, 69]. In ex vivo endarterectomy specimens it was confirmed that the VCAM-1-targeted contrast agents co-localized with VCAM-1 expressing endothelial cells in human plaques as well [69]. Additionally it was shown that statin therapy reduced the contrast enhancement caused by the VCAM-1-targeted contrast on MRI and fluorescence imaging (Fig. 24.6), which correlated with reduced expression of VCAM-1 on histology [69]. (Table 24.2).

A VCAM-1-targeted contrast agent has also been developed for ultrasound [70]. In vitro experiments showed that VCAM-1-targeted microbubbles were able to attach to activated murine endothelial cells, even under a pulsatile high shear stress condition. Subsequent in vivo experiments showed ultrasound signal enhancement in the aortic plaques of apoE-deficient mice within 10 min after contrast injection [70]. These results suggest that VCAM-1-targeted microbubbles could provide a fast molecular imaging technique. The availability of a fast molecular imaging technique could be advantageous for clinical practice.

Similarly, ICAM-1-targeted microbubbles were shown to specifically bind to endothelial cells expressing ICAM-1 in vitro [71]. In vivo ICAM-1-targeted microbubbles were found to attach to what are described as early stages of the atherosclerotic plaque (Fig. 24.7) [72]. Though this study showed that ultrasound might be capable of identifying the early stages of atherosclerotic vascular disease, no histology was performed to confirm this finding.

Selectin-targeted contrast agents have been developed but not yet investigated for the imaging of atherosclerotic plaques. Both e-selectin- and p-selectin-targeted SPIO compounds have shown binding to human endothelial cells in vitro and a concomitant significant T2 signal decrease on MRI [73–75]. e-Selectin-targeted MRI contrast agents have been used in vivo to identify inflammation in hepatic and muscle tissue of mice [76, 77].

Inflammatory Cells The activated endothelium releases chemoattractants to recruit monocytes. These subsequently enter into the sub-endothelial space where they differentiate in mature inflammatory cells. Macrophages are the most prevalent inflammatory cell in the atherosclerotic plaque and play a major role in the pathophysiology of plaque vulnerability [78]. The macrophages can cause a maladapted chronic inflammatory response that will aid the expansion of the sub-endothelial layer due to the accumulation of cells, lipids, and matrixmolecules [78]. The presence of macrophages in the plaque has been found to be closely associated with intraplaque neovascularization [79]. Macrophages both use the vasa vasorum neovascularization

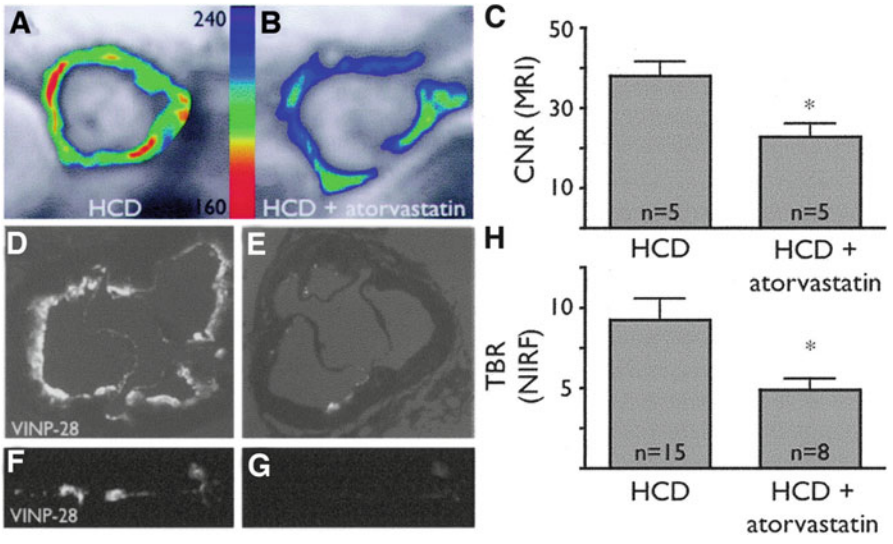

Fig. 24.6 Noninvasive MRI assessment of VCAM-1 expression after atorvastatin administration. (**a**) Short-axis MRI of the aortic root of an untreated apoE$^{-/-}$ mouse on a high cholesterol diet (HCD) after injection of a VCAM-1-targeted nanoparticle (VINP-28) with color-coded signal intensity. The *red color* encodes high VCAM-1 expression. (**b**) MRI of HCD + atorvastatin-treated apoE$^{-/-}$ mouse after VINP-28 injection. An attenuated signal drop in the aortic root wall compared with untreated mouse was noted. (**c**) After injection of VINP-28, the MRI contrast-to-noise ratio diminished in atorvastatin-treated mice (mean ± SD; $^*P < 0.05$ versus HCD). (**d**, **e**) Near-infrared (NIR) microscopy of the aortic roots depicted in **a** and **b**. Fluorescent signal originating from VINP-28 comprised the whole-root circumference (**d**), but less so in atorvastatin-treated mice (**e**). (**f**, **g**) Fluorescent reflectance imaging of the excised aorta of an untreated (**f**) and atorvastatin-treated (**g**) mouse showed reduced NIR signal in statin-treated mice. (**h**) The target-to-background ratio was reduced in aortas of treated mice (mean ± SD;$^*P < 0.05$ treated vs. untreated mice). Reproduced with permission from Nahrendorf et al. [69]

Table 24.2 Available studies on potential molecular targets involved in neovascularization and inflammation of the atherosclerotic plaque

Target	Nuclear imaging	MRI	Ultrasound	CT	In vivo imaging	Atherosclerosis model
Leukocyte adhesion molecules						
VCAM-1		[68, 69, 75]	[70, 132]		Animal	Yes
ICAM-1		[155]	[71, 72, 133]		Animal	Yes
e-Selectin		[73, 74, 76, 77]	[133]		Animal	No
p-Selectin		[75]	[132, 134]		No	Yes
Inflammatory cells						
Phagocytosis		[80–87]		[56]	Animal	Yes
Macrophage metabolism	[88–100]				Animal	Yes
					Human	Yes
MMP	[103]	[102]			Animal	Yes
Myeloperoxidase		[104]			Animal	Yes
Angiogenesis						
VEGFR2			[113–115, 134]		Animal	No
Endoglin	[112]		[113]		Animal	No
Integrin αvβ3	[122–125]	[120, 121]	[114, 126, 127, 134]		Animal	Yes
					Human	No
Fibronectin ED-B	[130, 131]				Animal	No
					Human	No

CT computed tomography, *ED-B* extra-domain B, *MRI* magnetic resonance imaging, *VEGFR2* vascular endothelial growth factor receptor 2, *ICAM-1* intercellular adhesion molecule-1, *MMP* matrix metalloproteinase, *MRI* magnetic resonance imaging, *VCAM-1* vascular cell adhesion molecule-1

as a port of entry into the plaque and excrete a myriad of proangiogenic molecules aiding the expansion of the microvascular network.

Macrophages provide a number of attractive targets for molecular imaging. Their ability to phagocytose molecules can be utilized to accumulated contrast agent. This should improve the target-to-background ratio and thus the accuracy with which contrast agent can be detected. Activated macrophages have been shown to internalize and concentrate a number of nanoparticles. For example, in

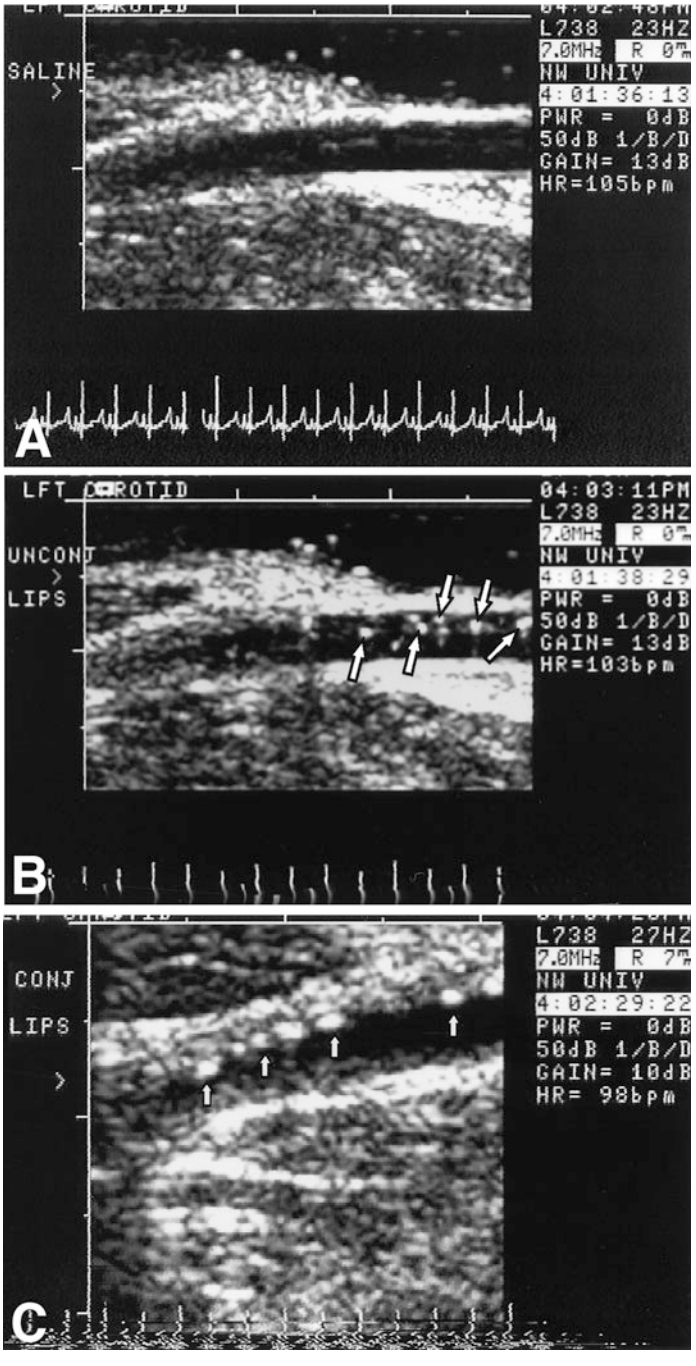

Fig. 24.7 Transvascular ultrasound images of an atherosclerotic left carotid artery of a Yucatan miniswine. (**a**) After injection of saline. (**b**) After injection of unconjugated liposomes (*arrows* point to liposomes within the lumen). (**c**) After injection of anti-ICAM-1-labeled liposomes (*arrows* point to liposomes attached to the atherosclerotic plaque). Reproduced with permission from Demos et al. [72]

vitro macrophages have been shown to actively phagocytose dextran-coated SPIO nanoparticles under the influence of cytokines, serum components, and statin treatment [80]. Similarly, both gadolinium micelles and iodinated nanoparticles have been shown to be internalized by macrophages [56, 81].

Dextran-coated SPIO nanoparticles have been investigated in human endarterectomy patients. The SPIO nanoparticles were shown to be to be able to identify macrophages in vivo [82–86]. However, due to the long interval between pre- and post-contrast scans (≥24 h) the clinical application of SPIO nanoparticles seems limited.

The Atorvastatin Therapy: Effects on Reduction of Macrophage Activity (ATHEROMA) Study investigated the effects of low-dose (10 mg) and high-dose (80 mg) atorvastatin on carotid plaque inflammation as determined by ultrasmall SPIO compound. The primary endpoint was the change in signal intensity from baseline after 6 and 12 weeks of either low-dose or high-dose atorvastatin. Both at 6 and 12 weeks there was a significant reduction in signal intensity from baseline in the high-dose group (Fig. 24.8). There was no difference observed in the low-dose group [87].

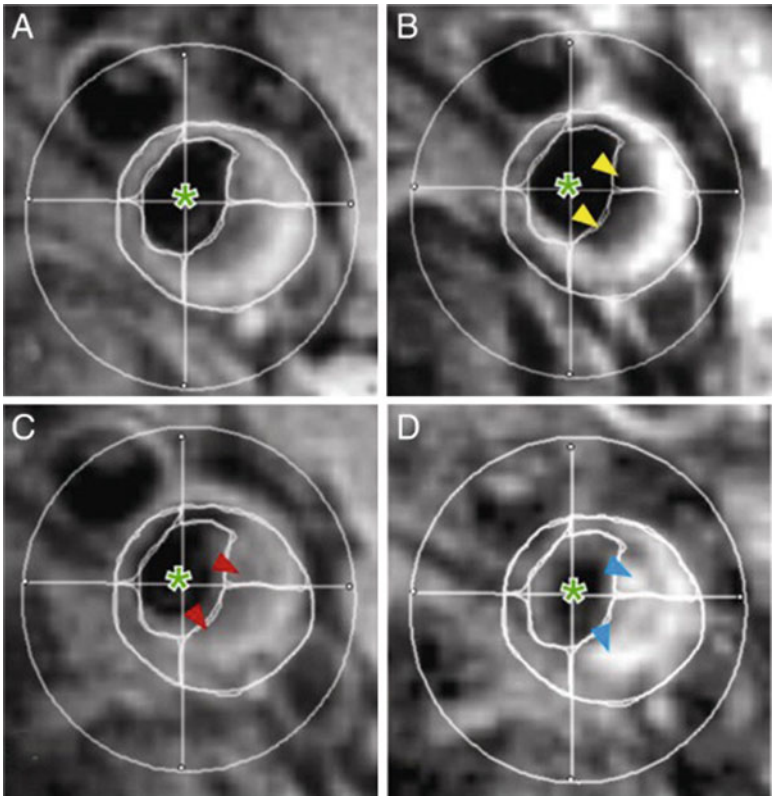

Fig. 24.8 T2*-weighted MRI images of the right common carotid artery of a patient receiving 12 weeks of high-dose atorvastatin (80 mg) treatment. Imager were taken before (*left*) and after (*right*) ultrasmall superparamagnetic iron oxide (USPIO) infusion at time points 0 (**a** and **b**) and 12 weeks (**c** and **d**). (**b**) USPIO uptake can clearly be seen in the plaque at baseline (*yellow arrowheads*). (**c**) USPIO has been cycled out of the plaque before reinfusion at 12 weeks (*red arrowheads*). (**d**) The plaque enhances at 12 weeks (*blue arrowheads*), indicating that the high-dose statin treatment has damped the USPIO-defined inflammation. Plaque segmentation was performed using a combination of multicontrast sequences. The cross hairs centered through the middle of the lumen divide the vessel into quadrants. Signal from artifact, extravascular structures, and the luminal blood pool (*green asterisks*) are excluded from the analysis. Reproduced with permission from Tang et al. [87]

To further improve the accumulation of contrast agent molecular contrast agents have been targeted at the macrophage scavenger receptors, to induce uptake of the molecule. In an in vivo study Lipinski et al. showed that the uptake of gadolinium immuno-micelles targeted at the macrophage scavenger receptor was significantly higher than nontargeted micelles. These promising results suggest that scavenger receptor-targeted contrast agents may improve the detection of macrophages [81].

A second characteristic that can be identified is the high metabolic activity of activated macrophages. The presence of activated macrophages in the atherosclerotic plaque will increase the metabolic activity at that location. The increased metabolic activity can be visualized by ^{18}F-fluorodeoxyglucose (FDG) PET, a radionuclide-labeled glucose analogue taken up by cells in proportion to their metabolism, especially glycolysis. FDG-PET is readily used in clinical practice to identify the presence of malignant metastasis. In cancer patients it was observed that the presence of FDG uptake in the arterial wall was associated with the presence of atherosclerotic vascular disease [88] Subsequently, the in vivo visualization and quantification of plaque inflammation by FDG-PET has been validated against histology in animals [89–92] and humans [93–97].

The use of FDG-PET has been shown to identify possible culprit lesions that were not identified by angiography. Davies et al. [98] investigated 12 patients who had all suffered a recent transient ischemic attack. Ten patients had a high FDG uptake in a plaque in the vascular territory compatible with the symptoms. Three of those were non-stenotic plaques which were not identified as the culprit lesion on angiography. This study shows the possibility of FDG-PET to identify relevant carotid lesions beyond stenosis. However, no histology was obtained to confirm the findings [98].

Rominger et al. [99] followed a cohort of 334 cancer patients asymptomatic for cardiovascular disease who had undergone FDG-PET/CT. Maximal standard uptake values were measured and calcifications were recorded for in both common carotid arteries, ascending aorta, aortic arch, descending aorta, abdominal aorta, and both iliac arteries.

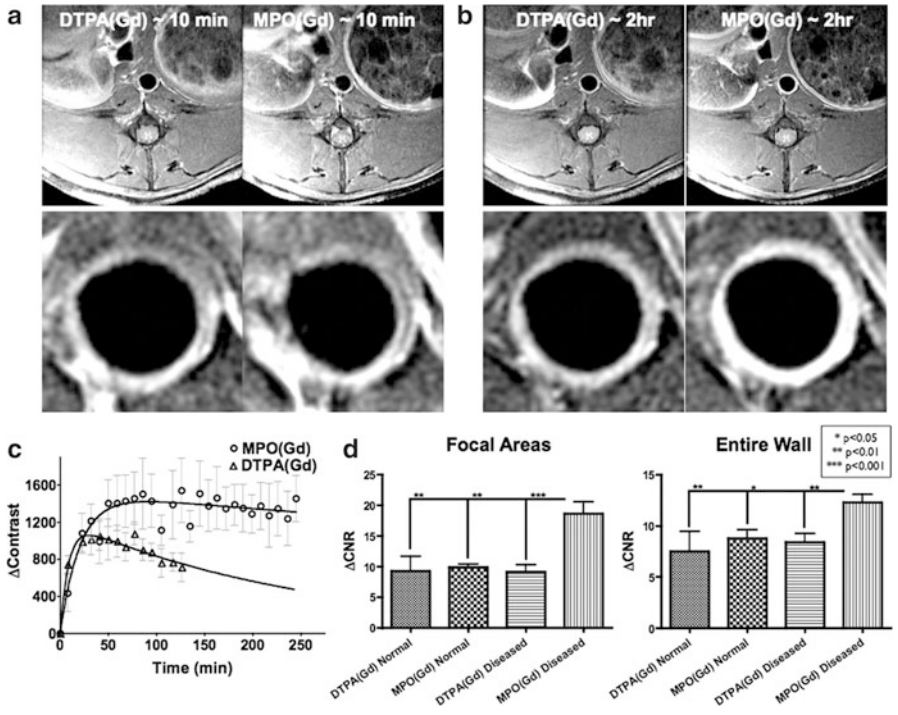

Fig. 24.9 (**a**) As-acquired (*top*; 5-cm field-of-view) and higher magnification (*bottom*; centered around aorta) early-phase (≈10 min) MRI images of diseased wall in rabbit fed a cholesterol diet for 17 months, taken after administration of a gadolinium contrast agent (DTPA(Gd)) (*left*) and a functional myeloperoxidase activity imaging sensor (MPO(Gd)) (*right*). Similar levels of enhancement were seen at this time point with both agents. (**b**) Delayed MPO(Gd) images (≈2 h; *right*) showed substantially increased enhancement compared with both late-phase (≈2 h; *left*) and early-phase (seen in **a**) DTPA(Gd) images. (**c**) Kinetics study. Increased and prolonged contrast was found with MPO(Gd) compared with DTPA(Gd) ($n = 3$ animals). (**d**) Analysis of pre-contrast and 2-h post-contrast [MPO(Gd) and DTPA(Gd)] MR images of rabbits fed a cholesterol diet for 28–29 months ($n = 8$) and age-matched controls ($n = 4$). Δ contrast-to-noise ratio (CNR) in both focal wall areas (*left*) and the entire wall (*right*) revealed no difference from MPO(Gd) and DTPA(Gd) in normal wall ($n = 4$, 11 sections analyzed). Diseased wall imaged with DTPA(Gd) ($n = 8$, 24 sections analyzed) also showed no difference compared with normal wall imaged with either agent. In distinction, diseased wall imaged with MPO(Gd) ($n = 8$, 24 sections analyzed) showed significantly higher ΔCNR (≈2×) than all other values. Reproduced with permission from Ronald et al. [104]

Fifteen patients developed a cardiovascular event in a median follow-up of 29 months. The mean target-to-background ratio (hazard ratio, 14.144; $p = 0.001$) and calcified plaque sum (hazard ratio, 3.560; $p = 0.025$) were significant independent predictors for the occurrence of cardio- or cerebrovascular events [99]. Additionally Tahara et al. [100] have shown the potential of FDG-PET to evaluate the effect of statin treatment on plaque inflammation. After 3 months of statin treatment FDG uptake in the atherosclerotic plaque was significantly decreased, compared to dietary management only [100].

Macrophages also secrete numerous pro-angiogenic factors that are associated with plaque vulnerability, such as matrix metalloproteinases (MMPs). MMPs are a group of enzymes that aid in angiogenesis by degrading the ECM. ECM degradation is necessary to allow for the migration of endothelial cells across the basement membrane. Besides aiding in angiogenesis MMPs have a direct effect on plaque vulnerability by weakening the fibrotic cap overlying the lipid necrotic core [101]. MMP-targeted tracers have been developed for MRI and SPECT [102, 103]. Ohshima et al. investigated a ^{99m}Tc-labeled broad spectrum MMP inhibitor to identify MMP activity in vivo. The tracer uptake was a significantly correlated with regions stained positive for macrophages, MMP-2 and MMP-9 on histology [103]. Enzymatic activity provides a possibility to use functional contrast agents that are only expressed in after enzymatic conversion. These agents are expected to improve the target-to-background ratio. Ronald et al. [104] investigated a functional contrast agent that was expected to oligomerize and bind to resident proteins as a result of myeloperoxidase-mediated activation. It was expected that this would result in a higher magnetic resonance signal and prolonged retention of the contrast agent within myeloperoxidase-rich plaque. The functional contrast agent created focal areas of twofold MRI signal intensity increase in the diseased vessel wall of NZW rabbits, while untargeted contrast agents showed no increase in signal intensity (Fig. 24.9) [104]. Functional contrast agents are an interesting development in in vivo imaging and might result in significant improvements in molecular imaging.

Neovascularization Angiogenesis is seen in numerous malignant, inflammatory, and ischemic diseases. In a healthy person the vascular endothelium is quiescent with less than 0.01% of the endothelial cells undergoing division. This makes angiogenic activity a specific marker for the presence of a disease process. In vascular disease excessive angiogenesis is seen in vascular malformations, hemangioma, hemangioendothelioma, and atherosclerosis [105].

Both MRI and ultrasound can identify the presence of vascularization in an atherosclerotic plaque, using a nontargeted contrast agent. The capability of ultrasound to detect individual microbubbles, which are obligatory intravascular, allows it to detect individual vessels in the plaque [106]. Several studies have shown an association between contrast enhancement in the plaque and intraplaque neovascularization on histology [107–109]. Kerwin et al. investigated dynamic contrast-enhanced MRI measurements of K^{trans} (a contrast transfer constant) and plasma volume in the plaque as measurement of intraplaque neovascularization. A significant correlation was found between dynamic contrast-enhanced MRI measurements and the amount of plaque neovascularization seen on histology [110, 111]. However, both ultrasound and dynamic contrast-enhanced MRI do not show whether there is active angiogenesis in the plaque.

Active angiogenesis can be identified by imaging targets that are overexpressed by proliferating endothelium but not by normal endothelium. The VEGF receptors and the transforming growth factor-β binding receptor endoglin are promising targets which are upregulated in the proliferating endothelium under the influence of HIF-1α [39]. Known for their involvement in tumor angiogenesis both have been targeted in vivo for the detection of tumor angiogenesis in mice using microbubbles or radionuclides [112–115]. The first study using VEGF receptor 2-targeted microbubbles in humans is currently being performed in patients with prostate cancer (clinicaltrials.gov; study no: NCT01253213). Studies investigating the molecular imaging of the VEGF receptors or endoglin have not yet been performed in an atherosclerosis model.

Integrin αvβ3 is a cell surface receptor involved in the migration of endothelial cells across the basement membrane during angiogenesis. Integrin αvβ3 is part of a large family of cell surface receptors, present in both healthy and angiogenic vessels [116]. However, the expression of integrin αvβ3 has been shown to be a marker for angiogenesis present in the adventitial vasa vasorum and intraplaque neovascularization [117–119].

Integrin αvβ3-targeted contrast agents have extensively been investigated in tumor models using MRI [120, 121], PET [122], SPECT [123–125], and ultrasound [114, 126, 127]. In vivo imaging of an atherosclerosis model has only been performed using integrin αvβ3-targeted gadolinium compounds. These compounds were shown to create a significant increase in the MRI signal in the vessel wall at locations of atherosclerosis. The expression of integrin αvβ3, proliferation of angiogenic vessels, and neointima formation was confirmed by histology [120, 121]. However, the results of a clinical trial investigating a ^{99m}Tc-labeled anti-αvβ3 antibody in metastatic cancer patients have thus far been disappointing [128].

During angiogenesis ECM molecules are seen that are not present otherwise. The fibronectin extra-domain B (ED-B) is an isoform of fibronectin, resulting from alternative splicing, which is present in the temporary extracellular matrix formed during tissue remodeling and is hardly present in normal vascular tissue [129]. Increased expression of ED-B has been found in both murine and human plaques. The expression of ED-B in human plaques was predominantly found around the vasa vasorum [130]. Matter et al. developed ^{125}I-labeled monoclonal antibodies against ED-B and found it to specifically target atherosclerotic plaques in apoE knockout mice [130]. However, only ex vivo imaging was performed.

In vivo imaging of the ED-B has been performed in patients with brain, lung, or colorectal cancer. Twenty patients with several different types of malignant tumors received an injection of a ^{123}I-labeled monoclonal antibody against the ED-B (L19). SPECT images were obtained at 4 and 24 h after contrast injection. Sixteen of the patients showed uptake in the tumor or metastasis. Of the four negative tumors one was an astrocytoma that of which it is known that it does not express ED-B. The other three could not be explained. Importantly no adverse events were seen [131]. This study showed that accurate specific targeting of the ED-B is possible. However, the spatial resolution of SPECT will probably not be sufficient to image atherosclerotic targets.

Multitargeted Contrast Agents Recently dual- and triple-targeted contrast agents have emerged in an attempt to improve ligand to target binding. Especially under high shear stress conditions attachment of the contrast agent to the target can be impaired. A number of studies have shown that the use of multitargeted contrast agent significantly improves contrast to target binding [75, 114, 132–134]. The investigated multitargeted contrast agents are of relatively large size (microbubbles and microparticles of iron oxide) and are therefore only targeted at intravascular targets.

Dual combinations of VEGF receptor 2 and $\alpha_v\beta_3$-integrin [114], p-selectin and VCAM-1 [132], and ICAM-1 and sialyl Lewis^x (selectins) [133] have been developed for ultrasound and p-selectin and VCAM-1 for MRI [75]. A triple-targeted microbubble targeting p-selectin, VEGF-receptor2, and $\alpha_v\beta_3$-integrin has been developed for ultrasound [134].

5 Theranostics

Molecular imaging allows the simultaneous detection of therapeutic targets and monitoring of treatment effect, a diagnosis-treatment strategy referred to as *theranostics*. Future theranostic strategies in the field of stabilization of atherosclerotic plaques could be targeted against inflammation and modulation of angiogenesis.

Theranostic Probes The delivery of targeted contrast agents to the atherosclerotic plaque presents clear opportunities for simultaneous drug delivery [135] Nanoparticles and microbubbles can be used for both in vivo diagnostic imaging and therapeutic drug delivery (theranostic probes). By localized delivery of drugs lower dosages of more potent drugs can be used, while reaching higher concentrations at the disease location. Due to decreased concentration at non-diseased sites the adverse effects of the drugs may be reduced. Theranostic agents can also transport drugs that cannot be administered otherwise (lipophilic drugs, proteins, silencing RNAs, DNA, etc). The development of theranostic nanoparticles is rapid and several types of nanoparticles have been developed [136–138].

Winter et al. [139] demonstrated the potential of theranostics in atherosclerosis. They used theranostic nanoparticles to identify the presence of integrin αvβ3 expressing vasa vasorum in the aortas of cholesterol fed rabbits and evaluate the effect of targeted treatment on angiogenesis. The lipid soluble anti-angiogenic agent fumagillin was incorporated in a integrin αvβ3-targeted paramagnetic nanoparticle. They evaluated the presence of integrin αvβ3 expressing vasa vasorum by MRI during treatment and 1-week posttreatment. The expression of integrin αvβ3 significantly decreased in the targeted fumagillin treated group, while the nontargeted fumagillin and no-drug group showed no change [139].

In the field of theranostic probes ultrasound microbubbles have a special interest because they can both deliver drugs and actively stimulate the uptake of the drugs. Microbubbles can be loaded with drugs and destroyed at the location of interest by the application of a high acoustic pressure ultrasound wave (within the limits of standard ultrasound equipment), releasing the drug [140, 141]. Besides the transportation of drugs to the target location this has also been shown to cause sonoporation and induction of endocytosis, which increases the local uptake of the drug (Fig. 24.10) [142–144]. Sonoporation is the creation of transient micropores in the cellular membrane due to the oscillation and implosion of microbubbles in an ultrasound beam, thus temporarily increasing cellular membrane permeability. Ultrasound has been shown to be able to induce the uptake of DNA and RNA molecules giving it an interesting prospective for gene therapy [140, 145, 146].

6 Angiogenesis Modulating Therapy

Anti-angiogenic Treatment Treatment of intraplaque neovascularization has been proposed as a possible method to stabilize the atherosclerotic plaque [147]. Inhibition of intraplaque neovascularization in animals has already shown to reduce the macrophage accumulation and progression of atherosclerosis [148–150]. Several anti-angiogenic agents are available or under evaluation in clinical trials for the treatment of cancer (http://www.cancer.gov/clinicaltrials/).

However, there are potential problems that need to be accounted for in transferring the anti-angiogenic strategy from cancer to atherosclerosis. First and foremost, the goal for the treatment of cancer is destruction of the tumor, while destruction of the vessel wall, atherosclerotic or not, is not necessarily a good idea. Atherosclerosis demands a different strategy to attack the vasculature. Furthermore, inhibition of angiogenesis might aggravate ischemic end-organ damage. Several strategies for inducing angiogenesis are being investigated to restore blood flow to regions affected by ischemia

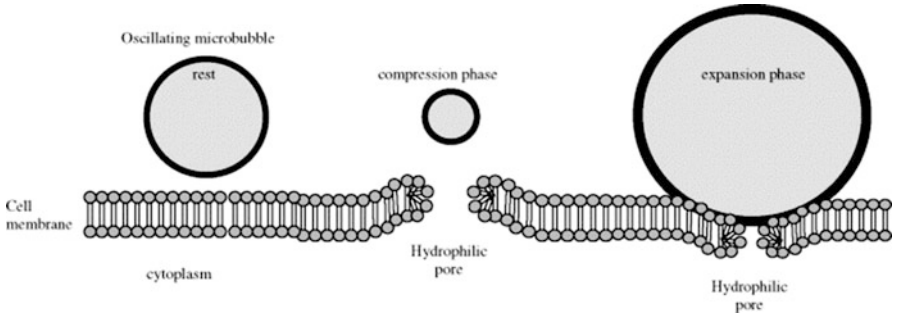

Fig. 24.10 Proposed model of the oscillating microbubble enforced pore formation (sonoporation) in the cell membrane. The pushing and pulling behavior of the microbubble causes rupture of the cell membrane creating a hydrophilic pore allowing trans-membrane flux of fluid and macromolecules. Reproduced with permission from van Wamel et al. [143]

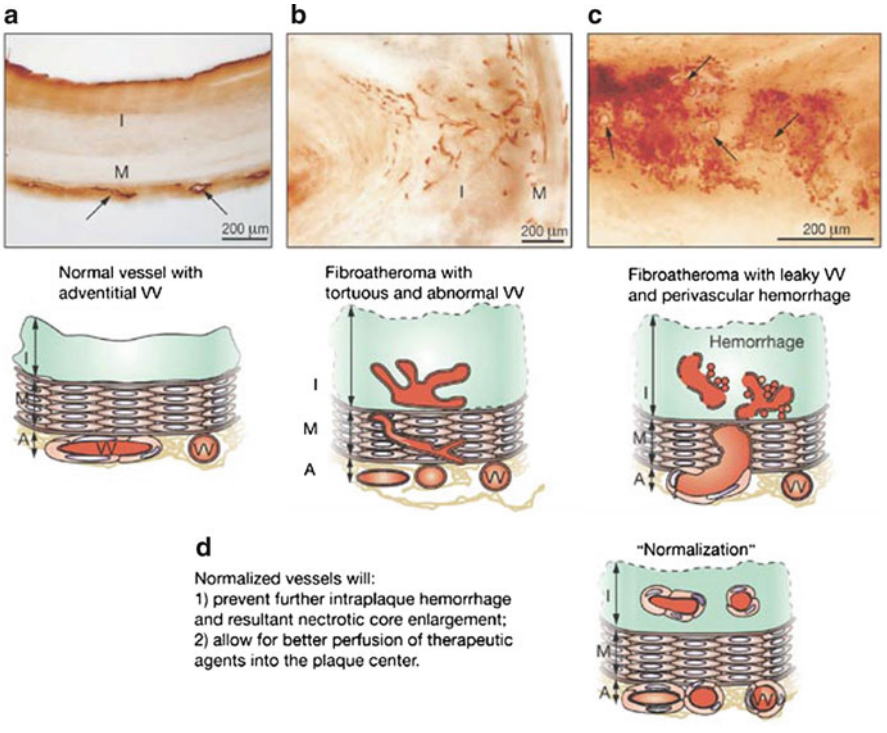

Fig. 24.11 Proposed 'normalization' of plaque microvasculature and its implications in atherosclerotic angiogenesis. Images of 150 m-thick sections of (**a**) normal human coronary artery, and (**b**) fibroatheroma without and (**c**) fibroatheroma with intraplaque hemorrhage. The endothelium was visualized by use of *Ulex europaeus* immunohistochemical staining. (**a**) Adventitial vasa vasorum can be seen (arrows). (**b**) In non-hemorrhagic fibroatheroma the vasa vasorum are intimal and show tortuosity and branching. (**c**) In fibroatheromas with intraplaque hemorrhage the vasa vasorum are disrupted (*arrows*) with surrounding hemorrhage. Intraplaque hemorrhage has been shown to contribute to the necrotic core enlargement and vulnerability to rupture. These specimens (**a**–**c**) are illustrated in corresponding schematics below them. (**d**) Jain et al. hypothesize that normalization of the vasa vasorum with "muscularization" of the capillaries leads to stable vessels that will prevent plaque progression. The absence of leaky vessels should promote plaque stabilization by preventing plaque hemorrhages. *A* adventitia, *I* intima, *M* media, *VV* vasa vasorum. Reproduced with permission from Jain et al. [156]

[151]. This might be overcome by using theranostics to locally deliver antiangiogenic therapy to the plaque.

Destruction of the intraplaque neovasculature could lead to sustained or increased hypoxia. This in turn could lead to further upregulation of genes that promote plaque vulnerability. Rather than eliminating the neovasculature it has been proposed that normalization of the vasculature could help stabilize the plaque [152]. The normalization of the immature intraplaque neovascularization should prevent leakage of erythrocytes, extravasation of lipids, and inflammatory cells that contribute to plaque progression (Fig. 24.11). Furthermore, the presence of these vessels should alleviate hypoxia, thus removing the underlying cause of angiogenesis.

Pro-angiogenic Treatment The induction of angiogenesis by ultrasound contrast agents is currently being explored as a means to restore blood flow in regions affected by ischemia. Targeted stimulation of neovascularization could be of clinical relevance for patients with myocardial ischemia or critical limb ischemia as an alternative treatment strategy for surgical revascularization. Chappell et al. [151] studied microvascular remodeling in a mouse gracilis muscle model. After high-dose administration of microbubble contrast agent and ultrasonic destruction of the microbubbles an impermanent microvascular remodeling response occurred. In contrast to that study, Johnson et al. [152] reported on the bioeffects of microbubble destruction in a gracilis muscle model of 23 Sprague–Dawley rats. Ultrasonic destruction of microbubble contrast agent caused an acute decrease in capillary density, followed by an incomplete angiogenic healing response. In a subsequent study, the gracilis muscles of 150 Sprague–Dawley rats were studied. A statistically significant change in vascular endothelial growth factor (VEGF) was observed, while capillary density was not changed by ultrasonic destruction of microbubble contrast agent [153]. Clearly, further studies are needed to explore the mechanism of action and treatment effect of pro-angiogenic therapy.

7 Conclusions

– Inflammation and angiogenesis are closely related and important factors in early plaque development and plaque vulnerability.

- Molecular imaging can aid in the early detection of plaque formation, provide insights into the natural history of cardiovascular diseases, and function as a surrogate endpoint in clinical trials.
- Several molecular targets involving inflammation and angiogenesis have been identified and tested in vivo; however, the number of contrast agents available for human studies is limited.
- Multimodality imaging and multitargeted contrast agents may improve the accuracy with which a biological process can be identified.
- Future developments in theranostics and antiangiogenic therapy might provide a noninvasive technique for stabilizing the vulnerable plaque.

References

1. Giroud D et al (1992) Relation of the site of acute myocardial infarction to the most severe coronary arterial stenosis at prior angiography. Am J Cardiol 69(8):729–732
2. Pasterkamp G et al (1998) Relation of arterial geometry to luminal narrowing and histologic markers for plaque vulnerability: the remodeling paradox. J Am Coll Cardiol 32(3):655–662
3. Schoenhagen P et al (2000) Extent and direction of arterial remodeling in stable versus unstable coronary syndromes: an intravascular ultrasound study. Circulation 101(6):598–603
4. Hardie AD et al (2007) The impact of expansive arterial remodeling on clinical presentation in carotid artery disease: a multidetector CT angiography study. AJNR Am J Neuroradiol 28(6):1067–1070
5. Naghavi M et al (2003) From vulnerable plaque to vulnerable patient: a call for new definitions and risk assessment strategies: part I. Circulation 108(14):1664–1672
6. Schaar JA et al (2004) Terminology for high-risk and vulnerable coronary artery plaques. Eur Heart J 25(12):1077–1082
7. Virmani R et al (2000) Lessons from sudden coronary death: a comprehensive morphological classification scheme for atherosclerotic lesions. Arterioscler Thromb Vasc Biol 20(5):1262–1275
8. Virmani R et al (2006) Pathology of the vulnerable plaque. J Am Coll Cardiol 47 (8 Suppl):C13–C18
9. Ylä-Herttuala S et al (2011) Stabilisation of atherosclerotic plaques. Thromb Haemost 106(1):1–19
10. Vancraeynest D et al (2011) Imaging the vulnerable plaque. J Am Coll Cardiol 57(20): 1961–1979
11. Cai W et al (2006) How molecular imaging is speeding up antiangiogenic drug development. Mol Cancer Ther 5(11):2624–2633
12. Weissleder R, Pittet MJ (2008) Imaging in the era of molecular oncology. Nature 452(7187):580–589
13. Sanz J, Fayad ZA (2008) Imaging of atherosclerotic cardiovascular disease. Nature 451(7181):953–957
14. Mankoff DA (2007) A definition of molecular imaging. J Nucl Med 48(6):18N–21N
15. Jaffer FA, Weissleder R (2005) Molecular imaging in the clinical arena. JAMA 293(7):855–862
16. Libby P, DiCarli M, Weissleder R (2010) The vascular biology of atherosclerosis and imaging targets. J Nucl Med 51(Suppl 1):33S–37S
17. Maiellaro K, Taylor WR (2007) The role of the adventitia in vascular inflammation. Cardiovasc Res 75(4):640–648
18. Gössl M et al (2010) Segmental heterogeneity of vasa vasorum neovascularization in human coronary atherosclerosis. JACC Cardiovasc Imaging 3(1):32–40
19. Hildebrandt HA et al (2008) Differential distribution of vasa vasorum in different vascular beds in humans. Atherosclerosis 199(1):47–54
20. Wolinsky H, Glagov S (1967) Nature of species differences in the medial distribution of aortic vasa vasorum in mammals. Circ Res 20(4):409–421
21. Heistad DD et al (1981) Role of vasa vasorum in nourishment of the aortic wall. Am J Physiol Heart Circ Physiol 240(5):H781–H787
22. Wilens SL, Malcolm JA, Vasquez JM (1965) Experimental infarction (medial necrosis) of the dog's aorta. Am J Pathol 47(4):695–711
23. Stefanadis C et al (1995) Aorta: structure/function: effect of vasa vasorum flow on structure and function of the aorta in experimental animals. Circulation 91(10):2669–2678
24. Wolinsky H, Glagov S (1969) Comparison of abdominal and thoracic aortic medial structure in mammals. Circ Res 25(6):677–686
25. Gössl M et al (2003) Functional anatomy and hemodynamic characteristics of vasa vasorum in the walls of porcine coronary arteries. Anat Rec A Discov Mol Cell Evol Biol 272(2):526–537
26. Jeziorska M, Woolley DE (1999) Local neovascularization and cellular composition within vulnerable regions of atherosclerotic plaques of human carotid arteries. J Pathol 188(2):189–196
27. Moreno PR et al (2004) Plaque neovascularization is increased in ruptured atherosclerotic lesions of human aorta: implications for plaque vulnerability. Circulation 110(14):2032–2038
28. Mofidi R et al (2001) Association between plaque instability, angiogenesis and symptomatic carotid occlusive disease. Br J Surg 88(7):945–950
29. Purushothaman KR et al (2003) Neovascularization is the most powerful independent predictor for progression to disruption in high-risk atherosclerotic plaques. J Am Coll Cardiol 41(6 Suppl 2):352–353
30. Hellings WE et al (2010) Composition of carotid atherosclerotic plaque is associated with cardiovascular outcome. A prognostic study. Circulation 121(17):1941–1950
31. Mause SF, Weber C (2009) Intrusion through the fragile back door: immature plaque microvessels as entry portals for leukocytes and erythrocytes in atherosclerosis. J Am Coll Cardiol 53(17):1528–1531
32. McCarthy MJ et al (1999) Angiogenesis and the atherosclerotic carotid plaque: an association between symptomatology and plaque morphology. J Vasc Surg 30(2):261–268
33. Dunmore BJ et al (2007) Carotid plaque instability and ischemic symptoms are linked to immaturity of microvessels within plaques. J Vasc Surg 45(1):155–159
34. Sluimer J et al (2009) Thin-walled microvessels in human coronary atherosclerotic plaques show incomplete endothelial junctions relevance of compromised structural integrity for intraplaque microvascular leakage. J Am Coll Cardiol 53(17):1517–1527
35. Sluimer JC, Daemen MJ (2009) Novel concepts in atherogenesis: angiogenesis and hypoxia in atherosclerosis. J Pathol 218(1):7–29
36. Kolodgie FD et al (2003) Intraplaque hemorrhage and progression of coronary atheroma. N Engl J Med 349(24):2316–2325
37. Moulton KS (2006) Angiogenesis in atherosclerosis: gathering evidence beyond speculation. Curr Opin Lipidol 17(5):548–555
38. Carmeliet P (2000) Mechanisms of angiogenesis and arteriogenesis. Nat Med 6(4):389–395

39. Semenza GL (2003) Targeting HIF-1 for cancer therapy. Nat Rev Cancer 3(10):721–732
40. Pugh CW, Ratcliffe PJ (2003) Regulation of angiogenesis by hypoxia: role of the HIF system. Nat Med 9(6):677–684
41. Sluimer JC et al (2008) Hypoxia, hypoxia-inducible transcription factor, and macrophages in human atherosclerotic plaques are correlated with intraplaque angiogenesis. J Am Coll Cardiol 51(13):1258–1265
42. Bjornheden T et al (1999) Evidence of hypoxic areas within the arterial wall in vivo. Arterioscler Thromb Vasc Biol 19(4):870–876
43. Jeziorska M, Woolley DE (1999) Neovascularization in early atherosclerotic lesions of human carotid arteries: its potential contribution to plaque development. Hum Pathol 30(8):919–925
44. Fleiner M et al (2004) Arterial neovascularization and inflammation in vulnerable patients: early and late signs of symptomatic atherosclerosis. Circulation 110(18):2843–2850
45. Kwon HM et al (1998) Enhanced coronary vasa vasorum neovascularization in experimental hypercholesterolemia. J Clin Invest 101(8):1551–1556
46. Herrmann J et al (2001) Coronary vasa vasorum neovascularization precedes epicardial endothelial dysfunction in experimental hypercholesterolemia. Cardiovasc Res 51(4):762–766
47. Lusis AJ (2000) Atherosclerosis. Nature 407(6801):233–241
48. Gössl M et al (2009) Low vasa vasorum densities correlate with inflammation and subintimal thickening: potential role in location – determination of atherogenesis. Atherosclerosis 206(2):362–368
49. Bayer I et al (2002) Experimental angiogenesis of arterial vasa vasorum. Cell Tissue Res 307(3):303–313
50. Dobrucki LW, Sinusas AJ (2010) PET and SPECT in cardiovascular molecular imaging. Nat Rev Cardiol 7(1):38–47
51. Sosnovik D, Nahrendorf M, Weissleder R (2008) Magnetic nanoparticles for MR imaging: agents, techniques and cardiovascular applications. Basic Res Cardiol 103(2):122–130
52. Kuo PH et al (2007) Gadolinium-based MR contrast agents and nephrogenic systemic fibrosis. Radiology 242(3):647–649
53. Powers J, Averkiou M, Bruce M (2009) Principles of cerebral ultrasound contrast imaging. Cerebrovasc Dis 27(Suppl 2):14–24
54. Main M, Goldman J, Grayburn P (2009) Ultrasound contrast agents: balancing safety versus efficacy. Expert Opin Drug Saf 8(1):49–56
55. Main ML, Goldman JH, Grayburn PA (2007) Thinking outside the "box" – the ultrasound contrast controversy. J Am Coll Cardiol 50(25):2434–2437
56. Hyafil F et al (2007) Noninvasive detection of macrophages using a nanoparticulate contrast agent for computed tomography. Nat Med 13(5):636–641
57. Cormode DP et al (2008) Nanocrystal core high-density lipoproteins: a multimodality contrast agent platform. Nano Lett 8(11):3715–3723
58. Cormode DP et al (2010) Atherosclerotic plaque composition: analysis with multicolor CT and targeted gold nanoparticles. Radiology 256(3):774–782
59. Rabin O et al (2006) An X-ray computed tomography imaging agent based on long-circulating bismuth sulphide nanoparticles. Nat Mater 5(2):118–122
60. Pontone G et al (2009) Diagnostic accuracy of coronary computed tomography angiography: a comparison between prospective and retrospective electrocardiogram triggering. J Am Coll Cardiol 54(4):346–355
61. Nash K, Hafeez A, Hou S (2002) Hospital-acquired renal insufficiency. Am J Kidney Dis 39(5):930–936
62. Gaemperli O, Kaufmann PA (2011) PET and PET/CT in cardiovascular disease. Ann N Y Acad Sci 1228(1):109–136
63. Izquierdo-Garcia D et al (2009) Comparison of methods for magnetic resonance-guided [18-F]fluorodeoxyglucose positron emission tomography in human carotid arteries: reproducibility, partial volume correction, and correlation between methods. Stroke 40(1):86–93
64. Mulder WJ et al (2007) Magnetic and fluorescent nanoparticles for multimodality imaging. Nanomedicine 2(3):307–324
65. Nahrendorf M et al (2008) Nanoparticle PET-CT imaging of macrophages in inflammatory atherosclerosis. Circulation 117(3):379–387
66. O'Brien KD et al (1993) Vascular cell adhesion molecule-1 is expressed in human coronary atherosclerotic plaques. Implications for the mode of progression of advanced coronary atherosclerosis. J Clin Invest 92(2):945–951
67. O'Brien KD et al (1996) Neovascular expression of e-selectin, intercellular adhesion molecule-1, and vascular cell adhesion molecule-1 in human atherosclerosis and their relation to intimal leukocyte content. Circulation 93(4):672–682
68. Kelly KA et al (2005) Detection of vascular adhesion molecule-1 expression using a novel multimodal nanoparticle. Circ Res 96(3):327–336
69. Nahrendorf M et al (2006) Noninvasive vascular cell adhesion molecule-1 imaging identifies inflammatory activation of cells in atherosclerosis. Circulation 114(14):1504–1511
70. Kaufmann BA et al (2007) Molecular imaging of inflammation in atherosclerosis with targeted ultrasound detection of vascular cell adhesion molecule-1. Circulation 116(3):276–284
71. Villanueva FS et al (1998) Microbubbles targeted to intercellular adhesion molecule-1 bind to activated coronary artery endothelial cells. Circulation 98(1):1–5
72. Demos SM et al (1999) In vivo targeting of acoustically reflective liposomes for intravascular and transvascular ultrasonic enhancement. J Am Coll Cardiol 33(3):867–875
73. Kang HW et al (2002) Magnetic resonance imaging of inducible e-selectin expression in human endothelial cell culture. Bioconjug Chem 13(1):122–127
74. Kang HW et al (2006) Targeted imaging of human endothelial-specific marker in a model of adoptive cell transfer. Lab Invest 86(6):599–609
75. McAteer MA et al (2008) Magnetic resonance imaging of endothelial adhesion molecules in mouse atherosclerosis using dual-targeted microparticles of iron oxide. Arterioscler Thromb Vasc Biol 28(1):77–83
76. Boutry S et al (2005) Magnetic resonance imaging of inflammation with a specific selectin-targeted contrast agent. Magn Reson Med 53(4):800–807
77. Radermacher KA et al (2009) In vivo detection of inflammation using pegylated iron oxide particles targeted at e-selectin: a multimodal approach using MR imaging and EPR spectroscopy. Invest Radiol 44(7):398–404
78. Moore KJ, Kathryn J, Tabas I (2011) Macrophages in the pathogenesis of atherosclerosis. Cell 145(3):341–355
79. de Boer OJ et al (1999) Leucocyte recruitment in rupture prone regions of lipid-rich plaques: a prominent role for neovascularization? Cardiovasc Res 41(2):443–449
80. Rogers WJ, Basu P (2005) Factors regulating macrophage endocytosis of nanoparticles: implications for targeted magnetic resonance plaque imaging. Atherosclerosis 178(1):67–73
81. Lipinski MJ et al (2006) MRI to detect atherosclerosis with gadolinium-containing immunomicelles targeting the macrophage scavenger receptor. Magn Reson Med 56(3):601–610
82. Schmitz SA et al (2001) Magnetic resonance imaging of atherosclerotic plaques using superparamagnetic iron oxide particles. J Magn Reson Imaging 14(4):355–361

83. Kooi ME et al (2003) Accumulation of ultrasmall superparamagnetic particles of iron oxide in human atherosclerotic plaques can be detected by in vivo magnetic resonance imaging. Circulation 107(19):2453–2458
84. Trivedi RA et al (2004) In vivo detection of macrophages in human carotid atheroma: temporal dependence of ultrasmall superparamagnetic particles of iron oxide-enhanced MRI. Stroke 35(7):1631–1635
85. Trivedi RA et al (2006) Identifying inflamed carotid plaques using in vivo USPIO-enhanced MR imaging to label plaque macrophages. Arterioscler Thromb Vasc Biol 26(7):1601–1606
86. Kawahara I et al (2008) Potential of magnetic resonance plaque imaging using superparamagnetic particles of iron oxide for the detection of carotid plaque. Neurol Med Chir (Tokyo) 48(4):157–161
87. Tang TY et al (2009) The ATHEROMA (Atorvastatin Therapy: Effects on Reduction of Macrophage Activity) study: evaluation using ultrasmall superparamagnetic iron oxide-enhanced magnetic resonance imaging in carotid disease. J Am Coll Cardiol 53(22):2039–2050
88. Yun M et al (2001) F-18 FDG uptake in the large arteries: a new observation. Clin Nucl Med 26(4):314–319
89. Lederman RJ et al (2001) Detection of atherosclerosis using a novel positron-sensitive probe and 18-fluorodeoxyglucose (FDG). Nucl Med Commun 22(7):747–753
90. Ogawa M et al (2004) (18)F-FDG accumulation in atherosclerotic plaques: immunohistochemical and PET imaging study. J Nucl Med 45(7):1245–1250
91. Tawakol A et al (2005) Noninvasive in vivo measurement of vascular inflammation with F-18 fluorodeoxyglucose positron emission tomography. J Nucl Cardiol 12(3):294–301
92. Ogawa M et al (2006) Application of 18F-FDG PET for monitoring the therapeutic effect of antiinflammatory drugs on stabilization of vulnerable atherosclerotic plaques. J Nucl Med 47(11):1845–1850
93. Rudd JHF et al (2002) Imaging atherosclerotic plaque inflammation with [18F]-fluorodeoxyglucose positron emission tomography. Circulation 105(23):2708–2711
94. Tawakol A et al (2006) In vivo 18F-fluorodeoxyglucose positron emission tomography imaging provides a noninvasive measure of carotid plaque inflammation in patients. J Am Coll Cardiol 48(9):1818–1824
95. Tahara N et al (2007) Vascular inflammation evaluated by [18F]-fluorodeoxyglucose positron emission tomography is associated with the metabolic syndrome. J Am Coll Cardiol 49(14):1533–1539
96. Tahara N et al (2007) The prevalence of inflammation in carotid atherosclerosis: analysis with fluorodeoxyglucose positron emission tomography. Eur Heart J 28(18):2243–2248
97. Rudd JHF et al (2008) Atherosclerosis inflammation imaging with 18F-FDG PET: carotid, iliac, and femoral uptake reproducibility, quantification methods, and recommendations. J Nucl Med 49(6):871–878
98. Davies JR et al (2005) Identification of culprit lesions after transient ischemic attack by combined 18F fluorodeoxyglucose positron-emission tomography and high-resolution magnetic resonance imaging. Stroke 36(12):2642–2647
99. Rominger A et al (2009) 18F-FDG PET/CT identifies patients at risk for future vascular events in an otherwise asymptomatic cohort with neoplastic disease. J Nucl Med 50(10):1611–1620
100. Tahara N et al (2006) Simvastatin attenuates plaque inflammation: evaluation by fluorodeoxyglucose positron emission tomography. J Am Coll Cardiol 48(9):1825–1831
101. Galis ZS, Khatri JJ (2002) Matrix metalloproteinases in vascular remodeling and atherogenesis: the good, the bad, and the ugly. Circ Res 90(3):251–262
102. Lancelot E et al (2008) Evaluation of matrix metalloproteinases in atherosclerosis using a novel noninvasive imaging approach. Arterioscler Thromb Vasc Biol 28(3):425–432
103. Ohshima S et al (2009) Molecular imaging of matrix metalloproteinase expression in atherosclerotic plaques of mice deficient in apolipoprotein E or low-density-lipoprotein receptor. J Nucl Med 50(4):612–617
104. Ronald JA et al (2009) Enzyme-sensitive magnetic resonance imaging targeting myeloperoxidase identifies active inflammation in experimental rabbit atherosclerotic plaques. Circulation 120(7):592–599
105. Carmeliet P, Jain RK (2000) Angiogenesis in cancer and other diseases. Nature 407(6801): 249–257
106. Staub D et al (2010) Contrast-enhanced ultrasound imaging of the vasa vasorum: from early atherosclerosis to the identification of unstable plaques. JACC Cardiovasc Imaging 3(7):761–771
107. Shah F et al (2007) Contrast-enhanced ultrasound imaging of atherosclerotic carotid plaque neovascularization: a new surrogate marker of atherosclerosis? Vasc Med 12(4):291–297
108. Coli S et al (2008) Contrast-enhanced ultrasound imaging of intraplaque neovascularization in carotid arteries: correlation with histology and plaque echogenicity. J Am Coll Cardiol 52(3):223–230
109. Giannoni MF et al (2009) Contrast carotid ultrasound for the detection of unstable plaques with neoangiogenesis: a pilot study. Eur J Vasc Endovasc Surg 37(6):722–727
110. Kerwin W et al (2003) Quantitative magnetic resonance imaging analysis of neovasculature volume in carotid atherosclerotic plaque. Circulation 107(6):851–856
111. Kerwin WS et al (2008) MR imaging of adventitial vasa vasorum in carotid atherosclerosis. Magn Reson Med 59(3):507–514
112. Bredow S et al (2000) Imaging of tumour neovasculature by targeting the TGF-[beta] binding receptor endoglin. Eur J Cancer 36(5):675–681
113. Korpanty G et al (2007) Monitoring response to anticancer therapy by targeting microbubbles to tumor vasculature. Clin Cancer Res 13(1):323–330
114. Willmann J et al (2008) Dual-targeted contrast agent for US assessment of tumor angiogenesis in vivo. Radiology 248(3):936–944
115. Pochon SP et al (2010) BR55: a lipopeptide-based VEGFR2-targeted ultrasound contrast agent for molecular imaging of angiogenesis. Invest Radiol 45(2):89–95
116. Hynes RO (1987) Integrins: a family of cell surface receptors. Cell 48(4):549–554
117. Hoshiga M et al (1995) Alpha-v beta-3 integrin expression in normal and atherosclerotic artery. Circ Res 77(6):1129–1135
118. Brooks PC, Clark RA, Cheresh DA (1994) Requirement of vascular integrin alpha v beta 3 for angiogenesis. Science 264(5158):569–571
119. Haubner R (2006) Alpha v beta 3-integrin imaging: a new approach to characterise angiogenesis? Eur J Nucl Med Mol Imaging 33(Suppl 1):54–63
120. Winter PM et al (2003) Molecular imaging of angiogenesis in early-stage atherosclerosis with alpha(v)beta3-integrin-targeted nanoparticles. Circulation 108(18):2270–2274
121. Burtea C et al (2008) Molecular imaging of alpha v beta 3 integrin expression in atherosclerotic plaques with a mimetic of RGD peptide grafted to Gd-DTPA. Cardiovasc Res 78(1):148–157
122. Haubner R et al (2005) Noninvasive visualization of the activated alphavbeta3 integrin in cancer patients by positron emission tomography and [18F] Galacto-RGD. PLoS Med 2(3):e70
123. Meoli D et al (2004) Noninvasive imaging of myocardial angiogenesis following experimental myocardial infarction. J Clin Invest 113(12):1684–1691

124. Sadeghi MM et al (2004) Detection of injury-induced vascular remodeling by targeting activated {alpha}v{beta}3 integrin in vivo. Circulation 110(1):84–90
125. Hua J et al (2005) Noninvasive imaging of angiogenesis with a 99mTc-labeled peptide targeted at [alpha]v[beta]3 integrin after murine hindlimb ischemia. Circulation 111(24):3255–3260
126. Ellegala DB et al (2003) Imaging tumor angiogenesis with contrast ultrasound and microbubbles targeted to [alpha]v[beta]3. Circulation 108(3):336–341
127. Leong-Poi H et al (2003) Noninvasive assessment of angiogenesis by ultrasound and microbubbles targeted to alpha(v)-integrins. Circulation 107(3):455–460
128. Posey JA et al (2001) A pilot trial of vitaxin, a humanized anti-vitronectin receptor (anti αvβ3) antibody in patients with metastatic cancer. Cancer Biother Radiopharm 16(2):125–132
129. Castellani P et al (2002) Differentiation between high-and low-grade astrocytoma using a human recombinant antibody to the extra domain-B of fibronectin. Am J Pathol 161(5):1695–1700
130. Matter CM et al (2004) Molecular imaging of atherosclerotic plaques using a human antibody against the extra-domain B of fibronectin. Circ Res 95(12):1225–1233
131. Santimaria M et al (2003) Immunoscintigraphic detection of the ED-B domain of fibronectin, a marker of angiogenesis, in patients with cancer. Clin Cancer Res 9(2):571–579
132. Ferrante EA et al (2009) Dual targeting improves microbubble contrast agent adhesion to VCAM-1 and P-selectin under flow. J Control Release 140(2):100–107
133. Weller GER et al (2005) Targeted ultrasound contrast agents: in vitro assessment of endothelial dysfunction and multi-targeting to ICAM-1 and sialyl Lewisx. Biotechnol Bioeng 92(6):780–788
134. Warram JM et al (2011) A triple-targeted ultrasound contrast agent provides improved localization to tumor vasculature. J Ultrasound Med 30(7):921–931
135. Lee DY, Li KCP (2011) Molecular theranostics: a primer for the imaging professional. AJR Am J Roentgenol 197(2):318–324
136. Wickline SA et al (2006) Applications of nanotechnology to atherosclerosis, thrombosis, and vascular biology. Arterioscler Thromb Vasc Biol 26(3):435–441
137. Sahoo SK, Labhasetwar V (2003) Nanotech approaches to drug delivery and imaging. Drug Discov Today 8(24):1112–1120
138. Sandhiya S, Dkhar SA, Surendiran A (2009) Emerging trends of nanomedicine – an overview. Fundam Clin Pharmacol 23(3):263–269
139. Winter PM et al (2006) Endothelial alpha(v)beta3 integrin-targeted fumagillin nanoparticles inhibit angiogenesis in atherosclerosis. Arterioscler Thromb Vasc Biol 26(9):2103–2109
140. Newman CMH, Bettinger T (2007) Gene therapy progress and prospects: ultrasound for gene transfer. Gene Ther 14(6):465–475
141. Frinking PJA et al (1998) Effect of ultrasound on the release of micro-encapsulated drugs. Ultrasonics 36(1–5):709–712
142. Ohl CD et al (2006) Sonoporation from jetting cavitation bubbles. Biophys J 91(11): 4285–4295
143. van Wamel A et al (2006) Vibrating microbubbles poking individual cells: drug transfer into cells via sonoporation. J Control Release 112(2):149–155
144. Meijering BDM et al (2009) Ultrasound and microbubble-targeted delivery of macromolecules is regulated by induction of endocytosis and pore formation. Circ Res 104(5):679–687
145. Kobulnik J et al (2009) Comparison of gene delivery techniques for therapeutic angiogenesis: ultrasound-mediated destruction of carrier microbubbles versus direct intramuscular injection. J Am Coll Cardiol 54(18):1735–1742
146. Suzuki JI et al (2010) Ultrasound-microbubble-mediated intercellular adhesion molecule-1 small interfering ribonucleic acid transfection attenuates neointimal formation after arterial injury in mice. J Am Coll Cardiol 55(9):904–913
147. Finn AV, Jain RK (2010) Coronary plaque neovascularization and hemorrhage: a potential target for plaque stabilization? JACC Cardiovasc Imaging 3(1):41–44
148. Moulton KS et al (2003) Inhibition of plaque neovascularization reduces macrophage accumulation and progression of advanced atherosclerosis. Proc Natl Acad Sci USA 100(8):4736–4741
149. Gössl M et al (2009) Prevention of vasa vasorum neovascularization attenuates early neointima formation in experimental hypercholesterolemia. Basic Res Cardiol 104(6):695–706
150. Moulton KS et al (1999) Angiogenesis inhibitors endostatin or TNP-470 reduce intimal neovascularization and plaque growth in apolipoprotein E-deficient mice. Circulation 99(13):1726–1732
151. Chappell JC, Klibanov AL, Price RJ (2005) Ultrasound-microbubble-induced neovascularization in mouse skeletal muscle. Ultrasound Med Biol 31(10):1411–1422
152. Johnson CA, Sarwate S, Miller RJ, O'Brien WD (2010) A temporal study of ultrasound contrast agent-induced changes in capillary density. J Ultrasound Med 29(9):1267–1275
153. Johnson CA, Miller RJ, O'Brien WD (2011) Ultrasound contrast agents affect the angiogenic response. J Ultrasound Med 30(7):933–941
154. ten Kate GL et al (2010) Molecular imaging of inflammation and intraplaque vasa vasorum: a step forward to identification of vulnerable plaques? J Nucl Cardiol 17(5):897–912
155. Sipkins DA et al (2000) ICAM-1 expression in autoimmune encephalitis visualized using magnetic resonance imaging. J Neuroimmunol 104(1):1–9
156. Jain RK et al (2007) Antiangiogenic therapy for normalization of atherosclerotic plaque vasculature: a potential strategy for plaque stabilization. Nat Clin Pract Cardiovasc Med 4(9):491–502
157. Schoenenberger F, Mueller A (1960) Ueber die vaskularisierung der rinderaortenwand. Helvet Physiol Pharmacol Acta 18:136–150

Carotid Angioplasty and Stenting

25

Sebastián Baldi, Luis García Nielsen, Tobias Zander, Rafael Feldman, and Manuel Maynar

1 Introduction

Stroke is a leading cause of functional impairment in adults, with approximately 20% of survivors requiring institutional care and up to one-third having a permanent disability. This is of great importance due to economic and social impact on each community. Most strokes are ischemic and caused by atherosclerotic emboli from the carotid artery or the aortic arch, or they are related to thromboembolism from the heart chambers [1].

Carotid occlusive disease is responsible for 25% of these strokes. The most common condition affecting the carotid arteries is atherosclerosis. Atherosclerosis is a systemic disease that affects the arteries of medium and large size, which commonly affects the carotid artery bifurcation. There are other conditions affecting the carotids that can lead to stroke such as extracranial carotid aneurysms and traumatic, iatrogenic, or spontaneous dissections. Large population-based studies indicate that the prevalence of carotid stenosis is approximately 0.5% after age 60 and increases to 10% in persons older than age 80 years [2].

The primary mechanism involved in strokes in patients with carotid stenosis is atherosclerotic debris or thrombotic material embolism from the plaque into the distal cerebral vasculature [3]. The annual risk of stroke is between 1% and 4.3% for asymptomatic patients with >50% stenosis of the carotid artery [4]. Symptomatic patients have a worse prognosis that is related to the degree of stenosis [5]. In the North American Symptomatic Carotid Endarterectomy Trial (NASCET) study, the risk of recurrent ipsilateral stroke rose to 4.4% in patients with stenosis between 50% and 69%, and 13% in those with a stenosis greater than 70% [6].

1.1 Background

Being atherosclerotic disease the most common condition, treatment is usually referred to revascularization. In 1953, DeBakey performed the first successful carotid endarterectomy (CEA) for the treatment of an occluded cervical carotid artery [7]. In 1954, Eastcott performed the first successful CEA in which the circulation to the brain was intentionally interrupted to remove a stenotic plaque [8]. Since then, CEA was performed worldwide despite a temporary decline in the mid-1980s, when a number of critical reports suggested unacceptable rates of perioperative stroke or death, and a high rate of procedures performed for inappropriate indications [9, 10].

The standard of care for symptomatic and asymptomatic patients has been established by the results of four large prospective randomized trials comparing medical therapy with CEA: NASCET [6, 11, 12], the European Carotid Surgery Trial (ECST) [13, 14], the Asymptomatic Carotid Atherosclerosis Study (ACAS) [15], and the Asymptomatic Carotid Surgery Trial (ACST) [16]. These trials have demonstrated that surgical carotid endarterectomy confers a significant benefit over best current medical management in patients with symptomatic carotid stenosis >70% with lesser, albeit significant, degrees of benefit in symptomatic lesions of 50–69% and asymptomatic lesions of >60%.

Carotid endarterectomy was accepted as the standard of treatment in this set of patients. However, it is important to notice that in the daily practice, CEA is commonly performed in patients who would have been excluded from these randomized trials. In higher risk patients, particularly those with contralateral occlusion, previous ipsilateral CEA, severe cardiopulmonary comorbidities, prior neck irradiation,

S. Baldi (✉) • T. Zander • M. Maynar
Department of Endovascular Therapy, Hospiten Rambla Hospital, Rambla General Franco 115, 38001 Santa Cruz de Tenerife, Spain
e-mail: js.baldi@yahoo.com; tobiaszander@gmx.net; mmaynar@yahoo.com

L.G. Nielsen • R. Feldman
Department of Interventional Cardiology and Cardiovascular Surgery, Clínica Sarmiento, San Miguel de Tucumán, Argentina
e-mail: lgarcianielsen@yahoo.com.ar; rafafeldman@gmail.com

L. Saba et al. (eds.), *Multi-Modality Atherosclerosis Imaging and Diagnosis*,
DOI 10.1007/978-1-4614-7425-8_25,

and inaccessible lesions above the C2 level, morbidity and mortality related to CEA have been reported in up to 18% of patients [17, 18].

Endovascular treatment arrived as an alternative to CEA. It may offer some advantages: general anesthesia is usually not required which allows to control the patient's clinical status during the procedure; shorter recuperation period; and no cervical incision is made eliminating the risk of cranial nerve palsies, wound infections, or neck hematomas. Kerber et al. reported the first percutaneous transluminal balloon angioplasty for carotid artery stenosis in 1980 [19]. In 1987, Theron et al. published the first large series of internal carotid angioplasty. Technical success was achieved in 94% of cases, with a 4.1% rate of serious morbidity [20]. In a review of the literature, Kachel et al. reported a 96.2% rate of technical success, with a 2.1% rate of morbidity, 6.3% rate of transient minor complications, and no deaths over 523 procedures [21].

1.2 Status of Clinical Trials and Registries

The first randomized trial comparing endovascular and surgical treatments, the Carotid and Vertebral Artery Transluminal Angioplasty Study (CAVATAS), included 504 patients enrolled between 1992 and 1997 and was designed to compare balloon angioplasty alone versus CEA. Stents, when they became available, were incorporated as well, but only accounted for 26% of cases. The CAVATAS trial demonstrated no difference between endovascular and surgical treatment in the rate of disabling stroke or death within 30 days [22]. Despite these favorable results, balloon angioplasty has a number of potential limitations, including vessel wall recoil, intimal dissection, and plaque dislodgement with embolization.

Carotid artery stenting (CAS) was then proposed to replace balloon angioplasty alone; it is feasible and safe and shows comparable procedural outcomes in patients with or without contralateral stenosis. Therefore, as technology evolved, technical skills of different operators improved and the results of comparative studies were published, widespread use of CAS has been accepted. Unlike CEA, CAS is not limited to the cervical portion of the carotid artery.

The Wallstent was the first multicenter randomized trial designed to evaluate CEA and CAS equivalence. The trial was stopped due to worse outcomes for the CAS group. Critical to interpreting these results is the fact that in the Wallstent trial distal embolic protection devices (EPDs) were not used [23, 24]. Between 1996 and 2001, 11 large carotid stent series have been published. Patients at high risk were excluded in these studies. The overall reported rate of technical success was >95%; procedure-related mortality rates (including cardiac deaths) were 0.6–4.5%; and major stroke rates were 0–4.5% [2]. Many reports also demonstrated that CAS is feasible and safe in high-risk patients [25]. A report consisting exclusively of symptomatic NASCET-ineligible patients with a high proportion of anatomic, medical, and neurological risk factors (Sundt grades 3 and 4) [26] concluded that carotid stent angioplasty can be performed in this set of patients with a periprocedural risk of stroke and death comparable to those of NASCET and other published endarterectomy series [27].

The Stenting and Angioplasty with Protection in Patients at High Risk for Endarterectomy Investigation (SAPPHIRE) was the first randomized multicenter trial comparing CEA and CAS in patients at increased risk for surgery. Among high-risk patients CAS was associated with a 56% reduction in perioperative death, stroke, and myocardial infarction (MI) compared with CEA, and a 39% reduction in death and ipsilateral stroke at one year. After 3 years of follow-up, there were no differences between the groups [28].

After this, five large randomized controlled trials have compared CAS with CEA in usual- or average-surgical-risk patients: the SPACE (Stent-supported Percutaneous Angioplasty of the Carotid artery versus Endarterectomy) [29], EVA-3S (Endarterectomy Versus Angioplasty in Patients with Symptomatic Severe Carotid Stenosis) [30], ICSS (CAVATAS-2-International Carotid Stenting Study) [31], CREST (Carotid Revascularization and Endarterectomy versus Stenting Trial) [32], and CaRRESS (Carotid Artery Endarterectomy Stenting Study) [33].

The EVA-3S, a randomized trial to assess the non-inferiority of CAS versus CEA, was stopped early for safety concerns with a superior 30-day stroke and death outcome in the CAS group. However, the EVA-3S trial allowed very inexperienced CAS operators, and the use of embolic protection was not required.

The SPACE compared CAS vs. CEA in 1,200 patients with symptomatic carotid artery stenosis: CAS ($n = 605$) or CEA ($n = 595$). The 30-day stroke and death rate was not different between the groups (6.84% for CAS and 6.34% for CEA). After 2 years of follow-up there continued to be no differences between the CEA or CAS groups; however, patients >68 years had a statistically significant better outcome with CAS compared with CEA.

ICSS is a multinational prospective trial randomizing symptomatic patients equally suited for CAS or CEA. Although the ICSS trial found an excess of minor strokes in the CAS group, there was no difference for the primary end point of disabling stroke or death between CAS and CEA. Once again, there was a significant imbalance in the experience level of the investigators between types of procedures.

The CREST trial enrolled 2,502 patients with an average surgical risk. There was no difference between CAS and CEA for the primary end point: death, stroke, or MI at 30

days, and ipsilateral stroke within 60 days. Patients were followed up to 4 years without any difference between CAS and CEA.

Finally, the CaRRESS was a non-randomized study comparing protected CAS with CEA in symptomatic (32%) and asymptomatic patients (68%) with low and high surgical risk. Nonsignificant difference in the rate of stroke and death at 30 days and 1 year (2.1% vs. 3.6% and 10% vs. 13.6%, respectively) was found.

In the high-risk stent registry ARCHeR (Acculink for Revascularization of Carotids in High Risk Patients) the primary end point (death, stroke, MI at 30 days plus ipsilateral stroke at 1 year) was 9.6% [34]. The BEACH trial demonstrated that CAS using the WALLSTENT in combination with the Filter Wire emboli protection system is non-inferior to (equivalent or better than) CEA in high-surgical-risk patients [35].

The German Carotid Artery Stent (ALKK-CAS) registry studied the safety of carotid artery stenting in unselected patients with contralateral occlusion and significant ipsilateral stenosis. They found low risk of periprocedural events, supporting CAS as an attractive option for the treatment of these patients [36].

Most of the registries and well-conducted trials demonstrated that the risk of death or nonfatal stroke following CAS is equivalent to CEA in a broad category of patients with carotid stenosis.

2 High-Risk Plaque

The term high-risk or "vulnerable" plaque has been proposed because it has been recognized that an ischemic complication—not only in the cerebral territory—can occur even in low-grade stenosis. Other factors than the degree of luminal stenosis have been reported to be determinants, such as the composition or the superficial structure of an atherosclerotic plaque [37]. Vulnerable plaques are prone to rupture and are associated with increased risk for cerebrovascular complications. Major and minor criteria have been proposed to characterize high-risk plaques, but the predictive value has not been evaluated yet.

2.1 Major Criteria

Active Inflammation: Active inflammation plays a major role in the initiation and progression of an arteriosclerotic plaque, and therapeutic approaches are directed to treat the inflammatory process. Neovessel formation in carotid plaques contributes to plaque instability with a significant increase of plaque hemorrhage and fibrous cap rupture [38]. MRI imaging has the potential to detect the inflammatory process depicting increased contrast enhancement and thickening of the vascular wall.

Thin Cap with Large Lipid Core: The fibrous cap separates the inner lipid content from the blood flow. A large lipid-necrotic core and a thin fibrous cap are associated with an increased risk of cerebrovascular events as thinner caps are more likely to rupture [39]. Radiological imaging methods should be able to quantify the lipid-necrotic core and the thickness of the fibrous cap (Fig. 25.1).

Endothelial Denudation with Superficial Platelet Aggregation and Fibrin Deposition: Endothelial Denudation is defined as the absence of an endothelium [39]. Here platelet aggregation or fibrin deposition increases the risk of cardiovascular events [40]. MRI can be useful to identify overlaying intraluminal thrombus.

Fissured Plaque: Once a fibrous cap is ruptured, its inner thrombogenic content is exposed and platelet aggregation is originated. Platelet activation and thrombin formation

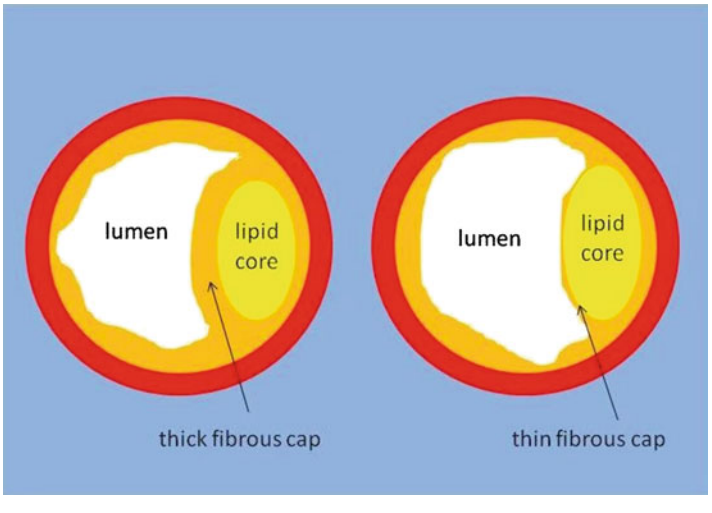

Fig. 25.1 Importance of the fibrous cap thickness as predictor of the embolic risk

in combination with the plaque content can produce acute vessel occlusion [41]. This explains the importance for diagnosing plaque rupture at an early stage, which can be accomplished by MRI imaging.

Severe Stenosis >90%: A severe stenosis refers to abnormal narrowing of the artery lumen, which reduces blood flow. Shear stress on the surface of severely stenosed plaque imposes a significant risk of thrombosis and sudden occlusion [42]. Several radiological imaging methods have the potential to diagnose a severe stenosis such as Doppler ultrasound (DUS), computed tomography angiography (CTA), magnetic resonant angiography (MRA), or Digital subtraction angiography (DSA).

2.2 Minor Criteria

Superficial Calcified Nodule: The superficial calcified nodule refers to a calcification close to the fibrous cap with the potential to cause cap rupture [40]. Calcified nodules might be diagnosed using US, CT, and MRI images.

Yellow Plaque on Angioscope: Yellow plaques on angioscope are believed to carry a high lipid burden and are, therefore, prone to rupture [40]. As the color is an angioscopic finding, this information cannot be depicted by radiological imaging methods.

Intra-plaque Hemorrhage: Hemorrhage inside an arteriosclerotic plaque accelerates plaque progression and increases the risk for thromboembolic complications by creating new destabilizing factors such as increase in lipid core and plaque volume [43]. Intra-plaque hemorrhage is considered a minor criterion; however, recent publications cast doubt on this ranking and suggest a more important role [43–45]. Two different types of intra-plaque hemorrhage can be distinguished: type I refers to histologically intact erythrocytes with intracellular methemoglobin and, meanwhile, type II is characterized by lysed erythrocytes and extracellular methemoglobin. MRI can accurately differentiate both types [40].

Endothelial Dysfunctions: Endothelial impairment plays a major role in the initiation of arteriosclerosis and its progression. Increased adhesion molecule expression and reduced anticoagulant properties increase the risk for cardiovascular disease [46]. Arterial stiffness and endothelial dysfunction commonly coexist and can be assessed by MRI or DUS [46].

Positive Remodeling: Positive Remodeling refers to an enlargement or growth of an arteriosclerotic plaque without reduction of the luminal area [40]. MRI can assess the positive remodeling.

Radioloical imaging methods should not only be able to detect the degree of a stenosis but must also provide information about superficial structure and morphology of the plaque. Here, the challenge is to identify asymptomatic high-risk patients, differentiate stable from unstable plaques, and predict the risk of a stroke.

3 Measurements

The North American Symptomatic Carotid Endarterectomy Trial (NASCET) and European Carotid Surgery Trial (ECST) have established criteria for stenosis quantification of images based on DSA. These criteria are currently used for CTA and MRA to determine vascular diameter and to quantify the degree of carotid artery stenosis. The NASCET method estimates a stenosis by calculating the ratio between the patent lumen diameter at the highest degree of stenosis and the patent lumen diameter at the distal "normal" internal carotid artery beyond the carotid bulb [11]. The ECST method calculates the ratio between the patent lumen diameter at the greatest stenosis and the total outer diameter of the arterial wall at the same level [5]. Comparing NASCET and ECST methods for determining the degree of a stenosis, the NASCET criteria underestimate the degree of a stenosis if compared to ECST; however, the higher the degree of stenosis, the less the difference between both methods [47, 48]. Most of the published trials are based on the NASCET criteria for evaluating the degree of a carotid artery stenosis (Fig. 25.2).

Some limitations have been reported when applying NASCET criteria. Incorrect NASCET measurements on

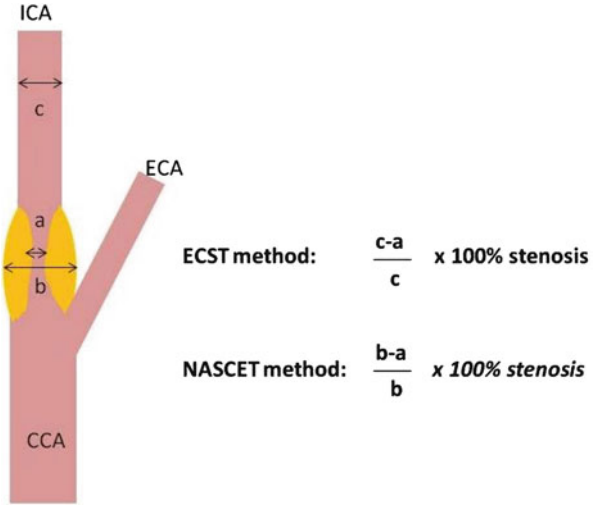

Fig. 25.2 Graphic shows anatomic sites of measurement in the carotid artery for calculating percent stenosis for the North American Symptomatic Carotid Endarterectomy Trial (NASCET) and the European Carotid Surgery Trial (ECST)

reconstruction images can overestimate the degree of stenosis. It is of crucial importance to correctly choose the distal "normal" ICA for NASCET measurement because the carotid bulb is larger than the outflow ICA. The measurement should be performed perpendicular to the vessel and only in parallel artery walls. Furthermore, for near occlusion NASCET criteria are lacking. The distal ICA diameter is reduced owing to the decreased blood flow in the distal ICA which leads to underestimation of the stenosis degree [11].

4 Indications for Treatment

4.1 General Aspects

Recommendations for the selection of revascularization techniques for patients with carotid artery stenosis mostly depend on the patient's clinical situation and the presence of comorbid medical conditions and anatomical factors. CEA is an efficient technique to prevent strokes in patients with carotid artery stenosis, and CAS, as a less invasive treatment alternative, has to be compared with the open surgical revascularization procedure. CAS can be performed under local anesthesia; therefore patients with comorbid medical conditions (cardiopulmonary diseases, open heart surgery within 6 weeks, etc.) may benefit from the CAS procedure. CAS has the clear advantage that it does not injure cranial nerves which occurs after CEA [22, 49]. Unfavorable anatomy such as surgically inaccessible high carotid bifurcation has also been considered an indication [50]. CAS should furthermore be performed instead of CEA in carotid artery dissection, tandem lesions, contralateral laryngeal nerve palsy, carotid artery stenosis with occlusion of the contralateral ICA, restenosis after CEA, and stenosis after radiotherapy [50, 51]. CAS should not be performed in patients who have contraindications to dual antiplatelet therapy [50].

4.2 Symptomatic Patient

Patients with carotid artery disease are considered symptomatic when they experience non-disabling ischemic stroke or transient cerebral ischemic symptoms including hemispheric neurological deficit or amaurosis fugax [5]. For these conditions, recommendations have been made for CEA but cannot be transferred to CAS due to lack of scientific evidence. For stenosis >70%, based on the NASCET criteria, operative treatment is strongly recommended; meanwhile symptomatic patients with stenosis >50% will probably benefit from CEA [51]. Other guidelines suggest ICA revascularization if a symptomatic stenosis >70% is documented by noninvasive imaging modalities or >50% as documented by catheter angiography [52]. At present, CAS is recommended in patients who need a revascularization and are at high risk for surgery or as an alternative to CEA, if high-volume centers have a documented death or stroke rate of ≤6% [50]. Both CEA and CAS should be performed in the early period after a symptomatic event, and CEA within 2 weeks thereafter [51, 53].

4.3 Asymptomatic Patient

Meanwhile in the presence of symptoms 5 patients have to undergo surgery to prevent 1 ipsilateral stroke in 5 years; 12 men or 24 women have to be treated if patients are asymptomatic [51]. The selection of asymptomatic patients for carotid revascularization requires an evaluation of comorbid conditions and life expectancy. CEA could be beneficial in asymptomatic patients with >60% carotid stenosis if their life expectancy is >5 years and if the perioperative stroke and death rate for the procedure performed by the surgical team is <3% [50]. In asymptomatic individuals with indication for revascularization, CAS can be an alternative in high-volume centers with a documented stroke and death rate of <3% [50, 51].

4.4 Chronic Total Occlusion

Chronic total occlusion of the ICA usually has a benign and asymptomatic course. Revascularization procedures are currently not recommended because they do not offer any benefit compared with best medical therapy regarding stroke prevention [50, 52]. However, it has been reported that endovascular revascularization can be performed in a very selected group of symptomatic patients despite the risk of distal embolization, vascular rupture, perforation, or hyperperfusion syndrome [52, 54].

4.5 Acute Total Occlusion

On the other hand, revascularization of internal carotid artery occlusion in the setting of an acute stroke is feasible and has shown a high rate of technical success with a favorable clinical outcome (Fig. 25.3). These data indicate that this technique can be useful in patients with severe stroke symptoms if it is performed within the first 6 h [55]. Outcomes after carotid artery stenting in acute stroke depend less on the result of the stent placement than on timing, efficacy, and complications of the cerebral thrombectomy.

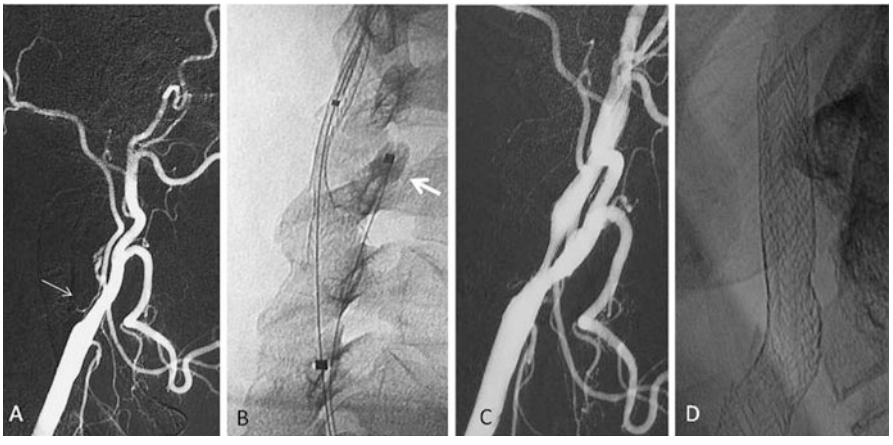

Fig. 25.3 Patient presenting with sudden left hemiplegia. (**a**) DSA performed within the 3 h shows complete right ICA occlusion (*thin arrow*). (**b**) Immediate tentative of revascularization was started using a flow reversal device (Mo.Ma, Invatec) as cerebral protection. See the distal balloon placed in the proximal ECA (*arrow*); the proximal balloon cannot be seen in this image. (**c**) Recanalization could be achieved by means of stent placement alone without balloon dilatation in order to avoid a hyperperfusion syndrome. (**d**) Plain film performed before discharge shows almost complete expansion of stent rendering angioplasty unnecessary

4.6 Near Occlusion

A near occlusion is defined as a carotid artery stenosis of 99% with reduced antegrade blood flow in the ICA and distal lumen collapse ("string sign"). In contrast to complete chronic occlusion, near occlusion burdens the risk of cerebral embolic events. CEA has little or no benefit for reducing future stroke risk compared with medical therapy alone [50, 52]. For CAS, no general recommendation can been made due to lack of scientific evidence; however, CAS in this condition has been reported with a low intraprocedural stroke and death rate and a good stroke prevention at long term [56, 57]. The presence of a sufficient collateral circulation has been discussed in asymptomatic patients, and in this condition, medical treatment is the recommended therapy. However, if recurrent or crescendo symptoms are present despite a medical therapy, an invasive treatment should be considered [58].

4.7 Stenosis Less than 50%

For stenosis <30% CEA increases the 5-year risk of stroke and has no beneficial effect for stenosis ranging from 30 to 49%. Therefore, neither CEA nor CAS is recommended in symptomatic patients with stenosis <50% and optimal medical treatment should be the primary therapy consisting of long-term dual antiplatelet therapy and long-term statins [50]. As said before, vulnerable plaques are likely to cause ischemic events and symptoms can appear even in the presence of low-grade stenosis despite medical management [59] (Fig. 25.3). These patients might benefit from revascularization procedures to prevent further stroke; however, no recommendation can be made and indication for an invasive treatment should be made individually [52, 59].

4.8 Patients Undergoing Cardiac Surgery

Patients with high-grade carotid stenosis undergoing coronary bypass or other cardiac surgeries present with a higher risk of stroke than patients without carotid disease.

The decision to treat an ICA stenosis before cardiac surgery should be discussed by a multidisciplinary team. Optimal time between a carotid intervention and cardiac surgery depends on clinical presentation, level of emergency, and severity of carotid and cardiac disease. With a <6-month history of TIA, revascularization is recommended for stenosis >70%, and can be considered for stenosis 50–69% in certain conditions. For asymptomatic patients, revascularization is only recommended for men who present with a bilateral 70–99% stenosis, an ipsilateral 70–99% stenosis with contralateral ICA occlusion, or previous silent ipsilateral cerebral infarction [50].

5 Noninvasive Imaging

5.1 Ultrasound

Ultrasound (US) is the most important tool for evaluation of carotid artery disease since it is widely available, low cost, and noninvasive. It is operator dependent, and therefore, criteria have been developed for reproducibility and reliabil-

ity of ultrasound examinations. The carotid arteries should be evaluated using gray-scale, color Doppler, and spectral Doppler examinations.

US Before Stent Placement: It is of utmost importance to correctly identify the degree of a carotid artery stenosis since indication for a carotid artery intervention depends on the clinical presentation and the degree of a stenosis. Therefore following categories for measuring the degree of ICA stenosis have been suggested: (1) Normal, (2) Stenosis <50%, (3) Stenosis 50–69%, (4) Stenosis ≥70%, (5) Near occlusion, (6) and Total occlusion [60]. For high-grade carotid artery stenosis (stenosis 70–99%) the US examination is an excellent screening method but with less accuracy for low-grade stenosis [61].

The gray-scale US has the potential to localize an arteriosclerotic lesion, measure intima-media thickness, and can identify the morphological degree of a stenosis by differentiating the lumen from the arterial wall. Gray-scale US has furthermore the potential to evaluate the superficial structure of a plaque and to detect plaque ulcer. The echogenicity of a plaque, assessed by gray-scale US, can further determine the risk for ipsilateral ischemic complications, since echolucent plaques are associated with a higher risk of future stroke than echogenic plaques [62]. Due to similar echolucency characteristics, a differentiation between fibrous intra-plaque tissue and the lipid core is not possible and intra-plaque bleeding might not correctly be diagnosed.

The DUS provides functional and hemodynamic information. The DUS can detect flow disturbances in plaque depressions and can be used to calculate the area of stenosis [63]. For area measurements US images should be obtained in a transverse fashion, since arteriosclerotic plaques can be eccentric. For determining the degree of a stenosis, the spectral Doppler examination is essential. The primary criterion for diagnosing an ICA stenosis is the ICA peak systolic velocity (PSV) in combination with the gray-scale evaluation [60]. If the stenosis is uncertain for the primary parameters, then additional parameters are used, such as ICA end diastolic velocity (EDV) and the ratio of ICA PSV/CCA PSV [60] (Table 25.1). The evaluation of ICA/CCA PSV is especially important in certain conditions such as aortic stenosis, low cardiac output, or detection of contralateral carotid occlusion [64].

For correct evaluation of flow velocities, technical aspects have to be considered. The PSV should be measured after a regular heartbeat. For determining flow velocities, a transversal view is preferable and the pulsed Doppler sample volume should be placed precisely within the area of the maximum stenosis. A wrong angulation of the Doppler gate leads to erroneous flow velocities. Therefore it has been recommended to use an angle within 45–60%, which ensures minimizing errors of flow velocity measurements [65]. In tortuous vessels the cursor should be placed tangential to the curvature of the artery.

US After Stent Placement: The US is the standard technique for screening after stent placement, to detect a residual stenosis or restenosis due to hyperplasia. Gray-scale US may provide morphologic information about the degree of a stenosis; however, blood flow velocities for stenosis detection, as previously described, fail. A "normal" carotid artery has an elastic vessel wall, which is reflected in the low-resistance waveform of a spectral DUS. After stent placement the artery will lose this condition due to the rigid device. Furthermore, wall stress produced by the stent can cause endothelial dysfunction, which is responsible for hyperplasia and restenosis. For this reason, the above-mentioned blood flow velocities for the evaluation of in-stent restenosis are not applicable. Although different thresholds for blood flow velocity have been proposed, it could have been demonstrated that current velocity criteria to assess in-stent restenosis after CAS yield a high false-positive rate [66]. Baseline control within 48 h after stent placement should be performed with consecutive control to document changes in blood flow velocities over time rather than applying absolute velocity criteria [67, 68]. If an in-stent restenosis is suspected, other imaging modality such as CTA has been proposed to confirm the degree of stenosis [69].

US Limitations: US can be of limited value in special conditions. Severe calcifications produce ultrasonic shadows, which limits the morphologic evaluation of the gray-scale US. For the same reason, the DUS might not be able to assess blood flow velocity at the greatest stenosis. In this condition, velocity measurements proximal and distal to the shadow could determine the degree of the stenosis.

Anatomic patient conditions influence quality of the US image. A high carotid artery bifurcation might not be assessed as well as in obese patients with a short neck. Tandem lesions might not correctly be depicted on gray-scale US evaluation; however, if there is inconsistency between a severe stenosis diagnosed on gray-scale US and the distal spectral waveform detected by DUS, an upstream lesion has to be suspected. Anatomic variants might cause confusion such as carotid artery kinking. In this condition it might be difficult to distinguish the external from the internal carotid artery. Elevated flow velocity and high-resistance flow pattern as well as outgoing branches help to differentiate the external from the internal carotid artery. US has a limited value for discriminating near occlusions from total occlusions [70]. The lack of detection of a residual flow might lead to false-positive results. Alternative imaging modalities such as DSA, MRA, or CTA can be useful to differentiate near from total occlusions.

Table 25.1 Doppler parameters for carotid stenosis Grant EG et al. [60]

Degree %	ICA PSV (cm/seg)	Plaque estimate %	ICA/CCA PSV (cm/seg)	ICA EDV (cm/seg)
Normal	<125	None	<2.0	<40
<50	<125	<50	<2.0	<40
50–69	125–230	≥50	2.0–4.0	40–100
≥70	>230	≥50	>4.0	>100
Near occlusion	High, low, indetectable	Visible	Variable	Variable
Total occlusion	Undetectable	Visible, no detectable lumen	Not applicable	Not applicable

5.2 Computed Tomography

The CT is a noninvasive technique for the workup of carotid artery stenosis and for follow-up after carotid stent placement. Meanwhile a non-enhanced CT has the potential to detect ischemic and hemorrhagic cerebral complications; the contrast-enhanced CTA can be used to determine the degree of a carotid artery stenosis and to evaluate the intracranial circulation. Currently, the mutidetector CT angiography (MDCTA) permits a fast evaluation with a high spatial resolution. Different reconstruction algorithms such as three-dimensional (3D) reconstructions, major intensity projections (MIP), and multiplanar or curved reconstruction images have contributed to improved accuracy [71].

CT Before Stent Placement: CTA is a valuable method for carotid artery disease evaluation [72]. Since MDCTA was used to diagnose ICA stenosis, improved accuracy has been demonstrated [73]. The highest accuracy was reported for detecting complete ICA occlusion [74]. MDCTA can furthermore discriminate total from near occlusion, with an excellent correlation with catheter angiography [75]. For high-grade stenosis (70–99%) without near occlusion, the CTA is an accurate method [74]. In contrast to high-grade stenosis, the diameter of the distal ICA is reduced in near occlusion, which can accurately be depicted by MDCTA. This is of special importance since patients with severe stenosis and a normal distal ICA but no near occlusion are at higher risk to develop a future stroke. Quantitative millimeter measurement of ICA stenosis has also been proposed to estimate the risk of stroke and to overcome ambiguities with NASCET criteria [76, 77]. Special care has to be taken in the group of 50–69% stenosis because symptomatic patients would receive invasive treatment and meanwhile patients with stenosis <50% receive medical treatment only. Here, CTA has the lowest specificity, compared to other noninvasive imaging methods [78]. On the other hand, CTA has an excellent negative predictive value for demonstrating <70% stenosis [79].

CTA can provide morphological information about the vascular wall and atherosclerotic plaques. It is very sensitive for detection and measurement of carotid plaques calcification and plaque ulcerations [80, 81]. Different plaque components such as fibrous connective tissue and fat may be distinguished from plaques containing calcifications due to their dissimilar densities (Fig. 25.4).

However, this differentiation is not possible for the lipid core, fibrous tissue, and intra-plaque hemorrhage. The Dual-Energy-CT is a new CT technique that uses two independent radiation sources with different voltages and has the potential to identify patients with vulnerable plaques better than conventional CTA [82–113]. Dual-Energy-CT is therefore a valuable tool for the noninvasive assessment of different plaque components and can discriminate mixed plaques from low-density fatty plaques [83].

CT After Stent Placement: The MDCTA has emerged as a noninvasive modality for surveillance after stent placement [84, 85]. DUS is the primary choice for assessing in-stent restenosis. However, it is of limited use because not all stents are assessable due to severe calcifications with dorsal sonic shadowing or due to anatomic localization. Here the CTA has proven to be an alternative for in-stent restenosis detection. Intimal hyperplasia on CTA images appears as variable hypodense ring between the hyperdense stent and the contrast filled artery lumen. Compared to DUS, MDCTA shows comparable results regarding detection of in-stent restenosis [68]. However, the dense metal struts can lead to local artifact that can degrade the image in the immediate vicinity of the vessel wall, which leads to overestimation of the degree of stenosis [50]. Other limitations of CTA imaging include motion artifacts, small stent diameter surrounded by heavy calcifications, and strike artifacts caused by the stent or stent markers such as tantalum or gold [86]. This is of extreme importance since artifacts caused by stent markers can masquerade as in-stent restenosis which is frequently found at the extremities of a stent. Therefore, the MDCTA has been recommended as an alternative technique if the stent is not completely assessable by DUS.

CT Limitations: The CTA has certain limitations. Even if it is a noninvasive method, iodine contrast has to be applied,

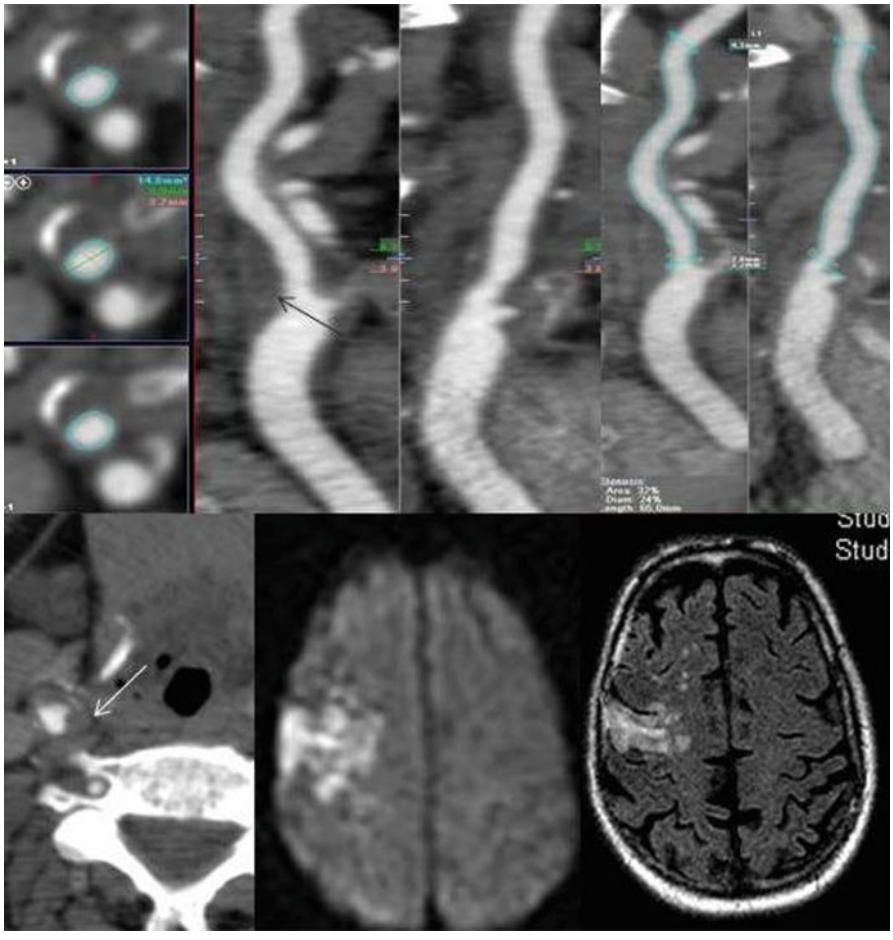

Fig. 25.4 Soft plaque depicted by CT (*arrows*). Although the stenosis measures by NASCET were not significant (<50%), this plaque embolized causing a right hemisphere infarct

which burdens the risk of contrast-induced nephropathy and the potential for allergic contrast reactions. Furthermore, the patient is exposed to ionizing radiation. Image quality might be limited in the uncooperative patient due to motion artifacts or in case of severe obesity. Metal structures such as surgical clips, endodontic prosthesis, or even vascular stents cause strike artifacts that may impede an appropriate evaluation of the patent vascular lumen. Very hyperdense structures like heavily calcified lesions, especially if circumferential, cause a hardening effect, which results in overestimation of the hyperdense structure and underestimates the lumen diameter [87].

5.3 Magnetic Resonance Imaging

With the technical advances of the past years the MRI has become a valuable noninvasive screening tool for detection of carotid atherosclerotic disease. Meanwhile the CT is the preferred method to differentiate a hemorrhagic from an ischemic stroke; the MRI is superior for early detection of ischemic lesions [88]. MRI has also an excellent soft-tissue contrast, which makes it a valuable technique for evaluating the vulnerability of a carotid plaque [40, 83]. MRI has further been used for the follow-up after carotid stent placement [84].

MRI Before Stent Placement: Some technical aspects have to be considered when using this technique. A 1.5 T MRI might be sufficient for an adequate vascular screening of the extra- and intracranial structures; however 3 T MRI machines provide better spatial resolution. For the assessment of plaque morphology, phased-array superficial coils must be used to optimize signal-to-noise ratio [85].

The MRI provides cross-sectional images in any plane including oblique planes. For detection of the degree of a stenosis, different sequences have been applied such as contrast-enhanced MR angiography (CE-MRA), time-of-flight (TOF) MRA, and phase-contrast MRA [89]. Since CE-MRA is fast, it has become the technique of choice for studying the carotid bifurcation [90]. The flow-dependent TOF MRA or phase-contrast MRA is of less importance due to their distinct susceptibility to motion or flow-related artifacts [91]. On the other hand, TOF MRA is the recommended technique for evaluation of steno-occlusive disease in the intracranial arteries, since it has a higher spatial resolution compared with CE-MRA [92, 93].

For the grading of a carotid artery stenosis CE-MRA is an excellent technique. For detecting carotid artery disease, CE-MRA is comparable with CTA and DUS. For detecting severe stenosis (70–99%) it is superior to CTA and DUS and is the most accurate method [78, 94–96]. CE-MRA is also very accurate for detecting total occlusions and can precisely discriminate near from total occlusion [70, 97]. For moderate ICA stenosis CE-MRA and especially TOF MRA appear to be poor diagnostic tools [97].

MRI is the preferred technique for the evaluation of stroke or transient ischemic attacks before and after stent placement, because it is the most sensitive technique for detecting early ischemic complications [88]. Diffusion-weighted images (DWI) should be obtained since patients who present with lesions visualized in DWI, especially when multiple, are at higher risk of recurrent ischemic events [88].

In the last years different MRI protocols have been evaluated for detecting different plaque characteristics. A multisequence MRI protocol has been proposed by different authors and can be used as a guide to assess the vulnerability of a carotid plaque [37, 98]. T1-weighted images before and after the application of contrast, proton density (PD)-, and T2-weighted images as well as TOF help to differentiate morphological characteristics [37]. Fat suppression should be used in all sequences to avoid signal from the subcutaneous fat.

For identifying an active inflammation of a carotid plaque, contrast has to be used and the inflammatory process can be detected by contrast enhancement of the vascular wall [40]. The lipid-necrotic core can accurately be differentiated from the surrounding tissue comparing pre- and post-contrast T1-w images since the lipid-necrotic core does not show enhancement after contrast [99]. The fibrous cap is hyperintense relative to the lipid-necrotic core after contrast on T1-w images [100, 101]. Calcified nodules appear hypointense on all 4 weightings and can be differentiated from the vascular lumen after the application of contrast or might be distinguished from the bright lumen in the TOF images [100, 102]. Intra-plaque hemorrhage can appear hyperintense on TOF and T1-w images and iso- or hypointense on PD- and T2-weighted image if type I hemorrhage is present but can have a high signal intensity on all sequences in case of type II hemorrhage [100].

MRI After Stent Placement: CE-MRA has been reported for the follow-up as it has the potential to visualize the patent stent lumen [103, 104]. Two techniques have been used to evaluate carotid stents, the CE-MRA and TOF MRA. The main problems of MRI are stent-related artifacts that lead to artificial lumen narrowing [84]. Artifacts depend on the stent material; here, different magnetic susceptibility characteristics of the stent influence the image quality [84, 105]. On the other hand, stent geometry and size of stents have an impact on the visualization of the stent lumen [84]. Currents induced inside the stent struts reduce signal strength leading to artificial lumen narrowing. In contrast to CE-MRA, the TOF MRA is based on rapid radiofrequency pulses, which furthermore increases susceptibility artifact [104]. For this reason, MRA in the follow-up after carotid stent placement has only limited value.

MRI Limitations: MRI is not as widely available as CT and is generally more expensive. It is contraindicated in patients with pacemakers, cochlear implants, neurostimulators, and metallic foreign objects. The application of contrast carries the risk of allergic reactions and renal complications, including nephrogenic systemic fibrosis [84]. Claustrophobic patients might need sedation due to the long and narrow gantry. To entirely assess extra- and intracranial vascular structures and plaque morphology and evaluate intracerebral lesions, it is a time-consuming method. Acquisition time of certain MRI sequences might be long and MRI is therefore sensible to motion artifacts. As described previously and depending on the sequences used, image quality can be restricted by factors, such as limited spatial resolution or scan range, flow signal intensity loss as a result of saturation or phase dispersion, and susceptibility artifacts [106]. Furthermore, MRA is reported to overestimate the degree of ICA stenosis, especially in non-contrast sequences such as TOF [50, 71].

Until recently, indication for carotid revascularization was related to patient symptoms and the degree of stenosis assessed by imaging techniques measuring the vessel's caliber, giving no information on plaque characteristics (stable or instable "vulnerable plaque").

Recent studies demonstrate how a 40% stenosis with a 0.2 mm thick "fibrous cap" is associated with the same wall stress and has risk of rupture as an 80% stenosis with a 0.5 mm thick "fibrous cap" [107].

In the next years, treating patients with "high-risk plaque morphology" will become a proven practice and standard of care supported by improvements in CT and MRI characterization of plaques.

6 Techniques of Carotid Artery Stenting

The efficacy of CAS in preventing stroke depends on careful patient selection and technical details. Although CAS is generally associated with low intraprocedural and postprocedural adverse neurologic events, it is mandatory to continuously undertake efforts to further reduce the rate of adverse events because these have a major effect on patient outcome.

Techniques and materials used for CAS are constantly evolving in order to make this procedure effective and safer.

One major concern with CAS is the potential distal embolization of particles from the treated site during the procedure. Embolic particles are classified as either macroemboli (>150 μm) or microemboli (<150 μm). Macroemboli, especially >200 μm, are associated with neurological events. To avoid this, various cerebral embolic protection devices (EPDs) have been developed and improved during the last years. However, published data to date do not clearly demonstrate the usefulness or safety with respect to clinical complications [108]. The use of EPDs, for some authors including us, increases the procedural complexity and risk of embolization during device manipulation. Since EPDs are expensive and prolong procedure time, it is important to determine the clinical value of this practice [109].

In 2000 our group started to treat carotid stenoses treated by CAS without using EPDs and without performing balloon dilatation neither before nor after stent placement, with encouraging results in the short and long term [110–112].

Herein, we will provide a step-by-step approach to the clinical and technical aspects that ensures the safe performance of carotid stenting. This includes the technique mostly performed worldwide with the use of EDPs and balloon angioplasty; the less used technique in which balloon angioplasty and stenting are performed without neuroprotection; and finally we will describe the author's technique for CAS without neuroprotection and balloon angioplasty, and discuss, from our point of view, the advantages of it.

6.1 Considerations for Safe CAS

6.1.1 Clinical Protocol (Table 25.2)

All patients should undergo a neurologic examination by a neurologist in order to document the pre-procedural clinical status using the baseline N.H.I.S.S (National Institute of Health Stroke Scale) or other functional scales.

The indication for stenting is given by DUS and DSA in most of the cases. In selected cases CTA or MRA can be also performed.

We pay close attention to the morphological aspect of the plaque which is assessed by ultrasonography. The plaque morphology is classified into 4 grades: grades 1 and 2 (echolucent or predominantly echolucent plaque) are considered as high-risk plaque morphology; grade 3 (predominantly echogenic) is medium risk, and grade 4 (echogenic) was low risk for stroke [5]. In our protocol, all patients with a high-risk plaque are treated if stenosis was more than 50%. Consider, if available, plaque characterization with MRI or CT (see high-risk plaque).

Angiography is performed prior to the endovascular intervention. The degree of stenosis before stenting is quantified using the NASCET criteria [6].

Table 25.2 Clinical protocol

Clinical protocol
Pre-procedure: • Carotid Duplex Ultrasound • 4-Vessel DSA (whenever possible previous to procedure) • MRI with DWI. If not possible CT-Scan • Neurological evaluation • ASA 100 mg PO bid × at least 3 days • Clopidogrel 75 mg or Ticlopidine 250 mg PO bid × at least 3 days
Procedure: • No sedation • 5,000 IU of heparin IV bolus • Squeezing toy in contralateral hand • Placement of devices directly in the carotid to be treated • Sheath removal
Post-procedure: • Post-procedural neurological evaluation • Carotid Duplex Ultrasound • MRI with DWI. If not possible CT-Scan within 48 h post-procedure • ASA 100 mg PO bid × life • Clopidogrel 75 mg × 3 months • Clinical and US F/U: 1, 3, 6, 12 month, annually thereafter

Before treatment, and whenever possible, a baseline cerebral MRI including diffusion weighted images (DWI) is recommended. If contraindicated or not available, CT should be done.

Patients must receive either a combination of clopidogrel 75 mg and aspirin 100–325 mg for at least 3 days prior to carotid stenting or, alternatively, loading doses of clopidogrel 600 mg and aspirin 325 mg at least 3 h prior to the procedure.

The intervention is performed under local anesthesia at the site of the vascular access. Neurological status, electrocardiogram, and blood pressure are monitored through the procedure. After procedure patient is sent to the intensive care unit to be monitored for 24 h (if balloon dilatation is performed) and neurologic status is evaluated. In our institution, patients go to a regular room because angioplasty is not done (see below our experience in CAS) and are discharged 48 h after procedure. During this time, DWI is repeated in order to document any new ischemic lesion.

6.1.2 Technique

The current technique of carotid and angioplasty used by most teams around the world can be divided into the following ten steps:

1. Vascular access
2. Angiographic evaluation
3. Common carotid engagement
4. Crossing the stenosis
   a. With EPD
   b. Without EPD
5. Predilatation of the stenosis
6. Stent Placement
7. Post dilatation

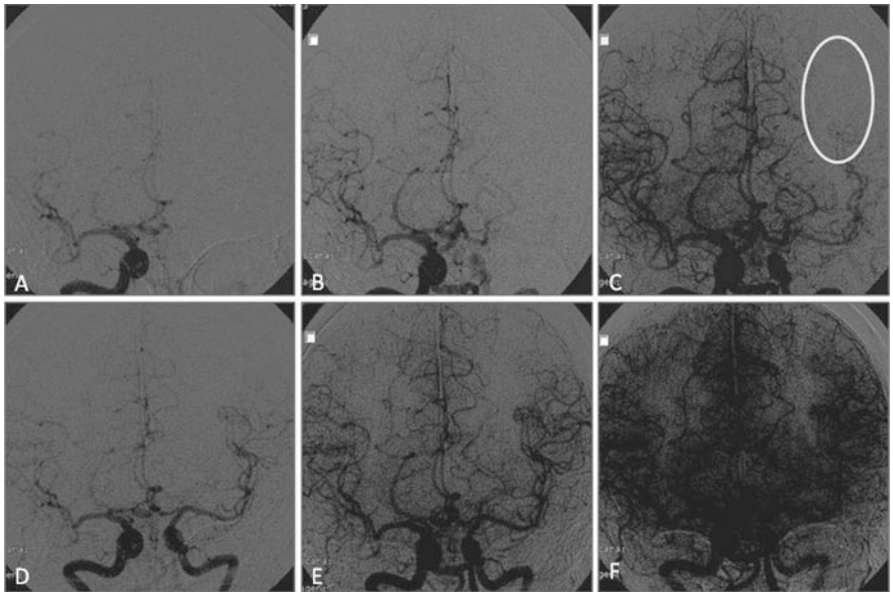

Fig. 25.5 Pre-procedure parenchymogram performed with a pigtail catheter placed on the ascendant aorta injecting a volume of 30–40 ml of nonionic contrast media with a debit of 15 ml/seg. (**a–c**) show a delay of contrast media through the left carotid artery, and a perfusion defect (*circle*) in the left hemisphere. (**d**, **e**) after CAS show no more delayed and perfusion deficit

8. Removal of EDP
9. Control angiogram
10. Sheath removal and Hemostasis

Vascular Access

Femoral arterial access is the preferred approach. Alternatives, in case of interrupted ilioaortic pathway or extremely tortuous aortic arch, are the radial/brachial access, and a direct carotid puncture.

Angiographic Evaluation

In most cases, brachiocephalic angiography can be performed using a single vertebral catheter. Sometimes, other catheters with different shapes may be useful, especially in cases of aortic arch type II or III.

Diagnostic angiography consists of visualization of the origins of the brachiocephalic arteries (this can be accomplished by a global injection using a pigtail catheter with a 30°–45° left anterior oblique projection, LAO), both carotids in at least two orthogonal projections, both vertebral arteries, and the intracranial circulation. In addition, our team performed a parenchymogram to assess areas of perfusion deficit (Fig. 25.5).

The advantages of performing a complete brachiocephalic angiography rely on the demonstration of anatomical conditions which could be unfavorable for carotid stenting or increase the difficulty of the procedure (e.g., severe vessel tortousity, heavy calcified stenosis, floating thrombus), knowledge of contralateral carotid stenosis or occlusion and status of the intracranial circulation that impacts on the stenting technique (e.g., choice of occlusive protection devices or filters), and the possibility of comparing final control angiograms with the baseline images in case of intraprocedural neurological complications.

Common Carotid Engagement

Once the carotid lesion is identified, a roadmap through the diagnostic catheter is performed in order to depict the external carotid. Then a 0.035″ 260 cm stiff Terumo type wire is advanced distally into the external carotid. The diagnostic catheter is withdrawn and an 8 Fr guiding catheter or a long 6 Fr sheath (Shuttle, Cook Inc., Blomington, IN; or Destination, Terumo, Japan) is advanced into the common carotid artery over the exchange length Terumo wire (coaxial technique). If diagnostic angiography has been previously done, the stenting procedure starts by placing from the beginning a 6 Fr long sheath over a 0.035” guide wire via the femoral approach into the descending aorta at a short distance from the origin of the left subclavian artery. After withdrawing the dilator from the long sheath, a long 125 cm catheter (Vertebral, Headhunter, Simmons) is introduced into the sheath and used to catheterize with the common carotid. Through it, and using roadmapping, a stiff 0.0035” Terumo guide wire is placed in the distal external carotid artery. Fixing the inner catheter and the wire with the right hand, the long sheath is advanced using the left hand into the common carotid artery 2 cm below the bifurcation (telescopic technique) (Fig. 25.6).

As soon as the introducer or a long sheath is placed into the arterial system, a dose of 5,000 units of heparin is administered through the sheath.

Engaging CCA in a safe way is the most important part of a successful carotid stenting procedure.

Crossing the Stenosis

Baseline angiograms are performed with different angle views in order to choose the one that depicts better the maximum severity of the stenosis. If the angio suite counts with

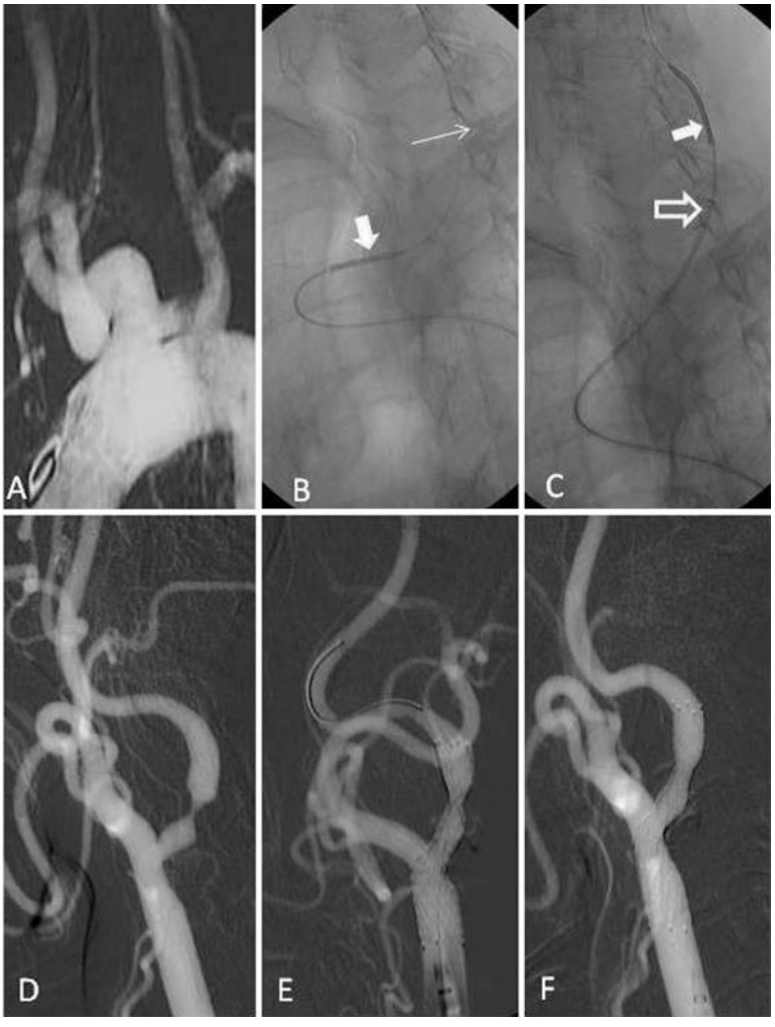

Fig. 25.6 Telescopic technique. (**a**) Aortogram showing a Type III aortic arch with the left carotid originating from the brachiocephalic trunk. (**b**, **c**) A 125 cm long Simmons catheter (*thick arrow*) is used through a 6 Fr 90 cm long Sheath (*hollow arrow*) to catheterize the left CCA. First the Simmons catheter is advanced into the CCA through a 0.035′ Terumo stiff guide wire placed in the external carotid artery, and then the long sheath is advanced over the catheter and positioned 2 cm below carotid bifurcation. (**d**–**f**) Finally, after retrieving the catheter and the guide wire, the stenosis is crossed with a 0.014 micro guide wire and the stent is advanced and released at the site of stenosis. No EPD was used in this case achieving a good result with a residual stenosis <20%

rotational angiography, a 3D reconstruction can be useful to better depict the carotid stenosis and choose the working projection, which should maximally separate the internal and external carotid artery. Measures of the diameters of the common and internal carotid are taken (Fig. 25.7).

The next step depends on whether the procedure is going to be done with or without EPDs.

CAS with EPDs

EPDs can be classified into two groups: filters and balloon occlusion systems (Figs. 25.8 and 25.9). In turn, balloon occlusion systems can be divided into distal and proximal balloon occlusion.

The main advantage of filters is that they do not interrupt blood flow to the brain (Fig. 25.10). It is also possible to verify the stent position prior to its deployment by contrast injections. However, they present some limitations: the crossing profile of almost all filters is larger than that of the distal occlusion balloon. In certain anatomical situations such as tight eccentric stenosis or marked tortousity of the distal ICA, this may preclude filter placement into the distal ICA. The introduction of new generation of filters which are low profile (Fibernet, Invatec) or permit to manipulate the wire independently from the filter (Sider, ev3; Emboshield, Abbot) may allow us to overcome these difficulties. Other drawbacks of filters include the possibility of debris dislodgement during the recapture phase (squeezing effect), and the fact that they can be an embolic source themselves due to intimal damage at the landing zone.

Filters must be placed far enough from the stenosis in a straight segment of the distal ICA. If the filter is opened close to the stenosis there will not be adequate place to allow stent placement, and, if it is positioned in a curve segment, incomplete wall apposition may occur and allow even macroemboli to bypass the protection device.

Characteristics of the main filter protection devices are summarized in Table 25.3.

Distal balloon occlusion systems (e.g., Percusurge Guardwire, Medtronic), in contrast to filters, do not allow flow into the distal bed; therefore its use is contraindicated in cases of isolated hemisphere (absence of collaterals from the contralateral carotid or vertebrobasilar system).

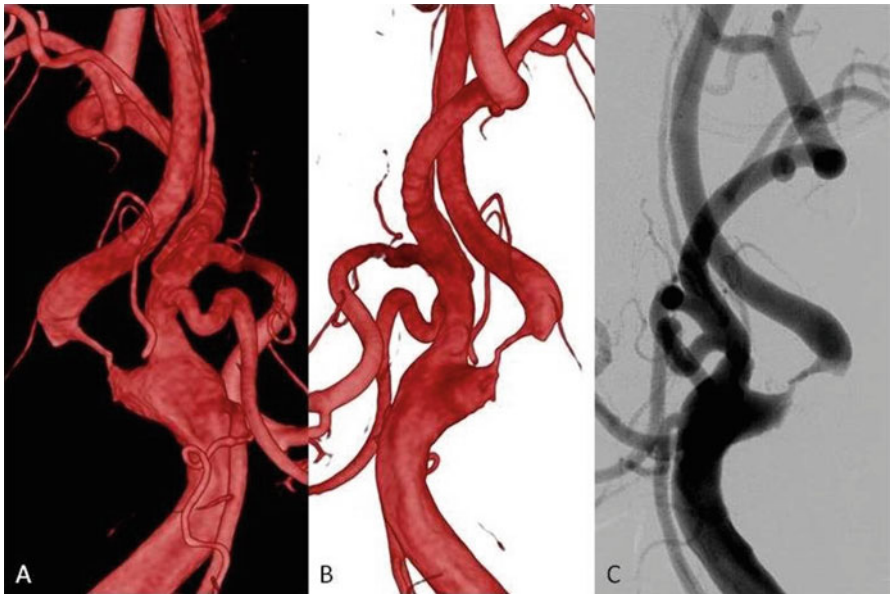

Fig. 25.7 3D images obtained from a rotational angiography depict well the stenosis, allow taking measures (**a**, **b**), and choosing the working projection on DSA (**c**)

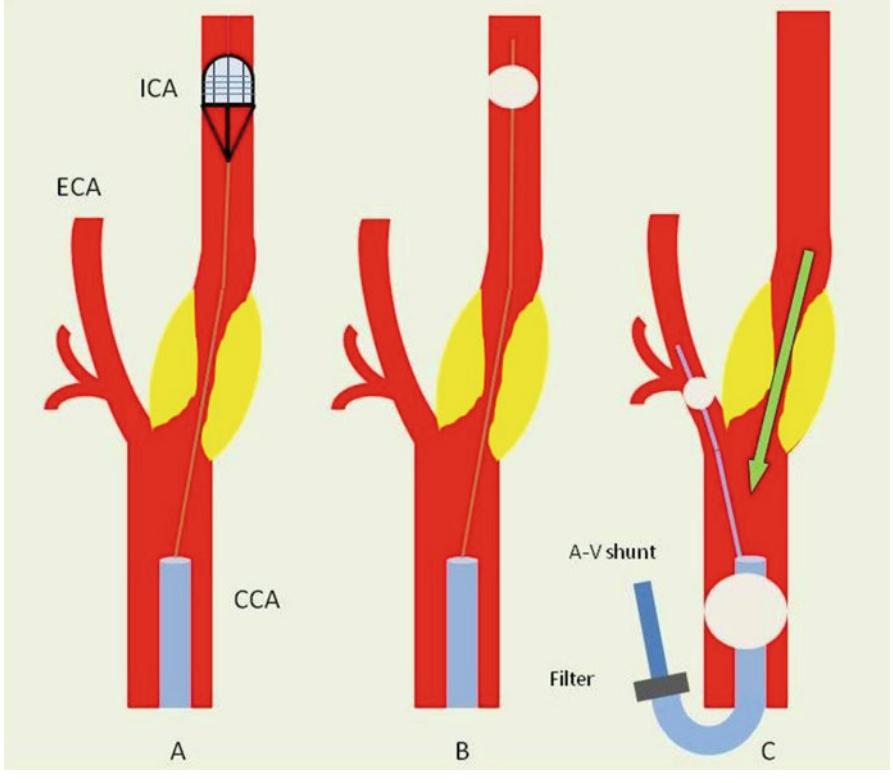

Fig. 25.8 Graphic showing a filter (**a**), distal occlusion balloon (**b**), and proximal occlusion balloon with flow reversal (**c**)

Both filters and distal balloon occlusion systems may increase the risk of arterial vasospasm, thrombosis, and dissection.

Proximal balloon occlusion systems consist of 8–9 Fr sheaths with and integrated balloon that is positioned in the CCA and an extended integrated (e.g., MO.MA, Invatec) or an independent (Neuroprotection System NPS, Gore) balloon catheter that is positioned in the ECA. The dual inflation of balloons reverses flow in the index carotid artery; therefore any emboli generated during procedure will travel in the direction of the flow towards the femoral artery. This allows the stenosis to be crossed with the micro guide wire of choice under protection. The use of these systems is more cumbersome; they are also contraindicated in case of isolated hemisphere, and their use is restricted in case of severe disease of the ECA and CCA.

CAS Without EPDs

There are many physicians who perform CAS without the use of EDPs. The only difference with protected CAS is that

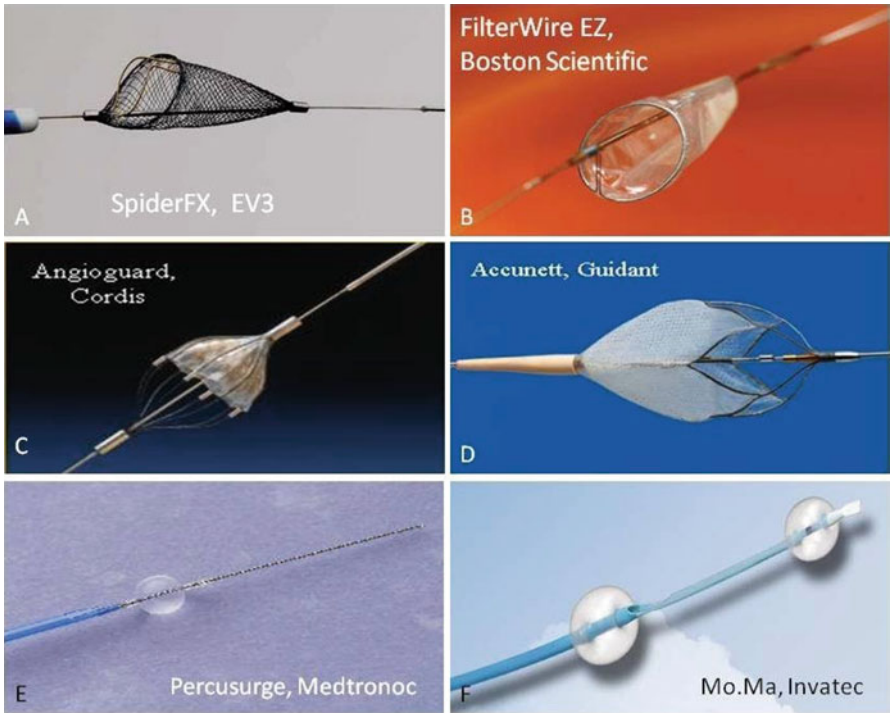

Fig. 25.9 Carotid protection systems: (**a**) The SPIDER filter with nitinol basket (ev3, Plymouth, MN). (**b**) The Filter Wire EZ (Boston Scientific). (**c**) The Angioguard filter with porous polyurethane membrane (Cordis, Miami, FL). (**d**) The Accunet filter basket (Guidant, Santa Clara, CA). (**e**) The PercuSurge GuardWire distal balloon occlusion system (Medronic, Santa Rosa, CA). (**f**) Mo.Ma proximal balloon occlusion system (Invatec, Roncadelle, Italy)

instead of using EDPs, the stenotic lesion is crossed with a steerable 0.014" guide wire after appropriate shaping of its tip and then placed close to the skull base. Balloon pre- and post dilatation are performed, although cerebral protection is not used.

In our team CAS is performed mostly without the use of balloon angioplasty neither pre- nor post-stent deployment and therefore without the use of cerebral protection devices. In our opinion EDPs add further manipulation, cost, and risk to the procedure, so we consider that by reducing the number of endovascular maneuvers in the supraortic vasculature, the risk of plaque material dislodgment can be reduced.

Predilatation of the Stenosis

Many authors perform predilatation routinely with a non-compliant balloon to permit the larger stent to cross the lesion in a less traumatic fashion. We only predilate in case of a very tight or calcified lesion precluding stent passage and positioning. In these cases, predilatation with a 2.5–3.5 mm monorail angioplasty balloon is necessary prior to stent deployment.

Following the predilatation, the wire of the EDP or the wire alone (in case of non-protected CAS) is left in position and used to advance the stent.

Stent Deployment

At the present time, only self-expanding stents are used to treat stenosis at the carotid bifurcation. The only indications for using balloon expandable stents are stenosis at the ostium of the common carotid, at the petrous segment, or in cases in which self-expandable stents cannot be advanced through the stenoses despite balloon predilatation. In this case a 4–6 mm balloon expandable stent is first deployed at the stenosis to prevent recoil and to allow the passage and deployment of a definitive self-expandable stent.

Currently, there are two types of stent material: cobalt chromium alloy (elgiloy) and nickel titanium alloy (nitinol). See characteristics in Table 25.4.

The stent must be deployed from "normal to normal" vessel, positioning the lesion in the middle. The stent diameter is oversized 10–40% versus the reference vessel diameter. Since there is usually a mismatch between the diameter of the internal and the common, the stent diameter should be chosen taking into account the latter one.

The choice of the optimal carotid stent depends mainly on arterial anatomy and lesion morphology. When treating a tortuous anatomy, stents with a flexible and conformable open-cell configuration are preferred. In arteries with a significant mismatch between common carotid artery and internal carotid artery diameter, elgiloy or tapered nitinol stents are selected. Lesions with suspected high emboligenicity (see high-risk plaque) are best covered with stents with a closed-cell configuration, whereas highly calcified lesions need treatment with nitinol stents (Fig. 25.11).

Postdilatation

The sized of the postdilatation balloon is matched to the diameter of the internal carotid artery at the site of stenosis. The most used balloon diameter is 5 mm (rarely 6 mm diameter). Since hemodynamic depression with bradycardia and

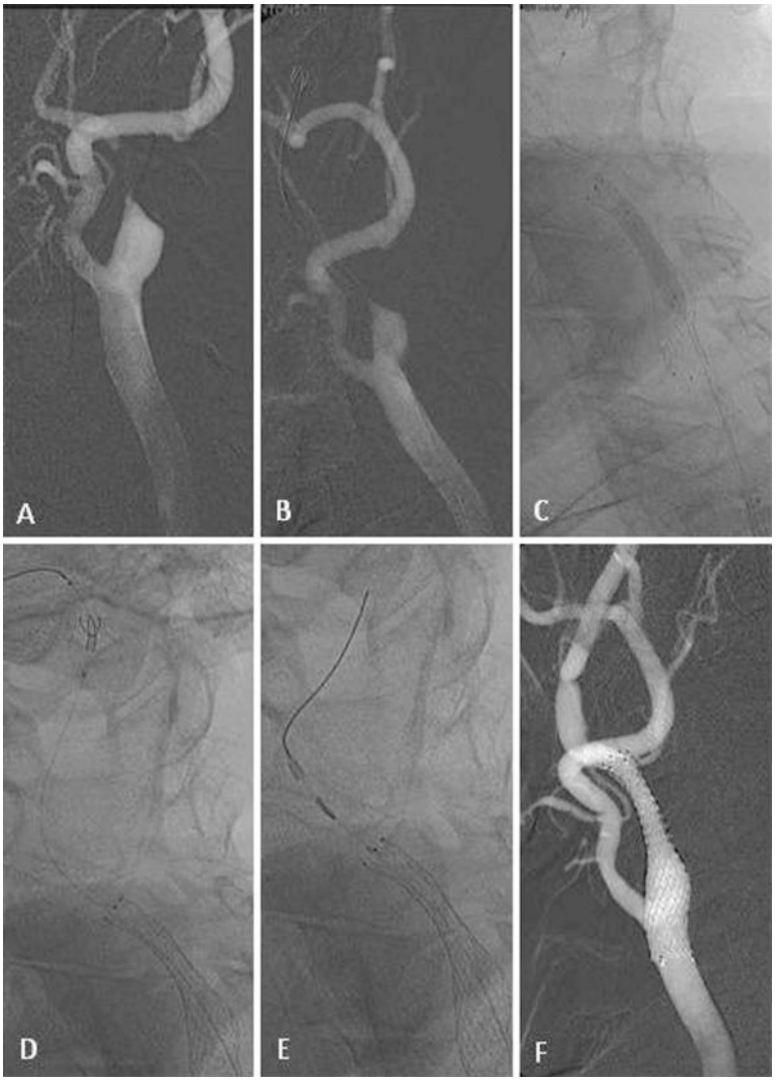

Fig. 25.10 (**a**) Suboclusive stenosis of the ICA. (**b**) Filter positioned distally in a straight segment of the ICA (*arrow*). (**c**) After stent placement a 5 × 20 mm monorail balloon is used to expand the stent. (**d**, **e**) The recovery catheter is advanced into the filter wire in order to envelop and retrieve it (*double arrow*). (**f**) Final control angio

Table 25.3 Characteristics of the main filter protection devices

Filter	Relationship to guide wire	Basket position	Pore size (μm)	Crossing profile (Fr)
Accunet (Abbott)	Wire-mounted torque independent	Concentric	125	3.5–3.7
Angioguard (Cordis)	Wire-mounted	Concentric	100	3.2–3.9
Emboshield (Abbott)	Wire-mounted Free-wire[a]	Concentric	120	2.8–3.2
Fibernet (Invatec)	Wire-mounted	Concentric	40	2.4–2.9
Spider (ev3)	Free-wire[a]	Eccentric	167–209	3.2

[a]Filters are independent and are loaded in a free guide wire

asistolia is not uncommon during balloon dilatation, atropine 1 mg is routinely given just before balloon postdilatation.

Remember that postdilatation is the most critical step concerning neurological events. The greatest amount of emboli is released during dilatation, so it should be carried out with extra care: do not use balloon larger than 5 mm, inflate to nominal pressure, and accept up to 30% residual stenosis.

Removal of EDPs

Filters: by fixing the filter wire with the right hand, the retrieval catheter is advanced with the left hand towards the distal filter such that its distal retrieval pod fully envelops the filter, which can then be withdrawn.

Distal occlusion balloon: prior to deflation of the balloon, an aspiration catheter is advanced till just before the inflated

Table 25.4 Characteristics of the main self-expandable stent

Stent type	Advantages	Disadvantages	Name of stents
Cobalto alloy braided mesh stents	• Small and flexible delivery system • High scaffolding properties (plaque covering) • Ability to accommodate to carotid bifurcation	• Potential unpredictable shortening during deployment • Loss of structural flexibility when inserted into vessels • Unpredictable radial force (depending on the angle formed between the braided mesh)	Wallstent-Boston Scientific
Nitinol open-cell stents (cylindrical or tapered)	• Absence of shortening during deployment • Conformability and flexibility • High vessel wall adaptability • Predictable radial force	• Moderate scaffolding properties (plaque covering) • Stent strut malalignment in complex carotid lesions	Precise-Cordis Exponent-Medtronic Viviexx-Bard Protégé-ev3 Acculink-Abbot Sinus-Optimed
Nitinol closed-cell stents (cylindrical or tapered)	• Absence of shortening during deployment • High scaffolding (plaque covering) • High predictable radial force	• Significant stiffness of the structure • Poor conformability and flexibility	Xact-Abbot NexSstent-Boston Scientific
Hybrid Nitinol Stent	• Absence of shortening during deployment • High conformability and flexibility on both extremities • High vessel wall adaptability on both extremities • High scaffolding at the mid-portion • Predictable radial force	• Fixed length of the closed-cell portion (10 13 mm) • Lower scaffolding propriety at the closed-and open-cell junction	Cristallo Ideale-Invatec

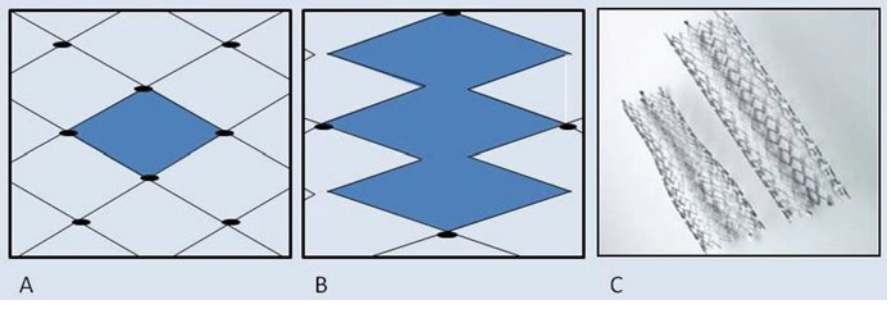

Fig. 25.11 The free cell area is shown in *blue*. (**a**) Closed-cell design; (**b**) Open-cell design; (**c**) Straight and tapered-stent configurations

balloon over the wire. Maintaining constant aspiration with a 20 cc syringe, the aspiration catheter is advanced to the occlusion balloon and pulled back to the carotid bifurcation several times till approximately 50 cc of blood is aspirated. This maneuver aspirates debris preventing distal embolization once the occlusion balloon is deflated.

Proximal occlusion balloon: after balloon postdilatation, three 20 ml syringes of blood are aspirated and checked for debris before deflating the balloons. Further aspiration must be done if debris are still present in the third syringe until no more particulate debris is seen. Following a control angiogram the system is pulled back to disengage the balloon catheter in the ECA from behind the stent and removed.

Control Angiogram

Final angiograms should be acquired in the same baseline projections. If a distal protection device has been used, the intracranial segment of the ICA has to be checked carefully. In case of vasospasm, nimodipine 1–4 mg or 200–400 μg of nitroglycerine can be administered through the guiding catheter or sheath. In case of spiral dissection, adjunct stent placement is required in most cases.

AP-lateral intracranial angiography should be acquired routinely and compared with the same projections as baseline.

In our working group, parenchymogram is performed at the end of procedure to evaluate the improvement of the initial perfusion deficit.

Sheath Removal and Hemostasis

If manual compression is used to achieve hemostasis, ACT has to be <150, before removing the sheath.

Whenever possible, we prefer to use a percutaneous closure device (AngioSeal, St Jude Medical Inc) to achieve hemostasis in these patients who are receiving aspirin and clopidogrel in addition to the low weight heparin that we prophylactically administer them until discharged 48 h later.

6.1.3 Complications

Carotid Artery Spasm

The most frequent complications with distal protection devices are spasm and slow-flow. Slow-flow may occur with filters when their pores are partially or completely occluded with debris. If this occurs it is important to first aspirate the column of stagnant blood proximal to the filter as this may contain suspended particles through the guiding catheter or guiding sheath which are advanced as closer as possible, and, when recovering the filter, it is important to just envelop the proximal portion of the filter to avoid squeezing the debris.

Spasm of the distal ICA usually resolves spontaneously within several minutes after removal of the device or with intra-arterial administration of nimodipine or nitroglycerine

Distal Embolization

The most frequent sites are the distal ICA and the middle cerebral artery including its major branches which is easy to detect. Every physician performing CAS should have a thorough knowledge of the intracranial vascular anatomy and expertise in advanced neurorescue techniques including chemical and mechanical fibrinolisis. Embolism in the smaller branches requires careful scrutiny utilizing the preprocedural angiogram. For a symptomatic small and peripheral branch occlusion adequate hydration, blood pressure, and anticoagulation should be carried out to increase chances of recovery.

Bradycardia and Hypotension

Bradycardia, hypotension, and/or asystole are common during balloon dilatation at the carotid bifurcation and are routinely prevented with 1 mg atropine just before balloon postdilatation. These events are less common in case of treating stenosis beyond the carotid bulb or restenosis after CEA because the receptors are not located at the site of stenosis or because they have been denervated by surgical dissection. Hypotension due to stimulation of the baroreceptors from both balloon dilatation and the persisting stretch of the self-expanding stent is not uncommon and is usually managed by adequate intravascular volume expansion. Continued hemodynamic monitoring in an Intensive Care Unit for at least 24 h in the post-procedural period is crucial.

Hyperperfusion Syndrome

The hyperperfusion syndrome is a clinical triad of ipsilateral headache, seizure, and focal neurological symptoms occurring in the absence of cerebral ischemia. Intracranial hemorrhage may also occur. It is related to long-standing hypoperfusion that results in impaired autoregulation of the microcirculation; thus following revascularization the increased perfusion pressure overwhelms the ability of the dilated arterioles to constrict.

This typically occurs in patients with severe carotid stenosis and poor collateral circulation. Strict control of blood pressure and anticoagulation in patients at risk is essential to prevent it.

Carotid Dissection

Carotid dissection is a rare complication, favored by severe tortousity, poor control of distal EDPs position, postdilatation of the distal stent edge within the ICA, and aggressive manipulation of the guiding catheter in the CCA. Management options depend on the severity of flow restriction and include additional stent implantation, or a conservative therapy with anticoagulants and/or antiaggregants.

Intracranial Hemorrhage

Intracranial hemorrhage is a life-threatening complication. A severe headache, followed by sudden loss of consciousness in the absence of vessel occlusion, should alert the operator. Heparinization should be reversed, an emergency CT scan performed, and the neurosurgeons put on alert.

Acute Stent Thrombosis

Acute stent thrombosis is a rare event in which a correct double antiplatelet therapy is essential to decrease at minimum the rate of stent thrombosis and the periprocedural embolic events.

Carotid Perforation

Carotid perforation is an extremely rare complication that occurred mostly due to an aggressive dilatation with an oversized balloon. It is important to always count with a covered stent to manage this situation.

7 Our Experience in CAS Without Cerebral Protection and Balloon Angioplasty

From 2001 we started to perform CAS using a simplified technique. On the basis of our experience, we considered that the use of EPDs is mostly not required to treat carotid stenoses, since balloon angioplasty is not performed either before or after stent placement. It is well known that the

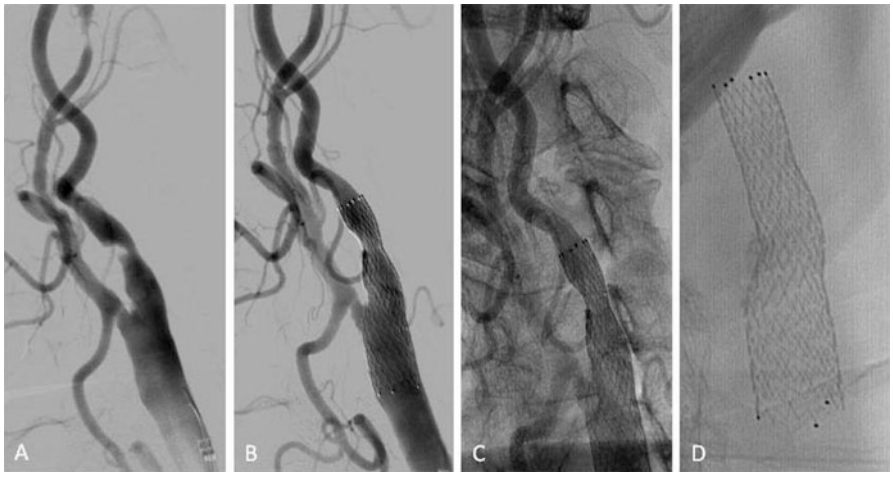

Fig. 25.12 (**a**) DSA reveals a severe internal carotid stenosis. (**b**, **c**) Final angiogram shows an optimal result with a residual stenosis of <10%. (**d**) Plain film obtained 1 month after procedure showing complete expansion of the stent

highest potential for embolization occurs in the postdilatation when the balloon crushes the plaque against the stent struts.

The rationale for performing CAS in this way is that, unlike peripheral or coronary stenoses, carotid stenoses are very infrequently symptomatic due to hemodynamic compromise. Rather, symptoms arise from embolization from a carotid plaque. Therefore, it remains to be determined what degree of correction of carotid stenosis is necessary to reduce the risk of embolization, because it is known that balloon dilation to achieve total expansion at once might produce a higher risk of procedural complications such as additional emboli.

In our series, the 30-day composite rate of any stroke or death was 1.2% (0.8% for symptomatic and 0.4% for asymptomatic patients). These results are considerably below the 3% and 6% of maximum complication rates recommended in the American Heart Association guidelines for carotid endarterectomy of asymptomatic and symptomatic patients, respectively.

In our series, the degree of stenosis decreased from a mean of 82% before the procedure to a mean of 30% immediately after stent placement. In 156 patients, the immediate residual stenosis was <30%; in 79, between 30% and 50%; and in 20 patients, >50% (in all these patients, there was at least a 20% improvement of stenosis) (Fig. 25.12).

Most in-stent restenoses that occur during the follow-up are asymptomatic, as evidenced by the low rates of ipsilateral stroke during follow-up. Although the criteria for re-intervention are not well defined, we perform angioplasty with cerebral protection in all patients presenting with >70% restenosis.

Carotid sinus reaction including bradycardia, asystole, and hypotension is one of the most common complications of internal carotid artery angioplasty. In the published literature, the rate of hypotension after CAS varies from 10% to 42%, and the rate of bradycardia from 27% to 37%, whereas in our patients occurred in 5.1%. The sustained outward force of a self-expanding stent seems to be a weak stimulus to the baroreceptors of the carotid sinus, whereas forceful dilation with a balloon is a strong stimulus; therefore, these adverse events can be drastically reduced if balloon dilation is not used.

DWI is currently the most sensitive tool for detecting early cerebral ischemia and offers the possibility of revealing small and thus asymptomatic lesions occurring during CAS, so it would have considerable use in evaluating the efficacy of EPDs. In 82 patients, MR imaging with DWI could be performed before and within 48 h after the procedure, depicting 8.5% of silent infarcts. This result compares favorably with previous reports that reveal a number of silent ischemic lesions after neuroprotected CAS, ranging from 15.3% to 50%. This finding supports the idea that less device manipulation, including EPDs, across the lesion minimized emboli dislodgment.

Finally, with this technique, in which a CPD is not needed because angioplasty is not performed, indications for CAS can be extended. There are some anatomic difficulties such as tortuous vessels, in which CPDs are not suitable for navigation or placement; in these cases, our technique may overcome such difficulties, making the procedure possible and safer (Fig. 25.13).

8 Conclusion

CAS is a well-established therapy for the carotid artery disease with a very low rate of complications when performed by experimented operators. Most of the registries and well-conducted trials demonstrated that CAS and CEA are equivalent in terms of stroke prevention in a broad category of patients with carotid stenosis.

Indication for carotid revascularization should no longer be based only on the clinical data and the degree of stenosis assessed by imaging techniques measuring percentage of stenoses, but also on plaque characteristics. Improvements

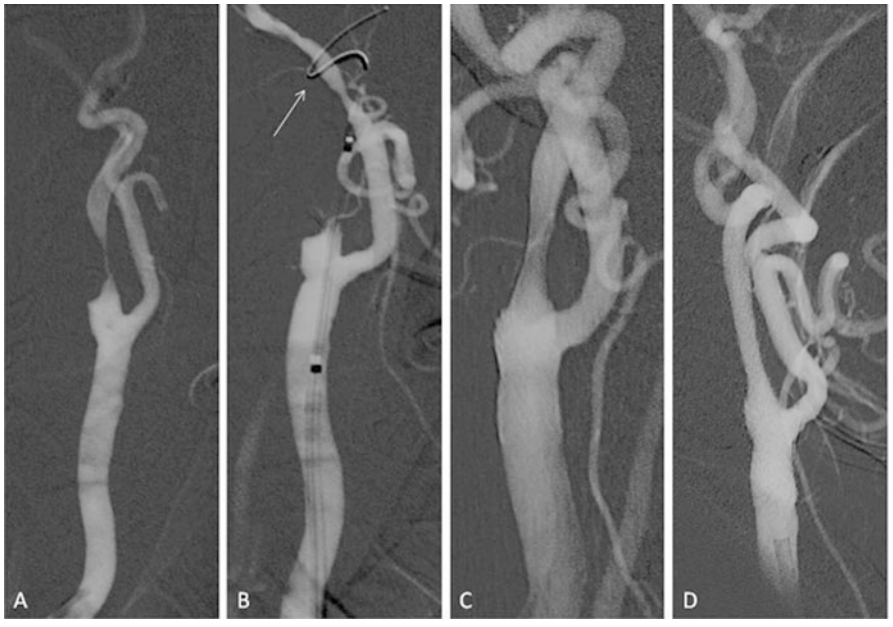

Fig. 25.13 (**a**) Severe carotid artery stenosis. (**b**) The tortousity of the post-stenotic segment of the ICA might have precluded filter placement (*arrow*). (**c**) Without the use of CPDs the stent could be placed easily obtaining a good self-expansion of the stent in the immediate angio control. (**d**) Final angio control 5 min later shows that the stent continued to expand without residual stenosis

in CT and MRI characterization of plaques may help in the identification of high-risk atherosclerotic plaque and in the quantification of biological markers, especially inflammation, that carry an increased embolic risk.

Based on our experience, stenting alone without the use of balloon angioplasty and therefore without using EDPs might be enough to treat patients who have symptomatic or asymptomatic severe carotid stenosis. In case of in-stent restenosis or lack of expansion angioplasty may be performed a second time safely if necessary.

Stenting alone may reduce the occurrence of hemodynamic depression during and after the procedure, avoiding the need of vasopressor support and ICU, thus reducing in-hospital stay and costs.

Further improvements in device technology are expected, making CAS procedure safer and positioning it as the preferred method to treat carotid artery disease in a wide range of patients.

References

1. The National Advisory Neurological Disorders and Stroke Council (1992) Stroke and cerebrovascular disease. National Institutes of Health Report. The National Advisory Neurological Disorders and Stroke Council, Bethesda, MD, pp 26–27
2. Higashida RT, Meyers PM, Phatouros CC, Connors JJ III, Barr JD, Sacks D III (2004) Reporting standards for carotid artery angioplasty and stent placement. Stroke 35:e112–e133
3. Molloy J, Markus HS (1999) Asymptomatic embolization predicts stroke and TIA risk in patients with carotid artery stenosis. Stroke 30:1440–1443
4. (1995) Risk of stroke in the distribution of an asymptomatic carotid artery. The European Carotid Surgery Trialists Collaborative Group. Lancet 345:209–212
5. (1998) Randomised trial of endarterectomy for recently symptomatic carotid stenosis: final results of the MRC European Carotid Surgery Trial (ECST). Lancet 351:1379–1387
6. North American Symptomatic Carotid Endarterectomy Trial (1991) Methods, patient characteristics, and progress. Stroke 22:711–720
7. DeBakey ME (1996) Carotid endarterectomy revisited. J Endovasc Surg 3:4
8. Eastcott HH, Pickering GW, Rob CG (1954) Reconstruction of internal carotid artery in a patient with intermittent attacks of hemiplegia. Lancet 267:994–996
9. Warlow C (1984) Carotid endarterectomy: does it work? Stroke 15:1068–1076
10. Barnett HJ, Plum F, Walton JN (1984) Carotid endarterectomy an expression of concern. Stroke 15:941–943
11. North American Symptomatic Carotid Endarterectomy Trial Collaborators (1991) Beneficial effect of carotid endarterectomy in symptomatic patients with high-grade carotid stenosis. N Engl J Med 325:445–453
12. Barnett HJ, Taylor DW, Eliasziw M, Fox AJ, Ferguson GG, Haynes RB, Rankin RN, Clagett GP, Hachinski VC, Sackett DL, Thorpe KE, Math M, Meldrum HE (1998) Benefit of carotid endarterectomy in patients with symptomatic moderate or severe stenosis. North American Symptomatic Carotid Endarterectomy Trial Collaborators. N Engl J Med 339:1415–1425
13. European Carotid Surgery Trialists' Collaborative Group (1991) MRC European Carotid Surgery trial: interim results for symptomatic patients with severe (70–99%) or with mild (0–29%) carotid stenosis. Lancet 337:1235–1243
14. MRC European Carotid Surgery Trialists (1998) Randomised trial of endarterectomy for recently symptomatic carotid stenosis: final results of the MRC European Carotid Surgery Trial (ECST). Lancet 351:1379–1387
15. Executive Committee for the Asymptomatic Carotid Atherosclerosis Study (1995) Endarterectomy for asymptomatic carotid artery stenosis. JAMA 273:1421–1428
16. MRC Asymptomatic Carotid Surgery Trial (ACST) Collaborative Group (2004) Prevention of disabling and fatal strokes by successful carotid endarterectomy in patients without recent neurological symptoms: randomised controlled trial. Lancet 363:1491–1502

17. Rothwell PM, Slatterg J, Waslow CP (1996) A systematic review of the risks of stroke or death due to endarterectomy for symptomatic carotid stenosis. Stroke 27:260–265
18. Safian RD, Bresnahan JF, Jaff MR, Foster M, Bacharach JM, Maini B, Turco M, Myla S, Eles G, Ansel GM, on behalf of the CREATE Pivotal Trial Investigators (2006) Protected carotid stenting in high-risk patients with severe carotid artery stenosis. J Am Coll Cardiol 47:2384–2389
19. Kerber CW, Cromwell LD, Loehden OL (1980) Catheter dilatation of proximal carotid stenosis during distal bifurcation endarterectomy. AJNR Am J Neuroradiol 1:348–349
20. Theron J, Raymond J, Casasco A, Courtheoux F (1987) Percutaneous angioplasty of atherosclerotic and postsurgical stenosis of carotid arteries. AJNR Am J Neuroradiol 8:495–500
21. Kachel R (1996) Results of balloon angioplasty in the carotid arteries. J Endovasc Surg 3:22–30
22. CAVATAS Investigators (2001) Endovascular versus surgical treatment in patients with carotid stenosis in the Carotid and Vertebral Artery Transluminal Angioplasty Study (CAVATAS): a randomised trial. Lancet 357:1729–1737
23. Alberts MJ, McCann R, Smith TP et al (1997) A randomized trial of carotid stenting vs. endarterectomy in patients with symptomatic carotid stenosis: study design. J Neurovasc Dis 2:228–234
24. Alberts MJ, for the Publications Committee of WALLSTENT (2001) Results of a multicenter prospective randomized trial of carotid artery stenting vs. carotid endarterectomy. Stroke 32:325
25. Shawl F, Kadro W, Domanski MJ, Lapetina FL, Iqbal AA, Dougherty KG, Weisher DD, Marquez JF, Shahab T (2000) Safety and efficacy of elective carotid artery stenting in high-risk patients. J Am Coll Cardiol 35:1721–1728
26. Sundt TM Jr, Whisnant JP, Houser OW, Fode NC (1990) Prospective study of the effectiveness and durability of carotid endarterectomy. Mayo Clin Proc 65:625–635
27. Malek AM, Higashida RT, Phatouros CC, Lempert TE, Meyers PM, Smith WS, Dowd CF, Halbach VV (2000) Stent angioplasty for cervical carotid artery stenosis in high-risk symptomatic NASCET-ineligible patients. Stroke 31:3029–3033
28. Yadav JS, Wholey MH, Kuntz RE et al (2004) Protected carotid-artery stenting versus endarterectomy in high-risk patients. N Engl J Med 351:1493–1501
29. The SPACE Collaborative Group (2006) 30 day results from the SPACE trial of stent-protected angioplasty versus carotid endarterectomy in symptomatic patients: a randomised non-inferiority trial. Lancet 368:1239–1247
30. Mas JL, Chatellier G, Beyssen B (2004) Carotid angioplasty and stenting with and without cerebral protection: clinical alert from the endarterectomy versus angioplasty in patients with symptomatic severe carotid stenosis (EVA-3S) trial. Stroke 35:e18–e20
31. International Carotid Stenting Study Investigators (2010) Carotid artery stenting compared with endarterectomy in patients with symptomatic carotid stenosis (International Carotid Stenting Study): an interim analysis of a randomised controlled trial. Lancet 375:985–997
32. Brott TG, Hobson RW II, Howard G, Roubin GS, Clark WM, Brooks W, Mackey A, Hill MD, Leimgruber PP, Sheffet AJ, Howard VJ, Moore WS, Voeks JH, Hopkins LN, Cutlip DE, Cohen DJ, Popma JJ, Ferguson RD, Cohen SN, Blackshear JL, Silver FL, Mohr JP, Lal BK, Meschia JF, for the CREST Investigators (2010) Stenting versus Endarterectomy for Treatment of Carotid-Artery Stenosis. N Engl J Med 363:11–23
33. CaRESS Steering Committee (2005) Carotid revascularization using endarterectomy or stenting systems (CaRESS) phase I clinical trial: 1-year results. J Vasc Surg 42(2):213–219
34. Gray WA, Hopkins LN, Yadav S, Davis T, Wholey M, Atkinson R, Cremonesi A, Fairman R, Walker G, Verta P, Popma J, Virmani R, Cohen DJ, for the ARCHeR Trial Collaborators (2006) Protected carotid stenting in high-surgical-risk patients: the ARCHeR results. J Vasc Surg 44:258–268
35. Iyer SS, White CJ, Hopkins LN, Katzen BT, Safian R, Wholey MH, Gray WA, Ciocca R, Bachinsky WB, Ansel G, Joye J, Russell ME, for the BEACH Investigators (2008) Carotid artery revascularization in high-surgical-risk patients using the carotid WALLSTENT and FilterWire EX/EZ. J Am Coll Cardiol 51:427–434
36. Mehta RH, Zahn R, Hochadel M, Mudra H, Ischinger T, Hauptmann KE, Jung J, Seggewiß H, Zeymer U, Senges J (2009) Effectiveness and safety of carotid artery stenting for significant carotid stenosis in patients with contralateral occlusion. Am J Cardiol 5:725–731
37. Saam T, Schoenberg SO, Hatsukami TS, Reiser M, Yuan C, Nikolaou K (2008) [High-resolution magnetic resonance imaging of carotid atherosclerotic plaque]. Rofo 180:100–111
38. McCarthy MJ, Loftus IM, Thompson MM et al (1999) Angiogenesis and the atherosclerotic carotid plaque: an association between symptomatology and plaque morphology. J Vasc Surg 30:261–268
39. Virmani R, Kolodgie FD, Burke AP, Farb A, Schwartz SM (2000) Lessons from sudden coronary death: a comprehensive morphological classification scheme for atherosclerotic lesions. Arterioscler Thromb Vasc Biol 20:1262–1275
40. Saam T, Hatsukami TS, Takaya N et al (2007) The vulnerable, or high-risk, atherosclerotic plaque: noninvasive MR imaging for characterization and assessment. Radiology 244:64–77
41. Falk E, Shah PK, Fuster V (1995) Coronary plaque disruption. Circulation 92:657–671
42. Naghavi M, Libby P, Falk E et al (2003) From vulnerable plaque to vulnerable patient: a call for new definitions and risk assessment strategies: Part I. Circulation 108:1664–1672
43. Takaya N, Yuan C, Chu B et al (2005) Presence of intraplaque hemorrhage stimulates progression of carotid atherosclerotic plaques: a high-resolution magnetic resonance imaging study. Circulation 111:2768–2775
44. Altaf N, Beech A, Goode SD et al (2007) Carotid intraplaque hemorrhage detected by magnetic resonance imaging predicts embolization during carotid endarterectomy. J Vasc Surg 46:31–36
45. Saam T, Yuan C, Chu B et al (2007) Predictors of carotid atherosclerotic plaque progression as measured by noninvasive magnetic resonance imaging. Atherosclerosis 194:e34–e42
46. Oliver JJ, Webb DJ (2003) Noninvasive assessment of arterial stiffness and risk of atherosclerotic events. Arterioscler Thromb Vasc Biol 23:554–566
47. Saba L, Mallarini G (2010) A comparison between NASCET and ECST methods in the study of carotids: evaluation using Multi-Detector-Row CT angiography. Eur J Radiol 76:42–47
48. Rothwell PM, Gibson RJ, Slattery J, Sellar RJ, Warlow CP (1994) Equivalence of measurements of carotid stenosis. A comparison of three methods on 1001 angiograms. European Carotid Surgery Trialists' Collaborative Group. Stroke 25:2435–2439
49. Liapis CD, Satiani B, Florance CL, Evans WE (1981) Motor speech malfunction following carotid endarterectomy. Surgery 89:56–59
50. Tendera M, Aboyans V, Bartelink ML et al (2011) ESC Guidelines on the diagnosis and treatment of peripheral artery diseases: Document covering atherosclerotic disease of extracranial carotid and vertebral, mesenteric, renal, upper and lower extremity arteries: the Task Force on the Diagnosis and Treatment of Peripheral Artery Diseases of the European Society of Cardiology (ESC). Eur Heart J 32:2851–2906
51. Liapis CD, Bell PR, Mikhailidis D et al (2009) ESVS guidelines. Invasive treatment for carotid stenosis: indications, techniques. Eur J Vasc Endovasc Surg 37:1–19
52. Brott TG, Halperin JL, Abbara S et al (2011) 2011 ASA/ACCF/AHA/AANN/AANS/ACR/ASNR/CNS/SAIP/SCAI/

SIR/SNIS/SVM/SVS Guideline on the management of patients with extracranial carotid and vertebral artery disease: executive summary. A Report of the American College of Cardiology Foundation/American Heart Association Task Force on Practice Guidelines, and the American Stroke Association, American Association of Neuroscience Nurses, American Association of Neurological Surgeons, American College of Radiology, American Society of Neuroradiology, Congress of Neurological Surgeons, Society of Atherosclerosis Imaging and Prevention, Society for Cardiovascular Angiography and Interventions, Society of Interventional Radiology, Society of NeuroInterventional Surgery, Society for Vascular Medicine, and Society for Vascular Surgery Developed in Collaboration With the American Academy of Neurology and Society of Cardiovascular Computed Tomography. J Am Coll Cardiol 57:1002–1044

53. Lin R, Mazighi M, Yadav J, Abou-Chebl A (2010) The impact of timing on outcomes of carotid artery stenting in recently symptomatic patients. J Neurointerv Surg 2:55–58
54. Iwata T, Mori T, Tajiri H, Miyazaki Y, Nakazaki M (2012) Long-term angiographic and clinical outcome following stenting by flow reversal technique for chronic occlusions older than 3 months of the cervical carotid or vertebral artery. Neurosurgery 70:82–90 (discussion 90)
55. Papanagiotou P, Roth C, Walter S et al (2011) Carotid artery stenting in acute stroke. J Am Coll Cardiol 58:2363–2369
56. Terada T, Tsuura M, Matsumoto H, et al (2006) Endovascular treatment for pseudo-occlusion of the internal carotid artery. Neurosurgery 59:301–309 (discussion 301–309)
57. Gonzalez A, Gil-Peralta A, Mayol A et al (2011) Internal carotid artery stenting in patients with near occlusion: 30-day and long-term outcome. AJNR Am J Neuroradiol 32:252–258
58. Yadav JS (2010) Functional occlusions of the carotid artery (string signs): to treat or not to treat? JACC Cardiovasc Interv 3:305–306
59. Yoshida K, Sadamasa N, Narumi O, Chin M, Yamagata S, Miyamoto S (2012) Symptomatic low-grade carotid stenosis with intraplaque hemorrhage and expansive arterial remodeling is associated with a high relapse rate refractory to medical treatment. Neurosurgery 70(5):1143–1150
60. Grant EG, Benson CB, Moneta GL et al (2003) Carotid artery stenosis: gray-scale and Doppler US diagnosis–Society of Radiologists in Ultrasound Consensus Conference. Radiology 229:340–346
61. Sabeti S, Schillinger M, Mlekusch W et al (2004) Quantification of internal carotid artery stenosis with duplex US: comparative analysis of different flow velocity criteria. Radiology 232:431–439
62. Gronholdt ML, Nordestgaard BG, Schroeder TV, Vorstrup S, Sillesen H (2001) Ultrasonic echolucent carotid plaques predict future strokes. Circulation 104:68–73
63. Gaitini D, Soudack M (2005) Diagnosing carotid stenosis by Doppler sonography: state of the art. J Ultrasound Med 24:1127–1136
64. Tahmasebpour HR, Buckley AR, Cooperberg PL, Fix CH (2005) Sonographic examination of the carotid arteries. Radiographics 25:1561–1575
65. Oates CP, Naylor AR, Hartshorne T et al (2009) Joint recommendations for reporting carotid ultrasound investigations in the United Kingdom. Eur J Vasc Endovasc Surg 37:251–261
66. Cumbie T, Rosero EB, Valentine RJ, Modrall JG, Clagett GP, Timaran CH (2008) Utility and accuracy of duplex ultrasonography in evaluating in-stent restenosis after carotid stenting. Am J Surg 196:623–628
67. Setacci C, Chisci E, Setacci F, Iacoponi F, de Donato G (2008) Grading carotid intrastent restenosis: a 6-year follow-up study. Stroke 39:1189–1196
68. Nolz R, Wibmer A, Beitzke D et al (2012) Carotid artery stenting and follow-up: value of 64-MSCT angiography as complementary imaging method to color-coded duplex sonography. Eur J Radiol 81:89–94
69. Nederkoorn PJ, Brown MM (2009) Optimal cut-off criteria for duplex ultrasound for the diagnosis of restenosis in stented carotid arteries: review and protocol for a diagnostic study. BMC Neurol 9:36
70. El-Saden SM, Grant EG, Hathout GM, Zimmerman PT, Cohen SN, Baker JD (2001) Imaging of the internal carotid artery: the dilemma of total versus near total occlusion. Radiology 221:301–308
71. Sameshima T, Futami S, Morita Y et al (1999) Clinical usefulness of and problems with three-dimensional CT angiography for the evaluation of arteriosclerotic stenosis of the carotid artery: comparison with conventional angiography, MRA, and ultrasound sonography. Surg Neurol 51:301–308 (discussion 308–309)
72. Hollingworth W, Nathens AB, Kanne JP et al (2003) The diagnostic accuracy of computed tomography angiography for traumatic or atherosclerotic lesions of the carotid and vertebral arteries: a systematic review. Eur J Radiol 48:88–102
73. Puchner S, Popovic M, Wolf F, Reiter M, Lammer J, Bucek RA (2009) Multidetector CTA in the quantification of internal carotid artery stenosis: value of different reformation techniques and axial source images compared with selective carotid arteriography. J Endovasc Ther 16:336–342
74. Koelemay MJ, Nederkoorn PJ, Reitsma JB, Majoie CB (2004) Systematic review of computed tomographic angiography for assessment of carotid artery disease. Stroke 35:2306–2312
75. Chen CJ, Lee TH, Hsu HL et al (2004) Multi-Slice CT angiography in diagnosing total versus near occlusions of the internal carotid artery: comparison with catheter angiography. Stroke 35:83–85
76. Bartlett ES, Walters TD, Symons SP, Fox AJ (2007) Carotid stenosis index revisited with direct CT angiography measurement of carotid arteries to quantify carotid stenosis. Stroke 38:286–291
77. Saba L, Sanfilippo R, Montisci R, Mallarini G (2012) Carotid artery stenosis at MSCT: is there a threshold in millimeters that determines clinical significance? Cardiovasc Intervent Radiol 35:49–58
78. Wardlaw JM, Chappell FM, Stevenson M et al (2006) Accurate, practical and cost-effective assessment of carotid stenosis in the UK. Health Technol Assess 10:iii–iv, ix–x, 1–182
79. Josephson SA, Bryant SO, Mak HK, Johnston SC, Dillon WP, Smith WS (2004) Evaluation of carotid stenosis using CT angiography in the initial evaluation of stroke and TIA. Neurology 63:457–460
80. Miralles M, Merino J, Busto M, Perich X, Barranco C, Vidal-Barraquer F (2006) Quantification and characterization of carotid calcium with multi-detector CT-angiography. Eur J Vasc Endovasc Surg 32:561–567
81. U-King-Im JM, Fox AJ, Aviv RI et al (2010) Characterization of carotid plaque hemorrhage: a CT angiography and MR intraplaque hemorrhage study. Stroke 41:1623–1629
82. Korn A, Bender B, Thomas C et al (2011) Dual energy CTA of the carotid bifurcation: advantage of plaque subtraction for assessment of grade of the stenosis and morphology. Eur J Radiol 80:e120–e125
83. Saam T, Ferguson MS, Yarnykh VL et al (2005) Quantitative evaluation of carotid plaque composition by in vivo MRI. Arterioscler Thromb Vasc Biol 25:234–239
84. Frolich AM, Pilgram-Pastor SM, Psychogios MN, Mohr A, Knauth M (2011) Comparing different MR angiography strategies of carotid stents in a vascular flow model: toward stent-specific recommendations in MR follow-up. Neuroradiology 53: 359–365

85. Hayes CE, Mathis CM, Yuan C (1996) Surface coil phased arrays for high-resolution imaging of the carotid arteries. J Magn Reson Imaging 6:109–112
86. Kwon BJ, Jung C, Sheen SH, Cho JH, Han MH (2007) CT angiography of stented carotid arteries: comparison with Doppler ultrasonography. J Endovasc Ther 14:489–497
87. Renker M, Nance JW Jr, Schoepf UJ et al (2011) Evaluation of heavily calcified vessels with coronary CT angiography: comparison of iterative and filtered back projection image reconstruction. Radiology 260:390–399
88. Easton JD, Saver JL, Albers GW et al (2009) Definition and evaluation of transient ischemic attack: a scientific statement for healthcare professionals from the American Heart Association/American Stroke Association Stroke Council; Council on Cardiovascular Surgery and Anesthesia; Council on Cardiovascular Radiology and Intervention; Council on Cardiovascular Nursing; and the Interdisciplinary Council on Peripheral Vascular Disease. The American Academy of Neurology affirms the value of this statement as an educational tool for neurologists. Stroke 40:2276–2293
89. Ho KY (2004) MR angiography of carotid arteries. JBR-BTR 87:29–32
90. Aoki S, Nakajima H, Kumagai H, Araki T (2000) Dynamic contrast-enhanced MR angiography and MR imaging of the carotid artery: high-resolution sequences in different acquisition planes. AJNR Am J Neuroradiol 21:381–385
91. Schuster L, Hauser T, Essig M (2010) [Significance of MR angiography for imaging diagnostics of carotid artery diseases]. Radiologe 50:597–606
92. Gizewski ER, Ladd ME, Paul A, Wanke I, Goricke S, Forsting M (2005) Water excitation: a possible pitfall in cerebral time-of-flight angiography. AJNR Am J Neuroradiol 26:152–155
93. Ozsarlak O, Van Goethem JW, Maes M, Parizel PM (2004) MR angiography of the intracranial vessels: technical aspects and clinical applications. Neuroradiology 46:955–972
94. Chappell FM, Wardlaw JM, Young GR et al (2009) Carotid artery stenosis: accuracy of noninvasive tests–individual patient data meta-analysis. Radiology 251:493–502
95. Nederkoorn PJ, van der Graaf Y, Hunink MG (2003) Duplex ultrasound and magnetic resonance angiography compared with digital subtraction angiography in carotid artery stenosis: a systematic review. Stroke 34:1324–1332
96. Nederkoorn PJ, Mali WP, Eikelboom BC et al (2002) Preoperative diagnosis of carotid artery stenosis: accuracy of noninvasive testing. Stroke 33:2003–2008
97. Debrey SM, Yu H, Lynch JK et al (2008) Diagnostic accuracy of magnetic resonance angiography for internal carotid artery disease: a systematic review and meta-analysis. Stroke 39:2237–2248
98. Yuan C, Mitsumori LM, Beach KW, Maravilla KR (2001) Carotid atherosclerotic plaque: noninvasive MR characterization and identification of vulnerable lesions. Radiology 221:285–299
99. Yuan C, Kerwin WS, Ferguson MS et al (2002) Contrast-enhanced high resolution MRI for atherosclerotic carotid artery tissue characterization. J Magn Reson Imaging 15:62–67
100. Saam T, Underhill HR, Chu B et al (2008) Prevalence of American Heart Association type VI carotid atherosclerotic lesions identified by magnetic resonance imaging for different levels of stenosis as measured by duplex ultrasound. J Am Coll Cardiol 51:1014–1021
101. Cai J, Hatsukami TS, Ferguson MS et al (2005) In vivo quantitative measurement of intact fibrous cap and lipid-rich necrotic core size in atherosclerotic carotid plaque: comparison of high-resolution, contrast-enhanced magnetic resonance imaging and histology. Circulation 112:3437–3444
102. Yuan C, Mitsumori LM, Ferguson MS et al (2001) In vivo accuracy of multispectral magnetic resonance imaging for identifying lipid-rich necrotic cores and intraplaque hemorrhage in advanced human carotid plaques. Circulation 104:2051–2056
103. Borisch I, Hamer OW, Zorger N, Feuerbach S, Link J (2005) In vivo evaluation of the carotid wallstent on three-dimensional contrast material-enhanced MR angiography: influence of artifacts on the visibility of stent lumina. J Vasc Interv Radiol 16:669–677
104. Rizzo JA, Dodge A, White P, Martin ED (2010) Magnetic resonance angiography in the evaluation of carotid stent patency. Perspect Vasc Surg Endovasc Ther 22:261–263
105. Buecker A, Spuentrup E, Ruebben A, Gunther RW (2002) Artifact-free in-stent lumen visualization by standard magnetic resonance angiography using a new metallic magnetic resonance imaging stent. Circulation 105:1772–1775
106. Choi CG, Lee DH, Lee JH et al (2007) Detection of intracranial atherosclerotic steno-occlusive disease with 3D time-of-flight magnetic resonance angiography with sensitivity encoding at 3 T. AJNR Am J Neuroradiol 28:439–446
107. Li Z-Y, Howarth PS, Tang T, Gillard JH (2006) How critical is fibrous cap thickness to carotid plaque stability? A flow−plaque interaction model. Stroke 37:1195–1199
108. Cardaioli P, Giordan M, Panfili M et al (2004) Complication with an embolic protection device during carotid angioplasty. Catheter Cardiovasc Interv 62:234–236
109. Bussiére M, Pelz DM, Kalapos P et al (2008) Results using a self-expanding stent alone in the treatment of severe symptomatic carotid bifurcation stenosis. J Neurosurg 109:454–460
110. Maynar M, Baldi S, Rostagno R, Zander T, Rabellino M, Llorens R et al (2007) Carotid stenting without use of balloon angioplasty and distal protection devices: preliminary experience in 100 cases. AJNR Am J Neuroradiol 28:1378–1383
111. Baldi S, Zander T, Rabellino M, Llorens R et al (2007) Carotid artery stenting without angioplasty and cerebral protection: a single-centre experience with up to 7 years' follow-up. AJNR Am J Neuroradiol 28:1378–1383
112. Rabellino M, Garcia-Nielsen L, Baldi S, Zander T, Casasola C, Estigarribia A, Chevez H, Llorens R, Maynar M (2010) Non-protected carotid artery stent without angioplasty in high risk patients with carotid and coronary artery disease undergoing cardiac surgery. Minim Invasive Ther Allied Technol 19(3):184–188
113. Das M, Braunschweig T, Muhlenbruch G et al (2009) Carotid plaque analysis: comparison of dual-source computed tomography (CT) findings and histopathological correlation. Eur J Vasc Endovasc Surg 38:14–19

New Approaches for Plaque Component Analysis in Intravascular Ultrasound (IVUS) Images

26

Arash Taki, Alireza Roodaki, Sara Avansari, Ali Bigdelou, Amin Katouzian, and Nassir Navab

1 Introduction

The aim of this part of the project is to classify pixels from plaque area of IVUS images into three tissue classes: dense calcium (DC), fibro-fatty (FF), and necrotic core (NC). These plaque components appear with different texture patterns in IVUS images (Fig. 26.1).

Thereby, texture analysis methods are best suited to characterize coronary plaque compositions. In most texture analysis methods, for each pixel (i, j) of the image I_{D_D} (or I), a $(M+1)\times(N+1)$ neighborhood $I\{i+m, j+n\}$ with $m \in \{-\frac{M}{2}, \frac{M}{2}\}$ and $n \in \{-\frac{N}{2}, \frac{N}{2}\}$ calling sweeping window is being processed. Then, textural features are extracted from this sweeping window and assigned to the central pixel. Finally, according to the extracted features, pixels are classified into predetermined classes by the means of a classifier. It is worth mentioning that since IVUS images are circular cross section of the blood vessel, input images are converted into polar coordinates before applying texture analysis methods so that rectangular sweeping windows used for feature extraction are utilizable (Fig. 26.2).

Figure 26.3 shows the outline of the project and the steps of Tissue Characterization stage. However, each of the proposed algorithms later explained in this chapter may follow some or all of these steps. It is worth defining the materials of these steps before stating the proposed algorithms.

Note: In this chapter, the plaque area is taken directly from the VH examples, in order for us to be able to validate the classification algorithms proposed here.

A. Taki (✉) • A. Bigdelou • A. Katouzian • N. Navab
Informatic Department, Technical University of Munich, I16, Boltzmannstr. 3, Garching b. Munich, 85748, Germany
e-mail: taki@cs.tum.edu

A. Roodaki
Department SSE, SUPELEC, Gif-sur-Yvette, France

S. Avansari
Department of Computer Science, University of Tehran, Tehran, Iran

2 Materials and General Background

2.1 Feature Extraction Methods

Co-occurrence matrix and statistical properties: A co-occurrence matrix, C, is used to describe the patterns of neighboring pixels in an image at a given distance d, and a given direction $\theta \in \{0°, 45°, 90°, 135°\}$ corresponding to horizontal, diagonal, vertical, and anti-diagonal directions (Fig. 26.4). This matrix is somehow a second-order histogram of the image and gives information about the relative positions of the various gray levels within the image [1].

Let us consider the neighborhood centered on the pixel (i, j) from image I. Its co-occurrence matrix is defined in a certain direction as $C_{d,\theta}(a, b)$,where $a, b \in [1, \ldots, P]$, where P refers to maximum gray level in image I and d is the gray level distance in the direction θ. Figure 26.5 gives a graphical description of this process for $C_{1,0°}$.

Various textural features can then be derived from co-occurrence matrix. For defining these textural features it is necessary to calculate the following statistical parameters in the first step:

$$P^{d,\theta}(a,b) = \frac{C_{d,\theta(a,b)}}{\sum_{a=1}^{P}\sum_{b=1}^{P} C_{d,\theta(a,b)}} \tag{26.1}$$

$$P_x^{d,\theta}(a) = \sum_{b=1}^{P} P^{d,\theta}(a,b) \tag{26.2}$$

$$P_y^{d,\theta}(b) = \sum_{a=1}^{P} P^{d,\theta}(a,b) \tag{26.3}$$

L. Saba et al. (eds.), *Multi-Modality Atherosclerosis Imaging and Diagnosis*,
DOI 10.1007/978-1-4614-7425-8_26,

Fig. 26.1 Different tissue types in plaque area of IVUS images: (**a**) dense calcium, (**b**) necrotic core, and (**c**) fibro-lipid

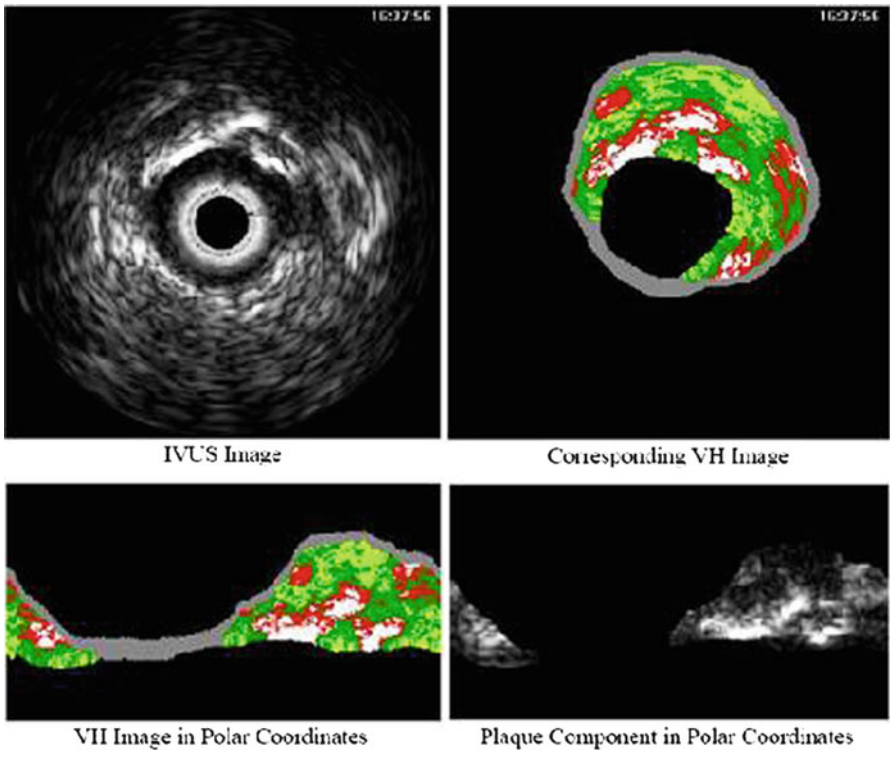

Fig. 26.2 Cartesian–Polar conversion of IVUS images for feature extraction

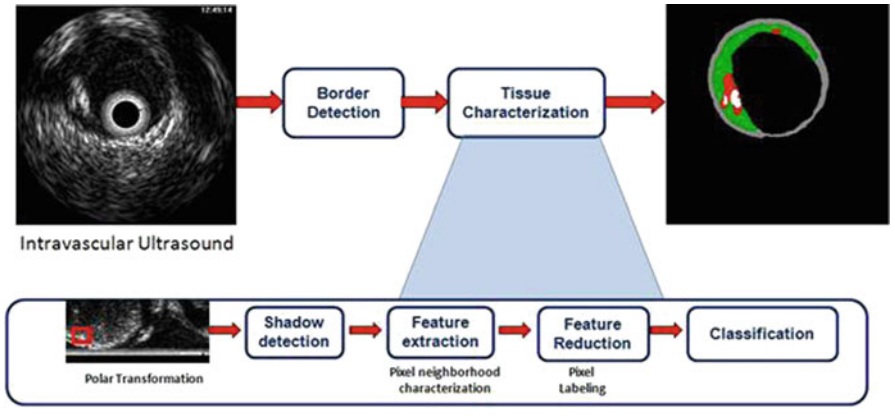

Fig. 26.3 Outline of the project and steps of Tissue Characterization stage

$$P_{x+y}^{d,\theta}(k) = \sum_{a=1}^{P}\sum_{b=1}^{P} P^{d,\theta}(a,b), \quad a+b=k, \quad k = 2,\ldots,2P \tag{26.4}$$

$$P_{x-y}^{d,\theta}(k) = \sum_{a=1}^{P}\sum_{b=1}^{P} P^{d,\theta}(a,b), \quad |a-b|=k, \quad k = 1,\ldots,P-1 \tag{26.5}$$

$$HX^{d,\theta} = -\sum_{a=1}^{P} P_x^{d,\theta}(a)\log(P_x^{d,\theta}(a)) \tag{26.6}$$

$$HY^{d,\theta} = -\sum_{b=1}^{P} P_y^{d,\theta}(b)\log(P_y^{d,\theta}(b)) \tag{26.7}$$

$$HXY_1^{d,\theta} = -\sum_{a=1}^{P}\sum_{b=1}^{P} P^{d,\theta}(a,b)\log(P_x^{d,\theta}(a)P_y^{d,\theta}(b)) \tag{26.8}$$

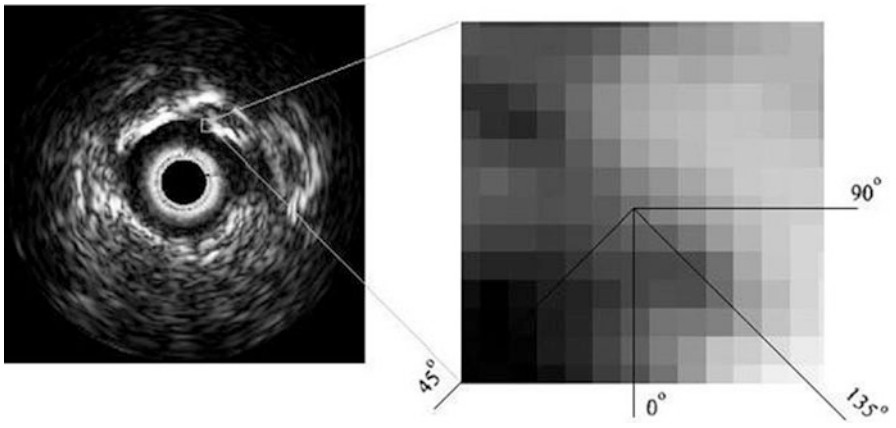

Fig. 26.4 The four directions used to form the co-occurrence matrix

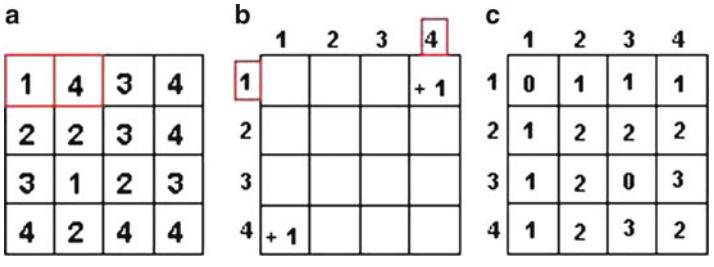

Fig. 26.5 Construction of the co-occurrence matrix in horizontal direction: (**a**) the original image, (**b**) horizontal neighboring of gray levels 1 and 4 with distance 1 occurred once in the image, and (**c**) the final result of the horizontal co-occurrence matrix

$$HXY_2^{d,\theta} = -\sum_{a=1}^{P}\sum_{b=1}^{P} P_x^{d,\theta}(a)\,P_y^{d,\theta}(b)\log(P_x^{d,\theta}(a)\,P_y^{d,\theta}(b)) \tag{26.9}$$

$$Q^{d,\theta}(a,b) = \sum_{k=1}^{P} \frac{P^{d,\theta}(a,k)\,P^{d,\theta}(b,k)}{P_x^{d,\theta}(a)\,P_y^{d,\theta}(b)} \tag{26.10}$$

Based on these statistical parameters, the 14 Haralick texture features are defined as follows:

1. Angular second moment (ASM): this feature is a measure of smoothness of the image. The less smooth the image is, the lower is the ASM.

$$f_1^{d,\theta} = \sum_{a=1}^{P}\sum_{b=1}^{P} P^{d,\theta}(a,b) \tag{26.11}$$

2. Contrast: This feature is a measure of local gray-level variations.

$$f_2^{d,\theta} = \sum_{k=0}^{P-1} k^2\, p_{x-y}^{d,\theta}(k) \tag{26.12}$$

3. Correlation:

$$f_3^{d,\theta} = \frac{\sum_{a=1}^{P}\sum_{b=1}^{P} ab\,p^{d,\theta}(a,b) - \mu_x\,\mu_y}{\sigma_x\sigma_y} \tag{26.13}$$

4. Variance:

$$f_4^{d,\theta} = \sum_{a=1}^{P}\sum_{b=1}^{P} (a-\mu)^2\,p^{d,\theta}(a,b) \tag{26.14}$$

5. Inverse difference moment:

$$f_5^{d,\theta} = \sum_{a=1}^{P}\sum_{b=1}^{P} \frac{1}{1+(a-b)^2}\,p^{d,\theta}(a,b) \tag{26.15}$$

6. Sum average:

$$f_6^{d,\theta} = \sum_{k=2}^{2P} k\,p_{x+y}^{d,\theta}(k) \tag{26.16}$$

7. Sum variance:

$$f_7^{d,\theta} = \sum_{k=2}^{2P} (k - f_6^{d,\theta})\,p_{x+y}^{d,\theta}(k) \tag{26.17}$$

8. Sum entropy:

$$f_8^{d,\theta} = \sum_{k=2}^{2P} p_{x+y}^{d,\theta}(k)\log(p_{x+y}^{d,\theta}(k)) \tag{26.18}$$

9. Difference variance:

$$f_9^{d,\theta} = -\sum_{k=1}^{P-1} p_{x-y}^{d,\theta}(k)\log(p_{x-y}^{d,\theta}(k)) \tag{26.19}$$

10. Difference variance:

$$f_{10}^{d,\theta} = -\sum_{k=1}^{P-1} p_{x-y}^{d,\theta}(k)\log(p_{x-y}^{d,\theta}(k)) \tag{26.20}$$

11. Entropy: This feature is a measure of randomness of the image and takes low values for smooth images.

$$f_{11}^{d,\theta} = -\sum_{a=1}^{P}\sum_{b=1}^{P} p^{d,\theta}(a,b)\log(p^{d,\theta}(a,b)) \tag{26.21}$$

12. Information measure:

$$f_{12}^{d,\theta} = \frac{f_{11} - HXY_1^{d,\theta}}{\max(HX^{d,\theta}, HY^{d,\theta})} \tag{26.22}$$

$$f_{13}^{d,\theta} = \sqrt{1-\exp^{-2(HXY_2^{d,\theta}-f_{11}^{d,\theta})}} \tag{26.23}$$

13. Maximal correlation coefficient:

$$f_{14}^{d,\theta} = \sqrt{\text{second largest eigenvalue of } Q^{d,\theta}} \tag{26.24}$$

Local binary pattern (LBP): LBP is a structure-related measure in which a binary number is allocated to the circularly symmetric neighborhoods of the center pixel of the window being processed and the histogram of the resulting binary patterns can be used as a discriminative feature for texture analysis [2, 3]. Actually, in this method N neighbors of the center pixel (i, j) on a circle of radius R with coordinates $\left(-R\sin\frac{\pi n}{N}, R\cos\frac{\pi n}{N}\right)$ $(n \in \{0,\ldots,N-1\})$ are processed. Typical neighbor sets (N, R) are (8, 1), (16, 2), and (24, 3), as shown in Fig. 26.6.

As these coordinates do not match the coordinates of the processing window, their corresponding gray levels are estimated by interpolation. Let g_c correspond to the gray value of the center pixel and g_n correspond to the gray values of the N neighbor pixels. A binary digit is then allocated to each neighbor based on the following function:

$$s(g_n - g_c) = \begin{cases} 1, g_n - g_c \geq 0 \\ 0, g_n - g_c < 0 \end{cases} \tag{26.25}$$

Then, by rotating the neighbor set clockwise the least significant resulting binary string is assigned to the processing as its binary pattern $L_{R,N} = \{L_{R,N}^0, \ldots, L_{R,N}^{N-1}\}$. This way the local binary pattern is rotation invariant. The basic steps for calculating $L_{R,N}$ and some microstructures that binary patterns can detect in images are illustrated in Fig. 26.7.

Based on the binary pattern $L_{R,N}$ and the gray values of neighbor pixels g_n, three texture features are defined as follows (Figs. 26.8, 26.9, and 26.10):

$$f_{R,N}^1 = \sum_{n=0}^{N-1} L_{R,N}^n 2^n \tag{26.26}$$

$$f_{R,N}^2 = \text{var}\{g_n\} \tag{26.27}$$

$$f_{R,N}^3 = \begin{cases} \sum_{n=0}^{N-1} L_{R,N}^n, & U(L_{R,N}) \leq 0 \\ N+1, & \text{otherwise} \end{cases} \tag{26.28}$$

Function U is a transition counter that counts the transition between 0 and 1 and vice versa in the binary pattern.

Run-length matrix: One of the methods that has been extensively used in segmentation and texture analysis is run-length transform [1]. A gray-level run is a set of consecutive pixels having the same gray-level value. The length of the run is the number of pixels in the run. Run-length features encode textural information related to the number of times each gray-level appears in the image by itself, the number of times it appears in pairs, and so on. Let us consider the neighborhood centered on the pixel (i, j) from image I. Its run-length matrix is defined in a certain direction as $R_k(a,\ b)$, where $a \in [1,\ldots,P]$, where P is maximum gray level and b is the run length, i.e., the number of consecutive pixels along a direction having the same gray-level value. In this approach each neighborhood is characterized with two run-length matrices: $R_v(a,\ b)$ and $R_h(a,\ b)$ corresponding to vertical and horizontal directions, respectively. Figure 26.11 shows the formation of run-length matrix.

Let R be the maximum run-length, N_r be the total number of runs, and N_p be the number of pixels in the processing window. Run-length features are then defined as follows:

1. Galloway (traditional) run-length features: the five original features of run-length statistics derived by Galloway [6] are as follows:
   - Short run emphasis (SRE) (Fig. 26.12):

$$f_1^k = \frac{1}{N_\tau}\sum_{a=1}^{P}\sum_{b=1}^{R}\frac{R_{k(a,b)}}{b^2} \tag{26.29}$$

   - Long run emphasis (LRE) (Fig. 26.13):

$$f_2^k = \frac{1}{N_\tau}\sum_{a=1}^{P}\sum_{b=1}^{R} R_k(a,b)\cdot b^2 \tag{26.30}$$

   - Gray-level nonuniformity (GLN) (Fig. 26.14):

$$f_3^k = \frac{1}{N_\tau}\sum_{a=1}^{P}\left(\sum_{b=1}^{R} R_k(a,b)\right)^2 \tag{26.31}$$

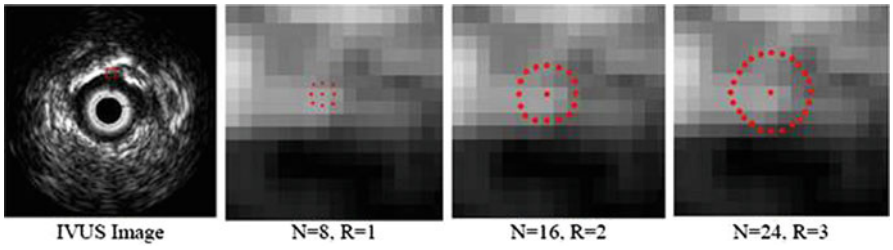

Fig. 26.6 Typical LBP binary patterns [4]

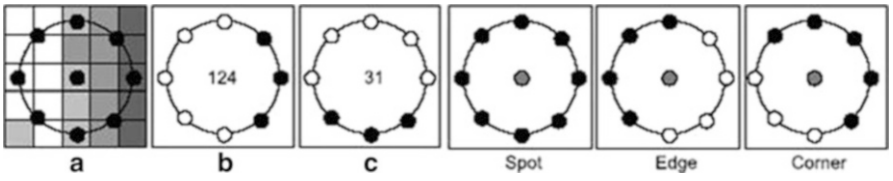

Fig. 26.7 Illustration of LBP, *Left*: the basic steps in computing the LBP code for a given pixel position: (**a**) the operator is centered on the given pixel and equidistant samples are taken on the circle of radius around the center; (**b**) the obtained samples are turned into 0's and 1's by applying a sign function with the center pixel value as threshold; (**c**) rotation invariance is achieved by bitwise shifting the binary pattern clockwise until the lowest binary number is found. *Right*: some of the microstructures that LBP are measuring [5]

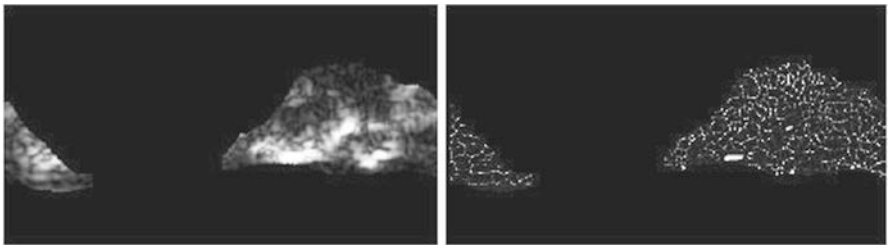

Fig. 26.8 Illustration of $f^1_{R,N}$ feature for $P = 8$, $R = 1$: plaque area in polar coordinates (*left*) and $f^1_{R,N}$ (*right*)

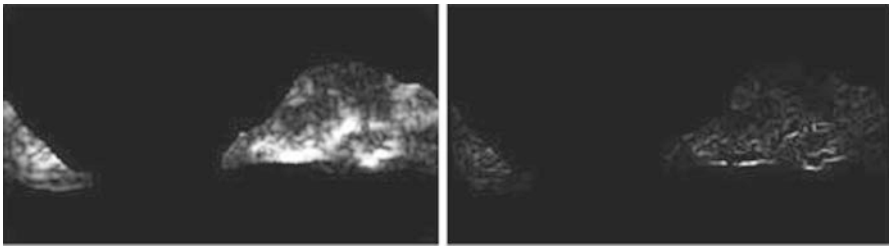

Fig. 26.9 Illustration of $f^2_{R,N}$ feature for $P = 8$; $R = 1$: plaque area in polar coordinates (*left*) and $f^2_{R,N}$ (*right*)

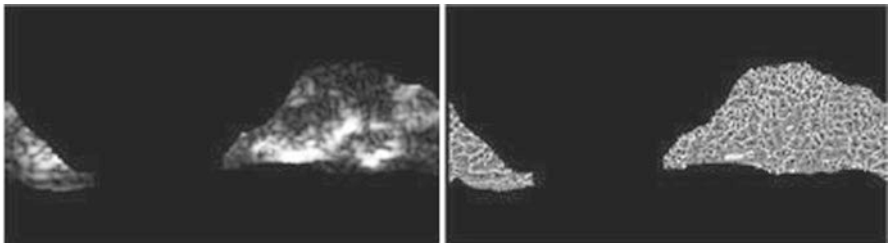

Fig. 26.10 Illustration of $f^3_{R,N}$ feature for $P = 8$; $R = 1$: plaque area in polar coordinates (*left*) and $f^3_{R,N}$ (*right*)

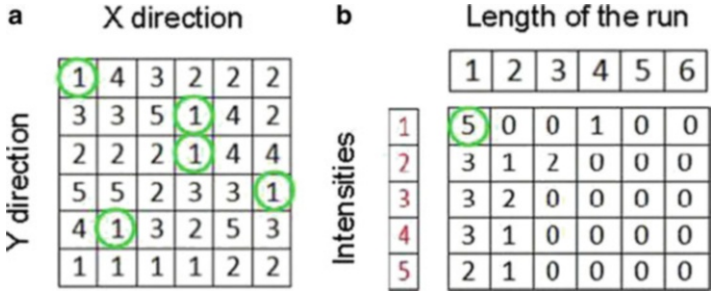

Fig. 26.11 Run-length matrix (in *horizontal direction*) formation: (**a**) original intensity matrix and (**b**) run-length matrix

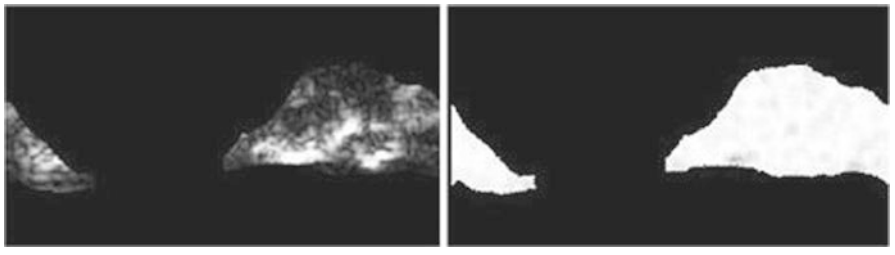

Fig. 26.12 Illustration of feature SRE: plaque area in polar coordinates (*left*) and SRE (*right*)

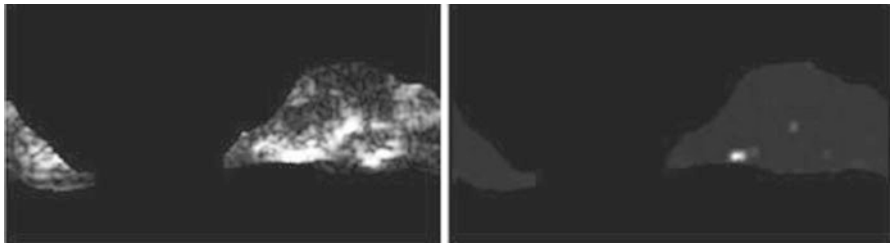

Fig. 26.13 Illustration of feature LRE: plaque area in polar coordinates (*left*) and LRE (*right*)

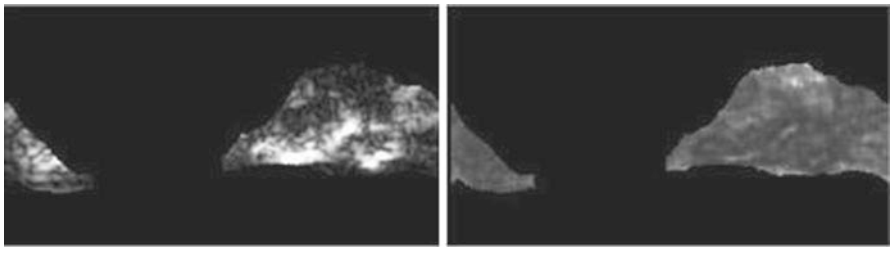

Fig. 26.14 Illustration of feature GLN: plaque area in polar coordinates (*left*) and GLN (*right*)

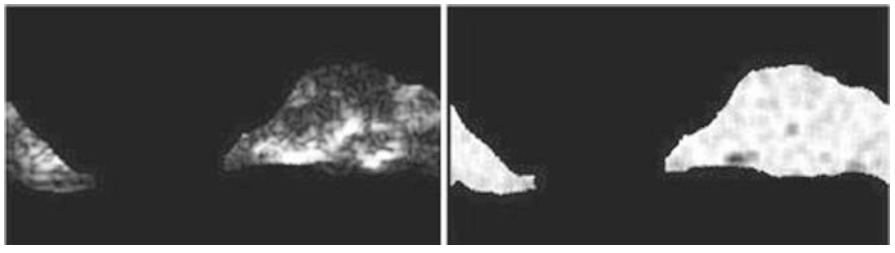

Fig. 26.15 Illustration of feature RLN: plaque area in polar coordinates (*left*) and RLN (*right*)

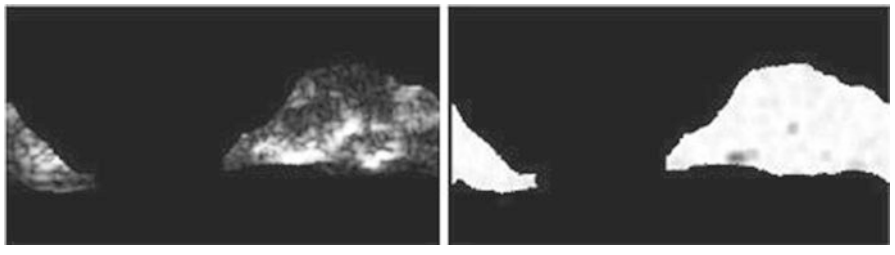

Fig. 26.16 Illustration of feature run percentage: plaque area in polar coordinates (*left*) and run percentage (*right*)

- Run-length nonuniformity (RLN) (Fig. 26.15):

$$f_4^k = \frac{1}{N_\tau} \sum_{b=1}^{R} \left(\sum_{a=1}^{P} R_k(a,b) \right)^2 \tag{26.32}$$

- Run percentage (Fig. 26.16):

$$f_5^k = \frac{N_\tau}{N_p} \tag{26.33}$$

2. Chu run-length features: the following features proposed by Chu et al. extract gray-level information in run-length matrix:
   - Low gray-level run emphasis (LGRE) (Fig. 26.17):

$$f_6^k = \frac{1}{N_\tau} \sum_{a=1}^{P} \sum_{b=1}^{R} \frac{R_k(a,b)}{a^2} \tag{26.34}$$

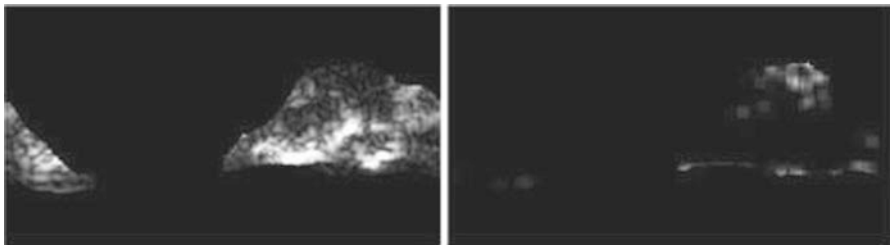

Fig. 26.17 Illustration of feature LGRE: plaque area in polar coordinates (*left*) and LGRE (*right*)

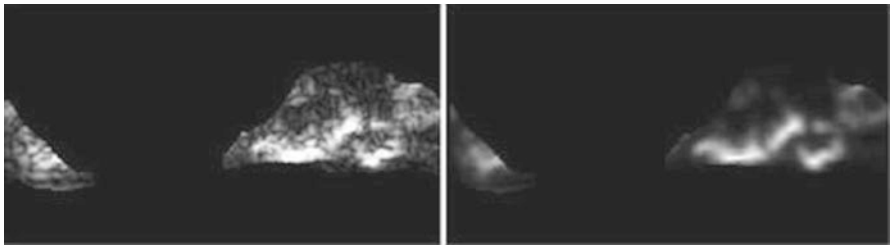

Fig. 26.18 Illustration of feature HGRE: plaque area in polar coordinates (*left*) and HGRE (*right*)

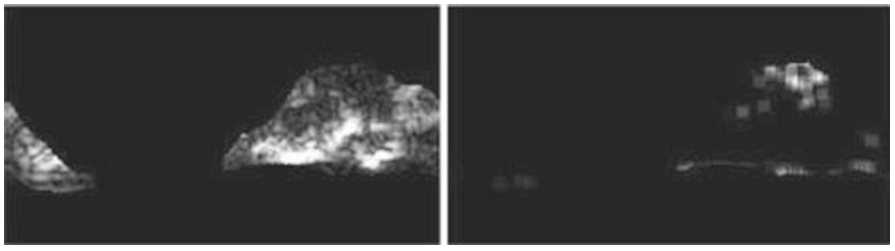

Fig. 26.19 Illustration of feature SRLGE: plaque area in polar coordinates (*left*) and SRLGE (*right*)

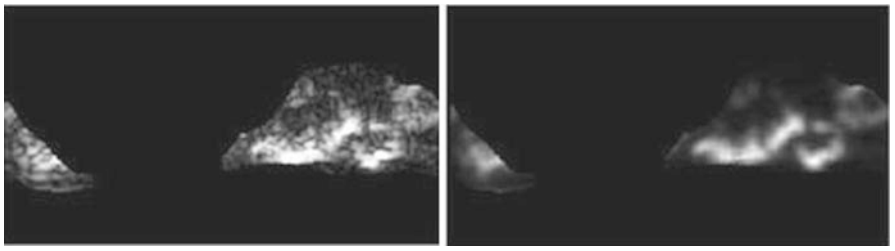

Fig. 26.20 Illustration of feature SRHGE: plaque area in polar coordinates (*left*) and SRHGE (*right*)

- High gray-level run emphasis (HGRE) (Fig. 26.18):

$$f_7^k = \frac{1}{N_\tau} \sum_{a=1}^{P} \sum_{b=1}^{R} R_{k(a,b)\cdot a^2} \tag{26.35}$$

3. Dasarathy and holder features: these features follow the idea of joint statistical measure of gray level and run length:
   - Short run low gray-level emphasis (SRLGE) (Fig. 26.19):

$$f_8^k = \frac{1}{N_\tau} \sum_{a=1}^{P} \sum_{b=1}^{R} \frac{R_k(a,b)}{a^2 \cdot b^2} \tag{26.36}$$

   - Short run high gray-level emphasis (SRHGE) (Fig. 26.20):

$$f_9^k = \frac{1}{N_\tau} \sum_{a=1}^{P} \sum_{b=1}^{R} \frac{R_{k(a,b)\cdot a^2}}{b^2} \tag{26.37}$$

   - Long run low gray-level emphasis (LRLGE) (Fig. 26.21):

$$f_{10}^k = \frac{1}{N_\tau} \sum_{a=1}^{P} \sum_{b=1}^{R} \frac{R_k(a,b) \cdot b^2}{a^2} \tag{26.38}$$

   - Long run high gray-level emphasis (LRHGE) (Fig. 26.22):

$$f_{11}^k = \frac{1}{N_\tau} \sum_{a=1}^{P} \sum_{b=1}^{R} R_{k(a,b)} \cdot a^2 \cdot b^2 \tag{26.39}$$

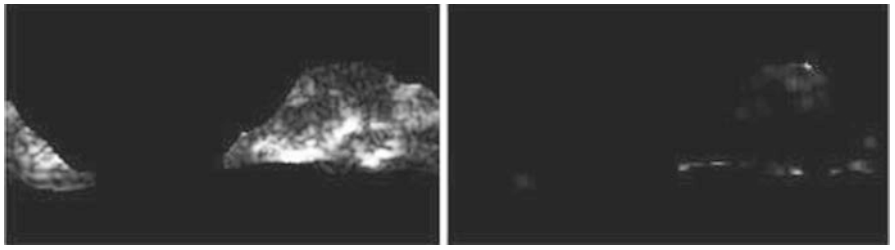

Fig. 26.21 Illustration of feature LRLGE: plaque area in polar coordinates (*left*) and LRLGE (*right*)

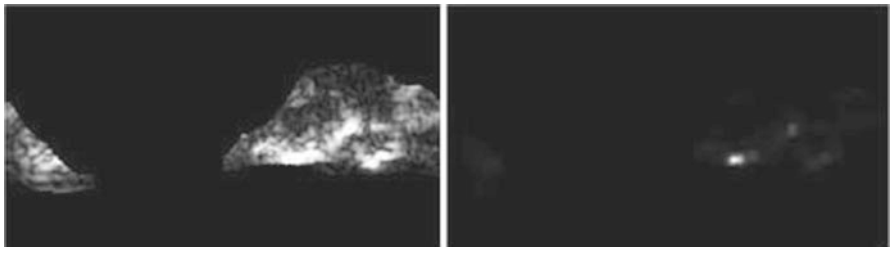

Fig. 26.22 Illustration of feature LRLGE: plaque area in polar coordinates (*left*) and LRHGE (*right*)

Above-mentioned methods have been previously used by several groups for IVUS plaque characterization. In next sections the proposed methods are introduced and discussed.

2.2 Feature Reduction

Linear discriminant analysis (LDA): LDA are methods which are used in statistics and machine learning to find the linear combination of features which best separate two or more classes of objects or events. The resulting combination may be used as a linear classifier or, more commonly, for dimensionality reduction before later classification. Suppose that the feature vectors come from C different classes (each class with mean μ_i and covariance Cov_i), then the between class and within class scatter matrices are defined as follows:

$$S_\mathrm{b} = \frac{1}{c}\sum_{i=1}^{c}(\mu_i - \mu)(\mu - \mu)^\mathrm{T}, \quad \mu = \frac{1}{c}\sum_{i=1}^{c}(\mu_i) \tag{26.40}$$

$$S_\mathrm{w} = \sum_{i=1}^{c}\mathrm{Cov}_i \tag{26.41}$$

It is proved that eigenvectors of $S_\mathrm{w}^{-1}S_\mathrm{b}$ are the directions that best separate these classes from each other [7]. Projecting feature vectors to the L ($L <$ # of features) largest eigenvectors results in a new reduced feature vector that better suited to classification methods. Figure 26.23 shows a Fisher direction for a three class problem.

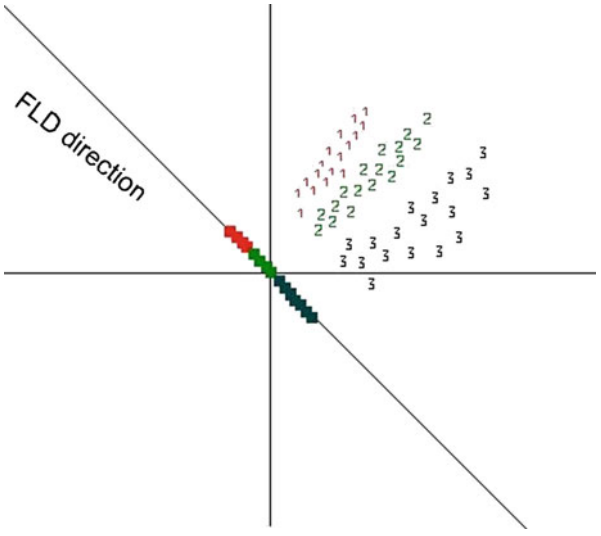

Fig. 26.23 Distribution of three classes and the Fisher direction that best separates these classes from each other

2.3 Classification

2.3.1 SVM Classifier

Support vector machines (SVM) are the classifiers based on the concept of decision planes that define decision boundaries. A decision plane is one that separates between a set of objects having different class memberships. A schematic example is shown in the illustration below. In this example, the objects belong either to class Black or White. The separating line defines a boundary on the right side of which all objects are Black and to the left of which all objects are White. The above is a classic example of a linear classifier, i.e., a classifier that separates a set of objects into their respective groups (Black and White in this case) with a line. Most classification tasks, however, are not that simple, and often more complex structures are needed in order to make an optimal separation, i.e., correctly classify new objects (test cases) on the basis of the examples that are available (train cases). Classification tasks based on drawing separating lines to distinguish between objects of different

class memberships are known as hyperplane classifiers. Support vector machines are particularly suited to handle such tasks. Support vector machine (SVM) is primarily a classifier method that performs classification tasks by constructing hyperplanes in a multidimensional space that separates cases of different class labels. To construct an optimal hyperplane, SVM employs an iterative training algorithm which is used to minimize an error function. According to the form of the error function, SVM models can be classified into different distinct groups. The C-SVM type is used in all proposed algorithms. In a two-class case, if the training dataset consists of feature vectors $\{f_1, \ldots, f_n\}$ with class labels $y_i \in \{-1, 1\}$, then the SVM training problem is equivalent to finding W and b such that training involves the minimization of the error function [8] and [9]:

$$\frac{W^{\mathrm{T}}W}{2} + C\sum_{i=1}^{N}\zeta_i \tag{26.42}$$

subject to the constraints:

$$y_i(W^{\mathrm{T}}\varphi(x_i) + b) \geq 1 - \zeta_i \text{ and } \zeta_i \geq 0, \quad i = 1, \ldots, N \tag{26.43}$$

where $\zeta_i \geq 0$ are the so-called slack variables that allow for misclassification of noisy data points, and parameter $C > 0$ controls the trade-off between the slack variable penalty and the margin [8]. In fact, W and b are chosen in a way that maximize the margin, or distance between the parallel hyperplanes that are as far apart as possible while still separating the data (Fig. 26.24). The function $\varphi(x)$ maps the data to a higher dimensional space. This new space is defined by its kernel function:

$$K(f_i, f_j) = \varphi(f_i)^{\mathrm{T}}\varphi(f_j) \tag{26.44}$$

The above problem can be formulated as a quadratic optimization process. The details of the solution and its implementation can be found in [10]. The Gaussian Radial Basis Function (RBF) kernel was used:

$$K(f_i, f_j) = \mathrm{e}^{-\gamma\|f_i - f_j\|^2} \tag{26.45}$$

This was firstly due to the fact that RBF kernel has only one parameter (γ) to adjust. Also, SVM classifiers based on RBF kernel were found more accurate than linear, sigmoid, and polynomial kernels in case of our problem. The publicly available C++ implementation of the SVM algorithms known as LIBSVM [10] was used. The entire dataset was normalized prior to training by setting the maximum value of each feature to 1 and the minimum to 0. For each set of parameters, fivefold cross validation was performed: the SVM was trained using 80% of the data samples, classified the remaining 20%, and repeated the procedure for all five portions of the data (Fig. 26.25).

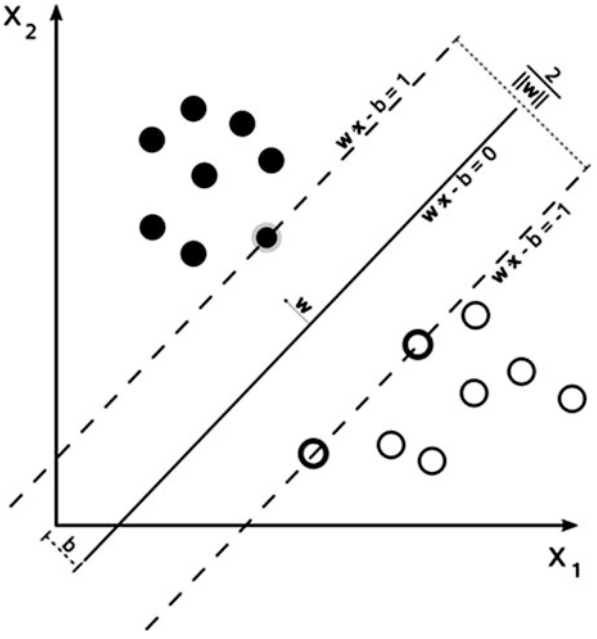

Fig. 26.24 Maximum-margin hyperplane and margins for a SVM trained with samples from two classes. Samples on the margin are called the support distribution

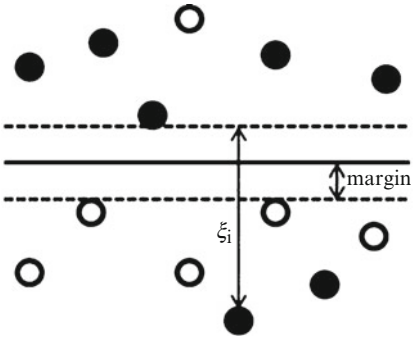

Fig. 26.25 Example of misclassification that shows slack variables

2.4 Post-processing

Studying intensity variety of each plaque component in VH images of the dataset through histogram analysis reveals that useful information can be extracted via this simple analysis. Figure 26.26 illustrates the histogram of pixels for three different plaque components. As this gray-scale-derived information might be ignored among many textural features in the classification steps, another step is added to the algorithm after the classification by SVM. In this step the given label of a pixel by SVM is confirmed or altered based on some prior information derived from the histogram

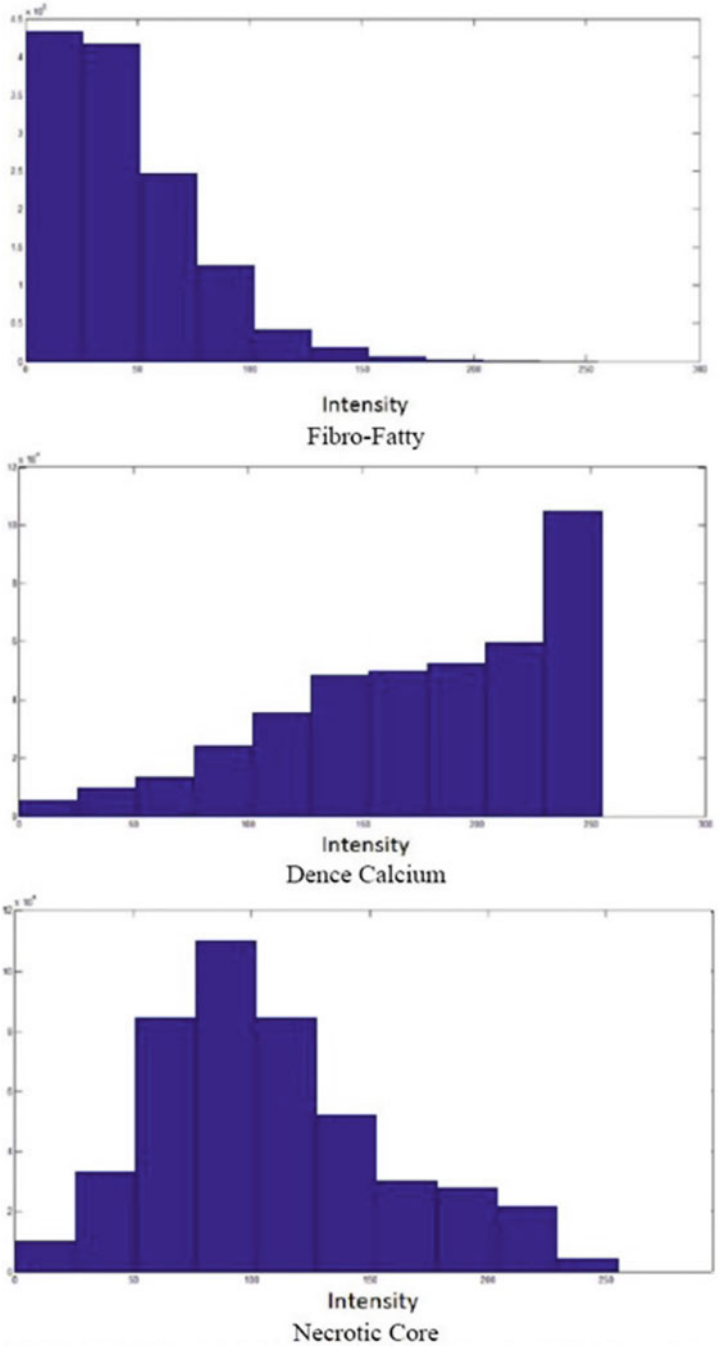

Fig. 26.26 The histogram of pixels belonging to FF, DC, and NC classes for 400 out of 500 IVUS images

of the IVUS image. Some useful information is pointed out below that can be inferred from the histograms displayed in Fig. 26.26:

- The majority of samples belong to FF class; however, there are few FF pixels whose their intensities exceed the gray level 150 (ThFF = 150).
- Most of the pixels with intensities above the gray level 200 [ThDC (low) = 200] belong to the DC class, whereby few pixels with value under 50 [ThDC (high) = 50] belong to this class.
- Pixels belonging to the NC are concentrated more between 30 and 200 gray levels [ThNC (low) = 30] and [ThNC (high) = 200].

So, based on these additional thresholds, the system will decide on whether to change the decision of SVM classifier or not.

2.5 Dataset

The data were acquired from 10 patients, which included about 2,263 gray-scale IVUS images and their corresponding VH images. These IVUS images of size 400×400 pixels were acquired using an electronic probe (In-Vision Gold, Volcano Therapeutics, Inc.) with a synthetic aperture 2.9 F and a frequency of 20 MHz. A motorized pullback was performed along the entire vessel with a speed of 1.0 mm/s using a dedicated pullback device. A total number of 500 frames from 12 vessels [6 left anterior descending (LAD), 3 right coronary artery (RCA), 3 left circumflex (LCX)] of 10 patients were available for VH analysis and comparison with IBH. In the VH analysis the total average amount of fibrous/fibro-fatty, dense calcium, and necrotic core was (1,505,907 pixels) 37,647 mm^2, (388,073 pixels) 9,701 mm^2, and (516,711 pixels) 12,917 mm^2, respectively. The relative average amounts per cross section were 63%, 16%, and 21%.

2.6 Statistical Analysis

The measures of sensitivity, specificity, and predictive accuracy for the three plaque components were calculated and reported as statistical analysis in this thesis. The standard formulae for these measures were the same commonly accepted in the medical literature [11].

$$\text{Sensitivity} = \frac{\text{True Positive Decisions}}{\text{Decisions Actually Positive}} \tag{26.46}$$

$$\text{Specificity} = \frac{\text{True Negative Decisions}}{\text{Decisions Actually Negative}} \tag{26.47}$$

$$\text{Accuracy} = \frac{\text{All Correct Decisions}}{\text{Total Cases}} \tag{26.48}$$

$$\text{CI}_{0.95\%} = X \pm 1.96 \times \frac{X \times (1 - X)}{N} \tag{26.49}$$

where X is either the sensitivity or specificity and N is the number of decisions used in denominator for calculating the sensitivity or specificity. In addition to the above-mentioned measures, Cohen's Kappa index is calculated to quantify the degree of agreement between the Algorithm IV and VH classification for in vivo validation, and Algorithm IV and manual painted images for ex vivo validations. A kappa value of 0.41–0.60 indicates moderate (fair) agreement, 0.61–0.80 indicates good agreement, and 0.81–1.0 indicates excellent agreement. This metric was originally introduced by Cohen to determine the level of agreement between two observers [11]. The kappa is calculated as

$$\kappa = \frac{\rho_o - \rho_c}{1 - \rho_c} \tag{26.50}$$

where ρ_o is the observed proportion of agreement and ρ_c is the expected proportion of agreement resulting from chance.

3 Algorithm I

3.1 Textural Feature Extraction

As it was mentioned in the previous section, various textural features can be derived from run-length matrix such as the short run emphasis, the long run emphasis, the gray-level nonuniformity, the run-length nonuniformity, and the run percentage. These features have been previously used on IVUS images; however, the results were not fulfilling [12]. Hence, two new features are proposed characterizing each gray-level a (i.e., every row) of the run-length matrix. The first feature $f_1^k(a), \quad k \in \{h, v\}$ where h and v represent horizontal and vertical respectively is defined as the maximum number of occurrences multiplied by the length of the run with maximum occurrence b_m:

$$f_1^k(a) = R_k(a, b_\text{m}) \times b_\text{m}, b_\text{m} = \arg_b \max(R_k(a, b)) \tag{26.51}$$

And the second feature $f_1^k(a), \quad k \in \{h, r\}$ is defined as the sum of every occurrences multiplied by its corresponding run length:

$$f_2^k(a) = \sum_b b \times R(a, b) \tag{26.52}$$

This way, each pixel (i, j) is mapped to a feature matrix, j:

$$F_{i,j} = \begin{pmatrix} f_1^h(1) & f_2^h(1) & f_1^v(1) & f_2^h(1) \\ \vdots & \vdots & \vdots & \vdots \\ f_1^h(a) & f_2^h(a) & f_1^v(a) & f_2^h(a) \\ \vdots & \vdots & \vdots & \vdots \\ f_1^h(P) & f_2^h(P) & f_1^v(P) & f_2^h(P) \end{pmatrix} \tag{26.53}$$

Let us consider now each column $F_{i,j,c}$ of matrix $F_{i,j}$ as a signal that is a function of the gray level a. As shown in Fig. 26.27, these signals reveal different frequency contents. This motivates us to extract discriminative features from spatial-frequency representation of the signals. Therefore, each signal is decomposed into a detail $F_{i,j,c}^d$ and an approximation $F_{i,j,c}^a$ by means of 1D discrete wavelet transform (DWT):

$$F_{i,j,c}^a[u] = (F_{i,j} * l)[u] \tag{26.54}$$

$$F_{i,j,c}^d[u] = (F_{i,j} * h)[u] \tag{26.55}$$

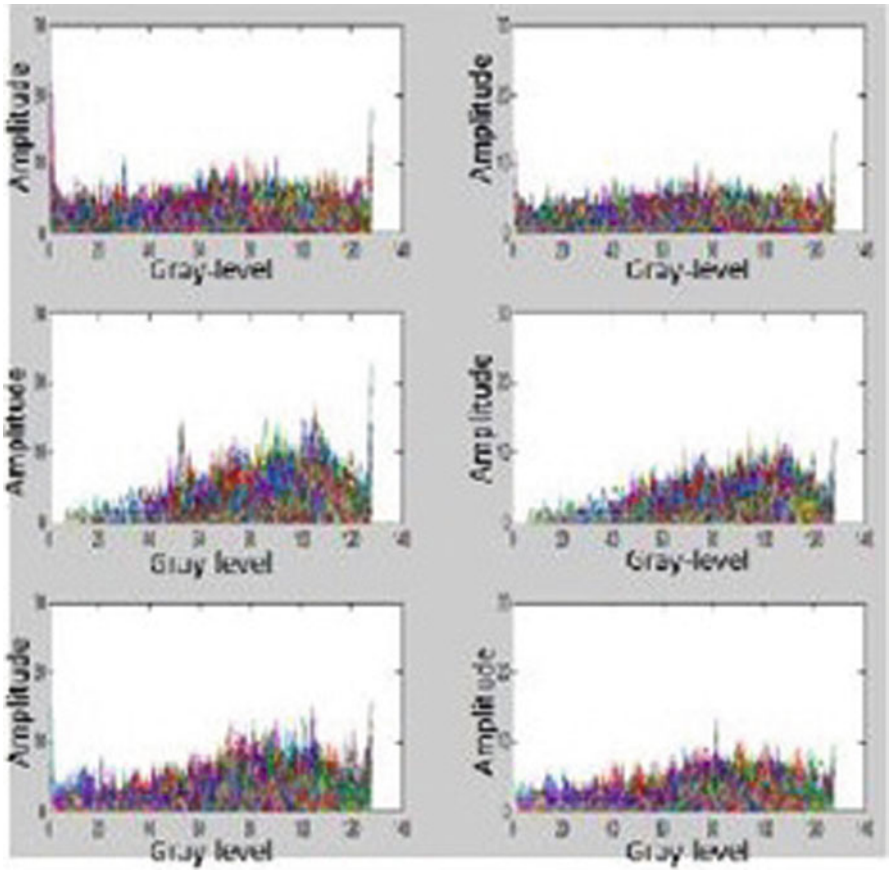

Fig. 26.27 Distribution of 5,000 bundle feature vectors for each plaque type. *Top* to *down*: DC, fibro lipid, and NC. *Left* to *right*: f_1^h and f_2^h

Then, each DWT component $((F^a_{i,j,c}[u])$ and $(F^d_{i,j,c}[u]))$ is characterized by a set of statistical features, namely, its weighted mean, weighted variance, maximum of signal, and its index:

$$\rho^k_{1,c} = \frac{1}{P}\sum_{u=1}^{P} u \times F^k_{i,j,c}(u) \tag{26.56}$$

$$\rho^k_{2,c} = \frac{1}{P}\sum_{u=1}^{P} \left(u \times F^k_{i,j,c}(u) - \rho^k_{1,c}\right)^2 \tag{26.57}$$

$$\rho^k_{3,c} = \max F^k_{i,j,c}(u) \tag{26.58}$$

$$\rho^k_{3,c} = \arg_u \max F^k_{i,j,c}(u) \tag{26.59}$$

Furthermore, spectral behavior of these components is also characterized by means of autoregressive (AR) model of order 5:

$$F^k_{i,j,c}(u) = \sum_{t=1}^{5} F^k_{i,j,c}(u-t) \times \varphi^k_{t,c} + n(u) \tag{26.60}$$

where $n(u)$ is the white noise and $\varphi^k_{t,c}$ are the coefficients of the AR model. These coefficients are also used as features.

Finally, the feature vector of each pixel $(i,\ j)$ is defined as follows:

$$X_{i,j} = \{\rho^k_{l,c}, \varphi^k_{t,c}, l \in \{1,\ldots,4\}, t \in \{1,\ldots,5\}, c \in \{1,\ldots,4\}, k \in \{a,d\}\} \tag{26.61}$$

This vector is the input of the SVM classifier. This classifier was explained in the classification subsection previously.

The block diagram of the proposed algorithm is shown in Fig. 26.28.

3.2 Result and Discussion of Algorithm I

The three feature extraction mentioned methods were then applied on the set of 200 frames. The characterized IVUS images were validated by their corresponding VH images and the accuracy, sensitivity, and specificity parameters were calculated for each technique. The results for this approach were compared to methods using LBP or co-occurrence-based features. The size of the neighborhood was empirically chosen to be 11×11 for all methods. This was done to get the optimum results for every method separately. For LBP method, five circles were then constructed in each neighborhood. Then, three features were extracted from each circle,

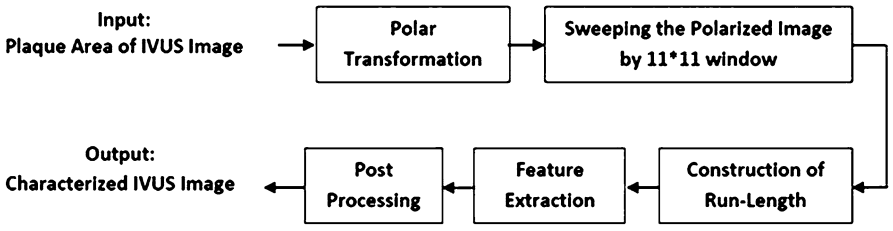

Fig. 26.28 Block diagram of the newly proposed modified run-length method

Table 26.1 The results of Algorithm I versus other techniques

	DC		FF		NC		
Method	Sensitivity (%)	Specificity (%)	Sensitivity (%)	Specificity (%)	Sensitivity (%)	Specificity (%)	Overall accuracy (%)
LBP	45	96	97	42	30	95	71
Co-occurrence	67	95	84	80	53	83	75
Proposed method	70	95	84	75	55	82	77

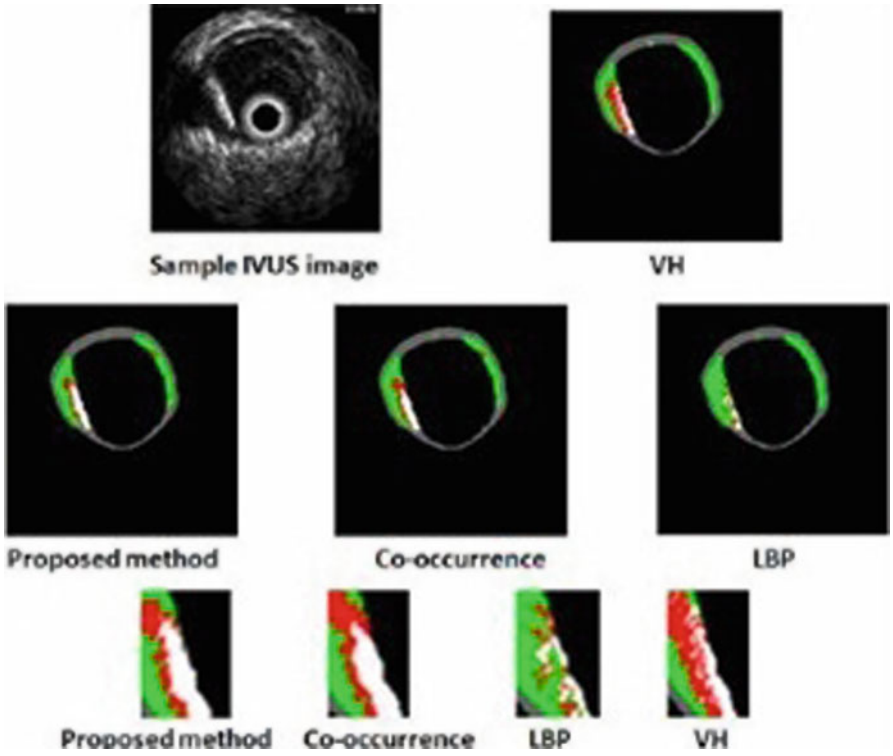

Fig. 26.29 The result of the feature extraction method in comparison with the co-occurrence and LBP methods from *left* to *right* (*white* is DC, *green* is fibro-lipid, and *red* is NC) (Color figure online)

and the number of features for every pixel in LBP method thus sums up to 15. Extracting features from five circles with different radii can be thought of as a multi-resolution textural analysis. Total number of features in the co-occurrence method was 14 which include, e.g., homogeneity, contrast, inverse difference moment, and so on. Results using different methods are presented below in Table 26.1. According to the results, Algorithm I is more capable of classifying DC and NC plaques in comparison to LBP or co-occurrence methods.

Although this approach reveals a higher overall accuracy, the co-occurrence and LBP methods perform better in characterizing the fibro-lipid regions. Figure 26.29 illustrates the images characterized by all methods with their corresponding IVUS and VH images.

In this study, the sensitivity of all methods for the detection of NC was low (55%). This fact was caused by similarities between NC and DC in gray-level IVUS images [13]. Furthermore, previous studies have shown that plaque areas adjacent to DC are frequently coded as NC tissue in VH images [14]. For a typical frame the proposed method took approximately 12 s to characterize the pixels, whereas the LBP took 2.6 min and the co-occurrence took nearly 60 min. Thus, in terms of time efficiency, the proposed method further outdoes the other two. A MATLAB implementation on an Intel Core 2 CPU2.00 GHz computer with 2.0 GB RAM was used in this work.

4 Algorithm II

For proposing this algorithm, this fact was taken into account that since each tissue shows different echogenic characteristics, the different plaque components can be characterized by their local frequency components. The best tool for this purpose is wavelet transform (WT). WT provides the best approximation of a space-frequency representation of an image, i.e., it permits to know which spectral components exist at which position in the input image. The main drawback of the WT is that it is translation non-invariant due to the decimation applied to the image after each decomposition level. Recently, another type of wavelet transforms known as redundant wavelet transforms (RWT) has been introduced [15]. Contrary to the classical WT, there is no decimation step after filtering the input image. This provides the decomposition to be translation invariant, and since it preserves the size of images in each level of decomposition, the local spectral components can be retrieved without any interpolation step. To generalize such transform, the wavelet packet transform (WPT) [16] has been introduced to decompose the whole-frequency spectrum into multiple sub-bands of varying sizes. It has been shown to provide a more redundant representation for the analysis of complex textural information. By combining the RWT and WPT, image can be decomposed into multiple sub-band images (Fig. 26.30). This decomposition provides translation invariance in addition to the rotation invariance gained by the initial polar transform.

4.1 Textural Feature Extraction

Let $\{l_k\}, k \in \{1, N\}$ be a collection of N sub-band images extracted from image I through redundant wavelet packet transform (RWPT). This section presents how to characterize each pixel (i, j) from I with textural descriptors extracted from the $\{I_k\}$. This provides an enhanced extraction of texture information by analyzing the different sub-band of the frequency spectrum. In this algorithm, the approach which is based on run-length features is compared to co-occurrence, and local binary pattern (LBP) methods. Each neighborhood is characterized with two run-length matrices $R_k^x(a, b)$ and $R_k^y(a, b)$ corresponding respectively to x and y directions in sub-band k. The 11 run-length-based features introduced in Sect. 2.1 in (26.29)–(26.39) were used. Let us denote $f_k^{\theta,\lambda}(i, j)$ where $\theta = \{x, y\}$ and $\lambda = \{1, 2, \ldots, 11\}$. The 22 features extracted from the neighborhood $\{I_k(i + m, j + n\}_{m,n}$ of each pixel (i, j) of each image I_k are then characterized by the following set of features $V_{i,j}^k$:

$$V_{i,j}^k = \{f_k^{\theta}(i, j)\}_{\theta,\lambda} \tag{26.62}$$

As the principal objective in a classification problem is to extract features that are capable of discriminating different classes as much as possible, the best subset of the $\{V^k\}_{k\in\{1,N\}}$ has to be chosen out to provide an optimal discrimination power. To this end, an adapted discriminant measure (Fisher criterion) is introduced:

$$D(k, \theta, \lambda) = \frac{(\mu_p^{k,\theta,\lambda} - \mu_q^{k,\theta,\lambda})^2}{\sigma_p^{k,\theta,\lambda^2} - \sigma_q^{k,\theta,\lambda^2}} \tag{26.63}$$

where $\mu_p^{k,\theta,\lambda}$ and $\sigma_q^{k,\theta,\lambda^2}$ are respectively the mean and the variance of the component $f_k^{\theta,\lambda}$ of V^k in the Pth class. This measure takes high values when the feature is varied in classes such that it has maximum differences in the mean and minimum variances. After computing the Fisher criterion

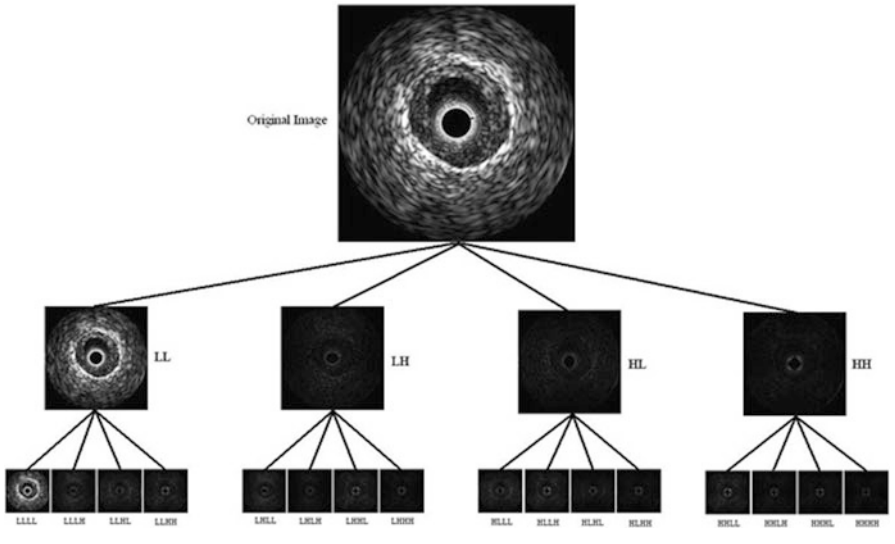

Fig. 26.30 Two level decomposition of RWT + WPT for an IVUS image

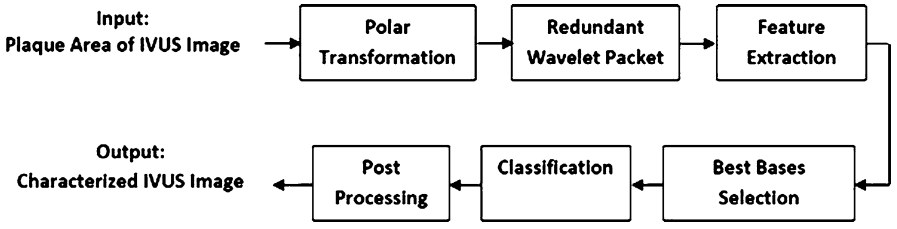

Fig. 26.31 Block diagram of Algorithm II

Table 26.2 Accuracy of different techniques

Technique	Overall accuracy		DC	FF	NC
Run-length	(73%) 72%	Sensitivity (%)	(76) 73	(97) 85	(9) 42
		Specificity (%)	(93) 93	(57) 79	(96) 84
Co-occurrence	(71%) 71%	Sensitivity (%)	(72) 70	(97) 84	(14) 46
		Specificity (%)	(96) 96	(58) 80	(94) 82
LBP	(66%) 70%	Sensitivity (%)	(40) 59	(97) 85	(8) 47
		Specificity (%)	(95) 95	(37) 78	(96) 80

Numbers within parenthesis and without relate respectively to before and after post-processing

for each component of all the $\{V^k\}_{k\in\{1,N\}}$ sub-bands which have higher values offer the best discrimination power. A variant of the Local Discriminant Basis (LDB) algorithm was proposed here which was introduced by Saito and Coifman [17] with Fisher's criterion. This algorithm selects the best subset of the $\{V^k\}_{k\in\{1,N\}}$ by computing its discrimination power as follows:

$$D(k) = \sum_{\theta}\sum_{\lambda} D(k,\theta,\lambda) \tag{26.64}$$

Each pixel $(i,\ j)$ of I is then characterized by the subset of features denoted $\{V^k\}_{k\in\{1,N\}}$ with $M \subset \{1, N\}$.

4.2 Weighted Classification Structure Based on SVM

For classification purposes, a structure of multiclass support vector machines is used. For each selected sub-band k with $k \in M$, an SVM is associated. However, all sub-bands do not have the same discrimination ability. Therefore, a weight is assigned to each classifier based on its discrimination ability. The final decision for a pixel is attained by considering the weighted votes of all SVMs. The block diagram of the proposed algorithm is shown in Fig. 26.31.

4.3 Result and Discussion of Algorithm II

The study group used for Algorithm II is the same as the one used for Algorithm I. The characterized IVUS images were validated by their corresponding VH images and the accuracy, sensitivity, and specificity parameters were calculated for each technique. Since the most important plaque components for atherosclerosis staging are lipid-rich tissues, necrotic core, and calcifications, the classification was concentrated into these three classes.

The Daubechies 4 wavelet, which has the ability of following small variations, is used for the RWPT decomposition. The number of decomposition levels was set to two, giving 21 sub-band images. The size of neighborhoods, on which features were extracted, was empirically chosen to be 9×9 for all methods. For LBP method, four circles were then constructed in each neighborhood. Then, three features were extracted from each circle.

After computing Fisher criterion for feature vectors of every sub-band images, a subset of 12 were selected based on their discrimination power and LDB procedure. Then, a weight was assigned to each based on their Fisher measure. The computed weights show that sub-band two (low frequency) has the best discrimination power in comparison with the others. Again, the LIBSVM C++ implementation of the SVM algorithms was used. A grid search was performed for optimal parameter selection and a fivefold cross validation to evaluate the performance of all three methods. For a typical frame the run-length method took 2 min to extract the features, whereas the LBP needed 20 min and the co-occurrence nearly 120 min. In terms of time efficiency, the run-length method outperforms the other two. A MATLAB implementation on an Intel Core 2 CPU 2.00 GHz computer with 2.0 GB RAM was used in this work. Table 26.2 illustrates the results using different methods besides the influence of the post-processing step. It can be inferred from the results that the run-length feature extraction method has a better capability for classifying DC plaques, while LBP and co-occurrence for NC. Results also show the influence of the post-processing step on the sensitivity of the NC class. Therefore, one might use the textural features and the classification procedure for dividing the plaque

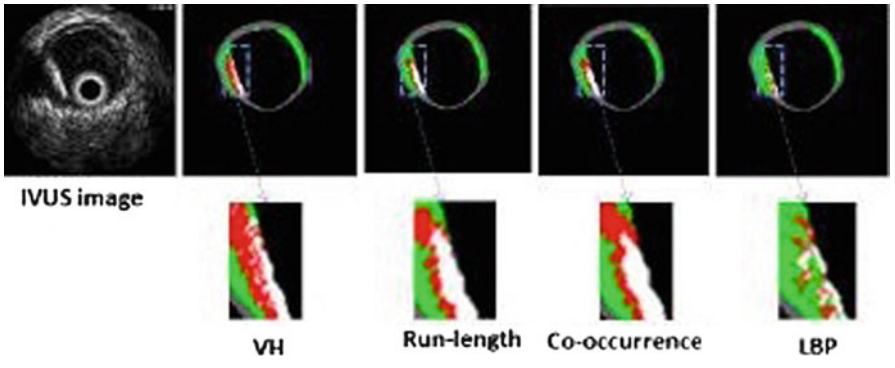

Fig. 26.32 The result of feature extraction methods (*white* is calcium, *green* is fibro-fatty, and *red* is necrotic) (Color figure online)

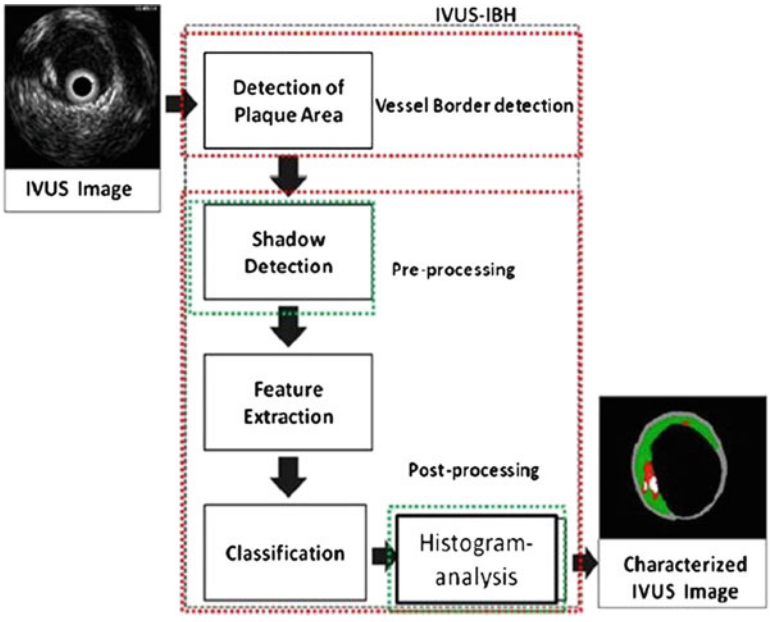

Fig. 26.33 Scheme of the workflow in the IBH-System (in GUI). First, an IVUS image is loaded. Then, the vessel's borders are detected using automatic border detection. Next, the textural feature are extracted from the plaque area and then, SVM classifier is applied to classify the pixels of the plaque area in order to generate the color-coded image representing the different plaque components. Finally, the post-processing is applied on SVM output

area into two classes, i.e., DC and FF, and then use prior information on their intensity distributions to distinguish the NC regions from them. Still, the sensitivity of all methods for the detection of the NC was low (46%). This fact was caused by similarities between NC and DC in gray-level IVUS images [14].

Also Fig. 26.32 illustrates the images characterized by all methods with their corresponding IVUS and VH images.

5 Algorithm III

In this algorithm some new facts were taken into account that were not noted in the previous algorithms. An important fact, which is mostly ignored in characterizing atherosclerosis plaques via features extracted from IVUS images, is to detect the acoustic shadowing behind dense calcified (DC) regions and treat them differently. These shadow regions which exist and displayed in the plaque area of some IVUS images appear as echo-soft; so, when treated within other parts of plaque area they are mostly Calcium and Necrotic Core plaques but normally should be classified to the lipid or fibro-fatty classes [18, 19]. The block diagram of the proposed algorithm is shown in Fig. 26.33.

5.1 Shadow Detection

Shadow areas appearing in IVUS gray scale images usually do not represent any useful information for plaque component analysis. However, the IVUS-VH method does not detect such regions and blindly treats them as normal plaque area which often leads to classification errors. By defining a specific plaque region as shadow region shown in Fig. 26.34 [17], we aim at reducing mentioned errors, which are caused by the nature of ultrasound imaging. Shadow regions are characterized by infra-low intensity regions behind ultrahigh intensity areas along a scan line. Thereby, detection of these regions by using two thresholds is proposed: one threshold T_{high} to detect ultrahigh intensity regions, which might belong to calcification or necrotic core, and the other threshold T_{low} to detect infra-low intensity regions. Let us consider an

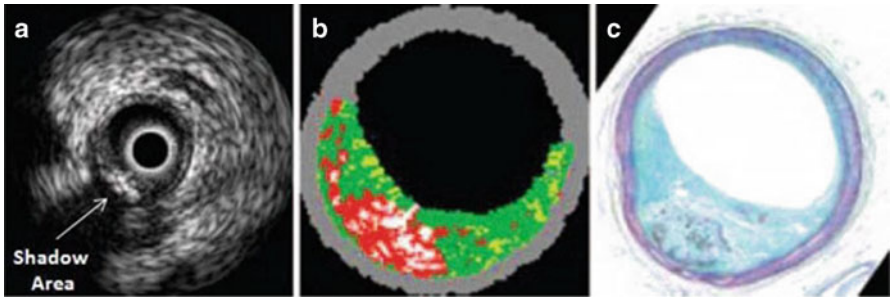

Fig. 26.34 The *shadow region* in a typical IVUS gray-scale image (*left*), its plaque constituents in IVUS-VH (*middle*), and its corresponding histopathalogy (*right*) [20]

image I from gray-level IVUS in polar domain. If $\sum$ denoted as the ensemble of pixels belonging to a shadow region, these pixels x can be detected along a scan line as follows:

$$x = (i, j) \in \sum \text{ if } \begin{cases} I(i, j) < T_{\text{low}} \text{ and } I(i, j-1) \in \sum \\ \text{or } I(i, j) < T_{\text{low}} \text{ and } I(i, j-1) > T_{\text{high}} \end{cases} \tag{26.65}$$

5.2 Feature Extraction Methods

In order to characterize the rest of plaque area into the three predefined plaque components, two feature extraction methods are examined and compared. To achieve this purpose, local binary pattern (LBP) [2] and co-occurrence [21] feature extraction methods have been studied in [14] and have been reported to outperform other feature extraction methods. Moreover, it was reported in [12] that the run-length method [22] is not an appropriate feature extraction method for characterizing IVUS images plaque area. In [23], both signal and image-based features were extracted. The co-occurrence, LBP, and Gabor-filtering feature extraction methods are used for texture-based feature extraction. Their results are compared to manual characterization of IVUS images by two experts and 90% accuracy is achieved. However, the manual characterization of IVUS images suffers from both inter-observer and intra-observer variability and especially uncertainty in characterizing soft plaques from each other, e.g., distinguishing between the FF and the NC tissues. Here, the performance of the features extracted from the run-length matrix is compared with those extracted from the LBP method in both accuracy and time efficiency aspects. The co-occurrence feature extraction method is not included in this study, since the previous studies reveal that despite good performance of this method in atherosclerotic plaque characterization, its heavy computational burden leads to poor time efficiency. IVUS imaging provides circular cross-section areas of the blood vessel and it uses 256 scan lines so the lateral resolution is $360/256 = 1.41^\circ$ and the axial resolution is about 40 μm.

For the analysis, IVUS images are converted into polar coordinates to be orientation independent for the feature extraction. In this manuscript, the data refer to the converted data. The polar transformed image is then swept by a sweeping window. The size of the sweeping window for both feature extraction techniques was empirically chosen as 9×9 pixels in which each pixel is equal to 0.025 mm.

5.3 Practical Implementation

The proposed methods for border detection and plaque characterization in this study were implemented in MATLAB and to obtain a stand-alone executable application, the program with a graphical user interface (GUI) was compiled by C++ compiler in Microsoft Visual Studio 2005. An example of the GUI is illustrated in Fig. 26.35.

5.4 Result of Algorithm III

Considering the shadow region detection procedure, 8% of plaque area pixels belong to the shadow region. The characterized IVUS images were validated by their corresponding VH images. In order to demonstrate the influence of applying the pre-processing step, i.e., detecting the shadow region and assigning it to the fourth class, the post-processing derived from the histogram analysis. In the post-processing step, the label assigned to a sample pixel and its gray level are considered. Then, final labels of the pixel are decided by this step. For instance, suppose the classification section assigns a pixel to the FF class and also the gray level of that pixel is above 150. In this case, based on ThFF, the current label is declined and whether the gray level is above ThDC (low) = 200 or not, it will be assigned to the DC or NC class, respectively. Tables 26.3 and 26.4 illustrate the comparative results of the two different feature extraction methods considering different conditions. Considering the VH as validating standard, the Kappa is computed to be 0.61 for the extended run length for both pixel-based and region-based (with a 9×9 pixels in a window) validations in the case of applying both pre-processing and post-processing steps.

Table 26.5 illustrates the P-value for the case of applying both shadow detection (pre-processing) and histogram-based

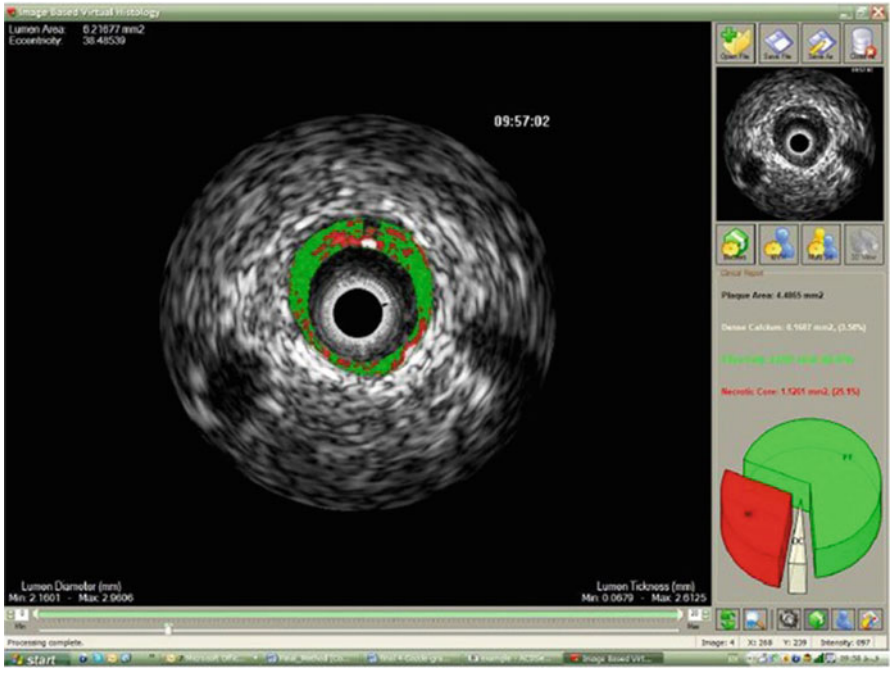

Fig. 26.35 An example of the GUI window: besides analysis of plaque components the GUI also allows calculation of other vessel parameters such as total plaque areas or the degree of stenosis

Table 26.3 Results of pixel-based plaque characterization of vessels' plaque area using the run-length method as feature extraction and SVM classifier. The cases of including the pre- and post-processing steps or not is distinguished using "Yes" and "No" signs in the two left columns. The parameter ± confidence interval is shown for the sensitivity, specificity, and accuracy parameters

Histogram-based post-processing	Shadow detection	DC		FF		NC		
		Sensitivity	Specificity	Sensitivity	Specificity	Sensitivity	Specificity	Overall accuracy
No	No	79% ± 6.5	93% ± 3.8	87% ± 5.1	38% ± 5.3	07% ± 3.3	97% ± 2.5	72% ± 6.3
No	Yes	79% ± 6.5	93% ± 3.7	96% ± 3	55% ± 6.6	12% ± 4.2	96% ± 2.7	74% ± 5.8
Yes	No	80% ± 6.5	93% ± 3.7	73% ± 6	64% ± 6.5	43% ± 6.6	80% ± 5.3	74% ± 6.4
Yes Pixel-based	Yes Pixel-based	79% ± 6.5	85% ± 3.6	81% ± 5.6	90% ± 5.3	52% ± 6.6	82% ± 5.5	75% ± 6.1
Yes Region-based: 9 × 9 pixels	Yes Region-based: 9 × 9 pixels	71% ± 4	97% ± 1	88% ± 1	87% ± 2	57% ± 4	88% ± 1	85% ± 3

Table 26.4 Results of pixel-wise plaque characterization of vessels' plaque area using the LBP method as feature extraction and SVM classifier. The cases of including the pre- and post-processing steps or not is distinguished using "Yes" and "No" signs in the two left columns. The parameter ± confidence interval is shown for the sensitivity, specificity, and accuracy parameters

Histogram-based post-processing	Shadow detection	DC		FF		NC		
		Sensitivity	Specificity	Sensitivity	Specificity	Sensitivity	Specificity	Overall accuracy
No	No	68% ± 6.6	96% ± 3.2	97% ± 3	42% ± 6.6	06% ± 4.6	95% ± 3.2	66% ± 6.1
No	Yes	68% ± 6.6	94% ± 3.1	95% ± 3	45% ± 6.6	13% ± 4.5	94% ± 3.2	69% ± 6.6
Yes	No	69% ± 6.4	96% ± 3.2	70% ± 5.8	61% ± 5.2	39% ± 6.1	79% ± 5.7	67% ± 6.1
Yes	Yes	69% ± 6.4	95% ± 3.1	75% ± 5.8	81% ± 5.2	42% ± 6.6	76% ± 5.7	72% ± 5.8

Table 26.5 The *P*-value shows differences of the case of applying both shadow detection pre-processing and post-processing and using the run-length method as a technique for feature extraction against the run-length method without pre-processing and histogram-based post-processing

	Sensitivity			Specificity			
Parameter	DC	FF	NC	DC	FF	NC	Accuracy
P-value	0.02781	0.01827	0.00497	0.02607	0.00695	0.01397	0.02345

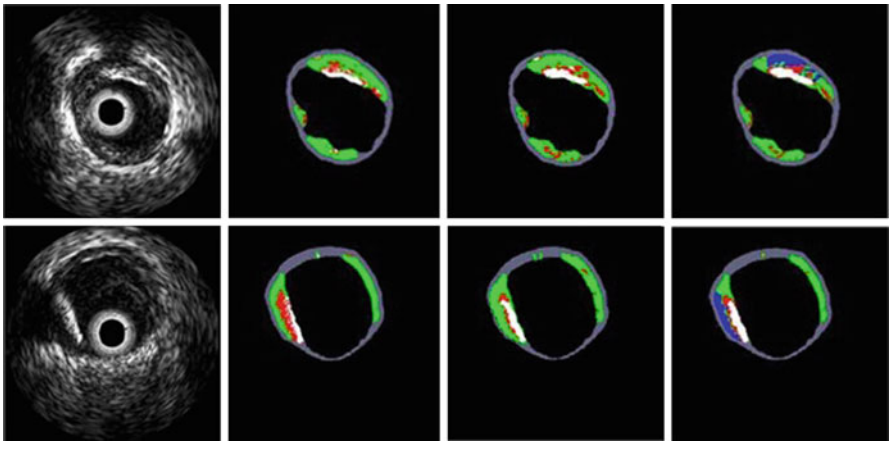

Fig. 26.36 The influence of applying the shadow detection section in the final constructed colorcoded IBH images. The images are from *left* to *right*: a typical IVUS image, its corresponding VH image, and IBH images without shadow section and with shadow detection section using the run-length feature extraction method. Note that the illustrated IBH images are after applying the histogram-based post processing technique (the FF, NC, and DC plaques are shown in *green*, *red*, and *white colors*, respectively. The *shadow region* is colored with *blue*)

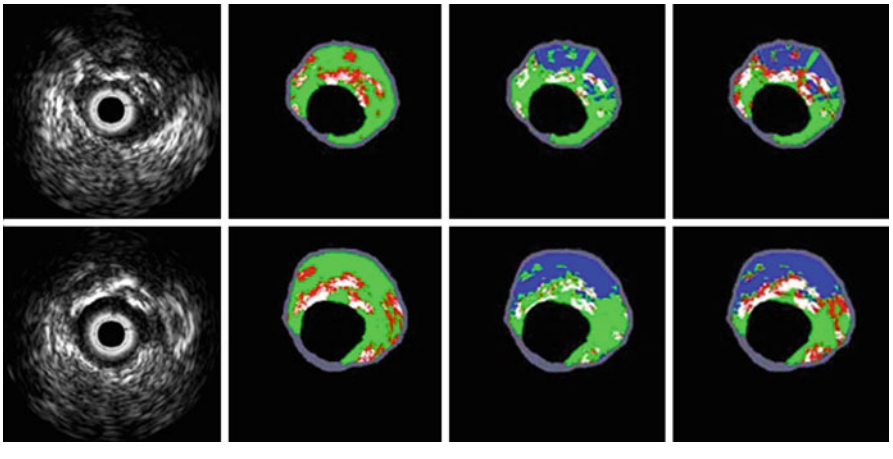

Fig. 26.37 The influence of applying the histogram-based post-processing section in the final constructed color-coded IBH images. The images are from *left* to *right*: a typical IVUS image, its corresponding VH image, and IBH images before applying the histogram-based post-processing and after that using the LBP feature extraction method. Note that the illustrated IBH images are after applying the shadow detection technique (the FF, NC, and DC plaques are shown in *green*, *red*, and *white colors*, respectively. The *shadow region* is colored with *blue*)

post-processing and also using the new extended run-length method as a technique for feature extraction. Figure 26.36 shows the influence of shadow region detection pre-processing on the final reconstructed IBH image. Figure 26.37 illustrates the influence of post-processing derived from histogram analysis on the final reconstructed IBH image. Finally, Fig. 26.38 shows the final reconstructed IBH images for two feature extraction methods.

Moreover, Table 26.3 also shows the statistical results of applying the proposed algorithm to these images. In most similar studies, when one wants to validate with correlated images a region-based validation method is used. It means that instead of comparing the result and its corresponding label pixel by pixel, the validation step is done by comparing regions, a window which contains more than one pixel. For example, the size of validation regions in Nair et al. is 1/3 mm × 1/3 mm, i.e., approximately a window of size 13 × 13 pixels. To handle this, a validation window of size $n \times n$ pixels is defined, where n can vary from 1, i.e., pixel-based validation, to 9. The label of a validation window is selected by looking at labels of its constituent pixels. In fact, it is assigned to a plaque component which is the majority. This experiment shows that the size of regions affects the results.

5.5 Discussion of Algorithm III

In Algorithm III, a complete algorithm was introduced for the IVUS image analysis including border detection (only

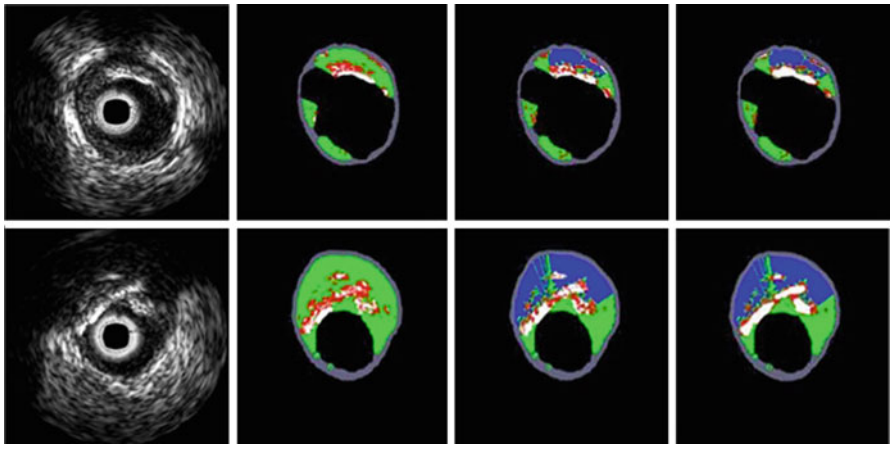

Fig. 26.38 The final constructed color-coded IBH images using the proposed algorithm. From *left* to *right*: an IVUS image, its related VH image, and its IBH images using the run-length and the LBP feature extraction methods

in GUI) to plaque characterization with more emphasis in the latter part. This comprehensive image-based algorithm provides cardiologists with not only the vessel's intima and media-adventitia borders but also a color-coded IBH image in which the location and distribution of different plaque components of atherosclerotic plaques are illustrated. Furthermore, when cardiologists analyze a sequence of IVUS images, additional clinical parameters together with the percentage of different plaque components can be useful.

Perhaps, one of the important advantages of the proposed algorithm is to increase the longitudinal resolution of plaque composition analysis. The present VH-derived plaque composition analysis provides only ECG-triggered images. As mentioned above, in an imaging procedure with the rate of 30 frames/s only 1 IVUS frame out of 30 IVUS frames is considered to generate the color-coded VH image.

As it is shown in Fig. 26.33, the proposed algorithm contains different sections including plaque area detection, shadow region detection as a pre-processing, textural feature extraction, classification by SVM, and post-processing based on the data derived from the histogram analysis. The differences in the results of the Tables 26.3 and 26.4 and also those illustrated in Fig. 26.37 show the influence of adding the shadow region detection as a pre-processing section. One of the obvious advantages to add the shadow region detection is to help algorithm to improve the detection of all three kinds of atherosclerosis plaque components.

Moreover, this technique provides us with a more general algorithm which can be more reliable when in studying patients with calcified plaques in which a lateral shadow region behind the calcified area exists. Out of the total number of 191,582 pixels was contained in the shadow region, 63%, 36%, and about 1% was respectively characterized into FF, NC, and DC plaques by the VH algorithm. Therefore, Tables 26.3 and 26.4 show that in addition to improving the distinction of three plaque components, the shadow detection procedure has a direct influence on the detection of FF and NC. Differences of relative amounts of DC and NC between after and before shadow detection were calculated 5% and 4%, respectively.

One should note that the IVUS-IBH images in the third and fourth column of Fig. 26.37 show small islands of green within the blue shadow regions. Once shadowing occurs due to calcium, the RF signal is attenuated and one doesn't expect to see these islands. This may be due to multiple reflections between the catheter and the calcium causing artifact. By comparing the results of the Tables 26.3 and 26.4, it can be concluded that the new extended run-length feature extraction method outperforms the LBP in classifying all plaque components. However, as illustrated in Fig. 26.38, it is quite clear that the color-coded image reconstructed with the use of LBP feature extraction method is more detailed.

This may be caused by the multi-resolution characteristic of this method. Perhaps, one future direction is to combine these two feature extraction methods in order to benefit from their both detailed and accurate results.

The computation times of the feature extraction methods are as follows: for a typical frame, i.e., the plaque area containing around 5,000 pixels out of the total 160,000 IVUS image's pixels, the new extended run-length method took 7–20 s to extract the features whereas the LBP took 2–5 min. Thus, in terms of time efficiency, the new extended run-length method further outperforms the LBP method. However a more optimized implementation in C++ will further speed up the algorithms as expected. The influence of the post-processing step after classification is highlighted in the differences in the sensitivity and specificity of the algorithm in characterizing NC and FF plaques, respectively. The extensive textural similarities between the NC regions and other plaque components defined by VH lead to preventing the classification part of the algorithm from identifying it; however, by studying the distribution of plaques' intensities in the dataset, it is concluded that in addition to textural fea-

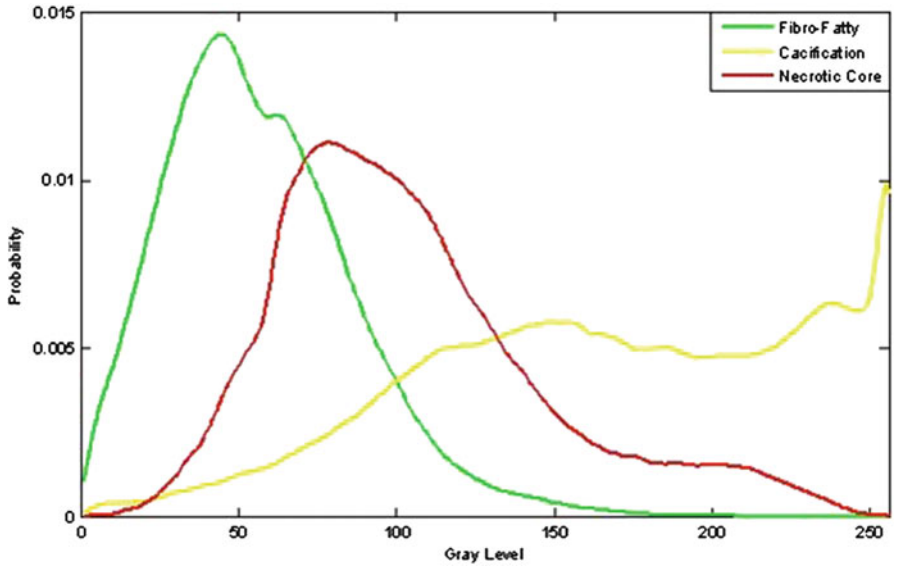

Fig. 26.39 Histogram of three plaque types in IVUS images: fibro-fatty (*green*), necrotic core (*red*), and calcification (*yellow*)

tures, there exists some rules for distinguishing the plaques in it (Fig. 26.33).

This $\kappa = 0.61$ (for both pixel-based and region-based validation) clearly represents that the classification results are in good agreement with VH after detecting and removing shadow regions. Moreover, the low values of CI and *P*-value show the reliability and consistency of these results obtained for this dataset. The *P*-values indicated in Table 26.5 answer the following question: If the method's performance is the same as the before applying shadow detection and post-processing, what is the probability of observing the current result? From a statistical point of view, the observed difference in these results compared to the results of the methods before detecting shadow and applying post-processing is not accidental.

An interesting point that should be mentioned here is that the results presented suggest that the texture-based algorithm based on IVUS gray-scale images produces similar images and has a modest co-relation to VH-IVUS, suggesting that most of the information in VH-IVUS tissue characterization comes from the intensity of the ultrasound signal, and less so on the underlying radiofrequency data. In this study, all methods' sensitivity to detect the NC was low (maximum value is 57%). The fact that detection of NC by studying the IVUS images is not a straightforward procedure has also been previously discussed in [4] and [24]. This phenomenon was caused by similarities between NC and DC in gray-level IVUS images. This fact supports the previous studies which have shown that plaque areas adjacent to dense calcium are frequently coded as necrotic tissue in VH images [14]. By considering selected cross sections that contained plaque areas with a homogeneous tissue composition as reported in [4], the accuracy results can be increased significantly. Although the sensitivity of detecting the calcified region was 79%, the algorithm performance to detect the focal calcified region in the images was more than 85%, which is another important point about these results. It derives from the fact that in the VH method the variation of pixels intensities assigned to the calcium class is very high (from 0 to 256) as can be observed in Fig. 26.26. However, since identifying focal calcified regions is more important than speckled calcification in the plaque area, the proposed algorithm shows increased reliability [25].

6 Algorithm IV

A definition of LBP and new extended run-length (NRL) features and the experiences of the previous algorithms indicates that these two feature extraction methods assess the texture from two different aspects. Hence their combination may enhance the accuracy of texture analysis methods and in this case the accuracy of plaque characterization. Moreover, in the previous algorithms, post-processing was applied to take advantage of the gray-level distribution of each plaque type to confirm or correct the labels given to each pixel by the classifier. Improvement of the results after applying the post-processing stage proved that gray-level information is valuable information that is not completely included in the LBP, NRL, or other structural features. However, as the histograms of plaques are not distinctly separated from each other (Fig. 26.39), the post-processing method is not sufficiently reliable. Furthermore, shapes of histograms may differ from one dataset to another that demands the histogram analysis be repeated for every new dataset. This imposes an unnecessary computational load. Moreover, the sharp decision thresholds in the post-processing can destroy the effect of discriminative hyperplanes detected by the classifiers.

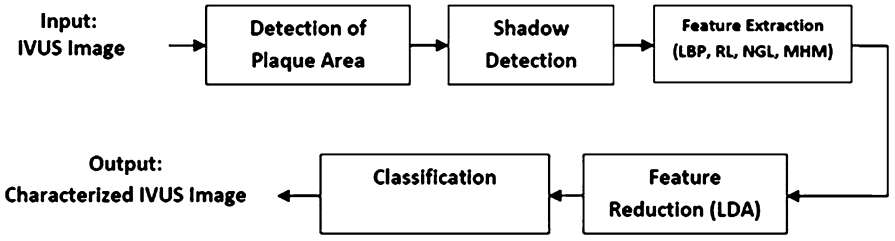

Fig. 26.40 Block diagram of Algorithm IV

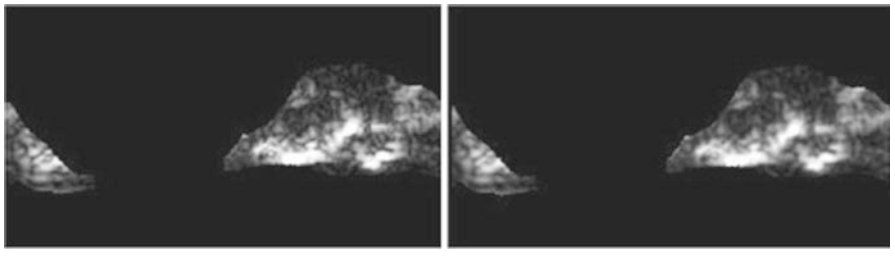

Fig. 26.41 Illustration of the neighboring gray-level feature (mean value of gray levels is shown): plaque area in polar coordinates (*left*) and mean neighborhood gray level (*right*)

Table 26.6 Hu Moments mathematical expressions [14]

$$\phi_1 = \eta_{20} + \eta_{02} \qquad \phi_2 = (\eta_{20} - \eta_{02})^2 + 4\eta_{11}^2$$

$$\phi_3 = (\eta_{30} + 3\eta_{12})^2 + (3\eta_{21} - \eta_{03})^2 \qquad \phi_4 = (\eta_{30} + \eta_{12})^2 + (\eta_{21} + \eta_{03})^2$$

$$\phi_5 = (\eta_{30} - 3\eta_{12})(\eta_{30} + \eta_{12})[(\eta_{30} + \eta_{12})^2 - 3(\eta_{21} + \eta_{03})^2] + (3\eta_{21} - \eta_{03})(\eta_{21} + \eta_{03})[3(\eta_{21} + \eta_{03})^2 - (\eta_{21} + \eta_{03})^2]$$

$$\phi_6 = (\eta_{20} - \eta_{02})[(\eta_{30} + \eta_{12})^2 - (\eta_{21} + \eta_{03})^2] + 4\eta_{21}(\eta_{30} + \eta_{12})(\eta_{21} + \eta_{03})$$

$$\phi_7 = (3\eta_{21} - \eta_{03})(\eta_{30} + \eta_{12})[(\eta_{30} + \eta_{12})^2 - 3(\eta_{21} + \eta_{03})^2] + (3\eta_{12} - \eta_{30})(\eta_{21} + \eta_{03})[3(\eta_{30} + \eta_{12})^2 - (\eta_{21} + \eta_{03})^2]$$

$$\text{where } \eta_{pq} = \frac{\mu_{pq}}{\mu_{02}{}^{\gamma}}, \quad \gamma = \frac{p+q}{2} + 1, \text{for}: p + q = 2.3.\ldots$$

In this algorithm, Algorithm IV, LBP and NRL were combined to benefit the advantages of both features. Also, in order to dispose of the post-processing stage and its shortcomings mentioned above, adding the gray-level information in the form of features was proposed in combination with LBP and NRL features to better classify the plaque types. These new features are the modified Hu Moments (MHM) and a newly proposed neighboring gray-level (NGL) feature (Fig. 26.40).

6.1 Neighboring Gray-Level Feature

As mentioned above, the features used in the previous algorithms are structural features and do not take into account directly the gray-level values of the pixels contained in the sweeping windows. However, there exists valuable discriminative information in the distribution of the gray levels and a new set of features capable of describing the useful gray-level information is proposed here. Suppose for each pixel (i, j) of the image $I, a(M + 1) \times (N + 1)$ neighborhood $I\{i + m, j + n\}$ with $m \in \{-\frac{M}{2}, \frac{M}{2}\}$ and $n \in \{-\frac{N}{2}, \frac{N}{2}\}$ is adopted. For the newly proposed gray-level feature, $M = N = 2$ is considered to have the smallest neighborhood, i.e., a 3×3 window. Let g_c be the gray value of the center pixel and $g_n, n = 1, 2, \ldots, 8$ be the gray values of the 8 neighbor pixels. So, nine gray levels of the pixels contained in that window are used as a feature vector $F = (g_c, g_1, g_2, \ldots, g_8)$. Since these features are sensitive to translation and rotation, the features are sorted in an ascending order to get rid of these effects. An illustration of the mean neighborhood gray level is shown in Fig. 26.41.

6.2 Modified Hu Moments

The moments mix gray-level and position information of pixels of an image to yield a new feature for texture analysis [1]. Actually, the moments show how gray levels distribute in an image. They are defined as follows:

$$m_{pq} = \sum_i \sum_j i^p j^q I(i, j) \tag{26.66}$$

That is called a moment of order $p + q$. However, these moments lack the invariance property (i.e., they are rotational, translational, and scale variant). Thereby, central moments are defined that are invariant to translation:

$$\mu_{pq} = \sum_i \sum_j (i - \bar{i})^p (j - \bar{j})^q I(i, j)$$

$$\bar{i} = \frac{m_{10}}{m_{00}}, \quad \bar{j} = \frac{m_{10}}{m_{00}} \tag{26.67}$$

But central moments are still scale and rotational invariant. A commonly used group of moments in texture analysis are Hu Moments described in Table 26.6. Although Hu

moments are rotational, translational, and scale invariant, but they are not invariant to affine transforms, for example, multiplication of whole image pixels by a numeric constant.

These affine transforms are associated to images with different acquisition gains. In order to solve this problem, a new set of invariants were proposed in [26]. Suppose that:

$$F_P(u) = \text{sign}\,(u) \cdot |u|^P \tag{26.68}$$

the new features are then described as follows (Figs. 26.42, 26.43, 26.44, 26.45, 26.46, and 26.47):

$$f_1 = \frac{F_2(\Phi_2)}{\Phi_1} \tag{26.69}$$

$$f_2 = \frac{F_3(\Phi_3)}{\Phi_1} \tag{26.70}$$

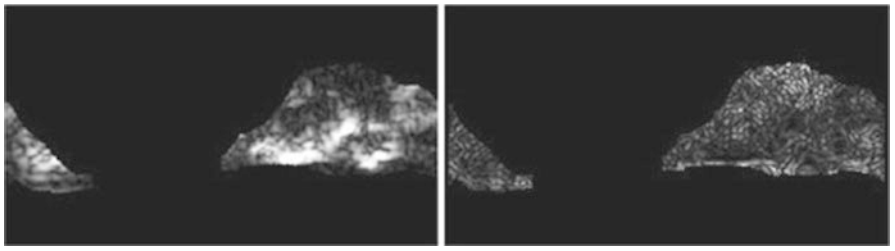

Fig. 26.42 Illustration of Hu feature f_1: plaque area in polar coordinates (*left*) and f_1 (*right*)

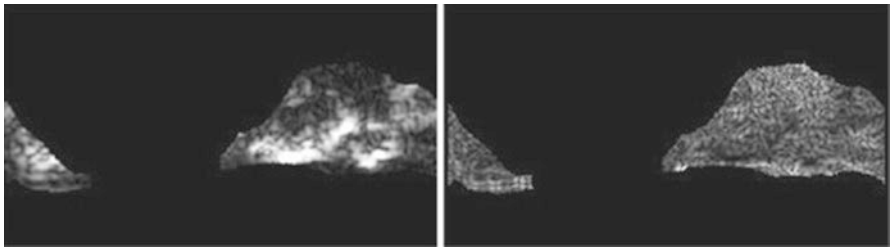

Fig. 26.43 Illustration of Hu feature f_2: plaque area in polar coordinates (*left*) and f_2 (*right*)

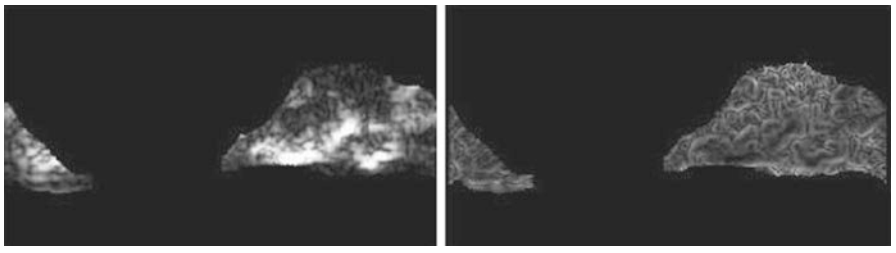

Fig. 26.44 Illustration of Hu feature f_3: plaque area in polar coordinates (*left*) and f_3 (*right*)

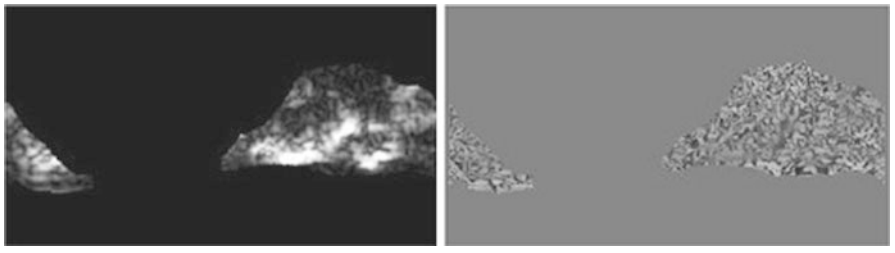

Fig. 26.45 Illustration of Hu feature f_4: plaque area in polar coordinates (*left*) and f_4 (*right*)

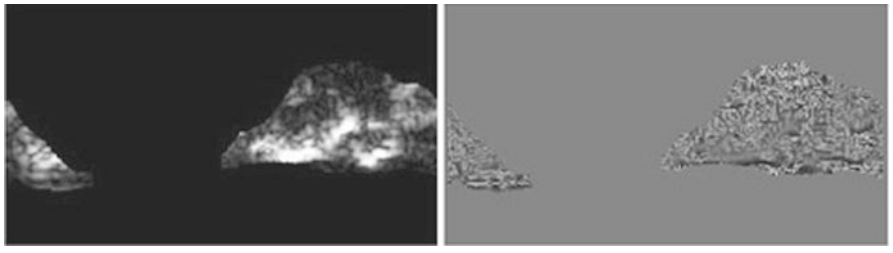

Fig. 26.46 Illustration of Hu feature f_5: plaque area in polar coordinates (*left*) and f_5 (*right*)

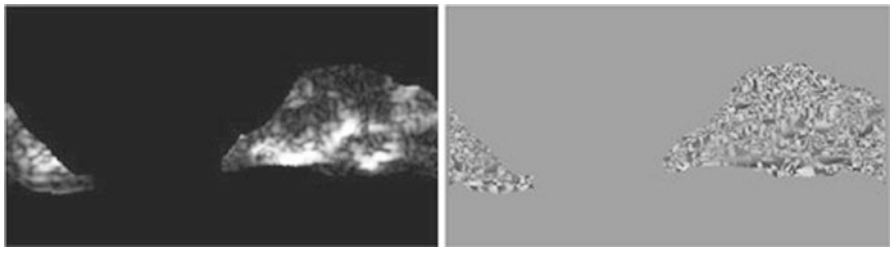

Fig. 26.47 Illustration of Hu feature f_6: plaque area in polar coordinates (*left*) and f_6 (*right*)

$$f_3 = \frac{F_3(\Phi_4)}{\Phi_1} \tag{26.71}$$

$$f_4 = \frac{F_6(\Phi_5)}{\Phi_1} \tag{26.72}$$

$$f_5 = \frac{F_4(\Phi_6)}{\Phi_1} \tag{26.73}$$

$$f_6 = \frac{F_6(\Phi_7)}{\Phi_1} \tag{26.74}$$

This set has shown lower sensitivity to translation, rotation, scale, and affine transforms than the conventional Hu Moments.

6.3 Result of Algorithm IV

The study group used for Algorithm IV is the same as the one used for Algorithm III. After shadow detection, the LBP, NRL, NGL, and MHM features were extracted from the remaining plaque area. The characterized IVUS images were validated by their corresponding VH images. Sensitivity, specificity, and accuracy parameters were then calculated in order to assess the performance of the new algorithm. Results are shown in Table 26.7. In order to find out the impact of the new features the results were compared to the case that NRL and LBP was concerned.

Results of Table 26.7 show that the combination of features enhanced the classification accuracy and especially the detection of necrotic core (concluded based on sensitivity and specificity of NC). Also Figs. 26.48 and 26.49 illustrate the images characterized by all methods with their corresponding IVUS and VH images.

Combination of different types of features results in large feature vectors and hence a complex feature space. Classification in such feature spaces is very time-consuming. In such cases, in order to increase the efficiency of classifiers, feature reduction methods are applied to feature vectors before they are fed to the classifiers. LDA was chosen that has been best suited to this work.

6.4 Linear Discriminant Analysis

LDA was applied to the feature space. However, the question is how to choose the L ($L <$ # of features) most significant directions? In LDA method, each direction is given a value that indicates the separation ability of that direction. In order to choose the L most significant directions, we start with the most significant direction and determine its separation ability (i.e., the ratio of its value to the sum of all directions' values). Then the second most significant direction is added to the first one and its separation ability is calculated. This procedure is repeated until adding directions does not change the separation value effectively.

Thereby, the number at which this happens is the optimum number of directions.

For example in this case, adding more directions to the five first most significant directions does not affect the percentage of separation (Fig. 26.50) so five is the optimum number of directions.

6.4.1 Error-Correcting Output Codes Classifier

The error-correcting output codes (ECOC) technique can be broken down into two distinct stages: encoding and decoding. Given a set of classes, the coding stage designs a codeword (a sequence of bits of a code representing each class, where each bit identifies the membership of the class for a given binary classifier) for each class based on different binary problems. The decoding stage makes a classification decision for a given test sample based on the value of the output code [27]. Given a set of N_C classes to be learned, at the coding step of the ECOC framework, different bi-partitions (groups of classes) are formed, and binary classifiers (dichotomies) are trained. As a result, a code word of length n is obtained for each class, where each bit of the code corresponds to the response of a given dichotomy: ± 1 if the class is considered by the dichotomy ($+$ or $-$ is decided by the dichotomy) and 0 if the class is not considered by the dichotomy. Figure 26.51 shows an example of ECOC for

Table 26.7 The results of Algorithm IV versus other techniques

	DC		FF		NC		
Method	Sensitivity (%)	Specificity (%)	Sensitivity (%)	Specificity (%)	Sensitivity (%)	Specificity (%)	Overall accuracy (%)
LBP	58	85	83	81	46	77	62
NRL	79	85	81	90	52	82	71
LBP + NRL	78	86	82	90	56	82	72
LBP + NRL + NGL + MHM	80	86	80	92	60	81	73

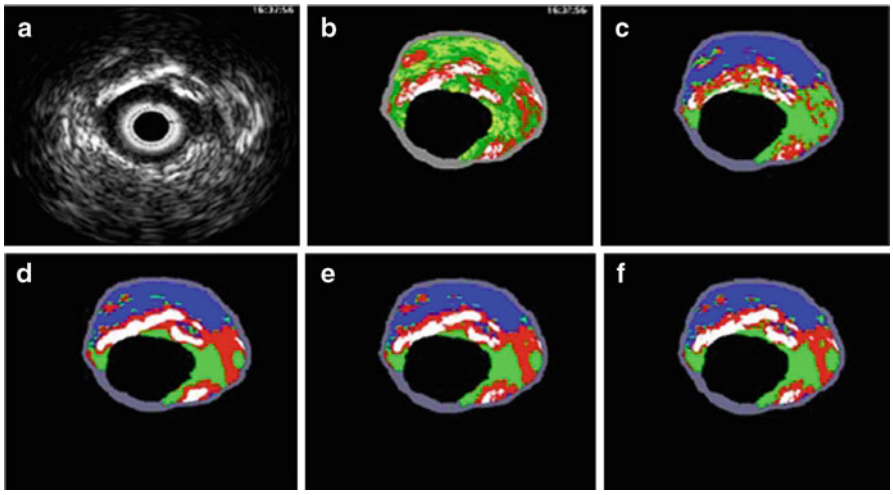

Fig. 26.48 (**a**) IVUS image, (**b**) its corresponding VH image, (**c**) reconstructed image by LBP method, (**d**) reconstructed image by NRL method, (**e**) reconstructed image by LBP + NRL method, and (**f**) reconstructed image by Algorithm IV

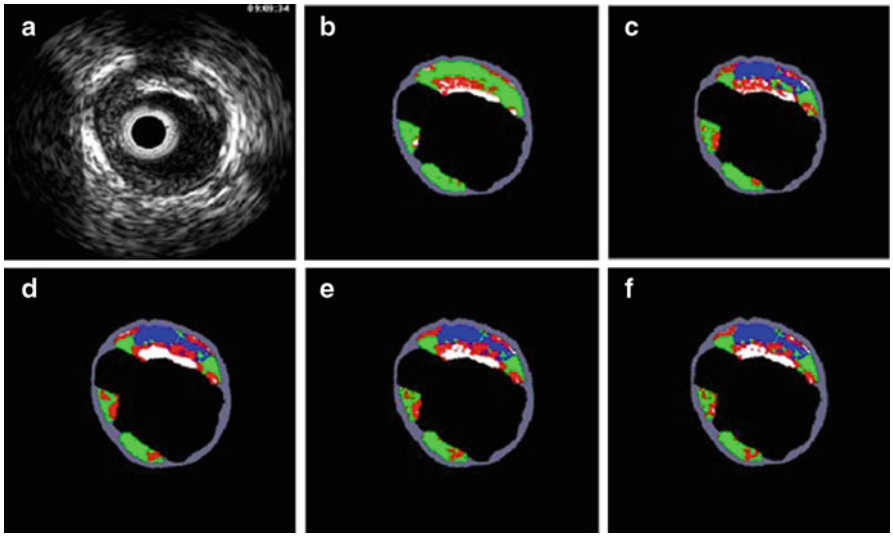

Fig. 26.49 (**a**) IVUS image, (**b**) its corresponding VH image, (**c**) reconstructed image by LBP method, (**d**) reconstructed image by NRL method, (**e**) reconstructed image by LBP + NRL method, and (**f**) reconstructed image by Algorithm IV

a three-class problem ($C_1, C_2,$ and C_3). Three dichotomies (h_1, h_2, h_3) are formed for a three-class problem where each dichotomy learns to split a pair of classes. For example, the first classifier h_1 is trained to discriminate C_1 versus C_2 ignoring C_3. According to these dichotomies, a code is assigned to each class. The white regions represent the code 1 (considered as positive for its respective dichotomy h_i), the dark regions represent the code -1 (considered as negative for its respective dichotomy h_i), and the gray regions represent the code 0 (not considered classes by the current dichotomy) (Table 26.8).

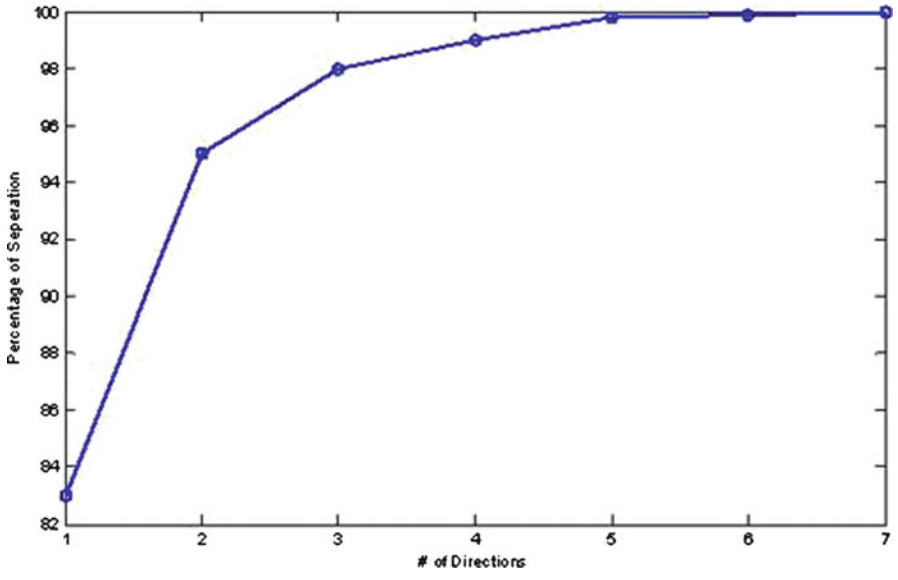

Fig. 26.50 Separation percentage does not change effectively selecting more than five LDA directions

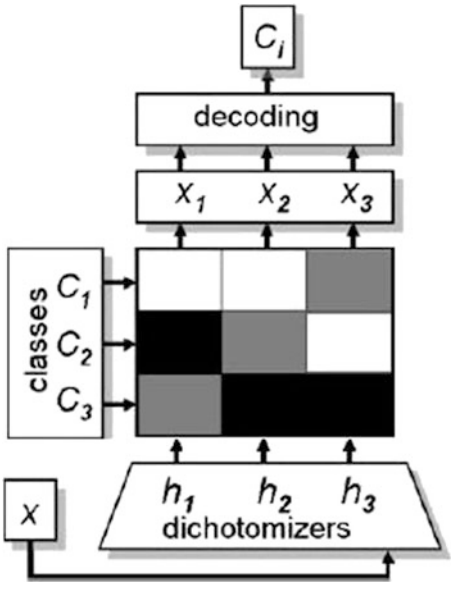

Fig. 26.51 Example of ECOC classification for a three-class problem [24]

Table 26.8 ECOC code map used in the classification

Classes	Classifier 1	Classifier 2	Classifier 3
Dense calcium	1	1	0
Fibro-lipid	−1	0	1
Necrotic core	0	−1	−1

6.5 Result of Algorithm IV After Applying LDA and ECOC

Results are shown in Table 26.9. According to the results, applying LDA would not severely affect the results while reducing the classification time. Furthermore, as SVM and ECOC result in nearly same accuracies, it can be concluded that this is the highest results achievable with these features.

6.5.1 Discussion of Algorithm IV

Algorithm IV is an improvement of the previous algorithms. It is mainly designed for, first, removing the histogram-based post-processing stage by adding some gray-level features at the feature extraction stage and, secondly, assessing the performance of combination of the previously introduced texture features. Since combination of several features would lead to a high dimensional feature vector of (49 features), LDA is used to optimally reduce the number of features. At the classification stage, also ECOC classifier is used (rather than SVM classifier) in order to assess the reliability of the obtained results.

It is concluded from Table 26.7 that the proposed gray-level-based features, NGL and MHM, can successfully play the role of histogram-based post-processing step. Furthermore, combination of features not only increases the feature vector dimension, but also improves the accuracy of plaque characterization algorithm especially in identifying NC plaque component. Moreover, comparison of Fig. 26.48e to Fig. 26.48c, d shows that a more detailed image is produced combining NRL and LBP.

Also, the results in Table 26.9 show that applying LDA would not severely affect the results and almost the same results are yielded. However, using this method reduces the complexity of feature space that helps SVM to find the discrimination hyperplanes faster and easier. Furthermore, based on this table, the results obtained with SVM and ECOC are close to each other. An interpretation is that this is the highest achievable accuracy using image-based methods in comparison to VH.

Table 26.9 The results of Algorithm IV evaluated with different classifiers with and without LDA

Method	Feature reduction	Classifier	Metric	DC	FF	NC	Overall accuracy (%)
NRL + LBP + NGL + MHM	None	SVM	Sensitivity (%)	80	80	60	73
			Specificity (%)	86	92	81	
NRL + LBP + NGL + MHM	LDA	SVM	Sensitivity (%)	79	78	59	72
			Specificity (%)	86	92	81	
NRL + LBP + NGL + MHM	None	ECOC	Sensitivity (%)	79	80	61	74
			Specificity (%)	87	91	82	
NRL + LBP + NGL + MHM	LDA	ECOC	Sensitivity (%)	80	80	60	73
			Specificity (%)	87	91	82	

Table 26.10 Summary of four algorithms proposed in this chapter

Method	Contribution	DC Sensitivity (Specificity)	FF Sensitivity (Specificity)	NC Sensitivity (Specificity)	Accuracy
Algorithm I (published in ISBI 2009)	Modified run-length	70% (95%)	84% (75%)	55% (82%)	77%
Algorithm II (published in SPIE 2010)	Redundant wavelet packet transform	73% (93%)	85% (79%)	42% (84%)	72%
Algorithm III (accepted in UBM journal)	Shadow detection GUI	79% (85%)	81% (90%)	52% (82%)	75%
Algorithm IV (SVM)(ECOC)(under submission IEEE TITB journal)	Introducing new feature Feature combination Removing post-processing LRE	79% (86%) 80% (87%)	78% (92%) 80% (91%)	59% (81%) 60% (82%)	72% 73%

The major contribution of this algorithm is the improvement of in detecting NC class comparing to the previous algorithms. Considering loss of information in the procedure of transforming RF signal to IVUS image and the reverberation phenomenon in the shadow region, it is really promising to obtain these results. These results support the idea that most discriminative information used in VH analysis comes from the amplitude of RF signals.

Table 26.10 shows a comparison chart of four algorithms proposed in this chapter.

7 Validation

A fivefold cross-validation approach is considered for validating the proposed algorithms. In this validation scheme, first, the feature vectors extracted from all images of the dataset are joined with each other to form a feature matrix. Then, this matrix is shuffled so that the feature vectors of different classes are distributed randomly. After shuffling, this matrix is divided into five equal parts. In each validation step, four parts are considered as training dataset used to train the classifier. The trained classifier is then tested with the remaining part. This procedure is repeated five times, each time with a new part as test data. The steps of a fivefold cross validation are shown in Fig. 26.52. Finally, the averages of the results derived from all steps are reported as the total result of classifier. These results are known to be more reliable than the other validation methods when sufficient number data is available.

8 In Vivo Validation

For in vivo validation, 120 new IVUS images, which were not included in the classification neither as training data nor as test data, were considered to be characterized using Algorithm IV. For this purpose, an SVM classifier was trained using the whole dataset excluding these images. Figure 26.53 shows the reconstructed images after applying Algorithm IV to three different IVUS images. Average accuracy for the images that participated in in vivo validation was measured 78%.

8.1 Statistical Analysis of In Vivo Validation

The VH and Algorithm IV interpretation of the plaque components of 120 images tested in vivo are reported in Table 26.11. The sensitivity, specificity, and accuracy of each plaque components are listed in Table 26.12. The kappa value was calculated to be 0.639 indicating good agreement.

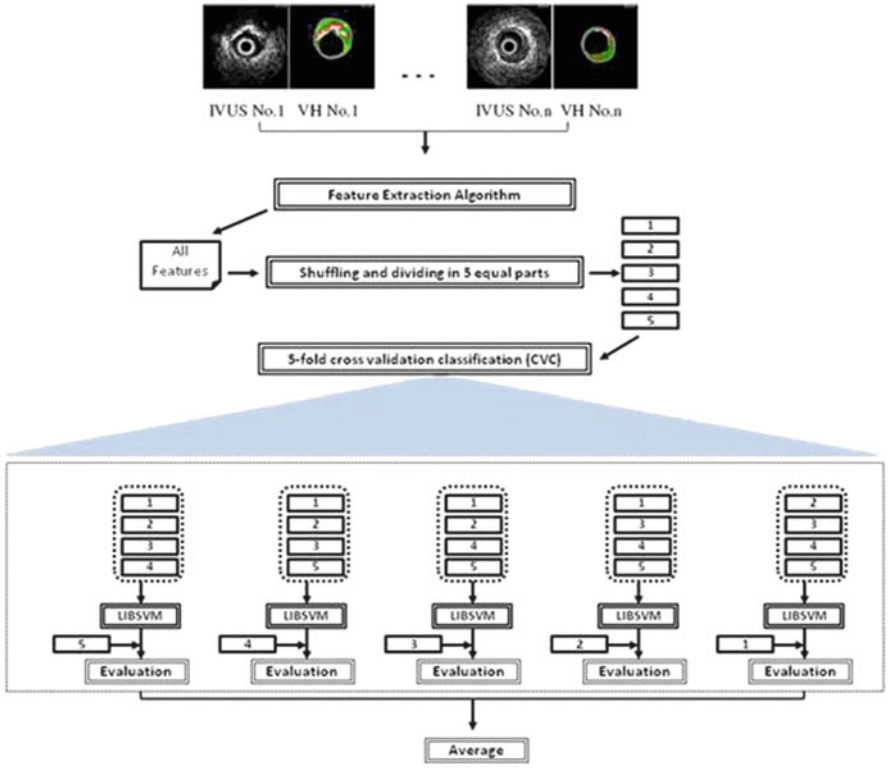

Fig. 26.52 Illustration of fivefold cross validation

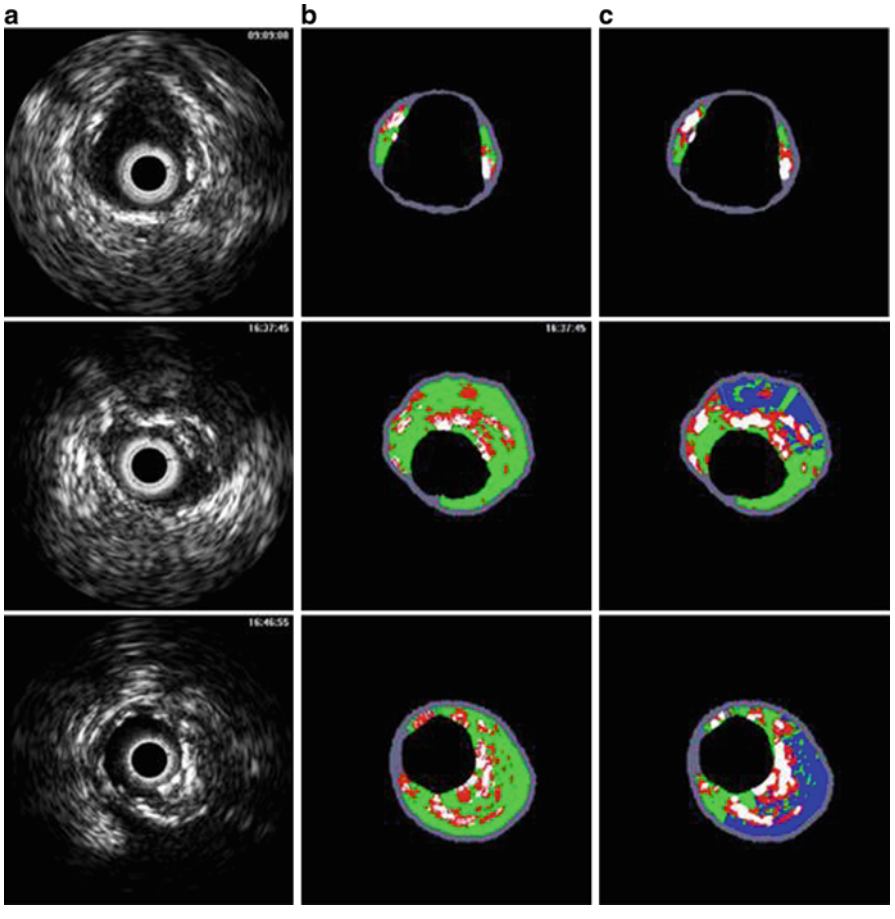

Fig. 26.53 (**a**) IVUS image, (**b**) its corresponding VH image and (**c**) reconstructed image by Algorithm IV

Table 26.11 Truth table to show the degree of agreement between the Algorithm IV and VH classification for in vivo validation

VH plaque component	DC in proposed method	FF in proposed method	NC in proposed method	Total in VH
DC in VH	54,425	4,431	15,384	74,240
FF in VH	2,430	359,326	19,229	380,985
NC in VH	10,884	37,279	45,221	93,384
Total in proposed method	67,739	401,036	79,834	548,609

The bold numbers in Table 26.11 illustrate the number of pixels characterized as the same plaque component by two methods, and the bold number at the last column shows the total number of pixels which have been characterized in 120 images collectively. The truth table shown in Table 26.11 contains a great amount of information which one can use to compare the proposed method to VH. First, the number of pixels detected in the proposed method is explicitly compared to VHs'. For example, on the one hand the first row of the numbers shows that among 74,240 pixels which detected as DC in VH images used in this test collectively, the proposed algorithm classified the 54,425 pixels as DC correctly (True Positive for DC), 4,431 pixels as FF plus 15,384 pixels as NC which are not correct (False Negative for DC). On the other hand, the first column of the numbers shows that among the 67,739 pixels which the proposed method classified as DC, excluding the 54,425 pixels which are true, 2,430 pixels misclassified as FF (False Positive for DC) and 10,884 pixels misclassified as NC (False Positive for DC). Analyzing the other rows and columns will determine the similar parameter for FF and NC too.

Table 26.12 The results of Algorithm IV as in vivo validation with 120 images

	Sensitivity	Specificity	Accuracy
Dense calcium (DC)	80.1% ± 0.3	94.5% ± 0.2	92.8%
Fibro-lipid (FF)	89.6% ± 0.09	98.91% ± 0.03	92.1%
Necrotic core (NC)	56.6% ± 0.3	86.8% ± 0.2	82.4%

9 Ex Vivo Validation

In order to test the reliability of the newly proposed algorithm (Algorithm IV), it was decided to validate with two reliable histology datasets considered as ex vivo validation. The first histology samples were processed and prepared as mentioned in 9.1.i and 9.5.ii by our medical partner group at Cardiology Department in University of Munich [28]. The second one is the dataset used in Katouzian et al. [29]. In addition to histology images, this dataset contains the images reconstructed from the plaque characterization algorithm proposed by Katouzain et al. [30].

9.1 Dataset 1

(a) Specimen handling and processing

Six human coronary arteries (two left anterior descending arteries; two left circumflex arteries; two right coronary arteries) from three cadavers (mean age 70 ± 9 years, all men, all noncardiac death) were imaged with IVUS within 12 h postmortem (mean time: 9 ± 1 h). After harvesting, the hearts were stored at 9 °C until imaging. The study was approved by the Institutional Ethics Committee of the University of Munich.

(b) IVUS imaging

After cannulation of the ostium of each coronary artery a pressure of 90 mmHg was established using a 0.9% sodium chloride solution. A 0.014-inch guide wire was inserted into the coronary artery lumen under fluoroscopic guidance. An external marker (surgical suture) was applied to the vessel at the distal (first image) and proximal (final image) position of the probe, which later enabled accurate correlation of IVUS and histology images. The IVUS probes were inserted and advanced to distal end of the vessel. An electronic probe (In-Vision Gold, Volcano Therapeutics, Inc., Rancho Cordova, California, USA) with a synthetic aperture 2.9 F and a frequency of 20 MHz was used. A motorized pullback was performed along the entire vessel with a speed of 1.0 mm/s using a dedicated pullback device (R-100 research pullback device, Volcano Therapeutics, Inc.). IVUS images were stored digitally in DICOM format. Immediately after the IVUS imaging, specimens were fixed with the 10% neutral-buffered formalin and histology was performed.

(c) Histology

All vessel specimens were dissected from the heart and 5 mm blocks were cut starting from the distal marker. Each tissue block was numbered, decalcified in a standard ethylene diamine-tetra-acetic acid-4 Na–20% citric acid solution for 10 h, and then embedded in paraffin. From each block, at least two consecutive 4 mm thick slices were cut every millimeter using a microtome. All cross sections were stained with hematoxylin and eosin and every second slice with Elastica-van Gieson. These stains routinely allow for the identification of necrotic lipid-rich, calcium, and fibrous tissue. See Fig. 26.54b.

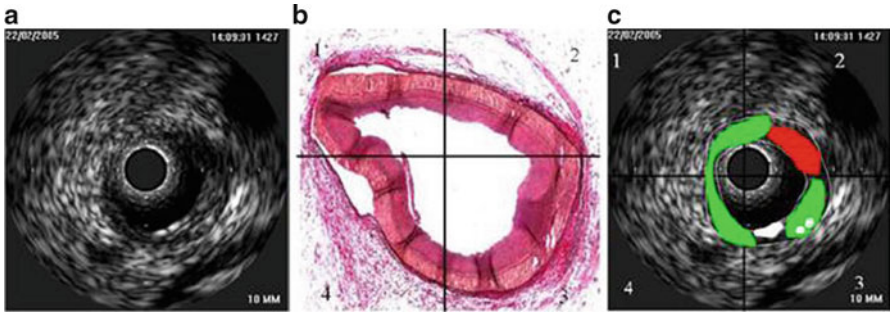

Fig. 26.54 (**a**) IVUS image, (**b**) histology, and (**c**) manually analyzed image

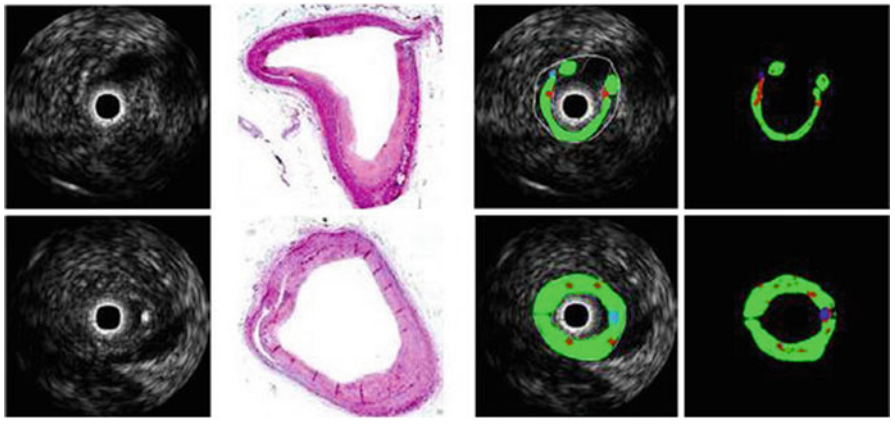

Fig. 26.55 (**a**) IVUS cross section, (**b**) histology image, (**c**) manually analyzed image, and (**d**) result of Algorithm IV

Table 26.13 The result of ex vivo validation: Algorithm IV validated with histology pictures using pixel-based and region-based validation (Dataset 1)

	DC		FF		NC		
	Sensitivity	Specificity	Sensitivity	Specificity	Sensitivity	Specificity	Overall accuracy
Algorithm IV	55% ± 15	97% ± 2	77% ± 9	50% ± 15	47% ± 9	77% ± 9	74% ± 8
Algorithm IV (9 × 9)	47% ± 19	98% ± 2	82% ± 8	58% ± 9	38% ± 17	83% ± 8	77% ± 8

(d) Manual image analysis

IVUS images were correlated with the corresponding histology slides. All images were divided into four quadrants. Four plaque components for tissue characterization of the vessel wall: normal, fibrous-lipid, calcium, and necrotic lipid-rich (necrotic) plaques were used. Each of the plaque components was assigned to a different color: gray for normal, green for fibrous-lipid, white for calcium, and red for necrotic tissue. Every part of the vessel wall in the IVUS images within the lumen–intima and media–adventitia borders was classified to consist of one of these tissue types using histology as the gold standard (see Fig. 26.54c). For histological classification, a modified grading system in accordance with the Committee on Vascular Lesions of the Council on Atherosclerosis [31] and [32] was used. Normal vessel wall was defined as a regular three-layered appearance without evidence of intimal thickening. In addition, early lesions (corresponding to plaque type I–III [32]) were defined as normal because these early changes are to a certain degree reversible [13] and due to their inferior resolution are not detectable in IVUS. Fibrous plaque was defined as accumulation of predominant fibrous tissue corresponding to plaque type VIII [32]. Necrotic-lipid rich plaque was defined as accumulation of predominant lipid-rich necrotic tissue corresponding to plaque type IV [32]. Plaques were defined as calcified when there was evidence of calcium deposits in the tissue corresponding to plaque type VII [32].

9.2 Results of Ex Vivo Validation (Dataset 1)

The images used in ex vivo validation were not considered in previous analysis of this research. For ex vivo validation, a SVM classifier was trained using the whole dataset and VH images as labels. Figure 26.55 shows the results of applying the Algorithm IV to two different IVUS images. These results are validated and compared with ten manually analyzed images considered as reference in this work. Also, Table 26.13 shows the statistical results of applying Algorithm IV to these images.

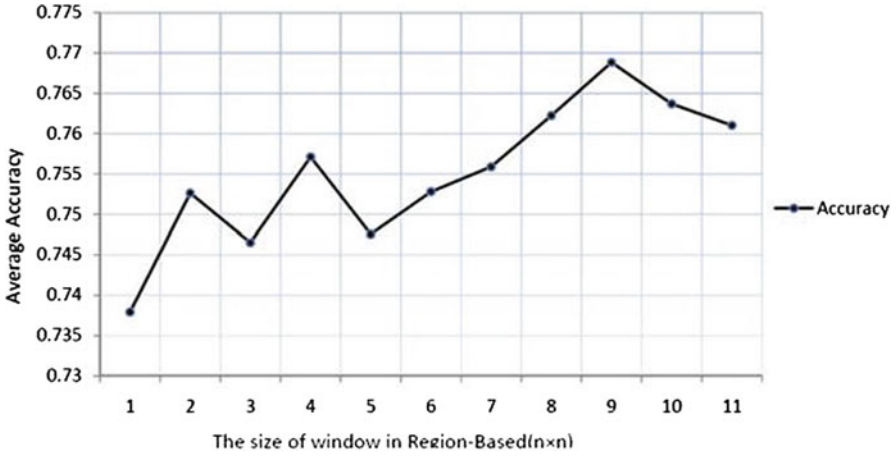

Fig. 26.56 Variable accuracies show the effect of window size in validation against the pixel-based validation ($n = 1$ on x-axis)

Table 26.14 Truth table to show the degree of agreement between the Algorithm IV and histology images of dataset 1 for ex vivo validation (pixel-based)

VH plaque component	DC in proposed method	FF in proposed method	NC in proposed method	Total in VH
DC in VH	1,169	149	654	1,972
FF in VH	261	36,908	4,785	41,954
NC in VH	812	3,815	5,668	10,295
Total in proposed method	2,242	40,872	11,107	54,221

In most similar studies, when one wants to validate with histology images a region-based validation method is used. It means that instead of comparing the result and its corresponding label pixel by pixel, the validation step is done by comparing regions, a window which contains more than 1 pixel. For example, the size of validation regions in Nair et al. [11] is 1/3 mm × 1/3 mm, i.e., approximately a window of size 13 × 13 pixels. To handle this, a validation window of size $n \times n$ pixels, where n can vary from 1 (pixel-based validation) to 13, was defined. The label of a validation window was selected by looking at labels of its constituent pixels. In fact, it is assigned to a plaque component which is the majority. Figure 26.56 shows different accuracies achieved through different window sizes from the pixel-based validation (0.025 mm × 0.025 mm pixels) till the region-based validation (0.3 mm × 0.3 mm regions). This figure shows that the size of regions affects the results.

9.3 Statistical Analysis of Ex Vivo Validation (Dataset 1)

As mentioned in previous section, dataset one in ex vivo validation was validated using both the pixel-based and region-based validation methods. Their sensitivity, specificity, and accuracy for three plaque components are reported separately in Tables 26.14 and 26.15. When predicting the tissue types in ex vivo validation, the kappa value for pixel-wise method ($\kappa = 0.487$) was a little less than region-based method ($\kappa = 0.533$) but both presenting the moderate agreement.

9.4 Dataset 2

An acquisition of the cross-sectional ultrasound images of right coronary arteries (RCA), left anterior descending (LAD), and left circumflex (LCX) coronary arteries for this dataset were performed with a 40-MHz rotating single-element Boston Scientific (Fremont CA) transducer. The catheter pullback speed was equal to 0.5 mm/s and the frame rate was 30 frames/s. Each raw frame contains 256 lines with 2,048 samples per line. In order to construct a 256 × 256-pixel IVUS image, the envelope of each RF signal was computed by the corresponding analytical signal and then it was decimated by eight samples. A logarithmic compression was also used to enhance the image quality. Then, the 8-bit quantization was used, and the resulting gray-scale image transformed to Cartesian coordinates to generate a typical IVUS frame (Fig. 26.58a). For extraction histology images, arteries of human hearts obtained from two sources, i.e., autopsy and transplant surgery, are dissected from the heart and oriented in a tissue cage fixture (Fig. 26.57). Then, they are stained with Movat Pentachrome. Movat

Table 26.15 Truth table to show the degree of agreement between the Algorithm IV and histology images of dataset 1 for ex vivo validation (region-based: 9 × 9)

VH plaque component	DC in proposed method	FF in proposed method	NC in proposed method	Total in VH
DC in VH	32	6	20	58
FF in VH	11	973	88	1,072
NC in VH	13	85	131	229
Total in proposed method	56	1,064	239	1,350

Fig. 26.57 Tissue cage fixture: the artery is fixed in the cage and an automatic pullback is performed in saline and human blood. The histology sections are taken at every 2 mm using side rods after the artery was fixed by formaldehyde [32]

Pentachrome colors cytoplasm in red, elastic fibers in black, collagen and reticulum fibers in yellow to greenish, and proteoglycans in blue. Then pictures are taken from these sections and homogenous parts are marked by pathologists (Fig. 26.58b). Then these marked images are mapped on IVUS images (Fig. 26.58c) and tissue color map images are extracted (Fig. 26.58d).

9.5 Results of Ex Vivo Validation (Dataset 2)

In the dataset two, which was used for ex vivo validation, an SVM classifier was trained using 50 tissue color map images extracted through histology pictures as shown in Fig. 26.58d (i.e., manually painted image based on histology image by expert pathologist). Figure 26.59c shows the results of applying the Algorithm IV to four different gray-scale IVUS images. These results were validated with other tissue color map images which were not included in training dataset (Table 26.16).

9.6 Statistical Analysis of Ex Vivo Validation (Dataset 2)

Kappa value 0.454 for this ex vivo validation indicates the moderate agreement between Algorithm IV and histology images in Table 26.17 as gold standard. Furthermore kappa value 0.628 for comparing the result of Algorithm IV with histology images shown in Table 26.18 indicates the good agreement. Table 26.19 shows a comparison of in vivo and ex vivo validation methods in this chapter (Table 26.20).

10 Longitudinal Resolution Enhancement (LRE)

As mentioned before, one of the limitations of VH is its ECG-gated acquisition. Using the ECG-gated acquisition, in one cardiac cycle, the RF spectrum from only one IVUS frame with the synchronization of R-wave is acquired and analyzed. Therefore the distance between each VH images can be derived from the R–R interval (s) and the pullback speed of the IVUS catheter (mm/s) as follows [24]:

$$\text{Distance between two V H images (mm)} = \text{R–R interval} \times \text{pullback speed}$$

At the same time, gray-scale IVUS images are, normally, produced at a rate of 30 frames/s. Therefore, comparing to gray-scale IVUS, the longitudinal resolution for VH is highly reduced. Considering a heart rate of 60 beats/min and pullback speed of 1 mm/s, for example, RF analysis is performed for only 1 frame/mm (1 frame/s). However, using the proposed algorithms of Image Based Histology (IBH), the longitudinal resolution would increase up to 30 frames/mm (Fig. 26.60).

In order to envisage the longitudinal resolution enhancement, plaque characterization based on the proposed algorithms was implemented on IVUS frames between each two consequential VH images. Plaque component abundances, which contribute to each tissue type characterized by the proposed method, are displayed in three different charts in Figs. 26.61, 26.62, and 26.63. The points in each chart refer to the plaque component abundances in VH images. The ones of other IVUS frames between two sequential VH frames are computed using the proposed method and displayed by

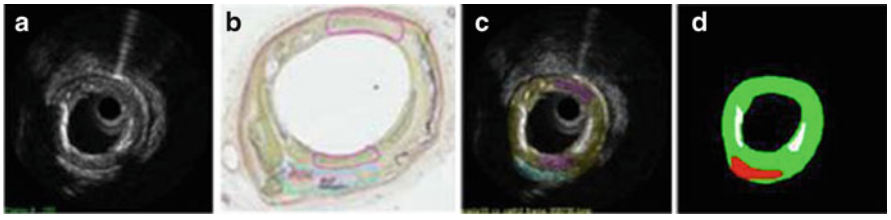

Fig. 26.58 (**a**) IVUS cross section, (**b**) Movat Histology image, (**c**) tissue color map imposed on the IVUS image, and (**d**) tissue color map: *White* is DC, *green* is fibro-lipid and *red* is NC [32]

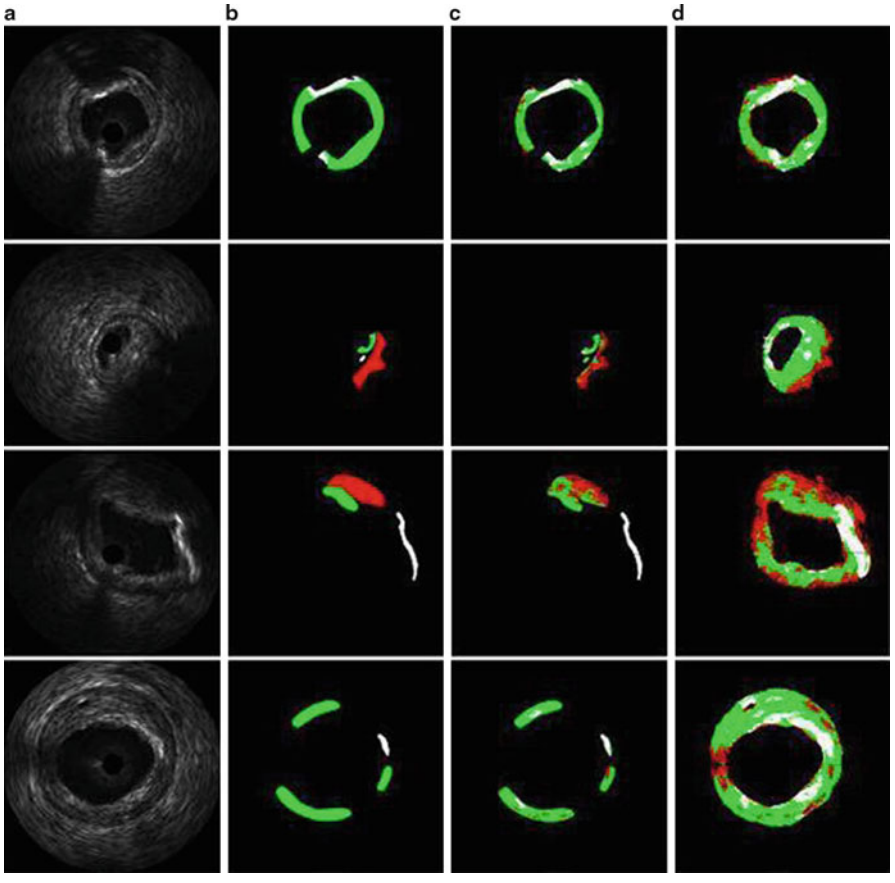

Fig. 26.59 (**a**) Gray-scale IVUS image, (**b**) manually painted image based on histology image with fibrotic + fibro-fatty (*green*), calcium (*white*), and necrotic (*red*) components, (**c**) characterized image using Algorithm IV after training by (**b**) on the manually detected plaque area, and (**d**) Characterized image using Algorithm IV after training by (**b**) on the whole plaque area detected by expert

Table 26.16 The result of ex vivo validation: Algorithm IV validated with histology pictures (dataset 1). The parameter ± confidence interval is shown for the sensitivity, specificity, and accuracy parameters

	Sensitivity		Specificity		Accuracy	
	Pixel-wise	Region-based	Pixel-wise	Region-based	Pixel-wise	Region-based
Dense calcium (DC)	59.3 ± 2.2	55.2% ± 13	97.5% ± 0.6	98% ± 3.4	96%	96%
Fibro-lipid (FF)	87.9% ± 0.31	90.8% ± 1.7	67.7% ± 0.45	68.3% ± 2.8	85.4%	86%
Necrotic core (NC)	55.1% ± 0.1	57.2% ± 6.4	87.6% ± 0.7	90.4% ± 3.8	79.9%	85%

Table 26.17 Truth table to show the degree of agreement between the Algorithm IV and histology images of dataset 2 for ex vivo validation (pixel-based)

VH plaque component	DC in proposed method	FF in proposed method	NC in proposed method	Total in VH
DC in VH	5,503	4,710	40	10,253
FF in VH	2,760	26,776	1,629	31,165
NC in VH	142	2,040	2,208	4,390
Total in proposed method	8,405	33,526	3,877	45,808

Table 26.18 Truth table to show the degree of agreement between the Algorithm IV and histology images of dataset 2 for ex vivo validation (region-based)

VH plaque component	DC in proposed method	FF in proposed method	NC in proposed method	Total in VH
DC in VH	136	85	0	221
FF in VH	23	844	26	893
NC in VH	1	39	61	101
Total in proposed method	160	968	87	1,215

Table 26.19 Summary of applied validation methods (in vivo and ex vivo)

Validation	Datasets	Pixel-based Accuracy	κ	Region-based Accuracy	κ
In vivo	120 IVUS images	>82%	0.639	–	–
Ex vivo	Data set #1	>79%	0.487	>85%	0.533
	Data set #2	>75%	0.454	>86%	0.628

Table 26.20 The result of ex vivo validation: Algorithm IV validated with histology pictures (dataset 2). The parameter ± confidence interval is shown for the sensitivity, specificity, and accuracy parameters

	Sensitivity Pixel-wise	Region-based	Specificity Pixel-wise	Region-based	Accuracy Pixel-wise	Region-based
Dense calcium (DC)	65.5% ± 1	85% ± 5.5	87.3% ± 0.7	92% ± 4.2	83.3%	91%
Fibro-lipid (FF)	79.9% ± 0.4	87% ± 2	64.3% ± 0.5	80% ± 2.5	75.7%	86%
Necrotic core (NC)	56.9% ± 1.6	70% ± 9.6	94.8% ± 0.7	96.54% ± 3.9	91.6%	95%

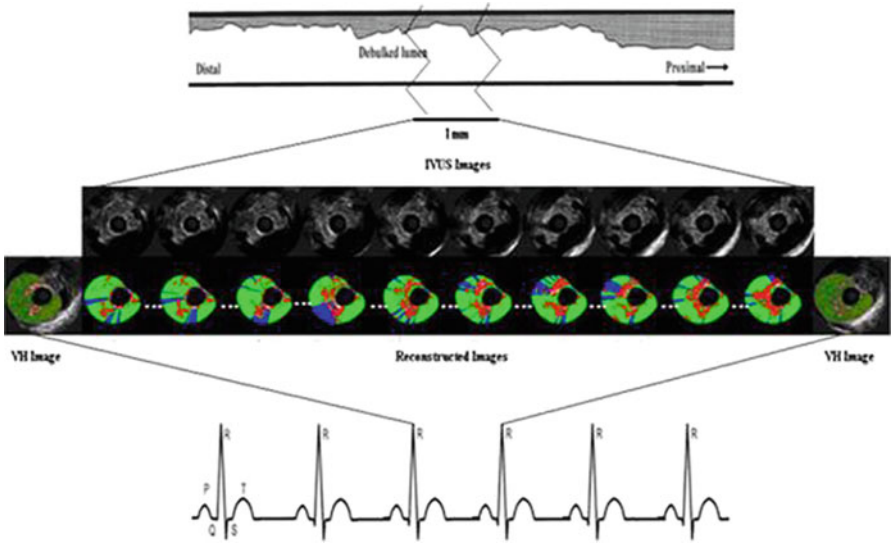

Fig. 26.60 Illustration of enhancement of the longitudinal resolution of atherosclerosis plaque composition characterization of gray scale IVUS using IVUS-IBH method compared to VH. Gray-scale IVUS images are, normally, produced at a rate of 30 frame/s. Considering a heart of 60 beats/min and pullback speed of 1 mm/s, for example, RF analysis is performed for only 1 frame/mm (or 1 frame/s). Therefore VH has a much lower longitudinal resolution than gray-scale IVUS

lines. The large changes in plaque component abundances between two VH-IVUS frames are reasonable, since they can be related to different sections of the vessel of about 1 mm distance. However, the rapid changes between two points on the line, which is described and highlighted using an IVUS and its corresponding characterized image, are because of existing different plaque components which were ignored by using VH. Moreover, one should note that these variations might be resulted from differences in the detected plaque area as well.

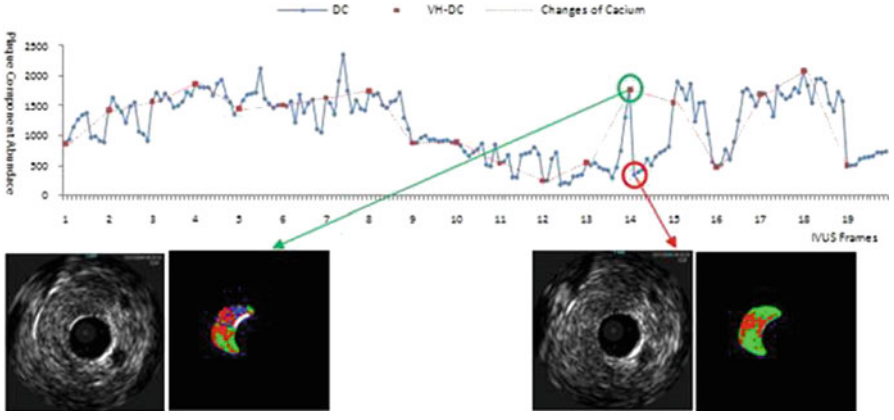

Fig. 26.61 Illustration of calcium plaque changes between VH slides

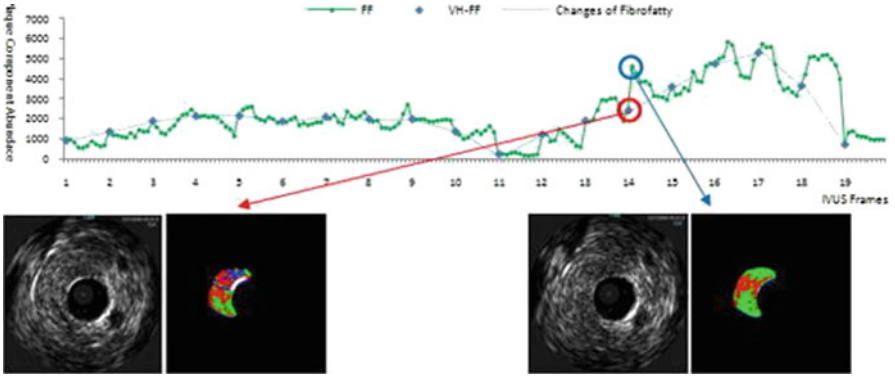

Fig. 26.62 Illustration of fibro-fatty plaque changes between VH slides

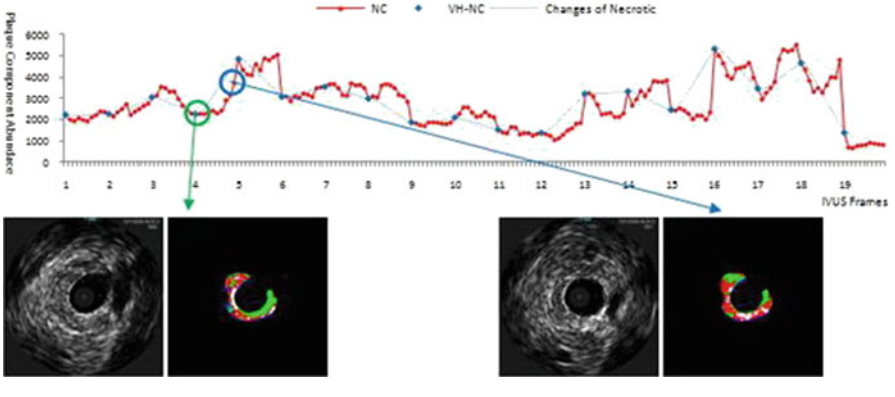

Fig. 26.63 Illustration of necrotic plaque change between VH slides

References

1. Theodoridis S, Koutroumbas K (2006) Pattern recognition, 5th edn. Elsevier
2. Ojala T, Pietikainen M, Maenpaa T (2002) Multiresolution gray-scale and rotation invariant texture classification with local binary patterns. IEEE Trans Pattern Anal Mach Intell 24(7):971–987
3. Sertel O, Kong J, Shimada H, Catalyurek U, Saltz J, Gurcan M (2008) Computeraided prognosis of neuroblastoma on whole-slide images: classification of stromal development. SPIE Medical Imaging
4. Gonzalo N, Garcia-Garcia HM, Ligthart J, Rodriguez-Granillo G, Meliga E, Onuma Y, Schuurbiers JCH, Bruining N, Serruys PW (2008) Coronary plaque composition as assessed by grayscale ultrasound and radiofrequency spectral data analysis. Int J Cardiovasc Imaging 24:811–818
5. Sorensen L, Shaker SB, de Bruijne M (2008) Texture classification in lung CT using local binary patterns. Med Image Comput Comput Assist Interv 11:934–941
6. Galloway MM (1975) Texture analysis using gray level run lengths. J Comput Graph Image Process 4:172–179
7. Welling M (2007) Fisher linear discriminant analysis. Class notes. Department of Computer Science, University of Toronto, Toronto, ON
8. Bishop CM (2006) Pattern recognition and matchine learning, 1st edn. Springer
9. Chang C, Lin C (2001) Libsvm: a library for support vector machines. http://www.csie.ntu.edu.tw/cjlin/libsvm
10. Fan RE, Chen PH, Lin CJ (2005) Working set selection using the second order information for training support vector machine. Mach Learn Res 6:1889–1918
11. Nair A, Margolis MP, Kuban BD, Vince DG (2007) Automated coronary plaque characterization with intravascular ultrasound backscatter: ex-vivo validation. EuroIntervention 3:113–120

12. Vince DG, Dixon KJ, Cothren RM, Cornhill JF (2000) Comparison of texture analysis methods for the characterization of coronary plaques in intravascular ultrasound images. Comput Med Imaging Graph 24:221–229
13. Kass M, Witkin A, Terzopoulos D (1987) Snakes: active contour models. Int J Comput Vis 1(4):321–331
14. Sales FJR, Falcao JLAA, Falcao BAA, Lemos PA, Furuie SS (2008) Evidences of possible necrotic-core artifact around dense calcium in virtual histology images. Comput Cardiol 35:545–548
15. Nason GP, Silverman BW (1995) The stationary wavelet transform and some statistical applications. Lect Notes Stat 35:281–300
16. Coifman RR, Wickerhauser MV (1992) Entropy based algorithm for best basis selection. IEEE Trans Inf Theory 38(2):713–718
17. Rodriguez-Granillo GA, McFadden EP, Valgimigli M, Van Mieghem CA, Regar E, De Feyter PJ, Serruys PW (2006) Coronary plaque composition of nonculprit lesions, assessed by in vivo intracoronary ultrasound radio frequency data analysis, is related to clinical presentation. Am Heart J 151(5):1020–1024
18. Mintz GS, Nissen SE, Anderson WD, Bailey SR, Erbel R, Fitzgerald PJ, Pinto FJ, Rosenfield K, Siegel RJ, Tuzcu EM, Yock PG (2001) Clinical expert consensus document on standards for acquisition, measurement and reporting of intravascular ultrasound studies (ivus). J Am Coll Cardiol 37:1479–1491
19. Bruining N, Verheye S, Knaapen M, Somers P, Roelandt JRTC, Regar E, Heller I, De Winter S, Ligthart J, Van Langenhove G, De Feijter PJ, Serruys PW, Hamers R (2007) Three-dimensional and quantitative analysis of atherosclerotic plaque composition by automated differential echogenicity. Catheter Cardiovasc Interv 70(7):968–978
20. König A, Margolis MP, Virmani R, Holmes D, Klauss V (2008) Technology insight: in vivo coronary plaque classification by intravascular ultrasonography radiofrequency analysis. Cardiovasc Med 5(4):219–229
21. Haralick R, Shanmugam K, Dinstein I (1973) Textural features of image classification. IEEE Trans Syst Man Cybern 6:610–621
22. Tang X (1998) Texture information in run length matrices. IEEE Trans Image Process 7(11):1602–1609
23. Gil D, Radeva P, Saludes J, Mauri J (2000) Segmentation of artery wall in coronary IVUS images: a probabilistic approach. Comput Cardiol: 687–690
24. Nasu K, Tsuchikane E, Katoh O, Vince DG, Virmani R, Surmely JF, Murata A, Takeda Y, Ito T, Ehara M, Matsubara T, Terashima M, Suzuki T (2006) Accuracy of in vivo coronary plaque morphology assessment: a validation study of in vivo virtual histology compared with in vitro histopathology. J Am Coll Cardiol 47(12):2405–2412
25. Virmani R, Burke AP, Farb A, Kolodgie FD (2006) Pathology of the vulnerable plaque. J Am Coll Cardiol 47(8):c13–c18
26. Sales FJR, Falcao JLAA, Falcao BAA, Furuie SS, Lemos PA (2009) Estimation of coronary atherosclerotic plaque composition based only on gray scale intravascular ultrasound images. Comput Cardiol
27. Escalera S, Pujol O, Mauri J, Radeva P (2009) Intravascular ultrasound tissue characterization with sub-class error-correcting output codes. J Signal Process Syst 55(1–3):35–47
28. Rieber J, Meissner O, Babaryka G, Reim S, Oswald M, Koenig A, Schiele TM, Shapiro M, Theisen K, Reiser MF, Klauss V, Hoffmann U
29. Katouzian A, Baseri B, Konofagou EE, Laine AF (2008) An alternative approach to spectrum-based atherosclerotic plaque characterization techniques using intravascular ultrasound (IVUS) backscattered signals. 2nd Workshop on computer vision for intravascular and intracardiac imaging, MICCAI
30. Katouzian A, Sathyanarayana S, Baseri B, Konofagou EE, Carlier G (2008) Challenges in atherosclerotic plaque characterization with intravascular ultrasound (ivus): from data collection to classification. IEEE Trans Inf Technol Biomed 12(3): 315–327
31. Topol EJ (2007) Textbook of cardiovascular medicine, 3rd edn. Lippincott Williams & Wilkins, Philadelphia, PA
32. Virmani R, Kolodgie FD, Burke AP, Farb A, Schwartz SM (2000) Lessons from sudden coronary death a comprehensive morphological classification scheme for atherosclerotic lesions. Arterioscler Thromb Vasc Biol 20:1262–1275

Visualization of Atherosclerotic Coronary Plaque by Using Optical Coherence Tomography

27

Plaque Characterization by OCT

Takashi Kubo and Takashi Akasaka

Abbreviations

ACS	Acute coronary syndrome
AMI	Acute myocardial infarction
IVUS	Intravascular ultrasound
OCT	Optical coherence tomography
TCFA	Thin cap fibroatheroma
UAP	Unstable angina pectoris
SAP	Stable angina pectoris

1 Introduction

Acute coronary syndrome (ACS) results from sudden luminal narrowing caused by thrombosis. There are multiple substrates for coronary thrombosis overlying an atherosclerotic plaque. Plaque rupture is the most frequent cause of coronary thrombosis (55–60%). Plaque rupture develops in the thin cap fibroatheroma (TCFA), which is characterized by the presence of a necrotic core and an overlying thin fibrous-cap (<65 μm) heavily infiltrated by activated macrophages. Erosion also leads to coronary thrombosis, accounting for 30–35% of all coronary thrombi. Eroded lesions are characterized by abundant surface smooth muscle cells and proteoglycans, and a small or absent lipid-rich core. Calcified nodule is the least common of all lesions that cause coronary thrombi (2–7%). These lesions typically contain calcified plates along with bony nodules that penetrate the lumen, which contains disrupted endothelium.

In vivo assessment of plaque characteristics is a key to getting a better understanding of vulnerable plaque. Several imaging techniques are currently in use for evaluation of coronary atherosclerosis. Recently, optical coherence tomography (OCT) has emerged as a technological breakthrough in the field of intracoronary imaging by providing high-resolution images with near histological detail. In vitro and in vivo studies have affirmed the excellent quality of OCT images making it an attractive technology for the analysis of atherosclerotic plaque and coronary microstructure. In this chapter, we will summarize the assessment of coronary atherosclerosis by using OCT.

2 OCT Technology

OCT is a novel, catheter-based, intravascular imaging modality using near-infrared light to create images [1]. The light wavelength ranges from 1,250 to 1,350 nm, which minimizes absorption of the light waves by water, protein, lipids, and hemoglobin. The light from the source is split in half, with part directed toward the arterial wall and part toward a mirror. The reflected signals are overlaid on a photodetector. The intensity of interference signal is detected and used to create images. The axial resolution in catheter-based OCT is 10–20 μm compared with 100–200 μm for IVUS, and the lateral resolution is typically 25–30 μm as compared with 200–300 μm for IVUS. However, the tissue penetration is limited to 1–3 mm as compared with 4–8 mm achieved by IVUS.

The OCT system consists of a catheter, imaging engine, and computer. The monorail 2.7-F OCT catheter is delivered over a conventional 0.014-in. coronary guidewire through a 6-F guide catheter. Because the infrared light is unable to penetrate red blood cells, OCT imaging is performed in a blood-free environment using a bolus injection of contrast (approximately 4 ml/s). The current frequency-domain OCT system acquires images at a rate of 100 frame/s. The OCT catheter is withdrawn using an automated pullback system at a speed of 20 mm/s. Thus, a 5-cm length of a coronary artery can be scanned in less than 3 s.

T. Kubo (✉) • T. Akasaka
Department of Cardiovascular Medicine, Wakayama Medical University, 811-1 Kimiidera, Wakayama, 641-8510, Japan
e-mail: takakubo@wakayama-md.ac.jp; akasat@wakayama-md.ac.jp

L. Saba et al. (eds.), *Multi-Modality Atherosclerosis Imaging and Diagnosis*,
DOI 10.1007/978-1-4614-7425-8_27,

3 Normal Coronary Artery

The coronary artery wall appears as a three-layer structure in OCT images (Fig. 27.1). Intima is depicted as a signal-rich layer nearest the lumen, media as a signal poor middle layer, and adventitia as a signal-rich outer layer of artery wall [2]. Intimal thickening is considered to be an early phase of atherosclerosis. The media becomes thinner as a result of positive vessel remodeling in the presence of atherosclerosis. Because of its much higher resolution compared with IVUS, OCT detects even the subtle atherosclerotic changes of the coronary artery wall.

4 Atherosclerotic Plaque

OCT has shown effectiveness in characterizing plaque composition. Fibrous plaques are characterized by homogeneous, signal-rich regions, fibrocalcific plaques by signal-poor regions with sharp borders, and lipid-rich plaques by signal-poor regions with diffuse borders (Fig. 27.2). With use of histopathologic diagnosis as the gold standard, these OCT criteria yielded a high sensitivity and specificity ranging from 71 to 79% and 97 to 98% for fibrous plaques, 95 to 96% and 97% for fibrocalcific plaques, and 90 to 94% and 90 to 92% for lipid-rich plaques, respectively [3]. Interobserver and intraobserver agreements for the plaque characterization with OCT were also high ($k = 0.88$ and 0.91, respectively) [3].

5 Vulnerable Plaque

Plaque Rupture: Plaque rupture is defined as a presence of fibrous-cap discontinuity and a cavity formation of the plaque in OCT (Fig. 27.3). The high resolution of OCT allows for a clear visualization of disrupted fibrous-cap and an accurate measurement of its thickness [4]. OCT revealed that the frequency of plaque rupture was 73% in patients with acute myocardial infarction (AMI) [5]. In patients with unstable angina (UAP), plaque rupture was often observed in Braunwald clinical class III (angina at rest within 48 h) compared with class I (new onset of severe angina or accelerated angina) and II (angina at rest within previous month but not within preceding 48 h) (71% vs. 43% vs. 13%, $p < 0.001$) [6].

OCT showed that the morphologies of plaque rupture differed between rest-onset and exertion-triggered rupture in patients with AMI. The thickness of disrupted fibrous-cap was significantly higher in exertion-triggered rupture compared with rest-onset rupture (exertion: 90 μm [interquartile median 65 μm]; rest onset: 50 μm [interquartile median 15 μm], $p < 0.01$) [7]. OCT suggests that some plaque rupture could occur in thick fibrous-caps >65 μm thick.

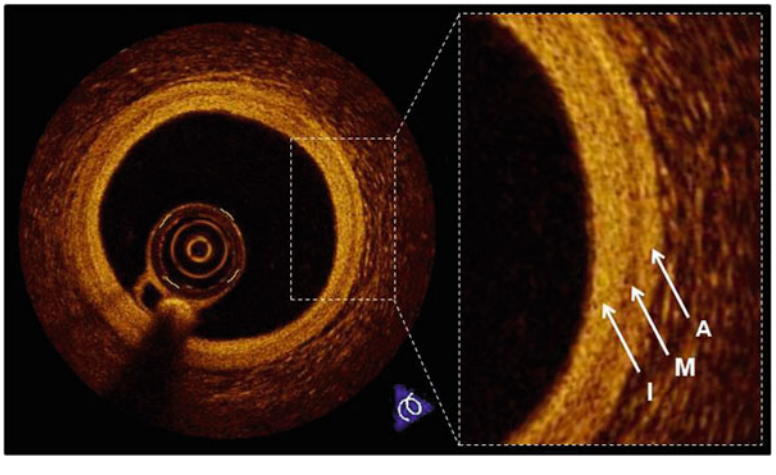

Fig. 27.1 Normal coronary artery. OCT demonstrates good contrast of the three layers of normal vessel. The media (M) is seen as a *dark band* delimited by the intima (I) and adventitia (A)

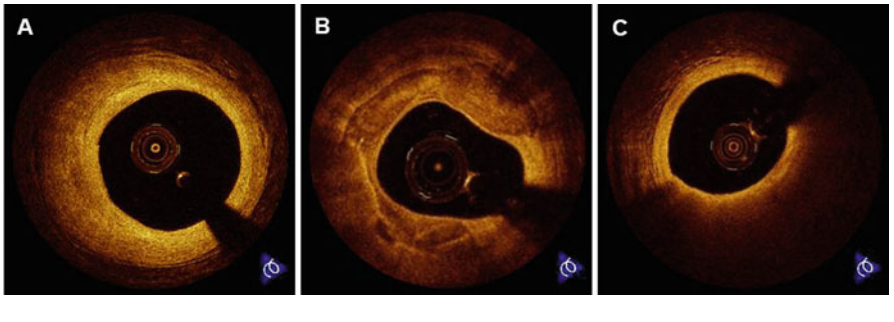

Fig. 27.2 Coronary atherosclerotic plaques. (**a**) OCT images of fibrous plaque show a homogeneous, signal-rich region. (**b**) OCT images of fibrocalcific plaque show a signal-poor region with sharply delineated borders. (**c**) OCT images of lipid-rich plaque show a signal-poor region with poorly delineated borders beneath a thin homogeneous band

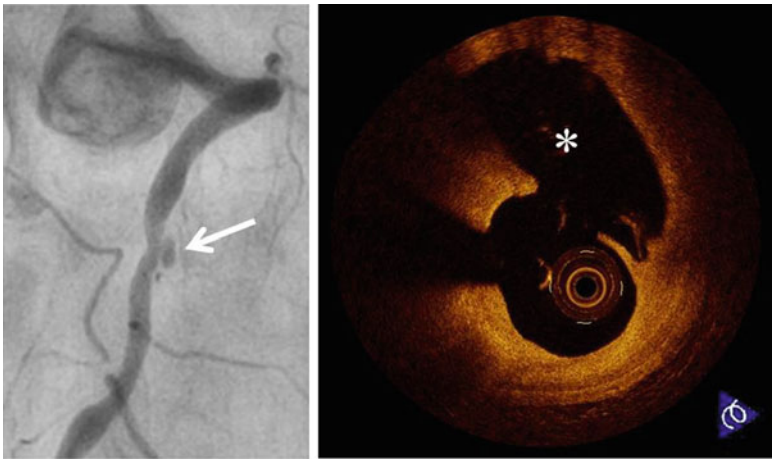

Fig. 27.3 Plaque rupture in patient with acute myocardial infarction. Coronary angiogram shows an ulcerated lesion in the mid right coronary artery (*arrow*). OCT demonstrates plaque rupture with a disrupted fibrous-cap and core cavity (*asterisk*) at the lesion site

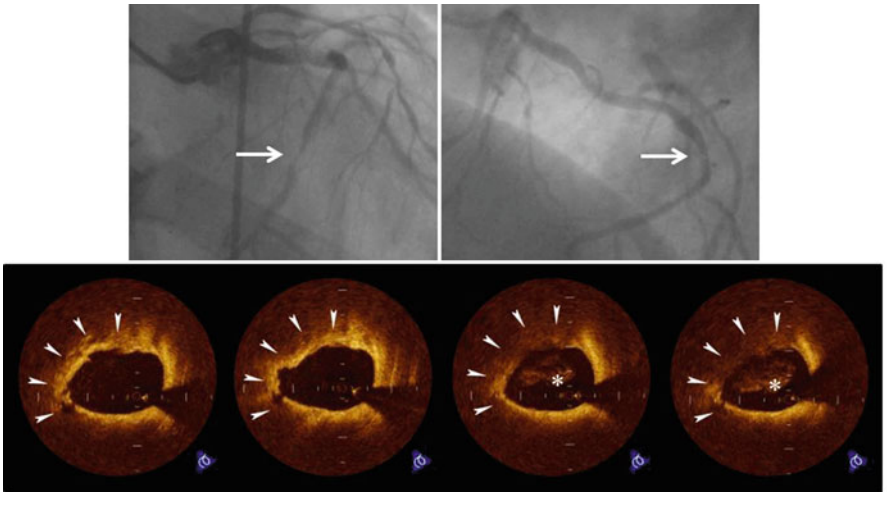

Fig. 27.4 Plaque erosion in patient with unstable angina pectoris. Coronary angiogram shows a subtotal lesion in the mid left circumflex coronary artery (*arrow*). OCT demonstrates plaque erosion with an irregular lumen surface (*arrowheads*) and intracoronary thrombus (*asterisks*) at the lesion site

OCT proposed two risk factors linking ruptured plaques to ACS: greater degree of plaque rupture and smaller lumen. Ruptured cavity area was significantly larger in AMI compared with UAP ($2.52 \pm 1.36\ mm^2$ vs. $1.67 \pm 1.37\ mm^2$, $p = 0.034$) [8]. Lumen area at rupture site was significantly smaller in symptomatic plaque rupture in UAP compared with asymptomatic plaque rupture in stable angina pectoris (SAP) ($3.00 \pm 0.86\ mm^2$ vs. $3.45 \pm 1.18\ mm^2$, $p = 0.030$) [9]. The greater degree of plaque rupture provokes more increased thrombus formation, and the smaller lumen requires less thrombus to precipitate an acute coronary event.

Three-vessel OCT imaging showed multifocal plaque destabilization during ACS [10–12]. Plaque rupture was often detected not only in culprit lesions but also in nonculprit lesions. Although one single lesion is clinically active at the time of ACS, the syndrome is associated with overall coronary instability.

Erosion: Plaque erosion is defined as a presence of an irregular luminal surface and no evidence of cap rupture evaluated in multiple adjacent frames (Fig. 27.4). Erosion is usually comprised of OCT evidence of thrombus [13]. Conventional imaging techniques are not sensitive enough to detect plaque erosions. OCT revealed that the frequency of plaque erosion was 23% in patients with AMI [5], and this data was comparable with previous autopsy results. Erosion may be less potently thrombogenic and lead smaller infarctions in comparison with plaque rupture.

Calcified Nodule: Calcified nodule is defined as a protrusion of a signal-poor and heterogeneous region with OCT signal attenuation (Fig. 27.5). Because light penetrates calcium in contrast with ultrasound, OCT allows precise, in vivo assessment of calcified nodules [14]. The origin of this lesion remains unclear, but it appears to be associated with healed thrombus or, potentially, with intraplaque hemorrhage.

Thrombus: Intracoronary thrombus was defined as a mass protruding into the vessel lumen from the surface of the vessel wall (Fig. 27.6). OCT can determine the presence, location, and size of a thrombus and even discriminate between white and red thrombus [15]. Red thrombus, predominantly consisting of red blood cells, appears in OCT as high backscattering structures with signal-free shadowing

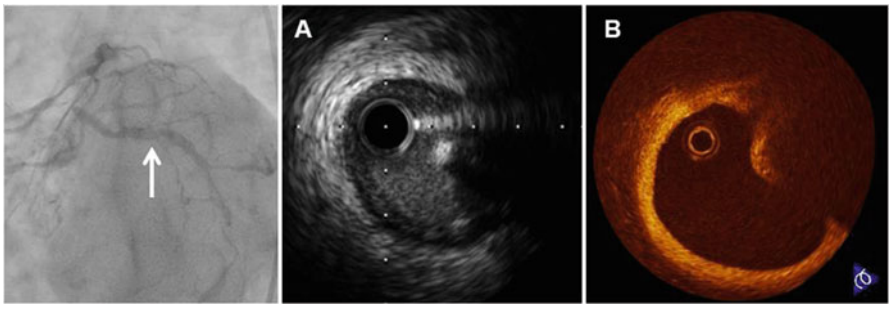

Fig. 27.5 Calcified nodule in patient with accelerated angina. Coronary angiogram shows intraluminal haziness in the proximal left circumflex coronary artery (*arrow*). (**a**) IVUS demonstrates a convex lumen surface with bright echo that obstruct the penetration of ultrasound. (**b**) OCT discloses a protrusion of a heterogeneous region with signal attenuation

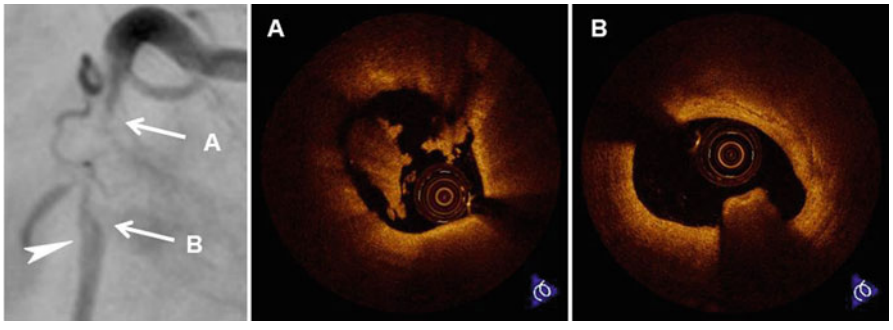

Fig. 27.6 Intracoronary thrombi in patient with acute myocardial infarction. Coronary angiogram shows a subtotal lesion with luminal filling defect (*arrowhead*) in the proximal right coronary artery. (**a**) OCT demonstrates white thrombi, predominantly consisting of platelets and white blood cells, which appears as low backscattering structures at the proximal site of the culprit lesion. (**b**) OCT discloses red thrombus, predominantly consisting of red blood cells, which appears as a high backscattering structure with signal-free shadowing at the distal site of the culprit lesion

while white thrombus, predominantly consisting of platelets and white blood cells, appears as a low backscattering structure [16]. In practice, pure white or red thrombi are rarely found; mixed thrombi, on the other hand, are common.

A coronary thrombus is observed by OCT even in patients with SAP. This may help to explain the benefit of antiplatelet therapy for the prevention of acute coronary events in the SAP patient population.

TCFA: OCT-derived TCFA is defined as a plaque with lipid and fibrous-cap of <65 μm thick (Fig. 27.7). OCT is the only modality with the resolution required for direct quantitative measurement of the fibrous-cap thickness [17]. The fibrous-cap thickness is defined as the minimum distance from the coronary artery lumen to inner border of lipid, which is characterized by signal-poor region in OCT image. An excellent correlation was found in the measurements of the fibrous-cap thickness between OCT and histological examination ($r = 0.90$, $p < 0.001$) [18].

OCT-derived TCFA has been investigated with other imaging techniques to confirm its instability. Recent IVUS studies have demonstrated that hypoechoic plaque with deep ultrasound attenuation is common in ACS. Such "attenuated plaque" is thought to be an IVUS characteristic of unstable lesion. OCT-derived TCFA was more often seen in IVUS-derived attenuated plaques compared with non-attenuated plaques (48% vs. 16%, $p < 0.001$) [19].

Spectral analysis of the radiofrequency (RF) ultrasound backscatter signals, known as Virtual Histology (VH), offers an in vivo opportunity to identify the four different types of atherosclerotic plaques (e.g., fibrous, fibro-fatty, dense calcium, and necrotic core). A natural history study of atherosclerosis using VH-IVUS showed that VH-derived TCFA, which is characterized by absence of visible fibrous-cap overlying a necrotic core, has a high risk for future adverse cardiovascular events. OCT-derived TCFA is associated with this vulnerable feature of VH-IVUS (diagnostic concordance rate = 86%) [20].

Angioscopy allows direct visualization of the internal surface of a coronary vessel wall. Several angioscopic studies revealed that yellow plaque was common in the culprit lesion of ACS. Therefore, angioscopy-identified yellow plaque has been considered vulnerable. OCT showed significant negative correlation between yellow color intensity and

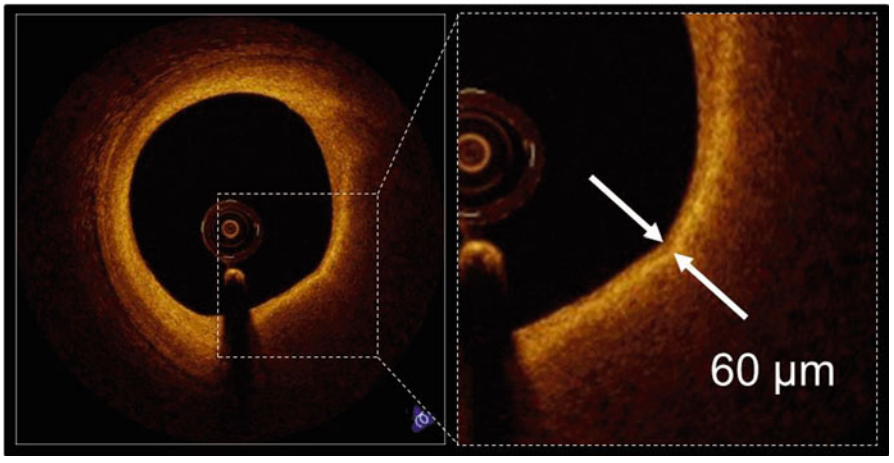

Fig. 27.7 Thin-cap fibroatheroma (TCFA). A fibrous-cap (*arrows*) is identified as a signal-rich homogenous region overlying a lipid core, which is characterized by a signal-poor region in OCT image. OCT-derived TCFA is defined as a plaque with a fibrous-cap measuring <65 μm

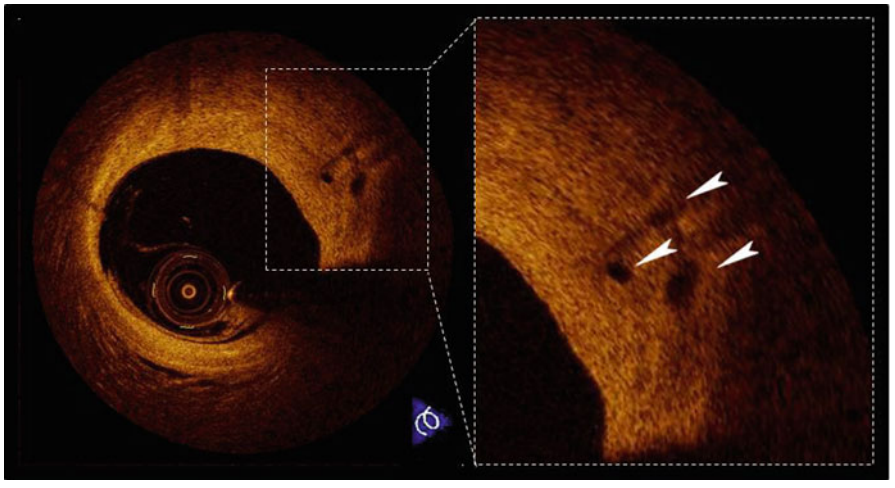

Fig. 27.8 Intraplaque neovascularization. Microvessels within the plaque (*arrowheads*) appear as signal poor voids that are sharply delineated

fibrous-cap thickness ($p < 0.001$) [21]. Furthermore, 80% of intensive yellow plaques were OCT-derived TCFA.

Recent advances in multi-detector computed tomography (CT) technology have allowed for a noninvasive assessment of coronary atherosclerotic plaques. A prospective CT study showed that the low-density plaque with positive vessel remodeling was an independent predictor of subsequent ACS. These CT characteristics were observed more frequently in OCT-derived TCFA compared with non-TCFA (76% vs. 31%, $p < 0.001$) [22].

OCT has been used to evaluate prevalence of TCFA in vivo. OCT-derived TCFA was more frequently observed in patients with AMI or ACS than SAP (72% vs. 50% vs. 20%, $p = 0.012$) [23]. In accordance with a previous pathological study [24], OCT-derived TCFA was detected not only in culprit lesions but also in non-culprit segments [10–12]. The distribution of OCT-derived TCFA in the right coronary artery was relatively even (proximal vs. mid vs. distal: 12% vs. 29% vs. 18%, $p = 0.420$), whereas TCFA in the left coronary artery was common in proximal sites (proximal vs. mid vs. distal: 27% vs. 9% vs. 0%, $p = 0.018$) [25]. Moreover, OCT-derived TCFA is associated with serum high sensitive C-reactive protein level [26]. These OCT data provide further evidence of the multifocal nature of inflammation in coronary atherosclerosis and support the hypothesis that the inflammation is manifested by thinning of the fibrous-caps of both culprit and non-culprit lesions.

Neovascularization: Increased microvessels in atherosclerotic plaques are associated with plaque vulnerability. Microvessels could contribute to intraplaque hemorrhage, resulting in expansion of the plaque. The high resolution of OCT offers an opportunity to directly visualize microvessels in the atherosclerotic plaque in vivo. The microvessel in the plaque is defined as a no-signal tubuloluminal structure without a connection to coronary artery lumen in OCT (Fig. 27.8). OCT showed that the microvessel density was increased in TCFAs (54% vs. 21%, $p = 0.012$) and lesions with positive remodeling (67% vs. 36%, $p = 0.020$) [27]. In addition, serum high sensitive C-reactive protein levels were significantly different according to the presence or absence of microvessels (median 0.27 mg/dl vs. 0.13 mg/dl,

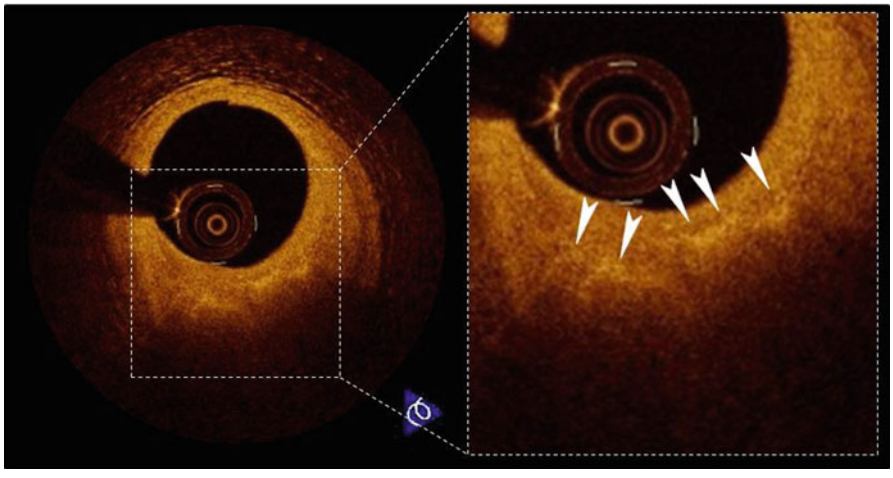

Fig. 27.9 Macrophages. Macrophages (*arrowheads*) are seen as signal-rich, distinct, or confluent punctuate regions that exceed the intensity of background speckle noise in OCT image

$p = 0.015$) [27]. Assessment of plaque neovascularization by using OCT might be useful for identifying lesions more prone to destabilization and rupture.

Macrophage: The high resolution of OCT has a potential to identify inflammatory cells such as clusters of macrophages/foam cells. Streaks of macrophages/foam cells are seen as signal-rich bands with signal-free shadowing in OCT images (Fig. 27.9). An autopsy study demonstrated a high degree of positive correlation between OCT and histological measurements of fibrous-cap macrophage density ($r < 0.84$, $p < 0.001$) [28]. A range of OCT signal standard deviation thresholds (6.15–6.35%) yielded 100% sensitivity and specificity for identifying caps containing >10% CD68 staining [28]. A clinical OCT study disclosed a significant relationship between the clinical presentation and the macrophage concentration in the coronary atherosclerotic plaques. Macrophage density was found to be significantly higher in culprit site of AMI ($5.54 \pm 1.48\%$) and ACS ($5.86 \pm 2.01\%$) compared with SAP ($4.14 \pm 1.81\%$) ($p = 0.003$) [29]. Sites of plaque rupture showed a greater macrophage density than non-ruptured sites ($6.95 \pm 1.60\%$, $5.29 \pm 1.17\%$, $p = 0.002$) [29]. In addition, surface macrophage infiltration was a stronger predictor of unstable clinical presentation than subsurface infiltration ($p = 0.035$) [29]. The possibility of seeing macrophages in OCT could open opportunities for studying the role of these inflammatory cells in coronary atherosclerosis.

6 Limitations

Because of its limited tissue penetration (1–1.5 mm), OCT does not appear to be suited to study vessel remodeling, which is well addressed by IVUS. Previous IVUS studies have shown that positive remodeling is often observed in the culprit lesion of ACS. OCT was used to assess the plaque characteristics in the lesion with positive remodeling that was determined by IVUS. Positive remodeling compared with absent or negative remodeling was more commonly associated with lipid-rich plaque (100 vs. 60 vs. 47.4%, $p = 0.01$), a thin fibrous-cap (median 40.2 vs. 51.6 vs. 87 μm, $p = 0.003$) and the presence of TCFA (80 vs. 38.5 vs. 5.6%, $p < 0.001$) [30]. Fibrous-cap macrophage density was also higher in plaques with positive remodeling showing a positive linear correlation with the remodeling index ($r = 0.60$, $p < 0.001$) [30]. These OCT results might explain the link between positive remodeling and unstable clinical presentations.

Thrombus may affect assessment of the atherosclerotic plaque. Because red blood cells cause severe signal attenuation, OCT cannot visualize coronary plaques behind the thrombus. In the OCT assessment of vulnerable lesions, thrombus may preclude identification of plaque rupture or erosion [31]. Furthermore, non-protruding red thrombi can be misinterpreted for necrotic lipid cores. This may occur due to the similar OCT signal pattern of the two tissue components.

Quantitative measurement of lipid core size is limited in OCT. Because the OCT signal is absorbed by the lipidic tissue, the boundary is not clearly visualized behind the lipid core. Therefore, lipid is semiquantified as the number of involved quadrants on the cross-sectional OCT image. When lipid is present in ≥2 quadrants in any of the images within a plaque, it was considered a lipid-rich plaque [23].

7 Future Developments in OCT Technology

OCT has a capability of identifying plaque components (Table 27.1). However, interpretation of the OCT image in terms of tissue type is still a complex and often ambiguous task for trained readers. To overcome this limitation, automated methods for plaque characterization are currently under development [32]. The application of a

Table 27.1 Criteria for plaque characterization in OCT

Histology	OCT findings
Intima	Signal-rich layer near lumen
Media	Signal-poor layer in middle of artery wall
Adventitia	Signal-rich outer layer of artery wall
Fibrous	Signal-rich, homogeneous region
Calcification	Signal-poor, well-delineated region
Lipid	Signal-poor, poorly delineated region
Fibrous-cap	Signal-rich layer overlying signal-poor region
Red thrombus	High-backscattering protrusion with signal-free shadowing
White thrombus	Low-backscattering protrusion
Microvessel	Signal-poor, well-delineated void within plaque
Macrophages	Signal-rich, distinct, or confluent punctuate regions with shadowing

post-processing color-coding software-based algorithm on analysis of either spectral OCT backscattered data or other optical tissue properties should improve the characterization of atherosclerotic coronary plaques and provide a more objective assessment.

High frame rate and fast pullback speed of OCT may facilitate the acquisition of three-dimensional data from longitudinal image sequences. The combination of automatic tissue characterization and three-dimensional reconstructions is further promising areas of research in OCT [33]. The localization analysis of elements related to plaque vulnerability such as necrotic core, thin fibrous-cap, or inflammatory cells could be improved by multidimensional assessment. These future technologies would develop our understanding of vessel and plaque pathology.

8 Conclusions

OCT enables real-time, full tomographic, in-situ visualization of coronary vessel microstructure with a unique high resolution. In vitro and in vivo studies have demonstrated the feasibility of OCT to visualize vulnerable plaques. At present, OCT is the only imaging technology with a resolution high enough for detection of TCFA. Furthermore, this technology would permit longitudinal trails to study the dynamic nature of coronary atherosclerosis. OCT could provide a greater understanding of the pathophysiology of coronary artery disease.

References

1. Takarada S, Imanishi T, Liu Y, Ikejima H, Tsujioka H, Kuroi A, Ishibashi K, Komukai K, Tanimoto T, Ino Y, Kitabata H, Kubo T, Nakamura N, Hirata K, Tanaka A, Mizukoshi M, Akasaka T (2010) Advantage of next-generation frequency-domain optical coherence tomography compared with conventional time-domain system in the assessment of coronary lesion. Catheter Cardiovasc Interv 75:202–206
2. Kume T, Akasaka T, Kawamoto T, Watanabe N, Toyota E, Neishi Y, Sukmawan R, Sadahira Y, Yoshida K (2005) Assessment of coronary intima-media thickness by optical coherence tomography: comparison with intravascular ultrasound. Circ J 69:903–907
3. Yabushita H, Bouma BE, Houser SL, Aretz HT, Jang IK, Schlendorf KH, Kauffman CR, Shishkov M, Kang DH, Halpern EF, Tearney GJ (2002) Characterization of human atherosclerosis by optical coherence tomography. Circulation 106:1640–1645
4. Akasaka T, Kubo T, Mizukoshi M, Tanaka A, Kitabata H, Tanimoto T, Imanishi T (2010) Pathophysiology of acute coronary syndrome assessed by optical coherence tomography. J Cardiol 56:8–14
5. Kubo T, Imanishi T, Takarada S, Kuroi A, Ueno S, Yamano T, Tanimoto T, Matsuo Y, Masho T, Kitabata H, Tsuda K, Tomobuchi Y, Akasaka T (2007) Assessment of culprit lesion morphology in acute myocardial infarction: ability of optical coherence tomography compared with intravascular ultrasound and coronary angioscopy. J Am Coll Cardiol 50:933–939
6. Mizukoshi M, Imanishi T, Tanaka A, Kubo T, Liu Y, Takarada S, Kitabata H, Tanimoto T, Komukai K, Ishibashi K, Akasaka T (2010) Clinical classification and plaque morphology determined by optical coherence tomography in unstable angina pectoris. Am J Cardiol 106:323–328
7. Tanaka A, Imanishi T, Kitabata H, Kubo T, Takarada S, Tanimoto T, Kuroi A, Tsujioka H, Ikejima H, Ueno S, Kataiwa H, Okouchi K, Kashiwaghi M, Matsumoto H, Takemoto K, Nakamura N, Hirata K, Mizukoshi M, Akasaka T (2008) Morphology of exertion-triggered plaque rupture in patients with acute coronary syndrome: an optical coherence tomography study. Circulation 118:2368–2373
8. Ino Y, Kubo T, Tanaka A, Kuroi A, Tsujioka H, Ikejima H, Okouchi K, Kashiwagi M, Takarada S, Kitabata H, Tanimoto T, Komukai K, Ishibashi K, Kimura K, Hirata K, Mizukoshi M, Imanishi T, Akasaka T (2011) Difference of culprit lesion morphologies between ST elevation myocardial infarction and non ST elevation acute coronary syndrome: an optical coherence tomography study. JACC Cardiovasc Interv 4:76–82
9. Kubo T, Tanaka A, Kitabata H, Matsuo Y, Tanimoto T, Ishibashi K, Orii M, Shiono Y, Shimamura K, Ozaki Y, Ino Y, Imanishi T, Akasaka T (2011) Optical coherence tomography analysis of clinical and subclinical plaque rupture. J Clin Exp Cardiol S1-002:1–5. doi:10.4172/2155-9880.S1-002, available at: http://www.omicsonline.org/2155-9880/2155-9880-S1-002.pdf. ISSN:2155-9880
10. Kubo T, Imanishi T, Kashiwagi M, Ikejima H, Tsujioka H, Kuroi A, Ishibashi K, Komukai K, Tanimoto T, Ino Y, Kitabata H, Takarada S, Tanaka A, Mizukoshi M, Akasaka T (2010) Multiple coronary lesion instability in patients with acute myocardial infarction as determined by optical coherence tomography. Am J Cardiol 105:318–322
11. Tanimoto T, Imanishi T, Tanaka A, Yamano T, Kitabata H, Takarada S, Kubo T, Nakamura N, Hirata K, Mizukoshi M, Akasaka T (2009) Various types of plaque disruption in a culprit coronary artery visualized by optical coherence tomography in a patient with unstable angina. Circ J 73:187–189
12. Kitabata H, Kubo T, Akasaka T (2008) Identification of multiple plaque ruptures by optical coherence tomography in a patient with acute myocardial infarction: a three-vessel study. Heart 94:544
13. Kubo T, Ino Y, Tanimoto T, Kitabata H, Tanaka A, Akasaka T (2011) Optical coherence tomography imaging in acute coronary syndromes. Cardiol Res Pract 2011:312978. doi:10.4061/2011/312978, available at: http://www.hindawi.com/journals/crp/2011/312978/

14. Kubo T, Akasaka T (2011) Identification of vulnerable plaques with optical coherence. In: Pesek K (ed) Atherosclerotic cardiovascular disease. InTech – Open Access, Rijeka, Croatia, pp 71–88, available at: http://www.intechopen.com/articles/show/title/identification-of-vulnerable-plaques-with-optical-coherence-tomography. ISBN 978-953-307-695-9
15. Kubo T, Akasaka T (2009) OCT-ready for prime time?: Clinical applications of optical coherence tomography. Card Interv Today 4:35–37
16. Kume T, Akasaka T, Kawamoto T, Ogasawara Y, Watanabe N, Toyota E, Neishi Y, Sukmawan R, Sadahira Y, Yoshida K (2006) Assessment of coronary arterial thrombus by optical coherence tomography. Am J Cardiol 97:1713–1717
17. Kubo T, Akasaka T (2008) Recent advances in intracoronary imaging techniques: focus on optical coherence tomography. Expert Rev Med Devices 5:691–697
18. Kume T, Akasaka T, Kawamoto T, Okura H, Watanabe N, Toyota E, Neishi Y, Sukmawan R, Sadahira Y, Yoshida K (2006) Measurement of the thickness of the fibrous cap by optical coherence tomography. Am Heart J 152:e1–e4
19. Kubo T, Matsuo Y, Ino Y, Tanimoto T, Ishibashi K, Komukai K, Kitabata H, Tanaka A, Kimura K, Imanishi T, Akasaka T (2011) Optical coherence tomography analysis of attenuated plaques detected by intravascular ultrasound in patients with acute coronary syndromes. Cardiol Res Pract 2011:687515. doi:10.4061/2011/687515, available at: http://www.hindawi.com/journals/crp/2011/687515/
20. Kubo T, Nakamura N, Matsuo Y, Okumoto Y, Wu X, Choi SY, Komukai K, Tanimoto T, Ino Y, Kitabata H, Kimura K, Mizukoshi M, Imanishi T, Akagi H, Yamamoto T, Akasaka T (2011) Virtual histology intravascular ultrasound compared with optical coherence tomography for identification of thin-cap fibroatheroma. Int Heart J 52:175–179
21. Kubo T, Imanishi T, Takarada S, Kuroi A, Ueno S, Yamano T, Tanimoto T, Matsuo Y, Masho T, Kitabata H, Tanaka A, Nakamura N, Mizukoshi M, Tomobuchi Y, Akasaka T (2008) Implication of plaque color classification for assessing plaque vulnerability: a coronary angioscopy and optical coherence tomography investigation. JACC Cardiovasc Interv 1:74–80
22. Kashiwagi M, Tanaka A, Kitabata H, Tsujioka H, Kataiwa H, Komukai K, Tanimoto T, Takemoto K, Takarada S, Kubo T, Hirata K, Nakamura N, Mizukoshi M, Imanishi T, Akasaka T (2009) Feasibility of noninvasive assessment of thin-cap fibroatheroma by multidetector computed tomography. JACC Cardiovasc Imaging 2:1412–1419
23. Jang IK, Tearney GJ, MacNeill B, Takano M, Moselewski F, Iftima N, Shishkov M, Houser S, Aretz HT, Halpern EF, Bouma BE (2005) In vivo characterization of coronary atherosclerotic plaque by use of optical coherence tomography. Circulation 111: 1551–1555
24. Kolodgie FD, Burke AP, Farb A et al (2001) The thin-cap fibroatheroma: a type of vulnerable plaque: the major precursor lesion to acute coronary syndromes. Curr Opin Cardiol 16: 285–292
25. Tanaka A, Imanishi T, Kitabata H, Kubo T, Takarada S, Kataiwa H, Kuroi A, Tsujioka H, Tanimoto T, Nakamura N, Mizukoshi M, Hirata K, Akasaka T (2008) Distribution and frequency of thin-capped fibroatheromas and ruptured plaques in the entire culprit coronary artery in patients with acute coronary syndrome as determined by optical coherence tomography. Am J Cardiol 102:975–979
26. Kashiwagi M, Tanaka A, Kitabata H, Tsujioka H, Matsumoto H, Arita Y, Ookochi K, Kuroi A, Kataiwa H, Tanimoto T, Ikejima H, Takarada S, Kubo T, Hirata K, Nakamura N, Mizukoshi M, Imanishi T, Akasaka T (2009) Relationship between coronary arterial remodeling, fibrous cap thickness and high-sensitivity C-reactive protein levels in patients with acute coronary syndrome. Circ J 73:1291–1295
27. Kitabata H, Tanaka A, Kubo T, Takarada S, Kashiwagi M, Tsujioka H, Ikejima H, Kuroi A, Kataiwa H, Ishibashi K, Komukai K, Tanimoto T, Ino Y, Hirata K, Nakamura N, Mizukoshi M, Imanishi T, Akasaka T (2010) Relation of microchannel structure identified by optical coherence tomography to plaque vulnerability in patients with coronary artery disease. Am J Cardiol 105:1673–1678
28. Tearney GJ, Yabushita H, Houser SL, Aretz HT, Jang IK, Schlendorf KH, Kauffman CR, Shishkov M, Halpern EF, Bouma BE (2003) Quantification of macrophage content in atherosclerotic plaques by optical coherence tomography. Circulation 107:113–119
29. MacNeill BD, Jang IK, Bouma BE, Iftimia N, Takano M, Yabushita H, Shishkov M, Kauffman CR, Houser SL, Aretz HT, DeJoseph D, Halpern EF, Tearney GJ (2004) Focal and multi-focal plaque macrophage distributions in patients with acute and stable presentations of coronary artery disease. J Am Coll Cardiol 44: 972–979
30. Raffel OC, Merchant F, Tearney GJ et al (2008) In vivo association between positive coronary artery remodelling and coronary plaque characteristics assessed by intravascular optical coherence tomography. Eur Heart J 29:1721–1728
31. Kubo T, Xu C, Wang Z, van Ditzhuijzen NS, Bezerra HG (2011) Plaque and thrombus evaluation by optical coherence tomography. Int J Cardiovasc Imaging 27:289–298
32. Kubo T, Akasaka T (2010) Optical coherence tomography imaging: current status and future perspectives. Cardiovasc Interv Ther 25:2–10
33. Tearney GJ, Waxman S, Shishkov M, Vakoc BJ, Suter MJ, Freilich MI, Desjardins AE, Oh WY, Bartlett LA, Rosenberg M, Bouma BE (2008) Three-dimensional coronary artery microscopy by intracoronary optical frequency domain imaging. JACC Cardiovasc Imaging 1:752–761

Image Fusion Technology

28

Gerd Brunner, Eric Y. Yang, Joel D. Morrisett, Zsolt Garami, and Vijay Nambi

1 Introduction

Medical imaging is of vital importance in modern medicine and of special interest in diagnostic medicine. Current medical imaging consists of a wide range of instrumentation including but not limited to computed tomography (CT), magnetic resonance imaging (MRI), ultrasonography (US), fluoroscopy, plain film radiography, positron emission tomography (PET), and single-photon emission computed tomography (SPECT). Each of these imaging modalities has certain advantages and limitations.

Clear advantages of one imaging system can be a limitation of another. Hence fusion of these imaging technologies may provide an approach for maximizing imaging information, as illustrated in Fig. 28.1.

We will first consider briefly advantages and limitations of common medical imaging technologies. Since the 1970s, CT usage has increased rapidly, and it is estimated that today more than 72 million scans are performed annually in the USA alone [1]. Although CT imaging is user-friendly and allows rapid image acquisition, concerns have been voiced recently regarding repetitive usage and radiation exposure resulting in a possible increase of life-time cancer risk [2]. Additionally, contrast agents that are required for some studies can lead to renal impairment and hence renal function should always be considered in image modality selection.

MR imaging provides excellent soft-tissue contrast and is free of ionizing radiation. MRI utilization is rapidly growing and today approximately 30 million annual scans are performed in the USA [3]. However, availability of MRI systems is limited and imaging costs are high compared to those of CT. The major contraindications to MRI are metallic implants in the body such as aneurysm clips, cochlear devices, spinal nerve stimulators, pacemaker, implantable cardioverter-defibrillator (ICD), and deep brain stimulators. Patients are frequently imaged using Gadolinium-based contrast agents. Gadolinium chelates are extravascular MRI contrast agents that are cleared by the renal system. Individuals with severe renal impairment may therefore experience adverse effects with the use of these contrast agents, and hence clinically, patients are screened for their kidney function by estimating the glomerular filtration rate (GFR).

PET is a functional imaging modality involving a radionuclide such as fluorodeoxyglucose (18F-FDG) which is intravenously injected after which the location of the tracer throughout the body can be determined for diagnostic purposes [4]. PET imaging has been very successful, especially in oncology [5]. One of the concerns regarding PET/CT imaging studies is the level of radiation exposure that can be in the order of ten to above 30 mSv per scan, depending on imaging protocols [6]. Moreover, at present the availability of PET imaging is limited and scanning costs are high. One of the major technical limitations of PET imaging is poor resolution when compared with other imaging modalities. The fusion of PET/CT systems alleviated the limitation of image resolution in part and also increased availability to approximately 2,000 installed systems in 2010 [7].

Ultrasound imaging is among the safest of imaging modalities with several advantages including portability and excellent temporal resolution. Moreover, US is a widely available versatile medical imaging technology. US has no known long-term side effects, and the modality can be used to image soft tissue, vasculature, blood flow, muscle,

G. Brunner • E.Y. Yang • J.D. Morrisett
Division of Atherosclerosis and Vascular Medicine, Department of Medicine, Baylor College of Medicine, Houston, TX 77030, USA

Z. Garami
Methodist DeBakey Heart and Vascular Center, The Methodist Hospital, Houston, TX 77030, USA

V. Nambi (✉)
Division of Athero, Baylor College of Medicine, Staff Cardiologist Ben Taub General Hospital and center for cardiovascular prevention Methodist DeBakey Heart and Vascular Center, Michael E DeBakey Veterans Affairs Hospital, Houston, TX 77030, USA
e-mail: vnambi@bcm.edu

L. Saba et al. (eds.), *Multi-Modality Atherosclerosis Imaging and Diagnosis*,
DOI 10.1007/978-1-4614-7425-8_28, © Springer Science+Business Media, LLC 2014

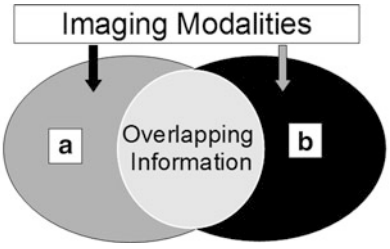

Fig. 28.1 Information content from two imaging modalities typically overlaps in certain aspects. Image fusion can merge complementary information from two or multiple imaging modalities

and bone surfaces (Fig. 28.2). US technology is based on sound waves that are generated and detected by piezoelectric elements inside the US transducer. Sound waves travel in a beam originating from the transducer that also acts as receiver for the reflected and scattered echo signals that are subsequently converted into an image. Clinical US imaging systems utilize acoustic waves in the low MHz range resulting in limited tissue penetration depth and inability to penetrate bone. US imaging is, however, more operator dependent than CT or MR imaging and hence the sonographer training and experience are important factors of image quality. Another limitation of ultrasound imaging is its "lateral drop out" or loss of detail in the lateral segments of the image, i.e., the segments away from the ultrasound beam—which is a consideration in assessing atherosclerosis [8].

2 Image Fusion

Image fusion presents the clinician and researcher with the opportunity to merge content from multiple imaging modalities, thereby possibly alleviating limitations of individual scanning technologies (Fig. 28.3). Image fusion can be implemented at the hardware or the software level. Table 28.1 lists clinically available image fusion systems such as, for example, PET/CT [4, 9] and recently available PET/MRI systems [10, 11]. Although image fusion is commonly understood as an inter-imaging modality technology, it can also be applied to intra-modality fusion; for instance to analyzing pre- and postoperative imaging data.

Table 28.2 shows a summary of important characteristics of major imaging technologies. Broadly speaking, image fusion between one or more imaging modalities can be accomplished by hardware or software fusion.

Image fusion can be broadly classified into two categories, namely hardware fusion and software fusion.

2.1 Hardware Image Fusion

In the hardware-based approach to image fusion, data are acquired simultaneously by different imaging modalities. The advantage of these systems is that the resulting imaging data are co-registered, and data fusion is performed in real time. The disadvantages include the possible requirement of larger equipment.

2.1.1 Ultrasonography

Compound imaging or the fusion of information obtained through multiple scans of the same anatomy or region of interest has been one of the main approaches toward improving information obtained through ultrasound-based imaging. Compound imaging systems fuse images from separate sequential scans of the area of interest [24–28]. Jeong and Kwon [29] obtained US scans of human breast tissue using two opposing array transducers. Although these efforts improved the image quality and resolution, imaging was done sequentially and hence resulted in long scan times or suboptimal co-registration, i.e., the ability to obtain information in the same plane. The simultaneous usage of multiple transducers might exacerbate the known US limitation of lateral dropout leading to potential loss of information.

The issue of lateral dropout in US imaging has been addressed by fusing images obtained from different angles using a technique known as spatial compounding which has been an active field of ultrasound research aimed at reducing intensity variations due to interference patterns from tissue echoes known as speckles [28]. Jespersen et al. [27] developed a scanning method known as multi-angle compound imaging (MACI) that uses a linear phased array to create iteratively a beam at one of n-angles at a time producing a set of acquisitions from different angles. MACI averages all n-images resulting in better tissue contrast and reduced speckle noise. The basic concept of MACI was extended by Behar et al. [28] to improve lateral resolution and speckle contrast by simultaneous image acquisition using three laterally separated transducers with only one acting as transmitter resulting in a compound image. Spatial compounding and MACI reduce speckle and improve tissue contrast at the cost of a reduced image frame rate.

2.1.2 PET/CT/MRI

PET/CT is a very successful imaging technology that combines functional imaging with anatomical imaging [9]. Although technical designs and specifications differ among vendors, the PET detectors and CT components are mounted typically inside a single gantry resulting in a co-registered data acquisition of both modalities [30, 31]. The major CT components such as detectors, readout electronics, and the

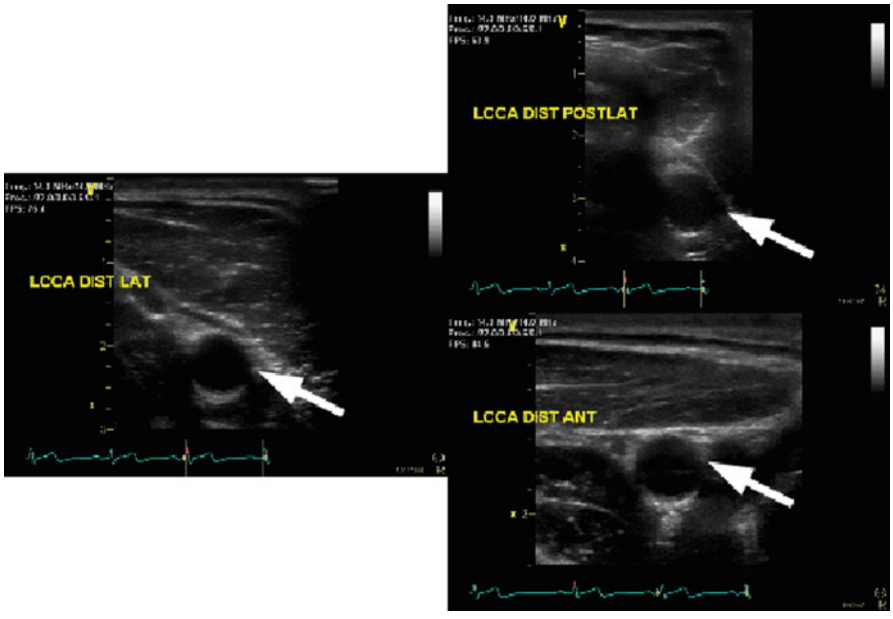

Fig. 28.2 US images of the left common carotid artery (LCCA) of one subject from different angles (views points). The *white arrows* indicate the same location in the LCCA illustrating changes in speckle patterns

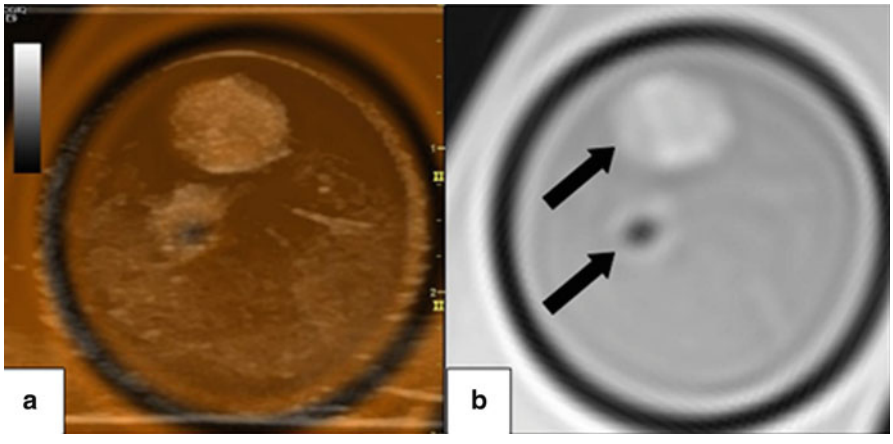

Fig. 28.3 Axial images of a carotid endarterectomy (CEA) sample. Panel (**b**) shows a proton density weighted MRI slice of the internal and external carotid artery (*arrows*). Note the hypointense region in the external carotid artery indicating the absence of plaque. Panel (**a**) depicts a fused image composed of the MRI slice and the corresponding ultrasound image

Table 28.1 Image fusion systems

Imaging modalities	MRI	US	CT	PET
MRI	X	X	X	X
US		X	X	X
CT			X	X

X-ray tube are mounted on a rotating ring. The PET detectors and electronics are mounted on a separate ring, partial ring, or are integrated in a stationary setup, depending on vendor specifications. Technical details on PET/CT scanner instrumentation can be found in an article by Alessio et al. [32].

In 2011 the US Food and Drug Administration approved the first commercial PET/MRI system for US market. PET/MRI is a promising technology, given its capability to simultaneously image function with increased soft tissue contrast at a significantly lower radiation burden [33, 34]. PET/MRI can reduce ionizing radiation by approximately 70 % when compared to state of the art PET/CT systems. Hence, this new technology might be especially of interest to vulnerable populations such as individuals receiving multiple scans and children.

2.2 Software Image Fusion

The software-based approach to image fusion is routinely used for the co-registration of images obtained with two or more modalities (Fig. 28.4). The process of image fusion involves several algorithmic steps that can vary substantially in number depending on the application at hand. Image fusion techniques integrate algorithms from the broad areas of computer vision and object recognition [35, 36]. Common problems that arise in image fusion are due to inherent differences in the underlying imaging technologies. For instance, in-plane resolution is quite different between US and

Table 28.2 Summary of important parameters for the most commonly used clinical imaging modalities

Properties/imaging modality	MDCT/DS-MDCT	MRI	US	PET
Ionizing radiation	Yes	No	No	Yes
Temporal resolution	165 ms/83 ms [12]	30–50 ms [13] [14, 15] (6 ms [16])	12 ms [17]	1 breathing cycle
Spatial resolution	0.4 × 0.4 × 0.5 mm [18, 19]	0.4 × 0.4 × 0.4 mm [20–22]	0.1–0.3 mm [23]	5–8 mm [4]
Reproducibility	Excellent	Excellent	Good but operator dependent	High
Acquisition time	Excellent	Moderate	Excellent	Moderate
Tissue contrast	Limited	Excellent	Limited	–
Function	Yes	Yes	Yes	Yes

MDCT multi-detector computed tomography, *MRI* magnetic resonance imaging, *US* ultrasonography, *PET* positron emission tomography

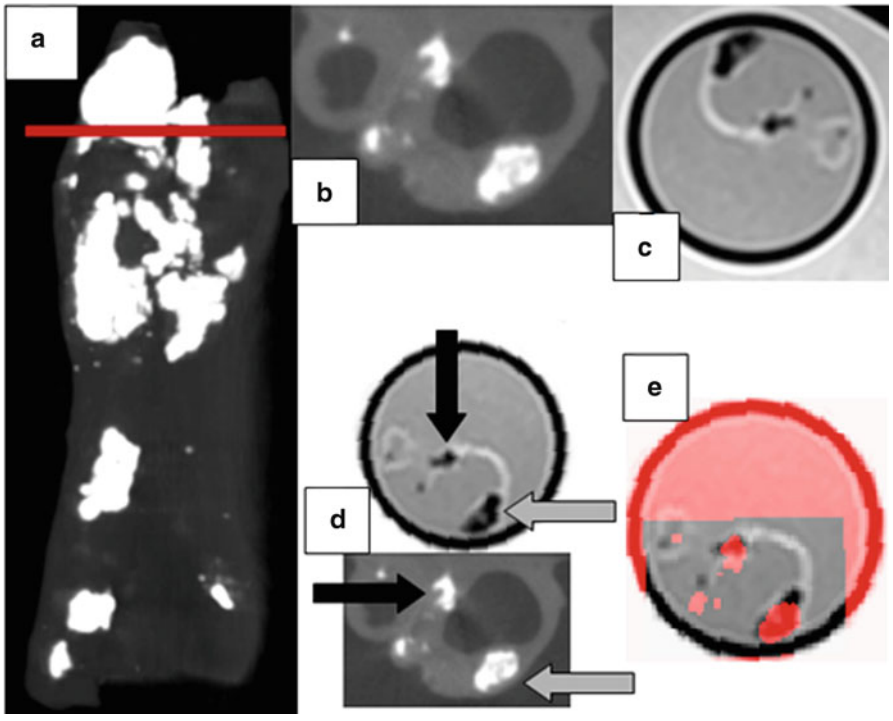

Fig. 28.4 Carotid endarterectomy (CEA) sample imaged with μCT and MRI. (**a**) Coronal view obtained with μCT for the CEA sample. Note the heavily calcified regions (*bright areas*). The *horizontal red line* indicates the location of the axial images in panels (**b**)–(**e**). (**b**) Axial slice at bifurcation of the μCT scan showing the internal and external carotid arteries with calcified nodules and increased wall thickness. (**c**) Co-registered MRI image acquired with a proton-density weighted turbo spin echo sequence on 3.T Siemens Verio system. (**d**) Euclidean transformed MRI slice in order to align with the μCT image. The *black* and *gray arrows* indicate calcified areas (hyperintense) serving as fiducial markers for image fusion. Note that calcified regions appear hypointense in MRI. (**e**) Representation of the fused μCT-MRI slices using transparency (best viewed in color) (Color figure online)

MRI images. The image fusion algorithms need to be able to tackle these differences in a robust fashion. Figure 28.5 shows the typical steps used in software-based image fusion techniques.

One of the most important steps in the image fusion workflow is the co-registration of the multi-modality imaging data. This aspect requires the identification of anatomical landmarks that are present in all of the source images. Depending on the approach, these landmarks, which are commonly referred to as fiducial markers, need to be extracted automatically or manually. Clinically, semiautomatic approaches have proven superior since automatic algorithms may perform poorly in the presence of imaging artifacts. Subsequently, these fiducial markers are used to extract *features* which in turn play a vital role in the quality of the final image fusion output.

Features are a compact representation of an image's content and of central importance in software-based image fusion systems. In the case of image fusion, the complexity of features can extend from simple coordinates of a set of fiducial markers to wavelet descriptors of selected regions of interest or include a set of features combining texture, structure, shape, motion, or entropy information [37–43]. The construction of features is of central importance in image

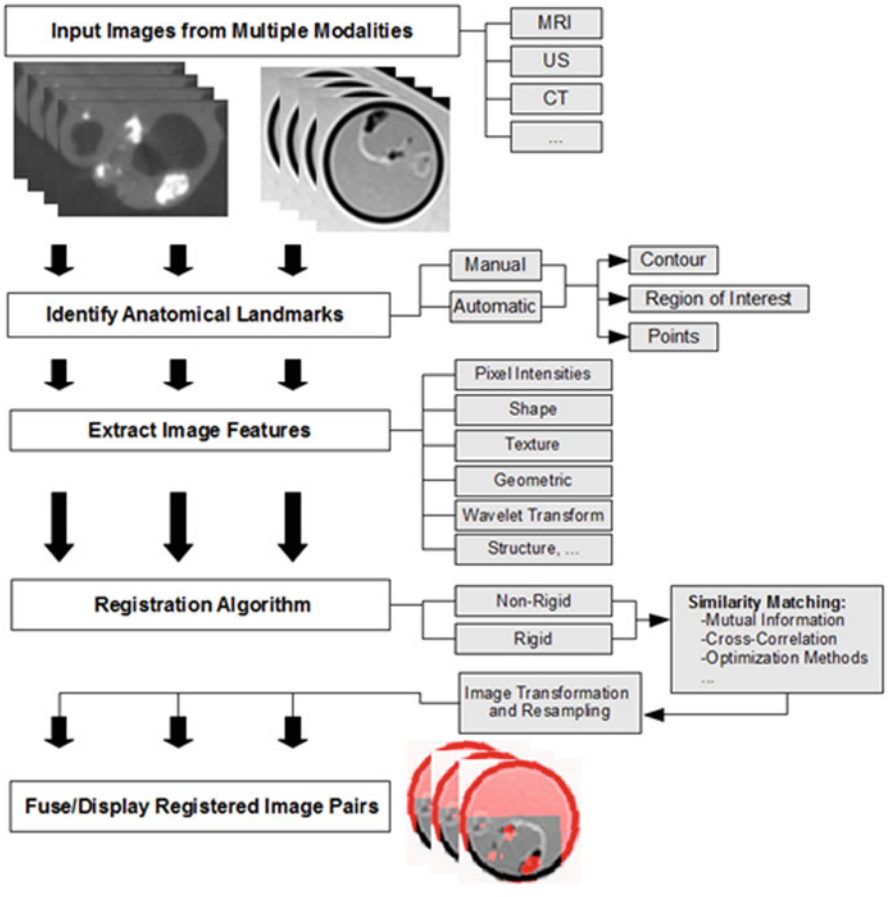

Fig. 28.5 Multi-modality image fusion workflow

analysis and image registration algorithms. It is beyond the scope of this chapter to discuss feature extraction in detail. Therefore, we will focus on the conceptual aspects, and the interested reader is referred to specialized literature on feature computation [35, 41, 44–52]. An important property of features for image fusion applications is *invariance*. Invariant features remain unchanged in case the image content is transformed according to a group action, i.e., the features obtained for an unaltered or a transformed image are mapped to the same point in feature space. A simple example is the color histogram of an image that remains identical under any permutation of the image pixels. However, a slight change in illumination, i.e., changing the actual values of pixels, may significantly change a simple color histogram. The concept of invariance considerably simplifies semi-automatic or fully automatic image co-registration. Instead of comparing images in all transformed instances, only one comparison has to be performed.

The next step in the workflow outlined in Fig. 28.5 is the actual registration algorithm that uses the features extracted from both modalities to establish correspondence between the imaging data sets. The most commonly used registration approach assumes a rigid scenario meaning that a set of rotations, translations, and perhaps a uniform scaling operation results in a correspondence between the imaging data. These operations are also known as a similarity transformation that consists of 4 degrees of freedom (DoF) in the case of a two-dimensional image, i.e., translation in x and y direction (2 DoF), in plane rotation (1 DoF), and uniform scaling (1 DoF). In order to solve the similarity transformation, a total of 2 points is sufficient. In the general 3D case such as a volumetric US or MRI study, the similarity transformation has a total of 7 DoF (3 translation, 3 rotation, 1 scaling) and requires at least 3 fiducial markers to obtain a co-registration between the data sets. The rigid registration approach works favorably for many applications. However, in cases where a patient's anatomy changes such as, for example, when scans were taken pre and post a surgical or endovascular intervention, the rigid registration approach delivers suboptimal results. In these cases image fusion can be attempted by using nonrigid registration algorithms. There is a broad spectrum of nonrigid registration methods that basically allow to transform elastically the content of one image to match the content of another one. In general, nonrigid registration algorithms are complex and time consuming as the number of degrees of freedom can be very large [53, 54]. In order to alleviate this limitation, nonrigid registration algorithms commonly incorporate expert knowledge of the underlying anatomical change that improves performance and accuracy.

2.3 US-CT and US-MRI Fusion

Ultrasound is a real time cost-effective and widely available imaging technology that can be fused with other modalities such as CT or MRI. US is of special interest in intraprocedural and postoperative imaging due to its noninvasive nature. Any other technique would require image viewing, processing pauses, or prolonging the procedure. Crocetti et al. [55] examined in a recent study the feasibility of a commercial multimodality fusion imaging system (Virtual Navigator System, Esaote SpA, Genoa, Italy), for real-time fusion of preprocedure CT scans with intraprocedure US. The study was conducted ex vivo using calf livers prepared with radiopaque internal targets to simulate liver lesions. Subsequently, acquired CT scans were fused with real time US images resulting in mean registration errors of 3.0 ± 0.1 mm.

Nakano et al. [56] used a commercially available image fusion system (Real-time Virtual Sonography, Hitachi Medical, Tokyo, Japan) to perform breast imaging. The system was tested in 51 patients who presented with 63 lesions. Patients underwent MR imaging on a 1.5 T imager followed by a sonographic evaluation of the same lesions. Lesion size measured by real-time virtual sonography and MRI was similar ($r = 0.848$, $p < 0.001$). Similarly, positioning errors for the sagittal and transverse planes and relative depth from the skin were small (6.9 mm, 7.7 mm, and 2.8 mm).

Wein et al. [57] developed an automatic CT-US registration framework for diagnostic imaging. Liver and kidney CT and US scans from 25 patients were fused to assess registration errors of the proposed algorithm. One expert defined ground truth data by manually locating fiducial landmarks (lesions) in both imaging modalities. Subsequently, registration errors were compared between the automatic algorithm and the fiduciary point-based registration method. The point-based method using manually identified lesions yielded more accurate results than the automatic method with respective fiducial registration errors of 5.0 mm and 9.5 mm. However, the point-based method involved up to 10 min of identifying fiducial markers, whereas the automatic method required approximately 40 s. Although the automatic method is not readily usable in the clinical setting, it could provide a means to reduce the time necessary to fuse CT and US data sets.

In another study, Caskey et al. [58] developed an US–CT fusion system with the capability to combine real-time US images with pre-acquired CT images. The system was tested using Met-1 tumors in the fat pads of 12 female mice. The CT data were used to identify the Hounsfield units of the tumor which in turn were validated histologically. The US and CT data were fused using fiducial markers with an accuracy of approximately 1 mm.

3 Clinical Research Applications

As multi-modality imaging becomes more prevalent, attention will be directed toward systematic, reproducible methods for inter-modality comparison of image sets for a given biological system. The fusion imaging techniques discussed above allow for such comparisons to be conducted.

With regard to ultrasound imaging, one can envision fusion ultrasound protocols using baseline ultrasound scans as a reference for true serial comparisons (i.e., ultrasound–ultrasound comparisons) for monitoring cardiac function and wall motion abnormalities. Fusion with more detailed structural scans such as MRI or CT may also allow for overlaying of functional information from real-time ultrasounds. We describe our experience for ex vivo and in vivo imaging toward development of these protocols in the subsequent sections, using a commercially available ultrasound system capable of fusion imaging.

Figure 28.6 illustrates the four main image fusion steps after uploading data from a secondary imaging modality:

1. Locking the plane (Fig. 28.6a)
2. Presenting markers and orientation, zoom out/in to view area of interest (Fig. 28.6b)
3. Co-registration: Choosing at least three reference points on each imaging modality (Fig. 28.6c)
4. Displaying the fused images in cross section and longitudinal views (Fig. 28.6d–f)

In Fig. 28.6, the carotid bifurcation and calcified plaques were used as intrinsic landmarks for co-registration. Below, we describe in detail the various considerations both for in-vivo and ex-vivo fusions.

3.1 Registration of Landmarks

As previously stated, one of the main challenge with inter-modality fusion of image sets comes from linking recognizable image landmarks through co-registration. Techniques for hardware- and software-based co-registration have been described in depth in the previous sections. Image landmarks, or fiducial markers, chosen for co-registration can be intrinsic or extrinsic to the biological system of interest.

The simplest co-registration techniques with intrinsic landmarks use anatomic features [59]. Anatomy common to a given biological system (e.g., carotid bifurcations) also allows for standardization of in vivo imaging protocols. When extrinsic landmarks are introduced into a biological system, compatibility of the chosen markers between various imaging modalities should be considered. For ex vivo imaging, spatial features of these landmarks aid with identifying spatial orientation within an imaging modality, since the native anatomic orientation (e.g., left–right,

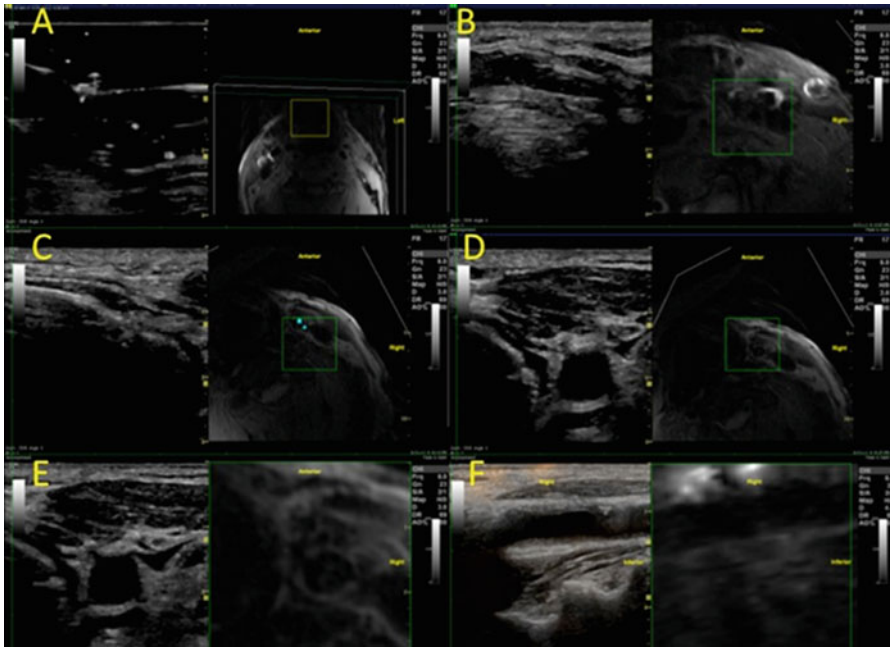

Fig. 28.6 (**a**–**f**) Carotid duplex and neck MR fusion imaging

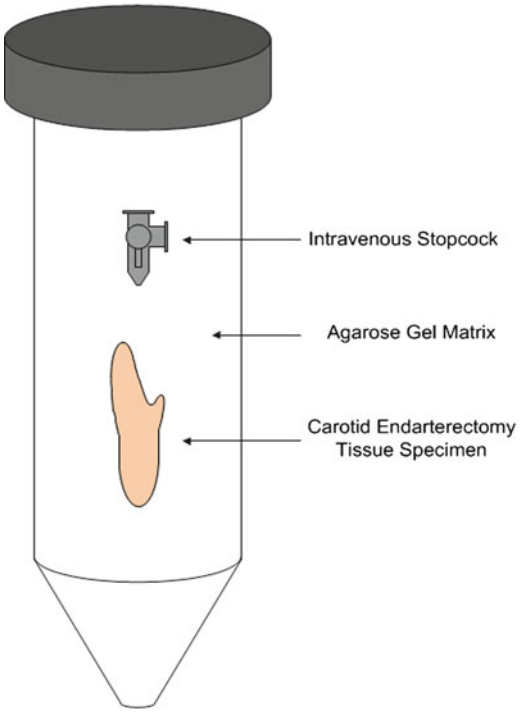

Fig. 28.7 Schematic of carotid tissue specimen embedded with an extrinsic landmark (intravenous 3-way stopcock) in an agarose gel matrix to preserve spatial configuration

anterior–posterior, cranial–caudal) may no longer be present. We encountered these issues in our ex vivo experiments with carotid endarterectomy tissue specimens and have found plastic intravenous 3-way stopcocks to be adequate 3D markers for this system (Fig. 28.7).

3.2 Preparation for Inter-Modality Imaging

Maintaining spatial orientation of the biological system of interest has become so important for inter-modality comparisons that entire medical imaging fields have been developed to address this issue [59]. Again, hardware and software processing techniques have been covered in detail in the above sections. Steps may still be taken with preparing a given biological system to standardize quality assessment protocols of inter-modality comparisons and to assist with such comparisons.

In the ex vivo setting, soft tissues such as vessels are easily deformable and thus do not maintain their shape. Furthermore, the ultrasound imaging modality requires a substrate/media through which the sound beam can travel, ideally a substrate/media with acoustic properties resembling those of soft tissue. Agarose gels maintain the spatial arrangement of embedded tissues and can be mixed to have such desired acoustic properties. Additionally, agarose has minimal chemical interaction with biological tissue. Such a gel has been used for ultrasound imaging of carotid endarterectomy tissues ex vivo [60]. Furthermore, these constructs are compatible with other imaging modalities such as MRI and CT and have also been used for imaging phantoms for these modalities. We have used an agarose gel media (3 % by mass [g]–volume [mL]) for our studies [61].

Carotid endarterectomy tissues were obtained 1–3 h after surgical resection and preserved in phosphate-buffered saline/50 % glycerol at −20 °C to maintain the ultrastructural properties of the tissue. Prior to use, specimens were dialyzed for 24 h against phosphate-buffered saline to remove the

Fig. 28.8 Carotid tissue specimen embedded in an agarose gel matrix for MR imaging. Thread was used to suspend the specimen in the matrix

Fig. 28.9 Custom-designed holder for MR imaging of tissue specimens

glycerol and then embedded in an agarose mixture. The low-melting agarose mixture was created by heating to 60 °C and then degassing under vacuum. Degassing minimized the presence of bubbles in the mixture, which are hyperechogenic on ultrasound and interfere with ultrasound imaging. Each tissue was suspended with an intravenous plastic 3-way stopcock as an extrinsic fiducial marker (Fig. 28.8).

For MRI, tissues and markers were suspended in empty 50 mL tubes, then filled with agarose and placed in a specially constructed MRI compatible holder (Fig. 28.9) [61]. After MRI each tissue was extruded intact as an agarose cylinder from the tube and then transferred to a plastic box ($10.5 \times 2.5 \times 4.0$ cm), and additional degassed molten agarose was added to form an agarose bed (Fig. 28.10). This procedure was performed to provide adequate surface contact for the ultrasound probe.

For in vivo experiments, we observed and recorded the subject's head position for the MRI scan. Having the subject reproduce this positioning for the 3D ultrasound scan helps minimize MRI-US co-registration issues. In theory, extrinsic landmarks may be employed for in vivo multimodality imaging. However, such landmarks would either be limited to the skin surface, interfering with the contact by the ultrasound probe, or be necessarily invasive, requiring needle insertion of the marker. Other external reference systems, such as the Meijer's arc, may also be considered. However, their reliability for co-registration should be compared with that of the above markers.

Fig. 28.10 Carotid endarterectomy tissue embedded in an agarose gel bed for ultrasound imaging

3.3 Three-Dimensional Ultrasound Imaging

3.3.1 MR Imaging

For in vivo experiments involving subjects with known carotid atherosclerosis, individuals were positioned supine in a Signa Excite 3.0 T MRI scanner (GE Healthcare, Wauwatosa, WI). The carotid arteries were imaged using a 6-cm phased array 4-channel carotid coil (Pathway Med Tech, Redmond, WA). A standard 3-plane localizer was used to identify the carotid arteries. Subsequently, a 2D time of flight (TOF) sequence was applied as a localizer to identify both the right and left common carotid bifurcation (flow divider) and to obtain high quality blood flow and vessel wall imaging. Three 2D fast spin echo scans were acquired using proton-density weighting, T2-weighting, and T1-weighting. The longitudinal coverage of this set of images was centered at the carotid bifurcation and covered a large part of the carotid artery below and above the bifurcation.

For ex vivo experiments, carotid endarterectomy tissue specimens were imaged using the same 3.0 T scanner and phased array coil as for the subjects. Serial axial proton-density weighted (PDW), T1-weighted, and T2-weighted images were acquired (2-mm slice thickness, matrix 512×512, field of view 100×100 mm) using a fast-spin echo sequence, providing 10–31 slices with an in-plane resolution of $\sim$0.195 mm. Correction algorithms adjusted for magnetic field strength gradients across the sample image. More recently, we also imaged the carotid tissue specimens using a 3.0 T Siemens Verio system with a 32-channel head coil. The CEA samples were imaged using a turbo spin echo sequence with the following parameters: repetition time (TR) = 3010 ms; echo time (TE) = 6.1 ms; number of averages = 4; slice thickness = 2 mm; echo train length = 7; pixel bandwidth = 521 Hz/pixel; flip angle = 123°; x–y pixel spacing = 0.364 mm; and number of slices = 63.

3.3.2 3D Ultrasound Imaging

3D ultrasound images can be acquired using probes (a) with motors set to move elements over a certain length, (b) with two-dimensional arrays of transducer elements, or (c) with freehand techniques. With free-hand techniques, the probe is moved in a direction perpendicular to the scan plane or rotated in place, and internal or external reference systems are used to combine a series of B-mode ultrasound images acquired during the sweep. Internal reference systems may consist of (a) timing through clocks or (b) image processing algorithms that recognize large movement in the scan plane. These internal reference systems are beyond the scope of this chapter, but the interested reader is directed to relevant citations for more detail [63]. External reference systems have also been used. Some ultrasound systems have included accelerometers with the transducer probe, capable of detecting probe motion and direction [63]. Others have acquired position information through electromagnetic transmit–receive setups.

For our experiments, we have used one such commercially available position-sensing system as the external reference. This system consists of a mid-range DC magnetic transmitter for generating a weak magnetic field. Sensor arrays attached to the two-dimensional vascular ultrasound probes sensed this field and transmitted the information to an in-built circuit system. Thus, information on the position and orientation of the ultrasound probe can be acquired with the system from the signal detected by the attached sensor arrays. The system can also be used independent of a three-dimensional image data set to generate a three-dimensional reference "map" or image set.

After calibration through a semiautomated co-registration process, real-time B-mode ultrasound images were mapped to the co-registered three-dimensional image sets in a manner similar to that used by the Global Positioning System (GPS) navigation devices to map the device location to stored maps. For our experiments, we used a plane-point co-registration technique. First, the corresponding image set (e.g., MRI scans) for a biological system that was imaged was loaded into the ultrasound system, which performed multiplanar reconstruction of the image data set to form a three-dimensional "map." The reconstruction was used to navigate to a landmark of interest (e.g., an extrinsic landmark such as a plastic marker for ex vivo experiments or the chin of a volunteer for in vivo experiments). Then, the plane for the loaded three-dimensional image set was locked. The corresponding plane on the live B-mode ultrasound scan was found and locked on the system, completing the plane-lock step. The system then tracked motion of the live ultrasound scan with freehand navigation through the loaded three-dimensional image set. Next, an intrinsic landmark (e.g., calcification in tissue or carotid bifurcation) was located, and the three-dimensional image set was rotated in-plane to align the corresponding images. Finally, the intrinsic landmark was marked with a point on both the live ultrasound scan to refine the real-time co-registration.

3.3.3 Ultrasound Imaging Fusion Experiments

For ex vivo experiments, we have validated use of the system for three-dimensional co-registration against manual co-registration based on anatomic landmarks with 13 carotid endarterectomy tissue specimens [64]. We found that on average, 13.92 (standard error [SE] 1.95) MRI slices each 2 mm thick and 265.77 (SE 28.58) ultrasound frames were necessary to image the tissue samples, translating to 19.66 (SE 2.07) ultrasound scan frames per MRI slice [64]. There were excellent inter-reader agreements between semi-automated GPS-like system and two different readers

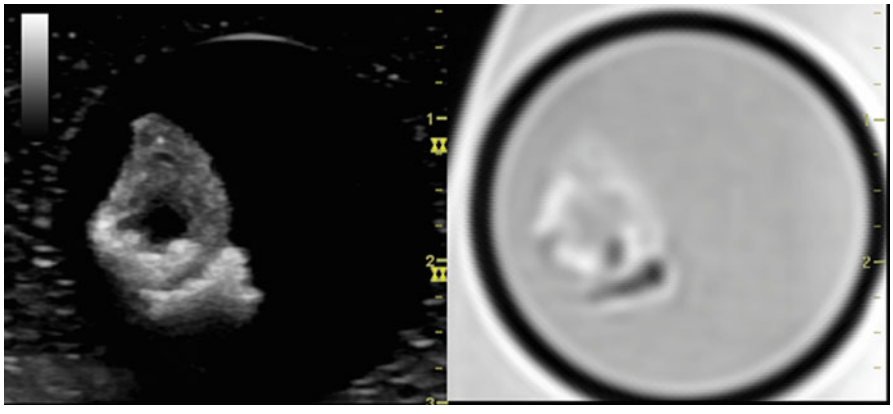

Fig. 28.11 Real-time B-mode ultrasound scan (*left*) of a carotid tissue specimen co-registered to corresponding MR image set (*right*). The faint circular pattern on the ultrasound scan corresponds to the agarose cylinder used to hold the specimen for MR imaging, also seen on the *right*

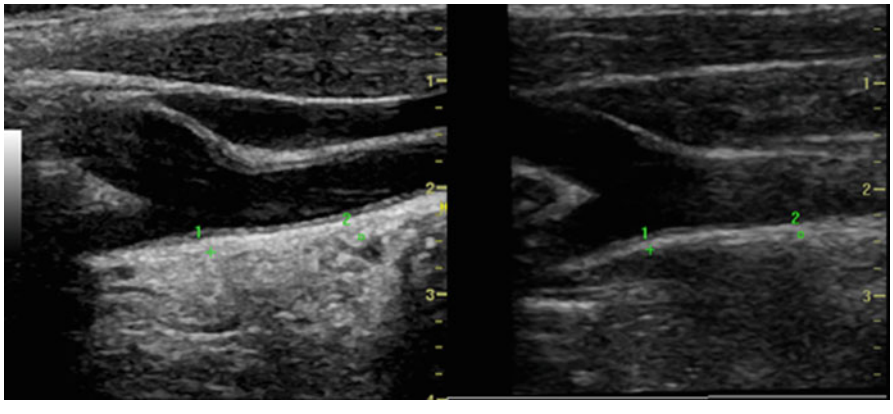

Fig. 28.12 Real-time B-mode ultrasound scan (*left*) of a carotid bifurcation co-registered to a three-dimensional ultrasound image set (*right*) taken 2 weeks previously. *Green markers* identify corresponding points. A cross at position 1 signifies a marker within the scan plane. A box at position 2 signifies a marker outside the scan plane (i.e., in a neighboring scan plane or in a position coming out or going into the screen)

(intraclass correlation coefficients [ICC] > 0.99) for 33 landmarks (Fig. 28.11) [64]. Further experiments with additional specimens have suggested modestly better agreement between ultrasound and volumes measured by water displacement (ICC 0.85) than between MRI and water volumes (ICC 0.81) [65].

We have also examined if in vivo repeatability of carotid intima-media thickness (CIMT) measurements can be improved using the same system. CIMT measures using the Meijer's arc and the GPS-like system were 0.61 (SE 0.03) mm and 0.63 (SE 0.03) mm at the initial visit, respectively [64]. On the second visit (~2 days apart), CIMT measures were 0.64 (SE 0.03) mm and 0.64 (SE 0.04) mm, respectively. There was good agreement (ICC > 0.7) between the two methods (ICC 0.92). Overall, we found greater repeatability C-IMT measures with the registered images (ICC 0.91) than those with the Meijer's arc (ICC 0.84) (Fig. 28.12) [64]. However, because of the 3-D map, the image quality was not as good as when performed with regular 2D approaches.

We have also used the same co-registration technique for our in vivo study of carotid atherosclerosis, using carotid bifurcations as the intrinsic landmark (Fig. 28.13).

So far, our three-dimensional evaluations have been limited to structural measurements of thicknesses and volumes. Future work may include more complex analyses such as physiologic functional assessment. In fact, others have begun work to incorporate color Doppler information from echocardiography with cine cardiac MRI, paving the way for four-dimensional co-registration [66]. One group has extracted color Doppler blood flow from transthoracic echocardiograms in ten volunteers, co-registered the flow information with corresponding cardiac MR images in time and space using the mitral annular root and root of the aortic valve as intrinsic landmarks, and fused the two data sets into one image set. Registration quality was assessed in this study using the variation in distance of a landmark between echocardiograms and cardiac MRI.[66] The fusion process was conducted off-line using in-house built algorithms, but one can already envision fusion of real-time ultrasonography with cine cardiac MRI using electrocardiography gating with existing technologies [66]. Challenges with algorithm development and temporal resolution would need to be overcome to bring these advanced analyses to research, and eventually clinical, settings.

4 Clinical Applications and the Future

Clearly the capability to fuse imaging technologies will have significant value in both diagnostic and therapeutic medicine. With respect to ultrasound the major advantage of portability, safety and providing real time functional and anatomical

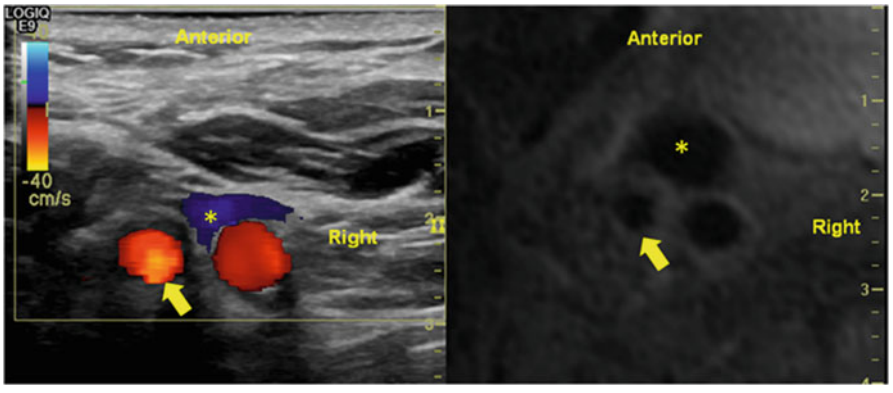

Fig. 28.13 Real-time B-mode ultrasound scan with color Doppler (*left*) of a carotid bifurcation co-registered to corresponding MR image set (*right*). *Arrows* indicate the internal carotid artery, and the *asterisk* indicates the internal jugular. A difference in scale between panes exists due to zooming with the ultrasound window, and hence the slight offset between modalities. The system maintained the scale for the MR image sets because of the native MRI resolution

information can be harnessed to complement the excellent anatomic tomographic information that can be provided by MRI and CT.

Ultrasound-based fusion is already beginning to show value both in the clinical and research arenas. Ultrasound on its own is already used to guide biopsies. However, the limitations of ultrasound (drop out, tissue penetration) have to be circumvented by the physician. Although this is clearly possible, it is not optimal. The ability to get in addition the excellent anatomical information as can be provided by a CT scan or MRI will allow the physician performing the procedure more confidence and accuracy in performing the procedure. For example, during a biopsy, images can be fused and an ultrasound be used to guide the biopsy in real time. With image overlays, the physician will be able to simultaneously look at the CT scan/MRI to know if he is in the right anatomical location. These approaches have been already shown to improve prostate biopsies [67]. Similarly, ultrasound-based radiofrequency ablation can be used to treat some tumors. However, ultrasound drop out, isoechoic tumors, prior treatment, etc. may make it difficult for ultrasound to adequately identify these tumors for therapy. The fusion with CT/MRI may allow increased accuracy in the identification of these [55, 68]. In a recent animal study, ultrasound-ultrasound fusion was applied to improve the delivery of radiofrequency ablative therapy. In this study, gold pellets were inserted into the renal parenchyma in a canine model and then 3D ultrasound images were obtained. These 3D ultrasound images were used to plan ablative therapies. Then, using real time, 2D ultrasound, registered to the 3D data set, radiofrequency ablative therapy was delivered, and this overall improved the accuracy of delivery of therapy [69]. From a cardiovascular imaging perspective, in addition to the improved anatomical information, fusion could be an excellent educational tool when we try to resolve artifactual findings.

Ultrasound, on the other hand, can be used to complement other modalities as well. The functional information that can be obtained through ultrasound can be fused with the anatomical information on a MRI/CT to allow better interpretation of a MRI finding. For example, once a stent is placed, MR images in the region of the stent may not be helpful and functional information may be difficult to get. Fusing the images could allow ultrasound to get functional (Doppler) based information related to the same. Figure 28.14 shows an example of an MRA of the middle cerebral artery in the brain that was fused with ultrasound (transcranial Doppler) information to gain knowledge about how the stent was functioning. In such cases, fusion imaging can abrogate the need for a follow-up angiogram (Fig. 28.14).

Several potential uses of ultrasound–ultrasound fusion (similar to our efforts to fuse CIMT data and improve reliability) can be thought of as well including, for example, monitoring abdominal aortic aneurysms for expansion, cardiac chambers, and change in lumen dimensions in arterial segments. This may allow meaningful comparisons and a better appreciation of the progression/stability of disease. Clearly, there are innumerable clinical situations where one can think of possible uses of fusion.

However, one must be cognizant of limitations as well [64]. The time taken for the procedure will clearly increase. Further there is a learning curve: the advantages offered by the fusion technology will be limited by the accuracy of registration that the sonographer performs. There may be occasions where a small error in registration may not matter. However, there may equally be situations (such as during a biopsy/therapy) where any error will be critical. Then, when one images a dynamic structure such as the heart, changes in heart rate and rhythm between studies may all affect the ability to fuse the images without additional processing.

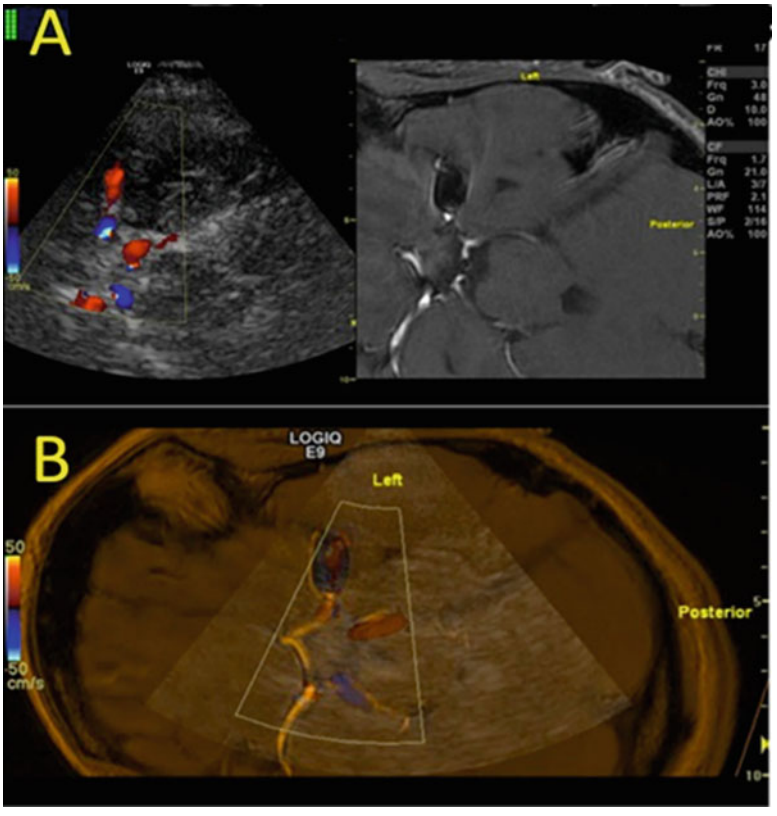

Fig. 28.14 Transcranial duplex and brain MRA fusion imaging

5 Conclusion

Image fusion, be it hardware or software has the potential to enable us to improve imaging-based assistance in diagnostics and therapeutics. Image fusion may be of particular value to ultrasound imaging given its clear differences (vis a vis advantages and disadvantages) with other imaging modalities. Although additional work is required, this developing application offers great promise.

Acknowledgments

1. We thank the SMART RISK study (ClinicalTrials.gov Identifier: NCT00860184) for allowing us to use images generated from the study
2. We thank the Gulf Coast Medical Foundation whose grant awarded to one of the authors supported part of the research described/images generated
3. We thank Drs. Ching-Hsuan Tung and Xukui Wang for micro-CT data acquisition.
4. We thank Dr John Volpi and Rasadul Kabir for their kind assistance with the ultrasound imaging

Support This work was partly supported by the following grants: NIH/NHLBI T32HL007812 training grant, American Heart Association South Central Affiliate Postdoctoral Fellowship grant, NIH/NHLBI K23HL096893 grant, NIH/NHLBI HL63090, Gulf Coast Medical foundation. Dr. Nambi was supported by a NIH/NHLBI K23 HL096893 grant. Dr Nambi has research collaboration with GE. Clinical trial NCT00860184 is sponsored by VPDiagnostics, Inc. (Seattle, WA) and supported by NIH/NHLBI R44HL070576. The views expressed in this chapter are those of the authors and do not necessarily represent the views of the Department of Veterans Affairs.

References

1. Berrington de Gonzalez A, Mahesh M, Kim KP, Bhargavan M, Lewis R, Mettler F, Land C (2009) Projected cancer risks from computed tomographic scans performed in the United States in 2007. Arch Intern Med 169(22):2071–2077
2. Brenner DJ, Hall EJ (2007) Computed tomography–an increasing source of radiation exposure. N Engl J Med 357(22):2277–2284
3. IMV (2008) Benchmark report: MRI 2007. IMV Medical Information Division, Des Plaines, IL
4. Ben-Haim S, Israel O (2006) PET/CT for atherosclerotic plaque imaging. Q J Nucl Med Mol Imaging 50(1):53–60
5. Hillner BE, Siegel BA, Hanna L, Shields AF, Duan F, Gareen IF, Quinn B, Coleman RE (2012) Impact of 18F-FDG PET used after initial treatment of cancer: comparison of the national oncologic PET registry 2006 and 2009 cohorts. J Nucl Med 53(5):831–837
6. Huang B, Law MW, Khong PL (2009) Whole-body PET/CT scanning: estimation of radiation dose and cancer risk. Radiology 251(1):166–174
7. Buck AK, Herrmann K, Stargardt T, Dechow T, Krause BJ, Schreyogg J (2010) Economic evaluation of PET and PET/CT in oncology: evidence and methodologic approaches. J Nucl Med 51(3):401–412
8. Nambi V, Chambless L, Folsom AR, He M, Hu Y, Mosley T, Volcik K, Boerwinkle E, Ballantyne CM (2010) Carotid intima-media thickness and presence or absence of plaque improves prediction of coronary heart disease risk: the ARIC (atherosclerosis risk in communities) study. J Am Coll Cardiol 55(15):1600–1607
9. Townsend DW, Beyer T (2002) A combined PET/CT scanner: the path to true image fusion. Br J Radiol 75(Spec No):S24–S30
10. Calcagno C, Cornily JC, Hyafil F, Rudd JH, Briley-Saebo KC, Mani V, Goldschlager G, Machac J, Fuster V, Fayad ZA (2008)

Detection of neovessels in atherosclerotic plaques of rabbits using dynamic contrast enhanced MRI and 18F-FDG PET. Arterioscler Thromb Vasc Biol 28(7):1311–1317
11. Nishioka T, Shiga T, Shirato H, Tsukamoto E, Tsuchiya K, Kato T, Ohmori K, Yamazaki A, Aoyama H, Hashimoto S, Chang TC, Miyasaka K (2002) Image fusion between 18FDG-PET and MRI/CT for radiotherapy planning of oropharyngeal and nasopharyngeal carcinomas. Int J Radiat Oncol Biol Phys 53(4):1051–1057
12. Flohr TG, McCollough CH, Bruder H, Petersilka M, Gruber K, Suss C, Grasruck M, Stierstorfer K, Krauss B, Raupach R, Primak AN, Kuttner A, Achenbach S, Becker C, Kopp A, Ohnesorge BM (2006) First performance evaluation of a dual-source CT (DSCT) system. Eur Radiol 16(2):256–268
13. Kellman P, Chefd'hotel C, Lorenz CH, Mancini C, Arai AE, McVeigh ER (2009) High spatial and temporal resolution cardiac cine MRI from retrospective reconstruction of data acquired in real time using motion correction and resorting. Magn Reson Med 62(6):1557–1564
14. Christodoulou AG, Brinegar C, Haldar JP, Zhang H, Wu YJ, Foley LM, Hitchens T, Ye Q, Ho C, Liang ZP (2010) High-resolution cardiac MRI using partially separable functions and weighted spatial smoothness regularization. Conf Proc IEEE Eng Med Biol Soc 2010:871–874
15. Hansen MS, Sorensen TS, Arai AE, Kellman P (2012) Retrospective reconstruction of high temporal resolution cine images from real-time MRI using iterative motion correction. Magn Reson Med 68(3):741–750
16. Krishnamurthy R, Pednekar A, Cheong B, Muthupillai R (2010) High temporal resolution SSFP cine MRI for estimation of left ventricular diastolic parameters. J Magn Reson Imaging 31(4):872–880
17. Poepping TL, Nikolov HN, Rankin RN, Lee M, Holdsworth DW (2002) An in vitro system for Doppler ultrasound flow studies in the stenosed carotid artery bifurcation. Ultrasound Med Biol 28(4):495–506
18. Bardo DM, Brown P (2008) Cardiac multidetector computed tomography: basic physics of image acquisition and clinical applications. Curr Cardiol Rev 4(3):231–243
19. Choe YH, Choo KS, Jeon ES, Gwon HC, Choi JH, Park JE (2008) Comparison of MDCT and MRI in the detection and sizing of acute and chronic myocardial infarcts. Eur J Radiol 66(2):292–299
20. Duivenvoorden R, de Groot E, Elsen BM, Lameris JS, van der Geest RJ, Stroes ES, Kastelein JJ, Nederveen AJ (2009) In vivo quantification of carotid artery wall dimensions: 3.0-Tesla MRI versus B-mode ultrasound imaging. Circ Cardiovasc Imaging 2(3):235–242
21. Bachmann R, Nassenstein I, Kooijman H, Dittrich R, Stehling C, Kugel H, Niederstadt T, Kuhlenbaumer G, Ringelstein EB, Kramer S, Heindel W (2007) High-resolution magnetic resonance imaging (MRI) at 3.0 Tesla in the short-term follow-up of patients with proven cervical artery dissection. Invest Radiol 42(6):460–466
22. Qiao Y, Steinman DA, Qin Q, Etesami M, Schar M, Astor BC, Wasserman BA (2011) Intracranial arterial wall imaging using three-dimensional high isotropic resolution black blood MRI at 3.0 Tesla. J Magn Reson Imaging 34(1):22–30
23. O'Leary DH, Bots ML (2010) Imaging of atherosclerosis: carotid intima-media thickness. Eur Heart J 31(14):1682–1689
24. Adam D, Beilin-Nissan S, Friedman Z, Behar V (2006) The combined effect of spatial compounding and nonlinear filtering on the speckle reduction in ultrasound images. Ultrasonics 44(2):166–181
25. Bercoff J, Montaldo G, Loupas T, Savery D, Meziere F, Fink M, Tanter M (2011) Ultrafast compound Doppler imaging: providing full blood flow characterization. IEEE Trans Ultrason Ferroelectr Freq Control 58(1):134–147
26. Vogt M, Ermert H (2008) Limited-angle spatial compound imaging of skin with high-frequency ultrasound (20 MHz). IEEE Trans Ultrason Ferroelectr Freq Control 55(9):1975–1983
27. Jespersen SK, Wilhjelm JE, Sillesen H (1998) Multi-angle compound imaging. Ultrason Imaging 20(2):81–102
28. Behar V, Adam D, Friedman Z (2003) A new method of spatial compounding imaging. Ultrasonics 41(5):377–384
29. Jeong MK, Kwon SJ (2010) Multimode ultrasound breast imaging using a new array transducer configuration. Ultrasound Med Biol 36(4):637–646
30. Townsend DW, Beyer T, Blodgett TM (2003) PET/CT scanners: a hardware approach to image fusion. Semin Nucl Med 33(3):193–204
31. Townsend DW, Carney JP, Yap JT, Hall NC (2004) PET/CT today and tomorrow. J Nucl Med 45(Suppl 1):4S–14S
32. Alessio AM, Kinahan PE, Cheng PM, Vesselle H, Karp JS (2004) PET/CT scanner instrumentation, challenges, and solutions. Radiol Clin North Am 42(6):1017–1032, vii
33. Lee WW, Marinelli B, van der Laan AM, Sena BF, Gorbatov R, Leuschner F, Dutta P, Iwamoto Y, Ueno T, Begieneman MP, Niessen HW, Piek JJ, Vinegoni C, Pittet MJ, Swirski FK, Tawakol A, Di Carli M, Weissleder R, Nahrendorf M (2012) PET/MRI of inflammation in myocardial infarction. J Am Coll Cardiol 59(2):153–163
34. Zaidi H, Del Guerra A (2011) An outlook on future design of hybrid PET/MRI systems. Med Phys 38(10):5667–5689
35. Hartley RI, Zisserman A (2004) Multiple view geometry in computer vision, 2nd edn. Cambridge University Press, Cambridge
36. Faugeras O (1993) Three-dimensial computer vision: a geometric viewpoint. MIT Press, Cambridge, MA
37. Alexander SK, Azencott R, Papadakis M (2007) Isotropic multiresolution analysis for 3D-textures and applications in cardiovascular imaging. Paper presented at the proceedings of SPIE wavelets XII
38. Arivazhagan S, Ganesan L (2003) Texture classification using wavelet transform. Pattern Recogn Lett 24(9–10):1513–1521
39. Ali A, Farag A, El-Baz A (2007) Graph cuts framework for kidney segmentation with prior shape constraints. Med Image Comput Comput Assist Interv 10(Pt 1):384–392
40. Belongie S, Malik J, Puzicha J (2002) Shape matching and object recognition using shape contexts. IEEE Trans Pattern Anal Mach Intell 24(4):509–522
41. Brunner G, Chittajallu DR, Kurkure U, Kakadiaris IA (2010) Patch-cuts: a graph-based image segmentation method using patch features and spatial relations. Paper presented at the proceedings of the IAPR conference on British machine vision conference (BMVC), September 2010
42. Boykov Y, Kolmogorov V, Cremers D, Delong A (2006) An integral solution to surface evolution PDEs via geo-cuts. Paper presented at the proceedings of the 9th European conference on computer vision
43. Yu W, Yan P, Sinusas AJ, Thiele K, Duncan JS (2006) Towards pointwise motion tracking in echocardiographic image sequences – comparing the reliability of different features for speckle tracking. Med Image Anal 10(4):495–508
44. Haralick RM, Shanmugam K, Dinstein I (1973) Textural features for image classification. IEEE Trans Syst Man Cybernet 3:610–621
45. Jamie Shotton MJ (2008) Semantic texton forests for image categorization and segmentation. Paper presented at the proceedings of the computer vision and pattern recognition (CVPR 2008)
46. Bishop CM (2006) Pattern recognition and machine learning (information science and statistics). Springer, New York
47. Boykov Y, Veksler O (2006) Graph cuts in vision and graphics: theories and applications. In: Paragios N, Chen Y, Faugeras O (eds) Handbook of mathematical models in computer vision. Springer, New York

48. Gonzalez RC, Woods RC (2008) Digital image processing, 3rd edn. Prentice Hall, Upper Saddle River, NJ
49. Jain AK (1989) Fundamentals of digital image processing. Prentice-Hall, Englewood Cliffs
50. Petrou M, Sevilla PG (2006) Image processing: dealing with texture. Wiley, Chichester
51. Pratt WK (1991) Digital image processing. Wiley, New York
52. Sonka M, Hlavac V, Boyle R (1999) Image processing, analysis and machine vision, 2nd edn. Brooks/Cole, Pacific Grove
53. Rueckert D, Sonoda L, Hayes C, Hill D, Leach M, Hawkes D (1999) Nonrigid registration using free-form deformations: application to breast MR images. IEEE Trans Med Imaging 18(8):712–721
54. Yang J, Blum RS, Williams JP, Sun Y, Xu C (2006) Non-rigid image registration using geometric features and local salient region features. Paper presented at the proceedings of the CVPR '06: proceedings of the 2006 IEEE computer society conference on computer vision and pattern recognition, Washington, DC
55. Crocetti L, Lencioni R, Debeni S, See TC, Pina CD, Bartolozzi C (2008) Targeting liver lesions for radiofrequency ablation: an experimental feasibility study using a CT-US fusion imaging system. Invest Radiol 43(1):33–39
56. Nakano S, Yoshida M, Fujii K, Yorozuya K, Kousaka J, Mouri Y, Fukutomi T, Ohshima Y, Kimura J, Ishiguchi T (2012) Real-time virtual sonography, a coordinated sonography and MRI system that uses magnetic navigation, improves the sonographic identification of enhancing lesions on breast MRI. Ultrasound Med Biol 38(1):42–49
57. Wein W, Brunke S, Khamene A, Callstrom MR, Navab N (2008) Automatic CT-ultrasound registration for diagnostic imaging and image-guided intervention. Med Image Anal 12(5):577–585
58. Caskey CF, Hlawitschka M, Qin S, Mahakian LM, Cardiff RD, Boone JM, Ferrara KW (2011) An open environment CT-US fusion for tissue segmentation during interventional guidance. PLoS One 6(11):e27372
59. Maintz JB, Viergever MA (1998) A survey of medical image registration. Med Image Anal 2(1):1–36
60. Wilhjelm JE, Jensen MS, Gammelmark KL, Sahl B, Martinsen K, Hansen JU, Brandt T, Jespersen SK, Falk E, Fredfeldt KE, Sillesen H (2004) A method to create reference maps forevaluation of ultrasound images of carotid atherosclerotic plaque. Ultrasound Med Biol 30(9):1119–1131
61. Culjat MO, Goldenberg D, Tewari P, Singh RS (2010) A review of tissue substitutes for ultrasound imaging. Ultrasound Med Biol 36(6):861–873
62. Choudhary S, Higgins C, Chen I, Reardon M, Lawrie G, Gr V, Karmonik C, Via D, Morrisett J (2006) Quantitation and localization of matrix metalloproteinases and their inhibitors in human carotid endarterectomy tissues. Arterioscler Thromb Vasc Biol 26(10):2351–2358
63. Prager RW, Ijaz UZ, Gee AH, Treece GM (2010) Three-dimensional ultrasound imaging. Proc Inst Mech Eng H 224(2):193–223
64. Yang EY, Polsani VR, Washburn MJ, Zang W, Hall AL, Virani SS, Hodge MD, Parker D, Kerwin WS, Lawrie GM, Garami Z, Ballantyne CM, Morrisett JD, Nambi V (2011) Real-time co-registration using novel ultrasound technology: ex vivo validation and in vivo applications. J Am Soc Echocardiogr 24(7):720–728
65. Kumar A, Yang EY, Brunner G, Murray TO, Garami Z, Volpi J, Virani SS, Washburn MJ, Zang W, Lawrie GM, Kabir R, Ballantyne CM, Morrisett JD, Nambi V (2011) Plaque volume of carotid endarterectomy (CEA) specimens measured using a novel 3-dimensional ultrasound (3DUS) technology. Circulation 124(21S):A14405
66. Wang C, Chen M, Zhao JM, Liu Y (2011) Fusion of color Doppler and magnetic resonance images of the heart. J Digit Imaging 24(6):1024–1030
67. Hadaschik BA, Kuru TH, Tulea C, Rieker P, Popeneciu IV, Simpfendorfer T, Huber J, Zogal P, Teber D, Pahernik S, Roethke M, Zamecnik P, Roth W, Sakas G, Schlemmer HP, Hohenfellner M (2011) A novel stereotactic prostate biopsy system integrating pre-interventional magnetic resonance imaging and live ultrasound fusion. J Urol 186(6):2214–2220
68. Sandulescu DL, Dumitrescu D, Rogoveanu I, Saftoiu A (2011) Hybrid ultrasound imaging techniques (fusion imaging). World J Gastroenterol 17(1):49–52
69. Hung AJ, Ma Y, Zehnder P, Nakamoto M, Gill IS, Ukimura O (2012) Percutaneous radiofrequency ablation of virtual tumours in canine kidney using global positioning system-like technology. BJU Int 109(9):1398–1403

Symptomatic Versus Asymptomatique Plaque Classification in Carotid Ultrasound*

29

U. Rajendra Acharya, Oliver Faust, S. Vinitha Sree, Filippo Molinari, Luca Saba, Andrew Nicolaides, and Jasjit S. Suri

1 Introduction

The World Health Organization (WHO) estimates that almost 23.6 million people will die mostly from heart disease and stroke by 2030 [1]. Deposition of plaques results in thickening of arteries which causes atherosclerosis, which is the primary cause for both heart disease and stroke [2]. It has been shown that the presence of carotid stenosis (thickening of the carotid artery) is a strong predictor of death in the general population [3]. The common treatment options to unblock the stenosis are Carotid Artery Stenting (CAS) and Carotid Endarterectomy (CEA). It has been shown that surgical removal of plaques reduced the risk of ipsilateral stroke [4, 5]. However, in the Carotid Revascularization Endarterectomy versus Stenting Trial (CREST) [6], it was concluded that there was a higher risk of stroke with CAS and a higher risk of myocardial infarction with CEA. It has been observed that symptomatic patients [who have had retinal or hemispheric symptoms such as stroke, Transient Ischemic Attack (TIA), and Amaurosis Fugax (AF)] have more frequent plaque ruptures that cause life-threatening embolization. Plaque rupture was seen in 74% of symptomatic plaques and in only 32% of plaques from asymptomatic patients [7]. Since there is a considerable risk for the patient undergoing either CEA or CAS, techniques are needed to effectively select only those symptomatic patients who are at a higher risk of stroke for these procedures. Thus, effective diagnosis systems not only aid in the successful treatment of atherosclerotic cardiovascular diseases but also reduce healthcare cost and patient anxiety. Successful carotid atherosclerosis detection can also be used for treatment, in addition to the surgery. The genome identification in the human genome project led to the development of apolipoprotein A1 Milano which protects, to a certain extent, against vascular events that carries this disease. The therapy, based on this protein, resulted in the regression of coronary atherosclerosis in few weeks [8].

*Credit/copyright notice: Based on "An Accurate and Generalized Approach to Plaque Characterization in 346 Carotid Ultrasound Scans," by U.R. Acharya, O. Faust, S. Vinitha Sree, F. Molinari, L. Saba, A. Nicolaides, J.S. Suri, which will appear in IEEE Trans Instrum Meas, 2012, IEEE (Article in Press).

U.R. Acharya
Department of Electronics and Computer Engineering, Ngee Ann Polytechnic, 599 489 Singapore, Singapore

Department of Biomedical Engineering, Faculty of Engineering, University of Malaya, Malaysia
e-mail: aru@np.edu.sg

O. Faust
Department of Electronics and Computer Engineering, Ngee Ann Polytechnic, 599 489 Singapore, Singapore
e-mail: fol2@np.edu.sg

S.V. Sree (✉)
Global Biomedical Technologies, Inc., 208 Otter Glen CT, Roseville, CA 95661, USA

35, GRG Chandragandhi Nagar, Coimbatore 641028, Tamil Nadu, India
e-mail: vinitha.sree@gmail.com

F. Molinari
Biolab, Department of Electronics, Politecnico di Torino, Torino 10129, Italy
e-mail: filippo.molinari@polito.it

L. Saba
Department of Radiology, Azienda Ospedaliero Universitaria di Cagliari, Cagliari 09124, Italy
e-mail: lucasaba@tiscali.it

A. Nicolaides
Vascular Screening and Diagnostic Centre, London W1G 7BS, UK

Department of Biological Sciences, University of Cyprus, Nicosia 1678, Cyprus
e-mail: a.nicolaides@imperial.ac.uk

J.S. Suri
Global Biomedical Technologies, Inc., 208 Otter Glen CT, Roseville, CA 95661, USA

Biomedical Engineering Department, Idaho State University (Aff.), Pocatello, ID 83209, USA
e-mail: jsuri@comcast.net

L. Saba et al. (eds.), *Multi-Modality Atherosclerosis Imaging and Diagnosis*,
DOI 10.1007/978-1-4614-7425-8_29, © Springer Science+Business Media, LLC 2014

Since atherosclerosis is a common disease, diagnosis support systems must be economical in order to keep the financial burden on society as low as possible. The Common Carotid Artery (CCA) is routinely used to detect the presence of plaques. Ultrasound imaging is cost-effective and affordable, and hence, is a good choice for imaging the carotid artery. In spite of significant advantages of diagnostic ultrasound, there are still limitations. The correlation between ultrasonographic features and the histological evaluation of carotid plaques was often poor [9]. The limiting factors responsible for these deficits include low spatial resolution and ultrasound artifacts. Therefore, improving the image quality using adequate image preprocessing techniques and extraction of good features is necessary. In this chapter, we present a low-cost noninvasive Computer-Aided Diagnosis (CAD) system that uses image processing and data mining techniques for classifying symptomatic and asymptomatic plaques in B-mode ultrasound images. We call this system as a class of Atheromatic™ systems (Global Biomedical Technologies, Inc., California, USA). In this system, grayscale features based on Discrete Wavelet Transform (DWT) were extracted and fed to the Support Vector Machine (SVM) classifier for automated classification.

The flow of the chapter is as follows: Sect. 2 briefly describes: (Sect. 2.1) the overall methodology of the proposed system; (Sect. 2.2) the data acquisition and preprocessing steps; (Sect. 2.3) the method used to extract features using DWT; (Sect. 2.4) the statistical *t*-test technique used to select the significant features for input to the classifier, and (Sect. 2.5) the SVM classifier and its various kernel functions. Classification results are presented in Sect. 3. The results are discussed in Sect. 4, and finally the chapter concludes in Sect. 5.

2 Materials and Methods

2.1 Methodology

The proposed CAD system is depicted in Fig. 29.1. It consists of an online system (shown on the right side of Fig. 29.1) which processes an incoming patient's test image. This system predicts the class label based on the transformation of the online grayscale feature vector by the training parameters determined by an off-line learning system (shown on the left side of Fig. 29.1). The off-line classification system is composed of a classification phase which produces the training parameters using the combination of grayscale off-line training features and the respective off-line ground truth training class labels (0/1 for asymptomatic/symptomatic). In both systems, the grayscale features are several DWT-based features extracted from the manually segmented plaque regions from the input images. Significant features among the extracted ones are selected using the *t*-test. We evaluated the Support Vector Machine (SVM) classifier as the off-line learning classifier. The above CAD system was developed using an image database that is split into a training set and a test set. The training set images were used to develop the learning classifiers. The built classifiers were evaluated using the test set. For evaluation, we used a *k-fold* cross-validation protocol. The predicted class labels of the test images and the corresponding ground truth labels (0/1) were compared to determine the performance measures such as sensitivity, specificity, accuracy, and positive predictive value (PPV).

2.2 Data Acquisition and Preprocessing

We used 150 asymptomatic and 196 symptomatic (a total of 346) carotid plaque ultrasound images in this work. These images were collected from patients referred to the Vascular Screening Diagnostic Center, Nicosia, Cyprus, for diagnostic carotid ultrasound to detect both presence and severity of internal carotid stenosis. Approval from Institutional Review Board and consent from patients were obtained prior to conducting the study. Subjects with cardioembolic symptoms or distant symptoms (>6 months) were not included in this work. The plaques with less than 50% stenosis were not included in the database [5]. We also excluded plaques from emergency cases scanned after normal working hours as the scanning was often performed by personnel not trained in plaque image capture. The ultrasonographers who conducted the examinations and obtained the plaque images knew the reason for referral, as they performed routine diagnostic testing for the presence and grading of stenosis. However, for the purpose of studies such as the present, the database images were anonymized and the persons who subsequently did the image normalization and image analysis did not know whether the plaques were symptomatic or asymptomatic [10].

The following prerequisites essential for successful image normalization were carried out: (1) Dynamic range adoption. (2) Frame averaging (persistence). (3) Time gain compensation curve (TGC) was sloping through the tissues was positioned vertically through the lumen of the vessel because the ultrasound beam was not attenuated when passed through blood. This ensured that the adventitia of the anterior and posterior walls had similar brightness. (4) Gain adjustment. (5) Postprocessing with a linear transfer curve. (6) The ultrasound beam was at 90° to the arterial wall. (7) The minimum depth was used so that the plaque occupied a large part of the image. (8) The probe was adjusted so that Adventitia adjacent to the plaque was clearly visible as a hyperechoic band which may be used for normalization.

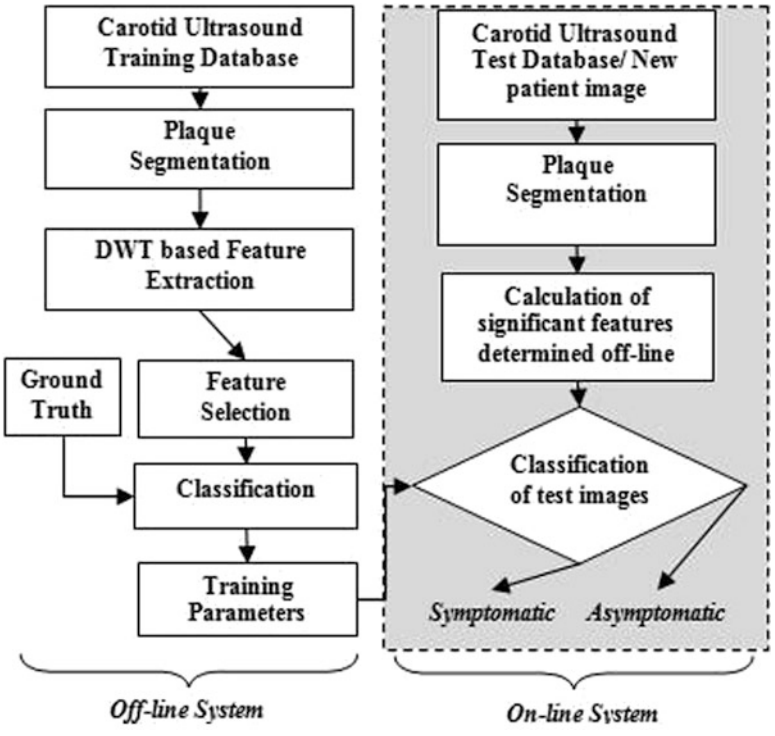

Fig. 29.1 Block diagram of the proposed technique; the blocks outside the *dotted shaded rectangular box* represent the flow in the *off-line system*, and the blocks within the *dotted box* indicate the *online system*

The grayscale images were normalized (using blood and adventitia as reference points) manually by adjusting the image linearly so that the median gray level value of blood was in the range of 0–5, and the median gray level of adventitia (artery wall) was in the range of 180–190.

The plaques from patients having retinal or hemispheric symptoms (unstable plaques), such as stroke, Transient Ischemic Attack (TIA), and Amaurosis Fugax (AF), were grouped as symptomatic plaques (88 stroke, 70 TIA, and 38 AF) 196. Asymptomatic plaques were from patients who had no symptoms in the past. During preprocessing, the Region of Interest (ROI) was selected by medical practitioner from each of the studied images prior to feature extraction. The vascular surgeons and sonographers are trained to identify the hypoechoic region representing hard plaque or stenosis. Therefore, we adapted the manually segmented plaque regions in this work. The nature of the disease is focused on the vessel wall that specifically changes the morphology of the lumen-intima interface from slow gradual lipid formation and maturing into hard plaque or loose island of hemorrhage [11]. Thus, the young and old plaques are all focused towards the vessel disease which yields the information in the form of echogenicity in the ultrasound image [10]. Therefore, the focused ROI constitutes <25% of the image frame, and hence, the vascular surgeons are keenly interested in characterization of plaque in this regional information. We, therefore, focused on analyzing this small ROI traced by the vascular surgeon. Typical symptomatic and asymptomatic carotid images are shown in Fig. 29.2a, b. Figure 29.3a, b shows the ROIs of symptomatic and asymptomatic carotid images.

2.3 Feature Extraction

In this work, we used two-dimensional (2D) DWT and averaging algorithms for feature extraction. The DWT transform of a signal x is determined by sending the signal through a sequence of down-sampling high and low pass filters. The low pass filter is defined by the transfer function $g[n]$ and the high pass filter by $h[n]$. The output of the high pass filter $D[n]$, known as the detail coefficients, is obtained as follows:

$$D[n] = \sum_{k=-\infty}^{\infty} x[k]h[2n-k] \tag{29.1}$$

The output of the low pass filter, known as the approximation coefficients, is found by using the following equation.

$$A[n] = \sum_{k=-\infty}^{\infty} x[k]g[2n-k] \tag{29.2}$$

The frequency resolution is further increased by cascading the two basic filter operations. To be specific, the output of the first level low pass filter is fed into the same low and high pass filter combination. The detailed coefficients are output at each level, and they form the level coefficients. In

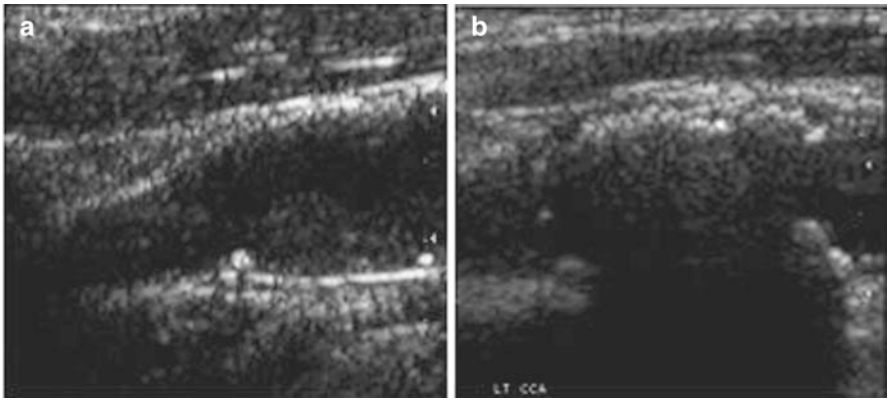

Fig. 29.2 Carotid images: (**a**) symptomatic (AF) and (**b**) asymptomatic (AS). *Source*: [12], © IEEE, 2012

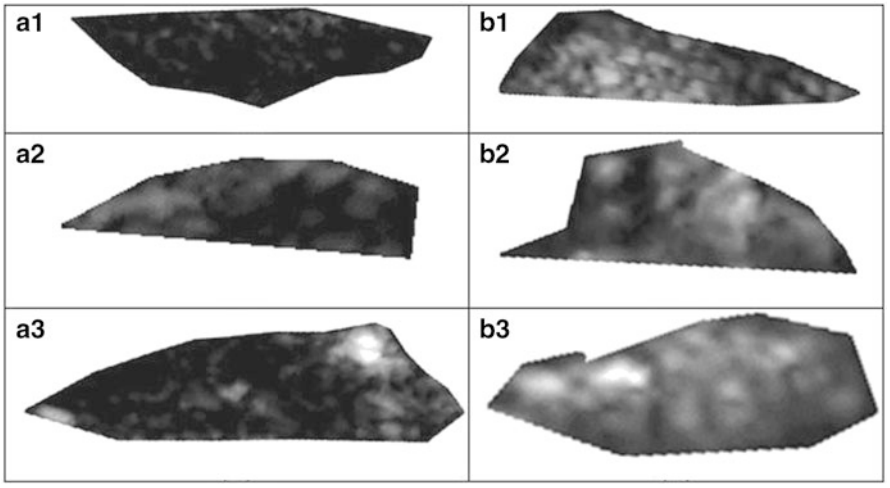

Fig. 29.3 Region of interest extracted from the carotid plaque ultrasound images of (**a**) symptomatic (AF) and (**b**) asymptomatic (AS) patients. *Source*: [12], © IEEE, 2012

general, each level halves the sample number and doubles the frequency resolution. Consequently, in the final level, both detail and approximation coefficients are obtained as level coefficients. For 2D signals, the 2D DWT can be used. We used wavelet packet decomposition (WPD) for images. These images are represented as an $m \times n$ grayscale matrix $I[i, j]$ where each element of the matrix represents the intensity of 1 pixel. All non-border pixels in $I[i, j]$, where $i \notin \{0, m\}$ and $j \notin \{0, n\}$, have eight immediate neighboring pixels. These eight neighbors can be used to traverse through the matrix. However, changing the direction with which the matrix is traversed just inverts the sequence of pixels, and the 2D DWT coefficients are the same. For example, the WPD result is the same when the matrix is traversed from left to right as from right to left. Therefore, we are left with four possible directions, which are known as decomposition corresponding to 0° (horizontal, *Dh*), 90° (vertical, *Dv*), and 45° or 135° (diagonal, *Dd*) orientations. The implementation of this algorithm follows the block diagram shown in Fig. 29.4. The diagram shows the $N \times M$ dimensional input image $I[i, j]$ and the results for level 1. In this work, we found that the results from level 1 were sufficient to obtain significant features.

In this work, we evaluated several wavelet functions. Each of these wavelet functions has both a unique low pass filter transfer function $g[n]$ and a unique high pass filter transfer function $h[n]$. Figure 29.5 shows the transfer functions for the Biorthogonal 3.1 (*bior3.1*) family used in this work.

The first level 2D DWT yields four result matrices, namely Dh_1, Dv_1, Dd_1, and A_1, whose elements are intensity values. Figure 29.6 shows a schematic representation of these result matrixes. Unfortunately, these matrixes cannot be used for classification directly, because the number of elements is too high. Therefore, we defined two averaging methods that represent result matrixes with just one number. The first method is used to extract average measures from 2D DWT result vectors.

$$\text{Average } Dh_1(Ah) = \frac{1}{N \times M} \sum_{x=<N>} \sum_{y=<M>} |Dh_1(x, y)| \tag{29.3}$$

$$\text{Average } Dv_1(Av) = \frac{1}{N \times M} \sum_{x=<N>} \sum_{y=<M>} |Dv_1(x, y)| \tag{29.4}$$

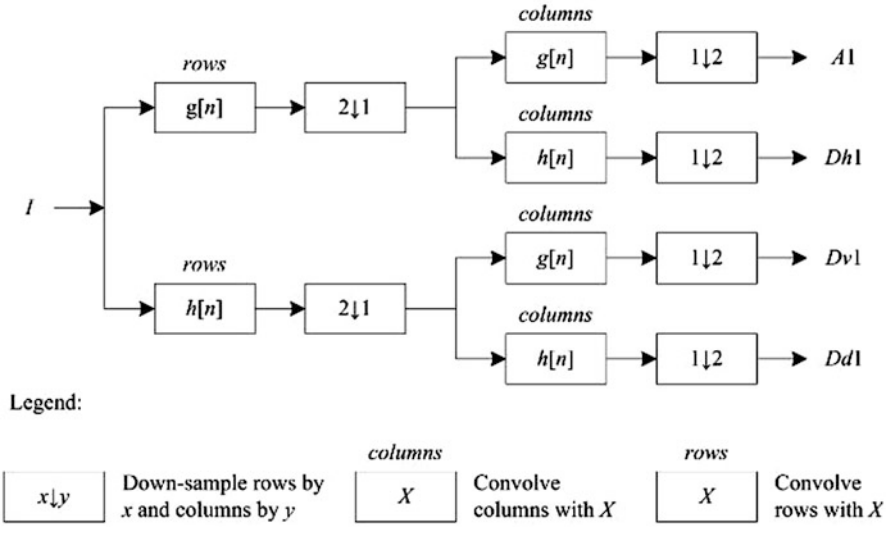

Fig. 29.4 Discrete wavelet transform (DWT) decomposition. *Source*: [12], © IEEE, 2012

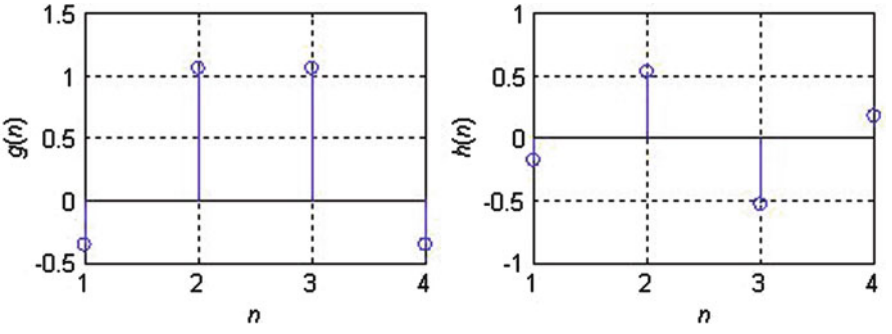

Fig. 29.5 Transfer functions of the Biorthogonal 3.1 wavelet (*bior3.1*). *Source*: [12], © IEEE, 2012

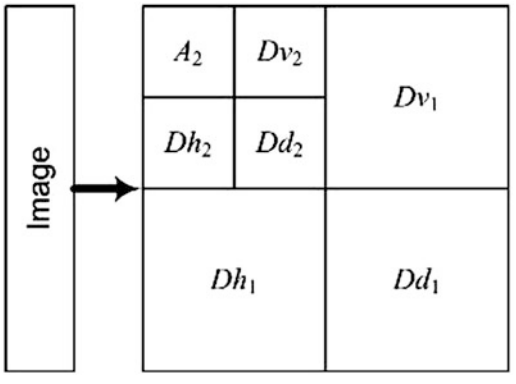

Fig. 29.6 Wavelet-based image decomposition. *Source*: [12], © IEEE, 2012

The final averaging method uses averages not the intensity values as such but the energy of the intensity values.

$$\text{Energy}\ (E) = \frac{1}{N^2 \times M^2} \sum_{x=<N>} \sum_{y=<M>} (Dv_1(x,y))^2 \tag{29.5}$$

These three elements form the feature vector.

2.4 Feature Selection

We have used *t*-test [13] to verify if the features are significant enough to be able to accurately discriminate the symptomatic and asymptomatic classes. In this test, initially, the null hypothesis is assumed that the means of the feature from the two classes are equal. Then, the *t*-statistic, which is the ratio of difference between the means of a feature from two classes to the standard error between class means, and the corresponding *p*-value are calculated. The *p*-value is the probability of rejecting the null hypothesis given that the null hypothesis is true. In our case, we assumed a normal distribution of the features, but the scaling term in the test statistic was known. Therefore, it was replaced by an estimate based on the data. A low *p*-value (<0.01 or 0.05) indicates that the means are significantly different for the two classes, and hence, the feature is significant.

2.5 Classification

SVM is a hyperplane-based nonparametric classifier. When it is trained using input features–output ground truth class label pairs, it outputs a decision function which can be used to test new input features. Assuming that the class label

$c=-1$ for asymptomatic class and $+1$ for symptomatic class, the SVM algorithm maps the training set into a feature space and attempts to locate in that space a hyperplane that separates the positive from the negative examples. During the testing of a new unlabeled image, the algorithm maps the image's feature vector into the same feature space and determines the class based on which side of the separating plane the vector is present. Thus, the main objective of SVM is to determine a separating hyperplane that maximizes the margin between the input data classes that are plotted in the feature space [14–16]. In order to determine the margin, two parallel hyperplanes are constructed, one on each side of the separating hyperplane with the help of the training data. Consider two-class classification using a linear model of the form

$$y(x) = w^{\mathrm{T}}\phi(x) + b \tag{29.6}$$

where $\phi(\cdot)$ denotes the feature transformation kernel, b is the bias parameter, and w is the normal to the hyperplane. The training data consists of the input feature vectors x and the corresponding classes c. $c=-1$ for asymptomatic class and $+1$ for symptomatic class. During the testing phase, the new feature vector is classified based on the sign of y. The perpendicular distance to the closest point from the training data set is the margin, and the objective of training an SVM classifier is to determine the maximum margin hyperplane and also to assign a soft penalty to the samples that are on the wrong side of the margin. Support vectors are those points that the margin pushes up against. The problem becomes an optimization problem where we have to minimize

$$C\sum_{i=1}^{N}\xi_i + \frac{1}{2}\|w\|^2$$
$$c_i\, y(x_i) \geq 1-\xi_i, \quad \xi \geq 0 \tag{29.7}$$

where ξ_i are the penalty terms for samples that are misclassified, and C is the regularization parameter which controls the tradeoff between the misclassified samples and the margin. The first term in (29.7) is equivalent to maximizing the margin. This quadratic programming problem can be solved by introducing Lagrange multipliers a_n for each of the constraints and solving the dual formulation. The Lagrangian is given by

$$L(w,b,a) = \frac{1}{2}\|w\|^2 + C\sum_{i=1}^{N}\xi_i - \sum_{i=1}^{N}a_i[c_i\, y(x_i) - 1 + \xi_i] - \sum_{i=1}^{N}\mu_i\xi_i \tag{29.8}$$

where a_i and μ_i are the Lagrange multipliers. After eliminating w, b, and ξ_i from the Lagrangian, we obtain the dual Lagrangian which we maximize.

$$\tilde{L}(a) = \sum_{i=1}^{N}a_i - \frac{1}{2}\sum_{i=1}^{N}\sum_{j=1}^{N}a_i a_j c_i c_j k(x_i, x_j)$$
$$k(x_i, x_j) = \phi(x_i)^{\mathrm{T}}\cdot\phi(x_j)$$
$$0 \leq a_n \leq C, \sum_{i=1}^{N}a_i c_i = 0 \tag{29.9}$$

The predictive model is now given by

$$y(x) = \sum_{i=1}^{N}a_i c_i k(x, x_i) + b \tag{29.10}$$

and b is estimated as:

$$b = \frac{1}{N_M}\sum_{i\in M}\left(c_i - \sum_{j\in S}a_j c_j k(x_i, x_j)\right) \tag{29.11}$$

M is the set of indices such that $0 < a_i < C$. A solution to the quadratic programming problem of maximizing the dual Lagrangian (29.9) is given in [17]. In the case of linearly non-separable data, the features are first mapped to a higher dimensional space using kernel functions [17, 18], and then the hyperplane is determined, i.e., every dot product in (29.9) is replaced by a nonlinear kernel function. Several standard kernels are often used. We have used the linear kernel, polynomial kernel of order 1, 2, and 3, and the Radial Basis Function (RBF) kernel. The polynomial kernel is defined as

$$k(x_i, x_j) = (1 + x_i.x_j)^p \tag{29.12}$$

where p is the order of the kernel. The RBF kernel is defined as

$$k(x_i, x_j) = \exp\left(-\|x_i - x_j\|^2\right) \tag{29.13}$$

During classification, the training data are used to determine the training parameters C (i.e., the Lagrange multipliers a_i and μ_i) and b so that new data x can be input into (29.10) in order to obtain the value of corresponding y. The class c is then determined based on the sign of the resultant y value.

3 Results

3.1 Selected Features

The features selected were: energy, average horizontal and vertical DWT coefficients. These features were fed to the SVM classifier for automatic detection of the unknown class.

Table 29.1 Symptomatic (AF) versus asymptomatic (AS) features obtained using the discrete wavelet transform (DWT) method using *bior3.1* wavelet function

Features	AF (mean ± SD)	AS (mean ± SD)	*p*-value
Average Dh_1 (Ah)	0.10 ± 0.04	0.14 ± 0.03	<0.0001
Average Dv_1 (Av)	3.82E-02 ± 1.55E-02	5.49E-02 ± 1.47E-02	<0.0001
Energy (*E*)	5.47E-08 ± 2.22E-08	7.17E-08 ± 1.99E-08	<0.0001

Source: [12], © IEEE, 2012

Table 29.2 Classification results obtained using the discrete wavelet transform (DWT) features in the various configurations of the support vector machine (SVM) classifier

SVM	TN	FN	TP	FP	*A* (%)	PPV (%)	Sn (%)	Sp (%)
Linear	48	8	37	11	81.7	77	82.2	81.3
Polynomial order 1	48	8	37	11	81.7	77	82.2	81.3
Polynomial order 2	51	9	36	8	83.7	81.8	80	86.4
Polynomial order 3	53	12	33	6	82.6	84.6	73.3	89.8
RBF	50	11	34	9	80.8	79	75.5	84.7

Source: [12], © IEEE, 2012
A accuracy, *Sn* sensitivity, *Sp* specificity

Table 29.1 presents the features obtained using DWT with the *bior3.1* wavelet. A *p*-value of <0.0001 indicates that the features are significant.

3.2 Classification Results

In this work, we compared the performance of 54 different wavelet functions and 15 classifiers. The mother wavelet families that were analyzed were Reverse Biorthogonal wavelet family (*rbio*), Daubechies wavelet (*db*), Biorthogonal 3.1 wavelet (*bior*), Coiflets, Symlets, Discrete Meyer (FIR approximation) (*dmey*), and Haar family. The biorthogonal (*bior3.1*) performed better compared to the other wavelet functions. Threefold stratified cross-validation method was used to evaluate these classifiers. In this method, the dataset of 346 images was split into three parts, each part containing the same proportion of images from both classes. In the first fold, two parts were used for training, and the third part was used for testing. Specifically, 242 images were used for training and 104 images were used for testing the classifier, i.e., 137 symptomatic images (26 AF, 49 TIA, and 62 stroke), and 105 asymptomatic images were used for training. The testing group consisted of 59 symptomatic (12 AF, 21 TIA, and 26 stroke) and 45 asymptomatic images were used. This protocol was repeated such that each part was given a chance to become a test set. As a result, two more runs were executed. Thus, in this technique, there were three parts of data, and therefore, three iterations of testing. The averages of the performance measures obtained during the testing phase of each fold are reported as the final performance measures for that classifier.

Since SVM performed better among the 15 classifiers used, we have presented the performance measures (sensitivity, specificity, accuracy, and PPV) obtained using various kernel configurations of SVM in Table 29.2. TN (True Negative) is the number of asymptomatic plaques identified as asymptomatic. TP (True Positive) is the number of symptomatic samples identified as symptomatic. FN (False Negative), on the other hand, is the number of symptomatic samples identified as asymptomatic, and FP (False Positive) is the number of asymptomatic samples identified as symptomatic. Sensitivity, which is probability that the technique will identify symptomatic cases, is calculated as TP/(TP + FN) and specificity, which is probability that the technique will identify asymptomatic cases, is determined as TN/(TN + FP). PPV, which is the proportion of symptomatic subjects among those who were labeled symptomatic by the technique, is calculated as TP/(TP + FP), and accuracy, which is the ratio of the number of correctly classified samples to the total number of samples, is calculated as (TP + FP)/(TP + FP + TN + FN).

Our results show that the SVM classifier with the polynomial kernel of order 2 achieved an average accuracy of 83.7%, sensitivity of 80%, specificity of 86.4%, and PPV of 81.8%. In order to select an optimal classifier, one has to choose a classifier which gives equally high values for both sensitivity and specificity. Such equal values indicate that the classifier has good capability in discriminating both the classes without bias towards a particular class. Moreover, the overall accuracy of the classifier should also be high. Based on these criteria, the SVM classifier with a polynomial kernel of order 2 was found to be suitable for this carotid plaque classification problem.

4 Discussion

The classification of carotid plaque is a difficult and multifaceted problem. A scale/frequency approach, based on the wavelet transform, was used in an attempt to characterize carotid atherosclerotic plaque from B-mode ultrasound [19]. Two wavelet decomposition schemes, namely the DWT and wavelet packets (WPD), and three basis functions, namely Haar, symlet3, and biorthogonal3.1, were investigated in terms of their ability to discriminate between symptomatic and asymptomatic cases. A total of 12 detailed sub-images were extracted using the DWT and 255 using the WP decomposition schemes. It was shown that WP analysis by the use of Haar filter and the 1-1 norm as texture descriptor could reveal differences not only in high but also in low frequencies, and therefore, could characterize efficiently the atheromatous tissue. It was concluded that additional studies applying and further extending the above methodology were required to ensure the usefulness of wavelet-based texture analysis of carotid atherosclerosis. Therefore, in this study, we explored the utility of wavelet-based features for plaque classification.

Kyriacou et al. [20] used ten texture and morphological features in neural and statistical classifiers and obtained an accuracy of around 71.2%. Normalized pattern spectra computed for both structural and multilevel binary morphological model were used as classification features in two classifiers, Probabilistic Neural Network and SVM, for automated diagnosis of symptomatic and asymptomatic classes [21]. Using SVM classifier on 137 samples in each class, a classification efficiency of 73.7% for multilevel binary morphological image analysis and 66.8% for grayscale morphological analysis were obtained. The texture and motion patterns of carotid atherosclerosis features were extracted and fed to a fuzzy C-means classifier for classification into symptomatic and asymptomatic plaques [22]. On evaluating the classifier using features from ten symptomatic and nine asymptomatic plaque images, it was observed that the technique could correctly classify 74% of plaques based on texture features only, and 79% of plaques based on motion features only. Classification performance reached 84% using a combination of motion and texture features. In another study [23], 61 texture and shape features from manually segmented ROIs of 230 plaques were used in a modular neural network. A classification accuracy of 73.1% was reported.

It is evident from the above discussed studies that there is a need for techniques that are more accurate and that use lesser number of features. Most of these studies employ texture features for plaque classification. In our earlier study [24], we extracted four texture features (standard deviation, entropy, symmetry, and run percentage) from the same dataset used in this work (manual ROI selection was used) and used them in Adaboost and SVM classifiers. SVM (RBF kernel) presented an accuracy of 82.4%. In order to improve the accuracy further, in this work, we decided to study the capability of DWT-based features for the plaque classification problem. Our proposed method resulted in accuracy, sensitivity, and specificity of 83.7%, 80%, and 86.4%, respectively. The accuracy of our work is relatively higher than that reported by previous studies, and this accuracy has been obtained with only a very low number of features (three).

In the case of the plaque ROI classification, an accuracy of 83.7% has been registered by the SVM classifier. A higher accuracy is difficult to achieve for the following reasons. All plaques are initially asymptomatic. In this cross-sectional study, when the dataset was collected, 196 plaques had already become symptomatic. Over time, some additional plaques are likely to rupture and become symptomatic. However, according to their texture, such plaques would be classified by our technique as high risk and symptomatic, but they would have been labeled as clinically asymptomatic at the time of imaging. This discrepancy leads to lower accuracy. This issue can only be resolved by prospective longitudinal studies.

The following are the key features of our proposed technique:

(a) *Use of a small feature set*: The feature set is small (only three features), and yet is powerful enough to effectively classify symptomatic and asymptomatic plaques with good accuracy of 83.7%. The significant features were the average of the horizontal coefficients from level 1 decomposition, average of vertical coefficients from level 1, and the energy of the level 1-vertical coefficients. Since these features had a low p-value (Table 29.1), on using them in the SVM classifier, good accuracy was obtained. We observed that the best accuracy was registered when the data was transformed into a higher dimensional space using the polynomial kernel of order 2.

(b) *Robustness*: In order to obtain a robust system, we evaluated the technique using a large database consisting of an almost equal number of samples in both classes: 150 asymptomatic and 196 symptomatic plaques. Moreover, we trained and built the SVM classifier using stratified threefold cross-validation data resampling technique to get generalized training parameters that are suitable to handle any new patient image.

(c) *Real-time*: The system is real time as no manual interaction is necessary except for the selection of the ROI. The ROI can be easily traced by expert ultrasonographers. No mathematical modeling is required. The system allows selecting the ROI region with the help of the Doppler ultrasound as an adjunct tool.

(d) *Generalized*: The proposed CAD framework can be extended to study other medical images. This is a generalized system and we have already extended this classical

framework to Thyroid and Liver Ultrasound, except that the feature set here is tuned to pick up the textural information present due to atherosclerotic formations such as hard and soft plaque.

(e) *Low-cost and safe*: The technique is low cost as it used features extracted from images acquired using the widely available and affordable ultrasound modality. Moreover, the technique can be easily written as a software application which can be installed in any computer at no cost. Furthermore, the technique does not use radiation unlike Computed Tomography and is much economic unlike Magnetic Resonance Imaging.

We have been able to achieve a good accuracy of 83.7% using a novel combination of three wavelet-based features using a large dataset. However, we do have the following future directions with respect to this work:

1. There is a scope of improving accuracy by adding more advanced features which can represent atherosclerotic deposits in wall region, and our group is committed towards improving this system for next generation.
2. The proposed protocol requires the sonographers to manually delineate the ROI. We hope that in future the ROI segmentation can potentially be done automatically.
3. In this work, the ground truth information of whether the plaque symptomatic or asymptomatic has been obtained based on the presence or absence of symptoms. A drawback of such a ground truth determination is that some of the asymptomatic plaques might have been wrongly labeled as symptomatic when the symptoms might have occurred due to plaque in heart and not in the carotid artery. Also, patients who do not recollect their history of symptoms may be classified as asymptomatic. To alleviate this problem, in our future studies, we intend to determine the ground truth from pathological studies on the plaque instead of from the clinical report on the patient's symptoms.

5 Conclusions

Only experienced physicians or vascular ultrasonographers have the ability to efficiently detect symptomatic and asymptomatic plaques in ultrasound images. The CAD system proposed in this work can help doctors in giving a valuable second opinion on the nature of the detected plaques, thereby enabling them to confidently decide on the treatment protocol. Our system uses DWT for feature extraction and can diagnose the two classes automatically with an accuracy, sensitivity, and specificity of more than 83%. We have achieved a classification accuracy of 83.7%, sensitivity of 80%, and specificity of 86.4%. This accuracy is relatively higher than those recorded in similar studies in the literature. Hence, we believe that the proposed technique can be considered as an *effective image mining technique* which can serve as an efficient adjunct tool for the vascular surgeons in selecting patients for risky stenosis treatments. However, these accuracies may not be sufficient enough for the system to be incorporated into routine clinical work flow. More research is needed to improve the classification results. Since we have tested a wide range of classifiers in this study, future work would include studying more feature extraction techniques in order to improve the accuracy. Specifically, we intend to study more texture-based methods and the combination of various feature extraction methods in our future studies.

References

1. WHO, CVD. http://www.who.int/mediacentre/factsheets/fs317/en/index.html. Accessed 28 Dec 2011
2. Agabiti-Rosei E, Muiesan ML (2007) Carotid atherosclerosis, arterial stiffness and stroke events. Adv Cardiol 44:173–186
3. Joakimsen O, Bonaa KH, Mathiesen EB et al (2000) Prediction of mortality by ultrasound screening of a general population for carotid stenosis: the Tromsø Study. Stroke 31:1871–1876
4. European Carotid Surgery Trialists' Collaborative Group (1998) Randomised trial of endarterectomy for recently symptomatic carotid stenosis: final results of the MRC European Carotid Surgery Trial (ECST). Lancet 351:1379–1387
5. North American Symptomatic Carotid Endarterectomy Trial Collaborators (1991) Beneficial effect of carotid endarterectomy in symptomatic patients with high-grade carotid stenosis. N Engl J Med 325:445–453
6. Brott TG, Hobson RW, Howard G et al (2010) Stenting versus endarterectomy for treatment of carotid-artery stenosis. N Engl J Med 363:11–23
7. Carr S, Farb A, Pearce WH et al (1996) Atherosclerotic plaque rupture in symptomatic carotid artery stenosis. J Vasc Surg 23:755–765
8. Chiesa G, Sirtori CR (2003) Recombinant apolipoprotein A-I(Milano): a novel agent for the induction of regression of atherosclerotic plaques. Ann Med 35:267–273
9. Droste DW, Karl M, Bohle RM et al (1997) Comparison of ultrasonic and histopathological features of carotid artery stenosis. Neurol Res 19:380–384
10. Griffin MB, Kyriacou E, Pattichis C et al (2010) Juxtaluminal hypoechoic area in ultrasonic images of carotid plaques and hemispheric symptoms. J Vasc Surg 52:69–76
11. Carter-Monroe N, Yazdani SK, Ladich E et al (2011) Introduction to the pathology of carotid atherosclerosis: histologic classification and imaging correlation. In: Suri JS, Kathuria C, Molinari F (eds) Atherosclerosis disease management. Springer, New York, NY
12. Acharya RU, Faust O, Vinitha Sree S et al (2012) An accurate and generalized approach to plaque characterization in 346 carotid ultrasound scans. IEEE Trans Instrum Meas 61(4):1045–1053
13. Box JF (1987) Guinness, gosset, fisher, and small samples. Stat Sci 2:45–52
14. Vapnik V (1998) Statistical learning theory. Wiley, New York, NY
15. Cortes C, Vapnik V (1995) Support-vector networks. Mach Learn 20:273–297
16. Burgess CJC (1998) A tutorial on support vector machines for pattern recognition. Data Min Knowl Discov 2:1–47

17. David V, Sanchez A (2003) Advanced support vector machines and kernel methods. Neurocomputing 55:5–20
18. Muller KR, Mika S, Ratsch G et al (2001) An introduction to kernel based learning algorithms. IEEE Trans Neural Netw 12:181–201
19. Tsiaparas N, Golemati S, Stoitsis J et al (2009) Discrete wavelet transform vs. wavelet packets for texture analysis of ultrasound images of carotid atherosclerosis. In: Proceedings of the 9th international conference on information technology and applications in biomedicine, pp 1–4
20. Kyriacou E, Pattichis MS, Christodoulou CI et al (2005) Ultrasound imaging in the analysis of carotid plaque morphology for the assessment of stroke. Stud Health Technol Inform 113:241–275
21. Kyriacou E, Pattichis MS, Pattichis CS et al (2009) Classification of atherosclerotic carotid plaques using morphological analysis on ultrasound images. J Appl Intell 30:3–23
22. Stoitsis J, Golemati S, Nikita KS et al (2004) Characterization of carotid atherosclerosis based on motion and texture features and clustering using fuzzy c-means. In: Proceedings of the 26th annual international conference of the IEEE EMBS, pp 1407–1410
23. Christodoulou CI, Pattichis CS, Pantziaris M et al (2003) Texture based classification of atherosclerotic carotid plaques. IEEE Trans Med Imaging 22:902–912
24. Acharya RU, Faust O, Alvin AP et al (2011) Symptomatic vs. asymptomatic plaque classification in carotid ultrasound. J Med Syst 36(3):1861–1871. doi:10.1007/s10916-010-9645-2

Biographies of the Editors

0.1 Dr. Luca Saba

Luca Saba received the M.D. from the University of Cagliari, Italy, in 2002. Today he works in the A.O.U. of Cagliari. Dr Saba research fields are focused on Multi-Detector-Row Computed Tomography, Magnetic Resonance, Ultrasound, Neuroradiology, and Diagnostic in Vascular Sciences.

His works, as lead author, achieved more than 60 high impact factor, peer-reviewed, journals as *American Journal of Neuroradiology, European Radiology, European Journal of Radiology, Acta Radiologica, Cardiovascular and Interventional Radiology, Journal of Computer Assisted Tomography, American Journal of Roentgenology, Neuroradiology*, *Clinical Radiology, Journal of Cardiovascular Surgery, Cerebrovascular Diseases.* Dr Saba presented more than 400 papers in National and International Congress (RSNA, ESGAR, ECR, ISR, AOCR, AINR, JRS, SIRM, AINR).

He is member of the Italian Society of Radiology (SIRM), European Society of Radiology (ESR), Radiological Society of North America (RSNA), American Roentgen Ray Society (ARRS), and European Society of Neuroradiology (ESNR)

0.2 Dr. João Miguel Sanches

João M. Sanches received the E.E., M.Sc., and Ph.D. degrees from the Instituto Superior Técnico (IST) in the Technical University of Lisbon, Portugal, in 1991, 1996, and 2003, respectively. Today he is Assistant Professor at the Department of Electrical and Computer Engineering (DEEC) at the Systems, Decision and Control Section from the Instituto Superior Técnico (IST), where he has taught in the area of signal processing, systems, and control. He has been actively involved in the course of Biomedical Engineering advising master thesis of the Biomedical Engineering course and Ph.D. students of the doctoral program in Biomedical Engineering. He has proposed a Ph.D. course of Medical Image Reconstruction that he has been taught in the last years. Now is actively involved in the creation of the new department of Bio-Engineering where the Biomedical and Biological Engineering are two of the most important components.

He is researcher at the Institute for Systems and Robotics (ISR) and in the last years his work has been focused in Biomedical Engineering, namely, in Biomedical Image Processing, Physiological based Modeling of Biological Systems in the perspective of the Systems and Control theory, and statistical signal processing of physiological data. His research activity is focused in the morphological and tissue characterization of tissues from Ultrasound (US) images for the diagnosis of the atherosclerotic disease of the carotids and diffuse diseases of the liver. He is also working in functional Magnetic Resonance Imaging (fMRI) and Fluorescence Confocal Microscope (FCM) imaging in collaboration with the Institute of Molecular Medicine at the Medical School of the University of Lisbon. He is also involved in the development of signal processing algorithms and biomedical

L. Saba et al. (eds.), *Multi-Modality Atherosclerosis Imaging and Diagnosis*,
DOI 10.1007/978-1-4614-7425-8, © Springer Science+Business Media, LLC 2014

applications for mobile phones for the diagnosis of sleep disorders in collaboration with the Electroencephalography and Clinical Neurophysiology Center (Centro de Electroencefalografia Neurofisiologia Clínica— CENC), also with the Medical School of the University of Lisbon.

He is member of the IEEE Engineering in Medicine and Biology Society and Associate Member of the Bio Imaging and Signal Processing Technical Committee (BISP-TC) of the IEEE Signal Processing Society. He is also president of the Portuguese Association of Pattern Recognition (APRP).

0.3 Dr. Luís Mendes Pedro

Luís Mendes Pedro, M.D., Ph.D., FEBVS received the M.D. and the Ph.D. degrees in the Medical School of the University of Lisbon in 1987 and 1993, respectively. In 2000 he achieved approval in the European Board of Vascular Surgery examinations becoming Fellow of the European Board of Vascular Surgery (FEBS).

His present positions are:

- Associated Professor of "Vascular Surgery" and "Introduction to Clinical Medicine" at the Medical School of the University of Lisbon.
- Consultant Vascular Surgeon at the Santa Maria Hospital in Lisbon and at the "Lisbon Cardiovascular Institute ("Instituto Cardiovascular de Lisboa").

He is also involved in the course of Biomedical Engineering (Instituto Superior Técnico – Technical University of Lisbon and Medical School of the University of Lisbon) being co-responsible for the discipline of "Biomaterials 2" and co-advisor of master thesis in Biomedical Engineering and PhD students of the doctoral program in Biomedical Engineering.

The main research areas are:

- Vascular ultrasound characterization of the arterial wall.
- Ultrasonographic and computer-assisted atherosclerotic plaque characterization.
- Carotid surgery.
- Synchronous cardiac and carotid surgery.

Member of the Portuguese Medical Association (presently with place in the Board of Angiology and Vascular Surgery), the Portuguese Society for Angiology and Vascular Surgery (SPACV), the European Society for Vascular Surgery (ESVS), the International Society of Endovascular Specialists (ISES), and the International Union of Angiology (IUA).

Member of the Editorial Board of the European Journal of Vascular and Endovascular Surgery (EJVES) (2006–2010) and Chief Editor of the journal "Angiologia e Cirurgia Vascular" (SPACV) since 2006.

Reviewer of the EJVES, "Revista Portuguesa de Cardiologia", "Acta Médica Portuguesa," and "Acta Reumatológica Portuguesa".

0.4 Dr. Jasjit Suri

Jasjit S. Suri, M.S., Ph.D., MBA, Fellow AIMBE, is an innovator, visionary, scientist, and an internationally known world leader, has spent over **25** years in the field of biomedical engineering/sciences, software and hardware engineering, and its management. During his career in biomedical industry/imaging, he has had an upstream growth and responsibilities from scientific Engineer, Scientist, Manager, Director R&D, Sr. Director, Vice President to Chief Technology Officer (CTO) level positions in industries like *Siemens Medical Systems, Philips Medical Systems, Fisher Imaging Corporation, and Eigen Inc. & Biomedical Technologies, respectively, and managed up to 100 people.*

He has developed products and worked extensively in the areas of breast, mammography, orthopedics (spine), neurology (brain), angiography (blood vessels), Atherosclerosis (plaque), ophthalmology (eye), urology (prostate), image-guided surgery, and several kinds of biomedical devices from inception phase to commercialization phase, including 510(K)/FDA clearances. Under his leadership he has obtained over five FDA clearances in Urology, Angiography, and Image Guided Surgery Product Lines ranging from

1,000 pages to 5,000 pages submissions. He has conducted in vivo and ex vivo validations on biomedical devices and surgery systems. Dr. Suri has developed several collaboration programs between University–Industry partnerships. He has managed funds ranging upto $10 million dollars. He has very successfully built IP portfolios during his career bringing attraction for larger OEMs spin-offs. ***Dr. Suri has written over 400 articles which includes 60 US/European Patents, over 25 books*****. He is well-known speaker and has spoken over 50 times at national and international levels. Dr. Suri has won over 50 scientific and extracurricular awards during his career.**

He received his Masters from University of Illinois, Chicago, Doctorate from University of Washington, Seattle, and Executive Management from Weatherhead School of Management, Case Western Reserve University (CWRU), Cleveland. Dr. Suri was crowned with President's Gold medal in 1980 and the *Fellow of American Institute of Medical and Biological Engineering (AIMBE)* for his outstanding contributions at Washington DC. He believes in "getting a job done" using his strengths of innovation, strategic partnerships, and strong team collaborations by bringing cross-functional and multidisciplinary teams together both in-house and outsourcing relationships.

Index

L. Saba et al. (eds.), *Multi-Modality Atherosclerosis Imaging and Diagnosis*,
DOI 10.1007/978-1-4614-7425-8, © Springer Science+Business Media, LLC 2014